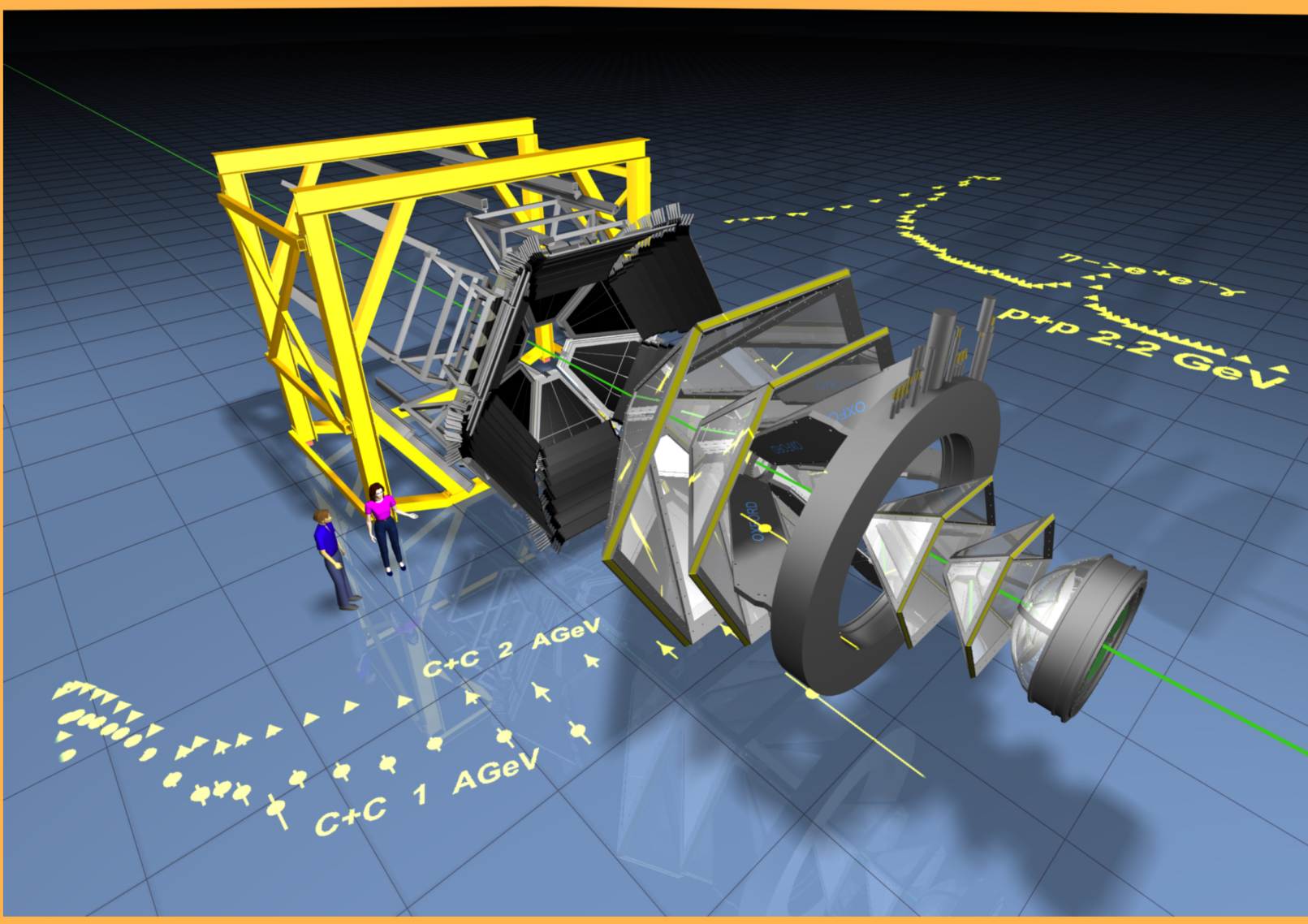
GSI

GSI Report 2006-1
May 2006

SCIENTIFIC REPORT 2005



Gesellschaft für Schwerionenforschung mbH Darmstadt
Member of the Helmholtz Association

Cover illustration:

The front cover shows an artist's view of the High Acceptance Dielectron Spectrometer HADES installed in the target hall served by the SIS18 accelerator. The spectrometer detects rare leptonic decays of neutral vector mesons which are produced in the central reaction volume of heavy-ion collisions. The detector is capable of digitizing and filtering all relevant signals produced by reaction products at collision rates of up to 20 kHz. The detectors, which are moved apart along the beam axis in the image, are packed closely around the target for experiments to achieve polar angle coverage between 18 and 85 degrees. Six superconducting coils provide a toroidal magnetic field with a maximum bending power of 0.3 Tm.
So far, the electron pair (i.e. e^+ e^-) production has been investigated in C+C, Ar+KCl and p+p reactions. The pair emission rate was measured over almost six orders of magnitude in the pair invariant mass range between 50 and 1000 MeV/c^2 (spectrum shown in the foreground). The experimental data clearly evidences contributions to the pair yield from the early phase of the collision. Information about the properties of mesons imbedded in dense nuclear medium can be obtained by careful analysis of the spectral distribution of emitted electron pairs. Elementary reactions are exploited to scrutinize our knowledge about the various emission processes. The histogram in the background exemplarily shows the exclusive reconstruction of η-meson production in p+p reactions. HADES will continue its experimental program with p and π-induced reactions, and, after replacing the inner time-of-flight system by a novel RPC detector and upgrading the data acquisition system, with experiments addressing heavier collision systems.

Cover illustration:

The front cover shows an artist's view of the High Acceptance Dielectron Spectrometer HADES installed in the target hall served by the SIS18 accelerator. The spectrometer detects rare leptonic decays of neutral vector mesons which are produced in the central reaction volume of heavy-ion collisions. The detector is capable of digitizing and filtering all relevant signals produced by reaction products at collision rates of up to 20 kHz. The detectors, which are moved apart along the beam axis in the image, are packed closely around the target for experiments to achieve polar angle coverage between 18 and 85 degrees. Six superconducting coils provide a toroidal magnetic field with a maximum bending power of 0.3 Tm.
So far, the electron pair (i.e. e^+ e^-) production has been investigated in C+C, Ar+KCl and p+p reactions. The pair emission rate was measured over almost six orders of magnitude in the pair invariant mass range between 50 and 1000 MeV/c^2 (spectrum shown in the foreground). The experimental data clearly evidences contributions to the pair yield from the early phase of the collision. Information about the properties of mesons imbedded in dense nuclear medium can be obtained by careful analysis of the spectral distribution of emitted electron pairs. Elementary reactions are exploited to scrutinize our knowledge about the various emission processes. The histogram in the background exemplarily shows the exclusive reconstruction of η-meson production in p+p reactions. HADES will continue its experimental program with p and π-induced reactions, and, after replacing the inner time-of-flight system by a novel RPC detector and upgrading the data acquisition system, with experiments addressing heavier collision systems.

GSI Scientific Report 2005

GSI Report 2006-1
<http://www.gsi.de/library/GSI-Report-2006-1/>

ISSN: 0174-0814
and GSI Report 2006-1

Publisher: Gesellschaft für Schwerionenforschung mbH (GSI),
Planckstr. 1, 64291 Darmstadt, Germany, <http://www.gsi.de>
The GSI is a member of the Helmholtz Association of National Research Centres <http://www.helmholtz.de>.

Publication dates: August 2006 (online version), October 2006 (printed version)
Editor: Katrin Große, Technical team for the printed and the Internet version: Ingo Giese, Katrin Große, Volker Schaa, and Kerstin Schiebel.
Design of the cover illustration: Alexander Schmah/GSI.

Copyright © 2006 by GSI Darmstadt, all rights reserved.
Limited edition. Copies are available by order (gsilibra@gsi.de, phone: +496159 712610, fax: +496159 713049).
Printed by: typographics, Darmstadt, Germany.

For the production of this report templates and scripts of the JACoW collaboration (Joint Accelerator Conferences on Web <www.jacow.org>) were used.

The complete scientific report is also available with supplementary colored figures and illustrations on the Internet: <http://www.gsi.de/library/GSI-Report-2006-1/>

Foreword

This year's Scientific Report shows a noticeable increase in the number of contributions, a trend already seen last year. The reason for this will be no surprise: with preparations for the Facility for Antiproton and Ion Research (FAIR) a broad range of additional research and development has started, both in the accelerator area as well as in the preparation of the experimental program. These are included in the present Report. In the future, once FAIR is formally formed, we expect that this will lead to a separate annual report. At present, however, during the so-called preparatory phase for FAIR, it seems that the most expedient way to distribute information is as a part of the annual GSI Scientific Report.

FAIR went through major developments over the last twelve months. 'Technical Reports' for all components related to accelerators, infrastructure, and civil construction, as well as 'Technical Proposals' for the experiments were prepared for the beginning of 2005. They were subsequently carefully reviewed and scrutinized by high-level expert committees, with members from leading laboratories around the world. Key aspects were feasibility, appropriateness for the specific task, forefront technology, scientific and technical soundness, and realistic estimates of effort and cost. This has resulted in the so-called Baseline Technical Report (BTR), with more than 3000 pages and about 2400 authors. The BTR is now complete and, after approval by the FAIR Steering Committee which represents all international partners of FAIR, will be distributed this summer. The present Report provides, in its traditional form of short summary pages, many of the R&D details but also in its totality an overview of the current scientific and technical status of FAIR.

While the FAIR activities have required a very substantial effort from everybody involved, the ongoing program at the existing GSI accelerators has continued at full level and with a large number of interesting results.

Developments at the accelerators, from ion sources, beam diagnostics, beam dynamics of high-intensity beams up to new modes of operation for the storage ring, have increased accelerator performance and operation. 2005 saw record target times with beams on target of 6132 h at the UNILAC, 6315 h at SIS-18, and 1374 h at the ESR.

In nuclear structure research a set of radioactive-beam experiments with the RISING detector provided new spectroscopic results via relativistic Coulomb excitation for a range of nuclei: from light mirror nuclei to heavy nuclei, both neutron and proton rich. A surprising result was obtained from the analysis of previous data from the on-line mass separator at the UNILAC: two-proton decay from a long-lived high-spin isomer was unambiguously observed and reveals unexpectedly strong proton-proton correlations. The experimental nuclear structure work is supported by a range of theoretical calculations. An important component of this work is related to nuclear astrophysics. The previously developed Fermionic Molecular Dynamics (FMD) model for nuclear structure is being extended for resonance and scattering reactions. A new, antineutrino induced nucleosynthesis process, the νp-process, has been recently suggested to occur in supernova explosions and to drive the production of medium mass nuclei.

In nuclear matter research, interesting results now emerge from the analysis of recent heavy-ion (C+C) and proton (p+p) collision experiments at GSI with the HADES di-electron spectrometer. In the 2 AGeV Ar+KCl run in August 2005 almost complete coverage with the outer multi-drift chambers and thus good momentum resolution was achieved. This is confirmed by narrow peaks observed in missing-mass distributions, which permit the exclusive reconstruction of η-production in pp reactions. The C+C measurements show an enhancement of di-electrons over conventional sources at intermediate masses. Analysis of previous SPS experiments at CERN with GSI participation show scale dependence of mean transverse momentum fluctuations, an observable considered important for the determination of the critical point on the hadron-to-quark gluon plasma phase boundary (CERES), and production yields for phi mesons (NA49) which indicate non-smooth behavior similar to what was observed earlier for negative kaons. An analysis of all existing data on hadron production in a thermal model provides an updated freeze-out curve which tentatively indicates intriguing structure in the region towards higher baryochemical potential. Also in the nuclear-matter area the experiments are paralleled by intensive theoretical work, ranging from various approaches to the QCD phase diagram, to the calculation of spectroscopic functions of hadrons in the nuclear medium, and to transport calculations of the collision processes.

In atomic physics, work has continued to focus on radiative processes and high-resolution spectroscopy in highly-stripped very heavy atoms. Dielectronic recombination has been successfully established as a novel, effective and precise tool to measure isotope shifts. The work on traps has continued with ISOLTRAP at ISOLDE. with precision measurements of medium-mass nuclei on the neutron-rich side. At GSI, SHIPTRAP started its routine operation. SHIPTRAP is pursuing atomic and nuclear properties of heavy elements, produced in heavy-ion fusion reactions and with charge numbers greater than 100. As a first step, the masses of more than 20 nuclei were determined near the proton dripline around mass 147 and around ^{105}Sn near the rp-process end point. The experimental work goes

parallel with developments in instrumentation, including in particular significant advances in the development and construction of the HITRAP facility. Theoretical support is provided by calculations of both, atomic collision processes and related spectroscopy and of fundamental aspects of QED and general symmetries.

Progress in plasma physics has been made in experimental investigations of heavy-ion beam generated states of high energy density in matter (warm dense matter, WDM). Recent developments of diagnostics tools and methods have provided for new data on thermo-physical and hydrodynamic responses of high-energy density states near the boiling curve, the regions of two-phase liquid-gas and the critical point.

Major progress has been achieved in the physics and engineering design efforts and construction of the PHELIX petawatt laser project at GSI. Technical developments were concerned with the pulsed power and control system of the preamplifier, extensive operation tests of the main amplifiers, in-situ inspections of large-sized lenses (involving an illumination and an image processing system, both specifically designed or this purpose), the general PHELIX control system, the petawatt compressor, beam diagnostics and simulations of pulse propagation. In terms of physics performance, a grazing incidence pumped zirconium x-ray laser was experimentally demonstrated at the PHELIX lasers. Recently a first experiment for proton beam generation was performed. The theory effort in plasma physics is closely connected to the experimental studies in terms of extensive simulations and phase diagram studies.

The material science work at GSI on ion tracks continues with the characterization and improved understanding of irradiated materials such as, for example, the ionic conduction and rectification properties in conical nanopores. A new major focus is on the production and investigation of the basic physical properties of nano-structures. These include, among others: the demonstration of Rayleigh instabilities during isothermal heating of metallic nanowires (considered important for future nano-scale devices); infrared and electrical transport properties of single nanowires with a manifestation of quantum size effects; and the production of sharp metallic nanotips.

The bio-physical and bio-medical research program continues along two major thrusts: the basic studies of biological systems to ionizing radiation and the tumor therapy activities. DNA fragmentation, in particular double strand breaks (DSB), were investigated in atomic force and scanning tunneling microscope high-resolution studies, together with other experiments on characterization and repair of DSB. Cell behavior, chromosomal aberrations and genetic instabilities, low- and high-dose effects, bystander responses, tumor cell migration are other examples of a broad and unique research program in radiation biology.

Tumor therapy at the pilot facility at GSI continued in 2005. By now, well above 300 patients have been treated (which involves more than 5000 field settings, more than 3000 fractions and individual treatments). New indications, such as prostate tumor, have been approved for treatment. Technical developments have continued which are directed at various topics, such as multiple field optimization procedures, irradiation of moving organs, detector optimizations and reconstruction algorithms for PET scanners etc.

The Heidelberg ion beam cancer therapy centre HIT, for which GSI has technical project responsibility, has seen major progress. The accelerator section of the building was completed to the point that installation of accelerator components started in the last quarter of 2005. Many factory acceptance tests of accelerator components have been performed as well as numerous commissioning activities at GSI.

This brief survey of the present Report can only provide a small glimpse into the various areas of activities. There are many more excellent examples that could not be touched upon within the scope of this introduction. The reader is encouraged to explore the full Report. As previously, the enormous amount of high-quality research and innovative technical developments - with respect to the ongoing program as well as for FAIR - would definitely not have been possible were it not for the broad involvement and dedication of the research community, the GSI users and the GSI staff. This is an opportunity to express our heartfelt thanks to everybody involved!



W. Henning
Scientific Director

Contents

Foreword . . .
Contents . . .

The FAIR Project

FAIR-GENERAL-01 – The FAIR Project in 2005 . . . 1
FAIR-APPA-BIOMAT-01 – High-Energy Irradiation Facility for Biophysics and Materials Research 3
FAIR-APPA-FLAIR-01 – FLAIR Collaboration: a Status Report . . . 4
FAIR-APPA-FLAIR-02 – Machine Experiments at CRYRING for Antiproton Operation at FLAIR 5
FAIR-APPA-FLAIR-03 – An Ultra-low Energy Electrostatic Storage Ring at FLAIR . . . 6
FAIR-APPA-FLAIR-04 – Double-Strangeness Studies at FLAIR . . . 7
FAIR-APPA-FLAIR-05 – A novel Penning trap design for the measurement of the (anti)proton g-factor . . . 8
FAIR-APPA-HEDGEHOB-01 – Simulations of HIHEX Experiments at FAIR Using Porous Material 9
FAIR-APPA-HEDGEHOB-02 – The LAPLAS experiment: Rayleigh-Taylor instability in elastic solids . . . 11
FAIR-APPA-HEDGEHOB-03 – Dynamic confinement in spherical geometry for WDM experiments 13
FAIR-APPA-SPARC-01 – Combined laser and electron cooling of bunched C^{3+} beams at the ESR 14
FAIR-APPA-SPARC-02 – Beam Lifetimes and Cross Sections for 10-75 MeV/u U^{28+} and Xe^{18+} Ions 15
FAIR-APPA-SPARC-03 – Novel target development for FAIR . . . 16
FAIR-APPA-SPARC-04 – Projectile electron losses in the collision with neutral targets . . . 17
FAIR-APPA-SPARC-05 – A Reaction Microscope with Toroidal Sectors . . . 18
FAIR-APPA-SPARC-06 – Development of a Crystal Spectrometer for Low-energy X-ray Measurements. . . . 19
FAIR-APPA-SPARC-07 – Development of a Double-Sided Si(Li) Strip Detector for Hard X-Ray Polarimetry . . . 20
FAIR-APPA-SPARC-08 – Performance Test of a 2D μ-Strip Ge(i) Detector at the Sychnrotron Facility ESRF . . . 21
FAIR-APPA-SPARC-09 – Development of digital signal processing for the readout of complex Ge(i)-detectors . . . 22
FAIR-NUSTAR-ELISE-01 – ELectron-Ion Scattering in a storage ring (eA collider) - ELISe . . . 24
FAIR-NUSTAR-EXL-01 – R&D on Large-Volume Position-Sensitive Si(Li) Detectors . . . 27
FAIR-NUSTAR-EXL-02 – Simulations for the in-ring spectrometer of EXL . . . 28
FAIR-NUSTAR-EXL-03 – Charge-exchange reactions on ^{136}Xe: Gamow-Teller strength distributions 29
FAIR-NUSTAR-DESPEC-01 – Decay Spectroscopy (DESPEC) . . . 30
FAIR-NUSTAR-DESPEC-02 – Simulations of possible Ge arrays for the DESPEC setup at FAIR . 31
FAIR-NUSTAR-LASPEC-01 – LASPEC - A setup for laser spectroscopy at the low energy beamline at FAIR . . . 32
FAIR-NUSTAR-LASPEC-02 – First ion pulses out of a laser ion source trap . . . 33
FAIR-NUSTAR-LASPEC-03 – Optical pumping in an RF cooler buncher . . . 34
FAIR-NUSTAR-LASPEC-04 – Setup for a Charge Radius Measurement of the Beryllium Halo Nuclei . . . 35
FAIR-NUSTAR-HISPEC-01 – The HISPEC Project . . . 36
FAIR-NUSTAR-HISPEC-02 – Beam particle detection for HISPEC . . . 37
FAIR-NUSTAR-HISPEC-03 – A Plunger Apparatus for Relativistic Radioactive Beams . . . 38
FAIR-NUSTAR-ILIMA-01 – ILIMA Project: Towards Pure Isomeric Beams . . . 39
FAIR-NUSTAR-ILIMA-02 – The Isochronous Mode for Mass Measurements in the CR Storage Ring . . . 40

FAIR-NUSTAR-LEB-01 – On-line test of the Ion Catcher setup at the FRS . . . 41
FAIR-NUSTAR-MATS-01 – The Future Penning Trap Facility MATS at FAIR . . . 42
FAIR-NUSTAR-MATS-02 – An electron beam ion trap for charge breeding of radioactive isotopes 43
FAIR-NUSTAR-MATS-03 – Detection Techniques for On-Line Mass Determination with Penning Traps . . . 44
FAIR-NUSTAR-R3B-01 – Recoil detector system of R3B setup . . . 45
FAIR-NUSTAR-R3B-02 – Heavy Ion CVD-Diamond Detectors for R3B . . . 46
FAIR-NUSTAR-SuperFRS-01 – Progress of Ion-optical and Technical Layout at the Super-FRS . . . 47
FAIR-NUSTAR-SuperFRS-02 – Ion optical design of the focusing system in front of the Super-FRS target . . . 49
FAIR-NUSTAR-SuperFRS-03 – Calculation of activation and dose spatial distributions induced by high intensity uranium beams at the Super-FRS fragment separator at FAIR . . . 50
FAIR-NUSTAR-SuperFRS-04 – Liquid Jet Lithium Target for Super-FRS Fast Extraction Scheme: Comparison Between 2D and 3D Simulations . . . 51
FAIR-NUSTAR-SuperFRS-05 – 3D hydrodynamic calculations of the Super-FRS liquid lithium target . . . 54
FAIR-NUSTAR-SuperFRS-06 – Luminosity calculations for NESR experiments . . . 55
FAIR-QCD-CBM-01 – The CBM experiment at FAIR . . . 56
FAIR-QCD-CBM-02 – A Silicon Tracking System for CBM . . . 58
FAIR-QCD-CBM-03 – Achievements of Monolithic Active Pixel Sensors for the CBM Vertex Detector . . . 59
FAIR-QCD-CBM-04 – Event Reconstruction in the CBM Experiment . . . 60
FAIR-QCD-CBM-05 – Open charm measurement in Au+Au collisions at 25 AGeV in the CBM experiment . . . 61
FAIR-QCD-CBM-06 – Strategies for electron pair reconstruction in CBM . . . 62
FAIR-QCD-CBM-07 – Simulation studies of electron identification with the RICH detector for CBM 63
FAIR-QCD-CBM-08 – Track Reconstruction in the Transition Radiator Detector of CBM . . . 64
FAIR-QCD-CBM-09 – Vector meson detection via $\mu^+\mu^-$ decay in CBM . . . 65
FAIR-QCD-CBM-10 – CbmRoot: Simulation and Analysis framework for CBM Experiment . . . 66
FAIR-QCD-CBM-11 – High efficiency Transition Radiation Detectors for high rate environment . 67
FAIR-QCD-CBM-12 – New developments in timing RPC for the CBM-TOF . . . 68
FAIR-QCD-CBM-13 – MWPC rate capability measurements with an X-ray tube . . . 69
FAIR-QCD-CBM-14 – Hardware Implementation of a Hough Tracker for CBM . . . 70
FAIR-QCD-CBM-15 – Front End Electronic Building Blocks for CBM . . . 71
FAIR-QCD-CBM-16 – Fast TRD Pre-Amplifier Shaper for the CBM experiment . . . 72
FAIR-QCD-PANDA-01 – Integration and Infrastructure of the PANDA Detector . . . 73
FAIR-QCD-PANDA-02 – Installation of the Genova/Fermilab Cluster-Jet Target at GSI . . . 74
FAIR-QCD-PANDA-03 – The inner tracking detector of the PANDA experiment . . . 75
FAIR-QCD-PANDA-04 – Measurement of photon angles for highly resolved TOF detectors . . . 76
FAIR-QCD-PANDA-05 – Towards a DIRC-Detector for the PANDA Experiment . . . 77
FAIR-QCD-PANDA-06 – Proton irradiation of Large Area APDs for the PANDA-EMC . . . 78
FAIR-QCD-PANDA-07 – Pulse shape analysis for germanium detectors operated under magnetic field . . . 79
FAIR-QCD-PANDA-08 – Calculations for the PANDA Magnet System . . . 80
FAIR-QCD-PAX-01 – PAX: Polarized Antiproton eXperiments . . . 81
FAIR-ACC-01 – Status Report of the FAIR-Accelerator Complex . . . 85
FAIR-ACC-02 – Preparation Status of the HIPPI Experiments . . . 87
FAIR-ACC-03 – Progress of the Layout of the FAIR Proton Linac . . . 88
FAIR-ACC-04 – Status of the CH-DTL for the FAIR Proton Injector . . . 89
FAIR-ACC-05 – SIS100/300 Status Report . . . 90
FAIR-ACC-06 – Layout of the FAIR Beam Line System . . . 91
FAIR-ACC-07 – The Storage Rings of the FAIR Project . . . 92
FAIR-ACC-08 – Design Work for the High-Energy Storage Ring (HESR) . . . 94
FAIR-ACC-09 – Beam Performance and Luminosity Limitations in the High-Energy Storage Ring (HESR) . . . 96
FAIR-ACC-10 – Simulation of Modified Yoke Configurations and Coil Geometries for the Laminated Nuclotron Magnet . . . 97

FAIR-ACC-11 – Development of FAIR superconducting magnets and cryogenic system 98
FAIR-ACC-12 – SIS100/300 Acceleration 100
FAIR-ACC-13 – Bunch Compressor System for the SIS 12/18 upgrade 101
FAIR-ACC-14 – Pick-Up and Kicker Electrodes for Stochastic Cooling at FAIR 102
FAIR-ACC-15 – Study of Secondary Rare Isotopes Stochastic Cooling for CR Project 103
FAIR-ACC-16 – Stacking of 3 GeV Antiprotons with a Moving Barrier Bucket Method at the RESR 104
FAIR-ACC-17 – Beam Position Monitor System Development for FAIR 105
FAIR-ACC-18 – BIF Monitor and RGM System Development for FAIR 107
FAIR-ACC-19 – Energy-Loss Dependence of the Ion-Induced Desorption Yield measured with Ar^{10+} Ions at GSI-HHT 109
FAIR-ACC-20 – UHV-ERDA Investigations on Ion Induced Desorption 110
FAIR-ACC-21 – Non evaporable film getters technology at GSI: first results 112
FAIR-ACC-22 – Tools for Far Remote Accelerator Operation 113
FAIR-ACC-23 – Emittance Coupling Stopband in the SIS100 114
FAIR-ACC-24 – Transverse Instabilities for the High-Current Upgrade of SIS18 115
FAIR-ACC-25 – Measurement of the Energy Deposition Profile by U ions of Energies 500 and 950 MeV/u in Cu Targets 116
FAIR-ACC-26 – Loss Analysis for a β-Beam Operation in existing CERN Synchrotrons 117
FAIR-ACC-27 – Beam Loss Studies for the AGS Booster Operation with Intermediate Charge State Heavy Ions 118
FAIR-SAFETY-01 – Monte Carlo shielding calculations for FAIR 119
FAIR-SAFETY-02 – Dose equivalent from 500 MeV neutrons 120

Research to the Programme Hadrons and Nuclei

ACC-STATUS-01 – UNILAC Status and Developments 121
ACC-STATUS-02 – Ion Source Development and Operation 122
ACC-STATUS-03 – SIS18 Status Report 124
ACC-STATUS-04 – ESR Operation and Development 125
ACC-STATUS-05 – Accelerator Operation Report 127
ACC-R+D-01 – Beam Diagnostics Developments for Current Operation of SIS18 and HEBT . . . 129
ACC-R+D-02 – Commissioning of the SIS12/18 Cavity Synchronization System 132
ACC-R+D-03 – High Current Ion Source Development and HOSTI 133
ACC-R+D-04 – Parametrization of Kicker Coupling Impedances 134
ACC-R+D-05 – Status 28 GHz Superconducting ECR Ion Source Project ISIBHI-MSECRIS 135
ACC-R+D-06 – Test of the 350 MHz Superconducting CH-Cavity 136
ACC-R+D-07 – Planned Installations and Experiments at the Frankfurt High Current Injector . . 137
ACC-R+D-08 – Experimental Investigation of Resonance Induced Effects in SIS18 138
ACC-R+D-09 – Excitation of atoms and molecules by highly relativistic ions 139
ACC-R+D-10 – Scattering of residual gas atoms by fast HCI beams 140
NUSTAR-SPECTROSCOPY-01 – Progress in Direct Mass Measurements of Stored Exotic Nuclei 141
NUSTAR-SPECTROSCOPY-02 – Improved analysis method for bound state beta decay experiment of $^{207}Tl^{81+}$ 143
NUSTAR-SPECTROSCOPY-03 – Rare Isotope Investigation at GSI (RISING) Using Relativistic Ion Beams 144
NUSTAR-SPECTROSCOPY-04 – Mirror symmetry of new subshell closures: ^{36}Ca vs ^{36}S 145
NUSTAR-SPECTROSCOPY-05 – Relativistic Coulomb excitation of neutron-rich ^{54,56,58}Cr 146
NUSTAR-SPECTROSCOPY-06 – Gamma-decay of the GDR in the exotic nucleus ^{68}Ni excited via Coulomb excitation 148
NUSTAR-SPECTROSCOPY-07 – ^{108}Sn studied with intermediate-energy Coulomb excitation . . 149
NUSTAR-SPECTROSCOPY-08 – Proton-Proton Correlations Observed in the Two-Proton Radioactivity of the (21+) Isomer of ^{94}Ag 150
NUSTAR-SPECTROSCOPY-09 – Beta decay of ^{101}Sn 152
NUSTAR-SPECTROSCOPY-10 – Gamow-Teller beta decay of ^{105}Sn 153
NUSTAR-SPECTROSCOPY-11 – β-decay properties of nuclei in the region around ^{132}Sn 154
NUSTAR-EXOTIC-BEAMS-01 – Investigation of the reaction ^{20}Ne(p,γ)^{21}Na in the astrophysical interesting energy region 155
NUSTAR-EXOTIC-BEAMS-02 – Measurements of the Interaction Cross-Sections of Proton-Rich Kr Isotopes 156

NUSTAR-EXOTIC-BEAMS-03 – Production Cross-Sections of Isotopes Formed by Fragmentation of 1 AGeV ^{80}Kr Beam . . . 157
NUSTAR-EXOTIC-BEAMS-04 – Longitudinal velocity distributions measured with FRS and fundamental ideas on fragmentation . . . 158
NUSTAR-EXOTIC-BEAMS-05 – Production of residual nuclides in the spallation of ^{238}U . . . 159
NUSTAR-EXOTIC-BEAMS-06 – Systematic comparison of ISOLDE-SC yields with calculated in-target production rates . . . 160
NUSTAR-THEORY-01 – Correlated Realistic Two-Body Interactions and the Tjon Line . . . 161
NUSTAR-THEORY-02 – RPA and ERPA with Correlated Realistic NN Interactions . . . 162
NUSTAR-THEORY-03 – Self-consistent Green's function calculations of finite nuclei . . . 163
NUSTAR-THEORY-04 – Shell Model Monte Carlo Applications . . . 164
NUSTAR-THEORY-05 – Shell Model Monte Carlo method in the pn-formalism . . . 165
NUSTAR-THEORY-06 – Beyond the relativistic mean field approximation: configuration mixing of angular momentum projected wave functions . . . 166
NUSTAR-THEORY-07 – Relativistic Mean-Field Model with Momentum-Dependent Self-Energies 167
NUSTAR-THEORY-08 – Superdeformed Pb isotopes with large neutron excess . . . 168
NUSTAR-THEORY-09 – Determination of spherical mean field nuclei . . . 169
NUSTAR-THEORY-10 – Constraining a nuclear energy density functional by low-energy QCD . 170
NUSTAR-THEORY-11 – Low-momentum Hyperon-Nucleon Interactions . . . 171
NUSTAR-THEORY-12 – Electron scattering on two-neutron halo nuclei with full inclusion of final state interactions . . . 172
NUSTAR-THEORY-13 – Assessment of saddle-point-mass predictions for astrophysical applications . . . 173
NUSTAR-THEORY-14 – Collisions of ^{16}O+^{16}O in a Full Skyrme-Force TDHF Treatment . . . 174
NUSTAR-THEORY-15 – Microscopic Calculation of Fusion Cross Sections . . . 175
NUSTAR-THEORY-16 – Diabatic states from nodal-structure conservation . . . 176
NUSTAR-THEORY-17 – Dynamical calculations of charge distribution for the reaction of ^{238}U at 1 A GeV on a (CH_2)n target . . . 177
NUSTAR-THEORY-18 – Isospin effects on particle production . . . 178
NUSTAR-THEORY-19 – Modification of the ρ^0 meson mass spectrum at HADES energies . . . 179
NUSTAR-THEORY-20 – Production of Hot Nuclei in Nuclear Reactions and Supernova Explosions 180
NUSTAR-THEORY-21 – Resonances, Scattering and Bound States in Fermionic Molecular Dynamics . . . 181
NUSTAR-THEORY-22 – Tunneling of a composite object . . . 182
NUSTAR-THEORY-23 – Transport study of charged current interactions in neutrino-nucleus reactions . . . 183
NUSTAR-THEORY-24 – The outer crust of non-accreting cold neutron stars . . . 184
NUSTAR-THEORY-25 – Weak-interaction processes during stellar collapse . . . 185
NUSTAR-THEORY-26 – The neutrino-process . . . 186
NUSTAR-THEORY-27 – The νp-process . . . 187
NUSTAR-THEORY-28 – Neutron captures and the r-process . . . 188
NUSTAR-THEORY-29 – Constraints on the high density EoS from HIC and compact stars . . . 189
NUSTAR-SHE-PHYS-01 – Search for Element 112 Using the Hot Fusion Reaction ^{48}Ca + ^{238}U . . 191
NUSTAR-SHE-PHYS-02 – Single-particle effects in the decay of ^{269}Ds . . . 193
NUSTAR-SHE-PHYS-03 – Decay Studies of K-Isomeric States in ^{254}No and ^{252}No . . . 194
NUSTAR-SHE-PHYS-04 – New isotopes ^{193,194}Rn . . . 196
NUSTAR-SHE-PHYS-05 – Search for the "missing" α-Decay Branch in ^{239}Cm . . . 197
NUSTAR-SHE-PHYS-06 – Projectile Energy Control by Cusp-electrons . . . 198
NUSTAR-SHE-PHYS-07 – Giant quasi-atoms and superheavy nuclei obtained in collisions of transactinides . . . 199
NUSTAR-SHE-CHEM-01 – Fully Relativistic ab initio Calculations of the Electronic Structures of the Superheavy Atoms . . . 200
NUSTAR-SHE-CHEM-02 – Adsorption of Element 112 on a Au (100) surface . . . 201
NUSTAR-SHE-CHEM-03 – Theoretical Predictions of Complex Formation of Group-4 Elements Zr, Hf, and Rf in H_2SO_4 Solutions . . . 202
NUSTAR-SHE-CHEM-04 – Gas Chemical Investigation of Hexafluoroacetylacetonates of Zr and Hf with Preseparated Isotopes . . . 203

NUSTAR-SHE-CHEM-05 – Pb/Hg Separation on the Surface of Au, Pd and Pt . . . 204
NUSTAR-SHE-CHEM-06 – Electrochemical Deposition of Short-lived Pb Isotopes on a Pd Coated Ni Tape . . . 205
NUSTAR-SHE-CHEM-07 – Simulation of Elution Curves for Chromatography Columns with a Low Number of Theoretical Plates . . . 206
NUSTAR-SHE-CHEM-08 – Molecular plating of uranium on thin aluminum backings . . . 207
NQMA-01 – Radial flow in central Al+Al and Ni+Ni reactions at 2 AGeV . . . 208
NQMA-02 – Hadron production at chemical freeze-out . . . 209
NQMA-03 – Statistical production of J/ψ at RHIC . . . 210
NQMA-04 – Z-Boson Simulations with the central barrel of ALICE . . . 211
NQMA-05 – Statistical Model Predictions for Particle Ratios at sqrt(s_{NN}) = 5.5 TeV . . . 212
NQMA-EXPERIMENTS-01 – Comparison of the isotopic cross sections measured in the fragmentation of ^{136}Xe and ^{124}Xe projectiles with the EPAX parameterization . . . 213
NQMA-EXPERIMENTS-02 – Systematic investigation of the spectator response to the participant blast in the reactions ^{197}Au+^{27}Al, ^{197}Au at 0.5 A GeV and ^{197}Au+^{197}Au at 1.0 A GeV . . . 214
NQMA-EXPERIMENTS-03 – Δ-Scaling in Spectator Fragmentation . . . 215
NQMA-EXPERIMENTS-04 – Reaction Plane Dispersion at Intermediate Energies . . . 216
NQMA-EXPERIMENTS-05 – Dielectron production in C+C and pp collisions . . . 217
NQMA-EXPERIMENTS-06 – Search for kaonic clusters in p+CH_2/CD_2 reactions . . . 222
NQMA-EXPERIMENTS-07 – Strangeness production using a π^- beam at 1.15 GeV/c with FOPI . . . 223
NQMA-EXPERIMENTS-08 – K^+/K^0 ratio in $^{96}_{44}$Ru+$^{96}_{44}$Ru and $^{96}_{40}$Zr+$^{96}_{40}$Zr collisions at 1.528 AGeV . . . 224
NQMA-EXPERIMENTS-09 – Recent results from the NA49 experiment . . . 225
NQMA-EXPERIMENTS-10 – Production of ϕ mesons in central Pb+Pb collisions at SPS energies 227
NQMA-EXPERIMENTS-11 – Charged particle multiplicity in Pb+Au collisions at 158 GeV per nucleon . . . 228
NQMA-EXPERIMENTS-12 – Multiplicity fluctuations in nuclear collisions at 158A GeV . . . 229
NQMA-EXPERIMENTS-13 – Pion-proton correlations in central Pb+Au collisions at 158 AGeV . 230
NQMA-EXPERIMENTS-14 – Scale dependence of mean transverse momentum fluctuations at 158 AGeV . . . 231
NQMA-EXPERIMENTS-15 – Two-particle azimuthal correlations at high transverse momentum in Pb-Au at 158 AGeV/c . . . 232
NQMA-EXPERIMENTS-16 – Leading hadron azimuthal correlations in ALICE central barrel . . 233
NQMA-EXPERIMENTS-17 – Quarkonia measurements with the central detectors of ALICE . . . 234
NQMA-THEORY-01 – Chiral extrapolation of nucleon properties from lattice QCD . . . 235
NQMA-THEORY-02 – Coupled-channel study of baryon resonances with charm . . . 236
NQMA-THEORY-03 – Quantum interferences in the γ, N -> e^+e^-N reaction close to the vector meson production threshold . . . 237
NQMA-THEORY-04 – Hadron Resonances from Lattice-QCD with Chiral Fermions . . . 238
NQMA-THEORY-05 – Transversity from Lattice QCD . . . 239
NQMA-THEORY-06 – On the Faddeev-Popov operator in topological field configurations . . . 240
NQMA-THEORY-07 – Phases of QCD . . . 241
NQMA-THEORY-08 – Realistic phase diagram in a chiral hadronic model . . . 242
NQMA-THEORY-09 – Approaching the strongly coupled regime of color-superconductivity . . 243
NQMA-THEORY-10 – Phase diagram of neutral quark matter: Self-consistent treatment of quark masses . . . 244
NQMA-THEORY-11 – Quark Fluctuations in a Chiral Model at finite chemical potential . . . 245
NQMA-THEORY-12 – Self-consistent in-medium masses of light, scalar and vector mesons from the linear σ-model . . . 246
NQMA-THEORY-13 – Critical Region around the QCD Critical End Point . . . 247
NQMA-THEORY-14 – The D-meson spectral density in hot and dense nuclear matter . . . 248
NQMA-THEORY-15 – Open-charm systems in cold nuclear matter . . . 249
NQMA-THEORY-16 – Asymmetric neutrino emission in quark matter and pulsar kicks . . . 250
NQMA-THEORY-17 – Decoherence time and entropy production in high energy Heavy Ion Collisons . . . 251
NQMA-THEORY-18 – Dilepton production in heavy ion reactions at intermediate energies . . . 252
NQMA-THEORY-19 – Entropy per baryon of dense QCD matter at GSI-FAIR . . . 253
NQMA-THEORY-20 – Thermal production of glueballs in high-energy heavy-ion collisions . . . 254

NQMA-THEORY-21 – Probability of n-body collisions in BUU . . . 255
NQMA-THEORY-22 – Charge Fluctuations from Cluster Hadronization and the D-puzzle . . . 256
NQMA-THEORY-23 – Di-Jet Suppression plus Mono-Jet Emission - induced Mach Shocks in the Quark-Gluon Plasma at the LHC . . . 257
NQMA-THEORY-24 – Improving the Hartree-Fock approximation by including nonzero decay widths . . . 258
NQMA-THEORY-25 – Finite Volume effects from Renormalization Group flows . . . 259
INSTRUMENTS-METHODS-01 – A Multiple-Reflection Time-of-Flight Mass Spectrometer for Resolution of Isobaric Ions . . . 260
INSTRUMENTS-METHODS-02 – A modular setup to monitor a detector's operation conditions 261
INSTRUMENTS-METHODS-03 – The TASCA Project . . . 262
INSTRUMENTS-METHODS-04 – Development of the TASCA Control System . . . 263
INSTRUMENTS-METHODS-05 – Modelling the Differential Pumping of the TASCA Gas-Vacuum System . . . 264
INSTRUMENTS-METHODS-06 – TASCA Target Group Status Report . . . 265
INSTRUMENTS-METHODS-07 – A High-Resolution Time-of-Flight Spectrometer with Tracking Capabilities for Fission Fragments and Beams of Exotic Nuclei . . . 266
INSTRUMENTS-METHODS-08 – Single-Crystal CVD-Diamond Detectors Progress Report . . . 267
INSTRUMENTS-METHODS-09 – A diamond start detector for FOPI . . . 269
INSTRUMENTS-METHODS-10 – Go4 Analysis Framework v3.0 . . . 270
INSTRUMENTS-METHODS-11 – Extension of ROOT I/O for XML Files and SQL Databases . . . 271
INSTRUMENTS-METHODS-12 – EPICS - Experimental Physics and Industrial Contral System at GSI . . . 272
INSTRUMENTS-METHODS-13 – New Slow Control System for FOPI . . . 273
INSTRUMENTS-METHODS-14 – InfiniBand Test Cluster for FAIR DAQ . . . 274
INSTRUMENTS-METHODS-15 – PCI to GTB (GTBP) Interface for Data Acquisition . . . 275
INSTRUMENTS-METHODS-16 – Interface between CAD (CATIA) and ROOT/Geant4 . . . 276
INSTRUMENTS-METHODS-17 – Electronic gain dependence of the time resolution for FOPIs Multi-strip Multi-gap Resistive Plate Counters (MMRPCs) . . . 277
INSTRUMENTS-METHODS-18 – Status of the HADES RPC Project . . . 278
INSTRUMENTS-METHODS-19 – Progress on Pion Beam for HADES . . . 280
INSTRUMENTS-METHODS-20 – 128 channel high resolution TDC with integrated DAQ-system 281
INSTRUMENTS-METHODS-21 – Status of the ALICE Time Projection Chamber . . . 282
INSTRUMENTS-METHODS-22 – Alice TRD Manufacturing at GSI, Status of Chamber Production and Testing . . . 283
INSTRUMENTS-METHODS-23 – Mass production of the ALICE TRD chambers at IKF Frankfurt 284
INSTRUMENTS-METHODS-24 – Surface electrical conductivity of cured Araldite 2011 Epoxy System, a study initiated during Alice TRD production . . . 285
INSTRUMENTS-METHODS-25 – The ALICE HLT Read-Out Receiver Card . . . 286
INSTRUMENTS-METHODS-26 – The Readout Boards for the ALICE TRD . . . 287
INSTRUMENTS-METHODS-27 – FPGAs - Reconfiguration for Radiation Tolerance . . . 288
INSTRUMENTS-METHODS-28 – Optical Readout Interface for the ALICE TRD . . . 289
INSTRUMENTS-METHODS-29 – Electronics Integration for the ALICE TRD . . . 290
INSTRUMENTS-METHODS-30 – Grid Activities at GSI . . . 291

Research to the Programme in Atomic Physics, Plasma Physics and Materials Science

AP-EXP-SPECTROSCOPY-01 – Test of Relativistic Time Dilation at the ESR . . . 293
AP-EXP-SPECTROSCOPY-02 – Laser Spectroscopy of Heavy Elements at SHIPTRAP . . . 294
AP-EXP-SPECTROSCOPY-03 – Nuclear Charge Radius of Lithium-11 . . . 295
AP-EXP-SPECTROSCOPY-04 – Isotope Shift Measurements of Li-like $^{142}Nd^{57+}$-$^{150}Nd^{57+}$ by Means of Dielectronic Recombination . . . 296
AP-EXP-SPECTROSCOPY-05 – High-precision mass measurements with ISOLTRAP . . . 297
AP-EXP-SPECTROSCOPY-06 – Mass Measurements of rare-earth radionuclides at SHIPTRAP . 298
AP-EXP-SPECTROSCOPY-07 – First observation of the Lyman-α transition in hydrogen-like heavy ions with high-resolution calorimetric low-temperature detectors . . . 299
AP-EXP-SPECTROSCOPY-08 – State Selective Formation of Excited L-Shell Levels in Li-Like Uranium . . . 300

AP-EXP-SPECTROSCOPY-09 – Radiative Processes Studied in Collisions of Decelerated Bare Uranium Ions with H_2 Target . . . 301
AP-EXP-COLLISIONS-01 – Mutual ionization in 200 keV H^- -He collisions . . . 302
AP-EXP-COLLISIONS-02 – Longitudinal Momentum Distribution in Simultaeous Ionization of Target and Projectile in 3.6 AMeV Ne^{3+} + Ar Collisions . . . 303
AP-EXP-COLLISIONS-03 – Radiative Electron Capture to the Continuum Cusp(RECC) in 90 AMeV U^{88+} + N_2 . . . 304
AP-EXP-COLLISIONS-04 – Simultaneous Electron Capture to Bound and Continuum States in 90AMeV U^{88+} + N_2 . . . 305
AP-EXP-COLLISIONS-05 – X-ray study of the enhancement effect in radiative recombination of bare U^{92+} ions with low-energy electrons . . . 306
AP-EXP-COLLISIONS-06 – X-ray emission in few-electron heavy ion - atom collisions . . . 307
AP-EXP-COLLISIONS-07 – Deceleration of H-like uranium ions in a crystal . . . 308
AP-EXP-COLLISIONS-08 – Fragmentation of Acetylene in Collisions with 3.6 MeV/u Xe^{40+}-ions 309
AP-METHODS-01 – Status of the HITRAP Decelerator Project . . . 310
AP-METHODS-02 – Status of the HITRAP DTL decelerator at GSI . . . 311
AP-METHODS-03 – The cooler Penning trap for the HITRAP project . . . 312
AP-METHODS-04 – The HITRAP RFQ . . . 313
AP-METHODS-05 – Chargebreeding with the MAXEBIS . . . 314
AP-METHODS-06 – Implementation of a sensitive, narrow-band Fourier Transform Ion Cyclotron Resonance (FT-ICR) detection for short-lived radionuclides at SHIPTRAP . . . 315
AP-METHODS-07 – Efficiency improvement studies for ion-catcher devices . . . 316
AP-METHODS-08 – Status of the g-factor experiment for highly charged calcium . . . 317
AP-METHODS-09 – The FOCAL Spectrometer for Accurate X-Ray Spectroscopy of Fast Heavy Ions . . . 318
AP-THEORY-01 – Hyperfine Splitting in Heavy Ions with the Nuclear Magnetization Distribution Determined from Experiments on Muonic Atoms . . . 319
AP-THEORY-02 – Electron angular and energy distributions in relativistic ion-atom collisions . . 320
AP-THEORY-03 – $K\alpha_1$ decay of helium-like uranium ions following radiative electron capture . 321
AP-THEORY-04 – Correlated double-electron capture with emission of a single photon . . . 322
AP-THEORY-05 – Quantum interference between nuclear excitation by electron capture and radiative recombination . . . 323
AP-THEORY-06 – Tests of Fundamental Interactions with Heavy Ions and Atoms . . . 324
AP-THEORY-07 – Preservation of polarization for polarized ions in magnetic system of a storage ring . . . 325
AP-THEORY-08 – New level diagrams for superheavy collision systems . . . 326
AP-THEORY-09 – Electron Cooling of bare Uranium in HITRAP . . . 327
PLPY-01 – Progress on HEDP/WDM experiments at GSI . . . 328
PLPY-EXP-01 – Heavy-Ion-Beam Pumped Excimerlaser . . . 329
PLPY-EXP-02 – Influence of non-gaussian laser beam profile on proton acceleration . . . 330
PLPY-EXP-03 – Charge state and energy loss of heavy ion beam interacting with porous and solid matter . . . 331
PLPY-EXP-04 – Energy Loss of C-ions in Ar-plasma and -gas in the Gap-target Configuration . . 332
PLPY-EXP-05 – Calcium projectile ion radiation dynamics in gaseous target . . . 333
PLPY-EXP-06 – Influence of f number variation on the properties of laser produced plasmas . . . 334
PLPY-METHODS-01 – CAST - Probing Axions from the Core of the Sun . . . 335
PLPH-THEORY-01 – Hydrodynamic Stability of LAPLAS Target Using an Annular Focal Spot at the Future FAIR Facility . . . 336
PLPH-THEORY-02 – Simulations of Damage to Carbon Collimators Caused Due to Full Impact of LHC Beam . . . 339
MATERIALS-01 – Thermo-stimulated luminescence in LiF and NaCl crystals irradiated at 8 K . 341
MATERIALS-02 – Characterisation of surface hillocks formed on CaF_2 under ion irradiation . . 342
MATERIALS-03 – Influence of ion velocity on the track morphology in dark mica . . . 343
MATERIALS-04 – Improved fission-track length measurements using ion irradiation . . . 344
MATERIALS-05 – Quasi One-Dimensional Electrical Conductors Created by Swift Heavy Ion Tracks in Tetrahedral Amorphous Carbon Films . . . 345
MATERIALS-06 – Laser Spectroscopy of the $^6P_{7/2}$ Multiplet of Gd^{3+} in a LaF_3 Host Crystal . . . 346

MATERIALS-07 – Radiation sensitivity of polyimide at low temperature . . . 347
MATERIALS-08 – Current-Voltage curves in synthetic conical nanopores as described by a simple Poisson/Nernst - Planck model . . . 348
MATERIALS-09 – Protein Biosensors Based on Conical Gold Nanotubes . . . 349
MATERIALS-10 – Morphological Changes in Au Nanowires Influenced by Rayleigh Instability . 350
MATERIALS-11 – Electrical transport properties of single bismuth nanowires . . . 351
MATERIALS-12 – Infrared properties of single metal nanowires . . . 352
MATERIALS-13 – Field emission of copper nanowires grown in polymer ion-track membranes . 353
MATERIALS-14 – Sharp metallic nanotips produced by the ion-track template technique . . . 354
MATERIALS-15 – Improvements of the GSI microprobe for the targeted irradiation of single cells 355
PHELIX-01 – PHELIX Progress Report . . . 356
PHELIX-02 – Grazing Incidence Pumped Zr X-Ray Laser at PHELIX . . . 359
PHELIX-03 – Laser produced proton beams as a tool for EOS measurements . . . 360
PHELIX-04 – ILIAS - Ion and Laser beam Interaction and Application Studies . . . 361

Research to the Programme Health in Field of Cancer Research

RAD-BIOPHYSICS-01 – DNA fragmentation induced by ionizing radiation - AFM study . . . 363
RAD-BIOPHYSICS-02 – High resolution STM study on small dsDNA plasmid . . . 364
RAD-BIOPHYSICS-03 – Quantification of ion-induced DNA double strand breaks with flow cytometry . . . 365
RAD-BIOPHYSICS-04 – Repair of high-LET induced DSBs . . . 366
RAD-BIOPHYSICS-05 – Cluster Effects within the Local Effect Model (LEM) . . . 367
RAD-BIOPHYSICS-06 – Characterisation of p21 foci at heavy ion induced DNA lesions . . . 368
RAD-BIOPHYSICS-07 – Identification of TGF-β1-dependent signalling cascades mediating radiation-induced ATM activity . . . 369
RAD-BIOPHYSICS-08 – Radiation-induced terminal differentiation and cellular senescence: Do they share common pathways? . . . 370
RAD-BIOPHYSICS-09 – Radiation-induced telomerase activity in peripheral blood mononuclear cells . . . 371
RAD-BIOPHYSICS-10 – Induction of chromosomal aberrations in human primary B lymphocytes by ionising irradiation . . . 372
RAD-BIOPHYSICS-11 – Radiation-induced genetic instability in normal human fibroblasts . . . 373
RAD-BIOPHYSICS-12 – Chromosomal instability in T-lymphocyte long-term cultures irradiated with carbon ions and X-rays. . . . 374
RAD-BIOPHYSICS-13 – Analysis of chromosome damage induced by 177 MeV/u Fe-ions based on the time-course of aberrations . . . 376
RAD-BIOPHYSICS-14 – Role of soluble factors in mediating bystander response after carbon ion exposure . . . 377
RAD-BIOPHYSICS-15 – First insights into the cellular basis of different radiosensitivities of squamous carcinoma cells after high LET irradiation . . . 378
RAD-BIOPHYSICS-16 – Neoplastic Transformation Induced by Carbon Ions . . . 379
RAD-BIOPHYSICS-17 – Impact of conventional and heavy ion irradiation on tumour cell migration in-vitro . . . 380
RAD-BIOPHYSICS-18 – Investigation of substrate- and radiation-dependent cell motility using videomicroscopy . . . 381
RAD-BIOPHYSICS-19 – ALTEA: FM Particle Telescope tested at GSI . . . 382
RAD-BIOPHYSICS-20 – Radiation tolerance of the rat spinal cord after single and fractionated doses of photon and carbon ions . . . 383
RAD-BIOPHYSICS-21 – Complete Double Differential Cross Sections for Low Energy Electron Emission in Solids Induced by Swift heavy ion Impact . . . 384
RAD-BIOPHYSICS-22 – Experimental Fragmentation Studies with ^{12}C Therapy Beams . . . 385
RAD-BIOPHYSICS-23 – Fragmentation of 200 MeV/u ^{3}He beams in water . . . 386
RAD-BIOPHYSICS-24 – Synthetic diamonds for heavy-ion therapy dosimetry . . . 387
RAD-BIOPHYSICS-25 – Recent progress in the development of a fron-end electronic for diamond aplications based on the NINO ASIC . . . 388
RAD-BIOPHYSICS-26 – Multiple field optimization and biological dosimetry of a 2D-treatment plan . . . 389
RAD-BIOPHYSICS-27 – Verification of Complex 3D-Dose Distributions in Carbon Ion Irradiation 390

RAD-BIOPHYSICS-28 – Dose calculation in the presence of organ motion . . . 391
RAD-BIOPHYSICS-29 – Comparison of In-Beam PET Data Taken in the ^{3}He-Experiment with ^{12}C-Data . . . 392
RAD-BIOPHYSICS-30 – Analysis of MLEM and OSEM Reconstruction Algorithms for Different Geometries of PET Scanners . . . 393
RAD-BIOPHYSICS-31 – A Method of Processing of the Elements of the System Matrix for Iterative Reconstruction of PET Data . . . 394
RAD-BIOPHYSICS-32 – Optimum detector arrangements for in-beam PET with direct time-of-flight . . . 395
EXTERNAL-HIT-01 – Status Report of the HIT Project . . . 396
EXTERNAL-HIT-02 – Beam Diagnostics for the HIT and CNAO medical accelerators . . . 398
EXTERNAL-HIT-03 – Testbench of the HIT RFQ . . . 400
EXTERNAL-HIT-04 – Optimised raster scan dose delivery with RF-knockout extracted pencil beams . . . 401
EXTERNAL-HIT-05 – Beam monitors for the high-energy beam line of HIT . . . 402
EXTERNAL-HIT-06 – Patient monitors for HIT and transfer of know-how to Siemens-Med . . . 403

Annex

ANNEX-PUBL-01 – Publications to FAIR: Future experiments . . . 405
ANNEX-PUBL-02 – Publications to FAIR: Accelerator Research & Development . . . 407
ANNEX-PUBL-03 – Publications to the programme 'Physics of hadrons and nuclei': Accelerator Research & Development . . . 409
ANNEX-PUBL-04 – Publications to the programme 'Physics of hadrons and nuclei': Experiments 413
ANNEX-PUBL-05 – Publications to the programme 'Large-scale facilities for research with photons, neutrons and ions' . . . 438
ANNEX-PUBL-06 – Publications to the programm 'Health' in the field 'Cancer research' . . . 447
ANNEX-PUBL-07 – Patents and patent applications . . . 448
ANNEX-PUBL-08 – GSI as publisher . . . 449
ANNEX-COLLABORATIONS-01 – International and national collaborations . . . 451
ANNEX-COLLABORATIONS-02 – EU projects at GSI . . . 479
ANNEX-EVENTS-01 – Invited talks at conferences and at other institutions . . . 484
ANNEX-EVENTS-02 – Seminars and talks at the GSI . . . 501
ANNEX-EVENTS-03 – Workshops and meetings . . . 509
ANNEX-UNIV-01 – PhD, Master, Bachelor, Habilitation and Diploma theses . . . 510
ANNEX-UNIV-02 – Teaching activities of GSI staff at universities . . . 514
ANNEX-EXPERIMENTS-01 – Experiments performed at the GSI accelerators in 2005 . . . 519
ANNEX-ORGANIGRAM-01 – Scientific bodies of the GSI as at January 15th, 2006 . . . 521
ANNEX-ORGANIGRAM-02 – Organigram of the GSI . . . 525
ANNEX-ORGANIGRAM-03 – Facts and Figures . . . 526
List of Authors . . . 527

The FAIR Project

FAIR-GENERAL
FAIR General

- FAIR-GENERAL : The FAIR Project in 2005 (1p.)

FAIR-APPA
Reports of the Collaborations in the Atomic, Plasma Physics and Applications Programme

- FAIR-APPA-BIOMAT : The BIOMAT Collaboration (3p.)
- FAIR-APPA-FLAIR : The FLAIR Collaboration (4p.)
- FAIR-APPA-HEDGEHOB : The HEDgeHOB Collaboration (9p.)
- FAIR-APPA-SPARC : The SPARC Collaboration (14p.)

FAIR-NUSTAR
Preparations to Experiments of the Collaborations of the NUSTAR Community

- FAIR-NUSTAR-ELISE : The ELISe Collaboration (24p.)
- FAIR-NUSTAR-EXL : The EXL Collaboration (27p.)
- FAIR-NUSTAR-DESPEC : The DESPEC Collaboration (30p.)
- FAIR-NUSTAR-LASPEC : The LASPEC Collaboration (32p.)
- FAIR-NUSTAR-HISPEC : The HISPEC Collaboration (36p.)
- FAIR-NUSTAR-ILIMA : The ILIMA Collaboration (39p.)
- FAIR-NUSTAR-LEB : The LEB Collaboration (41p.)
- FAIR-NUSTAR-MATS : The MATS Collaboration (42p.)
- FAIR-NUSTAR-R3B : The R^3B Collaboration (45p.)
- FAIR-NUSTAR-SuperFRS : R&D to the SuperFRS Facility (47p.)

FAIR-QCD
R&D to Experiments to the Quantum Chrono Dynamics Theory

- FAIR-QCD-CBM : The CBM Collaboration (56p.)
- FAIR-QCD-PANDA : The PANDA Collaboration (73p.)
- FAIR-QCD-PAX : The PAX Collaboration (81p.)

FAIR-ACC
R&D for the Future FAIR Accelerator Complex (85p.)

FAIR-SAFETY
Radiation Safety and Security (119p.)

The FAIR Project in 2005

Ingo Augustin[1], Thomas W. Beier[1], Katharina Berghöfer[1], Jürgen Eschke[1]and Hans H. Gutbrod[1]

FAIR Project Coordination, [1]GSI, Planckstr. 1 64291 Darmstadt, Germany

1. Introduction

In 2001, GSI, together with a large international science community, presented a Conceptual Design Report (CDR) [1] for a major new accelerator facility for beams of ions and antiprotons in Darmstadt. The concept for the Facility for Antiproton and Ion Research (FAIR) is based on extensive discussions and a broad range of workshops and working group reports, organized by GSI and by the international user communities over a period of several years.
It builds and substantially expands on many seminal developments made by GSI and its international users over the last decade in cooler-ring technology and physics for high-energy heavy ion beams. The central part of the FAIR facility are two superconducting synchrotrons which will deliver high intensity ion beams up to 35 GeV per nucleon for experiments with primary beams of ions up to uranium and with secondary (radioactive) ion beams and antiprotons. FAIR will open up unique opportunities for a broad spectrum of research programs comprising QCD studies with cooled beams of antiprotons, nucleus-nucleus collisions at highest baryon density, nuclear structure and nuclear astrophysics investigations with nuclei far off stability, high density plasma physics, atomic and material science studies, radio-biological investigations and other interdisciplinary studies.

2. Organization as an International Project Status of the FAIR project

Following an in-depth evaluation by the German Wissenschaftsrat (the science advisory committee of the German government) and its recommendation to realize the facility, the German Federal Government announced in February 2003 approval of the project, with Germany providing up to 75% of the needed funding (65% federal, 10% State of Hessen).

The International Steering Committee (ISC) of the FAIR project has been installed in February 2004 with the intention to work out and agree on a contract for the establishment of the international accelerator laboratory FAIR. Until the end of 2005 the following member countries have signed a Memorandum of Understanding (MoU), which expresses the intention to participate in the construction and operation of FAIR: China, Finland, France, Germany, Greece, India, Italy, Poland, Russia, Spain, Sweden, and the United Kingdom.

The new German government has affirmed in November 2005 that the financing of the German share of the FAIR construction cost (total investment) of approximately 1 billion € will be assured. Negotiations with the other FAIR member countries concerning their contributions are in progress.

In 2006, it is foreseen to sign an inter-governmental agreement (convention) that defines the legal and organizational form of FAIR and the contributions of all member countries.

The start of the construction is projected for 2007. FAIR shall be constructed in three phases until 2014. The full performance with the parallel operation of all experimental programs will be reached in 2015.

3. The FAIR Baseline Technical Report

The FAIR project developed significantly from the CDR in 2001 to the Baseline Technical Report (BTR) in 2006. The proposed research program and the accelerator concept have been worked out in more than 100 workshops. Significant R&D has been carried out and detailed design has been developed. A large fraction of this effort is funded by the European Commission.
About 2500 scientists from 44 countries have organized themselves in collaborations and have submitted Letters of Intent in 2004 and Technical Proposals in 2005 for the experiment programs at FAIR.



Figure 1: *The six volumes of the FAIR Baseline Technical Report contain about 3500 pages.*

The working group for Scientific and Technical Issues (STI) of the International Steering Committee has performed an evaluation of the proposed scientific research programs by three Program Advisory Committees (PACs).
In addition, the Technical Advisory Committee (TAC) and several expert groups (Mini-TACs) played an important role in the advancement of the technical design of the FAIR accelerator facilities and civil construction planning with the evaluation of the Technical Reports in 2005.

Also the costs of the experiments, the accelerators and for civil construction have been reviewed by Cost Review Committees. The feedback of the committees in an iterative evaluation process led to the optimisation of the scientific and technical concepts and to a reduction of cost.
Many technical details have been improved to reduce the costs. The accelerator layout has been optimized. Finally the FAIR topology (see Figure 2) and accelerator design was frozen by the TAC in November 2005.
This design is the basis of the FAIR Baseline Technical Report (BTR). It contains the following information in 6 volumes with about 3500 pages:

Volume 1: Executive Summary
Volume 2: Technical Report on Accelerators and Scientific Infrastructures
Volume 3: Technical Experiment Proposals on QCD physics
Volume 4: Technical Experiment Proposals on Nuclear Structure and Nuclear Astro Physics
Volume 5: Technical Experiment Proposals on Atomic Physics, Plasma Physics and Applied Physics
Volume 6: Technical Report on Civil Construction

In addition, a Supplement on Construction Costs, Schedule and Manpower and the Costbook with the individual costs for components has been issued as draft.

The FAIR Baseline Technical Report is based on the STI recommendations. It defines the FAIR project.
The BTR will be published after approval by the International Steering Committee.

4. The FAIR Accelerator Facility

The concept and design of the FAIR accelerator facility has been adapted to the requirements of the planned scientific programs. The specifications of the synchrotrons, storage rings and the achievable beam parameters for the various research programs are explained in detail in reference [2].
As major change of the original layout described in the CDR, the HESR has been moved towards the experimental target hall.
This became possible after cancellation of the antiproton re-injection into SIS100. The mode of operation has also been modified. The HESR will now be capable of accelerating antiproton beams from 3 GeV up to the maximum beam energy of 14.5 GeV. Moreover a proton beam line for commissioning and possible later injection of polarized beams into the HESR from SIS18 has been added.

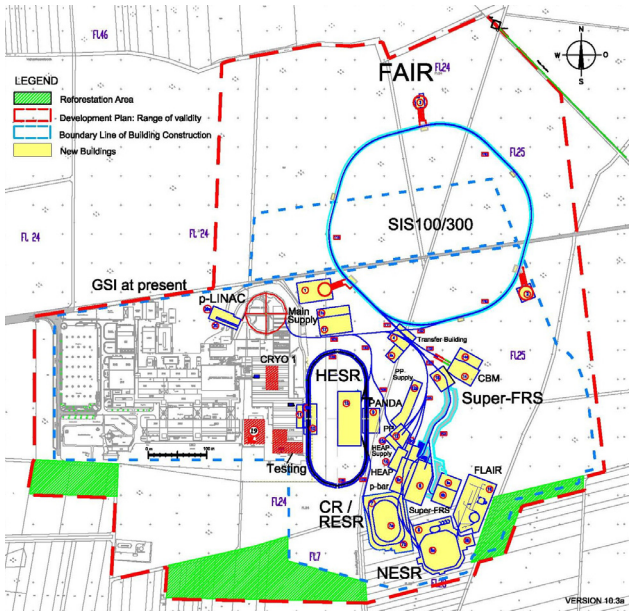


Figure 2: *New layout of the FAIR facilities. The new accelerators and buildings are located east of the existing GSI facilities.*

5. Preparation of the legal documents for establishing the FAIR company as international laboratory

The working group for Administrative and Funding Issues (AFI) of the International Steering Committee has prepared a final draft of an inter-governmental agreement (convention) that defines the legal and organizational form of FAIR and will describe the contributions of all member countries. AFI has also worked out a draft of the Articles of Association of the FAIR (GmbH) company. It is foreseen for the construction period to establish FAIR as an independent legal entity besides GSI with the FAIR member countries as shareholders. The shares per shareholder depend on the contribution of each country to construction and operation of FAIR. The contribution of the participating countries can be financial or in-kind.
It is foreseen to finalize all legal documents, to conclude the negotiation with the ministries or funding agencies of the FAIR member countries and to sign the convention in the course of 2006, so to start construction in 2007.

[1] **An International Accelerator Facility for Beams of Ions and Antiprotons** Conceptual Design Report (http://www.gsi.de/fair/reports/)
[2] **Facility for Antiproton and Ion Research (FAIR)** Vol. 16, No. 1, 2006, Nuclear Physics News

High-Energy Irradiation Facility for Biophysics and Materials Research

R. Neumann, D. Schardt, M. Scholz, C. Trautmann, GSI Darmstadt, Germany
for the BIOMAT-Collaboration

The BIOMAT collaboration, formed by the biophysics and materials research groups at GSI and 29 international user groups, is planning a high-energy irradiatioin facility for experiments in biophysics, space research, and materials science. The facility will be part of the FAIR High-Energy Cave which is shared by the SPARC-Collaboration and will provide unique experimental conditions for irradiations with heavy ions covering the energy range from 100 MeV/u up to 10 GeV/u.

Solar and cosmic radiation represents a major hazard in all space explorations. The interactions and transport properties of cosmic radiation should be known as precisely as possible in order to reduce shielding to the necessary minimum. Moreover, shielding of humans and spacecraft is difficult and costly in space. At the new facility, irradiation experiments will simulate cosmic rays exploiting shielding properties and radiation stability of materials such as the spacecraft hull and electronic equipment. Materials research activities will primarily focus on modifications of solids induced by relativistic ions. The large range of the projectiles will allow the exposure of samples embedded in high-pressure anvil cells.

Experiments in both fields require high flexibility concerning irradiation conditions and target area. Access to a broad range of beams (protons up to uranium) and ion energies from the SIS18 as well as the SIS100 synchrotron is therefore mandatory.

To allow high-quality irradiations of large sample areas, a magnetic beam scanner will be installed. Additionally, a passive scattering system will be provided. The main target station will comprise various flexible set-ups such as a remote-controlled moving belt for positioning of smaller samples and larger devices (e.g. detectors, space devices) together with a robotic system for automatic handling of biological samples. Irradiation experiments on samples exposed to extreme pressure conditions will be performed in a large-volume multi-anvil device. Finally, for basic studies allowing in-situ und on-line monitoring of ion-induced processes, a multi-purpose UHV-chamber is planned. An additional target set-up in close vicinity of the beam dump will allow experiments with extreme beam conditions with respect to fluence and beam energy.

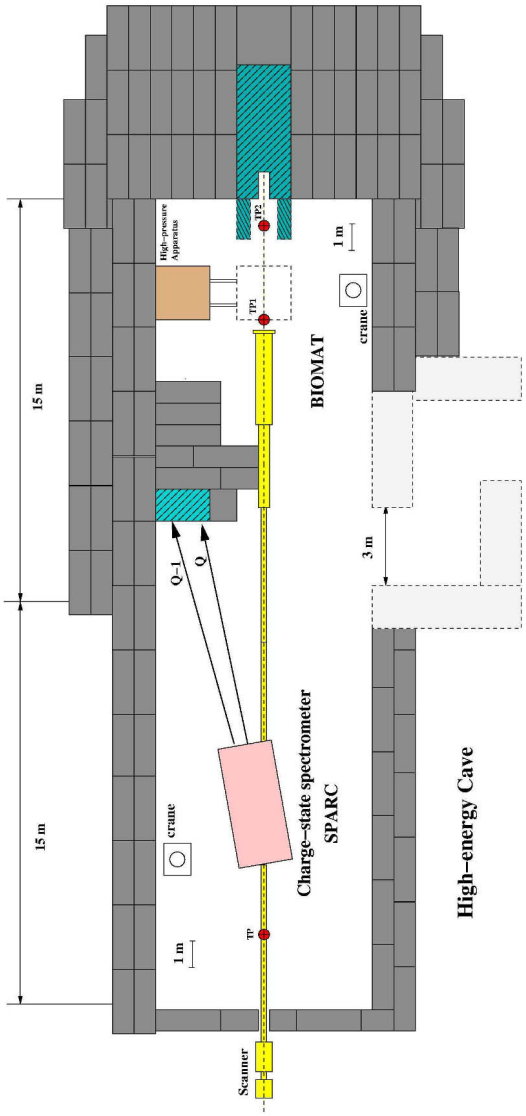


Figure 1: *Schematic layout of the planned High-Energy Cave shared by the SPARC and BIOMAT collaborations.*

FLAIR Collaboration: a Status Report

A. Braeuning-Demian[1], W. Quint[1,2], E. Widmann[3]
[1]GSI Darmstadt; [2]Universität Heidelberg, Germany; [3]Stefan Meyer Institute for Subatomic Physics, Austrian Academy of Science, Vienna, Austria; for the FLAIR Collaboration

FLAIR - the **F**acility for **L**ow-energy **A**ntiproton and Heavy-**I**on **R**esearch - will provide cooled and intense beams of low-energy antiprotons as well as stable and unstable highly-charged ions for atomic, nuclear and particle physics research. The combination of two storage rings - the Low-energy Storage Ring, LSR, and the Ultra-low energy Storage Ring, USR - and the ion trap facility HITRAP will deliver beams of excellent emittance covering energies from 100 MeV/u down to few eV/u. Over 15 different experiments have been proposed to be located at FLAIR and will make use of the provided beams. Details about the scientific goals and technical aspects of these experiments are presented in the FLAIR Letter of Intent and the Technical Proposal [1].

Based on the recommendations of the Program Advisory Committee (APPA-PAC), the Scientific and Technical Issues working group (STI) decided in summer 2005 to include the proposed research program with low-energy antiprotons as an integral part of the FAIR project. Due to the fact that the FLAIR and SPARC research programs rely largely on the same accelerator infrastructure the committee suggested a strong cooperation between the two collaborations.

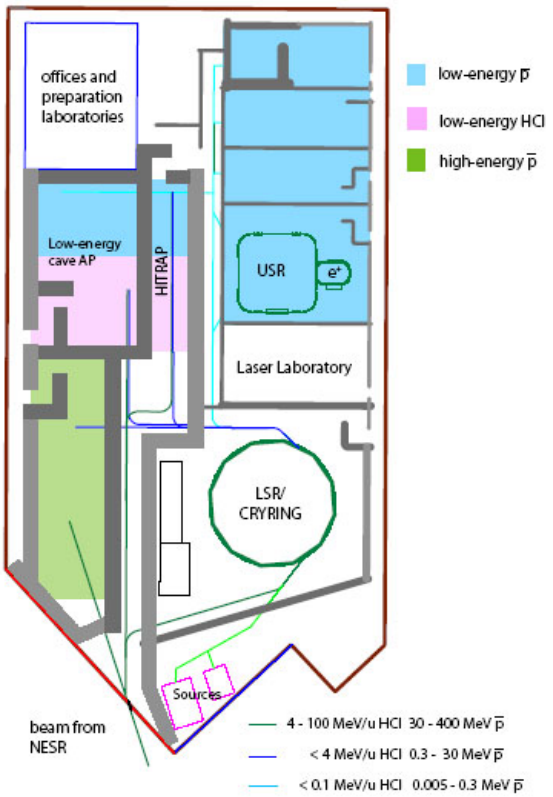


Figure 1: Layout of the FLAIR building.

With this decision, the FLAIR collaboration received the 'green light' to proceed with the preparation of the technical developments. As an immediate consequence of this decision, the FLAIR building was integrated into the FAIR general layout and became part of the civil construction planning. Based on the requirements presented in the Technical Proposal by the FLAIR experiments, a concerted activity for design optimisation of the facility was performed during the second half of 2005. The optimised building layout presented in Fig. 1 satisfies the requests of the planned experimental setups under the observance of safety and radiation protection rules and cost saving. Together with the radiation protection group at GSI, detailed simulations of the radiation field, produced in the different experimental areas, and the required shielding have been performed. Details about these simulations are presented in the present Annual Report [2].

Another important activity of the collaboration is connected to the integration of the LSR storage ring into the larger frame of the FAIR accelerator system. For most of the FLAIR experiments, the antiproton and ion beams will be delivered via LSR, USR or HITRAP. The large diversity of the experiments planned at FLAIR requires a complex beam sharing inside the facility (see Fig. 2) and a good matching with the FAIR accelerator system.

In December 2005 a FLAIR-SPARC coordination meeting was organised at GSI [1]. Part of the meeting was dedicated to presentation of experiment proposals with highly-charged ions at FLAIR. Also the building layout and the Baseline Technical Report, due December 15, 2005, were discussed and accepted by the participants.

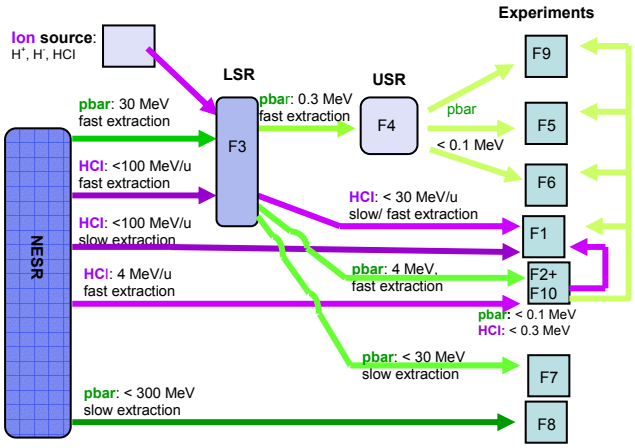


Figure 2: Beam distribution scheme at FLAIR.

References

[1] http://www.oeaw.ac.at/smi/flair/
[2] G. Fehrenbacher at al., present Report

Machine Experiments at CRYRING for Antiproton Operation at FLAIR

H. Danared, A. Källberg and A. Simonsson, Manne Siegbahn Laboratory, Stockholm, Sweden

It is planned that the synchrotron and storage ring CRYRING at the Manne Siegbahn Laboratory in Stockholm will be transfered to the future FAIR facility, where it will be used for deceleration of antiprotons and heavy ions at FLAIR. This report presents results from machine experiments at CRYRING using protons and H^- ions, simulating antiproton operation at FLAIR.

At the FLAIR facility, antiprotons of maximum 30 MeV kinetic energy and heavy ions of 4 MeV/u will be decelerated down to very low energies and ultimately to rest. The first step in the deceleration at FLAIR is made in the magnetic Low-Energy Storage Ring (LSR). CRYRING at the Manne Siegbahn Laboratory in Stockholm will be closed down within the next few years, and since it has an energy range quite similar to the proposed LSR, is equipped with beam cooling, and has several other features required for a deceleration ring, plans are being made for the transfer of CRYRING to FAIR and for its use at FLAIR.

During the past year, several weeks of beamtime at CRYRING have been devoted to machine experiments relevant to the new role that the ring is expected to have at FLAIR. These experiments were performed using protons or, in the case of electron cooling tests, H^- ions, since the interaction between ions and electrons may depend on the sign of the ion charge.

Tests of deceleration from 30 MeV, which is the expected injection energy for antiprotons, down to 300 keV have been performed with protons. Since the present injection energy in CRYRING for protons is 300 keV, the particles were first accelerated to 30 MeV and then decelerated again. Some results from these tests were presented already in the previous GSI Annual Report [1].

More recently, it has been shown that the loss that occurred at the start of the deceleration during the initial tests can be avoided if the beam is cooled a second time at an energy above the injection energy, in this case at 1.3 MeV, where cooling is more efficient than at 300 keV. In particular, the longitudinal emittance of the beam was reduced in this way. These experiments will continue, however, with the aim of improving the overall transmission of the acceleration–deceleration cycle.

Another investigation concerned the maximum number of cooled protons (or antiprotons) that can be stored at 300 keV. This maximum should be determined by the space-charge limit which depends on the (1σ) emittance of the beam, ε, and the maximum tune shift, ΔQ, through the expression

$$N = \frac{4\varepsilon\beta^2\gamma^3\Delta Q}{r_0},$$

where β and γ are the usual relativistic factors and r_0 is the classical particle radius.

In this experiment, the particles were injected in batches every 0.5 s while the electron cooling was on, leading to an accumulation of particles during several minutes. The highest particle number observed was 4.7×10^9. The emittance could be estimated, using residual-gas beam-profile monitors in both planes, to 15π mm mrad horizontally and 5π mm mrad vertically, indicating a ΔQ of approximately 0.1.

This beam was, however, quite unstable. Taking into account also the bunching factor of a beam that is being decelerated, one should not expect stable, decelerated antiproton beams of more than 1×10^9 particles at an emittance in the order of 10π mm mrad.

A third set of measurements were made in order to get an estimate of the time it takes to electron-cool antiprotons at 3 MeV energy. It is anticipated that cooling at an intermediate energy in this neighbourhood is required for the deceleration of antiprotons from 30 MeV to 300 keV. Fig. 1 shows transverse beam profiles of an H^- beam during cooling. The electron current was only 18 mA, producing an electron density of 3.8×10^{12} m^{-3}.

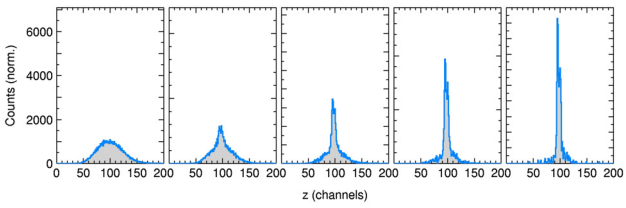


Figure 1: Transverse beam profiles during electron cooling of H^- ions. The full horizontal scale of 200 channels corresponds to 40 mm, and the time interval between the profiles is 300 ms.

It can be estimated from the figure that the cooling time (reduction of beam radius with a factor e) is 0.8 s in the outer parts of the beam, where the cooling is the slowest. The beam reached a cold equilibrium state in about 1.5 s. The uncooled beam had an emittance of approximately 5π mm mrad. The cooling time agrees quite well with cooling times for singly and multiply charged positive ions, properly scaled, that have been measured previously at CRYRING [2].

References

[1] A. Bräuning-Demian *et al.*, GSI Report 2004-1 (2005) p. 33.

[2] H. Danared *et al.*, Proc. EPAC 2000, Vienna 2000, p. 301.

An Ultra-low Energy Electrostatic Storage Ring at FLAIR

C. P. Welsch[1], M. Grieser, K.-U. Kühnel, A. Wolf and J. Ullrich, MPI-K, Heidelberg, Germany

The Facility for Low-energy Antiproton and Ion Research (FLAIR) recently got part of the FAIR core project. A large part of the wide physics program decisively relies on new experimental techniques to cool and slow down antiprotons to 20 keV, namely on the development of an ultra-low energy electrostatic storage ring (USR).

For the USR to fulfil its key role in the FLAIR project, the development of novel and challenging methods and technologies is necessary: the combination of the electrostatic storage mode with a deceleration of the stored ions from 300 keV to 20 keV, electron cooling at all energies in both longitudinal and transverse phase-space, bunching of the stored beam to ultra-short pulses in the nanosecond regime and the development of an in-ring reaction microscope for antiproton – matter rearrangement experiments.

Ring Layout

The symmetric, four-sided machine consists of 90° cylinder deflectors and quadrupole doublets that are used for transverse modulation of the beam. As can be seen in figure 1, the experimental sections and the integrated electron cooler mainly determine the overall size of roughly 9 m × 9 m of the storage ring [1].

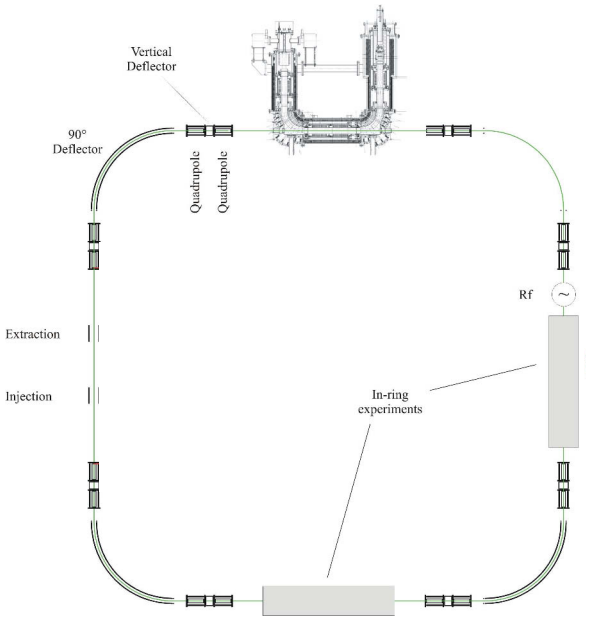


Figure 1: Layout of the USR.

Single-turn injection and extraction of the beam will be realized by pulsed deflectors. In contrast to existing or planned fixed energy electrostatic machines [2–3] an rf operated drift tube with voltages < 100 V is used in combination with an electron cooler to obtain short bunches for in-ring experiments.

Until now there is nearly no experience on cooling forces and cooling times in this energy region, but preliminary estimates indicate that antiprotons can be cooled quite efficiently within less than a second cooling times [2,3].

Aiming to be a true multi-user facility, the ring will provide an antiproton beam that can be used by various in-ring and external experiments. High luminosity, low emittance and low momentum spread are some of the main characteristics of the electron-cooled antiproton beam that shall be achieved and that the various experiments may take advantage of. The storage time in the USR is limited by the interaction of the stored antiprotons with the residual gas. At pressures around $1 \cdot 10^{-11}$ mbar storage times in the order of 10 seconds can be envisaged. About $5 \cdot 10^7$ antiprotons are intended to be transferred from the LSR to the USR at an emittance of 1 mm mrad at 300 keV. Depending on the experimental demands, strong or moderate electron cooling is realized providing 10^6 to 10^7 stored antiprotons at energies down to 20 keV. With typical revolution times of 20 μs, an effective rate of more than $R_{eff} = 10^{10}$ antiprotons/s is reached for in-ring experiments.

Presently, there are two further options under discussion. First, the USR could be used for a much broader physics program if the storage of highly-charged stable and radioactive ions would be included. Nuclear properties of isotopes far-off stability could be investigated with unprecedented precision by laser spectroscopy of the hyperfine transition in one- or few-electron systems or by dielectronic resonances since uncertainties due to many-electron contributions are avoided. Collisions of highly charged ions with atoms involve few to many-electron transfer reactions proceeding within the collision time between a few femtoseconds down to a few attoseconds, thus being ideal prototype reactions to explore ultra-fast, correlated electron dynamics.

A second option is a merged positron beam for in-flight creation of anti-hydrogen. Even though technical requirements would be similar to the original design, modifications in the machine layout are necessary to guarantee easy access to the neutral hydrogen beam. Both options are investigated at present.

References

[1] C.P. Welsch, M. Grieser, J. Ullrich, A. Wolf, "An ultra-low-energy storage ring at FLAIR", NIM A 546 (2005) 405–417

[2] C.P. Welsch, A.V. Smirnov, “Cooling Rates of the USR as Calculated with BETACOOL”, AIP Conf. Proc. (Cool05) to be published, 2006

[3] A. Wolf et al, "The Heidelberg CSR: Low-Energy Ion Beams in a Cryogenic Electrostatic Storage Ring", ”, AIP Conf. Proc. (Cool05) to be published, 2006

[1]Present address: CERN, Geneva, Switzerland

Double-Strangeness Studies at FLAIR

D. Grzonka, A. Gillitzer, K. Kilian, W. Oelert, J. Ritman, T. Sefzick
Institut für Kernphysik, Forschungszentrum Jülich, D-52425 Jülich, Germany
P. Winter
University of Illinois at Urbana-Champaign, Urbana IL 61801-3080, USA
B. Bassalleck
University of New Mexico, Dep. of Physics and Astronomy, Albuquerque, NM 87131, USA
P. Kingsberry
T.U.N.L., Duke University, Box 90308, Durham, NC 27708-0308

Studies of hadronic systems involving double strangeness (S = -2) are practically limited to searches for the H-particle, a system of B = 2, S = -2, first proposed by Jaffe [1] which up to now was not observed. Apart from this exotic object the measurement of the interaction in hadronic systems with double strangeness is of general QCD interest and will result in a better understanding of the strong interaction.

The proposed experiment [2] for the observation of strangeness -2 baryonic states is based on the production of Ξ-baryons in the special condition of recoil-free kinematics. A direct production of Ξ hyperons with zero momentum in a nuclear environment is a very efficient way to produce strongly interacting S = -2 baryonic systems. To achieve such recoil-free kinematics for the Ξ production a K* 'beam' would be particularly suitable where the K* momentum should be about 160 MeV/c for m_{K*}= 982 MeV/c^2. The K* momenta resulting from the antiproton annihilation via: $\bar{p}\ p \rightarrow \bar{K}^*K^*$ are about 290 MeV/c at the nominal K* mass.

Taking into account the K* mass width of about 50 MeV/c^2 the produced K* momenta very well match the required condition for recoil-free kinematics.

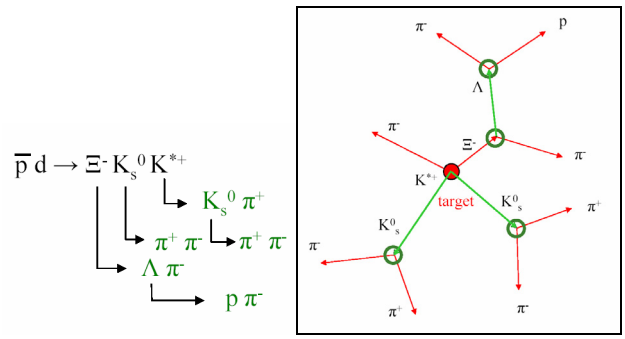


Fig. 1: Sketch of a suitable reaction channel to study the production of Ξ. The primary produced K^{*+} decays within a few fermi into a K_s^0 and a π^+ resulting in 3 delayed decays.

The first stage in these studies to be performed at the FLAIR facility [3] will be solely the Ξ production with the most suitable reaction channel: $\bar{p}$ d → Ξ⁻ K_s^0 K^{*+} resulting in 8 charged particle tracks in the exit channel. A sketch of this reaction channel is shown in Fig. 1.

The high multiplicity of charged particles in the final state and the multiplicity increase due to the delayed decays in this multi-strangeness production gives a clean trigger signal and the event identification is possible via the geometry of the particle tracks. From the charged pions the decay vertices of the K_s^0 are reconstructed and with the known target vertex their tracks are determined. The track of the unobserved neutral Λ hyperon is given from both vertices reconstructed from the (p, π^-) and the (Ξ^-, π^-) tracks. With this information all momentum directions of all particles are known and applying a mass hypothesis for the detected particles the events are completely reconstructed.

For the study of the Ξ-N, Λ-Λ or H system ^{3}He has to be used as target gas. The particle configuration in the exit channel is similar, but an additional proton appears in the exit channel. To perform these experiments a well defined target vertex is required. Therefore a cooled beam with small emittance is necessary. A slow stochastic extraction with a high duty factor from LSR, the Low Energy Storage Ring at FLAIR, is required. The measurement of the S=-2 channel needs a low energy antiproton beam in the range of a few MeV adjusted to an optimum stopping within the target material. For tests of the detector performance higher energy antiprotons or protons could be used.

The planned detection system will include Si-μ-strips close around the target to determine the tracks of the Ξ^-, followed by a segmented scintillation layer for triggering and straw tubes as tracking device. At a distance of about 1 m a second scintillator hodoscope is installed to detect the multiplicity increase. The total detector size will therefore amount to about 2 m length and a diameter of 2 m. For more details on the detection system we refer to the FLAIR Technical Proposal [3].

References

[1] L. Jaffe, Phys. Rev. Lett. 38 (1977) 195.
[2] K. Kilian, Proc. 4th LEAR Workshop, Villars-sur-Ollon 1987, C. Amsler et al., ed., Harwood Academic Publishers, Chur, 1988 p. 529; K. Kilian et al., Memorandum PSCC CERN 1990.
[3] http://www.oeaw.ac.at/smi/flair/

A novel Penning trap design for the measurement of the (anti)proton *g*-factor*

S. Kreim†[1], S. Ulmer‡[1,3], K. Blaum[1,2], W. Quint[2,3], S. Stahl[4], J.Verdu[3], J. Walz[1]

[1]Institut für Physik, Johannes Gutenberg-Universität, 55099 Mainz, Germany, [2]GSI, Planckstraße 1, 64291, Darmstadt, Germany

[3]Ruprecht-Karls-Universität, 69047 Heidelberg, Germany, [4]www.Stahl-Electronics.com, 67582 Mettenheim, Germany

The precise determination of the *g*-factor of the proton and the antiproton together with their comparison is a stringent test of the CPT invariance theorem in the baryonic sector [1]. In our experiment, which is part of the FLAIR collaboration, the *g*-factor of a single, isolated (anti)proton will be determined by utilizing the continuous Stern-Gerlach effect [2] in a double Penning trap setup [3]. The system consists of a precision trap (PT) and an analysis trap (AT). In the PT, we have a homogeneous magnetic field. Introducing an inhomogeneous magnetic field $B = B_0 + B_2 z$ via a ferromagnetic ring electrode in the AT couples the axial oscillation frequency and the direction of the magnetic moment of the (anti)proton. Due to this coupling, an induction of a spin-flip in the precision trap will affect a change of the particles axial frequency in the AT, given by

$$\Delta\omega_z = \frac{B_2}{m_p \omega_z}\mu_p \quad . \tag{1}$$

This frequency shift can be measured by a phase-sensitive detection method, applied in the AT [4]. From the measurement of the characteristic eigenfrequencies of the (anti)proton in the Penning trap via the FT-ICR method (Fourier transform - ion cyclotron resonance), the free cyclotron frequency ω_c of the particle can be extracted. The *g*-factor can be evaluated by the relation

$$g = 2\frac{\omega_L}{\omega_c} \quad , \tag{2}$$

where ω_L is the Larmor-frequency. The oscillating particle induces image currents in the electrodes of the trap, which can be detected by high-Q resonance circuits. Therefore, superconductive inductances will be used, so that the whole experiment has to be operated at cryogenic temperatures. Other essential effects of the low temperature surroundings are an increase of the signal-to-noise ratio and a rise of the storage time [5]. Another important effect is the reduction of the line width of the g-factor resonance. This is caused by a smaller thermal drift in the axial frequency space, due to the small temperature in the Boltzmann-factor [6].
In well-known past experiments, Dehmelt and Van Dyck measured the electron g factor. Since the magnetic moment of the proton is smaller than the Bohr-magneton by a factor of 658, common cylindrical geometries are improper to detect the spin-flip. Therefore we developed a novel trap design with a toroidal ring electrode. A sketch of the trap is shown in Fig. 1a. The substantial advantage of the toroidal trap design is an increase of the B_2 term by a factor of ≈ 3 compared to the cylindrical geometry. The axial frequency shift, that is caused by a spin-flip, does not only depend on the shape of the ring electrode, it is also influenced by the length of the correction electrodes (Fig. 1b), the inner radius of the trap, the full trap length and the axial dimensions of the ring electrode. In a detailed study, the frequency shift caused by a spin-flip has been optimized with respect to other experimental parameters, like the sensitivity of the axial frequency with respect to voltage fluctuations, the electronic detection sensitivity, the harmonicity range of the trapping potential and the time constants for resistive cooling. The complete trap setup is in construction now. Furthermore, in 2005 the pulse tube cooler has been characterized and the design of the cryostat has been finished. Next the details for the electronic detection will be developed. After the measurement of the proton *g*-factor, the experiment will be continued at the FLAIR facility with a single trapped antiproton

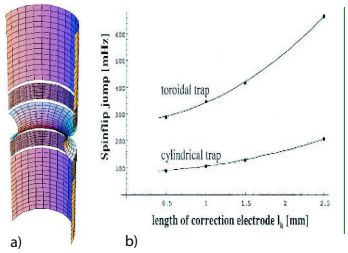


Figure 1: a) Inner surfaces of the cylindrical Penning trap with a toroidal ring. b) Comparison of the axial frequency shift in a toroidal and a cylindrical trap as a function of the length l_k of the correction electrode

References

[1] R. Bluhm, Phys. Rev. Lett. **79**, 1432 (1997).

[2] R.S. Van Dyck, P.B. Schwinberg, H. G. Dehmelt, Phys. Rev. Lett. **59**, 26 (1987).

[3] N. Hermanspahn et al., Phys. Rev. Lett. **84**, 427 (2000).

[4] S. Stahl et al., J. Phys. **B 38**, 297 (2005).

[5] G. Gabrielse et al., Phys. Rev. Lett. **74**, 3544 (1995).

[6] J. Verdu et al., Phys. Rev. Lett. **92**, 093002 (2004).

* work supported by HGF under contract number VH-NG-037 and DFG under contract number QU122/3-1-2

† kreim@uni-mainz.de

‡ ulmers@uni-mainz.de

Simulations of HIHEX Experiments at FAIR Using Porous Material*

N.A. Tahir, D.H.H. Hoffmann, GSI, Darmstadt, Germany
A. Shutov, I.V. Lomonosov, V.E. Fortov, IPCP, Chernogolovka, Russia
A.R. Piriz, University of Castilla-La Mancha, Ciudad Real, Spain
C. Deutsch, LPGP, University of Paris–Sud, Orsay, France

Abstract

Heavy **I**on **H**eating and **Ex**pansion (HIHEX) technique [1, 2] has been proposed to study the equation-of-state (EOS) of high-Energy-Density (HED) matter using intense uranium beam at the future Facilit for Antiprotons and Ion Research (FAIR) [3]. Previously we considered solid material for such studies whereas in the present work we use porous targets that are heated by the above ion beam. Numerical simulations of the hydrodynamic and thermodynamic response of the beam–heated material has been carried out using a two–dimensional hydrodynamic computer code, BIG-2 [4].

Introduction

The basic idea of the HIHEX experiment is to exploit the intrinsic feature of heavy ion beam–volume character of heating in contrast to generating a shock wave. A large volume of a sample of solid material is heated by a heavy ion beam uniformly and quasi-isochorically, inducing high pressure, high-entropy states. The heated material is then allowed to expand isentropically, passing through many interesting physical states including that of an expanded hot liquid, two-phase liquid-gas region, critical point region and if sufficient specific energy is deposited in the target, one would achieve a strongly coupled plasma. The feasibility of this proposed technique has been studied previously [1, 2]. In the present work we consider a porous target in which the grains will be heated by the beam and the heated material will expand, filling the pours homogeneously, that will lead to uniform physical conditions in the sample. In this case, the overall volume of the sample remains unchanged and required density can be obtained by choosing the correct level of porosity. A schematic diagram for such a scheme is ahown in Fig. 1.

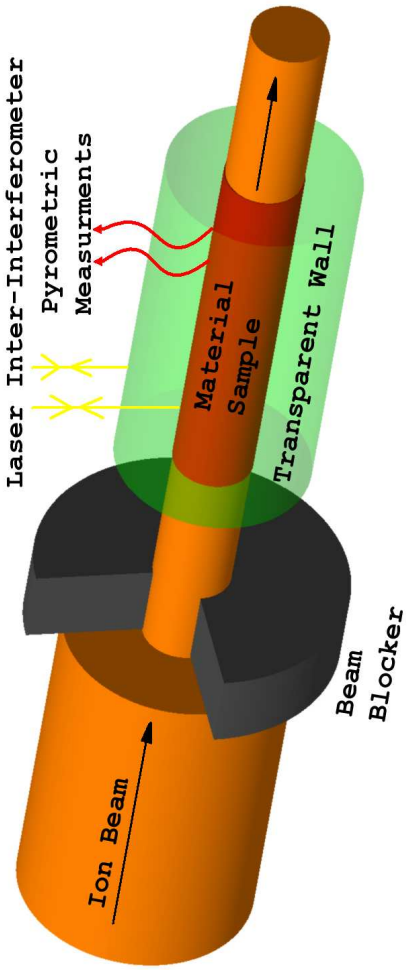


Figure 1: A schematic diagram for proposed HIHEX scheme using porous sample material.

Simulation Results

In the study presented in this section, we consider porous copper with various levels of porosity that correspond to different HED states of interest. Present technology allows production of porous copper with grain sizes of 5 to 10 nm. For the sake of simplification, we neglect the initial porous structure of the sample and start the calculations with an initial uniform subsolid density that corresponds to a given physical state. By adjusting the beam parameters, one can achieve the required temperature and the pressure in the sample.

Despite the fact that critical point region is a very important regime of HED states, there is practically no experimental data available for critical point parameters for most of the materials. Theoretical estimates for critical temperature of metals obtained using various models differ significantly which demonstrates the pressing need for such studies. Table 1 lists estimated critical point parameters for a few metals [5]. It is seen that the critical temperatures for most of the metals are very high and are very difficult to access using traditional methods. Employing the HIHEX

* Work supported by BMBF

technique, one can easily generate the required temperature by depositing an appropriate amount of specific energy.

In Fig. 2 we present physical conditions in the target after it is heated by the beam. We show the sample region (porous copper) which is a cylinder with length = 5 mm and radius = 500 μ that is enclosed in a cylindrical shell of LiF which has an outer radius of 2 mm. A 1 GeV/u uranium beam with an intensity of 5 $\times$ 10^{11} ions that are delivered in a single bunch, 50 ns long has been used to heat the target. Although the beam diameter (FWHM of the transverse Gaussian intensity distribution) is considered to be 4 mm, only the sample material is irradiated by the ions while the LiF is protected from the ions by the beam blocker. Three different cases are considered and the results are presented in Fig. 2(a) – 2(c).

In the case presented in Fig. 2(a), we assume a target density which is 10% of the solid copper density (0.89 g/cm^3) and as a result of beam heating, the target material enters into two–phase liquid–gas (2PLG) region. In case of Fig. 2(b), on the other hand, we start with the calculated critical point density for copper (2.28 g/cm^3, see Table 1). Beam heating in this case leads to estimated values of critical temperature and pressure for copper. Using these beam-target parameters, one can therefore access the critical point region for copper. Calculations presented in Fig. 2(c) assume an even higher density of 5.7 g/cm^3 that leads to the state of an expanded hot liquid after beam heating. The accessible parameter range is further extended using different values of the beam intensity in the range of 10^{11} – 10^{12} ions per bunch.

This work has shown that varying beam intensity or the focal spot size, one can generate all the interesting physical states of HED matter in copper over a wide range of physical parameters, as summarized in Table 2. These calculations have shown that one will be able to generate a strongly coupled copper plasma with a coupling parameter, Γ = 1 – 5 [6].

Table 1: Calculated Critical Parameters of Different Metals

Element	T_c (K)	P_c(kbar)	ρ_c (g/cm^3)
lead	5500	2.30	3.10
gold	8500	6.14	6.10
copper	7800	9.00	2.28
uranium	9650	7.70	4.50
tungsten	13500	3.10	2.17
niobium	19200	11.10	1.7
tantalum	14550	7.95	3.85
aluminum	6390	4.45	0.86
tin	8175	2.39	1.59
silver	7050	10.64	3.29
irridium	11650	6.20	3.10

(please contact: n.tahir@gsi.de).

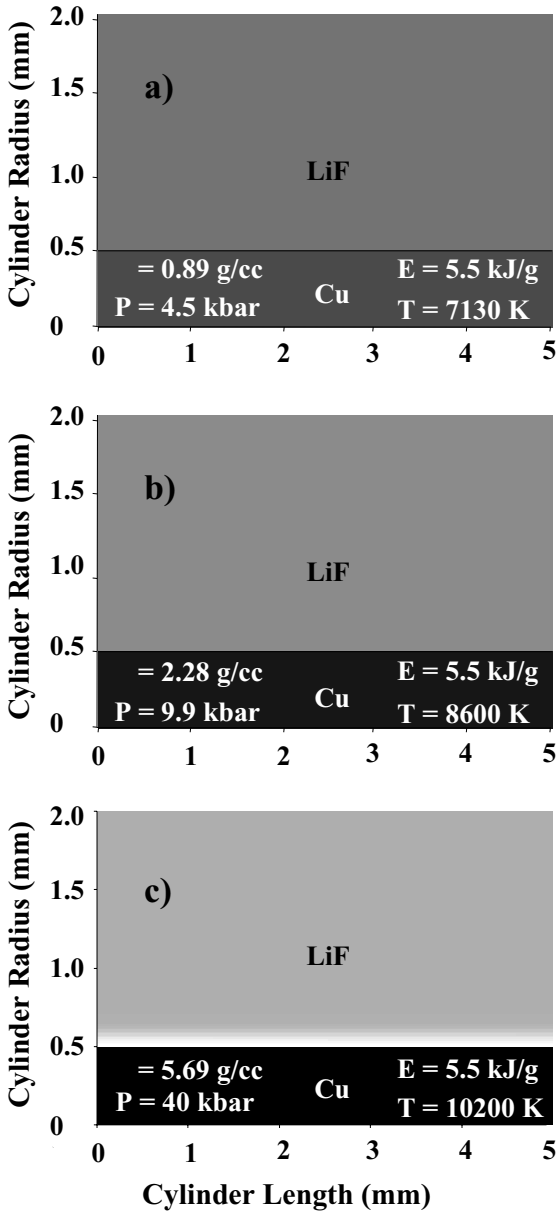


Figure 2: Physical conditions in porous copper sample after beam heating, beam intensity = 5 $\times$ 10^{11}, bunch length = 50 ns, FWHM of transverse Gaussian intensity distribution = 4 mm, (a) density = 0.89 g/cm^3 [10 % solid Cu density], (b) density = 2.28 g/cm^3 [estimated critical density] and (c) density = 5.7 g/cm^3.

References

[1] D.H. Hoffmann et al., Phys. Plasmas 9(2001) 3651.

[2] N.A. Tahir et al., Phys. Rev. Lett. 95 (2005) 035001.

[3] W.F. Henning, Nucl. Instr. Meth. B 214 (2004) 211.

[4] V.E. Fortov et al., Nucl. Sci. Eng. 123 (1996) 169.

[5] I.V. Lomonosov, private communication.

[6] V. Gryaznov et al., Zh. Eksp. Teor. Fiz. 114, 1242 (1998).

The LAPLAS experiment: Rayleigh – Taylor instability in elastic solids

A. R. Piriz, J. J. López Cela, O. D. Cortazar,M. C. Serna Moreno, U. Castilla-La Mancha, Spain
N. A. Tahir, and D. H. H. Hoffmann, GSI Darmstadt, Germany

LAPLAS (Laboratory of Planetary Sciences) experiment [1] is one of the most interesting experimental schemes proposed for the study of equation of state and transport properties of high energy density matter in the framework of the FAIR (Facility for Antiproton and Ion Research) project [2]. This experiment involves a cylindrical implosion of a thick shell of Au or Pb driven by a heavy ion beam with annular focal spot. The region of the shell heated by the ion beam (the absorber) expands accelerating the pusher layer that surrounds the sample in the internal axial region. During this process in which the hot and less dense absorber accelerates the denser pusher, the conditions for the growing of the Rayleigh –Taylor instability (RTI) arise. Therefore, this is an issue of possible concern that is presently under investigation. The classical RTI is a very well known phenomenon that has been extensively studied during the last 50 years but the LAPLAS experimental conditions are quite far from such a classical situation. In fact, during the implosion the pusher remains in solid state retaining its elastic and plastic properties whilst the absorber is melted remaining in liquid state. So, the elastic – plastic properties of the pusher as well as the liquid internal frictional forces (viscosity) will affect the evolution of RTI.

The RTI physics in solids is significantly determined by the elastoplastic properties of the material and exhibit a series of complex phenomena that are note well understood yet. For this, it results of great help to analyze situations involving materials with pure elastic or plastic properties. In this regards, the problem of the linear instability in perfectly elastic solids has been studied in the past by using different methods. On one side, simple models are very suitable for describing more physics as, for instance, the effect of the transient phase between the initial conditions and the asymptotic regime, the effect of the Atwood number A_T [$A_T= (\rho_2-\rho_1)/ (\rho_2+\rho_1)$, where ρ_2 is the density of the solid and ρ_1 is the density of the lighter solid or fluid below it] [3]. However, such models have given so far only a qualitative description of the RTI whislt quantitative results are needed for an adequate design of the experiments. Exact results for the perfectly elastic case were obtained in Ref [4] but this work is limited to $A_T =1$ and it is so involved mathematically to make difficult to generalize it for including more physics. Recently, a new exact solution has been presented in Ref.[5] that can deal with arbitrary values of A_T but it is based in a normal mode analysis so that it is limited to the asymptotic regime. Although limitations of the exact solutions of Ref.[4] and [5] they are very valuable for testing the accuracy of more general but approximate models.

Here we present an analytic model that can describe the transient initial phase as well as the asymptotic regime[6]. Besides, the model is very simple and accurate so that more physics can be included conveniently as, for instance, the effect of arbitrary A_T. This model may be the first step to a more complete elastoplastic theory yet inexistent.

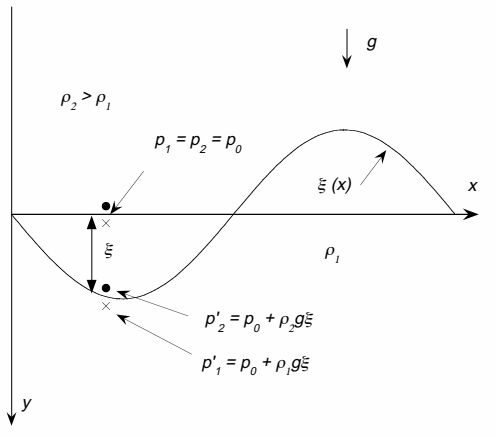


Fig. 1 Diagram of the perturbed interface

Let us show first how the classical results can be obtained from this model [6]. For this we consider two inviscid fluids in a gravitational field g as in Fig.1. If the interface is perfectly planar and it is in equilibrium, the fluid elements on each side of the interface immediately above and below it, respectively, have the same pressure $p_1=p_2=p_0$. If we introduce a small perturbation $\xi(x)$ in the surface, so that these fluid elements originally at $y=0$ are translated to a lower position $y = \xi(x)$, the pressure of the fluid elements will increase as they are in a deeper place within the fluid. However, pressure in the denser fluid increases more than pressure in the lighter one:

$$p_1' = p_0 + \rho_1 g\xi,\ p_2' = p_0 + \rho_2 g\xi \qquad (1)$$

Therefore, a pressure difference $\Delta p = (\rho_2-\rho_1)g\xi$ is created which tends to deform the interface fatherly. According to the Newton second law, the equation of motion of the interface can be written as follows:

$$m\ddot{\xi} = \Delta pA \qquad (2)$$

where A is the area of the interface and m is the mass of both fluids involved in the motion. Since in the RTI we have to deal with surface modes, we can assume that in the linear regime only the fluid within a distance equal to $1/k$ participates in the motion ($k= 2\pi/\lambda$ is the perturbation wave number and λ is the wave length). Therefore, we get:

$$m = m_1 + m_2 = \rho_1 \frac{A}{k} + \rho_2 \frac{A}{k} \quad , \qquad (3)$$

where m_1 and m_2 are, respectively, the masses of the light and heavy fluids that participate in the motion. Thus the equation of motion reads:

$$(\rho_2 + \rho_1)\frac{\ddot{\xi}}{k} = (\rho_2 - \rho_1)g\xi \quad . \qquad (4)$$

As it is well known this equation can easily be solved to get the classically exponential growth rate $\gamma = (A_T kg)^{1/2}$.

This very simple model clearly shows how the interface motion is driven by the buoyancy force $(\rho_2-\rho_1)g\xi A$. If other forces F_i are present, for example due to viscosity, surface tension, elasticity, etc, they must be added to the equation of motion [6]:

$$(m_1 + m_2)\ddot{\xi} = (\rho_2 - \rho_1)g\xi A + \sum_i F_i \quad . \qquad (5)$$

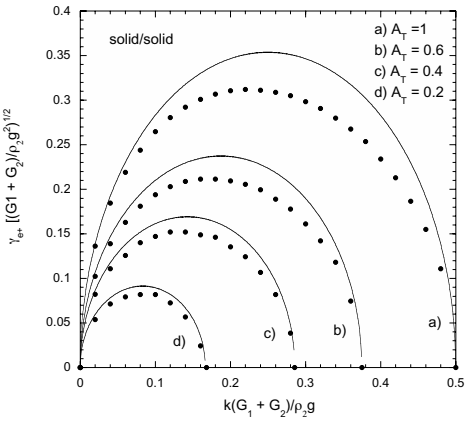


Fig. 2 Asymptotic growth rate as a function of the perturbation wave number for a solid/solid interface and for several values of the Atwood number. Dots are the results of Ref.[5].

So, provided that we can calculate the corresponding forces F_i acting on the interface, this equation will describe the evolution of the interface. For the particular cases of viscous fluids and elastic solids, the forces that act on the interface can be calculated approximately from the constitutive relationships of the material by assuming the velocity field of an inviscid fluid [6]. Then, for a viscous fluid we get:

$$F_v = -2\mu k\dot{\xi}A \quad , \qquad (6)$$

where μ is the fluid viscosity. In the same way, for an elastic (Hookean) solid we obtain:

$$F_e = -2Gk(\xi - \xi_0)A \quad , \qquad (7)$$

where G is the shear modulus of the material and ξ_0 is the perturbation initial amplitude. Using these results we can analytically solve the equation of motion for the cases of solid/solid and solid/fluid interfaces. In Figs. 2, 3 and 4 we show the asymptotic growth rate as a function of the perturbation wave number for different cases. Dots correspond to the exact results of Ref.[5]. The model also describes the transient phase between the initial conditions and the asymptotic regime for arbitrary Atwood numbers. For the particular case of $A_T = 1$ treated in Ref.[4] the result of the present model are also in excellent agreement.

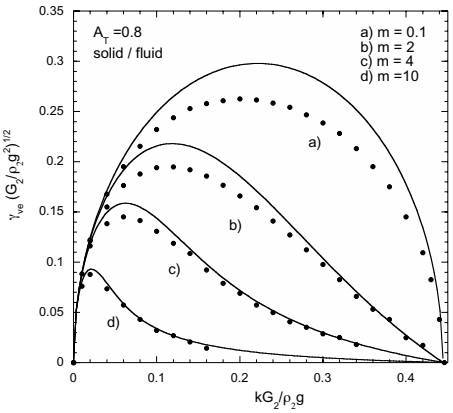


Fig. 3. Asymptotic growth rate as a function of the perturbation wave number for a solid/fluid interface, for an Atwood number 0.8 and for several values of the dimensionless viscosity parameter $m=[\mu_1 g(\rho_2/G_2^3)^{1/2}]^{1/2}$. Dots are the results of Ref.[5].

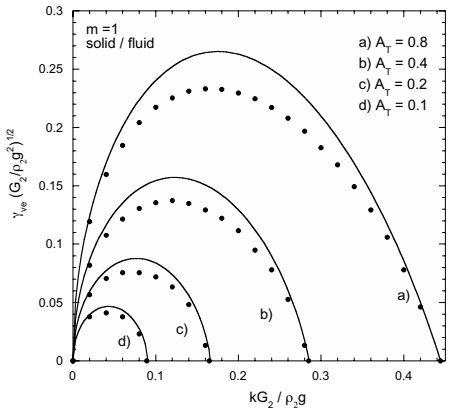


Fig. 4. Asymptotic growth rate as a function of the perturbation wave number for a solid/fluid interface, for several Atwood numbers and for a dimensionless viscosity parameter $m=[\mu_1 g(\rho_2/G_2^3)^{1/2}]^{1/2}=1$. Dots are the results of Ref.[5].

References

[1] N.A.Tahir et al. *Nucl. Intrum. Methods Phys. Res. A* **544**, 16 (2005).
[2] W.F. Henning, *Nucl. Intrum. Methods Phys. Res. B* **214**, 211 (2004).
[3] J. W. Swegle and A. C. Robinson, *J. Appl. Phys.* **66**, 2859 (1989).
[4] B.J. Plhor et al., *Z. angew. Math. Phys*. **49**, 786 (1998).
[5] G. Terrones., *Phys. Rev E*. **71,** 036309 (2005).
[6] A. R. Piriz et al. *Phys. Rev. E* **71**, 056313 (2005).

Dynamic confinement in spherical geometry for WDM experiments*

An. Tauschwitz, J.A. Maruhn, J. Jacoby, Johann Wolfgang Goethe-Universität, Frankfurt am Main, Germany
F.B. Rosmej, Université de Provence et CNRS, Marseille, France
S. Borneis, A. Tauschwitz, Gesellschaft für Schwerionenenforschung, Darmstadt, Germany

The "WDM" (Warm Dense Matter) collaboration proposes to investigate the radiation properties of matter under extreme conditions created by the intense SIS-100 heavy ion beam at FAIR [1]. The ion beams expected at this facility will be able to heat matter within a short time, so that the condition of isochoric heating which is preferable for heavy ion beam experiments is fulfilled. To start the WDM experiments with the SIS-18 heavy ion beam a special target configuration is needed to control the hydrodynamic response of the heated matter. The possibility for diagnostics access is also critical for the proposed target. The use of the PHELIX laser will provide X-ray scattering diagnostics yielding the temperature, density, charge state, and ion-ion correlations. This requires that the target is transparent for the diagnostics X-rays with an energy of few keV. A dynamic confinement scheme employing a thin low-Z tamper heated by the wings of the ion beam to produce confining pressure on the core target material was proposed recently in cylindrical geometry [2]. The performed hydrodynamic calculations have shown that the dynamic confinement of heavy ion beam targets can be extended to spherical geometry which allows using the mature technology for the production of ICF pellets. The target materials and the parameters of the ion beam are the same as in the cylindrical target [2]. Frozen hydrogen is used as a core, an appropriate tamper is a carbon phenolic composite. The 100 ns ion beam pulse consists of 8×10^{10} U ions with 200 MeV/u focused to a 350 μm spot (standard deviation of the Gaussian distribution). The calculations were made with the 2D Caveat code [3] using the Arbitrary Lagrangian-Eulerian technique. The radius of the target core and the thickness of the tamper were optimized to obtain the conditions of quasi-isochoric heating. The smallest density variation during ion beam heating was achieved for an H-core radius of $R_{\mathrm{H}} = 400\,\mu$m and tamper thickness $\Delta R_{\mathrm{c}} = 50\,\mu$m. Figure 1 shows the density distribution in hydrogen for different times. At $t = 50$ ns the density near the target center is depressed, the tamper moves inwards and launches a weak shock wave. In the radial plane the core is less compressed than along the z-axis. At $t = 80$ ns the reflected shock wave and the C/H interface are moving outwards. At the end of the beam pulse the density distribution in the core is nearly uniform, which is an advantage for the diagnostics. In Fig. 2, the mean hydrogen density is plotted as a function of time. For a tamper thickness $\Delta R_{\mathrm{c}} = 65\,\mu$m the mean density at the end of the bunch is equal to the initial density. The dynamic confinement scheme works in spherical as well as cylindrical geometry.

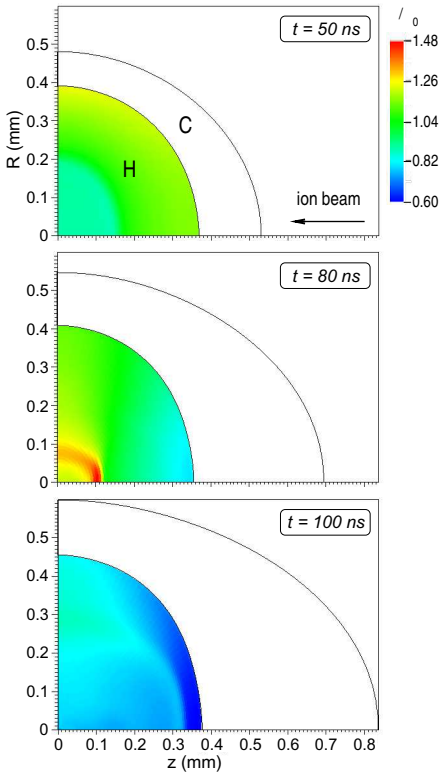


Figure 1: Density distribution of the hydrogen core in length - radius plane. The solid line shows the expansion of the carbon tamper.

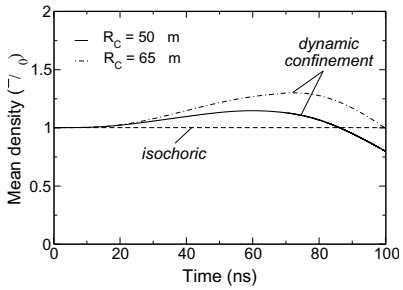


Figure 2: Evolution of the mean hydrogen density during ion beam heating for different tamper thickness.

References

[1] http://www.gsi.de/forschung/phelix/Experiments/FAIR/WDM/.

[2] A. Kozyreva et al., Phys. Rev. E **68**, 056406 (2003).

[3] F. Addessio, Los Alamos Rep. LA-10613-MS-Rev. 1, 1990.

* Work supported by BMBF Projects # 06 F 132, # 06 F 130

Combined laser and electron cooling of bunched C^{3+} beams at the ESR *

U. Schramm†, M. Bussmann, D. Habs, Department für Physik, LMU München, Garching
T. Kühl, P. Beller, B. Franzke, F. Nolden, M. Steck, GSI, Darmstadt
G. Saathoff, S. Reinhard, MPI-K, Heidelberg, S. Karpuk, Inst. f. Physik, Univ. Mainz

Laser cooling of bunched relativistic ion beams at the FAIR synchrotrons is expected to provide fast cooling to unprecedented low momentum spread [1, 2]. Yet, the steep momentum gradient of the resonant force comes at the expense of a narrow momentum acceptance range and predominantly collinear action. An increase in the momentum acceptance can be achieved by adapted tuning of the momentum distribution, as demonstrated for laser cooled C^{3+} beams at the ESR [3] or by direct tuning or broadening of the laser force, planned for an upcoming ESR beamtime.

Here, we report complementary results of the recent ESR C^{3+} beam time, where the phase space density of the ion beam was measured as a function of the beam current for a fixed tuning of the laser force close to the bucket center that corresponds to a relative momentum deviation of only $\Delta p/p \sim 10^{-6}$. Still, every ion in the bucket experiences the laser force once per synchrotron period.

In Figs. 1 and 2 the spatial bunch length, the momentum spread and the transverse width of electron-cooled beams, following the expected intra-beam scattering scaling (dashed lines) [1, 4], are plotted for reference (filled symbols). Regarding the bunch length below 10 μA, laser cooling (open symbols) leads to a reduction by a factor of two. Bunches are longitudinally space-charge dominated [3] matching the expected equilibrium length (solid line) [4]. For higher currents it seems that only a fraction of the ions is efficiently laser-cooled as larger detuning provides longer bunches. For the momentum spread (derived from Schottky spectra for electron cooled reference beams) a momentum dependent measurement of the laser fluorescence (marked HV) yields a reduction of $\Delta p/p$ by about one order of magnitude - far below the solid line that corresponds to the constant equilibrium bunch length. Indirect transverse laser cooling cannot be observed above 10 μA. For lower currents, an onset might be visible. Yet, with little additional electron cooling the behaviour changes (stars). Though the momentum spread slightly increases, the beam becomes transversally as cold as for strong electron cooling.

Summarizing, combined cooling of low current C^{3+} beams leads to unprecedented phase space densities at a plasma parameter of the order of unity. Broad-band laser cooling is presently prepared for an increased momentum acceptance as well as complementary optical methods for the detection of the momentum spread, the bunch length and Schottky noise for a better understanding of space-charge and potential ordering phenomena.

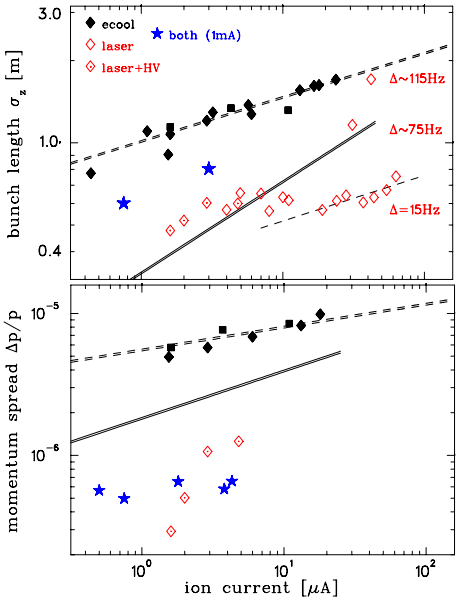


Figure 1: Spatial bunch length (pick-up) and mometum spread (Schottky signal and fluorescence diagnostics) for electron- and laser-cooled ion beams of decreasing current.

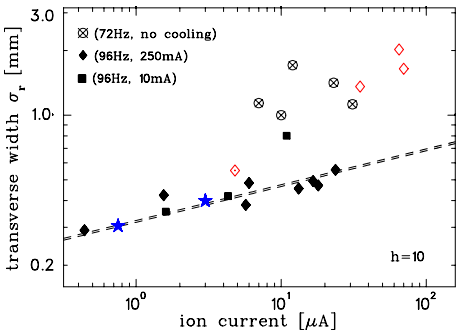


Figure 2: Transverse width (beam-profile-monitor) as above ($\sigma_r = 0.4$ mm corresponds to $\varepsilon = 4 \times 10^{-3}\pi$ mm mrad).

References

[1] U. Schramm, D. Habs, Prog. Part. Nucl. Phys.**53**, 583–677 (2004)

[2] U. Schramm, et al., FAIR LoI#18 APPA–PAC (2004), GSI annual report, 275 (2003)

[3] U. Schramm, et al., GSI annual report, 198 (2004), Proc. LASER 2004 Poznan, Hyp. Int. in press (2006)

[4] U. Schramm, et al., Proc. PAC05, JACoW, FOAD004 (2005) and COOL05 (2005), AIP Proc. in press

* Supported by BMBF 06ML183
† www.ha.physik.uni-muenchen.de

Beam Lifetimes and Cross Sections for 10-75 MeV/u U^{28+} and Xe^{18+} Ions*

R.D. DuBois, O. de Lucio and M. Thomason
University of Missouri-Rolla, Rolla, MO 65409, U.S.A.

G. Weber, Th. Stöhlker, K. Beckert, P. Beller, F. Bosch, C. Brandau, A. Gumberidze, S. Hagmann, C. Kozhuharov, F. Nolden, R. Reuschl, J. Rzadkjewicz, P. Spiller, U. Spillmann, M. Steck, S. Trotsenko
GSI, Darmstadt, Germany

Several GSI future projects require intense beams of heavy ions, in particular uranium ions. To obtain the desired beam intensities and energy densities, space charge effects need to be minimized; this means using low-charge state ions, i.e., ions having charge states far below the equilibrium charge state. When these ions interact with background gases contained in the beamlines and storage rings, electron loss (stripping) occurs. This increases the mean charge state of the beam which decreases its energy density. It also reduces the overall beam intensity, limits storage lifetimes, and generates major detrimental effects such as wall erosion, excessive heat and vacuum loads, radiation buildup, etc. However, until recently, virtually no experimental data were available for low charged heavy ions. Therefore an experimental program accompanied by theoretical studies has been started recently in order to obtain a reliable basis for cross-section and luminosity estimates[1,2].

Our current work assesses the importance of electron stripping at MeV/u energies by measuring storage lifetimes for U^{28+} and Xe^{18+} ions within normal SIS and ESR vacuum environments. For modeling the interaction probabilities and storage lifetimes at higher energies or for other ions, lifetimes and cross sections for stripping by H_2 and N_2 were also measured. This was done using the ESR gas target.

Beam lifetimes were measured in the SIS and ESR for 10-75 MeV/u Xe^{18+} and 10-50 MeV/u U^{28+}. Lifetimes were measured for both cooled and uncooled beams. In addition, using cooled beams, lifetimes were measured at 50 MeV/u for Xe^{18+} - N_2 collisions and at all energies for U^{28+} - H_2 and N_2 collisions. For lifetimes resulting from interactions with hydrogen and nitrogen, ions were injected into the ESR, electron cooling was applied long enough to cool the beams, the electron cooler was turned off and a fast valve was opened to admit the supersonic jet from the ESR gas target. Preliminary measurements were performed to determine the best beam-jet overlap conditions. By monitoring the density of the injected molecular beams, the H_2 and N_2 lifetime data can be converted into absolute stripping cross sections.

Figure 1 shows our measured lifetimes for U^{28+} as a function of beam energy. The data are for interactions with H_2, N_2, and the "normal" background gases within the ESR. The ESR base vacuum was 2 x 10^{-11} mbar with the primary components being H_2 (87%), H_2O (5%), CH_4 (5%), CO_2 (2%) and Ar (1%).

Figure 1 shows that the uranium beam lifetimes due to interactions with N_2 are approximately a factor of ten smaller than for interactions with H_2, i.e., the cross sections for stripping by N_2 are approximately a factor of ten larger than for H_2. In addition, since the lifetimes are proportional to the cross section times the beam velocity, σv, the data show that above 20 MeV/u the stripping cross sections for interactions with N_2 have a v^{-1} dependence in the energy range investigated. In contrast, the stripping cross sections for interactions with H_2 have a faster, perhaps v^{-2}, dependence. The measured beam lifetimes in the ESR ring demonstrate a velocity dependence between these two values since they are determined by a weighted average of cross sections for the various gas constituents.

Most importantly, the data demonstrate that for base vacuum environments that can be achieved in storage rings, the lifetimes for these low-charge-state uranium ions are adequate (~50 seconds) for research associated with several future GSI projects.

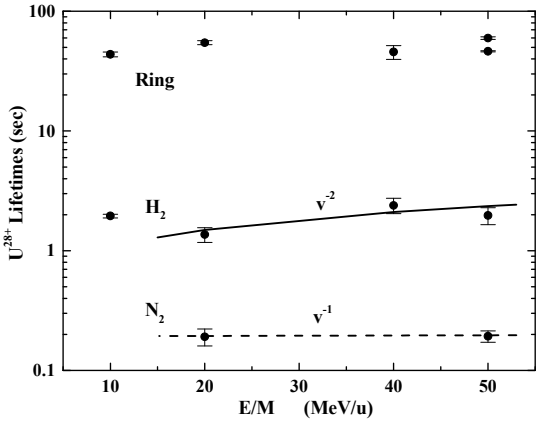


Figure 1: Preliminary lifetime data for beams of U^{28+} ions stored in the ESR ring. The data label "Ring" refer to lifetime data obtained without any additional internal target.

References

[1] R. D. DuBois et al., Phys. Rev. A **70**, 032712 (2004)
[2] R. E. Olson, R. L. Watson, V. Horvat, K. E. Zaharakis, R. D. DuBois, and Th. Stöhlker, NIM A 544, 331-336 (2005)

*Work supported in part by the Office of Fusion Energy Research, US Department of Energy

Novel target development for FAIR*

R. E. Grisenti and R. Dörner, IKF, J. W.-Goethe Universität, Frankfurt/M, Germany

Most of the future experiments at FAIR-NESR require high-density targets to achieve the projected luminosity. One example is the "EXL" collaboration, aiming at the study of nuclear structure properties in light-ion induced reactions (i.e., by using hydrogen or helium beams as internal target). The central part of the experiment is represented by a detector system for the light-ion target-like recoil. The dimensions of the detector system are essentially determined by the spatial extension of the target-beam and the stored ion-beam. Standard gas-jet targets spread out over several millimetres providing an area density of about 10^{14} atoms/cm^2. A challenging issue is thus represented by the search for new methods aiming to significantly reduce the detector size by increasing at the same time the area density to 10^{15}-10^{16} atoms/cm^2 as desirable at the NESR.

Standard internal gas-jet targets make use of Laval-type nozzles with diameter $d \geq 100$ μm. However, such large orifice diameters preclude cooling of the source to temperatures lower that about 80 K as the corresponding flux increase would lead to a strong degradation of the beam properties. The use of very small orifice diameters (d~1 μm) appears thus here to be the essential step towards the possibility to increase the target area density by further cooling of the nozzle source to temperatures well below the liquid nitrogen temperature.

The feasibility to producing continuous droplet beams with $N>10^5$ atoms/droplet by discharging normal liquid and superfluid ^{4}He through 2 μm diameter nozzles into vacuum has been demonstrated recently [1]. These experiments allowed a precise characterization of the *true* beam angular profile as a function of the source pressure P_0=1-22 bar and source temperature T_0=1.3-4.2 K, and a dramatic decrease in the beam divergence either by *increasing* the source pressure or by *decreasing* the source temperature was observed [1]. These results indicate that any angular beam spread in the range 1-100 mrad can be achieved by appropriately choosing the source parameters. This provides a broad range of atomic densities at a given distance downstream from the nozzle exit. In particular, by assuming a uniform droplet beam density and a droplet beam diameter of 1 mm as required for the NESR, area densities in the range 10^{12}-10^{16} atoms/cm^2 are indeed achieved.

Systematic investigations of droplet beams have been reported so far only for ^{4}He. Much less data are available for molecular hydrogen droplet beams. Most of the work with H_2 concerns studies in the Rayleigh-breakup regime, especially by the Uppsala group [2], who reported on the generation of "pellets" (frozen droplets) by discharging liquid hydrogen through 20 μm-diameter nozzles. However, the local area density of $\approx 10^{20}$ atoms/cm^2 makes the possible use of these pellets as internal target at the NESR questionable. In addition, in order to avoid jet freezing at the nozzle exit the liquid hydrogen was discharged into a H_2 atmosphere kept near triple-point conditions, thereby considerably increasing the complexity of the vacuum injection system and the corresponding vacuum pumping stages. Since the nucleation rate decreases with decreasing size, the use of smaller nozzle orifices appears to be crucial to avoid freezing in expansions *into vacuum*.

Preliminary investigations [3] on hydrogen beam generation in the Rayleigh regime by discharging liquid normal hydrogen through a 2 μm diameter nozzle into vacuum demonstrate the feasibility to provide area densities more than one order of magnitude smaller than previously reported [2], as shown in Fig. 1. Most importantly, these results open up the possibility to achieve a broad range of area densities, including those required for the NESR, in close analogy to helium droplet beams [1].

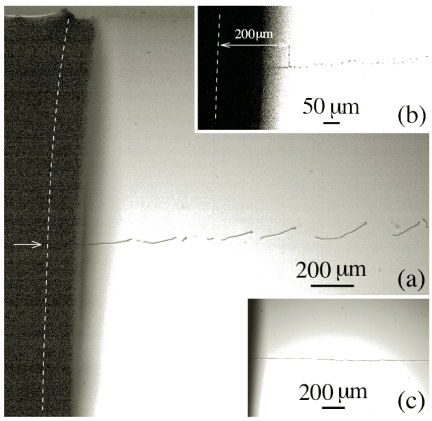


Figure 1: Different breakup modes of a 2 μm diameter hydrogen microjet [3]. (a) The initial filament breaks up into a sequence of rods as a result of apparatus vibrations. The arrow indicates the orifice. (b) Close-up view of Rayleigh breakup. The length of the continuous liquid filament is about 0.2 mm. (c) Example of a continuous solid filament.

References

[1] R. E. Grisenti and J. P. Toennies, Phys. Rev. Lett. 90 (2003) 234501.
[2] B. Trostell, Nucl. Instr. And Meth.: Phys. Res. A 362 (1995) 41.
[3] R. E. Grisenti *et al*., Europhys. Lett. (2006), in print.

*Work supported by GSI and EU

Projectile electron losses in the collision with neutral targets*

V.I. Matveev[1], D.U.Matrasulov[2], Kh.Yu. Rakhimov[2], Th. Stöhlker[3], G.Baur[4]

[1] Pomor State University, Arkhangelsk, Russia [2] Uzbek Academy of Sciences, Tashkent ,Usbekistan

[3] GSI, Darmstadt, Germany; [4] FZ Jülich, Germany

An important issue in the acceleration of U^{28+}at the forthcoming FAIR/GSI [1] is the projectile electron loss in the collision with the rest gas atoms(molecules). It can lead to degraded focusing and loss of the beam to the walls. These charge-changed fast ions strike the accelerator container walls and give rise to sputtering and activation of the surface. Evidently, it is important to study the interaction of highly charged heavy ions with neutral (rest gas) targets, for practical as well as theoretical reasons. It is a theoretical challenge to treat the many-electron (relativisic) scattering problem in a realistic nonperturbative way.

In the spirit of high energy Glauber theory we present a nonperturbative approach for the treatment of single and multiple electron losses of intermediate as well as relativistic highly charged ions colliding with neutral atom targets[2].

We introduce an average impact dependent probabilty p(b) as

$$p(b) = \frac{1}{n_0}\sum_n \frac{1}{M_n}\sum_{l,m}\int d^3k| < \vec{k}|\exp -i\chi(\vec{b},\vec{r})|nlm > |^2 \tag{1}$$

where $\chi(\vec{b},\vec{r})$ denotes the eikonal phase. The number of all possible values of l and m in a given shell n is denoted by M_n, n_0 is the number of shells, further details can be found in [2].

Now we can write the probability $W^{(N_e)+}$ for the loss of $N_e = N_p - N$ electrons, where N_p is the number of electrons of the highly charged ion ($N_p = 64$, in the case of our application to U^{28+}) as

$$W^{(N_e)+}(b) = \frac{N_p}{N!N_e!}p(b)^{N_e}(1-p(b))^N \tag{2}$$

The corresponding cross section is obtained by an integration over the impact parameter d^2b using the Laplace method [2]. In Fig. 1 (taken from [2]) we show the dependence of the multiple electron loss cross section on the number $N_e = N_p - N$ of electrons lost.

In our approach we used a parametrisation for p(b) where we have to fix two parameters [2]. This was done by fitting to the experimentally observed cross section [3] for $N_e = 14, 15$. The agreement is very good, in view of the approximations made.

It is our aim to calculate ionisation cross sections in a more detailed way using the LOSS code[4], which we intend to modify in order to include impact parameter depence as well as relativistic effects.

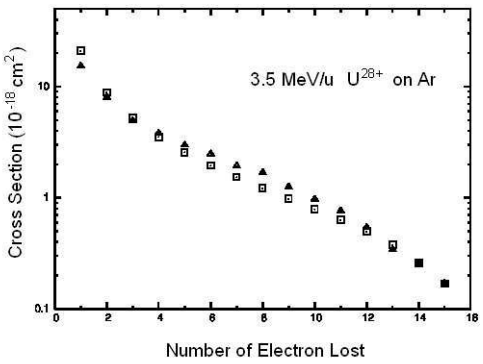


Figure 1: Dependence of the multiple electron loss cross section(in $10^{-18}cm^2$) on the number of loss electrons. triangles are the experimental data [3], squares are the result of our calculation [2]. For further explanation see text and[2].

References

[1] "An International Accelerator Facility for Beams of Ions and Antiprotons", Conceptual Design Report. GSI November 2001.

[2] V.I. Matveev, E.S. Gusarevich, D.U. Matrasulov, Kh. Yu. Rakhimov, Th. Stöhlker and G.Baur, submitted to J.Phys. B

[3] R.D. DuBois, A.C.F. Santos, Th. Stöhlker et al. Phys. Rev. A 70(2004)032712 ;R.E.Olson, et al. J.Phys. B37(2004)4539

[4] V.P. Shevelko, I.Yu. Tolstikhina and Th. Stöhlker, Nucl. Inst. and Meth. in Phys. Res. B184(2001)295

* Work supported by INTAS

A Reaction Microscope with Toroidal Sectors

X.. Wang[1,3], S. Hagmann[1,2], Y. Zou[1]

[1] Fudan University, China
[2]Institut für Kernphysik University Frankfurt; [3]GSI-Darmstadt, Germany

Reaction Microscopes have established themselves as superbly suited for kinematically complete measurements of single and multiple ionization, transfer and excitation processes in the categories of ion-atom and electron-ion collisions [1]. They are utilised in a) dynamics of multiple ionization of atomic and molecular targets for very strong perturbations, b) kinematically complete cross sections for the fundamental process (e, 2e) for ions [2] and c) kinematically complete study of the short wavelength limit of the electron nucleus Bremsstrahlung. They permit to detect simultaneously the momentum vectors of all collision partners, e.g. of all electrons emitted and, too, of recoiling target ions with large solid angle close to 4π and momentum resolutions about 0.01 a.u. Moreover, in combination with an imaging forward electron spectrometer they cover a large range of momentum transfer q from small q for target ionization (outer shell) to large q for (inner shell) target and projectile ionization and electron capture. In the linear geometry the large area 2D position sensitive detectors for electrons and recoil ions are close to the beam axis. However, when a large dynamic range of cross sections is to be measured in a storage ring environment, one must remove the detectors from the immediate vicinity of the coasting beam in order to enable dispersion of unwanted high yields of recoil ions of low charge states and to reduce exposure of detectors to background. The attempt to preserve symmetry as much as possible in view of the wanted variability of parameters leads us to study a toroidal geometry for the low energy electron branch of a reaction microscope.

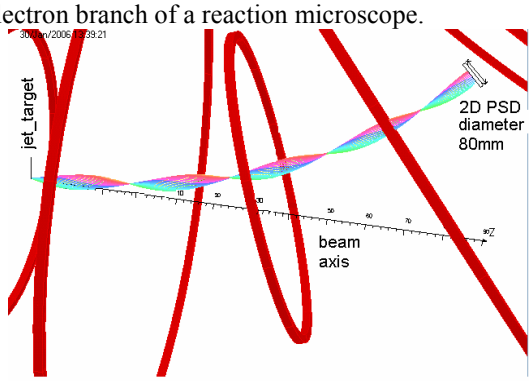


Fig.1 Helical trajectories of electrons in a section of a toroidal field generated by a configuration of 5 coils

Here we describe simulation calculations of a magnetic toroidal sector with 2D position sensitive detector for electrons using OPERA. Trajectories of electrons of the same longitudinal and transverse energy are shown below in Fig.1. A toroidal magnetic B field differs from the solenoidal field in that B is not a constant over the cross section, i.e., in the inner part of the toroidal sector the B field is higher than in the outer part $B(r)=\mu_0 IN/2\pi r$.

In a linear (conventional) reaction microscope, the helical motion frequency ω is independent of the azimuthal angle around the field axis. However, in the new toroidal geometry, as the B-field depends on the azimuth about the field axis, the cyclotron frequency now as well is related to the azimuth of emission $\omega=qB(r)/m$.

Additionally, also the distance traveled by the electron along the outer part is longer than the corresponding distance along the inner part of the toroidal sector, thus the time of flight also is related to the azimuth of emission:

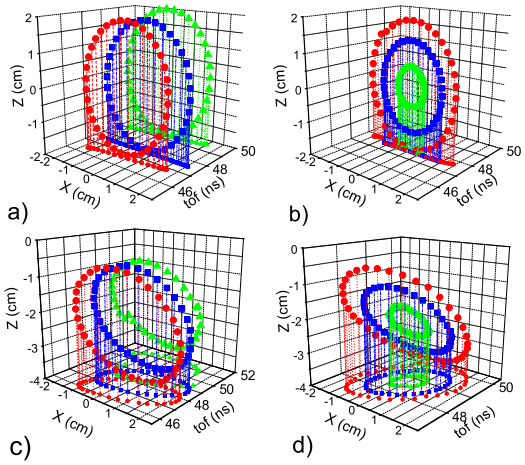


Fig.2 Transverse position and time of flight of electrons in the detector plane In the left column the transverse electron energy is 10 eV, triangle, square and circle correspond to 210,200 and 190 V extraction voltage. In the right column the extraction voltage is 200V and transverse electron energies of 1,5,10 eV are chosen.

In a conventional reaction microscope, the longitudinal momentum (corresponding to the extraction energy) is determined by the time of flight (see Fig.2 b) while the transverse momentum (corresponding to the perpendicular energy) is determined by the radius or the position on the detector (see Fig.2 a). However, with a toroidal magnetic field the position is coupled with the time of flight (see Fig.2 c and d), the circles in (momentum-time) space evolves into an ellipse (Fig.2 c,d). Still this configuration conserves the symmetry almost entirely. A prototype for a toroidal sector will be tested using Unilac beams in X4.

[1] J.Ulrrich et al Rep. Prog. Phys. **66**(2003) 1463
[2] H.Kollmus et al., PRL**88**(2002)103202

Development of a Crystal Spectrometer for Low-energy X-ray Measurements

D. Banaś, P. Jagodziński, M. Pajek, Świętokrzyska Academy, 25-406 Kielce, Poland
Th. Stöhlker, M. Trassinelli, R. Reuschl, U. Spillmann, GSI, D-64291 Darmstadt, Germany

He-like heavy ions are the simplest atomic multibody systems. They are in particular well suited to study electron-electron effects in the presence of strong Coulomb fields where QED contributions are of considerable importance. Recent progress in the spectroscopy of these ions [1] and in related theoretical investigations [2] opened new perspectives for such studies up to He-like uranium. A further important motivation for such investigations is the fact that heavy He-like ions provide also very promising possibilities for studying parity non-conservation in simple atomic systems at high-Z [3] as a test of the standard model. Experimentally, the $\Delta n = 0$ intra shell transitions provide most favorable conditions for such studies, e.g. the $1s2p\,^3P_2 \rightarrow 1s2s\,^3S_1$ transition in He-like uranium located at an energy of close to 4.5 keV.

For future experiments on this topic at the ESR storage ring and within the SPARC collaboration, a dedicated x-ray Bragg spectrometer was designed for the energy range between 1 and 10 keV. Using such an instrument it will also be possible to perform high resolution measurements of the Doppler shifted Balmer x-ray transitions. The constructed spectrometer operates in the Johann geometry [4] with a Rowland circle radius equal to 0.5 m (see Fig. 1). The Si(111) crystal (Carl Zeiss Inc.), with a lattice spacing of 3.136 Å, has a diameter of 75 mm and a radius of curvature of $2R$ equal to 1 m. This arrangement maximizes the number of x-rays diffracted towards the detector, due to the focusing properties of the spherical crystal, essentially increasing the efficiency without an significant influence on the resolution. The spectrometer plane is placed vertically with a fixed sample position adjusted to the height of the ESR experimental storage ring. The crystal and detector can move independently in x and y directions, respectively. The spectrometer is equipped with two linear motorized stages for the x-axis and one pneumatic linear stage for the y-axis movement, both with a 1 μm resolution and two rotation motorized stages with an angular resolution of 0.001°, one for the crystal and the second for the detector rotation. The crystal is mounted using a Newport Ultima Precision Mounting System, which allows for a precise crystal position adjustment. All motors are controlled by two motion controllers (Newport MM4006) connected to a PC. The first version of the software for moving the motors, written in C++ using Newport C++ libraries, has already been developed and tested. For a direct x-ray detection a deep depleted back illuminated CCD camera (Andor Technology DY420-BR-DD) will be used. It consists out of an array of 1024x256 square pixels with a pixel size of 26 μm, what provides the best dynamic range versus resolution and has a negligible dark current at low operating temperatures using a water cooled Peltier module. The quantum efficiency of the CCD is around 90 % for 1 keV and 50 % for 10 keV x-rays.

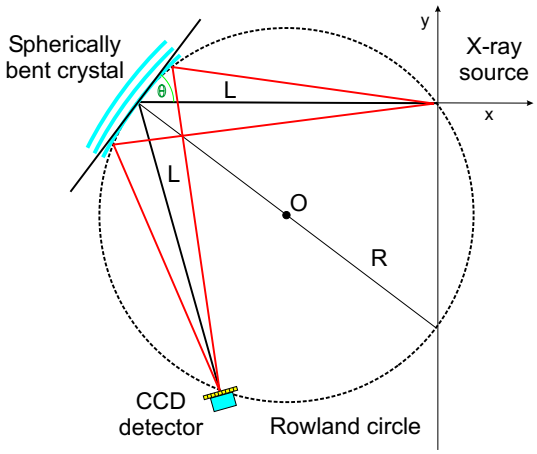


Figure 1: The Johann geometry of the spherical crystal spectrometer showing the positions of the x-ray source, the crystal and the detector (R - Rowland circle radius, θ - Bragg angle, 2R - radius of crystal curvature, L denotes the x-ray source-crystal and crystal-detector distance).

The spectrometer geometry arrangement, in connection with the Si(111) crystal characteristics, allows for an adjustment of the Bragg angle from 15° to 80°, what corresponds to a diffracted x-ray energy range from 2 to 7.5 keV. The expected energy resolution of the crystal spectrometer calculated from the source-crystal-detector geometry, crystal characteristic and detector parameters, is of the order of 0.5 eV. The estimated spectrometer efficiency calculated using a dynamical theory of the crystals reflectivity is about 10^{-6}. The spectrometer will be operated soon and tested in a series of dedicated experiments using a x-ray Mo tube.

This work has been supported by I3 EURONS under EC contract No. 506065 and by Polish Ministry of Education and Science under Grant No. 1P03B-00629

References

[1] A. Gumberidze et al., Phys. Rev. Lett. 92, 203004 (2004)

[2] A. N. Artemyev et al., Phys. Rev. A 71, 062104 (2005)

[3] L. N. Labzowsky et al., Phys. Rev. A 63, 054105 (2001)

[4] H. H. Johann, Zeitschrift fur Physik 69, 185 (1931)

Development of a Double-Sided Si(Li) Strip Detector for Hard X-Ray Polarimetry

D. Protić [1], Th. Stöhlker [2], T. Krings [1], I. Mohos [1], U. Spillmann [2]
[1]IKP, FZ-Jülich, Germany; [2]GSI-Darmstadt, Germany

Heavy ions colliding with electrons or low-density gaseous matter induce electron-ion recombination processes which are of great relevance for plasma- and astrophysics. For high-Z ions and fast collisions, electron-ion recombination in general produces strongly polarized x-rays in the energy regime between 50 and 500 keV [1,2]. First results achieved with the two-dimensional microstrip germanium detector [3] for x-ray spectroscopy of highly-charged heavy ions demonstrated its excellent sensitivity for polarisation effects via Compton scattering [4]. But for photons in the energy regime between 50 and 150 keV (very important range in electron-ion recombination processes at ESR in Darmstadt) a similar silicon detector would clearly outperform this germanium detector. The reason is that in case of germanium the dominance of Compton scattering over the photoelectric absorption begins at ~140 keV. For silicon, in contrast, the latter takes place already at 55 keV. In addition, the relatively low-Z of silicon has the advantage of a reduced width of the Compton profile as compared to germanium. The latter is most important for x-ray imaging on the basis of the Compton effect [5]. Therefore, a Si(Li)-polarimeter would substantially support the research activities of the SPARC-collaboration.

Diameter	36 cm
Length	62 cm
Entrance window	0.5 mm Be
Weight (full)	41 kg
LN_2 content	11 liter (9 kg)
Vacuum	1.4 10^{-7} mbar (zeolite and ion pump)
Operation temperature	120 K

Table l: Some technical specifications of the double-sided Si(Li) polarimeter under construction.

For the above mentioned reasons we have projected the realization of a powerfull Si(Li) polarimeter. The Si(Li) detector of the polarimeter system will be ~15 mm thick with a boron-implanted p^+-contact and a thin Li-diffused n-contact. Both contacts will receive the same strip structure, orthogonally oriented, consisting of 32 strips on an area of 64 mm x 64 mm, surrounded by a ~8 mm wide guard-ring [Fig. 1]. A 15 mm thick diode having 4" in diameter, designated for this purpose, is being in the Li-drift process.
The design of the cryostat and the detector holder is already finished. The schematic view of the Si(Li) polarimeter is shown in Fig. 2.

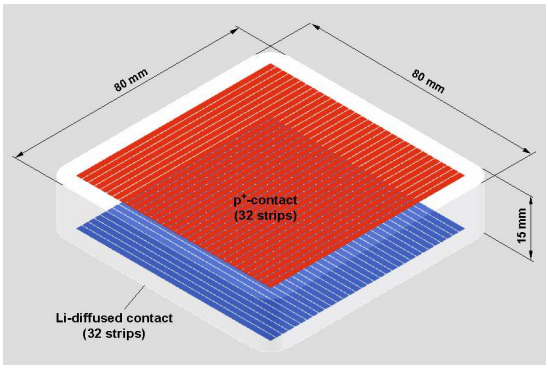


Figure 1: Schematic view of the structured Si(Li) detector

Any orientation of the polarimeter will be possible due to the special dewar (commercially available) that prevents the loss of liquid nitrogen at any position. Low capacitance feedthroughs will be applied to achieve a good energy resolution. Using proved preamplifiers supplied by MTA-ITA-LAI-Budapest (Hungary) an energy resolution below 2 keV will be possible.

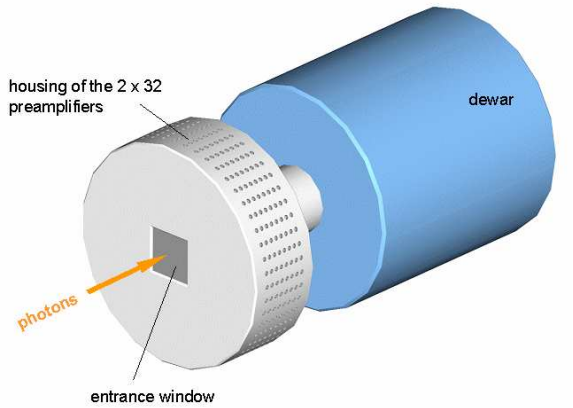


Figure. 2: Schematic view of the Si(Li)-polarimeter.

References:

[1] A. Surzhykov, S. Fritzsche, Th. Stöhlker, Phys. Lett. A 289 (2001) 213
[2] Th. Stöhlker, D. Banas, S. Fritzsche, A. Gumberidze, C. Kozhuharov, X. Ma, A. Orsic-Muthig, U. Spillmann, D. Sierpowski, A. Surzhykov, S. Tachenov and A. Warczak, Physica Scripta. Vol. T110, 384–388 (2004)
[3] D. Protić, Th. Stöhlker, T. Krings, I. Mohos, U. Spillmann, IEEE 52, 3194 – 3198 (2005)
[4] U. Spillmann et al., contribution to the current scientific report 2005
[5] E. A. Wulf, B. E. Phlips, W. N. Johnson, et al., IEEE Trans. Nucl. Science 50 (4): 1182 (2003)

Performance Test of a 2D µ-Strip Ge(i) Detector at the Sychnrotron Facility ESRF

U. Spillmann, Th. Stöhlker , H.F. Beyer, S. Hess, C. Kozhuharov, R. Reuschl, S. Tashenov, S. Trotsenko
GSI-Darmstadt, Germany and IKF, University of Frankfurt, Germany

T. Krings and D. Protic
IKP, FZ-Jülich, Germany

D. Banas
Swietokrzyska Academy, Kielce, Poland

J.Cl . Dousse, M. Kavcic, J. Szlachetko
University of Fribourg, Switzerland

The x-ray spectroscopy program of the SPARC collaboration strongly relies on the availability of two-dimensional, energy dispersive strip detectors with their inherent advantages concerning spectroscopy and imaging capabilities as well as polarization sensitivity [1]. Here we report on a performance test of a first prototype 2D µ-strip germanium detector developed at IKP Jülich. This germanium diode has on the front contact 128 strips on an area of 32 mm x 56 mm (pitch of 250 µm) and on the rear contact 48 strips (pitch of 1167 µm), respectively (for details compare [2]). For an accurate determination of the response characteristics of this detector (accuracy in position determination and polarization sensitivity) in-beam test measurements were performed at the European Synchrotron Radiation Facility (ESRF) in Grenoble. At the ESRF, the high energy beam line ID15A has been chosen where 98% linearly polarized synchrotron radiation at energies of 60 keV and 210 keV was provided for the experiment. The beam size on the detector was close to 50 µm x 50 µm, ideally suited for this test purpose. For the experiment, each detector segment was connected to a separate electronic readout. This allowed us to register simultaneously for every segment the energy deposition and the hit probability as a function of the beam position on the detector. For the latter purpose, the photon beam was scanned over the active detector area in steps of 50 µm. From this scanning technique detailed information on the effects of electronic cross talk and in particular of charge splitting for the different photon energies used is obtained. A further important aspect of this study was to utilize the detector as a Compton polarimeter and to investigate its polarization sensitivity. Sample 2D images for Compton scattering of 210 keV photons are depicted in Fig. 1 as observed for different energies of the Compton scattered photons. Utilizing the kinematical relation between Compton scattering angle θ and the energy of the scattered photons, the various images displayed refer to the spatial intensity distributions related to different scattering angles (from almost 0 deg up to 180 deg). In the figure, an almost dipolar intensity pattern is observed close to scattering angles of 90 deg (cluster plot in the middle). This finding visualizes that for our initial energy of 210 keV, Compton scattering is most sensitive to the linear polarization at scattering angles close to 90 deg. To illustrate the excellent performance in more detail, we display in Fig. 2 the intensity distribution for 90 deg scattering along an arbitrarily chosen radius vector of 5 mm around the center of the image (position of the beam spot on the detector). The solid line displayed gives the result of the Klein-Nishina formula [3] for 100% linearly polarized light and a scattering angle of 90 deg. An excellent agreement between the data and the calculation must be stated.

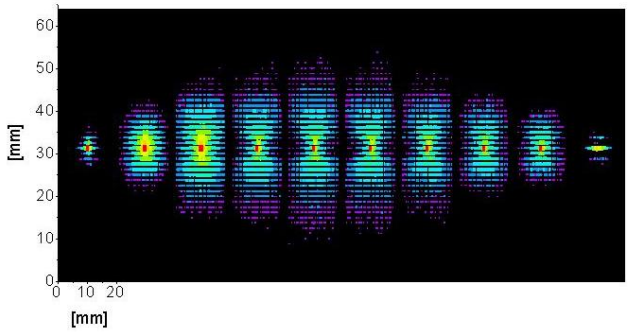


Figure 1: Preliminary 2D images for Compton scattering of 210 keV photons (for details compare text).

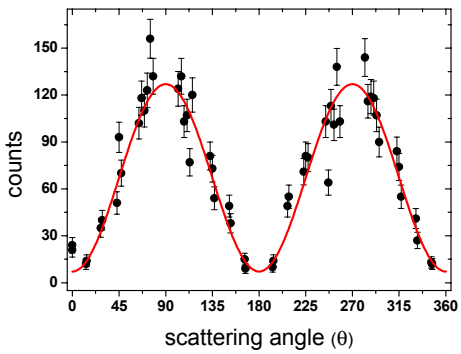


Figure 2: Preliminary result for the intensity distribution for Compton scattering of 210 keV photons at 90 deg .

[1] Technical Report of the SPARC collaboration
http://www.gsi.de/fair/experiments/sparc/index_e.html
[2] D. Protić, Th. Stöhlker, T. Krings, I. Mohos, U. Spillmann, IEEE **52**, 3194 – 3198 (2005)
[3] K. Siegbahn Alpha-, Beta- and Gamma-Ray Spectroscopy, Vol. 2, North-Holland, 1968

Acknowledgment: The authors would like to thank the staff of the ESRF beamline ID15A and especially Dr. Th. d'Almeida for the excellent support during the experiment.

Development of digital signal processing for the readout of complex Ge(i)-detectors

M.Kajetanowicz, S.Samek, D.Sierpowski, A.Warczak, A.Wilk, Jagiellonian University, Cracow, Poland

U. Spillmann, Th.Stöhlker, GSI Darmstadt, Germany

Advanced experiments, associated with the investigation of atomic processes in heavy-ion atom collisions, require application of complex solid state detectors for the detection of X-ray photons [1-3]. Very recently, particular attention has been paid to precise X-ray measurements at the ESR storage ring at GSI in Darmstadt, concentrated around the Lamb shift in hydrogen-like high-Z ions [3]. However, in order to achieve considerable advance in the field, further accuracy improvements of the measurements are required. This should be allowed in the next generation of experiments because of the application of a focusing crystal spectrometer combined with a position sensitive micro-strip detector, equipped with up to 200 strips [1]. In the X-ray energy region of interest, i.e. above 15 keV, germanium seems to be the best material for the fabrication of such detectors, foreseen for position sensitive x-ray spectroscopy [4].

A segmented germanium pixel detector (16 pixels) was successfully tested for the polarization study of radiative electron capture (REC) into the K shell of bare uranium ions [2]. To simplify fast and reliable processing of signals from segmented germanium detectors, a new flexible multi-channel read-out and data acquisition system was developed and tested. The idea comprises both hardware and software development. This digital system, based on the continuous signal sampling, is presented below.

The voltage pulses provided by the charge sensitive preamplifiers, connected directly to Ge detectors, form the inputs for the designed read-out board. The height of these pulses, for the lowest X-ray energies of interest, is in the mV range and, on average, only slightly exceeds the noise level. In the case of the weakest pulses registered, a typical signal to noise ratio is of about two. Timing parameters of the rising edge of the pulse determine the position of the X-ray interaction within the detector crystal. To extract the time and amplitude (energy) information, the noisy input signals are amplified first, without any shaping, and then digitized. Only a simple CR high-pass filter is used to reject the omnipresent 50 Hz hum (Fig. 1).

The read-out electronics is split into 16-channel boards. Each channel on the read-out board contains the input amplifier, the ADC (Analog to Digit Converter) and the FIFO (First In First Out) memory. The logic controller on the board controls the operation of the input channels and the digital data transmission to the receiving device. The structure of one input channel is presented in Fig. 1.

The boards are read sequentially. The digital data from all the boards are transmitted with one 50-way cable to the VME crate in the event by event mode. The acceptable distance between the detector and the VME crate is up to 100 meters.

The data packets will be further on-line processed in the SAM3 VME module developed at GSI Darmstadt [5], and will be accessible to the user via the VME crate controller.

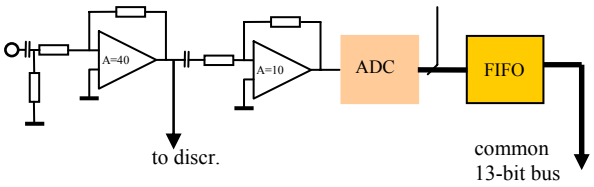


Fig.1 Structure of one input channel

The main advantages of the new read-out electronics are: reduced noise pick-up, low channel to channel cross talk, improved signal to noise ratio, high reliability, modular structure (easy to upgrade), low cost per channel, fast on-line data processing. In order to obtain information on the energy and time of the detected photon from the digitized data stream, special algorithms have been developed and prepared.

When the trigger signal appears, the pre-defined number of digital samples, taken before and after the trigger signal, is stored in the FIFO memory of each channel. The length of the time window is approximately in the range of 0.1– 4.0 μs.

A single channel planar Ge(i) detector (ORTEC GLP 16195/10-S) has been used for test purposes, utilizing ^{241}Am and ^{133}Ba standard calibration sources. The signal output from the read-out board were filtered and cleaned by DSP algorithms. An example spectrum of the amplitude of the signal is shown in Fig. 2. The amplitude (energy) resolution is approximately 1.3% (800eV) for the 60 keV line.

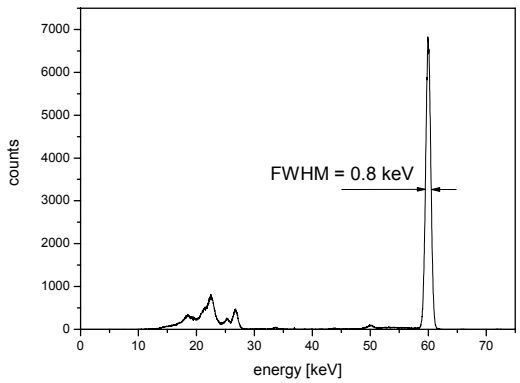


Fig 2. Energy spectrum for ^{241}Am source registered via new read-out board.

Next, measurements of the time difference between trigger and energy signal were performed. Here, the ^{133}Ba source was used. For a single X-ray line, the achieved time resolution is of a few ns.

The board was also used to measure the ^{241}Am energy spectrum with a 16-fold pixel Ge(i) detector. Fig. 3 presents an example spectrum measured by one of the pixels (pixel number 14).

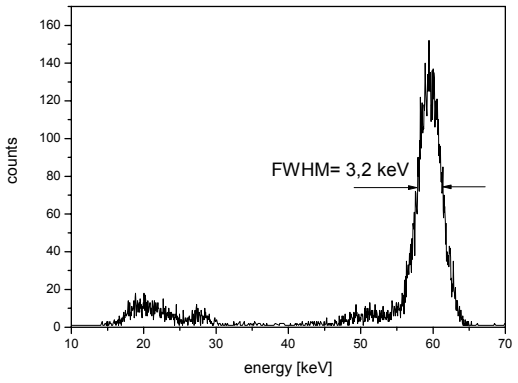


Fig. 3 ^{241}Am energy spectrum registered by one pixel of the 16-fold detector

The designed read-out board along with the prepared software shows excellent energy and time resolution. Moreover, the results point to the possibility of improvement, particularly on the software side. This development is in progress and will be concentrated on multi-dimensional detectors which goes towards precise X-ray tracing.

Acknowledgments

The work presented in this paper was supported by the EU within the contract HPRI-CT-2001-50036 an by I3 EURONS under EC contract No. 506065.

Access to the VME module SAM3, developed and produced by the DVEE division at GSI Darmstadt, is highly appreciated. Here, special thanks are due to J. Hoffmann.

References

[1] Beyer, H.F., Stöhlker, Th., Banaś, D., Liesen, D., Protić, D., Beckert, K., Beller, P., Bojowald, J., Bosch, F., Förster, E., et al., Spectrochimica Acta Part B 59 (2004) 1535

[2] Tachenov, S., Stöhlker, Th., Banaś, D., Beyer, H.F., Fritsche, S., Gumberidze, A., Hagmann, S., Kozhuharov, C., Krings, Th., Ma, X., et al., Scientific Report 2003, GSI Report 2004-1, p. 107.

[3] Gumberidze, A., Stöhlker, Th., Banaś, D., Beckert, K., Beller, P., Beyer, H.F., Bosch, F., Hagmann, S., Kozhuharov, C., Liesen, D., et al., Phys. Rev. Lett. (in print).

[4] Protić, D., Stöhlker, Th., Beyer, H.F., Bojowald, J., Borchert, G., Gumberidze, A., Hammacher, A., Kozhuharov, C., Ma, X., Mohos, I, IEEE Trans. Instrum. Meas. 48 (2001), 1048.

[5] Hoffmann, J., Ott, W., Scientific Report 2002, GSI Report 2003-1, p. 211.

[6] Smith S. W., 1999, The Scientist and Engineer's Guide to Digital Signal Processing, California Technical Publishing, p. 277, p. 297.

ELectron-Ion Scattering in a storage ring (eA collider) – ELISe *

C. A. Bertulani, University of Arizona, Tuscon, USA
L.V. Chulkov, RRC "The Kurchatov Institute", Moscow, Russia
V. Nedorezov, Y. L. Grishkin, A. Turinge, INR-RAS, Moscow, Russia
A. Kelic, K.-H. Schmidt, H. Simon#, GSI, Darmstadt, Germany
G. Schrieder, IKP, TU Darmstadt, Germany
J. Jourdan, D. Rohe, Universität Basel, Switzerland
J. Udias Moinelo, Universidad Complutense, Madrid, Spain
H. Wörtche, N. Kalantar-Nayestanaki, KVI, Groningen, The Netherlands,
for the ELISe collaboration

The ELISe project pages can be found on:
http://www.gsi.de/fair/experiments/elise/

Abstract

The ELISe experiment will be part of the installations envisaged at the NESR for FAIR. It offers worldwide unique opportunities to scatter electrons off exotic nuclei.

Physics opportunities

For all stable nuclei, it has been shown [1] that the central densities are about the same ($\approx$ 0.17 nucleons/fm^3) and that the matter density radius is roughly proportional to the atomic number to the power of minus one-third ($R \sim A^{-1/3}$). The surface thickness (or diffuseness, $a \approx 1$ fm, see Fig. 1) is approximately independent of the mass number A. The spatial proton and neutron distributions have approximately the same form and only differ in magnitude. This is no longer the case for nuclei far from stability where skins ($R_p \neq R_n$ with $a_p \approx a_n$) and halos ($R_p \neq R_n$ with $a_p > a_n$, or $a_n > a_p$) were found. Heavy bubble-like nuclei (strong depression of central density) are also theoretically predicted. A pure electromagnetic probe like the electron allows to measure, with excellent precision, the proton distribution using elastic scattering. Together with elastic hadron scattering (e.g. p,p at medium energies) where only the matter density distribution can be measured, also the neutron density distributions can be extracted.

The determination of charge radii and extraction of nuclear matter radii are crucial for studying the evolution of neutron and proton skins along isotopic chains. For theory, the precise knowledge of the skin thickness is decisive (e.g. [2]) to understand isovector interactions and the symmetry energy. The quantity $R_n - R_p$ is not only related to the symmetry energy but also to the slope of the equation of state (EOS) for neutrons which is proportional to the pressure. Several modern Skyrme Hartree-Fock models using different parameters [3] predict a clear linear and strong dependence between the neutron skin thickness $S = R_n - R_p$ for lead and the slope of the neutron EOS. In ref. [4] the relation of S to several quantities like the nuclear binding energy, the compressibility etc. is studied for a large amount of mean field theories.

The diffuseness parameter reflects the behaviour of the nuclear potential (e.g. spin-orbit) and eigenfunctions at the nuclear surface. It is an important ingredient for computing the asymptotic behaviour of the wave function. This is relevant to understand e.g. hadron-nucleus reactions which are sensitive only to the outer region of the nucleus due to strong absorption. See for example the large differences between the spectroscopic factors measured via *(e,e'p)* and (d,^{3}He) [5].

Since ELISe can measure *elastic form factors* that are not accessible by other means, the diffuseness of charge density distributions will be uniquely determined. The isotopic dependence of higher moments of the charge distributions will also be determined. These are again related to the isovector interaction since the proton density follows the neutron density due to static polarization.

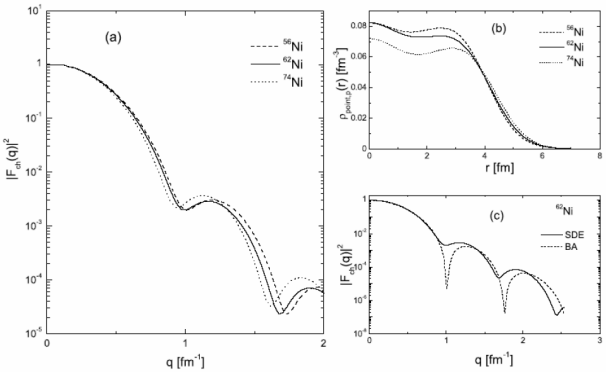


Figure 1: Elastic charge form factor for different Ni isotopes (a), the corresponding point proton distributions (b) and the effect of the Coulomb distortion of the electrons(SDE curve includes it, BA doesn't) on the form factor (c). Taken from ref. [6].

In recent years, experimental and theoretical investigations have been refocused on the nuclear electric dipole (E1) response. The investigations have been stimulated by results of nuclear resonance fluorescence and Coulomb dissociation experiments which yielded a significant concentration of E1 strength below the particle threshold in stable and non-stable nuclei (for a recent overview we refer to [7] and references therein). Besides the implica-

*Work supported by EC under INTAS contract number 03-54-6545
#H.Simon@gsi.de

tions for the r-process nucleosynthesis, where the low-lying strength could significantly increase the neutron capture cross-section [8], there are clear indications that the strength is correlated to the neutron-excess [9] and especially prominent in exotic neutron-rich nuclei. Up to now, however, the isospin character and the structure of the dipole excitations are far from being settled (see e.g. [10]) and the correlation between the differences in the radial neutron-proton density distribution (neutron skin) and the low-lying E1 strength distribution are still speculative. In addition, there are recent theoretical investigations in the framework of the Relativistic Random-Phase Approximation [11], which predict the existence of low-lying E1 transitions also as a fundamental feature of proton-rich exotic nuclei. As an example, results of recent calculations of the electron scattering on the ^{6}He nucleus [12] demonstrates the enhancement of low-energy dipole modes in electron scattering at small momentum transfers. For the nucleus ^{6}He, which is a benchmark nucleus for all theoretical models of two-neutron halo nuclei, the scattering experiments can be realized at the ELISe *eA*-collider. *Transition formfactor measurements* will offer the unique opportunity to study the momentum-transfer dependency of E1 transitions below and above the particle threshold and contribute to pin down their structure by means of their q-dependence.

In addition, *break-up reactions* induced by electron scattering on halo nuclei can reach the order of ten millibarns for 10 MeV electrons and increase logarithmically at higher energies [13]. This means, that information about the continuum structure of weakly-bound nuclei (e.g. scattering lengths and effective ranges) are easily accessible in the electron-ion collider mode.

Nuclear fission is best suited to study the dynamic properties of cold and moderately excited nuclear matter. At low excitation energies, the onset of dissipation in a super-fluid Fermionic system and the influence of nuclear structure on nuclear level densities can be studied. Nuclear fission is also a unique tool to explore shell effects at extreme deformation. The measurement of the $\sigma_{ee'f}$ cross section with well defined momentum and energy transfer provides additional information on the nuclear fission process, e.g., on the multipolarity of the nuclear excitation [14] prior to the decay as well as it allows to study the fission barriers, neutron separation energies, branching ratios of neutron to fission decays and the level density parameter. One can study by this way the dependence of nuclear fissility on the dynamics of nuclear motion (dipole, monopole, quadrupole etc). The advantage of ELISe for fission studies with unstable nuclei, namely the possibility to determine precisely and in a model independent way multipole excitation functions, even when the resonant strength is spread over an excitation range of some MeV, has been already demonstrated for stable uranium isotopes by Th. Weber et al. [15]. Although in e-scattering the isoscalar and isovector resonances are equally excited, the interaction of the electron with the nucleus is well understood. The coincidence between the scattered electron and the fission fragments eliminates the radiative tail of elastic scattering, which in heavy nuclei can overshoot the resonant strength by some orders of magnitude.

The ELISe project offers also the unique possibility to study nucleon-nucleon (N-N) correlations as a function of the proton to neutron ratio in *quasi-free electron scattering* experiments. In symmetric nuclear matter the single particle states are depleted by ≈ 15%. This amount can be found at high missing energy and momentum. In asymmetric matter with neutron excess a larger depletion occurs for protons while for neutrons the occupation probability increases. With ELISe one could measure occupation probabilities for neutron-rich as well as proton-rich nuclei up to an asymmetry of 0.4. The distortion due to final state interaction on medium-light nuclei can be kept under control in parallel kinematics [16]. The identification of the residual system will also allow to perform (e,e'p) experiments from deep shells (as 1s ones) under exclusive conditions and thus a comparison of the spectral response of all the shells of light and medium nuclei in exclusive conditions will be obtained for the first time.

Spectrometer Design

Simulation of the ELISe (electron-ion collider) electron spectrometer [17] consisting of a predeflector system in the NESR in combination with a second vertical dipole stage has been performed for real experimental conditions. The achievable momentum resolution was studied with variable parameters, i.e.:

- initial electron energy (125 - 500 MeV),
- angle of turn of the electrons by the first magnet **a** (70^0 - 90^0),
- mean value H (1.8 - 2.5T) and coefficient of focusing of magnetic field in the second magnet **b**,
- vertical aperture of the first magnet (±1.5 mrad - ±150 mrad),
- length of interaction region for electrons and ions (0.1 - 10 cm),
- coordinate component of the vertical emittance **Δy** of the electron beam (0 - 0.2 mm).

The initial parameters were taken from Report [18]. The studies were calculated for ^{132}Sn ions. The electron tracking inside the magnets was realized using a stepwise integration of the trajectories according to the value of the magnetic field with a minimal step size of 1 mm. The magnetic field inside the first magnet was parameterized using: $H = H_0 \cdot (r/r_0)^{\mathbf{b}}$, were r_0 is the radius of the central electron trajectory in the second magnet, and **b** is the coefficient of focusing while $H_0 = 2.2$ T.

The electron tracking inside the electron spectrometer takes into account the multiple scattering which limits the thickness of the first coordinate detector. The coordinate resolution of these position detectors should be 0.2 mm in order to provide the necessary momentum resolution. Here, the distance between the beam line and entrance of the second magnet was chosen to be 1 m, and the distance from the beam plane to the output from the second magnet equals to 92 cm.

The coordinate detectors in front of the second magnet are assumed to be equipped with 100 micron mylar windows. They can be filled with a argon gas mixture (10mm thickness) with about 1/3 of atmospheric pressure. Their spatial resolution should be about 0.2 mm. Under these conditions the angular uncertainty due to multiple scattering is negligible (much less than 1 mrad), the single plane efficiency is about 70%.

The second coordinate detector at the quasi focus of the second dipole stage, should be operated under atmospheric pressure. The efficiency then is about 98%/plane, keeping the spatial resolution at 0.2 mm.

Simulations show, that using only the position information at the second magnet's quasi focal plane, results to a momentum resolution of only 0.4%, which is not yet enough to distinguish elastic and inelastic scattering. Therefore full tracking through the spectrometer is required in order to achieve the necessary resolutions of 0.01% and 1 mrad in momentum and scattering angle, respectively. As an example, one may take into account the value for the vertical angles β_j at the entrance of the second magnet. If one builds a calibration table of average values $\mathbf{u}(p_i)$ where **u** is the coordinate along the second position detector (stepsize for p_i, electron's momentum, 100 keV/c) for each value of β_j (stepsize of 0.2 mrad), one ends up with 3.75 million elements that are used to interpolate tracks in order to achieve maximum resolution. The final resolution for different momentum ranges is shown in Figure 2. Here the length of the interaction zone of electrons and ions is taken to be 10 cm, the coordinate component of the vertical emittance is 0.087 mm. It can be shown, that the best result corresponds to the case **a** = 90°, **b** = 0.5.

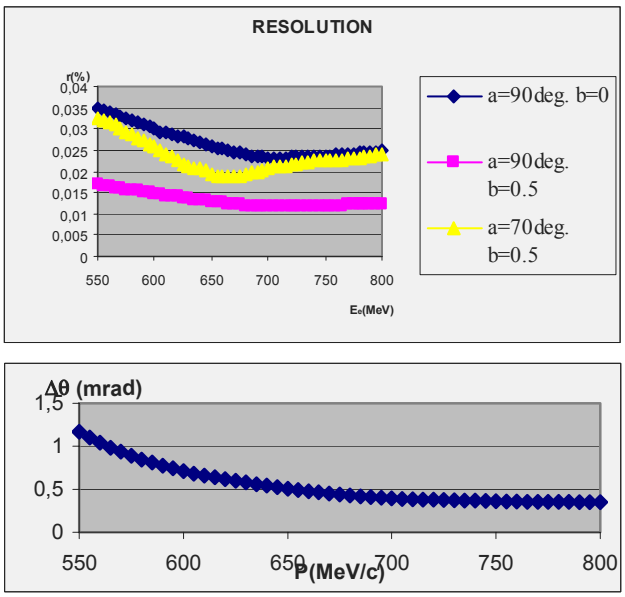


Figure 2: Dependence of the achievable resolution in angle and momentum. For details, see text.

Straw tube prototypes (see Fig. 3) have been build and put into operation at the GSI detector laboratory. They will soon be tested in a test experiment at TU-Darmstadt. They seem to be especially favourable for the first coordinate detector system due to their mechanical properties.

In a separate study, the sources of errors in the luminosity measurements using bremsstrahlung quanta have been investigated. It can be shown, that the luminosity can be reliably determined within a few percent, taking into account realistic offsets of beam and collimation axis, the influence of different ion velocities, and the variations in the absolute position of the interaction zone



Figure 3: Straw tube prototypes: straw thickness 126µm; capton on Al (0.2 µm) covered by C-layer (5 µm). Length = 60 cm; Inner diameter = 7.5 mm. Ar/CO_2 (80/20) atmospheric pressure at 1850 V.

References

[1] R. Hofstadter, Nobel Lectures, available at http://nobelprize.org/physics/laureates/1961/hofstadter-lecture.pdf

[2] F. Hoffmann, C.M.Keil, H.Lenske, Phys.Rev. **C64** (2001) 034314

[3] B.A. Brown, Phys. Rev. Lett. **85** (2000) 5296

[4] R.J. Furnstahl, Nucl. Phys. **A706** (2002) 85

[5] G.K. Kramer, H.P. Blok, L. Lapikás, Nucl. Phys. **A679** (2001) 267

[6] A.N. Antonov, D.N. Kadrev, M.K. Gaidarov, E. Moya de Guerra, P. Sarriguren, J.M. Udias, V.K. Lukyanov, E.V. Zemlyanaya, G.Z. Krumova, Phys.Rev. **C72** (2005) 044307

[7] D. Vretenar, Nucl. Phys. **A751** (2005) 264c

[8] S. Goriely and E.Khan, Nucl.Phys. **A706** (2002) 217; S. Goriely, E. Khan, and M. Samyn, Nucl. Phys. **A739** (2004)331

[9] R.Palit et al., Nucl. Phys. **A731** (2004) 235; P. Adrich et al., Phys. Rev. Lett. **95**, 132501 (2005)

[10] A. Zilges, M. Babilon, T. Hartmann, D. Savran, S. Volz, Prog. Part. and Nucl. Phys. **55** (2005) 408

[11] N. Paar, P. Papakonstantinou, V. Yu. Ponomarev, and J. Wambach, arXiv:nucl-th/0506010

[12] S.N.Ershov, B.V.Danilin, J.S.Vaagen, Phys. Rev. **C72**, 044606 (2005).

[13] C.A. Bertulani, Phys. Lett. **B624** (2005) 203

[14] D.F.Herring, I.C.Nascimento, R.B.Walton et al. Phys.Rev.B139, 3, (1965) 562

[15] Th. Weber et al., Nucl. Phys. A510 (1990) 1

[16] D. Rohe et al., Phys. Rev. Lett. **93** (2004) 182501

[17] Technical proposal (ELISe): http://www.gsi.de/documents/DOC-2005-Oct-93-1.pdf

[18] Conceptual Design of an Electron-Nucleus Scattering Facility at GSI, BINP 2001: http://www.gsi.de/documents/DOC-2004-Nov-111-1.pdf

R&D on Large-Volume Position-Sensitive Si(Li) Detectors

D. Protić, T. Krings, FZ Jülich, Germany
P. Egelhof, GSI, Darmstadt, Germany
E. C. Pollacco, CEA Saclay, France

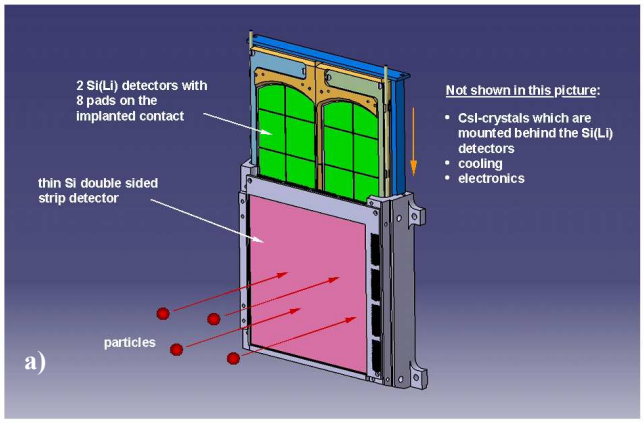
Research and development of large-volume position-sensitive Si(Li) detectors are of great importance for future activities of the EXL-Collaboration.

In the course of the work on large-diameter diodes a serious problem concerning the Li-driftability of the p-type silicon has become more and more apparent. As was feared [1], even relatively thin (4-5 mm) slices of the 5-inch p-type silicon could not be completely compensated even for 4 times longer drifting time. Unfortunately, also some of the 4-inch slices (purchased as Li-driftable p-type silicon) needed prolonged drifting time, especially in their central parts. Now, we are preparing a gettering procedure to eliminate defects inside the starting material that prevent the Li-drift process.

Each position-sensitive structure on our Si(Li) detectors are generally surrounded by an about 5 mm wide guard-ring which prevents the influence of usually high surface leakage current generated on the surface of the Li-compensated region between the detector contacts. Therefore, the area of a guard-ring is practically dead area of a contact surface. Normally, the detector user would like to have the guard-rings as narrow as possible. Concerning only the surface leakage, 1-2 mm wide guard-rings would be a possible solution. But an additional problem has been known since long time: "Surface states" on the Li-compensated region between the contacts distort the normally parallel electric field lines inside a Si(Li) detector. As a result, position and energy information for interactions several mm apart from the edge of the detector contacts could not be correct. Extensive investigations have been undertaken, applying three different methods, to explore the influence of the surface states on the detector response as function of bias voltage, temperature, shaping time constant and the time since the last surface treatment. The first results were presented in [2].

For the experiments at ESR (GSI-Darmstadt) two 7 mm thick Si(Li) diodes with a diameter of 4 inch are under preparation. To relieve the efforts for the first experiments a telescope configuration very similar to that of the MUST II experiment (Saclay, Orsay, GANIL) will be applied, as sketched in Fig. 1. Two Si(Li) detectors equipped with 8 pads on the implanted p^+-contact (the same position-sensitive structure as for the MUST II experiment) will be mounted in a frame which can be inserted in the telescope holder. For illustration, a 5 mm thick Si(Li) detector, under preparation for the MUST II experiment is shown in Fig. 1b.

An important aspect will be the development of UHV-capable detector telescopes for the ESR experiments. All these activities have been partly funded by (R II 3)-EURONS program, contract No. 506065.



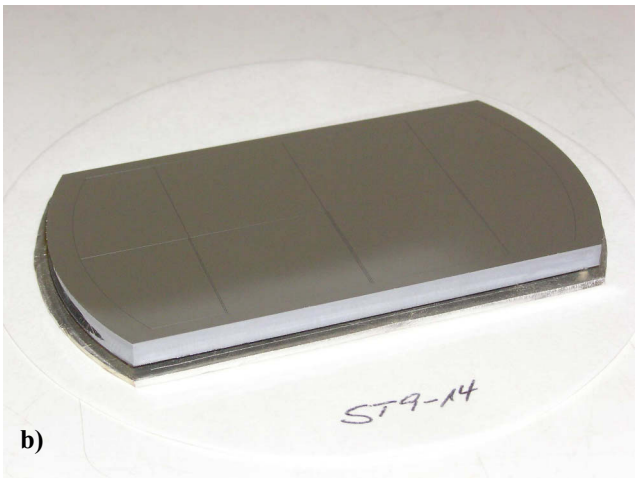


Figure 1: a) First two detector layers of a MUST II telescope for recoil particles (the sketch was made by the MUST II collaboration). Two Si(Li) pad detectors are mounted in a frame which can be inserted into the telescope holder. b) One of the transmission Si(Li) detectors, about 5 mm thick, with 8 pads on the implanted p^+-contact.

References

[1] Annual report IKP 2004.
[2] D. Protić and T. Krings, "Detection Characteristics Near Edges of Large-Volume Si(Li) Detectors", 10th European Symposium on Semiconductor Detectors, Wildbad Kreuth, 2005.

Simulations for the in-ring spectrometer of EXL

M. Mahjour-Shafiei[1], N. Kalantar-Nayestanaki[2], O. Kiselev[3,4], H. Weick[5], and the EXL Collaboration
[1]Tehran University, Iran; [2]Kernfysisch Versneller Instituut, The Netherlands;
[3]Mainz University, Germany; [4]PNPI, St. Petersburg, Russia; [5]GSI, Darmstadt, Germany

The forward spectrometer of the EXL setup is meant to detect heavy projectile fragments emerging from the gas-jet target [1]. It consists of a cascade of magnetic lenses, which are part of NESR storage ring, and three position sensitive detectors. The first detector is placed at 2 meters away from the target, while the second and third ones are located before and after the third dipole, respectively; for more information see [1].

The simulations of the forward spectrometer are being performed using GEANT4 toolkit [2]. As the first step in the simulations, the geometry of the lenses was created. The interaction of the magnetic fields with charged fragments is described using transfer matrices. Simple implementation and saving CPU time were the main motivations to use transfer matrices instead of direct implementation of magnetic fields. One should note that obtaining the trajectory of projectiles by means of transfer matrices is fair if the life-time of the projectile is much longer than its time of flight inside the lenses.

Since this setup is designed to study exotic nuclei, which are not stable, the decay process was also needed to be included in the `PhysicsList` as well. The decay tables for ions needed for the description of the decay process were obtained from the decay data provided by GEANT4. Fortunately, these decay tables are written in an easy to understand format and can, consequently, be simply edited, if necessary.

Event generation is done by a FORTRAN-based code, called GENBOD [3]. It generates a multi-particle weighted event according to Lorentz-invariant Fermi phase space. The total center of mass energy as well as the number and masses of the outgoing particles are specified by the user. GENBOD then generates momentum vectors of the outgoing particles in the center of mass and gives the weight which must be associated with each event. The momenta of the particles in the exit channel were put in a ROOT tree [4]. In order to feed the events generated by the GENBOD to the simulations, a method capable of opening a ROOT-file and reading in events off a tree was added to the `PrimaryGeneratorAction`.

The data analysis part of the simulation was done by developing and adding a ROOT-based class to save the desired information, for instance the coordinates of fragments at the moment of impact on position-sensitive detectors, in a ROOT tree. The off-line analysis of these data can be done using ROOT software [4], interactively.

In order to compare the response of the spectrometer to light and heavy nuclei, elastically scattered ^{24}F (^{132}Sn) nuclei off a proton target with the incident beam energy of 783 MeV/u (796 MeV/u) were generated by GENBOD and tracked in the simulations. As the simulations reveal, the outgoing ^{24}F reaches the first position-sensitive detector but hardly makes it to the second and third detectors. However, almost 20% of $^{132}Sn^{50+}$ can be detected by the third detector. This has simply to do with the fact that the recoil that ^{24}F receives in the scattering process is big enough to push the outgoing ^{24}F out of the ring before arriving at the second detector. This test implies that, contrary to heavy nuclei, light nuclei with different charge states cannot be distinguished using position sensitive detectors together with the magnetic elements. Moreover, for kinematic reconstruction of events for light nuclei one has to rely merely on information delivered by recoil detectors and there would be no information from the second and third detectors. A typical charge state separation for $^{132}Sn^{50+}$ and $^{132}Sn^{49+}$ ions is shown in figure 1. This work is partially supported by EURONS/EXL project.

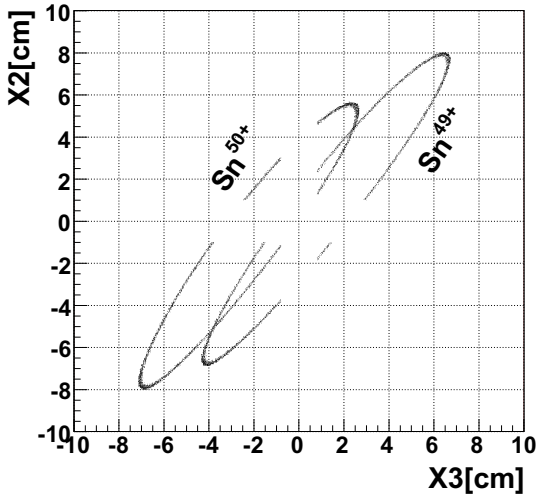


Figure 1: Separation of $^{132}Sn^{49+}$ and $^{132}Sn^{50+}$ obtained with the second and third tracking detectors. The openings in the elliptical-shape rings indicate the space that has to be free of matter for the circulating beam. The vertical (horizontal) axis is the x-coordinate of ion, in the reference plane, detected by the second (third) position sensitive detector.

References

[1] EXL technical proposal; http://www-linux.gsi.de/ wwwnusta/tech_report/05-exl.pdf

[2] S. Agostinelli *et al.*, Nucl. Instr. Meth. Phys. Res. A 506 (2003) 250; http://geant4.web.cern.ch/geant4/

[3] F. James, Monte Carlo Phase Space, CERN 68-15 (1968).

[4] http://root.cern.ch/

Charge-exchange reactions on ^{136}Xe: Gamow-Teller strength distributions*

O. Moreno[1], R. Álvarez-Rodríguez[1], P. Sarriguren[1], E. Moya de Guerra[1,2†]
[1]IEM, CSIC, Serrano 123, E-28006 Madrid, Spain.
[2]Dpto. FAMN, UCM, Ciudad Universitaria, E-28040 Madrid, Spain.

Abstract

We present here theoretical calculations regarding the first experimental test of EXL feasibility at GSI with ^{136}Xe. Our results concern the Gamow-Teller strength distributions of this nucleus, which are directly related to the cross section of charge-exchange reactions. Results on ^{132}Xe isotope have also been obtained for spherical and for stable deformed shapes.

Our theoretical framework starts with an axially-deformed Hartree-Fock mean field with effective two-body Skyrme interactions which includes pairing correlations within BCS approximation. Gamow-Teller excitations are described within QRPA with a spin-isospin residual interaction in the particle-hole (*ph*) and in the particle-particle (*pp*) channels, with coupling constants consistent with the mean field approximation.

We first obtain the Hartree-Fock energy as a function of the quadrupole deformation parameter β using several Skyrme forces for the sake of comparison. For ^{136}Xe a minimum of the energy is found corresponding to a spherical nuclear shape. For this spherical solution we have obtained the GT$^-$ and GT$^+$ strength distributions, which could be extracted, under the appropriate kinematic conditions, from the following charge-exchange reactions:

GT$^-$:
^{136}Xe(p,n)^{136}Cs; ^{136}Xe(^{3}He,^{3}H)^{136}Cs; ^{136}Xe(d,2n)^{136}Cs

GT$^+$:
^{136}Xe(n,p)^{136}I ; ^{136}Xe(^{3}H,^{3}He)^{136}I ; ^{136}Xe(d,2p)^{136}I

Fig.1 shows GT$^-$ and GT$^+$ strength distributions for a spherical nuclear shape using Sk3 Skyrme force. Discrete, gaussian-folded and accumulated strength distributions are included up to an excitation energy of the residual nucleus of 20 MeV.

Calculations of cross sections as well as results of calculations for other isotopes are under way and will be presented in our next report.

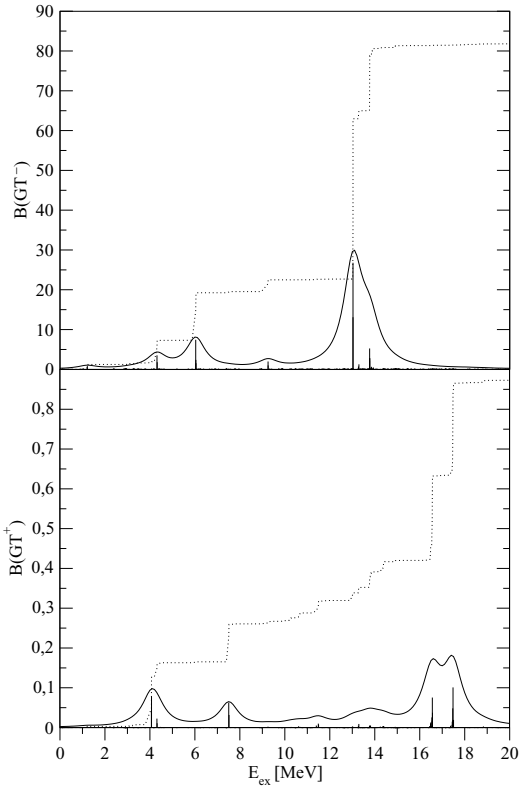


Figure 1: ^{136}Xe GT$^-$ and GT$^+$ strength distributions a) discrete b) folded (—) and c) accumulated (····). Results are obtained for the spherical ground state using Sk3 Skyrme force and fixed pairing gap.

* Work supported in part by European Commission R113-EURONS-506065.
† elvira.moya@iem.cfmac.csic.es

Decay Spectroscopy (DESPEC)

B. Rubio[1], Zs. Podolyák[2], P.J. Woods[3], M. Górska[4], J. Gerl[4], for the DESPEC collaboration
[1]CSIC-University, IFIC, Valencia, Spain; [2]University of Surrey, Surrey, UK; [3]Edinburgh University, Edinburgh, UK; [4]GSI Darmstadt.

Abstract
The access to the first structure information of the most exotic nuclei will be possible with the implantation of radioactive beams from the Super-FRS into an active stopper detector. The subsequent α, β, γ, proton and neutron decays of those species will be measured with a compact multi task array. The main objective of DESPEC (Decay Spectroscopy) are the doubly magic nuclei placed at the extremes of the chart of nuclides, as ^{100}Sn, the new magic numbers and shell evolution for the very neutron rich isotopes e.g. ^{122}Zr, and exploration of astrophysical r- and rp- process paths.

Physics focus

Decay studies lie at the frontier of our understanding of nuclei far from stability, since once the existence of an isotope has been demonstrated, the next elementary piece of information we seek is how it decays. Experiments can be performed with very high sensitivity and key physics information such as particle decay branching ratios, half-lives, first excited states, isomeric decays can be gleaned from a relatively small number of events. The Super-FRS system will allow the fast, efficient transportation of short-lived ($t_{1/2}$>100ns) exotic nuclei, with clean in-flight ion identification. On the other hand the intense beams provided by the Super FRS will allow complete decay studies where not only delayed particle and gamma emission branching ratios can be extracted but also detailed spectroscopic information, such as ß-strength functions, nuclear moments and spins as well as electro-magnetic transition probabilities. Decay studies will be vital for the first insights into the evolution of shell structure towards the neutron drip line. This is of particular importance for the mass regions before and after the classical magic neutron numbers 50, 82 and 126 where phase transitions may occur associated with new magic numbers. This is a key issue for both nuclear structure and astrophysics. Measuring the β -decay of ^{110}Zr and the heavier isotopes towards ^{122}Zr would be a key test of N=82 shell quenching and the predicted development of new shell gaps very far from stability. The interplay between explosive astrophysical scenarios (novae, X-ray bursters etc.) and the properties of exotic nuclei is in evidence on the proton-rich side of stability. Waiting point nuclei created by the proton drip-line could be explored by the β -decay half-lives, β-delayed proton emission, 1 and 2-proton radioactivity measurements. There is a great interest from the scientific community working in theory in these exotic decay modes. At the neutron rich side the FAIR Super-FRS will provide access to regions where the waiting points for the r-process nucleo-synthesis of heavy elements occur.The ground and low excitation energy properties of the nucleus can be studied using α decay, a very good example is the triple shape co-existence of 0+ states in neutron-deficient Pb isotopes. Of particular interest is the exploration of nuclear structure around doubly-magic ^{100}Sn where very high α -decay reduced widths are found, and more specifically of the alpha decay of ^{104}Te with an expected lifetime in the range of 10-100 ns. Increased particle yields will also enable a first high precision β -decay study of ^{100}Sn. Isospin symmetry can be tested in studies of the β -decays of mirror nuclei, and β -decays provide a tool for exploring the strength of T=0 and T=1 pairing effects in nuclei.

Instrumentation

The radioactive species to be studied will be delivered as beams by the energy buncher of the Low Energy Branch of the Super-FRS. The DESPEC set-up will comprise Si based implantation and decay detectors, a compact Ge array, neutron detectors, fast BaF_2 detectors, a total absorption spectrometer and equipment for g-factor and quadrupole moment measurements. In most of the experiments within this project the implantation prior to the decay will involve an active DSSD system to correlate in time and space the implanted ions with the subsequent decay in the case of charged particle emission Such system will require high resolution, both for signal to noise discrimination and because the physics (eg 2p decay studies) demands such precision to compare with theory. In nearly all of the setups it will be sensible to incorporate high efficiency and highly segmented Ge detectors in close-packed geometry around the active stopper for the ions. The segmentation is necessary to compensate for the gamma flash and for ray tracing capability in the case of isomeric decays where correlations with the implanted position are difficult. In order to avoid the “Pandemonium effect” (caused by the low efficiency of Ge detectors at high gamma-ray energies) in decay studies with high Q values and large beta-delayed gamma branching ratios, complementary measurements with a Total Absorption Spectrometer are foreseen. An important task will be the development of modern high efficiency neutron detector arrays for measurements of beta delayed or direct one or two neutron emitters. Complementary measurements of electromagnetic transition probabilities based on levels half life measurements will be possible with the fast timing technique using BaF_2 detectors and dedicated electronics. Electromagnetic moments of isomeric states will be measured using the TDPAD method.

The varied nature of these experiments indicates a flexible, modular detector system optimally adoptable to the requirements of individual experiments.

Simulations of possible Ge arrays for the DESPEC setup at FAIR

A. Algora[1*], A. Jungclaus[2], L. Caballero[1], B. Rubio[1], J. L. Tain[1], J. Gerl[3] for the DESPEC Collaboration
[1]IFIC,CSIC-Univ. Valencia, Spain; [2]Univ. Autónoma Madrid, Spain, [3]GSI, Germany

At the Low Energy Branch of the future FAIR facility, the fragmented beams from the Super-FRS are slowed down in energy or completely stopped. One of the experiments proposed at this branch is DESPEC (decay spectroscopy) where studies of the decay of short-lived nuclei, either in their ground state or in an isomeric state are planned.

The ions at some tens of MeV/u will be deeply implanted in an active stopper; a highly pixellated Si detector which allows correlating in time and space the signal from the implanted ion with the subsequent signal produced by the β in case of β-decay. This detector together with gamma-ray and neutron detectors arranged in a compact geometry around the stopper are the heart of the experimental setup.

The present report deals with the simulations for the Ge array. For the moment the collaboration is considering two possibilities. The first one is to use an array of planar Ge detectors specifically designed to fulfill the DESPEC requirements. The other alternative is to use more standard segmented Ge detectors of EXOGAM [1] or TIGRESS [2] type. The R&D phase requires the realization of Monte Carlo simulations in order to determine the optimal and most cost-effective setup for the future facility.

The "planar setup" consists of an array of 24 composite planar detectors (see Fig. 1 for a schematic view). The detector unit is a stack of three planar Ge detectors with dimensions $72 \times 72 \times 22\ mm^3$. Each planar has a guard ring of 2 mm, which leaves an active Ge volume of $68 \times 68 \times 22$ mm^3. The distance between the planars is 3 mm and the stack is encapsulated in an Al capsule of 1.5 mm thickness. They are situated around a focal plane of $24 \times 8\ cm^2$ surface.

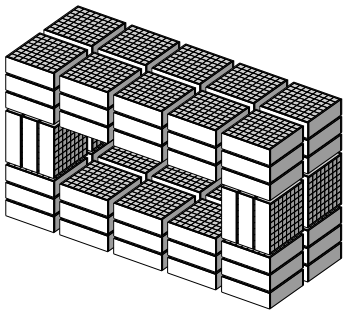


Figure 1: Schematic view of the planar setup. Each detector unit is an stack of three segmented planar detectors.

The "CLOVER" setup is an array of 6 CLOVER detectors of the EXOGAM type. Each detector consists of four co-axial n-type Ge crystals arranged in the configuration of a four-leaf clover and housed in the same cryostat. The individual crystals considered are 60 mm diameter and 90 mm long before shaping. In this setup the detectors were positioned in an annular arrangement around the focal plane. Four CLOVER detectors are facing the longer side of the focal plane (two detectors on the top, two detectors on the bottom), while the other two detectors face the shorter sides of the focal plane.

The two described geometries have been implemented using the Monte Carlo code GEANT4 [3]. In this framework, we have studied the detection efficiency of the two setups either for point-like or extended monoenergetic sources. In Table 1 the results for the two "standard" setups are presented for centered point-like sources. The quoted peak efficiencies correspond to the sum of the individual detector efficiencies of each setup.

As part of our study, efficiencies have been also calculated for other possible geometrical arrangements with more detectors (8 CLOVER detectors), and for a focal plane of $8 \times 8\ cm^2$. The possibility of an arrangement that can be optimal to couple with neutron detectors has been also considered. The next step of our work will be the study of the performance of tracking algorithms for the different setups as well as their γ-imaging efficiency.

Table 1: Calculated efficiency (%) of the studied setups.

Energy	Eff. planar setup		Eff. clover setup	
(MeV)	(Peak)	(Total)	(Peak)	(Total)
0.10	48.4	53.7	36.4	46.3
0.25	34.5	57.4	30.7	46.2
0.50	21.0	55.6	23.5	43.6
1.00	13.3	50.3	18.0	40.7
2.00	8.9	44.5	12.9	36.6
5.00	4.1	39.6	7.1	32.8
10.00	1.8	36.7	4.0	28.7

References

[1] http://www.ganil.fr/exogam/

[2] H. C. Scraggs *et al.*, Nucl. Inst. and Meth. A543 (2005) 431

[3] S. Agostinelli *et al.*, Nucl. Inst. and Meth. A506 (2003) 250; http://wwwasd.web.cern.ch/wwwasd/geant4/geant4.html

* on leave from MTA ATOMKI, Debrecen, Hungary

LASPEC – A setup for laser spectroscopy at the low energy beamline at FAIR

W. Nörtershäuser, GSI Darmstadt & Johannes Gutenberg-Universität Mainz, Germany
P. Campbell, University of Manchester, UK
and the LASPEC Collaboration

Laser spectroscopy of radioactive isotopes is an efficient and successful approach for the determination of nuclear ground state properties, which can also be applied to isomers that have lifetimes exceeding a few ms [1]. Hyperfine structures and isotope shifts in electronic transitions exhibit readily accessible information on the nuclear spin, magnetic dipole and electric quadrupole moments as well as root-mean-square charge radii. The nuclear parameters measured by optical techniques are extracted in a manner that is completely free of any nuclear model dependency. They provide vital information on both bulk and valence nuclear properties at the limits of stability with exceptional sensitivity to changes in nuclear deformation.

At FAIR the Super Fragment Separator (S-FRS) will provide a rich spectrum of isotopes that are not and will not be available at any other facility. From the view of optical spectroscopic research the proposed facility will afford unique access to regions of particular nuclear interest that would otherwise remain inaccessible, including the study of isotopes of refractory elements, high-K isomers and a vast region of heavy, neutron-rich isotopes.

The LASPEC collaboration has designed a laser spectroscopic station that will receive beams from the Low-Energy Branch (LEB) ion catcher at FAIR and will be capable of matching, in its spectroscopic capabilities, the universal production of the S-FRS. We have combined specialized spectroscopic techniques into one compact and multi-functional laser spectroscopy station, which is shown in Fig. 1. A full description of the setup, its function and costing is detailed in the Technical Design Report which was delivered in 2005.

The station consists of two beamlines of which one will allow the neutralization of an incoming ion beam in a charge exchange cell to form a fast beam of neutral atoms, while the other one is optimized for collinear spectroscopy of ion beams. Collinear laser spectroscopy on ions and atoms was performed with production rates as few as 100 ions per second [2] and has been the workhorse for high-precision laser spectroscopy on short-lived isotopes for many years. Bunched and cooled beams will be delivered by an RFQ cooling and bunching station that will be jointly designed and operated with the MATS collaboration. Similar devices are already in operation, *e.g.*, at ISOLDE and Jyväskylä.

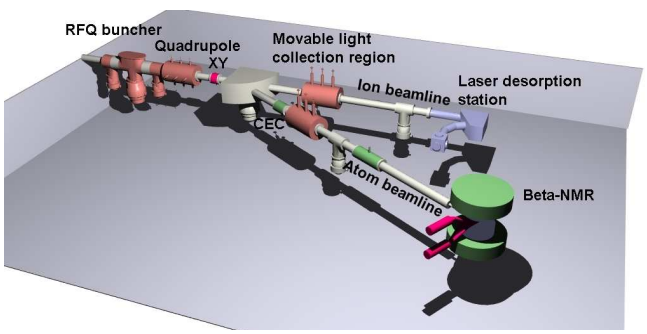


Fig. 1: The LaSpec laser spectroscopic station

At the end of the ion-beamline the beam can be stopped inside a target and then desorbed with a laser pulse to provide thermal atoms that can be detected and studied using resonance ionization spectroscopy (LD-RIS). When used in conjunction with Time-Of-Flight (TOF) and decay-tagged photo-ion detection an extremely sensitive spectroscopy can be achieved, able to detect signals with production rates as low as a few atoms per second [3]. The fast atom beamline will allow collinear laser spectroscopy on neutral beams, optical pumping and -NMR, a well-established technique that is able to deliver nuclear moments with far higher accuracy then those obtained from standard laser spectroscopy [4].

Besides laser spectroscopic work at this station, the collaboration aims to implement a laser resonance ionization ion source (RILIS) at the FAIR facility's Low Energy Branch gas-stopper. The RILIS will add to the selectivity inherent in the production method of the S-FRS and ion catcher device and will be used to enhance the production of isotopic (or even isomeric) enriched or pure ion beams. The type of RILIS that will be used depends critically on the choice of ion-catcher. At present both a gas-filled stopper cell and a superfluid helium catcher (as demonstrated by Huang and colleagues [5]) are being considered.

Currently, the LaSpec collaboration continues with the development of new laser spectroscopic techniques, a few of which will be presented in this annual report, namely the development of a laser ion source trap (LIST, K. Wies *et al.*), the application of optical pumping in the RFQ buncher to manipulate atomic sub-states to those optimal for high-resolution laser spectroscopy (P. Campbell *et al*.) and the development of an on-line Paul-trap for laser and sympathetic cooling of rare isotopes (Ch. Geppert *et al*.)

References

[1] E.W. Otten, *Nuclear radii and moments of unstable isotopes*, in Treatise on heavy-ion science, D.A. Bromley (Ed.) (1989) 517.
[2] P. Campbell *et al*., Phys. Rev. Lett. 89 (2002) 082501.
[3] V. Sebastian, Dissertation, Johannes Gutenberg - Universität: Mainz (1999).
[4] R. Neugart, Hyperf. Int. 127 (2000) 101
[5] W.X. Huang *et al*., Europhys. Lett. 63 (2003) 68.

First ion pulses out of a laser ion source trap*,°

K. Wies[1], K. Blaum[1,2], K. Brück[1], C. Geppert[1,2], H.-J. Kluge[2,3], W. Nörtershäuser[1,2], G. Passler[1], S. Schwarz[4] , K. Wendt[1]
[1]Universität Mainz, Germany [2] GSI Darmstadt, Germany
[3] Universität Heidelberg, Germany [4]MSU, East Lansing, USA

Resonance ionization laser ion sources (RILIS) are applied for the production of exotic ion beams with high isotopic and isobaric purity [1], limited only by surface ionization of unwanted atomic species. A new type of resonance ionization laser ion source is presently being deve-loped and tested at the RISIKO mass separator at Mainz University [2] for future use at on-line radioactive ion beam facilities. For highest isobaric selectivity, this RILIS approach [3] decouples the evaporation and ionization region by a combination of atomizer - ion repeller - ion cooler and trap, which is operated together with a titanium:sapphire (Ti:Sa) laser system [4].

The central part of this laser ion source trap (LIST) approach is a segmented and gas-filled radio-frequency quadrupole (RFQ) structure. A cross section through the atom source-repeller-trap combination is shown in Figure 1 togther with a typical potential distribution applied for trapping.

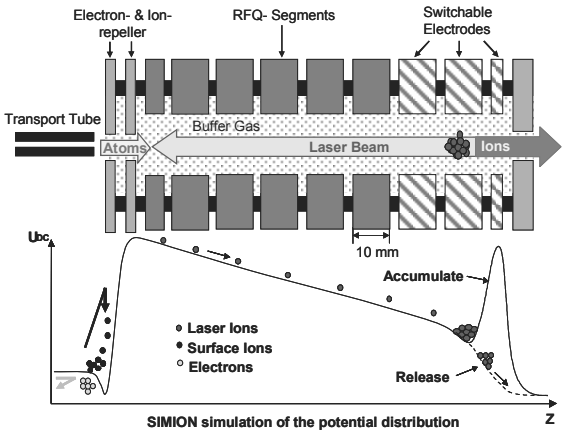


Figure 1: Working principle and potential distibution of the repeller trap system.

The atoms are delivered through the transport tube from the location of evaporation, the latter acting as an atomic beam source. Two repeller electrodes serve for suppression of electrons and unwanted surface ions from the source. Each of them has an aperture diameter of 6 mm and a thickness of 2 mm. The RFQ rods have a length of 96 mm and consist of nine segments. The free field radius between opposite rods is 12 mm. The last three electrodes are switchable to open and close the trap. A final electrode with an inner diameter of 6 mm and a thickness of 5 mm shields the internal of the trap against the acceleration field of the isotope separator. The RF-frequency used is set to ν_{RF} = 1 MHz with an amplitude of up to U_{RF} = ±200 V. DC-voltages on the order of up to 100 V are supplied for the longitudinal storage field and the repelling electrodes. Atoms inside the trap are exposed to laser light and element-selective excited and ionized. For cooling of the ions, helium (He) buffer gas is used.

First operational tests of the laser ion source trap LIST have been carried out using stable Ga, Ca and Ni isotopes. Figure 2 shows a trapped but uncooled Ca ion pulse (dotted line) as well as a trapped and cooled bunch (solid line).

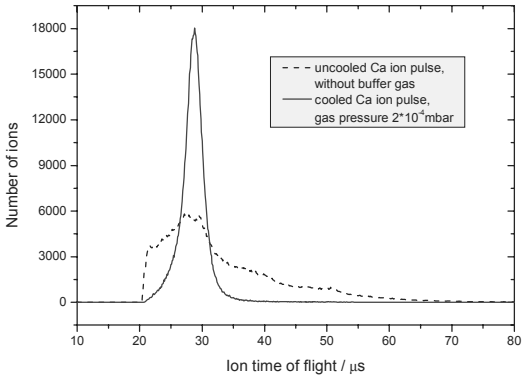


Figure 2: Trapped Ca ion pulses with and without buffer gas cooling.

The cooling effect of the helium buffer gas is obvious. The pulse width of the ion pulse is significantly reduced down to about 3.5 µs FWHM resulting in a narrow Gaussian like time profile. The cooled ion pulse contains 75 % of the ions from the initial uncooled pulse. No measurable background due to surface ionization was observed in Figure 2. During these tests, the laser system was operated at a repetition rate of 7 kHz. Reasonable cooling has been obtained for accumulating and storing ions created within 10 laser pulses and skipping the succeeding 10 laser pulses for proper cooling of the trapped ions. With a He gas pressure of $5 \cdot 10^{-4}$ mbar, storing ions created in 6 laser pulses and operating the trap at 350 Hz, the pulse width of the cooled Ca ions was further reduced down to 1.4 µs. Specification measurements with Ca ions demonstrated a maximum loading capacity of the trap of $4 \cdot 10^{6}$ ions per cooling cycle.

References

[1] U. Köster et al., Spectrochim. Acta 58B (2003), 1047
[2] K. Wendt et al., Radiochim. Acta 79 (1997), 183
[3] K. Blaum et al., NIM B 204 (2003), 331
[4] J. Yi et al., Jpn. J. Appl. Phys. 42 (2003), 5066

*Work supported by BMBF Mz 179
°Supported by EU/FP6 EURONS (see Annex)

Optical pumping in an RF cooler buncher*

P. Campbell, University of Manchester, for the
Birmingham - Jyväskylä - Helsinki - Manchester members of the LaSpec collaboration, FAIR, GSI

The Super-Fragment Separator, S-FRS, at FAIR will have a production capability unparallelled in Europe. The device will be able to deliver exotic nuclear isotopes and isomers, of any chemical element, well beyond the limits of all present facilities. The gas stopper of the low energy branch of FAIR will be used to slow and thermalize these reaction products and, in doing so, prepare them for laser spectroscopic study. The LaSpec collaboration, who will perform these studies, must match their spectroscopic capabilities to the facilities universal production abilities in order to fully exploit the opportunities afforded. We report here on the progress of one of the developmental projects aimed at providing spectroscopic access to elements which are presently inaccessible or prohibitively challenging.

Although multi-functional, the LaSpec station at FAIR will use the collinear beams technique as the workhorse for the majority of its research. In the technique an atomic or ionic beam is overlapped with a collinear beam of counter-propagating laser light and, for fluorescence observation, a length of the overlap region is imaged onto a photomultiplier. The cooling and bunching of radioactive beams possible at FAIR permits a highly efficient and low background variant of collinear laser spectroscopy to be performed [1]. In this variant the signal from the photomultiplier is gated and only opened as an ion bunch traverses the interaction region. The bunching of the ion beam allows fluorescent photons to be counted at a greatly reduced background (which is otherwise dominated by a continuous non-resonant scattering of photons from the laser beam).

For ionic spectroscopy the cooling and bunching of the reaction products limits the optical spectroscopy to transitions from the electronic ground state (with all other atomic metastable state populations relaxed during the beam preparation). The laser excitation frequency, electronic spin, hyperfine structure and transition strength are thus limited and often one or more of these parameters is not optimal, or for some elements, fatally restricted. At JYFL, Jyväskylä, UK-Finnish members of the LaSpec collaboration are developing methods for the preparation of cooled and bunched ionic beams in states other than the ground state. The collaboration have now succeeded in efficiently manipulating state populations in ionic ensembles using optical pumping within an RF cooler buncher.

Figure 1 shows two resonance fluorescence spectra observed in the singly charged yttrium ion (using a continuous 1 pA flux of ions). For both spectra the optical transition is excited from the same metastable state and the effect of optical pumping in the cooler buncher can be observed. During the acquisition of the spectrum labelled 'TiSa on' $\sim$ 200 mW of 363.3nm light from a pulsed titanium-sapphire (Ti:Sa) laser illuminated the thermalisation axis of the cooler. Population transfer is observed at a level that remains constant while the ion beam is bunched. The fluorescent intensity is likewise constant, unlike that from unpumped ensembles which decreases to zero as the relaxing metastable population is held in the cooler.

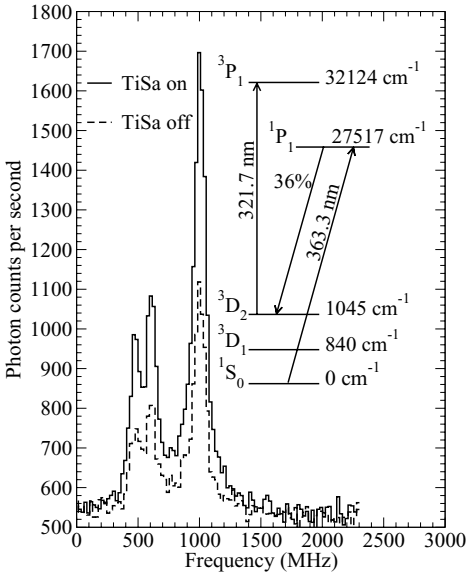


Figure 1: Fluorescence spectrum of cooled $^{89}Y^+$. The optical transition is excited from the second metastable state of Y^+ and the effect of laser optical pumping is shown.

The ability to manipulate state populations using broad bandwidth pulsed lasers is intended to greatly extend the prospects for collinear laser spectroscopy at FAIR. The pulsed lasers used for the state manipulation can readily access a far greater range of wavelengths, via harmonic generation, than that possible with the high-resolution single mode lasers used in the collinear spectroscopy. It is thus possible to use pulsed lasers to manipulate the ionic state and populate levels from which transitions suitable for single mode CW lasers can be studied. The choice of transition can then be optimised and for many elements previously impossible investigations can then be made.

References

[1] A. Nieminen *et al.*, Phys. Rev. Lett. 88 (2002) 094801

* Work supported by EPSRC, Academy of Finland and FP6 EURONS

Setup for a Charge Radius Measurement of the Beryllium Halo Nuclei *

C. Geppert[1,4], G. Ewald[2], H.-J. Kluge[1,3], N. Miski-Oglu[1,4], W. Nörtershäuser[1,4], R. Sánchez[1], F. Schmidt-Kaler[5], D. Tiedemann[1,4], C. Zimmermann[2]
[1]GSI Darmstadt [2]University Tübingen [3]University Heidelberg
[4]University Mainz [5]University Ulm

Although light nuclei with extraordinary large nuclear matter radius are known since the eighties of the last century [1,2], charge radii of such halo isotopes have been determined in a series of laser based high precision measurements just during the last three years. The charge radii of the neutron-rich helium isotopes ^{6}He and ^{8}He are studied in a magneto-optical trap at the Argonne National Laboratory [3], while the charge radius of ^{11}Li has been successfully determined with two- photon spectroscopy by the ToPLiS group from GSI [4 and Sanchez *et al*. in this annual report].

A new experiment aims to measure the charge radius of the Beryllium halo nuclei. ^{11}Be with a lifetime of 13.6 s is the prototype of a one-neutron halo, while ^{14}Be ($t_{1/2}$ = 4.8 ms) is assumed to be a four-neutron halo. Some properties of the beryllium isotopes are listed in Table 1. The charge radius of the halo nuclei is determined by high-resolution measurements of the isotope shift. For these light nuclei a theoretical prediction of the mass shift contribution with adequate precision is required as input parameter. Up to now this can only be provided for two- or three-electron systems [5] and thus the study of the beryllium charge radius has to be carried out on the singly charged positive beryllium ion. Calculations of the mass shift contributions for all beryllium isotopes in the $2s_{1/2} - 2p_{1/2}$ transition are currently performed [6].

The proposed setup for the new experiment consists of a rather compact vacuum chamber system and a dedicated laser system, which has to be transferred to an on-line facility with sufficient beryllium yields. At the current stage it is planed to adapt this setup at the trap experiments at ISOLDE, CERN. A beryllium ion beam from the on-line laser ion source will be accumulated and cooled at the ISOLTRAP buncher [7], extracted and focused by adapted ion optics into a linear Paul trap. Inside the trap the velocity of the low-energy ions will be further reduced by laser cooling with the second harmonic of a continuous wave dye laser at 626 nm. A second dye laser will be used for the spectroscopic study on the $2s_{1/2} - 2p_{1/2}$ transition. For precision laser wavelength control a frequency comb will be used. Detection of the fluorescence in the trap will be provided by a photomultiplier system. At present an off-line setup of the suggested experiment is assembled at GSI and the institute for nuclear chemistry at the University of Mainz. There, stable beryllium ions will be provided by non-resonant laser desorption from a beryllium foil with a low-repetition rate nitrogen laser. This has been successfully tested recently. Off-line tests shall provide the ideal ion trap parameters, increase the trapping and single ion detection efficiency as well as help to eliminate systematic effects and uncertainties on the isotope shift measurement.

This trap and laser cooling development is also performed with respect to other applications. Once cold beryllium ions are stored in the trap, other ion species can be injected and sympathetically cooled, removing the necessity to develop laser systems for direct laser cooling of such systems. This will provide efficient laser spectroscopy of rarely produced radioactive ions and might be applied at SHIPTRAP for the spectroscopy of heavy and super-heavy elements or at the LaSpec setup at FAIR's low-energy beamline. Moreover, the laser system will also be used for cooling of beryllium ions in the RETRAP Penning trap setup to sympathetically cool highly charged ions, which are delivered from the HITRAP facility. At RETRAP, cold highly-charged ions will allow precision tests of QED in strong electric and magnetic fields as well as studies of the nuclear magnetization distribution (Bohr-Weisskopf effect).

Table 1: Spins, half-lifes, matter- [2] and charge radii [8] of known beryllium isotopes.

Isotope	I	$T_{1/2}$	R_{rms}^{matter} [fm]	R_{rms}^{charge} [fm]
^{7}Be	$3/2^-$	53d	2.33 (2)	?
^{9}Be	$3/2^-$		2,38(1)	2,52(1)
^{10}Be	0^+	1,6 My	2.28(2)	?
^{11}Be	$1/2^+$	13,8 s	2,71(5)	?
^{12}Be	0^+	21,3 ms	2,57(5)	?
^{14}Be	0^+	4,4 ms	3,11(38)	?

* Supported by EU/FP6 EURONS (see Annex)

References

[1] I. Tanihata, H. Hamagaki, O. Hashimoto *et al.*, Phys. Rev. Lett. 55, (1985) 2676.
[2] I. Tanihata, T. Kobayashi, O. Yamakawa *et al.*, Phys. Lett B 206, (1988) 592.
[3] L.B. Wang, P. Müller, K. Bailey *et al.*, Phys. Rev. Lett. 93 (2004) 142501A.
[4] R. Sanchez, W. Nörtershäuser, G. Ewald *et al*., PRL 96 (2006) 033002.
[5] Z.-C. Yan and G.W.F. Drake, Phys. Rev. A 66 (2002) 042504, Phys. Rev. Lett. 91 (2003) 113004.
[6] Z.-C. Yan, priv. comm. (2005)
[7] F. Herfurth, J. Dilling, F. Kellerbauer *et al.*, Nucl. Inst. Meth. Phys. Res. A 469 (2001) 254
[8] J.A. Jansen, R. T. Peerdeman, and C. De Vries, Nucl. Phys. A 188 (1972) 337.

The HISPEC Project

J. Gerl, GSI, Darmstadt, Germany; J. Jolie, Univ. Köln, Germany; W. Korten, CEA, Saclay, France and Zs. Podolyák, Univ. Surrey, UK for the HISPEC/DESPEC collaboration

Abstract

HISPEC (High-resolution in-flight spectroscopy) deals with a versatile, high resolution, high efficiency spectroscopy set-up to address questions in nuclear structure, reactions and astrophysics using radioactive beams from the Super FRS with energies of 3-150 MeV/u. The radioactive beams will be used for γ-ray, charged particle and neutron spectroscopy. The HISPEC set-up will comprise beam tracking and identification detectors placed before and behind the secondary target, the AGATA Ge array, charged particle detectors, a plunger, a magnetic spectrometer and other ancillary detectors.

Physics focus

The HISPEC (High-resolution in flight spectroscopy) project [1] is part of the NUSTAR facility. It shares the common goals of attempting to understand nuclear structure and nuclear reactions and related questions in nuclear astrophysics

Due to the large overlap in physics, instrumentation and participants HISPEC and the DESPEC work jointly together.

Detailed spectroscopic information can be deduced by γ-ray spectroscopy in reactions of secondary beams at intermediate energies of several tens to ~100 MeV/u. Thick targets, of the order of several 100 mg/cm^2, can be used and relevant cross sections are of the order of 0.1 barn. Thus, experiments are feasible with modest beam intensities. Examples of type of measurements to be performed within HISPEC are given below.

Nuclear collectivity

Projectile Coulomb excitation in heavy ion collisions at beam energies of 40 MeV/u to 100 MeV/u can deliver accurate B(E2) values for states excited in a one-step process. Measurements of this type allow mapping the evolution of nuclei over the full range of structural dynamics from single-particle to deformation degrees of freedom. Islands of octupole deformations or of other multipolarity can be accessed by the same method. At the proposed facility, the region of nuclei with large neutron excess between the N = 50 and N = 126 shells, will be accessible for the first time.

High-spin states

The population of high-spin states in fragmentation reactions is a very novel concept that just starts to be understood and exploited. The process of multi-nucleon knockout in a fragmentation reaction leaves the residual nucleus in a highly excited state with considerable angular momentum. This opens up the spin degree of freedom for structure investigations.

Nuclear moments

Another unique feature of intermediate-energy reactions concerns the atomic charge state of the fragments. Choosing the appropriate kinetic energy, hydrogen-like and few-electron ions will emerge from the reaction target. In heavy ions extraordinary strong hyperfine fields will thus arise. These can be utilized for the measurement of nuclear moments of short-lived excited states, which enables to determine specific nucleonic (proton/neutron) components of the nuclear wave functions as well as nuclear shapes. The technique used for lifetimes in the range of 10^{-12} s is projectile Coulomb excitation in combination with strong transient magnetic hyperfine fields and electric field gradients. Precessions of the nuclear moments are observed in measurements of particle-γ-angular correlations. For the detection of quadrupole precessions, sufficient polarization of the nuclear state is provided by the Coulomb excitation process.

Instrumentation

Generally, the set-up will be similar to the RISING experiment [2], taking advantage of all the experience gained with this first generation in-flight spectroscopy system.

The set-up is aiming at complete spectroscopy of the particles and gamma rays which are emitted, as well as event-by-event identification of the nucleus of interest.

The following detector systems will be used for the HISPEC experiments.

- Detectors for beam tracking and particle identification.
- The AGATA [3] gamma-ray spectrometer.
- Devices for precision lifetime measurements (plungers, BaF_2 arrays).
- Charged-particle Si detector arrays optimized for reaction and structure studies.
- TOF-dE-E detector system for particle identification after the secondary target.
- A large acceptance magnetic spectrometer with “tagging” detectors in the focal plane.

References

[1] www.gsi-linux.de/~wwwnusta/tech_report
[2] H.J. Wollersheim et al., NIM A 537 (2005) 637.
[3] "AGATA Technical Proposal", ed. J. Gerl, W. Korten., GSI Darmstadt 2001

Beam particle detection in HISPEC

J. Gerl, GSI, Darmstadt, Germany; J. Jolie, Univ. Köln, Germany; W. Korten, CEA, Saclay, France and Zs. Podolyák, Univ. Surrey, UK for the HISPEC/DESPEC collaboration

Abstract

The beam particle detectors of the HISPEC (High-resolution in-flight spectroscopy) set-up need to determine position and direction as well as nuclear charge and mass. They will be placed before and behind the secondary target. A rate capability of 10^7 p/s, a time resolution of < 100 ps as well as a position resolution of < 1 mm is envisaged.

Beam particle detection

HISPEC [1] will use secondary radioactive ion beams from the Super-FRS at a wide energy range from about 3 A·MeV to 150 A·MeV and with masses A > 10. Two sets of particle detectors, for Coulomb barrier energies and relativistic energies, are foreseen.

The incoming ions will pass through beam particle detectors. These will provide on event-by-event basis the position, energy (TOF) and charge (ΔE) of the incoming ion. Identification and tracking of the reaction products will be done with a calorimeter and/or magnetic spectrometer, suitably coupled to similar beam detectors.

Simulations showed that the time resolution has to be <100 ps (FWHM), and the position resolution needs to be <1 mm. Moreover, the detectors should run at rates up to 10^7 ion/s. To avoid excessive energy and angular spread of the incoming particles all detectors need to be very thin and the whole set-up needs to run in vacuum. Velocity will be obtained from TOF on a flight path of 8 m, both before and behind the secondary target.

Work is going on within the NUSTAR collaboration to develop suitable diamond detectors, which are fast and able to give both position and energy loss measurements. Presently the main problem is the limited size. The biggest polycrystalline CVD (chemical vapor deposition) diamond detector (used at GSI) has the following characteristics: time resolution FWHM=70 ps (measured for 650 A·MeV ^{52}Cr), rate >10^7 p/s, thickness 200 μm, area 60×40 mm^2, 1.8 mm × 38 mm strips. The thickness can be reduced by a factor of 10. Energy resolution adequate for nuclear charge determination requires single crystal detectors. Here the size is currently limited to about 10 mm^2 and cost is still prohibitive for large area detectors.

At Coulomb barrier energies very thin detectors (<1μm) must be used. For that purpose it is foreseen to use detectors based on secondary electron emission. These are fast (FWHM~100ps), cover large areas and can give sub-millimeter position resolution [2].

With currently available technologies the tracking at Coulomb barrier energies can be performed at rates of 10^5-10^6 ion/s. This can be done considering the following detectors:

- TOF start detector: scintillator with Δt<100ps
- TOF stop + x,y position: secondary electron detector (mylar foil) with the electron being detected with a gas detector. Δt~300ps, Δx,Δy=1-2mm
- ΔE: an array of 5×5 cm^2 Si strip detectors. ΔE/E<2%.

Simulations for thin target experiments (considering existing VAMOS SED type detectors [2] show that a velocity measurement with a precision of Δv/v=0.4-0.5% can be obtained for ^{19}B and ^{220}Rn ions of E = 5-20 A·MeV and rate 10^6 ion/s. Tests with SED detectors will be preformed at the Universities of Köln and Huelva.

ΔE-E calorimeter

The design for the ΔE-E calorimeter, for experiments at relativistic energies, is based on the experience with the existing calorimeter telescope CATE, used at RISING [3]. The revised design, called Lund-York-Cologne CAlorimeter (LYCCA), will enable event-by-event energy loss, total energy and position measurement, resulting in the determination of both Z and A. At the same time, a second part of the system will be sensitive to light-charged particles produced in the secondary reactions at the target or emitted by the secondary fragments.

LYCCA's design foresees nine Δ*E*-*E* telescopes each consisting of a double-sided silicon strip detector backed by an array of nine CsI elements. Using 32×32-strip double-sided silicon detectors of size 6 × 6 cm^2 and a thickness of 520 μm, available today, an opening angle per pixel of ~0.06º can be reached at a distance of 2 m from the secondary target.

Magnetic spectrometer

In the first stage of the project the existing ALADIN magnet can be used as magnetic spectrometer at intermediate energies. It will be available with minimal additional cost. Its older tracking detectors will be replaced with new more powerful ones. First ion-optical calculations have been done for a configuration QQ-ALADIN. The second quadrupole is necessary to achieve focusing in x-direction. Ion-optical simulations predict that with relative large acceptance in x of ± 70 mm a slice in y of ±8 mm can be accepted by this configuration. Calculations done for a test ion of A = 132 and E = 10 A·MeV result in a mass resolution of ΔA/A of 1/250.

References

[1] www.gsi-linux.de/~wwwnusta/tech_report
[2] A.Drouart et al., NIM A477 (2002) 401)
[3] H.J. Wollersheim et al., NIM A 537 (2005) 637.

A Plunger Apparatus for Relativistic Radioactive Beams*

A. Dewald[1], B. Melon[1], O. Möller[1], J. Jolie[1], C. Fransen[1], K. Jessen[1], K.O.Zell[1], K. Starosta[2]

[1] Institut für Kernphysik, Universität zu Köln, Germany; [2] NSCL, MSU, Michigan, U.S.A.

Nuclear structure investigations with radioactive beams are at present one of the most interesting and active fields in nuclear physics. Absolute transition probabilities are of crucial importance for these studies which can be directly deduced from the lifetimes of excited levels. The aim of this work is to investigate the feasibility of Doppler shift methods to measure level lifetimes of exotic nuclei by using radioactive beams and to provide a first plunger device for such experiments. So far only two RDM experiments with radioactive beams were performed. The first one was done with the RISING spectrometer using secondary fragmentation of a ^{37}Ca beam at 200MeV/u. The second experiment was performed at RIKEN using Coulomb excitation to excite the first 2^+ state in ^{30}Mg. In both experiments set-ups with fixed target and degrader foils were used.

At the NSCL/MSU a RDM experiment was performed with a ^{124}Xe beam at 55 MeV/u in order to test the recoil distance technique under the same conditions as for radioactive beam experiments and with good statistics. The final data analysis where relativistic effects, gamma angular distribution, deorientation and efficiency effects had to be considered, gave a 2^+ lifetime consistent with a recent precise and lifetime measurement Ref. [1]. Details can be found in Ref. [2]. This experiment provided important input for the design of the present plunger device which is shown in Figs. 1 and 2. It is designed to meet the specific requirements of experiments with radioactive beams produced in a production target by fragmentation at relativistic energies resulting from low beam intensities, the large phase space occupied by the radioactive beam causing the need of beam tracking. The plunger device consists of an outer tube, about 1m long and 160mm in diameter (Fig.1) and an inner part (Fig.2) with the frames for the target and the degrader foils, a piezo-motor with an optical device for measuring the target-degrader separation and an additional piezo crystal used in a feedback system for holding adjusted target-degrader distances. In the existing version the target foil can be moved whereas the degrader foil is kept at a fixed position. The target and degrader foils have to be clamped between two rings screwed tightly together and then stretched by screwing the rings to conically shaped support frames. In this way target foils of about 50-70 mg/cm^2 can be stretched.

Some more technical details:
Target/ degrader diameter: 50mm
Target-degrader separation: ≤ 20 mm
Accuracy: ≤ 5μm

For thicker target or degrader foils new target frames and stretching procedures have to be developed.

The plunger will be used first in a measurement for lifetimes in neutron rich Pd nuclei (accepted proposal at NSCL/MSU).

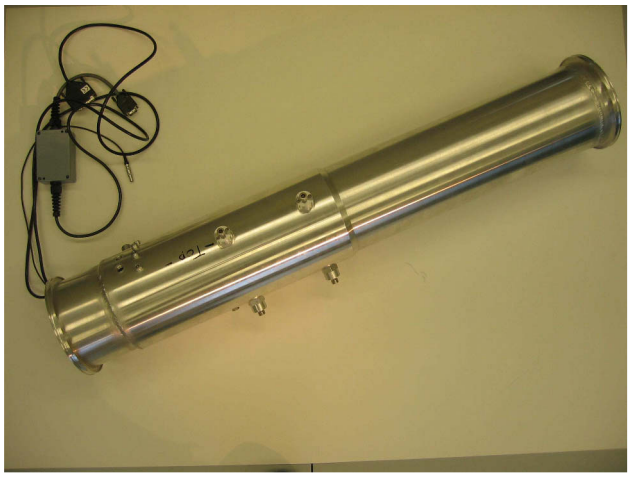


Figure 1: Housing of the inner plunger part shown in Fig. 2.



Figure 2: Plunger removed from the housing shown in Fig.1. At the left side frames and cones for stretching the target and degrader foils can be seen. The black cylinder is the housing of the piezo-motor including an optical device for measuring the target-degrader separation.

References

[1] B. Saha et al., Phys. Rev. C 70 (2004) 034313.
[2] A. Chester et al., submitted to NIM, (2005).

*Work supported by BMBF, contract no.: 06K167 and GSI, F. u. E. contract no. : OK/JOL

ILIMA Project: Towards Pure Isomeric Beams

H. Weick[1], H. Geissel[1,2], Yu.A. Litvinov[1,2], M. Steck[1], K. Beckert[1], P. Beller[1], F. Bosch[1], D. Boutin[1], L. Chen[2], O. Klepper[1], R. Knöbel[1,2], C. Kozhuharov[1], J. Kurcewicz[1], S.A. Litvinov[1,2], M. Mazzocco[1], G. Münzenberg[1], C. Nociforo[1], F. Nolden[1], W. Plaß[2], C. Scheidenberger[1], B. Sun[1], M. Winkler[1]
[1] *GSI Darmstadt,* [2] *JLU Giessen,*

Although the present experimental program at the SIS-FRS-ESR facilities has been quite successful and has led to several basic discoveries [1], the field of research is expected to be drastically extended by the next-generation facility FAIR [2]. It will consist of a more powerful driver accelerator, a large acceptance in-flight separator Super-FRS [3], and a new storage-cooler ring system specially adapted to the large phase space and short half-lives of the exotic nuclear beams [4].

Within the FAIR framework, ILIMA [5] is an accepted proposal which will be an extension of the present successful program at the FRS-ESR. One goal is to provide pure isomeric beams circulating in the new storage ring system to be used in reactions with the internal target or collision zones with other stored particles as electrons or antiprotons. An important demonstration of the feasibility in this direction has been achieved in the present experiment by scraping off one component of an isobaric doublet recorded with Schottky Mass Spectrometry [6]. The goal was achieved by a precise mechanical scraper at a dispersive plane in the ESR. This mechanical separation in the micrometer range brought the success as demonstrated in Figure 1. The technique which has been applied is very similar to one developed for the measurements of the horizontal beam size of cooled ion beams with micrometer resolution [7]. More sensitive methods for the micrometer separation are proposed [7] which should give access to beams of isomers with lower excitation energy.

References

[1] H. Geissel et al., Proc. FINUSTAR-05; *nucl-ex/0510009*.

[2] An international accelerator facility for beams of ions and antiprotons, Conceptual Design Report, GSI 2001, *http://www.gsi.de/GSI-Future/CDR/*

[3] H. Geissel et al., Nucl. Instr. and Meth. B204 (2003) 71.

[4] P. Beller et al., Proc.: 9^{th} Eur. Part. Acc. Conf., Lucerne, Switzerland, 2004, p. 1174, *http://accelconf.web.cern.ch/accelconf/*, and references therein.

[5] Yu.N. Novikov, Yu.A. Litvinov, H. Weick et al., Study of isomeric beams, lifetimes and masses, ILIMA, Letter of Intent, GSI, 2004.

[6] Yu.A. Litvinov et al., Nucl. Phys. A756 (2005) 3.

[7] M. Steck et al., Proc.: 9^{th} Eur. Part. Acc. Conf., Lucerne, Switzerland, 2004, p. 1966, *http://accelconf.web.cern.ch/accelconf/*.

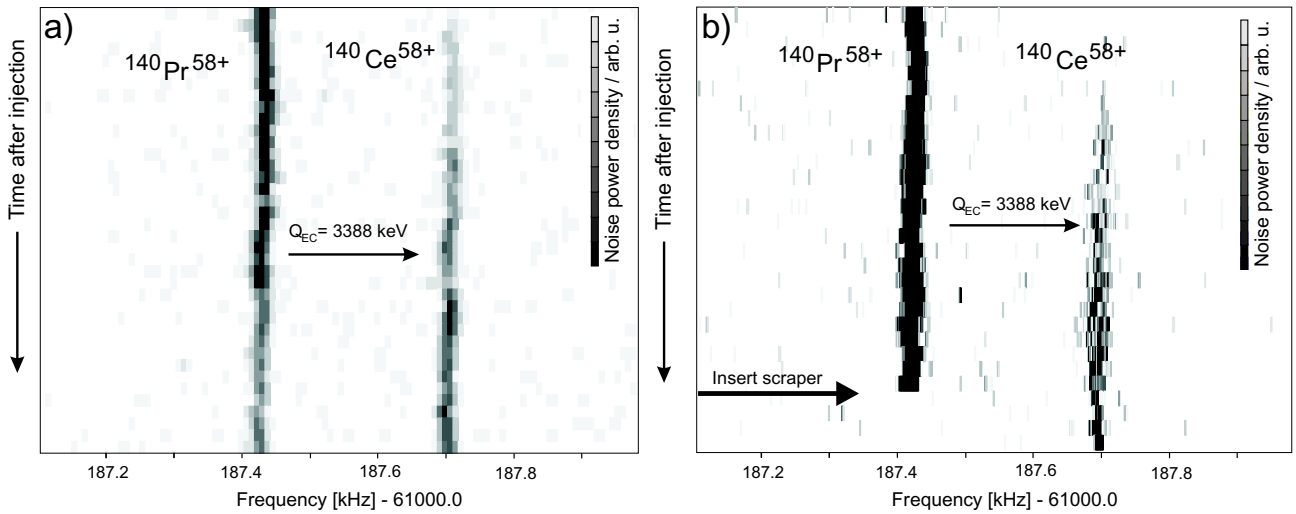


Figure 1: Schottky frequency spectra of well resolved isobaric doublet characterized by a Q-value of about 3.4 MeV. Note, that we can inject monoisotopic fragment beams in the ESR. It has been proven many years ago. Left panel: undisturbed traces in time of hydrogen-like Pr and fully ionized Ce ions recorded for about 520 s. Right panel: 170 s after the injection into the ESR, the beam of Pr ions was eliminated by mechanical scraping. This is a demonstration for the feasibility to provide pure isomeric beams in the storage ring.

The Isochronous Mode for Mass Measurements in the CR Storage Ring

S.A. Litvinov, A. Dolinskii, H. Geissel, Yu.A. Litvinov, H. Weick, GSI Darmstadt

Exotic nuclei will be produced and separated in flight with the Super-FRS [1] at FAIR. The separated fragments will be injected and stored in the 13 Tm Collector Ring (CR) [2]. It will be used in the isochronous mode as a time-of-flight (TOF) spectrometer for short-lived exotic nuclides ($T_{1/2} > 20\mu s$), a method which has been developed at the ESR [3]. The mass-to-charge ratio m/q of the stored ions circulating in the ring can be measured from the revolution frequency (f) and the velocity (v) of the ions.

$$\frac{\Delta f}{f} = -\frac{1}{\gamma_t^2} \cdot \frac{\Delta(m/q)}{(m/q)} + \left(1 - \frac{\gamma^2}{\gamma_t^2}\right)\frac{\Delta v}{v},$$

where γ is the relativistic Lorentz factor and γ_t the transition point of the ring. The isochronous condition is reached when ($\gamma = \gamma_t$). The CR can be operated at a γ_t of 1.84. This condition can be achieved by an increased dispersion function. Although, we kept the maximum of the dispersion function below 30 m, it still reduces the momentum acceptance to $\pm 0.5\%$. The transverse acceptance is 100 mm mrad in the both planes, see Fig. 1. The calculation was done with the GICOSY and MIRKO codes.

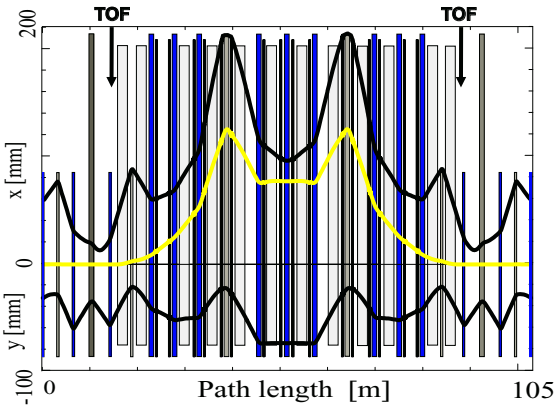


Figure 1: The Calculated beam envelope in x (upper part) and y (lower part) directions and the dispersion function (white line) for one half of the CR. The positions for two TOF detectors are indicated.

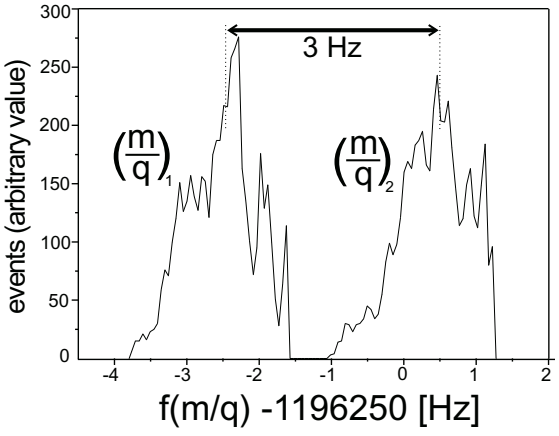


Figure 2: Calculated frequency spectrum with 10 mm mrad transverse emittances. The beam consists of two species of particles separated by $\Delta(m/q) = 2.1 \cdot 10^{-5}$.

We developed a special code which allows us to simulate the motion of stored ions and to obtain frequency spectra of isochronous particles with different m/q values. An example of such calculations is presented in Fig. 2. With this code we calculated the dependence of the revolution frequency on the transverse emittance, see Fig. 3. The calculations were done under ideal conditions, i.e. without the influence of the chromaticity, the fringing fields, and multipole components of the magnets.

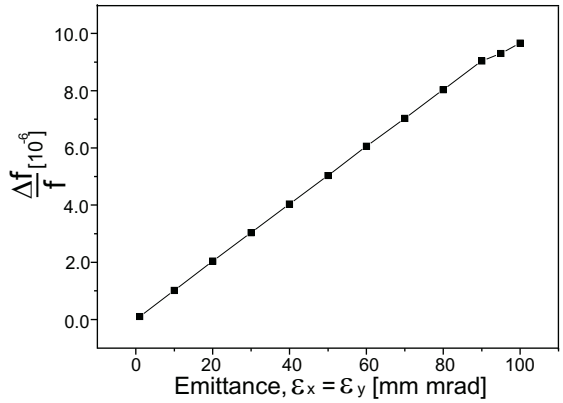


Figure 3: Calculated spread of revolution frequency as a function of transverse emittances. The change of the slope is due to particle loss in the ion motion.

In reality ions are mainly injected at velocities which do not perfectly match γ_t [5]. For analysis and calibration of such data we need to measure the velocity or magnetic rigidity of each ion in addition to the revolution frequency since:

$$\frac{(m/q)_1}{(m/q)_2} = \frac{f_2 \cdot \gamma_2}{f_1 \cdot \gamma_1}.$$

The velocity measurement can be done with two TOF detectors placed in a straight section of the CR. The distance between them is about 30 m. The aimed accuracy in magnetic rigidity is $\Delta B\rho/B\rho \sim 10^{-4}$ [6].

References

[1] H. Geissel et al. Nucl. Instr. and Meth. B204 (2003) 71.
[2] A. Dolinskii et al., Nucl. Instr. and Meth. A552 (2004) 483.
[3] M. Hausmann et al., Nucl. Instr. Meth. A446 (2000) 569.
[4] A. Dolinskii et al., Proc. EPAC'04, Lucerne, p. 1177.
[5] L. Chen, et al., GSI Annual Report 2005 (this volume).
[6] ILIMA TP, http://www-linux.gsi.de/∼wwwnusta/tech_report/

On-line test of the Ion Catcher setup at the FRS

M. Maier[1], M. Petrick[2], G. Savard[3], C. Scheidenberger[1] , K. H. Behr[1], A. Brünle[1], L. Caceres[1], G. Chubaryan[3], J. A. Clark[4], Z. Di[2], S. Eliseev[2], H. Geissel[1,2], W. Hüller[1], M. Huyse[5], C. Karagiannis[1], R. Knöbel[1,2], Y. Kudryavtsev[5], T. Levand[4], Y. Litvinov[1], I. Mukha[5], D. Morrissey[6], G. Münzenberg[1], N. Scielzo[4], P. Van Duppen[5], H. Weick[1], M. Winkler[1], W. R. Plaß[2], M. Portillo[6], Z. Wang[2], B. J. Zabransky[3]

[1]GSI Darmstadt, Germany; [2]JLU Giessen, Germany; [3]Texas A&M University, USA, [4]Argonne National Laboratory, USA; [5]KU Leuven, Belgium; [6]Michigan State University, USA

The FRS Ion Catcher [1] was tested in a first on-line experiment. The system is designed to efficiently stop in-flight separated exotic nuclei from the FRS in a helium-filled gas-cell and to provide them as cooled, low-energy (a few 10 eV) beams for different experimental setups. It is a prototype for an ion catcher system at the Low-Energy Branch of the Super-FRS. The primary goal of the experiment was a proof-of-principle with relativistic exotic nuclei. Besides that, stopping and extraction efficiency, extraction times and possible conceptual limitations should be studied.

A schematic view of the setup placed at the final focal plane of the FRS is shown in figure 1. In the experiment,

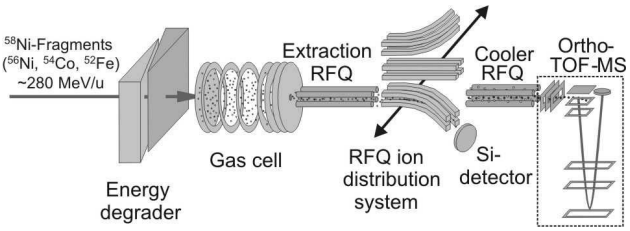


Figure 1: Schematic view of the experimental setup. Detectors placed in front of the energy degrader for particle identification of the incoming secondary beams are not shown.

exotic nuclei were produced by projectile fragmentation of a ^{58}Ni primary beam of 10 ms spill length in an Al target. Fragments with N=Z were separated with the FRS and energy-focused [2] with the second stage and a wedge-shaped degrader at its exit. This led to the mono-energetic secondary nuclides indicated in figure 1 with approximately 280 MeV/u. The various N=Z-fragments have different ranges. Due to the energy focusing, the range differences exceed the range straggling. This imposes an additional separation and thus, varying the degrader thickness allows to stop isotopically pure beams in the gas cell. This cell, developed at ANL [3], is the key component of the setup. It has a length of 1.25 m and works with a sophisticated configuration of DC and RF fields, which guide and extract the stopped ions. A longitudinal DC potential drop is applied to swiftly transport the ions close to the exit nozzle where they are extracted, dragged by the gas flow. An additional RF field applied to the extraction cone repels the ions from the gas-cell surface. In the experiment, the gas cell was filled with helium and mostly operated at a pressure of 100 mbar, corresponding to an areal weight of 2,3 mg/cm^2. The extracted radioactive ions were separated from the gas by two differential pumping stages. Using a newly developed RFQ-based beam-distribution system [4], the radioactive ions extracted from the gas cell could be alternatively guided to a Si-detector and a high-resolution time-of-flight mass spectrometer (Ortho-TOF-MS). The beam-distribution system ensures that the extracted, cooled ion beams are guided throughout by the pseudo potential created by an RF field and transmission losses are thus minimized. The Si-detector was used to count the - decays from the stopped radioactive ions and with the Ortho-TOF mass spectrometer it was possible to detect and identify the created molecular ions and adducts. It also allowed to study the time-scale of ion extraction.

The most important result of the experiment is the fact, that relativistic exotic nuclei can be stopped in and extracted from the cell. The total transmission time is of the order of several 10 ms thus allowing for experiments with short-lived nuclei. This is confirmed by our measurement of the half-life of isomeric state ^{54m}Co with the result (202±5)ms, in agreement with the literature value 198 ms. The extraction times increase, as expected, with increasing mass number. The overall efficiency of the setup, defined as the ratio of decays of ^{54}Co measured with the Si detector and the number of incoming ions of the same species, is depicted in figure 2 as a function of the cone RF voltage. A detailed analysis is in progress.

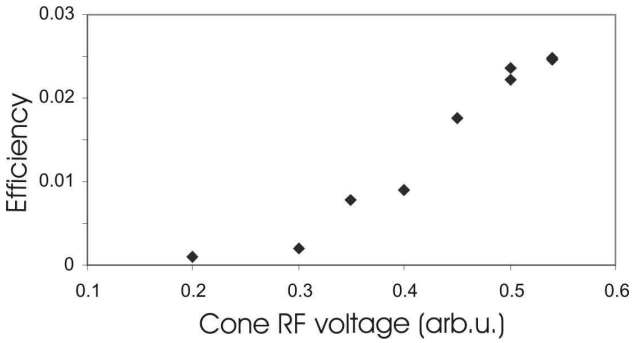


Figure 2: Preliminary data of the overall efficiency of the setup as a function of the cone RF voltage (see text for details).

[1] M. Maier et al., GSI Report 2005-1, 331 (2005).
[2] C. Scheidenberger et al.,N.Instr.Meth. B204, 119 (2003)
[3] G. Savard et al., Nucl. Instr. Meth. B204, 582 (2003).
[4] M. Petrick et al., GSI Report 2005-1, 330 (2005).

The Future Penning Trap Facility MATS at FAIR*

K. Blaum[#], Johannes Gutenberg-Universität Mainz and GSI Darmstadt, Germany
F. Herfurth[¶], GSI Darmstadt, Germany
J. R. Crespo López-Urrutia[§], Max-Planck-Institut für Kernphysik, Heidelberg, Germany
for the MATS Collaboration

The mass is a unique property that distinguishes each nucleus. The binding energy, i.e. the difference between the total mass and the mass of the constituents, is the result of the strong force and the Coulomb force acting within the nucleus. Investigating nuclides with systematically varying numbers of protons and neutrons provides important insights. Precise mass measurements of all nuclei, especially short-lived radionuclides, provide a versatile testing ground for the understanding of complex nuclear structure such as shell closures, deformation, shape transitions, pairing, and isospin symmetry. Beyond nuclear structure physics, precise mass values are important for a variety of applications, ranging from nuclear-decay studies of the weak interaction and of the Standard Model to astrophysical models for X-ray bursts and the creation of heavy elements in stars.

Precise mass measurements combined with decay spectroscopy help to answer questions like: Is the nuclear shell structure concept applicable to very exotic nuclei? How does the deformation of the nucleus come about? Is the weak force sufficiently described in the Standard Model? How were the heavy elements created and distributed over the Universe?

The required relative uncertainty ranges from 10^{-5} to below 10^{-8} for radionuclides, which most often have half-lives well below 1 s. Substantial progress in Penning trap mass spectrometry has made this method a prime choice for precision mass measurements on rare isotopes. The technique has the potential to maintain high accuracy and sensitivity even for very short-lived nuclides. Furthermore, ion traps can be used and offer advantages for precision decay studies due to the well-defined storage conditions that are free of impurities.

With MATS (Precision Measurements of very short-lived nuclei using an Advanced Trapping System for highly-charged ions) at FAIR [1] we aim for applying two techniques to very short-lived radionuclides: high-precision mass measurements and in-trap spectroscopy of conversion-electron and alpha decays. The experimental setup of MATS as schematically shown in Fig. 1 is a unique combination of an electron beam ion trap for charge breeding, Paul and Penning traps for beam preparation, and a high-precision Penning trap system for mass measurements and decay studies.

MATS offers both, high precision and high sensitivity. A relative mass uncertainty of 10^{-9} can be reached by employing highly-charged ions and non-destructive Fourier-Transform-Ion-Cyclotron-Resonance (FT-ICR) detection technique on a single stored ion. The high charge state of the ions can also be advantageously used to reduce the required storage time, hence making measurements on even shorter-lived isotopes possible.

Decay studies in ion traps will become possible with MATS. Novel spectroscopic tools for in-trap high-resolution conversion-electron and charged-particle spectroscopy from carrier-free sources will be developed, aiming *e.g.* at the measurements of quadrupole moments and *E0* strengths. With the possibility of both, high-precision mass measurements of shortest-lived isotopes and sensitive decay studies, MATS is ideally suited to the investigation of very exotic nuclides that will only be produced at the FAIR facility.

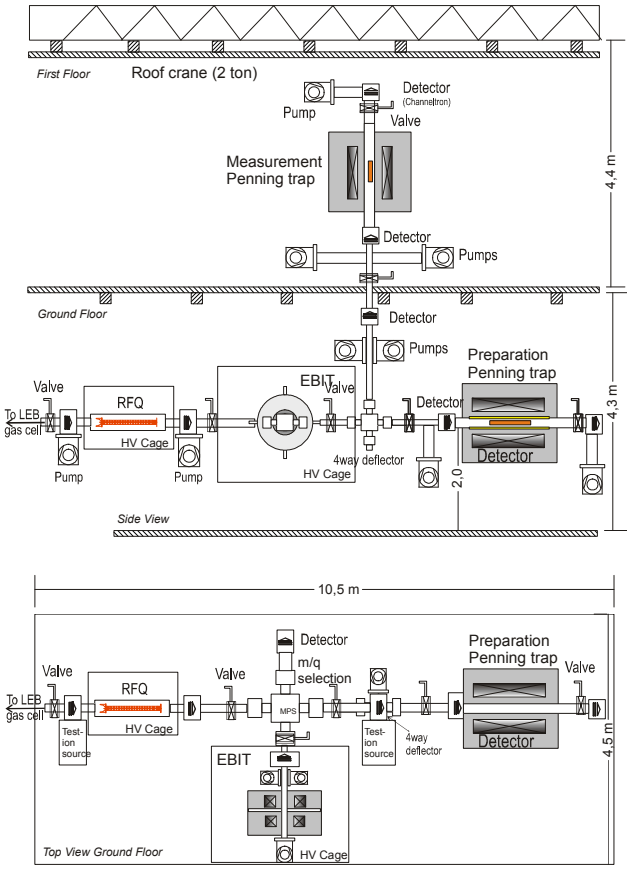


Figure 1: High-precision Penning trap mass spectrometer and in-trap conversion electron spectroscopy setup.

References

[1] MATS Collaboration, Technical Design Report, submitted to GSI/FAIR Darmstadt (2005).

* K.B. is supported by the HGF under contract number VH-NG-037.
# blaumk@uni-mainz.de ¶ f.herfurth@gsi.de § crespojr@mpi-hd.mpg.de

An electron beam ion trap for charge breeding of radioactive isotopes

G. Sikler, S. Epp, M. Froese, C. Osborne, J. R. Crespo López-Urrutia, and J. Ullrich, Max-Planck-Institut für Kernphysik, D-69117 Heidelberg, Germany
J. Dilling, TRIUMF, Vancouver, BC 60439, Canada

Abstract

Rapid charge breeding of short-lived radioactive isotopes produced in ISOL facilities or through fragment separation is a prerequisite for the viability of schemes aiming at accurate mass measurements using Penning traps and the reacceleration of such ions with compact accelerators. We have developed a new electron beam ion trap (EBIT) with short breeding times for these purposes, which is currently undergoing performance tests.

Rapid charge breeding with EBITs

To reduce the time needed to remove as many electrons of a given ion as possible, the primary means is to use a high density electron beam. This can be accomplished in an EBIT by magnetic compression; currently operational devices have already reached values of about 10000 A/cm^2. The new generation of EBITs constructed at the MPI für Kernphysik in Heidelberg is designed for an electron beam current of 5A, thus increasing the current density by nearly one order of magnitude and reducing the time needed to prepare highly charged ions (HCI) accordingly.

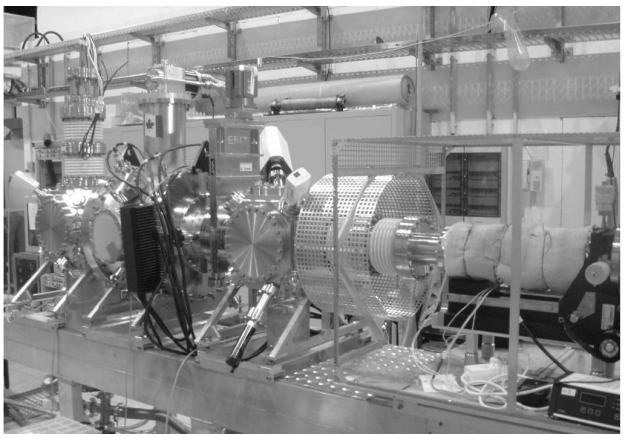


Fig. 1. View of one of the new charge breeding EBITs during assembly at the MPI-K in Heidelberg.

The production rates of the isotopes of interest can be quite low, and therefore the breeding apparatus should be able to handle bunches of may be only a few hundred ions. This implies severe conditions for the background current. An important advantage of EBITs is the very small ion inventory and the low emission current out of the trap when injection is suppressed, both due to the extreme vacuum level in the cryogenic trap region. Typical contaminants, such as O^{6+} ions, can be reduced to pA or even fA emission levels, low enough to allow for good resolution of the interesting species.

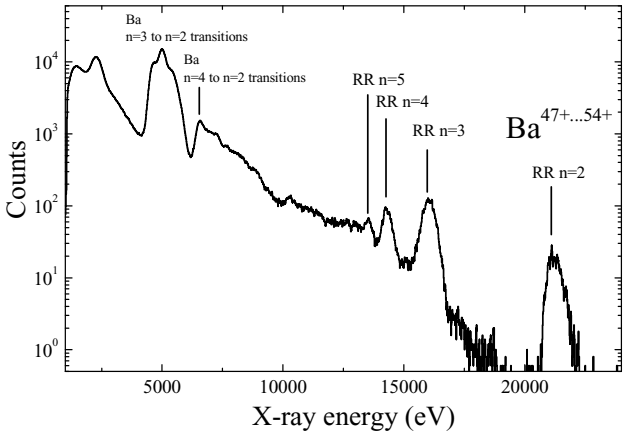


Fig. 2. Recombination x-ray spectrum of Ba ions produced at the new Heidelberg EBIT at 12.5 keV beam energy and 90 mA during initial tests.

By a judicious choice of the electron beam energy and appropriate breeding schemes, the majority of the singly charged ions injected into an EBIT can be brought simultaneously to almost any desired charged state. Closed-shell configurations, such as He-, Ne- or Ni-like, are particularly convenient, since very high degrees of charge purity (of more than 80%) for the final ionization state have been already demonstrated. X-ray diagnostics of the trapped ions (see Fig. 2) is extremely useful for optimization of the breeding process. By tuning the beam energy onto certain dielectronic resonances, selective recombination of the HCI into interesting *q/m* ratios can be attained in a very short time (see, for instance, Ref.[1]). Optimized use of the rare species and a reduction of the beam line contamination can be achieved in this way. The present EBIT performances are ideally suited for charge breeding in the mass measurement program of MATS at FAIR.

References

[1] J. R. Crespo López-Urrutia, J. Braun, G. Brenner, H. Bruhns, A. Lapierre, A. J. González Martínez, V. Mironov, R. Soria Orts, H. Tawara, M. Trinczek, and J. Ullrich, *"Optimization of the charge state distribution of the ion beam extracted from an EBIT by dielectronic recombination"*, Rev. Sci. Instrum. 75, 1560 (2004)

Detection Techniques for On-Line Mass Determination with Penning Traps*

C. Weber[1,2,#], K. Blaum[1,2], M. Block[2], R. Ferrer[1], A. Herlert[3], J. Ketelaer[1],
D. Neidherr[1], and C. Yazidjian[2,3] for the MATS collaboration
[1]Johannes Gutenberg-Universität, D-55099 Mainz.
[2]GSI, D-64291 Darmstadt, [3]CERN, CH-1211 Genève 23.

A Penning trap mass spectrometer is a well established instrument for the precise mass determination of both, stable and short-lived nuclides. For this purpose two different concepts are employed. Masses of stable species are mostly determined by the non-destructive detection of image currents induced in the trap electrodes and a subsequent Fourier transformation (FT). For short-lived nuclides the destructive time-of-flight ion-cyclotron-resonance technique (TOF-ICR) appeared to be the method of choice, since the ions have to be released from the trap prior to their detection. Approaching rarely produced nuclides with prolonged half-lives $T_{1/2}$ or pushing forward to ions with multiple charge states q, the non-destructive Fourier-transform ion-cyclotron-resonance (FT-ICR) technique [1] is very promising. In the first case, the limited ion statistics can be overcome by an extended observation time and secondly, with $q > 1$, single ion detection sensitivity is easily feasible. Both, the destructive detection with microchannel plate (MCP) detectors or Channeltrons and the detection with the FT-ICR technique will be implemented for advanced mass spectrometric studies with the Penning trap system MATS within NUSTAR at the future GSI facility FAIR.

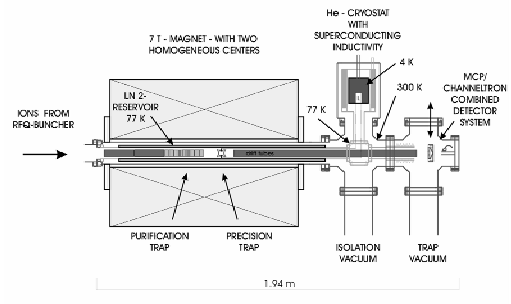


Figure 1: Schematic for a non-destructive detection of image currents in a cryogenic trap enabling the subsequent extraction to an additional detector system.

A corresponding trap system is depicted in Fig. 1. In the precision Penning trap narrow-band FT-ICR detection will be used. The cryogenic environment and the optimized, low-noise electronics enable the detection of single ions and thus a non-destructive detection and mass analysis of the stored ions. The current development at the University of Mainz mostly concentrates on the preparation of this sensitive detection technique for heavy ions at SHIPTRAP [2]. Alternatively, the geometry of the setup allows the ejection of ions for destructive techniques.

For TOF-ICR mass spectrometry [3,4] the ions are ejected from the trap towards a MCP detector or a Channeltron. Figure 2 shows such a combined detector setup. With a linear feedthrough the MCP array can be retracted and the beam line is open to a conversion electrode detector with a Channeltron. The setup with a conversion electrode, where ions are accelerated to, allows an improved detection efficiency of almost 100% compared to the typical efficiency of about 30% for the MCP.

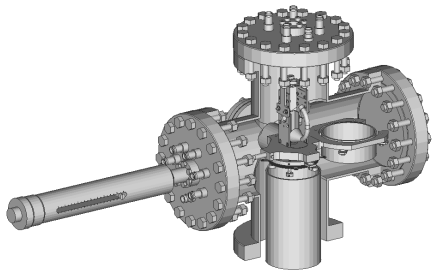


Figure 2: Combined detector system of a retractable MCP and a Channeltron as used for the time-of-flight registration at ISOLTRAP and MATS/Mainz.

The experimental comparison of both detector types using residual gas ions is shown in Fig. 3. An improved detection efficiency of the Channeltron by a factor of three could be verified in this test. The shift in the position of the maximum is due to the respective position of the detector on the beam axis resulting in a different focussing condition corrected by the voltage of an einzel lens. With the current development studies both techniques are well established and ready to use at MATS [5] at FAIR.

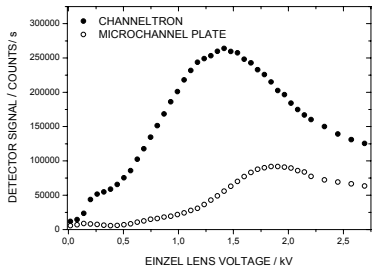


Figure 3: Relative detection efficiencies of a channeltron and a microchannel plate using ionized residual gas.

References

[1] M.B. Comisarow, *et al.*, Chem. Phys. Lett. **25**, 282, 1974.
[2] C. Weber, *et al.*, EPJ A **25**, Supplem.1, 65, 2005.
[3] G. Gräff, *et al.*, Z. Phys. A **297**, 35, 1980.
[4] M. König, *et al.*, Int. J. Mass Spec. **142**, 95, 1995.
[5] Technical Design Report, submitted to FAIR/GSI (2005).

* Work supported by the Association of Helmholtz Research Centers (contract VH-NG-037)
# email: c.weber@gsi.de

Recoil detector system for the R3B setup

O.A. Kiselev, T. Aumann, W. Catford, M. Chartier, P. Egelhof, H. Emling, M. Freer, J.V. Kratz, M. Labiche,R. Lemmon, T. Nilsson, G. Nyman, G. Schrieder, H. Simon, A. Shrivastava, M Stanoiu, K. Sümmerer for the R3B Collaboration

A new universal setup with high efficiency, acceptance, and resolution for kinematically complete measurements of reactions with high-energy radioactive beams is planned to be installed at the focal plane of the high-energy branch of the Super-FRS at FAIR. The experimental configuration is based on a concept similar to the existing LAND setup introducing substantial improvement with respect to resolution and an extended detection scheme including a detector system for light (target-like) recoil particles in coincidence with the heavy fragments, neutrons and protons. The experimental setup is aiming at utilizing a wide variety of scattering experiments. Among them are light-ion (in)elastic and quasi-free scattering in inverse kinematics. The combination of the detection of fragments in forward direction with the target-recoil detection allows for the first time a kinematical complete measurement of, e.g., quasi-free nucleon knockout reactions.

The recoil particle detector provides precise tracking, vertex determination, energy and multiplicity measurement with high efficiency and acceptance. A general overview of the light ion detector has been given in the R3B Letter of Intent [1] and the Technical Proposal [2]. A thick liquid hydrogen target ($\sim$200 mg/cm^2 or $\sim$3 cm) will be used to reach the required luminosity for the radioactive beams. The use of an extended target requires the determination of the interaction vertex with a precision of 1-2 mm. This corresponds to an effective target thickness below 20 mg/cm^2 thus making possible a precise correction for the energy loss of the fragments in the target.

The barrel-like tracking system consists of two layers of position sensitive detectors placed into a vacuum chamber in order to minimize multiple scattering. The whole tracking system will be placed inside the gamma-ray calorimeter. The calorimeter will cover approximately 75% of the total solid angle with an opening in the backward hemisphere. This space free of the detectors will be used by the infrastructure of the liquid hydrogen target and the electronics of the tracker detectors. Study of knockout reactions and quasi-free scattering in inverse kinematics requires detection of recoils with energies in the range of 50 - 300 MeV, which corresponds to an angular range of 20° to 70° for an incident energy of 700 MeV/u. Extensive simulations using the GEANT4 package have been done in order to optimize the system performance. The first preliminary results show that the first layer of the barrel should be as thin as possible to reduce multiple scattering of the recoils, while the second layer can be 300 - 400 μm thick. The noise of the readout electronics and the small energy deposition of the fast particles, especially protons, limit the minimum thickness of the Si detectors; a reasonable thickness of the first layer is $\sim$100 μm. A strip pitch size on both sides of 100 μm is needed to obtain the required angular resolution of a few mrad.

Silicon microstrip detector have been developed in collaboration with the University of Geneva, Switzerland. The compact modules consist of double sided sensors mounted together with the readout electronics. The modules will serve as the prototypes of the recoil proton detectors for the R3B setup and will be used at the same time for experiments with the existing LAND reaction setup at Cave C. They will be installed into the target section for precise coordinate and ΔE measurements; the total energy of the recoils will be measured with the surrounding NaI Crystal ball. The suggested prototypes will be able to detect many particles at the same time due to their granularity and individual-strip readout. Each sensor has a size of 72$\times$41 mm^2, a thickness of 300 μm and a 110 μm readout pitch.

The detector prototypes have been tested with a β-source and cosmic rays. A good signal-to-noise ratio was observed even for very low energy deposit. Several detectors have been installed in a vacuum chamber and were tested using a ^{12}C beam at 350 MeV/u in November 2005 at the FRS. The beam has been fragmented in a thick target to check the Z separation of the detectors. An example of the measurements with a secondary ^{8}B beam is shown in a Fig.1 (the energy spread of the beam is not corrected for). The

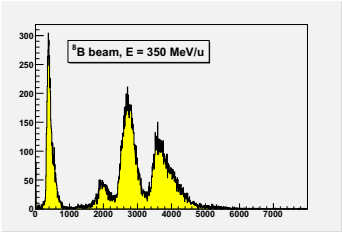


Figure 1: Z separation of Si microstrip detectors obtaned with a secondary ^{8}B beam, X-axis represents an energy loss in Si detector in arbitrary units.

preliminary results show very good beam profiles, a small noise level and a good energy loss measurement. The detectors will be used to detect recoiling protons in scattering experiments with the LAND setup in 2006 and 2007. This work is partially supported through EURONS (EC contract Nr. 506065), BMBF contract 06MZ174 and HGF Virtual Institute VH-VI-061 (VISTARS).

References

[1] http://www-land.gsi.de/r3b/docu/R3B-LoI.pdf

[2] http://www-land.gsi.de/r3b/docu/R3B-TP-Dec05.pdf

Heavy Ion CVD-Diamond Detectors for R3B*

K. Eppinger, R. Gernhäuser, R. Krücken, S. Schwertel† and S. Winkler, TU München
W. Koenig and J. Pietraszko, GSI, Darmstadt

CVD-diamond is a detector material with fast signals, high charge carrier mobility, smallest lattice constant, and large band-gap [1] resulting in radiation hardness, very good timing and high count rate capability. These properties make it an ideal material for heavy ion tracking and TOF detectors. Polycrystalline diamond is successfully used as detector material at GSI for some years at several experiments (HADES, FOPI,...). Especially for the R3B experiment where a minimum material budget around the target is essential, we carry on this development towards highly segmented, thin, large area ($50 \times 50\,\mathrm{mm}^2$) devices.

First investigations were made with a new material from the IAF Fraunhofer Institute Freiburg. We have produced small test detectors of $10 \times 10\,\mathrm{mm}^2$ area with different thicknesses ranging from 20 μm up to 100 μm and a segmentation of four strips in x and y direction on the front and the back side respectively. Leakage currents of typically 5 nA/cm^2 are constant up to fields of 5 V/μm and increases by a factor of 10 between 5 - 7 V/μm. We applied a field of 3 V/μm.

Basic tests were performed at the Munich Tandem accelerator using ^{16}O and ^{7}Li beams of 117 MeV and 48 MeV. The detectors were set up as a stack consisting of a diamond detector and a Si diode. After passing through the diamond detector the beam was stopped in the diode which provided a trigger and the residual energy signal.

The detector efficiency was measured for a 50 μm thick diamond substrate. Using the Li beam and an energy cut of 20 % of the average signal, 98 % of all particles passing the diamond are recognized. This value is consistent with the segmentation gaps of 50 μm at a pitch of 2 mm.

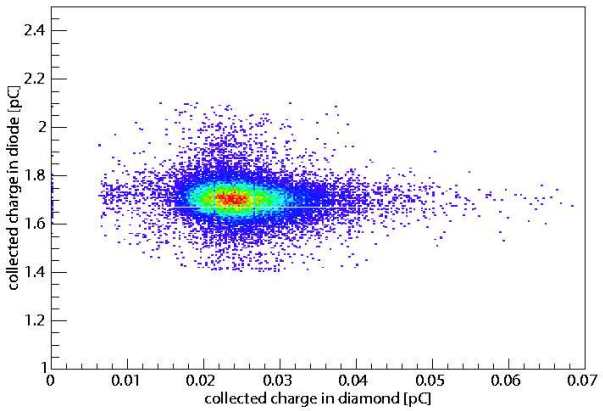


Figure 1: The collected charge in the diamond detector versus the collected charge in the diode.

In polycrystalline CVD-diamond material the electrons and holes only drift a fraction of the thickness in the electric field and recombine preferred at the grain boundaries. This charge collection capability typically widens the energy distribution (see fig. 1). An average collected charge of 25 fC corresponds to a charge collection depth of 12 μm which is already sufficient for heavy ions and has to be verified for different material thickness.

Another main task of the measurement was to test the radiation hardness of this material. Up to a dose of 10^{11} ^{16}O ions per mm^2 the average signal amplitude linearly dropped to about 70 %.

After these tests this type of detector was already used as start detector in the HADES experiment in 2005. It is only half the thickness of the old start detector and mounted closer to the target. Therefore particle background is reduced. The four fold segmented detector in this case was mounted on a new developed circuit board based on a fast, low-noise, low power 2 GHz broad band preamplifier in a SC70 package. It was tested in an 1 AGeV ^{27}Al beam from SIS/GSI and used in a beam time in September using ^{40}Ca of 1.9 AGeV.

The efficiency of the new start detector was measured in relation to the old one. 1.5 % of all particles were seen in the old start detector but not in the new one. This result is very similar to the Munich measurement reported before.

Investigating the time of flight between the old and the new start detector a time resolution of $\sigma\tau \approx 60$ ps for each individual detector was measured. This did not depend on the signal amplitudes and is about a factor of two worse than expected from the signal rise time and the noise figure. Reasons for this have to be investigated in further tests.

A special feature of the detector material are particle induced persistent currents which have decay times of several seconds after switching off the beam. This effect also seen in laser excitation of CVD-diamond results from material impurities and the grain boundaries [1].

At beam intensities of $2 \cdot 10^6\,\mathrm{s}^{-1}$ a maximum current of 2 μA was observed in the first days of operation. This value dropped to 500 nA after 10 days.

Next steps in the development will be a higher segmentation with 30 μm gap and 110 μm pitch utilizing lithographic methods. The handling of large area diamonds has to be practiced. New readout schemes have to be implemented for these detectors and a first large area prototypes is expected end of 2006.

References

[1] C. Nebel, Semicond. Sci. Technol. 18 No 3 (March 2003) S1-S11, PII: S0268-1242(03)58317-1

* Supported through EURONS (EC contract no. 506065)
† sabine.schwertel@ph.tum.de

Progress of Ion-optical and Technical Layout at the Super-FRS*

M. Winkler, B. Achenbach, K.-H. Behr, H. Emling, H. Geissel, M. Gleim, W. Hüller, H. Iwase, C. Karagiannis, A. Kelic, H. Leibrock, Y. Litvinov, G. Moritz, C. Mühle, G. Münzenberg, C. Nociforo, C. Scheidenberger, H. Simon, K. Sümmerer, N.A. Tahir, H. Weick, GSI, Darmstadt, Germany
D. Boutin, W. Plass, Z. Wang, H. Wollnik, Justus-Liebig University , Giessen, Germany
Anna Tauschwitz, J.A. Maruhn, Frankfurt, Germany
M. Berz, S. Manikonda, NSCL-MSU, East-Lansing, USA
M. Svedentsov, M. Yavor, Institute of Analytical Instrumentation, RAS, St. Petersburg, Russia

Introduction

The Super-FRS [1] will be the next-generation in-flight separator for exotic nuclei up to relativistic energies, which will efficiently separate rare isotopes produced via projectile fragmentation of all primary beams up to ^{238}U and via fission of ^{238}U. It is a large-acceptance two-stage superconducting fragment separator with three branches serving different experimental areas including the new storage ring complex.

The primary beam intensities planned for SIS100/ SIS300 [2] will exceed by a factor of up to 1000 the present intensities. This requires challenging designs of the high-power production targets, the beam-dumps to catch the remaining primary beam, and radiation resistant magnets. In this report we summarize the recent developments on these issues.

Layout of the Super-FRS

General Layout

Figure 1 shows the layout of the Super-FRS. It consists of two separator stages, the Pre-Separator and the Main-Separator. Both separator stages use the Bρ-ΔE-Bρ method, where a two-fold magnetic rigidity analysis is applied in front and behind a specially shaped energy degrader. The Main-Separator has three exits: the High-Energy Branch (HEB), the Ring-Branch (RB), and the Low-Energy Branch (LEB).

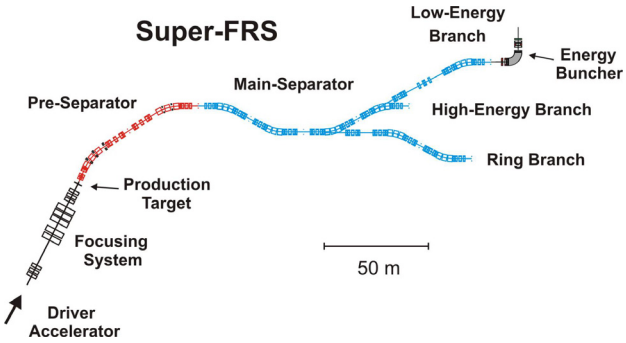


Figure 1: Layout of Super-FRS indicating the three different branches.

*Work supported by the European Community under the FP6 DESIGN STUDY (contract 515873 - DIRACsecondary-Beams).

Ion-optical Design

Each separator stage is an achromatic system with an intermediate dispersive focus, where the energy degrader is placed. The Super-FRS accepts a transversal phase space of 40 π mm mrad, both in x- and y-direction, and a momentum deviation of ±2.5 %, which guarantees a high transmission also for very neutron-rich nuclei produced by uranium fission. The target spot size is assumed to be ±1 mm and ±2 mm in x- and y-direction, respectively, corresponding to a momentum resolution of 1500 at the mid plane of the Main-Separator.

The Pre-Separator

The Pre-Separator consists of two dipole stages, where each dipole stage is divided into three dipole units [3]. This concept allows installing beam catchers at dedicated positions as indicated in Figure 2. Approximately 80-90 % of the primary beam will not react with the production target but has to be stopped in these beam catchers. Due to a high flux of energetic particles the first magnets have to be radiation resistant.

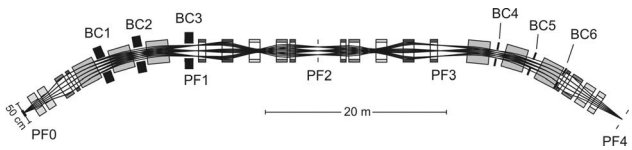


Figure 2: Layout of the Pre-Separator, indicating the focal planes (PF1-PF4) and the positions of the beam catchers (BC1-BC6) [3].

High-Power Targets

The requirements of the target technology for the Super-FRS can be summarized:

- The Super-FRS will use slowly extracted beams from SIS100/SIS300 for counter experiments in the HEB and LEB as well as fast extracted beams for storage ring experiments.
- The optimum target thickness will range up to 8 g/cm^2 depending on the atomic number Z of the projectile and the selected energy.

Targets for slow-extracted beams

The typical extraction time in the slow extraction mode is 1 s. The power deposited by a ^{238}U primary beam into the production target will be about 12 kW. We intend to

use a rotating graphite target wheel, with a radius of 22.6 cm. The graphite ring will be subdivided into several circles in order to achieve adjustable thicknesses. Cooling will be achieved by thermal radiation from the surface. Special attention has to be paid to the bearings which have to be kept at rather low temperatures. This requirement can be fulfilled by connecting the target ring and the bearing housing by spokes. Figure 3 shows the temperature distribution for our planned target wheel rotating with 60 rpm. ANSYS calculations yield a maximum temperatures of 1037 °C for the graphite and 368 °C for the axle [4].

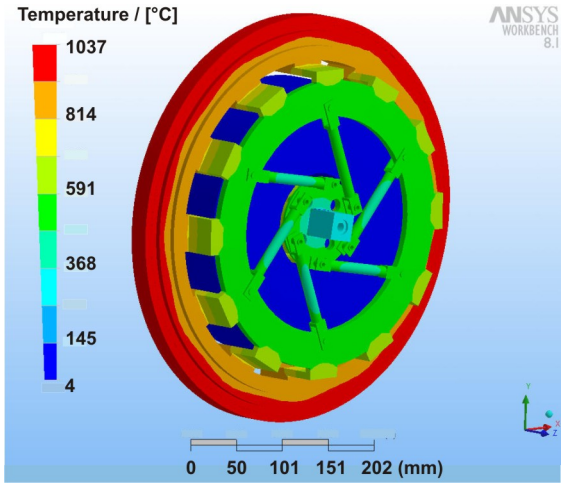


Figure 3: Calculated surface temperature distribution of the graphite target wheel which is irradiated with a ^{238}U beam with 1 GeV/u and an intensity of 10^{12} ions/s. The wheel rotates with 60rpm [4].

Targets for fast-extracted beams

The very high instantaneous power deposition in the target for fast extracted beams ($\tau \approx 50$ ns, $P < 200$ GW) could lead to the destruction of the production target by a single beam pulse. Thus special care has to be taken for the design of such targets:

- For small deposited specific beam powers (i.e. low projectile Z, low intensities, enlarged beam spot size) the use of the rotating graphite wheel as described above is considered.
- For the highest power densities a windowless liquid-metal jet is considered. First calculations of a Super-FRS liquid-metal target for the fast-extraction scheme are reported in Refs. [5,6].

Beam Catcher

The beam catcher has to stop the primary beam and to shield the subsequent parts of the separator from a high level of secondary radiation. Consequently the design of the beam catcher consists of two parts (see Figure 4). The V-shaped graphite block at the entrance widens the range distribution and thus distributes the heat. The subsequent iron part will reduce the neutron radiation of the magnets. The beam catchers will be installed at dedicated positions in the Pre-Separator.

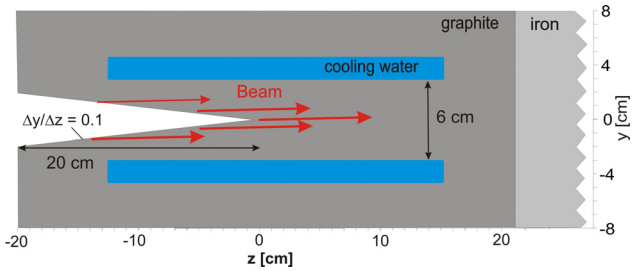


Figure 4: Cut through the beam catcher consisting of a graphite part and an iron part. The arrows indicate the primary beam.

Radiation Resistant Magnets

The magnetic elements located in the high-radiation areas have to be reliably operated for the lifetime of the facility, i.e. their material has to be radiation resistant. Detailed Monte Carlo simulations using the PHITS code [7] were performed assuming a ^{238}U primary beam with an energy of 1500 MeV/u and an intensity of 10^{12} ions which is focused on a carbon target. Figure 5 shows the results for the first quadrupole magnet (PQ_{11}) behind the production target.

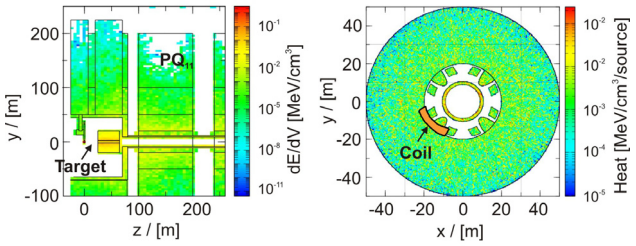


Figure 5: Energy deposition per primary 1.5 GeV/u ^{238}U ion impinging on a 4 g/cm^2 C target. The left side shows the distribution along the optical axis and the right side shows the distribution at the entrance surface of PQ_{11}.

In average the energy deposition on the coil surface is $\langle \Delta E \rangle / M \approx 1$ mJ/g, which is equivalent to a dose rate of 1 Gy/s. Assuming a 4000 h/year operation time this sums up to an accumulated dose of 14 MGy/year which require the use of inorganic insulators, the most crucial parts concerning radiation resistance magnets. Magnet designs based on Mineral Insulation Cables (MIC) are being performed [8].

References

[1] H. Geissel et al., Nucl. Inst. & Meth. B 204 (2003) 71
[2] FAIR – Technical Report of the Subproject 'Accelerato (2005) unpublished;
[3] H. Geissel et al., Nucl. Inst. & Meth., submitted for publication.
[4] B. Achenbach, Dipl. Thesis, FH Hagen, (2005)
[5] N. Tahir et al., this report.
[6] An. Tauschwitz et al., this report.
[7] H. Iwase et al., J. Nucl. Sci. Tech. 39 (2002) 1142.
[8] M. Winkler et al., IEEE Trans. on Appl. Supercond., accepted for publication

Ion-optical design of the focusing system in front of the Super-FRS target*

D. Boutin†, W. Plass, Justus-Liebig Universität Giessen
H. Geissel, G. Münzenberg, H. Weick, M. Winkler, GSI, Darmstadt, Germany
M. Yavor, Institute of Analytical Instrumentation, RAS, St. Petersburg, Russia

Ion-optical design studies of the focusing system in front of the Super-FRS [1] have been performed. The following will give an overview of the two options which have been studied.

System description

The new heavy-ion synchrotron SIS100 [2] will provide high-intensity beams at relativistic energies in the rigidity range (27-100) Tm. In order to produce secondary fragments, the ion beam will interact with the Super-FRS production target, where the beam spot is required to be about (1×2) mm^2 in size. Therefore it is necessary to perform careful investigations of the transport beam line between the SIS100 and the Super-FRS. The last part, which consists of a large acceptance strong focusing system, has been investigated. Two options have been chosen for the construction planning:

1. System using cos(ϕ) magnets,
2. system using superferric magnets (also used in the Super-FRS).

The two systems have been studied with the ion optical code GICOSY [3]. Two limitations have to be taken into account for the simulations. At maximum energies the field strength of the magnets have to stay below the limitations given below. At low energies, the phase space is getting larger and the system must be able to keep a full transmission. Table 1 gives an overview of the magnets specifications used for both options.

System	Length	Aperture	Max. Gradient
1	2.2 m	$\pm$120 mm	30 T/m
2	0.75 m	$\pm$80 mm	20 T/m
2	1.2 m	$\pm$190 mm	10 T/m

Table 1: Specifications of the magnets described in this report.

Cos(ϕ) magnets design (system 1)

In this design the magnets have all the same specifications. This option will reduce the construction cost of the system, and its overall length will be kept small. The aperture has been chosen to be the minimum required to fully transport the ions. This is shown for $^{238}U^{28+}$ ions at 400 MeV/u as presented in Fig. 1.

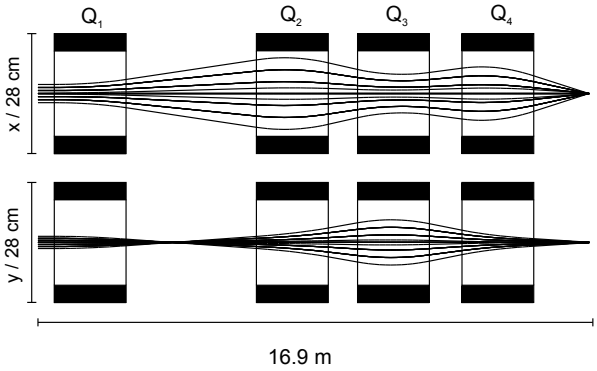


Figure 1: Beam enveloppes for system 1. The initial phase spaces are ϵ_x = 25 mm mrad, ϵ_y = 10 mm mrad. The final spot size is (1×2) mm^2.

Superferric magnets design (system 2)

Here, each quadrupole is divided in several parts (2 or 3). This system improve the flexibility with beams having a rigidity range (27-100) Tm. Parts of the split magnets can be switched off, depending on the magnetic rigidity. An example is displayed in Fig. 2, where the magnets marked in black are used. Another advantage of this system is to use the same magnet design as planned in the Super-FRS.

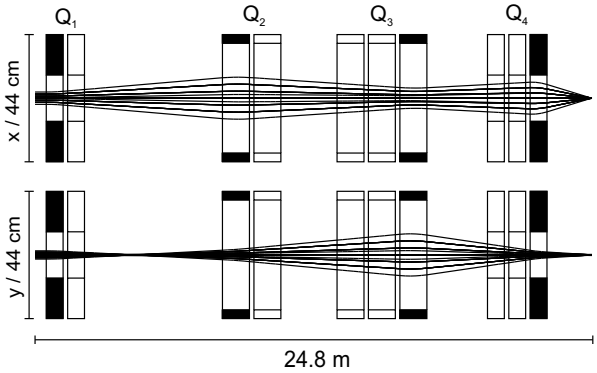


Figure 2: Beam enveloppes for system 2. The initial and final phase spaces are the same as in Fig. 1. The magnets used for this Bρ setting (27 Tm) are marked in black.

The further studies will mainly consist on correction of higher-order aberrations.

References

[1] H. Geissel *et al.*, GSI Report **2005-02**.

[2] Technical Status Reports - Accelerator Facilities, Darmstadt, January 2005 (unpublished).

[3] http://www-linux.gsi.de/∼weick/gicosy/

* Work supported by European Community under the FP6 program DESIGN STUDY (contract 515873 - DIRACsecondary-Beams)

† d.boutin@gsi.de

Calculation of activation and dose spatial distributions induced by high intensity uranium beams at the Super-FRS fragment separator at FAIR

H. Iwase, H. Weick, T. Radon, F. Gutermuth, M. Winkler, and H. Geissel, GSI Darmstadt

Abstract

A calculation of activation and induced dose spatial distribution caused by 1.5 GeV/u ^{238}U irradiation was carried out for the design of the shielding of the Super-FRS[1], which is under development for the future project at FAIR GSI. The calculation is based on a model newly developed in this study and it is divided into; (1) Residual nuclei calculation (2) activation calculation, (3) dose conversion, and (4) dose attenuation calculation.

Residual nuclei calculation

Residual nuclei in a quadrupole magnet (180 cm ϕ) irradiated by 1.5 GeV/u ^{238}U were calculated using the heavy ion transport code PHITS[2]. The quadrupole was constructed of an assembly of 20 $\times$ 20 $\times$ 20 cm^3 bricks in the calculation (see Fig. 2) and production rates $Y(M,Z)$ of residual nuclei in each brick per projectile were obtained.

Activation calculation

The radioactivity caused by each residual nucleus $A(M,Z)$ in the brick is calculated by the equation

$$A(M,Z) = Y(M,Z) \cdot N_{spill} \cdot (1 - e^{-\lambda(M,Z)\cdot T}) \cdot e^{-\lambda(M,Z)\cdot t}. \quad (1)$$

where $Y(M,Z)$ is the production rate of the nucleus (M,Z) per projectile and N_{spill} is the number of projectiles per second. $\lambda(M,Z)$ is the decay constant of the nucleus, T is the irradiation time, and t is a waiting time between the end of the irradiation and the evaluation time. Both are in the unit of sec. It is noted that the decay chain is NOT included in this study.

Dose conversion

The radioactivity $A(M,Z)$ can be converted to a dose value using the conversion factor in the unit of (mSv·h^{-1}·GBq^{-1}) listed in table A2 in reference [3]. Then the sum of the doses represents the total dose of the brick D_0.

Dose attenuation and spatial distribution

The attenuation of the dose in a certain brick D_0 to the evaluation point (x, y, z), D, can be calculated by the Moyer model[5]. Attenuation length by Conner et al.[4] are used. Fig. 1 is a benchmark calculation to check the model developed in this study, and it shows that the model gives a very good agreement with data. Finaly the calculated dose distribution around the quadrupole is shown in Fig. 2.

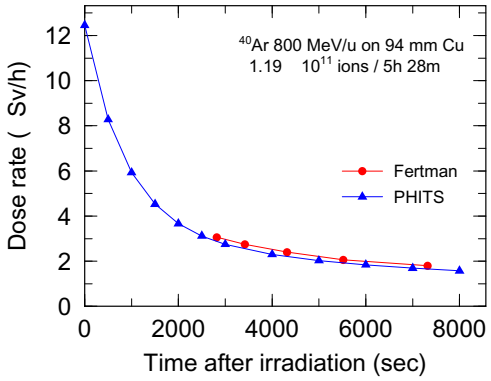


Figure 1: Calculated and experimental [6] decay of the dose rate for a copper target of 97mm thickness irradiated by 1.2 $\times$ 11^{11} Argon beams of 800 MeV/u during 5 h 28 min at 30 cm distance from the target.

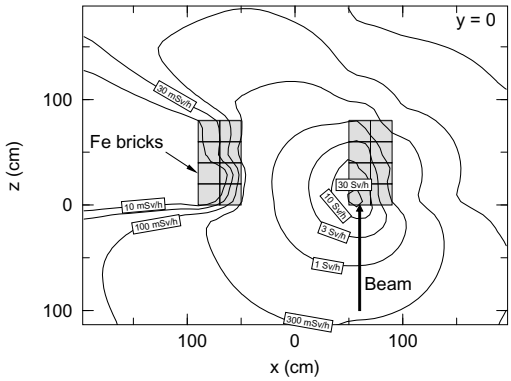


Figure 2: Spatial dose distribution caused by activation of the quadrupole after 30 days irradiation and 1 days cooling.

References

[1] H. Geissel, M. Winkler et al., *Technical report on the design, construction, comissioning and operation of the Super-FRS of FAIR*, GSI (2005).

[2] H. Iwase, K. Niita and T. Nakamura, Journal of Nucl. Sci. and Technol., Vol. 39, No. 11, p 1142-1151 (2002)

[3] N. Petoussi, et al., GSF - Bericht 7/93, March (1993).

[4] A. L. Conner, H. F. Atwater, and Elizabeth H. Plassmann, Phys. Rev. A Vol. 1 No. 3 (1970)

[5] B. J. Moyer, in Proc. 1st Int. Conf. Shielding around High Energy Accelerators, Paris, (1962) p65.

[6] A. Fertman, A. Golubev, B. Sharkov, et al., Annual Report GSI 2004-03, p19, (2004).

Liquid Jet Lithium Target for Super-FRS Fast Extraction Scheme: Comparison Between 2D and 3D Simulations *

N.A. Tahir, GSI, Darmstadt, Germany
A.Shutov, V. Kim, I.V. Lomonosov, IPCP Chernogolovka, Russia
K. Sümmerer, A. Kelic, B.Achenbach, H. Weick, M.Winkler, H. Geissel,
D.H.H. Hoffmann, GSI, Darmstadt, Germany

Abstract

Previously we have shown [1] that using the highest intensity uranium beam with 10^{12} ions delivered in a single bunch with a duration of 50 ns, a solid graphite target will be destroyed in a single experiment if one uses a small focal spot size necessary to have good ion optical resolution and sufficient transmission of the secondary particles. It is therefore essential to develop novel target designs like a windowless liquid jet target. In Ref. [1] we presented first calculations of interaction of the beam with a liquid lithium target using a two–dimensional computer code, BIG-2 [2]. This computer code uses a semi-empirical equation-of-state model to simulate the target physical conditions [3]. In the meantime we have carried out three-dimensional calculations of this problem and in this contribution we present more detailed calculations together with a comparison between 2D and 3D results.

Introduction

The new heavy ion synchrotron, SIS100 that will be built at the future **F**acility for **A**ntiprotons and **I**on **R**esearch (**FAIR**) [4], will generate a very intense uranium beam with an intensity of 10^{12} ions that will be delivered in a single bunch, 50 ns long. A wide range of particle energy between 400 MeV/u–2.7 GeV/u will be available to the experimentalists. The beam intensity in transverse direction will be Gaussian while the focal spot geometry could be circular or elliptic. Super-FRS will be one of the important experiments that will be carried out at FAIR. Calculations have shown [1] that if one uses a focal spot with dimensions required for reasonable ion optical resolution and tolerable transmission of the fragments, a solid carbon target will be destroyed in a single experiment whereas one needs to use the same target over an extended period of time. Using a two-dimensional computer code, BIG-2, calculations have been reported [1] in which a novel target design, namely a windowless liquid lithium jet target has been used. Recently, we have performed calculations using a three-dimensional hydrodynamic code and a comparison between the results obtained from the two codes shows excellent agreement.

* European Community RESEARCH INFRASTRUCTURES ACTION under the FP6 programme

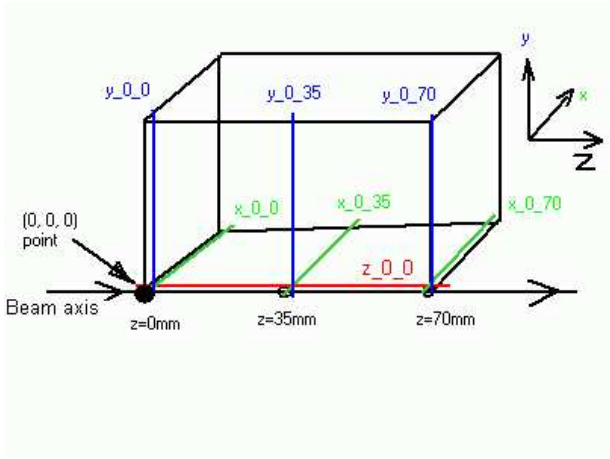


Figure 1: A quater of the target in plane geometry, length = 7 cm, height = 1.5 cm, thickness = 1 cm, beam is directed along Z-axis.

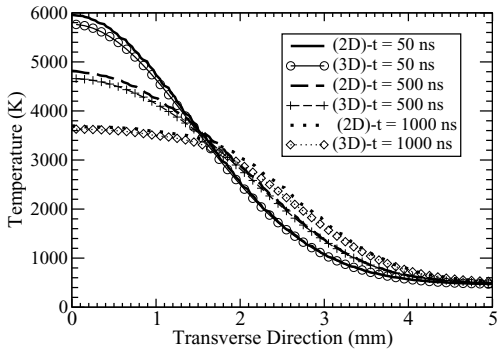


Figure 2: Temperature vs transverse coordinate (Y–axis) at different times, circular focal spot with σ = 1.414 mm, 2D and 3D results

Simulation Results

The target initial conditions are shown in Fig. 1 which is quarter of a target in plane geometry. The beam is incident along the Z-axis and target length, height and thickness are 7 cm, 1.5 cm and 1 cm respectively. It is advantageous to use an elliptic focal spot instead of a circular one in these experiments. This is because the ion optical resolution of the fragments is determined by the X–dimensions whereas the transmission is controlled by the Y-dimensions. One can therefore increase the focal spot area to reduce the tar-

get temperature while keeping reasonable levels of resolution and transmission. However, for a comparison between 2D and 3D results we assume a circular focal spot with a standard deviation, σ = 1.414 mm that is equivalent to an elliptic focal spot with σ_x = 1 mm and σ_y = 2 mm. An initial temperature of 460 K is required to keep lithium in liquid state.

In Fig. 2 we plot temperature along transverse direction (along the height) at three different times using 2D and 3D codes respectively. It is seen that at t = 50 ns when the beam has delivered its total energy, the temperature at the maximum of the Gaussian distribution is of the order of 6000 K and the 2D and 3D results agree very well. At later times the temperature decreases because of the low density caused in the beam heated region as a result of the shock wave moving outwards, but the level of agreement between the 2D and 3D results remains excellent. Corresponding pressure nd density profiles are plotted in Figs. 5 and 6 respectively. It is again seen that the 2D and 3D results show excellent agreement which means that it may be sufficient to use two–dimensional code to study most aspects of this problem.

One of the most important conditions required for the survival of a liquid jet target is that the target temperature remains well below the boiling temperature of the material. The boiling temperature of lithium is 1343 K which means that the target will be destroyed if irradiated with above beam parameters. It has been shown [1] that if one uses an elliptic focal spot with a two-dimensional Gaussian intensity distribution in X–Y plane with standard deviation, σ_x = 2 mm and σ_y = 12 mm along X and Y directions respectively, sufficient resolution and transmission can be achieved. In order to study this problem with a 2D code, one can consider a circular focal spot which has an equivalent area that leads to $sigma$ = 4.9 mm. The BIG-2 code has been used to carry out these calculations and the results are plotted in Figs. 5 – 7 respectively. It also to be noted that in this case we consider a cylindrical target that has a length of 7 cm and a radius of 1.5 cm while the beam is incident along the cylinder axis. The results are plotted along the transverse coordinate (radius).

We note that it has been shown that if one uses the full intensity of the uranium beam (10^{12} ions per bunch), a solid carbon target will survive only if one uses a beam spot with σ_x greater than 4 mm and σ_y = 12 mm. Such a value of σ_x would decrease the resolution to a value that will not be acceptable. Using a liquid jet target one can operate with a focal spot that has σ_x = 2 mm, which is a substantial gain. It is therefore very likely that one would use such a liquid jet target for the Super-FRS.

Figure 5 shows that at t = 50 ns (at the end of the ion pulse), a maximum temperature of 970 K is generated in the target that leads to a maximum pressure of 0.7 GPa, as seen from Fig. 6. The high pressure launches a compression wave outwards in transverse direction that leads to a 15 % reduction in the density at t = 2000 ns (see Fig. 7). Figure 6 shows that at t = 2000 ns the pressure t the target center decreases to almost zero while in the outer part of the target in the compressed part of the target the pressure is of the order of 0.2 GPa. These calculations show that the target may be used with the above beam parameters, however more work is needed in order to come to a final conclusion concerning this problem. For example it is important to calculate the minimum height of the target so

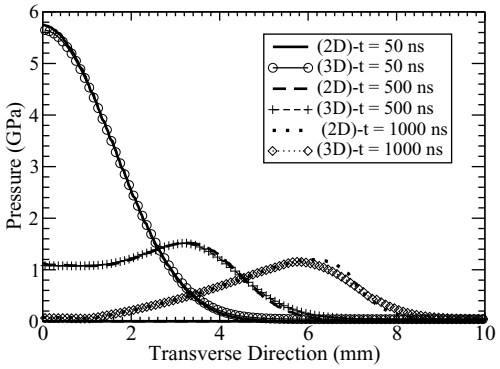


Figure 3: Pressure vs transverse coordinate (Y–axis) at different times, circular focal spot with σ = 1.414 mm, 2D and 3D results.

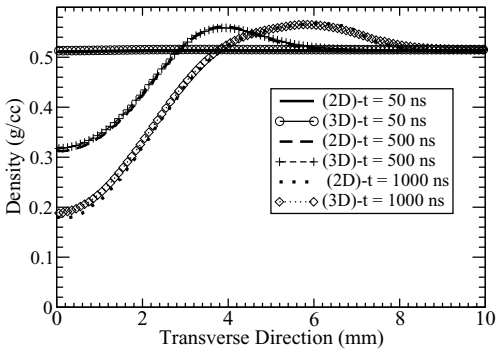


Figure 4: Density vs transverse coordinate (Y–axis) at different times, circular focal spot with σ = 1.414 mm, 2D and 3D results.

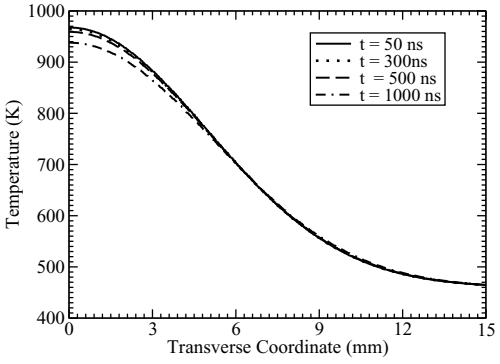


Figure 5: Temperature vs transverse coordinate (cylinder radius) at different times, circular focal spot with σ = 4.9 mm, 2D calculations using BIG-2 code.

that the amplitude of the pressure wave decreases to a level that it does not destroy the jet nozzle.

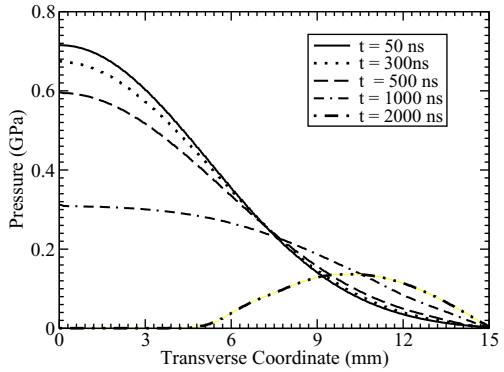


Figure 6: Pressure vs transverse coordinate (cylinder radius) at different times, circular focal spot with σ = 4.9 mm, 2D calculations using BIG-2 code.

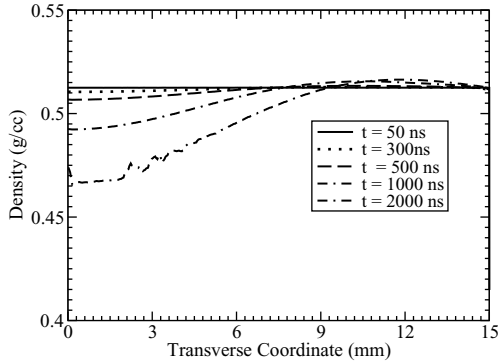


Figure 7: Density vs transverse coordinate (cylinder radius) at different times, circular focal spot with σ = 4.9 mm, 2D calculations using BIG-2 code.

(please contact: n.tahir@gsi.de).

References

[1] N.A. Tahir et al., J. Phys. D: Appl. Phys. 38 (2005) 1828.

[2] V.E. Fortov et al., Nucl. Sci. Eng. 123 (1996) 169.

[3] A.V. Bushman and V.E. Fortov, Sov. Tech. Rev. B 57 (1987) 219.

[4] W.F. Henning, Nucl. Inst. Meth. B 214 (2004) 211.

3D hydrodynamic calculations of the Super-FRS liquid lithium target*

An. Tauschwitz, J.A. Maruhn, Johann Wolfgang Goethe-Universität, Frankfurt am Main, Germany
K. Sümmerer, Gesellschaft für Schwerionenenforschung, Darmstadt, Germany

A careful choice of the production target is very important for SUPER-FRS experiments at FAIR. A windowless liquid Lithium jet is one of the target configurations that are discussed [1]. Focusing of the primary beam improves the resolution of the isotopes and the transmission of the secondary beam, but can destroy the target. Analysis of the target behavior after the beam irradiation provides the beam focusing limits. A fast extracted SIS-100 ion beam with 6×10^{11} Uranium ions at 1000 MeV/u energy is assumed for the simulations. SUPER-FRS will operate in a regime with an energy deposition in the target of a few kJ/g within 50-60 ns. Under these conditions the hydrodynamic energy transport in the liquid target dominates over heat conduction. The hydrodynamic response of an ion beam heated liquid lithium target was calculated with the three-dimensional CFDLIB code [2] developed in Los Alamos. The ion beam coupling and implementation of the SESAME equation-of-state library [3] were made by the Frankfurt group.

For the above mentioned beam parameters the energy deposition of the ion beam is fast on the hydrodynamic time scale. The created pressure gradients give rise to pressure waves in the target. The target can become unstable if the matter gets into the two-phase region, where liquid and gas can coexist. Before the liquid matter becomes unstable it passes through the meta-stable region of an overheated liquid which extends to the spinodal. The spinodal separates the meta-stable from the unstable regime within the two-phase region. For this simulation we assume that the integrity of the liquid jet is no longer given once the matter undergoes spinodal decomposition.

In the calculations an elliptical beam spot with a Gaussian intensity profile is assumed. The horizontal size of the beam σ_x is fixed to 2 mm. By changing the transverse beam size, σ_y we have found that the spinodal decomposition of the target material will be avoided if $\sigma_y \geqslant 4$ mm. For this limiting beam spot size the energy deposition in the center of the heated spot is 3.3 kJ/g. This corresponds to a temperature of 1560 K. The target has a depth $L_z = 7$ cm along the beam axis, the line density is 3.7 g/cm^2. The horizontal size $L_x = 1.6$ cm is dictated by the stability in the jet flow, a length of $L_y = 6.4$ cm is considered in the flow direction. The center of the target is placed at the origin of the coordinate system. After the ion beam energy is deposited, a compression wave is launched in the xy-plane. The free surface of the heated region moves outwards, and an expansion wave runs along the z-axis to the target center.

* Work supported by BMBF Project # 06 F 132

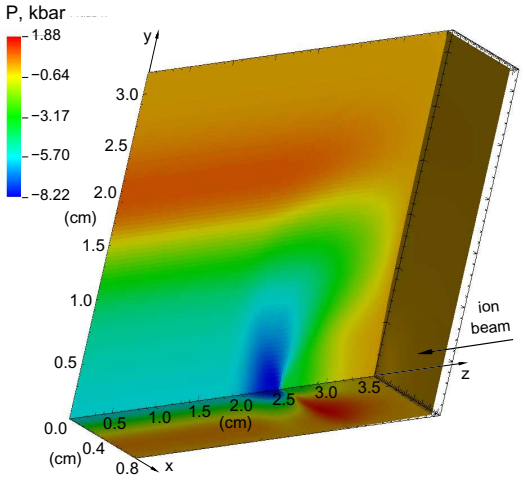


Figure 1: Pressure distribution in the target volume at $t = 3.7\,\mu$s.

When the compression wave propagating in the x-direction reaches the target surface, an expansion wave starts to move inwards. Figure 1 shows a pressure distribution in the target at $t = 3.7\,\mu$s when the two expansion waves overlap and the pressure has the lowest value of $P = -8.2$ kbar.

The negative pressure means that the matter is not compressed but expanded. Under these conditions the liquid can be unstable because the negative pressure may lead to cavitation. The negative pressure threshold for cavitation depends very much on the measures taken to degas the liquid. It is generally assumed that the degassing process removes large size bubbles. A next step for our investigations will be the evaluation of the heated Li-jet behavior under conditions of gas bubble existence. However, theoretical considerations of wave propagation in a bubbly liquid assume that the initial diameter of the bubbles and the initial bubble volume fraction are known. Therefore, improved conclusions about the ion beam focusing limits for the SUPER-FRS liquid lithium target will require experimental data.

References

[1] FAIR, Conceptual Design Report, 2001.

[2] J.R. Baumgardner et al., Los Alamos Report LA-UR-90-1361.

[3] SESAME'83: Report on the Los Alamos Equation-of-State Library, T4-Group, Los Alamos National Laboratory Report No. LALP-83-4, Los Alamos 1983

Luminosity calculations for NESR experiments*

K.-H. Schmidt, H. Simon#, Th. Stöhlker, H. Weick, GSI, Darmstadt, Germany
A. Mol, KVI, Groningen, The Netherlands
V.A. Volokov, RRC "The Kurchatov Institute", Moscow, Russia
M. Pikulskiy, University of Kiev, Ukraina

.

The obtainable isotope intensities in the NESR are of prime interest for e.g. the AIC, ELISe, EXL, ILIMA and SPARC experiments. This paper describes briefly a newly developed programme that allows reliably predicting them. At energies around 1 GeV/u, the isotope production process can be well described by the intra-nuclear cascade model, or - in the case of heavy-ion collisions - by the abrasion model. For quantitative predictions these have been modelled in terms of two-step (abrasion plus evaporation) codes (ABRABLA), with a careful description of fission included [1]. Alternatively, fragmentation cross sections of non-fissile projectiles have been fitted to an empirical formula, EPAX [2]. The transport through the SuperFRS [3] is calculated using a parameterization that is obtained from a full ion optics simulation, together with a model calculation for the nuclear and electromagnetic breakup processes in the Nb degrader material. The degrader thickness is herby optimized to allow for the necessary fragment resolution while restricting the maximum energy loss in the material. The new primary beam intensities and cycling schemes [4] for the SIS cyclotron installations have been taken into account. A more refined full production simulation is planned. The beam life time (τ) for cooled and stored ion beams in the NESR is determined by recombination processes in the electron cooler and charge changing collisions with residual gas atoms / molecules. In addition, for the case that the internal target is used, charge exchange in collisions with the gas atoms of the jet target must be considered. Usually, this gives the most important contribution to beam losses and determines the overall beam lifetime. Target density ρ (p/cm^2) and charge exchange rate λ are simply connected by $\lambda = 1/\tau = \rho \sigma f$, where f denotes the revolution frequency of the circulating ion beam and σ the atomic charge-exchange cross-section, respectively. Assuming a stored beam of bare ions, the two most important charge exchange processes for bare ions are Radiative and Non-Radiative Electron Capture (REC and NRC) [5]. In case of H- and He-like ions K-shell ionization occurring in atomic collisions have to be considered in addition [6]. Together with the tabulated nuclear life times and an optimized measurement cycle in the NESR e.g. the result shown in Fig. 1 is obtained.

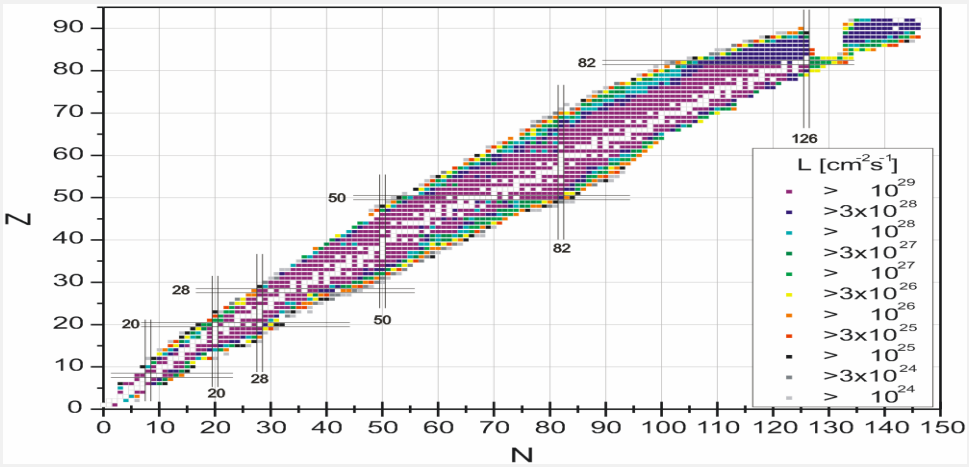


Figure 1: Luminosities for the EXL experiment ($\rho = 10^{14}$ p/cm^2) in the NESR using the newly implemented options in the luminosity calculation programme. For details, see text.

References

[1] J.-J. Gaimard, K.-H.S., Nucl. Phys. **A531**, 709 (1991)
J. Benlliure et al., Nucl. Phys. **A628**, 458 (1998).
[2] K. Sümmerer,B.Blank,Phys.Rev.**C61**,034607 (2000).
[3] H. Geissel et al., Nucl. Inst. Meth **B 204** (2003) 71
[4] FAIR Newsletter No. 1 , December 2005
[5] Th. Stöhlker et al., Phys. Rev. A58, 2043 (1998)
[6] J. Eichler and Th. Stöhlker, in Atomic Physics with Heavy Ions, Editors: H. F. Beyer, V. P. Shevel'ko, (Springer 1999) ISBN: 3540648755

*Supported by the EC under INTAS contract number 03-54-6545
#h.simon@gsi.de

The CBM experiment at FAIR*

V. Friese, W.F.J. Müller, P. Senger, GSI Darmstadt, and the CBM Collaboration

The high-intensity heavy-ion beams of the FAIR accelerators, together with the planned Compressed Baryonic Matter (CBM) experiment [1], offer unique possibilities to produce and to investigate baryonic matter at highest densities in the laboratory. According to calculations, baryon densities of up to 10 times saturation density (comparable to the ones in the inner core of neutron stars) and energy densities of up to 5 GeV/fm^3 can be reached in central collisions of heavy nuclei at top SIS 300 energy. These values exceed by far the densities where nucleons are expected to exist as individual entities. The baryonic matter in the reaction volume is highly excited, and most probably it undergoes a transition from hadronic to parton dominated matter. Calculations predict that already at beam energies above 10 AGeV the system spends part of its lifetime beyond the hadronic world [2].

The goal of the CBM research program is to explore the QCD phase diagram in the region of high baryon chemical potentials. Of particular interest are the structure and the equation-of-state of baryonic matter at high densities, the location of the phase boundary between hadronic and partonic matter (including the QCD critical endpoint), and the onset of chiral symmetry restoration at high net-baryon densities. The most promising observables are particles with charm, low-mass vector mesons decaying into dilepton pairs, (multi-)strange particles, event-by-event fluctuations, and collective flow. The task of the experiment is to identify hadrons and leptons in collisions with up to 1000 charged particles at event rates of up to 10 MHz. A particular experimental challenge is the selection of secondary vertices with high accuracy. The measurements require a high-speed data acquisition (DAQ) architecture and an appropriate high-level event selection concept.

A schematic view of the proposed CBM detector concept is shown in figure 1. The core of the setup is a Silicon Tracking System (STS) located inside the large gap of the dipole magnet. The STS consists of several planar layers of silicon-pixel and silicon microstrip detectors which have to provide the capabilities for track reconstruction, determination of primary and secondary vertices, and momentum determination. Electrons from low-mass vector-meson decays will be identified with a Ring Imaging Cherenkov (RICH) detector. The TRD detector will provide charged particle tracking and the identification of high energy electrons and positrons. Hadron identification will be performed using a TOF wall consisting of a RPC array. The ECAL will be used for the identification of electrons and photons.

* Work supported by EU/FP6 HADRONPHYSICS (see Annex) and by INTAS

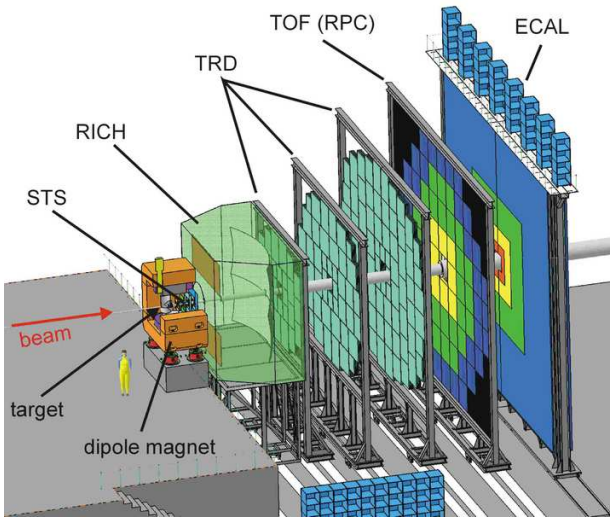


Figure 1: Schematic view of the Compressed Baryonic Matter (CBM) experiment planned at FAIR. The setup consists of a high resolution Silicon Tracking System (STS), a Ring Imaging Cherenkov detector (RICH), three stations of Transition Radiation Detectors (TRD), a time-of-flight (TOF) system made of Resistive Plate Chambers (RPC) and an Electromagnetic Calorimeter (ECAL).

Feasibility studies

The feasibility studies- which were performed within the CBM software framework [3] - concentrated on the optimization of the detector configuration in order to assure that the key observables are accessible with sufficient precision. Major progress has been made in track- and vertex reconstruction taking into account a realistic Silicon detector response, including pile-up events in the pixel vertex detectors and fake hits in the Strip detectors. STS track reconstruction efficiencies of more than 90% could be obtained when using a Cellular Automaton track finder and a Kalman filter for track fitting [4]. Similar results are obtained for track reconstruction in the TRD [5].

Open charm

One of the benchmark observables are the D-mesons which will be identified via their hadronic decay into one or two pions and a kaon. This measurement poses a major challenge to the Silicon tracker: the decay vertex of the D-meson - which is displaced from the main vertex of the collision by several 10 μm - has to de determined with an accuracy of about 50 μm in order to suppress the overwhelming combinatorial background caused by pions and kaons directly emitted from the fireball. The simulations

show that an event suppression factor of about 1000 can be achieved when using a thin and highly granulated vertex pixel detector. This factor is sufficient for an online selection of D-meson candidates even in gold-on-gold collisions at reaction rates up to 10 MHz [6].

Vector mesons

Another key observable are low-mass vector-mesons which decay into lepton pairs with a branching ratio of $10^{-4} - 10^{-5}$. The major challenge, both for the measurement and for the data analysis, is to reject the physical background of electron-positron pairs from Dalitz decays and gamma conversion. According to simulations based on an optimized Silicon tracker configuration one expects a signal-to-combinatorial background ratio of about 0.5 for ω- and ϕ-mesons in central gold-on-gold collisions at an energy of 25 GeV/nucleon. This analysis requires a pion suppression factor of 10^4 which can be achieved by the combined performance of RICH and TRD [7].

As an alternative approach to the dielectron measurement we have studied the possibility of detecting vector mesons (ρ, ω, ϕ, J/ψ) via their decay into $\mu^-\mu^+$ pairs. The idea is to identify the muons just behind the Silicon Tracking System with a combination of absorber and detector layers. The simulations are based on track reconstruction algorithms taking into account a realistic response of the Silicon pixel and strip detectors (STS) and of the muon chambers. Reconstructed charged particle tracks with hits in the muon chambers located behind the last absorber layer are associated with muons. The results of the preliminary studies demonstrate the feasibility of dimuon measurements with the CBM detector setup using an active absorber system for Au+Au collisions at 25 AGeV. This is particularly true for J/ψ mesons which can be identified within the full phase-space acceptance of the CBM setup with a signal-to-background ratio of 10 - 100. In the case of low-mass vector mesons the phase-space acceptance, the efficiency, and the signal-to-background ratio are reduced [8].

Detector R&D

Silicon Tracker System

The Silicon Tracking System (STS) serves for track and momentum measurement and for determination of primary and secondary vertices. The current STS layout consists of minimum 7 layers and is placed inside a magnetic dipole field which provides the bending power required for momentum determination with an accuracy of about $\Delta p/p$ = 1 %. The first 2 stations serve for vertex determination and will consist of silicon pixel detectors. Monolithic Active Pixel Sensors (MAPS) with a pixel size of 40x40 μm^2 and a thickness of 100 μm would perfectly fulfill our requirements concerning vertex resolution which is needed to measure the displaced vertices of D mesons [6]. The R&D on MAPS concentrates on the improvement of radiation hardness and readout speed [9].The next two Silicon layers (distance from the target 20 and 40 cm) may consist of hybrid pixel detectors, and the for last three layers (distance from the target about 60, 80, and 100 cm) we consider to use Silicon micro-strip detectors. Simulations are being performed to optimize the number of layers, the layout and material budget of the detectors [10].

Ring Imaging Cherenkov detectors

The RICH detector is designed to provide identification of electrons and suppression of pions. Detector R&D concentrates on the radiator gas, on the mirror, and on the photon detector. Ring recognition algorithms are developed to accurately determine the ring radii and the ring centers. The electron identification efficiency depends crucially on the matching of Cherenkov rings to particle trajectories. Performance studies are in progress, taking into account track reconstruction and more realistic detector properties, in order to optimize the detector layout [11].

Transition radiation detector

The task of the TRD is charged particle tracking and identification of high energy electrons and positrons from charmonium decays. Detector R&D concentrates on the development of highly granular and fast gaseous detectors which can stand the high-rate environment of CBM. Prototype gas detectors (based on MWPC and GEM technology) have been built and tested with particle rates of up to 100 kHz/cm^2 without deterioration of performance [12, 13].

Resistive plate chambers

RPC detector R&D is focussed on high rate capability, low resistivity material, long term stability and the realization of large arrays with overall excellent timing performance [14].

References

[1] CBM Technical Status Report, Januar 2005, `www-linux.gsi.de/~hoehne/report/cbmtsr_public.pdf`

[2] Yu.B. Ivanov, V.N. Russkikh, V.D. Toneev, nucl-th/0503088

[3] M. Al-Turany, D. Bertini, see FAIR-QCD-CBM-9

[4] S. Gorbunov, I. Kisel, see FAIR-QCD-CBM-03

[5] S. Gorbunov et al., see FAIR-QCD-CBM-07

[6] I. Vassiliev et al., see FAIR-QCD-CBM-04

[7] T. Galatyuk et al., see FAIR-QCD-CBM-05

[8] A. Kiseleva et al., see FAIR-QCD-CBM-08

[9] S. Amar-Youcef et al., see FAIR-QCD-CBM-02

[10] J. Heuser et al., see FAIR-QCD-CBM-01

[11] C. Höhne, see FAIR-QCD-CBM-06

[12] M. Petrovici et al., see FAIR-QCD-CBM-10

[13] C. Garabatos, F. Uhlig, see FAIR-QCD-CBM-12

[14] E. Cordier, see FAIR-QCD-CBM-11

A Silicon Tracking System for CBM *

J. M. Heuser, W. F. J. Müller, P. Senger – GSI, Darmstadt, Germany
C. Müntz, J. Stroth – J. W. Goethe-Universität, Frankfurt/Main, Germany
and the CBM Collaboration

The Silicon Tracking System (STS) is the central component of the CBM experiment. The challenging task of the STS is the reconstruction of the particle tracks, the measurement of their momenta, and the detection of primary and secondary vertices. A benchmark observable is the D meson ("open charm") which has to be identified via its hadronic decays $D^0 \rightarrow K^-\pi^+$ and $D^\pm \rightarrow K^\mp\pi^\pm\pi^\pm$. This task requires a vertex detector with high position resolution, very low material budget, extreme radiation tolerance and a fast self-triggered readout.

Detector Concept

The actual concept of the STS is shown in Fig. 1. Seven detector stations with a geometrical acceptance between 50 and 500 mrad are arranged in the 1 m long gap of a superconducting dipole magnet with 1 Tm bending power. Three very thin pixel detector stations in the upstream part close to the target provide true space points with high position resolution for the vertex measurement. They cover about 150 cm^2 active area and are installed in vacuum. Charged particle tracking is realized in the downstream section of the telescope with four thin micro-strip detector stations. They cover about 1.5 m^2. Already their size alone calls for the application of micro-strip technology that can be produced on large wafers.

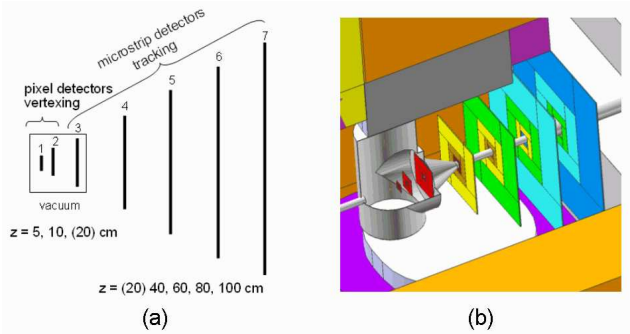


Figure 1: (a) Concept of the Silicon Tracking System. (b) Detector stations in the dipole magnet (design study).

Detector Layout Studies

Several detector configurations with different sensor types and material budgets were assessed. One option comprised three stations of Monolithic Active Pixel Sensors (MAPS) [1] for the vertex measurement, with 150 μm silicon equivalent thickness, 5 μm spatial resolution but event pile-up due to limited readout speed, and four stations of double-sided micro-strip sensors for the tracking with 200 μm thickness and 15 μm spatial resolution. As micro-strip detectors are limited by fake tracks in high track-density conditions, we also studied a detector configuration with a fast hybrid pixel detector of 750 μm effective silicon thickness and 50 μm pixel pitch replacing the third MAPS station. With this configuration, minimum-bias 25 GeV Au+Au collisions could be reconstructed with 98% average single-track efficiency. The D^0 signal was detected with about 8% efficiency [2]. Further ongoing studies focus on optimizing the positions and number of stations for best tracking, momentum and vertex measurements with more redundancy.

Detector R&D

Current pixel detector technologies combine only two out of four performance requirements essential to CBM: Either very small pixel size and very low total thickness (CMOS sensors, MAPS), or fast readout and radiation hardness (hybrid pixel detectors). We started to develop a pixel detector prototype for the vertexing stations based on MAPS [3]. Attractive is their already excellent position resolution and small thickness of ultimately around 50 μm. We focus on improving the radiation tolerance of the sensor to 10^{13} n_{eq} and the readout time to 10 μs. However, the harsh radiation conditions at the first pixel station, 4×10^{15} n_{eq} for one year of 10^7 interactions/s, suggest to apply this detector only at lower beam intensities in the initial phase of CBM. Alternative sensor technologies, as new developments of thin hybrid or SOI-monolithic pixel detectors with small sensor cells, have to be considered for the future.

For the tracking stations, we started to develop thin double-sided AC-coupled micro-strip sensors with 200 μm thickness, 50 μm pitch and 15° stereo angle. As the experiment will comprise only high-level triggers, the front-end electronics must be capable of self-triggered data output. A micro-strip readout chip with this feature, matching also others of the CBM specifications, has been developed by the DETNI [4] consortium. We plan to explore and to adapt this chip.

References

[1] G. Deptuch et al., NIM **A535** (2004) 366-369
[2] I. Vassiliev et al., see FAIR-QCD-CBM-04
[3] S. Amar-Youcef et al., see FAIR-QCD-CBM-02
[4] http://jra1.neutron-eu.net/jra1

* Supported by EU/FP6 HADRONPHYSICS (see Annex) and INTAS

Achievements of Monolithic Active Pixel Sensors for the CBM Vertex Detector

S. Amar-Youcef[a], A. Besson[b], G. Claus[b], M. Deveaux[b,c], A. Dorokhov[b], W. Dulinski[b], S. Heini[b], A. Himmi[b], K. Jaaskelainen[b], C. Müntz[a], F. Rami[b], J. Stroth[a], I. Valin[b], M. Winter[b]
[a]Johann-Wolfgang-Goethe-Universität-Frankfurt, [b]IReS-Strasbourg, [c]GSI-Darmstadt

The development of Monolithic Active Pixel Sensors for the CBM vertex detector is mainly driven by two issues: the read-out speed and the tolerance to non-ionising radiation. Significant progress was achieved in 2005 in these two areas, as well as for the tolerance to ionising radiation and for the sensor thinning [1, 2]. Simulation studies were also performed in order to optimize the design of the detector.

Fast read-out architecture

The most advanced fast read-out architecture, which is incorporated in the MIMOSA-8 prototype, was tested with an ^{55}Fe source and on a $\sim$ 5 GeV e$^-$ beam at DESY. The sensor features 32 columns read out in parallel. Each column contains 128 pixels equipped with Correlated Double Sampling (CDS). 24 of these columns are ended with a discriminator, while the other 8 deliver an analog output allowing to assess the performance of the analog part of the architecture. The measured noise after CDS came out to be $\sim$ 15 e$^-$ ENC only. However, the signal-to-noise (S/N) ratio was rather modest, i.e. $\sim$ 9, reflecting an epitaxial layer thickness of less than 7 μm for the TSMC-0.25 technology, in which the chip was manufactured.

The performance of the architecture was assessed by computing the detection efficiency of the chip when the discriminator thresholds were set to a value corresponding to a S/N ratio of 4. An efficiency better than 99 % was observed (with a fake cluster rate of $\sim 10^{-3}$), despite the modest S/N ratio. Overall, these tests demonstrate that the chip architecture performs very well and can be extended by replacing each discriminator with a 4-5 bits ADC. On the other hand, the chip should be manufactured in a technology offering a thicker epitaxial layer, in order to ensure a higher S/N ratio. The AMS 0.35 OPTO technology is at present the best candidate, since it offers a 11 - 12 μm thick epitaxial layer, which translates into a typical S/N ratio of 20 - 30. A prototype (MIMOSA-15) featuring only the pixels with integrated CDS of MIMOSA-8 (but not yet its columns ended with discriminators) was fabricated in this technology. First tests with an ^{55}Fe source show that the noise performances are very close to those of the analog part of MIMOSA-8.

Radiation tolerance

The first chip fabricated in the AMS 0.35 OPTO technology (MIMOSA-9) was exposed to $\sim$ 1 MeV neutrons in Dubna, and consecutively tested on the DESY electron beam. It was observed that even for a fluence of $\sim 10^{12}$n$_{eq}$/cm^2, the sensor still exhibits a S/N ratio of $\sim$ 19, and a detection efficiency of $\sim$ 99.5 % at a temperature of -20°C. This promising result was obtained with standard pixels, not equipped with CDS micro-circuits, which exhibit a noise of $\sim$ 10 e$^-$ ENC only before irradiation, while pixels with CDS have a noise of $\sim$ 15 e$^-$ ENC. The study will therefore be repeated with such pixels and fluences of up to 10^{13}n$_{eq}$/cm^2 will be explored.

The tolerance to ionising radiation was significantly improved by modifying the pixel design in order to reduce the increase of the leakage current consecutive to large integrated dose exposures. Arrays of MIMOSA-11 and -15 were designed for this purpose with pixels where the thick oxide near the sensing diode was removed and a P+ guard ring was implemented around the diode. In absence of irradiation, these pixels exhibit a noise of $\sim$ 12 e$^-$ ENC to be compared to $\sim$ 10 e$^-$ ENC for standard pixels. Tests of chips irradiated with integrated doses of up to 1 MRad show that the noise of the standard pixels increases rapidly, contrary to the radiation tolerant pixel, for which the noise remains below 15 (resp. 11) e$^-$ ENC after 1 MRad exposure, at an operating temperature of +10°C (resp. – 25°C).

Thinning

Industrial procedures are being investigated which allow to thin the sensors to $\sim$ 50 μm or less. 1 wafer of reticle size sensors (i.e. 3.5 cm^2 wide) was successfuly thinned to 50 μm and diced. The thinning makes the chips lose their flatness due to the release of internal mechanical constraints. A handling procedure is under study, which accounts for the sensor curvature and fragility and allows to bond them on their support.

Simulation studies

Extensive simulations were carried out in order to estimate the radiation dose corresponding to the reconstruction of 10^4 D^0-mesons. Preliminary results of this study show that a radiation hardness of 10^{13} n_{eq}/cm^2 is sufficient to reach this goal. Slight modifications in the detector design are supposed to reduce this requirement by a factor of four to five.

References

[1] A.Besson et al., “Status of CMOS sensor R&D”, talk presented at the ECFA-ILC Workshop, November 2005, Vienna

[2] A.Besson et al., ”Status of CMOS Sensors: 2005 outcome”, talk presented at the SOCLE Wokshop, 12-13 January 2006, IPNL, Lyon; http://lyoinfo.in2p3.fr/socle06/.

Event Reconstruction in the CBM Experiment*

S. Gorbunov, DESY Zeuthen, Platanenallee 6, 15738 Zeuthen, Germany
I. Kisel, Kirchhoff Institute for Physics, University of Heidelberg, 69120 Heidelberg, Germany
and the CBM Collaboration

Large track density together with the presence of a non-homogeneous magnetic field make reconstruction of events in the CBM experiment [1] complicated.

A cellular automaton method is used to reconstruct tracks in the silicon tracking system (STS). The algorithm was applied to central Au+Au collisions at 25 AGeV beam energy simulated by UrQMD and transported through the CBM detector setup [2].

Track category	Efficiency (%)			
	Ideal.	Realistic with pile-up		
	-	0	5	10
Reference set ($p \geq 1$)	99.45	97.38	96.85	96.43
All set	96.98	93.90	93.05	91.59
Extra set ($p < 1$)	89.46	84.64	82.90	78.71
Ghost	0.61	4.02	9.91	17.52

Table 1: Track reconstruction efficiency for the idealistic and realistic STS setups.

The efficiency of track reconstruction for particles detected in at least four stations is presented in Table 1. Two STS detector setups have been investigated. In the idealistic setup all stations are pixel-like detectors. The realistic setup consists of (going downstream) 2 MAPS detectors, 1 pixel detector and 4 double-sided silicon strip detectors with 15^o stereo angle. Different number of pile-up events in the MAPS stations have been investigated.

Track fitting [1, 2] is done using the Kalman filter technique. A special analytic formula [3] has been derived for fast track extrapolation in a non-homogeneous magnetic field. The precision of extrapolation does not depend on the shape of the magnetic field. The extrapolated track parameters are expanded in a power series of the magnetic field components. The formula with terms up to the third order has the quality of propagation equal to the fourth-order Runge-Kutta method.

Parameter	PV	SV_G	SV_{GM}	SV_{GT}	SV_{GMT}
x_v	0.71	7.6	7.6	1.8	1.7
y_v	0.61	7.1	7.0	1.9	1.7
z_v	3.99	47.7	46.1	46.0	44.4

Table 2: Accuracy (in μm) of the primary (PV) and secondary (SV) vertex parameters obtained from Au+Au collisions at 25 AGeV with D^0 decays included [2].

A vertex fitting package is also based on the Kalman filter. The precision of the reconstructed primary and secondary vertex positions are given in Table 2. The secondary vertex parameters obtained in the geometrical (G) vertex fit can be improved by taking into account several assumptions on tracks associated to the vertex. The mass (M) constraint is applied in the case one or several combinations of particles in the vertex are known to originate from a narrow width mass state. The topological (T) constraint is used to point a mother particle to the (already reconstructed) primary vertex.

Rings set	Performance (%)
Reference set efficiency	94.3
All set efficiency	74.0
Extra set efficiency	65.5
Ghost rate	12.8

Table 3: Performance of the standalone ring finding algorithm [4].

A standalone ring finding algorithm [4] for the RICH detector is based on the elastic net method. The method does not require any prior track information and can be used for triggering. The algorithm has a high efficiency (Table 3) and is very fast (5 ms/ev).

The next steps include tracking in the TRD and muon detectors, global event reconstruction and investigation of tracking problems at the trigger stage of the event reconstruction.

References

[1] CBM Collaboration, Compressed Baryonic Matter Experiment. Technical Status Report, GSI, Darmstadt, 2005.

[2] S. Gorbunov, I. Kisel and Iou. Vassiliev, Analysis of D^0 meson detection in Au+Au collisions at 25 AGeV, CBM-PHYS-note-2005-001, 23 June 2005.

[3] S. Gorbunov and I. Kisel, An analytic formula for track extrapolation in an inhomogeneous magnetic field, CBM-SOFT-note-2005-001, 18 March 2005.

[4] S. Gorbunov and I. Kisel, Elastic net for standalone RICH ring finding, CBM-SOFT-note-2005-002, 22 September 2005.

* Supported by EU/FP6 HADRONPHYSICS (see Annex)

Open charm measurement in $Au + Au$ collisions at 25 AGeV in the CBM experiment*

Iouri Vassiliev, GSI, Darmstadt, Germany, S. Gorbunov, DESY, Zeuten, Germany,
I. Kisel, KIP, Heidelberg, Germany and the CBM Collaboration

One of the major experimental challenges of the CBM experiment is to trigger on the displaced vertex of the D-meson hadronic decay in the environment of a heavy-ion collision. This task requires fast and efficient track reconstruction algorithms and high resolution secondary vertex determination. Particular difficulties in recognizing the displaced vertex of the rare D meson decays (lifetime of the D^0 and D^+ mesons are $c\tau$ = 123 μm and 312 μm correspondingly) are caused by: weak hyperon decays which produce displaced vertices closed to the target, very low multiplicity and branching ratio of the D meson production ($5.8 \cdot 10^{-6}$ for neutral and $1.2 \cdot 10^{-5}$ for charged Ds), multiple scattering in the detectors and beam pipe.

To study the feasibility of open charm mesons measurement in the CBM experiment 10^4 central $Au+Au$ UrQMD events at 25 AGeV have been simulated. The K^- and π^+ pair in case of D^0 decay or K^-, π^+ and π^+ in case of D^+ decay have been added as a signal to each event in order to simulate a signal in the environment of the background hadrons. The primary vertex was determined with high accuracy (4 μm in z-direction, 0.7 μm in x and y) from about 450 tracks fitted in the STS with inhomogeneous magnetic field by the Kalman filter procedure [1]. Two MAPS (10 μm x 10 μm, 200 μm thickness) and five (35 μm x 35 μm) pixel silicon stations (200 μm thickness) allow to achieve z-resolution of the secondary vertex of 39 μm for D^0 and 37 μm for D^+ decay. It is sufficient to separate detached secondary vertices from the primaries [1, 2]. Different STS configurations (varying number of stations, type of detectors, interaction rates, radiation tolerance etc.) with hybrid pixels and strip silicon detectors are under study now.

The D meson decays through a week process, consequently, K^- and π^+(s) tracks have relatively large impact parameters and, therefore, the distance between the primary vertex and the decay point is measurable. Since the majority of the primary tracks have very small impact parameter, significant part of the combinatorial background can be rejected using a cut on the χ^2 distance to primary vertex. This increases the D^0 reconstruction efficiency up to 25% keeping the same background rejection factor [1].

The main background contributions are due to combinatorics (multiple scattering in the detectors) and due to hyperon decays. The combinatorial background is suppressed mainly by the χ^2 distance cut on the impact parameter, z-vertex cut to select detached vertices, the requirement for D meson momentum to point to the primary vertex, the p_t-cut and the vertex χ^2 cut for good quality secondary vertices. Signal to background ratio is about 3.0 for D^0 and about 5.3 for D^+ (see Fig. 1) mainly due to different shape of the combinatorial backgrounds (two and three tracks correspondingly).

cut	D^0, D^+	**eff.** D^0	**eff.** D^+
χ^2 dist. to PV	3.5 σ, 3.5 σ	53	67
$p_{K\pi}$-cut (GeV/c)	1.0, 0.9(0.5)	72	76
$p_{t\ K\pi}$-cut (GeV/c)	0.5, 0.25(0.15)	61	70
z-vert. cut (μm)	250, 250	54	81
geo. vertex χ^2	$\leq$5, $\leq$5	91	83
GT 3 track χ^2	–, $\leq$5	–	72
all cuts	–	8.5%	5.3%

Table 1: Optimized cut values

After applying all cuts the background is suppressed by a factor of 10^5 in the signal mass region. The optimized cut values together with the signal efficiency are shown in the table. D^0 and D^+ reconstruction efficiencies are 8.5% and 5.3% (lower geometric acceptance) correspondingly. The shape of the background in the signal IM region was estimated using MC super event technique. The resulting background plus D^+ signal spectrum is shown in Figure 1.

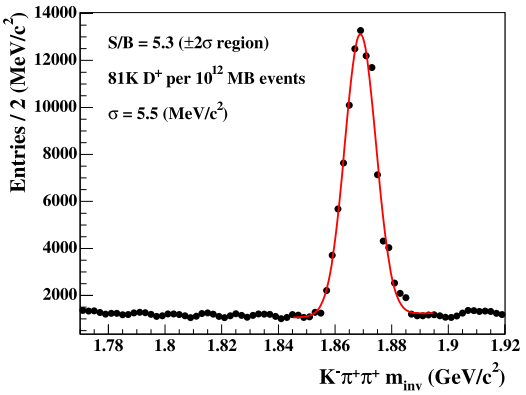


Figure 1: D^+ and background invariant mass spectrum. Estimated spectrum corresponds 10^{12} minimum bias events.

References

[1] S. Gorbunov, I. Kisel and Iouri Vassiliev, Analysis of D^0 Meson Detection in Au+Au Collisions at 25 AGeV, CBM-PHYS-note-2005-001, June 2005.

[2] Iouri Vassiliev, S. Gorbunov, I. Kisel, CBM Collaboration meeting, September 2005.

* Supported by EU/FP6 HADRONPHYSICS (see Annex)

Strategies for electron pair reconstruction in CBM

T. Galatyuk, V. Friese, D. Kresan, P. Senger, GSI, Darmstadt, Germany
J. Stroth, Institut für Kernphysik, Frankfurt, Germany

The investigation of the inmedium properties of short lived neutral vector mesons (ρ, ω, ϕ) via detection of their decay in electron-positron pairs is one of the major issues of the CBM physics program. The strategies to reduce the combinatorial background in electron pair measurements with the CBM detector are discussed here.

The simulations were performed for the collision system $Au + Au$ at a beam energy of 25 AGeV. The final state phase space distributions of hadrons and photons were generated using the UrQMD code. To study the most extream case the simulation was done for zero impact parameter. The phase space distribution of electrons and positrons from purely leptonic and semi-leptonic (i.e. Dalitz) decays of ρ, ω, ϕ were obtained using the PLUTO event generator. The ρ meson mass distribution was generated by including a Breit-Wigner shape around the pole mass, thermal phase space factors, and a factor $1/M^3$ to account for vector dominance in the decay into e^+ e^-. All particles were finally propagated through the detector system using the GEANT3 package.

The dominant background sources are random combinations of electrons and positrons from π^0-Dalitz decay and γ conversion. In a central $Au + Au$ collision about 360 π^0 mesons are produced, which decay into $e^+e^-\gamma$ ($\Gamma/\Gamma_{tot} = 0.012$) and to 2γ ($\Gamma/\Gamma_{tot} = 0.988$).

Hitherto existing electron pair spectrometers (DLS [1], HADES [2], CERES [3]) provide electron identification in front of the magnetic field, this permits the rejection of electron-positron pairs with small opening angle, which most probably originate from π^0-Dalitz decay and γ conversion. At CBM there is no electron ID in front of the Silicon Tracking Station and the magnetic field. Hence, the rejection strategy has to rely to a large extend on the track topology of pairs in the compact Silicon Tracking Station.

To increase the acceptance for low momentum particles the magnetic field was reduced to $B_{max} = 0.33$ T and shifted 20 cm downstream. A single 25 μm gold target was assumed. The first STS station was not used in the analysis due to its limited acceptance for tracks with small laboratory polar angles. A track was considered fully reconstructed if tracking station 2 to 7 were traversed and the RICH and the 3 TRD detectors were hit. Perfect particle identification was assumed for fully reconstructed tracks. Tracks were considered partially reconstructed if a minimum of 4 STS stations were traversed. For these tracks only the charge sign information and the Monte-Carlo momentum were used. The Monte-Carlo momenta where smeared assuming 1 % momentum resolution independent of particle momentum.

The strategy of background rejection comprises three steps. First step is to identify and reject true pairs originating from conversion, second step is to remove single tracks where the true partner was not fully reconstructed, third step is to assign pairs with a characteristic pattern to π^0-Dalitz pairs. All cuts are summarized in Table 1.

cut	optimum value
invariant mass cut	0.025 GeV/c^2
closest neighbor hits cut	0.045 cm
p_t of closest neighbor cut	0.05 GeV/c
$(\theta_{1,2} + m_{e^-e^+})$ of closest neighbor cut	5^o + 0.01 GeV/c^2
p_t of identified leptons cut	0.2 GeV/c
opening angle cut	2^o
Dalitz decay reconstruction	0.2 GeV/c^2

Table 1: Optimized cut values

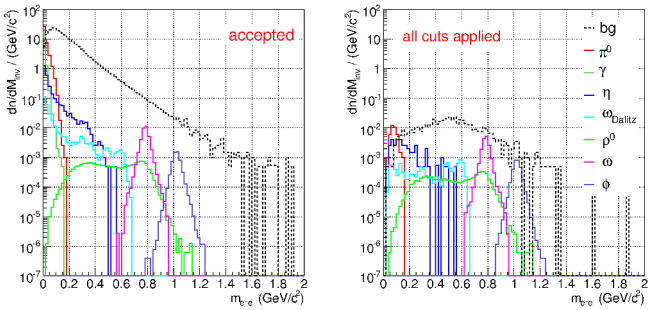


Figure 1: Invariant mass spectra before (left) and after (right) all cuts. Red: π^0-Dalitz, dark green: γ, dark blue: η-Dalitz, blue: ω-Dalitz, magenta: ω, green: ρ^0, violet: ϕ, black: combinatorial background.

The invariant mass spectrum for electron pairs arising after applying all cuts is shown in Figure 1 (right panel). For comparison, the respective contribution before background rejection is shown in the left panel. The S/B ratio steadily increases with each cut applied. The ω and ϕ signal are visible above the combinatorial background. The S/B ratio in a ± 1.4 σ_m range around the vector meson peaks are about 0.5 for ω and 0.3 for ϕ, for π^0-Dalitz the S/B is about 2.

References

[1] R.J. Porter et al. [DLS Collaboration]. Phys. Rev. Lett. 79 (1997) 1229.

[2] R. Holzmann for the HADES Collaboration. Quark Matter 2005 proceedings, to be published in Nucl. Phys. A.

[3] CERES Collaboration. arXiv:nucl-ex/9712008 v1 23Dec 1997.

Simulation studies of electron identification with the RICH detector for CBM *

C. Höhne, GSI Darmstadt, Germany, S. Gorbunov, DESY Zeuthen, Germany,
I. Kisel, KIP Heidelberg, Germany, S. Lebedev, JINR-LIT, Dubna, Russia,
B. Polishchuk, IHEP Protvino, Russia, and the CBM collaboration

The RICH detector of CBM

The measurement of dielectron pairs in heavy-ion collisions at FAIR energies requires detectors which identify electrons with high efficiency and reject pions by a factor of 10^4 at least. Electron identification in CBM will be performed by a Ring Imaging Cherenkov (RICH) detector (for momenta up to about 10 GeV/c) and a Transition Radiation Detector (TRD) [1, 2]. Main sources of a misidentification of pions as electrons in the RICH are mismatches of electron rings with pion tracks, e.g. from secondary electrons without a reconstructable track in the STS and primary vertex pions. Moreover, misidentification of pions at higher momenta due to the finite resolution of the ring radius measurement will occur. In order to study the proposed RICH detector layout with respect to the π rejection requirements simulations have been started and first results are presented in this report for both of these sources.

Cherenkov angle resolution

The separation power between electrons and pions for higher momenta is determined by the resolution of the ring radius or Cherenkov angle of the rings in the photodetector plane. Different contributions to the resolution can be separated, the main components for single photons are presented in table 1. Clearly, the values depend in particular on the finally chosen photodetector (pixel size, $\lambda_{\rm min}$). In addition, small contributions from angular deviations of the mirror surface as well as due to different emission angles are expected. Since the momentum dependent contributions are inversely proportional to p they play a minor role for the high momenta. Nevertheless, assuming a total resolution of 4-5 mrad and – depending on the finally chosen photodetector – 10-30 hits per ring, a ring resolution of 0.36-0.7 mrad is expected which corresponds to 2-3% of the Cherenkov angle (24.4 mrad for N_2). A 3% resolution would still correspond to a 6σ separation power of electrons and pions at $p = 12$ GeV. The π misidentification in the electron sample from this source is thus expected to be negligible for the momentum range in question.

Ring reconstruction

The geometrical acceptance of the RICH detector, requiring at least 6 hits in the STS in addition is presented in figure 1 (left). The lower cutoff at $p = 0.5$ GeV is given by the magnetic field. For ring recognition, first standalone ring finders have been implemented (Hough Transform, Elastic Net Method [2, 3]) and were run on single electrons embedded into UrQMD events for central Au+Au collisions at 25 AGeV beam energy. The resulting ring finding efficiency is shown in figure 1 (right). In general, the efficiency is good, however, for larger momenta it suffers from the high ring density in the central part of the detector. In addition, many fake rings are found in this region picking up randomly hits from close by rings. An optimization of the current implementations of the ring finders concerning these problems including the development of quality criteria for finally selected rings is under way. The efficiency of matching found rings to tracks extrapolated from the STS is between 0.8 and 1 for all momenta. These first simulations show, that due to ring-track mismatches about 1.5% of the main vertex electrons are misidentified only which would correspond to a π rejection of a few times 10^3. Including the e-π separation from the TRD the envisaged factor of 10^4 is in reach.

Table 1: Main contributions for Cherenkov angle resolution of single photons; 10-30 hits are expected per ring; $\lambda_{\rm min}$ is the lower wavelength cutoff.

source	**resolution [mrad]**
multiple scattering	~ 1 ($p = 1$ GeV)
magnetic stray field	< 1 ($p = 1$ GeV)
chromatic dispersion	> 1 ($\lambda_{\rm min} \sim 120$ nm)
pixel size	1-2

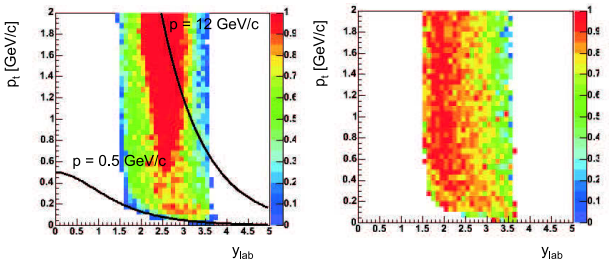


Figure 1: Geometrical acceptance of e^- requiring at least 6 hits in the STS (left), and ring finding efficiency for accepted electrons embedded in central UrQMD events (25 AGeV, $y_{\rm beam} = 2$, right).

References

[1] V. Friese et al., see FAIR-QCD-CBM-00.

[2] Technical Status Report of the CBM experiment (2005).

[3] S. Gorbunov, I.Kisel, see FAIR-QCD-CBM-03.

* Supported by EU/FP6 HADRONPHYSICS (see Annex)

Track reconstruction in the Transition Radiation Detector of CBM

S. Gorbunov, DESY, Hamburg; M. Kalisky, GSI, Darmstadt
I. Kisel, KIP, Heidelberg; D. Kresan, GSI, Darmstadt

The TRD system of the CBM detector will serve as the device for electron ID and track reconstruction. High efficiency track reconstruction up to the TOF-RPC is required for the measurement of event-by-event observables.

The TRD consists of three stations each containing three layers. The material budget is 1.5% per layer and 13.5% in total. The hit position resolution is determined by the pad size and is 0.3 – 0.5 mm across and 2.7 – 33 mm along the pad (depending on the polar angle). Each station has two layers with horizontally and one layer with vertically oriented pads, thus it provides precise measurement of both coordinates. This TRD layout was simulated using a dedicated hit producer algorithm. A sketch of the TRD together with the Silicon Tracking System (STS) is depicted in Figure 1.

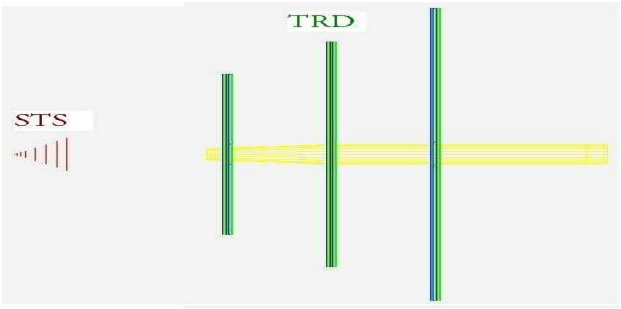


Figure 1: Schematic view of the STS and TRD systems of the CBM detector

Tracking Algorithm

The tracking method is based on the track extrapolation from the STS and can be described by following steps:

1) Extrapolation of the track parameters from the plane of last STS hit to first TRD station.
2) Attachment of the TRD hits in the current station to the track.
3) Update of the track parameters.
4) Filtering of the fake tracks.
5) Extrapolation of the track parameters to the next TRD station (step 2).

For track parameter extrapolation and update the Kalman Filter method is used.

A hit is attached to the track if the normalized distance (distance divided by the sum of the track parameter error and the hit position resolution) between hit and track less than certain cut value. If several hits fulfill the attachment criteria, the track is duplicated and all combinations are considered.

The fake filtering procedure is based on the assumption, that one hit can be attached to one track only. If two track candidates have a common hit, the track with higher χ^2 is marked as a fake and is not processed further.

Performance

The tracking algorithm was tested on central Au + Au collisions at 25 AGeV, generated by the UrQMD transport code. The cut on the normalized distance to hit was set to 6. Figure 2 shows distribution of number of true TRD hits in track. A track was considered as reconstructed if it contains more than 70% of true hits. Figure 3 shows the efficiency of the track reconstruction as the function of momentum.

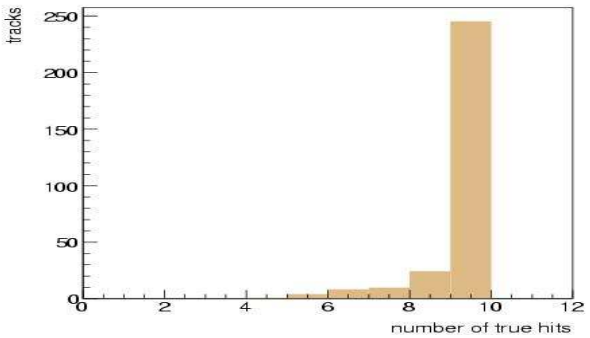


Figure 2: Distribution of number of true hits attached to the track

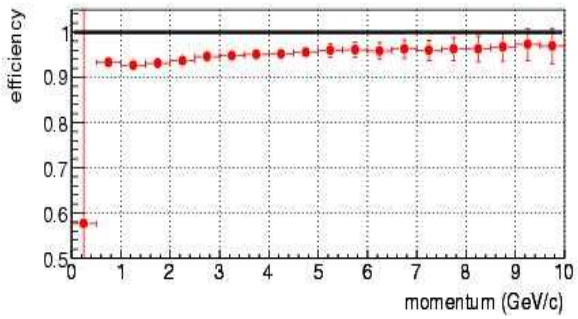


Figure 3: Track finding efficiency as the function of momentum

Outlook

In the next step the track reconstruction performance will be studied with different TRD layout parameters such as material budget, granularity and number of layers per station.

References

[1] CBM Technical Status Report http://www.gsi.de/onTEAM/dokumente/public/DOC-2005-Feb-447.html

Vector meson detection via $\mu^+\mu^-$ decay in CBM *

A. Kiseleva, I. Vassiliev, GSI, Germany,
V. Baublis, PNPI, Russia, S. Gorbunov, DESY, Zeuthen, Germany,
I. Kisel, University, Heidelberg, Germany

As an alternative approach to the dielectron measurement, the possibility of the detection of vector mesons (ρ, ω, ϕ, J/ψ) via their decay into $\mu^+\mu^-$ has been studied. This measurement would require a muon detector located after the STS. The current design of the muon system consists of 16 detector layers with 100 μm position resolution and 5 absorber layers made of carbon and iron of variable thickness. The structure of the muon detector is following: one sensitive layer is in front of the first absorber, three sensitive layers are between each two absorbers and three — behind last absorber.

The vector meson decays were simulated with the PLUTO generator assuming a thermal source with a temperature of 170 MeV. The multiplicities of the signals for central $Au + Au$ collisions at 25 AGeV beam energy were taken from the HSD transport code [1]. The background, consisting mainly of decays of charged pions and kaons, was calculated with the UrQMD event generator for the same system. Both signal and background are transported through the detector setup with cbmroot v.APR05 employing GEANT3. The L1 tracking procedure [2] has been used for the track finding at STS and muon system and momentum reconstruction at STS.

Table 1: Cuts for the signal selections: "high" cuts - for the J/ψ, "low" cuts for the ρ, ω and ϕ selection.

cuts	"high" cuts	"low" cuts
opening angle (^{o})	> 12	> 12
p_t (GeV/c)	> 1	> 0.23
scalar product	[-2.4, -2.05]	[-0.26, 0.04]

Table 1 shows the cuts, which were used for the background rejection: "high" cuts — for the J/ψ,"low" cuts for the ρ, ω and ϕ selection.

Table 2 and table 3 show the efficiency for vector meson detection and the signal to background ratio, calculated in a $\pm 2\sigma$ window around the signal peaks, for the different versions of the muon detector.

The preliminary results presented hier demonstrate the feasibility of dimuon measurements with the CBM detector setup using an active absorber system for $Au + Au$ collisions at 25 AGeV. The next steps towards an optimized muon detector setup include: performing more realistic simulations (reduction of the energy cutoff value from 1 MeV to 100 keV for particles hitting the muon detectors), optimization of the muon system (type, number and geometry of the detectors, position resolution, granularity), absorber study (material, thickness), and energy dependence (10 to 45 AGeV).

* Work supported by EU/FP6 HADRONPHYSICS (see Annex) and by INTAS

Table 2: Efficiency of the J/ψ signal and signal to background ratio for the versions of the muon system with carbon (5C) and iron (5Fe) absorbers.

muon system with absorbers:	after tracking J/ψ	after "high" cuts J/ψ
efficiency (%)		
5C	24	12
5Fe	20	12
S/B ratio		
5C	0.8	> 90
5Fe	0.3	> 20

Table 3: Efficiency of the low vector meson signals and signal to background ratio for the different versions of the muon system: with carbon (5C), with iron (5Fe), with 4 iron and 1 carbon absorbers (4Fe+C) and with increased (4Fe+C+15%) and decreased (4Fe+C-15%) absorber thickness of the last version by 15%.

muon system with absorbers:	after tracking ρ	ω	ϕ	after "low" cuts ρ	ω	ϕ
efficiency (%)						
5C	4.1	2.6	3.8	2.3	6.3	6.0
5Fe	0.6	0.4	1.1	0.5	1.6	1.5
4Fe+C	1.8	0.9	2.3	1.4	4.1	3.7
4Fe+C-15%	3.1	1.9	3.3	2.3	5.3	4.6
4Fe+C+15%	1.6	0.8	1.3	0.7	2.4	2.2
S/B ratio						
5C	0.005	0.009	0.1	0.2	0.06	0.1
5Fe	0.3	0.005	0.07	0.2	0.01	0.02
4Fe+C	0.004	0.01	0.2	0.7	0.04	0.2
4Fe+C-15%	0.001	0.005	0.04	0.2	0.01	0.004
4Fe+C+15%	0.01	0.05	0.2	1.3	0.06	0.2

References

[1] W. Cassing, E. Bratkovskaya, A. Sibirtsev, Nucl. Phys. A 691 (2001) 74.

[2] S.Gorbunov, I.Kisel, I.Vassiliev, "Analysis of D0 Meson Detection in $Au + Au$ Collisions at 25 AGeV", CBM-PHYS-note-2005-001.

CbmRoot: Simulation and Analysis framework for CBM Experiment

M. Al-Turany and Denis Bertini

Abstract

The Virtual Monte Carlo concept allows performing simulations using Geant3, Geant4 or Fluka without changing the user code. The same framework is then used for the data analysis. An Oracle database with a build-in versioning management is used to efficiently store the detector geometry, materials and parameters.

Design and implementation

The schematic design of the CBM framework (CbmRoot) is shown in Fig.[1].

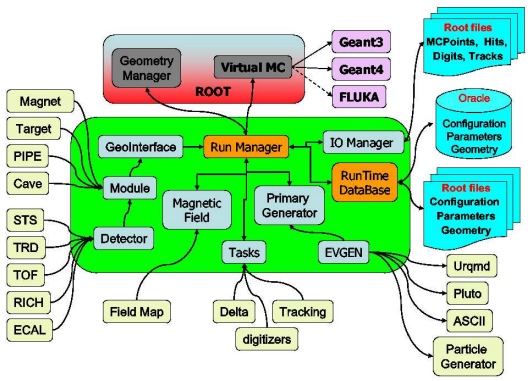


Figure 1: Schematic design of the CBM simulation and analysis framework

In this design, the framework is fully based on the ROOT system [1].The user can create simulated data and/or perform analysis with the same framework. Moreover, Geant3, Geant4 and Fluka transport engines are supported, however the user code that creates simulated data do not depend on a particular monte carlo engine.

Basic functionalities

Input/Output procedures

The storage of all information collected by the different sensitive detectors is done on an event by event basis (an event means in this context one interaction between one beam particle and the target) . All persistent objects are serialized and stored into binary ROOT files. An interface class (CbmMCPoint) is provided to define the structure of registered hit in a detector. Each detector can then provide a more specific implementation following the CbmMCPoint API. All registered hits will be collected into dedicated lists, one list corresponding to one detector entity. The ROOT class TTree is used to organize the output data into a "ntuple like" data structure . In the analysis case, the CbmRootManager provides methods to read this information. A partial input/ouput mechanism is also supported.

Parameters definition

In order to analyze the simulated data, several numerical parameters are needed, as for example, calibration/digitization parameters or geometry positions of detectors. One common characteristic to most of these parameters is that they will go through several different versions corresponding, for example, to changes in the detectors definition or any other condition. This makes necessary to have a parameter repository with a well-defined versioning system. The runtime database (realized through the CbmRuntimeDb class) is such a repository. Different inputs are supported : Ascii format , ROOT binary format and Oracle Database input.

Implementation of the algorithms

The analysis (Reconstruction) is organized in tasks. For each event we need to accomplish various tasks or reconstruction algorithms. The CbmTask is an abstract class defining a generic API allowing to execute one task and to navigate through a list of tasks. The user can create his own algorithm inheriting from CbmTask. Each task defines the relevant input data and parameter and creates its particular output data during the initialization phase. During the execution phase, the relevant input data and parameters are retrieved from the input file and the output data objects are stored in the output file.

summary

A VMC based framework for CBM has been implemented, the first release was in march 2004. The October 2004 release was used to produce and analyze data for the CBM technical Status report[2]. The Parameter containers and the initialization scheme is now added. Work on digitizers and full tracking is going on.

References

[1] R. Brun, F. Rademakers, P. Canal, I. Antcheva, D. Buskulic, O. Couet, A. and M. Gheata *ROOT Users Guide* (CERN, Geneva, 2005)

[2] CBM Collaboration *Technical Status Report* (GSI, Darmstadt, 2005)

High efficiency Transition Radiation Detectors for high rate environments

M. Petrovici, V. Simion, M. Petriş, D. Moisă, A. Radu, D. Bartoş,
I. Berceanu, V. Cătănescu, A. Herghelegiu, C. Măgureanu, NIPNE-Bucharest
M. Hoppe, A. Wilk, J.P. Wessels, University of Münster

The Transition Radiation Detector considered to be implemented in the CBM experiment at the future FAIR facility at GSI Darmstadt will be used for particle tracking and identification of high energy electrons and positrons for J/Ψ meson reconstruction [1]. The specific challenge for such a detector in the CBM experiment is the high granularity and a good performance in a high counting rate environment.

Based on the experience of the TRD for ALICE [2] and of the TRT for ATLAS [2], various prototypes of fast Multiwire Proportional Chambers (MWPC) [4] -[7] were designed, built and tested. Up to intensities of 100 kHz/cm^2, no major deterioration of the performance has been observed. However, this performance of the prototypes was reached decreasing drastically the conversion efficiency of the transition radiation in a single layer of such a MWPC based TRD. In order to circumvent this aspect, we designed and built a few prototypes of TRD based on double sided pad read-out electrode. The main idea is to increase by a factor of ∼2 the conversion efficiency obtaining the same performance and number of read-out channels of the protypes mentioned above. This can be reached by symmetrizing the counter structure relative to the readout electrode using a double sided pad-plane electrode. A sketch of the counter structure and a photo of the prototype is shown in Fig.1. The anode-cathode gap and the anode wire pitch

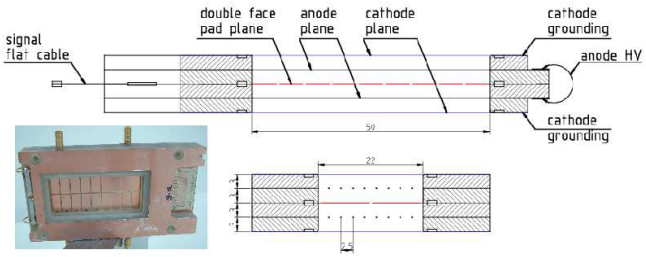


Figure 1: Exploded view of the counter structure

were kept the same as in the former, one sided, prototype built by us [5], i.e. 3 mm and 2.5 mm, respectively. The pad size is 5x10 mm^2. Three versions of such prototypes were built. The first one, used to test the functionality of such a structure, has the intermediate read-out electrode made out of a PCB with two rows of 9 pads on either side. The prototype was tested using ^{55}Fe source. Custom built charge-sensitive preamplifier/shapers were used to process the detector signals which were digitized by an AD811 peak sens ADC. In Fig.2 we show the energy spectra of ^{55}Fe source taking the signal from the anode wires (Fig.2a)) or from the pads (Fig.2b)), respectively. These results indicate that the counter can be operated as designed. In order to test the performance of such a structure even for low energy X rays, a second prototype was built in which the middle electrode was made out of mylar foil of 3 μm thickness, aluminized on both sides. The energy resolution for an ^{55}Fe source is shown in Fig.2c). The observed 12.5% resolution is mainly due to the high capacity of the intermediate electrode, the pad size being equal to the counter surface ∼22 x 50 mm^2. For such an intermediate electrode the measured transmission is 98.5%. All these measure-

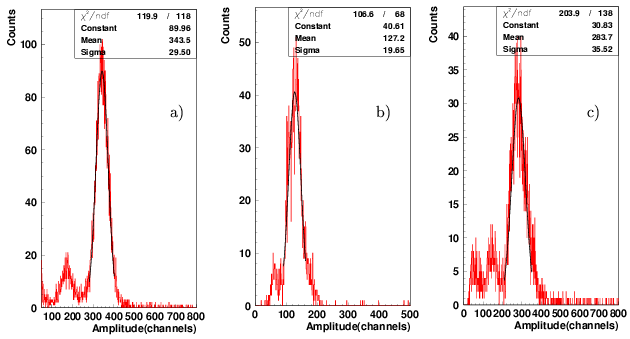


Figure 2: Energy spectra of ^{55}Fe source

ments were performed at 1700 V anode voltage using an Ar/CO_2(70%/30%) gas mixture. The third prototype, ready to be tested, combines the features of the previous two, i.e. the double sided pad read-out electrode is obtained by etching the pad structure on a double sided copperized kapton foil of 25 μm. Based on detailed measurements done with the ALICE-TRD configuration [2], these prototypes would have a TR conversion efficiency of more than 80% relative to the ALICE-TRD counters which have a drift zone of 30 mm, for Xe/CO_2(70%/30%) gas mixture. In-beam tests will be done in the near future at GSI-Darmstadt. In conclusion, this type of TRD is recomended as a candidate for the TRD subdetector at small polar angles, where the counting rate could exceed 100 kHz/cm^2, with particle densities of about 0.05/cm^2. High efficiency is important in order to reduce the number of electronic channels and the overall material budget.

Acknowledgment: The Bucharest group would like to thank Nikolaus Kurz from GSI Darmstadt for his support in implementing the MBS GSI-type DAQ in NIPNE.

References

[1] CBM - Technical Status Report, 2005
[2] CERN/LHCC 2001-021, ALICE TRD 9 - TDR, 2001
[3] ATLAS, IDTDR, v.2, CERN/LHCC/97-17
[4] A. Andronic et al, GSI Ann. Rep. 2005-1,INSTMETH-33
[5] M. Petris et al,CBM Coll. Meet., March 9-12, 2005, GSI
[6] V. Golovatiouk et al., Coll. Meet., March 9-12, 2005, GSI
[7] C. Garabatos et al., Coll Meet., March 9-12, 2005, GSI

New development in timing RPC for the CBM-TOF*

E. Cordier[1] for the ATOF (JRA12)/ CBM-Collaboration.
[1]Physikalisches Institut, Universität Heidelberg, Germany

In 2005 a lot of efforts was invested in the R&D of high performance timing RPC by the different groups of the CBM-TOF Hadron-ID collaboration. Several new material samples have been studied, new prototypes have been built and tested with radioactive sources and beams. In addition new developments in fast electronics were carried out (ASIC-Design).

Concerning the investigations on low resistivity material the IHEP group has built and tested four-gap double-stack prototypes made out of silicate semiconductive glass doped by Fe, Ti and Ge (MRPC-1). The glass volume resistivity was measured to be $1.2 \cdot 10^{12}$ Ω.cm. Its rate capability and aging effect were compared to a counter with the same glass but a different Ge/Ti composition (MRPC-2). Under irradiation with a high gamma flux in the order of $10^7 \gamma/cm^2 s$ the counting rate and currents strongly deviate from linear increase of the gamma flux. As expected MRPC-2 shows less saturation and less distortion of signals.

In Coimbra the low resistivity material studies have continued with ceramic glass material (controlled resistivity alumina Al940CD). The electrode has been made from a commercial material free from charge depletion effects. The results show that the efficiency is kept for rate less than 100 kHz/cm^2. A time resolution $\sigma_t \leq 100$ ps was measured for rates below 75 kHz/cm^2. After several weeks of irradiation the observation shows no degradation of the performance.

In Bucharest a prototype of a multistrip RPC with an electrode made out of Glaverbel float glass has been developed and tested with radioactive source and in beam at GSI. The results with a gamma source have shown good performance with a resolution under 100 ps.

The Hades group has developed a detector prototype with electrically shielded RPCs and tested it on fragmented C-beam at GSI. The cells show uniform and reliable performances and robustness. Crosstalk measured between channels is negligeable and the counter fulfills the Hades requirements.

FOPI has tested a full size prototype of supermodule with 5 Multistrip Multigap RPCs (MMRPC) at different gap sizes between 220 μm and 270 μm and the readout electronics. For a rate of 100 Hz/cm^2 was measured a time resolution $\sigma_t \leq 60$ ps and an efficiency $\epsilon \geq 99\%$ (see Fig. 1). This type of counter has also been tested in electron beam at ELBE and shows similar performance. Also first efforts in the development of a multichannel electronics have been done. A new front-end electronics prototype

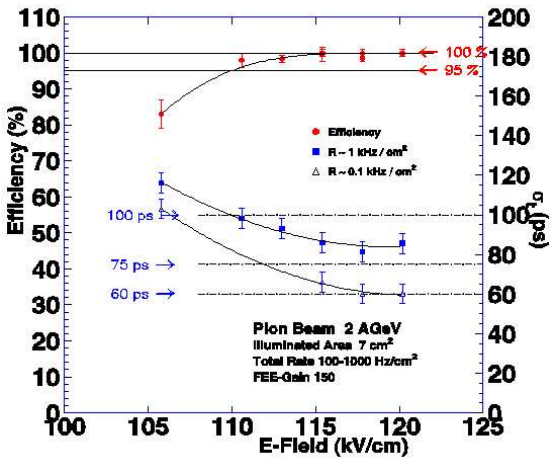


Figure 1: FOPI MMRPC timing and effi ciency results

(FEE-NINO [1]) has been made in GSI and was compared to the FOPI electronics (FEE-3). The single channel time resolution as a function of the signal amplitude is shown in Figure 2. There is no significant difference between NINO and FEE-3 for large input signals. The next step is to evaluate the performance of the NINO with a full differential counter.

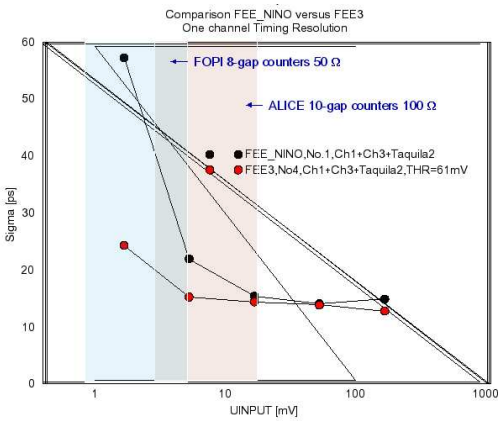


Figure 2: Single channel time resolution FEE-NINO and FEE-3

References

[1] F. Anghinolfi , P. Jarron, A.N. Martemyanov, E. Usenko, H. Wenninger, M.C.S. Williams, A. Zichichi, *Nucl.Instrum.Meth.A533: 183-187 (2004)*

[2] CBM Collaboration, *Tech. Status Report CBM (2005)*

* Supported by EU/FP6 HADRONPHYSICS

MWPC rate capability measurements with an X-ray tube

C. Garabatos, F. Uhlig, GSI, Darmstadt, Germany

G.. Hamar, Eötvös Loránd University,. Budapest, Hungary

Abstract

A Cu target X-ray tube operated at 8 kV and several mA is used to perform systematic measurements of the rate capability of Multi-Wire Proportional Chambers (MWPC), and its dependence on chamber geometry, gas composition and gas gain. We describe the experimental set-up, system calibration and first results.

Introduction

The CBM TRD is a xenon-based gaseous detector that will perform particle tracking and electron identification at rates of up to 10^5 Hz/cm^2. At these rates, space-charge effects due to build up of charge in the counting gas may appear, thus reducing the effective gain of the detector. Although many novel devices have proven to deal with such rates at no gain degradation, MWPC have only rarely been studied in this facet. Wire chambers are however very robust and inexpensive, and therefore it is worth to systematically study their rate behaviour, in order to find a configuration that would allow one to use them in CBM.

Experimental set-up and calibration

The experimental set-up consists of a Cu target X-ray tube powered with a generator able to provide up to 20 kV to the filament and 20 mA current. The collimated X-ray beam is attenuated with aluminium foils before entering a CBM TRD MWPC prototype (in this case 2 mm anode pitch and 6 mm total gas thickness). The rate of absorbed X-rays in the detector, typically of 8 keV, as a function of the current in the tube is measured for each set of Al foils and suitably corrected for pile-up in the readout electronics. The size of the irradiated spot is determined by exposing a regular Polaroid film stack to the photon beam. The gain of the detector is measured at low rates and, with the above calibration, its gain dependence with rate can be determined by measuring the detector current with increasing X-ray generator current. This procedure can be repeated for different gas mixtures and compositions.

First results

Figs. 1 and 2 show first, calibrated measurements of the rate capability of the prototype MWPC for two Ar-CO_2 gas mixtures and different initial gains. The effect of space-charge effect is clearly visible and its onset occurs at lower rates for higher gains. The solid lines are a fit to Mathieson's formula $\ln(G/G_0)/G = KR$, where K is a phenomenological constant which characterises the chamber geometry and the gas properties. The link between gain and rate capability is thus demonstrated, and the experimental goal is shown to be within reach.

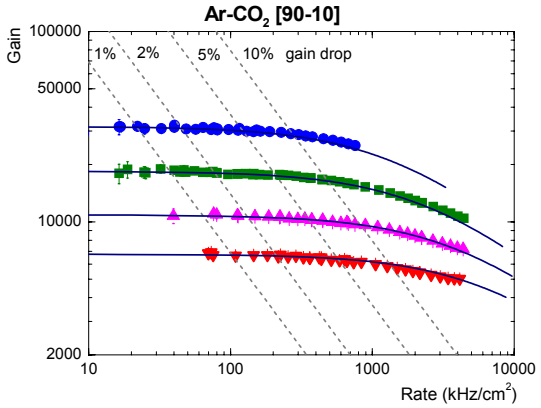


Figure 1: Rate capability for different gains for Ar-CO2 [90-10].

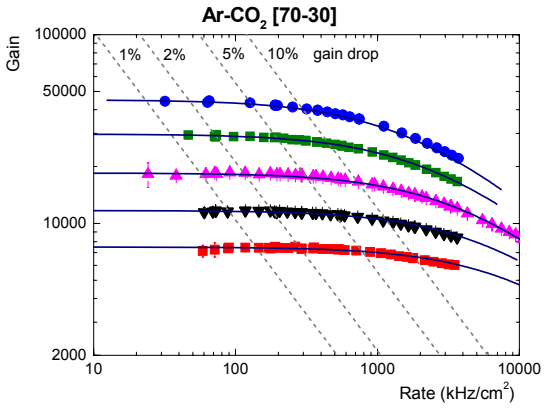


Figure 2: Rate capability for different gains for Ar-CO2 [70-30].

References

[1] E. Mathieson and G. C. Smith, Nucl. Instrum. Meth. A316 (1992) 246.

Hardware Implementation of a Hough Tracker for CBM *

J. Gläss, R. Männer, C. Steinle, Mannheim University, Germany

Abstract

In this report we describe an adaptation of the Hough transform for the tracking of particles in the CBM STS detector, together with a possible implementation of the algorithm in hardware using FPGA (field programmable gate array) as a level-1 trigger. A first FPGA based R&D hardware prototype that can be used also for a variety of other application (e.g. Data Combiner and Active Buffer) is also described.

Hough Transform

The most demanding task concerning trigger processing for CBM is an open-charm trigger on D mesons via their detached vertex position in the first trigger level.

The Hough-transform is a global method. The coordinates of all STS detector hits have to be transformed into a parameter space according to the components of the track momentum p (e.g. $1/p_z$, p_x/p_z and p_y/p_z), leading to a 3-dimensional Hough-transform [1].

The goal for the implementation is to process the tracking with maximum speed, e.g. to process one detector hit per clock cycle. Therefore the complicated calculations of the Hough transform according to the real detector geometry and the magnetic field are implemented with LUTs. Using LUTs also inhomogeneities of the magnetic field can be considered.

The 3-dimensional Hough histogram is decomposed into several 2-dimensional Hough histograms. First the y-z projection of a track as a straight line applies to select the appropriate 2-dimensional histogram. In the second step the 2-dimensional Hough histograms according to a parabolic approximation of the track are calculated. The accumulation of the Hough curves in a 2-dimensional histogram is done in a systolic array of simple processing elements (see fig. 1). An efficient implementation within a FPGA was elaborated.

Simulations of Au+Au Monte Carlo (MC) data, within the CBM framework showed, that better results can be expected for events with less tracks and detector setups with more detector layers. Using six instead of five detector layers improves the efficiency by 2 to 3 %, and the ghost rate is only half. At present the algorithm is further developed, in particular the adjustment to strip detectors and the optimization of the detector layout.

* Supported by EU/FP6 HADRONPHYSICS (see Annex)

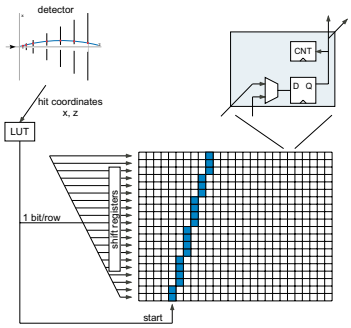


Figure 1: Implementation of a Hough transform unit as a systolic array of simple processing elements.

R&D Hardware Prototype

A first R&D prototype was designed and produced. It consists of a state-of-the-art FPGA (XC4VFX20) with integrated processor and multi gigabit transceivers, external DDR-memory, Ethernet, optical SFP connector and mezzanine connectors to add modules for data transfer or memory. It serves as a test bed not just for tracking algorithm implementation. It also provides a platform to evaluate the essential architecture elements of the CBM FEE-DAQ concept, like the combined data, time, control, and RoI traffic of the Data Combiner Boards, and the event building and storage architecture of the Active Buffer Boards.

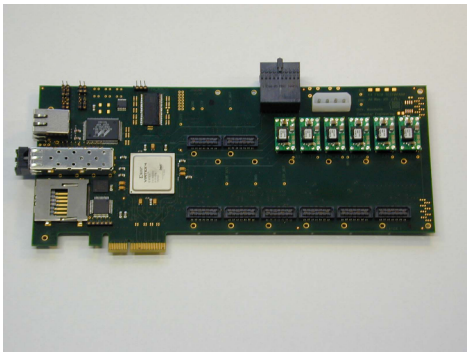


Figure 2: FPGA based R&D prototype board.

References

[1] J. Gläss, C. Steinle, R. Männer, “Tracking in the Silicon Tracker System of the CBM Experiment using Hough Transform”, 14th IEEE-NPSS REAL TIME Conference, June 2005, Stockholm, http://www.sysf.physto.se/RT2005/.

Front End Electronic Building Blocks for CBM

M. Bernert, U. Brüning*, P. Fischer†, F. Giesen, I. Perić, M. Ritzert, University of Mannheim, Germany
H. Deppe‡, GSI, Darmstadt, Germany
M. Dorn, V. Lindenstruth§, University of Heidelberg, Germany
D. Muthers, R. Tielert¶, S. Tontisirin, University of Kaiserlautern, Germany
E. Atkin‖, Moscow Engineering Physics Institute, Russia

Abstract

The CBM experiment will require novel electronics for sensor readout and fast data communication. Several prototyping designs and test structures in the UMC $0.18\,\mu\mathrm{m}$ target technology have been put together by the groups contributing to the development of chip-level electronics for CBM. The multi project run has been financed by GSI. Examples of submitted structures are a fast ADC, clock/data recovery circuits, a content addressable memory, charge sensitive preamplifiers for micro strip detectors, time-to-digital converters, DACs and transistor test structures.

FEE Building blocks for CBM

The various detector components and the data readout system of CBM will require several specialized VLSI circuits in order to meet the challenging requirements. In particular, a self triggered operation with autonomous time-stamping of all hit data is required in the front end electronics because no first level trigger will be available, the data readout system must be able to handle a huge data volume due to the untriggered operation and it should also be able to communicate neighbor information with very low latency between detector subcomponents to initiate the readout of regions of interest. In order to be able to share building blocks and know-how, the groups involved in chip design are concentrating on one target technology, which presently is the UMC $0.18\,\mu\mathrm{m}$ CMOS process. A first common prototyping run has been financed by GSI in 2005. It contains several different building blocks and test structures which will be the basis of future work for CBM. Examples of submitted designs are:

A **fast, low power pipeline ADC** will be an essential component in all front end chips. The implemented design is based on the successful TRAP ADC [1]. The power dissipation of the switched capacitor architecture is proportional to the clocking speed. The measured value is $0.7\,\mathrm{mW/MS/s}$. An effective number of bits (ENOB) of $10.9\,\mathrm{bit}$ has been measured for low signal frequencies at a clocking rate of $75\,\mathrm{MHz}$ at a dissipation of $53\,\mathrm{mW}$.

Clock/data recovery circuits are essential components of the serial communication system. The local chip clocks must be extracted from the serial data stream with very low jitter to accommodate the requirements of ADCs, serializers and time stamping units. Several inductor-based voltage controlled oscillators (VCO) / data recovery designs have therefore been submitted. The best design reduces an input clock jitter of $280\,\mathrm{ps}$ (peak-peak) to an output clock jitter of only $5.9\,\mathrm{ps}$ (rms).

A **content addressable memory** can be used for efficient address translation in the planned network communication chips. The design has 512 entries of 2×18 bit. It uses a pipelined, low power architecture. The first stage uses normal CAM cells, the second stage uses 'ternary' cells where bits can be set to a 'don't care' state. A simple test interface is included.

A **charge sensitive amplifier** for micro strip detectors has been optimized for input capacitances of $30-100\,\mathrm{pF}$ and rise times of $10-200\,\mathrm{ns}$ at a power consumption of $1\,\mathrm{mW}$ per channel. 8 identical channels in $50\,\mu\mathrm{m}$ pitch and some other blocks ($3.3\,\mathrm{V}$ version, clocked comparator, general purpose rail to rail amp) are grouped onto one chip.

A **CMOS TDC** is based on a Delay Locked Loop (DLL) with 128 voltage adjustable delay elements, a phase detector controlling a charge pump and a loop filter. The regulation loop locks to a $80\,\mathrm{MHz}$ reference clock so that the width of the time bins of $97.65\,\mathrm{ps}$ is independent of temperature or process variations. The clock driven architecture of the design allows for reading out one hit in every clock cycle.

A **differential TDC** uses a Phase Locked Loop (PLL) based on a constant current differential logic style. The VCO is based on a 16 stage ring oscillator. It has been optimized for good linearity, not for highest speed, with a measured bin width of $75\,\mathrm{ps}$ at $500\,\mu\mathrm{A}$ per delay element.

Other blocks are a **12 bit current mode DAC** and the essential building blocks for a medium speed, low power **algorithmic current mode ADC**. A large set of **transistor test structures** with standard and enclosed layouts is used for technology evaluation and for precise dc-modelling of radiation hard devices.

References

[1] D. Muthers, R. Tielert, A $0.11\,\mathrm{mm}^2$ low-power A/D converter cell for 10b 10MS/s operation, proceedings of the EESSCIRC 2004, 21-23 Sept. 2004, pp. 251–254

* ulrich@ti.uni-mannheim.de
† peter.fi scher@ti.uni-mannheim.de
‡ h.deppe@gsi.de
§ ti@kip.uni-heidelberg.de
¶ tielert@rhrk.uni-kl.de
‖ atkin@eldep.mephi.ru

Fast TRD Pre-Amplifier Shaper for the CBM experiment

H.K. Soltveit, Physikalisches Institut, University of Heidelberg, Germany
I. Rusanov, Physikalisches Institut, University of Heidelberg, Germany
J. Stachel, Physikalisches Institut, University of Heidelberg, Germany

One of the challenges in research and development for fast PASA suitable for MWPC-based detectors in future experiments (like TRD in CBM) is to achieve low noise with short shaping time and high pulse rate, low power consumption and small chip size. We present here a prototype using standard technology (0.35 μm) to show that the requirements can be fulfilled.

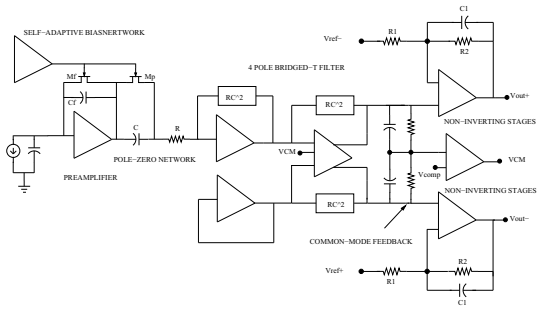


Figure 1: Schematics of the fast PASA done in 0.35μm technology

In order to achieve an overall noise of less than 1000 electrons per channel for a typical input capacitance of a total of 5-10 pF, the use of a low-noise circuit is required. A well proven topology to fulfil such a requirement is shown in fig. 1. Each channel consist of a low noise charge-sensitive amplifier, an active CR-$(RC)^4$ pulse shaper. The main noise contributor is the input transistor of the preamplifier that is based on the folded cascode topology. The cascode consist of a common-source stage followed by a common-gate stage. It combines two transistors (a wide input transistor and a narrower cascode transistor) to obtain: i) high transconductance and low noise of a wide transistor, ii) high output resistance and low output capacitance of a narrow transistor, and iii) reduced capacitance between output and input. In addition a Pole-Zero network is included to avoid undershoot that will strongly limit the counting rate behaviour. In the design a MOS transistor (MF) is used with a feedback capacitance Cf that is continously discharged with a decay time $td = Cf \cdot Rds$ (MF). This continuously sensitive design is particularly suitable for a detector with high occupancy and high counting rate. A typical impulse response is shown in fig. 2. In this first prototype the peaking time is 70 ns (t0/100), and the FWHM is about 70 ns. In terms of noise this circuit fulfil the requirement with an ENC of less than 400 electrons for an input capacitance of 10 pF. In terms of power consumption the circuit uses 16 mW/channel. The chip is fabricated in 0.35 μm standard CMOS technology, and it has a pad pitch of 200 μm and a total area of 12 mm^2.

A first prototype using this design was submitted in October 2005 and it has just been received from the foundry. The first tests in lab and in test beam show that the chip responds according to specifications, in particular with very good noise level, a good uniformity of the baseline and high yield. This circuits are now under preparation to be used in the Fast-TRD test beam in February 2006.

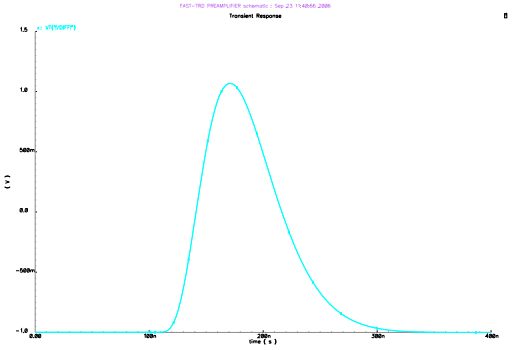


Figure 2: Typical impulse response of the fast PASA done in 0.35μm technology

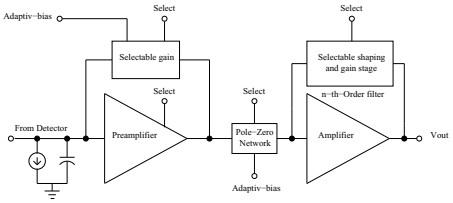


Figure 3: Schematics of the fast PASA under development in 0.13μm technology

The next step now is to migrate from 0.35 μm technology to a smaller technology that will bring less power and less area, and that will be the standard in few years. A prototype development of a new circuit done in 0.13 μm IBM technology is already under way. The proposed schematic layout is shown in fig. 3. This circuit consist of a low noise, selectable gain, preamplifier that can detect both polarities. The choice of gain range in the preamplifier is made by switching the relevant range capacitors. The reason of choosing a selectable gain preamplifier is to provide a versatile preamplifier potentially suitable for several of the proposed CBM detectors (RICH, ECAL and TRD). The core preamplifier is based on the same topology as used in ALICE-TPC/TRD [1]. The change in decay time (due to change in gain range) also influence the P-Z network, that has to change to preserve to same relation to avoid undershoot. The shaper/gain circuit is also made selectable. The purpose of the selectable shaper/gain circuit is to amplify the input signal to the full scale voltage of the ADC ensuring that the maximum signal resolution is achieved. Several programmable shaper/gain topologies are under investigation to find the best candidate for the proposed detectors.

References

[1] H.K. Soltveit *et al.,* GSI Annual Report 2003, p 244

Integration and Infrastructure of the PANDA Detector

B. Lewandowski*, L. Schmitt
GSI, Darmstadt, Germany

Integration

The design of a universal state-of-the-art detector as PANDA starts with the sub-detector elements represented by their active volumes. The task of the integration process is to realize an apparatus matching components of the sub-detector systems including mechanical structure, supplies and cabling.

A first step of the integration already during the R&D phase of the evolving sub-detectors is the determination of the overall volumes for each system. Within these volumes the realisation of the detector components including mechanical structures and electronics as part of the readout chain is done by the responsible working groups. Figure 1 shows a snapshot of the CAD drawings used to determine the subsystem volumes and check for possible clashes.

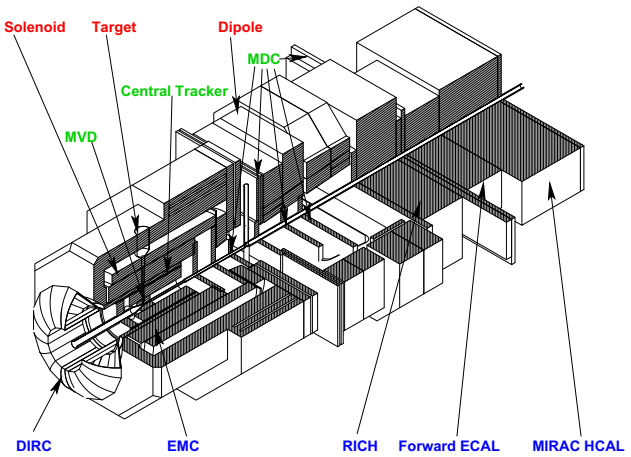


Figure 1: The PANDA sub-detector volumes.

A further objective of the integration work is the realisation of the support infrastructure for all detector systems. This includes the details of mounting sequences during installation as well as dismounting procedure for maintenance purposes. Furthermore the operation requirements of the individual subsystems have to be coordinated to ensure a reliable running of the experiment.

Infrastructure

The hall for the PANDA experiment (fig. 2) will be located at the east side of the HESR. The floor space of 29×43 m is divided into the beam area, where the detector will be located during the running experiment and the assembly and service area, which will be used for the initial installation of the detector and where it will be located during maintenance times. The separation of these two areas will be realised by a dismountable radiation shielding made of concrete blocks. The transfer of the target spectrometer and the forward detector requires rail systems connecting the two different positions of the detector.

The operation of the PANDA experiment is planned as factory mode with the experiment taking data 24 hours a day, 7 days a week for running periods in the order of six months. While the radiation shielding is in place, controlled access to the beam area will be possible using an additional entrance tunnel.

In the south part of the service area a three story counting house with a floor space of 10×15 m is foreseen. The lowest floor will comprise supplies for the detector. The middle floor will house the data acquisition electronics and the upper floor is foreseen for the online computing farm.

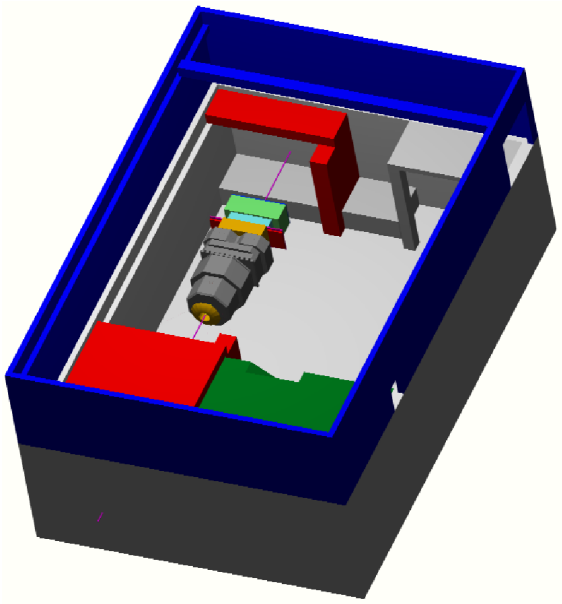


Figure 2: The PANDA experimental hall.

The entrance to the hall will be in the north-east corner, where a platform for deliveries is planned at ground level. This platform in a height of 10 m above the hall floor offers sufficient space for a truck to enter the hall. From this place a hall crane can transfer the load to any place in the hall. An opening of 8×8 m in the roof allows the delivery of detector parts, which exceed the maximum load capacity of 15 t of the hall crane. An additional person entrance to the hall is foreseen at the counting house. The control room for the experiment will be located in a neighboring building.

* B.Lewandowski@gsi.de

Installation of the Genova/Fermilab Cluster-Jet Target at GSI

W. Quick, J. Lühning, H. Orth, C. Schwarz, GSI Darmstadt
M. Marinelli, A. Bersani, M. Macri, INFN Genova,
A. Gruber, J. Zmeskal, SMI Vienna
K. Kendziora, D. Miller, FNAL Batavia

The PANDA experiment[1] uses the antiproton-proton annihilation process for copious production of mesons and baryons with heavy quark content, namely strange and charm. In particular the formation of charmonium states with subsequent precision spectroscopy of their mass, life time, and branching ratios of decay, requires a well controlled coasting beam of anti-protons with small momentum spread and fine-focus for interactions with protons in a ultra-high vacuum. This can be provided with sufficient luminosity by a hydrogen cluster-jet target. A cluster jet is a homogeneous, variable density, stationary stream of protons forming a target with the least amount of disturbance to the antiproton beam minimizing beam heating and consequently losses. It is therefore best suited for precision charmonium spectroscopy.

A cluster-jet target was used in earlier experiments at Fermilab: E760 [2] and, with major upgrade, E835 [3]. The experiment E835 has been discontinued in the year 2000, so the target apparatus, originally designed by the Genova group, was available to resume developments for use at FAIR. We hauled the jet apparatus in a 40'container from Chicago to Darmstadt and started installation of the components at GSI. The laboratory infrastructure which we had to implement at its new location was: electrical power, connection to the central water cooling system, installation of a safe hydrogen handling and exhaust system and a robust multi-stage roots pumping station (5000 m^3/h).

This cluster jet apparatus routinely provided target densities between 1×10^{14} and 6×10^{14} protons/cm^2 at Fermilab, however, for PANDA the density of 1 to 3×10^{15} protons/cm^2 is required to achieve the anticipated luminosity of $L > 10^{32}$ cm^{-2} s^{-1}. Although the jet-platform cannot be reused within the 4π PANDA detector because of the severe spatial constraints, the set-up can be used to further improve the cluster formation. This consists of:

- increasing the gas pressure at the nozzle up to 25 bar.
- decreasing the nozzle capillary to 10 micron.
- enhancing the cluster density going to < 10 K.
- developing diagnostic tools to study clusterization.

At present the target apparatus is operational at GSI. Cluster beams of both Ne and H_2 have been made. Hydrogen clusters were formed between 2 and 6 bars input pressure at temperatures slightly above the phase transition boundary from liquid to gas (28 K at 6 bar). Since the pumping speed may have changed from earlier values, we cannot yet deduce the reached jet density. It will be one of the next steps to measure the pumping speed for hydrogen in the individual sections of the jet vacuum chamber (see Fig. 1).

Using a needle with a thickness of 0.8 mm transversely crossing the hydrogen jet and observing the pressure rise in the interaction section (AA in Fig. 1), the jet profile could be measured (Fig. 2). The lateral extension of 7 mm is in agreement with the former behavior. The jet boundaries are much steeper than the falling edges of this plot suggest, since this data is not de-convoluted over the circular jet cross-section.

In summary, we are ready to investigate and optimize hydrogen cluster-jets for the PANDA experiment.

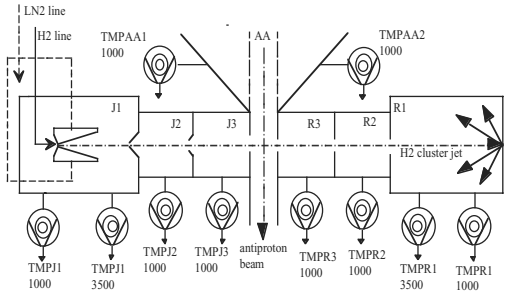


Figure 1: Cluster-jet target with differential pumping stations J1, J2, J3 for production and R1, R2, R3 for sink.

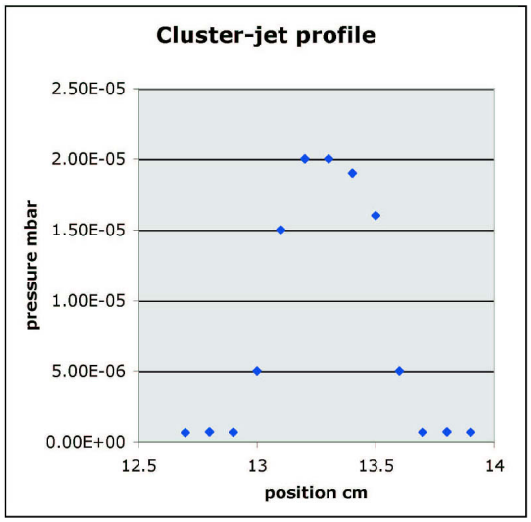


Figure 2: Transverse profile of the hydrogen cluster-jet demonstrating the operational readiness of the apparatus

References

[1] Technical Progress Report for PANDA, Darmstadt 2005.

[2] M.Macri et al., Nucl. Phys. A558, 27C (1993), FNAL-TM-1915, Nov 1994, 15.

[3] D.Allspach et al., Nucl. Inst. Meth. A410 (1998), 195-205.

The inner tracking detector of the PANDA experiment*

The PANDA collaboration

The PANDA experiment will have an inner tracking detector close to the interaction point. This device will consist of silicon detectors. The presently favored layout of the Micro-Vertex-Detector (MVD) is shown in figure 1. The MVD has to provide tracking points with a high resolution in $r\phi$ as well as in z direction. The main focus of the work of the last year was the optimization of the design concerning the most demanding requirements, like high track density in forward direction, radiation background and low material budget. Altogether four sensitive layers are foreseen in the barrel part and six in the disk part covering the forward region.

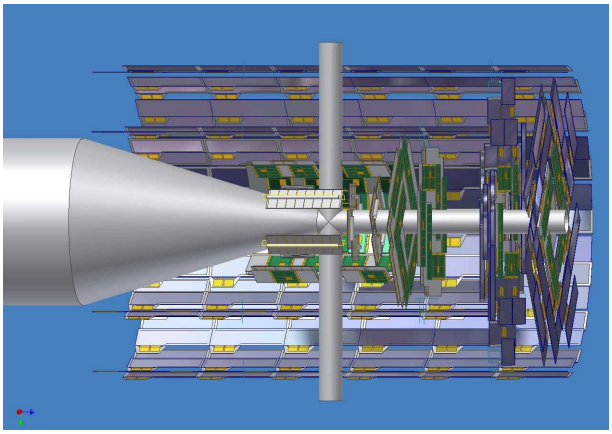


Figure 1: Schematic view of the micro vertex detector, for visibility parts of some layers are omitted.

Since PANDA will have a stationary internal target, most of the outgoing particles from various reaction channels will go in the forward direction as can be seen in the lower frame of figure 2. Due to the high occupancy and the radiation dose close to the interaction point the two innermost barrel layers and all inner parts of the disks have to be pixel detectors. For the outer layers, strip detectors will be used to fill the space to the outer tracking device taking advantage of their smaller material budget and fewer readout channels. The thinner strip detectors will also reduce the conversion probability in the detector material and feed the outer tracking with precise space points to help resolving ambiguities in the outer tracking detector.

To provide reliable simulation results for various physics channels a complex simulation framework is under construction. The Micro-Vertex-Detector simulations are part of a software framework organizing the detector simulation, reconstruction and physics analysis [2]. Included in

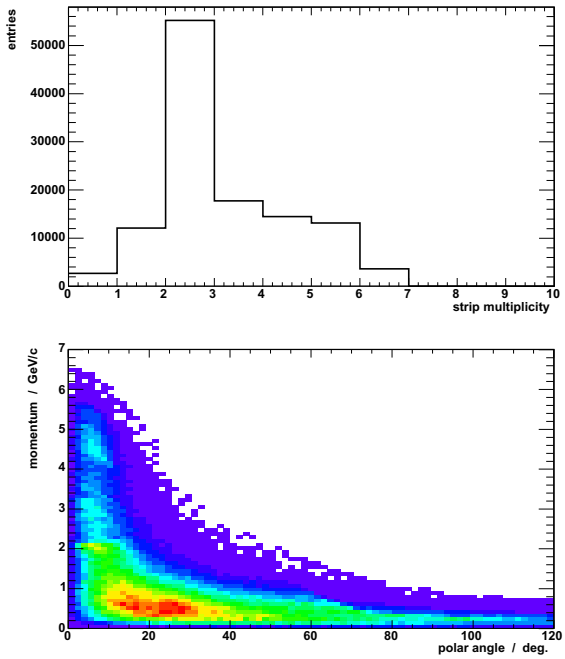


Figure 2: upper: Estimated cluster size of particle hit in strip detector; lower: Momentum distribution of background particles at 6.6 GeV/c beam momentum

.

the software framework is the digitization of simulated data. The aim is to produce a data format which is of the same kind as real detector data and is useful also for detector development of the MVD to fix parameters such as readout frequencies of frontend chips, raw data size per event, power consumption of a single module and cooling needs. These simulation results are essential for the hardware design of the subdetectors as well as for the development of efficient reconstruction algorithms. As an example the mean cluster size in the strip detectors is shown in the upper part of figure 2. This will influence the detector resolution and therefore the physics performance of the whole detector.

References

[1] The PANDA "Technical Progress Report", March 2005; available at: http://www.ep1.rub.de/∼panda/auto/doc/_home.htm

[2] for more information see: http://www.ep1.rub.de/∼panda/auto/com/_home.htm; and more details about physics investigation in [1]

* Work supported by BMBF and EU

Measurement of photon angles for highly resolved TOF detectors*

P. Achenbach†, J. Pochodzalla, S. Sánchez Majos
Inst. für Kernphysik, Joh. Gutenberg-Universität, Mainz, Germany

Particle identification by means of the Time-of-Flight (TOF) technique is widely used in modern spectrometers. Stringent requirements on high resolving power (time resolutions $\sigma < 200$ ps) and small scintillator thicknesses ($d < 0.5\% X_0$) push the technique close to its limits. One intrinsic limit on the time resolution of low mass scintillation counters comes as a consequence of the statistical processes involved in the generation of the signal. In general, the voltage pulse, $V_{\rm PMT}$, can be expressed as a linear superposition of N_{pe} single photoelectron pulses, v_i, arriving at individual times due to time uncertainties in the energy transfer to the optical scintillator levels, $t_{\rm dep}$, the decay time of the light emitting states, $t_{\rm emit}$, the propagation time, $t_{\rm pro}$, and the photomultiplier transit time, $t_{\rm TT}$:

$$V_{\rm PMT}(t) = \sum_{i=1}^{N_{pe}} v_i(t - (t_{\rm dep} + t_{\rm emit} + t_{\rm pro} + t_{\rm TT})_i)$$

The spread of photon arrival times due to propagation length differences is given by $\Delta t_{\rm pro} = \frac{nd}{c}(\frac{1}{\cos\theta} - 1)$ for a point like source of light placed at a distance d from the end face of a cylindrical scintillator with refractive index n. Fig. 1 illustrates the geometry where $d = L/2$ and θ represents the complement of the total internal reflection angle, $\theta = \arccos\frac{n_{ext}}{n}$. The geometry of the problem gets more complicated for rectangular shaped scintillators, but is solveable with Monte Carlo simulations.

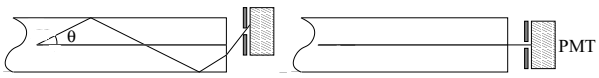


Figure 1: Cross section of the scintillator set-up.

One example, where the contribution of the propagation time spread $\sigma_{\rm pro}$ gets significant is provided by the Cylindrical Time-of-Flight Counter being developed for Panda [1]. A thickness of only 5 mm would allow to mount the scintillator strips together with the DIRC radiators, but reduces the number of photoelectrons to $\langle N_{pe}\rangle \simeq 100$ at $d = 1$ m. A Monte Carlo simulation including a finite decay time of the scintillator predicts a minimum achievable time resolution of $\sigma_{\rm min} \simeq 130$ ps, depending a little on threshold.

In our experiment two tubes of type R4998 from Hamamatsu are placed on the extremes of the rectangular scintillator of type BC408 from Bicron of dimensions $32 \times 10 \times 2000\,{\rm mm}^3$. The transit time spread of the tubes is only $\sigma_{\rm TTS} = 160$ ps and the decay time of the scintillator $\tau = 2.1$ ns. At one end the photomultiplier stays fixed keeping the contact with the scintillator by a suitable set of springs. At the other end a set of two linear position stages permits the scanning of the position. A resolution of 2.5 μm can be achieved with two motorised positioning modules. A thin slit plate is mounted in front of the tube window for the study of the correlation between timing and position. The basic idea was to measure the exit angles of the photons as these carry the information of the propagation time by displacing the tube by 1 cm. An analogy of this method is used successfully in DIRC-like detectors using glass slabs for measuring the Cherenkov angle, but was never investigated in scintillators. The 2 m long scintillator was placed along the longitudinal axis of a black metallic tube in which a set of connectors for the scintillator excitation have been installed. A ^{90}Sr source and a fast pulsed ultraviolet laser can be used for the measurements. The laser has a pulse duration FWHM < 100 ps.

Fig. 2 shows the variation of the mean pulse timing as a function of the position of the slit with respect to the centre, when the laser light is injected at $d = 1$ m. The light propagation is simulated in detail with a Monte Carlo code. The observed variation of the mean pulse timing with position was verified. These simulations serve as an important guide for the TOF detector development.

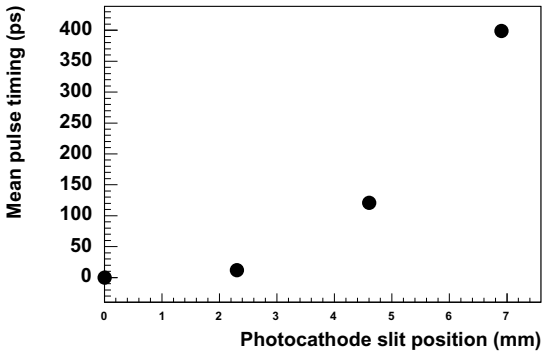


Figure 2: Mean pulse timing as a function of photocathode slit position as measured with the scintillator set-up.

These results have brought forward the idea of improving the timing resolution of a scintillation counter through position sensitive photon detection.

References

[1] Technical progress report for Panda: strong interaction studies with antiprotons, Jan. 2005.

* Work supported by F+E project MZ/POC and by the EU Design Study DIRACsecondary-Beams under contract number 515873.

† patrick@kph.uni-mainz.de

Towards a DIRC-Detector for the PANDA Experiment*

G. Schepers, K. Götzen, J. Lühning, H. Orth, W. Quick, C. Schwarz, GSI, Darmstadt, Germany
K. Peters, GSI, Darmstadt and Johann Wolfgang Goethe-Univ. Frankfurt, Germany

Abstract

The PANDA Experiment aimes for high quality hadron spectroscopy using the antiproton source of the FAIR facility planned at GSI. Situated in the barrel section of the fixed target experiment the DIRC (Detection of Internally Reflected Cherenkov photons) detector provides a positive kaon identification and serves for the destinction of gammas and relativistic charged particles. The velocity derived from the Cherenkov angle together with the momentum information of the tracking detectors determines the mass of the particles.

Investigated DIRC Concepts

As a first attempt a scaled copy of the BABAR DIRC [1] made from quarz glass is envisaged. However, at the same time R&D is done to replace the two dimensional photon detector by 1.) the readout of only one dimension plus the timing imformation of the detector as in the TOP-project (Belle) [2] or 2.) the usage of a small mirror at the end of each radiator and a APD array working in Geiger mode [3]. The first option demands a timing resolution in the order of 100 ps. Here a wider slab is favoured over a bar shaped radiator and the use of acrylic glass gets interesting. Material tests also with acrylic glass as well as quality control of the radiator surfaces and edges are performed at GSI. The developement of a selfquenching Geiger mode APD is required in the second option.

For the investigations of the surface quality of the Cherenkov radiator material an optical test stand was set up (figure 1b). Collimated light of either a red diode laser (635 nm) or a green diode pumped solide state laser (532 nm) can be shined under controlled angles into the radiator bar and simulates the internally produced and reflected Cherenkov photons (figure 1a and figure 2). Behind the radiator internal reflected laser light is measured with a photo diode. The diode as well as the bar are fixed each on two linear x-y-sledges. One scans the complete inner surface of the radiator with the laser spot the other carrying the diode allows to scan the two dimensional shape of the transported laser light. For the latter purpose the diode is enclosed in a metall box having a hole that is small against the spot size of the laser. The light that enters the hole is defocused by a lense to cover the whole area of the light diode avoiding the influence of inregularities on the sensitive area. The aim is the quality measurement of a variaty of different radiators as well as of bigger numbers of bars from the same material. These tests are accompanied by simulations of the light propagation in different radiator materials, radiator shapes and of particle reconstruction, tracking and identification within the PANDA-framework.

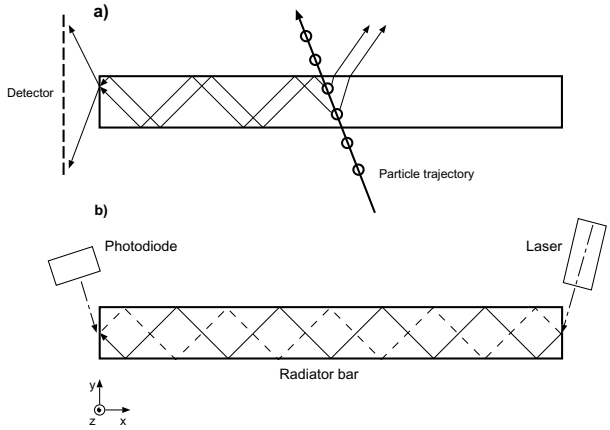


Figure 1: On the DIRC test stand (b, top view) the internal reflection of the Cherenkov photons (a) is simulated with a laser. The bar and the photodiode can be moved via each two step motors in y and z direction to scan the inner surface as well as the gauss shape of the transmitted laser beam.

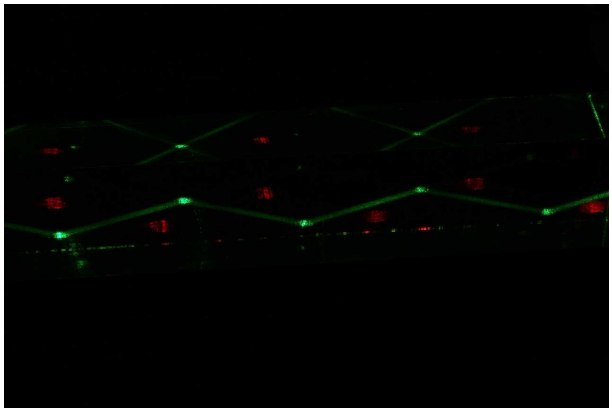


Figure 2: The internal reflection of the laser light in an acrylic glass bar.

References

[1] G. Vasileidis, Nucl. Inst. Meth.A384, 175 (1996)

[2] Y. Enari et al., Nucl. Inst. Meth.A494, 430 (2002)

[3] R. Wilson, Nucl. Inst. Meth.A433, 487 (1999)

* Work supported by the European Community RESEARCH INFRASTRUCTURES ACTION under the FP6 programme: Structuring the European Research Area - Specific Support Action - DESIGN STUDY (contract 515873 - DIRACsecondary-Beams)

Proton irradiation of Large Area APDs for the PANDA-EMC*

A. Wilms, H. Nowak, GSI, Darmstadt, Germany

Experimental overview

For the readout of the electromagnetic calorimeter of the PANDA detector large area APDs (LAAPDs) with an active area of $10 \times 10\, mm^2$ are envisaged. Several new developed devices have been tested in terms of radiation damage.

The LAAPDs were irradiated with 90 MeV protons at KVI Groningen at two different temperatures: at room temperature and at $T = -25°C$, corresponding to the temperature value which is envisaged in case of using lead tungstate as scintillator material for the EMC. The current, which includes the dark current of the device and the current caused by irradiation, was monitored up to an integrated fluence of $10^{13}\ p/cm^2$ using two different beam currents ($I_{beam} = 0.4\ nA$ and $I_{beam} = 4\ nA$). The dark current of the devices after irradiation was determined by using the measured currents without beam at the end of each measurement.

Two different APD types were tested: the device S8664-1010SPL which was developed in cooperation with Hamamatsu Photonics and one device (C30703F) manufactured by Perkin Elmer with the same size of active area.

Irradiation results

The results of the current measurements during proton irradiation are shown in fig.1 - fig.2.

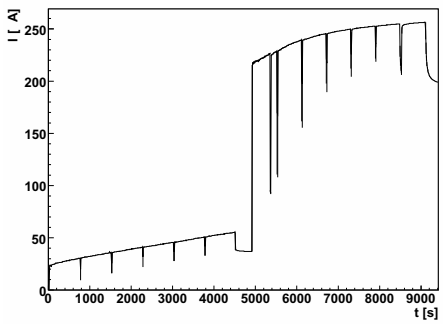


Figure 1: Current of the Perkin Elmer LAAPD C30703F measured at room temperature using two different beam currents.

The irradiation of the device manufactured by Perkin Elmer was done at room temperature. At the end of the irradiation the value of the dark current was approx. $I_d = 200\ \mu A$ (see fig.1). In case of the Hamamatsu APD S8664-1010SPL the irradiation was done at two different temperatures. The dark current of this APD type after irradiation was $I_d = 55\ \mu A$ at room temperature and $I_d = 5.4\ \mu A$ at $T = -25°C$ (see fig.2).

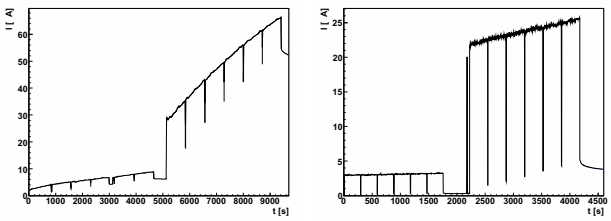


Figure 2: Current of the LAAPD S8664-1010SPL measured at room temperature (left) and at $T = -25°C$ (right).

In all measurements the integrated fluence of $10^{13}\ p/cm^2$, which corresponds to the estimated value of 10 years of detector operation, was reached in a few hours. To extend this exposure an additional measurement of the device current was done with one S8664-1010SPL APD. The result of this measurement is shown in fig.3 and was done at $T = -25°C$ using only the beam current value of $I_{beam} = 4\ nA$.

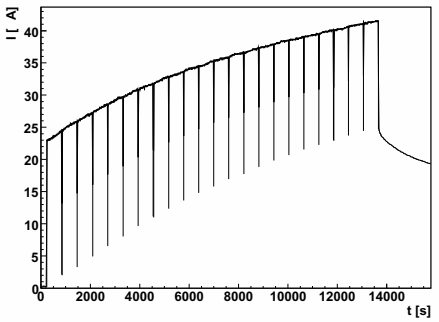


Figure 3: Measured current of S8664-1010SPL at $T = -25°C$ using a constant beam current.

Conclusion

The dark current of the APDs from Hamamatsu after proton irradiation is nearly a factor four smaller than the corresponding value of the device manufactured by Perkin Elmer (both measured at room temperature). Therefor more R&D has to be done to reduce the dark current of the APD type C30703F. A decrease of the device temperature by a value of $\Delta T \approx 45°C$ decreases the measured dark current of the APD type S8664-1010SPL by nearly a factor of 10. The measurement of the device current using only one beam current value (see fig.3) shows the expected exponential behavior which corresponds to a saturation curve and is caused by point defects. More detailed studies of the radiation damage caused by proton irradiation are in progress.

* Work supported by EU/FP6 HADRONPHYSICS (see Annex) and GSI

Pulse shape analysis for germanium detectors operated under magnetic fields*

A. Sanchez Lorente†, P. Achenbach, M. Kavatsyuk, J. Pochodzalla,
N. Saito, T.R. Saito, C. Sfienti for the HYPERGAMMA Collaboration, U Mainz, GSI, Germany

Pulse shape Analysis for VEGA and EUROBALL detectors [1] under high magnetic field were investigated. The scope of this analysis is the extraction of the energy resolution from the preamplifier signal by using digital signal processing. With this result the investigation of the feasibility of germanium detectors under high magnetic fields will be fully addressed. [1]

For the measurements of the pulse shape, a SIS3300 8 channel 100 MHz 12-bits FADC(www.struck.de) was used. It was directly connected to the preamplifier of one of the channels of Super Segmented Clover detector VEGA(see [2]). A typical preamplifier signal is illustrated in the upper part of Fig. 1. The output signal of a charge integrating preamplier with continuous discharge consist of a fast rising step due to the charge collection, followed by an exponential tail due to the discharge of the capacitors over the resistor. The exponential tail reduces the final peak height depending on the rise time of the signal, therefore in order to extract the whole amplitude of the signal which corresponds to the energy of a gamma ray, the influence of the preamplifier has to be removed. This is accomplished by the moving window deconvolution algorithm (MWD) [3]. It consists of two parts: the first part is a deconvolution, which transforms the continuous discharge preamplifier signal into a signal from a transistor reset preamplifier, which is a staircase signal. By applying numerical differentiation of such signal the moving window deconvolution equation is obtained. It converts an exponential signal into a step signal of length M, being M the width of the deconvolution window as shown in the lower part in Fig. 1. Knowing the decay time and the start time of the signal, the initial amplitude can be determined from any data point of the decaying signal. The decay time for VEGA is about 50 μs.

In Fig. 2, the energy resolution of the 4 segments of the analysed channel at VEGA, extracted by using the method explained above, is shown as a function of the length M, for differents values of the magnetic field. Even though each segment shows a different character, all segments exhibit a common trend, i.e, the energy resolution improves by increasing M. The investigation for larger M value with longer FADC sampling time is in progress. [4]

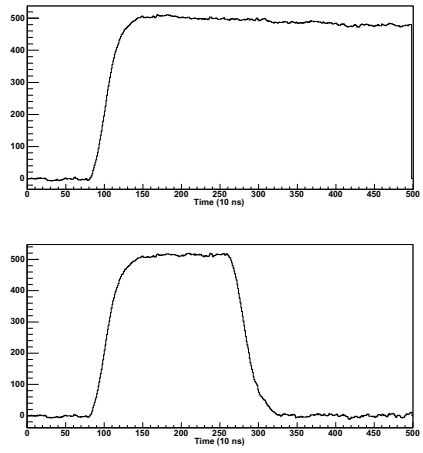


Figure 1: Upper part corresponds to the preamplifier signal of the VEGA detector, which ideally follows an exponential decay. Lower part illustrates the step signal of length M=1.8 μs, after the application of MWD method.

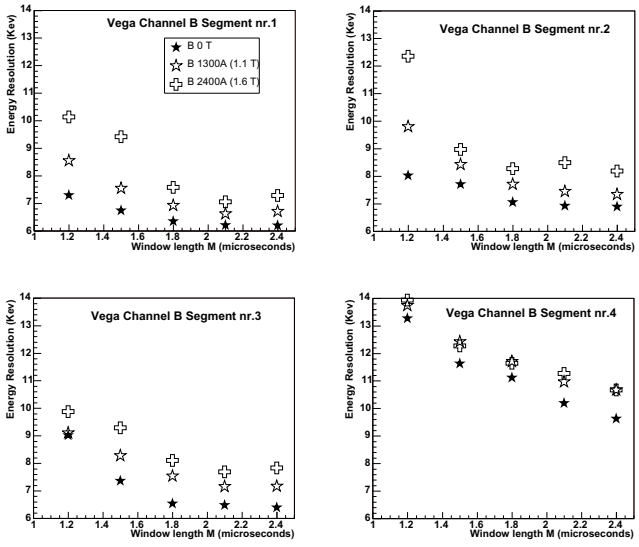


Figure 2: Energy resolution for 4 segments of the Channel B at VEGA as a function of the length M of the deconvolution window and for different magnetic fields.

References

[1] A. Sanchez Lorente et al., Performance of germanium detectors in high magnetic fi elds, in GSI Sci. Rep. 2004, p.32

[2] J. Gerl, H. Grawe, and E. Roeckl, 1998. http://www-gsi-vms.gsi.de/eb/html/vegaproject.html.

[3] A. Georgiev, W. Gast and R.M. Lieder, An Analog-to-Digital Conversion Based on a Moving Window Deconvolution, IEEE Trans. Nucl. Sci. NS-41(4) (1994), 1116.

[4] A. Sanchez Lorente. PhD thesis, U Mainz.

* This research is part of the EU integrated infrastructure initiative Hadronphysics project under contract number RII3-CT-2004-506078 and by the BMBF under contract number 06MZ176.

† lorente@kph.uni-mainz.de

Calculations for the PANDA-Magnet System*

J. Lühning, H. Orth, L. Schmitt, GSI, Darmstadt, Germany
E.K. Koshurnikov, A.S. Vodopianov, JINR, Dubna, Russia

Abstract

Several finite element models of the PANDA solenoid and the PANDA-dipole [1] were created and analyzed in order to optimize the design of the magnets and the configuration of the detectors. The extensive design work done at JINR Dubna is published elsewhere [2].

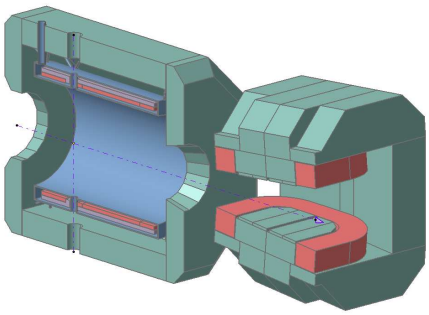


Figure 1: Cut through the PANDA solenoid and dipole models.

Solenoid

For the spectroscopy of low momentum particles at larger angles PANDA will use a superconducting solenoid surrounding the target region. Operation of acluster jet or pellet target requires piping close to the interaction point. Therefore openings for incoming and outgoing pipes through the solenoid are needed causing field distortions.

The nominal field in the tracking area is 2 Tesla. The main question in the solenoid design was concerning the inhomogeneity in the tracking area. In order to get a value of less than ± 2.5 % the axial length of the coil was increased from 50 to 80 cm upstream of the target axis. For the inhomogeneity, the ratio of the current density in the end sections of the coil and the density in the middle section has an important influence. A ratio of 1.6 results in an inhomogeneity of ± 4 %, a ratio of 2.0 gives a value of ± 2 %.

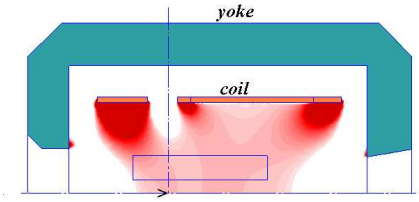


Figure 2: B-field contours in the solenoid. The vertical dahesd line indicates the target axis.

A higher ratio would improve the homogeneity but it would also enhance the maximum field at the windings, and this would require more stabilization of the superconductor.

Since the iron yoke of the solenoid can not be made mirror-symmetric, the axial force on the coil is not proportional to the excitation current. Depending on the design of the yoke the direction of the axial force might even change during the ramp-up. If the opening angle of the downstream end-cap is 22^o the axial force is in the order of 100 t. In the latest design proposal with an angle of 10^o, the axial force can be limited to less than 40 t, furthermore the homogeneity in the tracking area can be improved and the stray field between the solenoid and the dipole can be reduced.

Dipole

The main requirements for the Dipole magnet are a bending power of 2 Tm, and horizontal and vertical opening angles of $\pm 10^o$ and $\pm 5^o$, respectively. Other requirements are low power consumption, a low stray field, and a small length in beam direction.

Different coil shapes were analyzed. Complex shapes like the classical bedstead-type give a more uniform field distribution than the simple racetrack-type and require less iron in the return yoke. The disadvantages of the complex types are higher manufacturing costs and higher power consumption.

Using copper or aluminium conductors with low current density the power consumption is in the order of 400 kW. Superconducting coils would require less electric power for the refrigeration, but manufacturing and maintenance cost are higher and the complex support structure required for the magnetic forces is disadvantageous. Like for other dipoles, for instance the one at LHCb [3], normal conductivity is more favourable.

For the choice of the length of the dipole different aspects have to be considered. A small length results in smaller dimensions of the forward spectrometer because it can be positioned nearer to the target. On the other hand, a longer dipole gives less stray field, less power consumption and less field saturation in the iron poles where an average value of 2 T should not be exceeded. Taking this value, a minimum length of 2.5 m is required for a 400 kW racetrack-type dipole made of low-carbon steel.

References

[1] Technical Progress Report for PANDA, Darmstadt 2005.

[2] E. K. Koshurnikov et al., *Conceptual Design of the PANDA Magnet System*, Proceedings of the MT-19, Genoa 2005, to be published in IEEE TAS, 2006.

[3] LHCb Magnet TDR, CERN/LHCC/2000-007.

* Work supported by INTAS Ref.Nr. 03-54-3710

PAX: Polarized Antiprotons eXperiments

P. Lenisa, University and INFN, Ferrara, Italy
F. Rathmann, FZJ, Jülich, Germany

Abstract

Polarized antiprotons produced by spin filtering with an internal polarized gas target provide access to a wealth of single– and double–spin observables, thereby opening a window to physics uniquely accessible with the HESR at FAIR. This includes a first measurement of the transversity distribution of the valence quarks in the proton, and a first measurement of the moduli and the relative phase of the time–like electric and magnetic form factors $G_{E,M}$ of the proton. In polarized and unpolarized $p\bar{p}$ elastic scattering open questions like the contribution from the odd charge–symmetry Landshoff–mechanism at large $|t|$ and spin–effects in the extraction of the forward scattering amplitude at low $|t|$ can be addressed.

Introduction

The possibility to achieve polarized proton-antiproton interactions at the High Energy Storage Ring (HESR) at FAIR has been proposed last year by the PAX Collaboration [1]. Polarized antiproton-proton interactions will provide unique access to a number of new fundamental physics observables, which can be studied neither at other facilities nor at HESR without transverse polarization of protons and antiprotons.

Physics case

Transversity

The transversity distribution is the last leading–twist missing piece of the QCD description of the partonic structure of the nucleon. It describes the quark transverse polarization inside a transversely polarized proton [2]. Unlike the more conventional unpolarized quark distribution $q(x,Q^2)$ and the helicity distribution $\Delta q(x,Q^2)$, the transversity $h_1^q(x,Q^2)$ can neither be accessed in deep–inelastic scattering of leptons off nucleons nor can it be reconstructed from the knowledge of $q(x,Q^2)$ and $\Delta q(x,Q^2)$. It may contribute to some single–spin observables, but always coupled to other unknown functions. The transversity distribution is directly accessible uniquely via the **double transverse spin asymmetry** A_{TT} in the Drell–Yan production of lepton pairs. The theoretical expectations for A_{TT} in the Drell–Yan process with transversely polarized antiprotons interacting with a transversely polarized proton target at HESR are in the 0.3–0.4 range [3, 4]; with the expected beam polarization achieved using a dedicated low–energy antiproton polarizer ring (APR) of $P \approx 0.3$ and the luminosity of HESR, the PAX experiment is uniquely suited for the definitive observation of $h_1^q(x,Q^2)$ of the proton for the valence quarks. The determination of $h_1^q(x,Q^2)$ will open new pathways to the QCD interpretation of single–spin asymmetry (SSA) measurements [5].

Magnetic and electric form factors

The origin of the unexpected Q^2–dependence of the ratio of the magnetic and electric form factors of the proton as observed at the Jefferson laboratory [6] can be clarified by a measurement of their relative phase in the time–like region, which discriminates strongly between the models for the form factor. This phase can only be measured via SSA in the annihilation $\bar{p}p^{\uparrow} \to e^+e^-$ on a transversely polarized target [7, 8]. The first ever measurement of this phase at PAX will also contribute to the understanding of the onset of the pQCD asymptotics in the time–like region and will serve as a stringent test of dispersion theory approaches to the relationship between the space–like and time–like form factors [9, 10, 11]. The double–spin asymmetry will allow independently the $G_E - G_M$ separation and serve as a check of the Rosenbluth separation in the time–like region which has not been carried out so far.

Hard scattering

Arguably, in $p\bar{p}$ elastic scattering the hard scattering mechanism can be checked beyond $|t| = \frac{1}{2}(s - 4m_p^2)$ accessible in the t–u–symmetric pp scattering, because in the $p\bar{p}$ case the u–channel exchange contribution can only originate from the strongly suppressed exotic dibaryon exchange. Consequently, in the $p\bar{p}$ case the hard mechanisms [12, 13, 14] can be tested at t almost twice as large as in pp scattering. Even unpolarized large angle $p\bar{p}$ scattering data can shed light on the origin of the intriguing oscillations around the s^{-10} behavior of the 90^0 scattering cross section in the pp channel and put stringent constraints on the much disputed odd–charge conjugation Landshoff mechanism [15, 16, 17]. If the Landshoff mechanism is suppressed then the double transverse asymmetry in $p\bar{p}$ scattering is expected to be as large as the one observed in the pp case.

The PAX proposal

Accelerator scheme

The possibility to test the nucleon structure via double spin asymmetries in polarized proton–antiproton reactions at the HESR ring of FAIR has been suggested by the PAX collaboration with a Letter–of–Intent submitted on January

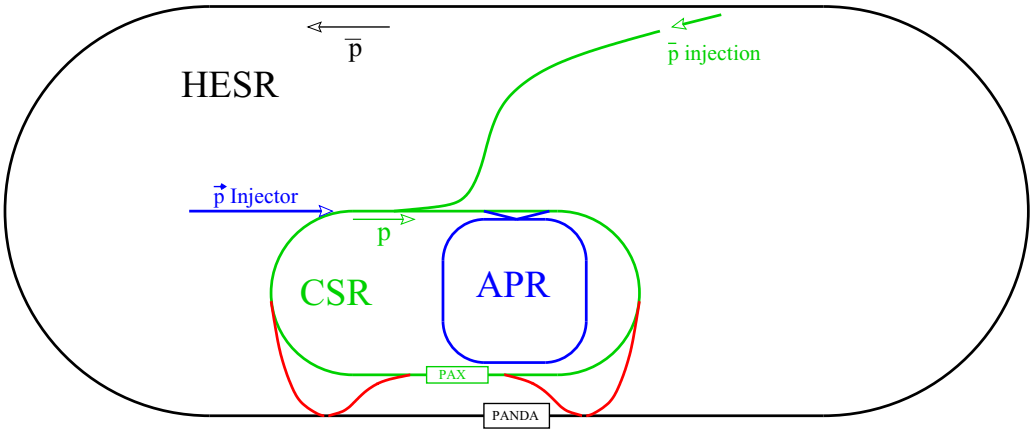


Figure 1: The proposed accelerator set–up at the HESR (black), with the equipment used by the PAX collaboration in Phase I: CSR (green), APR, beam transfer lines and polarized proton injector (all blue). In Phase II, by adding two transfer lines (red), an asymmetric collider is set up. It should be noted that, in this phase, also fi xed target operation at PAX is possible.

15, 2004 [1]. The physics program of PAX has been positively reviewed by the QCD Program Advisory Committee (PAC) on May 14–16, 2004. Following the QCD–PAC report and the recommendation of the Chairman of the committee on Scientific and Technological Issues (STI) and the FAIR project coordinator, the PAX collaboration has optimized the technique to achieve a sizable antiproton polarization [18] and a Technical Proposal for experiments at GSI with polarized antiprotons [19].

The overall machine setup of the HESR complex is schematically depicted in Fig. 1. Its main features are:

1. An Antiproton Polarizer (APR) built inside the HESR area with the crucial goal of polarizing antiprotons, to be accelerated and injected into the other rings. The polarization method is based on spin-filtering of the circulating beam by an internal target to the storage ring. This technique has been successfull demonstrated with protons [20] and tests are foreseen with an antiproton beam.

2. A second Cooler Synchrotron Ring (CSR, COSY–like) in which protons or antiprotons can be stored with a momentum up to 3.5 GeV/c. This ring shall have a straight section, where a PAX detector could be installed, running parallel to the experimental straight section of HESR.

3. By deflection of the HESR beam into the straight section of the CSR, both the collider or the fixed–target mode become feasible.

It is worthwhile to stress that, through the employment of the CSR, effectively a second interaction point is formed with minimum interference with PANDA. The proposed solution opens the possibility to run two different experiments at the same time.

Staging

The PAX collaboration proposes an approach that is composed of two phases. During these the major milestones of the project can be tested and optimized before the final goal is approached: An asymmetric proton–antiproton collider, in which polarized protons with momenta of about 3.5 GeV/c collide with polarized antiprotons with momenta up to 15 GeV/c. These circulate in the HESR, which has already been approved and will serve the PANDA experiment. The proposed phases are the following:

Phase I

A beam of unpolarized or polarized antiprotons with momentum up to 3.5 GeV/c in the CSR ring, colliding on a polarized hydrogen target in the PAX detector. This phase is independent of the HESR performance.

This first phase, at moderately high energy, will allow for the first time the measurement of the time–like proton form factors in single and double polarized $\bar{p}p$ interactions in a wide kinematical range, from close to threshold up to $Q^2 = 8.5$ GeV^2. It would enable to determine several double spin asymmetries in elastic $\bar{p}^{\uparrow}p^{\uparrow}$ scattering. By detecting back scattered antiprotons one can also explore hard scattering regions of large t: In proton–proton scattering the same region of t requires twice the energy. There are no competing facilities at which these topical issues can be addressed. For the theoretical background, see the PAX Technical Proposal [19] and the recent review paper [21].

Phase II

This phase will allow the first ever direct measurement of the quark transversity distribution h_1, by measuring the double transverse spin asymmetry A_{TT} in Drell–Yan processes $p^{\uparrow}\bar{p}^{\uparrow} \to e^+e^-X$ as a function of Bjorken x and Q^2 $(= M^2)$

$$A_{TT} \equiv \frac{d\sigma^{\uparrow\uparrow} - d\sigma^{\uparrow\downarrow}}{d\sigma^{\uparrow\uparrow} + d\sigma^{\uparrow\downarrow}} = \hat{a}_{TT} \frac{\sum_q e_q^2 h_1^q(x_1, M^2) h_1^{\overline{q}}(x_2, M^2)}{\sum_q e_q^2 q(x_1, M^2) \overline{q}(x_2, M^2)}\,, \tag{1}$$

where $q = u, \overline{u}, d, \overline{d} \ldots$, M is the invariant mass of the lepton pair and $\hat{a}_{TT}$, of the order of one, is the calculable double–spin asymmetry of the QED elementary process $q\overline{q} \rightarrow e^+e^-$. The most promising scenario forsees a beam of polarized antiprotons from 1.5 GeV/c up to 15 GeV/c circulating in the HESR, colliding on a beam of polarized protons with momenta up to 3.5 GeV/c circulating in the CSR. Deflection of the HESR beam to the PAX detector in the CSR is necessary (see Fig. 1). By proper variation of the energy of the two colliding beams, this setup would allow a measurement of the transversity distribution h_1 in the valence region of Bjorken-$x > 0.05$, with corresponding $Q^2 = 4 \ldots 100$ GeV^2 (Fig. 2).

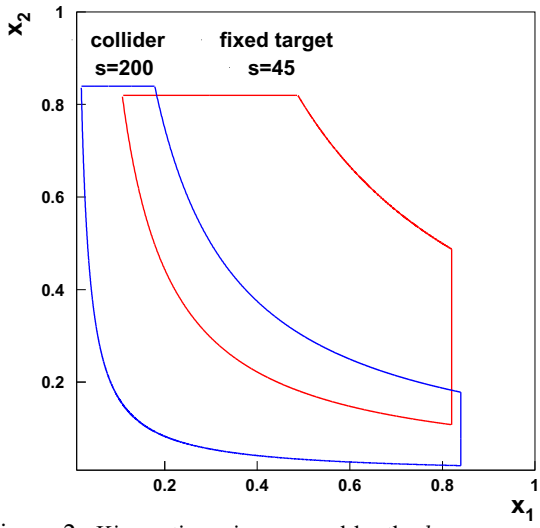


Figure 2: Kinematic region covered by the h_1 measurement at PAX in phase II. In the asymmetric collider scenario (blue) antiprotons of 15 GeV/c impinge on protons of 3.5 GeV/c at c.m. energies of $\sqrt{s} \sim \sqrt{200}$ GeV and $Q^2 > 4$ GeV^2. The fi xed target case (red) represents antiprotons of 22 GeV/c colliding with a fi xed polarized target ($\sqrt{s} \sim \sqrt{45}$ GeV).

A_{TT} is predicted to be larger than 0.3 over the full kinematic range, up to the highest reachable center–of–mass energy of $\sqrt{s} \sim \sqrt{200}$ (Fig. 3).

The cross section is large as well: With a luminosity of $5 \cdot 10^{30}$ cm$^{-2}s^{-1}$ about 2000 events per day can be expected For the transversity distribution h_1, such an experiment can be considered as the analogue of polarized DIS for the determination of the helicity structure function g_1, i.e. of the helicity distribution $\Delta q(x, Q^2)$; the kinematical coverage (x, Q^2) will be similar to that of the HERMES experiment.

Detector

An extensive program of studies has been started to investigate different options for the PAX detector configuration, aiming at an optimization of the achievable performance. The primary goal of the PAX experimental program is to carry out a direct measurement of the h_1

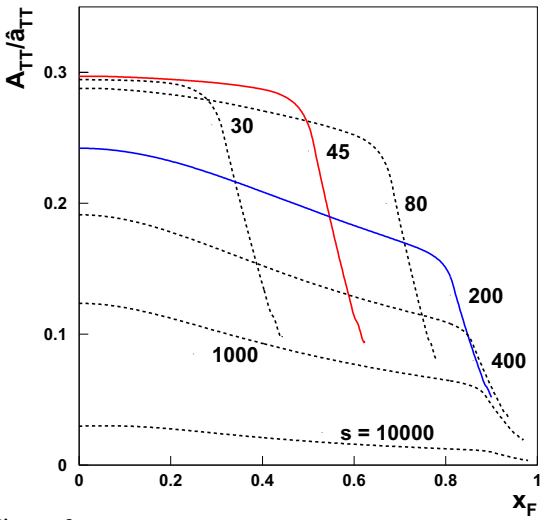


Figure 3: Expected asymmetry as a function of Feynman x_F for different values of s and $Q^2 = 16$ GeV^2.

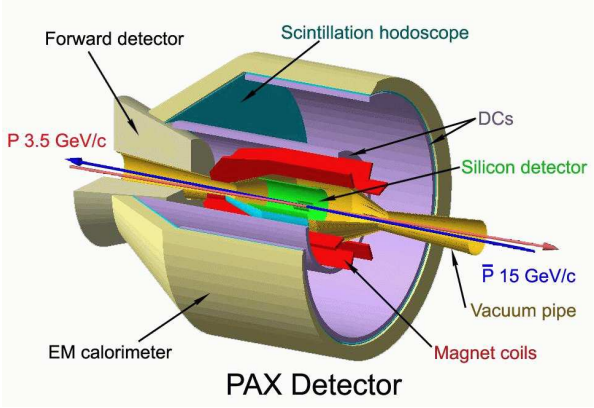


Figure 4: Conceptual design of the PAX detector.

transversity distribution. The proposed detector, described in the PAX technical proposal and shown in Fig. 4, is well-suited to provide large invariant-mass e^+e^- pair detection, from both Drell-Yan reactions and $\bar{p}p$ annihilations. In addition, such a detector is able to efficiently detect secondaries in two body reactions, like elastic scattering events, where the over-constrained kinematic simplifies the event reconstruction and reduces the particle identification requirements. Alternative detector scenarios, e.g. with $\mu^+\mu^-$ Drell-Yan pair detection capability, with an instrumented forward section or with extended hadron particle identification, are also under study.

Signal estimate

A detailed Monte Carlo study has been started to test the feasibility of the Drell-Yan measurement with the proposed detctor layout in Phase II. The achievable precision of the ratio between the transverse h_1^u and the well known unpolarized u(x) distributions of the proton, in different in-

tervals of the Bjorken-x and after one year of data-taking is shown in Fig. 5. The h_1^u distribution can be measured in a wide x range, from $x = 0.7$ down to $x = 0.05$, practically covering the whole valence region and extending to low value of x, where the theoretical predictions show the largest deviations. It should be noticed that in principle the beam energies in the two rings of the collider can be tuned to best explore different x intervals. Indeed the highest sensitivity is achievable for $x \approx 1/\sqrt{p_p p_{\bar{p}}}$.

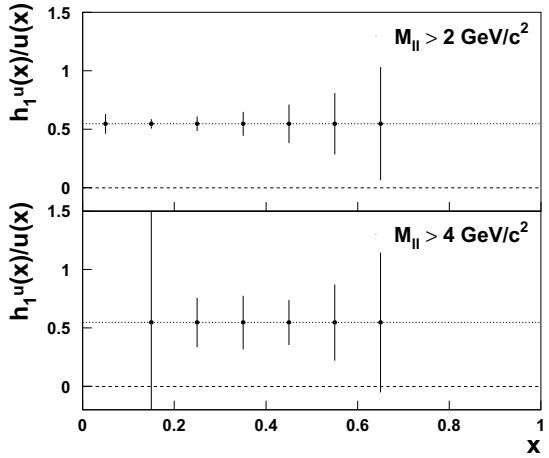


Figure 5: Expected precision of the $h_1^u(x)$ measurement for one year of data taking in the collider mode at PAX. A luminosity of $2 \cdot 10^{30}$ cm^{-2}s$^{-}1$ and a polar angle acceptance between 20° and 120° were assumed. The top panel shows the precision achievable within the full $Q^2 > 4GeV^2$ kinematic range, whereas the bottom panel shows the precision achievable in the restricted $Q^2 > 16GeV^2$ range.

Spin-filtering studies

As a first step towards the ambitious program of the PAX Collaboration a complete understanding of the mechanism of polarization buildup in a storage ring is mandatory. Therefore dedicated tests are forseen with protons at the COSY storage ring in Jülich, and a Letter of Intent [24] has been submitted to CERN in Nov. 2005 to perform spin filtering experiments using stored antiprotons in the AD ring. The final design for the APR ring will be defined only after these studies will be completed.

Conclusion

The PAX Collaboration has presented a rich and innovative physics program to be realized in the upcoming FAIR hadron facility. The storage of polarized antiprotons at HESR will open unique possibilities to test QCD in hitherto unexplored domains and make of FAIR a facility without competitors. In order to achieve a complete understanding of the spin-filtering process proposed for the production of the polarized antiprotons, dedicated studies are forseen in the next years at the COSY and AD ring.

References

[1] *PAX Letter of Intent*, Spokespersons P. Lenisa and F. Rathmann http://www.fz-juelich.de/ikp/pax

[2] A comprehensive review paper on the transverse spin structure of the proton can be found in: V. Barone, A. Drago and P. Ratcliffe, *Phys.Rep.* **359**, 1 (2002).

[3] M. Anselmino, V. Barone, A. Drago and N. Nikolaev, *Phys. Lett. B* **594**, 97 (2004).

[4] A. Efremov, K. Goecke and P. Schweitzer, *Eur. Phys. J. C* **35**, 207(2004).

[5] HERMES Collaboration, A. Airapetian et al., *Phys. Rev. Lett***84**, 4047 (2000); *Phys. Rev. Lett.***90** 092002 (2003); *Phys. Rev. D* **64** 097101 (2001); K. Rith, *Progress in Part. and Nucl. Phys.* **49**, 245 (2002).

[6] M. K. Jones et al., [Jefferson Lab Hall A Collaboration], *Phys. Rev. Lett.* **84**, 1398 (2000). O. Gayou et al., [Jefferson Lab Hall A Collaboration], *Phys. Rev. Lett.* **88**, 092301 (2002).

[7] A. Z. Dubnickova, S. Dubnicka, and M. P. Rekalo, *Nuovo Cimento* **109**, 241 (1966).

[8] S.J. Brodsky et al., *Phys.Rev. D* **69**, 054022 (2004).

[9] For a discussion on the validity of continuing space–like form factors to the time–like region, see, B. V. Geshkenbein, B. L. Ioffe, and M. A. Shifman, *Sov. J. Nucl. Phys.* **20**, 66 (1975); *Yad. Fiz.* **20**, 128 (1974).

[10] H.–W. Hammer, U.–G. Meißner and D. Drechsel, *Phys. Lett.B* **385** 343 (1996); H.–W. Hammer and U.–G. Meißner, *Eur. Phys. J.* A **20**, 469 (2004).

[11] E. Tomasi–Gustafsson and M.P. Rekalo, *Phys. Lett. B* **504** 291 (2001); *Nuovo Cimento A* **109** 241 (1996).

[12] V. Matveev et al., *Lett. Nuovo Cimento* **7**, 719 (1972).

[13] S. Brodsky and G. Farrar, *Phys. Rev. Lett.* **31**, 1153 (1973) and *Phys. Rev. D* **11**, 1309 (1973).

[14] M. Diehl, T. Feldmann, R. Jakob and P. Kroll, *Phys. Lett. B* **460**, 204 (1999).

[15] P. Landshoff, *Phys. Rev. D***10** 1024 (1974); P. Landshoff and D. Pritchard, *Z. Phys.* **C6**, 69 (1980).

[16] J.P. Ralston and B. Pire, *Phys. Rev. Lett.* **61** 1823 (1988); ibid. **49**, 1605 (1982); *Phys. Lett. B* **117** 233 (1982).

[17] G. P. Ramsey and D. W. Sivers, *Phys. Rev. D***52** 116 (1995); *Phys. Rev. D***47** 93 (1993); *Phys. Rev. D***45** 79 (1992).

[18] F. Rathmann et al., *Phys. Rev. Lett.* **94**, 014801 (2005)

[19] *PAX Technical Proposal*, Spokespersons P. Lenisa and F. Rathmann http://www.fz-juelich.de/ikp/pax

[20] F. Rathmann et al., *Phys. Rev. Lett.* **71**, 1379 (1993).

[21] S.J. Brodsky *Testing Quantum ChromoDynamics with Antiprotons* arXiv:hep-ph/0412206 (2004).

[22] G. Bardin et al. *Phys. Lett. B* **257** 514 (1991).

[23] C. G. White et al. *Phys. Rev. D* **70** 091102 (2004).

[24] *LoI for Measurement of the Spin-Dependence of the $\bar{p}p$ Interaction at the AD-Ring*, Spokespersons P. Lenisa and F. Rathmann http://www.fz-juelich.de/ikp/pax

Status Report of the FAIR-Accelerator Complex

H. Eickhoff for the GSI Project Group of the FAIR-Accelerator-Facility

1) Abstract

In 2005 major progress was achieved in further evaluation of the detailed ion-optical and technical design of the individual accelerator systems of the FAIR complex.
The according descriptions were summarized within two versions of Technical reports (TR) [1]. In addition a cost book for the accelerator system was created, that describes the costs of the individual systems within a 'buttom-up' cost estimate.
Numerous presentations and discussions of the technical and cost issues within international committees ('Technical Advisory Committee' (TAC), 'Cost Review Committee' (CORE-A), and various expert and 'MINITAC'-meetings) took place. In November the actual TR and Costbook were conditionally accepted by these committees.

2) Overall project description and status

a) Revisions of the topology

In 2005 the topology of the FAIR facility had been modified leading to an optimized situation both concerning the costs and the functions.

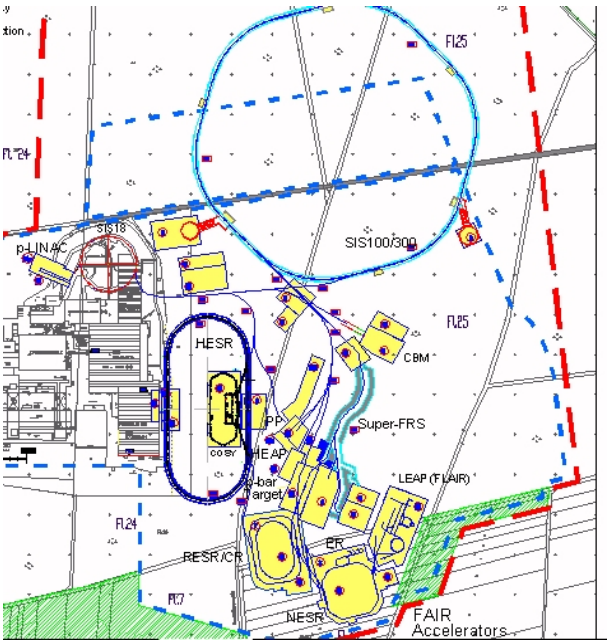


Fig. 1: Topology of the FAIR-accelerator facility

The modification led to a significant cost reduction for the individual accelerator sections and the buildings, especially for the High Energy beam transport system (HEBT).
Fig. 1 shows the actual layout with the different accelerator sections and the main buildings.

a) Upgrade programs (UNILAC, SIS18)

As both the UNILAC and SIS18 will be the injector facilities for the new FAIR accelerator sections, upgrade measures are foreseen within the next 3 years to achieve the demanded beam properties, especially the intensities.
At the UNILAC modifications at the high current ion-source are intended as well as upgrade procedures at the high current RFQ and at the quadrupole power supplies for the Alvarez structures; in addition a new charge separator section is intended. These measures will increase the transmission and enhance the beam brilliance in order to achieve the design current of 15 mA U^{28+} .
At SIS18 the major upgrade measures are the replacement of the electrostatic injection septum, the improvement of the vacuum system in order to reach XUV-conditions (p ~10^{-12} Torr), the insertion of collimators, the installation of 2 bunch compressor cavities and the power connection to a 110 kV grid, that allows a fast ramping (dB/dt = 10 T/s) .
The collimator system is necessary to prevent a dynamical pressure rise in case of U^{28+}-operation, that drastically reduces the beam-life-time and intensity. The improvement of the static pressure will mainly achieved by the usage of NEG-coated vacuum chambers.
At present these measures are in preparation; the grid connection will be ready in summer 2006.

In addition to the mentioned modifications new high current beam diagnostic systems have to be developed and the accelerator control system will be modified.
Whereas for the SIS upgrade costs major contributions from the EU-FP6 funding program could be reached, the UNILAC high current upgrade costs have to be financed mainly by GSI.

b) The FAIR accelerator sections

The FAIR accelerator facility consists of a double-ring synchrotron (SIS100 and SIS300) and a storage-ring complex with 4 storage rings (CR, RESR, NESR, HESR), that are also capable to accelerate /decelerate particle beams. These systems are designed to accelerate, accumulate and cool high intensity ion and proton beams. The proton beams, preaccelerated with a new proton linac, are mainly used for the production of antiprotons.
The new FAIR accelerator system consists of the following sections:

section	Circumference [m]	$(BR)_{max}$ [Tm]
SIS100	1083	100
SIS300	1083	300
CR	206	13
RESR	246	13
NESR	222	13
HESR	520	50

In addition to the synchrotron / storage ring facilities a new, large acceptance Super-Fragment Separator with a

maximum magnetic rigidity of 20 Tm, a pbar-Target section and the High energy beam transport systems to connect all these facilities has been designed. The major experimental facilities contain caves for High energy physics (CBM-cave), atomic physics, plasma physics and a FLAIR-building for low energy atomic and antiproton physics.

SIS100/300 complex

The double-ring synchrotron will provide ion beams of unprecedented heavy ion and proton beam intensities as well as of considerably increased energy.
SIS100 is the main accelerator of the FAIR project. It is a new large synchrotron (C=1083m) providing:

- up to $1 \cdot 10^{12}$ U^{28+}-ions per second at energies from 0.4 to 1.5 GeV/u in a single short bunch with lengths from 50 to 90 ns for the radioactive beam program;
- up to $2.5 \cdot 10^{13}$ protons at 29 GeV for the antiproton facility;
- up to $1 \cdot 10^{12}$ U^{28+} - ions at energies from 0.4 to 2.7 GeV/u in a single short bunch (30 to 90 ns) for plasma physics research;
- $2 \cdot 10^{9}$ U^{92+} -ions as booster for SIS300 for the research program on high energy nuclear collisions.

SIS300 will be operated in two different modes. First in a so called 'stretcher mode' and second in a 'high energy mode'. In the stretcher mode SIS300 shall provide un-interrupted slow extracted beams of high intensity in the energy range of SIS100. In the second operation mode, SIS300 will be supplied with fully stripped heavy ion beams from SIS100 (e.g. U^{92+}). U^{92+} beams will be accelerated up to an energy of 34 GeV/u and slowly extracted with spill durations of up to 100 s.

The storage-ring-complex

The storage ring complex contains three storage rings for Heavy Ion- and antiproton-accumulation and -experiments. While the 'Collector Ring' CR and the RESR mainly serve for beam cooling and beam accumulation, the NESR is a dedicated experimental ring mainly designed for in-ring experiments and equipped with electron cooling and electron target systems.

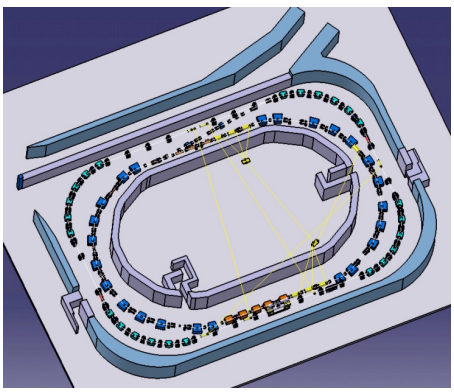


Fig. 2: Layout of the CR/RESR storage-rings (CR is the inner, RESR the outer ring)

In addition the NESR will provide the FLAIR experiment with low energetic antiproton beams.
All three storage rings will be capable to store both ions and antiprotons by means of changing current polarities of the magnets.
A fourth storage ring, the High Energy Storage ring HESR, will accelerate and cool antiprotons up to 15 GeV by means of stochastic and high energy electron cooling, mainly for the in-ring-experiment PANDA. The design of this ring is performed within a consortium, led by the Research Center of Jülich.

HEBT

The beam transport system for the FAIR project shall provide loss-free, emittance conserving transport of ion-, proton- and antiproton-beams to and from the synchrotrons and storage rings and to the experimental areas.
The system is designed such that every single experiment can be served with a static setting of all beam line magnets. It consists of sections, designed for different maximum magnetic rigidities.

Proton-Linac

Beside the research program with radioactive ion beams, a major part of the FAIR experimental program is dedicated to antiproton physics. Taking into account the pbar production & cooling rate, $2 \cdot 10^{16}$ primary protons/h have to be provided. Therefore a new 70 MeV proton linac is planned to generate proton beams with an intensity of 70 mA for injection into SIS18.

c) Main-R&D-activities

For the different technical systems various R&D-activities have been started within the last 2-3 years; these activities were partly covered by bilateral contracts between GSI and international institutes and firms. As superconducting and superferric magnets are foreseen for the synchrotrons SIS100, SIS300, the CR and HESR-storage rings and at parts of the Super-FRS and the HEBT, major R&D activities were devoted to these items, e.g. development of superconducting cables and tests of fast ramped sc model magnets and on the subject cryogenics. Within test measurements the technical feasibility of a fast ramped superconducting dipole could be demonstrated.

d) Schedule

The following table gives a rough overview of the intended construction periods for the individual realization stages:

Stage 0	Upgrade UNILAC, SIS	- 2008
Stage 1	Super-FRS, CR, NESR	2007 – 2011
Stage 2	SIS100, RESR, HESR, FLAIR, p-Linac	2011 – 2013
Stage 3	SIS300, caves for atomic and plasma-physics , CBM	2013 – 2015

3) References

[1] Technical Report (TR); GSI, Nov. 2005

Preparation Status of the HIPPI Experiments

W. Bayer, W. Barth, L. Dahl, L. Groening, M. Maier, S. Richter, S. Yaramyshev
GSI Darmstadt

Introduction

In order to meet the FAIR requirements for the acceleration of heavy ions (15 emA $^{238}U^{28+}$, 5 emA $^{238}U^{73+}$) a further improvement of the UNILAC performance is necessary. Therefore the correlation between space charge forces and focusing during acceleration of high intensity ion beams have to be understood in detail. The brilliance, i. e. ratio of beam current and beam emittance, is a suited quantity to study this correlation. It has to be determined and optimised for different phase advances σ_0 of the Alvarez-quadrupoles which can be achieved by the variation of their field strengths. Therefore an $^{40}Ar^{10+}$ beam is used, as the required field strengths of these quadrupole lenses for equivalent measurements with $^{238}U^{28+}$ cannot be reached yet. Regarding space charge beam transport of 6 emA ($^{40}Ar^{10+}$) corresponds to that of 12.8 emA ($^{238}U^{28+}$). In order to enable the acceleration of $^{238}U^{28+}$ with optimised brilliance the replacement of all Alvarez–quadrupole power supplies is hence part of the UNILAC upgrade program for FAIR.

Within the beam dynamics working package of the European network "**H**igh **I**ntensity **P**ulsed **P**roton **I**njector" (HIPPI) investigations of space charge forces are funded. Benchmarking calculations for different codes are performed with respect to the treatment of space charge forces on the theoretical side [1]. Experimentally the beam brilliance along the UNILAC will be investigated and optimised in all three dimensions for high beam currents. A schematic overview of the experimental setup for the planned measurements is shown in Figure 1. Due to beam destructive emittance measurements no parasitic beam delivery through the UNILAC will be possible. For the first time exclusive beam time (96 shifts) for UNILAC machine experiments was requested and approved for 2006.

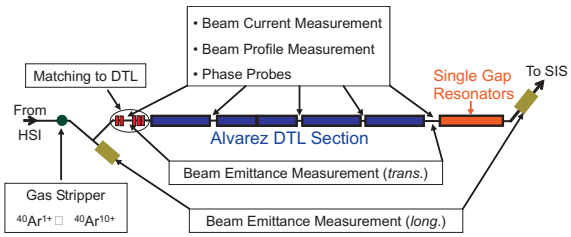


Figure 1: Overview of the experimental setup.

Machine Experiments in 2005

In 2005 UNILAC machine experiments were performed in preparation for the HIPPI experiments in 2006. It was intended to measure the beam emittance for different beam energies at the end of the DTL. This was performed for an $^{40}Ar^{10+}$ beam with low (1 emA) and high (9.5 emA) intensity. In a first step the horizontal and vertical emittances before the Alvarez DTL were measured. For 1 emA $^{40}Ar^{10+}$ usual field strengths of the quadrupole lenses in front of the DTL were used. For 9.5 emA these field strengths were recalculated to match the beam to the first periode of the first DTL section [3]. Afterwards the emittance measurements before the DTL were repeated. Finally the emittances behind the DTL for different beam energies were measured by switching off the Alvarez tanks successively starting from the last. The results are summarised in Figure 2.

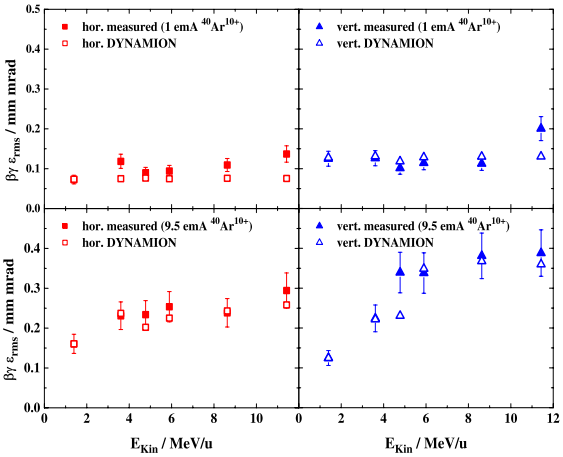


Figure 2: Measured and calculated horizontal (left) and vertical (right) beam emittance for a 1 emA (top) and 9.5 emA (bottom) $^{40}Ar^{10+}$ beam. The values at 1.4 MeV/u were used as input parameters for calculations with the DYNAMION code.

As shown in Figure 2 a significant emittance growth for different energies only exists for high intensity due to space charge effects while for 1 emA $^{40}Ar^{10+}$ the transverse beam emittance is preserved within the error tolerance. The error bars illustrate the maximum systematic error assumed to $\pm 15\,\%$. Calculations with the multiparticle tracking code DYNAMION [4] reproduce the measured emittances for 1 emA as well as for 9.5 emA $^{40}Ar^{10+}$ within the accuracy of the measurement.

Outlook

Until the next machine experiments further optimisations of the experimental setup and the data aquisition will be implemented. Especially the setups for the measurement of longitudinal emittances have to be tested. In preparation for the HIPPI experiments additional calculations with DYNAMION and measurements will be performed.

Acknowledgement

We acknowledge the support of the European Community-Research Infrastructure Activity under the FP6 Structuring the European Research Area programme (CARE, contract number RII3-CT-2003-506395)

References

[1] A. Franchi *et al.*, GSI Report 2004, p. 319
[2] P. Forck *et al.*, Proc. of LINAC 2000, Monterey, p. 166
[3] W. Barth *et al.*, GSI Report 2003, p. 207
[4] A. Kolomiets *et al.*, Proc. EPAC-98, p. 1201

Progress of the Layout of the FAIR Proton Linac

W. Barth, L. Dahl, P. Forck, L. Groening, R. Hollinger, O. Meusel, P. Spädtke, W. Vinzenz, S. Yaramyshev, GSI, Darmstadt, Germany
G. Clemente, U. Ratzinger, A. Schempp, R. Tiede, University of Frankfurt, Germany
S. Minaev, Institute for Theoretical and Experimental Physics, Moscow, Russia

Abstract

A first layout of the Proton Linac for FAIR was completed. Simultaneously, a detailed cost estimate including all subsystems was done. In 2005 special emphasis was put on the investigation of a appropriated proton source, the RFQ design, and on the design of the DTL.

Introduction

The proton linac has to provide the primary proton beam for the pbar production and its main beam parameters are listed in Tab. 1. This normal conducting machine will inject protons into the existing transfer channel from the UNILAC to the SIS18. The building complex will be located north of the existing UNILAC hall.

Final energy	70 MeV
Pulse current	70 mA
Pulse length	16 μs
Protons per pulse	$7\ 10^{12}$
Repetition rate	4 Hz
Transv. beam emittance	2.8 μm (tot. norm.)
Rel. momentum spread	10^{-3} (tot.)
Rf-frequency	352.21 MHz

Tab. 1: Main parameters of the proton linac for FAIR.

Proton Source and LEBT

The most appropriated source is a ECR type followed by a 2-solenoid-LEBT. Its design is aimed to be close to the set-up at CEA/Saclay [1], i.e. a proton current of 100 mA will be extracted at 95 keV with a pulse length of up to 1 ms. Vertical output phase space distributions were measured in a collaboration of CEA, GSI, and the University of Frankfurt for different solenoid settings, pulse lengths, and delay times within the pulse. Since the slit/grid method was used, the different components comprising the total beam current could be resolved. Although data reduction is still in progress it seems that the measured emittances fit well to the requirements of the RFQ being currently under design for the FAIR proton linac. Additionally, the source set-up did not fail a single time during the campaign lasting three weeks.

RFQ

The subsequent RFQ has to provide acceleration to 3 MeV with a transmission of 90% of accelerated particles. For its design two rf-structure types are followed, i.e. a 4-rod type at the University of Frankfurt and a 4-vane type at ITEP, Moscow. In simulations the 4-rod type design demonstrated all requirements with respect to rf- and to beam dynamic properties and it is ready for production. The 4-vane type still needs some refining with respect to the reduction of the longitudinal output emittances as well as to the reduction of the surface electric field strength. The final system decision will be made within 2006.

Layout of the DTL

Beam matching to the Drift Tube Linac (DTL) is done in a MEBT section comprising a single quadrupole lens and one re-buncher. The current DTL design comprises 11 Crossed-bar H-cavities (CH) separated by quadrupole triplets and beam diagnostic tools. A detailed description of the DTL is given in a separate report [2].

Several schemes for the rf-power alimentation are studied with respect to the number of rf-power sources, power converters, and to industrial providers for components. Especially concepts were and will be further studied that might allow to reduce the number of expensive rf-power sources to drive the structures. This survey is still in progress and a final layout is foreseen to be defined in summer 2006.

A second re-buncher installed behind the DTL will provide the required momentum spread at the injection to the SIS18. Injection into the transfer channel UNILAC-SIS18 will be done in a 90°-deflection chicane including horizontal scrapers for additional momentum cleaning. Alternatively to the deflection the beam can be transported in forward direction into a beam dump which allows detailed diagnostics including measurements of longitudinal and transverse beam emittances.

Project Reviewing

The main parameters of all relevant sub-components were defined. Their layouts (not including technical drawings) were presented in a Technical Report as well as twice to the Technical Advisory Committee (TAC) and to a MiniTAC. These layouts were used to provide a detailed cost estimate (cost book) of the overall project being evaluated twice by the COst REview (CORE) committee for the FAIR accelerators. Finally, the layout for the linac tunnel and supply building was refined in collaboration with the safety- and with the civil construction division, respectively.

References

[1] R. Gobin et al., "Saclay High Intensity Light Ion Source Status", Proc. of the 8th Europ. Part. Acc. Conf., Paris, France, (2002).

[2] C. Clemete et al., "Status of the CH-Proton Injector for FAIR", GSI-Annual Report 2005.

Status of the CH-DTL for the FAIR Proton Injector

G. Clemente, H. Podlech, R.Tiede, U.Ratzinger[#] , IAP Goethe University, Frankfurt, Germany
L. Groening, GSI, Darmstadt
S. Minaev, ITEP, Moscow

Abstract

A first 352 Mhz CH-cavity is under construction, which will demonstrate main production steps like stem welding and galvanic copper palting of the completed stainless steel tank module

Beam Dynamics

The beam dynamics investigtion from 3 to 70 MeV has been performed by use of the LORASR Code: several RFQ output distributions generated with PARMTEQ and representing realistic samples of an RFQ output distribution at 3 MeV and 70 mA were employed as initil distribution to design the whole linac lattice and, in particular, to design the matching section between the CH-DTL and the RFQ.

The overall Linac

To reach the final energy of 70 MeV required for the injection into the SIS18 several configurations were tested and analyzed: in this paper we present one technical solution consisting in 11 tanks with a total linac length of about 21 meter as schematised in Fig.1. Half a meter of free space is reserved for an extended diagnostics region after the 5th tank.

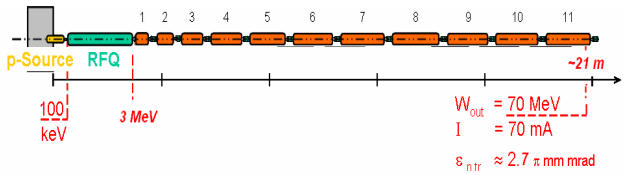


Fig.1: a schematic view of the FAIR Proton Injector.

To provide optimal matching between the RFQ and the CH-DTL an indipendently phased resonator will bunch the beam after the RFQ [2]. The main layout parameters are shown in Tab.1: compared to conventional linac designs, the increase in acceleration gradient is obvious.

Energy Range [MeV]	3-70
Pulsed Current [mA]	70
Norm.Rms emitt. X-X' (95 %) (mm mrad)	0.55
Norm.Rms emitt. Y-Y' (95 %) (mm mrad)	0.59
Rms emittance ΔW- Φ (95 %) (KeV/ns)	1.89
Energy Spread at 70 MeV	$< 10^{-2}$
Total Length	< 22 m

Tab.1: The main parameters of the CH Proton Injector: emittance values are calculated at 70 MeV.

Cavity Model

In order to improve the technical experience on this new kind of structure a cold model cavity consisting of 8 equidistant gaps is under construction

To achieve a good flatness of the electric field on the cavity's axis a new design for the end-cells has been conceived and, as shown in Fig.2, the linac will result in a very compact structure where each tank will be connected with the following one. The large end-half tubes will provide the desired flatness of the axis field and, at the same time, they will also be used to host the quadruple lenses and/or some beam diagnostics device such as phase probes. In this way the longitudinal beam dynamics, which depends a lot on short intertank sections, profits a lot.

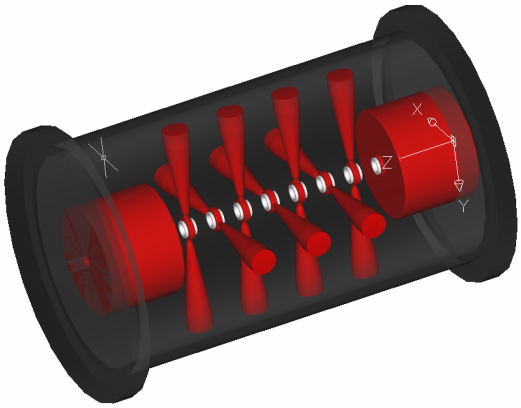


Fig.2 : view of the CH Prototype cavity under construction at the IAP of Frankfurt University.

All the components have been already fabricated and the cavity is now ready for the final assemblage and welding; after these operations the tank module will be ready for galvanic copper plating and preliminary RF and vaccum test.

References

[1] U.Ratzinger et Al. "The 70 MeV p-Injector for FAIR". U.Ratzinger et al, AIP Conference Proceedings, 2004, Volume 773, pp. 249-253 .

[2] G.Clemente et Al. "Beam dynamics of the first tank of a 70 mA CH-DTL Proton Injector". CARE NOTE 2005-016-HIPPI

*Work supported by EU Contract Nr . RII3-CT-2003-506395
[#]u.ratzinger@iap.uni-frankfurt.de

SIS100/300 Status Report

P. Spiller, K. Blasche, U. Blell, O. Boine-Frankenheim, P. Forck, B. Franczak, G. Franchetti, J. Stadlmann, I. Hofmann, P. Hülsmann, H. Klingbeil, A.D. Kovalenko(*), A. Krämer, G. Moritz, C. Omet, A. Peters, N. Pyka, H. Ramakers, H. Reich, H. Welker,
GSI, Darmstadt, Germany, (*) JINR, Dubna, Russia

Most of the critical design items of both synchrotrons could be addressed and technically feasible solutions were found. For all technical subsystems, technical concepts were defined which enable a systematic development of models and prototypes. Two major conceptual changes had to be accommodated: a) since HESR will be operated in a synchrotron like mode, antiproton acceleration is no more required in SIS100 and b) the minimum injection energy of SIS300 providing full beam intensity had to increased to 1.5 GeV/u.

Ion Optical Layout

The SIS100 lattice, using a missing dipole concept with 14 cells per sextant, was confirmed. In order to minimize the lateral displacement between SIS100 and SIS300 and to obtain sufficient space within each lattice cell, a lattice structure for SIS300 with only 13 lattice cells per sextant was developed. Furthermore, to maintain the possibility for using long bent dipole magnets instead of the short straight, the missing dipole concept was not assigned to SIS300. For both synchrotrons a suitable extraction scheme, fitting into the relatively short straight sections could be found. A combined horizontal-vertical extraction optics was chosen, enabling minimum loss slow extraction, respecting the Hardt condition. The originally considered external beam dump has been replaced by an internal beam dump. A bipolar kicker system in SIS100 is used in case of a fail function to dump the beam on this internal dump or extract the beam into the transfer system towards the experimental areas. A first ion optical solution using realistic parameters for the magnetic septa and kicker system was found for the vertical transfer between SIS100 and SIS300. Also here the tight geometrical conditions are crucial. Since a lateral displacement between both synchrotrons of about 0.5 m could not be avoided, the vertical transfer system must be tilted.

Beam Dynamics

Optimized working points were defined for the three operation modes of SIS100/300: a) proton operation, b) heavy ion operation with fast extraction and c) heavy ion operation with slow extraction. Dynamic aperture studies in the relevant areas of the working diagram are progressing. For the SIS100 tracking studies, measured field data of the Nuclotron magnet series were used. For the SIS300 calculations, scaled field data of the RHIC magnets were applied.

With the goal to define an impedance acceptance for both machines, theoretical models are being developed and improved. Impedance properties of crucial devices like kicker magnets, beam position monitors and collimation systems have been studied.

RF Systems

For cost saving reasons the RF systems for acceleration and compression has been reconsidered. The originally foreseen acceleration system for the generation of a second harmonic was cancelled. In order to compensate for the enhance space charge effects, the injection energy was raised. To save R&D effort with respect to the technical systems itself, but also for the beam-cavity interaction a conservative technical approach with ferrite load systems will be followed. Furthermore the total voltage for the compression systems was reduced from 1 MV to 600 kV. It is assumed that the final bunch length is not significantly affected and the distribution function may be influence by a proper pre-bunch concept. All RF units were distributed over the various straight sections and sufficient space could be declared between the quadrupole cryostats.

Vacuum System

Vacuum systems for both synchrotrons have been defined providing the extreme UHV conditions required for the operation with intermediate charge state heavy ions. In order to avoid freezing of molecules on the cold beam pipes, it is especially important to start with a sufficiently low residual gas pressure before cooling down. This is guaranteed by a large number of vacuum sectors and pumping stations. The operation with intermediate charge state heavy ions rely on the high pumping power of the cold surfaces. Therefore it is planned to equip the vacuum chambers with an independent active cooling system. A number of technical concepts for the thin wall SIS100 magnet chambers are actually under investigation.

Beam Diagnostics

The beam diagnostics system has to cover a large range in beam intensities and time structures for all ions from protons to uranium. Dedicated developments for crucial devices like the high current dc transformer (up to 200 A), and the beam position monitor system has been started. For cost saving reasons especially the number of beam loss monitors was drastically reduced.

Power Supply

A distributed power supply concept, including the dump units for the quench case has been developed. Both synchrotrons require three independent quadrupole circuits and one dipole circuits. A draft design of the power supply units and circuits could has been finished for the correction elements. Crucial components of the power units, like the active filter system and the quench protection circuit are under investigation.

Magnet R&D is described in dedicated annual reports.

Layout of the FAIR Beam Line System

S. Ratschow, K. Blasche, B. Franczak, P. Spiller, GSI, Darmstadt, Germany

The High Energy Beam Transport System had to be adapted to several changes in the layout of the various FAIR synchrotron and storage rings and was influenced by the common effort to reduce the overall cost of the FAIR facility:

- The circumference of SIS100 and SIS300 was reset to five times the circumference of SIS18. The circumferences of the storage rings were modified several times.
- The layout of the Super-FRS pre-separator was modified resulting in an increase of the total deflection angle from 56° to 66°.
- It was proposed to operate the HESR in a synchrotron like mode, such that the 13 Tm cooled antiproton beam can directly be transferred from RESR. Acceleration of antiprotons in SIS100 is no longer considered. Correspondingly the proton beam for the HESR machine setting will be supplied directly from SIS18 with a rigidity of 13 Tm. Protons from SIS100 at 50 Tm for the HESR are no longer required.

In order to minimize the distance of the HESR from SIS18 and RESR, and to make use of the existing infrastructure, the position of the HESR was changed (Fig. 1). As a result of the decision to supply the HESR directly from the RESR, further beam line sections could be optimized: The injection beam line from SIS18 to SIS100, originally used to transport 50 Tm beams to the HESR, could be shortened and moved closer to SIS18. This modification allowed changing the extraction direction from SIS100 and SIS300 from horizontal to vertical. The horizontal extraction from SIS100 required rather large underground buildings. By the new scheme using vertical extraction the building area could be considerably reduced. Furthermore, it was decided to foresee an internal beam dump for SIS100 and SIS300. Therefore the beam line to the originally considered external beam dump could be removed. A beam dump for setting the synchrotrons and for optimizing the parameters of the extracted beam has been introduced on half way to ground level.

The CBM cave, being the only experimental area which will be supplied with 300 Tm beams, was also moved to the intermediate underground level at -6 m. The underground position provides sufficient screening for the secondary particles emitted from the production targets. By moving the CBM cave to the intermediate height level another difficulty was solved. The maximum inclination of the SIS300-type s.c. dipoles could be limited to less than 6°, which is more suitable for the cryogenics system.

The requirement of a passive protection of the CBM cave by a beam line bend, was solved by means of the beam divider in front of the machine beam dump.

Until mid summer 2005 several competing concepts for the overall topology were studied. One of these concepts used a mirrored Super-FRS. As a consequence the whole FAIR layout was pretty much oriented in east-western direction.

The concept for the ion optical layout of the beam line system itself has been reconsidered. By limiting the acceptance to two times the maximum value of the emittance, many quadrupole magnets could be saved. Straight F0D0 focussing proved to be the most economic solution. All instances of triplet focussing were eliminated.

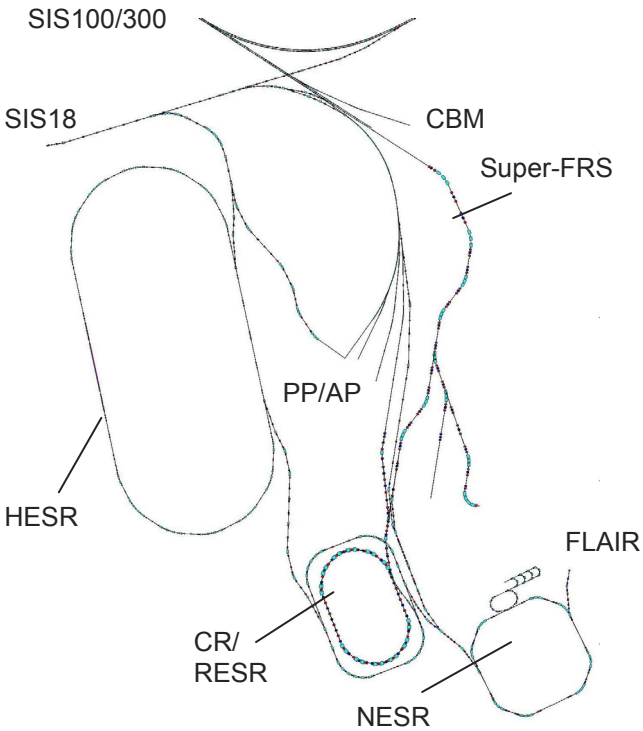


Figure 1: Beam Line Layout of the FAIR facility

The series connection of the quadrupole magnets was optimized. However, the numerous beam dividers and combiners, and many bends with varying angles needing beam or dispersion matching, limit the possible number of series connections. The supply buildings were defined and the required area for the power supply and other supply units and the cryogenics equipment was estimated.

The Storage Rings of the FAIR Project

P. Beller, K. Beckert, B. Franzke, A. Dolinskii, F. Nolden, C. Peschke, M. Steck, J. Yang

GSI, Darmstadt, Germany

Introduction

The storage ring complex is an important part of the FAIR project. Experiments with antiprotons and with highly charged heavy ions - stable and unstable- will be performed at the different storage rings. Furthermore, the storage rings supply the FLAIR complex with low energy antiproton and ion beams.

Since the release of the Conceptual Design Report (CDR) [1] the FAIR project has undergone some big changes. However, in the last year the positioning of the storage rings with respect to each other and the connections between the rings remained unchanged. The layouts of the rings and of the buildings are now more detailed. Figure 1 shows as an example how the Collector Ring CR and the Accumulator/Decelerator Ring RESR are located in their common building.

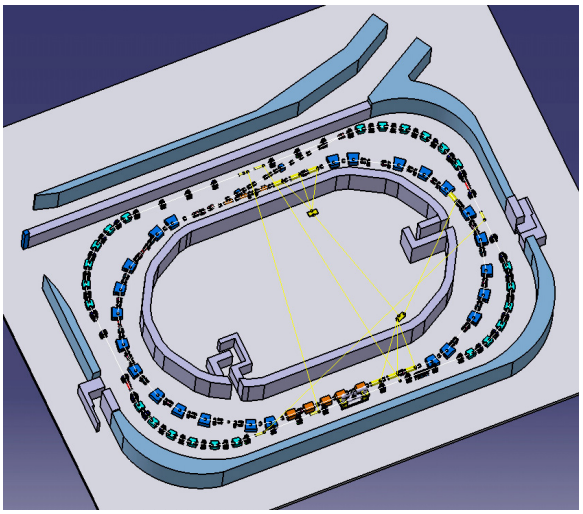


Figure 1: 3D bird's eye view of the CR/RESR area.

Major progresses have been made in the design of the stochastic cooling systems of CR and RESR. This includes also the decision about the accumulation scheme for antiprotons in the RESR. Another major progress has been made with beam dynamics calculations for the RESR and for the New Experimental Storage Ring NESR.

Some changes will lead to the reduction of performance of the rings. These changes were made due to the necessity to save investment cost. An example of this kind of change is the reduction of rf and cooling power in the CR which will lead to an increased momentum spread of the beam after injection and bunch rotation and longer cooling times. However, the possibility of an addition remains for all these systems and therefore, it is still possible to bring the rings to their initially envisaged performance.

The Collector Ring CR

The CR is optimized for fast cooling of secondary beams of antiprotons and rare isotopes [2]. Rare isotopes are injected at a fixed energy of 740 MeV/u while antiprotons have an energy of 3 GeV. The most recent design of the CR results in a circumference of 210.45 m. This design foresees the usage of super-ferric dipoles and normal conducting quadrupoles. A schematic drawing of the ring and its important installations is shown in Figure 2.

Due to the need to reduce investment costs the number of rf-cavities has to be reduced leading to a reduction of the maximum voltage for bunch rotation from 400 kV down to 200 kV. For the same reason the bandwidth of the stochastic cooling system has to be reduced from 3 GHz to 1 GHz. The first measure causes a larger momentum spread of the beam after bunch rotation. The second measure leads to distinctly longer cooling times. Now total cooling times of about 10 s for antiprotons and 1.5 s for rare isotopes are envisaged. However, it will be possible to upgrade these systems in a later stage. The required space for these systems has been foreseen.

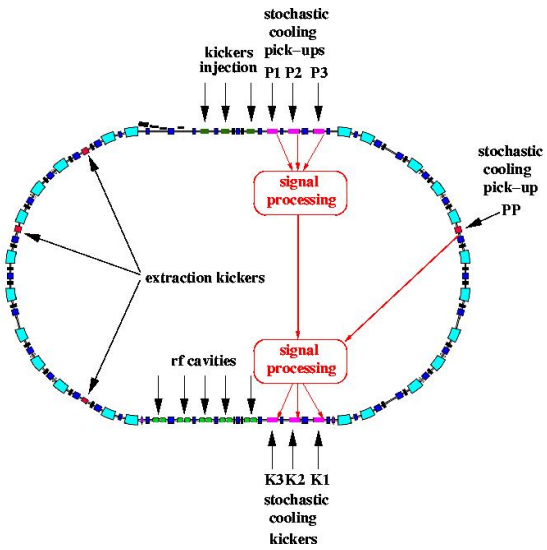


Figure 2: Schematic layout of the CR and important installations.

Major progress has been made in the design of stochastic cooling electrodes for the CR. The recent developments are described in a separate contribution of this annual report [3].

The Accumulator/Decelerator Ring RESR

The tasks of the RESR are the efficient accumulation of antiprotons at 3 GeV and the fast deceleration of rare iso-

topes to energies between 500 MeV/u and 100 MeV/u within 1 s. The RESR has a circumference of 245.5 m. The current design foresees normal conducting dipoles and normal conducting quadrupole magnets. To keep investment costs low the RESR will reuse parts of the existing storage ring ESR [4]. Due to the modification of the extraction scheme during the last year the number of RESR kickers could be reduced from four to two. The RESR uses now a common kicker for injection and extraction towards the HESR and one separate kicker for extraction towards the NESR.

In order to get an estimation of the useful aperture, dynamic aperture calculations have been carried out using MAD8, SIXTRACK and PTC. These calculations so far include sextupole components and higher order multipole components of the main dipole and the quadrupole magnets. The calculations were carried out for the central orbit and for orbits with a momentum offset of -1 % and +1 % with respect to the central orbit. The results show a dynamic aperture which is in all investigated cases larger than the geometric acceptance of the ring.

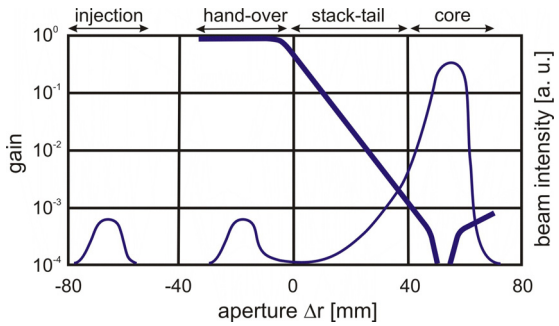


Figure 3: Gain profile of the momentum pick-ups and beam distribution.

Due to the prolongation of the cooling times in the CR the antiproton accumulation rate in the RESR has been reduced from 7×10^{10}/h to 3.5×10^{10}/h. A crucial point within antiproton accumulation is the reduction of the emittance and the momentum spread of the injected beam between successive injections. The stochastic cooling system must be capable of cooling a batch of 10^8 antiprotons to its final values with respect to emittance and momentum spread within 10 s. Two studies have been carried out concerning the antiproton accumulation scheme [5] [6] in the RESR. These studies resulted in the decision to use a stacking scheme which is very similar to the CERN AA stacking scheme [7]. The gain profile of the momentum pick-ups of such a system is shown in Figure 3. The momentum cooling system is divided into three different systems: the hand-over system, the stack-tail system and the stack-core system. An antiproton beam is injected to an inner orbit of the RESR with a momentum offset of $\Delta p/p = -0.8$ % with respect to the central orbit. This beam is transferred from the injection orbit to an orbit which is covered by the hand-over system using the standard rf-cavity of the RESR. The different cooling systems then will cool this beam towards the stack-core. In addition to the momentum cooling system the RESR is equipped with two transverse cooling systems.

The New Experimental Storage Ring NESR

The NESR is now designed with a circumference of 222.11 m. In the NESR the same normal conducting dipole and quadrupole magnets as in the RESR will be used. The NESR is the main instrument for nuclear and atomic physics experiments with stored ion beams [8]. Atomic and antiproton physics with low energy beams require the possibility of fast deceleration and subsequent fast or slow extraction towards the FLAIR complex.

To increase the intensity of rare isotope beams the NESR allows the accumulation of these particles using a barrier bucket accumulation scheme.

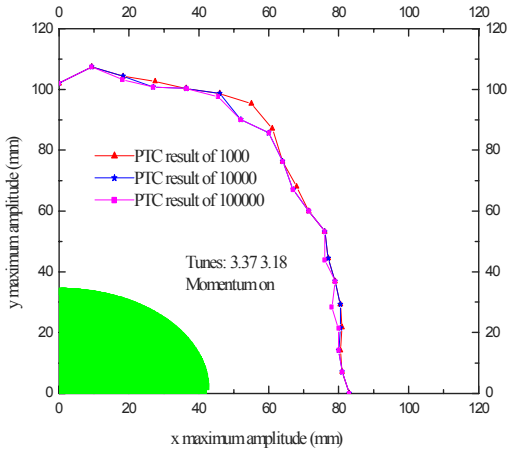


Figure 4: Dynamic aperture calculations for different numbers of turns using PTC. The green area represents the geometric acceptance of the ring.

For the NESR similar dynamic aperture calculations as for the RESR were carried out. The results also show a dynamic aperture which is larger than the geometric acceptance of the ring. Figure 4 depicts the results of these calculations.

References

[1] An International Accelerator Facility for Beams of Ions and Antiprotons, Conceptual Design Report, GSI, November 2001.
[2] A. Dolinskii et al., Proc. of the 8th European Particle Accelerator Conference, Paris, 2002, p 572.
[3] C. Peschke et al., this report.
[4] B. Franzke, Nucl. Instr. Meth. B24/25 (1987) 18.
[5] T. Katayama et al., Proceedings of COOL 2005, to be published.
[6] D. Möhl, internal note, 2004.
[7] H. Koziol, S. Maury, CERN-PS 95-15 (AR/BD), 1995.
[8] P. Beller et al., Proc. of the 8th European Particle Accelerator Conference, Paris, 2002, p. 545.

Design Work for the High-Energy Storage Ring (HESR)*

A. Lehrach#, S. An, K. Bongardt, J. Dietrich, R. Eichhorn, B. Lorentz, R. Maier, S. Martin, D. Prasuhn, A. Schnase, E. Senicheva, Y. Senichev, H. Stockhorst, R. Tölle, E. Zaplatin
Forschungszentrum Jülich, 52425 Jülich, Germany
O. Boine-Frankenheim, A. Dolinskii, R.W. Hasse, M. Steck
Gesellschaft für Schwerionenforschung, 64291 Darmstadt, Germany
F. Hinterberger
Helmholtz-Institut für Strahlen- und Kernphysik, Universität Bonn, 53115 Bonn, Germany
T. Bergmark, B. Gålnander, T. Johnson, T. Lofnes, G. Norman, D. Reistad
The Svedberg Laboratory, Uppsala University, 75121 Uppsala, Sweden

Abstract

The High-Energy Storage Ring (HESR) of the future International Facility for Antiproton and Ion Research (FAIR) at GSI in Darmstadt is planned as an antiproton synchrotron storage ring in the momentum range of 1.5 to 15 GeV/c. An important feature of this new facility is the combination of phase space cooled beams and dense internal targets (e.g. pellet targets), which results in demanding beam parameter requirements for two operation modes: high luminosity mode with peak luminosities of up to $2\cdot10^{32}$ cm^{-2} s^{-1}, and high resolution mode with a momentum spread down to 10^{-5}, respectively. To reach these beam parameters one needs a very powerful phase space cooling, utilizing high-energy electron cooling and high-bandwidth stochastic cooling.

Design Issues and Experimental Requirements

The HESR is dedicated to the field of antiproton physics over a broad momentum range from 1.5 to 15 GeV/c [1,2]. The lattice has a racetrack-shaped design, consisting of two 180° arc sections connected by two long straight sections (see Fig. 1). One straight section will mainly be occupied with the electron cooler. In a later stage a Siberian snake can be added to ensure a possible upgrade for polarized beams. The other straight section will host the experimental installation PANDA [3] with an internal frozen H_2 pellet jet target, injection kickers/septa and RF cavities. Two pickup tanks for stochastic cooling are located close to the ends of each straight section while the stochastic kicker tanks are placed opposite in the other straight section, diagonally connected with signal lines. Special requirements for the lattice are dispersion-free straight sections and betatron amplitudes of a few meters at the internal interaction point. Larger betatron amplitudes to get sufficient beam-target overlap are under discussion [2]. Furthermore imaginary transition energy and optimized ion optical conditions for beam cooling can be provided (e.g. matched betatron amplitudes at the pickups and kickers of the stochastic cooling system and in the electron cooler section, scaling with beam momentum for optimum beam overlap and cooling). Details of the ion optical layout and features of the lattice design are discussed in [4]. The antiproton beam is accumulated in the CR/RESR complex at 3.8 GeV/c before injected into the HESR [2]. Beam parameters at injection, experimental requirements and operation modes are summarized in Table 1.

TABLE 1. Design beam parameters and operation modes.

Injection Parameters	
Transverse emittance	1 mm·mrad (normalized, rms) for $3.5\cdot10^{10}$ particles, scaling with number of accumulated particles: $\varepsilon_\perp \sim N^{4/5}$
Relative momentum spread	$1\cdot10^{-3}$ (normalized, rms) for $3.5\cdot10^{10}$ particles, scaling with number of accumulated particles: $\sigma_p/p \sim N^{2/5}$
Bunch length	200 m
Injection Momentum	3.8 GeV/c
Injection	Kicker injection using multi-harmonic RF cavities
Experimental Requirements	
Ion species	Antiprotons
Production rate	$2\cdot10^7$ /s ($1.2\cdot10^{10}$ per 10 min)
Momentum / Kinetic energy range	1.5 to 15 GeV/c / 0.83 to 14.1 GeV
Number of particles	10^{10} to 10^{11}
Target thickness	$4\cdot10^{15}$ atoms/cm^2
Transv. beam size at IP	Range of one millimeter
Operation Modes	
High resolution (HR)	Peak luminosity $2\cdot10^{31}$ cm^{-2} s^{-1}, 10^{10} $\bar{p}$ rms momentum spread $\sigma_p/p \sim 10^{-5}$ 1.5 to 9 GeV/c, electron cooling
High luminosity (HL)	Peak luminosity $2\cdot10^{32}$ cm^{-2} s^{-1}, 10^{11} $\bar{p}$ rms momentum spread $\sigma_p/p \sim 10^{-4}$ 1.5 to 15 GeV/c, stochastic cooling above 3.8 GeV/c

* Work supported by European Community RESEARCH INFRASTRUCTURES ACTION under the FP6 program: DESIGN STUDY (Contract No. 515873 – DIRAC Secondary-Beams), and by INTAS-GSI grants (Ref. No. 03-54-5584).
# a.lehrach@fz-juelich.de

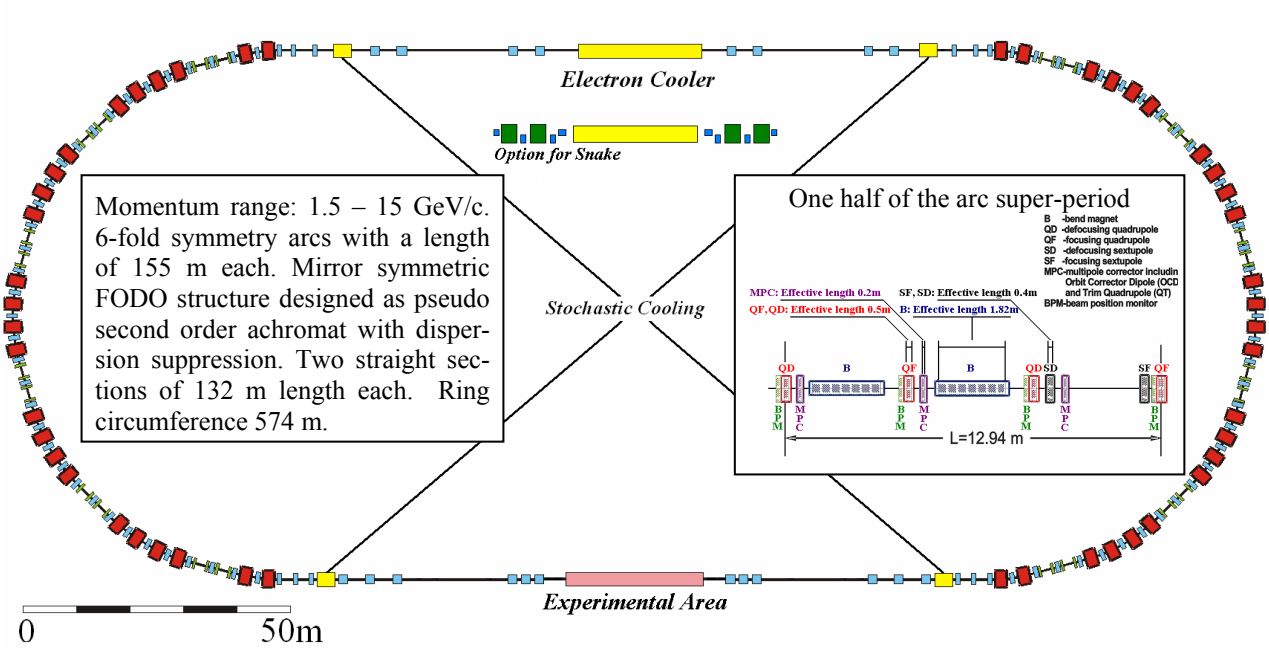


FIGURE 1. Schematic view of the HESR with 6-fold symmetry lattice. Tentative positions for injection, cooling devices and experimental installations are indicated. Also shown is the arrangement of elements in the super-period

The HESR was planned with one internal interaction point only, equipped with the PANDA detector [3]. Two other experimental groups (ASSIA [5] and PAX [6]) proposed antiproton spin physics experiments at HESR.

R&D work

Highest priority is assigned to the high-energy electron cooler. The main issue is the reliable operation of high-brilliance electron beams in a high-voltage environment. The design work is lead by TSL in cooperation with the Budker Institute, the Fermi National Accelerator Laboratory (FNAL), and industry.

With regard to maximum field strength, magnet aperture and ramping rate RHIC-type super-conducting "cosθ"-magnets installed in the interaction regions fit the HESR requirements except for the magnet length. Short straight super-conducting magnets demands a careful R&D work. Prototypes have to be built to ensure the design choice. In addition R&D work with high priority is allotted to curved super-conducting magnets for improved sagitta in the HESR energy range.

Prototyping of critical components for the stochastic cooling system has high priority. The main stochastic cooling parameters were determined for a system utilizing quarter-wave loop pickups and kickers. Stochastic cooling is presently specified above 3.8 GeV/c.

The development of low impedance kicker and septa is of great importance for an optimized injection scheme. Furthermore broad-band amplifiers for beam feedback, alignment and assembly issues for bent cryostats and super-conducting multilayer magnets combining several multipoles will be investigated.

The R&D work covers the years 2005-2008.

Conclusion

A correction scheme for the lattice is being developed to correct for field errors, misalignments and chromatic effects of magnets. Main R&D issues are feasibility demonstration for magnetized high-energy electron cooling, prototyping of super-conducting magnets and for high-bandwidth stochastic cooling. In parallel simulation codes for cooled beams interacting with internal targets are improved.

References

[1] An International Accelerator Facility for Beams of Ions and Antiprotons, Conceptual Design Report, GSI Darmstadt, November 2001, see http://www.gsi.de/GSI-Future/cdr/.

[2] FAIR Project, Technical Report, to be published.

[3] Strong Interaction Studies with Antiprotons, Letter-of-Intent, PANDA collaboration, January 2004, see http://www.gsi.de/documents/DOC-2004-Jan-1151.pdf.

[4] Y. Senichev et al., Lattice Design Study for HESR, Proc. of the European Accelerator Conference, Lucerne, 653 (2004).

[5] A Study of Spin-dependent Interactions with Antiprotons, Letter-of-Intent, ASSIA collaboration, January 2004, see http://www.gsi.de/documents/ DOC-2004-Jan-152-1.pdf.

[6] Antiproton-Proton Scattering Experiments with Polarization, Letter-of-Intent, PAX collaboration, January 2004, see http://www.gsi.de/documents/ DOC-2004-Jan-1251.pdf; F. Rathmann et al., Phys. Rev. Lett. 93, 224801 (2004).

Beam Performance and Luminosity Limitations in the High-Energy Storage Ring (HESR)

A. Lehrach, R. Maier, A. Prasuhn, FZ Jülich, F. Hinterberger, Universität Bonn, O. Boine-Frankenheim, R.W. Hasse, GSI Darmstadt

An important feature of the High-Energy Storage Ring [1,2] is the combination of phase space cooled beams and dense internal targets (e.g. pellet targets), which results in demanding beam parameter requirements for two operation modes: high luminosity mode with peak luminosities of up to $2 \cdot 10^{32}$ /cm²s, and high resolution mode with a momentum spread down to 10^{-5}, respectively. The effects of beam-target scattering and intra-beam interaction are investigated in order to study beam equilibria and beam losses for the two different operation modes [3].

Beam equilibrium is of major concern for the high-resolution mode. Calculations of beam equilibrium between electron cooling, intra-beam scattering and beam-target interaction are being performed utilizing different simulation codes like BETACOOL by I.N. Meshkov et al. (JINR, Dubna), MOCAC by A.E. Bolshakov et al. (ITEP, Moscow), and PTARGET by B. Franzke at al. (GSI, Darmstadt). Results from different codes for HESR conditions are compared in [4]. Studies of beam equilibria for the HESR are also carried out by D. Reistad for electron cooled beams [2] and by H. Stockhorst for stochastically cooled beams [5] utilizing the BETACOOL code. To simulate the dynamics of the core particles, an analytic rms model was applied for the calculation presented in this paper [6]. The empirical magnetized cooling force formula by V.V. Parkhomchuk was used for electron cooling [7], and an analytical description was applied for intra-beam scattering [8]. Beam heating by beam-target interaction is described by transverse and longitudinal emittance growth due to Coulomb scattering and energy straggling, respectively [9, 10]. The presently available numerical models to calculate beam equilibrium parameters of cooled beams interacting with internal targets will be further improved. Important tasks covered by an INTAS research project are studies of beam equilibria, and cooled beam distributions in the presence of intra-beam scattering and internal target scattering.

The main restriction for high luminosities is beam losses, since the antiproton production rate is limited. Three dominating contributions of the beam-target interaction have been identified: Hadronic interaction, single Coulomb scattering and energy straggling of the circulating beam in the target. In addition, single intra-beam scattering due to the Touschek effect has also to be considered for beam lifetime estimations. Beam losses due to residual gas scattering can be neglected compared to beam-target interaction, if the vacuum is better than 10^{-9} mbar. For beam-target interaction, the beam lifetime is independent of the beam intensity, whereas for the Touschek effect it depends on the beam equilibria and therefore on the beam intensity.

In order to calculate the average luminosity, machine cycles and beam preparation times have to be specified. After injection at 3.8 GeV/c, the beam is pre-cooled to equilibrium (with target off), and then ac-/decelerated to the desired beam momentum. Beam steering and focusing in the target region is required before beam cooling and pellet beam are switched on, and the physics experiment can be performed.

The main restriction for the high-resolution mode is intra-beam scattering. To reach the specified momentum spread, the beam has to be heated transversely. This is also required to get a sufficient beam-target overlap. In addition, simulation codes have to be improved to describe the dynamics of tail particles, especially with respect to the beam-target interaction. Beam losses are of major concern for the high-luminosity mode. Hadronic interaction, single Coulomb scattering, energy loss straggling and Touschek effect due to single intra-beam scattering are main causes of the beam loss. At lower momenta, the beam losses are too large compared to the antiproton production rate. An optimized beam cooling scenario and a factor of two larger longitudinal ring acceptance is required to reach average luminosities of the order of 10^{32} /cm²s.

[1] An International Accelerator Facility for Beams of Ions and Antiprotons, Conceptual Design Report, GSI Darmstadt, November 2001,
see http://www.gsi.de/GSI-Future/cdr/.
[2] FAIR Project (subproject HESR), Technical Report, to be published.
[3] A. Lehrach, O. Boine-Frankenheim, F. Hinterberger, R. Maier, D. Prasuhn accepted by Nucl. Instr. Meth. A.
[4] A. Dolinskii et al., Simulation Results on Cooling Times and Equilibrium Parameters for Antiproton Beams in the HESR, Proc. of the European Accelerator Conference, Lucerne, 1969 (2004).
[5] H. Stockhorst et al., Cooling Scenario for the HESR Complex, to be published in Proc. of International Workshop on Beam Cooling and Related Topics, Galena IL, USA (2005).
[6] O. Boine-Frankenheim et al., Cooling equilibrium and beam loss with internal targets in the High-Energy Storage Ring (HESR), to be published.
[7] V.V. Parkhomchuk, Nucl. Inst. Meth. A 441, 9 (2000).
[8] A.H. Sørensen, CERN Accelerator School (edited by S. Turner) CERN 87-10, 135 (1987).
[9] F. Hinterberger, T. Mayer-Kuckuk and D. Prasuhn, Nucl. Instr. Meth. A 275, 239 (1989).
[10] F. Hinterberger, D. Prasuhn, Nucl. Instr. Meth. A 279, 413 (1989).

Work supported by INTAS-GSI grants (Ref. No. 03-54-5584).

Simulation of Modified Yoke Configurations and Coil Geometries for the Laminated Nuclotron Magnet

H. De Gersem*, S. Koch†, T. Weiland, TEMF TU Darmstadt, Germany

Abstract

For the SIS-100 of FAIR, superconducting dipole magnets will be used. In order to further decrease the dynamic losses caused by eddy currents induced in the laminated yoke, modified designs for the end blocks are investigated. Simulations are performed using the original coil as well as an artificial one to analyse the impact of the end turns on the computed losses. The results show a strong dependence of the losses on the coil geometry.

Simulation Setup

Calculations are carried out using the magnetoquasistatic approximation of the Maxwell equations discretised by the Finite Integration Technique (FIT). The laminated yoke material is modelled by an anisotropic, nonlinear material characteristic [1]. Several modifications were proposed to break up the eddy-current paths in the end regions of the yoke in order to bring the losses during transient operation down to an acceptable level. While the yokes in the upper row of Fig. 1 are equipped with the original coil, the four configurations at the bottom feature flattened end turns. However the latter coil design can not be built up in practise due to mechanical restrictions. As the first column

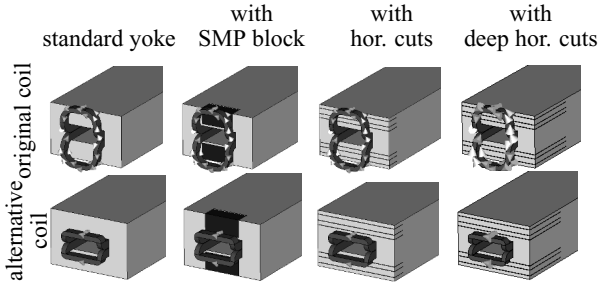


Figure 1: Eight considered magnet configurations.

shows the original design, the yoke configurations in the second column exhibit an insert of sintered magnetic powder (SMP) denoted by the dark brick, which has zero electric conductivity. The models in the third and fourth column are modified by horizontal slits of two different depths (50 mm and 200 mm) to inhibit eddy currents from circulating inside the lamination plane. Using a magnetic vector potential formulation within the FIT a nonlinear system of equations is obtained which is to be linearised and solved in every timestep. Time integration is performed by means of a θ-method with a constant timestep of 0.1 s while the arising linearised systems are solved with a Krylov subspace solver accelerated by an algebraic multigrid preconditioner.

* Supported by GSI, Darmstadt
† Supported by DFG under contract GraKo 410.

Numerical Results

Simulations were run for the eight configurations shown in Fig. 1 using two different discretisation levels. Results are shown for the more refined one. The total losses due to eddy currents are integrated over the yoke volume. Comparing the results for the different coil geometries, a reduction by approximately a factor of three is observed for the artificial coil independent of the yoke modifications (Fig. 2). In addition the losses in the yoke are integrated in time over one triangular excitation cycle and are plotted against the spatial coordinate along the magnet axis in Fig. 3. As expected the location of the losses is shifted away from the end plate in presence of a SMP block. For this configuration the total losses amount to 19.3 W whereas the other modifications of the end plates don't result in substantial benefits.

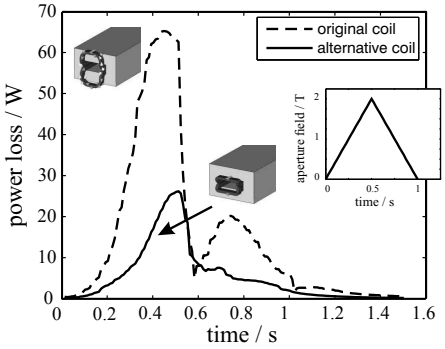


Figure 2: Power loss integrated over the yoke volume.

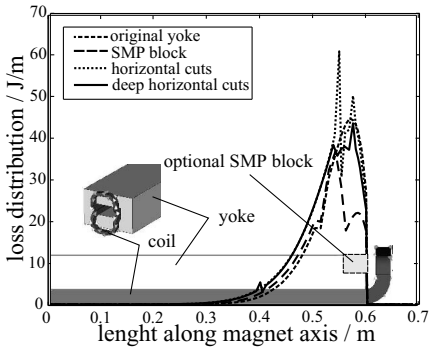


Figure 3: Power loss distribution integrated over one transient cycle, shown for the different yoke modifications.

References

[1] S. Koch, H. De Gersem, E. Fischer, G. Moritz and T. Weiland, "Simulation of Eddy-Current Losses in a Fast Ramped Superconductive Dipole Magnet", Proceedings of the 19th International Conference on Magnet Technology (MT19), 2005.

Development of FAIR superconducting magnets and cryogenic system

Egbert Fischer, Eric Floch, Guenther Hess, Hanno Leibrock, Juris Kaugerts, Marion Kauschke, Gebhard Moritz, Carsten Muehle, Pierre Schnizer, Claus Schroeder, Gertrud Walter, Birgit Weckenmann, Yu Xiang, GSI Darmstadt, Germany

Introduction

Generally speaking, R&D continued during 2005 for FAIR superconducting magnets, especially for the main dipoles and quadrupoles and the corresponding cryogenic distribution system as well. R&D was conducted by GSI employees, in collaborations or by contracts, funded by GSI or the European Union (EU FP6 Design study). Both fields, sc magnets and cryogenics, (besides normal conducting magnets) were reviewed by subcommittees of the Technical Advisory Committee (TAC), the cost estimates were approved by the Cost Review Committee-Accelerator (CORE-A).

Superconducting Magnets

SIS 100

Main dipole

Measurements and calculations with the goal to reduce the thermal losses at 4K in dipole yoke and coil continued [1, 2, 3]. The sources have been better identified and understood also quantitatively. A new cross section was defined following an aperture increase by the machine designer. With this information the lamination cross section and the structural elements of the yoke (stainless steel end plate, stainless steel brackets, etc.) are defined.

Besides coil loss reduction due to a new strand with reduced filament size the main work on the coil was directed to the design of the conductor (Nuclotron type cable) support structure [4,5] and the coil restrain in the magnet gap. The chosen G11 conductor support structure is an appropriate component to stabilize the coil and offers important advantages:

- Precise positioning of the conductor with certain defined distance between conductors providing better and reproducible field quality,
- More uniform distribution of loads on the CuNi tubes (no narrow pressure contact lines),
- Easier winding process on a guiding support.

Short models of that structure were produced and tested. Preliminary stress calculations showed that fatigue effects on the Cu-Ni-tube of the cable are tolerable. As cable alternative a novel CICC-cable has been developed and tested [6].

Main quadrupole

The AC loss reduction was proven by detailed experimental model tests. 2D and 3D field quality calculations have been performed [7].

SIS 300

The testing of dipole GSI001 (4T, 1 T/s) continued at BNL. Cryogenic losses were measured and compared with calculated data based on measured wire and cable parameters. Agreement was good besides some discrepancies for the eddy current contribution. The ramp rate test showed the expected behavior. Field harmonics (b3 and b5) were measured on the ramp of 2 T/s, the relative difference between DC and AC-values is less than 2 x 10-4 for b3 [8].

Design work for the 6T, 1 T/s dipole continued at IHEP, Protvino [9] and at CERN. 2D coil cross section was agreed on. Winding tests with a cored Rutherford-cable (bare cable dimensions identical to the LHC dipole outer layer cable) were performed. The results were the basis for 3D end design of the coil. Thermo-mechanical calculations of the magnet cross sections were performed, a temperature margin of 0.9 K under operating conditions was calculated. Cable contact resistances and time dependent strand magnetization was measured as the basis for the cryogenic AC loss calculations. A UNK collared coil was bent in a fixture (radius of 50 m) and successfully tested at 4K. The magnet did not show any performance degradation as far as critical current or field quality is concerned [10]. We will investigate a curved 8m long dipole with 4.5T and reduced aperture as a possible alternative for the SIS 300 main dipole.

Super-FRS / CR

The decision was made that the first 3 dipole, 3 quadrupole and 2 sextupole magnets in the high radiation area downstream of the Super-FRS target will be resistive with a special mineral-insulated conductor [11]. The remaining dipoles of the Super-FRS and the CR will be (almost) identical (superferric, H- type, warm iron, straight, laminated). Magnetic field calculations are finished. A conceptual design of the cryostat exists [12]. A contract with the FAIR-China-Group was signed for the further design and construction of a prototype to be delivered by March 2008.

The quadrupoles (with embedded octupoles) and sextupoles of the Super-FRS form a multiplett. Toshiba started a conceptual design study for such a multiplett. The same quadrupole and sextupole can be used in the CR ring.

NESR / RESR

Design work has started at GSI for a superferric version of the NESR / RESR dipole. In contrary to the DC-operated CR dipole this magnet is ramped at 1 T/s. Therefore a low inductance high current option with the Nuclo-

tron conductor was chosen. The cryostat must intercept the induced circumferential current.

Quench detection and protection

A protection scheme (dumping the current) was established for SIS100, SIS300, the CR ring, the Super FRS and the HEBT. The general quench detection scheme was also defined for these machines.

Test Facility for model and prototype magnets

The test facility has been described earlier [13]. The status is as follows: Refrigerator, distribution box, feed boxes and universal cryostat are commissioned. Power supply, quench protection and detection system are ready for the first tests of magnet GSI001 and a modified Nuclotron type dipole.
For magnetic measurement the so-called 'warm finger' is ordered. The drawing set for the mole was completed and the order prepared. The development of a 'stretched wire' continues.

Cryogenics

During the last year the list of consumers and their cryogenic needs was refreshed [14]. Now the experiments are mainly included into the main distribution system of FAIR. For the main consumers as SIS100, SIS300 and HEBT the cooling scheme and the local distribution system were concretized by flow schemes and distribution box designs [15]. For the warm bore, warm iron H-type superferric magnets –as required for CR and Super-FRS- alternative cooling schemes were discussed to lower costs and increasing the availability.

A more detailed version of the helium distribution system for FAIR was prepared and the integration into the buildings was started. The idea of having two independent cryogenic plants in different buildings, which share a common compressor station, was settled. During a cryogenic technical advisory committee meeting the critical components were identified and the requirements for the refrigeration power adjusted.

References

[1] New Results on Minimizing AC Power Losses in a Fast Cycling 2T Superferric Dipole with a Cold Yoke, Alexander Kovalenko et al., Proceedings of MT19, Genova, Italy, Sep. 2005

[2] 3D Transient Process Calculations For Fast Cycling Superferric Accelerator Magnets, Egbert Fischer et al., Proceedings of MT19, Genova, Italy, Sep. 2005

[3] Simulation of Eddy-Current Losses in a Fast Ramped Superconductive Dipole Magnet, S. Koch et al., Proceedings of MT19, Genova, Italy, Sep. 2005

[4] A Detailed Mechanical and Thermal Evaluation of the Hollow Cable Conductor for the Fast Cyclic SIS 100 Synchrotron, E. Bobrov et al., Proceedings of MT19, Genova, Italy, Sep. 2005

[5] EU FP6 Design study DIRAC- secondary-beam, task 22, D52: Design report on structural analysis, P. Schmidt et al., Accel, Bergisch Gladbach, 30.11.2005

[6] Development and test of a miniature novel Cable-In-Conduit-Conductor for use in fast ramping accelerators with superconducting magnets, V.E. Sytnikov et al., Proceedings of MT19, Genova, Italy, Sep. 2005

[7] Design of a Superferric Quadrupole Magnet with a High Field Gradient, Alexander Kalimov et al., Proceedings of MT19, Genova, Italy, Sep. 2005

[8] RECENT TEST RESULTS OF THE FAST-PULSED 4 T COSΘ DIPOLE GSI 001, Gebhard Moritz et al., Proceedings of PAC2005, Knoxville, Tennesee, USA, May 2005

[9] Optimization of a Dipole with Partially Keystoned Cable for the SIS 300, I. Bogdanov et al., Proceedings of MT19, Genova, Italy, Sep. 2005

[10]Tests of Straight and Bent Superconducting Dipoles, S.S. Kozub et al., Proceedings of MT19, Genova, Italy, Sep. 2005

[11] Radiation Resistant Quadrupole Magnet for the Super-FRS at FAIR, M. Winkler et al., Proceedings of MT19, Genova, Italy, Sep. 2005

[12] Conceptual design of cryostat for the superconducting CR dipole magnet, Q. Wang et al., Proceedings of MT19, Genova, Italy, Sep. 2005

[13] A test facility for fast-ramped superconducting magnets for FAIR, Gertrud Walter, Internal Note Nov. 2005, MT-INT-GW-2005-001

[14] M. Kauschke, C. H. Schroeder, H. Quack, 'FAIR Cryogenics- New Tasks on the Cryogenic System for the new Research Facility at GSI', CEC 2005, Keystone, USA, in press

[15] Y. Xiang, M. Kauschke, C. Schroeder, G. Moritz, A. Kutzschbach, H. Quack, 'Cryogenic Distribution for Beam Transfer Lines, Radioactive Secondary Beam Fragment Separator and Storage Ring of FAIR', CEC 2005, Keystone, USA, in press

SIS100/300 Acceleration

H. G. Koenig, K. Kaspar, GSI, Darmstadt, Germany

A short overview on two different RF systems is presented which were analysed as possible candidates for the SIS100/300 accelerating systems. More details about the RF systems are contained in [1] and the documents cited in [1].

Introduction

In the scope of the FAIR project, various types of accelerating and beam manipulation units for several synchrotrons have to be developed. For the SIS100/300 synchrotrons an accelerating system based on ferrite loaded cavities was chosen. Costs and power consumption aspects were the reasons to reject the alternative MA (magnetic alloy) concepts. In 2005 two different solutions for the cavities were under investigations. The first one is the well proven SIS18 cavity – the second can be found in the design study [2] presented by the Budker Institute of Nuclear Physics (BINP). This collaboration will continue with a detailed planning of a prototype.

Accelerating cavities

The existing SIS18 cavities - multiplied to the number needed for the desired voltage of 400kV for h=10 are the basis for this solution. It was verified that this cavity type is able to deliver 20kV peak in the desired frequency range with minor modification. The frequency tuning factor required in SIS100 (and SIS300) is by a factor of 2.5 lower than in the SIS18, so the threshold of the critical high-loss-effect is controllable [3]. One SIS18 cavity consists of two coaxial quarter-wave resonators, working in push-pull mode onto a common accelerating gap. The two quarter-wave sections are filled with ferrite material FXC8C12m made by Philips/Ferroxcube.

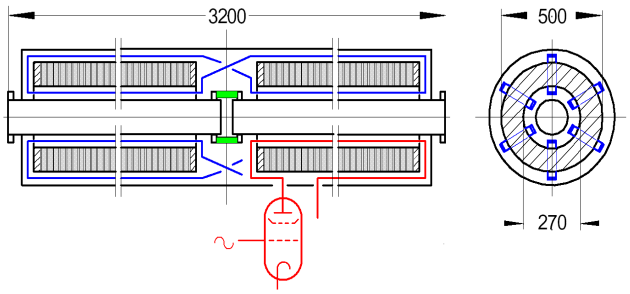


Figure 1: Sketch of SIS18 ferrite loaded cavity [3]

The resonant frequency of the cavity is controlled by DC bias magnetisation of the ferrite material. Six figure-of-eight bias windings with DC currents up to 200 A are used for this purpose. With closer adaptation of the ferrite material to the SIS100 frequency tuning requirements, further optimization of the maximum cavity voltage and an improved amplifier design, a slight reduction of the cavity length is possible but has to be investigated in more detail.

BINP-Solution

The proposed cavity of BINP is loaded with a Russian type of ferrite (400NN-2, Magneton St. Petersburg) and is water-cooled indirectly. Both halves are loosely coupled and biased with 30 A using encapsulated windings.

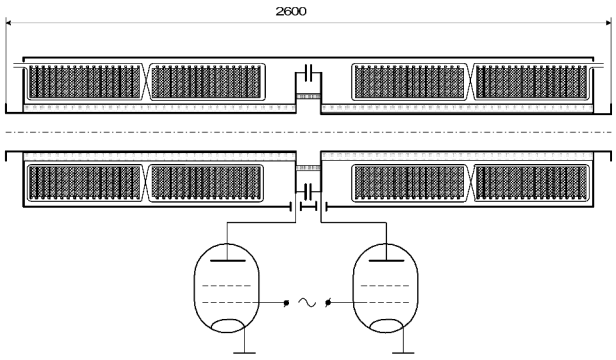


Figure 2: Cavity from BINP design study [2]

The RF power amplifier suggested by the BINP is a push-pull-arrangement running in class AB. The doubled number of power tubes proposed here may also mean an increased reliability risk, however. The single-ended SIS18 amplifier seems to be sufficient but the overall impedance has to be taken into account.

Outlook

The next step will be the detailed planning of a prototype that combines the advantages of the two systems described above. Using the SIS100 cavities for the SIS300 accelerating system is cost efficient. Both accelerating systems are identical in construction and placed in a framework on top of each other. A modular concept with an optimized multi-shift-usage for the cavity, power amplifier, filters and monitoring devices is an effective step to cost reduction. The accelerating system may be used for other FAIR rings as well.

References

[1] H.G.Koenig: "Technical Concept SIS100/300 Acceleration" – Version0V98; GSI internal Document

[2] G.Ya.Kurkin, V.N.Osipov, V.M.Petrov et al.: "Design Study of RF System for SIS100 Accelerating Facility"; Final Report

[3] K.Kaspar, H.G.Koenig, T.Winnefeld: "Studies on maximum RF Voltages in Ferrite tuned Accelerating Cavities"; EPAC2004

Bunch Compressor System for the SIS 12/18 upgrade

P. Hülsmann, R. Balß, W. Vinzenz, G. Hutter, J. Mohr, R. Scholz

1. Bunch Compressor Cavity

After realizing the design concept and finishing the construction phase, the assembly of the cavity and the built up for the whole test facility in the workshop are the next steps. Figure 1 shows the status of assembly of the new compressor cavity filled with 2x10 magnetic alloy ring cores [1].
The cavity should provide 40 kV gap voltage at an operating frequency of 0,8 and 1,2 MHz (harmonic number h=1). System challenges are for instance the very short rise time (≤ 10µs) of RF voltage and thus the development of a very fast MOSFET switch for shortening the gap during acceleration (switching time ≤ 10µs).



Fig. 1: compressor cavity assembly (not finished)

2. Final RF-power amplifier

The 600 kW RF-power amplifier feeds the cavity in push-pull mode using two Siemens RS 2054 tubes.
(tube working point 24kV; 28A)
Fortunately the low pulse duration (≤ 500µs) leads to a relatively low average power of 0,3 kW which is easy handle.



Fig. 2: final RF-power amplifier

3. Supply unit

The supply unit contains the supply sub-devices like anode-, screen grid-, control grid-, and filamentation-supply. Plug in modules for controls like amplitude- and phase control, the bunch compressor interface, the pre-amplifier and the PLC (programmable logic control) are also located here.



Fig. 3: Supply unit for the bunch compressor system

4. Low Level RF control

A DSP system, which can be used in different closed-loop control applications has been developed by the RF-Group. Among other things this system is able to synchronize two or more cavities, if they are running at the same frequency [2].

5. Outlook

The bunch compressor components and the whole system will be tested thoroughly. After successful lab tests and optimizations the cavity will be installed in the SIS18 tunnel.
In the future a second cavity-system is planned to reduce the bunch length further by increasing the overall voltage to 80 kV. But it will not be realized before the first system is running properly.

References

[1] P. Hülsmann, W. Vinzenz, G. Hutter: "The bunch compressor system for SIS18 at GSI", EPAC 2004 proceedings.

[2] H. Klingbeil: "Technical Concept Cavity Synchronization", Rev. 0.91, 24.08.2005.

Pick-Up and Kicker Electrodes for Stochastic Cooling at FAIR

C. Peschke, F. Nolden, GSI, Darmstadt, Germany

The main task of the collector ring (CR) is stochastic cooling of rare isotope beams (RIBs, $\beta = 0.83$) and antiprotons ($\bar{p}$, $\beta = 0.97$). Figure 1 shows the location of the stochastic cooling installations within the CR. The system consists of three pick-ups (P1-P3) at zero dispersion, a pick-up at high dispersion (PP), and three kickers (K1-K3) at zero dispersion. All systems will work in the frequency band 1-2 GHz. An upgrade to 2-4 GHz is foreseen.

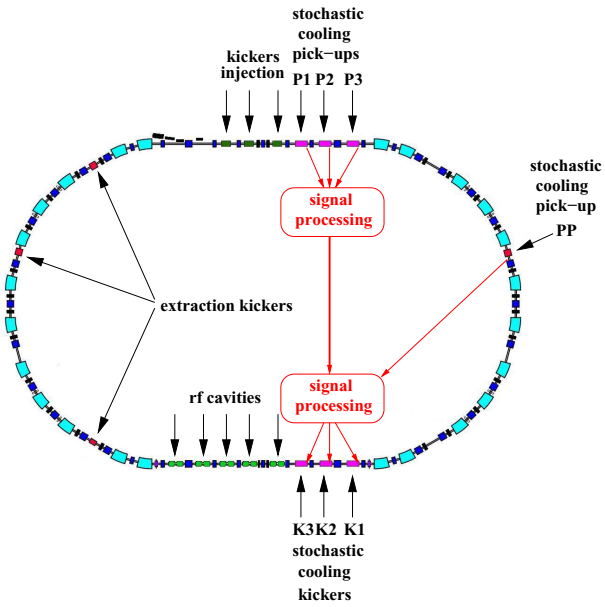


Figure 1: Schematic layout of the CR with installations.

Table 1 lists the signal paths for the different species and phases of the cooling process. For RIBs in the first phase, directly after debunching, only the Palmer pick-up PP is used. The pick-ups P1-P3 cannot be used due to the large undesired mixing.

from	to	antiprotons	rare isotopes (phase)
P1	K3	longitudinal	longitudinal (final)
P2	K2	vertical	vertical (final)
P3	K1	horizontal	horizontal (final)
PP	K1	-	horizontal (first)
PP	K2	-	longitudinal (first)
PP	K3	-	vertical (first)

Table 1: Stochastic cooling signal paths.

The pick-ups must have a large bandwidth and a high signal to noise ratio in spite of their large aperture of $120 \cdot 120\ \mathrm{mm}^2$. New planar slotline electrodes have been developed [1] to meet these requirements. The electrodes consist mainly of an alumina printed circuit board (Figure 2, top). The rear side is completely metallized, except for the slots (dashed in Figure 2). The mirror currents of the beam induce traveling waves in both directions of the slotlines. At a $\lambda/4$ distance from the end of the slotline, the signal is coupled out to the microstrip line on the front side. The signals from eight slots will be combined with proper phase relation with fixed delay lines on the combiner board. The modules will be cryogenically cooled and movable to lower the noise and to get enough signal at the final phase of the cooling. Each tank contains eight pairs of such modules. Their signals will be combined with switchable delays to correct the two different particle velocities.

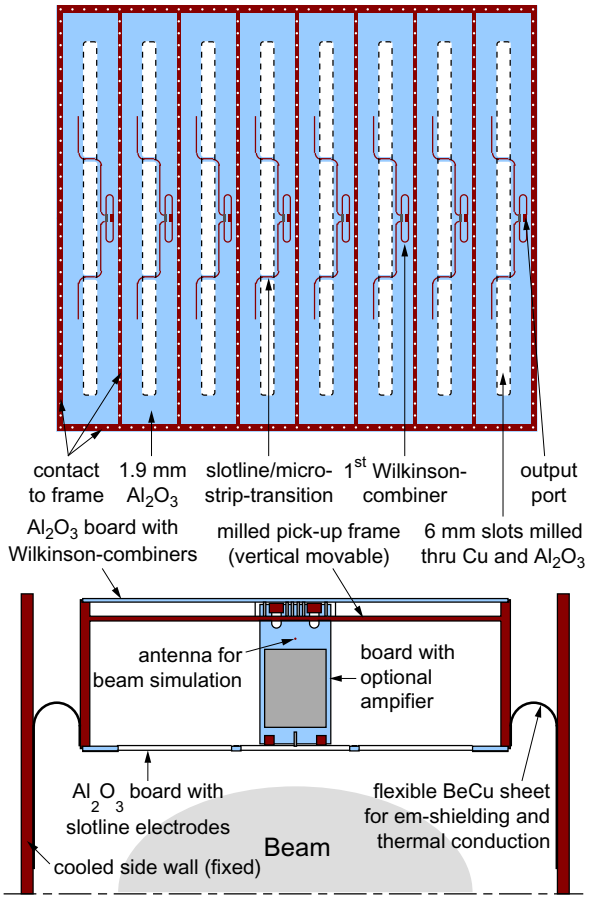


Figure 2: Current layout of a pick-up module.

References

[1] C. Peschke, F. Nolden, L. Thorndahl: "Pick-Up and Kicker Electrodes for the CR"; Conference COOL 05, Galena, Illinois, USA.

Study of Secondary Rare Isotopes Stochastic Cooling for CR Project

I. Nesmiyan, F. Nolden, GSI, Darmstadt, Germany

The CR stochastic cooling system [1] is required to cool secondary rare isotopes from $\varepsilon_{x,y}$=200 mm mrad to 0.5 mm mrad at 740 MeV/u in both transverse planes and longitudinally from δp/p=0.4% to 0.05%.

We investigated the stochastic cooling process of secondary rare isotopes at the CR storage ring with respect to cooling times and requirements on the system layout and electrical power. In particular, the effect of Schottky band overlap on longitudinal heating was studied.

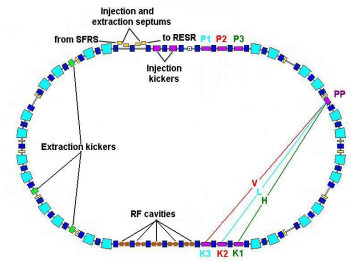


Fig.1. Layout of the CR with Palmer pick-up (PP).

In order to minimize the effect of undesired mixing caused by the low energy and the large initial momentum spread, the Palmer pick-up PP in the CR ring must be used to extract both a momentum cooling signal and a horizontal cooling signal, which cannot be disentangled electronically as they overlap in the frequency domain. This effect of band overlap can decrease the cooling performance, because Schottky noise always leads to heating. Fig. 2a shows as a function of frequency the limiting momentum width for overlapping longitudinal bands with each other and for overlapping longitudinal bands with horizontal bands.

Special slot-line couplers [2, 3] have been designed for the CR Palmer pick-up. As a function of the vertical coordinate *y*, their sensitivity is lowest in the middle of the vacuum chamber, i.e. for particles which do not perform any vertical betatron oscillations. In the simulations discussed below we have assumed an average vertical position *y*.

Palmer cooling of rare isotopes has been simulated based on a Fokker-Planck approach with parameters listed in Table 1.

Table 1: Parameter set used in the calculations

Cooling band, [GHz]	1-2
Number of electrode pairs	64
Electrode characteristic impedance, [Ω]	100
Average electrical power, [W]	350
Palmer pick-up effective noise temperature, [K]	80
Palmer kicker maximal sensitivity	0.7
Palmer pick-up maximal sensitivity	0.3

The evolution of the 1σ momentum width for a $^{238}U^{92+}$ beam with 10^7 particles is shown in Fig. 2b. The simulations are shown for two limiting cases:

1. No horizontal noise at all (horizontal cooling before longitudinal cooling)
2. Maximum horizontal noise all over the cooling process (no horizontal cooling)

The results show that according to Fig. 2b. the cooling time of 1 second and required equilibrium momentum width can be reached as soon as horizontal cooling decreases the Schottky power from the horizontal bands simultaneously. The strong influence from the overlapping horizontal bands is clearly visible. One should note that the calculations were performed under the pessimistic assumption that no electrode plunging is applied. As expected the cooling performance is worst for zero vertical position (*y*). This can be overcome by vertical plunging.

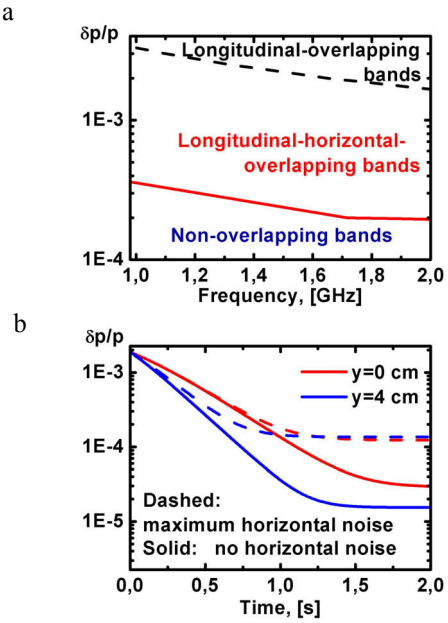


Figure 2 a) The lower limit of overlapping bands as a function of frequency and momentum width; b) Evolution of the momentum width for different vertical positions.

References

[1] B. Franzke, et al., Fast cooling of antiproton and radioactive ion beams in future storage rings at GSI, *Nucl. Inst. Meth*. A, 532 (2004), 97-104.

[2] F. Nolden, et al., Stochastic Cooling Electrode for a Wide Velocity Range in the CR, Proc. *PAC'05* (2005), 779-801.

[3] C. Peschke, et al., Pick-up and Kicker Electrodes for Stochastic Cooling at FAIR, this report.

I.Nesmiyan@gsi.de

Stacking of 3 GeV Antiprotons with a Moving Barrier Bucket Method at the RESR

P. Beller, B. Franzke, T. Katayama, I. Nesmiyan, F. Nolden, M. Steck (GSI),
D. Möhl (CERN) and T. Kikuchi (Utsunomiya Univ.)

At FAIR 3 GeV antiprotons are to be accumulated in the RESR up to an intensity of 10^{11}. If the CR is equipped for full performance, every 5 s a batch of 10^8 antiprotons will be transferred to the RESR. The antiprotons are pre-cooled to a momentum spread of 0.1% and an emittance of 5 mm mrad. As an option, azimuthal separation of injected and stacked beams with barrier buckets was studied. The process was simulated for 1000 injections.

The movement of the barrier pulses proceeds as follows (Fig. 1). After injection one of the barrier pulses (P2) is adiabatically moved to P1 within 200 ms. The energy spread of the particles confined between the two pulses grows as the distance of the pulses shrinks. Eventually ΔE becomes so large that the particles overflow the barriers and move into the accumulation area. When P2 reaches P1, all injected particles have overflown into the accumulation area and the barrier pulses are turned off. Now the beam is coasting with two streams separated by ± 4 MeV which corresponds to a barrier bucket height of 3 kV. Then stochastic cooling is applied. After 5 s stochastic cooling is stopped and P1 and P2 are adiabatically turned on at the same azimuth. P2 moves to the original position. The barrier pulses compress the cooled/stacked beam into the accumulation area and the injection area is empty. A new batch is injected. This process will be repeated according to the cooling time in CR.

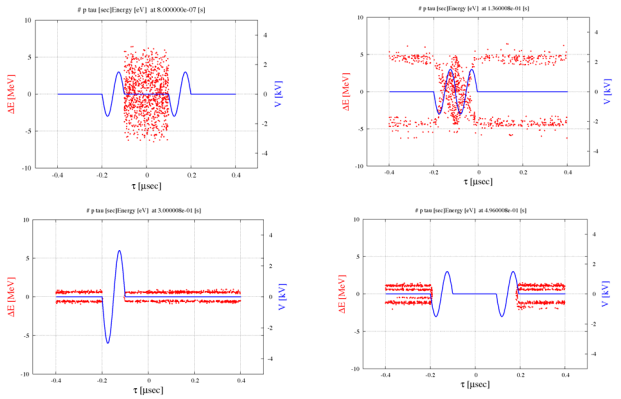


Figure 1: Barrier bucket injection and cooling. Blue curves represent the barrier voltage, red points represent the particle distribution. Top left to bottom right: beam injection, barrier pulses approaching each other, beam cooling, barrier pulses moved to their original position.

The principle of stochastic cooling and stacking of two coasting streams is similar to classical stacking. The two coasting beams are moved to the central core by the coherent term. Schottky noise from other particles and amplifier noise act as diffusion force and push the particles back to lower density regions. The coherent strength is adjusted to produce the maximal particle flux from the injection orbit to the central region. Within 5000 s up to 7.5×10^{10} antiprotons are accumulated in the stacking area within a momentum spread of less than $\pm\ 10^{-3}$.

Parameters of RESR and stacking system

Circumference	245.5 m
Revolution time	820 ns
Transition energy γ_τ	3.62
Slip factor η	0.020
BB Pulse voltage	± 3.0 kV
BB Pulse width	100 ns
Cooling system band width W	1.5 GHz
Voltage for injected batch ΔE_c	0.533 eV/turn
Voltage ratio injected batch/stack top	1.01×10^3

In Fig. 3 distributions calculated for these parameters are shown as a function of time. As explained before, the movement of barrier buckets produces two streams of coasting beam in the RESR.

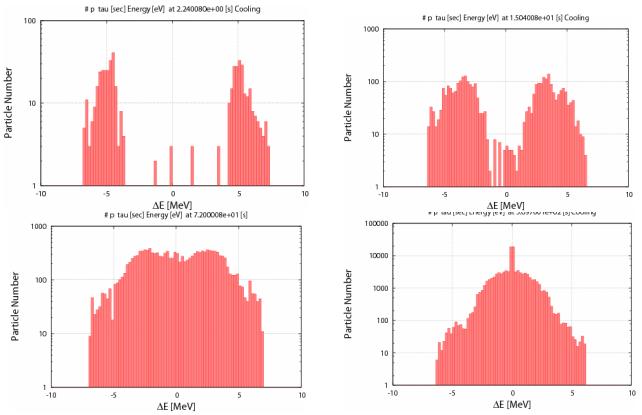


Figure 3: Spectrum of the stacked beam. Plots from top left to bottom right: distribution function after 22 s, 150 s, 720 s and 5000 s. The particle number is in units of 10^6.

The figure reveals the high density core produced in the central region during 1000 injections. The sharp peak in the central region is due to the antisymmetric gain function of the pickup with non zero value at the origin. However, in the real stacking process such a high-density peak will be smeared out due to the strong heating by intra-beam scattering. The number of antiprotons in the central core region defined by $|\Delta p/p| < 10^{-3}$ is 7.5×10^{10}.

References

[1] B. Franzke et al., NIM A 532, 97 (2004).
[2] S. van der Meer, CERN/PS/AA/78-22, 1978.
[3] Fermilab recycler ring TDR, FNAL Nov. 1996.
[4] J. Griffin et al., IEEE Trans. Nucl. Sci. 30, 3502 (1983).
[5] S. Y. Lee et al., Phys. Rev. E 55, 5992 (1998).

Beam Position Monitor System Development for FAIR*

A. Peters, A. Galatis, W. Kaufmann, P. Kowina, K. Lang, J. Schölles, GSI, Darmstadt, Germany

Abstract

The first steps of research and design made for the BPM (beam position monitor) system for the FAIR project, with partly use for the SIS-18 upgrade, will be described. It includes the evaluation software parts as well as the hardware part for the direct digitization of the position pick-up signals and, in addition, the first design steps for the cryogenic detector itself.

Design of the BPM detector using Finite Element Methods

There are a lot of requirements in the design of the BPM detector for the FAIR project, the most important are listed here:

- The BPM hast to fit in the cryogenic modules planned e.g. for SIS100, see Fig. 1 as an example for the straight section.
- The shape of the BPM should be elliptical as the beam pipe for impedance matching.
- The materials have to be compliant to the UHV and cryogenic requirements of the machine.
- The target value for the resolution of the BPM is 0.1mm, therefore the mechanical stability should be better than 50µm (because of additional error terms coming from thee electronics and data evaluation, see below).

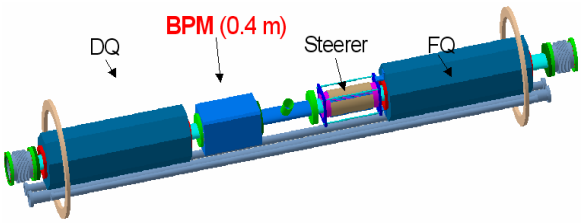


Figure 1: Layout of a cryogenic module for the straight section of SIS100 in the FAIR project

Based on studies done for the "shoe-box type" BPM used in the synchrotron of the HICAT facility [1] the cross- talk between the plates in one plane was investigated, which should be as low as possible. The different geometrical configurations and the calculated values are shown here:

	Metal coated Ceramics	Metal plates
No guard ring, 1mm gap	-5.1 dB	-7.9 dB
No guard ring, 2mm gap	-8.1 dB	-10.8 dB
With guard ring	-20.8 dB	-22.5 dB

*Work supported by the European Community-Research Infrastructure Action under the FP6 "Structuring the European Research Area" programme (DIRACsecondary-Beams, contract number 515873).

From these results one would deduce that a design based on metal plates containing a guard ring would be the best solution, but the mechanical stability would be a big problem due to the amount of parts, which have to be aligned within 50µm under cryogenic conditions. Therefore the other solution based on metal coated ceramics tubes will be investigated, a first sketch can be seen in Fig. 2.

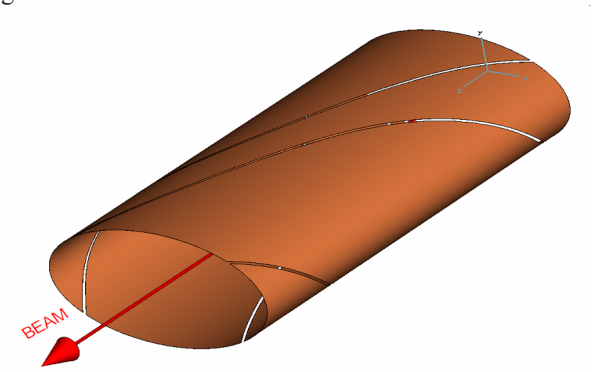


Figure 2: First layout of a BPM pick-up for SIS100

As the simulation tool "CST Microwave Studio" (CST-MW, version 5) is used, all calculations are performed using the transient solver. The work is on-going in 2006.

Digitisation of BPM signals and evaluation

Software

After the signal is treated by a high-performance amplifier chain for best possible utilization of the 14 bit ADC's, it will be digitized according to the Nyquist criteria with a minimum of 125MSa/s. This speed is needed for taking enough samples of very short bunches in the order of some tens of ns [2]. The hardware platform for digital signal evaluation and treatment should realize different working modes. It should combine a digitizer, capable of storing full acceleration cycles on board, transferring the data onto a central data storage device. In addition, it should be able to extract position measurements from the raw ADC data. The position information is then stored either direct on the device or on a central storage unit. It is also thought of to display the position data directly for visual evaluation of the accelerator setup. A fast feedback mode of operation is also planned, using the position information calculated to produce beam orbit correction signals.

The target is to build a system, which will track online beam position changes in the order of 0.1mm. Since the position has to be calculated online and the designated hardware runs at about the same clock frequency as the

ADCs efficient algorithms have to be designed to introduce a minimum in computational load as well as a minimum in delay.

In 2005, first software algorithms were developed which worked with no interaction from external parameters, e.g. the RF frequency. The simulation of these methods verified the assumption that free running methods could be utilised and used for the project. First results and methods where introduced at the DIPAC 05 [3]. Other algorithms were developed later that year, resulting in a preliminary system for offline evaluation, which can track changes in position in the order of 0.15mm.

Methods implemented concentrate more on the problem of the S/N ratio of the pick-up signal at the beginning of acceleration. In this region methods for suppressing noise and optimizing the bunch detection scheme. For the suppression, averaging techniques by means of mean/median filters were tested and evaluated. A fundamental point which is being investigated is the baseline restitution, which is needed to simplify the beam position calculation done through numerical integration.

Hardware

For evaluation of the hardware part, we use a *Libera* Beam Position Monitor from Instrumentation Technologies [4]. This device has the required components needed to digitize, filter and store the amplified pick-up signals.

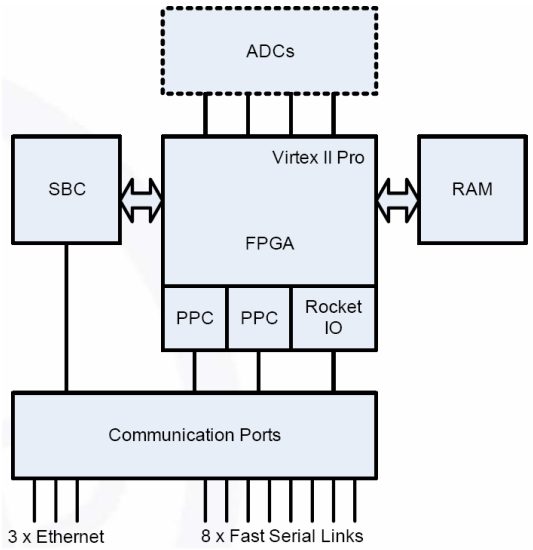


Figure 3: Scheme of the *Libera* hardware layout

The analogue board of the *Libera* (see Fig. 4) provides four fast 14 Bit ADCs for signal sampling, with the needed frequency. These ADCs bring the data to a Xilinx Virtex II Pro FPGA, which takes the control over a 256MB DDR2-RAM to use it as data storage.

As controller for the Libera a Single Board Computer (SBC) is used, which runs with an embedded Linux operating system. The SBC also establishes the connection to the outside world via Fast Ethernet.

The firmware for the Virtex II Pro from Instrumentation Technologies provides the necessary interfaces to get the data from the ADCs, to read and write the data to the DDR2-RAM and to send it to the control-system via the SBC. Between these interfaces, we have thereby the possibilities to integrate our filter-algorithm and can switch the data flows as we need them in the different operating modes (see Fig. 3)



Figure 4: Prototype of the *Libera* hadron beam version

Through several I/Os of the FPGA, we can synchronize our measurements with the machine- and system-clock and can receive events for triggering.

For the next steps, we started to implement our developed filter-algorithms in VHDL to test them under real conditions. Tests with beam signals from the existing SIS18 BPM pick-ups will start in 2006.

Acknowledgements

Many thanks also to all collaborators at CERN, Instrumentation Technologies, FZ Jülich and TU Darmstadt.

References

[1] P. Kowina, W. Kaufmann, J. Schölles and M. Schwickert, „Optimisation of ”shoe-box type” beam position monitors using the finite element methods”, Proc. of DIPAC 05, p. 114

[2] FAIR Beam Parameter List

[3] A. Galatis, A. Peters, et al "Digital Beam Position Measurement at GSI-SIS and CERN-PS ", Proc. of DIPAC '05, p.184

[4] www.i-tech.si

BIF Monitor and RGM System Development for FAIR*

P. Forck, C. Andre, F. Becker C. Dorn, , T. Giacomini, H. Graf, T. Hoffmann,
F. Peldzinski, A. Peters, H. Reeg, , GSI, Darmstadt, Germany
D. Lyakin, V. Skachkov, ITEP, Moscow, Russia

Beam Induced Fluorescence Monitor

Due to the high beam power expected for FAIR, novel methods for non-intersecting beam diagnostics for the High Energy Beam Transport Lines must be considered. We investigate the detection of fluorescence photons from the excited states of the residual gas N_2 with a **B**eam **I**nduced **F**luorescence (**BIF**) Monitor [1]. This method was successfully applied for high current measurements at UNILAC [2]. Photons in the wavelength range 390 nm < λ < 470 nm are generated by transitions in N_2^+ with about 60 ns lifetime [3]. 'Single-photon counting' is performed with an image intensifier [4], equipped with a double MCP for 10^6-fold photo-electron amplification. The light from the fast P46 phosphor screen with 300 ns decay time is taper-coupled to a digital CCD camera with a FireWire interface (Basler 311f).

The setup was installed behind SIS close to the beam dump HTP and tested with different ions (Xe, Ta, U) and varying energies (from 60 to 750 MeV/u) for fast and slow extraction. An example of such a measurement is shown in Fig. 1: The spots within the area of the vacuum window are created by single optical photons, their projection along the beam axis yield the horizontal profile. The correspondence to a SEM-Grid measurement proves the applicability. But the BIF method offers a higher spatial resolution (here 300 µm/pixel), which can be matched easily to other requirements by the choice of an appropriated lens/taper system, e.g. In addition, a BIF Monitor can be realized within a short insertion length.

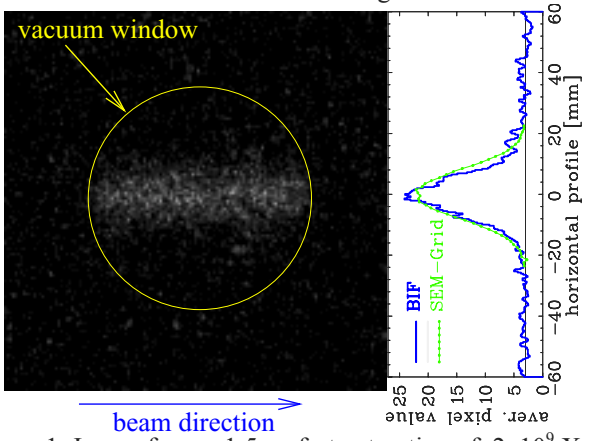


Figure 1: Image from a 1.5 µs fast extraction of $2x10^9$ Xe 48+ at 200 MeV/u and the projected horizontal profile compared to a SEM-Grid. The BIF data were recorded at $1x10^{-3}$ mbar and averaged over 20 shots.

The critical demand for a BIF Monitor is the amount of background caused by neutrons hitting the photo-cathode (Na2KSb)Cs of the image intensifier. It leads to a uniform distribution even outside of the optical path, as shown in Fig. 1. The background is larger than for UNILAC beam parameters due to the energy-dependence of neutron production and the location close to the dump. For the U73+ beam with 5 energy steps between 60 and 550 MeV/u noise increases by a factor of ~30. For fast extraction, a background decay time of 1.6(4) ms was determined by gating the photo-cathode of the image intensifier and independently by a plastic scintillator system. This long decay time can be understood qualitatively by the neutron moderation inside the beam dump and the surrounding concrete walls [5]. With an appropriate short gating of the image amplifier during the 1 µs beam delivery, this background can be reduced.

For sufficient signal strength on a single shot basis, a relatively large pressure bump of typically 10^{-3} mbar was required for the investigated beam currents. These currents are two to three orders of magnitude lower than expected for FAIR. To legitimate the necessary extrapolation for FAIR, the vacuum pressure was varied over 3 orders of magnitude to larger pressures. Fig. 2 confirms the pressure independence of the determined profile-width σ and the linearity of the total signal strength. This proves that the fluorescence is dominated by the above-mentioned N_2^+ transitions.

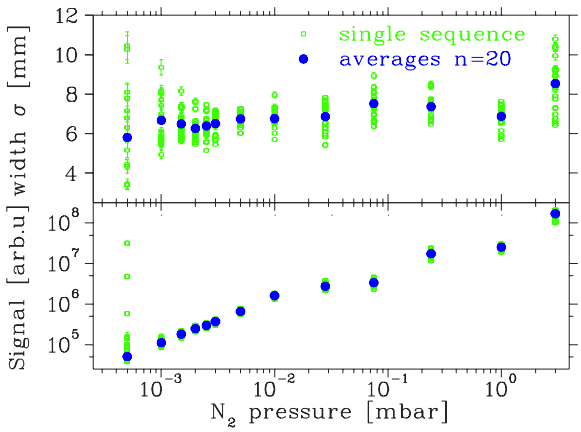


Figure 2: The horizontal profile width and the total signal strength as a function of vacuum pressure, determined by the BIF Monitor with the beam parameters of Fig. 1

The described and further systematic investigations [6] demonstrate the general applicability of BIF for the FAIR in fast and slow extraction mode. In particular for the final-focus adjustments at the S-FRS, anti-proton or Plasma-Physics targets. A local vacuum bump might still be necessary, but is probably tolerable close to these tar-

*R&D efforts supported by INTAS project Ref. No. 03-54-393, the technical realization is funded by the EU FP6 FAIR construction programme (EU CNI contract "DIRAC-PHASE-1", contract number 515876).

gets. A careful shielding of the image intensifier against neutrons is required. To enlarge the distance to the beam pipe, a commercially available 'Fibre Optics Image Bundle' might be a solution.

Residual Gas Monitor System for SIS100/300

The present Residual Gas Profile Monitor (RGM) in the SIS 18 is used up to now for several machine experiments like emittance exchange, tune resonance crossing and electron cooling [7]. The resolution limitations in time and space especially at high currents due to space-charge effects and the demands of the SIS100/300 made the development of a advanced RGM [8] necessary. The experiences with the RGM-SIS18 lead to several improvements in the different modules of the new device. It will provide two different readout techniques, a fast readout mode on a turn-by-turn basis at 1mm and a high resolution mode with 100 Profiles/s at 0.1mm resolution. The currently used RGM operates with residual gas ion detection, while the new one will be able to detect either ions or electrons [9]. The project is split into several sub-tasks like the design of the E-field and B-field, calculation of particle dynamics, calibration of MCPs, optical readout with digital CCD camera, fast readout with photodiodes or photomultipliers, analog- and digital electronics, development of data acquisition and analysing software tools as well as the mechanical design. The different tasks are achieved in parallel by a collaboration of different teams at ITEP and MSU (Moscow), MSI (Stockholm), COSY (Jülich) and GSI (Darmstadt). The intermediate results were exchanged at several meetings. The ITEP team develop the fast optical readout and compares the advantages of photo-diodes and Photo-multipliers and the needed low noise analogue and DSP-based digital electronics [10]. The MSU team develop the compact magnetic field by comparing permanent and electrical window frame magnets. The work includes kick compensation, fine tuning and validation with particle dynamics calculations inside the simulated magnetic and electric fields [11]. The GSI team developed the very uniform electric field (1‰ non-uniformity) with CST EM Studio© software tools and verified it with CST Particle Tracking© software. A special MCP-Phosphor screen assembly (optical readout device) that fits best the needs of a rectangular image was developed, manufactured and tested. Several tests were performed to design an electron emitting wire module. It will be used to calibrate the MCPs by time and for secondary electron suppression to prevent of disturbed beam profiles [12]. The tests with the special optical readout device and the electron emitting wire were observed with a digital CCD camera. Several software modules were developed under LabView© for the camera readout. This code was permanently improved and adjusted to the needs of reliable image acquisition and profile analysis. The already performed tasks will be tested in a prototype installation at the COSY facility in summer 2006. The prototype will not be equipped with a magnetic field and will therefore detect residual gas ions. The high system integration of the prototype leads to a very compact device with an overall length of 60cm for the horizontal and vertical RGM in combination. The large inner aperture of 175x175 mm^2 enable the installation at different synchrotrons and storage rings. It is planned to move it at end of 2006 from COSY to the ESR at GSI.

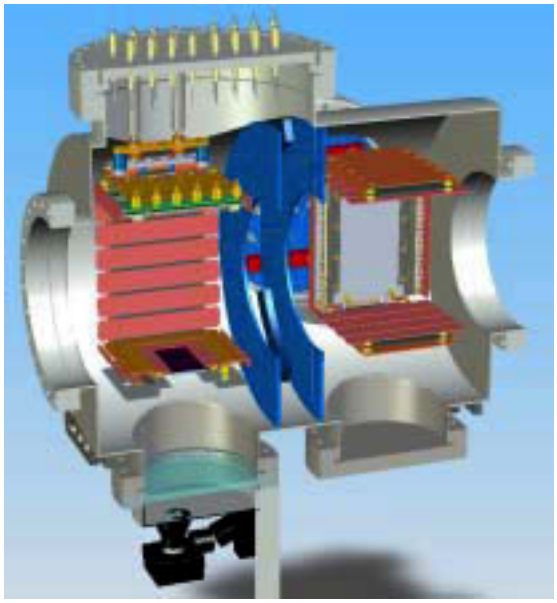


Figure 3: Set-up of the RGM prototype, completion planned for summer 2006

References

[1] P. Forck et al., Proc. DIPAC 2005, Lyon, p. 221 (2005).

[2] A. Bank, P. Forck, Proc. DIPAC 2003, Mainz, p. 137 (2003) and P. Forck et al., GSI Annual Report 2003, p. 217 (2003).

[3] R.H. Hughes et al., Phys. Rev. 123, 2084 (1961).

[4] www.proxitronic.de.

[5] H. Iwase, Phys. Rev. C 62, 044615 (2000)

[6] F. Becker, Diploma Thesis, Technische Universität Darmstadt (2006)

[7] G. Franchetti, T. Giacomini, M. Kirk, A. Parfenova, Resonance Induced Beam Loss in SIS18, GSI-Acc-Note-2005-12-001

[8] Andrea Franchi et al., Measurement of emittance exchange driven by betatron linear coupling in the SIS-18, GSI-Acc-Note-2006-02-001

[9] P.Forck, et al., Advanced Residual gas Profile Monitor for hig Current Synchrotrons and Cooler Rings, DIPAC03, Mainz

[10] T. Giacomini, P. Forck, D. Liakin, V. Skachkov, Development Of A Residual Gas Profile Monitor With High Resolution And Fast Readout, BIW04, Knoxville

[11] D.Liakin, Vl. Skachkov, et al., Current Status Of The Advanced Residual gas Monitor For Heavy Ion Synchrotron Applications, DIPAC05, Lyon

[12] T. Giacomini, et al., Improving The Reliability of IPM, DIPAC05, Lyon

Energy-Loss Dependence of the Ion-Induced Desorption Yield Measured with Ar^{10+} Ions at GSI-HHT

M. Bender, H. Kollmus, A. Krämer, GSI, Darmstadt, Germany
E. Mahner, CERN, Geneva, Switzerland
E. Hedlund, Uppsala University, Sweden

Introduction

In heavy ion synchrotrons like SIS 18 high energetic ions can impact on the beam pipe and release gas molecules. This so called "ion induced desorption" deteriorates the accelerator vacuum and, as a consequence, the beam life time and luminosity. Desorption yields η (released gas atoms or molecules per incident ion) of various materials have been studied at GSI since 2003. A scaling of the desorption yield with the electronic energy loss to the second power $(dE/dx)^2$ was found first for 1.4 MeV/u Pb^{27+}, Cr^{7+} and C^{2+} ions [1] and afterwards for U^{73+} ions (15-100 MeV/u) impacting on stainless steel, copper and aluminium targets [2]. In the energy regime investigated nuclear stopping can be neglected. In 2005, we studied the $(dE/dx)^2$ scaling of the desorption yield of argon on stainless steel (316LN, vacuum fired) at the same energies per nucleon as in [2]. The intension was to verify the observed scaling for a different projectile ion.

Experiment

The experimental setup was modified with the aim to achieve a lower base pressure. The stainless steel endflange itself represented the sample. The aperture of the pumping stages was increased and partially NEG coated. For beam alignment and diagnose a current transformer and a beam screen were added. The desorption yield η was calculated form the total pressure increase Δp using the ideal gas law,

$$\eta = \frac{\Delta p \cdot S}{\dot{N} \cdot k \cdot T}$$

where S is the pumping speed, $\dot{N}$ is the ion flux, k is the Boltzmann constant and T is the temperature. The total pressure was measured with an extractor ion gauge, a residual gas analyzer was not used. The base pressure after bakeout was in the low 10^{-10} mbar region.

Results and Discussion

The measurement parameters for Ar^{10+} ions, the pressure rise (Δp) and the corresponding yields (η) are summarized in Table 1. So far, we assume that the desorption yield is proportional to the squared electronic energy loss: $\eta = K \cdot (dE/dx)^2$. The 2005 desorption experiment with Ar ions confirms, within the given error bars, the previously measured scaling of η. The obtained measurement results for Ar ions are shown in Fig. 1 together with the calculated electronic energy loss using the SRIM code [3].

Table 1: Experimental Parameters

Energy [MeV]	**Flux [s^{-1}]**	**Δp [mbar]**	η
100	$1 \cdot 10^{10}$	$2.7 \cdot 10^{-11}$	3.6
80	$9 \cdot 10^{9}$	$3 \cdot 10^{-11}$	5.2
40	$7.5 \cdot 10^{9}$	$1.8 \cdot 10^{-10}$	47

The previously obtained results for U ions are also shown for comparison. The factor K is not identical for both experiments, probably due to the different experimental conditions (setup modification and different residual gas composition).

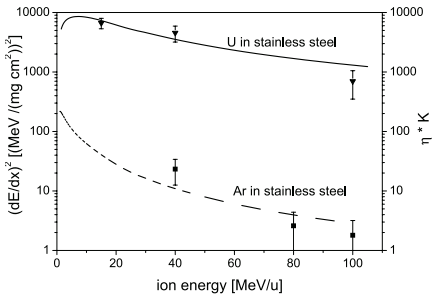


Figure 1: Electronic energy loss $(dE/dx)^2$ (lines) and measured desorption yield (points) for U and Ar ions impacting perpendicular onto a stainless steel target

Outlook

For a deeper understanding of the ion induced desorption process it is necessary to investigate the $(dE/dx)^2$ scaling in more detail for example using a dedicated setup and on "both sides" of the Bragg maximum. It would be also very interesting to measure the angular dependance of the desorption yield. Complementary to the study presented here, we presently perform material analysis with ERDA to investigate the material properties in correlation with the desorption yields [4].

We acknowledge the support of the GSI operating and the beam diagnostics group for delivering an excellent beam.

References

[1] H. Kollmus *et al.* AIP CP773 (2005), p. 207
[2] H. Kollmus *et al.* GSI Scientific Report (2004), p. 316
[3] SRIM 2003, http://www.SRIM.org
[4] H. Kollmus *et al.* GSI Scientific Report (2005)

UHV-ERDA Investigations on Ion Induced Desorption *

H. Kollmus and M. Bender, GSI, Darmstadt, Germany
W. Assmann, LMU, Munich, Germany
R. Dörner, University Frankfurt, Germany

Abstract

In heavy ion accelerators the beam line vacuum is effected by lost ions impinging on the beam pipe. Due to ion induced desorption gas is released from the walls into the vacuum. This vacuum degeneration effects the ion beam life time and is a serious luminosity limitation for a heavy ion synchrotron like SIS18. Here we report on a new approach to understand the physics of the ion induced desorption using ion beam analysis. The technique is briefly introduced and first results with a silicon target are presented, showing a clear correlation between the desorption yield and the material constitution.

Introduction

In 2003 an experimental program was started at GSI to measure desorption yields (desorbed particles per incident ion) in a dedicated test stand. Within this experiments, various materials and surface treatments have been investigated as well as a variety of beam parameters. One can observe a dependence of the desorption yield on the electronic energy loss of the projectile ion inside of the material [1].

In parallel to these phenomenological investigations an UHV-ERDA (**E**lastic **R**ecoil ion **D**etection **A**nalysis) setup was taken into operation 2005 in order to understand the effects of ion induced desorption in more detail. ERDA allows an element specific depth profiling of the first 1000 nm of a sample with a resolution of about 20 nm. This depth profiling can be carried out *in-situ* parallel to desorption yield measurements using the same ion beam.

UHV-ERDA Technique

ERDA is a well established ion beam analysis tool in material research and details are described elsewhere [2]. Uncommon is the need of an UHV environment during ion beam analysis. Here, this is necessary to be close to the application in the accelerator, where we have an average pressure in the lower 10^{-11} mbar range, to minimize readsorption of residual gas on the sample and to be sensitive to low desorption yields (low pressure rises). To our best knowledge there was only one UHV-ERDA apparatus existing at the LMU Munich in the group of W. Assmann. This UHV-ERDA apparatus was transfered to GSI and modified to meet our requirements. The essential parts of the UHV chamber, the radiation geometry and the pressure diagnostics are sketched in Fig. 1. In parallel to the ERDA measurements the desorption yield and the partial pressure distribution can be measured with an extractor gauge and a quadrupole mass analyzer (QMA). All data are acquired event-by-event in listmode format allowing a time resolved analysis.

All samples can be cleaned by a Xe-sputter gun in the lower part of the UHV chamber, see Fig. 1. The Xe-sputter gun can operate up to 8 keV total energy with an average flux of $1{\cdot}10^{13}$ ions s^{-1}. This sputter gun can be used to clean surface contaminations like an oxide layer effectively. Fig. 2 shows a typical ERDA spectrum of stainless steel bombarded with Xe^{18+} projectiles at 1.4 MeV/u: One can clearly see that stainless steel contains beside Cr, Fe and Ni also light components like C, N and O and intermediate components like Si.

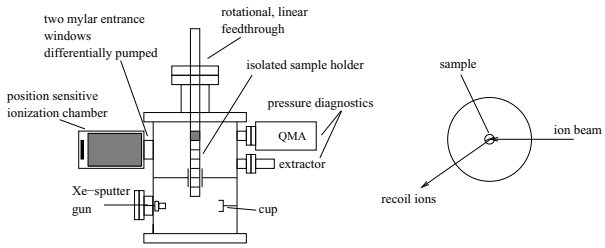


Figure 1: Schematic of the UHV setup and the scattering geometry.

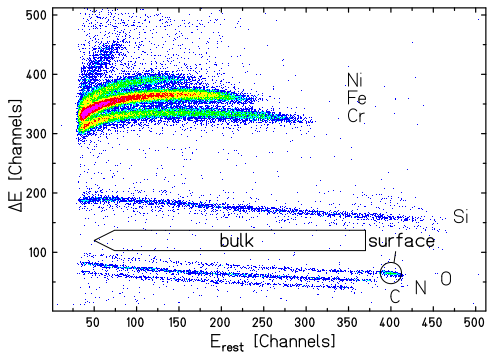


Figure 2: A typical ΔE - E_{rest} spectrum. Different elements are identified by their individual energy loss ΔE. The origin depth of the scattered target atom is given by the residual energy E_{rest}.

* We acknowledge the support of the European Community-Research Infrastructure Action under the FP6 "Structuring the European Research Area" program (DIRACsecondary-Beams, contract number 515873)

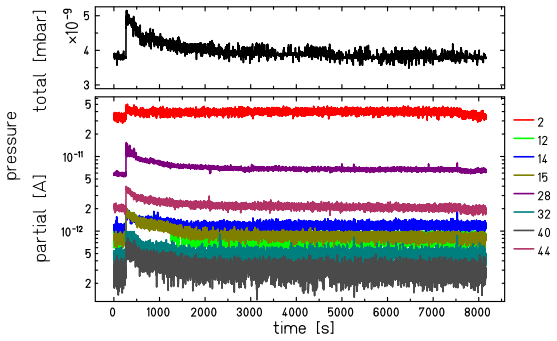


Figure 3: Desorption yield measurements of a Si wafer irradiated with 1.4 MeV/u Ca^{10+} ions. The upper black line shows the total pressure evolution (N_2 equivalent), the lower colored lines the ion currents from the QMA.

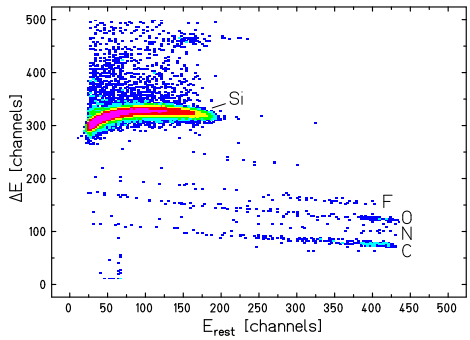


Figure 4: ΔE - E_{rest} spectrum for Si. The projectile ion was Ca^{10+} with 1.4 MeV/u impact energy.

Results from Silicon Samples

Silicium samples were already investigated in the desorption yield test stand [3] and have shown a quite low desorption yield of about 3 released particles per 1.4 MeV/u C^{2+} ion impact. The desorbed gases are dominantly H_2, CO and CO_2. It is well known that H is dissolved in nearly all materials, even in extremely pure Silicon wafers. Unclear, however was the origin of CO and CO_2. To understand this in detail ERDA measurements have been carried out in parallel to total and partial pressure measurements. Fig. 3 shows the total and partial pressure evolution for a Si wafer irradiated with 1.4 MeV/u Ca^{10+} projectiles with a time structure of 40 pulses per sec. and a pulse length of 5.5 ms. The number of ions per pulse is approximately $1{\cdot}10^8$. The beam spot is 20 mm^2. This corresponds to a flux of about $2{\cdot}10^{10}$ ions s^{-1} cm^{-2}. One can observe a total pressure increase of approx. $1{\cdot}10^{-9}$ mbar dominantly caused by H, CO and CO_2 desorption. In addition one can see, that this pressure increase is decaying as a function of the ion flux, sometimes called *beam scrubbing*. This cleaning or scrubbing can be observed for all gas components accept H, which is dissolved in the Si bulk and therefore represents a nearly "infinite" reservoir.

Parallel to the pressure measurements an ERD analysis of the target was performed and the result is shown in Fig.

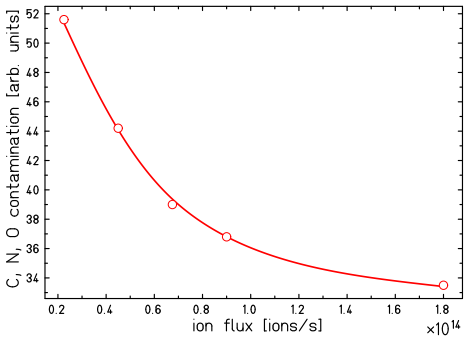


Figure 5: C, N and O content on Si as a function of the radiation dose.

4: In contrast to the stainless steel probe, the Si sample is quite "clean". Only few C, N, O and F contaminations are visible on the surface. Fig. 5 shows the evolution of the C, N and O contamination as a function of the ion flux. It is clearly visible that the surface contamination of C, N and O on the Si wafer is decreasing with the ion dose analogously to the pressure evolution shown in Fig. 3.

Discussion

Using the UHV-ERDA technique we have shown clear correlations between target properties and the corresponding ion induced desorption yield. The observed CO and CO_2 desorption from Si is caused by surface contamination. These contaminations are sputtered under ion beam bombardment leading to a cleaning of the target resulting in a decrease of the pressure rise down to the detection limit. Consequently, completely clean samples should show no desorption, except H and the sputtering of the target material itself.

Outlook

To verify the results further experiments have to be carried out, especially using materials which can be easily used in accelerators. Stainless steel is not suitable, since the C, N and O contaminations are not only on the surface but in the whole bulk, representing an "infinite" reservoir for desorption. A good candidate is Cu which can be produced in very high purity, comparable to Si. A disadvantage is the oxidation of Cu under atmosphere, which will again lead to a high desorption yield. In our ERDA setup this oxide layer can effectively be removed by the Xe-sputter gun, allowing a detailed study of the influence of the oxide layer on the Cu. In addition experiments will be performed with "terminated"Cu surfaces, e.g., by Au coatings.

References

[1] H. Kollmus et al., AIP CP773 (2005), p.207

[2] H.D. Mieskes et al., NIM B **146** (1998), p. 162

[3] H. Kollmus et al., GSI Scientifi c Report (2004), p. 316

Non Evaporable Film Getters Technology at GSI: First Results*

M.C. Bellachioma, J. Kurdal, and H. Reich-Sprenger

GSI, Darmstadt, Germany

Abstract

For the GSI future project FAIR an accelerator system with a base pressure of 10^{-12} mbar is required. The low pressure is needed to reduce the charge exchange rate between the accelerated ions and the residual gas molecules and to increase the ion beam lifetime.

Among the different measures undertaken to upgrade the existing UHV system, the installation of NEG coated dipole and quadrupole chambers is foreseen. For this purpose a license agreement for the non evaporable thin film getters was signed between GSI and CERN at the end of June 2005. A first magnetron sputtering system was designed and commissioned at GSI. The characterization of the first coated samples produced was performed by means of scanning electron microscopy and pumping speed measurements.

Experimental set-up and coating procedure

The experimental set-up, shown in Fig.1, consists of a vacuum pumping speed unit, a manifold, and a vertical solenoid. The vacuum pumping speed unit, driven by a rotary-turbomolecular pumping station, is equipped with a Kr injection line, a pumping by-pass, two wide range gauges, and a residual gas analyser (RGA). The electrical feedthrough for the cathode (made by intertwisted Ti, Zr and V wires-2mm diameter) is located on top of the manifold and it is fed by 1,5 kW dc power supply. The solenoid is 1,2 m long has a 350 mm internal diameter and provides a maximum magnetic field of about 200 Gauss. A 1 micron thick film is obtained by applying a cathode current of 100 mA, a discharge voltage of 500 V at a Kr pressure of about 10^{-2} mbar, and a magnetic field of 130 Gauss. The coating procedure foresees to bake the system over night at around 200°C and to maintain the chamber at 100°C during coating.

Thin film characterization results

To ascertain the quality of the thin film a 25x20 mm stainless steel sample is coated together with each chamber, and used to analyse the film morphology and thickness by means of the scanning electron microscopy. A very smooth film surface was observed for all produced samples. In addition, the performances of the thin films are characterised by measuring (by means of a standard Fischer-Mommsen dome [1]) the pumping speed. After the bakeout the sample is progressively heated at 200°C, 250°C, and 300°C for about 4 hours, without intermediate air venting. After each heating step the sample is cooled to room temperature and CO pumping speed measurements and saturation (see Fig. 2) are carried out.

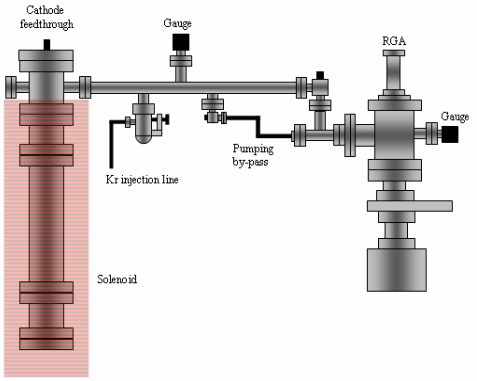


Figure 1: Schematic drawing of the experimental set-up.

Conclusions and outlook

The pumping speed (between 5 and 7 l s^{-1} cm^{-2}) and saturation (around 10^{15} molecules cm^{-2}) values obtained in our investigation are in complete agreement with those measured at Cern[2].

Motivated by these promising first results the design and commissioning of a new facility for the coating of the SIS dipole chambers started at the end of 2005. The first coating tests on dipole chambers are foreseen in February 2006.

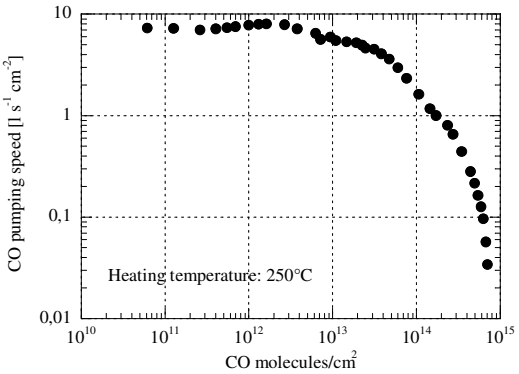


Figure 2: CO saturation curve obtained after activation of the sample at 250°C for about 4 hours.

References

[1] E. Fischer and H. Mommsen, Vacuum 17 (1967) 309.
[2] C. Benvenuti, Proceedings of the 2001 Particle Accelerator Conference, Chicago.

* Work supported by EU design study (contract 515876, DIRAC-PHASE-1, RP6 SIS 18-2).

Tools for Far Remote Accelerator Operation*

P. Schütt, A. Peters, H. Tang, GSI, Darmstadt, Germany

Abstract

The most likely scenario of a next generation linear collider as well as for FAIR is that it will be built by a collaboration of existing laboratories, which will remain involved during the operation of the accelerator. Advanced means of communication will be necessary to support efficient collaboration in the design and construction phase as well as far remote accelerator operation.

The GANMVL Project

GANMVL[1], the "Global Accelerator Network Multipurpose Virtual Laboratory" is a work package of EuroTeV[2], the European design study towards a global TeV Linear Collider. It is a collaboration of colleagues from DESY, ELETTRA, Fraunhofer-IGD, GSI, INFN-LNF, INFN-Mi, INFN-Ro2, and the Universities of Mannheim and Udine.

The goal of the project is to design and build a novel collaboration tool and test it on existing accelerator collaborations. The tool is a mobile communication centre which provides immersive video and audio capture and reproduction of an accelerator control room, a laboratory workplace environment or an accelerator hardware installation. It is able to connect to standard measurement equipment and to elements of accelerator controls and make these connections available to a remote client. The remote user should be enabled to participate in accelerator studies, assembly of accelerator components, trouble shooting of hardware or analysis of on-line data as if he or she would be present on site.

The GANMVL project will provide valuable experience of a new way in designing, building and operating large accelerator complexes, and will address the important psychological and sociological issues of the Global Accelerator Network.

Development of Prototypes

The present specification of the GANMVL tool is based on a world wide query of the user needs. About 170 accelerator scientists and engineers contributed in this query.

The MVL system is envisioned as a client-server system. The server is providing the information from an on-site activity as well as software tools for uploading, safety algorithm, authentification and authorization procedures and help information for a remote user or client.

On the client side it is assumed that any computer terminal equipped with commercially available audio and video equipment is sufficient. The access to control system is accomplished by a thin client technique which is based on a web service in order to be as platform independent as possible.

Three prototypes of the MVL server will be built to serve different types of application:

- a mobile server for work in the accelerator tunnel or other restricted areas
- a semi-mobile server for work in laboratories, electronic rooms etc.
- stationary server in control room for operation and commissioning or for observation of equipment behaviour.

Virtual Instruments

In 2005, the contribution of GSI was concentrated on the integration of virtual instruments into MVL based on a plug-and-play mechanism. The goal is to provide interfaces for most of the common off-the-shelf test and measurement (T&M) instruments such as oscilloscopes or spectrum analyzers.

Analysis of the problem led to the conclusion to base the first prototype on the IVI (Interchangeable virtual instruments) standard with generic instruments. A large number of devices are supported by this standard. The prototype version has been implemented and first tests with existing instruments are under way.

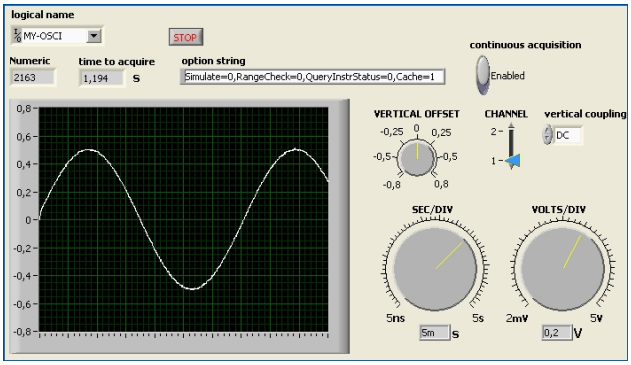


Figure 1: Screenshot of Virtual Instrument Prototype.

References

[1] https://ulisse.elettra.trieste.it/mvlgan
[2] http://www.eurotev.org/e558/e943

*Work supported in part by the Commission of the European Communities under the 6th Framework Programme "Structuring the European Research Area", contract number RIDS-011899.

Emittance Coupling Stopband in the SIS100

I. Hofmann and G. Franchetti
GSI, Darmstadt, Germany

The SIS100 requires careful conservation of both transverse emittances in order to keep beam loss due to nonlinear dynamics and space charge within the acceptable budget [1]. The choice of a horizontal to vertical emittance ratio of 3:1 implies that no transfer of the horizontal to the vertical emittance is allowed. The most dangerous source of emittance coupling is due to nonlinear space charge forces near the fourth order resonance condition $2Q_x - 2Q_y = 0$ ("Montague resonance" [2]). It leads to a very fast exchange keeping the sum of emittances roughly constant. Therefore, the associated stop-band should be avoided by the working point for high-current operation. We present a scaling law for this stop-band (for details see [3]), which has been calibrated by means of computer simulation and experimental data obtained at the CERN proton Synchrotron in the years 2002 and 2003 [4].

The driving force for this emittance exchange resonance is primarily the "octupolar" term in the space charge potential. It leads to a partial or complete emittance exchange, depending on how far the working point lies inside the stop-band. It has been shown [3] that for 2D coasting beams the stop-band falls entirely on that side of the resonance condition, where $Q_x < Q_y$. This applies to the case where $\epsilon_x > \epsilon_y$; for a reversed emittance ratio the sides have to be switched. The width in Q_x is given by

$$\Theta = \frac{3}{2}(\sqrt{\epsilon_x/\epsilon_y} - 1)\Delta Q_x. \qquad (1)$$

ΔQ_x is the space charge tune shift of an equivalent KV-beam, which is half the maximum tune shift of a Gaussian beam. Also, $\epsilon_x > \epsilon_y$ is assumed; if $\epsilon_x < \epsilon_y$, Eq. 1 still holds, if x is consistently replaced by y.

The ideal stop-band in 2D approximation has been derived ignoring finite bunch length, synchrotron oscillation as well as dispersive and chromaticity effects. It is, therefore, not surprising that the stop-bands for high-intensity bunched beams measured in experiments at the CERN Proton Synchrotron in 2002/2003 are somewhat broader than the ideal ones. We find that widening the stop-band on either side by 3/4 of the width in Eq. 1 is well containing these experimental data and "safe" to avoid an exchange. Although experimental data for different emittance ratios and tune shifts are not available, we scale this safety margin to the SIS100 parameters – taking advantage of the fact that the emittance ratio was the same in the experiment and only the tune shift was weaker. For the SIS100 and high-current operation it is assumed that the maximum vertical tune-shift (Gaussian beam) is -0.3, which corresponds to a horizontal KV tune-shift of -0.087. We thus find for the left edge of the stop-band $Q_{x,left} = Q_y - 0.17$, and for the right edge $Q_{x,right} = Q_y + 0.07$. The resulting stop-band is shown in Fig. 1. It is seen that the "Montague" stop-band enforces to use working points under the diagonal, with some distance from it. This narrows down the available region, if we also note that working points cannot approach the integer lines from below due to danger from the resistive wall instability.

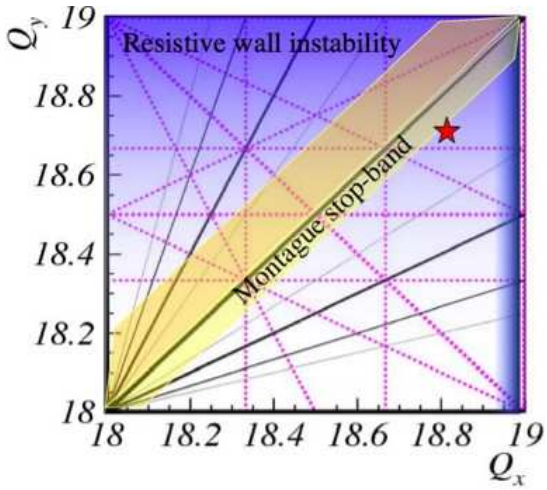


Figure 1: Tune diagram with high-intensity working point and Montague stop-band for SIS100.

For a working point well inside the stop-band the exchange time is fast and approximately given by [3]:

$$N_{ex}^{-1} \approx \frac{1}{2}\frac{\Delta Q_x}{Q_{0,x}}, \qquad (2)$$

where N_{ex} is the number of betatron periods. For the SIS100 and above parameters we would thus obtain ≈ 20 turns for the exchange.

During final bunch compression prior to extraction, where the maximum vertical space charge tune shift is expected to reach -0.6, the stop-band indicated in Fig. 1 would be doubled on either side of the resonance line. If the working point is not outside this new band, the rapid nature of the exchange would induce at least a partial exchange of emittances just a few turns before extraction. It needs to be checked whether this has any consequences for the manipulations beyond extraction.

References

[1] GSI Technical Design Report.

[2] B.W. Montague, CERN-Report No. 68-38, CERN, 1968.

[3] I. Hofmann and G. Franchetti, to be published in Phys. Rev. ST Accel. Beams (2006).

[4] E. Metral et. al., *AIP Conf. Proc.* **773**, New York, 2004, 122

Transverse Instabilities for the High-Current Upgrade of SIS 18

V. Kornilov, O. Boine-Frankenheim, R. W. Hasse and I. Hofmann, GSI, Darmstadt, Germany
A. M. Al-khateeb, Yarmouk University, Irbid, Jordan

Transverse collective instabilities lead to losses for high-intensity beams in ring accelerators and can limit the operation of the upgraded SIS 18 and the planned SIS 100 synchrotrons. Numerical investigations of the structure of collective modes and of the damping mechanisms together with the driving forces (with the beam surroundings described using coupling impedances) are in progress. In this report we focus on consequences of transverse collective instabilities for the SIS 18 Upgrade.

The first important damping mechanism (called linear Landau damping) is related to the spread in the particle revolution frequency (described using the slippage factor η) and to the spread in the betatron tune (described using the chromaticity ξ). Considering a slow wave with the coherent unshifted frequency $\omega_s = n\omega_0 - \omega_{\beta 0}$, where n denotes the mode index of the transverse collective perturbation, one obtains the dispersion relation for an arbitrary transverse impedance. One can use it to analyse the stability and general properties of different beam parameters for the KV distribution.

Another collective effect, called "nonlinear Landau damping", damps dipole perturbations due to the nonlinearities in the betatron oscillations. We considered nonlinearities induced by the space charge forces, external forces (e.g. octupoles) and by a combination of these two effects. Using the Vlasov equation for the particle distribution function, one obtains the dispersion relation, which contains the stationary betatron amplitude distribution and the nonlinear tune shift distribution. It was shown that there exists a complex interplay (also see e.g. [1]) between the two nonlinear damping mechanisms, i.e. combining the space-charge and external nonlinear effects, one observes a significant enhancement for the stability.

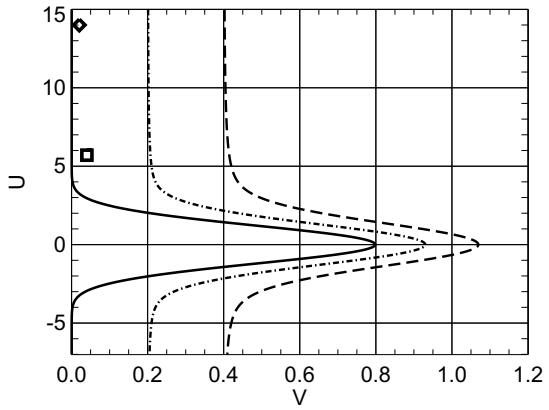


Figure 1: Stability diagram with linear Landau damping: level contours of the growth rate (the full line is the stability boundary) in the normalized impedance plane $V+iU \propto Z^{\perp}$, two working points for SIS 18 are given.

As an example, Fig. 1 shows the numerically obtained stability diagram (Gaussian distribution, for details see Ref. [2]) for the linear Landau damping (including the chromaticity and the slippage factor effects) with two working points: the square for the U^{28+} coasting beam in the SIS 18 at the injection energy (unstable, the growth time is τ =3.4 ms) and the diamond for the same at the flat-top stage (unstable, τ =4 ms). Each of these modes is the most unstable one for the corresponding beam and is excited by the resistive-wall impedance.

Aiming at the impedances budget definition and better understanding of the instabilities, the involved particle tracking simulations are necessary to investigate nonlinear dynamic effects and to study the effects, which were considered here analytically, more realistically and accurately. The solutions of the dispersion relations will serve as benchmark for the simulations.

As to the impedance investigations [3], the transverse space–charge and resistive–wall impedances were investigated analytically for a smooth resistive cylindrical beam pipe of thick wall. For an off–axis motion of the beam, the perturbed charge distribution of the beam becomes a function of the azimuthal angle, resulting to first order in the beam displacement in a dipole term which is the source of the transverse impedance. All six components of the electromagnetic field are different from zero and, therefore, both TM (transverse magnetic) and TE (transverse electric) modes will be excited in the beam–pipe and coupled to the beam at the inner surface of the resistive wall. Using the dipole source term, a linear combination of TM and TE modes is used to get closed form expressions for the transverse electromagnetic field components excited in the beam–pipe, and a generalized analytic expression for the corresponding transverse coupling impedance. It has been found that the contributions of the TM and the TE modes to the real part of the transverse resistive–wall impedance have similar dependence on the relativistic parameter γ_0 but with opposite signs, the sum of both always being positive.

References

[1] D. Möhl and H. Schönauer, Proceedings of the 9th International Conference an High Energy Accelerators, p. 380, May 2–7, Stanford, 1974.

[2] V. Kornilov, O. Boine-Frankenheim, I. Hofmann, B. Doliwa, GSI-Acc-Note-2005-10-001, GSI Darmstadt, 2005.

[3] A. M. Al-khateeb, W. Hasse, O. Boine-Frankenheim and I. Hofmann, Phys. Rev. E, 2006, to be submitted.

Measurement of the Energy Deposition Profile by U ions of Energies 500 and 950 MeV/u in Cu Targets*

E.Mustafin#, D.Schardt, K. Weyrich, GSI, Darmstadt, Germany
A. Golubev, A.Kantsyrev, V.Luckjashin, A.Fertman, ITEP, Moscow, Russia
A.Kunin, V.Vatulin, A. Gnutov, Y. Panova, VNIIEF, Sarov, Russia,
N.Sobolevskyi, L.Latysheva, INR RAS, Moscow, Russia.

Abstract

The results of the experimental research on precision measurements of total stopping range and energy deposition function of ^{238}U ion beam with kinetic energy E = 500 and 950 MeV/u in copper targets are presented and compared with the ones calculated with the help of different codes.

Motivation

The range of the U ions of energy E = 1 GeV/u in copper is about 1.5 cm. Assuming 17 mrad grazing incidence this would result in the Bragg peak energy deposition depth of 0.3 mm, which is the thickness of the vacuum tube foreseen for the superconducting (s.c.) magnets of the SIS100 synchrotron of the FAIR Project. Since the s.c. cables of the magnets are situated right next to the vacuum tube walls it is very important to know the energy deposition profile dE/dx with high accuracy. The measured values should be compared with the calculated ones in order to validate the numeric tools used for beam loss damage simulations.

"Thick target" method

The 'thick target' method was used for precision measurement of the total energy deposition by the U ions in solids. The method offers the following advantages [1] for our purpose:

1) provides a direct measurement of dE/dx, rather than its reconstruction from the differential energy deposition measurements using thin foils;

2) eliminates the 'edge effects' (the influence of ion entrance to the bulk and its exit from the bulk on the dE/dx), as compared to the 'thin foil' approach;

3) takes into account the beam straggling and fragmentation, secondary particles etc.

Measured values and calculations

The results of the dE/dx measurements were compared with dE/dx calculations using the ATIMA [2], SRIM [3] and SHIELD [4] codes.

All codes gave a good agreement with the measured data (within the accuracy of the measurement) for the case of U ions of energy E = 500 MeV/u.

We demonstrate the discrepancy of the calculations with the measurement (and with each other) on the example of the 950 MeV/u U ions in Cu target. The resulting dE/dx curves are presented in Fig. 1.

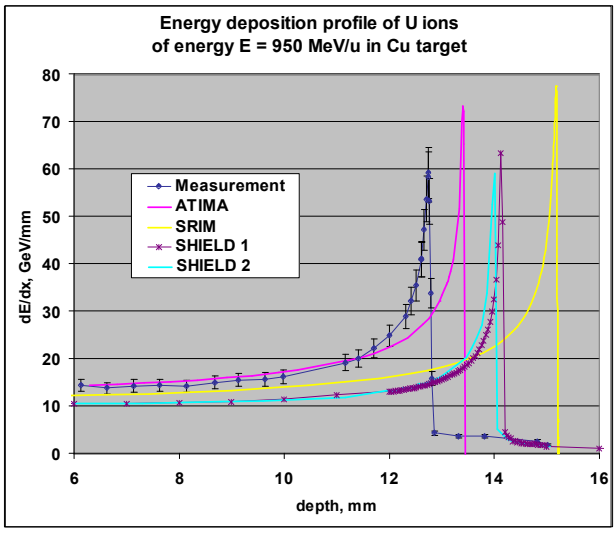


Fig.1 Comparison of the measured and calculated energy deposition profiles dE/dx for the case of 950 MeV/u U ions in Cu target. The "SHIELD 1" curve corresponds to dE/dx in a cylindrical Cu target. The "SHIELD 2" curve corresponds to more detailed modeling of the experimental set-up.

Note that SRIM and ATIMA calculate the stopping power without taking into account the nuclear reactions (besides the elastic recoils in case of SRIM) and the SHIELD code takes into account the nuclear reactions.

References

[1] E.G.Vasina, V.V.Vatulin, A.A.Golubev, D.H.H.Hoffmann. "Thick Target" Approach for Precise Measurement of Total Stopping Ranges: Motivation for Experimental Research". High Energy Density in Matter Produced by Heavy Ion Beams. GSI Annual Report, 1998, p.45.

[2] C. Scheidenberger, H. Geissel, Nucl. Instr. and Meth. B 135 (1998) 25 and B 136–138 (1998) 114, web interface http://www-aix.gsi.de/~weick/ATIMA

[3] J.F. Ziegler, J.P. Biersack, U. Littmark, The Stopping and Range of Ions in Solid, Pergamon Press, New York, 1985.

[4] N.M. Sobolevsky, The SHIED transport code: a tool for computer study of interaction of particles and nuclei with complex media, in: Proceedings of the YUNSC 2000, Belgrade, October 2–5, 2000, The VINCA Institute, Belgrade, 2001, pp. 539–564.

*Work was done in the frame of the GSI-INTAS Project #03-54-3588
#E.Mustafin@gsi.de

Loss Analysis for β-Beam Operation in existing CERN Synchrotrons*

M. Kirk, C. Omet, P. Spiller, J. Stadlmann, GSI, Darmstadt, Germany

The EURISOL β-beam collaboration was formed to address the issue of accelerator production of high flux neutrino beams. With the aim to exploit the existing PS and SPS synchrotrons at CERN, in combination with the planned EURISOL facility, it is proposed to create anti/neutrinos from high intensity radioactive beams boosted to high γ in the SPS and inject them into an elongated storage ring within which narrow cones of anti/neutrinos are produced due to the high γ of the decaying nuclei. The ions chosen are $^{6}He^{2+} \rightarrow {}^{6}Li^{3+} + \beta^{-} + \nu$ and $^{18}Ne^{10+} \rightarrow {}^{18}F^{9+} + \beta^{+} + \bar{\nu}$ because of their ISOL-production cross section and a reasonable short β-decay half life (0.81s for ^{6}He and 1.67s for ^{18}Ne) to achieve a reasonable decay rate at the high γ of 50 to 150 in the decay ring. We present here the beam loss and pressure rise analysis for the PS and SPS. At present there is no dedicated collimation system in either machine. It is important that in a well collimated accelerator the decay products of the β-decay should avoid as much as possible hitting the beam pipe in order to prevent pressure rise and radiation damage to the magnets due to neutron activation. Starting with the baseline scenario in [1] and considering the loss distribution at injection, the GSI *StrahlSim* code was used to calculate the tracking and pressure. Systematic losses i.e. injection, RF capture and extraction were ignored. The constituents of the vacuum rest gas were assumed the same for both rings. The distribution of impact positions along the existing PS of the Li and F ions is not very peaked (figure 1). Therefore the collimation efficiency is apparently just a few percent. Furthermore, there is no optimum collimation scheme for both ions due to their different charge-to-mass. The maxima in the distribution are caused by the focussing from the alternating gradient pairs of combined function magnets. We see that these maxima seldom coincide with a drift section.

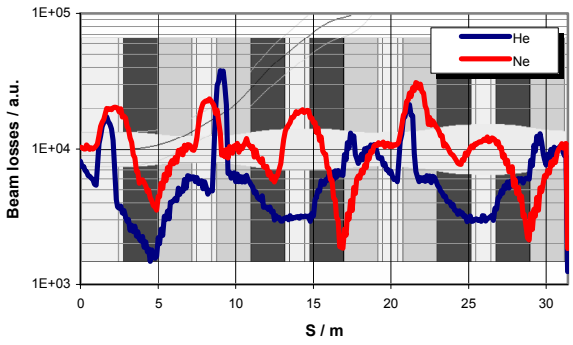


Figure 1. Loss distributions over one period of the PS.

*Work supported by the FP6 EURISOL design study.

As many of the Li and F ions as possible should ideally go into the collimators. The consequent beam induced desorption from the collimators could however be tolerated since enhanced pumping may be localised at the collimator positions. From a pressure point of view, it is He that produces the highest pressure bump which is ~2 orders of magnitude higher than Ne. This is caused by the much higher injected intensity and shorter half life of He. The SPS also has a relatively flat loss pattern. Furthermore, the maximum allowed collimator thickness could present a problem concerning stopping ranges. There are only 2 points along the beam line at which drift sections coincide with peaks in the losses. The relative drop in intensity in the SPS is larger for He because of the shorter decay half life. Coulomb scattering which goes as $\beta^{-3}\gamma^{-2}$ [2] was checked and found to be insignificant. We notice a maximum in the pressure of ~$3\cdot10^{-7}$ at 0.5 seconds (figure 2). This is due to the fast single turn injection. After this maximum the pumping rate exceeds desorption. The main concern here is the maximum pressure of the order of 10^{-7} Pa during the cycle. Final intensities just before injection into the decay ring were found to be lower than those calculated merely on the basis of β-decay in [1]. Primary beam intensities at the point of injection into the decay ring were $5.63\cdot10^{12}$ for He and $1.51\cdot10^{11}$ for Ne.

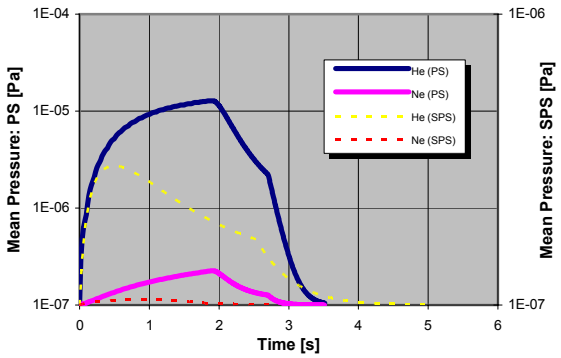


Figure 2: Example for a pressure evolution in PS and SPS calculated with the program STRAHLSIM.

Though not mentioned here, a new design to replace the PS similar to the SIS100 with an optimised loss distribution together with high collimation efficiency, and ramping at 4 T/s has recently been proposed.

References

[1] M. Benedickt et al., "The EURISOL Beta-Beam Facility. Parameter and Intensity values", EURISOL DS/TASK12/TN-05-03, July 2005.

[2] J. D. Jackson, Classical Electrodynamics, Second Edition, Wiley, New York (1975).

Beam Loss Studies for the AGS Booster Operation with Intermediate Charge State Heavy Ions

C. Omet([1]), W. Fischer([2]), A. Smolyakov([3]) and P. Spiller([1]),

([1]) GSI, Darmstadt, Germany, ([2]) BNL, Brookhaven, USA, ([3]) ITEP, Moscow, Russia

Introduction

In the context of the planned operation of SIS18 and SIS100 with intermediate charge state heavy ions, the simulation code StrahlSim has been developed which couples the beam dynamics, the atomic physics and the vacuum phenomena. This code was used to carry out a comparison between the current and planned SIS18 operation and the operation of the AGS Booster at BNL [1].

Stabilization of Dynamic Pressure in SIS18

For the stabilization of the pressure dynamics in SIS18 major upgrade measures are in preparation. The upgrade of the UHV system shall lead to a static pressure of p_0 $1*10^{-12}$ mbar. It is planned to replace the existing dipole and quadrupole magnet chambers by new chambers and to develop a new bake-out system for higher bake-out temperature of 300 °C (the existing one is operated up to 200 °C). In addition, NEG coating of all magnet chambers and the revision of all existing pumps shall provide the required high local and distributed pumping speed. Finally, the upgraded effective pumping speed will be about $2*10^5$ l/s, which is about 100 times higher than the total pumping speed at present.

Moreover, a collimation system is planned for beam losses generated by ionization processes and prevent the desorbed ions and molecules from interacting with the circulating beam. Furthermore, a reduction of systematic beam losses, in particular injection losses to 5% and RF-capture losses to 1% is desired.

All calculations of the beam lifetime and pressure evolution were done using the code StrahlSim. This code includes the simulation of different beam loss mechanisms like coulomb scattering, projectile and target ionization and couples these mechanisms to the induced gas desorption, the desorption collimation system and the resulting vacuum dynamics. Furthermore, realistic numbers for beam loss during injection, RF capture, acceleration and extraction in the AGS Booster and SIS18 acceleration cycle have been included. In order to demonstrate the perspectives, simulations were carried out for higher beam intensities in SIS18 and AGS Booster.

AGS Booster Operation

In fig. 1, a comparison of StrahlSim results with measured beam intensity profiles in an AGS Booster cycle with an initial intensity of $2.6*10^9$ (which is achieved in standard operation) and $6.1*10^9$ ions is plotted. In both cases, measured and simulated beam intensity profiles are in good agreement. No fast pressure measurement does exist for the Au^{32+}-case. However, in machine experiments with beam losses of about $3*10^9$ Au^{31+} ions, a maximum pressure in the order of 10^{-5} Pa was measured in the AGS Booster.

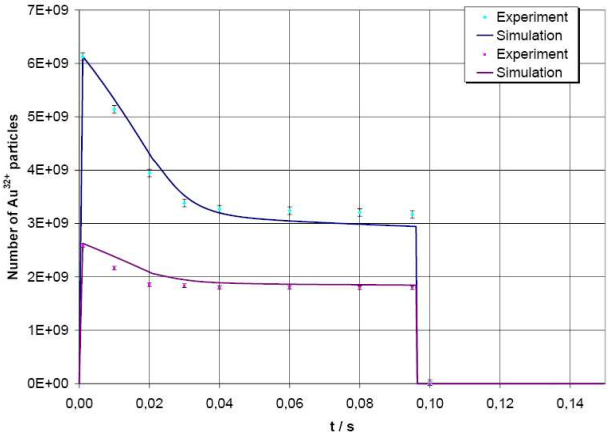


Figure 1: Calculated and measured intensity profiles in an AGS Booster cycle for different initial intensities

The results indicate that the operation with Au^{32+}-beam with an initial intensity of $6*10^9$ Au^{32+} ions can be assumed as a threshold for the AGS Booster.

At higher initial intensities and without any further upgrade measures, tremendous beam loss would occur in both synchrotrons. Due to the different injection energies, the beam lifetime in the AGS Booster is evidently lower than in SIS18. This can be explained by the much higher charge-exchange cross-sections. In SIS18, the dominant process for U^{28+} ions at the injection energy of 11.4 MeV/u is electron loss with cross sections of 10^{-18} to 10^{-17} cm^2/atom. In the AGS Booster the dominant process for Au^{32+} ions at 0.92 MeV/u is electron capture with cross sections of 10^{-17} to 10^{-16} cm^2/atom. At similar base vacuum conditions and also similar and relatively high injection losses this leads to much higher beam losses in the AGS Booster.

Furthermore, the potential operation with higher intensities in the fully upgraded SIS18 and the present AGS Booster has been simulated. SIS18 after reaching the planned upgrade parameters shows quite encouraging results evidently allowing the acceleration of U^{28+}-ion beams with intensities of 10^{11}. On the other side the planned increase of injection energy in the AGS booster will also improve the situation considerably.

References

[1] GSI-Acc-Report-2005-11-001

Monte Carlo shielding calculations for FAIR

G. Fehrenbacher, F. Gutermuth, A. Knapp, G. Moustafina, T. Radon
GSI, Darmstadt, Germany

Introduction

The examples of Monte-Carlo-calculations presented in this report are all performed with the latest version of the FLUKA code[1] (FLUKA2005). It is capable of simulating interaction and propagation in matter for a large variety of particles in a wide energy range. Recently the transport of heavy ions including nucleus-nucleus collisions has been added employing the RQMD [1] and the DPMJET [2] models.

A Maze for SIS 100/300

In order to shield the entrance area of the extraction building of the SIS 100/300 an elaborated maze is needed. The maze shown here (see Fig. 1) has a clearance of 2 m and a width of 2.5 m. Special removable struts (dashed squares) on the ceiling of the maze have been foreseen to further reduce the dose level in the extraction building. The beam loss is represented here by 6 discrete positions which amount in total to a loss of 10 %. Due to the absence of doors, the overall length of the maze reaches 25 m to limit the dose rate to max. $5 \cdot 10^{-7}$ Sv/h at the entrance of the maze. A duct for cables etc. which is located on top of the maze has also been taken into account for the dose rate calculation.

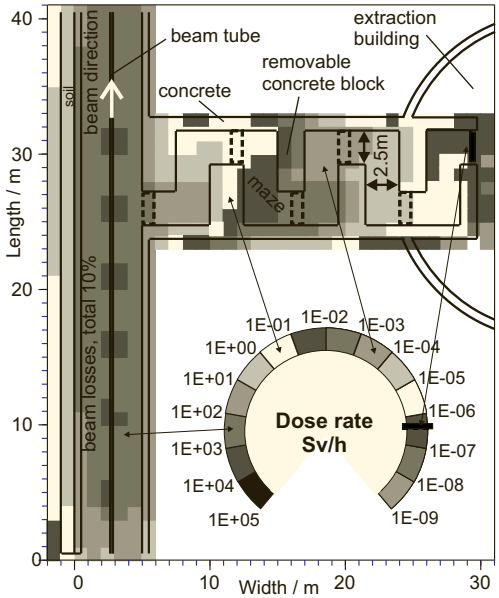


Figure 1: Layout of the maze for SIS 100/300.

The Low energy Storage Ring for FLAIR

Antiprotons ($\bar{p}$) coming from the NESR into the LSR have an energy of 30 MeV. With the LSR it is possible to accelerate the $\bar{p}$ up to an energy of 90 MeV. To calculate the required thickness of the concrete shielding two calculations are performed according to two different scenarios: During normal operation only a small fraction ($\approx$ 10 %) of the beam will be lost homogeneously in the ring. However, for the setup and conditioning of the LSR a total loss of 100 % of the beam must be assumed. The standard beam pipes in the LSR will be made from 2 mm thick steel. Taking into account the mass of all magnets ($\approx$ 100 tons) an average thickness of 10 mm steel of the beam tube demonstrates the total amount of steel. Figure 2 shows the two calculations according to a 10 % $\bar{p}$ beam loss, which is represented by 4 discrete positions, at an intensity of 10^8 particles per spill per 30 seconds (top) and a 100 % $\bar{p}$ beam loss for a reduced beam intensity by a factor of 10. The calculation shows that a 50 cm thick concrete wall is needed to assure a dose rate below $5 \cdot 10^{-7}$ Sv/h.

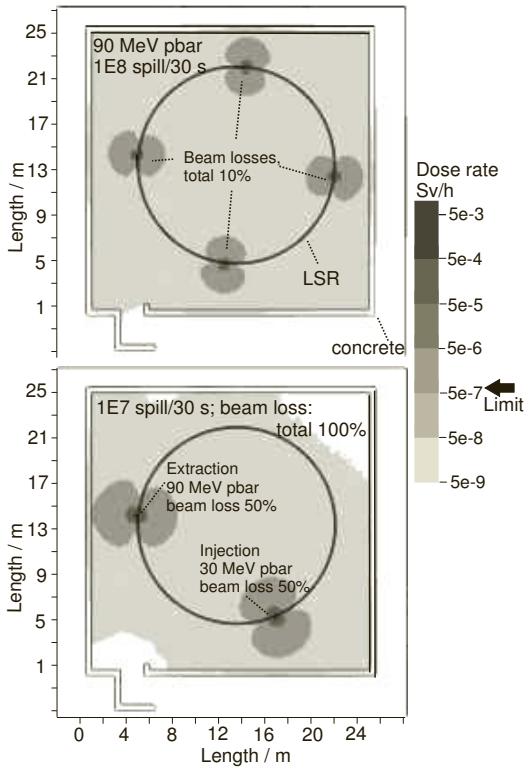


Figure 2: FLUKA calculations for two scenarios (i. coasting beam, ii. injection/extraction).

References

[1] H. Sorge. Flavor production in Pb(160A GeV) on Pb collisions: Effect of color ropes and hadronic rescattering. *Physical Review C*, 52(6):3291–3314, 1995.

[2] J. Ranft. New features in DPMJET version II.5. *Physical Review D*, 51:64, 1995.

[1] *www.fluka.org*

Dose equivalent from 500 MeV neutrons

S. Beceiro[1], G. Fehrenbacher[2], F. Gutermuth[2], E. Kozlova[2], T. Radon[2]

[1] Universidad de Santiago de Compostela, Spain

[2] GSI Darmstadt, Germany

Abstract

Neutrons constitute a major component in the radiation field outside the shielding of particle accelerators. Consequently appropriate neutron dose meters are needed to survey the radiation levels.

A thermo-luminescence based neutron dosemeter is used at the UNILAC as well as at the SIS. It has been modified to improve the response for high energetic neutrons (*extended range*). We report on a test of these devices in a quasi mono-energetic field of 500 MeV neutrons.

Neutron production in Cave C

A deuteron beam with particle kinetic energy of 1 GeV impinges on a 5 cm thick lead brick. The deuterons break up into protons and neutrons mainly through Coulomb interaction (lead Z=82). The protons are deflected by a dipole situated downstream to the lead target (ALADIN). The remaining neutrons are employed for the dosemeter tests. The flux of the deuterons is monitored with a 1 cm thick plastic scintillator for beam intensities up to 10^5 particles per second and with a high precision ionization chamber for higher beam intensities.

Characterization of the neutron field

The neutron yield in forward direction is measured with a 2m$\times$2m time-of-flight wall consisting of a multi-layer array of iron converters and plastic scintillators (LAND)[1]. The resulting neutron yield is 4.9 neutrons per 100 incoming deuterons. The distribution of the neutrons in energy is shown in figure 1. The most probable energy is $\approx$470 MeV which is a little lower than the 500 AMeV of the primary beam revealing a small energy loss in the lead brick.

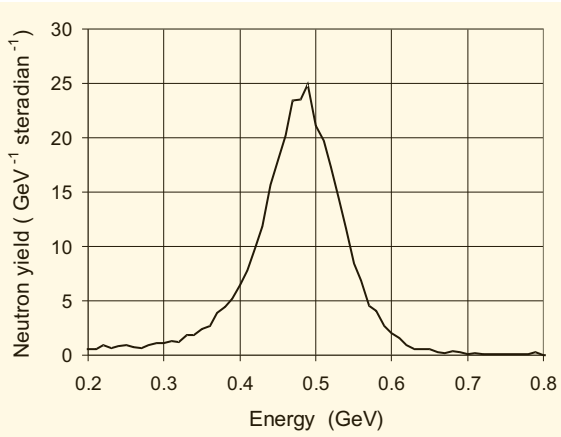


Figure 1: Energy spectrum of the neutron field as measured with LAND[1].

Neutron dose

The dose reading of the conventional TLD neutron dosemeter is 49 ± 6 pSv cm^2 which is approximately a factor of 5 lower than the result of 252 ± 47 pSv cm^2 from the extended range version (see figure 2). Both types are calibrated to the so-called ambient dose equivalent in the field of a Americium-241/Beryllium-neutron source.

FERRARI and PELLICCIONI [2] report a conversion factor of 290 pSv cm^2 for neutrons of energy 500 MeV which is in good agreement with the dose reading of the extended range TLD dosemeter (see figure 2).

Conclusion

We conclude that a conventional neutron dosemeter may significantly underestimate the dose from 500 MeV neutrons whereas the extended range version yields appropriate dose readings.

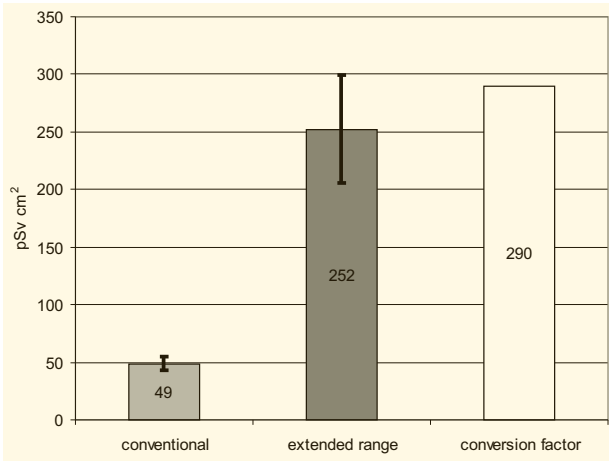


Figure 2: Dose readings of the conventional and the extended range neutron dosemeter and conversion factor from [2] for 500 MeV neutrons.

Acknowledgement

This investigation was largely supported by the LAND group which is greatly acknowledged. Work partly funded by EU grant EURONS-JRA10-SAFERIB.

References

[1] Th. Blaich et al. *Nucl.Instr.Meth.*, A314:136–154, 1992.

[2] A. Ferrari and M. Pelliccioni. *Rad.Prot.Dosim.*, 76(4):215–224, 1998.

Research to the Programme Hadrons and Nuclei

ACC
Reports of the GSI Accelerator Division

- ACC-STATUS : Accelerator Operation and Status Reports (121p.)
- ACC-R&D : Accelerator Research and Developments (129p.)

NUSTAR
Nuclear structure, astrophysics and reactions

- NUSTAR-SPECTROSCOPY : Spectroscopy (141p.)
- NUSTAR-EXOTIC-BEAMS : Exotic Beams and Reactions (155p.)
- NUSTAR-THEORY : Theoretical Nuclear Structure, Astrophysics and Reactions (161p.)
- NUSTAR-SHE-PHYS : Physics of Heavy and Superheavy Elements (191p.)
- NUSTAR-SHE-CHEM : Chemistry of Heavy and Superheavy Elements (200p.)

NQMA
Nuclear & Quark Matter Research

- NQMA : General (208p.)
- NQMA-EXPERIMENTS: Experimental Works (213p.)
- NQMA-THEORY: Theoretical Works (235p.)

INSTRUMENTS-METHODS
Instruments & Methods (260p.)

UNILAC Status and Developments

W. Barth, W. Bayer, L. Dahl, L. Groening, S. Richter, S. Yaramishev, GSI, Darmstadt, Germany

Status of Operation

During the beam time in 2005 for the GSI therapy program carbon beams from the Electron Cyclotron Resonance (ECR) ion source were mainly accelerated via the high charge state injector (HLI) in the UNILAC for the SIS-injection as in the years before [1]. Additionally several UNILAC experiments used the beam with high duty factor. The ECR source was in operation for the production of various isotopes (^{7}Li, ^{26}Mg, ^{48}Ca, ^{54}Cr, ^{112}Sn, ^{124}Sn, ^{132}Xe) as well. Mainly experiments for the Super Heavy Element synthesis (SHIP) and the nuclear chemistry requested beam time for the experimental hall. Additionally, ion beams from the ECR were injected into the SIS (Rising collaboration, ESR-experiments). The Penning (PIG) ion source provided calcium, aluminium, argon, chromium, nickel, samarium and neodymium beams with medium intensity, especially when the ECR was used for the irradiation of patients. For heavy ions (^{197}Au, ^{208}Pb, ^{238}U) a beam from the PIG source was accelerated via HSI in the UNILAC with short pulses mostly for the injection into the SIS 18. Additionally, ^{238}U and ^{208}Pb was delivered for material research experiments in the experimental hall, moreover ^{197}Au for the atomic physics program at the UNILAC. The MUlti Cusp Ion Source (MUCIS) provided high current beams for different high energy experiments with high intensities (H_2, $2D_3$, ^{40}Ar, ^{78}Kr, ^{132}Xe). The Metal Vapour Vacuum Arc (MEVVA) ion source delivered ^{94}Mo, ^{100}Mo and ^{142}Nd for SIS-injection. Due to serious problems with the delivery of uranium cathodes no high current uranium beam operation was performed in 2005 as already in the last year. Alternatively, ^{181}Ta was in use to perform SIS-machine experiments with a high intensity heavy ion beam. During (sweeper-) operation with high power heavy ion beams the thermal stress of the stripper foils in the transfer line to the SIS raises considerable problems (see Figure 1). In addition just 88 hours (209 hours in 2003, 96 hours in 2004) for accelerator tests were available, resulting in a reduced program for machine development.

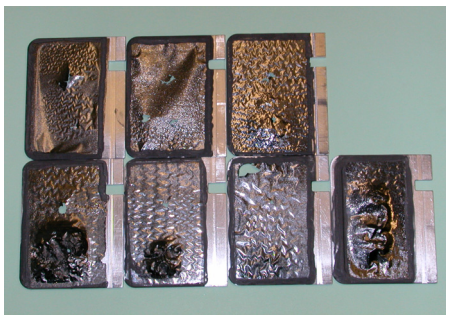


Figure 1: Destroyed carbon stripper foils (200 µm - 600 µm) after operation with high intensity heavy ion beams.

Machine Experiments

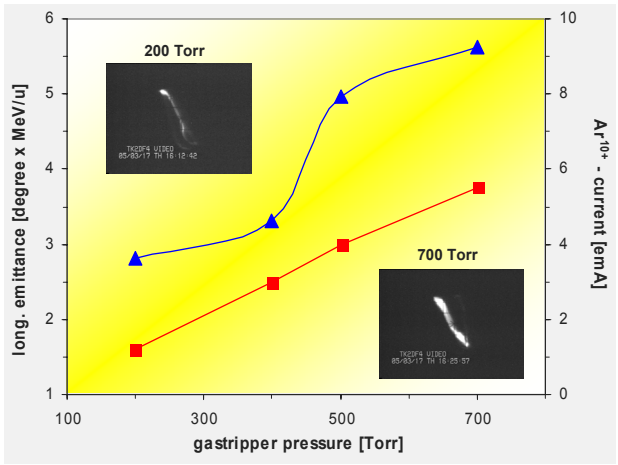


Figure 2: Measured longitudinal emittance of a high current argon beam at 11.4 MeV/u for different intensities adjusted by variation of the gas stripper density.

For the progressing machine development program at the end of beam time block 1 and 3 a high intensity argon beam from the MUCIS was in use for the preparation of the HIPPI (High Intensity Pulsed Proton Injector, CARE, contract number RII3-CT-2003-506395)-experiments, to be performed in June and November 2006. [2]

Additionally, software tests with the new emittance data acquisition program were performed. This software tool in combination with already mounted beam diagnostic devices will allow high performance emittance measurements at seven different positions along the whole UNILAC and transfer line to the SIS 18. Especially for the HIPPI-experiment program and the UNILAC upgrade program for FAIR all investigations are based on versatile emittance measurements to be carried out for low and high intensity heavy ion beams.

The improvement of the longitudinal beam quality for high intensity beams is strongly recommended as a key requirement to reach the required momentum spread for injection into the SIS 18. A longitudinal emittance measurement device is now established for further optimisation of heavy ion beams in the transfer line. As shown in Figure 2 the longitudinal beam emittance depends strongly on the ion intensity accelerated in the Alvarez Drift Tube Linac.

References

[1] U. Scheeler and D. Wilms, Accelerator Operation Report, (this report).
[2] W. Bayer, et. al., Preparation Status of the HIPPI Experiments, (this report).
[3] W. Barth, et. al., UNILAC Status and Development, scientific report 2004, p. 307-308.

Ion Source Development and Operation

P. Spädtke, J. Bossler, M. Galonska, F. Heymach, R. Hollinger, R. Iannucci, R. Lang, K.D. Leible, K. Ochs, K. Tinschert

ECR Ion Source (ECRIS)

Regular operation at the High Charge State Injector (HLI) was performed for: $^{7}Li^{+}$ (6 d), $^{12}C^{2+}$ (97 d), $^{26}Mg^{5+}$ (21 d), $^{48}Ca^{7+}$ (74 d), $^{54}Cr^{7+}$ (34 d), $^{124}Sn^{16+}$ (8 d), and $^{136}Xe^{18+}$ (7 d). For $^{48}Ca^{10+}$ a long run of 67 days could be provided characterized by exceptional stability at high intensity level. The lifetime of the oven exceeded 1500 hours while 3 fillings of the crucible were consumed. Taking into account the amount of material recovered from condensates a consumption of only 0.2 mg/h has been achieved which corresponds to an efficiency never reached before. Initiated by a request of a SHIP experiment for a ^{30}Si beam tests were performed at the ECR injector setup (EIS) using natural SiO to produce a $^{28}Si^{5+}$ beam by evaporation from the GSI standard oven (STO). SiO appeared to be the only choice, because the vapor pressure of Si and SiO_2 are by far to low. An appropriate source setting could be found to provide a stable beam of Si^{5+} at moderate intensity level for more than 20 hours.

Beam diagnostic tools have to be adapted to the specific requirements of an ECR ion source. To measure the beam emittance a pepper pot device has been reactivated. The pepper pot has a spatial resolution of 5 mm only, but provides information which is not available from a standard slit grid device. The difference between both measurements is that the pepper pot gives a two dimensional subspace of the transverse phase space, whereas the slit grid method is a two dimensional projection of the four dimensional phase space. As an example, the emittance of a singly charged helium beam, directly behind the extraction system is shown in Fig. 1. The ion source has been tuned to a low current mode. Even in that case the characteristic shape of an ion beam extracted from an ECR source can be seen.

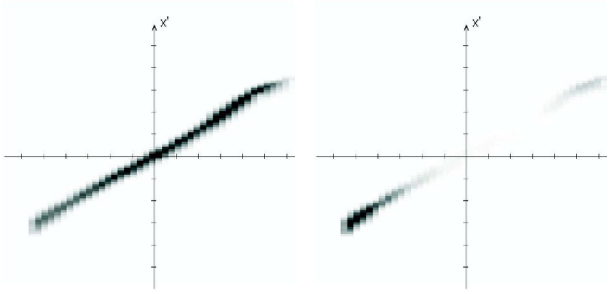


Figure 1: Emittance of a helium beam, measured by the pepper pot device. Left: integrated over all angles in y, right: angle resolved emittance.

A 3D model of the beam line has been developed (see Fig. 2) to investigate properties of beam transport. This model describes in four sections (extraction, solenoid section, quadrupole section, and dipole section) the full beam line. Coupling by the solenoid, as well as by space charge can be simulated because of the fully three dimensional simulation [2].

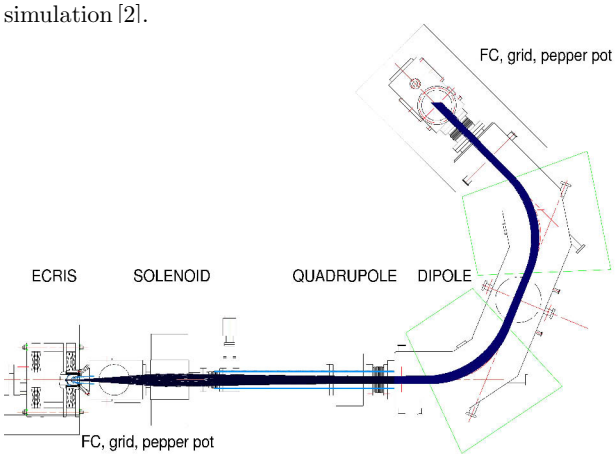


Figure 2: 3 dimensional beam tracking along the beam line, including space charge.

Penning Ion Source (PIG)

Regular operation was performed for: $^{20}Ne^{3+}$ (4 d), $^{22}Ne^{+}$ (4 d), $^{27}Al^{+}$ (18 d), $^{40}Ca^{+}$ (13 d), $^{40}Ar^{+}$ (2 d), $^{40}Ar^{2+}$ (11 d), $^{52}Cr^{2+}$ (12 d), $^{58}Ni^{2+}$ (13 d), $^{58}Ni^{3+}$ (6 d), $^{152}Sm^{3+}$ (22 d), $^{197}Au^{8+}$ (14 d), $^{208}Pb^{4+}$ (7 d), $^{238}U^{10+}$ (8 d), and $^{238}U^{4+}$ (52 d). The attempt to create a neodymium beam without previous experience failed, indicating the necessity to develop new beams at the test bench before offering them for the regular beam time schedule. Theoretical, experimental, and technical investigations to increase the available ion currents resulted in the design of an accel-decel extraction system [3].

High Current Ion Sources

Regular operation was performed for: $^{1}H_3^{1+}$ (14 d, 1 mA), $^{2}D_3^{1+}$ (20 d, 2 mA), $^{14}N_2^{1+}$ (3 d, 4 mA), $^{40}Ar^{+}$ (6 d, 20 mA), $^{40}Ar^{2+}$ (23 d, 0.1 mA), $^{40}Ca^{+}$ (6 d, 5 mA), $^{58}Ni^{2+}$ (12 d, 6 mA), $^{78}Kr^{2+}$ (9 d, 6 mA), $^{86}Kr^{2+}$ (22 d, 10 mA), $^{100}Mo^{2+}$ (9 d, 0.5 mA), $^{132}Xe^{3+}$ (12 d, 0.2 mA), $^{136}Xe^{3+}$ (16 d, 0.8 mA), $^{142}Nd^{3+}$ (10 d, 1.5 mA), $^{181}Ta^{3+}$ (7 d, 7 mA), and $^{238}U^{4+}$ (2 d, 5 mA). Ion beam current measured in front of the RFQ. In order to study and to compare the beam quality produced by the gaseous ion source CHORDIS and the vacuum arc ion source VARIS transversal beam emittance measurements were carried out with a slit-grid device at the high current test bench. Both ion sources were equipped with the same extraction system. The effective emittance using a multi-aperture system is approximated by a parallelogram that surrounds all single emittance ellipses. The emittance is then given by

$\epsilon_{eff} = 4R\phi/\pi + \epsilon_1$. R is denoting the outer hole circle of the apertures, ϕ the beam divergence, and ϵ_1 the emittance of one of the apertures. According to this relation the emittance is a function of the beam divergence only if the extraction geometry is given. Fig. 3 (left) shows the emittance pattern of a matched Argon beam (80 % Ar^+, 20 % Ar^{2+}) at 18 kV extraction voltage, screening voltage is -1.4 kV using the CHORDIS ion source with the multi aperture system. The azimuthal position of the extraction system with respect to the measurement device is such that seven single ellipses are visible in Fig. 3. The ion beam current measured in a Faraday cup is 60 mA. The perveance is $0.0604\, mA/(kV)^{1.5}$ for a single aperture.

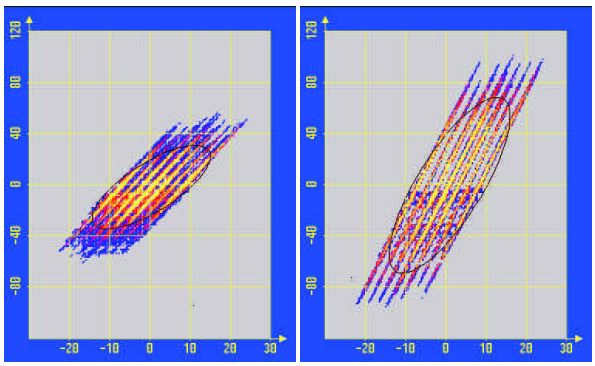


Figure 3: Emittance pattern of an argon beam (multi aperture, 60 mA, 18 kV) and emittance pattern of a nickel beam (multi aperture, 60 mA, 18 kV) in the y-y'-plane, y (horizontal) in mm, y' (vertical) in mrad.

The emittance (90 %, 4rms) is given as black ellipse. It amounts to 320 mm mrad, 0.32 mm mrad normalized. The effective emittance, only influenced by the beam divergence of 45 mrad, is 500 mm mrad. Fig. 3 (right) shows the emittance pattern of a nickel ion beam produced by the VARIS (74 % Ni^{2+}). Extraction voltage is 18 kV, screening voltage is -1.2 kV using the same extraction system as the CHORDIS. The ion beam current is 60 mA and thus the perveance is the same as for the argon beam. The emittance (90 %, 4rms) amounts to 645 mm mrad, 0.77 mm mrad normalized. The effective emittance (beam divergence of 90 mrad) is 1000 mm mrad. The different orientation of the emittance patterns is due to the different distance between the extraction system and the measurement device because of the different geometries of the ion sources. Transforming the emittance pattern of argon back to the position where the nickel emittance has been measured is yielding an emittance pattern with the same orientation. The small argon beam divergence of 45 mrad and therefore small effective emittance reflects the cold plasma which is produced by the CHORDIS. The ion temperature for the gaseous ion source is typically in the range of tenth of electron volts. Due to the ion generation process in a vacuum arc plasma the ion temperature is in the order of a few electron volts leading to a larger beam divergence of 90 mrad and therefore to a larger effective emittance which is two times higher as in the case of argon. The large beam divergence is intensified by the high transversal energy of ions in a vacuum arc ion source. The single ellipses of the argon beam are broader as the an in the nickel case. On the one hand this is due to the fact that these are a supperposition of two ellipses produced by the ion beam and by the coexisting neutral particle beam. The neutral particles are generated within the extraction system in the first gap between plasma and screening electrode by charge exchange. These ellipses have a slightly different orientation because the ion beam experiences the defocusing effect of the secreening electrode while the neutral particle beam remains unaffected by this. This is responsible for a broadening of the single emittance pattern. The measured fraction of these neutral particles may be as high as 20 % of the extracted beam.

Heidelberg Ion Therapy (HIT)

A proton beam has been provided for a period of 19 days for commissioning measurements of the RFQ, foreseen for the Heidelberg therapy accelerator. This beam has been provided by a MUCIS ion source at a temporarily build test bench. The dedicated ion sources (Supernanogan ECR ion sources) for this accelerator have been delivered by Pantechnik [5] to the accelerator site of HIT and are ready for assembly at the low energy beam lines.

Uranium Material for the Ion Sources

Future supply of uranium cathodes turned out to be a problem. For the PIG ion source as well as for the MEVVA ion source depleted, metallic uranium ($\leq 0.3\%$ U^{235}) is required. Whereas we simply could buy these kind of electrodes on the market up to 2001, we are now faced with the fact, that the available uranium material is either sintered material or is such as sensitive to atmosphere, that it is unusable within the ion source. Both, sintered materials, and the newly delivered material tends to become dusty during operation, finally the electrode becomes brittle and unusable. In addition, the ion source itself, imposed to the uranium dust become unusable. One problem is, that we are not allowed to machine uranium in our workshop, which makes any modification of the available material impossible. This problem is unsolved in the moment for the MEVVA ion source, but it will become a problem for the PIG source also as soon as all old electrodes have been used.

References

[1] K. Tinschert et al., "Status of the 28 GHz Superconducting ECR Ion Source Project ISIBHI–MSECRIS", this report.

[2] KOBRA3-INP, INP, Junkernstrasse 99, 65205 Wiesbaden, Germany

[3] P. Spädtke et al., "Accel-Decel Extraction System for PIG Ion Sources", GSI Report 2002-2, 2002

[4] R. Hollinger et al., "High Current Ion Source Development and HOSTI", this report.

[5] Pantechnik S. A.; 12, rue Alfred Kastler, Caen France

SIS18 Status Report

P. Spiller, K. Blasche, U. Blell, P. Forck, H. Klingbeil, G. Franchetti, B. Franczak,
C. Omet, M. Kirk, A. Peters, H. Reich, H. Ramakers, A. Redelbach, U. Scheeler, P. Schütt,

GSI, Darmstadt, Germany

In parallel to the beam production for the ongoing experimental programs, accelerator development have been conducted with various goals: a) Improvement of the beam performance for the running experimental programs, b) upgrade of SIS18 for the planned FAIR operation and c) experiments in preparation of the HIT therapy synchrotron operation.

a) Beam Performance for the Running Experimental Programs

Due to the lack of a suitable MEVVA source material, increasing the maximum intensity of uranium beam could not been addressed. However, an intensity of about $2x10^9$ ions can still be reached by multi-multi-turn injection using the Penning source. This beam intensity level is meanwhile achieved for a number of other heavy ions like, Ag, Pb or Ta, whether by standard multi-turn injection using the MEVVA source or by multi-multi-turn injection using the Penning source. Experiments have been conducted with the goal to improve the spill microstructure. It was tried to reduce the ripple by increasing the chromaticity setting. However, increasing the chromaticity with a gap voltages of 1-2 kV on the flattop appeared to show no significant signs of improvement in the microstructure, whereas theory shows that it should be the case. However, by misaligning the cooler's mean electron energy, a distinct improvement of the spill structure was observed.

Different changes in the data supply and machine operation were introduced. A pause time for data processing was introduced at the end of the machine cycle. The electron cooler control was simplified and the event mode operation completed. Furthermore, in order to avoid self bunching during high current operation the RF frequency setting was modified.

b) Upgrade of SIS18 for the Planned FAIR Operation

In preparation of the FAIR operation of SIS18, a first long shut down is planned for first upgrade measures in summer 2006. Preparations for the following hardware projects have been performed in 2005:

a) High Current Transformer

The maximum measurable beam current of about 100 mA of the existing high current transformer was touched in several machine runs during the last year. Therefore, a new DC high current transformer has been bought and tested. For the installation of the new transformer, the mechanical design has been finished and the manufacturing of the components has been started.

b) Injection Septum

In order to enable an injection of the low charge state U^{28+} ion beams with the reference injection energy of 11.4 MeV/u, the field strength of the electrostatic injection septum must be increased. To provide the required electrical strength a new septum with enlarged vacuum chamber and new electrode geometry has been designed. In parallel a new high voltage power supply unit for the generation of up to 300 kV has been ordered. The design of the new electrostatic septum incorporates also a profile monitor close to the septum entrance and a collimator for the protection of the septum in case of beam misalignment. All components are under construction.

c) UHV System Upgrade

The operation with low charge state heavy ions requires a very low static and a sufficiently stabilized dynamic vacuum. Therefore, all existing magnet chambers will be replaced by new NEG coated chambers, which shall provide a distributed pumping power which is about a factor of 100 higher than at present. It is planned to equip the first vacuum sector with the new coated chambers in the summer shut down 2006. The UHV group has acquired the licence for NEG coating and has built a coating facility at GSI. All chambers for the first UHV sector are available and being prepared for the NEG coating.

d) Bunch Compression Cavity

The first of two new RF compression cavities which will generate an RF voltage of 80 kV in total will be installed in the summer shut down 2006. All components of the cavity and the final amplifier stage have been ordered and manufactured and will be assembled and tested with the new supply unit. In parallel the development of a fast semiconductor gap switch is being performed in collaboration with the company BEHLKE.

e) Power Connection

In order to ramp SIS18 with the maximum possible magnetic field rate, a new independent power connection is required. The present connection restricts the maximum pulse power to 5 MW only. The new power connection which will be available in June 2006 allows running SIS18 with a maximum pulse power of up to 30 MW, which is the expected power at a ramp rate of 10 T/s up to 12 Tm. In parallel to the set-up of the new power connection, power- and mechanical measurements have been conducted in the surrounding power grid and the closest major power plants.

c) Experiments in Preparation of the HICAT Therapy Synchrotron Operation.

The knock out feedback to the exciter for slow extraction now works yielding more rectangular spills in the macrostructure. Latest therapy experiments have succeeded to eliminate the remaining beam in the spill interruptions. In parallel to the switching off of the exciter, a small shift of 0.5-1kHz in the cavity frequency was produced in order to shift the tunes temporarily away from the resonance.

ESR Operation and Development

K. Beckert, P. Beller, P. Forck, B. Franzke, V. Gostishchev, F. Nolden,
A. Peters, U. Popp, A. Schwinn, M. Steck
GSI Darmstadt

1 Machine Development

1.1 Deceleration

The main machine development activity was the first demonstration of deceleration of a beam of bare ions to an energy of 4 MeV/u and the fast extraction to the reinjection channel. This mode of operation is required to provide highly charged ions for the HITRAP project [1]. The deceleration to this low energy had been demonstrated before with modest beam intensity and a relatively low deceleration rate. Optimization of the deceleration process is one aspect of the machine development. The other aspect, which was tested for the first time, was the kicker extraction of the decelerated beam and the development of detection techniques for short pulses of low energy extracted beams.

These tests were performed with a beam of $^{48}Ca^{20+}$ injected into the ESR at an energy of 400 MeV/u. As in previous runs the beam was first cooled by the electron cooling system and then decelerated with a ramp rate of 0.1 T/s to 30 MeV/u. At this energy electron cooling was applied again before the beam was decelerated with a ramp rate of 0.05 T/s to 4 MeV/u. At 4 MeV/u cooling was applied again and the coasting beam was extracted by firing the fast kicker with a pulse length between 1 μs and 3 μs, which is the maximum flat top time of the kicker. This way between one and three quarters of the circulating beam, depending on the length of the kicker pulse, were extracted into the reinjection channel. The rest of the beam continued to circulate in the ESR and was cooled to a new equilibrium. The quality of the extracted beam is well reproducible as it is determined by electron cooling and consequently independent of the history of the beam.

The extracted beam was detected in the reinjection channel with a fluorescent screen. The camera picture was digitized, Figure 1.1 shows a sequence of horizontal and vertical beam profiles detected in the reinjection channel. The sequence shows successive extractions of the coasting beam which was cooled between the extractions. Due to the fact that only about half of the stored beam was extracted, for each extraction the intensity of the extracted beam is reduced by about a factor of two compared to the previous extraction.

The beam profiles reproduce the expected reduction of the beam emittance with decreasing intensity, which is a consequence of an equilibrium between intrabeam scattering and electron cooling. The beam profiles agree reasonably with measurements of the stored beam, which showed for 5×10^6 stored $^{48}Ca^{20+}$ ions at 4 MeV/u an emittance of 0.9 mm mrad and a momentum spread of 1.8×10^{-4}.

Another experiment with a decelerated $^{136}Xe^{54+}$ beam was aiming at maximum acceptance at the low magnetic rigidity after deceleration. By fine tuning of focussing (quadrupoles) and chromaticity correction (sextupoles) elements the momentum acceptance could be increased slightly above $\pm 1\%$ down to an energy of 7 MeV/u. This was evidenced by the simultaneous storage of the two charge states 54+ and 53+, which was produced in the ring by electron capture of the bare ion. By variation of the beam energy with the electron cooler, it could be confirmed that the full momentum range is available for stable beam storage.

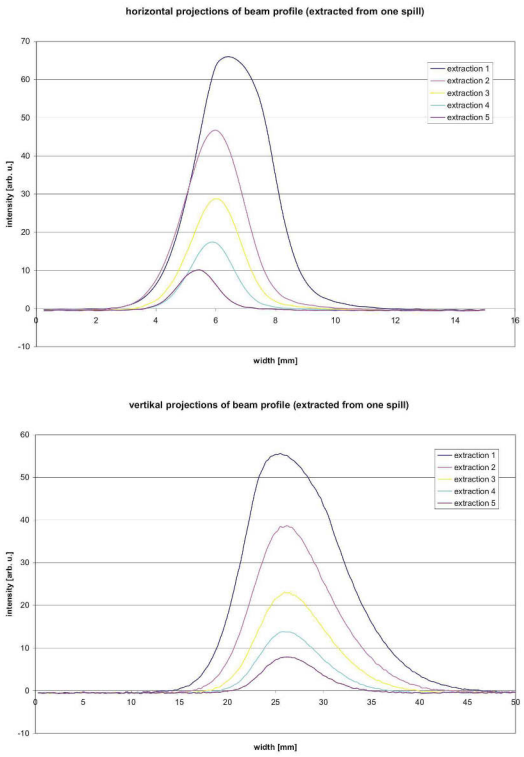


Figure 1: Horizontal and vertical profile of a $^{48}Ca^{20+}$ beam decelerated to 4 MeV/u and extracted to the reinjection channel. The different traces were taken after five successive extraction kicks. Each kick extracted about half of the stored beam leaving the other half in the ring. The initial intensity was about 6×10^6 stored ions.

1.2 Internal Target

Another goal of machine development is the preparation of high luminosity in experiments employing the internal target, particularly in operation with a hydrogen jet. A $^{136}Xe^{54+}$ at 350 MeV/u was injected for these experiments. More than 2×10^8 ions could be injected in a single bunch. By accumulation in the ESR the intensity could be increased beyond 1×10^9 stored ions, which corresponds to an electric current above 20 mA. The highest intensities, however, were rather unstable showing a reduced lifetime due to coherent transverse oscillations. For the long term operation a new bunch was injected every few minutes and added to the stored beam. This way the ion current was kept on a level of 5-10 mA, corresponding to $3 - 6 \times 10^8$ stored ions.

For the operation with highest thickness of the hydrogen target the nozzle of the internal target was cooled to liquid nitrogen temperature. A target thickness of up to 2×10^{12} cm^{-2} was reached. The operation of the hydrogen target was still rather unstable requiring typically one warm up of the nozzle per day. The reason for the unreliable operation of the cooled nozzle is under investigation.

An average stored current of 6 mA, which was easily achieved, and a target thickness of 1.5×10^{12} cm^{-2}, which could be maintained over typically one day, before the nozzle had to be warmed up for one to two hours, resulted in a luminosity of 2×10^{27} cm^{-2}s^{-1}. In addition to electron cooling with an electron current of 300 mA, which provided stronger cooling than required to compensate the heating in the target, a moderate rf voltage of 100 V was applied to provide a beam with a time structure and to have additional compensation for the energy loss in the target.

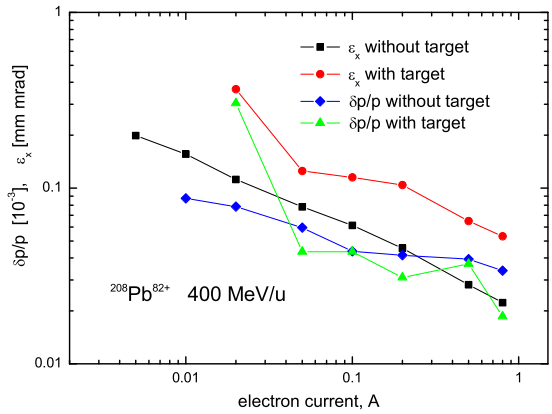


Figure 2: Comparison of momentum spread and horizontal emittance (1σ-values) of a ^{208}Pb^{82+} beam at 400 MeV/u with and without a gas jet in the internal target. The electron current applied for cooling was varied. The thickness of the krypton target was 5×10^{12} cm^{-2}.

The maximum target density which can be compensated by electron cooling was studied with heavy target gas and variation of the cooling rate. A plot showing emittance and momentum spread of the stored cooled beam of 2×10^8 bare lead ions at 400 MeV/u with and without a krypton gas jet target is shown in Figure 2. With target the emittance is significantly increased. Moreover, a clear increase of the beam emittance and momentum spread is observed for electron currents below 50 mA. The cooling with small electron currents cannot compensate the heating by the internal gas jet target. These measurements will allow benchmarking of simulation codes which are used for the design of experiments in the FAIR project.

1.3 Lifetime of low charge states

A series of measurements was performed to study the lifetime of ions in a low charge state as usually obtained after the first stripping stage of the UNILAC. These measurements were performed with U^{28+} in the energy range 11-75 MeV/u and with Xe^{18+} in the energy range 11-50 MeV/u [2]. The lifetimes in the ultrahigh vacuum and in selected gases injected in the internal gas jet target were measured. Lifetimes for the various energies in the vicinity of 1 min without target agree well with an average base pressure of the ESR slightly below 2×10^{-11} mbar and with the measured composition of the residual gas, which is dominated by hydrogen and contains a fraction of argon of less than 1 %.

2 Operation for Physics Experiments

A rather large range of beams has been provided for experiments. Singly charged $^7Li^{1+}$ ions were stored and cooled by electron cooling for an experiment studying the relativistic time dilatation by laser spectroscopy of fast moving ion beams. The lifetime of 130 s of the cooled Li beam provided good conditions for the experiment. The fraction of ions in the metastable state, which are required for laser excitation, will be increased in future by optimized parameters of the ion source.

Low beam energy, but highly charged ions were available with decelerated beams. The lowest energy with bare uranium ions and their extraction after electron capture in the electron cooler was 12 MeV/u. Up to 1×10^7 $^{238}U^{92+}$ could be decelerated to 12 MeV/u and prepared for extraction. The extraction period of the cooled beam by charge changing could be extended over several minutes.

Various experiments used incompletely stripped ions. $^{238}U^{88+}$ was stored to study electron emission after interaction with the internal target. Electron distributions were measured employing the electron spectrometer installed downstream of the internal target and a special imaging technique [3]. Ionized projectiles were detected in coincidence with the standard particle detectors systems installed in the bending section of the ESR. The program of dielectronic recombination studies was continued comparing two different isotopes (^{142}Nd, ^{150}Nd). Special care was taken to store both isotopes in the Li-like charge state under identical conditions, particularly in the interaction region with the electron beam of the cooling system, which was operated as an electron target with variable relative velocity.

Experiments with fragment beams from FRS where continued. Emphasis was on the time-resolved Schottky mass spectrometry employed in the study of the beta-decay of highly charged ions. $^{140}Pr^{58+}$ ions produced by fragmentation of a primary ^{152}Sm beam were stored and cooled in the ESR. A reduction of the total cooling time from 12 s to 6 s was achieved by a combination of stochastic pre-cooling and final electron cooling. The possibility of single ion detection by frequency analysis of the Schottky noise allowed a precise measurement of the decay time of the nucleus [4].

References

[1] J. Alonso et al., GSI Scientific Report 2004, GSI 2005-1, p. 212.
[2] R.D. Dubois et al., contribution to this report.
[3] M. Nofal et al. GSI Scientific Report 2004, GSI 2005-1, p. 214.
[4] F. Bosch et al., contribution to this report.

Accelerator Operation Report

U. Scheeler, D. Wilms
GSI Darmstadt

This report describes the operation statistics of the accelerator facility in the year 2005. The data has been collected with the help of the program PROST [1].

1. General overview

Altogether there were four beam periods scheduled in 2005. Operating time started on January 12th with a beam period of about nine weeks. The second block of operation started after a three week shutdown at the beginning of April and ended on June 9th. After a short shutdown of two weeks the third period started on June 22nd and lasted until August 25th. The following three weeks were used for shutdown and upgrade work again. The last beam period started on September 14th and was initially supposed to last until the end of November. Because of extensive experiment requests for additional beam time this block was prolonged until December 15th.

	Total beam time 2005	Target time 2005	Target time 2004
UNILAC	7208 h	6132 h	5449 h
SIS	8361 h	6315 h	5885 h
ESR		1374 h	1225 h

Table 1: Overall beam time of the accelerator facility

Table 1 shows total beam time and achieved target time for different experimental areas. In 2005 accelerator operating time (number of working hours) increased by 40 days compared to 2004, now amounting to 6928 hours, the equivalent of 866 accelerator operation shifts. The former annual maximum was 800 shifts. Thus the increased operation time has led to a considerable higher amount of target time for both accelerators.

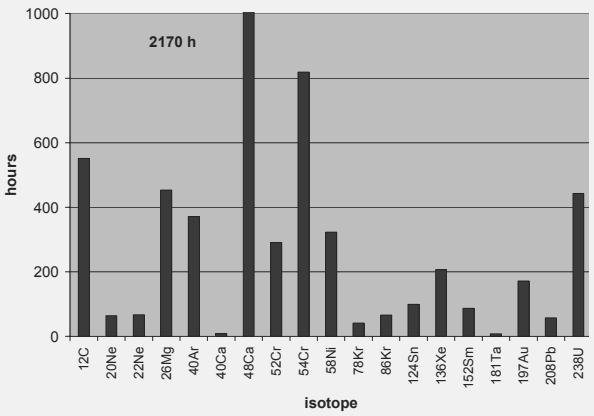


Figure 1:
Accelerated isotopes for UNILAC experiments

Over the year ion beams of 30 different isotopes from hydrogen to uranium were accelerated and delivered to 21 low energy experiments at UNILAC and 38 high energy experiments at SIS. As shown in Figure 1 UNILAC experiments mainly requested medium heavy elements. The synchrotron users preferred carbon and uranium beam (Figure 2).

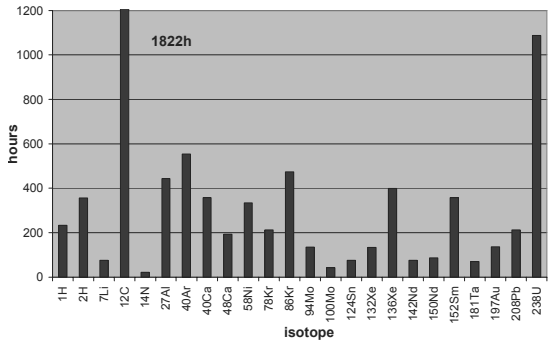


Figure 2:
Accelerated isotopes for SIS experiments

2. UNILAC Operation

The beam time for the UNILAC experiments is summarized in table 2. The ratio of "number of hours for listed category" to "total amount of beam time" is expressed as a percentage and indicates the efficiency of accelerator operation.
The increase in operation time and the reduction of unscheduled downtime by a factor of 2 led to a higher amount of beam time available for the experiments. The necessary tuning time remained on the same level as last year. The time for accelerator development was on the rise again in 2005, as it had been in 2004.
A closer look at the unscheduled down time reveals that it

	(h)	Percentage
Target time for exp. runs	6132	85%
Beam for experiment tests	14	0,2%
Accelerator development	236	3,3%
Accelerator tune-up	415	5,7%
Ion source replacement	112	1,6%
Unscheduled down time	209	2,9%
Retuning	70	1,0%
Stand-by	20	0,3%
Total beam time	7208	

Table 2: Beam delivered to UNILAC experiments

can be attributed to failures of rf-amplifiers (63h), injectors (30h), computer control (2h), beam diagnostics (3h) vacuum system (16h), magnet power supplies (37h), infrastructure (21h), and others (42h). Compared to 2004 the down time for rf system and injectors is significantly lower. Instabilities of beam position (mainly at the end of the poststripper section) sometimes led to difficulties in operation. Problems with the beam chopper and a vacuum leak in the RFQ at the High Charge State Injector caused changes of the beam time schedule in the 4th block. Besides this no major problems had to be reported.

	(h)	Percentage
Beam available for SIS injection	9025	92,2%
Accelerator development	39	0,4%
Ion source replacement	104	1,1%
Accelerator tune-up	282	2,9%
Unscheduled down time	317	3,2%
Retuning	21	0,2%
Total beam time	9788	

Table 3: UNILAC beam delivered to SIS in 2005

Table 3 displays the beam time provided by the UNILAC for SIS injection. Beam availability grew by 2.8 % compared to 2004, less time for tune up was needed and the share of down time decreased.

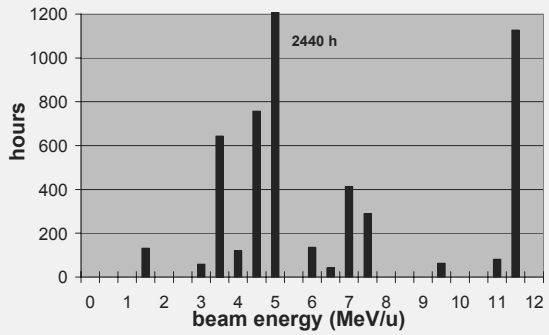


Figure 3: Beam energies of the UNILAC experiments

In Figure 3 the target time of the UNILAC experiments (without beam injected into SIS) is displayed versus beam energy. Beam energies in the range from 4 to 5 MeV/u mainly resulted from experiments for super heavy element synthesis, nuclear chemistry experiments took place at 7 MeV/u and energies at 11.4 MeV/u were used for material science, biology and plasma physics experiments.

3. SIS Operation

Operation statistics for SIS are shown in table 4. Compared to last year the total target time considerably increased. The amount of beam time for the ESR and for patient treatment remained constant. The time for SIS accelerator development increased as it did at the UNILAC.

The main part of down time was related to problems with magnet power supplies, at least 108 h. Vacuum down time was 42 hours in this year. Other categories of technical problems led to the following loss in beam time: infrastructure (21h), rf-amplifiers (increased to 22h), beam diagnostics (2h), controls (15) and others (80h). A four day operation break due to a vacuum leak at the end of the transfer channel to SIS is not included in down time statistics, because the experiments could be shifted. There were a lot of shorter breaks due to low reliability with the flow meters of magnet cooling in the

	(h)	Percentage
Beam for target area	5079	60,7%
Therapy	1236	14,8%
Beam for experiment tests	0	0,0%
Target time	6315	75,5%
Beam delivered to ESR	1374	16,4%
Accelerator development	248	3,0%
Accelerator tune-up	134	1,6%
Unscheduled down time	290	3,5%
Total beam time	8361	

Table 4: SIS operation time in 2005

beamlines behind SIS. Fluctuations in the spill structure (below 1µsec) have to be reduced at high intensities. At the moment there is unfortunately no tuning concept, but beam diagnostics were installed to investigate the behavior of the beam concerning time structure of the spill.

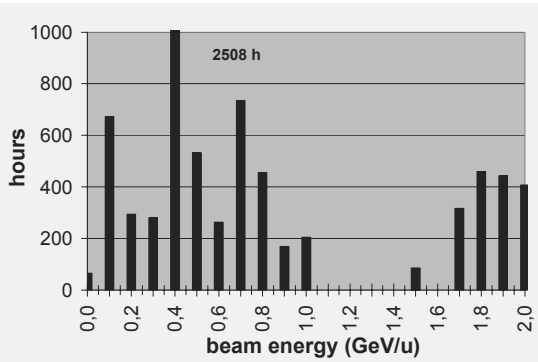


Figure 4: Beam energies of the SIS experiments

Figure 4 shows the beam time versus energy for the SIS experiments. The high amount of target time at energies at about 400 MeV/u stems from the acceleration of 12C beam for cancer therapy. As main users of gold, lead and uranium the ESR got beams with energies up to 500 MeV/u and the fragment separator up to 1GeV/u. The highest energies were delivered for pion production and for atomic physics experiments.

References

[1] **PR**ogramm für **O**perating und **ST**atistik

Beam Diagnostics Developments for Current Operation of SIS18 and HEBT

P. Forck, G. Fröhlich, T. Hoffmann, W. Kaufmann, A. Peters, J. Schölles, GSI, Darmstadt, Germany
D. Lyakin, ITEP, Moscow, Russia

Abstract

Three beam diagnostics developments for the current operation of the SIS18 and the high energy beam transport (HEBT) lines are described: a service program for SIS18 diagnostics, a tool for spill structure analysis and the renewed beam position monitor system in the HEBT lines.

Service program for SIS18 diagnostics

Since SIS operating started, a lot of measurements for beam characterisation within the synchrotron were done only by experts. With the help of a new service program called SPEKY, measurements especially in frequency domain are now prepared to be applied by the whole operator staff..

The handling of some relevant beam diagnostic devices such as phase probe or Schottky pick-up including a spectrum analyser has to be simplified for standard measurements during beam time. Every member of the operating staff has to be able for execution of the following standard measurements: determination of revolution frequency, determination of particles momentum-spread and monitoring of the bunched beam intensity.

A dedicated spectrum analyser that is integrated in the operating console for accelerator control, is fed by preselected signal sources and dedicated triggers (Fig. 1). Interfacing the spectrum analyser via IEC-bus allows a slim handling that fits the needs of the measurement.

Block diagram

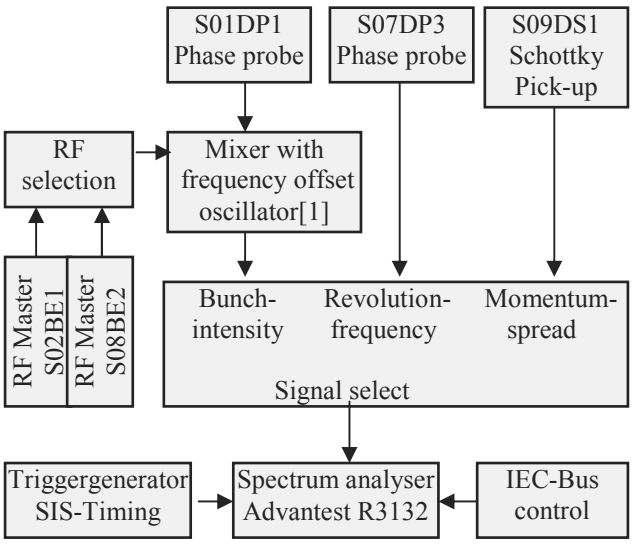


Figure 1: Fixed set-up for standard beam diagnostics in frequency domain at the SIS18

Signal selection and trigger parameters will be executed automatically depending on what measurement was chosen by the operator. In addition there is a status readout from all concerning devices. This status information is also available during a measurement. To give an impression how the service program looks like during the measurement of momentum spread with the Schottky pick-up , a screen shot is shown in Fig. 2.

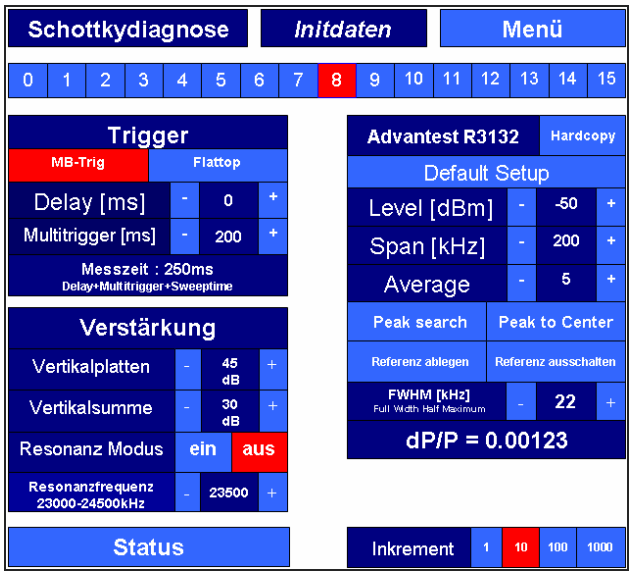


Figure 2: Graphical User Interface for diagnostics with the Schottky pick-up

For determination of the real revolution frequency or momentum spread the operating personnel has to select a virtual accelerator of interest and all parameters like trigger and analyser settings will be preset. Only the gain range of the probe signal has to be adapted depending on the beam current. Reading and interpretation of the displayed frequency peak delivers information that constitutes the basis for accelerator fine tune especially for high beam currents.

Spill-Structure Analysis

During the last years, a comprehensive VME-based data acquisition system for counter application at SIS and the High Energy Transfer Lines was developed [1]. This package ABLASS (**A** **B**eam **L**oss measurement **A**nd **S**caling **S**ystem) is frequently used during machine operation. The data evaluation on a LINUX server offers a versatile display of many measured parameters, among them the simultaneous time evolution of all chosen channels during the SIS18 cycles, the loss distribution as detected by Beam Loss Monitors and the long term trending (e.g. the

delivered particles per spill) with storage capabilities of several days

Due to the sensitive resonance driven slow extraction, the extracted particle flux exhibits significant fluctuations. These fluctuations can be flattened by extracting a bunched beam or by the proper choice of several SIS18-parameters, e.g. the chromaticity [2]. For several experiments, a smooth beam delivery is essential for target protection and maximization of experimental rate capability.

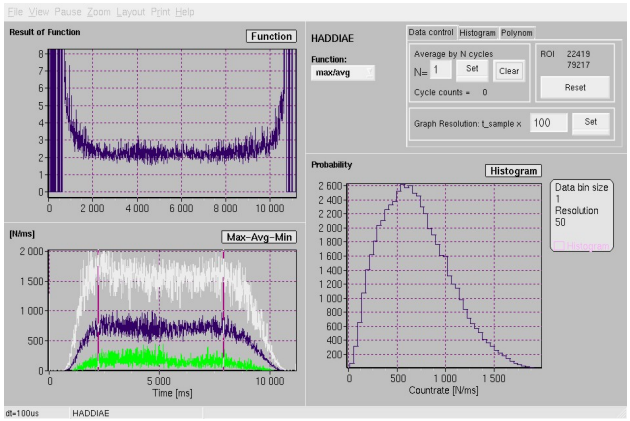


Figure 3: Online evaluation of a single spill of 1750 MeV/u Ar^{18+} delivered to HADES. The particle counter is read with 100 µs time increment for the 10 s spill. Upper left: Maximum-to-average ratio during the spill; Lower left: Minimum (bottom), average (middle) and maximum (top) within a 10 ms time slice; Right: Histogram of the count rate.

Online optimisation of the spill structure is achieved by using the new feature ABLASS – Q-Analysis. It allows a fast readout of the counts down to the µs region and a variable parameter adoption for the data analysis. The related functionality is described for the example shown in Fig. 3: The rate from a particle counter is recorded with a 10 kHz sampling frequency. Within a 10 ms time window the minimal, maximal and average count rate is displayed and the ratio maximum-to-average is used for a meaningful characterization of the spill quality. Due to the beam bunching during extraction, this ratio is decreased by a factor of ~3 compared to the un-bunched case.

For the adoption to the time requirements of the experiment, the max-to-average and min-to-average rate is calculated for different readout times, realized as a function of bin size, as displayed in Fig. 4. For the given example, interruptions during beam delivery are present for readout times below ~500 µs. For an un-bunched beam this would be typically several ms.

A further characterization is yielded for the probability distribution of the count rate. In the displayed case for a bunched beam extraction (Fig. 3, right), the maximum of this distribution histogram is slightly lower than the average rate. For an un-bunched beam, the maximum of this distribution would be about one order of magnitude lower, reflecting the occurrence of breaks during beam delivery.

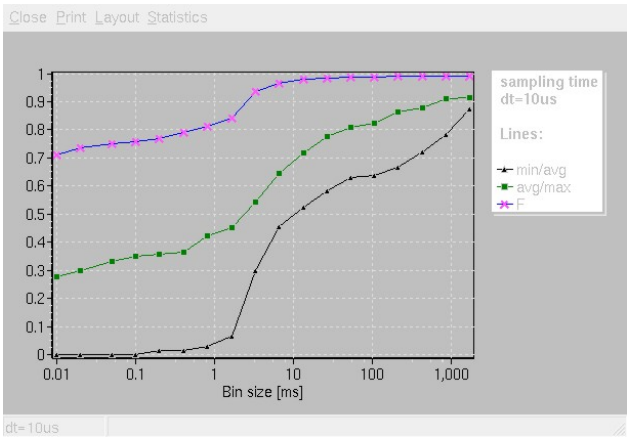


Figure 4: Minimum-to-average ratio (triangle), average-to-maximum ratio (cube) and duty factor (cross) as a function of time binning (from 10µs to 1s) for the spill of Fig. 3.

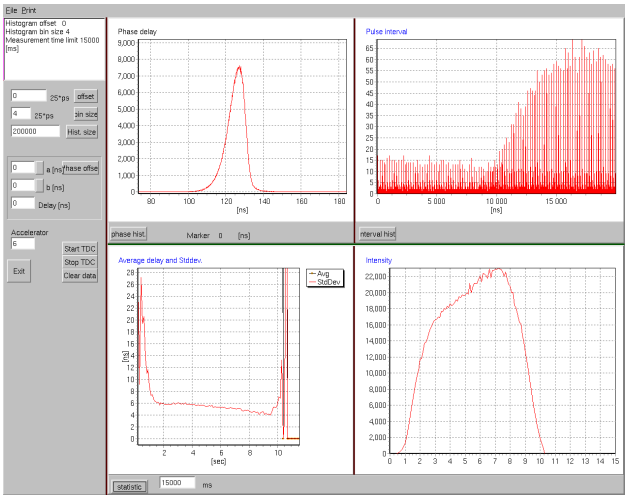


Figure 5: TDC-spectra recorded with same beam parameters as in Fig. 3. The bunch repetition frequency is 5.191 MHz, corresponding to 192 ns. Upper left: Time distribution of the particles relative to the bunching RF-phase, about half of an RF-period is shown. Lower left: The standard deviation σ of this distribution during the spill. Upper right: The probability distribution of ascending particle hits composed of ~6 ns broad peaks and 192 ns distances. Lower right: Intensity distribution during the spill.

For the characterisation of the bunched beam extraction on the ns time scale, the new feature ABLASS – TDC is used: A multi-hit Time-to-Digital converter measures the arrival time of the ions compared to the bunching rf-phase with 25 ps resolution. As displayed in Fig. 5, this distribution is strongly correlated with the RF. The standard deviation is only 6 ns in this case, which is about one order of magnitude shorter than the width of the circulating bunches. The TDC data also leads to the time spacing of

consecutive particle hits (Fig. 5, top right) and its display should be used to match the delivered particle current to the maximal count rate capability of the experiment. These measurements cover the time range from ns to s and are online available for beam optimisation.

Accuracy and the high performance of the measurements are gained by the chosen VME data acquisition hardware such as a CES RIO3 800 MHz CPU, a dedicated DSP (AD-BlackFin) board for the Manchester encoded GSI timing, a SIS3820 32-Bit-Multiscaler, a SIS3808 Pulse generator and the CAEN V1290N Multihit TDC 21 Bit with 25ps resolution.

Single Shot Beam Position Monitor for the HEBT Lines

Within the scope of the coming SIS-18 upgrade and the FAIR project, single bunch handling with intensities from 10^7 up to $3 \cdot 10^{13}$ charges/bunch and minimum lengths of 30ns (FWHM) are expected at the GSI high energy beam transfer lines. Thus, the demand of an accurate real-time position monitoring is mandatory. The basic principle (see Fig. 6) of the novel system is the use of digital storage oscilloscopes for data acquisition instead of conventional A/D-converter-cards [3], because this solution is cheap in comparison to the usage of commercial high speed samplers in standard crates like VME, CompactPCI or PXI.

At the moment, the HEBT is equipped with ten systems of broad-band beam position pick-ups (BPMs) with an aperture of 126mm. A variation in signal magnitude from µVolts up to several Volts is expected and signal conditioning before data acquisition is necessary. A recently developed 60dB amplifier optimised for the best common mode amplification covers a dynamic range from less than -80dBm up to +20dBm with a bandwidth of 200MHz [4]. This is sufficient to get the lower signals in reasonable DSO acquisition ranges.

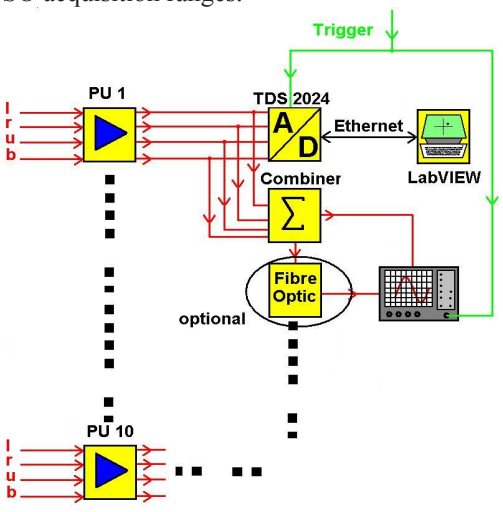


Figure 6: BPM system overview

For data acquisition four channel Tektronix TDS 2024 DSOs with 2GSa/s and vertical resolution of 8bit are in use. At the moment all pick-ups are equipped with the new amplifiers. In a first test run, five of them are connected to DSOs. The Tektronix TDSPCS1 OpenChoice® software is in use to observe the signals and a LabVIEW application controls the entire BPM-system.
The lower limit of the amplifier resolution is reached with about $1.8 \cdot 10^7$ charges per bunch (see Fig.7). In this case $(S/N)/N \approx 2$ is essential. This means that the worst case of the lower limit with 10^7 charges per bunch is nearly reached.

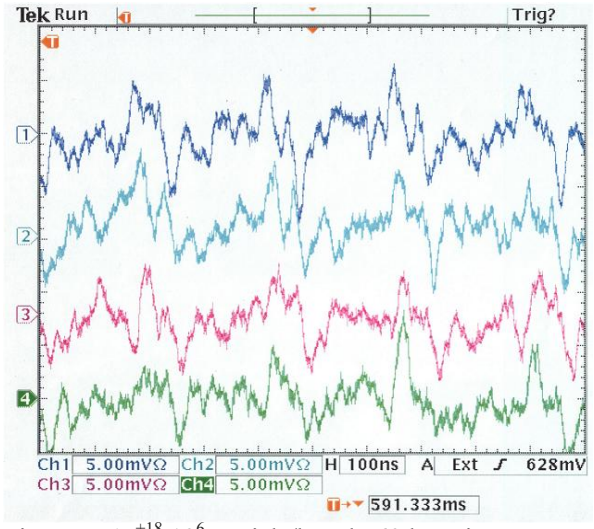


Figure 7: Ar^{+18} 10^6 particle/bunch, 60dB gain

With a maximal gain of 60dB over a bandwidth of 200MHz, there is sufficient gain reserve to fulfil the requirements. It is also succeeded to provide common mode gain matching for each position plane automatically. This will be done by a build-in variable voltage controlled attenuator.

To get an improvement for the low intensity limit, an additional low-pass-filtering close to the pick-up can produce relief. But this is not tested yet. Also an attenuator for limiting higher levels is still missing. The next necessary step will be further tests of the interaction between the DSOs, software and the entire electronics. A software solution for beam position calculation is also in progress. The project will be finished 2006 after installation of all components.

References

[1] T. Hoffmann et al., Proceedings of BIW 2004, Knoxville, USA, p. 294
[2] P. Forck et al., Proceedings of EPAC 2000, Vienna, Austria, p. 2237
[3] Y.Shoji, A.Ando, S.Hashimoto, "Single pass beam position monitor of NEWSUBARU", Himeji Institute of technology, Proceedings of the 2001 Particle Accelerator Conference, Chicago, USA, p. 1637
[4] J.Schoelles, W.Kaufmann, "New Single Shot Beam Position Monitor of the GSI High Energy Transfer Line", DIPAC´05, Lyon, June 2005, p.190

Commissioning of the SIS12/18 Cavity Synchronization System

H. Klingbeil, H. Damerau, M. Kumm, P. Moritz, G. Schreiber, GSI, Darmstadt, Germany
B. Zipfel, FH Fulda, Fulda, Germany

After initial tests of the synchronization system for the RF cavities in the SIS12/18 in 2004 [1], hardware development as well as commissioning have been continued in 2005. Potential improvements could be suggested from the data collected during machine development experiments with the new system. The cavity synchronization is now operational.

The Cavity Synchonization System

The key modules of the cavity synchonization system are the DSP system, the FPGA Interface Board and the DDS unit. The DSP sub-system is used for high-precision phase and amplitude detection and for fast closed-loop control algorithms. It includes analog preprocessing in the IF range, ADC and DAC modules, as well as digital interfaces and comfortable diagnostic features. A universal FPGA Interface Board has been developed that provides an interface to the central control system and several other interfaces which are used as standards in the GSI synchrotron RF group. This board is used as base for the new DDS that serves as actuator in closed loop RF control systems. To switch between different reference sources, a remote-controlled distribution amplifier has been developed and put into operation.

Performance of the Cavity Synchronization

Fig. 1 shows a measurement for the phase difference between the gap signals of the two SIS18 cavities when the cavity synchronization loop is closed (green: maximum and minimum, blue: average). A maximum phase difference of $\pm 2^\circ$ is achieved. The measured threshold of the closed loop is below 50V per cavity. The larger deviations at the beginning are due to the limited bandwidth of our automatic gain control (AGC). The development of a faster AGC is currently in progress.

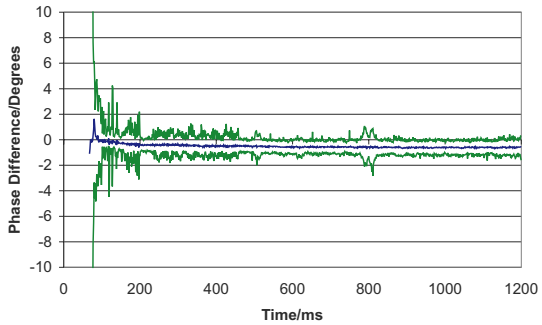


Figure 1: Closed loop phase difference of gap signals during acceleration

On-Line Measurement of the Longitudinal Beam Characteristics

During machine development experiments, the performance of the cavity synchronization system has been verified and no additional particle losses due to the operation of the SIS12/18 with two synchronized RF cavities instead of one has been observed. Additionally, the RF capture has been analyzed experimentally in more detail [3].

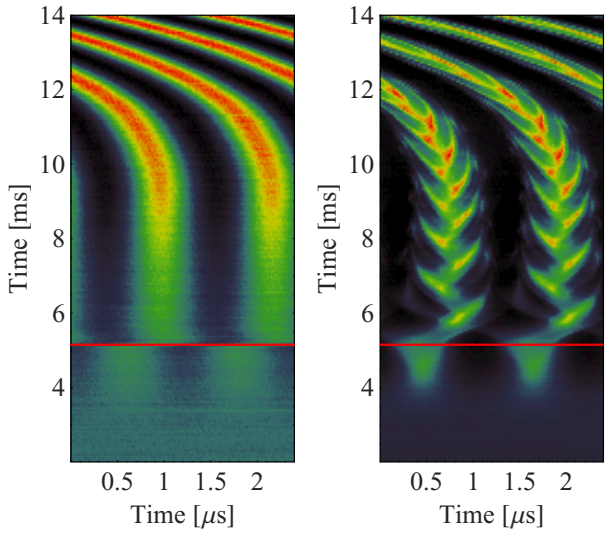


Figure 2: Density plot of gap (left) and bunch (right) signal during RF capture (time goes from bottom to top). Only two of the four bunches in the SIS are shown. The bunches start to oscillate coherently due to a phase jump of the RF voltage (red line).

A new quasi- online visualization technique has been developed and put into operation to observe the longitudinal behaviour of the bunches. The longitudinal bunch signal from a pick up and the gap voltage of an RF cavity are recorded in segments and directly displayed versus time in a density plot as presented in Fig. 2. This measurement and visualization technique has already been proven to be extremely versatile during the commissioning of the cavity synchronization, as well as during machine development experiments.

References

[1] H. Klingbeil, "RF Development for the SIS12/18 Upgrade Program", GSI Scientific Report 2004, GSI Report 2005-1, GSI, Darmstadt, Germany, 2005, pp. 312-313

[2] H. Klingbeil, "A Fast DSP-Based Phase-Detector for Closed-Loop RF Control in Synchrotrons", IEEE Trans. Inst. Meas., Vol. 54, 2005, pp. 1209-1213

[3] O. Chorniy, H. Damerau, G. Schreiber, B. Zipfel, "Machine Development Experiments on Cavity Synchronization in the SIS12/18", GSI internal note SIS04075.HF, GSI, Darmstadt, Germany

High Current Ion Source Development and HOSTI

R. Hollinger, M. Galonska, F. Heymach, K. D. Leible, K. Ochs, P. Spädtke, GSI, Darmstadt, Germany

As part of the FAIR project the beam intensity and quality at the high current injector have to be enhanced, in particular for uranium ion beams. For this purpose the high current test injector HOSTI assembly will be completed for the exploration of the matching of maximum ion currents to the post-acceleration gap [1]. The combined system of extraction system and the post-accleration gap accelerates ions to the desired energy of 2.2 keV/u while the technical installation can provide up to 5.87 keV/u. This combined system has been studied using the KOBRA3-INP simulation code [2], simulating an uranium ion beam with the correct charge state distribution [3]. The results of these theoretical studies are to be confirmed at HOSTI. The surveys on the effect of different electrode designs of the post acceleration gap on the ion beam quality and current are summarized in Fig. 1. It shows the presently installed electrode design of the post-acceleration gap (left) while Fig. 1 (right) is presenting an improved electrode design. Both designs are four electrode arrangements with a high voltage electrode, and encapsulated screening electrode. The necessary high voltage for a uranium beam is in the order 100 kV with a gap distance of several 10 mm, the screening voltage is typically several kilovolts with negative polarity.

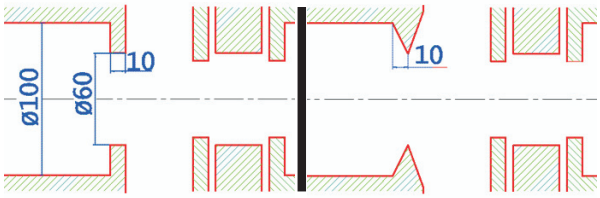


Figure 1: Present (left) and improved (right) electrode design by a better electrode shaping of the post-acceleration gap. The screening electrode is located between two grounded electrodes. Distances are in mm.

It is apparent that the improved electrode design is yielding an ion beam with a smaller emittance (340 mm mrad, rms) which is 15 % less than the emittance achieved with the present design (400 mm mrad, rms) while yielding the same ion beam current of 50 mA (Fig. 2). Consequently the beam brightness is increased by a factor of approximately 1.5. However, the emittance is still 2.5 times higher than the acceptance of the existing GSI RFQ accelerator at the high current injector HSI. Adapted to the specific situation, emittance values are not normalized. The aberrations of the ion beam are reduced which is leading to a decrease of the divergence angle of the accelerated ion beam. Momentarily it is 50 mrad with the present design, but it will be reduced to 25 mrad with the improved electrode design.
All these conditions will minimize beam losses in the low energy section and are therefore favorable for the beam transport.

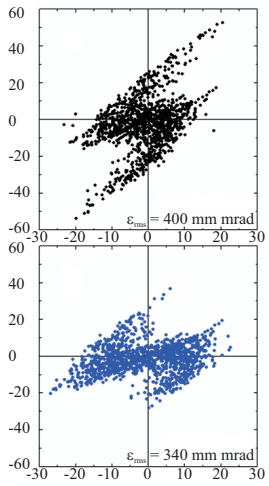


Figure 2: Emittance of the accelerated beam, top: present design, bottom: improved design. Horizontal: position in mm, vertical: angle in mrad.

The technical design of HOSTI is completed, and HOSTI is only partly assembled. It is envisaged to implement the improved acceleration gap in summer/autumn 2006 and to start emittance studies on the accelerated ion beam with a slit grid emittance scanner. In addition further electrode designs will be studied by experiment. Further improvement of the extraction system of the ion source will be a future option after optimizing the acceleration gap. A promising design is the use of a 19 hole multiaperture system instead of the commonly installed 13 hole system. An increase of the beam current of about 50 % is expected for this extraction system. The adoption of this extraction system implies that the acceleration gap will be optimized for the acceleration of such an intense ion beam. In order to fulfill the requirements of the FAIR project concerning intense uranium ion beams, it is inevitable to complete the assembly of the HOSTI and to put it into operation. Systematic emittance studies on the combined system of extraction system and post-acceleration with a high current emittance scanner are an essential instrument to achieve this aim.

References

[1] R. Hollinger et al., "Transversale Emittanzmessung am Injektor Nord", GSI Report 2001-02, Juli 2001
[2] KOBRA3-INP, INP, Junkernstr. 99, 65205 Wiesbaden, Germany
[3] W. Xiang, GSI Report 2004-02, July 2004

Parameterization of Kicker Coupling Impedances*

B. Doliwa[1], H. De Gersem[1], T. Weiland[1], U.Blell[2], and O. Boine-Frankenheim[2]
[1]Technische Universität Darmstadt, Institut für Theorie Elektromagnetischer Felder, [2]Gesellschaft für Schwerionenforschung, Darmstadt

The SIS-18 upgrade is an important step towards the realization of the FAIR project. Besides the resistive beampipe walls, the nine kicker modules mounted in the SIS-18 may have a parasitic influence on the beam stability. The general goal of our numerical field calculations is to quantify the latter effect in terms of coupling impedances [1]. Here we report on the development of a parametrized kicker model which may be helpful for reducing the coupling impedances through a modification of the external pulse-forming network (PFN).

Equivalent-Circuit Model

As is well known, the dominant contribution to the transverse kicker coupling impedance arises from the inductive coupling of the beam to the PFN of the kicker. A simplified model describing this phenomenon has already been proposed by Nassibian and Sacherer in [2]. Here we rephrase their argument, arriving at a slightly modified model.

The starting point is the observation that the horizontal coupling impedance can be written as

$$Z_x(\omega) = \frac{-v}{\omega \Delta^2 I_1^2} \int d^3 r j_z^* E_z, \qquad (1)$$

where v is the particle velocity, I_1 the beam current strength, and j_z describes an excitation consisting of two anti-parallel currents I_1 along the z-axis with separation Δ. The fictive current loop represented by j_z may be interpreted as the primary coil of a transformer, which inductively couples to the kicker-magnet coil via the mutual inductance, M. The current I_2 induced in the secondary coil in part flows through the external network -represented by the impedance Z_g- and the parallel impedance Z_p within the kicker module, which may arise from the capacitance at the PFN feed-throughs, for instance. In addition to the coupling to the external network, we introduce the impedance $i\omega L_s$ in series with the primary coil, accounting for the direct interaction of the beam with the kicker device, mainly with the ferrite blocks. With the respective self inductances L_1 and L_2 of the primary and secondary coils, the kicker transformer model has the form shown in Fig. 1.

Since $Z_x = \frac{v}{\omega\Delta^2} Z_{ab}$, with Z_{ab} measured between the points a and b in Fig. 1, we finally arrive at the expression,

$$Z_x = \frac{v}{\omega \Delta^2} \left[i\omega L_s + \frac{\omega^2 M^2}{i\omega L_2 + \frac{Z_g Z_p}{Z_g + Z_p}} \right]. \qquad (2)$$

*Supported in part by DFG under contract GraKo 410 and GSI, Darmstadt.

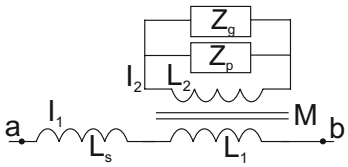


Figure 1: Kicker-PFN equivalent circuit

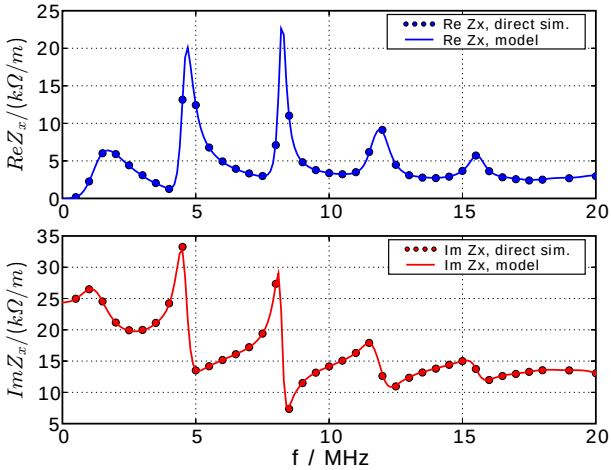


Figure 2: Comparison of direct simulation with simplified model.

In order to have a full parameterization of the SIS-18 kickers, the quantities L_s, L_2, M, and Z_p have to be determined from numerical field computations. However, a closer look at the last equation reveals that only three of the four parameters are independent. More specifically, one may rewrite the latter expression as $Z_x = [AZ_g + B]/[Z_g + C]$, with new parameters $A(\omega)$, $B(\omega)$, and $C(\omega)$.

Numerical Results

Using the measured impedance of the external network [3] as input we directly compute Z_x, see Fig. 2. In order to check the equivalence of the simplified model, we separately determine the parameters A, B, and C from three frequency sweeps with $Z_g = 0$, ∞ and 50Ω. As shown in Fig. 2, the agreement of the impedance model with the direct simulation is excellent.

References

[1] B. Doliwa, H. De Gersem, and T. Weiland, proceedings of the PAC 2005, p. 1820

[2] G. Nassibian, and F. Sacherer, NIM 159(1), p. 21, 1979.

[3] U. Blell, proceedings of the PAC 1997, p. 1727

Status of the 28 GHz Superconducting ECR Ion Source Project ISIBHI–MSECRIS*

K. Tinschert, GSI Darmstadt, for the ISIBHI collaboration [1]

Introduction

Besides regularly delivering C^{2+} ions for the heavy ion therapy the HLI is mainly serving the high duty cycle experiments investigating superheavy elements (SHE), which request beams of rare isotopes in most cases. The most suitable ion source for this purpose is an ECR ion source (ECRIS) with its high efficiency and low material consumption. At GSI there is the demand to increase the intensity of the ECRIS as it is also requested at other European accelerator laboratories. Within EURONS of FP6 the joint research activity ISIBHI (Ion Source for Intense Beams of Heavy Ions) started at the beginning of 2005. A prototype of a new generation of ECRIS will be built that can be adapted to the different requirements in cw and pulsed mode. Higher ion beam intensities from an ECRIS require an increase of the plasma density. According to semiempirical scaling laws and to experiments at present ECRIS [2, 3, 4] the electron density is directly related to the square of the microwave frequency. Considering the electron cyclotron resonance condition and following scaling laws for the magnetic flux in ECRIS [3] the increased microwave frequency requires an increase of the magnetic field above 2.2 T implying the use of superconducting magnets.

Superconducting Magnets and Cryostat

The minimum B configuration of MS–ECRIS will consist of a mirror field generated by 3 coaxial solenoidal coils and of a radial field generated by hexapolar coils which are coaxial with the mirror coils. The solenoid coils are surrounding the hexapole. The cryostat design includes high temperature superconducting (HTS) current leads and cryocoolers for operation in stand–alone mode. Four separate power supplies (3 for the solenoids and one for the hexapole) will be used to get optimal conditions for adjusting the magnetic plasma confinement. The magnetic system and the cryostat are under construction at ACCEL Instruments [5]. The double wall plasma chamber is water-cooled and should be able to dissipate a maximum RF power of 10 kW. It is placed in the central warm bore of the magnet cryostat. A 2 mm lead shield between the plasma chamber and the insulator will reduce the X-ray emission thereby reducing the heat load of the cryostat. High voltage insulation will be provided by a 4 mm thick polyetheretherketone (PEEK) cylinder between the chamber and the cryostat. The length of the plasma chamber will be about 650 mm.

Microwave Injection

The RF power to be injected into the plasma chamber of MS-ECRIS is estimated to be about 6 to 10 kW following the experiences of previous experiments [2]. The microwave injection line will reproduce the reliable layout used for the SERSE ECRIS including filters and bending unit [2]. A new design for the 60 kV dc break is under study, allowing the full power transmission for long time operation. The microwave will be provided by a 28 GHz transmitter based on a gyrotron tube of 10 kW maximum power. The cryostat provides magnetic shielding of the stray field produced by the superconducting magnet system using high permeability iron for the external walls. So the residual magnetic field will be lower than 2 mT at 4 m distance from the cryostat at the position of the transmitter in order to ensure the safety of the gyrotron tube.

Experimental Setup

The ECR injector test setup (EIS) at GSI [6] will be used to investigate the MS-ECRIS source. The presently installed CAPRICE ECRIS including support stand and extraction box will be replaced by the MS-ECRIS with its ancillary equipment while the beam transport line will be used in its present configuration but upgraded to handle the increased power dissipation caused by the high extraction currents of MS-ECRIS. The transport through the beamline has been studied with different computer codes to investigate the influence of space charge and its compensation. The maximum beam magnetic rigidity allowed by the beamline is 0.088 Tm, which is suitable for full characterization of any beam at a voltage of 40 kV or lower.

According to the time schedule of ISIBHI the experimental program will start after spring 2007 until the end of 2008.

References

[1] K. Tinschert, P. Spädtke, R. Lang, GSI, Darmstadt, Germany; G. Ciavola, S. Gammino, L. Celona, L. Torrisi, S. Passarello, L. Andò, INFN-LNS, Catania, Italy; M. Cavenago, A. Galatà, INFN-LNL, Legnaro, Italy; R. Leroy, C. Barue, GANIL, Caen, France; D. Hitz, P. Seyfert, CEA, Grenoble, France; H. Koivisto, P. Suominen, O. Tarvainen, JYFL, Jyväskylä, Finland; H. Beijers, S. Brandenburg, KVI, Groningen, Netherlands; D. Vanrooyen, TSL, Uppsala, Sweden; C. Hill, D. Küchler, CERN, Geneva, Switzerland; H. Homeyer, J. Röhrich, HMI, Berlin, Germany; L. Schachter, S. Dobrescu, NIPNE Bucharest, Romania

[2] S. Gammino et al.; Rev. Sci. Instr. 72 (2001) 4090

[3] D. Hitz et al.; Rev. Sci. Instr. 73 (2002) 509

[4] G. Ciavola et al.; Rev. Sci. Instr., in press

[5] ACCEL Instruments GmbH, Friedrich–Ebert–Str. 1, D–51429 Bergisch Gladbach

[6] K. Tinschert et al.; Rev. Sci. Instr. 69 (1998) 709

*Work supported by EU/FP6 EURONS

Test of the 350 MHz Superconducting CH-Cavity*

H. Podlech#, C. Commenda#, H. Liebermann#, I. Müller#, U. Ratzinger#
#Institut für Angewandte Physik der Johann-Wolfgang-Goethe-Universität, Germany

Abstract

The CH-structure is a new multi cell drift tube structure for the acceleration of low and medium energy proton and ion beams. Due to the mechanical stiffness of the cavity it can be realised for room temperature as well as for superconducting linacs [1]. A superconducting 350 MHz CH-cavity with a β=v/c of 0.1 has been developed. This prototype has 19 cells and is the first superconducting multi cell cavity. After room temperature tests first cryogenic tests have been performed successfully. With an obtained effective accelerating voltage of 3.6 MV the design voltage has been exceeded.

Test of the CH-structure

After the delivery of the cavity room temperature conditioning has been performed. An rf power of 300 W cw has been coupled to the cavity. Additionally, rf pulses up to 2 kW have been applied for the room temperature tests [2].



Figure 1: The superconducting CH-structure prepared for the first cryogenic test.

The cavity has been tested at 4.2 K in the new cryogenic laboratory in Frankfurt. At low levels some minor multipacting barriers occurred which could be processed within one hour. The maximum effective voltage which has been achieved so far was 3.6 MV in cw mode. This corresponds to an effective gradient of 3.4 MV/m for the full cavity length and 4.5 MV/m for the inner structure length of 9.5βλ. Figure 2 shows the Q-value as function of the gradient. The unloaded Q at low field levels was $5 \cdot 10^8$ at 4.2 K which corresponds to a total surface resistance of 110 nΩ. The BSC-resistance at 4.2 K is about 41 nΩ. A residual external magnetic field of 1 μT leads to a magnetic surface resistance of 4 nΩ. Therefore the residual resistance of the cavity is 65 nΩ. The rf power to reach tihs design voltage of 3.4 MV was about 15 W. At higher field levels field emission could be observed. In a next step the distribution of the emitted X-rays will be measured. Depending on these results an additional chemical preparation will be considered to increase the achievable fields.

Additionally, it is foreseen to test the prototype cavity in a horizontal cryostat under realistic conditions. For this reason the development of a mechanical as well as of a fast piezo tuner system has started. An existing horizontal cryostat will be modified to serve for this purpose.

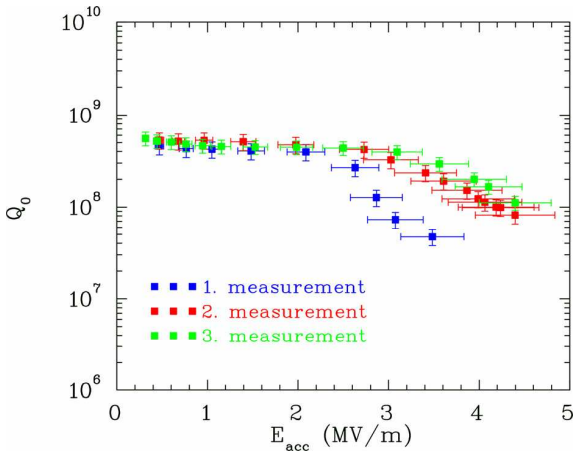


Figure 2: Measured Q-value as function of the gradient. The gradient definition is based on a length of 9.5βλ.

*Work supported by GSI, BMBF contr. No. 06F134I, EU contr. No. EFDA/99-507ERB5005, RII-CT-2003-506395

References

[1] H. Podlech, "Development of Room Temperature and Superconducting CH-Structures", LINAC'04, Lübeck, Germany, August 2004, p. 28-33, http://www.jacow.org.

[2] H. Podlech, H. Deitinghoff, H. Liebermann, H. Klein, U. Ratzinger, A. Sauer, R. Tiede, „ First Tests of the Superconducting CH-Structure", PAC'05, Knoxville, TN, USA, May, 2005, p. 3414-3416, http://www.jacow.org

Planned Installations and Experiments at the Frankfurt High Current Injector.

M. Droba, L. Chau, N. Joshi, O. Meusel, U. Ratzinger, IAP, J.W. Goethe-Universität D-60325, Ffm

M. Heil, FZ Karlsruhe/GSI Darmstadt.

Abstract

Two main experiments will be driven by the new 150 kV terminal at Frankfurt: The Frankfurt Neutron Generator at the Stern-Gerlach-Zentrum FRANZ and a novel High Current Storage ring based on a stellarator type magnetic guiding field.

High Current Ring

In the reports [1][2] we presented particle simulation results for the high current storage ring with respect to the toroidal magnetic field and its magnetic surfaces. It will allow high current beam accumulation experiments at different space charge compensation schemes as well as experiments in the fields of plasma, nuclear and atomic physics. One of the major tasks in this project is the development of an injection method.

Initial experimental setups are proposed to study beam injection into the high current accumulator ring. Various regimes should be tested and compared with theoretical and numerical predictions.

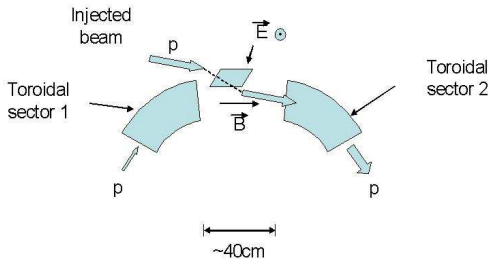


Figure 1: Two sectors with Toroidal 30° magnetic field at B_{centre}=0.6T.

An advanced setup will consist of two beams, where an injected beam is merged with a second beam passing two toroids (Fig. 1). Here the interaction between the beams and the ExB action will be studied. All elements for injection experiments are already specified.

Neutron generator

The second experiment driven by the new high current 150kV terminal will be the Frankfurt Neutron Generator at the Stern- Gerlach - Zentrum FRANZ. 40 ns Proton-Bunches with an energy of 120 keV will be produced at a repetition rate of 250 kHz, where a maximum pulsed current of 200 mA seems possible. The main acceleration will be done by a 175 MHz-RFQ with an output energy of 1.7 MeV (Fig. 2). In order to gain a high proton intensity and pulse lengths of 1 ns at the target a buncher-system of the Mobley-Type [3] is proposed, whereby periodic deflection at the one focus of a dipole-magnet will guide the bunches on suitable paths to the other focus, where a ^{7}Li-Target is located.

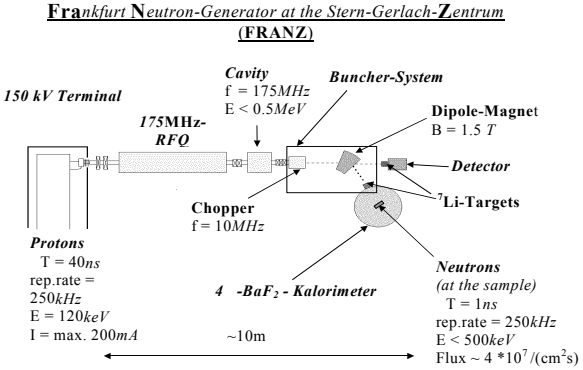


Figure 2: Schematic layout of acceleration part of neutron generator.

By $^7Li(p,n)Be^7$-reactions low-energy neutron-bunches will be produced with an average density of 4 10^7 cm^{-2} s^{-1} at a repetition rate of 250 kHz at a distance of 0.4m from the Li target. The upper limit for the neutron energy spectrum is 500 keV, depending of the final proton energy. Attractive neutron-capture-experiments can be performed by a 4 -BaF_2-Calorimeter, which has been built and successfully used at FZ Karlsruhe.

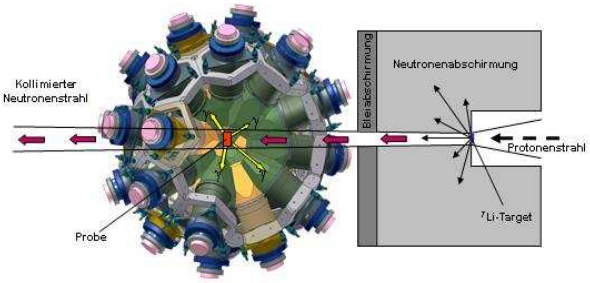


Figure 3: Neutron generation and gamma detector.

The outstanding beam parameters of FRANZ will be interesting for many experiments in the field of astrophysics, biology, chemistry, material sciences and of nuclear waste transmutation.

References

[1] M. Droba, Annual Reports 2003 High Energy Density Physics with Intense Ion and Laser Beams.

[2] N.Joshi, Annual Reports 2004 High Energy Density Physics with Intense Ion and Laser Beams.

[3] R.C. Mobley, „Proposed Method for Producting Short Intense Monoenergetic Ion Pulses“ , Phys. Rev. 88(2), 360-361 (1951).

Experimental Investigation of Resonance Induced effects in SIS18

G. Franchetti, A. Franchi, T. Giacomini, M. Kirk, A. Parfenova, A. Redelbach
GSI, Darmstadt, Germany

The upgrade of the SIS18 to become the injector of the SIS100 requires beam loss control/limitation at the percent level [1]. The storage of high intensity beams needs careful choice of the working point and of compensation of the resonances crossing the beam space charge tune spread (as large as $\Delta Q \sim 0.5$). However, the linear coupling may be useful for balancing beam emittances and improving multiturn efficiency. The study of the SIS18 resonances was carried out in a measurement campaign in 2004-2005 with low intensity beams. The correlation between beam loss

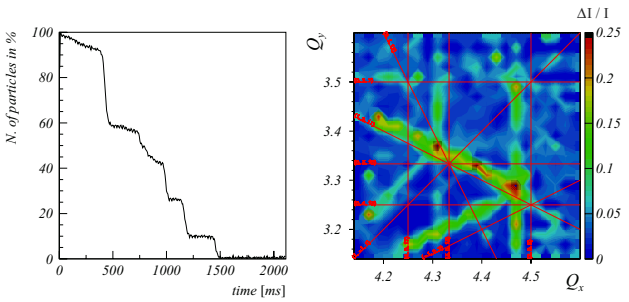


Figure 1: a) Beam intensity during crossing $(4.10, 3.15) \rightarrow (4.23, 3.6)$; b) Resonances in SIS18

and (setpoint) tune, obtained by varying dynamically the tunes within the machine cycle (Fig. 1a), allows the drawing of the resonance web and the identification of the resonances in SIS18 [2]. In Fig. 1b is plotted $(I_{i+1} - I_i)/I_i$ versus (Q_x, Q_y), where I_i is the beam current of an $^{40}Ar^{+18}$ DC beam at 11.4 MeV/u at the time t_i. The maximum beam current was 0.5 mA. Unfortunately the progressive beam degradation during the crossing of several resonances does not allow one to infer the beam profile prior to the crossing of each resonance and compare beam loss. To

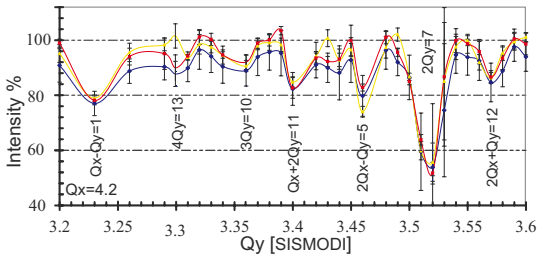


Figure 2: Relative beam loss for several tunes, inferred from both the BLM (black) and the IPM (pale grey x, dark grey y).

avoid this problem, in 2005 we measured beam survival of a $^{48}Ca^{+19}$ DC beam of intensity 33 μA at 11.4 Mev/u with beam loss monitor (BLM) and ionization profile monitor (IPM) [3]. In each measurement the tunes were fixed within the machine cycle. We measured beam loss for 32 working points along $Q_x = 4.2$, $3.2 < Q_y < 3.6$ which overlap with the high intensity tunespread discussed in [4]. Fig. 2 summarizes the findings in terms of % of beam survived after storage of 1.1 s. For every minima of beam intensity the correspondent resonance is identified. Note that the maximum beam loss for $2\,Q_y = 7$ is not consistent with Fig. 1a as the center of the resonance is not hit. The studies on the linear coupling were carried out by using 50μA of $^{40}Ar^{+10}$ DC beam at 11.4 MeV/u. The transverse beam profiles were measured every 10 ms for 0.5 ms with a spatial resolution of 2.1 mm which allows an acceptable estimate of the beam emittances. For the resonance center at $\overline{Q}_x = 4.26$ and $\overline{Q}_y = 3.30 \pm 0.01$ we measured a stop-band width of $|C| = 29 \pm 8 \times 10^{-3}$ being the amount of exchanged emittance in each plane equal to $\Delta\epsilon_{max} = |C|^2(|C|^2 + \Delta)^{-1}(\epsilon_{x0} - \epsilon_{y0})$ with $\Delta = Q_x - Q_y - 1$. The crossing of the resonance (in

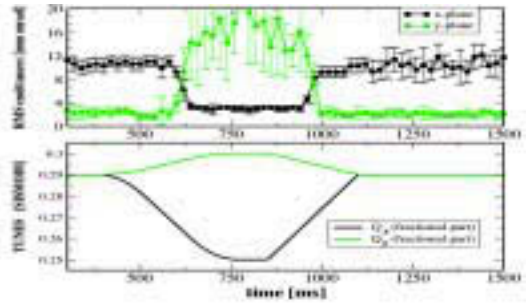


Figure 3: Emittance exchange driven by dynamic crossing the resonance $Q_x - Q_y = 1$.

500 ms) leads to emittance equalization in 250 ms (Fig. 3), whereas on the other side of the stop-band the emittances are, to within error, exchanged [5]. In Fig. 3 is also shown the reversed crossing (time $>$ 800 ms): the emittances are exchanged again returning to the original values. This behavior is consistent with the existence of an adiabatic invariant to which the beam distribution remains matched to. These studies show the existence in the SIS18 of 7 resonances (Fig. 2) which are relevant for high intensity beam storage and that emittance equilibration may be possible by slowly crossing the linear coupling line. The consequences of high intensity on beam loss in bunched beams and emittance control schemes are part of ongoing work in progress.

References

[1] GSI Technical Design Report.

[2] G. Franchetti *et al.*, GSI-Acc-Note-2005-02-001.

[3] T. Giacomini *et al.*, Proceedings of BIW 2004.

[4] R. Bär *et al.* EPAC 98.

[5] A. Franchi *et al.* GSI-Acc-Note-2006-03-001.

Excitation of atoms and molecules by highly relativistic ions

M. Bär*, B. Jakob, P.-G. Reinhard and C. Toepffer
Institut für Theoretische Physik II, Universität Erlangen-Nürnberg, Germany

Motivation

The inevitable interaction of the accelerated particles in a storage ring with the residual gas may serve as a future tool for beam analysis. In any case, one needs reliable theoretical estimates for the inelastic collision cross section. We report on an approach to acquire an inexpensive estimate for this cross section.

Formal Framework

The fast ion is described as a Coulomb charge moving on a straight line. The starting point and benchmark is to propagate the ground state single-particle wave functions of the target perturbed by the time-dependent electric and vector potentials of the projectile. This is done by time-dependent density functional theory (TD-DFT). The very fast collisions at small impact parameters b imply a very fast variation of the potentials requiring a tiny time step for TD-DFT calculations. This demands a lot of computational time, so two different approximations for the time evolution operator are derived. The first one based on Glauber theory is the "sudden approximation", which is valid for the very fast collisions at small b. A local operator can be derived [1, 2] whose applications on the ground state yields the state of the system after the collision. The approximation fails for large b, where the collisions are too slow to be "instantaneous". In that regime we use the time-dependent perturbation theory in dipole approximation [3, 4]. It can be shown that there is a range of b, where both approximations agree. The validity of both approximations is illustrated in figure 1 in the case of a hydrogen target by comparison with the time resolved TD-DFT calculations.

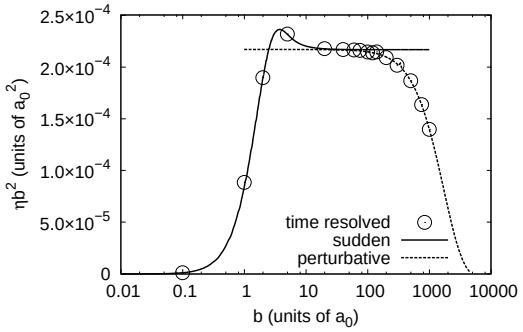


Figure 1: Total inelastic transition probability η for the proton-hydrogen collision with proton velocity $\beta = v/c = 0.99$ as function of the impact parameter b.

* Supported by the BMBF project 06 ER 128

Results

Combining sudden approximation and the perturbative approach yields a compact expression for the total inelastic transition cross section σ [3]. The contribution from small b must be calculated numerically in the sudden approximation, while the regime of large b only requires the knowledge of the transition energy to the first excited state and the variance of the dipole operator taken in the ground state: $G = \langle\Psi_0|\Delta^2 D|\Psi_0\rangle$. For many-electron systems, this can be easily calculated by DFT. We find that σ mainly scales with G, see figure 2. The relative deviation is less than 5%. Thus one can approximately get the cross section σ_{X} for a given system X by relating it to the hydrogen cross section σ_{H} as $\sigma_{\mathrm{X}}(\beta) \approx \frac{G_{\mathrm{X}}}{G_{\mathrm{H}}}\ \sigma_{\mathrm{H}}(\beta)$. Finally, for practical purpose, $\sigma_{\mathrm{H}}(\gamma)$ can be expanded and expressed by

$$\frac{\sigma_{\mathrm{H}}(\beta)}{a_0^2} \approx \frac{Z^2}{\beta^2}\left[5.287\cdot 10^{-3} + \pi 6.695\cdot 10^{-4}(-2.4037 + 2\ln(\gamma\beta))\right] . \quad (1)$$

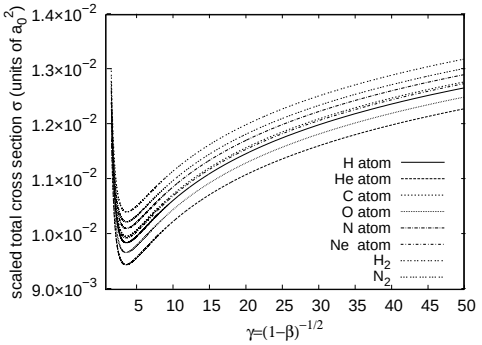


Figure 2: Total inelastic transition cross sections scaled by the relative dipole variances $\Delta^2 D_{\mathrm{H}}/\Delta^2 D_{\mathrm{X}}$

References

[1] B. Jakob, "Anregung von Wasserstoff durch Streuung hochenergetischer Ionen", Diplomarbeit, Erlangen (2002)

[2] B. Jakob, P.-G. Reinhard, C. Toepffer, G. Zwicknagel, "Excitation of Hydrogen by Relativistic Ions" GSI Annual Report (2002)

[3] M. Bär, B. Jakob, P.-G. Reinhard, C. Toepffer, accepted for publication in Phys. Rev. A (2006)

[4] M. Bär, "Anregungs- und Ionisationsquerschnitte von Atomen und Molekülen bei Streuung hochenergetischer Ionen", Diplomarbeit, Erlangen (2005)

Scattering of residual gas atoms by fast HCI beams

G. Zwicknagel
Institut für Theoretische Physik II, Universität Erlangen, Germany

The scattering of fast ion beams, circulating e.g. in a synchrotron, with the residual gas can lead to desorption when the scattered ions hit the aperture limiting devices of the structure [1]. Here, the impacts of recoiled residual gas particles may be an additional source for desorption. We are thus interested in the scattering of residual gas atoms or molecules by passing fast highly charged ions, focusing on the example of 1 GeV/u U^{92+}.

To make an estimate for the related cross section and the acquired recoil energies we treat the problem as elastic scattering between the nucleus (with charge $Z_R e$) of a residual gas atom and the projectile nucleus ($Z_P e$), neglecting the energy and momentum transfer to the bound electrons of the residual gas atoms or molecules. A classical description with classical trajectories can be employed because the Coulomb parameter $\eta = Z_R Z_P e^2/(4\pi\epsilon_0\hbar c\beta) = Z_R Z_P \alpha/\beta$ is for the envisaged energies and projectile charges ($\beta = v/c = 0.87$, $\gamma = 2$, $Z_P = 92$) about unity, or even larger for residual gas atoms heavier than hydrogen [2, 3]. As shown in [4], magnetic field effects and retardation corrections are rather small for relativistic (heavy) ion collisions at such energies ($\gamma = 2$) and will be neglected.

We then end up with classical scattering with an effective interaction potential $V(r)$ which accounts for the screening of the nuclei by the bound electrons. This can be treated by relativistic classical mechanics. Here closed expressions can be obtained for arbitrary spherically symmetric interactions $V(r)$ [5], if one collision partner remains at rest. As a next step of approximation we thus consider the scattering event in the frame where the heavy projectile (^{238}U) is (initially) at rest and treat it as infinitely heavy ($m_P \to \infty$). Replacing the effective $V(r)$ by the Coulomb potential, i.e. $V = \kappa/r$ ($\kappa = Z_R Z_P e^2/(4\pi\epsilon_0)$) and taking the screening into account only by restricting the allowed impact parameters b to values below a typical screening length $\lambda \approx 10^{-10}$m, the scattering angle $\theta(b)$ can be given explicitly [5] by

$$\theta(b) \;=\; \pi - \frac{2}{\zeta(b)}\mathrm{arccot}\left[\frac{b_0}{b\,\zeta(b)}\right],$$

where $b_0 = \kappa/(\gamma m_R c^2\beta^2) = Z_R Z_P \alpha\hbar/(\gamma m_R c\beta^2)$ and $\zeta^2 = 1 - \beta^2 b_0^2/b^2$. In the present case $\gamma = 2, \beta^2 = 3/4, Z_P = 92$ we get (with $m_R = A_R m_u$) $b_0 = (Z_R/A_R)\ 0.953\times 10^{-16}\mathrm{m} \approx 10^{-16}$m. For impact parameters b between $\approx 10^{-14}$m (sum of nuclear radii) and $\lambda \approx 10^{-10}$m (screening) we have $b_0/b \ll 1$, hence $\zeta \approx 1$. For the angle $\theta(b)$ and the cross section $d\sigma/d\Omega = [b(\theta)/\sin\theta]\,|db/d\theta|$ we thus arrive at

$$\theta(b) \;\approx\; 2\frac{b_0}{b} \;\ll 1, \qquad \frac{d\sigma}{d\Omega} \;\approx\; \frac{4b_0^2}{\theta^4}.$$

A Lorentz back-transformation (with $-\beta, \gamma$) to the lab-system, where the residual gas atoms are initially at rest, yields the scattering angle θ' and cross section

$$\tan\theta' = \frac{\sin\theta}{\gamma(1-\cos\theta)} \approx \frac{2}{\gamma\theta}, \quad \frac{d\sigma'}{d\Omega'}(\theta') \;\approx\; \frac{\gamma^2 b_0^2}{\left(\frac{\pi}{2}-\theta'\right)^3},$$

that is, the residual gas atoms are mainly scattered with angles close to $\pi/2$, i.e. perpendicular to the projectile beam, with a momentum (in the lab-frame) of

$$p'^2 = p^2\sin^2\theta + \gamma^2 p^2(1-\cos\theta)^2 \approx p^2\theta^2 = \gamma^2 m_R^2 c^2\beta^2\theta^2$$

i.e. $p'/m_R c = \gamma\beta\theta \ll 1$. This results in the corresponding non-relativistic recoil energies E_{kin} of the scattered residual gas particles (per u)

$$\epsilon = \frac{E_{\mathrm{kin}}}{\mathrm{u}} \approx \frac{1}{2}m_u v'^2 \approx \frac{1}{2}m_u c^2\gamma^2\beta^2\theta^2 \approx 1\mathrm{GeV}\theta^2\,.$$

These energies are varying from sub-eV for collisions with b around the screening length λ ($\theta \approx 10^{-6}, d\sigma'/d\Omega' \approx 10^{-14}$ m^2/rad) up to values of a few 100 keV for collisions where the nuclei almost touch ($\theta \approx 10^{-2}, d\sigma'/d\Omega' \approx 10^{-26}$ m^2/rad). As an estimate for the expected number of residual gas particles dN scattered per unit time with a recoil energy within $[\epsilon, \epsilon + d\epsilon]$ we get (since $\epsilon \propto \theta^2$)

$$\begin{aligned} dN(\epsilon) \;&=\; dN(\theta(\epsilon)) = J\frac{d\sigma}{d\Omega}(\theta)2\pi\sin\theta d\theta \approx J 8\pi b_0^2\frac{\theta d\theta}{\theta^4} \\ &\approx 2\pi b_0^2 m_u c^2\gamma^2\beta^2\, J\,\frac{d\epsilon}{\epsilon^2} \;\approx\; 10^{-25}\,\frac{J\,d\epsilon}{\epsilon^2}\ \mathrm{keV\,m^2} \end{aligned}$$

per one passing heavy ion (i.e. a 1 GeV/u U^{92+} ion). J is here the current density of the residual gas atoms in the frame where the heavy ion is (initially) at rest.

References

[1] H. Kollmus et al., GSI Annunal Report 2004, p. 316.

[2] J. Eichler, W.E. Meyerhof, *Relativistic atomic collisions*, San Diego CA, Academic Press 1995.

[3] N. Bohr, Kgl.Dan.Vidensk.Selsk. Mat.Fys.Medd. **18** (1948) no 8.

[4] R. Matzdorf, G. Soff, G. Mehler, Z. Phys. D**6** (1987) 5.

[5] R. G. Newton, *Scattering theory of waves and particles*, New York, McGraw-Hill 1966.

Progress in Direct Mass Measurements of Stored Exotic Nuclei

L. Chen[1,2], R. Knöbel[1,2], B. Sun[1], K. Beckert[1], P. Beller[1], F. Bosch[1], D. Boutin[1,2], J.J. Carroll[3], R.S. Chakrawarthy[4], D. Cullen[5], H. Geissel[1,2], J. Gerl[1], M. Hausmann[6], G. Jones[7], A. Kishada[5], O. Klepper[1], C. Kozhuharov[1], J. Kurcewicz[1], S. Litvinov[1,2], Yu. Litvinov[1,2], Z. Liu[7], S. Mandal[1], F. Montes[1], G. Münzenberg[1], A. Musumarra[8], C. Nociforo[1], F. Nolden[1], Z. Patyk[9], W.R. Plaß[2], Z. Podolyak[7], R. Propri[3], S. Rigby[5], N. Saito[1], T. Saito[1], H. Schatz[6], C. Scheidenberger[1], M. Shindo[10], M. Steck[1], P. Ugorowski[3], G. Vorobjev[1,11], P.M. Walker[7], H. Weick[1], S. Williams[7], N. Winckler[1,2], M. Winkler[1], H.-J. Wollersheim[1]

[1] *GSI Darmstadt,* [2] *JLU Giessen,* [3] *Uni. Yongstown,* [4] *TRIUMF Vancouver,* [5] *Uni. Manchester,* [6] *MSU East Lansing,* [7] *Uni. Surrey,* [8] *INFN-LNS Catania,* [9] *SINS Warsaw,* [10] *Uni. Tokyo,* [11] *PNPI Gatchina*

Two experimental methods for direct mass measurements were further developed at the FRS-ESR facilities. These are the time-resolved Schottky Mass Spectrometry (SMS) and Isochronous Mass Spectrometry (IMS).

Schottky Mass Spectrometry (SMS)

In the SMS, the exotic ions produced and separated with the FRS are stored and electron cooled in the ESR. Thus the velocity spread becomes negligible and the measured revolution frequencies characterize the mass-to-charge ratios of stored ions. The revolution frequencies are measured with the Schottky technique [1]. Peak areas in the frequency spectra are proportional to the number of stored ions and monitoring of their evolution in time provides half-lives. SMS has been very successful in recent years providing mass measurements for more than 600 neutron-deficient nuclides [1]. In 2004 the SMS measurements were extended to neutron-rich uranium projectile fragments. The details of the experiment are described in [2].

Nuclides in a wide mass range from A=238 down to about A=100 were identified in the Schottky frequency spectra. The lighter nuclides were produced by the in flight fission of the ^{238}U projectiles. They lie close to the valley of β-stability and have well-known mass values ideal for the calibration.

The heavier nuclides measured belong to the most neutron-rich nuclei presently known. A primary beam intensity of about $2 \cdot 10^9$ particles/spill and the ultimate sensitivity down to single stored particles were the prerequisites for measurement of the hitherto unknown isotopes. One example is illustrated in Fig. 1, where the frequency spectrum of the new isotope ^{235}Ac is shown. The half-life of hydrogen-like ^{235}Ac ions is derived from the time evolution of peak areas (panel "a"). Thus, the first identification and two fundamental properties are measured simultaneously in this experiment. According to the EPAX2 estimation [3] for the production cross-sections, more new isotopes are expected in the element range from Au to Ac.

Another goal of this experiment was the search for new long-lived isomers in neutron-rich heavy nuclides. Already in the preliminary analysis we identified a new isomeric state in ^{228}Fr.

A few hundred nuclides which are present in different frequency spectra will be combined in one correlation matrix for the final mass evaluation. In the future, the data obtained in this and other FRS-ESR experiments will be eval-

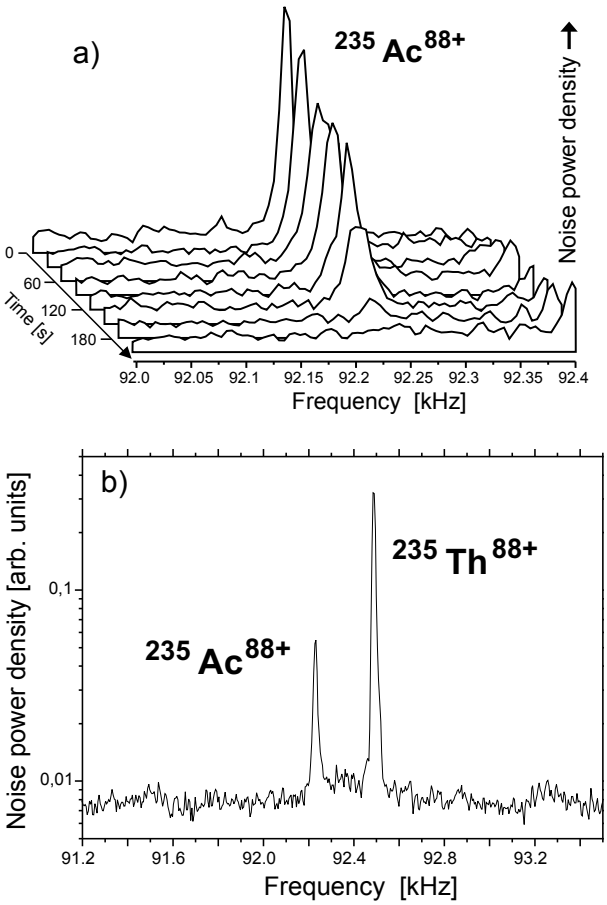


Figure 1: Discovery of the new isotope ^{235}Ac along with its mass and lifetime measurements applying time-resolved SMS [4]. The mass value has been extracted by calibrating with the known mass for ^{235}Th (panel "b"), whereas the half-life has been extracted from the time evolution of the peak-area (panel "a").

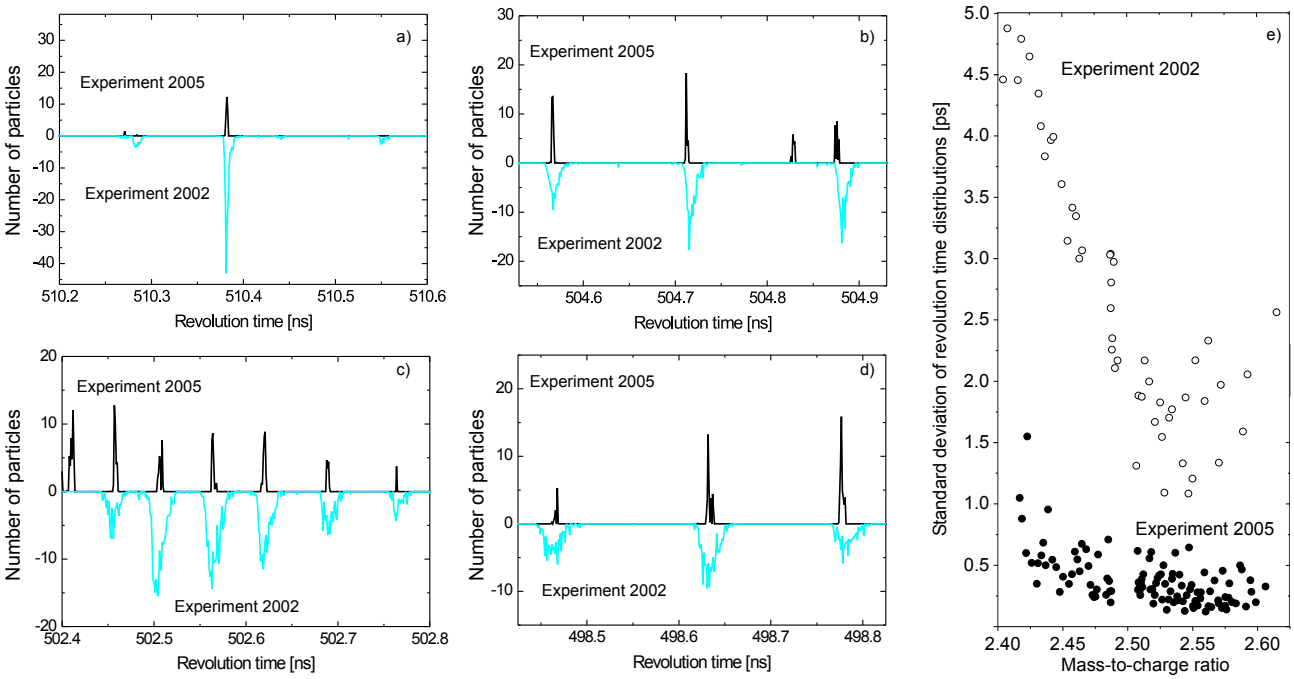


Figure 2: Measured time-of-flight spectra (panels "a"-"d") of uranium fission fragments. The time distribution for different isotopes are compared to an earlier run [7]. The new experiment is shown on the top, and our previous measurements are inverted for better comparison. The setting in these runs was almost the same. In panel "e" the improved peakwidths are shown as a function of m/q-ratio of the fragments.

uated in a common matrix. Thus the increasing number of correlations and of reference masses in the system should improve the mass accuracy (presently about 30 keV). One step in this direction was taken last year by measuring several tens of masses for stable and close-to-stability nuclides around mass number A=140 produced via fragmentation of ^{152}Sm projectiles.

Isochronous Mass Spectrometry (IMS)

In the IMS the storage ring is tuned to a special ion-optical mode in which the velocity spread of ions is in first order compensated by their orbit lengths. Mass-to-charge ratios of stored ions are obtained from the measured revolution times. The revolution times are measured with a time-of-flight detector placed inside the ESR. The IMS does not require cooling and can be applied to nuclides with half-lives as short as a few ten μs only [5].

A mass resolving power of 10^5 was achieved in previous experiments [6, 7]. Unfortunately, good isochronous conditions are valid only in a small part of the time-of-flight spectrum, which was used for the mass analysis [7].

In order to correct for the non-isochronicity the velocity or the magnetic rigidity of each particle has to be measured in addition. The power of this refined experimental method was tested last year. Uranium fission fragments have been investigated. The magnetic rigidity of the injected ions was determined to about $3 \cdot 10^{-4}$ in the dispersive midplane of the FRS.

This condition allowed us to improve the resolving power up to one order of magnitude and even for the best isochronous region by a factor of more than two. The obtained time-of-flight spectrum is compared to the one from [7] in Fig. 2. It is clearly seen that the resolving power in the new run stays almost constant for the entire spectrum, see panel "e".

This important achievement is presently obtained with slits at the FRS thus reducing the transmission. However, this reduction is compensated by the fact that much less statistics is now needed for each peak. For the future ILIMA project, a second time-of-flight detector is planned in the CR, which will provide turn-to-turn velocity measurements for each ion [8]. In this case there will be no reduction in transmission from the Super-FRS.

References

[1] Yu.A. Litvinov et al., Nucl. Phys. A756 (2005) 3.

[2] Yu.A. Litvinov et al., GSI Annual Report 2004 (2005) 79.

[3] K. Sümmerer, B. Blank, Phys. Rev. C61 (2000) 034607.

[4] H. Geissel et al., Proc. FINUSTAR-05; *nucl-ex/0510009*.

[5] M. Hausmann et al., Nucl. Instr. Meth. A446 (2000) 569.

[6] J. Stadlmann et al., Phys. Lett. B586 (2004) 27.

[7] M. Matoš, Doctoral Thesis, Universität Giessen 2004.

[8] S.A. Litvinov et al., GSI Annual Report 2005 (this volume).

Improved analysis method for bound state beta decay experiment of $^{207}Tl^{81+}$*

L.Maier[a], D.Boutin[b], F.Bosch[b], C.Scheidenberger[b], T.Yamaguchi[b,d], K.Beckert[b], P.Beller[b], T.Faestermann[a], B.Franczak[b], B.Franzke[b], H.Geissel[b,c], E.Kaza[b], P.Kienle[a], O.Klepper[b], C.Kozhurarov[b], Yu.Litvinov[b], M.Matos[b], G.Münzenberg[b,e], F.Nolden[b], Yu.Novikov[f], T.Ohtsubo[g], W.Plass[c], M.Portillo[b], J.Stadlmann[b], M.Steck[b], K.Takahashi[b], H.Weick[b], M.Winkler[b]
[a]TU-München; [b]GSI; [c]JLU Gießen; [d]Saitama University; [e]JGU Mainz; [f]NPI St. Petersburg; [g]Niigata University

In the bound state β-decay the created electron occupies a previously vacant orbit of the daughter atom. This process plays an important role in stellar nucleosynthesis which might strongly influence model calculations. Current lifetime measurements of bare nuclei at the ESR (GSI) are contributing to this field[1]

In the experiment described here (also see [2]) $^{207}Tl^{81+}$ ions were produced by fragmentation of a ^{208}Pb beam, separated in the FRS and injected into the storage ring ESR. To investigate the nuclear decay constants two experimental techniques were applied simultaneously. One is a detector telescope [3] inserted into the ring for directly counting the $^{207}Pb^{82+}$ ions from the free beta decay. In addition the Schottky-noise signal of the circulating ions was recorded in the usual way.

To compare the results from the two supplementary approaches a special software package was developed. A peak finder routine is able to trace all peaks in the Schottky spectra. The associated peak areas, which are proportional to the number of stored particles, are calculated including errors. This allows to observe both, the decrease of the $^{207}Tl^{81+}$ mother ions and the increase of the daughter $^{207}Pb^{81+}$ originating from the bound state beta decay channel (see fig 1). Providing a set of fixed parameters a complete analysis of the Schottky spectra is a matter of minutes per datafile without any user interference. This analysis can easily be accommodated to other applications, e.g. Schottky mass measurements.

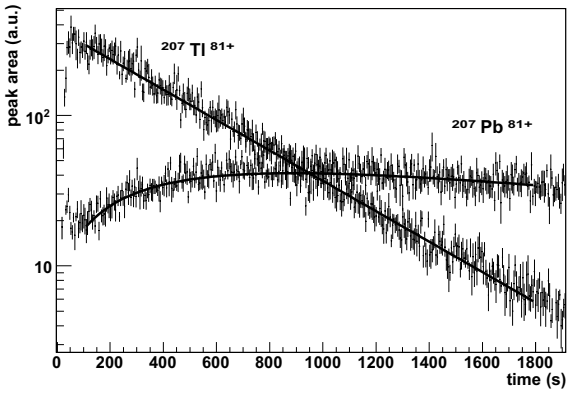


Figure 1: Example showing the progression of peak areas of the $^{207}Tl^{81+}$ and $^{207}Pb^{81+}$ ions in the Schottky spektra. Also drawn are the fits used to determine the decay constants.

The analysis of the data taken by the detector telescope delivers a classical decay rate (see fig. 2). Background suppression is achieved by determining the energy loss of the particles in a position sensitive stack of 14 Si-PIN-Diodes providing a charge resolution of $\Delta Z \approx 0.6$ (FWHM). Due to the statistics a maximum likelihood fit is required to derive the decay constant here.

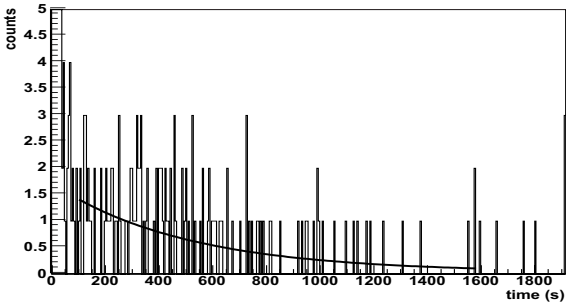


Figure 2: Exemplary decay curve measured with the detector telescope.

Figure 3 shows the results for the nuclear decay constant $\lambda_{\mathrm{nuc}} = \lambda_{\mathrm{bound\,beta}} + \lambda_{\mathrm{continuous\,beta}}$ of the two analysis methods (lab system). Obviously the error bars for the Schottky analysis are underestimated and a systematic uncertainty has to be included. The resulting decay constants $\lambda_{\mathrm{nuc}}^{\mathrm{Schottky}} = (1.93 \pm 0.02) \cdot 10^{-3}\,\mathrm{s}^{-1}$ for the Schottky analysis and $\lambda_{\mathrm{nuc}}^{\mathrm{Det}} = (1.92 \pm 0.03) \cdot 10^{-3}\,\mathrm{s}^{-1}$ for the detector telescope are in good agreement.

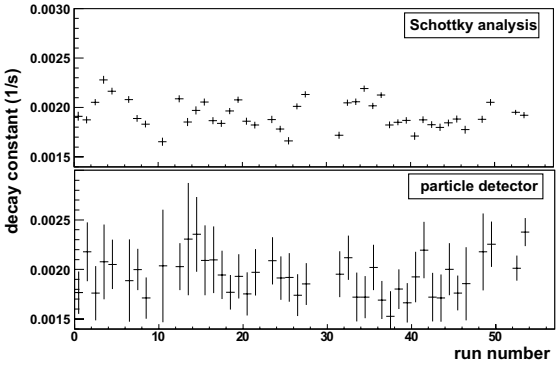


Figure 3: Decay constants as a function of the run number for the Schottky analysis and the detector telescope.

References

[1] T. Ohtsubo *et al.*, Phys. Rev. Lett. **95** 052501 (2005)

[2] D. Boutin *et al.*, GSI Scientifi c Report 2003, p. 18

[3] L. Maier *et al.*, GSI Scientifi c Report 1999, p. 210

* Work supported by GSI TM/KR-2 and BMBF 06 MT 190.

Rare Isotopes Investigation at GSI (RISING) Using Relativistic Ion Beams

H.J. Wollersheim[1] for the RISING Collaboration
[1]GSI, Darmstadt, Germany

Abstract

The Rare ISotopes INvestigation at GSI (RISING) project combines the former EUROBALL Ge-Cluster detectors, the MINIBALL Ge detectors, BaF_2-HECTOR detectors, and the fragment separator FRS at GSI for high-resolution in-beam γ-ray spectroscopy measurements with radioactive ion beams (RIB). RISING is aimed at frontier research in nuclear structure physics and will be of vital importance for the future FAIR and RIA facilities. The first results of the fast beam campaign are now available and a new series of experiments using stopped beams will be performed in 2006-7 to measure γ-rays following β-decay to excited states and to measure the direct decay of long lived isomers.

The RISING fast beam campaign

The SIS/FRS facility provides secondary beams of unstable rare isotopes after fragmentation reactions or secondary fission of relativistic heavy ions with sufficient intensity for in-beam γ-spectroscopy measurements. These exotic beams are used for Coulomb excitation or secondary fragmentation experiments in order to explore the nuclear structure of the projectiles or projectile like nuclei by measuring de-excitation photons. The set-up (see Fig. 1) was conceived in such a way that γ-ray detection efficiency was maximized, with the restriction that the energy resolution was at a percent level for each individual EUROBALL Cluster segment for recoil velocities of v/c=0.43.

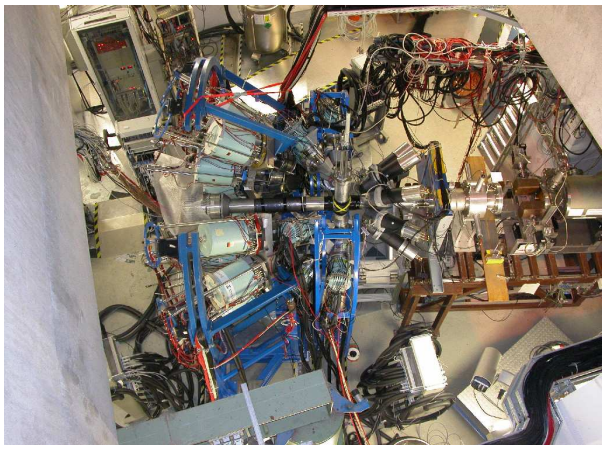


Figure 1: RISING fast beam set-up. The beam enters the set-up from the right. After hitting the target the ions are detected in the CATE detector. The γ-rays are detected using the HECTOR array (right), the MINIBALL detectors (middle) and the EUROBALL Cluster detectors (left).

Due to the Lorentz boost this implied a strongly asymmetric set-up whereby all detectors were mounted behind the target in three rings around the 16cm wide beam tube. With this set-up, a photopeak efficiency of 2.8% (at 1.33 MeV) and an energy resolution of 1.5% was attained [1]. In part of the fast beam experiments two additional rings holding seven additional MINIBALL triple detectors were added, increasing the photopeak efficiency to 7.3%. In the backward direction, eight BaF_2 detectors from the HECTOR array were mounted. These were used to measure very high energy γ-rays and also provide a very good timing reference. After the target the CAlorimetric TElescope array CATE was used to identify the scattered particles and breakup products. It consisted of position sensitive ΔE-E detectors from thin Si and thick CsI(Tl) telescope detectors. To analyze the data each event is tracked and reconstructed.

In a first experiment, a primary beam of ^{84}Kr was impinging on a ^{197}Au target mounted in the final focal plane of the FRS in order to investigate the feasibility of Coulomb excitation measurements under the best beam conditions. Fig. 2 shows a Doppler-corrected γ-ray spectrum and demonstrates that the set-up provides a new powerful instrument for high-resolution in-beam γ-spectroscopy at relativistic energies.

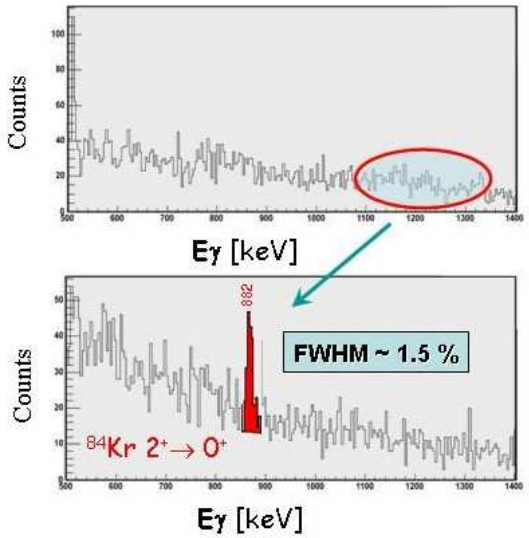


Figure 2: Gamma-ray spectra for 113 AMeV ^{84}Kr projectile Coulomb excitation on a 0.4g/cm2 thick gold target, (top) without and (bottom) with Doppler correction. The $2^+ \rightarrow 0^+$ transition at 882 keV is marked.

References

[1] H.J. Wollersheim et al. NIM A537 637 (2005).

Mirror symmetry of new subshell closures: ^{36}Ca vs ^{36}S

P. Doornenbal, H. Grawe, GSI, Darmstadt, Germany
and P. Reiter, IKP, Köln, Germany for the RISING collaboration

The new N, Z = 14(16) shell stabilization and the N = 20 shell quenching in ^{32}Mg are supposed to be dominated by the monopole part of the nucleon-nucleon residual interaction. Disregarding the different neutron binding energy an isospin symmetric scenario is expected for the N = 16-20 mirror region [1] and can be verified by experiments along the light Ca (Z = 20) isotopes by studying the Coulomb Energy Difference (CED), defined as

$$CED(I) = E_x(I, T_z = -T) - E_x(I, T_z = +T).$$

For the mirror pair ^{38}Ca and ^{38}Ar, the CED of the first excited 2^+ state (^{38}Ca;2^+- ^{38}Ar;2^+ = 39 keV) is positive, which is expected due to the different Coulomb repulsion in the 0^+ ground state. Here, we report on the first results of the ^{36}Ca;2^+- ^{36}S;2^+ measurement.

The RISING (Rare Isotope INvestigation at GSI) [2] setup was used to measure the $2^+ \rightarrow 0^+$ decay of ^{36}Ca via the two step fragmentation technique. A stable beam of ^{40}Ca was incident upon a 4 g/cm^2 ^{9}Be target at the entrance of the FRS (FRagment Separator) [3] with an energy of 420 A $\cdot$ MeV. The average beam intensity was 3 $\times$ 10^8 ions/s. Out of the produced beam cocktail ^{37}Ca was selected and identified in-flight using the Bρ-TOF-ΔE method. At the final focus, 2 $\times$ 10^3 ^{37}Ca ions/s impinged on a secondary 700 mg/cm^2 ^{9}Be target at an energy of 196 A $\cdot$ MeV. The reaction products could then be selected using the CAlorimeter-TElescope (CATE) [4] array. The measuring time amounted to approximately 100 hours beam on the secondary target.

The γ-rays emitted by the fragmentation products were measured with 15 CLUSTER Ge-detectors and positioned at extreme forward angles. In addition, 7 six-fold segmented MINIBALL Ge-detectors and the HECTOR (High Energy γ-deteCTOR) array, consisting of 8 large volume BaF_2, were placed around the secondary target. The high granularity of the MINIBALL detectors permitted to put them to very close target distances of 250 mm, while the CLUSTER and HECTOR detectors stayed at 700 mm and 400 mm, respectively.

In order to obtain good resolution for the γ-rays emitted in flight (β = 0.54), an excellent tracking of the moving nuclei was crucial. Therefore, a thin position sensitive Si ΔE detector directly after the target position and the same type CATE Si ΔE detectors at a distance of 1400 mm to the target determined the fragments' trajectories.

In the analysis the particles were selected and identified with the above mentioned detectors. The β for the Doppler-shift correction was taken on an event-by-event basis by correlating the measured TOF-β with the mean β in the center of the target obtained from MOCADI [5] simulations. The results for ^{36}Ca gated γ-spectra are shown in Fig. 1. For the CLUSTER detectors only the add-back spectrum is displayed, because then, in the case of high γ-energies measured at forward angles, single escape and Compton-scattering events were much suppressed.

The energy of the $2^+ \rightarrow 0^+$ decay of ^{36}Ca was determined to be 3014(20) keV, which is 276 keV lower than its T = 2 mirror ^{36}S. Preliminary shell model calculations using a ^{16}O core, the isospin symmetric interaction USD [6] and experimental single particle energies (SPE) from ^{17}O and ^{17}F reproduce the energy shift qualitatively, indicating that a major part of it is due to the Thomas-Ehrmann shift [7] [8] of A = 17 SPE.

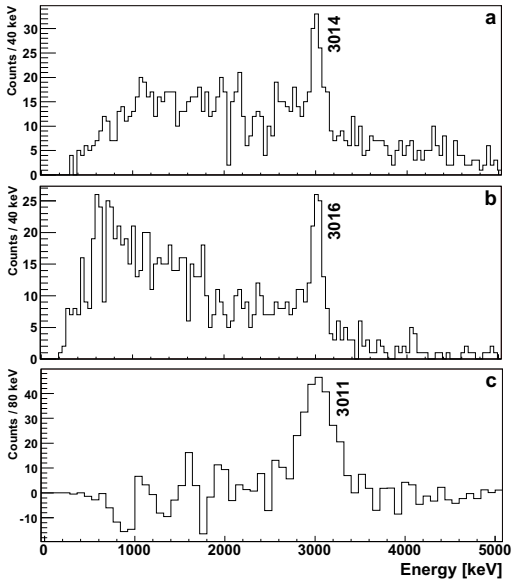


Figure 1: Doppler corrected ^{36}Ca gated γ-ray spectra measured with the MINIBALL (a) and CLUSTER detectors (b). The spectrum of the HECTOR detectors (c) was additionally background subtracted.

References

[1] H. Grawe et al., Act. Phys. Pol. B34, 2267 (2003)
[2] H.J. Wollersheim et al., Nucl. Instr. Meth. A 537 (2004) 637
[3] H. Geissel et al., Nucl. Instr. Meth. B 70 (1992) 286
[4] R. Lozeva et al., Acta Phys. Pol. B36 (2005) 1245
[5] http://www-linux.gsi.de/∼weick/mocadi
[6] B.A. Brown, B.H. Wildenthal: Ann. Rev. of Nucl. Part. Sci. 38, 29 (1988)
[7] R.G. Thomas, Phys. Rev. 80 (1950) 146
[8] J.B. Ehrmann, Phys. Rev. 81 (1951) 412

Relativistic Coulomb excitation of neutron-rich ^{54,56,58}Cr

A. Bürger[a], T.R. Saito[b], H. Grawe[b], H. Hübel[a], P. Reiter[c], J. Gerl[b], M. Górska[b], H.J. Wollersheim[b], A. Al-Khatib[a], A. Banu[b], T. Beck[b], F. Becker[b], P. Bednarczyk[b,d], G. Benzoni[e], A. Bracco[e], S. Brambilla[e], P. Bringel[a], F. Camera[e], E. Clément[f], P. Doornenbal[c], H. Geissel[b], A. Görgen[f], J. Gręboszb,d, G. Hammond[g], M. Hellström[b], M. Honma[h], M. Kavatsyuk[b,i], O. Kavatsyuk[b,i], M. Kmiecik[d], I. Kojouharov[b], W. Korten[f], N. Kurz[b], R. Lozeva[b,j], A. Maj[d], S. Mandal[b], B. Million[e], S. Muralithar[k], A. Neußer[a], F. Nowacki[l], T. Otsuka[m,n], Zs. Podolyák[o], N. Saito[b], A.K. Singh[a], H. Weick[b], C. Wheldon[q], O. Wieland[e] and M. Winkler[b]

[a]Helmholtz-Institut für Strahlen- und Kernphysik, Universität Bonn, Germany; [b]Gesellschaft für Schwerionenforschung (GSI), Darmstadt, Germany; [c]Institut für Kernphysik, Universität zu Köln, Germany; [d]The Henryk Niewodniczański Institute of Nuclear Physics, PAN, Kraków, Poland; [e]Dipartimento di Fisica, Università di Milano, and INFN sezione di Milano, Italy; [f]DAPNIA/SPhN, CEA Saclay, Gif-sur-Yvette, France; [g]Department of Physics, Keele University, Keele, UK; [h]University of Aizu, Fukushima 965-8580, Japan; [i]Taras Shevchenko Kiev National University, Ukraine; [j]Faculty of Physics, University of Sofia, Bulgaria; [k]Nuclear Science Centre, New Delhi, India; [l]IReS, Université Louis Pasteur, Strasbourg, France; [m]Department of Physics, University of Tokyo, Japan; [n]RIKEN, Hirosawa, Japan; [o]Department of Physics, University of Surrey, UK; [p]Department of Physics & Meteorology, Indian Institute of Technology Kharagpur, India; [q]Hahn-Meitner-Institut Berlin, Germany

Nuclei far off the valley of stability have become more accessible in recent years through the use of radioactive ion beams. The investigation of shell structures of such nuclei is a key topic of nuclear structure studies. It has become evident that shell and subshell closures may differ significantly from those of nuclei near stability, in particular for very neutron-rich nuclei, since they are intimately related to the monopole part of the nucleon-nucleon (NN) residual interaction [1]. However, experimental data, needed to test and refine the interactions used in the shell model calculations [2, 3, 4, 5], are still scarce. Modifications of the shell structure have far reaching consequences for nuclear properties and also beyond nuclear structure physics, e.g. for the rapid neutron-capture process (r-process) of stellar nucleosynthesis and the resulting isotopic abundances [6].

The neutron-rich Cr isotopes are located at a key point on the pathway from the $N = 40$ subshell closure via a deformed region to spherical nuclei at $N = 28$. Two large-scale shell model calculations have been performed based on different realistic effective interactions with empirically tuned monopoles [7, 8], which await experimental proof with respect to model space and evolution of subshells and deformation. Experimental 2_1^+ energies in the Ca isotopes show a rise at $N = 32, 34$, indicating a possible subshell closure beyond $N = 28$. The Cr and Ti isotopes show a maximum of those energies at $N = 32$ [4, 9, 10, 11, 12]. However, the Ni isotopes do not show such an effect. Within the $N = 34$ isotones, $E(2_1^+)$ is increasing from Fe to Cr in contrast to the expected trend towards mid-shell, which suggests an $N = 34$ closure [4]. Besides the 2_1^+ energies, masses (which are difficult to measure due to short half lives) and $B(E2)$ values are an important test of the evolution of the subshell structure. A recent determination of $B(E2, 0^+ \rightarrow 2_1^+)$ values in ^{52,54,56}Ti confirms the subshell closure at $N = 32$, but provides no evidence for the predicted $N = 34$ closure [13]. The measurement of $B(E2)$ values of the $N = 30 - 34$ isotopes of Cr, which is the subject of the present investigation, confirms the $N = 32$ subshell closure for $Z = 24$.

Three consecutive experiments were performed to measure Coulomb excitation of high-energy ^{54}Cr, ^{56}Cr and ^{58}Cr beams using the FRS-RISING setup at GSI [14]. From a ^{86}Kr beam from the SIS with an energy of $\approx 480 \cdot A\,\mathrm{MeV}$ and an intensity of 3 to $10 \cdot 10^8$ ions per second, fully stripped Cr ions were produced by fragmentation on a ^{9}Be production target with a thickness of $2.5\,\mathrm{g/cm^2}$ placed in front of the fragment separator FRS. The nuclei of interest were selected in the FRS by their magnetic rigidity and their specific energy loss in the degraders. In all three experiments, the energies of the Cr beams were set to reach $100 \cdot A\,\mathrm{MeV}$ after passing through the reaction target, a $7 \times 7\,\mathrm{cm^2}$ Au foil of $1\,\mathrm{g/cm^2}$ thickness. Scintillators, multi-wire-proportional-counters and the ionisation chamber MUSIC (MUlti-Sampling Ionisation Chamber) before the Au target and CATE (CAlorimeter TElescope) after the Au target were used to identify the ions in A and Z and to track their positions [14].

Gamma rays emitted after Coulomb excitation were measured in the array of 15 Ge-Cluster detectors of the RISING setup [14]. Coincidences between particles and γ rays were recorded by requiring a γ ray in one or more of the Ge detectors, an incoming particle in the scintillator in front of the Au target and an outgoing particle in one of the CsI detectors of CATE. To determine the number of beam particles, events without γ coincidence condition were recorded. The tracked path of each Cr ion and the position of the Ge crystal detecting a γ ray were used to correct for the Doppler shift of the γ rays emitted at $v/c \approx 0.43$.

The γ-ray spectra obtained after Coulomb excitation of ^{54,56,58}Cr ions at relativistic energies are displayed in Fig. 1. Gamma-ray transition intensities were obtained from the

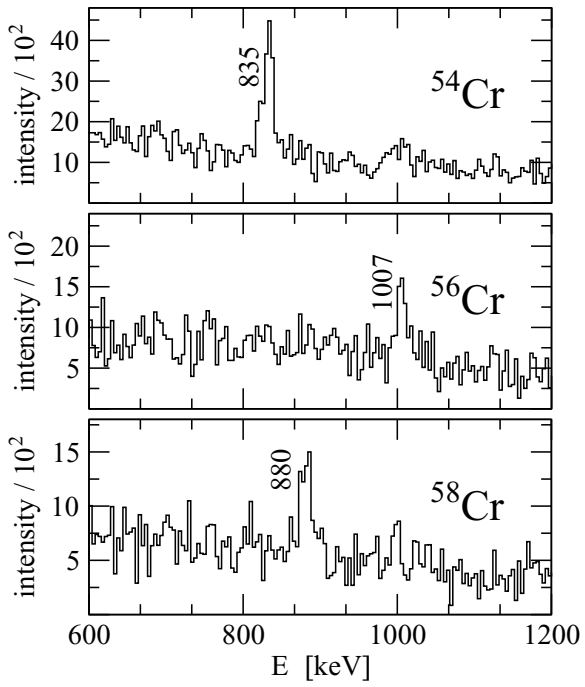


Figure 1: Examples of Doppler- and efficiency-corrected γ-ray spectra showing the $2_1^+ \rightarrow 0^+$ transitions in ^{54,56,58}Cr.

Isotope	$E(2_1^+)$ [keV]	$B(E2; 2_1^+ \rightarrow 0^+)$ [W.u.]	
		this work	previous work
^{54}Cr	835[a]	(norm.)	14.6(0.6)[a]
^{56}Cr	1007[a]	8.7(3.0)	
^{58}Cr	880[b]	14.8(4.2)	

[a] from ref. [15] [b] from ref. [4]

Table 1: Gamma-ray energies, E_γ, and $B(E2; 2_1^+ \rightarrow 0^+)$ values of ^{54,56,58}Cr.

measured counts in the Cr $2_1^+ \rightarrow 0^+$ peaks in the three spectra. The $B(E2)$ values for ^{56}Cr and ^{58}Cr were then calculated relative to the previous value of ^{54}Cr [15], see Table 1.

In Fig. 2 the experimental 2_1^+ excitation energies, $E(2_1^+)$, and the $B(E2, 2_1^+ \rightarrow 0^+)$ values for the Cr isotopes are compared to results of shell model calculations using two different approaches. The experimental $B(E2)$ values show that the collectivity of the 2_1^+ state in ^{56}Cr with $N = 32$ is significantly lower than that of the neighbouring isotopes, ^{54}Cr and ^{58}Cr with $N = 30$ and 34, respectively. In the calculations the effective interactions `GXPF1` [7] (and a modified version, `GXPF1A`, better reproducing $E(2_1^+)$ for Ti and Cr [16]) and `KB3G` [8], respectively, were used in the (p,f) model space. Despite the variations in the $E(2_1^+)$ energies, the $B(E2)$ values are virtually unchanged in the various shell model approaches and remain almost constant from $N = 30$ to 34 (see Fig. 2). The experimental value for ^{56}Cr lies clearly below the shell model predictions which is evidence for the $N = 32$ subshell closure already indicated by the higher 2_1^+ energy. This result is in

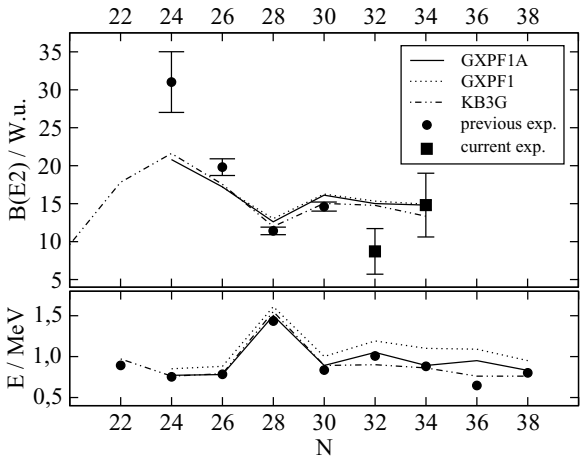


Figure 2: Calculated and experimental values for $E(2^+)$ and $B(E2, 2_1^+ \rightarrow 0^+)$ for Cr isotopes.

agreement with a recent measurement of $B(E2)$ values in ^{52,54,56}Ti [13] which also show a decrease in collectivity at ^{54}Ti with $N = 32$.

The authors wish to thank the technical staff at GSI for providing the Cr beams. The work was supported by the German BMBF under grant nos. 06BN-109, 06OK-167 and by the Polish State Committee for Scientific Research (KBN grant no. 620/E-77/SPB/GSI/P-03/DWM105/2004-2007).

References

[1] H. Grawe, Acta Phys. Pol. B **34**, 2267 (2003).
[2] T. Otsuka *et al.*, Phys. Rev. Lett. **87**, 082502 (2001).
[3] T. Otsuka *et al.*, Eur. Phys. J. A **13**, 69 (2002).
[4] J. I. Prisciandaro *et al.*, Phys. Lett. B **510**, 17 (2001).
[5] A. P. Zuker, Phys. Rev. Lett. **90**, 042502 (2003).
[6] B. Pfeiffer *et al.*, Nucl. Phys. A **693**, 282 (2001).
[7] M. Honma *et al.*, Phys. Rev. C **69**, 034335 (2004).
[8] E. Caurier *et al.*, Eur. Phys. J. A **15**, 145 (2002).
[9] R. V. F. Janssens *et al.*, Phys. Lett. B **546**, 55 (2002).
[10] B. Fornal *et al.*, Phys. Rev. C **70**, 064304 (2004).
[11] S. Liddick *et al.*, Phys. Rev. C **70**, 064303 (2004).
[12] S. N. Liddick *et al.*, Phys. Rev. Lett. **92**, 072502 (2004).
[13] D.-C. Dinca *et al.*, Phys. Rev. C **71**, 041302 (2005).
[14] H. Wollersheim *et al.*, Nucl. Instr. Meth. A **537**, 637 (2004).
[15] ENSDF database, `http://www.nndc.bnl.gov/ensdf/`.
[16] T. Otsuka *et al.*, Acta Phys. Pol. B **36**, 1213 (2005).

Gamma-decay of the GDR in the exotic nucleus ^{68}Ni excited via Coulomb excitation.

A. Bracco, G. Benzoni, N. Blasi, F. Camera, F.Crespi, S. Leoni, P. Mason, B. Million, M. Pignanelli, O. Wieland, INFN and University of Milano, Italia
A. Maj, M. Kmiecik, W. Meczynski, J. Styczen, Cracow
T. Aumann, F. Becker, P. Bednarczyk, H. Emling,J. Gerl, M.Gorska , J.Grebozs, P. Reiter, T.Saito, H. Wollersheim, et al. GSI
G. de Angelis, A. Gadea, D. Napoli, LNL
S. Lenzi, F. Della Vedova, E. Farnea, S. Lunardi, Padova
C. Petrache and G. Lo Bianco, Camerino
M. Castoldi and A. Zucchiatti, Genova
G. La Rana, Napoli
F. Azaiez, Orsay

The isovector giant dipole resonance (GDR) is one of the most important and easily accessible nuclear collective modes. This nuclear excitation carries information on the nuclear structure and in particular on the effective nucleon-nucleon interaction in the medium.

This topic has attracted much attention over several past decades and large amount of experimental data exists for nuclei in the proximity of the stability line. Almost nothing is known far from the stability line. In particular, the question on how the Giant Dipole Resonance strength evolves when going from stable to exotic, weakly bound nuclei with extreme neutron to proton ratio is presently under discussion both theoretically and experimentally [1-5] in connection with the existence of the so called pygmy resonances or soft mode.

A neutron rich nucleus in the medium mass region which is very interesting for the study of the GDR is ^{68}Ni. Recent theoretical calculations have predicted that the contribution of the low-energy region to the dipole strength distribution increases with the neutron excess. In particular, the ratio of the energy weighted moment in the low-energy region (E < 10 MeV) and in the high-energy region (E > 10 MeV) is predicted to be of the order of 8%.

The gamma emission from coulomb excited ^{68}Ni has been measured using the RISING array. A 900 MeV/u ^{86}Kr beam with an intensity of 10^{10} pps measured at the SEETRAM has been focused on a primary Be target. The ^{68}Ni fragments have been selected and focused by the FRS on a secondary Au target 2 gr/cm^2 thick.

The standard FRS-Rising setup [6], including a segmented scintillator placed at S2 was used. Figure 1 shows the incoming fragments selected by the FRS measured before the secondary Au target. The particle identification setup after the target is performed by the CATE calorimeter which, in the present experiment, consisted of nine position sensitive Si detectors coupled to four 6 cm thick CsI. High and low energy gamma rays have been measured using 15 HPGe clusters of the Euroball array, 7 HPGe segmented clusters from the Miniball array and 8 BaF_2 from the Hector array.

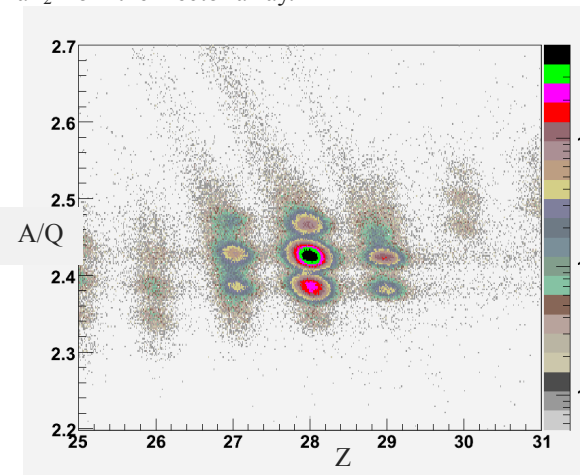


Figure 1: The identification matrix of the secondary fragments selected by the FRS. The ^{68}Ni fragments corresponds to the central stronger spot

During the experiment approximately 10^8 events of ^{68}Ni have been acquired before the Au target. From the preliminary analysis, in approximately 1-2 % of the cases a γ-ray coming from the target has been measured in coincidence in one of the gamma detectors.

The requirement of incoming ^{68}Ni fragments in the FRS and Ni isotope in CATE calorimeter cleanly eliminates most of the background. The analysis is in progress.

References

[1] H. Sagawa, T. Suzuki, Phys. Rev. C59(1999)3116
[2] D.Sarchi et al Phys. Lett. B601 (2004)27
[3] P. Adrich et al Phys. Rev. Lett. (2005)132501
[4] A. Leistenschneider et al Phys. Rev. Lett. (2001)5442
[5] E.Tryggestad et al Phys. Lett. B541 (2002)52
[6] H.J.Wollersheim NIM A537(2005)637

^{108}Sn studied with intermediate-energy Coulomb excitation*

A. Banu[1,2], J. Gerl[1], C. Fahlander[3], M. Górska[1], H. Grawe[1], T. R. Saito[1], H.-J. Wollersheim[1], E. Caurier[4], T. Engeland[5], A. Gniady[4], F. Nowacki[4], M. Hjorth-Jensen[5], and the RISING Collaboration

[1]*Gesellschaft für Schwerionenforschung (GSI), D-64291, Darmstadt, Germany*
[2]*Institut für Kernphysik, Universität Mainz, D-55099 Mainz, Germany*
[3]*Department of Physics, Lund University, S-22100 Lund, Sweden*
[4]*IReS, F-67037 Strasbourg Cedex 2, France*
[5]*Department of Physics and Center of Mathematics for Applications, University of Oslo, N-0316 Oslo, Norway*

^{100}Sn, the heaviest self conjugate doubly magic nucleus, lies at the proton drip-line. In this region of nuclei changes in the shell structure and the onset of the collectivity are predicted to be driven exclusively by the drift of the single-particle states and the proton-neutron interaction between identical shell model orbitals [1]. The latter is caused by the confinement of protons in the Coulomb barrier and/or the vicinity of the N=Z line. Therefore, studies of the ^{100}Sn core polarisation as well in spin (M1) as in the shape response (E2), proton-neutron pairing, and isospin symmetry are essential. In particular, Sn isotopes between the N = 50 and 82 shell closures provide the longest chain of semi-magic nuclei accessible to nuclear structure studies, both in the neutron valence space of a full major shell and with emphasis on excitations of the Z = 50 core. The reduced transition rate from the first excited 2^+ states to the ground state of a nucleus from that chain is most sensitive to details of shell structure and *E*2 core polarization.

The measurement of the B(E2;$0^+ \rightarrow 2^+$) in ^{108}Sn [2] triggered by this motivation was the first experiment on a non stable Sn isotope. This was caused by the existence of excited isomeric states in all light Sn isotopes which hampered the lifetime measurements of the 2^+ state. The availability of the first radioactive beams boosted a series of Coulomb excitation measurements at different energy ranges, starting at GSI followed by REX-ISOLDE [3] and MSU [4].

The measurement of the intermediate-energy Coulomb excitation of ^{108}Sn was carried out within the RISING project [5]. Experimental details of the measurements are given in [2], and presented at large in [6]. The neutron-deficient secondary beams of interest, ^{108,112}Sn, were produced by fragmentation of a primary ^{124}Xe beam, and identified before and after the reaction target by the fragment separator FRS [7] and the calorimeter telescope CATE [8], respectively. Gamma rays in coincidence with projectile residues were detected by the 15 RISING Ge-Cluster detectors. The resulting spectrum is show in Fig. 1. The extracted B($E2;0^+_{g.s.}\rightarrow 2^+_1$) value of 0.230(57)$e^2b^2$, measured for ^{108}Sn, has been determined relative to the known value in the stable ^{112}Sn, studied in the same experimental conditions.

The results are discussed in [2] in the framework of recent large-scale shell model (LSSM) calculations performed with realistic effective interactions, where the role of particle-hole excitations across the ^{100}Sn doubly magic core and the *Z=50* shell gap for the *E2* polarization correlations are investigated. Without these excitations and with only neutron degrees of freedom, one would need a neutron effective charge in the range of (1-1.5)*e* to explain the experimental data [9]. The LSSM calculations performed here involving up to 4 particle-4 hole excitation, being the present computational limit, and with a polarization charge of 0.5*e* for protons and neutrons can reproduce the increasing B(E2) trend towards the lighter Sn isotopes [2] indicating softness of the ^{100}Sn core and the Z=50 shell gap below N=64.

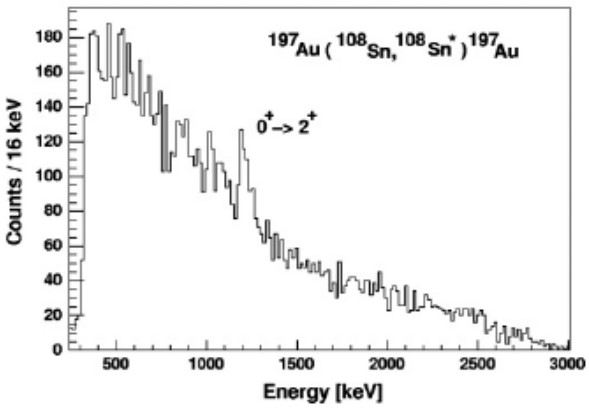


Figure 1: De-excitation γ-ray line following $0^+_{g.s.}\rightarrow 2^+_1$ Coulomb excitation of the ^{108}Sn projectile.

References

[1] H. Grawe, in The Euroschool Lectures on Physics with Exotic Beams, Vol. I, Lect. Notes Phys. **651** (Springer, Berlin Heidelberg, 2004), p. 33.
[2] A. Banu *et al.*, Phys. Rev. C **72**, 061305(R) (2005).
[3] J. Cederkäll, private communication
[4] K. Starosta, private communication
[5] H.J. Wollersheim *et al.*, Nucl. Instrum. Methods Phys. Res. A **537**, 637 (2005).
[6] A. Banu, Ph. D. thesis, University of Mainz, 2005; http://archimed.uni-mainz.de
[7] H. Geissel *et al.*, Nucl. Instrum. Methods Phys. Res. B **70**, 286 91992).
[8] R. Lozeva *et al.*, Acta Phys. Pol. B **36**, 1245 (2005).
[9] A. Holt, T. Engeland, M. Hjorth-Jensen, and E. Osnes, Nucl. Phys. **A704**, 60c (2002).

*Work supported by BMBF under Contract Nos. 06MZ176 and 06-K-167.

Proton-Proton Correlations Observed in the Two-Proton Radioactivity of the (21^+) Isomer in ^{94}Ag

I. Mukha[a,b,c], E. Roeckl[b], L. Batist[d], A. Blazhev[b,e], J. Döring[b], H.Grawe[b], L.Grigorenko[f], M. Huyse[a], Z. Janas[g], R. Kirchner[b], M. La Commara[h], C. Mazzocchi[b,i], S. L. Tabor[k], P. Van Duppen[a]

[a]KU, Leuven, Belgium; [b]GSI, Darmstadt, Germany; [c]RRC Kurchatov Institute, Moscow, Russia; [d]PNPI, St. Petersburg, Russia; [e]University of Sofia, Bulgaria; [f]JINR, Dubna, Russia; [g]University of Warsaw, Poland; [h]Università "Federico II" and INFN, Napoli, Italy; [i]University of Tennessee, Knoxville, USA; [k]Florida State University, Talahassee, USA

The (21^+) isomer occurring in the lightest known isotope of silver, ^{94}Ag, has properties that are unmatched in the entire nuclear chart. It is characterised by a long half-life of 0.39(4) s [1], a high spin [2] and, although its dominant disintegration modes are β-delayed γ-ray [2] or proton [1] emission, the excitation energy of 6.7(5) MeV [3] makes direct one-proton and two-proton (2p) radioactivity possible. The experimental results on the latter two decay modes have recently been published [3,4], those on the 2p radioactivity will be summarised here.

The 2p radioactivity of the (21^+) isomer was studied at the GSI on-line mass separator by using a ^{58}Ni(^{40}Ca,p3n) fusion-evaporation reaction. After ionisation and acceleration to 55 keV, the A=94 ions were mass separated and implanted into a tape positioned in the centre of an array of segmented silicon and composite germanium detectors. The tape was periodically removed from the implantation position in order to reduce the build-up of long-lived daughter activity. While the silicon detectors were used to record protons the germanium crystals served to 'tag' on known γ-ray transitions in the two-proton daughter, ^{92}Rh. In this way a 2p branch was discovered, having a decay energy of 1.9(1) MeV and a decay probability of 0.5(3) % which corresponds to a partial half-life of about 80 s. The cross-section for producing the 2p radioactivity in the fusion-evaporation reaction amounts to about 350 pb [5].

The experimental proton-proton correlation data are displayed in Fig. 1 together with predictions obtained from the break-up model [5-8]. The spectra displayed in Fig. 1 were derived out of the Si_1-Si_2-γ-γ coincidence matrix, with a total of 19 events fulfilling the triple condition set on two ^{92}Rh γ-transitions and on the 2p sum-energy in the range of 1.8-1.95 MeV. All proton-proton events shown in Fig. 1 are normalized by using their respective solid angles of the detectors. This leads to a normalization of the histogram and therefore the intensity is given in arbitrary units. The experimental uncertainties are calculated as weighted sums of the standard deviations of the respective proton-proton counts.

In general, 2p decay can proceed through sequential proton emission involving intermediate ^{93}Pd states, or through a simultaneous three-particle decay mechanism. The former decay should result in narrow peaks in the spectrum shown in Fig. 1b whose energies depend on the

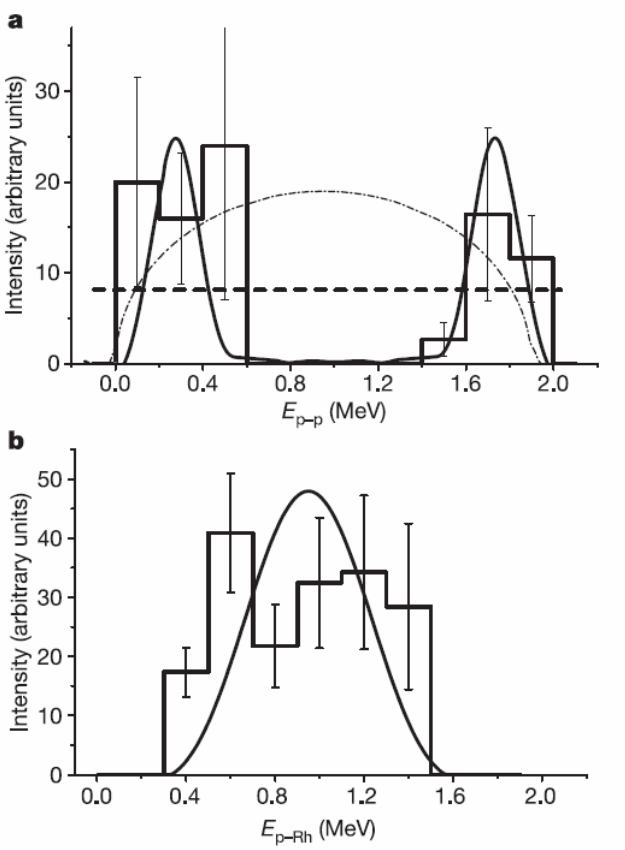


Figure 1: Correlations observed in the 2p decay of the (21^+) isomer of ^{94}Ag. Relative-energy spectra for proton-proton (E_{p-p}) and proton-^{92}Rh (E_{p-Rh}) correlations are shown by histograms in **a** and **b**, respectively. The solid curves are the predictions of our model of simultaneous proton emission from a deformed nucleus convoluted with an experimental uncertainty of 200 keV. The dashed line represents the fit obtained with a sequential emission mechanism. The dashed-dotted curve shows the calculated distribution when the 2p decay is isotropic in the absence of the mentioned decay mechanisms.

(unknown) energy of the ^{92}Rh state involved and should add up to a total of 1.9(1) MeV. As there is no evidence for peaks in Fig. 1b, their positions are not indicated in this figure.

The observed proton-proton correlations seem to be consistent only with ^{94}Ag decaying through a simultaneous 2p emission process. For ^{94}Ag such a 'true' 2p-decay model [9] should be much slower than the sequential decay mode [6]. Moreover, the 2p-decay half-life estimated with the 'simultaneous emission' model [7,8] exceeds the experimentally determined half-life by a factor of 10^3–10^6. The unexpectedly large 2p decay probability we observe can, however, be explained by assuming strong nuclear deformation of the (21^+) isomer. We used a simple breakup model to evaluate the probability of simultaneous 2p decay of a deformed nucleus, assuming that the two protons share the decay energy E and angular momentum L and that they are emitted from different points on an elliptically deformed nucleus with axes ratios of 1:1:a. The results of these calculations (which do not include proton–proton interactions) are shown in Fig. 2 for L=6, 8 and 10, and are seen to reproduce the experimental data when using nuclear deformation parameters a<0.3 or a>2 (corresponding to oblate or disk-like deformation, and prolate or cigar-like deformation, respectively). The extent of the nuclear deformation that is needed to replicate the experimental half-life is very large. For example, oblate nuclei with a≈0.3 have not been observed so far, whereas prolate deformations with $a \approx 2$ have only been seen in super-deformed nuclei (see e.g. [10]). For comparison, Fig. 2 also includes the predictions of the quasi-classical ^{2}He decay model [9] that assumes a very strong proton–proton attraction resulting in the emission of a ^{2}He cluster from the deformed nuclear surface. In the case of spherical nuclei, the ^{2}He model provides a lower limit for 2p-decay half-lives [7, 8] and is used here for reference purposes.

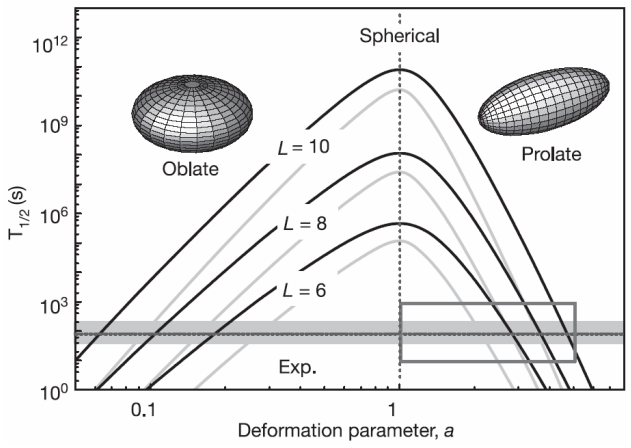


Figure 2: Nuclear deformation of ^{94}Ag (21^+) derived from its 2p decay. The partial 2p-decay half-life ($T_{1/2}$) of ^{94}Ag (21^+) is shown as a function of the nuclear deformation parameter a, which is a ratio of the long to the short axes of the ellipsoid. The simultaneous (black curves) and quasi-classical ^{2}He (grey curves) model estimates of the 2p decay are shown for the angular momenta L = 6, 8, 10. The nuclear shapes corresponding to the derived deformations are shown for the L = 6 calculation. The experimental $T_{1/2}$ value is shown by the dotted line (marked as 'Exp.') with the grey region of experimental uncertainties.

All in all, the experimental results on the 2p half-life and on the proton-proton energy correlation are interpreted as indicating a very large, prolate (cigar-like) deformation of the parent nucleus, with the emission of protons occurring either from the same or from opposite ends of the 'cigar' (see Fig. 3). This first measurement of correlation data in two-proton radioactivity calls for further experimental studies of the properties of this truly exotic isomer as well as for a quantitative theoretical description of the observed two-proton decay behavior.

References

[1] I. Mukha et al., Phys. Rev. C **70** (2004) 044311.
[2] C. Plettner et al., Nucl. Phys. A **733** (2004) 20.
[3] I. Mukha et al., Phys. Rev. Lett. **95** (2005) 022501.
[4] I. Mukha et al., Nature **479** (2006) 298.
[5] I. Mukha et al., Eur. Phys. J. A **25**, s01 (2005) 131.
[6] L. V. Grigorenko et al., Phys. Rev. C **64** (2001) 054002.
[7] L. V. Grigorenko, I. G. Mukha and M. V. Zhukov, Nucl. Phys. A **714** (2003) 425.
[8] L. Grigorenko and M. V. Zhukov, Phys. Rev. C **68** (2003) 054005.
[9] V. I. Goldansky, Nucl. Phys. **19** (1960) 482.
[10] P. J. Twin et al., Phys. Rev. Lett. **57** (1986) 811.

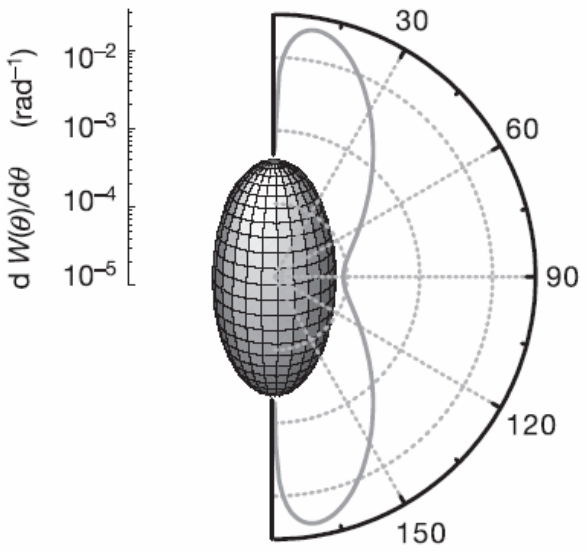


Figure 3: Intensity W of 2p-emission as a function of the angle θ between one emitted proton and the long ellipsoid axis (thick grey curve).

Beta decay of ^{101}Sn

O. Kavatsyuk[a,b], C. Mazzocchi[a,c], A. Banu[a], L. Batist[d], F. Becker[a], A. Blazhev[a], W. Brüchle[a], J. Döring[a], T. Faestermann[e], M. Górska[a], H. Grawe[a], Z. Janas[f], A. Jungclaus[g], M. Karny[f], M. Kavatsyuk[a,b], O. Klepper[a], R. Kirchner[a], M. La Commara[h], K. Miernik[f],I. Mukha[a], C. Plettner[a], A. Płochocki[f], E. Roeckl[a], M. Romoli[h], K. Rykaczewski[i], M. Schädel[a], K. Schmidt[a], R. Schwengner[k], J. Żylicz[f]

[a]GSI, Darmstadt, Germany; [b]National Taras Shevchenko Univ. of Kyiv, Ukraine; [c]Univ. of Tennessee, Knoxville, USA; [d]PNPI, Gatchina, Russia; [e]TU, München, Germany; [f]Univ. of Warsaw, Poland; [g]Instituto Estructura de la Materia, CSIC and Departamento de Fisica Teórica, UAM Madrid, Spain; [h]Università "Federico II" and INFN, Napoli, Italy; [i]ORNL, Oak Ridge, USA; [k] IKHP, FZ Rossendorf, Dresden, Germany

The β decay of the very neutron-deficient isotope ^{101}Sn, one of the four closest neighbours of the doubly-magic nucleus ^{100}Sn, was studied at the GSI on-line mass separator. ^{101}Sn was produced in the fusion-evaporation reaction induced by a 36 particle-nA, $\sim$5 MeV/u ^{58}Ni beam on a ^{50}Cr target. By adding CS_2 vapour to the ion source, high chemical selectivity for tin was achieved [1], thus strongly suppressing the isobaric contaminants. After ionisation and acceleration to 55 keV, the A=101+32 ions were mass separated and implanted either into thin carbon foils in front of a setup for measuring β-delayed protons (βp) or into a tape positioned in the centre of an array of silicon and germanium detectors (Si-Ge array) for β-delayed γ-ray ($\beta\gamma$) spectroscopy.

In the βp experiment the A=101+32 beam was periodically switched between two carbon foils in consecutive grow-in (12 s) and decay (12 s) intervals, the collected βp activity being recorded by two ΔE-E Si-detector telescopes (ΔE: 450 mm^2, 20 μm; E: 2000 mm^2, 500 μm). Each of them covered a solid angle of 17(2) %. The βp data allowed us to redetermine with improved accuracy the half-life of ^{101}Sn to be 1.9$\pm$0.3 s and to estimate the production cross-section in the ^{50}Cr(^{58}Ni, α3n) fusion-evaporation reaction to be about 60 nb.

In the $\beta\gamma$ experiment, three Si detectors (two 30 mm$\times$30 mm and one 14 mm$\times$14 mm) were placed inside of a small vacuum chamber, covering the solid angle of about 40 %. Around this camber two GSI VEGA-SuperClover detectors and one small Clover detector (i.e. a total of 12 Ge crystals) were mounted, yielding a total photopeak efficiency of 7.5 % at 1.3 MeV. The measurement was performed while the A=101+32 beam was continuously implanted into the tape at rest. Every 8 s the activity was removed from the implantation position. The $\beta\gamma$ data yielded for the first time weak evidence for the observation of β-delayed γ rays of ^{101}Sn which apparently form a cascade of 352 and 1065 keV transitions in ^{101}In.

Figure 1 shows the experimental βp energy spectrum together with theoretical predictions. The calculated spectra were obtained on the basis of estimated Q_{EC} and S_p values [2], a β-intensity distribution as predicted by a shell-model calculation [3] and a barrier-transmission calculation based on a statistical model [4]. The centre of gravity of the experimental βp energy spectrum is in good agreement with the prediction based on the 5/2$^+$ assignment for the ground-state of ^{101}Sn. In contrast, the theoretical spectrum obtained for a 7/2$^+$ assignment is concentrated in a more narrow energy range, the main intensity lying about 400 keV lower. Although, the theory based assignment of the ground-state of ^{101}Sn and the lowest-lying orbital above the $N = 50$ shell-closure is unambiguously a 5/2$^+$, the shell-model calculation [3] overestimate the energy of the GT resonance in ^{103}Sn by 500 keV.

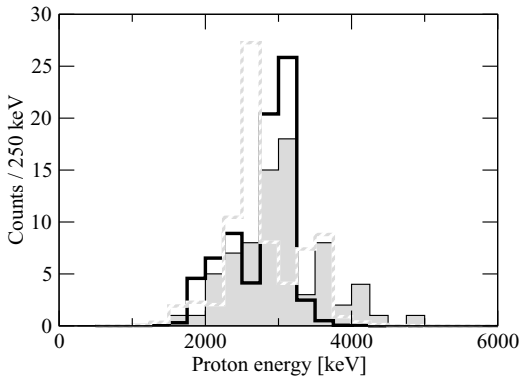


Figure 1: Experimental energy spectrum of β-delayed protons compared to predictions obtained on the basis of a shell-model calculation assuming a 5/2$^+$ (solid-line histogram) and 7/2$^+$ (dashed-line histogram) spin-parity assignment for the ^{101}Sn ground-state. Theoretical and experimental spectra are normalised to equal integral number of counts.

[1] R. Kirchner, NIM B **204**, 179 (2003).
[2] G. Audi *et al.*, Nucl. Phys. A **729**, 337 (2003).
[3] M. Hjorth-Jensen et al., Phys. Rep. **251**, 125 (1995).
[4] B. Jonson *et al.*, Proc. 3rd Intern. Conf. on Nuclei far from Stability, Cargèse (1976), CERN 76-13, p.277; P. Hornshøj *et al.*, Nucl. Phys. A **187**, 609 (1972).

Gamow-Teller beta decay of ^{105}Sn

M. Kavatsyuk[a,b], L. Batist[c,d], F. Becker[a], A. Blazhev[a,e], W. Brüchle[a], J. Döring[a], T. Faestermann[f], M. Górska[a], H. Grawe[a], Z. Janas[g], A. Jungclaus[h], M. Karny[g], O. Kavatsyuk[a,b], R. Kirchner[a], M. La Commara[d], S. Mandal[a], C. Mazzocchi[a], I. Mukha[a,i], S. Muralithar[a,k], C. Plettner[a], A. Płochocki[g], E. Roeckl[a], M. Romoli[d], M. Schädel[a], J. Żylicz[g]
[a]GSI, Darmstadt, Germany; [b]National Taras Shevchenko Univ. of Kyiv, Ukraine; [c]PNPI, St. Petersburg, Russia; [d]Universitá "Federico II" and INFN, Napoli, Italy; [e]University of Sofia, Bulgaria; [f]TU, München, Germany; [g]Univ. of Warsaw, Poland; [h]Departamento de Fisica Teórica, UAM Madrid, Spain; [i]Kurchatov Institute, Moscow, Russia; [k]Nuclear Science Center, New Delhi, India

The interest in studying nuclei in the ^{100}Sn region, in particular those "south-east" of this doubly magic shell closure, is partly motivated by the occurrence of a resonance-like β decay related to the Gamow-Teller (GT) transitions of a $g_{9/2}$ proton into a $g_{7/2}$ neutron. For odd-A tin isotopes, this transformation initiates from the even-even core, leading to three-quasiparticle states in the odd-Z, even-N daughter nucleus and a correspondingly complex structure of the GT resonance. A suitable tool for measuring the β-intensity distribution in such cases is total absorption spectroscopy. This method is based on recording cascades of β-delayed γ rays rather than single γ transitions. This allows one to determine the entire β-intensity distribution, including weak β transitions to high-lying excited states in the daughter nucleus. In this work a total absorption spectrometer (TAS) [1] was used for investigating the ^{105}Sn decay. The motivation for this study was to improve the data available from previous experiments on the β-delayed γ [2] and proton (βp) [3] emissions of ^{105}Sn, with the aim of determining the GT strength distribution and comparing it with shell-model predictions.

The experimental technique and data analysis procedure were the same as used for ^{103}Sn β-decay study, described in ref. [4]. With this investigation a dominant GT resonance occurring in the decay of ^{105}Sn was identified, peaking at 3.6 MeV and having a width of 300 keV. In fig. 1 the experimental GT strength distribution is compared with shell-model calculation based on an empirical interaction [5], yielding qualitative agreement with the shape of the measured GT resonance. However, the theoretical distribution is shifted by about 600 keV towards lower excitation energies, and the predicted summed GT strength is 4.5(6) times higher than the experimental one of 3.0(4) in units of $g_A^2/4\pi$. This hindrance is in agreement with the values obtained for other nuclei in the ^{100}Sn region. The shift may be ascribed to the inverted $d_{5/2} - g_{7/2}$ sequence in ^{101}Sn and/or a reduced neutron pairing in the shell model approach.

In addition the TAS allowed us to measure further decay characteristics of ^{105}Sn such as the Q_{EC} value of 6230(80) keV [6] and the contribution of 0.420(35) of the electron capture process to the total decay rate. The ^{105}Sn half-life of 32.7(5) s was remeasured with higher precision.

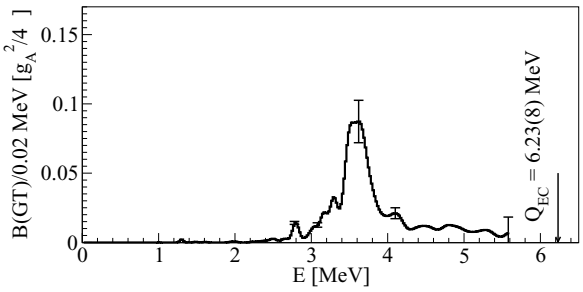


Figure 1: Gamow-Teller strength distribution for ^{105}Sn obtained from the TAS measurement (black-line histogram) and from the shell-model calculation (dotted histogram). The theoretical distribution was normalised to the experimental summed GT strength (see text).

The βp emission was detected using the ancillary silicon detectors of the TAS. This allowed us to measure the βp branching ratio to be $1.1(4) \times 10^{-4}$.

Using the main TAS crystal as an active background shielding for the ancillary germanium and silicon detectors, conversion coefficients of 0.055(6) and 0.07(2) were determined for the long-lived $1/2^-$ isomers in ^{105}In and ^{103}In that have excitation energies of 632 and 674 keV, respectively. A comparison of this result with the theoretical values of 0.062 and 0.075 [7], respectively, suggests $M4$ polarity of the transition. This confirms the previous multipolarity assignment [8].

References

[1] M. Karny *et al.*, Nucl. Instr. Meth. B **126**, (1997) 411.

[2] M. Pfützner *et al.*, Nucl. Phys. A **581**, (1995) 205.

[3] P. Tidemand-Petersson *et al.*, Z. Phys. A **302**, (1981) 343.

[4] O. Kavatsyuk *et al.*, Eur. Phys. J. A **25**, (2005) 211.

[5] K. Rykaczewski, GSI-95-09 (1995), B.A. Brown, K. Rykaczewski, Phys. Rev. C **50**, (1994) R2270.

[6] M. Kavatsyuk *et al.*, Intern. J. Mass Spectrometry, in print.

[7] I.M. Band *et al.*, Atomic Data and Nuclear Data Tables **81**, (2002) 1.

[8] J. Verplancke *et al.*, Z. Phys. A **315**, (1984) 307.

β-decay properties of nuclei in the region around ^{132}Sn*

R. Kessler, K.-L. Kratz, Institut f. Kernchemie, Mainz, Germany
J. Pereira Conca, H. Schatz, NSCL, Michigan State University, East Lansing, USA
The E040 Collaboration, GSI, Germany

Data analysis of experiment E040

About half of the elements heavier than iron have their origin in the rapid neutron capture process (r-process). To date, both the astrophysical scenarios as well as the precise r-process "boulevard" are not known for certain. The required conditions for the creation of the r-process isotopes depend – among other parameters – also on nuclear-physics properties of many extremely neutron-rich nuclei, from which so far about 50 have been investigated experimentally, mainly by the Mainz group.

In order to further improve the understanding of the r-process, it is necessary to know, for example, the β-decay half-lives and neutron emission probabilities (P_n) of additional nuclei in the r-process path. Since the abundance pattern is strongly depending on the properties of the "waiting-point" nuclei, there is a special interest in the region around ^{132}Sn with respect to the formation of the A=130 r-abundance peak.

Furthermore, experimental data in this region yield information about nuclear-structure effects far off stability such as the possible erosion of the classical N=82 neutron shell gap.

For this purpose, an experiment has been performed at GSI six years ago to measure $T_{1/2}$ and P_n values of nuclei in the region "north east" of ^{132}Sn.

The experiment used a ^{238}U primary beam of 750 MeV/u impinging on a Pb target. Several so far unknown nuclei were produced via projectile fission.

After subsequent separation and identification, the fragments were implanted into four double-sided Silicon strip detectors allowing a correlation of the implantation and β-decay events.

The whole β-detector array was surrounded by the Mainz 4π neutron long counter in order to measure the β-delayed neutron emission

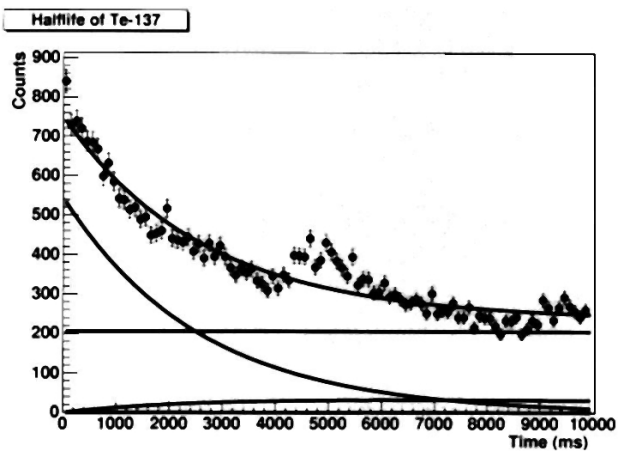


Figure 1: Decay curve of all data from isotope ^{137}Te.

Initially, the data have been analyzed by fitting the decay curves of all events from one isotope. Assuming that the fit function consists of the contributions from the mother, the daughter, the granddaughter and a background component, the half-life of the mother nuclide was derived by minimizing the χ^2.

Figure 1 shows a typical example of such a fit for the case of ^{137}Te, triggered on the corresponding implantation event. The bumps within the decay curve arise from the subsequent spill. Depending on the actual setting, the next package of ^{238}U ions from the primary beam produces an additional background component at positions between 4.5 and 9 seconds. The result is an obviously wrong half-life of the respective isotope.

As an alternative way to analyze the data, the Maximum-Likelihood method was chosen. It is the mathematically correct method even in those cases, where the isotope of interest has been produced only with low statistics.

First results for the half-lives of some isotopes are presented in Table 1. Due to the problems with the background, these values are still preliminary.

Additional work has to be done to determine the half-lives of all measured isotopes, as well as the P_n values.

Table 1: Comparison of β-decay half-lives determined in experiment E040 with literature values [1].

Isotope	**Known half-lives [ms]**	**Preliminary results of this work [ms]**
^{133}Sn	1450 (30)	1568 (135)
^{135}Sn	450 (50)	485 (37)
^{137}Sb	>150 ns	390 (18)
^{138}Sb	>300 ns	296 (35)
^{138}Te	1400 (400)	1151 (28)
^{139}Te	>150 ns	598 (20)
^{140}Te	>150 ns	334 (14)
^{142}In	~200	222 (12)
^{143}In	>150 ns	130 (45)

*Work supported by HGF VISTARS and the Joint Institut of Nuclear Astrophysics

[1] G. Audi et al., Nucl. Phys. A729 (2003), 3.

Investigation of the reaction $^{20}Ne(p,\gamma)^{21}Na$ in the astrophysical interesting energy region*

Sascha Falahat† and Karl-Ludwig Kratz, Institut für Kernchemie, Johannes Gutenberg Universität Mainz,‡
Joachim Görres, Edward J. Stech and Michael C. F. Wiescher
University of Notre Dame, Department of Physics§
Gottfried Münzenberg, Gesellschaft für Schwerionenforschung mbH, ¶

The nuclear reaction $^{20}Ne(p,\gamma)^{21}Na$ has been investigated in the astrophysical interesting energy region from $E_p = 600\,k\mathrm{eV}$ to $E_p = 1400\,k\mathrm{eV}$.
Furthermore several resonances of the reaction $^{27}Al(p,\gamma)^{28}Si$ have been measured in an energy range of $E_p = 400\,k\mathrm{eV}$ to $E_p = 1400\,k\mathrm{eV}$ to determine the calibration and efficiency of the detector setup.
The experiments and corresponding measurements have been performed at the Nuclear Structure Laboratory of the University of Notre Dame with the Van-de-Graaff accelerators KN and JN. Implanted or evaporated ^{20}Ne, respectively ^{27}Al beamstop targets have been bombarded with protons, and the induced reactions have been investigated. For the γ-spectroscopic measurements a Ge-detector and a pair of NaI-detectors have been used in 3 different setups.
The first setup included the positioning of the Ge-detector in an angle of 0° to the target. Here the Ge-detector and the target were surrounded completly by a pair of NaI-detectors.
For the second setup the NaI-detectors have been moved forward, so that the target was at the end of the NaI-detector annulus with the Ge-detectors positioned at 0°.
The difference between the second and the third setup is the mounting of a 45° target chamber and correspondingly the rotating of the Ge-detector.
For each setup, the NaI-detectors have been used as Veto-detectors to realize a cosmic background and a Compton continuum rejection.
To determine the setup with the best efficiency, several resonances of the reaction $^{27}Al(p,\gamma)^{28}Si$ have been measured and investigated.
Especially the behavior of the efficiency considering coincidence-summing has been taken into account.
Setup 1 has shown the best rejection while Setup 3 had the highest yields and was therefore chosen to measure the reaction $^{20}Ne(p,\gamma)^{21}Na$.
In our measurements, the resonance strength $\omega\gamma$ for the $^{20}Ne(p,\gamma)^{21}Na$ resonance at $E_p = 1169\,k\mathrm{eV}$ could be determined to a value of :

$$\omega\gamma = 1,12 \pm 0,02\,\mathrm{eV}$$

Tanner et al. [1] report a value of $\omega\gamma = 1,13 \pm 0,07\,\mathrm{eV}$ while E.Stech [3] published a value of $\omega\gamma = 1,17 \pm 0,06\,\mathrm{eV}$.

A measurement and correspondingly a detailed analysis of the direct capture reaction $^{20}Ne(p,\gamma)^{21}Na$ below the $E_p = 1169\,k\mathrm{eV}$ resonance allowed a comparison of the obtained results for the cross section of the $DC \rightarrow 2425\,k\mathrm{eV}$ component with previous results. Figure 1 shows our results in comparison to the results of Rolfs et al. [2] and Stech [3].

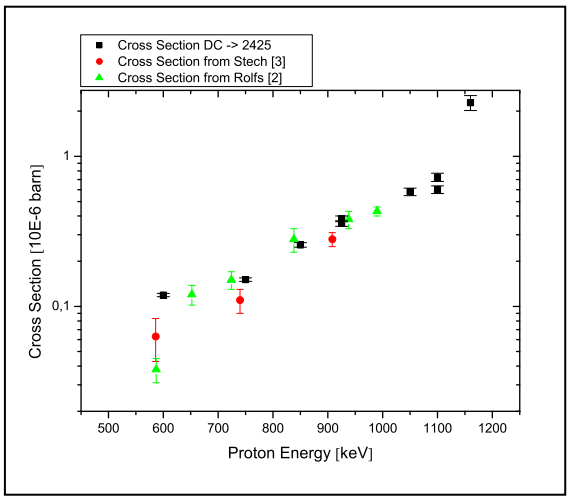


Figure 1: Comparison of the results from our experiments [4] and previous results [2], [3].

The results agree in their trend and partly in their absolute values. The detailed experimental procedures and analysis will be published in [4].

References

[1] Tanner N., 1959, Physical Review, 114, p. 1060

[2] Rolfs C.E., Rodney W.S., Shapiro M.H. and Winkler H., 1975, Nuclear Physics A, 241, p. 460

[3] Stech E., Ph. D. Dissertation, The Astrophyscial Impact of the $^{20}Ne(p,\gamma)^{21}Na$ Reaction, University of Notre Dame, USA

[4] Falahat S., Diploma Thesis, Untersuchung der Kernreaktion $^{20}Ne(p,\gamma)^{21}Na$ im astrophysikalisch interessanten Energiebereich, 2006, Johannes Gutenberg Universität Mainz, Fachbereich Physik; to be published

* Work supported by HGF Virtuelles Institut für Struktur der Kerne und Nukleare Astrophysik (VISTARS) and the Joint Institute for Nuclear Astrophysics (JINA)
† falahat@uni-mainz.de
‡ Fritz-Strassmann Weg 2, 55128 Mainz, Germany
§ ISNAP, 46556, Notre Dame, Indiana, USA
¶ Planckstr. 1, 64291 Darmstadt, Germany

Measurements of the Interaction Cross-Sections of Proton-Rich Kr Isotopes

T. Yamaguchi[1], T. Suzuki[1], T. Ohnishi[2], K. Sümmerer[3], H. Geissel[3], G. Münzenberg[3], F. Becker[3], K-H. Behr[3], A. Brünle[3], K. Burkard[3], M. Fukuda[4], M. Hosoi[1], R. Janik[5], C. Karagiannis[3], K. Kimura[6], S. Mandal[3], S. Nakajima[1], T. Ohtsubo[7], A. Ozawa[8], A. Prochazka[5], M. Shindo[9], B. Sitar[5], P. Strmen[5], T. Suda[2], K. Sugawara[1], I. Szarka[5], A. Takisawa[7], M. Takechi[4], K. Tanaka[2]

[1]Saitama Univ., Japan; [2]RIKEN, Japan; [3]GSI Darmstadt, Germany;
[4]Osaka Univ., Japan; [5]Comenius Univ., Slovak; [6]Nagasaki Inst. App. Sci., Japan;
[7]Niigata Univ., Japan; [8]Univ. Tsukuba, Japan; [9]Univ. Tokyo, Japan

Measurements of the interaction cross-sections ($\sigma_{\rm I}$) at relativistic energies allow us to derive nuclear matter radii [1]. Since nuclear matter radii are directly related to the density distributions, the measurements of $\sigma_{\rm I}$ are a good probe to search for unusual nuclear structures such as halo and skin.

We have successfully performed several experiments to determine nuclear matter radii using the fragment separator FRS [2–5]. A recent remarkable finding is the evidence of the proton skins in proton-rich Ar isotopes [6]. One would expect that the proton as well as neutron skin is a quite common phenomenon for nuclei close to the proton and neutron drip line. Up to now, however, only Ar isotopes and few other nuclei are known to have the proton skins [7]. The measurements of $\sigma_{\rm I}$ of Kr isotopes is expected to provide another example of the proton skins. The charge radii are available from the isotope-shift measurements [8] so that the proton skin thickness can be extracted experimentally.

Another interest for the $\sigma_{\rm I}$ measurements is to study the nuclear equation of state (EOS) of asymmetric systems. For Kr isotopes the thickness of nucleon skins can be studied in a certain range of the neutron excess $\delta = (N-Z)/A = 0.1$.

We have measured the interaction cross-sections for even-mass Kr isotopes, ^{72,76,80}Kr at FRS. The experiment is essentially the same as our previous works [2–7]. The principle is based on the transmission method, in which the cross sections are derived from the ratio of the numbers of incoming and non-interacting outgoing particles passing through the secondary target placed at the second focus S2 of FRS.

The measurements for Kr isotopes are an effort to extend a series of successful experiments with light nuclei ($A \leq 40$) [2–7] to heavier nuclei ($A \simeq 80$). The TOF resolution of less than 30 ps was required between the first and second foci S1 and S2 of FRS to unambiguously identify the mass of incident particles. We succeeded in obtaining TOF resolution of 13 ps (σ) for the ^{80}Kr beam by using the ultra-fast timing plastic scintillation counters developed at RIKEN [9]. The ΔE resolution was also good enough ($\leq$1%) to separate the charges of the fragments, by employing MUSIC [10] and TEGIC (Tilted Electrode Gas Ionization Chamber) which have a maximum counting rate of 10^6cps [11].

A preliminary result of the interaction cross-sections of Kr isotopes is shown in Figure 1. One can clearly see that the cross sections increase as the mass number decreases. This is consistent with an increase in the nuclear matter radii toward the proton drip line.

This work was supported by VEGA, Slovakia.

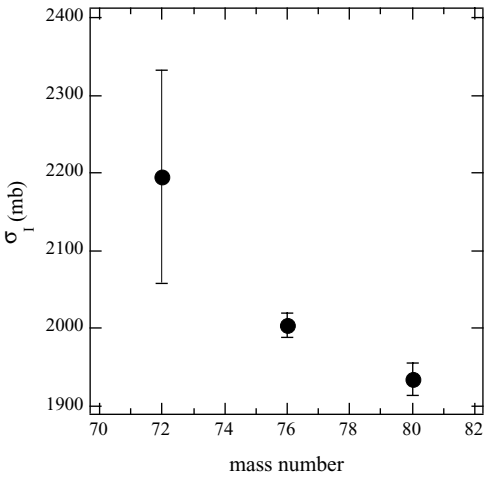


Figure 1: A preliminary result of $\sigma_{\rm I}$ of Kr isotopes as a function of the mass number.

References

[1] I. Tanihata et al., Phys. Lett. B 287 (1992) 307.
[2] T. Suzuki et al., Phys. Rev. Lett. 75 (1995) 3241.
[3] T. Suzuki et al., Nucl. Phys. A 658 (1999) 313.
[4] L.V. Chulkov et al., Nucl. Phys. A 674 (2000) 330.
[5] A. Ozawa et al., Nucl. Phys. A 691 (2001) 599.
[6] A. Ozawa et al., Nucl. Phys. A 709 (2002) 60.
[7] L.V. Chulkov et al., Nucl. Phys. A 603 (1996) 219.
[8] M. Keim et al., Nucl. Phys. A 586 (1995) 219.
[9] S. Nishimura et al., NIM A 510 (2003) 377.
[10] A. Stolz et al., GSI Scientific Report 1998 (1999) p. 174.
[11] K. Kimura et al., NIM A 538 (2005) 608.

Production Cross-Sections of Isotopes Formed by Fragmentation of ∼1 AGeV ^{80}Kr Beam

T. Yamaguchi[1], T. Ohnishi[2], K. Sümmerer[3], H. Geissel[3], G. Münzenberg[3], F. Becker[3], K-H. Behr[3], A. Brünle[3], K. Burkard[3], M. Fukuda[4], M. Hosoi[1], R. Janik[5], C. Karagiannis[3], K. Kimura[6], S. Mandal[3], S. Nakajima[1], T. Ohtsubo[7], A. Ozawa[8], A. Prochazka[5], M. Shindo[9], B. Sitar[5], P. Strmen[5], T. Suda[2], K. Sugawara[1], T. Suzuki[1], I. Szarka[5], A. Takisawa[7], M. Takechi[4], K. Tanaka[2]

[1] Saitama Univ., Japan; [2] RIKEN, Japan; [3] GSI Darmstadt, Germany;
[4] Osaka Univ., Japan; [5] Comenius Univ., Slovak; [6] Nagasaki Inst. App. Sci., Japan;
[7] Niigata Univ., Japan; [8] Univ. Tsukuba, Japan; [9] Univ. Tokyo, Japan

The proton drip line nuclei in the mass range 60< A <100 have received particular interest since they determine the astrophysical rapid proton capture process path [1, 2]. To produce the nuclei to be studied in this region, low energy fusion–evaporation reactions have been applied successfully for many years.

Recently, high- and intermediate–energy projectile fragmentation has also proved to be a powerful tool for producing nuclei far from stability [3, 4]. It is important to know their production cross-sections ($\sigma_{\rm F}$) to assess the feasibility of using them in radioactive beam experiment. It is difficult, however, to predict their $\sigma_{\rm F}$ with physical models, such as the abrasion–ablation model [5]. Another approach is to use an empirical parameterization, such as the EPAX formula [6, 7]. The quality of such a parameterization depends on the quality of the experimental data.

For krypton isotopes, data at high energy are available only for ^{84,86}Kr projectiles, at 200 and 500 AMeV, respectively [8, 9]. The present study was performed to extend the current database by studying the fragmentation of the relatively neutron–deficient krypton isotope ^{80}Kr.

The experiment was performed at the fragment separator facility FRS of GSI. Since the $\sigma_{\rm F}$ were obtained during the course of a secondary reaction experiment [10], the fragments were identified in the first half of the FRS, with a selection only according to their mass–over–charge ratios. A total of 3 different settings of FRS were used to select ^{72,74,76}Kr, as the central fragments. The experimental setup is essentially the same as that in our previous work [11].

As shown in Fig. 1(a), the TOF resolution of 33 ps [full width at half maximum (FWHM)] for primary beam, was sufficient to unambiguously identify the particles. The fragment nuclear charge number Z was determined by ΔE measurement in IC(see Fig. 1(b)) [12]. The nuclear charge resolution of $\Delta Z = 0.33$ (FWHM) was also sufficient. The magnetic field in the second dipole magnet gave $B\rho$ of the fragments. This allowed us to calculate A/Z from $B\rho$, TOF and Z, providing particle identification. We have observed neutron–deficient Kr to Ge isotopes. Further analysis is in progress.

This work was supported by VEGA, Slovakia.

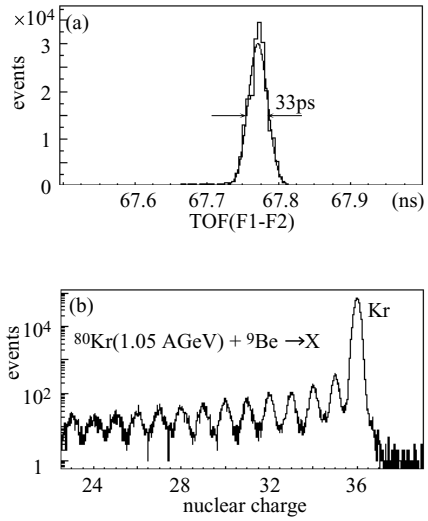


Figure 1: (a) TOF spectrum between the scintillators at the first and the second focus of FRS. (b) Nuclear charge spectrum of fragments from ^{80}Kr fragmentation at 1.05 AGeV, measured in an ionization chamber.

References

[1] B. Blank *et al*., Phys. Rev. Lett. **74**, 4611 (1995).
[2] M. J. López Jiménez *et al*., Phys. Rev. C **66**, 025803 (2002).
[3] C. Longour *et al*., Phys. Rev. Lett. **81**, 3337 (1998).
[4] T. Faestermann *et al*., Eur. Phys. J. A **15**,185 (2002).
[5] J. J. Gaimard and K.-H. Schmidt, Nucl. Phys. A **531**,709 (1991).
[6] K. Sümmerer *et al*., Phys. Rev. C **42**, 2546 (1990).
[7] K. Sümmerer and B. Blank, Phys. Rev. C **61**, 034607 (2000).
[8] C. Stéphan *et al*., Phys. Lett. B **262**, 6 (1991).
[9] M. Weber *et al*., Nucl. Phys. A **578**, 659 (1994).
[10] T. Yamaguchi *et al*., in preparation.
[11] A. Ozawa *et al*., Nucl. Phys. A **673**, 411 (2000).
[12] A. Stolz *et al*., Phys. Rev. C **65**, 064603 (2000).

Longitudinal velocity distributions measured with FRS and fundamental ideas on fragmentation*

A. Bacquias, V. Henzl, A. Kelić, M.V. Ricciardi, K.-H. Schmidt, GSI, Darmstadt, Germany

The study of the longitudinal-momentum width, $\sigma_{P//}$, of the spectator fragments produced in relativistic heavy-ions collisions is of great interest not only for the fundamental understanding of nuclear reactions but also for predictions of energy losses in accelerator-driven reactors and for the design of RIB facilities.

The experimental information on $\sigma_{P//}$ was for long time limited to fragments with mass close to the projectile and, to the other extreme, to the lightest fragments produced in more central collisions by multifragmentation [1]. The two classes of experimental data were compared with two predictions: the Morrissey formula [2] and the Goldhaber model, respectively [3]. The Morrissey's formula is based on an empirical systematic extracted from the experimental data available at the time. It is applicable only for fragments produced in very peripheral collisions. In the Goldhaber's model the momentum width of the prefragment is determined from the Fermi momentum of the abraded nucleons. The abrasion is seen as simple geometrical cut, ruled by statistical considerations. The effect of the sequential evaporation on the momentum width is not considered. This fact makes that the Goldhaber picture holds only for masses very close to the projectile and for very light fragments, since in these cases the effect of the following evaporation is negligible. The aim of this work is to create of physical model capable to predict $\sigma_{P//}$, which would take into account all the stages in the nuclear reaction, namely the abrasion, the following evaporation and the possible intermediate thermal instabilities.

In the last decade, with the use of magnetic spectrometers, high quality data were obtained over the almost mass range. Recently, devoted experiments were performed with the FRS at GSI to get full identification and extremely precise measurements of the longitudinal velocity of the fragments [4]. In Fig. 1, the velocity spectra for three fragments produced in the reaction ^{197}Au + ^{197}Au at 1 A GeV are presented [4]. The central gaussian peak is attributed to the fragmentation process.

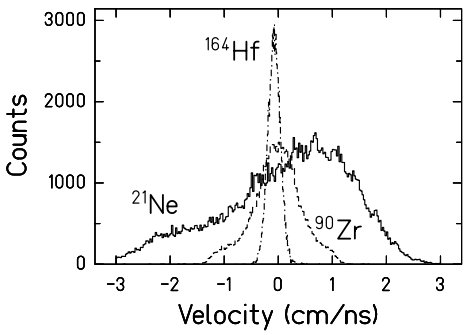


Figure 1: Velocity spectra for three fragments produced in the reaction ^{197}Au + ^{197}Au at 1 A GeV. Data are taken from [4].

The other humps, observable in the lightest fragments, are due to fission events, in which the coulomb repulsion pushes the fragment to higher velocities. From the fit of the central peak one can extract the values of $\sigma_{P//}$. The preliminary results are presented in Fig. 2 as a function of the mass of the final fragment A_f.

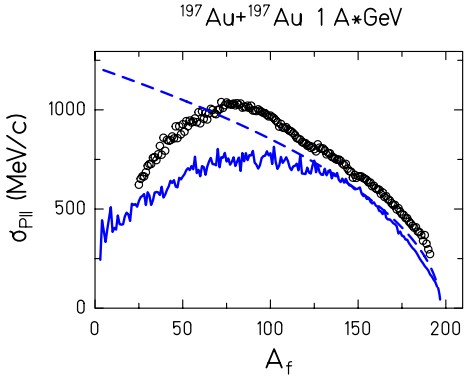


Figure 2: Preliminary data compared with the predictions of the Morrissey systematics (dashed line) and of ABRABLA (solid line).

A more careful analysis would include the simultaneous fit of all the components (fragmentation and fission humps). The simple fit, as performed in the present work, largely overestimates $\sigma_{P//}$ in the intermediate-mass region, where the presence of fission is not negligible. Nevertheless, the trend of the experimental data is correct. The data are compared with two predictions: the Morrissey systematic (dashed line) and the calculation ABRABLA. ABRABLA is an abrasion-evaporation statistical model. The momentum width acquired after the abrasion stage is calculated according to Goldhaber. Concerning the excitation energy reached by the prefragment, a limit is included to account for possible thermal instabilities. This limit corresponds to a temperature of 5 MeV. Beyond this limit, the nucleus breaks up simultaneously in several pieces. The prefragment finally decays by sequential evaporation of particles and very light nuclei, resulting in the enlargement of the momentum width due to the recoil of the nucleus when emitting particles. One can notice that for light fragment masses the Morrissey prediction deviates from the experimental data, as expected. Although the agreement between ABRABLA and the data is still not perfect, the model shows a right tendency, which reflects the physical content behind it.

[1] T. Odeh et al., Phys. Rev. Lett. 84 (2000).
[2] D.J. Morrissey, Phys. Rev. C 39, 460 (1989).
[3] A.S. Goldhaber, Phys. Lett. 53B (1974).
[4] V. Henzl, PhD Thesis, Univ. of Prague (2006).

*This work is part of A. Bacquias' PhD thesis.

Production of residual nuclides in the spallation of ^{238}U

E. Casarejos[2], M. V. Ricciardi[1], J. Taieb[1], F. Ameil[1], P. Armbruster[1], J. Benlliure[2], M. Bernas[3], A. Boudard[4], S. Czajkowski[5], T. Enqvist[1], R. Legrain[4], S. Leray[4], B. Mustapha[3], M. Pravikoff[5], F. Rejmund[1], K. -H. Schmidt[1], C. Stephan[4], L. Tassan-Got[3], C. Volant[4].
(1) GSI Darmstadt, (2) Univ. Santiago de Compostela, (3) IPN Orsay, (4) CEA Saclay, (5) CEN Bordeaux-Gradignan

The accurate prediction of formation cross sections of isotopes produced in spallation and fission reactions at intermediate energies is of extreme importance for the design of ADS and radioactive-ion-beam facilities. The predictive power of the computational tools is determined by the description of the reaction mechanisms involved. The physics involved in such reactions is still a subject of research, and precise experimental data are needed to test the reliability of theoretical models [1].

Residual nuclei from a ^{238}U beam at 1·A GeV on Be [2] and Pb [3] have already been produced in inverse kinematics at the FRS [3]. In this report, some preliminary results on reactions of proton and deuteron with ^{238}U at 1·A GeV are described. ^{238}U has been chosen as a reference material to investigate spallation and fission of fissile material at intermediate energy. Some attractive peculiarities of the in-flight separation are that fragments can be measured before they decay, the whole isotropic distribution can be obtained for every element, the velocity of the identified isotope can be precisely evaluated and used to deduce the reaction mechanism which generated that isotope (in this way, fission and fragmentation events can be disentangled). Although data have been taken for most of the produced residual nuclei from Z=6 to Z=93, only the formation cross sections and velocity distributions in *fragmentation* reactions and the velocity features of very light masses produced in strongly asymmetric *fission* (6<Z<20) have been analysed up to now.

In figure 1, the isotopic distributions of Yb (Z=70), Hg (Z=80), At (Z=85), U (Z=92), generated in the fragmentation of 1·A GeV ^{238}U in H_2 and D_2 targets are represented. Due to the heavier mass of the target nucleus, in the case of deuterium the higher energy transferred to the U nucleus leads to a longer evaporation chain and thus to a higher production of lighter residual masses. The drastic discrepancies between the data and a recent empirical systematics [4], which represents the actual knowledge on this field, demonstrates the important progress achieved by these new results.

Concerning the kinematics, the velocity of the fragments is lower than that of the beam due to momentum transfer in the collision. The surviving nucleus can then reach a stable configuration by an evaporation process or by fissioning. If the surviving nucleus fissions, the two fragments will run apart in opposite directions in the frame of the fissioning nucleus; the centre-of-mass velocity of the two ions must be equal to the velocity of the compound nucleus from which they were generated, thus slightly negative. This can be clearly observed in figure 2. There, the velocity of light elements produced in fission reactions is presented in the beam frame. The picture must be observed keeping in mind that, due to the limited angular acceptance of the spectrometer, fragmentation products can be almost entirely transmitted whilst only backward and forward emitted fission fragments succeed to pass through. Counts collected in the picture include a contribution from the titanium target windows. From data taken with a thin titanium target we deduced that the nuclei with the extreme velocity values are mostly due to the interaction of uranium with protons, while the central part is mostly due to the interaction of uranium with titanium. The velocities of very asymmetric fission fragments originated from the dichotomy of compound nuclei with masses around 180 to 240, estimated with a theoretical formula [3], perfectly overlap to the counts which fill the external wings of the distribution reported in fig. 2. Moreover, as already noted, the average value of the velocity of these two wings is consistent with the slightly negative value of the surviving nuclei observed in the fragmentation process. This allows us to interpret the counts in the two wings as very asymmetric fission products. So, neutron-rich light masses (like sodium), whose formation was already observed in direct kinematics in interactions of high-energetic protons with ^{238}U [5] [6], are produced in very asymmetric fission processes. The high value of the A/Z-ratio of formed isotopes is another sign that fission is the responsible production mechanism, since fragmentation generally produces isotopes on the neutron-deficient side of the beta-stability valley.

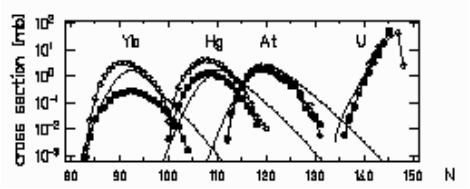


Figure 1: Preliminary experimental isotopic distributions for projectile fragments of 1·A GeV ^{238}U + p (•) and d (!). Relative error: 40%. Thick lines: Calculations [4] for 1 GeV p onto ^{238}U.

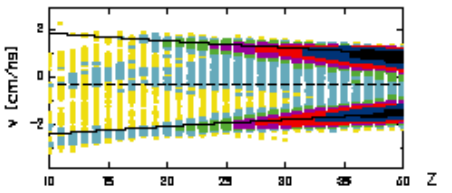


Figure 2: Shadowed area: plot of the preliminary experimental velocities versus element number. Lines: calculated velocities of fission fragments from the compound nucleus Z=84, A=214.

References

[1] F. Farget et al., GSI Scientific Report 1997, 33-34 (1998)
[2] Ch. Engelmann et al., GSI Scientific Report 1997, 36 (1998)
[3] T. Enqvist et al., Nucl. Phys. A 658, 47-66 (1999)
[4] C.H. Tsao, R. Silberberg, A.F. Barghouty, Astr. Phys. J. 501(1998)
[5] I. Amarel, R. Bernas, R. Foucher et al., Phys. Lett. 24B 402(1967)
[6] H.-J. Kluge, ISOLDE user's guide, CERN 86-05 (1986)

Systematic comparison of ISOLDE-SC yields with calculated in-target production rates *

S. Lukić,# F. Gevaert, A. Kelić, M. V. Ricciardi, K.-H. Schmidt, O. Yordanov
GSI, Darmstadt, Germany

Within the scope of the EURISOL project [1], the design of a large-scale European secondary-beam facility based on the ISOL (Isotope Separation On Line) method is actually being worked out. One of the tasks defined in the project is devoted to the predictions of the nuclide yields of the future facility.

The efficiency with which specific nuclides are extracted can vary over many orders of magnitude, thus strongly influencing the final yields. The information on the behaviour of the extraction efficiency with isotopic half-lives can help identifying the issues that need most attention in the process of target and ion-source development. The overall extraction efficiencies have been obtained earlier for some nuclides by measuring the extracted yields of stable [2] or radioactive [3] tracers implanted into a target. This method requires a dedicated experimental effort for every nuclide and every target and ion-source system.

We have used the ABRABLA code, benchmarked against recent GSI experimental cross-sections, to calculate the nuclide production rates in ISOLDE targets by proton-induced spallation at 600 MeV. We have compared these results to the published ISOLDE yields obtained with the proton beam from the CERN Synchrocyclotron (SC) [4]. In this way, we have systematically deduced the overall extraction efficiencies for a wide variety of isotopic chains from different target and ion-source systems, and studied their dependence on the isotope half-life. This dependence is found to follow a simple pattern in many different cases. For the shortest-lived isotopes, the extraction efficiency scales with a power function of the isotope half-life. For longer half-lives, the decay losses become negligible, and the extraction efficiency approaches the value valid for the stable isotopes. This behavior can be parameterized using the following function with three parameters that summarize the essential properties of the system in question:

$$\varepsilon\left(t_{1/2}\right) = \frac{\varepsilon_s}{1+\left(\frac{t_{1/2}}{t_0}\right)^{\alpha}} \qquad (1)$$

The parameters of the efficiency function are:

- The efficiency value ε_s in the limit of long half-lives.
- The exponent α of the power-function behaviour for the short half-lives.
- The value t_0 of the half-life around which the transition from the power-function to the constant behaviour occurs.

The efficiency in the limit of long half-lives reveals losses due to chemical reactions, sticking to the walls, condensation or escapes from the ionizer. The remaining two parameters directly relate to the decay losses and, thus, indicate the speed of the extraction.

As an example, the fit of the function (1) to the francium data is shown in the figure 1.

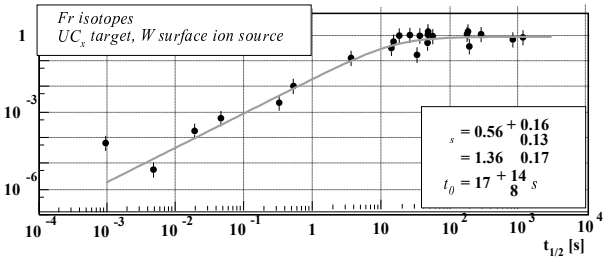


Figure 1: Overall release efficiency for Fr isotopes from a UC_x target with a W-surface ion source plotted in function of the isotopic half-life. The function described by the equation (1) was fitted to the data.

Several examples of fitted parameters for alkali elements are shown in the table 1.

Table 1: fitted parameter values for the alkali elements.

Element	Target	Ion Source	ε_s [%]	α	t_0 [s]
Na	UC_x	W surface	79^{+42}_{28}	1.26±0.32	$1.2^{+2.4}_{0.8}$
K	UC_x	W surface	108^{+45}_{32}	1.33±0.31	22^{+37}_{14}
Rb	UC_x	W surface	107^{+71}_{43}	0.45±0.40	$4.6^{+150}_{4.5}$
Cs	La molten	Ta surface	96^{+30}_{23}	2.78±0.32	56^{+22}_{16}
Fr	UCx	W surface	56^{+16}_{13}	1.36±0.17	17^{+14}_{8}

This kind of study is, in principle, applicable across the entire table of elements and for all targets and ion-sources. The present study comprises 35 cases of isotopic chains of elements from 4 different chemical groups, extracted from various target – ion-source systems [5].

References

[1] http://www.lnl.infn.it/~eurisol/
[2] R. Kirchner, Nucl. Inst. Meth. B70 (1992) 186
[3] N. Lecesne et al., Nucl. Inst. Meth. B126 (1997) 141
[4] H.-J. Kluge, "Isolde users guide", CERN, Geneva, 1986, web: http://isolde.cern.ch
[5] S. Lukic et al., Submitted for publication in Nucl. Inst. Meth. A

* We acknowledge the financial support of the European Community under the FP6 "Research Infrastructure Action - Structuring the European Research Area" EURISOL DS Project Contract no. 515768 RIDS. The EC is not liable for any use that may be made of the information contained herein.

s.lukic@gsi.de

Correlated Realistic Two-Body Interactions and the Tjon Line

R. Roth[a], T. Neff[b], H. Feldmeier[c]

[a] Technische Universität Darmstadt, Germany; [b] NSCL, Michigan State University, USA; [c] GSI, Darmstadt, Germany

With the advent of realistic nucleon-nucleon interactions, which reproduce the experimental NN scattering phase shifts and deuteron properties with high precision, the importance of three-body interactions became evident. Ab initio solutions of the nuclear many-body problem for p-shell nuclei, e.g. in the framework of Green's Function Monte Carlo or no-core shell model approaches, have demonstrated that the conventional realistic two-nucleon forces, e.g. the Argonne V18 or the Nijmegen I/II potentials are not sufficient to reproduce experimental binding energies and low-lying excited states. Typically, those potentials underestimate the binding energy of ^{4}He by approx. 4 MeV. In order to compensate for this deficiency, phenomenological three-nucleon forces are introduced, which depend on the underlying two-nucleon force. Some of the realistic potentials, e.g. the CD Bonn interaction, require significantly weaker three-body forces than the Argonne V18 potential.

Starting from one of the realistic two-nucleon forces we have employed the Unitary Correlation Operator Method (UCOM) to transform the original potential into a phase-shift equivalent correlated interaction $V_{\rm UCOM}$ [1]. Formally, this is achieved by a unitary transformation of the many-body Hamiltonian involving kinetic energy T and bare two-body potential V using unitary operators C_r and C_Ω

$$\mathrm{C}_r^\dagger \mathrm{C}_\Omega^\dagger (\mathrm{T}+\mathrm{V})\mathrm{C}_\Omega \mathrm{C}_r = \mathrm{T} + \mathrm{V}_{\rm UCOM} + \mathrm{V}^{[3]}_{\rm UCOM} + \cdots$$

The correlation operators C_r and C_Ω are tailored to describe short-range central and tensor correlations, respectively. Details on the construction of the correlation operators are given in [1]. The tensor correlator C_Ω has one parameter I_ϑ, which controls the range of the tensor correlations included via the transformation. In addition to the correlated two-body interaction $V_{\rm UCOM}$ the transformation generates a three-body interaction $V^{[3]}_{\rm UCOM}$ as well as higher-order terms. We focus on the application of $V_{\rm UCOM}$ in exact no-core shell model calculations for ^{3}H and ^{4}He using the code described in [3]. In this way we can asses the role of the omitted three-body terms $V^{[3]}_{\rm UCOM}$ and the range of the tensor correlation functions.

Figure 1 summarizes exact results for the ground state energies of ^{3}H and ^{4}He. Each symbol corresponds to a different interaction. The labeled symbols in the upper right quadrant show the results of exact calculations for different bare realistic NN interactions, which deviate significantly from the experimental values (Exp.). All realistic potentials seem to fall on a line in the $E(^3\mathrm{H})$-$E(^4\mathrm{He})$-plane known as Tjon line. If supplemented by a phenomenological three-nucleon force, fitted to the experimental binding energies, a good agreement can be achieved (cross symbols) [4].

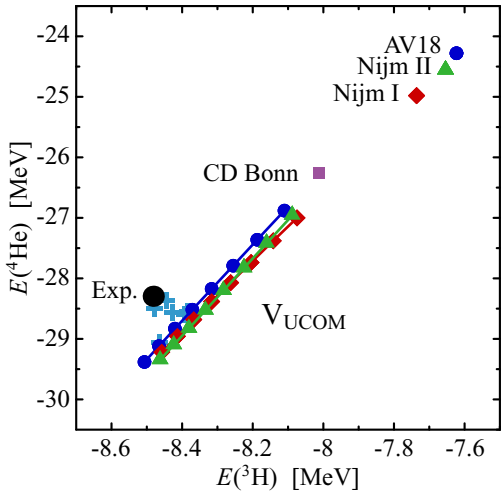


Figure 1: Exact ^{3}H and ^{4}He binding energies for different interactions in comparison with experiment (see text).

Now we add the results of no-core shell model calculations with $V_{\rm UCOM}$ to this picture. Using the range of the tensor correlators as a parameter, we can generate a manifold of phase-shift equivalent two-body interactions. The resulting ground state energies for the correlated Argonne V18 and Nijmegen I and II for $I_\vartheta = 0.05, 0.06, ..., 0.12\mathrm{fm}^3$ (from upper right to lower left) are depicted by the connected symbols. Obviously, one can choose the tensor correlator range such that the experimental binding energies are reproduced without employing an explicit three-body force and independent of the original interaction. This is a result of a cancellation between induced three-body interactions $\mathrm{V}^{[3]}_{\rm UCOM}$ and genuine three-body forces usually used to supplement the bare interaction.

The UCOM-transformation thus provides a way to construct phase-shift equivalent two-body potentials $V_{\rm UCOM}$ which require only minimal (or no) additional three-body components. Those are an ideal starting point for different many-body methods such as shell model, Hartree-Fock, perturbation theory, RPA, and Fermionic Molecular Dynamics, as discussed elsewhere (see [2] and references therein). Detailed no-core shell model calculations throughout the p-shell are presently in progress.

Supported by DFG under contract SFB634.

References

[1] R. Roth et al.; Phys. Rev. C 72, 034002 (2005).

[2] R. Roth et al.; nucl-th/0510036 (2005).

[3] P. Navrátil et al.; Phys. Rev. C 61, 044001 (2000).

[4] A. Nogga et al.; Phys. Rev. Lett. 85, 944 (2000).

RPA and ERPA with Correlated Realistic NN Interactions

P. Papakonstantinou, N. Paar, H. Hergert, R. Roth
Institut für Kernphysik, Technische Universität Darmstadt, Germany

The Unitary Correlation Operator Method (UCOM) provides a powerful scheme for carrying out ab initio nuclear structure calculations [1, 2, 3, 4]. In particular, it makes it possible to combine numerically affordable many-body Hilbert spaces with modern realistic NN interactions. Short-range correlations are explicitly taken into account. First results ranging from no-core shell model to Hartree-Fock (HF) and perturbation-theory calculations using correlated NN interactions have been reported previously.

In this work we employ correlated interactions in RPA studies of nuclear response. Only natural-parity excitations of spherical, closed-shell nuclei have been considered so far. First, HF calculations of the nuclear ground state are performed. The RPA is self-consistently formulated in the HF single-particle basis (HF+RPA model). We have also used an extended RPA version [5] (ERPA), which is built on top of the true RPA ground state and involves an iterative solution of the RPA equations. The influence of ground-state correlations on excitation properties can then be assessed. Corrected single-particle energies and occupation numbers can also be obtained.

We use the correlated interactions discussed in Ref. [4], based on the Argonne V18 potential. The results presented here were obtained in a harmonic-oscillator basis of 13 shells with the optimal value of the tensor correlation volume, $I_\vartheta^{(S=1,T=0)} = 0.09$ fm^3.

Our RPA results on the isoscalar (IS) giant monopole resonance (ISGMR), for various medium and heavy nuclei, are in good agreement with the experimental data. An example is shown in Fig. 1, where we see also that the ground state correlations taken into account in ERPA have a relatively small effect. In general, lower I_ϑ values result in lower ISGMR energies [6]. The isovector (IV) dipole strength (not shown) is distributed at energies which are too high compared with experiment; ERPA is not able to correct for this result. Inclusion of $2p2h$ configurations within second-order RPA is expected to bring the IVD strength to lower energies. Our results could be further improved by considering a phenomenological three-body correction to the correlated interaction.

Ground-state occupation numbers $n_i = \langle a_i^\dagger a_i \rangle$ (in standard notation) have been calculated within ERPA. In principle, UCOM-correlated operators should be used. The small depletion of the Fermi sea that we obtain using uncorrelated operators reflects the effect of the residual long-range correlations. Results for ^{40}Ca are presented in Fig. 2.

The UCOM scheme can be used in conjunction with other realistic (local or non-local) NN interactions, as well as with various many-body methods (Second RPA, QRPA, Shell Model, etc) for calculations across the nuclear chart. A next step in our exploration will be the use of second-order RPA as well as QRPA for open-shell systems.

Work supported by the DFG (SFB 634).

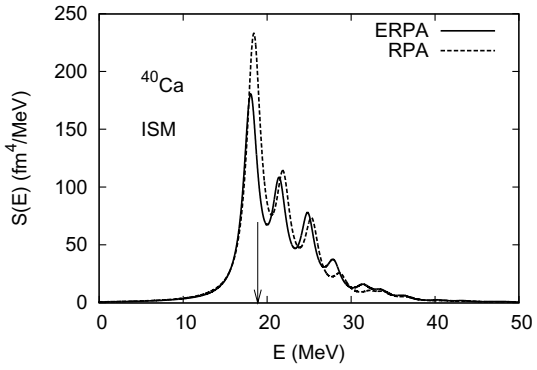


Figure 1: Isoscalar monopole resonance of ^{40}Ca, in HF+RPA (dashed lines) and ERPA (solid lines). An arrow indicates the experimental centroid.

References

[1] H. Feldmeier et al., *Nucl. Phys.* **A 632**, 61 (1998).
[2] T. Neff, H. Feldmeier, *Nucl. Phys.* **A 713**, 311 (2003).
[3] R. Roth et al., *Nucl. Phys.* **A 745**, 3 (2004).
[4] R. Roth et al., *Phys. Rev.* **C 72**, 034002 (2005).
[5] F. Catara et al., *Phys. Rev.* **B 58**, 16070 (1998).
[6] N. Paar et al., arXiv:nucl-th/0601026.

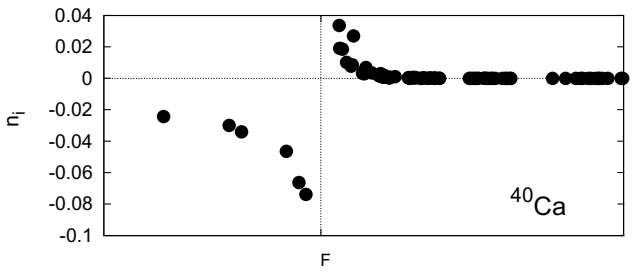


Figure 2: Change of the occupation probabilities of the HF single-particle states due to long-range correlations. Shown are ERPA results for proton orbitals in ^{40}Ca ($\varepsilon_{\rm F}$ is the Fermi energy).

Self-consistent Green's function calculations of finite nuclei

C. Barbieri*, GSI, Darmstadt, Germany

The properties of mean field orbits near the Fermi level can be strongly affected by collective excitations of the system. Such mechanisms are expected to have relevant effects on shell closure and spectroscopic factors for nuclei with extreme neutron/proton ratios. The coupling of single particle (sp) motion to excitations of the core, as well as to particle-particle (pp) and hole-hole (hh) correlations, is being computed employing the self-consistent Green's function (SCGF) approach [1, 2]. Calculations have been performed for the first time in a large no core model space, including up to eight major shells and partial waves $l \leq 4$.

The Lehmann representation of the sp propagator is

$$g_{\alpha\beta}(\omega) = \sum_n \frac{\langle \Psi^A | c_\alpha | \Psi_n^{A+1} \rangle \langle \Psi_n^{A+1} | c_\beta^\dagger | \Psi_0^A \rangle}{\omega - \left(E_n^{A+1} - E_0^A\right) + i\eta} + \sum_k \frac{\langle \Psi^A | c_\beta^\dagger | \Psi_k^{A-1} \rangle \langle \Psi_k^{A-1} | c_\alpha | \Psi_0^A \rangle}{\omega - \left(E_0^A - E_k^{A-1}\right) - i\eta} , \quad (1)$$

the poles of which are the transitions energies for the addition ($\varepsilon_n^+ = E_n^{A+1} - E_0^A$) and the removal ($\varepsilon_k^- = E_0^A - E_k^{A-1}$) of a nucleon. Applying the equations of motion to Eq. (1), one obtains a hierarchy of relations connecting the 2-, 4-, 6-point,... Green's functions. First is the Dyson equation, second the Bethe-Salpeter equation, third an expansion for the three-particle irreducible (3PI) propagator. It is at the level of the 3PI propagators for 2-particles–1-hole (2p1h) and 2h1p that the couplings between sp motion and collective modes become explicit. The example of a relevant diagram is shown in Fig. 1.

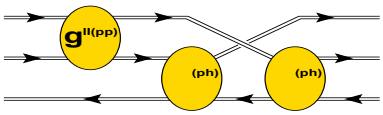


Figure 1: Example of diagrams contributing to the 3PI 2p1h propagator. $\Pi(\omega)$ and $g^{II}(\omega)$ are evaluated using dressed RPA. The double lines refer to the fully correlated sp propagator $g_{\alpha\beta}(\omega)$.

The formalism of Ref. [2, 3] evaluates the one-body response function $\Pi(\omega)$ and the pp/hh propagator $g^{II}(\omega)$ using the dressed random phase approximation (DRPA). These are coupled to the correlated $g_{\alpha\beta}(\omega)$ by solving a set of Faddeev equations for the 3PI propagators. A typical calculation starts with the Hartree-Fock (HF) approximation $g_{\alpha\beta}^{HF}(\omega)$ as a trial propagator, then the Dyson equation is solved for $g_{\alpha\beta}(\omega)$ and the whole procedure is iterated until convergence is reached.

Figure 2 shows the sp spectra for ^{16}O obtained using the unitary correlator operator method potential V_{UCOM} [4] and a G-matrix [5] as effective interactions. These were both derived form the Argonne V18 potential after removal of the electromagnetic terms (i.e., setting α=0). An oscillator parameter b=1.9 fm was used. The G-matrix interaction approximately reproduces the gap

* C.Barbieri@gsi.de

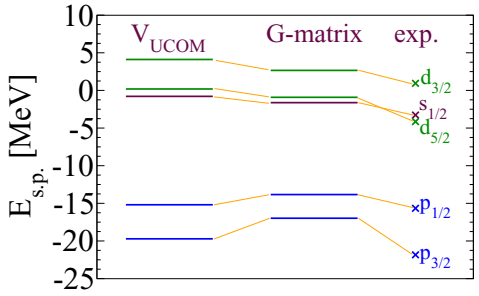


Figure 2: Single particle energies resulting from V_{UCOM} [4] and G-matrix. The experimental data refer to addition (removal) of a neutron to (from) ^{16}O.

between particle and hole energies but strongly underpredicts the splittings between spin orbit partners. Larger splittings are obtained using V_{UCOM}. The values obtained are compared to the HF results in Table 1. In both cases a strong reduction of the spin orbit interaction comes from coupling to collective modes. Phenomenological corrections or three-body forces may be needed to improve the comparison with the experiment. For the p shell, however, an additional correction from the coupling to the first excited 0+ level is expected in this case [3]. This involves 4p4h configurations not included in the present calculations.

The above formalism also allows the study of resonances using dressed RPA. Applications to neutron rich isotopes are planned.

Table 1: Spin orbit splittings (in MeV).

	$\Delta E_{p_{1/2}-p_{3/2}}$	$\Delta E_{d_{3/2}-d_{5/2}}$
V_{UCOM}-HF	6.30	4.61
V_{UCOM}-SCGF	4.52	3.92
$Gmtx$-HF	4.98	4.60
$Gmtx$-SCGF	3.14	3.57
exp. (^{15}O/^{17}O)	6.176	5.084

Acknowledgement. Part of this work was supported by the Natural Sciences and Engineering Research Council of Canada (NSERC).

References

[1] W. H. Dickhoff and C. Barbieri, Prog. Part. Nucl. Phys. **52**, 377 (2004).

[2] C. Barbieri and W. H. Dickhoff, Phys. Rev. C **63**, 034313 (2001).

[3] C. Barbieri and W. H. Dickhoff, Phys. Rev. C **64**, 064313 (2002).

[4] T. Neff abd H. Feldmeier, Nucl. Phys. **A713**, 311 (2003).

[5] M. Hjorth-Jensen, T. T. S. Kuo and E. Osnes, Phys. Rep. **261**, 125 (1995).

Shell Model Monte Carlo Applications

K. Langanke (GSI Darmstadt)
D.J. Dean and W. Nazarewicz (ORNL, Oak Ridge, USA)

The Shell Model Monte Carlo (SMMC) method allows shell model calculations in unprededently large model spaces and at finite temperatures. If the residual interaction between nucleons is described by an interaction of the pairing plus quadrupole type, the method is in principle exact and subject only to statistical errors. We have performed a series a calculation performed in the complete fp+gds model space, considering 50 active valence protons and neutrons each. The correlations, induced by the adopted pairing plus quadrupole interaction, reproduces the strong deformation in the $N \sim Z \sim 40$ region very well [1].

We have studied the thermal properties of four $N = 40$ medium-mass nuclei: ^{68}Ni, a substantially spherical and weakly paired nucleus; ^{70}Zr, a superfluid spherical nucleus; ^{72}Ge, a superfluid deformed nucleus which exhibits shape-coexistence; and the well-deformed, weakly-paired nucleus ^{80}Zr. A special focus of our SMMC calculations was on the competition between shape deformations and pairing correlations as a function of temperature. We find that shape and pairing changes contribute to the specific heat of the nucleus in a different way. While the superfluid-to-normal transition manifests itself as a pronounced peak in the specific heat around temperatures $T \approx 0.6 - 0.7$ MeV, the deformed-to-spherical transition is more gradually.

As an example, Fig. 1 shows the specific heat calculated for the nucleus ^{72}Ge. The pronounced peak at $T = 0.6$ MeV is related to the breaking of the proton and neutron pairs. The peak vanishes, if the pairing component in the residual interaction is switched off. The broad peak around $T = 3$ MeV is caused by the finite size of our model space ('Schottky peak'). The calculations have recently been extended to study the thermal properties of the nuclei as a function of rotation frequency by performing cranked SMMC calculations. A particular focus of these studies is the change of deformation and the pairing response.

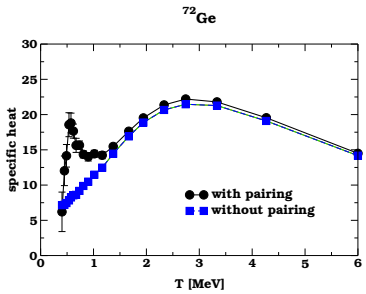


Figure 1: SMMC calculations of the specifi c heat for the nucleus ^{72}Ge performed with and without a pairing component in the residual interaction. (from [2]).

For a given many-body Hamiltonian the excitation energy $E(\beta)$ of a nucleus as a function of temperature $T = \frac{1}{\beta}$ is

$$E(\beta) = \frac{Tr[H \exp\{-\beta H\}]}{Tr[\exp\{-\beta H\}]} = \frac{\int dE \exp\{-\beta E\} E\rho(E)}{Z} \quad (1)$$

which allows to calculate the nuclear level density ρ by inversion. However, due to numerical difficulties with the Laplace transform, the integral is usually performed by saddle-point approximation. In (1), Z is the nuclear partition function.

We have calculated the level densities for several nuclei in the $A = 68 - 80$ mass range. By comparison to the standard backshifted Fermi gas treatment of the level densities, one finds that the model space is sufficient to yield reasonable level densities up to excitation energies of $E = 15 - 20$ MeV. An example is shown in Fig. 2 for the nucleus ^{72}Ge, considering of order 10^{26} configurations in the model space. Particular focus of the study is on the effect of pairing correlations on the level density. Due to the vanishing of proton and neutron pair correlations as function of temperature (excitation energy), the SMMC level density agrees well with a backshifted Fermi gas model with backshift $\Delta = 12/\sqrt{A}$ MeV at low excitation energies, while at large excitation energies it follows the Fermi gas model with $\Delta = 0$. The transition in between is well described if one assumes Δ to be energy-dependent and adopts the energy dependence from the expectation value of the SMMC pairing correlations as function of E. The calculation has been extended to odd-A and odd-odd nuclei. At low excitation energies, level densities are calculated in accord with standard Fermi gas model treatments ($\Delta \approx 0$ for odd-A and negative Δ for odd-odd nuclei).

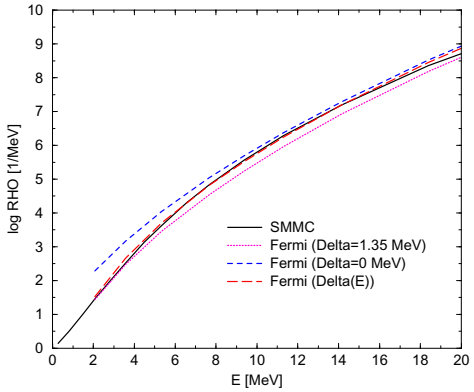


Figure 2: Comparison of SMMC level density for ^{72}Ge with backshifted Fermi gas models with backshift $\Delta = 12/\sqrt{A}$ MeV, $\Delta = 0$ and energy-dependent backshift.

References

[1] K. Langanke, D.J. Dean and W. Nazarewicz, Nucl. Phys. A728 (2003) 109

[2] K. Langanke, D.J. Dean and W. Nazarewicz, Nucl. Phys. A757 (2005) 360

[3] K. Langanke, to be published

Shell Model Monte Carlo method in the pn-formalism

C. Özen, GSI, Darmstadt, Germany
D. J. Dean, ORNL, Oak Ridge, USA

The Shell model Monte Carlo (SMMC) method [1] was developed as an alternative to direct diagonalization in order to study low-energy nuclear properties. It was successfully applied to nuclear problems where large model spaces made diagonalization impractical. One calculates the thermal canonical expectation values of observables of few-body operators by representing the imaginary-time many-body evolution operator as a superposition of one-body propagators in fluctuating auxiliary fields. Thus, one recasts the Hamiltonian diagonalization problem as a stochastic integration problem.

Recently a new approach to the SMMC method has been developed [2] in which the isospin symmetry is explicitly broken. This pn-implementation enables one to treat shell-model Hamiltonians that are not isospin invariant in the model space, or for which different model spaces are used for protons and neutrons. The method is general and may be used for realistic Hamiltonians, as well those of a more schematic variety.

As a first novel application of the new implementation, we performed SMMCpn calculations for the even-even $^{90-104}$Zr and $^{92-106}$Mo isotopic chains using a realistic effective interaction [3] derived with many-body perturbation theory techniques for the $1p_{1/2}, 0g_{9/2}$ proton and $1d_{5/2}, 2s_{1/2}, 1d_{3/2}, 0g_{7/2}, 0h_{11/2}$ neutron model spaces. Initial experimental studies [4] indicated that nuclei in this region have very large deformations, and that the transition from spherical shapes to highly deformed shapes occurs abruptly: ^{96}Zr is rather spherical while $^{100-104}$Zr nuclei are well deformed with a quadrupole deformation parameter of $\beta_2 = 0.35$ [5]. Furthermore, the spherical-to-deformed transition is more abrupt in the Zr isotopes than in the nearby elements Mo, Ru, and Pd. Generator-coordinate mean-field calculations in this region [6] are able to reproduce the shape transitions with particular Skyrme interactions. The region also exhibits significant shape-coexistence phenomena [7].

Shown in Fig.5-1 are calculations of the ground-state masses for the Zr and Mo isotope chains relative to the 88Sr core. Note that a very simple modification of the monopole part of the interaction (one that does not change the excitation spectrum) yields a reasonable description of masses along the isotope chains. Further work will be performed to understand the nuclear deformations in this region. Although nuclei above A=94 show significant deformation with this realistic interaction, there is still a factor of two difference between theory and experiment. We will investigate the origin of this problem in future work.

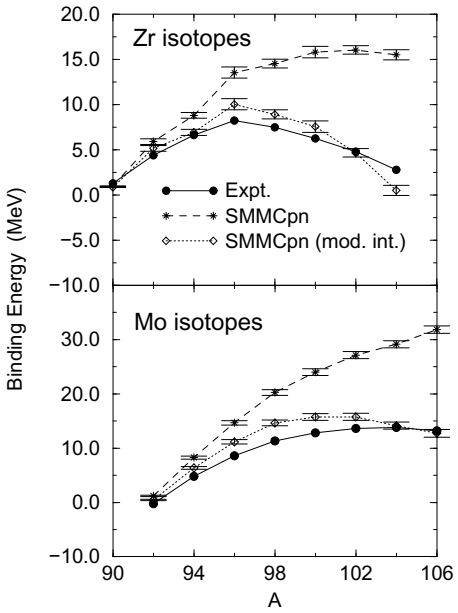


Figure 1: Binding energies of the Zr and Mo isotopes. Experimental values (full circles) and calculated values (asterisks) are shown. Calculations with monopole-corrected interactions (diamonds) are also plotted.

References

[1] S.E. Koonin, D.J. Dean, and K. Langanke, Phys. Reps. 278, 2 (1997)

[2] C. Özen and D.J. Dean, submitted to Phys. Rev. C (2005).

[3] A. Holt et al., Phys. Rev. C 61, 064318 (2000).

[4] E. Cheifetz et al., Phys. Rev. Lett. 25, 38 (1970).

[5] M. A. C. Hotchkis et al., Phys. Rev. Lett. 64, 3123 (1990).

[6] J. Skalski et al., Nucl. Phys. A559, 221 (1993).

[7] P.-G. Reinhard et al., Phys. Rev. C 60, 014316 (1999); J.L. Wood et al., Phys. Rep. 215, 101 (1992).

Beyond the relativistic mean-field approximation: configuration mixing of angular momentum projected wave functions

P. Ring and T. Nikšić*, Technische Universität München, Garching, Germany
D. Vretenar, Faculty of Science, University of Zagreb, Croatia

Abstract

We report the first study of restoration of rotational symmetry and fluctuations of the quadrupole deformation in the framework of relativistic mean-field models. A model is developed which uses the generator coordinate method (GCM) to perform configuration mixing calculations of angular momentum projected wave functions, calculated in a relativistic point-coupling model. The geometry is restricted to axially symmetric shapes, and the intrinsic wave functions are generated from the solutions of the constrained relativistic mean-field + BCS equations in an axially deformed oscillator basis.

Introduction

The rich variety of nuclear shapes, governed by the evolution of shell structure, has been the subject of extensive experimental and theoretical studies. Far from the β-stability line the energy spacings between single-particle levels change considerably with the number of neutrons and/or protons, resulting in reduced spherical shell gaps and even disappearance of spherical magic numbers. Although both the global shell-model and the self-consistent mean-field models have been employed in the description of shell evolution far from stability, the later approach is far more suitable for medium-heavy and heavy nuclei. In principle, it enables a description of the nuclear many-body problem in terms of a universal energy density functional. However, a quantitative description of shell evolution necessitates the inclusion of many-body correlations beyond the mean-field approximation. Among the most important ones are the rotational energy correction and the fluctuations of the quadrupole deformation. Both types of correlations can be included simultaneously by mixing angular momentum projected states corresponding to different quadrupole moments. The most effective approach for configuration mixing calculations is the generator coordinate method, with multipole moments used as coordinates that generate the intrinsic wave functions.

Applications: ^{32}Mg

In order to test our implementation of the GCM and angular momentum projection, a number of illustrative calculations have been carried out for the nuclei ^{194}Hg and ^{32}Mg [1]. The PC-F1 parameter set [2] has been used for the effective point-coupling Lagrangian, and the effective interaction in the particle-particle channel has been approximated by a density-independent δ-force.

* Supported by the Alexander von Humboldt Stiftung

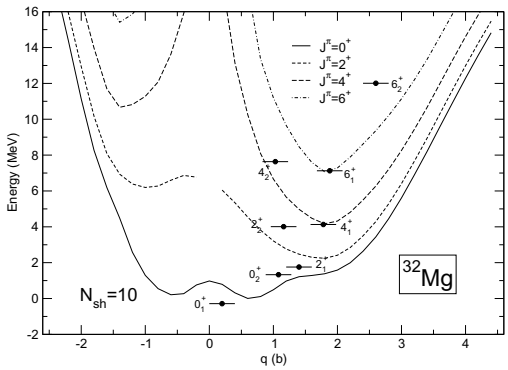


Figure 1: The GCM states in ^{32}Mg, together with the corresponding projected energy curves.

Our results are generally in very good agreement with the predictions of GCM calculations based on the non-relativistic effective interactions. In Fig. 1 we display the GCM states in ^{32}Mg, together with the corresponding angular momentum projected energy curves. The particular choice of the PC-F1 effective interaction results in an almost spherical ground state of ^{32}Mg and rather high value $E_{2_1^+} = 2.04$ MeV in comparison with the experimental data $E_{exp} = 0.885$ MeV [3]. This result, related to overestimated size of the spherical $N = 20$ neutron gap, points to an important problem. Virtually all global effective interactions have been adjusted to data, e.g. masses and radii, which already include correlations. On the other hand, those correlations that we wish to treat explicitly, should not be included in the effective interaction in an implicit way. The solution is to adjust global effective interactions to pseudodata, obtained by subtracting correlation effects from experimental masses and radii. Therefore, our next task is to adjust a new global effective point-coupling interaction which will not implicitly contain rotational energy corrections and quadrupole fluctuation correlations. Further developments will include the treatment of pairing fluctuations by particle number projection, the description of non-axial shapes, and the extension to odd nuclei.

References

[1] T. Nikšić, D. Vretenar, and P. Ring, submitted to Phys. Rev. C, as a preprint at http://xxx.lanl.gov, nucl-th/0601005.

[2] T. Bürvenich, D. G. Madland, J. A. Maruhn, and P.-G. Reinhard, Phys. Rev. C 65, 044308 (2002).

[3] C. Détraz et al., Nucl. Phys. A 426, 37(1984).

Relativistic Mean-Field Model with Momentum-Dependent Self-Energies

S. Typel, GSI, Darmstadt, Germany

Abstract

The conventional relativistic mean-field model with minimal meson-nucleon couplings is extended by introducing derivative meson-nucleon couplings. Combining this approach with a density dependence of the coupling vertices leads to an improved description of nuclear matter and atomic nuclei, especially of effective masses and the optical potential.

Introduction and Theoretical Model

The relativistic mean-field model (RMF) enjoys considerable success in the description of various properties of nuclear matter and atomic nuclei [1]. With nucleons and mesons as degrees of freedom and few parameters (masses and coupling strengths), basic features of these systems, e.g. the strong spin-orbit interaction, are readily explained. A density dependence of the effective in-medium interaction has to be introduced by assuming non-linear (NL) couplings of the mesons or a density-dependence (DD) of the meson-nucleon couplings in order to achieve a really quantitative description of experimental data. The nucleon self-energies in standard RMF models show a non-trivial density dependence but no momentum dependence as obtained, e.g., in microscopic Dirac-Brueckner calculations of nuclear matter.

The present model combines the flexibility of RMF models with density-dependent couplings with the feature of momentum-dependent self-energies in RMF models with derivative couplings. For details, see [2]. The parameters of the new model (D^3C) are found by fitting properties of doubly magic atomic nuclei (binding energy, charge and diffraction radii, surface thickness, neutron skin thickness, spin-orbit splittings) and the Schrödinger-equivalent optical potential in symmetric nuclear matter derived from the description of elastic proton-nucleus scattering in Dirac phenomenology [3].

Results and Outlook

The momentum-independent self-energies of conventional RMF models lead to a linear increase of the optical potential with much too large repulsion at high energies, see Fig. 1. In contrast, the self-energies in the D^3C model describe the energy-dependence of the empirical optical potential quite well. A binding energy of -15.981 MeV/nucleon, an incompressibility of 232.5 MeV, and a symmetry energy of 31.9 MeV at saturation density 0.151 fm^{-3} are obtained in the D^3C model, i.e. very reasonable values of the standard nuclear matter parameters. The effective Dirac mass $m_D = 0.541m$ at saturation is rather small. However, this is necessary to obtain the correct spin-orbit splitting in atomic nuclei. In contrast, the effective Landau mass m_L, that is related to the density of states, is much larger, see Fig. 1. Correspondingly, the density of single-particle levels at the Fermi surface in atomic nuclei increases. In standard RMF models, the level density is usually much too small because a large difference between m_D and m_L cannot be obtained without loosing a quantitative description of the spin-orbit interaction.

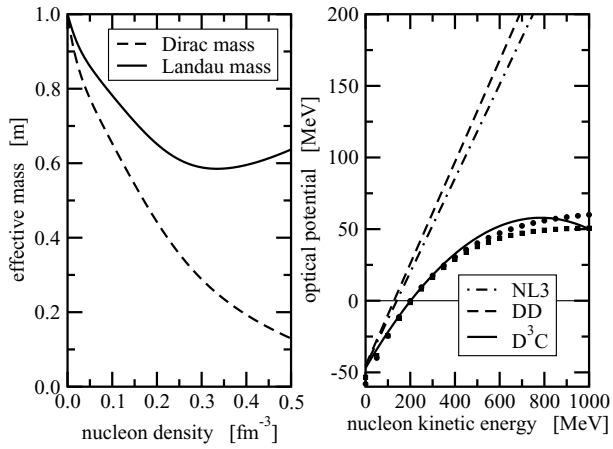


Figure 1: Left: Effective nucleon masses in symmetric nuclear matter of the D^3C model. Right: Schrödinger-equivalent central optical potential in symmetric nuclear matter at saturation density for standard RMF models (NL3 [4], DD [2]) and the D^3C model in comparison to results of Dirac phenomenology (circles, squares) [3].

A further improvement in the description of the optical potential and the level densities is possible by a readjustment of the model parameters assuming different functional forms for the density dependence of the meson-nucleon couplings. Also, it is worthwhile to apply the present model to the description of non-doubly magic and deformed nuclei. This will require the treatment of pairing effects and more elaborate numerical calculations.

References

[1] P. Ring, Prog. Part. Nucl. Phys. 37 (1996) 193.

[2] S. Typel, Phys. Rev. C 71 (2005) 064301.

[3] S. Hama et al., Phys. Rev. C 41 (1990) 2737. E.D. Cooper et al., Phys. Rev. C 47 (1993) 297.

[4] G.A. Lalazissis, J. König, and P. Ring, Phys. Rev. C 55 (1997) 540.

Superdeformation in Pb isotopes with large neutron excess

J. Daoutidis, P. Ring*, Technische Universität München, Garching, Germany
G. A. Lalazissis, Aristotle University, Thessaloniki, Greece

Abstract

Covariant Density Functional theory (CDFT) is used to investigate superdeformation in Pb isotopes on the neutron rich side of the periodic table. Energy surfaces and deformation parameters in this region are calculated by solving the constrained Relativistic Hartree Bogoliubov (RHB) equations.

Covariant density functional theory

Density functional theory is applied with great success in many areas of physics. In nuclear physics relativistic density functionals have gained much interest in recent years as for instance relativistic mean field (RMF) theory [1] or relativistic Hartree Bogoliubov (RHB) theory [2]. Lorentz invariance provides many features, which can be described in non-relativistic functionals only at the cost of additional parameters. In particular one hopes that relativistic functionals provide a more reliable description of the spin-orbit splitting far from stability.

Application to superdeformed Pb-isotopes

Shape coexistence in Pb isotopes on the proton rich side has been observed experimentally, as for instance in Ref. [3]. It also has been studied theoretically within the relativistic mean field model [4].

There are only few investigations of heavy nuclei on the neutron rich side of the valley of stability, mostly restricted to the area of fission products. So far it is experimentally very difficult to produce and to investigate very heavy nuclei on the neutron rich side. On the other hand, these nuclei are extremely important for our understanding of the nuclear synthesis of heavy elements above the Pb region. Nuclei with very large neutron excess play a dominant role on the r-process path. Therefore for the moment one has to rely on theoretical predictions

We have performed constrained RHB calculation in the isotopic chain of Pb nuclei [5]. Starting from the doubly magic ^{208}Pb up to very exotic isotopes with extremely large neutron excess. We use the Lagrangian parametrization DD-ME2, which has an explicit density dependence in both isoscalar and isovector channels, and the pairing force D1S of Gogny in the pairing channel. This study showed the existence of superdeformed minima in most of Pb nuclei at excitation energies which vary from a few MeV to large values. The heights of the barrier at superdeformation are larger for those Pb isotopes which favor spherical shape. The study also showed that the results are independent of the variation of the RHB model used in the analysis.

* ring@ph.tum.de

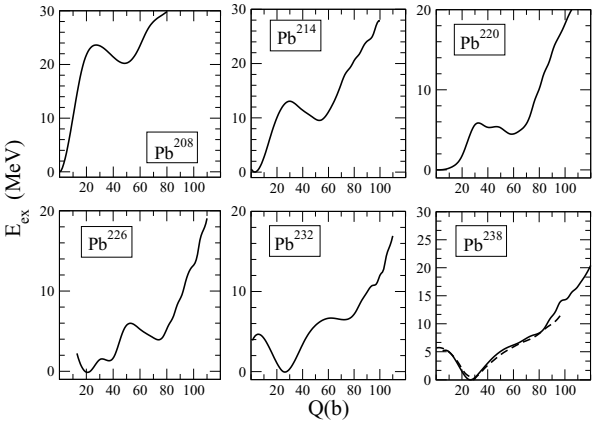


Figure 1: Potential energy surfaces for the nuclei ^{208}Pb, and ^{214}Pb, and ^{220}Pb, ^{226}Pb, ^{232}Pb and ^{238}Pb as a function of the quadrupole moment q. For ^{238}Pb the curve (dashed line) that corresponds to RHB calcualtions with the non-linear force NL3 is also included for comparison.

The potential energy surfaces (PES) of several Pb nuclei are shown in Figure 1. It is seen that in going from ^{208}Pb to heavier isotopes the g.s minimum at the beginning corresponds to the spherical shape. However, this behavior is changing rapidly at about A=226, where the Pb nuclei seem to favor a deformed shape. The deformation parameter β_2 reaches its maximum about ^{238}Pb and then starts gradually decreasing. Finally sphericity is restored again after ^{250}Pb. We find that nuclei betwee ^{238}Pb and ^{244}Pb practically do not show any superdeformed minimum.

A quantitative analysis of shape coexistence phenomena certainly goes beyond mean field theory. This has been shown recently on the proton rich side by investigations using of the Generator Coordinate Method (GCM) connected with angular momentum projection. Work in this direction on the neutron rich side is in progress.

References

[1] B. B. Serot and J. D. Walecka, Adv. Nucl. Phys. **16**, 1 (1986).

[2] T. Gonzales-Llarena, J. L. Egido, G. A. Lalazissis, and P. Ring, Phys. Lett. **B379**, 13 (1996).

[3] A. N. Andreyev *et al.*, Nature **405**, 430 (2000).

[4] D. Vretenar, A. V. Afanasjev, G. A. Lalazissis, and P. Ring, Physics Reports **409**, 101 (2005).

[5] J. Daoutidis and G. A. Lalazissis, J. Phys. **G31**, 659 (2005).

Determination of spherical mean field nuclei

P. Klüpfel*, P.–G. Reinhard, Universität Erlangen/Nürnberg, Germany
T.J. Bürvenich, J.A. Maruhn, Universität Frankfurt, Germany

Abstract

For the purpose of fitting nuclear mean-field models, we search for those spherical nuclei which are well reproduced by a mean-field description. To that end, we investigate the correlation energies for isotopic and isotonic chains of semi-magic nuclei. We find that isotonic chains provide the best pool of data.

Motivation

Self-consistent nuclear mean-field models are a widely used tool for a high quality description of nuclear structure and low-energy dynamics throughout the whole nuclear landscape (perhaps excluding the lightest elements), for a recent review see [1]. The form of the underlying energy functionals can be deduced from rather general arguments (e.g., low momentum expansion). The parameters of a model need to be adjusted phenomenologically. This is usually done by a fit to a selection of nuclei. Spherical nuclei are preferred for technical reasons. It is desirable that the chosen fit nuclei are well described within a mean-field approach, i.e. the correlation energy stemming from softness against deformation and from low-lying quadrupole modes is small. Semi-magic nuclei are usually supposed to meet these both conditions. It is the aim of this contribution to explore the amount of correlation effects in the chains of semi-magic nuclei.

Formal framework

We concentrate here on the Skyrme-Hartree-Fock model (SHF). The correlations are computed with the techniques as explained in detail in [2, 3]. The potential energy surface (PES) for deformation is determined by constrained Hartree-Fock (CHF) using the quadrupole operator as constraint. The quadrupole collective mass and related zero-point energies are computed by self-consistent cranking. This information from microscopic calculations determines the collective Hamiltonian for quadrupole motion. The ground-state solution of the collective Schrödinger equation provides the correlation energy associated with low-lying collective quadrupole modes.

Results and discussion

Figure 1 shows the correlations energy as computed with the Skyrme parameterization SkI3 [4] for a broad selection of semi-magic nuclei. The horizontal lines mark the intended uncertainties on the energies. Nuclei which stay within these bounds are considered as good mean-field nuclei. There are two exceptions: first, nuclei with $N = Z$ are uncertain due to an additional binding through the Wigner effect [1], and second, doubly-magic nuclei have, in fact, less correlation energy than the CHF method here predicts. Besides that, the figure suggests immediately two general rules: first, isotones provide longer chains of well behaved nuclei than isotopes, and second, the regions of $Z = 28$ and $N = 28$ are mostly dangerous. That result is surprising and needs yet to be taken care of in a more educated choice of fit nuclei when determining mean-field parameterizations.

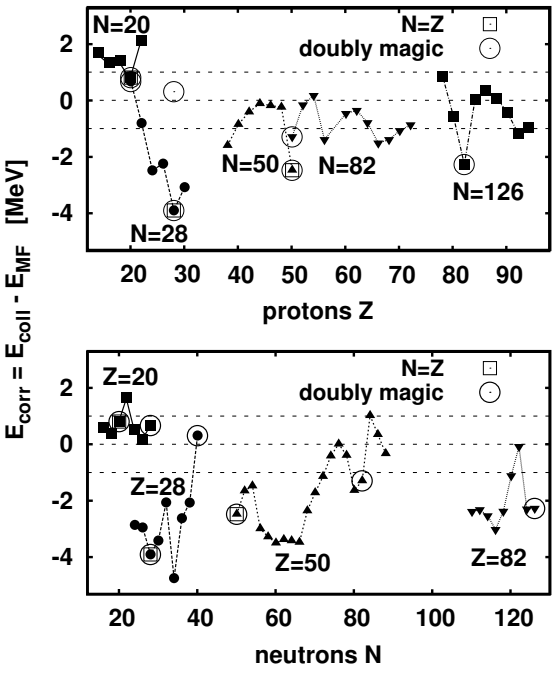


Figure 1: Correlation energies from the low-lying 2^+ state for isotopic (lower) and isotonic (upper) chains of semi-magic nuclei computed for the Skyrme force SkI3 [4]. The nuclei with $N = Z$ are marked by an open box and the doubly-magic nuclei by an open circle. The horizontal dashed lines mark the typical average uncertainty of energies achieved in fits of mean-field models.

References

[1] M. Bender *et al*, Rev. Mod. Phys. **75** (2003) 121

[2] P. Fleischer *et al*, Eur. Phys. J. A **22** (2004) 363

[3] P. Fleischer *et al*, Phys. Rev. C **70** (2004) 054321

[4] P.-G. Reinhard and H. Flocard, Nucl. Phys. A **584** (1995) 467

* Supported by the BMBF 06 ER 124

Constraining a nuclear energy density functional by low-energy QCD*

P. Finelli†, N. Kaiser and W. Weise, Technische Universität München, Germany
Dario Vretenar, Physics Department, Faculty of Science, University of Zagreb, Croatia

A relativistic nuclear energy density functional

$$E_0[\rho] = E_{\rm free}[\rho] + E_{\rm H}[\rho] + E_{\rm coul}[\rho] + E_\pi[\rho] \qquad (1)$$

has been developed, guided by two important features that establish connections with chiral dynamics and the symmetry breaking pattern of low-energy QCD:

1. large scalar and vector mean fields (with opposite sign) related to in-medium changes of QCD vacuum condensates [1], determining the Hartree energy functional $E_{\rm H}[\rho]$;
2. long- and intermediate-range interactions generated by one-and two-pion exchange and derived from in-medium chiral perturbation theory [2], with explicit inclusion of $\Delta(1232)$ excitations, determining the exchange correlation energy functional $E_\pi[\rho]$.

We have constructed a point-coupling model with density dependent interaction terms, in which the single terms of (1) reads [3]

$$E_{\rm free}[\rho] = \int d^3r\, \langle\phi_0|\bar\psi[-i\boldsymbol{\gamma}\cdot\boldsymbol{\nabla} + M_N]\psi|\phi_0\rangle \ , \qquad (2)$$

$$E_{\rm H}[\rho] = \frac{1}{2}\int d^3r\, [G_S^{(0)}\rho_S^2 + G_V^{(0)}\rho^2] \ , \qquad (3)$$

$$E_\pi[\rho] = \frac{1}{2}\Big\{\int d^3r\, [G_S^{(\pi)}(\rho)\rho_S^2 + G_V^{(\pi)}(\rho)\rho^2] + \int d^3r\, [G_{TS}^{(\pi)}(\rho)\rho_{S3}^2 + G_{TV}^{(\pi)}(\rho)\rho_3^2] - \int d^3r\, [D_S^{(\pi)}(\vec\nabla\rho_S)^2\Big\} \ , \qquad (4)$$

$$E_{\rm coul}[\rho] = \int d^3r\, A^0 e\frac{1+\tau_3}{2}\rho \ . \qquad (5)$$

The overall structure of $E_0[\rho]$ is reminiscent of what is commonly introduced for relativistic atomic systems in a DFT approach [4]. E_π plays the role of the exchange correlation term $E_{\rm exc}$ and $E_{\rm H}$ is the nuclear counterpart of the Hartree term.

This approach has been tested in the analysis of ground-state observables of spherical and deformed nuclei. In Fig. 1 we show recent results of an extensive study of ground-state properties of deformed isotope chains with $60 \le Z \le 80$, calculated in the Relativistic Hartree-Bogoliubov approximation [5].

The agreement with experimental data is very good over a wide range of isotopic chains and it demonstrates the validity of our basic assumptions. Study of collective excitations is in progress.

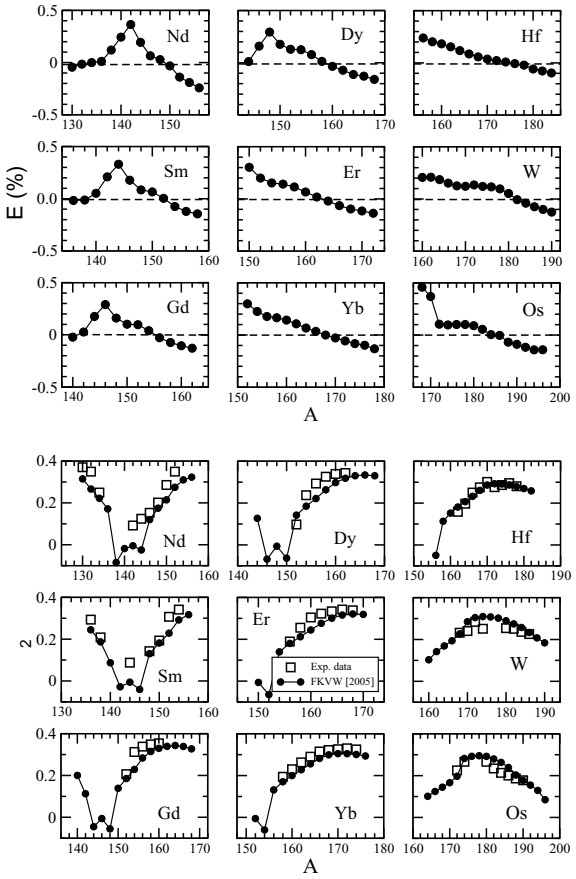


Figure 1: The deviations (in percent) of the calculated binding energies and the predictions for the ground-state quadrupole deformations of the Nd, Sm, Gd, Dy, Er, Yb, Hf, W, and Os isotopes.

References

[1] T. D. Cohen, R. J. Furnstahl, D. K. Griegel and X. m. Jin, Prog. Part. Nucl. Phys. **35** (1995) 221.

[2] S. Fritsch, N. Kaiser and W. Weise, Nucl. Phys. A**750** (2005) 259.

[3] P. Finelli, N. Kaiser, D. Vretenar and W. Weise, Nucl. Phys. A**735** (2004) 449.

[4] R. M. Dreizler and E. K. U. Gross, Density Functional theory, Spinger-Verlag, 1990; R. M. Dreizler, Lect. Notes Phys. **620** (2003) 123.

[5] P. Finelli, N. Kaiser, D. Vretenar and W. Weise, [arXiv:nucl-th/0509040] submitted to Nucl. Phys. A .

* Work supported by BMBF, GSI, MURST and INFN
† pfinelli@ph.tum.de

Low-momentum Hyperon-Nucleon Interactions

M. Wagner,[a] B.-J. Schaefer,[a,b] J. Wambach,[a,c] T.T.S. Kuo,[d] and G.E. Brown[d]

[a] Institut für Kernphysik, TU Darmstadt, Germany [b] Institut für Physik, Karl-Franzens-Universität, Graz, Austria
[c] GSI, Darmstadt, Germany [d] Department of Physics and Astronomy, State University of New York, Stony Brook, USA

Recently, it has become possible to calculate an 'universal' effective low-momentum potential $V_{\mathrm{low}\,k}$ for the nucleon-nucleon (NN) interaction by Renormalization Group (RG) techniques. These effective nucleon-nucleon potentials $V_{\mathrm{low}\,k}$ have been successfully applied to few-body and shell-model calculations [1].

Starting from realistic bare NN potentials one integrates out the high-momentum components in order to obtain the low-momentum effective potential $V_{\mathrm{low}\,k}$. It is constructed by introducing a cutoff Λ for the intermediate momenta in the Lippmann-Schwinger equation such that the physical quantities are cutoff independent. This is achieved by demanding the conservation of the half-on shell T-matrix. From this requirement one can derive the RG flow equation

$$\frac{d}{d\Lambda} V_{\mathrm{low}\,k}(k',k) = \frac{2}{\pi} \frac{V_{\mathrm{low}\,k}(k',\Lambda) T(\Lambda,k;\Lambda^2)}{1-k^2/\Lambda^2} \,.$$

Instead of using standard numerical (e.g. Runge-Kutta) methods for its solution we apply the Andreozzi-Lee-Suzuki (ALS) iteration technique [2].

We have generalized this method to the hyperon-nucleon (YN) sector [3]. The main difference, compared to the NN interaction, is the $\Lambda \leftrightarrow \Sigma$ coupling in the YN sector. The mass difference $m_\Sigma - m_\Lambda \approx 78\,\mathrm{MeV}$ cannot be neglected and shall be incorporated into the ALS iteration schema. Unfortunately, there exist only few YN scattering data and hence the YN interaction is not well constrained. As initial bare potentials for the RG equations we have used the Nijmegen SC97 models [4]. We have calculated the YN $V_{\mathrm{low}\,k}$ in the isospin as well as in the particle basis. For strangeness $S=-1$ there are two isospin channels $I=1/2$ and $I=3/2$ available. Only in the $I=3/2$ channel there is no coupling to the Λ particle. In Fig. 1 we show the results for the $\Sigma N \to \Sigma N$ $^1S_0$ partial wave. We have used three different NCS97 fits and a cutoff $\Lambda = 500\,\mathrm{MeV}$. By construction the phase shifts are preserved. In the $I=1/2$ channel the $\Lambda \leftrightarrow \Sigma$ coupling can emerge. This is a completely new situation for the $V_{\mathrm{low}\,k}$ approach because the mass difference has to be considered in the ALS iteration explicitly. By means of an energy-motivated cutoff we have generalized the $V_{\mathrm{low}\,k}$ approach to treat the $\Lambda \leftrightarrow \Sigma$ coupling appropriately.

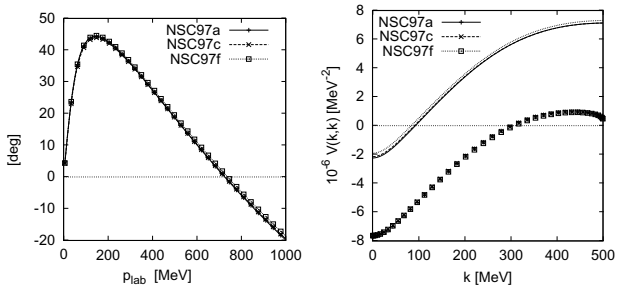


Figure 1: Left panel: $^1S_0$ phase shifts for three different bare potentials as a function of the momentum in the lab frame p_{LAB}. Right panel: Three diagonal bare potentials V_{bare} (NSC97a,c,f; dashed lines) and three (Hermitian) $V_{\mathrm{low}\,k}$ matrix elements (dotted) for $\Sigma N \to \Sigma N$ ($I=3/2$, $^1S_0$) versus the relative momentum k.

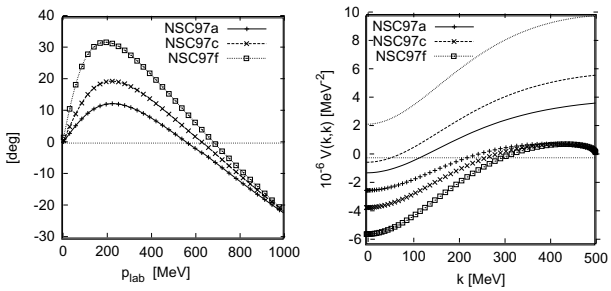


Figure 2: $^1S_0$ partial wave for the $I=1/2$ $\Lambda N \to \Lambda N$ channel. Same labeling as in Fig. 1.

In Fig. 2 we show results for the $\Lambda N \to \Lambda N$ $^1S_0$ partial wave. The phase shifts obey approximately the same shape but have different heights. For momenta near the cutoff the diagonal matrix elements collapse but they differ for lower momenta.

To conclude, in some partial waves we see a similar convergence to an universal softer low-momentum YN interaction as for the NN case. This can reduce the uncertainty in the potentials due to the unknown high-momentum physics. We also plan to use other realistic bare potentials and to perform Hypernuclei calculations.

References

[1] S. K. Bogner, T. T. S. Kuo, and A. Schwenk, Phys. Rept. **386**, 1 (2003), nucl-th/0305035.

[2] F. Andreozzi, Phys. Rev. C **54**, 684 (1996).

[3] B.-J. Schaefer, M. Wagner, J. Wambach, T. T. S. Kuo, and G. E. Brown, Phys. Rev. C (RC) in press (2005), nucl-th/0506065.

[4] T. A. Rijken, V. G. J. Stoks, and Y. Yamamoto, Phys. Rev. C **59**, 21 (1999).

Electron scattering on two-neutron halo nuclei with full inclusion of final state interactions

S.N. Ershov*, Joint Institute for Nuclear Research, 141980 Dubna, Russia
B.V. Danilin, Russian Research Center "The Kurchatov Institute", 123182 Moscow, Russia
J.S. Vaagen, SENTEF Department of Physics and Technology, University of Bergen, Norway

Abstract

A theory for electron scattering from Borromean two-neutron halo nuclei with full inclusion of final state interactions is developed. The halo nucleus is described as a three-body system ($core + n + n$). Nuclear wave functions for bound state and low-lying three-body continuum excitations are calculated by the method of hyperspherical harmonics. The model is applied to explore electron scattering on ^{6}He leading to nuclear excitations near the three-body breakup threshold.

One of the most interesting questions in the physics of radioactive beams is that of the structure of halo nuclei at the limits of nuclear existence. In Borromean two-neutron halo nuclei, like ^{6}He and ^{11}Li, the nature of the three-body continuum is currently most intriguing. The concentration of transition strength, experimentally observed in these nuclei at low excitation energy, may contain three-body resonances or new kinds of collective motion, such as a soft dipole mode corresponding to oscillations of the core against the halo neutrons. The continuum is usually explored via responses induced by one-step transitions from the ground state to the continuum.

We have developed a theory for description of electron scattering from two neutron Borromean halo nuclei in which effects of final state interactions between fragments are fully taken into account [1, 2]. The theory is coined for processes with small transferred momenta leading to low-energy nuclear excitations, the region which is most sensitive to the specific features of halo structure. The participant-spectator model is not applicable to this region. The nuclear structure was described within a cluster three-body model. This model reproduces rather well not only the properties of the ground state but is the natural basis for calculation of continuum states when the nucleus breaks into three fragments. The method of hyperspherical harmonics was used for solution of the three-body problem and for calculations of transition densities to the continuum.

The theory has been applied to make predictions for electron scattering from ^{6}He - the Borromean nucleus which is the test-bench example for theoretical studies of two-neutron halo structure. Our calculations of inclusive inelastic scattering show that dipole excitations dominate in spectrum at small transferred momenta. The position of the maximum and the shape of the dipole spectrum change with increasing transferred momenta. This differs from the behavior of the well known 2^+ true three-body resonance and gives additional evidence against a resonance nature for the soft dipole excitations. As an example of the theoretical calculations, Fig.1 shows the theoretical coincidence spectra for electron scattering angle θ = 10^o as function of the nuclear excitation energy E^* for different angles θ_y between the α-particle and the transferred momentum $\mathbf{q}$.

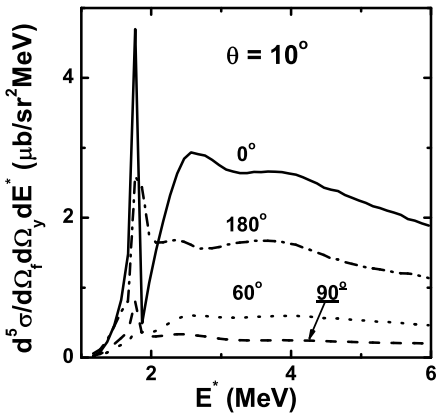


Figure 1: Cross sections $d^5\sigma/d\Omega_f d\Omega_y dE^*$ for electrons with energy ε_i = 500 MeV and scattering angle θ = 10^o as function of nuclear excitation energy E^*. The solid, dotted, dashed and dot-dashed lines correspond to angles $\theta_{\alpha q}$ equal 0^o, 60^o, 90^o and 180^o, respectively.

Future measurements of electrons in coincidence with fragments bear promise to give valuable information about halo structure. The pattern of energy and angular correlations are rather specific for different multipole excitations. Correlation measurements in general provide a unique tool for revealing the complex dynamics of nuclear excitations and pave a way to spectroscopy of the continuum, granted that rather small cross sections can be measured.

S.E. and B.D. acknowledge support from RFBR Grants No. 05-02-17535 and 1885.2003.2. and B.D.- from grant INTAS 03-54-6545.

References

[1] S.N. Ershov, B.V. Danilin, J.S. Vaagen, Phys. Rev. C **72**, 044606 (2005).

[2] B.V. Danilin, S.N. Ershov, J.S. Vaagen, Phys. Rev. C **71**, 057301 (2005).

* ershov@thsun1.jinr.ru

Assessment of saddle-point-mass predictions for astrophysical applications

Aleksandra Kelić and Karl-Heinz Schmidt, GSI, Darmstadt, Germany

In the r-process, fission has the decisive influence on the termination of the r-process as well as on the yields of transuranium elements and, consequently, on the determination of the age of the Galaxy and the Universe. Fission can also influence the abundances of nuclei in the region $A \sim 90$ and 130 due to the fission cycling. One of the common conclusions from extensive investigations on the beta-delayed, neutron- and neutrino-induced fission is that the role of fission in the r-process is very sensitive to the fission-barrier heights of heavy nuclei with A>190 and Z>84. Unfortunately, experimental information on the height of the fission barrier is only available for nuclei in a limited region of the nuclide chart, and for heavy r-process nuclei one has to rely on theoretically calculated barriers. Due to the limited number of available experimental barriers, in any model the constraint on the parameters defining the dependence of the fission barrier on neutron excess is rather weak. This leads to large uncertainties in estimating the fission-barrier heights of heavy nuclei involved in the r-process as can be seen in Fig. 1.

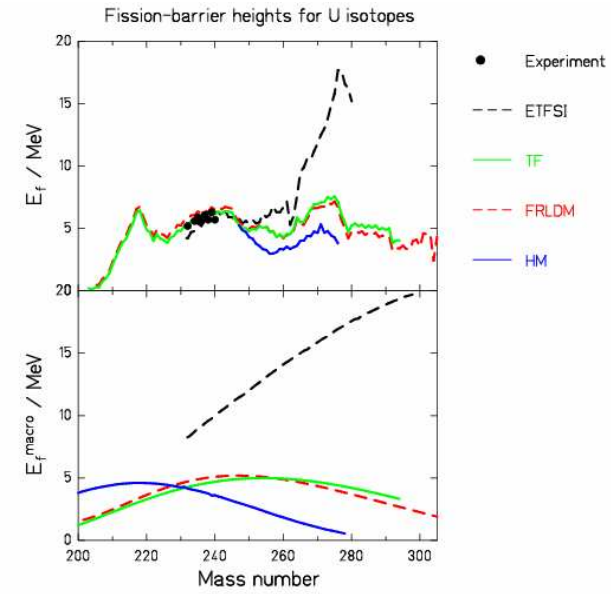


Figure 1: Full macroscopic-microscopic (upper part) and macroscopic part (lower part) of the fission barrier calculated for different uranium isotopes using the models mentioned in the text.

From the lower part of the figure it is evident that the largest discrepancies originate from the macroscopic part. Therefore, we have recently [1] examined the predictions of several macroscopic models by means of a detailed analysis of the isotopic trends of ground-state and saddle-point masses. We consider the macroscopic saddle-point masses given by the following models: Droplet model (DM) [2], Finite-range liquid drop model (FRLDM) [3], Thomas-Fermi model (TF) [4], Extended Thomas-Fermi model (ETF) [5]. In order to test the consistency of these models, we study the difference between the experimental saddle-point mass and the macroscopic part of the saddle-point mass given by models:

$$U_{sadd} = E_f^{\exp} + M^{\exp} \quad (E_f^{macro} + M^{macro}) \qquad (1)$$

with E_f being the height of fission barrier and M the ground-state mass. This quantity corresponds to the empirical shell-correction energy at the saddle point. At the saddle point configuration, due to the topographic theorem [5], the shell-correction energy is very small. Any general trend (e.g. increase or decrease) in δU_{sad} as a function of the neutron number would thus indicate severe shortcomings of a given macroscopic model in extrapolating to nuclei far from stability. The extracted slopes (A_1) of δU_{sad} as function of the neutron excess are shown in Fig. 2 for the different elements.

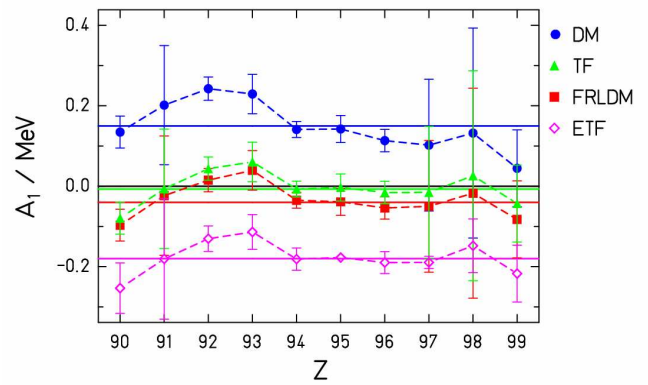


Figure 2: Slopes of δU_{sad} as a function of the neutron excess are shown as a function of the nuclear charge number Z.

The results of this study show that the most realistic predictions are expected from the Thomas-Fermi model and the finite-range liquid-drop model while inconsistencies in the saddle-point mass predictions of the droplet model and the extended Thomas-Fermi model were seen. Understanding the "extrapolatibility" of global nuclear-structure models is extremely important, and much attention has been paid to this test for ground-state masses. This work presents an important extension of these types of analyses to the question of reliably predicting fission-barrier heights for nuclei along the r-process path.

References

[1] A. Kelić and K.-H. Schmidt, accep. by Phys. Lett. B
[2] W.D. Myers, 1977 IFI/Plenum, ISBN 0-306-65170-X
[3] A. Sierk, Phys. Rev. C33 (1986) 2039
[4] W.D. Myers and W.J. Swiatecki, Phys.Rev.C60 (1999) 014606-1
[5] A. Mamdouh et al, Nucl. Phys. A 679 (2001) 337

Collisions of $^{16}O+^{16}O$ in a Full Skyrme-Force TDHF Treatment*

J. A. Maruhn, Institut für Theoretische Physik, Universität Frankfurt am Main, Germany
P.-G. Reinhard, Institut für Theoretische Physik, Universität Erlangen-Nürnberg, Germany
P. D. Stevenson, Department of Physics, University of Surrey, Guildford, UK

Abstract

A three-dimensional treatment of $^{16}O+^{16}O$ collisions with a complete modern Skyrme force shows enhanced energy loss and demonstrates the importance of time-odd parts introduced into the density functional to maintain Galilei invariance: these lead to additional energy loss due to excitation of a spin mode.

Motivation

Historically TDHF calculations were limited by the available computing power, necessitating symmetry restrictions such as axial geometry and simplified Skyrme forces. We have now constructed a new code that does away with all of these limitations: it allows the calculation in a three-dimensional Cartesian grid and the use of complete modern Skyrme forces. It was expected that the further relaxation of symmetries should lead to additional energy loss; the results of the calculations, however, also exhibited several surprising features.

New Spin Excitation

A Skyrme energy functional that contains current density contributions is not generally Galilei invariant in the sense that a static nucleus with all the wave functions multiplied by a common plane-wave factor should move uniformly. For example, for the spin-orbit term this requirement leads to a contributions containing $\times\mathbf{j}$, which will cause spin excitations even in spin-saturated matter.

In central heavy-ion collisions the net nucleonic current density shows a bit of sidewards streaming, which leads to the formation of a spin density with azimuthal character. The energy associated with this spin excitataion is of the order of 20 MeV. It is strongly excited up to impact parameters of 3-4 fm.

It should be noted that when the time-odd spin-orbit term is omitted in the calculation, the relative motion kinetic energy is no longer strictly conserved for separated nuclei. This was also seen in the calculations.

Energy Loss

The observed energy loss for several Skyrme forces in central collisions with incoming energy between 75 and 150 MeV is shown in Fig. 2 and compared to axial calculations from [1], in which SkM was employed and where a comparison to calculations with total omission of spin-orbit coupling was also given.

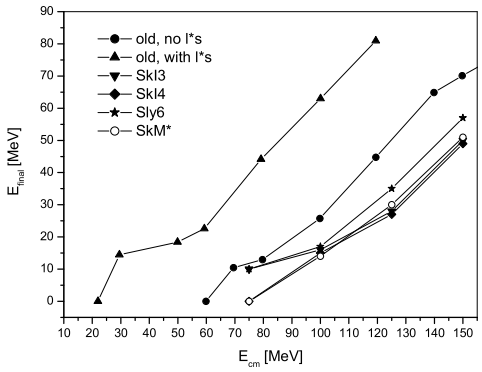


Figure 2: Energy loss in central collisions.

The additional energy loss is not as dramatic as the one caused by the inclusion of spin-orbit in [1], but what is surprising is the relatively good agreement for all the forces in the present calculation. The larger discrepancy at 75 MeV is caused by fusion, which was assumed to be realized after 1000 fm/c interaction time.

For noncentral collisions a comparison is shown in Fig. 2 for SkM* and 100 MeV. This figure also shows the reduced enrrgy loss without the time-odd terms discussed above. The full three-dimensional treatment now seems to lead to a qualitatively different behaviour for intermediate impact parameters compared to the "old" calculations of [1]. This clearly illustrates the additional dissipation due to lifting of symmetry constraints.

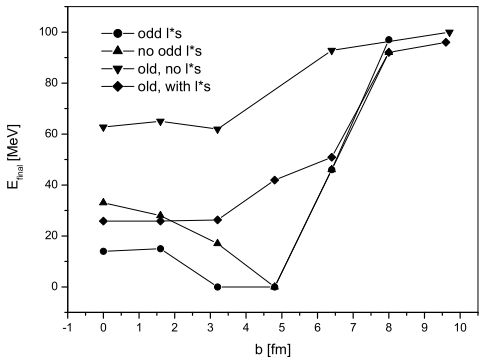


Fig. 2: Energy loss for noncentral collisions.

References

[1] P.-G. Reinhard et al., Phys. Rev C**37**, 1026 (1988).

* Work supported by BMBF under project no. 06 ER 124 and 06 F 131 and UK EPSRC under grant GR/S96425/01

Microscopic Calculation of Fusion Cross Sections

T. Neff, NSCL, Michigan State University, East Lansing, USA
H. Feldmeier, K. Langanke, GSI, Darmstadt, Germany

In the high density environment of the crust of a neutron star it is expected that electron capture dominates nuclear processes, driving nucleosynthesis towards the neutron drip line [1]. At sufficiently high densities and low temperatures pycnonuclear reactions are favoured to occur. The determination of fusion cross sections at extremely low energies is a critical issue for calculating reaction rates of astrophysical interest.

Our aim is to provide fully microscopic calculations of the fusion cross sections for some selected nuclei (^{16}O, ^{22}O and ^{24}O) that can be used to test the simpler models used in astrophysical network calculations. We perform these calculations in the framework of the Fermionic Molecular Dynamics (FMD) model. We use an effective interaction that is derived from realistic nucleon-nucleon forces by explicitly introducing short-range central and tensor correlations in the Unitary Correlation Operator Method (UCOM) [2].

The FMD ground states are obtained by minimizing the energy with respect to the parameters of all the nucleons. In the case at hand they are identical to spherical closed shell configurations. The FMD basis allows us to easily shift and boost the wave functions. We can therefore use our wave functions and interaction in the spirit of the microscopic cluster model to calculate nucleus-nucleus potentials. The system of two nuclei at a distance R is described by a Slater determinant built with the two ground state wave functions projected on angular momentum

$$\left| \Psi^{\ell}(R) \right\rangle = P^{\ell}_{00} \mathcal{A} \left\{ \left| \psi(-R\vec{e_z}/2), \psi(R\vec{e_z}/2) \right\rangle \right\} . \quad (1)$$

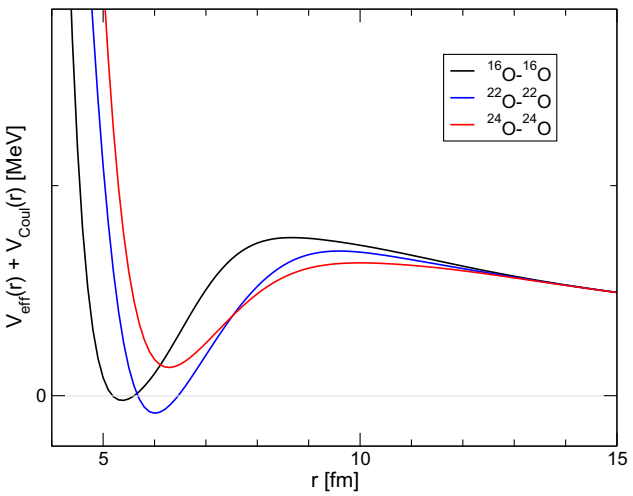


Figure 1: Effective Nucleus-Nucleus Potentials ($\ell = 0$) derived from the FMD energy surfaces. The barrier gets lower and shallower with increased neutron number.

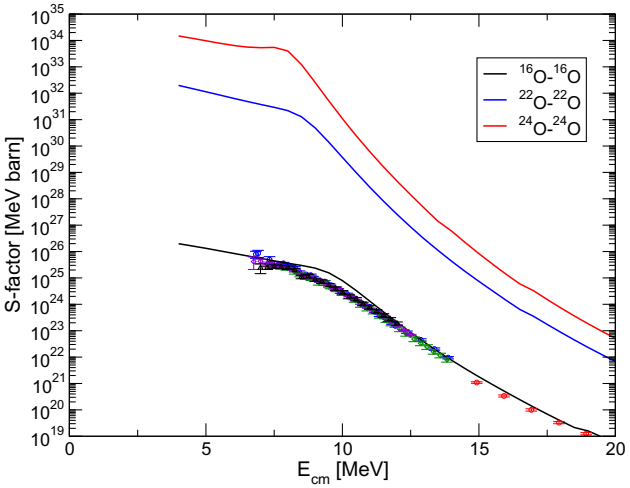


Figure 2: S-factor for the fusion of oxygen isotopes. Experimental data for ^{16}O are included.

The Slater determinants still contain the center of mass motion. In the case of equal widths for the Gaussians the center of mass wave function factorizes and we can define the corresponding RGM wave function [3]. The RGM wave function can not yet be identified with a wave function of two point-like nuclei as the basis states are non orthogonal because of the antisymmetrization. Therefore in a following step the RGM norm kernel is diagonalized numerically. Using these eigenstates we could now define a non-local potential for two point-like nuclei. Alternatively we can try to fit a local equivalent potential $V_{eff}(r) + \frac{\ell(\ell+1)}{2\mu r^2}$ to the matrix elements. This works remarkably well giving the same fit for the different partial waves. The potentials derived in this way are depicted in Fig. 1. These potentials are finally used to solve the Schrödinger equation with incoming wave boundary conditions. Here we assume that the two nuclei will fuse if they reach the minimum behind the Coulomb barrier. The penetration probabilities for all possible partial waves are finally summed up to get the total fusion cross section shown in Fig. 2. A remarkable agreement with the data for ^{16}O can be observed. For the neutron rich isotopes we find much enlarged cross sections.

References

[1] M. Beard, M. Wiescher, Revista Mexicana de Fisica **49**, supl. 4, (2003) 139

[2] R. Roth, T. Neff, H. Hergert, H. Feldmeier, Nucl. Phys. **A745** (2004) 3

[3] H. Horiuchi, Cluster model of the nucleus, World Scientifi c Publishing, 1986

Diabatic states from nodal structure conservation

F. A. Ivanyuk* and W. Nörenberg, GSI, Darmstadt, Germany

Many-body systems like nucleons in nuclei and electrons in atoms, molecules and clusters are basically described in the single-particle approximation, where the particles (or quasiparticles) move independently in a (self-consistent) mean potential V. The mean potential $V(\mathbf{q})$ depends on parameters $\mathbf{q} \equiv \{q_1, q_2, ..., q_f\}$ which denote e.g. deformation degrees of a nucleus or cluster, the coordinates of nuclei in a molecule, or the strengths of external fields acting on the many-body system. The eigenstates $|\alpha(\mathbf{q})\rangle$ and eigenvalues $e_\alpha(\mathbf{q})$ of the Hamiltonian $H(\mathbf{q}) = T + V(\mathbf{q})$ define the adiabatic basis. Problems arise when the Schrödinger equation is solved for a time-dependent potential $V(\mathbf{q}(t))$. Only for small enough velocities $\dot{\mathbf{q}}(t)$, the particles follow the time-dependent potential adiabatically, i.e. along the adiabatic states (Born-Oppenheimer approximation). With increasing velocities $\dot{\mathbf{q}}(t)$, however, the particle motion deviates more and more from adiabaticity, the deviation being caused essentially by the derivative coupling $\langle\alpha(\mathbf{q})|\nabla_{\mathbf{q}}|\alpha'(\mathbf{q})\rangle$. In fact near points, where two adiabatic states come close (quasicrossing), the derivative coupling becomes large, because the (nodal) structure of the wave functions change rapidly.

There are methods available for eliminating the derivative coupling within a subset of adiabatic states, and hence defining diabatic states which are smooth as function of $\mathbf{q}$. However in situations, where several quasicrossings mix strongly with each other, they become numerically difficult or unreliable.

We have introduced [1] a novel method for the construction of diabatic states, which is based on stable diagonalization procedures for a Hamiltonian $H(\mathbf{q})$ given by its matrix elements in a suitable set of basis states. For the diabatic states $|\nu(\mathbf{q})\rangle$ we require (1) that they are *eigenstates of a diabatic Hamiltonian* $H_d(\mathbf{q})$, which is uniquely defined in $\mathbf{q}$-space, and (2) that they *conserve their nodal structure* while following the variation of $H(\mathbf{q})$ in an optimal way. The first requirement is basic to assure one-valued single-particle energies (i.e. potentials) $e_\nu(\mathbf{q})$ and states $|\nu(\mathbf{q})\rangle$ as functions of $\mathbf{q}$. The second requirement is crucial for diabaticity and, satisfying this via a variational principle involving $H(\mathbf{q})$, renders uniqueness to the definition of diabatic states. Since only matrix elements of the Hamiltonian are needed, the method can be used in rather different (also self-consistent) approaches and applied in many fields of chemistry and physics.

The construction method [1] is illustrated for the deformed nucleus with 90 protons and 134 neutrons (^{224}Th). Figure 1 shows the results for the 1/2+ levels. In large parts of the diagram a remarkable correspondence between diabatic and adiabatic levels is observed.

To characterize the dependence of the wave functions on deformation, we consider the mass parameter in the cranking approximation shown in Fig. 2. The rapid variations of the adiabatic states with deformation, in particular around quasicrossings, are responsible for the large fluctuations in the adiabatic mass parameter. The smoothness of the diabatic states yields values which are one to two orders of magnitude smaller than the adiabatic values.

Our diabatic basis can be applied in various ways. For example in certain time-dependent problems one likes to know the diabatic motion starting at some initial deformation $\mathbf{q}_0$. This is simply accounted for by expanding the adiabatic states at $\mathbf{q}_0$ in terms of the diabatic states and keeping the expansion coefficients fixed for all $\mathbf{q}$-values. In other applications one is not interested in the diabatic states, but in approximations which lie in between the diabatic and adiabatic limits. Such quasidiabatic states should keep the diabatic crossings, but approach adiabaticity with respect to states which are well separated in energy. To construct these quasidiabatic states, one can for example adiabatize the diabatic basis taking interactions between distant diabatic levels into account.

[1] F.A. Ivanyuk and W. Nörenberg, Phys. Rev. Lett. **95**, 082501 (2005).

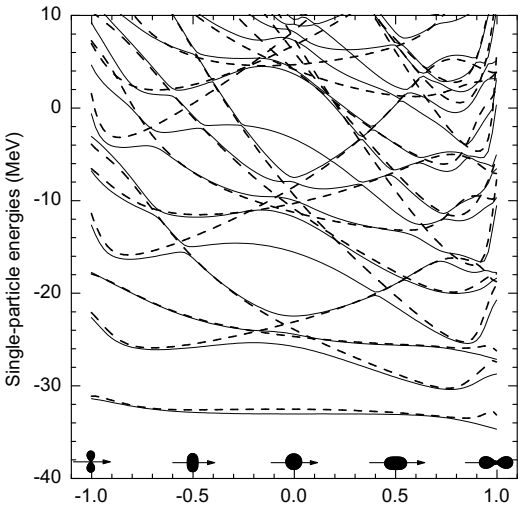


Figure 1: Adiabatic (solid lines) and diabatic (dashed lines) proton levels with $m\pi$=1/2+ as functions of deformation for ^{224}Th.

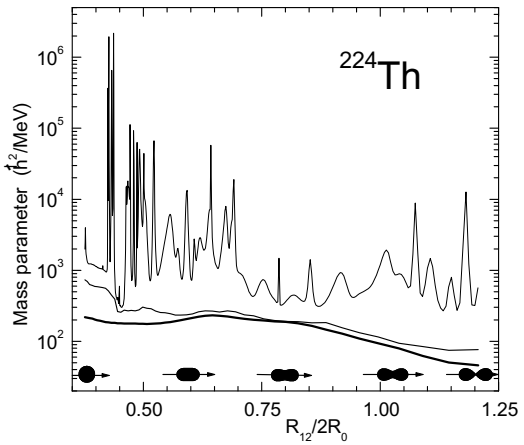


Figure 2: The adiabatic (thin line) and diabatic (heavy line) mass parameters as functions of deformation. The line in between is calculated for adiabatized diabatic states.

* On leave from the Institute for Nuclear Research, Kiev

Dynamical calculations of charge distribution for the reaction of ^{238}U at 1 A GeV on a (CH_2)n target*

P. N. Nadtochy, GSI, Darmstadt, Germany

The fragmentation-fission reactions [1] provide a very good opportunity to study fission dynamics from well definite initial conditions. These reactions are characterized by high excitation energy and low angular momentum L, so shell effects and the influence of L on the observables could be neglected in calculations. In Ref. [1] the experimental data on the variances of charge distributions of fission fragments σ_z and fission cross sections were reported for the reaction of ^{238}U at 1 A GeV on a (CH_2)n target. The analysis performed in Ref. [1] shows that the experimental data could be well reproduced using the statistical model, which takes into account transient effects in the calculations of the fission width. The dissipation coefficient $\beta = 2x10^{21}$ s^{-1} was used in Ref. [1] for the best fit of the experimental data. In this report the results of dynamical Langevin calculations for the reaction of ^{238}U at 1 A GeV on a (CH_2)n are presented.

The description of the dynamical model, as well as results of the calculations of different fusion-fission reactions could be found in Ref. [2]. The calculation for the reaction of ^{238}U at 1 A GeV on a (CH_2)n was performed using a modified version of a one-body dissipation mechanism with a reduction coefficient of a contribution from the wall formula ks [3]. The coefficient ks=0.5 has been used in the present dynamical calculations. This value of ks corresponds to $\beta = 10x10^{21}$ s^{-1} for the spherical shape of the nucleus. The results of the dynamical calculations are presented in Fig.1. In this figure, the experimental and calculated σ_z values are presented as a function of fission-fragment sum Z_1+Z_2. This sum approximately corresponds to the atomic number of the initial compound nucleus Z_{CN}. As can be seen from this figure for the compound nuclei with charge numbers $80<Z_{CN}<90$ the value of ks=0.5 could be used in order to reproduce the experimental σ_z values. The results of the preliminary calculations also show that in order to reproduce σ_z for the nuclei with $70<Z_{CN}<80$ the value of ks=1 is needed. This value of ks corresponds to $\beta = 20x10^{21}$ s^{-1}. The coefficients of $\beta = (10\text{-}20)x10^{21}$ s^{-1} obtained here are 5-10 times larger than the $\beta = 2x10^{21}$ s^{-1} obtained early in Ref. [1]. Such big difference in the β values could be explained by the different initial conditions used in the present calculations and in Ref. [1]. In modeling fission dynamics the initial deformed shape has been chosen in the present analysis. This shape corresponds to the ground-state deformation of ^{238}U, whereas the results of calculations [1] are obtained for the spherical initial deformation. The shift of the initial deformation from the spherical shape to the deformed one, which is closer to the saddle point, results in a considerable reduction (2-3 times) of the transient time. As a result, in order to suppress fission in the calculations starting from the deformed shape, larger β values are needed than in calculations starting from the spherical shape. However, the present analysis with $\beta = (10\text{-}20)x10^{21}$ s^{-1} leads to the same (or almost the same) transient time as in Ref. [1] with $\beta = 2x10^{21}$ s^{-1}. Dynamical calculations starting from the spherical shape of the compound nucleus also have been performed. Approximately the same result as in Ref. [1] has been obtained in this case, namely the $\beta \approx 2x10^{21}$ s^{-1} (ks $\approx$ 0.1) will result in reproduction of the experimental σ_z values.

The values of the ks=0.5-1 obtained in the present analysis could be compared with the previous analysis made in Ref. [2]. It was found that the experimental mass, kinetic-energy and angular distributions of the fission fragments, as well as the pre- and post-scission neutron multiplicities could be described using ks = 0.25 - 0.1 for heavy fissioning nuclei with fissility parameter $Z^2/A > 33$ and ks $\approx$ 0.5 for light nuclei with $Z^2/A < 33$. Thus a conclusion could be made that the coefficient $\beta = (10\text{-}20)x10^{21}$ s^{-1} of nuclear dissipation are realized for the compound nuclei with $70<Z_{CN}<90$.

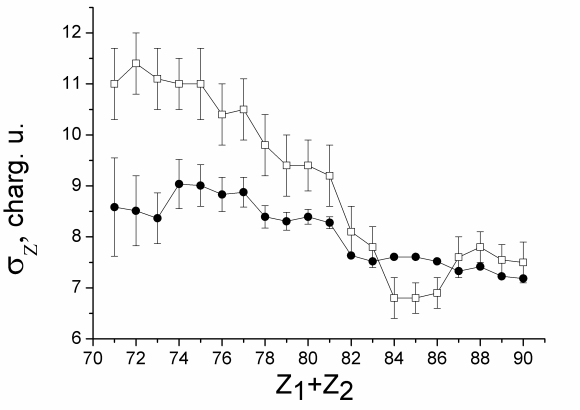


Figure 1: The comparison of the calculated σ_z values with the experimental one. The σ_z values are presented as a function of the fission fragments sum Z_1+Z_2. The filled circles are experimental data. The open squares are calculated results with the ks=0.5.

References

[1] B. Jurado et al, Phys. Rev. Lett. 93 (2004) 072501.
[2] G. D. Adeev et al, Fiz. Elem. Chastits At. Yadra 36 (2005) 732.
[3] J. R. Nix, Nucl. Phys. A502 (1989) 609.

*Work supported by Alexander von Humboldt Foundation

Isospin effects on particle production*

T. Gaitanos, H.H. Wolter, Dept. für Physik, Universität München, D-86748 Garching, Germany
G. Ferini, M. Colonna, M. Di Toro, LNS/INFN, Physics and Astronomy Dept., I-95123 Catania, Italy

Abstract

We investigate the Lorentz structure of the symmetry energy (E_{sym}) at supra-saturation densities in Heavy-Ion Collisions (HIC) at SIS/GSI energies. It turns out that particle yields, and in particular, the *strangeness ratio* K^+/K^0 presents a good probe in determining the high density isovector Equation of State (EoS).

HICs at intermediate relativistic energies (SIS/GSI regime, 0.1-2 AGeV) provide a unique tool to explore the nuclear EoS [1] under extreme conditions of density, temperature, and, particularly, of isospin-asymmetric nuclear matter (ANM). The density dependence of the isovector EoS is still unknown and theoretically differently predicted by various models [2]. On the other hand, its knowledge is important for the understanding of astrophysics, e.g. neutron stars [3].

In our work HICs are theoretically based on relativistic kinetic equations of Boltzmann type, i.e. the Relativistic Boltzmann Uhlenbeck Uheling (RBUU) transport equation. For the study of highly excited ANM matter we use the non-linear Walecka model (NL). The isovector part of the EoS is characterized by an isovector, vector ρ meson (NLρ) or by a ρ and an isovector, scalar δ fields (NL$\rho\delta$). The introduction of the δ field changes the high density behavior of E_{sym}; as in the isoscalar case (cancelation effects between strong repulsive vector ω and attractive scalar σ fields), the ρ field rises linearly with increasing baryon density ρ_B, whereas the δ meson is supressed due to the saturation of the isospin scalar density at high ρ_B. Thus, in order to describe the same bulk asymmetry parameter a_4 at saturation density, one has to increase the ρ meson coupling if the δ meson is accounted for. E_{sym} becomes therefore stiffer going from the NLρ to the NL$\rho\delta$ model [4]. The effect between them increases in the dynamical situation due to the additional Lorentz currents. One expects important transport effects in HICs.

Fig. 1 shows the energy dependence of the (K^+/K^0) and the (π^+/π^-) ratios [5]. Here the standard free parametrizations of the elastic and inelastic cross sections were used and for the kaons no potential were applied, except for some cases (open triangles and stars). In the NL model one does not consider any isovector mesons in the nuclear mean field, and it serves as a reference. It is seen that the variable stiffness of E_{sym} (NLρ, NL$\rho\delta$) influences differently the pionic and strangeness ratios. In particular, the isospin effect on kaons is more pronounced with respect to that for pions. This is because of the strong secondary re-scattering effects of pions. On the other hand, kaons ($K^{+,0}$) do not interact with the hadronic environment (large mean free path). Therefore they give directly information on the high density phase. As in detail discussed in [6], the stiffness of E_{sym} considerably influences the threshold condition of particle production via the isovector scalar and vector components of the hadron self energy; with increasing stiffness of E_{sym} the K^0 (K^+) yield is enhanced (reduced). Their opossite behavior with respect to the model leads to the observed strong isospin effect. Furthermore, a preliminary study shows the robustness of the strangeness ratio against density modifications of the elastic cross sections (open triangles) and of the kaon potential (stars). We note that the strangeness ratio remains also stable against in-medium changes of the inelastic cross sections for resonance production.

In summary, we have investigated the possibility to set stringent constraints on the high density behavior of the isovector EoS from HICs. Possible candidates for such studies turn out to be particle ratios, and in particular the strangeness ratio between isospin states of the kaon. Future experiments with radioactive beams will be an important issue in determining the symmetry energy at high isospin density.

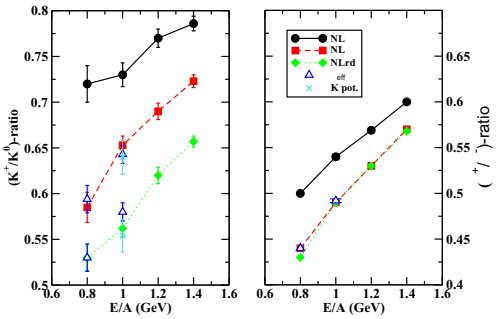


Figure 1: Energy depenence of the K^+/K^0 (left) and π^+/π^- (right) ratios for central Au+Au collisions. Transport calculations with the NL (solid-circles), NLρ (dashed-squares) and NL$\rho\delta$ (dotted-diamonds) models are shown. In some cases calculations with in-medium elastic cross sections (open triangles) and with the kaon potential (stars) are presented.

References

[1] C. Fuchs, Prog. Part. Nucl. Phys. **56** (2006) 1.
[2] V. Baran, et al., Phys. Rep **410** (2005) 335.
[3] G.Q. Li, C.-H. Lee, G.E. Brown, Nucl. Phys. **A625** (1997) 372.
[4] T. Gaitanos et al., Nucl. Phys. **A732** (2004) 24.
[5] G. Ferini, et al., in preparation.
[6] G. Ferini, et al., Nucl. Phys. **A762** (2005) 147.

* Work supported by BMBF 06ML981 and INFN

Modification of the ρ^0 meson mass spectrum at HADES energies

S. Vogel* and M. Bleicher†
Institut für Theoretische Physik, J.W. Goethe Universität Frankfurt am Main, Germany

Abstract

We report on the modification of the ρ^0 meson mass spectrum using a relativistic transport model. Our results can be tested with the HADES experiment and the upcoming CBM experiment at FAIR.

The data on the ρ meson spectral function by the NA60 collaboration [1] shows a clear modification of the mass spectrum of the ρ meson compared to a Breit-Wigner shape. This behaviour is expected to be measured by the HADES and the upcoming CBM experiment as well. In former publications this has been discussed as a signal for a partial chiral symmetry restoration [2, 3, 4].

For our studies we apply the UrQMD model. It is a non-equilibrium transport approach based on the covariant propagation of hadrons and strings. All cross sections are calculated by the principle of detailed balance or are fitted to data where available. The model allows to study the full space time evolution for all hadrons, resonances and their decay products. This permits to explore the emission patterns of the resonances in detail and to gain insight into the origin of the resonances. For further details of the model the reader is referred to [5, 6]. UrQMD has been successfully applied to study light and heavy ion reactions at SIS. Detailed comparisons of UrQMD with a large body of experimental data at SIS energies can be found in [7].

The mass distribution of the ρ^0 in min.bias C+C reaction at 2 AGeV is shown in Fig. 1. Open circles depict all decayed ρ^0's (this is similar to the di-leptons invariant mass distribution multiplied by the branching ratio and the vector meson dominance factor of $1/m^3$), while the ρ^0's reconstructable in $\pi\pi$ correlations are shown as full circles. In both distributions, one observes a clear double peak structure, with maxima at the ρ pole mass (770 MeV) and around 500 to 600 MeV. Usually an enhancement of the ρ spectral function in this mass region has been attributed to strong in-medium modifications, due to finite densities and temperatures. However, in the present calculation, we do not make explicit use of any in-medium modification, but only include the coupling of the ρ to pions and baryons via the employed cross sections calculated from detailed balance. Thus we conclude that the broadening of the ρ meson mass spectrum is not an unique signature for (partial) chiral symmetry restoration.

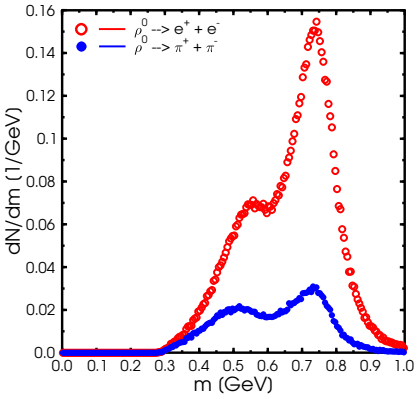


Figure 1: Mass distribution for ρ^0 mesons for min. bias C+C reaction at 2 AGeV. Open circles depict all decayed ρ^0's, whereas the closed circles depict those which are reconstructable in an invariant mass analysis of the di-hadronic decay channel. The peak around 500 MeV is due to a strong contribution from $N^*_{1520} \rightarrow N + \rho$ which amounts to 75% for masses below 600 MeV.

Acknowledgements:
The authors thank GSI and BMBF for financial support. Fruitful discussions with Drs. Horst Stöcker, Peter Zumbruch, Christian Sturm and Joachim Stroth are greatfully acknowledged. The computational resources have been provided by the Center for Scientific Computing in Frankfurt.

References

[1] S. Damjanovic *et al.* [NA60 Collaboration], arXiv:nucl-ex/0510044.

[2] G. E. Brown and M. Rho, Phys. Rev. Lett. **66** (1991) 2720.

[3] R. Rapp and C. Gale, Phys. Rev. C **60** (1999) 024903 [arXiv:hep-ph/9902268].

[4] W. Cassing, E. L. Bratkovskaya, R. Rapp and J. Wambach, Phys. Rev. C **57** (1998) 916 [arXiv:nucl-th/9708020].

[5] S. A. Bass *et al.*, Prog. Part. Nucl. Phys. **41** (1998) 225 [arXiv:nucl-th/9803035].

[6] M. Bleicher *et al.*, J. Phys. G **25** (1999) 1859 [arXiv:hep-ph/9909407].

[7] C. Sturm *et al.* [KAOS Collaboration], Phys. Rev. Lett. **86** (2001) 39 [arXiv:nucl-ex/0011001].

* e-mail: svogel@th.physik.uni-frankfurt.de
† e-mail: bleicher@th.physik.uni-frankfurt.de

Production of Hot Nuclei in Nuclear Reactions and Supernova Explosions

A.S. Botvina (GSI, Darmstadt, Germany, and INR, Moscow, Russia)
I.N. Mishustin (FIAS, Frankfurt University, Germany, and KI, Moscow, Russia)

It is well established experimentally that highly excited nuclear systems with temperatures $T > 3 - 5$ MeV can be formed in intermediate-energy heavy-ion collisions. Eventually they break up into many fragments with broad mass and charge distributions. These multifragmentation reactions have been intensively investigated in GSI and other world laboratories. It has also been established that a thermodynamical equilibrium is reached prior to such a break-up, and therefore, statistical models, like SMM [1], can be used for its description. In the nuclear phase diagram this state of matter corresponds to a mixed phase of the liquid-gas phase transition at subnuclear densities. The multifragmentation reactions give us a unique chance to investigate properties of the hot fragments embedded in a dense environment. Recently, extensive experimental efforts were undertaken to study the symmetry energy of hot nuclei $E^{sym}_{A,Z} = \gamma(A-2Z)^2/A$, where γ is a parameter ($\gamma \approx 25$ MeV for cold isolated nuclei). An essential decrease of γ, down to about 15 MeV, was found for the conditions corresponding to the multifragmentation reactions [2, 3, 4].

It is remarkable that similar conditions can be reached for stellar matter in some astrophysical processes. A type II supernova explosion is one of the most spectacular events in astrophysics, with huge energy release of about 10^{53} erg or several tens of MeV per nucleon. When the core of a massive star collapses, it reaches densities larger than the normal nuclear density $\rho_0 = 0.15$ fm^{-3}. The repulsive nucleon-nucleon interaction gives rise to a bounce-off and creation of a shock wave, responsible for the ejection of a star envelope that is observed as a supernova explosion. During the collapse and subsequent explosion the temperatures $T \approx (0.5 \div 10)$ MeV and baryon densities $\rho \approx (10^{-5} \div 2)\rho_0$ can be reached. The similarity of these conditions with those in multifragmentation reactions gives a ground for using the SMM model, after certain modifications, for describing the matter in the course of supernova explosions.

To describe the stellar matter we have modified the SMM by including electrons and neutrinos in the statistical ensemble under different assumptions concerning the weak reaction rates [5]. In Fig. 1 we present the SMM predictions for charge-to-mass ratios (Z/A) and mass distributions of hot nuclei for typical supernova conditions. We stress that a great variety of neutron-rich, and even exotic (large mass – small charge) nuclei can be formed during the explosion. Decreasing the symmetry energy, as expected from multifragmentation experiments, has a strong influence on the nuclear composition of supernova matter. As seen from Fig. 1, the masses and Z/A ratios of nuclei produced at standard $\gamma = 25$ MeV, and at $\gamma = 15$ MeV, are essentially different, by about factor 2. This effect may considerably influence macroscopic supernova dynamics, and nucleosynthesis in a supernova environment. In particular, the week reaction rates, e.g., the electron capture [6], will be modified. We plan to use the new experimental data on properties of hot fragments at subnuclear densities for calculations of the realistic nuclear composition, and construction of an improved equation of state of stellar matter. Therefore, the experimental and theoretical studies of multifragmentation reactions provide a valuable contribution to our understanding of matter properties in violent astrophysical processes.

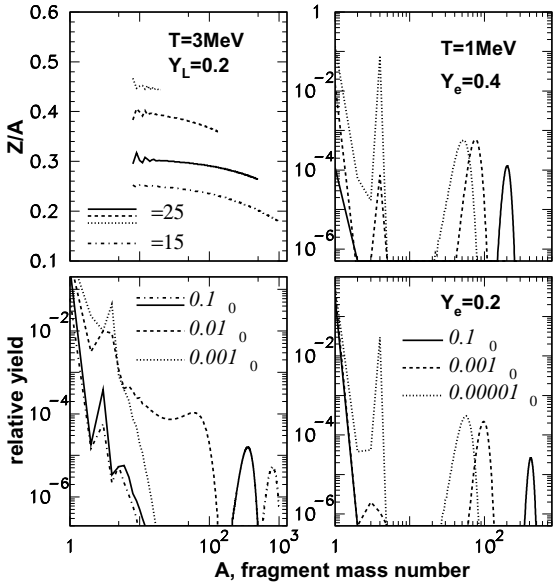


Figure 1: Mean charge-to-mass ratios (left top panel), and mass distributions of hot primary fragments (other panels) calculated with the SMM generalized for supernova conditions. Left panels are calculations for temperature $T = 3$ MeV and fi xed lepton fraction Y_L =0.2. Right panels, for temperature $T = 1$ MeV and fi xed electron fraction Y_e. Lines correspond to densities shown in the fi gure. Solid and dashed lines are calculations with the symmetry energy parameter γ =25 MeV, dot-dashed line is obtained for reduced γ =15 MeV.

References

[1] J.P. Bondorf et al., Phys. Rep. 257(1995)133.
[2] A.Le Fevre et al., Phys. Rev. Lett. 94(2005)162701.
[3] D. Henzlova et al., arxiv.org/abs/nucl-ex/0507003, 2005.
[4] D.V. Shetty et al., Phys. Rev. C71(2005)024602.
[5] A.S. Botvina and I.N. Mishustin, Phys. Lett. B584(2004)233; ibid., Phys. Rev. C72(2005) 048801.
[6] K. Langanke et al., Phys. Rev. Lett. 90(2003)241102.

Resonances, Scattering and Bound States in Fermionic Molecular Dynamics

A. Cribeiro, H. Feldmeier, K. Langanke, GSI, Darmstadt, Germany
T. Neff, NSCL, Michigan State University, East Lansing, USA

Radiative capture reactions like $^3\mathrm{He}(\alpha,\gamma)^7\mathrm{Be}$ play an important role in astrophysical scenarios. Experimental data are usually only available for higher energies and the extrapolation to the low energies relevant in astrophysical environments may be problematic. Theoretical calculations in the framework of microscopic cluster models [1] suffer from poor effective interactions and restricted cluster wave functions. Furthermore it is difficult to include configurations that are not of cluster nature but that are necessary to get a good description of the $^7\mathrm{Be}$ bound states.

We aim at using the Fermionic Molecular Dynamics (FMD) model to calculate such reactions. The FMD has been used successfully to describe the properties of nuclei in the p- and sd-shell [2] using an effective interaction that is derived from realistic nucleon-nucleon interactions by explicitly introducing short-range central and tensor correlations in the Unitary Correlation Operator Method (UCOM) [3]. The FMD wave functions use Gaussian wavepackets that are localized in phase space – cluster configurations can therefore be included naturally in the FMD model space. At small distances the clusters will loose their identity and we use FMD configurations that are obtained by minimizing the energy with respect to the parameters of all the individual nucleons. For larger distances the cluster configurations will become important and asymptotically the system can by described as a system of two point-like clusters. Outside the rang of the nuclear interaction the wave function has then to be matched to a Whittaker function (bound states) or a Coulomb wave function (resonances or scattering states).

This matching is not a trivial procedure as the Slater determinants used in the FMD description couple the relative motion of the clusters with the internal degrees of freedom of the clusters and the center of mass motion. If the same Gaussian width (the same oscillator parameter) is used for all wave functions the center-of-mass motion factorizes and an analytical deconvolution for the relative motion can be done. For the FMD this is not possible and a Collective-Coordinate Representation has been developed [4]. The center-of-mass problem is solved by explicit projection on total linear momentum. The deconvolution of the relative motion is done with the help of *localized states*. These are the eigenstates of the r^2 operator and asymptotically they can be matched to systems of point-like clusters whose distances are related to the eigenvalues.

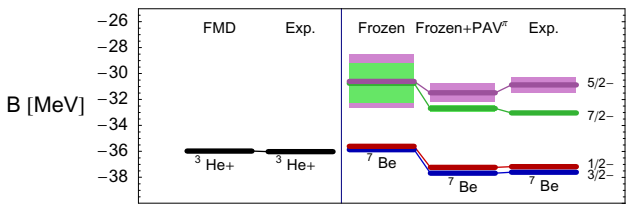


Figure 1: Calculated and experimental threshold energies (left). Bound State energies, resonance energies and widths obtained using only cluster configurations (Frozen) and an additional FMD (PAV$^\pi$) state (right).

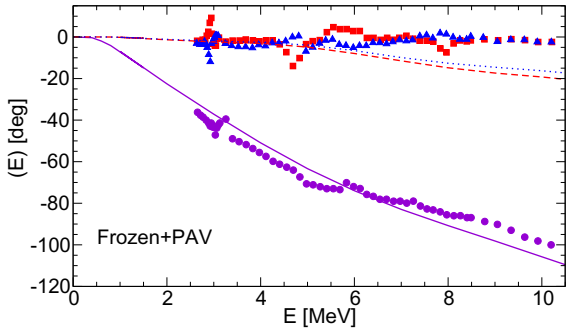


Figure 2: Phase shifts for the positive parity states ($1/2^+$, $3/2^+$ and $5/2^+$ correspond to solid, dashed and dotted lines, respectively) in the ^{3}He-α elastic scattering and comparison with experiment.

In Fig. 1 we show the results for the negative parity bound states and resonances. To reproduce the threshold energy quite sophisticated wave functions for the clusters have to be used. Linear combinations of Slater determinants and the use of two Gaussians of different width for each single-particle state are necessary for a good description especially of ^{3}He.

We depict the phase shifts for positive parity states in Fig. 2. A good agreement of this fully microscopic model with experiment is observed. With the inclusion of the dipole transition operator we will be able to calculate the reaction rates.

References

[1] A. Csótó, K. Langanke, Few-Body Systems **29** (2000) 121

[2] T. Neff, H. Feldmeier, Nucl. Phys. **A738** (2004) 357

[3] R. Roth, T. Neff, H. Hergert, H. Feldmeier, Nucl. Phys. **A745** (2004) 3

[4] A. Cribeiro, *Nuclear Many-Body Continuum States and their Boundary Conditions in a Collective-Coordinate Representation*, PhD thesis, 2005

Tunneling of a composite object

S. Bacca and H. Feldmeier (GSI Darmstadt)

The phenomenon of quantum tunneling is relevant in different areas of physics, from chemical reactions to nuclear fission and fusion below the Coulomb barrier. In most of the cases one has to deal with the tunneling of a complex object with internal degrees of freedom. In a one-dimensional model we investigate how an harmonically bound two-body system tunnels through an external gaussian barrier. The hamiltonian in the center of mass (C.M.) and relative coordinates, R and ξ, is

$$H(R,\xi) = K_R + K_\xi + \frac{1}{2}\mu\Omega^2\xi^2 + V\left(R+\frac{\xi}{2}\right) + V\left(R-\frac{\xi}{2}\right), \tag{1}$$

where $K_{R,\xi}$ denote the kinetic energy of the C.M. with mass $M = 2m$ and of the intrinsic system with mass $\mu = m/2$, respectively. The external potential, felt by both particles, is assumed to be $V(x) = V_0 e^{-\nu^2 x^2}$. We used $m = 938$ MeV, $\hbar\Omega = 1$ MeV, $V_0 = 10$ MeV and $\nu = 0.1$ fm^{-1}.

The standard theoretical approach to study the effect of internal excitations induced by the coupling potential is to solve the coupled-channel equation

$$-\frac{\hbar^2}{2M}\frac{d^2}{dR^2}\phi_{ji}(R) + \sum_{n=0}^{N}[V_{jn}(R) + (\epsilon_n - E)\delta_{jn}]\phi_{ni}(R) = 0\,, \tag{2}$$

with incoming boundary conditions, where $\phi_{ji}(R)$ is the C.M. wave function (with indices j and i denoting final and initial channel, respectively), while ϵ_n is the internal harmonic oscillator (H.O.) excitation energy. In Eq. (2) the potential matrix elements given by

$$V_{jn}(R) = \int_{-\infty}^{\infty} d\xi\; \chi_j^*(\xi)\left[V\left(R+\frac{\xi}{2}\right) + V\left(R-\frac{\xi}{2}\right)\right]\chi_n(\xi)\,, \tag{3}$$

can be interpreted as the effective potentials felt by the C.M. due to the presence of internal degrees of freedom. $\chi_n(\xi)$ denote the internal wave functions, which are H.O. wave functions in our case. In this model $V_{jn}(R)$ can be expressed analytically by a gaussian times a linear combination of Hermite polynomials [1]. We solved the coupled channel problem for a two level system, in which the only possible transition is that from the ground state to the second excited state, being the coupling $V_{01}(R)$ of Eq. (3) identically zero due to symmetry.

Fig. 1 shows the result of the total transmission coefficient T and its separate contributions T_{20} and T_{00}. Surprisingly, the penetration factor presents a peaked structure at low energies. This is mainly due to a Landau-Zener type transition to the intrinsic energy level ϵ_2, as can be seen from the fact that the elastic transmission T_{00} is rather flat in this energy region. Such a peaked structure is not obtained if one parametrizes the potential matrix elements as simple gaussian functions as in [2], without taking into account the fact that the $V_{jn}(R)$ are not independent of each other, as can be seen from Eq. (3).

In order to estimate the effect of the excitation of the internal degrees of freedom, we compare the coupled channel calculation with the uncoupled problem, where only the effective potential V_{00} is considered. In this case internal transitions are not possible,

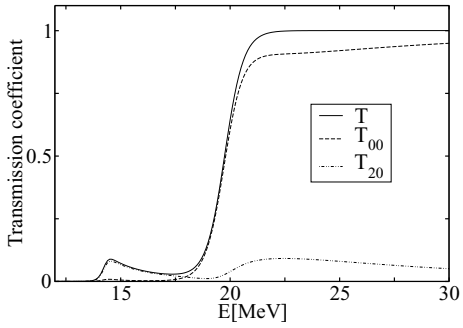


Figure 1: Total transmission coeffi cient and separate T_{20} and T_{00} contribution as a function of the total energy.

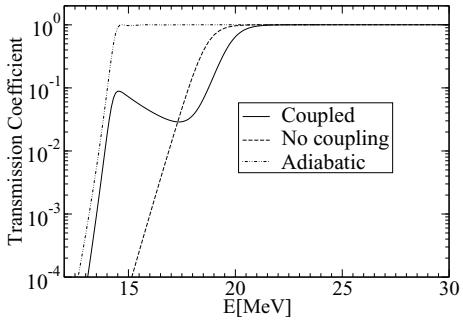


Figure 2: Comparison of the coupled channel transmission coeffi cient, with no-coupling and adiabatic case.

but V_{00} still accounts for finite size effects. As one can see from Fig. 2 the excitation of the internal degrees of freedom leads to an enhancement of the transmission coefficient of almost 3 orders of magnitude in the peak region. Comparison with the adiabatic tunneling shows that the exact transmission coefficient is however always lower than the adiabatic one.

The model results suggest to investigate more carefully fusion of soft nuclei [3] or electron screening at astrophysical energies [4, 5], paying attention to possible resonant effects.

References

[1] M. Razavy, *Quantum Theory of Tunneling*, World Scientific Publishing Co., Singapore (2003).

[2] K. Hagino, N. Takigawa and A.B. Balantekin, Phys. Rev. C **56**, (1997) 2104.

[3] A.B. Balantekin and N. Takigawa, Rev. Mod. Phys., Vol. **70** No.1, (1998) 77.

[4] H.J. Assenbaum, K. Langanke and C. Rolfs, Z. Phys. A **327**, (1987) 461.

[5] T.D. Shoppa, M. Jeng, S.E. Koonin, K. Langanke and R. Seki, Nucl. Phys. A **605**, (1996) 387.

Transport study of charged current interactions in neutrino-nucleus reactions

M. Kant and W. Cassing, Univ. of Giessen, Germany
K. Langanke, GSI Darmstadt, Germany
P. Vogel, California Institute of Technology, Pasadena, USA

The interest in neutrino induced reactions has been rapidly increasing during the last decade while current and future long base-line (LBL) experiments, K2K, MiniBoone, MINOS, CERN-GS, J2K *etc.* aim at determining the electro-weak response of nucleons and nuclei. In general the neutrino-nucleon/nucleus interaction consists of the quasi-elastic scattering, resonance production and deep inelastic scattering, the latter becoming dominant only for neutrino energies above about 1 GeV. Whereas at low neutrino energies $E_\nu < 0.3$ GeV the quasi-elastic channel clearly dominates, one observes an increasing contribution from resonance excitations at higher energies up to about 2 GeV [1]. Here charged current (CC) reactions offer the unique possibility to measure the μ^- in coincidence with e.g. the charged $\pi^\pm$ or neutral π^0 in order to extract information on the resonance transition form factors since the 4-momentum of the lepton fixes the transferred energy ν and 4-momentum squared q^2.

A variety of models (and event generators) treat neutrino nucleus reactions and incorporate selected aspects of scattering on nuclei like Pauli-blocking, nuclear Fermi motion, nucleon binding energies, pion rescattering and charge exchange reactions. However, most of the models lack an explicit propagation of the resonances and their in-medium decay to pions and nucleons as well as more realistic coordinate (and momentum) distributions of the target nucleons. In order to study the importance of these effects we employ a transport approach that has been tested in a wide range of π, p reactions on nuclei [2] as well as relativistic nucleus-nucleus collisions. This transport model – or related versions – have been also used and tested in the description of the photo-nuclear and electron induced reactions with the momentum and energy transfer comparable to those considered here [3].

For the description of the elementary process on nucleons we use the model of Rein and Sehgal [4] that has been often employed for an estimate of neutrino cross sections for resonance transitions. The differential cross sections are well known [5] and usually given in terms of helicity amplitudes. Our present investigation is focused on final-state-interactions (FSI) of the excited $\Delta(1232)$ resonance and the emitted pion. We point out that alternative forms of the neutrino-nucleon-resonance vertex will modify the double differential cross sections but have no severe impact on the strength of the FSI.

We mention that our calculated cross sections for π^+ meson production in CC reactions on ^{12}C targets from 0.5 to 1.5 GeV neutrino energy [6] compare well with the preliminary data from Ref. [7]. However, any agreement/disagreement is primarily due to the 'uncertain' axial-vector form factor $G^A(q^2)$ in the elementary amplitude such that no final conclusions can be drawn so far.

Here we quantify the strength of the FSI as a function of the pion momentum in the laboratory P_{lab} by considering the ratio R_+ of the π^+ spectra with/without FSI. The ratios R_+ displayed in Fig. 1 show a characteristic dip at small laboratory momenta P_{lab} which is more pronounced for the heavier Fe-target than for the light C-nucleus and reflects Δ-resonance absorption ($\Delta N \rightarrow NN$), momentum exchange and charge exchange reactions. The attenuation is found to be slightly stronger for neutral pions than for positive pions for both nuclei [6] at the neutrino energy E_ν = 1 GeV. These differential FSI effects can also be directly assessed by taking e.g. experimental differential ratios of spectra for heavy and light targets.

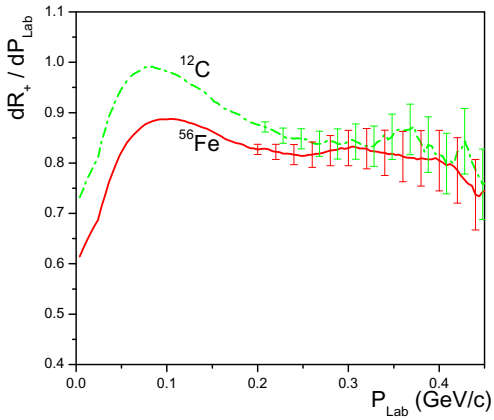


Figure 1: The differential ratios $R_+(P_{lab})$ for the reactions $\nu_\mu + ^{12}C(^{56}Fe) \rightarrow \mu^- + \pi^+ + X$ as a function of the pion momentum in the laboratory for a neutrino energy E_ν = 1 GeV. The error bars denote the statistical uncertainty in determining the ratios numerically due to the low cross sections at large pion momenta.

References

[1] E. A. Paschos, Nucl. Phys. B (Proc. Suppl.) 112 (2002) 89.

[2] W. Cassing *et al.*, Phys. Lett. B 396 (1997) 26.

[3] J. Lehr *et al.*, Nucl. Phys. A 671 (2000) 503.

[4] D. Rein and L. M. Sehgal, Ann. Phys. 133 (1981) 79.

[5] P. A. Schreiner, F. V. von Hippel, Nucl. Phys. B 58 (1973) 333.

[6] W. Cassing, M. Kant, K. Langanke, and P. Vogel, nucl-th/0601090.

[7] M.O. Wascko *et al.*, in NuInt 05, September 26 - 29, 2005, Okayama University, Okayama, Japan.

The outer crust of non-accreting cold neutron stars*

Stefan B. Rüster†, Matthias Hempel‡, and Jürgen Schaffner-Bielich§,
Institut für Theoretische Physik, J. W. Goethe-Universität, 60438 Frankfurt am Main, Germany

The outer crust of non-accreting cold neutron stars consists of electrons and nuclei. The latter are arranged in a body-centered-cubic (bcc) lattice. The outer crust of cold neutron stars begins at a mass density of about $\rho \simeq 10^4$ g/cm^3, where ^{56}Fe is the ground state. With increasing mass density, it is not the true ground state anymore because the nuclei capture electrons, emit neutrinos and become neutron richer. The outer crust of cold neutron stars ends when the neutron drip point is reached at $\rho \simeq 4.3 \cdot 10^{11}$ g/cm^3.

In Ref. [1], we used the model of Baym, Pethick, and Sutherland (BPS) [2] in order to obtain the equation of state and the sequence of nuclei in the outer crust of non-accreting cold neutron stars. For our investigation, we used up-to-date and state-of-the-art experimental [3] and theoretical nuclear models. We studied the differences of various nuclear models concerning the neutron dripline, magic neutron numbers, the equation of state, and the sequence of nuclei in the outer crust of non-accreting cold neutron stars. We utilize modern Skyrme Hartree-Fock-Bogoliubov (HFB) parameterisations as well as relativistic nuclear field theoretical ones for exploring effects of pairing and deformation of nuclei on the sequence of nuclei and the location of the dripline. We find that deformations have a crucial effect on the sequence of nuclei in the outer crust of non-accreting cold neutron stars.

In Fig. 1, we present the main result of our work [1], the sequences of nuclei in the outer crust of non-accreting cold neutron stars which are obtained by using the most modern nuclear models: SLy4 and BSk8 are Skyrme HFB mass tables, NL3 and TMA relativistic mean-field parameter sets, and FRDM stands for the newest version of the finite-range-droplet model. The neutron driplines appear to have a nearly linear behaviour extending $(Z, N) \simeq (20, 46)$ to $(Z, N) \simeq (50, 108)$. At the magic neutron number 82, the neutron driplines suddenly change their slope and rise vertically from $(Z, N) = (36, 82)$ to $(Z, N) = (40, 82)$. At $N = 82$, the neutron driplines of all most modern nuclear models are notably close to each other. But there are differences in the regions of the nuclide chart where $Z \simeq 28$ and $N \simeq 62$: If one compares the neutron driplines from the mass tables of sets TMA and NL3 which includes effects from deformations, then one can see that their neutron driplines differ by $\Delta Z = 4$ and $\Delta N = 16$. There are also differences of similar range for the neutron driplines at $(Z, N) \simeq (44, 100)$ if one compares the model TMA with SLy4 and NL3. The sequences of nuclei from all most modern nuclear models follow the magic neutron numbers 50 and 82 being located for a substantial part of the sequence on top of each other. Only the sequence of nuclei for the Skyrme set BSk8 shows a shift to larger proton numbers with $\Delta Z_{\max} = 4$. The sets BSk8 and NL3 have one nucleus in their sequence with $N = 52$. The endpoint of the sequence of nuclei for all the modern mass tables studied here is surprisingly similar and happens to be at $Z = 34$–38 with $N = 82$ ($N = 84$ for the set NL3) partially reflecting the fact that the neutron driplines of the models under study coincide in this region of the nuclear chart.

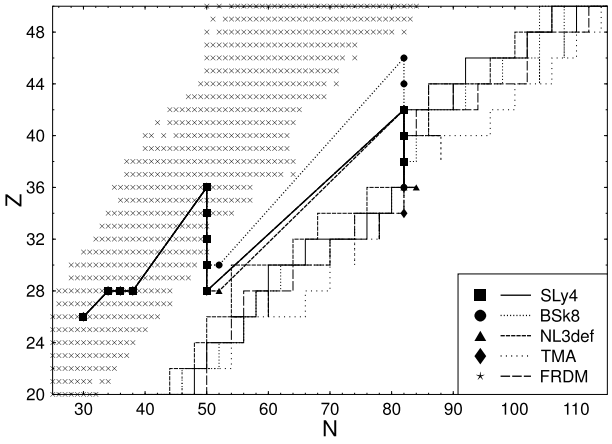


Figure 1: Nuclear chart for state-of-the-art models from Table 1 in Ref. [1] and their neutron driplines. The crosses mark the known nuclei taken from the atomic mass table of Ref. [3]. The thick lines and points show the sequence of nuclei in the outer crust of non-accreting cold neutron stars.

The sequence of neutron-rich nuclei in Fig. 1 are in reach to be measured by the FAIR facility at GSI.

* We thank Thomas Bürvenich, Thomas Cornelius, Stefan Schramm, and Lisheng Geng for providing the mass tables of the relativistic nuclear models used in this research project and J. A. Maruhn and P. G. Reinhard for useful discussions. This work is supported by the Gesellschaft für Schwerionenforschung (GSI) via the program "Fremde F&E-Mittel" in the research project OF/SAF "Struktur von neutronenreichen, exotischen Kernen in der Kruste von Neutronensternen".

† ruester@th.physik.uni-frankfurt.de
‡ hempel@astro.uni-frankfurt.de
§ schaffner@astro.uni-frankfurt.de

References

[1] S. B. Rüster, M. Hempel, and J. Schaffner-Bielich, astro-ph/0509325, accepted for publication in Phys. Rev. C.

[2] G. Baym, C. Pethick, and P. Sutherland, Astrophys. J. **170**, 299 (1971).

[3] G. Audi, A. H. Wapstra, and C. Thibault, Nucl. Phys. **A729**, 337 (2003).

Weak-interaction processes during stellar collapse

A. Juodagalvis, K. Langanke and G. Martinez-Pinedo (GSI Darmstadt)

Massive stars end their lifes as type II supernovae, triggered by a collapse of their central iron core with a mass of more than $1M_{\odot}$. The general picture of a core-collapse supernova is probably well understood and has been confirmed by various observations from supernova 1987A. Nevertheless, the most sophisticated supernova simulations [1, 2, 3] currently fail to explode indicating that improved input or numerical treatment is required. Among these microscopic inputs are nuclear processes mediated by the weak interaction, where recent progress has been made possible by improved many-body models and better computational facilities. Our research focussed on the electron capture on nuclei and on inelastic neutrino-nucleus reactions.

In recent years we have calculated electron capture rates for many nuclei present during the collapse [4]. The calculations were based on modern many-body theories (diagonalization shell model or Shell Model Monte Carlo) and have been performed for the density and temperature conditions appropriate for the core collapse of a massive star. Importantly our research showed that electrons are captured on nuclei rather than on free protons during the entire collapse phase until neutrino trapping and thermalization is achieved [5]. Supernova simulations, using the improved electron capture rates, have strongly modified collapse trajectories (density, temperature, Y_e profiles, where Y_e is the electron-to-nucleon ratio). In particular, the shock wave is created at smaller radii with more overlying stellar mass, but travels slightly further out due to modifications of the ram pressure [6].

Electron captures reduce the Y_e values. As a consequence, the abundant nuclei become more neutron-rich and heavier, as nuclei with decreasing Z/A ratios are more bound in heavier nuclei. Nuclei are in nuclear statistical equilibrium during the collapse phase guaranteed by sufficiently fast reactions mediated by the strong and electromagnetic interaction. With increasing temperature and density, more nuclei are abundant in the collapsing core and contribute to the total electron capture rate. We have therefore extended our calculation of the rates to a larger number of nuclei (about 300). Furthermore we have tested approximate methods to investigate strategies to include even larger numbers of nuclei in our evaluations.

Due to the energy exchange in inelastic neutrino-nucleus reactions, this process can help to thermalize neutrinos after trapping during the collapse phase. However, this reaction is currently not included in supernova simulations. To overcome this shortcoming we have studied inelastic neutrino-induced reactions on more than 50 nuclei in the iron mass range [7]. Our calculations are based on the diagonalization shell model for the allowed (Gamow-Teller) transitions and on the Random Phase approximation for forbidden transitions. During collapse the neutrino energies are relatively small (order 10 MeV) and allowed transitions dominate. As the spin part of the isovector M1 operator is proportional to the Gamow-Teller operator, it has been possible to validate the shell model calculations of the allowed transitions by detailed comparison to high-precision M1 data, obtained in electron scattering experiments (Fig. 1) [8]. Our calculations have been summarized as a table which gives the inelastic neutrino-nucleus cross sections as function of initial and final neutrino energies and for the relevant supernova temperatures. Fig. 2 shows typical neutrino-induced cross sections on nickel isotopes for selected temperatures.

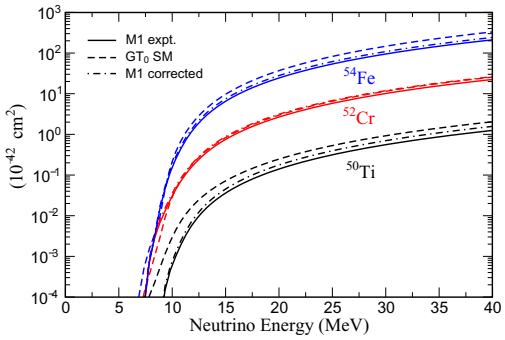


Figure 1: Neutrino-nucleus cross sections calculated from the M1 data (solid lines) and the shell-model GT_0 distributions (dotted) for ^{50}Ti (multiplied by 0.1), ^{52}Cr, and ^{54}Fe (times 10).

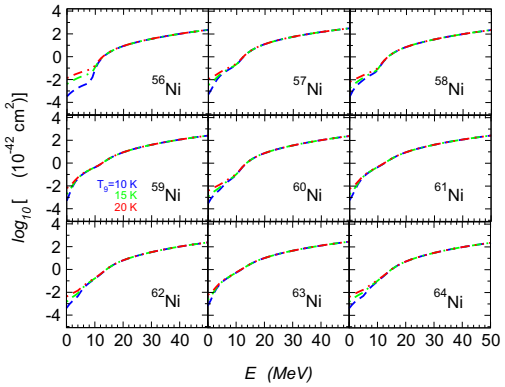


Figure 2: Cross sections for inelastic neutrino scattering on nuclei at finite temperature. The temperatures are given in MeV (from [7]).

References

[1] R. Buras, M. Rampp, H.-Th. Janka, K. Kifonidis, PRL 90 (2003) 241101

[2] H.-Th. Janka and M. Rampp, Astr. J. 539 (2000) L33

[3] A. Mezzacappa et al., PRL 86 (2001) 1935

[4] K. Langanke and G. Martinez-Pinedo, NPA 673 (2000) 481

[5] K. Langanke et al., PRL 90 (2003) 241102

[6] R.W. Hix et al., PRL 91 (2003) 210102

[7] A. Juodagalvis et al., NPA 747 (2005) 87

[8] K. Langanke, G. Martinez-Pinedo, P. von Neumann-Cosel, A. Richter, PRL 93 (2004) 202501

The neutrino-process

G. Martínez-Pinedo and K. Langanke, GSI, Darmstadt, Germany
A. Heger (Los Alamos), W.C. Haxton (INT Seattle) and S.E. Woosley (Santa Cruz)

Supernova neutrinos from SN1987a have been observed by the Kamiokande and IMB detectors and have confirmed the general supernova picture. The observed events were most likely due to $\bar{\nu}_e$ neutrinos. While supernova ν_μ, ν_τ and their antiparticles (combined called ν_x) and ν_e neutrinos are not directly observed yet, Heger et al. [1] point out that constraints on their spectra might be attainable from nucleosynthesis considerations within the ν process [2]. In the ν process certain nuclides can be made by neutrino-induced spallation off nuclei in the outer shells of a massive star during a supernova explosion. Woosley *et al.* [2] showed that the ν-process, i.e. nucleosynthesis by neutrino-induced reactions, can be responsible for most or a large fraction of the solar ^{11}B, ^{19}F, ^{138}La and ^{180}Ta abundance. For ^{11}B and ^{19}F the ν-process excites the parent nuclides ^{12}C and ^{20}Ne above the particle thresholds where they then decay by proton or neutron emission. As both nuclides have rather large particle thresholds, the neutrino nucleosynthesis of ^{11}B and ^{19}F is dominated by neutral-current reactions induced by supernova ν_x neutrinos which have the higher energy spectrum compared to ν_e and $\bar{\nu}_e$ neutrinos. However, as found in detailed stellar evolution studies [1] the rare odd-odd nuclide ^{138}La is mainly made by the charged-current reaction ^{138}Ba$(\nu_e, e^-)^{138}$La. Hence, the ν-process is sensitive to the spectra and luminosity of ν_e and ν_x neutrinos, which are the neutrino types not observed from SN1987a. The GT strength on ^{138}Ba has recently been measured by the (^{3}He,t) reaction in Osaka [**?**]; the ^{138}Ba$(\nu_e, e^-)^{138}$La cross section derived from these data agrees quite well with our calculated one.

To calculate the neutrino-spallation cross sections, a reliable reproduction of the Gamow-Teller (GT) distribution on the target nucleus is necessary. We have therefore performed no-core shell model calculations in $6\hbar\omega$ (for ^{12}C and $4\hbar\omega$ (^{20}Ne) model spaces [4]. As a sideproduct these calculations allow to study the shift of GT strength to higher energies, caused by mixing of excited configuration into the nuclear ground state. This phenomenon has been experimentally observed, it was, however, not yet been reproduced in microscopic model calculations.

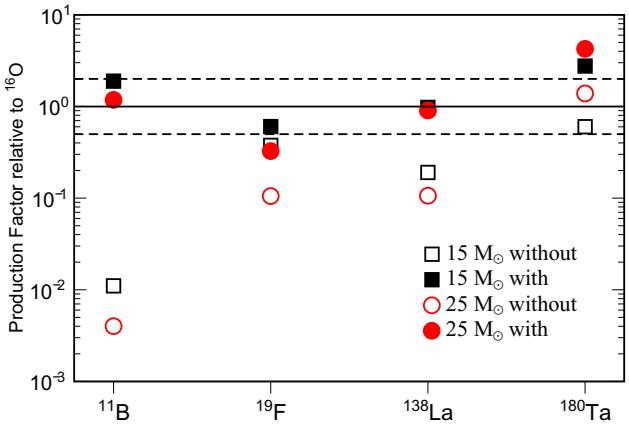


Figure 1: Abundance yields (normalized to solar) for selected nuclei in 15 $M_\odot$ and 25 $M_\odot$ stars with and without the consideration of neutrino nucleosynthesis reactions. (from [1].

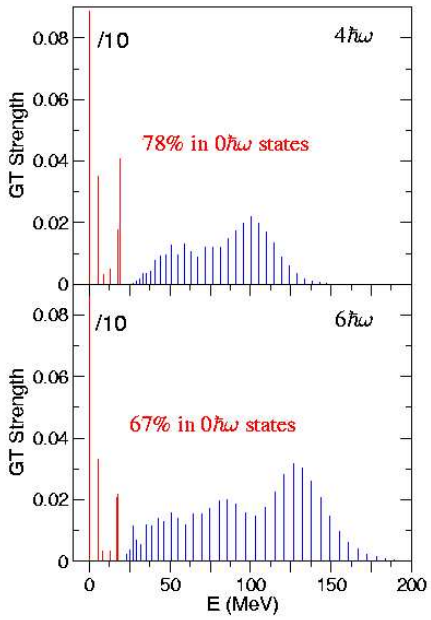


Figure 2: GT strength distribution on ^{12}C, obtained in $4\hbar\omega$ (upper) and $6\hbar\omega$ (lower) model spaces.

References

[1] A. Heger *et al.*, Phys. Lett. **B606** (2005) 258
[2] S.E. Woosley *et al.*, Astr. J. **356** (1990) 272
[3] P. v. Neumann-Cosel, private communication
[4] G. Martinez-Pinedo *et al.*, to be published

The νp-process

G. Martínez-Pinedo and K. Langanke, GSI, Darmstadt, Germany
C. Fröhlich, M. Liebendörfer, F.-K. Thielemann, Universität Basel, Basel, Switzerland
E. Bravo, Universitat Politècnica de Catalunya, Barcelona, Spain
W. R. Hix, Oak Ridge National Laboratory, Oak Ridge, USA
N. T. Zinner, University of Århus, Århus, Denmark

Supernova explosions (the cataclysmic endpoint of stellar evolution) produce iron and neighboring nuclei, underlined by their lightcurves powered by radioactive decay of ^{56}Ni. The production of elements beyond Fe has long been postulated by three classical processes, the r- and the s-process (caused by rapid or slow neutron capture) and the p-process, standing either for proton capture or alternative means to produce heavy neutron deficient, stable isotopes [1]. Currently, the mechanism for the production of the light p-nuclei, ^{92,94}Mo and ^{96,98}Ru, is still unknown.

Observations of extremely "metal-poor" stars in the Milky Way provide us with information about the nucleosynthesis processes operating at the earliest times in the evolution of our Galaxy. The recent detection of Sr/Fe, exceeding 10 times the solar ratio, in the most metal-poor star known to date [2] suggests the existence of a primary process, producing elements beyond Fe and Zn.

We have just suggested a new nucleosynthesis process that will occur in all core-collapse supernovae and could explain the existence of Sr and other elements beyond Fe in the very early stage of galactic evolution. We denote this process "νp-process" [3] and can also contribute to the nucleosynthesis of light p-process nuclei. The νp-process is primary and is associated with explosive scenarios. It occurs when strong neutrino fluxes create proton-rich ejecta. After the production of Fe-group elements, continued antineutrino absorptions by free protons produce free neutrons subject to immediate capture on neutron-deficient $N = Z$ nuclei with small proton-capture cross sections and long beta-decay half-lives, allowing for the synthesis of nuclei with $A > 64$.

Figure 1 compares the composition of supernova ejecta obtained from an hydrodynamical supernova model B07 described in detail in ref. [4] in two calculations, one including neutrino interactions and one neglecting neutrino interactions.

The sensitivity of the nucleosynthesis of some light p-nuclei to the proton-richness of the ejecta, Y_e is shown in figure 2. In particular the production of ^{92}Mo is sensitive to the experimentally unknown masses of the nuclei around ^{92}Pd. Future experimental determinations of these masses at FAIR will help to understand whether or not the νp-process can account for the solar system abundance of ^{92}Mo and will help us to understand the contribution of the νp-process to the chemical evolution of galaxies.

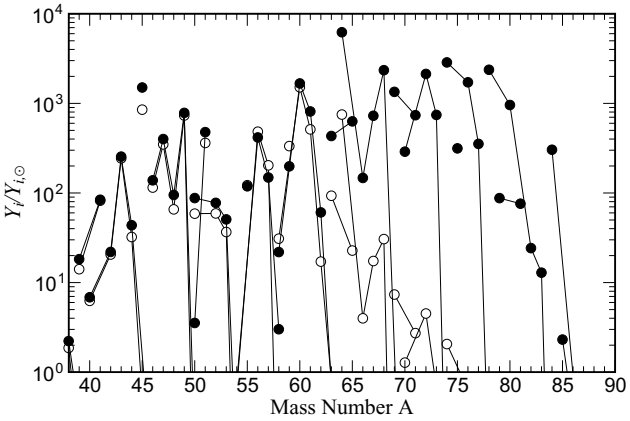


Figure 1: The filled circles represent calculations where (anti)neutrino absorption reactions are included in the nucleosynthesis while for the open circles neutrino interactions are neglected. The abundances are relative to solar.

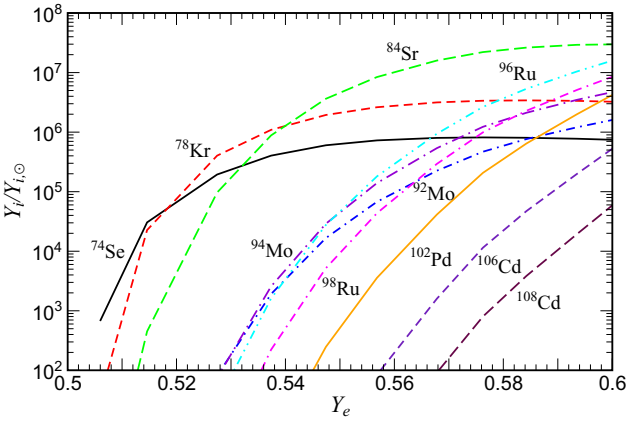


Figure 2: Light p-nuclei abundances in comparison to solar abundances as a function of Y_e. The Y_e-values given are the ones obtained at a temperature of 3 GK that corresponds to the moment when nuclei are just formed and the νp-process starts to act.

References

[1] G. Wallerstein, *et al.*, Rev. Mod. Phys. **69** (1997) 995.

[2] A. Frebel, *et al.*, Nature **434** (2005) 871.

[3] C. Fröhlich, *et al.*, Phys. Rev. Lett. (2006), submitted, `astro-ph/0511584`.

[4] C. Fröhlich, *et al.*, Astrophys. J. (2005), in press, `astro-ph/0410208`.

Neutron captures and the r-process*

Khalil Farouqi†, Johannes Gutenberg Universität Mainz, Institut f. Kernchemie,‡
Karl-Ludwig Kratz and Bernd Pfeiffer
Johannes Gutenberg Universität Mainz, Institut f. Kernchemie,
Friedrich-Karl Thielemann and Thomas Rauscher
Departement für Physik und Astronomie, Universität Basel§

Based on the early description of the electric dipole (E1) strength function of Kadmenskii et al. [1], in a more recent paper Goriely [2] has studied the possible relevance of the existence of a "pygmy" dipole resonance (PDR) in the low-energy tail of the giant dipole resonance (GDR) for neutron-capture cross-section ($\sigma_{n,\gamma}$) calculations. Under certain conditions, i.e. for nuclei where the PDR lies close to the neutron separation energy (S_n), the author predicts local enhancements of the Hauser-Feshbach cross sections by more than a factor 100. If confirmed experimentally, this would result in pronounced consequences for the r-abundance distribution.

To our knowledge, for the first time results from an experiment aimed on the determination of the GDR and the low-lying E1 PDR on medium-heavy, neutron-rich isotopes have been obtained at the LAND-FRS facility of GSI [3]. With respect to possible astrophysical consequences, the measured position of the PDR in ^{130}Sn and ^{132}Sn are of major interest, because some earlier models have predicted considerably lower energies of the PDR in neutron-rich nuclei, in the vicinity of their S_n values. With the known E(PDR)=9.8 MeV and S_n=7.3 MeV in ^{132}Sn, we now can conclude that at least for this isotope, and presumably for the whole A$\simeq$130 mass region of astrophysical interest, there will be no significant enhancement of the $\sigma_{n,\gamma}$ value due to the PDR. This is in contrast to what one would extract from e.g. Fig. 3 of [2].

Nevertheless, in order to investigate the possible impact of altered $\sigma_{n,\gamma}$ values of r-process nuclei, we have performed full dynamic network r-process calculations in the model of an adiabatically expanding hot entropy bubble [4, 5]. For the calculations shown below, the seed abundances for the r-process were obtained from an α-rich freeze-out of a charged-particle network. For the subsequent r-process, an almost instantaneous (n,γ)– (γ,n) equilibrium is established at the onset of the r-process. Therefore, only late-time neutron captures are important, which are then expected to mainly modify the abundances around the r-process peaks at A$\simeq$130 and 195.

Fig. 1 shows a snapshot for a parameter combination of Y_e=0.45, S=196 and an expansion time scale of 35 ms, which is representative for the formation of the A$\simeq$130 r-abundance peak. In order to take into account considerable uncertainties in the $\sigma_{n,\gamma}$ values, we have scaled the "standard" rates of [6] up and down by a factor 100. Fig. 2 shows the corresponding curves for the development of the neutron number densities as a function of time, again for the above three asumptions on the capture rates. As is clearly evident from Fig. 1, even these large variations in the $\sigma_{n,\gamma}$ values do not affect the final r-abundances in the A$\simeq$130 peak region, despite the different – but still "fast" – freeze-out behavior shown in Fig. 2. However, components with high entropies, which synthesize heavier r-process nuclei (A>140), tend to freeze out slower. Here, late-time neutron captures on nuclei near stability – and not on isotopes in the initial r-process path – can modify the final abundance pattern, in particular around the A$\simeq$195 peak [5].

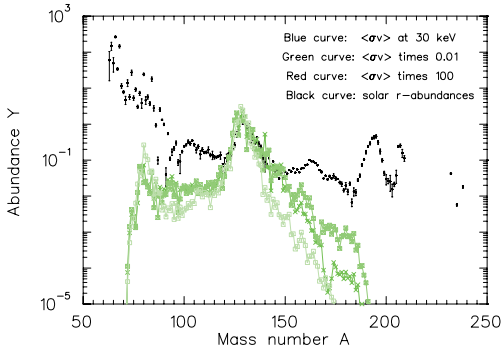


Figure 1: Decayed final abundances of the S=196-entropy component. The neutron capture rates are changed in a range of 4 orders of magnitude.

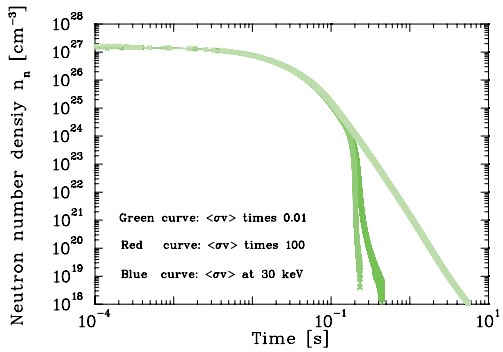


Figure 2: Time evolution of the neutron number density. For $n_n \leq 10^{17}$ ($<\sigma v>$) and $n_n \leq 10^{18}$ ($<\sigma v> \times 100$), the available neutrons are completely exhausted.

References

[1] S.G. Kadmenskii et al., Sov. J. Nucl. Phys. 37, 165 (1983)

[2] S. Goriely, Phys. Lett. B 436, 10 (1998)

[3] P. Adrich et al., GSI Scientific Report 2004, NUSTAR-E-22

[4] C. Freiburghaus et al., Ap. J. 516, 381 (1999)

[5] K. Farouqi, PhD Thesis, Mainz, 2005

[6] T. Rauscher and F.-K. Thielemann, ADNDT 75, 1 (2000)

* Work supported by Helmholtz Forschungsgruppe VISTARS and the Joint Institute for Nuclear Astrophysics

† farouqi@uni-mainz.de
‡ Fritz-Strassmann Weg 2, 55128 Mainz, Germany
§ Klingelberstrasse 82, 4056 Basel, Switzerland

Constraints on the high density EoS from HIC and compact stars

T. Klähn[1,2], D.B. Blaschke[3,4], S. Typel[3], A. Faessler[2], C. Fuchs[2], T. Gaitanos[5], H. Grigorian[1,6], A. Ho[7], E.E. Kolomeitsev[8], M.C. Miller[9], J. Trümper[10], G. Röpke[1], E.N.E. van Dahlen[2], D.N. Voskresensky[3,11], F. Weber[7], H.H. Wolter[5]

[1] Univ. Rostock, Germany; [2] Univ. Tübingen, Germany; [3] GSI Darmstadt, Germany; [4] JINR Dubna, Russia; [5] Univ. München, Germany; [6] Yerevan State Univ., Armenia; [7] San Diego State Univ., USA; [8] Univ. of Minnesota, USA; [9] University of Maryland, USA; [10] MPE Garching, Germany; [11] MEPI Moscow, Russia

The investigation of constraints for the high-density behavior of nuclear matter (NM) has recently received new impetus when the plans to construct a new accelerator facility (FAIR) at GSI Darmstadt were published. Since predictions critically depend on the underlying equations of state (EoS) they have to be carefully verified by comparison to available data. Here we review a set of constraints on the high density behavior of EsoS we suggested in [1]. Each constraint has been introduced within a *strict* and a *weak* interpretation.

(I) Elliptic flow constraint. A constraint on the stiffness of the EoS has been derived by analysing elliptic flow data from heavy ion collisions (HIC) at SIS and AGS. HIC have been described within a kinetic theory approach and the results have been compared to experimental data for the flow of symmetric nuclear matter (SNM) for densities up to $4.5 \times n_s$ [2], where n_s is the nuclear saturation density, see Fig. 1 (dark shaded region between UB and LB boundaries). Within the last decade the KaoS Collaboration at GSI has performed systematic measurements of the K^+ production. Analyses of the data implies a soft behaviour of the EoS, consistent with the flow constraint at moderate densities ($n \leq 3n_s$). At high densities ($n > 3n_s$) the flow constraint (in a weak interpretation) is based on flow data from the AGS energy regime ($E_{\rm lab} \sim 4 - 11$ AGeV).

(II) Maximum mass constraint. Recent measurements on PSR J0751+1807 imply a pulsar mass of $2.1 \pm 0.2\ (^{+0.4}_{-0.5})\ {\rm M}_\odot$ with 1σ (2σ) confidence [3]. Therefore a reliable EoS has to describe neutron star (NS) masses of at least $1.9 M_\odot$ (1σ) in a strong, or $1.6 M_\odot$ (2σ) in a weak interpretation. This condition limits the softness of EoS in NS matter.

(III) Direct Urca constraint. Direct Urca (DU) processes, e.g. the neutron β-decay $n \to p + e^- + \bar{\nu}_e$, are very efficient regarding their neutrino production, even in superfluid NM [4, 5], and cool NSs too fast to be in accordance with data from thermal observable NSs. Therefore we suppose that no DU processes should occur below the upper mass limit for "typical" NSs, i.e. $M_{DU} \geq 1.5\ M_\odot$ ($1.35\ M_\odot$ in a weak interpretation). These limits come from a population synthesis of young, nearby NSs [6] and masses of NS binaries [3].

(IV) Mass-radius constraint. A lower bound on the mass-radius relation of the isolated NS RX J1856 could be deduced from its photospheric radius $R_\infty = 16.8$ km [7] which requires EsoS allowing for compact stars with $M > 1.6 M_\odot$ (for $R \sim 12 - 13$ km) or $R > 14$ km for typical NSs.

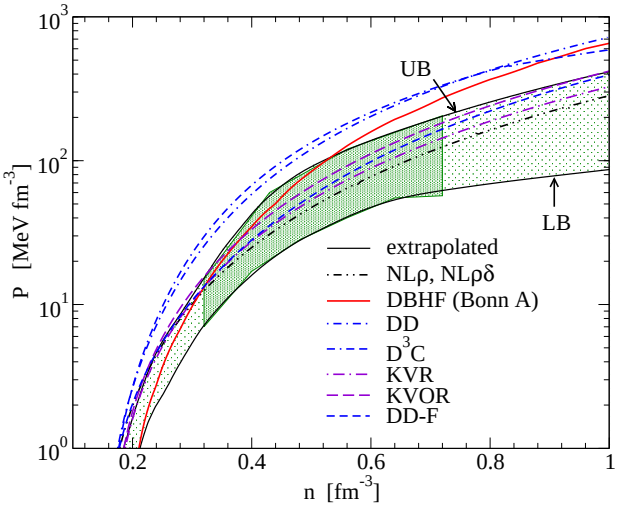


Figure 1: Constraint I: Pressure vs. density for a set of relativistic EsoS and flow constraint region (dark shaded) consistent with data from SIS and AGS. The light shaded region extrapolates this constraint within upper (UB) and lower (LB) bounds.

(V) ISCO constraint. From RXTE data of 4U 1636-536 the frequency of the innermost stable circular orbit (ISCO) has been estimated which corresponds to a mass in the limits 1.9 $M_\odot$ - 2.1 $M_\odot$ [8].

(VI) Gravitational binding constraint. It has been suggested that pulsar B in the double pulsar system J0737–3039 may serve to test EsoS [9]. Its mass of $1.249 \pm 0.001\ M_\odot$ [10] is the lowest reliably measured for any NS to date and could be an indication that pulsar B did form in a type-I supernova of an ONeMg white dwarf driven hydrostatically unstable by electron captures onto Mg and Ne. The well-established critical density at which such stars collapse corresponds to a critical core baryon mass of $M_N \sim 1.37\ M_\odot$ (using an atomic mass of $u = 931,5$ MeV) [9].

Models of the EoS. A wide range of densities up to and above 6 n_s is explored in the description of NSs and HIC. Therefore we use only relativistic EsoS. Phenomenological models NLρ, NL$\rho\delta$, DD, D^{3}C, KVR, KVOR and DD-F are based on a relativistic mean-field (RMF) description of NM with nucleon and meson degrees of freedom. We choose

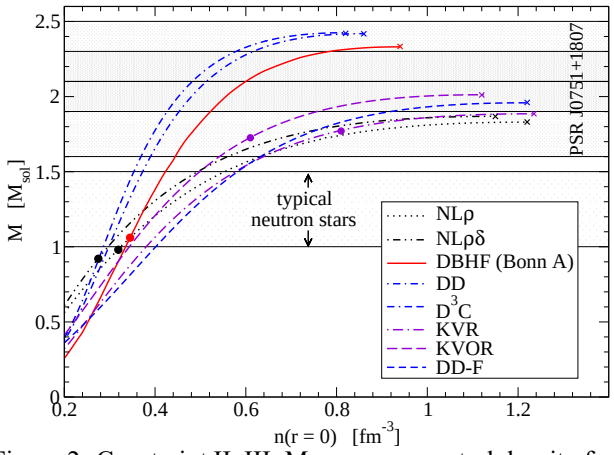


Figure 2: Constraint II, III: Mass versus central density for compact star configurations. Crosses denote the maximum mass configurations, filled dots mark the critical mass and central density values where the DU cooling process becomes possible. It should not occur in "typical neutron stars" which are expected to lie in the lower grey horizontal band. The dark(light) grey horizontal band around 2.1 $M_\odot$ denotes the $1\sigma(2\sigma)$ confidence level for the mass measurement of PSR J0751+1807 [3].

Model	Ref	I	II	III	IV	V	VI	Σ
NLρ	[11]	++	−+	−−	−−	−−	−−	1 2
NL$\rho\delta$	[11]	++	−+	−−	−−	−−	−−	1 2
DBHF	[13]	−+	++	−−	−+	++	−+	2 5
DD	[12]	−−	++	++	−+	++	−−	3 4
D^{3}C	[12]	−−	++	++	−+	++	−−	3 4
KVR	[5]	++	∘+	++	−−	−∘	−+	3 5
KVOR	[5]	++	++	++	−−	−+	−∘	3 5
DD-F	[1]	++	++	++	−−	−+	−+	3 5

Table 1: Results of the test scheme. Fulfilled (violated) constraints are indicated with $+(-)$, a marginal result with ∘. Left symbol stands for a strict, right for a weakened interpretation of the corresponding constraint. Σ: number of passed tests (out of 6).

two versions, NLρ and NL$\rho\delta$, of the non-linear (NL) RMF models with self-couplings of the σ meson field that were applied in the simulation of HIC [11]. The density dependent RMF models applied to finite nuclei are represented here by two parameter sets DD, D^{3}C [12]. The NL RMF models, KVR and KVOR, use couplings and meson masses decreasing with increase of the σ- meson field [5]. The parameters of KVR were adjusted to describe the EoS of the Urbana-Argonne group at densities below four times n_s. KVOR has a slightly modified parameter set and allows higher maximum NS masses. Finally, we present a new parametrization of the RMF model with density-dependent couplings, DD-F, that is fitted to properties of finite nuclei (binding energies, charge and diffraction radii, surface thicknesses, neutron skin in ^{208}Pb, spin-orbit splittings) as in Ref. [12] with an additional flow constraint by fixing the pressure of SNM to $P(3n_s) = 50$ MeV fm^{-3}. Also to compare with phenomenological models, we use recent results of (asymmetric) nuclear matter calculations in the DBHF approach with the relativistic Bonn A potential in the subtracted T-matrix representation, see [13].

Results. Fig. 1 demonstrates that the NLρ, NLδ, KVR, KVOR and DD-F model pass the flow test in both interpretations. In the weak interpretation DBHF passes too. Fig. 2 illustrates, that (II) is fulfilled for all EsoS in the weak (2σ) interpretation. The onset of DU-processes, however, is very sensitive to asymmetry behaviour of the EsoS and varies over a wide range of densities and corresponding NS masses. Only the DD, D^{3}C, KVR, KVOR and DD-F model pass this test.

Table 1 summarizes the results of all suggested tests and reveals the discriminative power of their combined application in a broad region of densities and isospin asymmetry. The whole scheme left four of eight EsoS, namely DBHF, DD-F, KVR and KVOR as most effective, whereby the violation of the DU constraint calls for an improvement of DBHF.

In [1] we found that the maximum NS mass constraint (II) allows to sharpen the flow constraint (I) and vice versa. Both are afflicted with uncertainties, represented by the region of possible pressures in Fig. 1 and the uncertain maximum NS mass. Very soft(stiff) EsoS, being in accordance with I(II), might violate II(I). For an intermediate stiffness both constraints are well fulfilled. It is interesting to note that the NS mass constraints (II,IV,V) demand a very stiff EoS which however most probably hardly passes the flow constraint (I).

We postpone the analysis of EsoS allowing for phase transitions to future work. Besides hyperonization, the possibility of a quark matter phase transition should be studied. The application of the introduced test scheme will help to constrain predictions for the behaviour of matter at large baryon densities to be created in the planned CBM experiment at FAIR.

Acknowledgment. This research was supported by the Virtual Institute *Dense Hadronic Matter and QCD Phase Transition* of the Helmholtz Association under grant No. VH-VI-041.

References

[1] T. Klähn et al., nucl-th/0602038 (2006)
[2] P. Danielewicz et al., Science **298**, 1592 (2002)
[3] D.J. Nice et al., Ap.J. **634**, 1242 (2005)
[4] D. Blaschke et al., A&A **424**, 979 (2004)
[5] E.E. Kolomeitsev et al., NPA **759**, 373 (2005)
[6] S. Popov et al., A&A**448**, 327 (2006).
[7] J.E. Trümper et al., NPProc. Suppl. **132**, 560 (2004)
[8] D. Barret, et al., MNRAS **361**, 855 (2005)
[9] P. Podsiadlowski et al., MNRAS **361**, 1243 (2005)
[10] M. Kramer et al., arXiv:astro-ph/0503386 (2005)
[11] T. Gaitanos et al., NPA **732**, 24 (2004)
[12] S. Typel, Phys. Rev. C **71**, 064301 (2005)
[13] E.N.E. van Dalen et al., NPA **744**, 227 (2004)

Search for Element 112 Using the Hot Fusion Reaction $^{48}Ca + ^{238}U$*

S. Hofmann[1,7], D. Ackermann[1], S. Antalic[2], H.G. Burkhard[1], R. Dressler[3], F.P. Heßberger[1], B. Kindler[1], I. Kojouharov[1], P. Kuusiniemi[1], M. Leino[4], B. Lommel[1], R. Mann[1], G. Münzenberg[1], K. Nishio[5], A.G. Popeko[6], S. Saro[2], H.J. Schött[1], B. Streicher[2], B. Sulignano[1,8], J. Uusitalo[4], A.V. Yeremin[6]

[1]GSI, Darmstadt, Germany; [2]Comenius University, Bratislava, Slovakia; [3]PSI, Villigen, Switzerland; [4]University of Jyväskylä, Jyväskylä, Finland; [5]JAEA, Tokai, Japan; [6]JINR, Dubna, Russia, [7] Johann Wolfgang Goethe-Universität, Frankfurt, Germany, [8] Johannes Gutenberg-Universität, Mainz, Germany

Recent literature data on the synthesis of element 112 using the hot fusion reaction $^{48}Ca + ^{238}U \rightarrow ^{286}112^*$ seem to be contradictory concerning cross-sections and half-lives of the produced nuclei (see [1–4]). The most comprehensive studies were performed at the DGFRS of FLNR [2], where not only the reaction $^{48}Ca + ^{238}U$, but also reactions leading to elements up to Z=118 were investigated.

In order to prepare an extensive experimental program at SHIP on the study of superheavy nuclei using hot fusion reactions and to confirm or disprove literature data, we selected the reaction $^{48}Ca + ^{238}U$ to start with.

The irradiations at SHIP, including various test reactions, took place from April 6th to June 9th, 2005. A detailed description of the experiment can be found in [5].

The ^{48}Ca beam was prepared from the ECR ion source of the UNILAC. Metallic, isotopically enriched ^{48}Ca (89.5 %) and the oven technique were used. Ions with charge state 10^+ were extracted and accelerated to Coulomb barrier energies. A mean current of 1.2 *p*μA was reached on target at a duty factor of 28 % (5.5 ms wide pulses at 20 Hz repetition frequency). The consumption of ^{48}Ca was 0.6 mg/h on the average.

The targets were prepared from the chemical compound UF_4. Layers of 488, 408 and 451 μg/cm^2 were evaporated on backing foils of 42 μg/cm^2 carbon and subsequently covered with carbon layers of 10 or 20 μg/cm^2. Details of the target preparation are given in [6]. The target thickness was controlled on-line by registration of elastically scattered projectiles and scattering of 20 keV electrons [7]. The data showed a continuous decrease of the thickness during irradiation. The target wheel was replaced at the latest, when the losses reached a value of 30 %. We estimated a mean fading of 20 % of target thickness for the calculation of the cross-section. A total of 14 uranium target wheels were used. The uranium content of new and irradiated targets including the performance of the whole experimental set-up was tested by measuring the yield of fusion products from reactions with a ^{22}Ne beam supplied for two days at half time of the experiment. This test confirmed the results obtained by the measurements using scattered projectiles or electrons.

Properties of SHIP and of the detector system are described in [8]. Since that time, however, the detector system was improved. A Si veto detector was mounted behind the stop detector and the single crystal Ge detector was replaced by a four crystal Ge clover detector. The new set-up is shown in Fig. 1. During the uranium irradiation the first of the TOF detectors was removed after few days, which resulted in reduced scattering of the ions and deeper implantation into the Si stop detector.

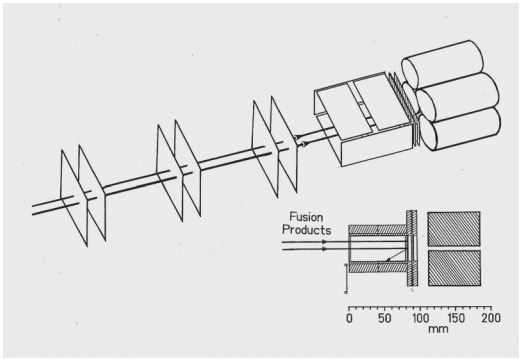


Figure 1: Detector set-up at SHIP. For details see text and description in [8].

We used three different ^{48}Ca beam energies during the experiment. Duration of the irradiations, beam energies, beam doses and cross-section data are summarized in Tab. 1. Chronologically, energies were chosen as given in the table from top to bottom.

Table 1: Parameters and results of the $^{48}Ca + ^{238}UF_4$ irradiation studied at SHIP.

days	E_{proj} / MeV	E* / MeV	dose / 10^{18}	n	σ / pb
20.9	239.3	37.0	12	0	<0.6
16.8	236.2	34.5	10	1	0.7 +1.6 –0.6
14.8	233.3	32.0	7	0	<0.8

E* is the excitation energy of the compound nucleus at half-thickness of the target layer; n is the number of events. Cross-section limits given are "one-event" limits which do not include statistical fluctuations.

No spontaneous fission (SF) events or α decay chains were measured at excitation energies of 37.0 and 32.0 MeV. Three SF events were measured at E* = 34.5 MeV. However, these events occurred within 12 hours after the test reaction $^{22}Ne + ^{238}UF_4$. The period of interest is shown in Fig. 2. The total kinetic energies (TKE) of these SF events are 149.4, 141.3, and 154.8 MeV (energy calibration based on α particles), respectively, which agrees well with the energies of SF events from ^{255}No or ^{256}Fm measured during the test reaction. We assign these three

* Work supported by EU, EURONS contract No. 506065.

events to the decay of ^{256}Fm produced in a p3n evaporation channel, taking into account well known half-lives and branching ratios of nuclei in the region of interest.

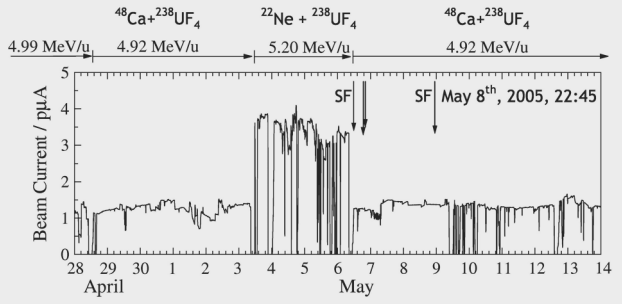


Figure 2: Mean beam currents in particle μA and appearance of SF events during the irradiation of an $^{238}UF_4$ target with ^{48}Ca projectiles. A ^{22}Ne beam was used for testing purposes from May 3rd to 6th.

A forth SF event was measured on May 8th, 2005, also marked in Fig. 2. The measured parameters clearly identify this event as SF. The energies, based on α calibration, are E_{stop} = 190.4 MeV and E_{box} = 15.3 MeV. These data are shown together with the energies from SF of ^{252}No (produced in the calibration reaction ^{48}Ca + ^{206}Pb) in Fig. 3. The considerable high TKE is clearly visible. In order to determine the true TKE we used the known TKE of the ^{252}No decay, which is 195 MeV [9]. The difference to the peak position at 158.7 MeV in Fig. 3 is 36 MeV. This energy difference was added to the TKE of the SF event from May 8th, which resulted in a TKE of 242 MeV. Assuming a width of the TKE distribution similar to that of ^{252}No, we determine a one σ uncertainty of ±15 MeV for the TKE of this one event.

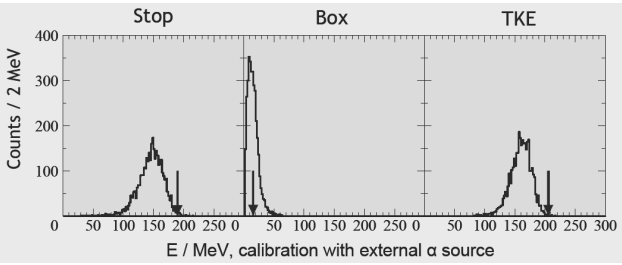


Figure 3: Detector response to SF fragments of ^{252}No produced in the test reaction ^{48}Ca + ^{206}PbS in comparison with the energy of the two SF fragments of the event measured during the ^{48}Ca + $^{238}UF_4$ irradiation.

The following further properties of the SF event were measured: No signals from the TOF detectors, coincident signals of 386 and 2068 keV in two of the Ge detectors, and appearance of the event during the beam pause at 12.508 ms after beginning of the macro-pulse period which starts with the 5.5 ms wide beam pulse. Finally, the event occurred in strip number 9 of the 16 strip stop detector at a vertical position of 30 mm from the bottom. The signal from the 28 segment box detector was derived from segment number 13.

At the position of the SF event in the stop detector we searched for preceding α particles and the implanted evaporation residue. Within a reasonable position window of ±1 mm and a time window of 1000 s, we found a total of 29 implantations (5 MeV < E < 30 MeV), but no α particle was measured. Due to the low discriminator level (200 keV) for detection of α particles escaping from the stop detector, we exclude non-registration of such events with high probability. Most (25) of the implantation events coincide with background events from elastically scattered target nuclei. Only one, the first one, appears within an energy-TOF window where we expect signals from implanted evaporation residues. The measured time difference between implantation and SF is 7.57 s, which corresponds to a half-life of (5.2 +25.1 –2.4) s.

Aiming at confirmation of results on element 112 using the hot fusion reaction ^{48}Ca + ^{238}U, we measured one SF event. Although we cannot assign this one event to a certain isotope on the basis of our present data, we find agreement with decay data which were assigned to the isotope ^{283}112 in [2], using the same reaction. However, if we tentatively assign our SF event to the isotope ^{283}112 in accordance with the interpretation given in [2], then we have to introduce an adequate SF branching of this nucleus, because no α particle was measured between implantation and SF. More experimental work is needed in order to obtain an independent and unambiguous confirmation of previous results. As a next step of technical improvement we explore the production of metallic uranium targets which result in higher efficiency of the SHIP separator than targets of chemical compounds. Using these targets we plan to study the reaction ^{50}Ti + ^{238}U → ^{288}114*. According to theoretical predictions, the evaporation of 4 neutrons is most likely at Coulomb barrier energies [10], and the produced isotope ^{284}114 should be the parent of at least three safely to correlate α decays with half-lives of a few hundred microseconds [11]. The chain could end at ^{272}Hs, ^{268}Sg or ^{264}Rf by SF after further α decays. With this next experiment we follow our strategy to fully exploit the use of relatively unproblematic uranium targets before starting experiments using more radioactive actinide targets like ^{242}Pu, ^{244}Pu, or ^{248}Cm.

References

[1] Yu.Ts. Oganessian et al., *Eur. Phys. J.* **A19** (2004) 3.
[2] Yu.Ts. Oganessian et al., *Phys. Rev.* **C70** (2004) 064609.
[3] A.B. Yakushev et al., *Radiochim. Acta.* **91** (2003) 433.
[4] K.E. Gregorich et al., *Phys. Rev.* **C72** (2005) 014605.
[5] S. Hofmann et al., *J. Nucl. Radiochem. Sciences*, submitted.
[6] B. Lommel et al., *Nucl. Instr. Meth.* **A480** (2002) 16.
[7] R. Mann et al., *GSI Scientific Report* **2004-1 (**2004) 224.
[8] S. Hofmann and G. Münzenberg, *Rev. Mod. Phys.* **72** (2000) 733.
[9] E.K. Hulet, *Physics of Atomic Nuclei* **57** (1994) 1099.
[10] G.G. Adamian et al., *Phys. Rev.* **C69** (2004) 44601.
[11] I. Muntian et al., *Acta Phys. Pol.* **B34** (2003) 2073.

Single-particle effects in the decay of ^{269}Ds*

A. Parkhomenko[1,2], F.P. Heßberger[2], S. Hofmann[2] and A. Sobiczewski[1,2]
[1]Soltan Institute for Nuclear Studies, Warsaw, Poland; [2]GSI, Darmstadt, Germany

A rather large number of decay chains of superheavy nuclei have been already observed (e.g. [1–3]). Most of them belong to odd-A nuclei. It is important then to see how well we are able to describe the chains for these nuclei.

The objective of this contribution is to perform a detailed theoretical analysis of the decay chain of the nucleus ^{269}Ds (Z=110), discovered in Darmstadt [4]. In particular, it is aimed to see, how large are the effects of an odd nucleon in description of this chain. Both measured quantities: transition energy in α decay, Q^{t}_{α}, (directly connected with kinetic energy of emitted α particle) and α-decay half-life T_{α} (directly connected with α-decay lifetime τ_{α}) are considered.

The theoretical model, which is used, is the macroscopic-microscopic approach. Alpha-decay energies are taken from [5]. Neutron single-particle excitation energies are obtained in the one-quasiparticle approximation [6]. It is assumed that transitions in the α-decay appear between the states with the same quantum structure (the same quantum numbers). If a transition goes to an excited state, the state tends to decay by γ transition before the next α-decay. Exceptions are the isomeric states.

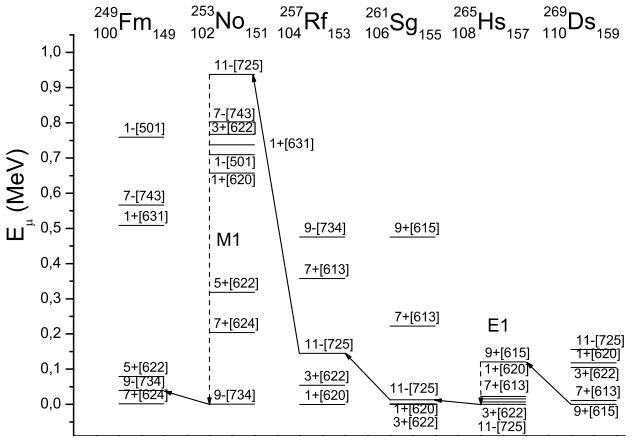


Figure 1: Calculated single-particle spectra and assumed decay chain of the nucleus ^{269}Ds.

With these assumptions, a most natural decay chain of ^{269}Ds is presented in Fig 1. The figure is done in a rather unconventional way, when the ground sates (g.s.) of all nuclei in the chain are put at the same level. This unconventional presentation has, however, a number of advantages. It better uses the space of the picture, allows one to see directly the excitation energy of single-particle states and to compare easily the spectra of all nuclei with each other. It is also easy to see how much is the transition energy Q^{t}_{α} changed with respect to the α-decay (g.s. to g.s. transition) energy Q_{α} by the odd-particle effect. Unconventional is also the specification of 2Ω instead of Ω (projection of spin on the symmetry axis of a nucleus) at each energy level, done for a simplification of the notation. One can see in the figure that the effects of odd nucleon are large. The effect is especially large in the decay of ^{257}Rf to ^{253}No, where it changes the transition energy Q^{t}_{α} by $\Delta E = -0.79$ MeV.

Table 1: Values of the quantities characteristic for the decay chain of ^{269}Ds.

Nucl.	$Q_{\alpha}^{t,th}$	$Q_{\alpha}^{t,exp}$	Q_{α}^{th}	ΔE	T_{α}^{th}	T_{α}^{exp}	f
-	MeV	MeV	MeV	MeV			
^{269}Ds	11.51	11.28	11.63	-0.12	39 μs	179 μs	4.6
^{265}Hs	10.35	10.72	10.36	-0.01	4.7 ms	701 μs	6.7
^{261}Sg	9.60	9.68	9.74	-0.14	96 ms	61 ms	1.6
^{257}Rf	8.42	8.80	9.21	-0.79	64 s	9.4 s	6.8
^{253}No	8.15	8.21	8.19	-0.04	91 s	92.4 s	1.0

Detailed values of the quantities characteristic for the chain are given in Table 1. Especially interesting in our study is the modification ΔE of the transition energy Q^{t}_{α} with respect to the α decay energy Q_{α} (g.s. to g.s. transition), $Q^{t}_{\alpha} \equiv Q_{\alpha} + \Delta E$, by the odd-particle effect. One can see that ΔE modifies Q^{t}_{α} in the chain by: 10-790 keV. Alpha-decay half-lives T_{α} are calculated according to a new formula, proposed recently in [7]. One can see that the calculated values reproduce experimental ones within a factor f ($f \equiv T^{th}_{\alpha}/T^{exp}_{\alpha}$ or $T^{exp}_{\alpha}/T^{th}_{\alpha}$), which is in about the range: 1-7. The average value of f for the 5 transitions is: $\bar{f}$=4.2. As no adjustable parameter is used, the result may be considered as good. Also the agreement between $Q^{t,th}_{\alpha}$ and $Q^{t,exp}_{\alpha}$ is satisfying.

References

[1] S. Hofmann and G. Münzenberg, Rev. Mod. Phys. **72**, 733 (2000).

[2] Yu.Ts. Oganessian *et al.*, Nucl. Phys. A 685, 17c (2001).

[3] K. Morita *et al.*, J. Phys. Soc. Jpn **73**, 2593 (2004).

[4] S. Hofmann *et al.*, Z. Phys. A **350**, 277 (1995).

[5] I. Muntian *et al.*, Acta Phys. Pol. B **34**, 2073 (2003).

[6] A. Parkhomenko and A. Sobiczewski, Acta Phys. Pol. B **36**, 3115 (2005).

[7] A. Parkhomenko and A. Sobiczewski, Acta Phys. Pol. B **36**, 3095 (2005).

* Work supported by EU, EURONS contract No. 506065.

Decay Studies of K-Isomeric States in ^{254}No and ^{252}No*

B. Sulignano[1,7], S. Hofmann[1,8], F.P. Heßberger[1], D. Ackermann[1], S. Antalic[2], H.G. Burkhard[1], B. Kindler[1], I. Kojouharov[1], P. Kuusiniemi[3], M. Leino[4], B. Lommel[1], R. Mann[1], K. Nishio[5], A.G. Popeko[6], S. Saro[2], H.J. Schött[1], B. Streicher[2], J. Uusitalo[4], A.V. Yeremin[6]

[1]GSI, Darmstadt, Germany; [2]Comenius University, Bratislava, Slovakia; [3]CUPP, University of Oulu, Finland, [4]University of Jyväskylä, Jyväskylä, Finland; [5]JAEA, Tokai, Japan; [6]JINR, Dubna, Russia, [7]Johannes Gutenberg-Universität, Mainz, Germany, [8]Johann Wolfgang Goethe-Universität, Frankfurt, Germany

The study of high spin K isomers offers an excellent possibility to get information on the properties of the nucleon orbits involved. In this respect nuclei in the region of ^{252}Fm (Z = 100, N = 152) are of special interest. The reasons are that nuclei in this region are deformed and that both at Z = 100 and at N = 152 large gaps exist between the energies of single particle Nilsson levels below and above these occupation numbers, which, vice versa, results in compression of levels below and above the gaps. As a result high spin K isomers are formed at relatively low energy, if within such a compressed band of levels not all levels are occupied and at least two levels with high spin exist.

Single particle energies in the region of interest were calculated, e.g. in [1,2] using the macroscopic microscopic model and in [3] using a self-consistent mean field approach. Already the results of these few examples show that the obtained energies depend sensitively on the deformation space used (in [1,2]) or on the selected effective nucleon interactions (in [3]). Therefore, calculated energies of K isomers are strongly model dependent.

Using the results of [1,2], the relevant Nilsson levels for neutrons below and above N = 152 are {9/2$^-$[734], 7/2$^+$[624], 5/2$^+$[622], 1/2$^-$[501], 1/2$^+$[631]} and {1/2$^+$[620], 3/2$^+$[622], 11/2$^-$[725], 7/2$^+$[613]}, respectively, and for the protons below and above Z = 100 {7/2$^+$[633], 3/2$^-$[521], 1/2$^+$[400], 5/2$^+$[642]} and {1/2$^-$[521], 7/2$^-$[514], 9/2$^+$[624]}. If large energy gaps exist at Z = 100 and N = 152, we would expect, qualitatively, high energies for K isomers in nuclei where the Fermi level is located within the gap and the K isomer must be formed by raising one or two quasiparticles to levels above the gap. Such cases are isotopes with Z = 100, isotones with N = 152 and as a special case the nucleus ^{252}Fm. Indeed, no K isomer is known experimentally in ^{252}Fm.

Using the argumentation given before, we conclude, that the lowest high spin K isomer in ^{250}Fm is formed from a neutron configuration, whereas the lowest isomer in ^{254}No is formed from a proton configuration. In ^{252}No, however, we expect K isomers at about equal energy formed by proton and neutron quasiparticles.

An extensive theoretical study on K isomers in the region of heavy and superheavy elements was recently published in [4]. In this investigation, however, neutron configurations for N = 150 and 152 isotones were not considered. However, the energy of K isomers formed from the proton configuration $K^{\pi} = 7^-$, $\pi(7/2^+[633],7/2^-[514])$ in isotopes of fermium and nobelium from N = 150 to 156 was calculated at relatively low excitations of about 1.0 and 1.6 MeV, respectively. For the K isomers in fermium the energy is even lower than in the case of nobelium. This result indicates that the energy spacing of proton levels used in [4] is different from that given in [1,2].

Experimentally, the first K isomers in the region of interest were measured already 33 years ago [5]. These were the $T_{1/2}$ = 1.8 s isomer in ^{250}Fm and the 0.28 s isomer in ^{254}No. The properties of ^{254}No were reinvestigated recently [6]. Our experiments at SHIP were planned to confirm data obtained on ^{254}No in [6] and to search for K isomers in ^{252}No.

^{254}No

In [6] the isotope ^{254}No was studied by in-beam as well as by focal plane spectroscopy, including conversion electron and γ coincidences. The reaction ^{48}Ca + ^{208}Pb was used. The 0.28 s isomer was confirmed. A more accurate half-life of 0.266 s was obtained and for the energy a value of 1293 keV was measured. Spin and parity of 8$^-$ were assigned on the basis of γ decay data. In addition, a second isomer with a half-life of 184 μs was measured. On its decay path to the first isomer, γ rays of 607 keV in coincidence with a total of 600 keV electron energy were measured. For the energy of this second isomer a value of 2.5 MeV was estimated, which is 1.2 MeV above the energy of the first isomer.

In our investigation of K isomeric states of nobelium isotopes at SHIP, we confirmed the data on ^{254}No obtained in [6]. Using the same reaction ^{48}Ca + ^{208}Pb, we measured in particular also the emission of γ rays in the decay paths of the 184 μs isomer. For the energy of the γ rays we measured a value of (605 ± 1) keV. In our experiment we observed coincidences between K-X-rays and these γ rays. Because the γ transition of 605 keV cannot be strongly converted, the observation of a high number of K-X ray – K-X ray coincidences proves that at least two transitions must follow or precede the γ transition.

In addition, a somewhat weaker γ line of (839 ± 1) keV with an intensity ratio of 0.7 compared to the 605 keV line was observed. Its half-life is in the range from 110 to 150 μs. This is slightly shorter than the 184 μs half-life of the second isomer. However, more data with better statis-

* Work supported by EU, EURONS contract No. 506065.

tical accuracy are needed in order to make a definite assignment.

^{252}No

The isotope ^{252}No was produced by the reaction ^{206}Pb(^{48}Ca,2n)^{252}No. In the focal plane of SHIP, γ spectra were studied using a delayed coincidence technique. In a first step the implanted ^{252}No nucleus ($T_{1/2}$ = 2.3 s) was identified by its subsequent α decay or spontaneous fission up to a maximum lifetime of 10 s. In a second step we searched for γ rays emitted during the lifetime of ^{252}No up to a maximum period of 500 ms after implantation, applying the additional condition that the γ rays are in coincidence with conversion electrons. A γ spectrum obtained this way is shown in Fig. 1a. A total of nine γ lines were assigned to the decay of ^{252}No. They are marked by their energies in Fig. 1a.

For the two lines at 755 and 862 keV a half-life of (53 ± 26) ms was measured. The energy difference of 107 keV equals the energy between the 4^+ and 2^+ rotational levels of the ground-state (g.s.) band which was measured in a recoil decay tagging experiment recently [7], see Fig. 1b. Therefore we assign the two lines to an isomeric state decaying directly into the g.s. rotational band. For the energy of the isomer we obtain a value of 908 keV.

For the other seven lines a half-life of (101 ± 14) ms was measured. Two of these lines at 166 and 224 keV have within error bars the same energies as the γ rays emitted from the 8^+ and 6^+ levels of the g.s. rotational band [7], see Fig. 1b. Therefore we assign the remaining five γ lines to the decay of a second isomeric state in ^{252}No. Because no difference between any of these five lines agrees with energies between the levels of the g.s. rotational band, we conclude that the four higher energy lines populating the g.s. band are emitted from different intermediate levels located below the second isomer. Due to the low number of detected γ rays, γ-γ coincidences were below the detection limit of the present experiment.

An estimate for the minimum energy of the 101 ms isomer follows from the sum of the energy of the 8^+ level of the g.s. band at 544 keV, because this level is populated with certainty, and the 827 keV γ energy. We obtain 1371 keV.

The population of the 8^+ level of the g.s. band in the decay of the isomer indicates a high spin value of the emitting state. In the context of K isomers as discussed before, we expect in ^{252}No two $K^\pi = 8^-$ states, one based on a proton and the other on a neutron configuration. Based on level density arguments, the two quasiparticle proton configuration should be lower in energy.

From the discussion of the single particle level energies we expect another lower spin ($K^\pi = 4^+$) two quasiparticle proton configuration in ^{252}No. Tentatively, we assign this configuration to the 53 ms isomer which decays into the 4^+ and 2^+ level of the g.s. band.

Four more lower spin ($K^\pi = 5^+$, 5^- and 4^+, 4^-) isomers can be formed by two quasiparticles neutron configurations. We tentatively assign the γ lines at 827, 886, 911, and 920 to the decay of levels from one of these states and the rotational states built on it. With these assignments the 134 keV transition fits quite natural to the decay of the 101 ms isomer. From intensity arguments we estimate M2 character for this transition, which excludes the negative parity states.

It is planned to continue the experiments on K isomers in nobelium and fermium isotopes. In particular, γ-γ coincidences are needed in order to confirm the tentative assignments given before. The data will be completed by search for possible α and spontaneous fission decay branches of the isomers.

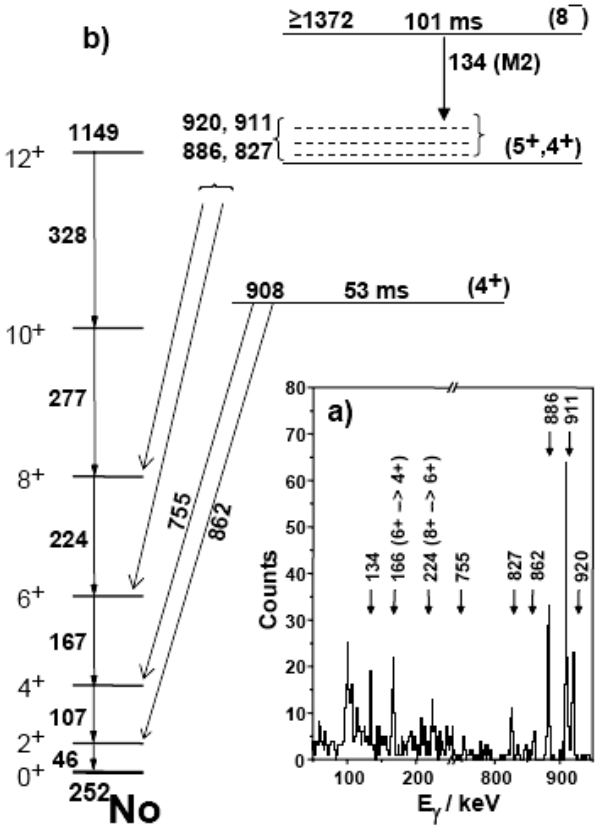


Figure 1: a) γ spectrum measured at the focal plane of SHIP in the reaction ^{206}Pb(^{48}Ca, 2n)^{252}No. For details of the measurement see text. The uncertainty of the γ ray energies is ±1 keV. b) Tentative decay schemes of the isomeric states in ^{252}No. Transition energies within the g.s. rotational band of ^{252}No were taken from [7]. All energies are given in keV.

References

[1] S. Cwiok et al., Nucl. Phys. **A 573** (1994) 356.
[2] Z. Patyk, A. Sobiczewski, Nucl. Phys. **A 533** (1991) 132.
[3] M. Bender et al., Nucl. Phys. **A 723** (2003) 354.
[4] F.R. Xu et al. Phys. Rev. Lett. **92** (2004) 252501.
[5] A. Ghiorso et al. Phys. Rev. **C 7** (1973) 2032.
[6] R.-D. Herzberg et al. Contrib. to the 'Int. Conf. on Finite Fermionic Systems' Lund, Sweden, 2005 (in press).
[7] R.D. Herzberg et al. Phys. Rev. **C 65** (2001) 014303.

New isotopes ^{193,194}Rn

A.N. Andreyev[1,9], S. Antalic[2], D. Ackermann[3], L. Bianco[4], D. Cullen[5], I. Darby[4], S. Franchoo[6], F. P. Heßberger[3], S. Hofmann[3*], M. Huyse[7], B.Kindler[3], I. Kojouharov[3], A.-P. Leppänen[8], B. Lommel[3], R. Mann[3], G. Münzenberg[3,§], R.D. Page[4], J. Pakarinen[8], J. J. Ressler[9], S. Šaro[2], B. Streicher[2], B. Sulignano[3,§], J. Thomson[4], P. Van Duppen[7]

[1]TRIUMF, Vancouver BC, V6T 2A3, Canada; [2]Comenius University, Bratislava, Slovakia; [3]GSI, Darmstadt, Germany; [4]University of Liverpool, L69 7ZE, U.K.; [5]Department of Physics and Astronomy, University of Manchester, M13 9PL, U.K.; [6]IPN Orsay, F-91406 Orsay Cedex, France; [7] IKS, University of Leuven, Belgium; [8]University of Jyväskylä, Jyväskylä, Finland; [9]Dept. of Chemistry, Simon Fraser University, Burnaby BC V5A-1S6, Canada

Theoretical calculations have suggested shape coexistence and the onset of strong ground-state deformation in Rn isotopes with A ≤ 201, see for example [1]. It is predicted that the $^{194\text{-}201}$Rn nuclei should possess the oblate-deformed ($\beta_2 \approx -0.22$) ground state, while a sharp transition to a strongly-deformed ($\beta_2 \approx 0.28$) prolate ground state should happen between ^{194}Rn and ^{193}Rn. However, until now no clear evidence for the onset of ground state deformation in the lightest Rn isotopes could be found experimentally, including the ^{195,196}Rn isotopes, being the lightest known Rn isotopes before the present study [2]. In contrast to this, the higher-lying yrast states (where known) do show evidence that deformed intruder configurations become important in the light Rn isotopes [3].

Complete-fusion reactions with heavy ions followed by α decay, is a powerful complementary tool to investigate low-energy shape coexistence and structure of the most neutron-deficient nuclei. By using this method, the new nuclides ^{193,194}Rn isotopes were produced in the 3n and 2n evaporation channels, respectively, of the ^{52}Cr+^{144}Sm → ^{194}Rn* reaction. The ^{52}Cr beam was provided by the UNILAC with a typical intensity of about 500-700 pnA on target which was rotating synchronously with the UNILAC macro-pulsing.

The evaporation residues were separated in-flight by SHIP and implanted in a position-sensitive silicon detector (PSSD) to measure subsequent particle decays. A 4-fold segmented Clover germanium detector was installed behind the silicon detector for prompt and delayed α-γ coincidence measurements. Preliminary data for ^{194}Rn are reported in this contribution, while the full account will be given elsewhere [4].

Fig. 1 shows a part of the α-decay spectrum, measured at the beam energy of E(^{52}Cr)=230 MeV in the middle of the target, within 10 ms after the recoil implantation in the PSSD. Based on the time-position correlation analysis with the daughter activities (e.g. ^{190}Po), the peak with 23 events at E_α=7696(20) keV was attributed to the new isotope ^{194}Rn. The half-life of $T_{1/2}$=0.8(2) ms was deduced for ^{194}Rn. About 15 recoil-α correlations were observed for the new isotope ^{193}Rn. The preliminary analysis shows that the α decay pattern of ^{193}Rn is more complex than that of ^{194}Rn with possible evidence for two α-decaying isomeric states in this nucleus, similar to the situation observed in the heavier odd-A $^{195\text{-}203}$Rn isotopes.

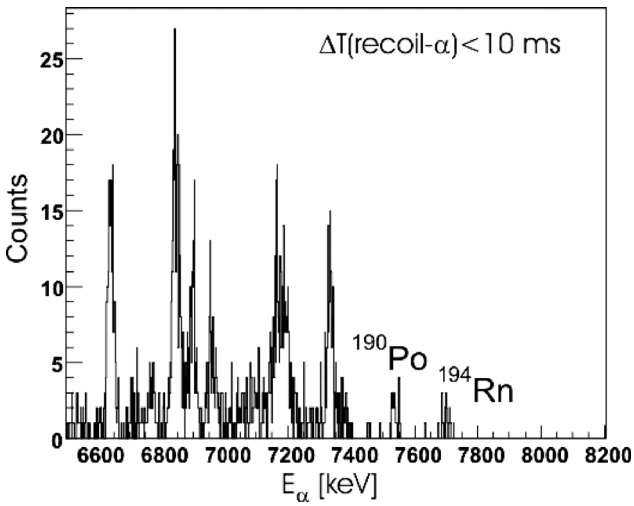


Figure 1: Spectrum of α particles measured in the ^{52}Cr + ^{144}Sm reaction at a beam energy of 230 MeV within 10 ms after the recoil implantation. The α decays of ^{190}Po and ^{194}Rn are marked.

We thank the UNILAC staff for providing the stable and high intensity ^{52}Cr beam. This work was supported by EURONS (European Commission contract no. 506065), by the FWO-Vlaanderen and by the Interuniversity Attraction Poles Programme-Belgian State-Federal Office for Scientific, Technical and Cultural Affairs (IAP grant P5/07) and UK EPSRC. A.N.A. and J.J.R. were partially supported by the NSERC of Canada.

References

[1] P. Möller et al., *At. Data Nucl. Tables* **59** (1995) 185.
[2] H. Kettunen et al., *Phys. Rev.* **C 63** (2001) 044315.
[3] R. Julin, K. Helariutta and M. Muikku, *J. Phys. G: Nucl. Part. Phys.* **27** (2001) R109.
[4] A.N. Andreyev et al., in preparation (2006).

*And Johann Wolfgang Goethe-Universität, Frankfurt, Germany
§ And Johannes Gutenberg-Universität, Mainz, Germany

Search for the "missing" α-Decay Branch in ^{239}Cm

Z. Qin [1,3], D. Ackermann[1], W. Brüchle[1], F.P. Hessberger[1], E. Jäger[1], P. Kuusiniemi[1], G. Münzenberg[1], D. Nayak[1], E. Schimpf[1], M. Schädel[1], B. Schausten[1], B. Sulignano[1,2], X.L. Wu[1,3], K. Eberhardt[2], J.V. Kratz[2], D. Liebe[2], P. Thörle[2], Yu. N. Novikov[1, 4]

[1]GSI, Darmstadt, Germany, [2]Johannes Gutenberg-Universität, Mainz, Germany, [3]IMP, Lanzhou, P.R. China,[4]Petersburg Nuclear Physics Institute, Gatchina, Russia

We continued our search for the "missing" α-decay branch of ^{239}Cm in a series of irradiations at the UNILAC making use of the ^{232}Th (^{12}C, 5n)^{239}Cm reaction and applying nuclear chemistry techniques. The goal of these experiments and a description of the irradiation and detection techniques were reported in Ref. [1]. In our recent experiments, ^{12}C beam intensities varied between 0.4 and 0.6 particle μA (available as a parasitic beam during nighttimes). Each irradiation lasted between 4 and 6 h. The radiochemical separation procedure [2] to prepare a purified Cm sample for α-spectroscopy was accomplished within 2.5 h.

The yield of extraction and precipitation was checked by adding ^{170}Tm radiotracer and was found to be typically about 75%. The yield of the evaporation step was determined with ^{151}Pm (product of ^{12}C induced ^{232}Th fission) and, for the evaluated experiments, it was close to 100%. The total chemical yield was assumed to be about 70% for curium. Samples were assayed for α-activities by 450 mm^2 PIPS detectors. The energy resolution of the evaporated samples was 60 keV (FWHM). All α-events were recorded together with detector numbers and associated times and were stored in a list mode.

In our recent series of experiments, two different ^{12}C beam energies were applied. 74 MeV (middle of target) was chosen as the first energy to reproduce our previous results and to increase the statistics. This energy is close to the maximum of the ^{239}Cm (5n) excitation function and it allows monitoring the stability of the experiment through the observation of ^{240}Cm and ^{238}Cm in 4n and 6n channel. Fig. 1(a) shows a typical α-spectrum of a Cm fraction obtained at 74 MeV and recorded for the first 10 hours. ^{240}Cm with α-energies of 6.29 and 6.25 MeV is clearly observed. A second, weaker α-peak around 6.52 MeV can be assigned to ^{238}Cm. A few events were observed in the region between 6.30 and 6.50 MeV, interesting for ^{239}Cm. However, tailing of ^{238}Cm into this region cannot be excluded. The time distribution of these events provides no additional information as ^{238}Cm and ^{239}Cm have very similar half-lives.

To be more sensitive in the interesting energy range, we lowered the beam energy to 70 MeV. In agreement with HIVAP calculations, which predict the 6n cross section to decrease by three orders of magnitude from 74 to 70 MeV - the 5n cross section should only be lowered by a factor of two or less -, no ^{238}Cm was observed anymore; see Fig. 1(b). Due to a smaller beam integral, the ^{240}Cm peak, which dominates the spectrum with energies of 6.29 and 6.25 MeV, is less intense in Fig. 1(b) as in Fig. 1(a).

No α events with energies between 6.30 and 6.50 MeV, which could be assigned to ^{239}Cm, were observed in this experiment at 70 MeV. From this we conclude that the corresponding α-events observed at 74 MeV ^{12}C energy were tails of the ^{238}Cm peak caused by self-absorption effects of the α source prepared by evaporation.

Cross sections were calculated from measured α activities, the ^{232}Th target thickness, beam integrals, and assuming that 100% of the Cm recoiled out of the target and was caught in the Cu catcher foil. As the measured cross section ratio of σ_{4n}:σ_{6n} at 74 MeV is consistent with HIVAP results (σ_{4n}:σ_{6n}=1:16) within a factor of 2 we trust the HIVAP σ_{4n}:σ_{5n}=1:1 ratio. From this, the total number of ^{240}Cm α-events and the non-observation of ^{239}Cm (taking 3 events for a 95% confidence limit) we calculated an upper limit of 3×10^{-5} for a ^{239}Cm α-branch.

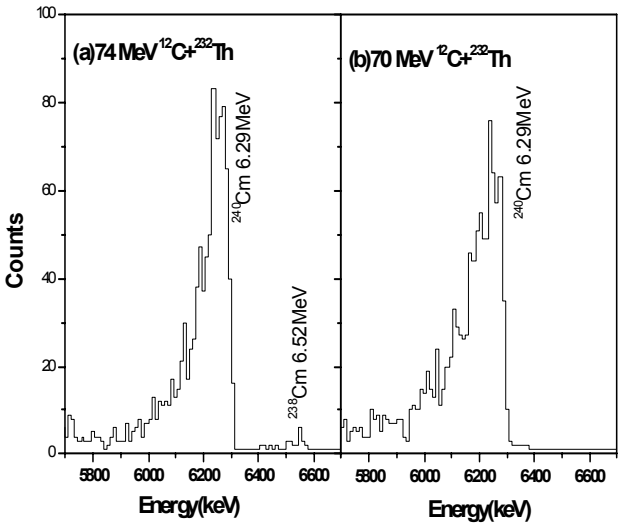


Figure 1: α-spectra of Cm fractions, for the first 10 h measuring time, from the reaction of (a) 74 MeV and (b) 70 MeV ^{12}C + ^{232}Th.

References

[1] Z. Qin et al, GSI Scientific Report 2004, p. 75
[2] Z. Qin et al., GSI Scientific Report 2004, p. 190, 191

Projectile Energy Control by Cusp–electrons

R. Mann[1], D. Ackermann[1,2], S. Antalic[3], F.P. Heßberger[1], S. Hofmann[1,4], B. Kindler[1], P. Kuusiniemi[1], B. Lommel[1], K. Nishio[1,5], S. Saro[3], H.G. Schött[1], B. Streicher[3], B. Sulignano[1,2]

[1]GSI Darmstadt, Germany, [2]Johannes Gutenberg-Universität, Mainz, Germany [3]Department of Nuclear Physics, Comenius University, Bratislava, Slovakia, [4]Johann Wolfgang Goethe-Universität, Frankfurt, Germany, [5]JAEA, Tokai, Japan

The cross-section for the synthesis of super heavy elements noticeably changes within a few percent of the nuclear excitation energy. Therefore, the knowledge of the projectile energy E_p is crucial. In order to have a control of E_p independent of the accelerator beam adjustment, we have developed a method based on measuring electrons moving along the projectile path with the projectile velocity v_p [1]. These electrons, denoted as cusp-electrons [2], result from distant collisions with target atoms either by exciting bound projectile electrons just to the continuum limit or by capturing target electrons just to the projectile continuum. Due to a small instrumental angular acceptance of only ±0.1° at zero degree in projectile direction, only electrons close to the projectile velocity are accepted resulting in a cusp shaped electron energy spectrum.

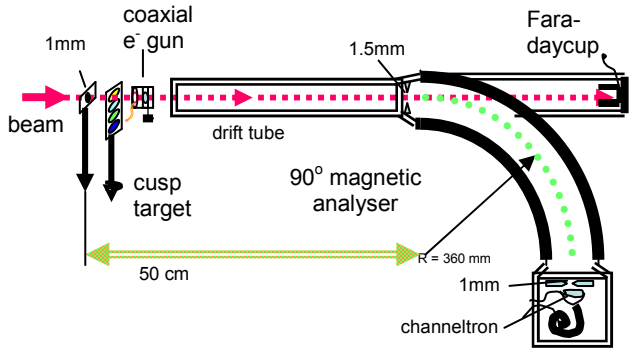


Figure 1: Set up for measuring cusp electrons.

The electrons are analyzed by a magnetic dipole momentum analyzer (Fig. 1). UNILAC beams (4.6 – 5.2 MeV/u $^{46}Ti^{12+}$, $^{51}V^{12+}$) penetrated a thin Au target. Behind a drift tube the electrons are analyzed by scanning the magnetic field and are detected by a channeltron multiplier. A small electron gun fixed in the beam line allows a quick calibration at any time and thereby a control of shifts of the analyzing system. Due to the high transparency of the gun, the fine collimated beam particles pass through with no intensity losses. For different projectile energies the cusp peaks clearly shift as seen in Fig. 2. These electron peak positions, of course, are independent from both, the projectile masse and ion charge state when the specific projectile energy (MeV/u) is fixed. Each measurement was cross checked by the gun measurement demonstrating a reproducibility within 10^{-3}. The overall agreement between accelerator energies and cusp measurements is $3x10^{-3}$, whereas variations within a series of repeated cusp measurements at a fixed accelerator energy are at a level of $\leq 10^{-3}$.

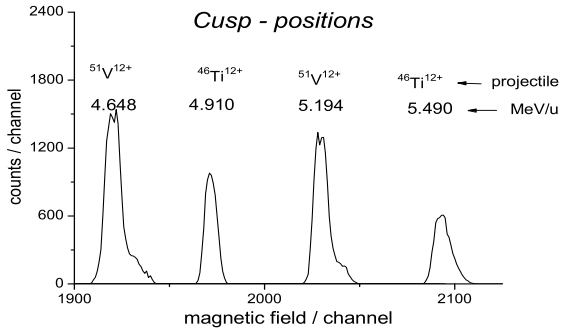


Figure 2: Cusp positions for different projectile energies. The magnetic field correspond to the electron velocity which equals the projectile velocity. The cusp target consisted of a 50 µg/cm² gold foil.

These values can be improved by a better analyser resolution. Uncertainties of cusp energies due to possible material dependent surface potentials [3] are minimized by using a target with high conductivity, e.g. gold. It was used for all measurements and compared with the electron gun calibration. A shift of cusp energy due to surface potentials depending on the beam current I_b was not observed when I_b was varied by a factor of 100. Hence, a detection of changes in beam energy with 10^{-3} accuracy is possible by this set up which can be applied for controlling accelerator adjustments.

In addition, projectile energy losses from different degrader foils (40 µg/cm² C, 97 µg/cm² C and 500+50 µg/cm² Pb+C) placed in front of the apparatus were determined for 4.91 MeV/u $^{46}Ti^{12+}$projectiles. The shifts of the cusp peaks were $\Delta E_p/E_p$ = 42% (0.41%), 1.03% (1%) and 1,64% (1,76%) in fair agreement with tabulated values (bracket values) from reference [4]. The positions of cusp peaks display shifts from energy losses. The shapes indicate broadening of the projectile energy also by straggling.

References

[1] R. Mann et al., *NIM* **B34** (1988) 403.
[2] F. Drepper and J.S. Briggs, *J.Phys.B* **9** (1976) 2063.
[3] G. Xiao et al., *NIM* **B115** (1996) 215.
[4] F. Huber et al., *Atom .Dat .and Nucl.Tabl.* **46** (1990) 1.

Giant quasi-atoms and superheavy nuclei obtained in collisions of transactinides

Valery Zagrebaev [1] and Walter Greiner [2]

[1] Flerov Laboratory of Nuclear Reactions, JINR, Dubna, Moscow Region, Russia

[2] Frankfurt Institute for Advanced Studies, J.W. Goethe-Universität, Frankfurt, Germany

For near-barrier collisions of heavy ions it is very important to perform a combined (unified) analysis of all strongly coupled channels: deep-inelastic scattering, quasi-fission, fusion and regular fission. A unified potential energy surface is derived determining the evolution of the nuclear system in all the channels and a unified set of dynamic Langevin type equations is proposed for the simultaneous description of deep-inelastic and fusion-fission processes. For the first time, the whole evolution of the heavy nuclear system can be traced starting from the approaching stage and ending in deep-inelastic, quasi-fission, and/or fusion-fission channels.

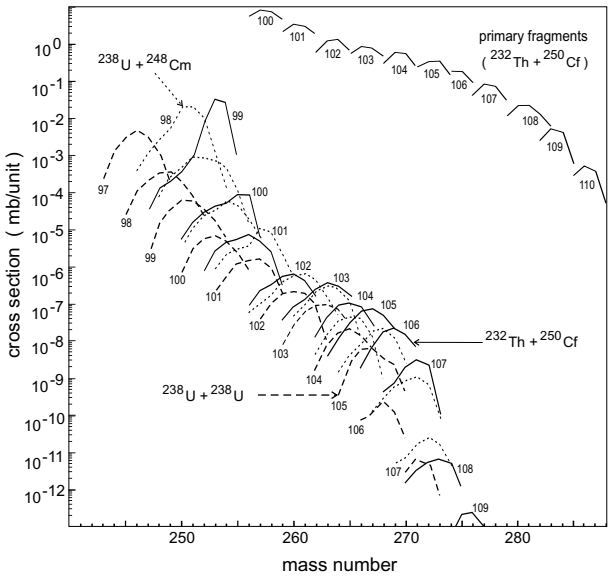


Figure 1: Yield of superheavy nuclei in collisions of ^{238}U+^{238}U (dashed), ^{238}U+^{248}Cm (dotted) and ^{232}Th+^{250}Cf (solid lines) at 800 MeV center-of-mass energy. Solid curves in upper part show isotopic distribution of primary fragments in the Th+Cf reaction. In the case of U+Cm the upper curve only is marked by Z-number (Z=98), the others are one by one up to Z=107.

Low energy collisions of very heavy nuclei (^{238}U+^{238}U, ^{232}Th+^{250}Cf and ^{238}U+^{248}Cm) have been studied within the proposed dynamical model. Large charge and mass transfer was found due to the "inverse" (anti-symmetrized) quasi-fission process caused by the Z=82 and N=126 nuclear shells. The production of survived long-lived neutron-rich superheavy nuclei in collisions of transuranium ions seems to be quite possible due to this quasi-fission process (see Fig. 1). Radiochemical identification of ^{267,268}Db and ^{271,272}Bh isotopes, produced in the Th+Cf or U+Cm reactions, could be performed, for example, to test this conclusion. If the found cross sections will be higher than several picobarns, then the subsequent experiments with such reactions could be planned aimed to the production of superheavy nuclei just in the region of the "island of stability".

Parallel search for spontaneous positron emission from a supercritical electric field of long-living giant quasi-atoms formed in these reactions is also quite promising. In many events lifetime of the composite system consisting of two touching nuclei turns out to be rather long (see reaction time distribution in Fig. 2); sufficient for spontaneous positron formation from super-strong electric field, a fundamental QED process.

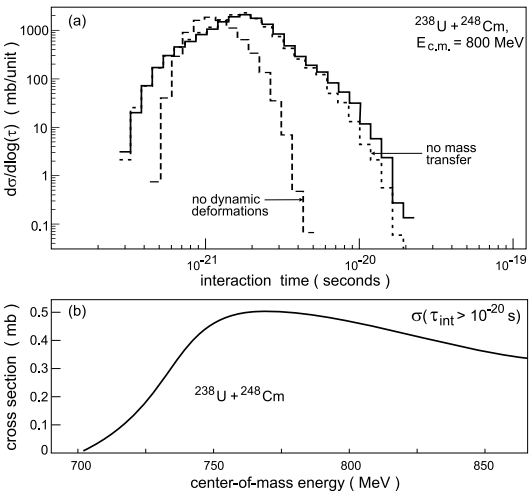


Figure 2: (a) Reaction time distribution for the ^{238}U+^{248}Cm collision at 800 MeV center-of-mass energy. Dashed and dotted histograms show the effect of switching-off dynamic deformations or mass transfer, respectively. (b) Cross section for events with interaction time longer than 10^{-20} s depending on beam energy.

Fully Relativistic *ab initio* Calculations of the Electronic Structures of the Superheavy Atoms

V. Pershina, GSI, Darmstadt, Germany
E. Eliav, U. Kaldor, Tel Aviv University, Israel

In order to obtain accurate results from quantum chemical calculations on systems containing heavy atoms, relativistic effects must be accounted for in a most straightforward way. This can be achieved via the four-component formulation applying original Dirac formalism with almost no approximations. Due to a considerable software development effort in recent years, two of those quantum chemical codes exist, one of them being a product of a European collaboration, called the DIRAC package [1]. In the present work we have performed calculations of ionization potentials (IP) and electron affinities (EA) of the heaviest atoms Rf through Ds using the DIRAC program. The EAs of all the elements and correlated IPs of Mt and Ds were calculated for the first time.

In the basis of the method lies the many-electron relativistic Dirac-Coulomb (DC) Hamiltonian

$$H_{DC} = \sum_i h_D + \sum_{i<j} 1/r_{ij} \,, \qquad (1)$$

where

$$h_D = c\vec{\alpha}\cdot\vec{p} + \beta c^2 + V_{nuc} \,. \qquad (2)$$

The four-component orbitals are spinors

$$\phi_{nk} = \begin{pmatrix} P_{nk}(r) \\ Q_{nk}(r) \end{pmatrix} , \qquad (3)$$

where $P_{nk}(r)$ and $Q_{nk}(r)$ are large and small component, respectively. The uncontracted Gaussian-type 33s29p20d16f9g universal basis set from [2] has been used for Rf through Ds. Though DIRAC has options to treat electron correlation at various levels of accuracy, MP2, CI (configuration interaction) and CC (coupled cluster), the calculations were performed for a small CI (treating open 7s, 6d and 7p shells as an active space) due to the limited capacity of a GSI 64-bit computer kindly offered to us by the theory department.* In addition, multireference CC, the most accurate scheme, is presently applicable only to elements with two or less valence electrons or holes beyond a closed shell, e.g., for elements 104, 111 and 112. Work on overcoming this limitation is presently in progress in TAU, Israel. The DC CI calculated IPs and EAs are given in Table 1 and Fig. 1 in comparison with IPs calculated using numerical multiconfiguration Dirac-Fock (MCDF) [3] and DCB Fock-space CC [4] methods for some elements.

*The author is thankful to the theory department (Prof. J. Knoll) and computing center for support. Calculations were also partially performed at computers of TAU, Israel.

Elements	IP			EA
	DC CI	MCDF [3]	CCSD [4]	DC CI
Rf	5.23	5.54	6.01	-0.10
Db	5.84	6.10	-	-0.15
Sg	6.49	7.03	-	-0.41
Bh	6.34	6.82	-	+0.17
Hs	6.35	6.69	-	-0.20
Mt	6.56	-	-	-0.23
Ds	6.68	-	-	-0.27

Our DC CI results for Rf through Hs are almost as accurate as MCDF obtained with a very large number of configurations and the trends in the row nicely agree.

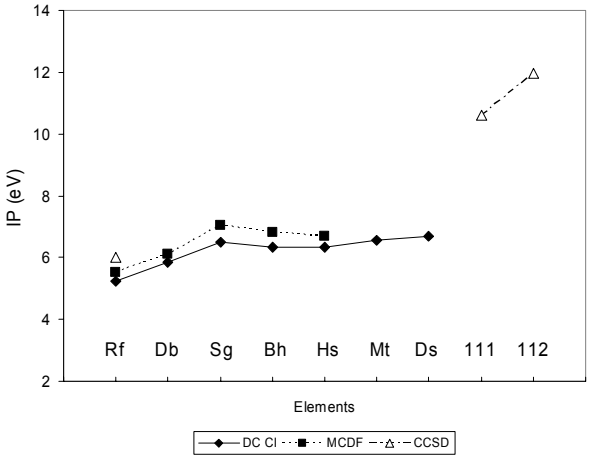


Figure 1: DC CI ionization potentials for elements Rf through 112 as compared to MCDF [3] and CCSD [4].

Thus, the results are very encouraging and we plan to perform large-scale CI calculations which will give even more accurate IPs and EAs (some might become positive), which will allow us to accurately determine some other important chemical properties of the heaviest elements like, e.g., chemical potentials. Further on, *ab initio* calculations for molecules of the heaviest elements using the DIRAC package are foreseen provided a 64-bit computer with the proper memory is at our disposal.

References

[1] DIRAC 04, written by H.J. Ja. Jensen, *et al*. (2004).
[2] G.L. Malli, *et al*., Phys. Rev. A **47** (1993).
[3] E. Johnson, *et al*. J. Chem. Phys. **93**, 8041 (1990); B. Fricke, *et al*. Radiochim. Acta, **62**, 17 (1993); E. Johnson *et al*. J. Phys. Chem. A **42**, 8458 (1999).
[4] U. Kaldor and E. Eliav, Adv. Quant. Chem. **31**, 313 (1998).

Adsorption of Element 112 on a Au (100) surface

C. Sarpe-Tudoran[1], V. Pershina[2], B. Fricke[1], J. Anton[1]
[1]Universität Kassel, D-34109 Kassel, [2]Gesellschaft für Schwerionenforschung, D-64291 Darmstadt

Element 112 is located in the Periodic system at the end of the 6d-series having a closed 6d and 7s shell [1]. This structure probably leads to a chemical behaviour which is expected to be somewhere between that of its homologue Hg and that of the noble gas Rn [2]. A summary of the state of the art of superhavy elements is given in Ref. [3].

In order to learn about the chemistry of this element already a number of years ago the experimental chemical groups which collaborate to detect the chemical behaviour of the superheavy elements have proposed to measure the position of the adsorption of element 112 in a thermochromatographic column.

In order to give a quantitative prediction for the adsorption energy of this element 112 on a gold (100) surface we have tried to finish our calculations and to present a final value. Due to the fact that there is no full relativistic solid state program available which is able to calculate this value we expanded our relativistic molecular density-functional code to tackle this problem [4].

Two methods are possible: The first is the calculation of larger and larger cluster which simulate the surface and then perform a calculation where the adatom is included on the surface. The difference of these total energies is by definition the adsorption energy. In order to accelerate the convergence with the cluster size, the above method is modified by adding many atoms around the inner cluster, which contribute only with their static potentials. This second method is the so called embedded cluster method.

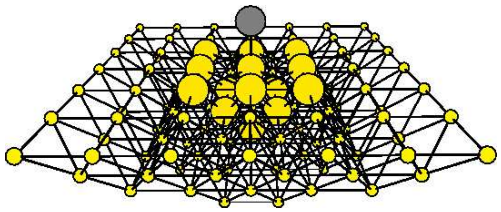


Figure 1: Structure of the atoms in the embedded cluster calculation for the case $Au_{14}(9, 4, 1)$.

A first prediction of the method 1 using the results for smaller clusters has been presented in a recent publication [5].

The main problem with both methods is the fact that the final result still was dependent on the cluster size and no convergence with the number of atoms in the cluster had been reached. The achievement of the last year is the fact that the difference of the adsorption energies of the two considered adsorbates became constant relative to the cluster size.

The results of our calculations are shown in Table1 for the three possible adsorption sites on a Au (100) surface:

Table 1: Adsorption energy of Hg and Element 112 on a (100) gold surface, for different adsorption sites.

top		bridge		hollow	
System	En. [eV]	System	En. [eV]	System	En. [eV]
$Au_{14}Hg$	1.64	$Au_{14}Hg$	1.68	$Au_{21}Hg$	0.86
$Au_{14}112$	1.47	$Au_{14}112$	1.18	$Au_{21}112$	0.82
$Au_{34}Hg$	1.02	$Au_{20}Hg$	1.31	$Au_{29}Hg$	0.84
$Au_{34}112$	0.65	$Au_{20}112$	0.96	$Au_{29}112$	0.74
		$Au_{36}Hg$	1.52		
		$Au_{36}112$	1.16		

top, bridge and hollow. The absolute values of the adsorption energies in eV of the elements Hg and 112 calculated in the GGA approximation (with B88 functional for exchange and P86 for correlation) are given.

First consequence of these calculations can be drawn from the absolute values of the adsorption energies. According to these data the "bridge" adsorption site is the preferred one. That is the reason why we have expanded our calculations to the very large Au_{36} cluster. The difference between the binding energies of Hg and Element 112 is the same for the clusters with 20 and 36 atoms, namely $\simeq 0.35$ eV. This number together with the experimental adsorption energy of Hg on Au surface (0.92 eV, reference [6]) allows us to estimate the adsorption energy of Element 112 on such a surface, namely 0.58 eV.

References

[1] B. Fricke, *Structure and Bonding* **21**, 89 (1975)

[2] R. Eichler, M. Schädel, *GSI Scientific Report*, (2001), p. 185

[3] Schädel, Matthias (Ed.), *The Chemistry of Superheavy Elements* (Ed.), Kluwer Academic Publisher, (2003)

[4] T. Jacob, J. Anton, C. Sarpe–Tudoran, et. al. *Surf. Sci.*, **536**, 45–54 (2003)

[5] V. Pershina, T. Bastug, C. Sarpe–Tudoran et al., *Nucl. Phys. A*, **734**, 200 (2004)

[6] J.-P. Niklaus, R. Eichler, S. Soverna, H. W. Gäggeler, *PSI Annual Report*, 8 (2000)

Theoretical Predictions of Complex Formation of Group-4 Elements Zr, Hf, and Rf in H_2SO_4 Solutions

V. Pershina, GSI, Darmstadt, Germany
D. Polakova, J. P. Omtvedt, Oslo University, Norway

Complex formation of Zr, Hf, and Rf in HF and HCl solutions has been studied both experimentally and theoretically [1,2]. Trends in K_d (distribution coefficient) values evidencing the strengths of formed complexes were shown to be influenced by such factors as pH of solution and acid concentration. Presently, experiments are under way to investigate complex formation of these elements in H_2SO_4 solutions using the SISAK technique [3]. To predict the outcome of these experiments, the present theoretical study has been undertaken. Accordingly, calculations of the free energy change, ΔG^r, of the following complex formation reactions were performed:

$$M(H_2O)_8^{4+} + nHSO_4^- \Leftrightarrow M(SO_4)_n^{4-2n},aq + nH^+ \quad (1)$$

$$MOH(H_2O)_7^{3+} + nHSO_4^- \Leftrightarrow M(SO_4)_n^{4-2n},aq + (n-1)H^+ \quad (2)$$

Electronic structures of the following complexes formed at various H_2SO_4 concentrations were calculated using the fully relativistic (4-component) density functional theory method (4c-DFT) [4]: $M(SO_4)(H_2O)_6^{2+}$, $M(SO_4)_2(H_2O)_4$, $M(SO_4)_3(H_2O)_2^{2-}$, where M = Zr, Hf, and Rf. Electronic structures of hydrated and hydrolyzed complexes of these elements were calculated earlier [5].

ΔG^rs were calculated via the model described in [5] as a sum of the ionic, ΔE^C, and covalent, ΔE^{OP}, constituents. Both ΔE^C and ΔE^{OP} were determined via Mulliken analysis implemented in the DFT method. Geometrical configurations of the complexes were chosen on the basis of an analysis of solid-state structure data of Zr sulphuric complexes. Bond lengths in the Hf and Rf complexes were estimated using optimized bond lengths in simpler gas-phase compounds and in accordance with ionic radii. The calculated ΔG^r for reactions of types (1) and (2) are summarized in Tables 1 and 2.

Table 1. Coulomb parts of the free energy change, ΔE^C (in eV), for reactions of type (1)

Complex	Zr	Hf	Rf
$M(SO_4)(H_2O)_6^{2+}$	-35.72	-35.84	-33.60
$M(SO_4)_2(H_2O)_4$	-42.43	-42.43	-39.37
$M(SO_4)_3(H_2O)_2^{2-}$	-45.14	-45.02	-41.38

Thus, trends in the formation of the three types of complexes via reactions of type (1) are Hf > Zr >> Rf, Zr = Hf >> Rf and Zr > Hf >> Rf, respectively. For reactions of type (2), trends are Hf > Zr >> Rf, Hf > Zr >> Rf, and Zr > Hf >> Rf for the three types of complexes, respectively. The same trends should be observed for the K_d values, since $K_d \cong f(\beta_i)$, and $\log\beta_i = -\Delta G^r/2.3RT$. The predicted K_d for Hf and Rf with respect to the measured K_d for Zr [6] in anion-exchange separations are shown in Fig. 1.

Table 2. Coulomb parts of the free energy change, ΔE^C (in eV), for reactions of type (2)

Complex	Zr	Hf	Rf
$M(SO_4)(H_2O)_6^{2+}$	-31.03	-31.23	-29.49
$M(SO_4)_2(H_2O)_4$	-37.74	-37.82	-35.26
$M(SO_4)_3(H_2O)_2^{2-}$	-40.45	-40.41	-37.27

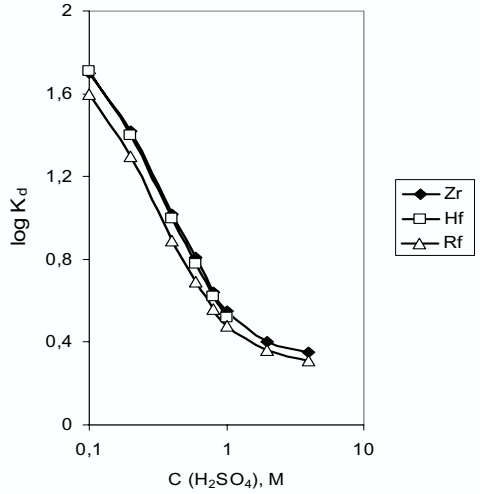


Figure 1: Predicted K_d values for Hf and Rf with respect to K_ds of Zr [6] in anion-exchange separations

Thus, trends in K_d of Zr and Hf are dependent on the pH of solution. With increasing H_2SO_4 concentration it should be Zr > Hf in agreement with experiments [6]. Complexes of Rf should be weaker than those of Zr and Hf at all pH, so that $K_d(Zr) > K_d(Hf) >> K_d(Rf)$ at the whole range of acid concentrations. The recent SISAK experiment on Rf confirmed this trend.

References

[1] J.V. Kratz in: "The Chemistry of Superheavy Elements", ed. M. Schädel, Kluwer, (2003), p. 159.
[2] V. Pershina, *ibid*, p. 31.
[3] J. P. Omtvedt, *et al*. J. Nucl. Radiochem. Sci. **3**, No. 1, (2002).
[4] T. Bastug, *et al*. Phys. B **28**, 2325 (1995).
[5] V. Pershina *et al*. Radiochim. Acta **90**, 869 (2002).
[6] R. Caletka, *et al*. J. Rad. Nucl. Chem. **142**,383 (1990).

Gas Chemical Investigation of Hexafluoroacetylacetonates of Zr and Hf with Preseparated Isotopes

Ch.E. Düllmann[*,#,†,‡], K.E. Gregorich[#], I. Dragojević[#,†], R. Eichler[§,¶], C.M. Folden III[†,#], M.A. Garcia[#,†], J.M. Gates[#,†], D.C. Hoffman[#,†], S.L. Nelson[#,†], H. Nitsche[#,†], G.K. Pang[#,†,‖], R. Sudowe[#]

[*]GSI, Darmstadt, Germany; [#]LBNL, Berkeley, CA, USA; [†]Univ. California, Berkeley, CA, USA; [§]PSI, Villigen, Switzerland; [¶]Univ. Bern, Switzerland; [‖]presently at: MSU, East Lansing, MI, USA.

Gas chemical methods have proven powerful for the investigation of the transactinide elements (TAN, Z≥104) which are produced in heavy-ion-induced fusion reactions. However, many chemical systems have not been accessible so far due to the plasma caused by the intense heavy-ion beam. Volatile metal complexes containing organic ligands, for example, would be immediately destroyed by this plasma. Recently, preseparation has been used as a new technique to overcome many of the current limitations in TAN chemistry [1,2]. In this technique, nuclear reaction products are separated from the heavy-ion beam and unwanted reaction products in a physical separator, extracted from this separator through a thin window and thermalized in a gas-filled Recoil Transfer Chamber (RTC) [3].

In first experiments conducted at the Lawrence Berkeley National Laboratory (LBNL) aiming at the chemical investigation of rutherfordium (Rf, Z=104), volatile metal complexes of its lighter homologs hafnium (Hf) and zirconium (Zr) with hexafluoroacetylacetone (hfa) were studied and some preliminary results are reported here.

Sort-lived ($T_{½}$ between 30 s and 8 min) Zr and Hf sotopes were produced at the LBNL 88-Inch Cyclotron. The nuclear reaction products were preseparated in the Berkeley Gas-filled Separator (BGS) [4] and thermalized in the RTC, which was flushed with hfa-vapor-containing helium and kept at a pressure of ~1 bar. The reaction products were transported with the gas flow to an oven installed directly at the exit of the RTC. There, formation of volatile complexes of the type $M(hfa)_4$ (M=Zr, Hf) occurred. Single molecules of these complexes are volatile at room temperature and were transported with the gas flow to activated charcoal catchers through a ~5-m long Teflon capillary. The absolute overall yield of this process was measured for ^{162,165,169}Hf. From these data, the overall "reaction plus transport" time was determined. Two settings were investigated: (i) relatively low hfa concentration and a gas-flow rate of 1.3 l/min, and (ii) relatively high hfa concentration and a gas-flow rate of 2.1 l/min. Preliminary results are shown in Fig. 1 for temperatures up to 400°C. At higher temperatures, decomposition of $hfa/M(hfa)_4$ was observed. As can be seen in Fig. 1, the minimum overall time with the current setup under the optimized current conditions is about 40 s.

In isothermal chromatography experiments, the whole 5-m long Teflon capillary was used as chromatography column. The relative yield of ^{162}Hf was measured at different isothermal temperatures. The obtained breakthrough curve is shown in Fig. 2. The experiments were modelled using a Monte Carlo Simulation (MCS) [5]. An adsorption enthalpy of $Hf(hfa)_4$ on Teflon of $-\Delta H_{ads} = (57\pm3)$ kJ/mol was evaluated.

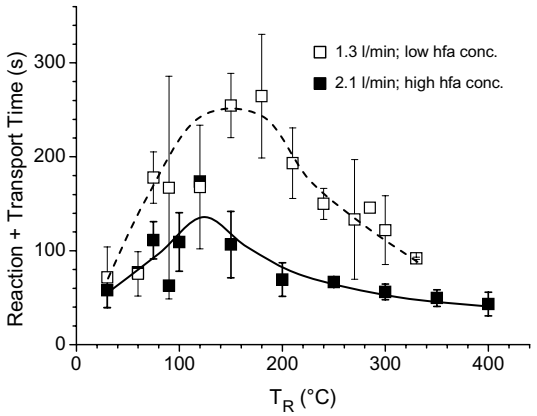


Figure 1: Total time *vs*. reaction temperature T_R for $Hf(hfa)_4$. The lines are shown to guide the eye.

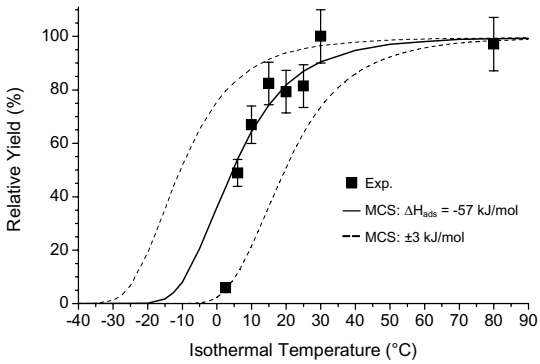


Figure 2: Isothermal chromatogram for $^{162}Hf(hfa)_4$.

References

[1] J.P. Omtvedt *et al*., J. Nucl. Radiochem. Sci. **3** (2002) 121.
[2] Ch.E. Düllmann *et al*., Nucl. Instrum. Meth. **A551** (2005) 528.
[3] U.W. Kirbach *et al*., Nucl. Instrum. Meth. **A484** (2002) 587.
[4] V. Ninov *et al.*, AIP Conf. Proc. **455** (1998) 704.
[5] I. Zvara, Radiochim. Acta **38** (1985) 95.

[‡]C.E.Duellmann@gsi.de

Pb/Hg Separation on the Surface of Au, Pd and Pt

A.Yakushev, J. Dvorak, Z. Novackova, A. Türler, B. Wierczinski, TUM, München, Germany
W. Brüchle, E. Jäger, M. Schädel, E. Schimpf, GSI, Darmstadt, Germany

Introduction

For experiments with E114 we are developing a method based on the chemical adsorption of E114 on a suitable metal surface followed by the desorption and detection of its α-decay daughter E112 [1]. To evolve this approach we performed test experiments on the gas chromatography of Pb and Hg to choose suitable materials for chemical filters and to select the best temperature regime. Results from estimates using semi-empirical models for metal-metal interactions between transactinides and transition metals indicate that noble metals are a good choice for the separation of E114 from E112 [2].

Experimental and results

Short lived isotopes of Pb ($^{184-189}$Pb) were produced at the UNILAC accelerator using ^{40}Ar beam and a ^{152}Gd target. A newly built, heated recoil chamber was employed and the dependence of the Hg yield from the recoil chamber temperature and the carrier gas composition was determined. In Fig. 1 the chemical yield of Hg as a daughter product after alpha-decay of Pb is shown. Hg is a very volatile metal and behaves like an inert gas – i.e. it does not adsorb on inert (oxidized) surfaces, even at room temperature. The upper line shows that some losses of Hg occur due to the adsorption of Pb on the stainless steel (SS) walls of the recoil chamber. At higher temperatures the yield of short-lived Hg isotopes from the recoil chamber increases due to desorption of Pb from the walls and diffusion of implanted daughter atoms back into the gas phase.

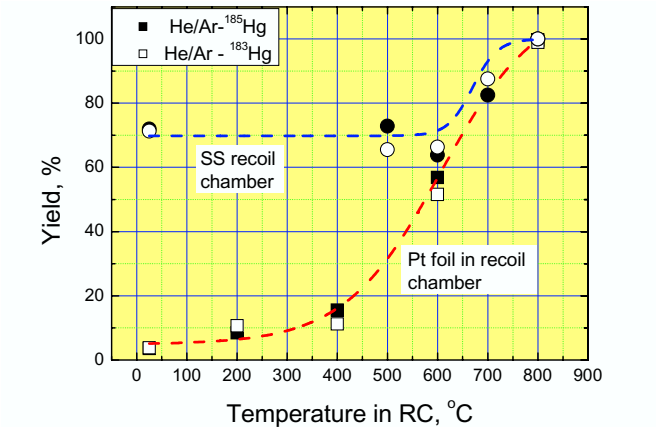


Fig. 1. Yields of ^{183,185}Hg (α-decay products of ^{187,189}Pb) as a function of the temperature and the exposed surface in the recoil chamber (stainless steel and Pt).

If Pt foil is inserted into the recoil chamber, Hg atoms are chemically adsorbed to the Pt surface at lower temperatures. A desorption of Hg takes place at temperatures well above 500°C.

Next the adsorption/desorption behavior of Pb and Hg nuclides was studied. The recoil chamber (stainless steel surface) was heated to 800°C. The flushed out short-lived Pb and its Hg daughter nuclei were adsorbed on the surface of metallic chromatographic columns, made from Pt, Pd, or Au. Desorption of Pb from the noble metal surface was negligible for temperatures up to 900°C. Desorption of Hg from Pt, Pd and Au surface was studied in the temperature region from room temperature up to 800°C. A typical chromatography curve is shown in Fig. 2. From these curves the enthalpy of adsorption of single Hg atoms on the column surface was evaluated using Monte-Carlo simulations, see Table 1.

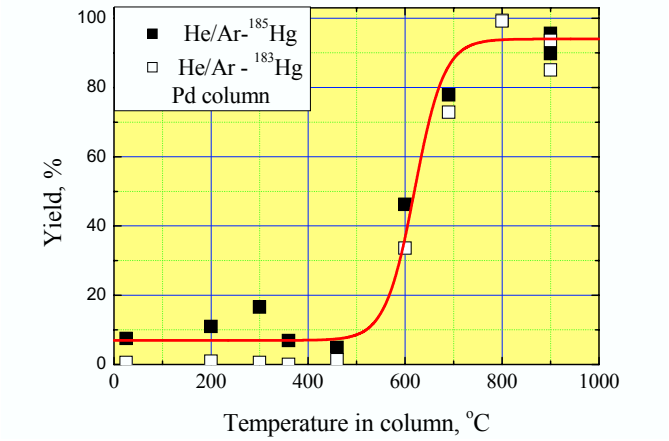


Fig.2. Desorption of Hg isotopes from Pd surface.

Table 1. Adsorption enthalpy of Hg on the surface of Pt, Pd and Au.

Adsorbent	$T_{50\%}$, °C	ΔH_{ads}, kJ/mol
Platinum	480	–112 ± 14
Palladium	620	– 128 ± 12
Gold	630	– 130 ± 12

References

[1] A. Yakushev et al., GSI Scientific Report 2003, p. 193.
[2] B. Eichler. Metallochemie der Transaktinoide. PSI-Bericht 00-09, PSI Villigen (2000).

Electrochemical Deposition of Short-lived Pb Isotopes on a Pd Coated Ni Tape

H. Hummrich, N.L. Banik, M. Breckheimer, R. Buda, J.V. Kratz, D. Liebe, L. Niewisch, N. Wiehl
Institut für Kernchemie, Johannes Gutenberg-Universität Mainz, Germany
W. Brüchle, E. Jäger, M. Schädel, B. Schausten, E. Schimpf, GSI, Darmstadt

The coupling of the ALOHA system to an electrolytic cell was successfully used to transfer Pb recoil nuclei from a ^{219}Rn emanation source into the liquid phase with subsequent electrodeposition on Pd electrodes [1].

So far, the transport of the electrodes from the electrolytic cell to the α-detector was performed manually. However, in an experiment with superheavy elements, an automated transport is necessary, preferably by using a metal tape as the electrode. For the deposition of Pb as the homolog of element 114, the electrode material of choice is Pd [1], but the production of several meters of Pd tape is too expensive. As a cheap and withstanding material, Ni tape is available, but the deposition of Pb on Ni was found to be slow and reversible. To combine the advantages of both materials, Pd was deposited onto a Ni tape (2 cm x 500 cm x 100 µm), which was wound onto a PE holder to ensure complete contact with the solution. The deposition was carried out in 1.5 L of 0.1 M HCl containing 50 mg/L Pd at -1000 mV vs. Ag/AgCl for 15 min. As counter electrode, a Pt gauze was used.

An electrolytic cell for electrodeposition experiments with tape shaped electrodes was constructed. The metal tape was sealed with two FEP coated o-rings to prevent the liquid from entering the detector system and to ensure a low frictional resistance for a smooth tape transport. A high volume magnetic stir bar was used for agitating the electrolyte. The α-detector system consisted of three PIN diodes, with (1 x 2) cm active surface, each. The detectors were mounted at 5 cm distance in an Al-case and were kept under He (see Fig.1).

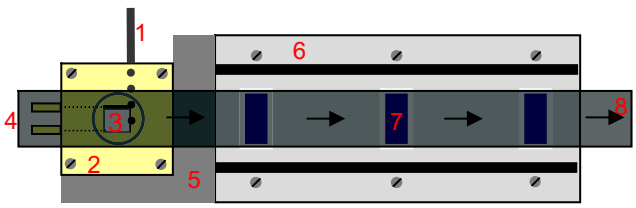


Fig. 1: Schematic of the electrolytic cell with the α-detection system for electrodeposition and detection of accelerator produced short lived isotopes. 1 Ag/AgCl reference electrode, 2 electrolytic call with o-rings, 3 high volume magnetic stir bar, 4 electrolyte in- and outlet, 5 spacer, 6 Al-case for detector system, 7 (1 x 2) cm PIN diodes, 8 Pd coated Ni-tape, arrows: stepping direction

The α emitting ^{188}Pb ($t_{1/2}$ = 25.5 s) was produced in the reaction ^{152}Gd (^{40}Ar, 4n). A ^{152}Gd (30% enrichment) target with a thickness of 300 µg/cm² on 15 µm Be backing was used. The recoil nuclei were swept out of the recoil chamber by a He/KCl cluster gas-jet at a flow rate of 1.5 L/min and transported through a PE capillary to the ALOHA device. To determine the overall deposition yield for ^{188}Pb, the activity was impacted for 3 min on a Kel-F disc. At this collection time, the activity of ^{188}Pb was nearly in radioactive equilibrium.

After impaction, the disc was switched to the dissolution position and the activity was transferred to the electrolytic cell by continuous cyclic pumping of the electrolyte (0.1 M HCl, T = 65°C).

The rest potential of the Ni(Pd) tape was -250 mV vs. Ag/AgCl. At this potential, Pb deposits spontaneously, so no external potential had to be applied.

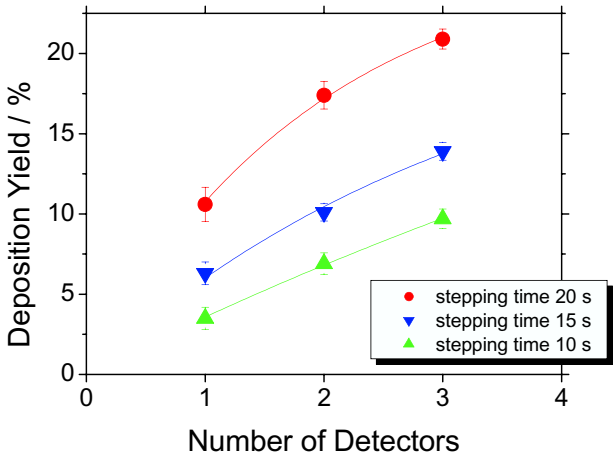


Fig. 2: Deposition yield vs. the number of detectors for various stepping times of the Pd coated Ni tape

The tape was stepped in intervals of 10, 15, and 20 s for several minutes. The deposition yield was calculated by comparing the count rates for each detector with a direct catch on a 0.1 µm nucleopore filter. A maximum deposition yield of 21 % was achieved for a stepping time of 20 s (see Fig. 2).

In this set-up, only three detectors were used. Especially for fast stepping times a big amount of activity was stepped out of the detection system. In a superheavy element experiment, up to 20 α detectors will be available. The yield may be increased significantly by using a pump system with a lower dead volume (now 250 µl) and a higher electrode surface. The latter can be achieved by using two tapes.

After improving the overall yield, the proposed set-up may be successfully used in aqueous chemistry with element 114. Experiments with homologs suggest, that also the electrochemical deposition of element 108 - 111, 113, 115, and 116 should be possible.

References

[1] Hummrich et al., *GSI Scientific Report 2004*, p. 189

Simulation of Elution Curves for Chromatography Columns with a Low Number of Theoretical Plates

W. Brüchle, GSI, Darmstadt, Germany

Chromatographic techniques are among the most effective chemical methods to separate and characterize closely related chemical substances or ions. More than half a century ago the main theoretical fundaments for these methods were developed; even a Nobel Price was awarded to Martin and Synge [1] for their theoretical and practical methodic developments. There is a lot of pioneering theoretical descriptions of peak position and peak width, often based on the molecular dynamic theory of chromatography, originally developed by Giddings and Eyring [2]. The model represents the progress of a single molecule through the column as a chain of elementary adsorption- desorption stochastic processes. The majority of these papers have started with partial differential equations leading to Bessel functions. The asymptotic expansion of the Bessel functions weighed by the probability of the initial state of the molecule should yield the distribution curve for the elution. Rather complicated calculations using the characteristic function method are described in [3]. An easier way to describe the chromatographic process is the "theoretical plate" concept. It is the imaginary section of a column in which a complete equilibrium step takes place. The model was successfully used in [1] for liquid-solid chromatography. In most cases textbooks dealing with chromatography will present the following formula without derivation:

$$K_d = (T_r - T_0)*F/m = (V - V_0)/m \qquad (1)$$

with T_r = retention time
T_0 = column hold-up time due to the free column volume
F = flow rate of the mobile phase [mL/min]
m = mass of the stationary phase (ion exchanger, reversed phase material) [g]
K_d= partition coefficient (distribution coefficient)
V_p = volume eluted until the peak maximum [mL]
V_0 = free column volume (dead volume) [mL]

During series of fast automated separations on rather small chromatographic columns (1.6 mm i.d., 8 mm long, and 1mm i.d., 3.5 mm long) with the ARCA and the AIDA systems [4,5] it was noticed that the peak shapes differed from a Gaussian; in addition it was often not possible to measure complete elution curves, but only two fractions. Still the distribution coefficient K_d should be determined. In [5] the Glueckauf equation of chromatography was used [6]:

$$A(V) = A_{max}\, exp(-N\,(V_P - V)^2 / 2V_P V) \qquad (2)$$

where N is the number of theoretical plates.
In a new stepwise simulation some discrepancies occurring in some pioneering publications could be removed. Some authors stated, that a dead volume of a chromatographic column is only the result of the discontinuous treatment, and with a K_d=0 the elution would start immediately without delay [6]. This problem could be solved by starting the simulation with the last theoretical plate, and going upwards with the calculation. The activity transported from plate number i to the next plate i+1 is given by:

$$\Delta a = a(i)(1 - K_d/(K_d + r_v)) \qquad (3)$$

In this formula, r_v is the ratio of the free column volume to the mass of the exchanger material v_l/m. The results of the simulation shows an obvious similarity of the elution curves with the Poisson-curves from [7]. A numerical comparison shows that the elution curves can very well be described by:

$$A(V - V_0) = A_{max} * \mu^{(N-1)}/(N-1)! * exp(-\mu) \qquad (4)$$

with $\mu = (V - V_0)*N/(m*K_d)$

One can determine the K_d- value from the peak of the Poisson curve using:

$$K_d = (V - V_0)*N/(N-1)/m \qquad (5)$$

The difference to the classical formula is the factor N/(N-1), that can be neglected for longer columns. The Glueckauf equation gives reasonable fits when a shift by V_0 is added.

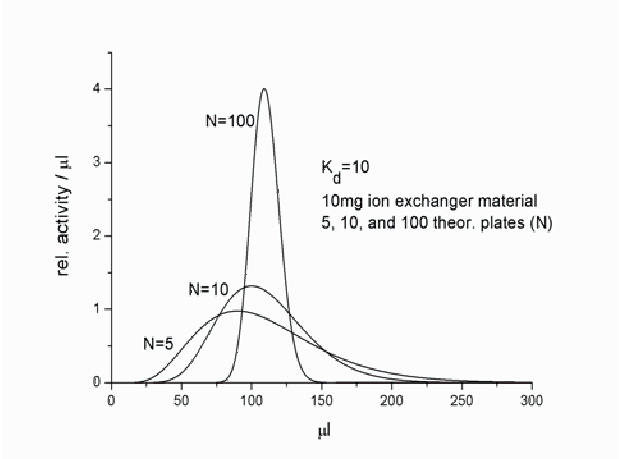


Figure 1: Simulation for different number of plates

References

[1] A.J.P. Martin, R.L.M. Synge, Biochem J. **35**, 1358-1368 (1941)
[2] J.C. Giddings, H. Eyring, J. Phys. Chem. **59**, 416-421 (1955)
[3] A. Cavazzini, M. Remelli, F. Dondi, J. Micro Sep. **9**, 295-302 (1997)
[4] M. Schädel, Radiochim. Acta ***89,*** 721-728 (2001) and references therein
[5] H. Haba *et al*., J. Am. Chem. Soc **126** (16) 5219-5224 (2004)
[6] E. Glueckauf, Trans. Faraday **51**, 34-44 (1955)
[7] W. Brüchle, Radiochim. Acta **91**, 71-80 (2003)

Molecular plating of uranium on thin aluminum backings*

D. Liebe, K. Eberhardt, J.V. Kratz, P .Thörle, Institut für Kernchemie,
Johannes-Gutenberg-Universität Mainz (UMZ), Germany
W. Hartmann, A. Hübner, B. Lommel, B. Kindler, J. Steiner, GSI, Darmstadt, Germany

Molecular plating is widely used for the deposition of lanthanide and actinide compounds on thin metallic backing foils [1]. At GSI and UMZ, this method has been previously applied on Ti or Be foils. Within the requirements of the TASCA-Project (**T**rans**A**ctinide **S**eparator and **C**hemistry **A**pparatus) very thin foils of Al (2-10µm) as backing material have been proposed [2].

The general usability of very thin Al was investigated by a test series with Gd and U. For these tests, plating conditions were adopted unchanged from previous practices [3]. Although Al foils of less than 10µm in thickness are difficult to manage, they show no significant disadvantages compared to Ti or Be with molecular plating.

2-Propanol (isopropanol) as organic solvent has previously been used for the preparation of actinide targets on Ti and Be backings. But on Al, the stability of the U layer is not acceptable. The surface of most of the targets looked scaly or cracked associated with irreproducible plating yields. In order to solve these problems, an alternative solvent, 2-Methyl-1-Propanol (isobutanol) was tested. Table 1 compares the plating condition of the previously used isopropanol and the newly tested conditions applying isobutanol.

Table 1: Plating conditions for isopropanol and isobutanol (U on Al-Backing)

Solvent	Voltage [V]	Current [mA]	Plating time [h]	Thickn. [µg/cm²]
Iso-propanol	100-1200 stepwise	0.5 -3.0	1	390#
Iso-butanol	150 V	0.01-0.5	4 - 5	650##

The hygroscopic character of isopropanol might have been the reason for the poor surface quality since the plating solution as always been exposed to air for a couple of hours prior to the plating. The content of water may cause the relative high current and, thus, it possibly effects the formation of obstructing hydroxides at the surface of the backing foil. Isobutanol, which is also used by the target laboratory of the Lawrence Berkeley National Laboratory, LBNL, is less polar and therefore poorly water-soluble [4]. During numerous experiments, the plating conditions were adjusted to a lower voltage resulting in a longer plating time as shown in Table 1. With isobutanol, the coating looks more homogenous without visible cracks. That has been approved with 25µm as well as 10µm Al backings. Fig 1 shows a light optical micrograph of an U-target, as usually prepared for the existing rotating actinide target wheel assembly at GSI.

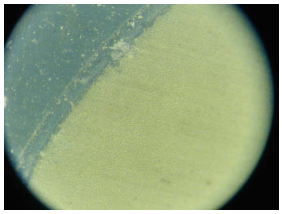


Fig 1: Uranium on Al Backing (25µm), plated from isobutanol within 3 h, Voltage 150 V

Furthermore, for U, a time dependence of the depositions yield has been determined. So far, a maximum yield at about 60 - 65 % is reached at a plating time of 5 h, as shown in Fig 2. In future investigations, the work will also focus on an increase of deposition yield to 75 % or more as achieved with isopropanol.

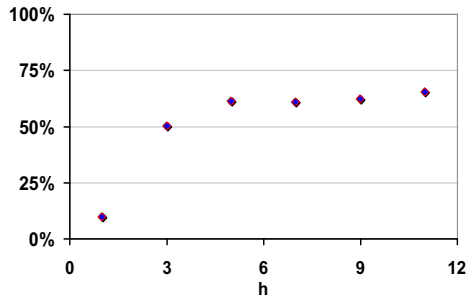


Fig 2: Time dependence of deposition yield at molecular plating of U on 25µm Al backing (from isobutanol with 150 V)

Next we plan to apply these conditions to other elements, especially various lanthanides. Also, the use of autoradiography [5] and REM/EDX will be further investigated to monitor target thickness, homogeneity and surface layer composition, respectively.

References

[1] W. Parker, R.Falk, Nucl. Instr and Meth 16 (1962), 355
[2] M. Schädel et al., contribution to this report
[3] D.Liebe, P. Thörle, J.V. Kratz "Further investigations on target preparation for heavy element studies",Annual report 2004, Institut f. Kernchemie, Universität Mainz, 2005
[4] P.M. Zielinsky, K. E. Gregorich, R. Sudowe, private communication at LBNL, Berkeley, March 2005
[5] K. Eberhardt et al., contribution to this report

* F+E Vertrag Mz/JVK Entwicklung und Herstellung von Transuran- u. sonstigen radioaktiven Targets
# corresponds to 74% at an intake of 500µg U /cm²
corresponds to 65% at an intake of 1000µg U/cm²

Radial flow in central Al+Al and Ni+Ni reactions at 2 AGeV*

M. Merschmeyer†, N. Herrmann, Physikalisches Institut, Universität Heidelberg,
Y.J. Kim, X. Lopez, GSI, Darmstadt, and the FOPI collaboration

The question whether a global freeze-out occurs in heavy-ion collisions below and up to energies of a few AGeV and to which extent this phenomenon is embedded into a collective radial expansion has been studied by various experiments [1, 2, 3]. Measurements performed at BEVALAC [1] indicate that the emission of light particles ($p, d, t, ^3He, \alpha$) around mid-rapidity in Au+Au collisions at 1 AGeV is well described by a thermal source of 81 MeV with a radial expansion velocity of $\beta_r = 0.32$. A similar investigation was done at SIS in the lighter Ni+Ni system at energies up to 2 AGeV [3]. The combined analysis of π^-, p, d yielded values of $T = 92$ MeV and $\beta_r = 0.32$ for the highest collision energy. A first attempt to incorporate strange particles into this framework was done in [2]. The study of Λ production in Ni+Cu reactions at 2 AGeV showed a temperature of $T = 51$ MeV and $\beta_r = 0.36$ in the mid-rapidity region. However, the statistics was limited and the phase space coverage rather small.

Recent advances in data processing now open up the possibility to collect statistics of several 100 million central (10-15%) heavy-ion collisions within a few weeks of beam time. FOPI was able to record about 110 million events of Ni+Ni collisions at 1.93 AGeV in 2003 and, recently, more than 300 million events of Al+Al reactions at 1.90 AGeV. By now huge data samples with 5-10·10^4 K^0_S or Λ (depending on the selection criteria) are available.

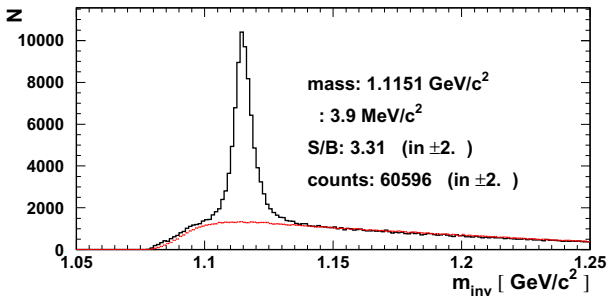


Figure 1: Invariant mass spectrum of $\pi^- p$ from Al+Al reactions. A subsample of the total statistics is shown.

All particles in this analysis are detected in the Central Driftchamber (CDC) of FOPI. Non-strange particles (π^-, p, d) are identified via their momenta and their differential energy losses. The neutral strange K^0_S and Λ, on the other hand, are reconstructed from their weak decays into charged decay products using the invariant mass method. An example of a $\pi^- p$ invariant mass spectrum for Al+Al collisions is given in figure 1.

For all particle species mentioned above, the transverse mass (m_T) spectra are generated as function of the longitudinal rapidity. The effective temperature T_{eff} at mid-rapidity is then extracted from an exponential fit to the $dN/(m_T^2 dm_T)$ spectrum. Figure 2 shows the mass dependence of the resulting T_{eff} for the Ni+Ni and Al+Al systems. Comparing the overall behaviour one finds that there scarcely is any radial flow in the lighter system since the effective temperatures are independent of the particle masses. Extrapolating to zero masses yields source temperatures of 100-110 MeV for both systems. Furthermore, the strange particles have systematically lower T_{eff} than the non-strange particles indicating that the concept of a common freeze-out in thermal equilibrium is too simplistic.

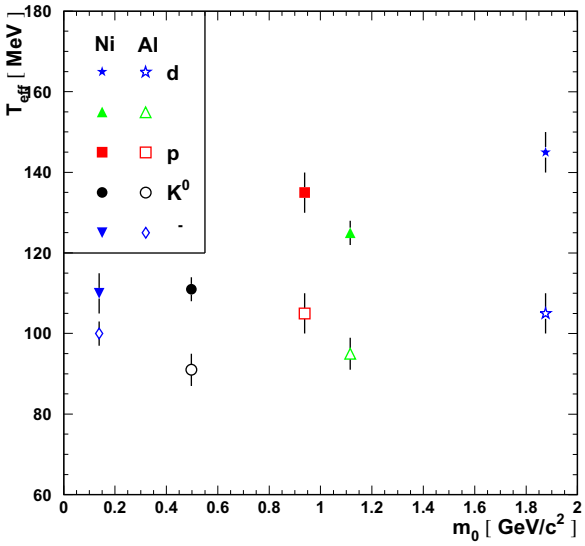


Figure 2: Mass dependence of the inverse slope parameters in Ni+Ni and Al+Al reactions extracted from transverse mass spectra at mid-rapidity.

References

[1] M.A. Lisa et al., Phys. Rev. Lett 75:2662-2665, 1995

[2] M. Justice et al., Phys. Lett. B 440:12-19, 1998

[3] B. Hong et al., Phys. Rev. C57:244-253, 1998

* Work supported by BMBF (06HD154)

† merschm@physi.uni-heidelberg.de

Hadron production at chemical freeze-out

A. Andronic, P. Braun-Munzinger, GSI, Darmstadt
J. Stachel, Physikalisches Institut, Universität Heidelberg

We perform, within the framework of the thermal model, an analysis of all available experimental data on hadron yields over a broad range of energies ($\sqrt{s_{NN}}$=2.7-200 GeV) for central nucleus-nucleus collisions [1]. The fits of the experimental data provide the thermal parameters, temperature (T) and baryo-chemical potential (μ_b) at chemical freeze-out.

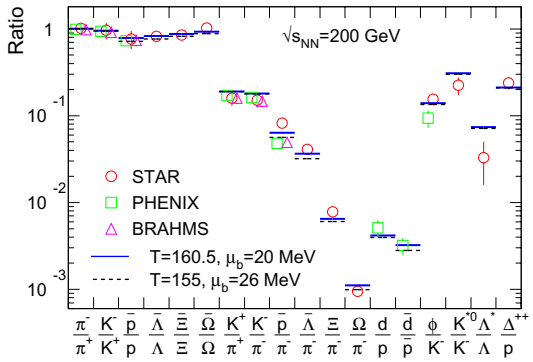


Figure 1: Hadron yield ratios with best fits at $\sqrt{s_{NN}}$=200 GeV. The last three ratios, involving resonances, were not included in the fits.

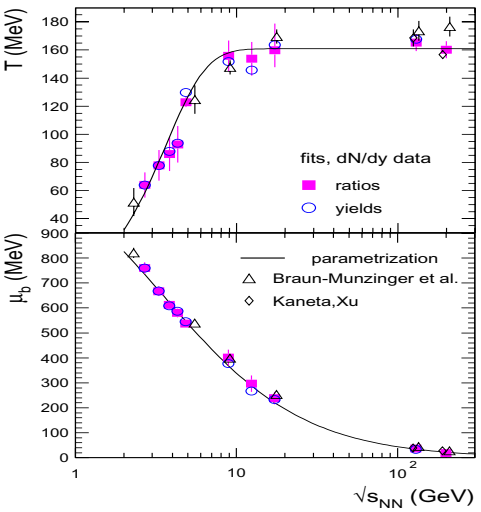


Figure 2: Energy dependence of the thermal parameters.

In general, the quality of the fits is good, providing support for the validity of the approach. An example of the fit of all available data at top RHIC energy of $\sqrt{s_{NN}}$=200 GeV is shown in Fig. 1. A combined fit of all available data, with the exception of strongly decaying resonances gives $T = 155 \pm 2$ MeV, $\mu_b = 26 \pm 5$ MeV, with $\chi^2/N_{df} = 34.1/23$. Excluding from the fit the ratios $\bar{p}/\pi^-$ and ϕ/K^- from PHENIX, the resulting parameters are: $T = 160.5 \pm 2$ MeV, $\mu_b = 20 \pm 4$ MeV, with an improved χ^2/N_{df}=16.0/21.

In Fig. 2 we show the energy dependence of T and μ_b extracted from our thermal fits. The temperature T exhibits a sharp rise up to $\sqrt{s_{NN}} \simeq$7-8 GeV, while μ_b sharply decreases all the way up to RHIC energies. Using the parametrizations of T and μ_b, shown by lines in Fig. 2, we could demonstrate that the model describes the main features observed in the data, but not the details. In addition, we can provide quantitative predictions for LHC energy.

The analysis presented here has also led to an updated version of the chemical freeze-out curve, shown in the phase diagram of QCD in Fig. 3 The results buttress previous observations that, from $\sqrt{s_{NN}} \approx 10$ GeV on, the chemical freeze-out points coincide with the phase boundary between hadrons and the QGP as predicted by solving QCD on the lattice [2].

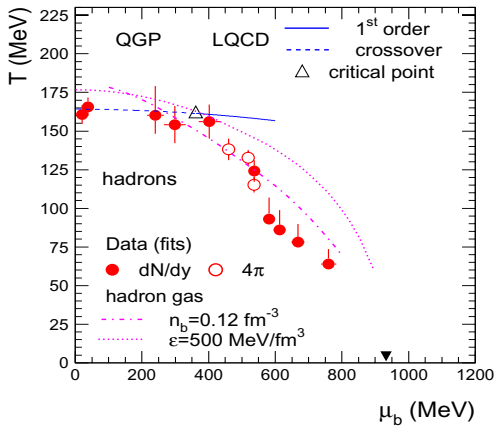


Figure 3: Phase diagram of QCD.

Although the exact location of the critical is far from being firmly established [3], it appears that the experimental freeze-out points for the SPS energies are located in the vicinity of the critical point [2]. It is interesting to speculate whether the deviations from the thermal model (including rather poor-quality fits) which we have encountered for the SPS energies are in connection with the critical point.

We have provided chemical freeze-out points, for the first time, at the 4 low AGS energies. In this energy range the freeze-out curve exhibits a peculiar and intriguing structure which needs further explanation.

References

[1] A. Andronic, P. Braun-Munzinger, J. Stachel, nucl-th/0511071 and refs. therein.

[2] Z. Fodor, S.D. Katz, JHEP 404 (2004) 50 [hep-lat/0402006].

[3] O. Philipsen, hep-lat/0510077.

Statistical production of J/ψ at RHIC

A. Andronic, A. Bercuci, P. Braun-Munzinger, GSI, Darmstadt; K. Redlich, University of Wrocław and CERN; J. Stachel, Physikalisches Institut, Universität Heidelberg

We study the production of charmonium in nucleus-nucleus collisions at RHIC ($\sqrt{s_{NN}}$=200 GeV)within the framework of the statistical hadronization model, SHM [1]. The model assumes that all charm quarks are produced in primary hard collisions and equilibrate in the quark-gluon plasma (QGP). In particular, no J/ψ mesons are preformed in the QGP, implying complete color screening [2]. Experimental results on the elliptic flow of electrons from charm mesons [3] argue in favor of the thermalization of charm quarks. However, there are indications from recent lattice QCD calculations that J/ψ mesons could survive in QGP well above the critical temperature [4]. The cross sections of charmed hadrons are too small to allow for their chemical equilibration in a hadronic gas.

The model has the following inputs: i) T and μ_b from thermal fits [5]; ii) the volume (for one unit of rapidity), obtained from the thermal densities and the experimental values of charged particles rapidity densities dN/dy; iii) the charm cross section. We have adopted the values calculated in FONLL perturbative QCD [6], corresponding to $d\sigma/dy = 63.7^{+95.6}_{-42.3}$ μb. This recent pQCD result [6] includes a careful estimate of the systematic errors in the calculations. We note that the experimental charm cross section at RHIC, extracted in an indirect way from single electron spectra [7], is compatible only with the upper limit of the errors on the pQCD calculations.

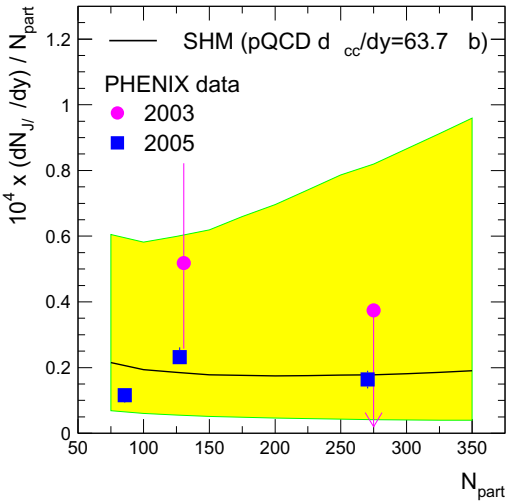


Figure 1: Centrality dependence of J/ψ yield. The line is our calculation for the central value of pQCD charm cross section, the band corresponds to its systematic uncertainties.

The centrality dependence of J/ψ yield at midrapidity (dN/dy) per participant is shown in Fig. 1. The model explains the recent PHENIX data [8] very well for the central value of the pQCD charm cross section, in agreement with our earlier results [1].

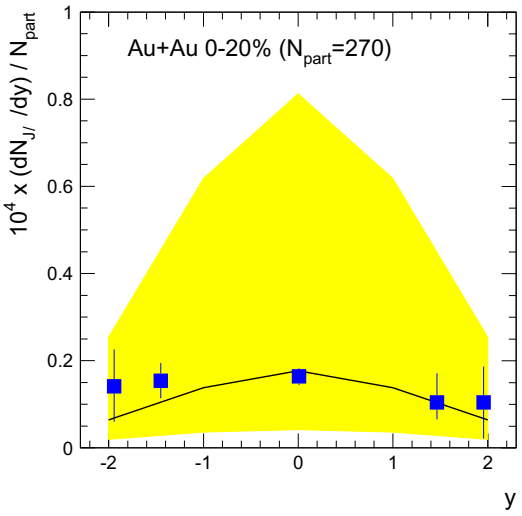


Figure 2: Rapidity dependence of J/ψ yield.

The rapidity dependence of the J/ψ yield is shown in Fig. 2 for 20% central Au-Au collisions. The model is in very good agreement with the data. Note that we have used the values of (T,μ_b) determined from mid-rapidity data [5] to calculate within the model the yields for all rapidity values.

These results demonstrate that the statistical production of J/ψ is a valid scenario for the RHIC energies. In order to increase the predictive power of our model, in particular for the upcoming data at LHC energy, more precise measurements of the charm cross section are needed.

References

[1] A. Andronic et al., Phys. Lett. B 571 (2003) 36

[2] T. Matsui, H. Satz, Phys. Lett. B 178 (1986) 416.

[3] S.S. Adler et al. (PHENIX), Phys.Rev. C72 (2005) 024901.

[4] M. Asakawa, T. Hatsuda, Phys.Rev.Lett. 92 (2004) 012001.

[5] A. Andronic, P. Braun-Munzinger, J. Stachel, nucl-th/0511071 (also this Report).

[6] M. Cacciari at el, Phys. Rev. Lett. 95 (2005) 122001.

[7] S.S. Adler et al. (PHENIX), Phys.Rev.Lett. 94 (2005) 082301; J. Adams et al. (STAR) Phys.Rev.Lett. 94 (2005) 062301.

[8] H. Pereira Da Costa (PHENIX), nucl-ex/0510051.

Z-Boson Simulations with the central barrel of ALICE

R. Bailhache, GSI, Darmstadt, Germany

The measurement of Z-boson in pp and PbPb collisions at the LHC could be alternatively used as a reference to measure the effect of the transition to a deconfined phase on the production of quarkonia. Z^0 is also a reference signal for detector performance in case of other high-momentum studies, like jets. We present simulation results on the ALICE central barrel capability for detecting the Z-boson through his electronic decay in pp-collisions at 14 TeV.

At the Tevatron energies (1.8-1.96 TeV) the $p\overline{p}\rightarrow Z+X$ process is usually simulated with the low-order single Z-production from Pythia and compared to the data by scaling with a k-factor. The absolute cross sections are not accurately approximated through an extrapolation with the same k-factor at the LHC, but the PDF uncertainties cancel in the ratio $\frac{\sigma_{tot}(Z)}{\sigma_{tot}(W)}$. Moreover, the inclusive W-production could be a source of background for the Z-boson. We find a k-factor for the process $p\overline{p}\rightarrow Z\rightarrow e^+e^-$ of about 1.5 for the Tevatron data. Through extrapolation we estimate for pp collisions at 14 TeV the inclusive cross-sections $\sigma(pp\rightarrow Z\rightarrow e^+e^-)$ and $\sigma(pp\rightarrow W\rightarrow e\nu_e)$ to be respectively 2.4 nb and 23.8 nb, which are higher than the NNLO calculations (about 1.95 nb and 19.6 nb). As expected, the ratio $\frac{\sigma_{tot}(Z)}{\sigma_{tot}(W)}$ is however consistent with the NNLO results. These cross-sections are very low. For 10^9 minimum-bias events ($\sigma_{mb}\approx$80 mb) per 8 months of data taking for pp collisions in ALICE the expected number of $Z\rightarrow e^+e^-$ events is only about 25.

The ALICE detector response is simulated with a fast-simulation program applied on the events from Pythia. The TRD provides an electron-identification efficiency of 90 % above 1 GeV. 5 % of the total $Z\rightarrow e^+e^-$-signal is reconstructed. The main restriction comes from the limited pseudorapidity range covered by the central barrel (8.5 % for $|\eta|<0.9$). The tracking and identification efficiency per e is about 76.7 %. The effect of a p_T-cut at 25 GeV has also been investigated, because the signature of $pp\rightarrow Z\rightarrow e^+e^-$ events is two high-p_T opposite charged electrons. It will reduce the signal by 8.5 % but also consistently reduce the possible sources of background.

Different sources of background have been investigated. $W\rightarrow e\nu_e$ events with an associated hadronic jet result in a high p_T electron and a second reconstructed electron, coming from a pion misidentified as electron. This kind of background remains negligeable for any reasonable pion efficiency. However the hard core (HC) cross-section has been simulated with Pythia, tuned for the minimal-bias events study at the CDF Tevatron experiment[2], to estimate the multiplicity p_T-distribution of charged particles above 25 GeV. $\frac{dN_{ch}}{d\eta}$ was found to be approximately 6.8 at midrapidity with a total cross-section of 64 mb. Mainly possible misidentified pions have to be taken into account above 25 GeV. The cross-sections and rates per minimum-bias events are summarized in Tab.1.

pp **at** $\sqrt{s}=$ **14 TeV**	Full [pb]	Rate per min-bias
$\sigma_{total}(Z\rightarrow e^+e^-)$	2400	3×10^{-8}
$\sigma_{total}(W\rightarrow e\nu)$	23800	2.98×10^{-7}
σ_{HC}	64 mb	

Table 1: Cross-sections and rates

The pion efficiency is about 0.5 % at 10 GeV but increases with the momentum in the energy range from 1 to 10 GeV. With an extrapolated value of 1.2 % at 25 GeV, misidenfitied pions are an issue. Fig.1 shows the invariant mass yield for minimum-bias events. Only a cut on p_T at 25 GeV has been applied. The signal-to-background ratio is about 1/10.

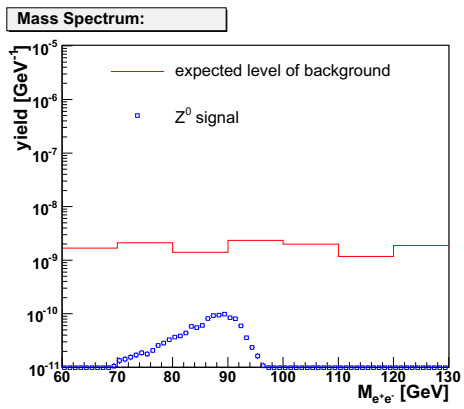


Figure 1: Invariant mass yield per minimum-bias event.

It appears to be very difficult to detect the Z-boson in pp-collisions. The low statistics speaks in favor of a dedicated trigger but the background is also expected to be very high. A condition on the e^+e^--opening angle and a more accurate study of the HC cross-section at high p_T momentum are under investigation.

References

[1] J. Fiete, http://qgp.uni-muenster.de/∼jfgrosse/www/elut/elut.html

[2] R. Field, CDF Collaboration, hep-ph/0510198

Statistical Model Predictions for Particle Ratios at $\sqrt{s_{NN}}$ = 5.5 TeV

I. Kraus, H. Oeschler, Institut für Kernphysik, University of Technology, D-64289 Darmstadt, Germany
J. Cleymans, S. Wheaton, UCT-CERN Research Centre and Department of Physics,
University of Cape Town, Rondebosch 7701, South Africa
K. Redlich, Institute of Theoretical Physics, University of Wrocław, Pl-45204 Wrocław, Poland

The Statistical Model has described very successfully particle ratios measured in heavy ion collisions over a wide range of center of mass energies [1]. The extracted chemical freeze-out conditions, the temperature T and the baryon chemical potential μ_B, drawn in the QCD phase diagram, appear on a common curve [2]. The extrapolation of this curve according to the parametrisation given in [3] results in $\mu_B(\sqrt{s_{NN}} = 5.5\ \text{TeV}) \approx 1$ MeV. The temperature T = 170 MeV was chosen in accordance with the chemical freeze-out temperatures at the top SPS and RHIC energies [1]. Predictions for different particle ratios are displayed in Table 1.

Table 1: Particle ratios in Pb+Pb collisions at freeze-out conditions expected at the LHC: T = (170±5) MeV and $\mu_B = 1^{+4}_{-1}$ MeV. The given errors correspond to the variation in the thermal parameters. Taken from [5].

h/h Ratio		mixed Ratio	
π^+/π^-	$0.9998^{+0.0002}_{-0.0010}$	K^+/π^+	$0.180^{+0.001}_{-0.001}$
$\mathrm{K}^+/\mathrm{K}^-$	$1.002^{+0.008}_{-0.002}$	K^-/π^-	$0.179^{+0.001}_{-0.001}$
$\bar{\mathrm{p}}/\mathrm{p}$	$0.989^{+0.011}_{-0.045}$	p/π^-	$0.091^{+0.009}_{-0.007}$
$\bar{\Lambda}/\Lambda$	$0.992^{+0.009}_{-0.036}$	Λ/p	$0.473^{+0.004}_{-0.006}$
$\bar{\Xi}^+/\Xi^-$	$0.994^{+0.006}_{-0.026}$	Ξ^-/Λ	$0.160^{+0.002}_{-0.003}$
$\bar{\Omega}^+/\Omega^-$	$0.997^{+0.003}_{-0.015}$	Ω^-/Ξ^-	$0.186^{+0.008}_{-0.009}$

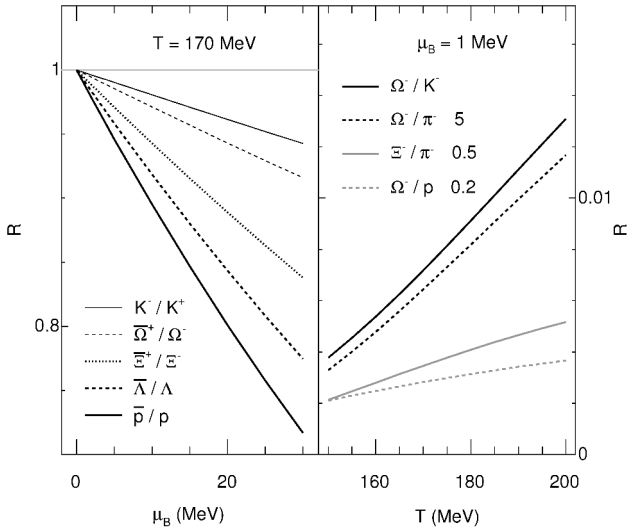


Figure 1: Antiparticle/particle ratios R as a function of μ_B for T = 170 MeV (left). The horizontal line at 1 is meant to guide the eye. Particle ratios R involving hyperons as a function of T for μ_B = 1 MeV (right). The calculations were carried out with the THERMUS package [4] in the grand canonical ensemble.

The ability to determine the freeze-out parameters experimentally is deduced from the sensitivity of well suited particle ratios on T and μ_B. Figure 1 (left) shows different antiparticle/particle ratios, $\bar{h}/h$ in dependence on μ_B. The decrease of the $\bar{h}/h$ ratios with increasing μ_B can be understood qualitatively from

$$\bar{h}/h \propto \exp[2(N_B\mu_B + N_S\mu_S)/T], \qquad (1)$$

with baryon number N_B and strangeness quantum number N_S of the antiparticle, $\bar{h}$, and strangeness chemical potential μ_S. In Eq. 1 feed-down contributions are neglected. In Antibaryon/Baryon ratios the dominating μ_B term is diluted by the μ_S term since N_S has the opposite sign of N_B. Consequently, the strongest sensitivity on μ_B can be observed in the $\bar{\mathrm{p}}/\mathrm{p}$ ratio.

Strong dependence on the temperature is expected in ratios built of particles with a large mass difference. Some ratios involving hyperons are shown in Fig. 1 (right). Here, the largest sensitivity is exhibited by the Ω^-/π^- ratio. However, hadronic decays of baryonic and, predominantly, from mesonic resonances contribute significantly to the pion yield. The large fraction of pions originating from heavier particles reduces the temperature dependence to the same level as the Ω^-/K^- ratio shows. For other particle ratios with smaller mass difference the sensitivity on temperature is weaker.

To summarise, the $\bar{\mathrm{p}}/\mathrm{p}$ ratio is best suited for the extraction of the baryon chemical potential μ_B. Two thermometers can be explored: The Ω^-/π^- and the Ω^-/K^- ratio exhibit the same sensitivity on the freeze-out temperature.

References

[1] P. Braun-Munzinger, K. Redlich and J. Stachel, Invited review for *Quark-Gluon Plasma 3*, edited by R. C. Hwa and Xin-Nian Wang (World Scientific Publishing, 2003), nucl-th/0304013.

[2] J. Cleymans and K. Redlich, Phys. Rev. Lett. **81**, 5284 (1998).

[3] P. Braun-Munzinger, J. Cleymans, H. Oeschler and K. Redlich, Nucl. Phys. **A697**, 902 (2002).

[4] S. Wheaton and J. Cleymans, THERMUS - A Thermal Model Package for ROOT, hep-ph/0407174.

[5] J. Cleymans, I. Kraus, H. Oeschler, K. Redlich and S. Wheaton, to be published.

Comparison of the isotopic cross sections measured in the fragmentation of ^{136}Xe and ^{124}Xe projectiles with the EPAX parameterization

D. Henzlova* for CHARMS, GSI, Darmstadt, Germany

It is one of the main interests of the present research to extend the experimental investigations towards the rarely produced isotopes with extreme *N/Z* in order to investigate their structure properties or to study the dependence of the nuclear equation of state on the isotopic composition of the system. To produce these exotic nuclei experimentally a reliable description of the production cross sections is necessary to predict the production rates. The most recent and frequently used parameterization of the production cross sections is EPAX developed in [1,2].

In two experiments recently performed at the Fragment Separator at GSI, the isotopically resolved residues over the broad range of the nuclear charge were measured in the fragmentation of ^{136}Xe and ^{124}Xe in a lead target at 1 A GeV. The isotopic distributions measured in these experiments form an extensive database for testing the predictive power of the cross-section parameterizations especially from the point of view of the *N/Z* dependence.

To obtain a more complete overview on the predictive power of EPAX, the measured isotopic distributions of elements *Z*=15,45,50 in both experiments are compared with EPAX in Figure 1.

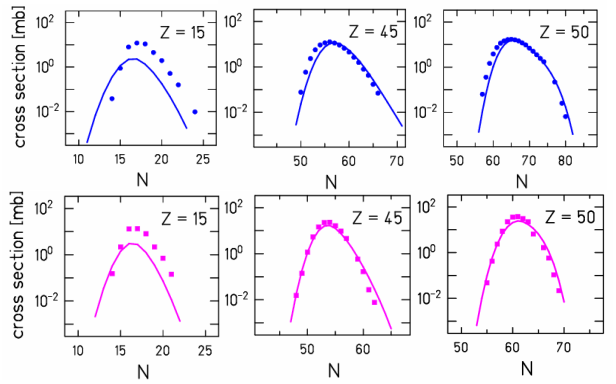


Figure 1: The isotopic distributions measured in ^{124}Xe+Pb (pink squares) and ^{136}Xe+Pb (blue squares) experiments for *Z*=15,45,50 compared with the EPAX (full lines).

It may be observed that the production cross sections of the lighter elements are strongly underestimated by EPAX in case of both projectiles. The production cross sections on the neutron-deficient side of the isotopic distributions for heavy elements are slightly underestimated by EPAX in case of the ^{136}Xe projectile. To obtain a complete overview on the isotopic composition of the final residues predicted by EPAX, the mean N-over-Z is compared with the experimental data in Figure 2.

The discrepancy between the experimental data and the EPAX in the vicinity of the ^{136}Xe projectile may be understood due to rather limited experimental information available for the n-rich system used to establish the EPAX parameterization. While in case of the less n-rich xenon projectiles (^{124}Xe, ^{129}Xe [3,4]) a broader range of heavy isotopes in the nuclear charge range *Z*~40-55 was available, the experimental data for the ^{136}Xe [5] projectile were much scarcer and concentrated only on the n-rich side of the isotopic distribution.

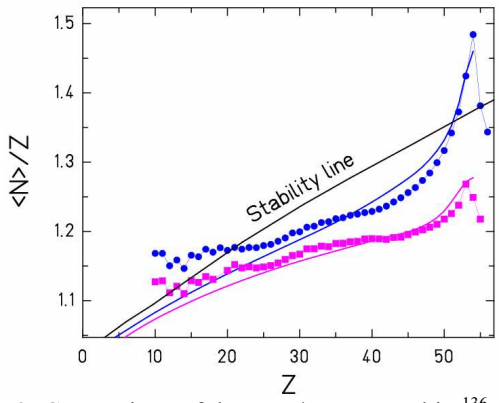


Figure 2: Comparison of the <*N*>/*Z* measured in ^{136}Xe+Pb (blue points) and ^{124}Xe+Pb (pink squares) reactions with the prediction of the EPAX parameterization (blue and pink lines).

Similarly, the discrepancy observed for the lighter residues may be traced back to the fact that only residues in the vicinity of the lighter projectiles were available to establish the EPAX parameterization. These residues are generally produced in more peripheral collisions where low to moderate excitation energies are introduced. On the contrary, the residues far away from the projectile are predominantly produced in more violent collisions, where considerably higher excitation energies may be expected. A highly excited nuclear system may undergo break-up into fragments of various sizes, a process, which contributes to an enhanced production of the intermediate-mass fragments (IMF, 3≤*Z*≤20). This may provide an explanation of the underestimation of the production cross sections by EPAX in this nuclear-charge range.

The presented experiments provide experimental data in a much broader mass and *N/Z* range than covered by previous experiments. This new information will help improving the EPAX parameterization for nuclei around mass 100.

References

[1] K. Sümmerer et al., Phys. Rev. C 42 (1990) 2546
[2] K. Sümmerer, B. Blank, Phys. Rev. C 61 (2000) 034607
[3] R. Schneider et al., Zeit. für Phys. A 348 (1994) 241
[4] J. Reinhold et al., Phys. Rev. C 58 (1998) 247
[5] J. Friese et al., Nucl. Phys. A 553 (1993) 7

* on leave from NPI Rez, Czech Republic

Systematic investigation of the spectator response to the participant blast in the reactions ^{197}Au+^{27}Al, ^{197}Au at 0.5 *A* GeV and ^{197}Au+^{197}Au at 1.0 *A* GeV

V. Henzl* for the CHARMS collaboration, GSI, Darmstadt, Germany

Recent theoretical work [1] suggested the longitudinal velocities of the fragmentation residues produced in relativistic heavy-ion collisions as an observable sensitive to the momentum dependent (MD) properties of the nuclear mean field (MF). Under certain conditions, the spectator remnant can acquire on average even a positive momentum during the collision This phenomenon has been named ***spectator response to the participant blast*** since the action of the expanding participant matter has been identified within this theoretical work [1] as the main source of the spectator reacceleration.

In several experiments performed at the Fragment Separator (FRS) at GSI, this theoretically predicted phenomenon was clearly observed [2,3]. In the present work [4], the dependence on the collision parameters such as projectile energy and reaction geometry was systematically studied. This may subsequently allow for better understanding the considered process and possibly contribute to the use of this observable for more detailed investigations of the MD aspects of the nuclear MF.

Three experiments were dedicated to the precise determination of the longitudinal velocities v_z of the fragmentation residues produced in the reactions ^{197}Au+^{197}Au at 1 *A* GeV and ^{197}Au+^{27}Al, ^{197}Au at 500 *A* MeV at GSI with use of the FRS as the high-resolution magnetic spectrometer allowing for very precise measurements of complete longitudinal velocity distributions of fully isotopically resolved reaction residues. Fig.1 displays the measured longitudinal velocity of the reaction residues in the frame of the projectile. The main ridge in these contour plots corresponds to the residues produced in fragmentation, while the edges are mainly composed of the residues produced in fission. A more quantitative insight is gained when the mean v_z is determined for the residues produced only by fragmentation, such as displayed in Fig.2. Projectile residues with masses A_{frag} > 150 produced in very peripheral collisions are decelerated in the reaction and follow the well established Morrissey systematics [5], however the $\langle v_z \rangle$ of the lighter residues level off, and progressively increase with decreasing mass and reach positive values with respect to the original projectile velocity (for A_{res} < 85).

Comparing the quantitative results of $\langle v_z \rangle$ with respect to A_{res} with the theoretical calculation, the differences between individual experiments are surprisingly small despite the great variation of the projectile energy or the size of the target nucleus. Therefore, we rather interpret the phenomenon as being the consequence of the dynamical evolution of the spectator matter itself, e.g. enhanced backward emission of nucleons and light clusters, possibly triggered (but not fully ruled) by the blast of the participating matter. Intensive theoretical investigations and additional experiments are underway to improve the understanding of the reacceleration of the fragmentation residues in mid-peripheral heavy-ion collisions.

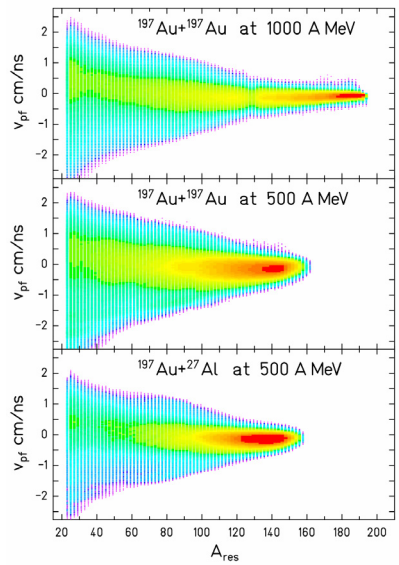


Fig.1: v_z of the projectile residues as a function A_{res} in the projectile frame. The color scale is logarithmic, and adjusted for illustrative purposes for each plot separately. The experiments performed at 500 *A* MeV did not cover residues with A_{res}>160.

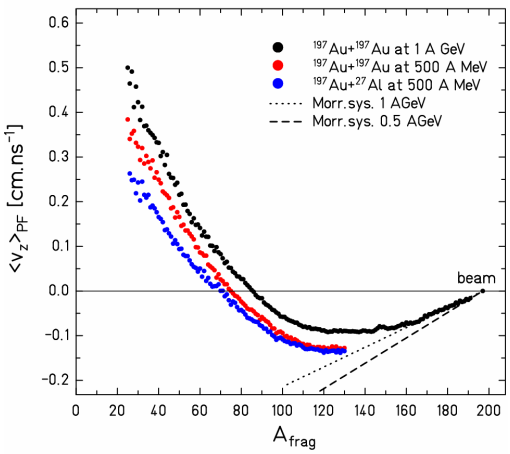


Fig.2: Mean longitudinal velocities of the fragmentation residues as a function of their mass A_{frag} in the reference frame of the corresponding primary beam. The black line represents the Morrissey systematics [5]. Experimental uncertainties typically do not exceed 0.01cm/ns.

References

[1] L.Shi *et al.*, PRC64, 034601 (2001).
[2] T.Enqvist *et al.*, NPA658 (1999) 47
[3] M.V.Ricciardi *et al.,* PRL90, 2123021 (2003).
[4] V. Henzl, PhD thesis, in preparation
[5] D.J.Morrissey, PRC39, 460 (1989).

Δ-Scaling in Spectator Fragmentation *

M. De Napoli, C. Sfienti, W. Trautmann and the ALADiN2000 Collaboration
GSI, Darmstadt, Germany

Universal scaling-laws of fluctuations (the Δ-scaling laws) have been derived for equilibrium systems, and shown to apply also in certain out-of-equilibrium situations. [1].

Recently looking for signals of a phase transition in multifragmentation reactions the model-independent theory of universal fluctuation has been used [2]. The Δ-scaling is observed when two or more probability distributions $P_N[m]$ of the observable m for a system size N collapse onto a single scaling curve $\phi(z_{(\Delta)})$ independent of system size when plotted in terms of the scaling variables. The scaling law with Δ=1/2 is associated with low temperature (*ordered*) systems, or with observables which are not related to an order parameter. Scaling with Δ=1 is seen at high temperature (*disordered* system) and also for critical systems. For m to be an order parameter it must exhibit a corresponding change of Δ-scaling regime when some suitable control parameter (e.g. available energy, temperature, etc.) is varied.

Using the data from the most recent ALADiN experiment [3], it has been investigated whether the $Z_{\max}$ distributions follow the Δ-scaling law. The multiplicity of charged particles measured in the Catania Hodoscope was used as impact parameter in oder to avoid possible autocorrelation with $Z_{\max}$.

An additional selection has, moreover, been applied to the data by defining two cuts on the asymmetry variable

$$\eta_{asy} = (Z_{\max} - (Z_2 + Z_3))/(Z_{\max} + (Z_2 + Z_3)):$$

$\eta_{asy} > 0.5$ and $\eta_{asy} < 0.3$ corresponding to the liquid and gas phases respectively. The correlation between the mean value and the fluctuation of $Z_{\max}$ is shown in Fig. 1. The dotted lines represent fits performed for Δ= 1 for high excitation energy (left-hand side of Fig. 1) and for Δ= 0.5 for low excitation energy (right-hand side of Fig. 1).

The form of the $Z_{\max}$ distributions also evolves with excitation energy: it is nearly Gaussian in the Δ=1/2 regime (bottom panel of Fig. 2); for Δ=1 the shape is asymmetric with a near-exponential tail for large positive values of the scaling variable, $z_{(\Delta)}$ (upper panel of Fig. 2): this distribution approaches that of the modified Gumbel-distribution [2].

The interpretation of this result is still an open question. The two Δ-scaling regimes seems to suggest that $Z_{\max}$is behaving like the order-parameter of a second-order phase transition. The fact that typical second-order phase transitions signals as scaling are observed in multifragmentation data may look surprising. The experimental observation of a flattening of the caloric curve, as well as recent studies in the framework of the SMM model, all point to a first-order phase transition. This apparent contradiction, however, can be understood as a finite-size effect [4].

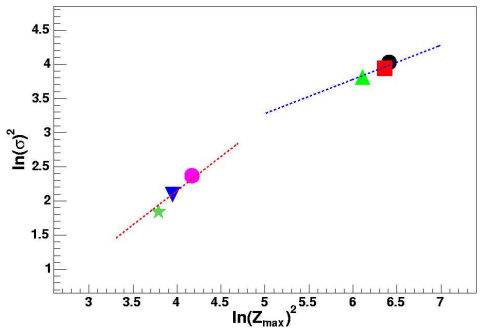


Figure 1: Correlation between the mean value and the fluctuation of $Z_{\max}$.

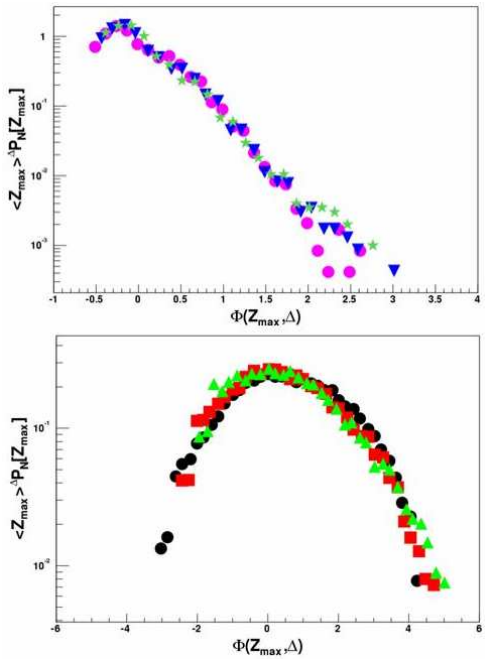


Figure 2: Upper panel: $Z_{\max}$ distributions for ^{124}Sn projectile spectator, scaled using Δ=1. Lower panel: Δ distributions for the same system scaled using Δ=0.5.

References

[1] R. Botet and M. Płoszajczak Phys. Rev. E 62 (2000) 1825

[2] J. D. Frankland et al, Phys. Rev. C 71 (2005) 034607

[3] C. Sfi enti et al., Nucl. Phys. A 749 (2005) 83c.

[4] F. Gulminelli et al., Phys. Rev. C 71 (2005) 054607

* Supported by EU/FP6/HADRONPHYSICS (see Annex)

Reaction Plane Dispersion at Intermediate Energies

J. Łukasik and W. Trautmann, GSI–Darmstadt, Germany

A new method to calculate the correction for the dispersion of the reaction plane at intermediate energies has been proposed. The existing standard methods, like those presented in [1, 2], have been developed and proved their usefulness to correct the measured flow values at high energies, for events with high multiplicities. They were however found inadequate for the Au+Au reactions studied with the INDRA detector at GSI, especially below about 100 AMeV. The range of energies studied during this campaign (40-150 AMeV) covers the 2 transitions of the collective flow, the one for the directed flow (v_1) around 50 AMeV and the one for the elliptic flow (v_2) around 100 AMeV. A precise knowledge of the behavior of the excitation function of both flow components is necessary to constrain the transport models in order to study the properties of the nuclear matter.

Since the detectors can not measure the positions, spins and momenta of the reaction products simultaneously, the reaction plane can only be estimated using the momenta, and the precision of the flow measurement will depend on the accuracy of this estimate.

The accuracy is large when the directed flow is large [2]. At energies close to the balance energy the directed flow is however small. In addition, the multiplicities get lower and the events are characterized by a broad range of charges of the reaction products. Thus, the applicability of the central limit theorem for devising the corrections is less obvious. Nevertheless, we argue that the assumption of the Gaussian distribution of the flow Q-vector [1] still holds, at least in the first approximation, even at energies as low as 40 AMeV. QMD-Chimera [3] calculations confirm this assumption, and, even more, show that the random sub-events are also normally distributed. The difference, as compared to the high energy case, is that the sub-events get strongly correlated and that the distributions of the Q-vector are no longer isotropic but rather elongated in the reaction plane, reflecting the increasing role of the in-plane emissions at low energies.

These observations, based on the results of the dynamical simulation and also resulting from the inspection of the experimental distributions of the relative angle between the Q-vectors for the random sub-events, led us to the conclusion that the joint probability distribution of the random sub-Q-vectors, $d^4P/d\vec{Q}_1 d\vec{Q}_2$, could be well approximated by the correlated non-isotropic Gaussian distribution of the form:

$$\frac{e^{-\frac{(Q_{1x}-\bar{Q})^2+(Q_{2x}-\bar{Q})^2-2\rho(Q_{1x}-\bar{Q})(Q_{2x}-\bar{Q})}{\sigma_x^2(1-\rho^2)}-\frac{Q_{1y}^2+Q_{2y}^2-2\rho Q_{1y}Q_{2y}}{\sigma_y^2(1-\rho^2)}}}{\pi^2\sigma_x^2\sigma_y^2(1-\rho^2)}$$

where we followed the conventions and notation of [2]. This distribution differs from those proposed in [2, 4, 5] in that it combines all three effects that influence the reaction plane dispersion at intermediate energies, namely the directed flow (through the mean $\bar{Q}$ or the resolution parameter $\chi_{sub} \equiv \bar{Q}/\sigma_x$ [2]), the elliptic flow (through the ratio $\alpha \equiv \sigma_x/\sigma_y$) and the correlation between the sub-events (through the correlation coefficient $-1 \leq \rho \leq 1$).

Making the division into sub-events random ensures that the distributions of the sub-Q-vectors are equivalent (in particular they have the same mean values and variances), and, since the total Q-vector $\vec{Q} = \vec{Q}_1 + \vec{Q}_2$, its distribution is characterized by the resolution parameter $\chi = \chi_{sub}\sqrt{2/(1+\rho)}$. As in [2] the use of the joint probability distribution is done by integrating it over the magnitudes of the Q-vectors and one angle, leaving the relative angle between the sub-events. Unlike in [2], the resulting distribution can not be presented in an analytical form, instead, it can be calculated numerically using e.g. the Gauss-Chebyshev quadrature. It depends now on 3 parameters (χ_{sub}, α, ρ) which can be obtained from the fit of the resulting distribution to the experimental or model one. The correction factors for the n-th harmonic v_n, depending now on χ and α, can be calculated (also numerically) from the corresponding mean values of the $\langle\cos(n\Delta\Phi)\rangle$ obtained from the total Q-vector distribution, in a similar way as in [2]. Introduction of 3 parameters was necessary to fit the whole family of shapes of the experimental distributions of the relative angle between the sub-events at low energies.

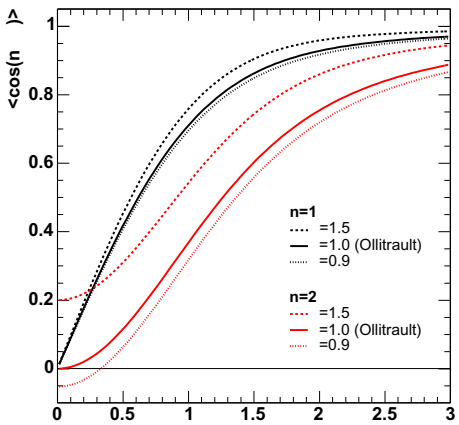


Figure 1: Correction factors for the first two harmonics as a function of the resolution parameter, χ, for different aspect ratios, α.

Figure 1 shows how the elongation of the Gaussian (α), or elliptic flow, modifies the correction factors for the 1^{st} (3 upper curves) and the 2^{nd} (3 lower curves) harmonics. It demonstrates that the in-plane emissions ($\alpha > 1$) enhance slightly the resolution for v_1 and considerably for v_2 – even in the absence of the directed flow. On the other hand, squeeze-out ($\alpha < 1$) deteriorates the resolution. The relation between χ_{sub} and χ indicates that the resolution improves in case the sub-events are anti-correlated ($\rho < 0$), a case at low energies and non-peripheral collisions.

References

[1] P. Danielewicz and G. Odyniec, Phys. Lett. 157B(1985)146.
[2] J.-Y. Ollitrault, preprint nucl_ex/9711003.
[3] J. Łukasik and Z. Majka, Acta Phys. Pol. B 24(1993)1959,
[4] J.-Y. Ollitrault, Nucl. Phys. A 590 (1995) 561c.
[5] N. Borghini et al., Phys. Rev. C 66 (2002) 014901.

Dielectron production in C+C and pp collisions

The HADES Collaboration

Introduction

In the previous annual report [1], preliminary dielectron invariant-mass distributions from C+C collisions at 2 AGeV were reported on. Here we present results from a more refined data analysis using better detector calibrations and improved pair reconstruction algorithms. A comparison of the measured invariant-mass distribution to predictions of a thermal cocktail based on the PLUTO event generator [2] is shown as well. In addition, we present first preliminary results obtained from the analysis of C+C collisions at 1 AGeV.

The interpretation of the HI results requires an independent verification of the HADES dielectron reconstruction efficiencies. For this purpose, the exclusive eta meson production in the *pp* reaction via the $\eta \rightarrow \pi^+\pi^-\pi^0$ (hadronic) and $\eta \rightarrow e^+e^-\gamma$ (electromagnetic) decays have been measured. The ratio of the two reconstructed channels can be compared to expectations based on simulations with a realistic detector response. Together with the well-known meson production and decay mechanisms, it then provides information on the looked-for efficiencies.

Dielectron production in C+C collisions

Dielectron production in C+C at collisions at 2 AGeV bombarding energy was studied with the HADES set-up in 2002, but without making use of the outer MDC system which was then not yet completely installed. A description of the experiment and of the analysis procedure has been given already in our previous report [1]. Here we just detail how the pair signal has been reconstructed from the lepton tracks.

With the identified single lepton tracks unlike-sign (e^+e^-) and like-sign (e^+e^+ and e^-e^-) pair distributions were built. Many of these pairs, however, are uncorrelated and represent combinatorial background (CB) which has to be suppressed. The CB arises mostly from multiple $\pi^0 \rightarrow \gamma\gamma$ decays followed by photon conversion, either in the target or in the RICH radiator, and from $\pi^0 \rightarrow e^+e^-\gamma$ Dalitz decays. Conversion pairs are emitted with small opening angles ($\theta^{conv}_{e+e-} < 4^\circ$) and can easily be distinguished from other sources, like $\eta \rightarrow e^+e^-\gamma$ or $\rho/\omega \rightarrow e^+e^-$, characterized by their much larger average pair angles. These so-called *close pairs* produce partially overlapping tracks in the inner tracking system and can be rejected efficiently by applying a condition on the fit quality of the reconstructed track segments. From dedicated Monte Carlo studies we have deduced that this cut rejects more than 90% of the close pairs with opening angles $\theta_{e+e-} < 3^0$, while still keeping 95% of the reconstructed track pairs from the relevant lepton sources.

From the remaining, well separated tracks only those involved in pairs with an opening angle $\theta_{e+e-} > 9^0$ were used in the further pair analysis. The resulting e^+e^- distributions comprise a signal part, originating from meson and baryon decays, and a CB contribution. To subtract the latter, we used the like-sign pair technique [3]. From the reconstructed like-sign invariant mass distributions dN^{++}/dM and dN^{--}/dM, the respective CB distribution was obtained as their geometric mean $N_{CB} = 2\sqrt{N^{++}N^{--}}$. We verified in Monte Carlo simulations that this prescription describes the CB for the HADES detector very well. The signal/background ratio is significantly better than 1 for the low-mass region, dominated by π^0 decays, and slightly above 1 in the high-mass region ($M > 300$ MeV/c^2).

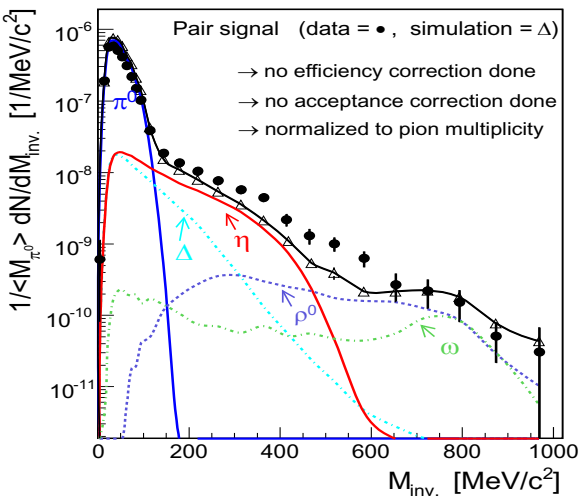


Figure 1: Raw invariant-mass distribution of unlike-sign signal pairs for experiment (circles) and fully simulated cocktail (triangles), normalized to the average charged-pion multiplicity in 2 AGeV $^{12}C + ^{12}C$ collisions. The various cocktail components are shown by the different lines. Error bars are statistical only.

In figure 1, the raw pair signal, obtained after subtracting combinatorial background, is compared to a simulated spectrum. In these simulations, the dielectron emission from thermal sources with temperatures $T_1 = 40$ and $T_2 = 80$ MeV was modeled with the PLUTO generator [2]. Artificially enhanced dielectron decay branching ratios were used for the heavy mesons to increase their event statistics with respect to the otherwise dominant π^0 decays. The generated events were transported through the full GEANT-based detector simulation and reconstructed (signal and combinatorial background) with the same anal-

ysis code as was used for the experimental data. After reconstruction, the dielectron rates were weighted appropriately to compensate for the enhancement factors. The π^0 and the η meson multiplicities were taken from published data [4], with quoted errors of 10% and 16%, whereas vector-meson production was estimated with a mt-scaling ansatz [5].

The contributions from meson and baryon decays to the cocktail are also shown in Fig. 1. The measured and simulated pair production probabilities were both normalized to the average charged-pion multiplicity $M_\pi = \frac{1}{2}(M_{\pi^+} + M_{\pi^-})$, taken from our data [6] for the former and from literature [7] for the latter. From the figure it appears that the data and cocktail agree within the estimated 30% systematic error (not shown) at low masses, dominated by the π^0 Dalitz decays, but show a clear excess at intermediate masses.

To allow a comparison with more refined theoretical models, we proceeded as follows: Instead of showing spectra corrected for, both, efficiency and acceptance, we chose to compare the data corrected for efficiency only with simulations filtered with the HADES acceptance. In this way we avoid the extrapolation to parts of the phase space for which we did not have coverage at all in the experiment. The experimental dielectron distributions must however be corrected for all distortions due to detector and reconstruction imperfections. Using dedicated Monte Carlo simulations for this purpose, electron tracks with a white, i.e. uniform, momentum distribution were imbedded into ^{12}C $+^{12}$ C events generated with the UrQMD transport model [8]. These compound events were digitized with a realistic detector response and processed through the same analysis chain as the measured data have been. The thus gained single electron reconstruction efficiencies account for losses due to (1) detector inefficiencies, (2) electron identification cuts, and (3) track reconstruction inefficiencies within the ^{12}C $+^{12}$ C event environment. Ideally, track embedding should be done, however, with real events and such a procedure is presently being developped. The pair reconstruction efficiency ϵ_{+-} was next calculated from the reconstruction efficiencies of those embedded single electron tracks which entered the HADES geometrical acceptance. Assuming independence of the two tracks, ϵ_{+-} was taken as the product of single electron efficiencies, i.e $\epsilon_{+-} = \epsilon_+\epsilon_-$, with the latter stored in three-dimensional arrays as function of the electron momentum, and its polar and azimuthal emission angles. It was verified in the simulation that the independence holds indeed for pairs with opening angles $\theta_{e+e-} > 9^0$. The experimental pair distributions were corrected event by event with these efficiencies and, after subtracting combinatorial background, compared directly to the cocktail generated with PLUTO and filtered with the HADES geometrical acceptance. In this procedure, the filtered electrons were momentum-smeared with the experimental resolution and were combined into pairs with $\theta_{e+e-} > 9^0$. Note that no extrapolation outside the HADES geometrical acceptance has been performed. Any comparison with a model will also require the application of the appropriate filter function, available from the HADES collaboration upon request [9].

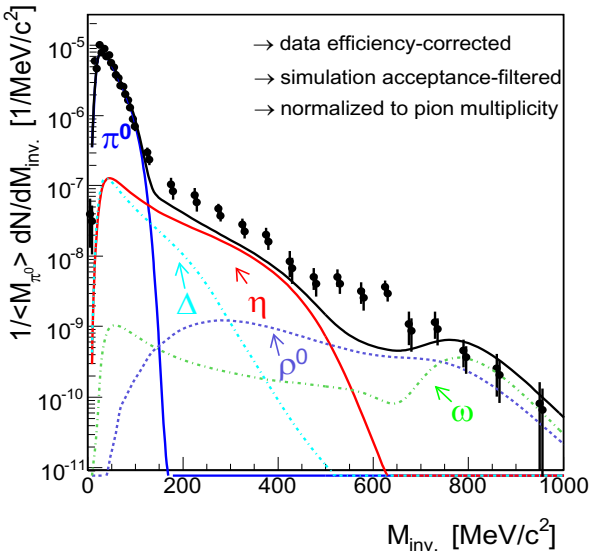


Figure 2: Efficiency-corrected invariant-mass distribution of unlike-sign signal (full symbols) and filtered PLUTO cocktail (full line), both normalized to the average charged-pion multiplicity. The various cocktail components are shown as well. Experimental errors include only statistical errors.

Figure 2 shows the comparison of the efficiency-corrected pair distribution with the acceptance-filtered PLUTO cocktail. Similarly as for uncorrected distributions, an enhancement at intermediate masses is visible, whereas the π^0 Dalitz yields agree, as expected, within the systematic error. Comparisons with theoretical predictions based on transport models (HSD, RQMD and URQMD) are presently in progress and first preliminary results have been shown in [10].

Dielectron production at 1 AGeV was measured in 2004. Preliminary on-line dielectron invariant-mass distributions were shown in the previous status report [1]. In this contribution, we present results of a data analysis obtained from $840 \cdot 10^6$ ($\simeq$ 80% of all data) first-level trigger (LVL1) events using full detector calibration and two independent methods for particle identification: the first is based on so-called "hard" cuts, as described for the 2 AGeV data, the second (BPID) takes advantage of a probabilistic approach guided by the Bayesian theorem and assigns the probability for a reconstructed track to be a particle of a given type based on: (i) measured detector (RICH, MDC, META) response and (ii) known (from simulation or measurement) relative particle abundances [11]. It was shown by careful analysis of experimental data and simulations [12] that the BPID method generally provides larger efficiency and similar background rejection capabilities. Figure 3 shows a comparison of the dielectron invariant-mass distribution obtained with both methods after combinato-

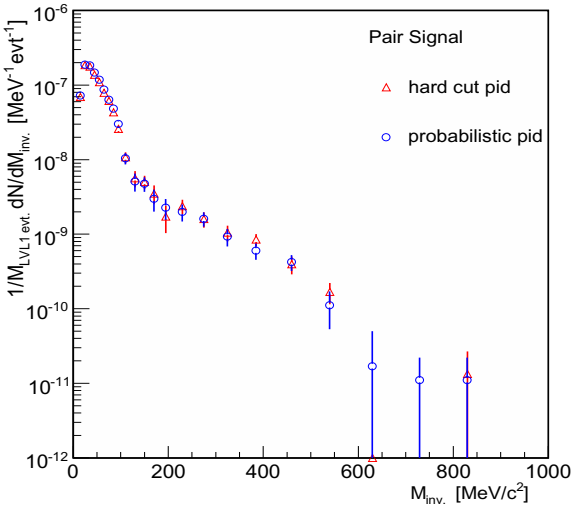


Figure 3: Raw invariant-mass distribution of unlike-sign signal pairs for "hard cut" (open triangles) and Bayesian PID analysis (open circles). Spectra are normalized to the number of LVL1 events recorded in 1 AGeV $^{12}C + ^{12}C$ collisions.

rial background subtraction. As one can see, both distributions agree very well in shape and, as expected, the pair yield obtained with BPID ($\simeq$ 8800 and 470 for $M < 140$ and $M > 140$ MeV/c^2, respectively) is slightly larger ($\simeq$ 20%). The distributions have been normalized to the number of LVL1 events and no corrections for reconstruction efficiencies has been applied.

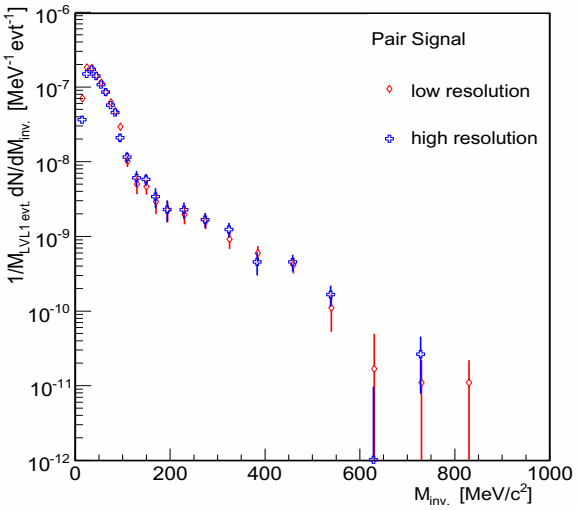


Figure 4: Raw invariant-mass distribution of unlike-sign signal pairs for the BPID analysis using low (open diamonds) and high-resolution tracking (open crosses). Distributions are normalized to the number of LVL1 events in 1 AGeV $^{12}C + ^{12}C$ collisions.

During the 1 AGeV experiment, almost complete coverage with the outer MDC chambers was achieved (6 sectors with MDCIII and 4 with MDCIV). Such a configuration allows of course for better momentum reconstruction (see next section). Furthermore, algorithms developed for the high-resolution tracking also offer the possibility to study systematic effects related to the low-resolution mode. Figure 4 shows invariant-mass distributions for the signal pairs reconstructed with the BPID in the low- (open diamonds) and the high-resolution (open cross) reconstruction modes. As one can see, both distributions agree well in shape and magnitude, hence one can conclude that systematic effects related to the low-resolution mode are small. The analysis of the 1 AGeV data set is on-going; it will allow for a direct comparison with the controversial results obtained by the DLS collaboration at the same beam energy [13].

Exclusive eta reconstruction in p+p collisions

The main goal of the 2004 p+p experiment was to verify the dielectron reconstruction efficiencies needed for a correct interpretation of the HI data. Eta meson production and its decay into hadronic [14] and electromagnetic channels [15] are well known. Therefore, the measured ratio of the respective decay rates, i.e. $Y(\eta \rightarrow \pi^+\pi^-\pi^0)$ and $Y(\eta \rightarrow e^+e^-\gamma)$, can be used to compare hadron and lepton reconstruction efficiencies.

In the simulation, we assumed resonant production of the η meson via $pp \rightarrow N(1535)p \rightarrow pp\eta$, with the Dalitz matrix element taken from [14]. For the eta hadronic decay, the matrix element from [16] has been implemented and for the eta electromagnetic Dalitz decay, the vector dominance model (VDM) was assumed. In addition, a full cocktail of reaction channels based on measured proton-proton cross sections [17] was generated. Simulated events were processed through the HADES GEANT code and reconstructed with the same analysis program as used for the experimental data.

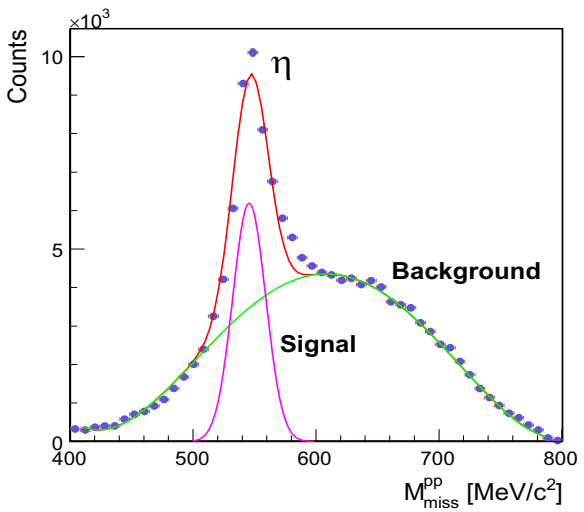


Figure 5: Proton-proton missing-mass distribution for $\eta \rightarrow \pi^+\pi^-\pi^0$ events measured in p+p reactions at 2.2 GeV. The η peak has been fitted with a Gauss function.

The η meson reconstruction was performed with the MDC tracking set-up complete, besides outer-most MDC

IV chambers still missing in two sectors. In a previous report we demonstrated the momentum resolution based on pp elastic scattering (for details of the experimental set-up and trigger setting see [1]). Since then, significant improvements in the momentum resolution and tracking efficiency have been achieved thanks to much better alignment procedures [18] and optimized tracking software. In particular, high-precision momentum reconstruction based on the Runge-Kutta method was implemented. As a result, the invariant-mass resolution for the pp elastic scattering in the sectors fully equipped with MDC chambers improved from $\sigma_M/M = 4.0\%$ to 2.4%.

The measurement of η mesons in the hadronic channel was performed with unbiased events, i.e. without second-level trigger (LVL2) condition, but selected only by a first-level trigger with a multiplicity condition $MUL > 3$ with at least two hits in opposite spectrometer sectors. Reconstruction of the $pp \to pp\eta \to pp\pi^+\pi^-\pi^0$ reaction started with particle identification (PID) based on time of flight and momentum [19]. After PID, a kinematical condition was imposed on events with two protons and two charged pions: to select the $pp \to pp\pi^+\pi^-\pi^0$ reaction channel, a proper condition on the four-particle missing mass was imposed as $(M_{miss}^{pp\pi^+\pi^-})^2 = (M_{\pi^0})^2 \pm 3\sigma$, σ being determined from a fit to the π^0 peak. The missing-mass resolution was further improved with a kinematical refit of the full $pp \to pp\pi^+\pi^-\pi^0$ event [20]. Finally, the η mesons were identified in the two-proton missing-mass distribution shown on Figure 5. A prominent η peak, centered at the expected position, is clearly visible on top of a non-resonant three-pion background.

By fitting the pp missing-mass peak in various $\cos\theta_\eta^{CM}$ slices, the angular distribution of the η meson emission has been evaluated. It is shown in Figure 6 together with a simulation. Since matrix elements for the η production and decay are known, most of the degrees of freedom describing the $pp\pi^+\pi^-\pi^0$ final state are fixed. Together with the fact that the beam axis has rotational symmetry, only two angles are left for the alignment of the $pp\eta$ plane. It has been checked with simulations that these variables are almost independent, thus allowing to compare directly 1-dimensional angular distributions without any multidimensional acceptance corrections. Two models have been used in Figure 6: an isotropic eta decay and a decay using the anisotropy coefficient of $c_2 = -0.32 \pm 0.10$ found in [14] at nearly the same beam kinetic energy. Correcting by the isotropic function and fitting with a 2^{nd}-order Legendre polynomial $\frac{d\sigma}{d\Omega} = c_0[1 + c_2 L_2(\cos\theta)]$, a value of $c_2 = -0.14 \pm 0.09$ has been found, which is consistent within error bars with the previous result, showing that the hadron efficiency is understood as a function of phase space.

The reconstruction of the $pp \to pp\eta \to pp e^+e^-\gamma$ reaction was done with events triggered by the HADES LVL2 trigger. In a first step, events with two protons and two electron tracks were identified by means of the RICH – MDC – META detectors. The $pp \to e^+e^-\gamma$ reaction channel was identified by means of a condition imposed on the four-particle missing mass $(M_{miss}^{pp e^+e^-})^2 = 0 \pm 3\sigma$, σ being obtained from a fit to the photon peak. Figure 7 shows the proton-proton missing mass obtained after a kinematical refit was applied to the $pp e^+e^-$ events with the constraint on a missing photon. The prominent peaks centered at 137 and 546 MeV/c^2 correspond to the π^0 and η mesons, respectively. The reconstructed yield stems from two main meson decays: (a) direct meson (X) Dalitz decays of the type $X \to e^+e^-\gamma$ and (b) two-photon meson decays $X \to \gamma\gamma$ followed by pair conversion of one of the decay photons in the target or RICH radiator.

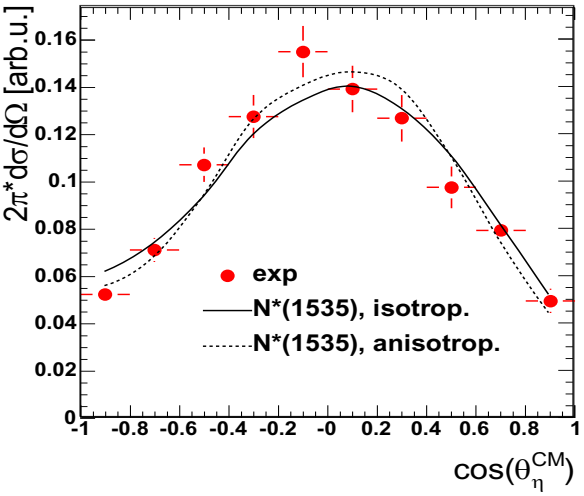


Figure 6: Distribution of the η center-of-mass polar angle for $\eta \to \pi^+\pi^-\pi^0$ events measured in $p+p$ reactions at 2.2 GeV. No correction for efficiency and acceptance is applied.

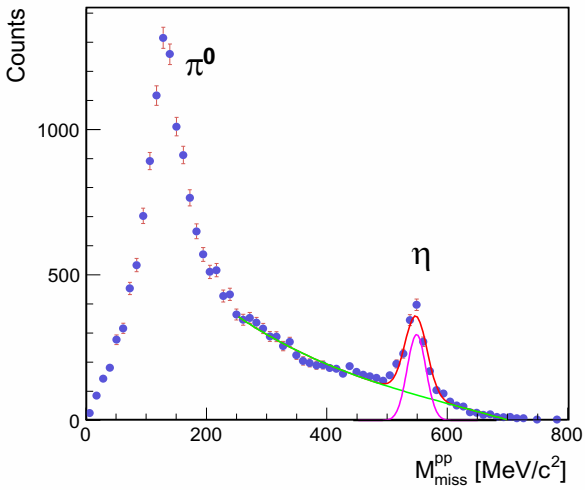


Figure 7: Proton-proton missing-mass distribution for $\eta \to e^+e^-\gamma$ events measured in pp reactions at 2.2 GeV. The η peak has been fitted with a Gauss function.

According to the simulation, the conversion contribution (b) dominates in the reconstructed η and $\pi 0$ yield ($\simeq 80\%$).

However, as the simulation also shows, it can be completely removed by conditions on χ^2 quality of the track reconstruction in the inner MDC planes and/or the pair opening angle. The analysis using the above-mentioned conversion rejection methods is currently on-going and final results are expected soon.

At this stage of the analysis one can compare the ratio R of the η yields reconstructed in the hadronic and electromagnetic decays (including conversion contribution) to the predictions of the simulation with the following results: $R^{EXP} = 21.4 \pm 1.6(stat) - 4.3(sys)$ and $R^{SIM} = 14.8 \pm 0.9(stat) + 0.5(sys)$. The large asymmetric systematic error quoted for the experimental ratio is due to the effect of the kinematical refit and is presently under investigation.

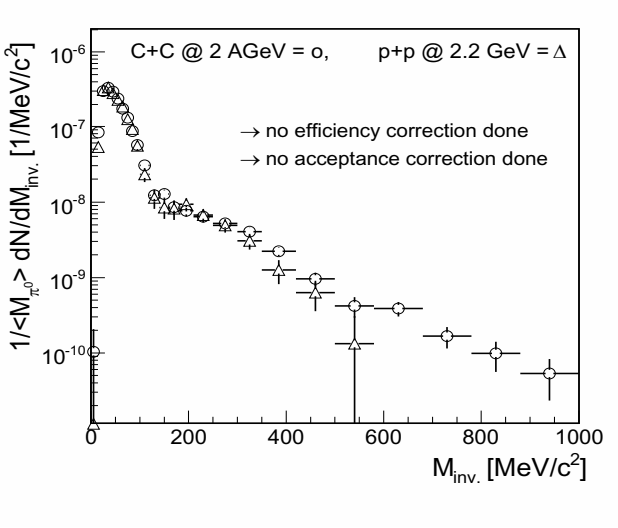


Figure 8: Raw invariant-mass distribution of unlike-sign signal pairs measured in pp collision at 2.2 GeV (open triangles) and C+C at 2 AGeV (open circles), normalized to the number of the pp LVL1 events. The pair distribution for C+C has been normalized to the π^0 yield as seen in p+p.

Inclusive pair production in pp collisions presents an important reference for HI collisions. Figure 8 shows (open triangles) the dielectron invariant-mass distribution obtained for pp collisions obtained with the high-resolution tracking and particle identification based on the "hard-cut" approach. In total, 10.100 pairs (9.400 for $M < 140$ and 700 for $140 < M < 600$) were reconstructed from 70% of the available statistics. The dielectron distribution has been normalized to the number of LVL1 triggers and has not been corrected for reconstruction efficiencies. It is compared to the pair distribution measured in 2 AGeV C+C (open circles) with normalization to the same yield in the π^0 region ($M < 140$ MeV/c^2). One can note that both distributions have similar shapes up to $M \simeq 350$ MeV/c^2, but for higher masses the pair yield measured in the C+C system systematically exceeds the one reconstructed in the pp system, though measured at a somewhat higher beam energy. However, final conclusions can be drawn only after application of full reconstruction efficiency corrections via a comparison to theoretical calculations filtered with the HADES acceptance and the trigger condition.

The collaboration gratefully acknowledges support by BMBF (06TM970I) and GSI (TM-FR1), GA CR 202/00/1668 and GA AS CR IAA1048304 (Czech Republic), KBN 5P03B 140 20 (Poland), INFN (Italy), CNRS/IN2P3 (France), MCYT FPA2000-2041- C02-02 and XUGA PGID T02PXIC20605PN (Spain), INTAS 03-51-3208 (EU), and, finally, an EU Access grant RII3-CT/506078.

References

[1] Hades collaboration, GSI Annual Report 2004.

[2] M.Kargalis, Pluto reference guide, GSI Report 2000-03.

[3] G. Agakishiev et al (CERES collaboration), Phys. Rev. Lett. 75 (1995) 1272.

[4] R. Averbeck et al. (TAPS collaboration), Z. Phys. A 359 (1997) 65.

[5] E. Bratkovskaya, W. Cassing, U. Mosel., Phys. Lett. B 424 (1998) 244.

[6] Hades collaboration, GSI Annual Report 2003.

[7] C. Sturm et al. (KAOS collaboration), Phys. Rev. Lett. 86 (2001) 39.

[8] S. Bass et al., Prog. Part. Nucl. Phys. 41 (1998) 225.

[9] The HADES acceptance filter can be obtained at http://www-hades.gsi.de.

[10] R. Holzmann (HADES collaboration), Proceedings of Quark Matter 2005 – Budapest 2005, to be published.

[11] P.Tlusty, Proceedings of XLII International meeting on Nuclear Physics – Bormio 2004, vol. 120.

[12] T. Wojcik, Proceedings of the XLIII Winter Meeting on Nuclear Physics – Bormio 2005, p. 295 and T. Christ, Proceedings of the 9^{th} ICATPP Conference – Como 2005 (World Scientific), to be published.

[13] R. J. Porter et al. (DLS collaboration), Phys. Rev. Lett. 79 (1997) 1229.

[14] F. Balestra et al. (DISTO collaboration), Phys. Rev. C 69 (2004) 064003.

[15] Particle Data Group, Phys. Rev. D 66 (2002).

[16] C. Amsler et al. (Crystal Barrel collaboration), Phys. Lett. B 346 (1995) 203.

[17] Landolt-Börnstein, New Series I/12b.

[18] Y. Pachmayer et al., GSI Annual Report 2004.

[19] S. Spataro, Proceedings of the XLIII Winter Meeting on Nuclear Physics – Bormio 2005.

[20] A. Rustamov, Proceedings of PANIC2005 – 2005 and A. Rustamov, Ph.D. thesis, TU Darmstadt 2006.

Search for kaonic clusters in p+CH_2/CD_2 reactions*

L. Fabbietti, P.Kienle, R.Krücken, K.Suzuki, TUM, Munich, Germany
for the FOPI Collaboration

A new exciting topic in nuclear physics has been investigated in different experiments that were aimed to look for the existence of deeply bound kaonic states. These states have been predicted by theory by means of a phenomenological K-nucleon potential [1] and then have been experimentally measured in K^- induced reactions [2, 3].
The formation of such states can also be investigated in heavy ion and elementary reactions at SIS energies to provide a solid evidence for the existence of such exotic states. A test experiment has been carried on during November 2005 for the reaction $p + CH_2/CD_2$ at 3.5 GeV to study the feasibility of the measurement of the state ppK^- using the FOPI spectrometer. Out of the p+n or p+p interaction, the formation of the ppK^- state can occur and then decay into the Λ-p channel.

$$p + n \rightarrow ppK^- + K^0 \rightarrow \Lambda + p + K^0 \quad (1)$$

$$p + p \rightarrow ppK^- + K^+ \rightarrow \Lambda + p + K^+ \quad (2)$$

Equation 2 shows two possible decay chains where the ppK^- is produced together with a kaon. One can see that the selection of such events strongly depends on the reconstruction capability for Λ and $K^{+,0}$ at the same time.
To enhance the resolution of the secondary vertex reconstruction, a silicon detector array has been installed around the target region 1. This detector is also meant to help in the tagging of very slow particles ($p_T < 100\ MeV/c$) that cannot be tracked in the FOPI CDC tracking detector.
The silicon array consists of 6 Eurisys double sided detectors,

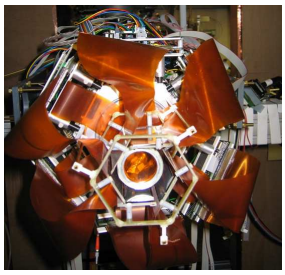


Figure 1: View of the installed silicon detector.

500 μm thick with an active area of $64 \times 25\ mm^2$. The array geometry has been configured such to achieve with the silicon detector the same phase space acceptance for the K^0 decay products as the CDC detector. The strips granularity corresponds to a resolution of about 0.5 mm in both the Z and the azimuthal angle coordinates. The readout electronics has been adopted in Munich on the basis of the modules developed for the R3B project (S248). These consist of a 64-channel preamplifier board (AMPLEX/GASSIPLEX) and a highly integrated digital data concentrator board. The whole detector readout was integrated into the MBS system with SAM3 GTB readout and achieved a rate of about 1 KHz by a multiplicity of 500 channels (50% occupancy). The energy range of the p and n side of the detectors has been set to detect slow particles with a maximal energy loss of 6 MeV. Figure 2 shows the energy distribution on the p and n side collected during the nov05 beam time. This translates into a gain of 22 $KeV/chan$ and 6 $KeV/chan$ for the p and n side respectively.
During the test experiment about $100 * 10^6$ events have been collected and a preliminary online analysis has estimated a multiplicity of reconstructed $K^0 s$ and K^+ in the CDC of $4 * 10^{-4}$/evt and $3 * 10^{-4}$/evt respectively. Figure 3 shows one event seen with the

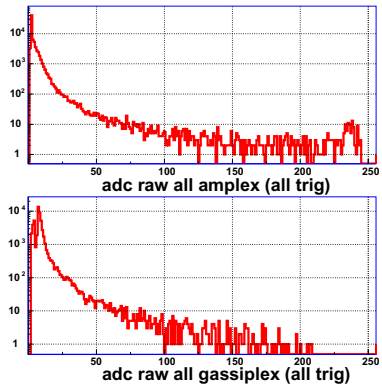


Figure 2: Raw data from the (top) p and (bottom) n side of the silicon detector.

CDC-silicon monitor, where the tracks reconstructed in the CDC can be traced down and matched with the silicon p-n hits. The ongoing correlation analysis will show whether the additional detector can improve the signal to background ratio in the K^0 and Λ reconstruction.

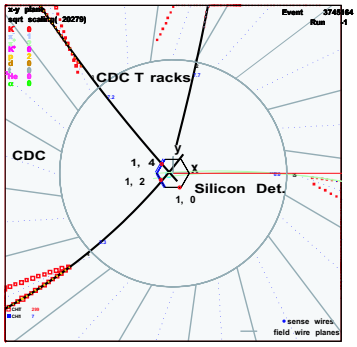


Figure 3: Online monitor for the CDC-Silicon correlations.

References

[1] Y. Akahishi and T. Yamazaki, Phys. Rev C 65 (2002) 044005.
[2] T. Suzuki et al., Phys. Lett B 597 (2004) 263.
[3] M. Agnello et al., Phys. Rev Lett. 94 (2005) 212303.

* Work supported by GSI TM/KR1

Strangeness production using a π^- beam at 1.15 GeV/c with FOPI

M.L. Benabderrahmane[1],N. Herrmann[1],Y.J. Kim[2],Y. Leifels[2]and the FOPI Collaboration
[1]Physikalisches Institut, Universität Heidelberg, Germany,[2]GSI, Darmstadt, Germany

In August 2004, for the first time, a π^- beam was delivered to the FOPI detector. During 15 days of beam time, altogether about 40 million events were collected for five targets: C, Al, Cu, Sn and Pb. The beam momentum was 1.15 GeV/c with an intensity of about 10^4 π^-/s .
At SIS energies, one of the important channels of kaon production for which the cross section in the nuclear medium is poorly known, is $\pi^- N \rightarrow YK$. The relevant cross sections were calculated theoretically by Tsushima et al. [1] in free space ($\rho = 0$) and at different nuclear matter densities. The aim of the experiment is to study the reaction $\pi^- A \rightarrow YK$ in order to extract the exclusive cross section of the elementary process $\pi^- p \rightarrow \Lambda K^0$ inside the nucleus and to compare it to theoretical predictions.
As a first step the inclusiveK^0-production cross section is analyzed. With the FOPI detector, we can only reconstruct the K^0_S that decays into ($\pi^-\pi^+$) pairs with a branching ratio of 68 %. For the current analysis only those K^0_S are reconstructed, for which both decay pions are registered in the central drift chamber (CDC). In order to extrapolate the reconstructed K^0_S to the primary 4π yield the detector efficiency has to be determined. The estimation of the acceptance-bias is model dependent. Hence, it is mandatory to compare the measured phase-space distribution inside the acceptance to the distribution resulting from model which was used for deducing the efficiency. The IQMD transport model [2] and the Geant3 based description of the FOPI experiment, was used in this case. In Fig. 1 the measured K^0_S rapidity distribution is shown in comparison to IQMD model calculations for the Pb target. In general, within the statistical errors the experimental and model-distributions agree very well. In the case of the carbon and lead targets the total K^0 reconstruction efficiency was found to be about 9%. In order to improve the signal-background ratio, a set of selection cuts is used. The transverse distance of $\pi^\pm$ tracks to the nominal vertex ($d^{\pi^\pm}_\perp > 1.5cm$) and the pointing angle of the mother particle with respect to that vertex ($\Delta\varphi < 30°$) are the most relevant among them. With this selection criteria a reconstruction efficiency of 1.2% is obtained at a signal to background ratio of typically 2 : 1. Under those conditions the inclusive $\pi^- A \rightarrow K^0 X$ reaction cross section is shown in Fig. 2 as a function of the number of protons Z of the target nucleus. One can parameterize the cross section according to a power law function like $\sigma = a \cdot Z^b$. The error bars of the cross sections are statistical only. Originating from typically several hundreds K^0_S-candidates (in Cu and Sn targets) and about thousand K^0_S-candidates (in C and Pb targets). In order to extract the cross section for the inclusive elementary channel $\pi^- p \rightarrow K^0 X$ process inside the nucleus, one has to separate the $\pi^- n \rightarrow K^0\Sigma^-$ reaction that is included in the cross section of Fig. 2. This will be attempted by the simultaneous analysis of the Λ production cross section that is currently in progress. In addition the K^+ production is being analyzed that exclusively tests the $\pi^- p \rightarrow K^+\Sigma^-$ reaction cross section.

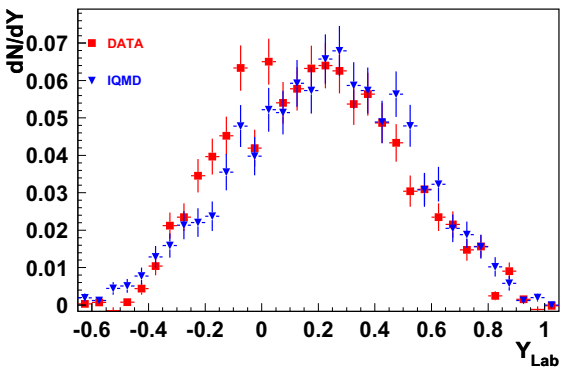


Figure 1: The phase space distribution of the K^0_S from the lead target, the square points are from data, triangle points are from IQMD calculations.

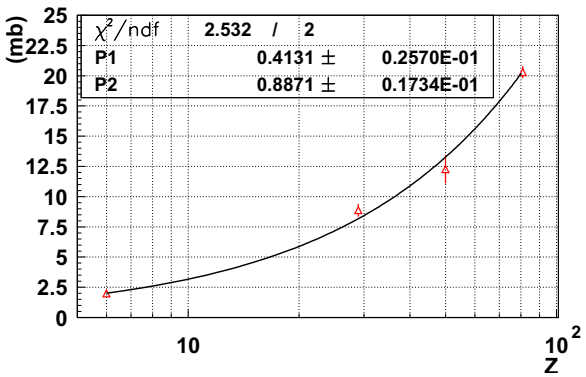


Figure 2: Inclusive K^0 reaction cross section as a function of charge number Z of the target nucleus.

References

[1] K. Tsushima, A. Sibirtsev, A.W. Thomas, Phys. Rev. C62 (2000) 064904; K. Saito, K. Tsushima, A.W. Thomas hep-ph/0506314

[2] C.Hartnack et al. Eur.Phys.J.,A1:151-169,1998

K^+/K^0 ratio in $^{96}_{44}$Ru+$^{96}_{44}$Ru and $^{96}_{40}$Zr+$^{96}_{40}$Zr collisions at 1.528 AGeV

X. Lopez[1], Y.J. Kim[1], M. Merschmeyer[2] and the FOPI Collaboration
[1]GSI, Germany, [2]Physikalisches Institut, Heidelberg, Germany

The equation of state of the asymmetric nuclear matter at baryonic density ρ_B and isospin asymmetry α is usually described as follows [1]:

$$E(\rho_B, \alpha) = E(\rho_B, \alpha = 0) + E_{sym}(\rho_B)\alpha^2 + O(\alpha^4) \quad (1)$$

where E_{sym} is the nuclear symmetry energy and α the asymmetry parameter which corresponds to the ratio:

$$\alpha = \frac{\rho_n - \rho_p}{\rho_n + \rho_p}. \quad (2)$$

Predictions based on various many-body theories diverge widely especially at high density [1, 2]. In fact, at densities $\rho \geq 3\rho_0$, even the sign of the symmetry energy is still uncertain.

We analysed collisions $^{96}_{44}$Ru+$^{96}_{44}$Ru and $^{96}_{40}$Zr+$^{96}_{40}$Zr with an asymmetry parameter α of 0.083 and 0.167, respectively. The incident energy of 1.528 AGeV corresponds to the threshold energy of K^+ and K^0 production. The K^+/K^0 ratio is predicted to be sensitive to the hot and dense system created during the earlier stage of the collision [2]. Details on the identification of K^+ and on the reconstruction of K^0 are provided in [3, 4].

The experimental ratio obtained in this analysis is:

$$\frac{(K^+/K^0)_{Ru}}{(K^+/K^0)_{Zr}} = 1.127 \pm 0.21. \quad (3)$$

This ratio is compared with model predictions based on the Relativistic Mean Field theory (RMF) [2, 5]. Two types of calculations are shown in Fig. 1. The first calculation has been performed under the assumption of an infinite nuclear matter (INM, full symbols) [2]; the second type, more realistic, discribes a finite system (HIC, heavy ion collision, open symbols) [5]. The differences between the INM and HIC calculations are obvious. In the INM calculations the system is in equilibrium (chemical, thermodynamical, isospin), in HIC it is not. In particular, particles could escape, which influences the isospin content of the fireball. Thus one should not expect that INM and HIC will provide the same results for kaons yields. A more equilibrated ratio due to isospin mixing in the collision is expected from the HIC calculation. The calculations done whith the HIC assumption have been done explicitely for Ru+Ru and Zr+Zr systems, while INM calculations are taken from [2]. This explains the differences observed on the statistical errors in the 2 different scenarios.

Different assumptions of the symmetry energy are taken into account in both scenarios of the collision [2, 5]. The non-linear Walecka model [2] (NL, illustrated by circles in Fig. 1) represents the prediction of the model using a soft symmetry energy. Calculations labeled NLρ (squares) and NL$\rho\delta$ (triangles) show the expectation of the model including the vector part (ρ) and the vector and scalar part ($\rho + \delta$) of the isovector, respectively, representing assumptions of a stiff and stiffer asymmetric behaviour of the symmetry energy [2].

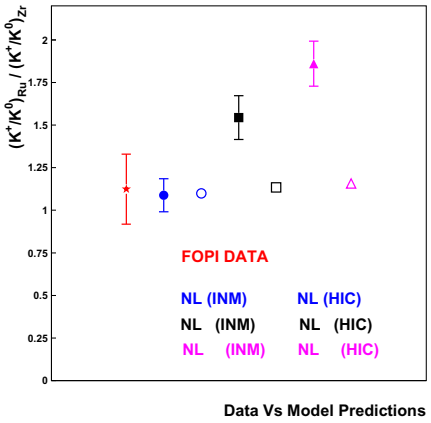


Figure 1: *Experimental ratio* $\frac{(K^+/K^0)_{Ru}}{(K^+/K^0)_{Zr}}$ *(star) and theoretical predictions (see text for more details).*

The trend of the ratio $\frac{(K^+/K^0)_{Ru}}{(K^+/K^0)_{Zr}}$ predicted with the two different scenarios is the same within the 3 different assumptions of the symmetry energy. An enhancement of the ratio is observed for a stiff and stiffer symmetry energy. But while this enhancement from the NL to NL$\rho\delta$ assumptions is very large for the INM scenario ($\sim$70%), it is rather small for a more realistic description (HIC, $\sim$5%). The comparison of the experimental ratio (star in Fig. 1) to the INM calculations shows that the NL model is closest to the experimental point. However, within the experimental uncertainity, one cannot conclude for the HIC scenario which assumption on the symmetry energy describes best the experimental data. A sensitivity of 5% between the two extreme cases, NL and NL$\rho\delta$, is too small to make this observable a possible probe of the isospin contribution to kaon production.

References

[1] B. an Li, Phys. Rev. C 71, 014608 (2005).

[2] G. Ferini, M. Colonna, T. Gaitanos, M. Di Toro, Nucl. Phys. A 762, 147 (2005).

[3] P. Crochet *et al.*, Phys. Lett. 486, 6 (2000).

[4] X. Lopez, M. Merschmeyer and the FOPI Collaboration, GSI-Report 2005-1 p125.

[5] T. Gaitanos, Private Communication (2005).

Recent results from the NA49 experiment

C. Alt[1], C. Blume[1], P. Dinkelaker[1], D. Flierl[1], V. Friese[2], M. Gaździcki[1], C. Höhne[2], S. Kniege[1], M. Kliemant[1], B. Lungwitz[1], M. Mitrovski[1], M. Otto[1], R. Renfordt[1], A. Sandoval[2], T. Schuster[1], R. Stock[1], C. Strabel[1], H. Ströbele[1], and the NA49 Collaboration

[1]Fachbereich Physik der Universität Frankfurt, [2]GSI Darmstadt

Energy dependence of hyperon production

One of the most interesting results from the NA49 energy scan program at the CERN SPS is an anomalous behaviour of the energy dependence of the $\langle K^+\rangle/\langle\pi^+\rangle$-ratio in central Pb+Pb reactions [1]. Also, results on the energy dependence of K^-- ϕ-, Λ-, $\bar{\Lambda}$-, and Ω-production have been reported [2, 3, 8]. The question whether all strange particles exhibit rapid changes in their yield relative to pions and what is the physics origin of these observed changes [4, 5], is of particular interest.

In order to complete the picture, a systematic study of the Ξ-production as function of beam energy and system size has been started. Figure 1 shows a preliminary result for the Ξ^-- and $\bar{\Xi}^+$-yield at mid-rapidity for the beam energies 20A, 30A, 40A, 80A, and 158A GeV, compared to data at higher energies as measured by the STAR collaboration [6]. While the $\bar{\Xi}^+$-yield is strongly rising in the SPS energy regime, the Ξ^--yield does not exhibit a very pronounced energy dependence over the depicted range of beam energies. With increasing beam energy $\bar{\Xi}^+$- and Ξ^--yields are getting closer as the the net-baryon density at mid-rapidity is approaching zero.

High-p_t spectra of identified particles

At RHIC energies an enhancement of the baryon/meson ratio above unity at higher p_t has been observed. This result was interpreted in terms of quark coalescence models, thereby implying that at these beam energies free quarks

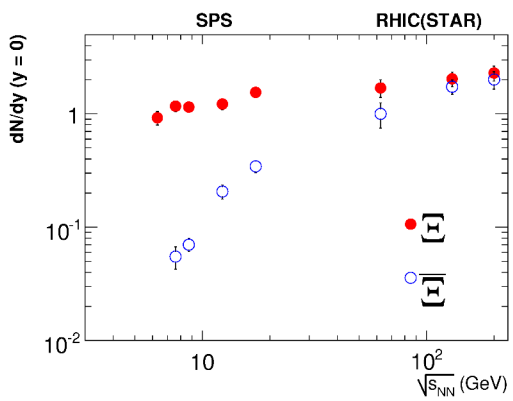


Figure 1: The Ξ^- and $\bar{\Xi}^+$ yields at mid-rapidity, measured by NA49 and STAR as a function of $\sqrt{s_{NN}}$.

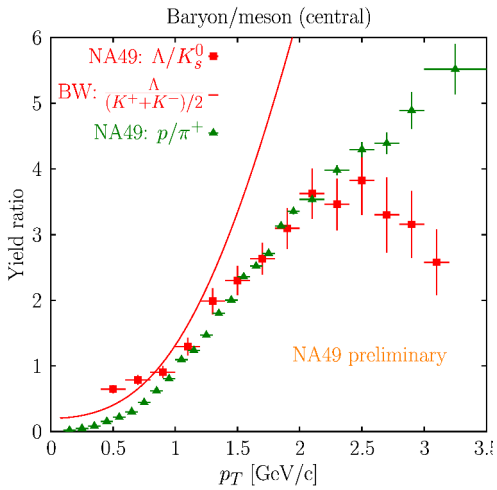


Figure 2: The baryon/meson ratio as a function of p_t. Shown are the Λ/K^0_s- and the p/π^+-ratio for central Pb+Pb collisions at 158A GeV (23.3% and 5% most central, respectively).

are the relevant degrees of freedom. A large statistics data set for central Pb+Pb reactions, taken by NA49 in 2000, allowed a similar study for top SPS energies [7]. As shown in Fig. 2 a similar rise of the baryon/meson ratio can also be observed here. The Λ/K^0_s-ratio, as well as the p/π^+-ratio, is steeply rising in the p_t-range of 1-2 GeV/c and cross unity around 1 GeV/c. While this behaviour is qualitatively the same for Λ/K^0_s and p/π^+ below 2 GeV/c there is an indication for a different p_t-dependence above. Also shown in Fig. 2 is the expectation from a hydrodynamically inspired blast wave model (solid line), which, however, does not describe the data above p_t = 1 GeV/c.

System size dependence of 2-pion correlations

The extraction of radius parameters from two-particle correlation functions are a well established technique to obtain information about the particle emitting source in space and time. NA49 has analysed two-pion correlations in central Pb+Pb collisions at beam energies from 20A to 158A GeV [8]. Our results confirm that from AGS to RHIC energies the transverse size parameters of the pion emitting source vary little although the number of produced pions

increases by a factor of 20. This intriguing finding asks for more differential experimental data which may help to find a consistent interpretation of the extracted size parameters. In this spirit we have extended the two-pion correlation analysis to Pb+Pb collisions at different centralities. Minimum bias Pb+Pb events obtained at 40A and 158A GeV were divided into 6 centrality classes according to the enery carried by the projectile spectators as measured by our Veto calorimeter. Class 1 corresponds to the 5% fraction of the most central collisions. The other fractions are 5 to 12.5%, 12.5 to 23.5%, 23.5% to 33.5%, 33.5 to 43.5%, and $>$ 43.5%. Details of the analysis procedure can be found in [9]. The results are summarised in Fig. 3. It shows the variation of the three radius parameters $R_{\rm side}$(upper), $R_{\rm out}$(middle) and $R_{\rm long}$(lower) with centrality the latter being quantified by the mean number of nucleons participating in the collision ($\langle N_{\rm part}\rangle$). The dots represent the 40A GeV and the triangles the 158A GeV data. The $R_{\rm side}$ values are the same at both beam energies for all centralities. $R_{\rm out}$ has a close to linear dependence on centrality with a smaller slope for the 158A GeV than for the 40A GeV data. This results in a slighly lower value of $R_{\rm out}$ at 158A GeV than at 40A GeV in central collisions. $R_{\rm long}$ increases from 40A GeV to 158A GeV by roughly 15% at all centralities. All three functional dependences extrapolate to finite radius parameters ($R \approx 2$ fm) at $\langle N_{\rm part}\rangle = 0$.

References

[1] M. Gaździcki (for the NA49 collaboration), J. Phys. **G 30** (2004), S701.

[2] V. Friese et al. (for the NA49 collaboration), J. Phys. **G 31** (2005), s911.

[3] C. Blume et al. (for the NA49 collaboration), J. Phys. **G 31** (2005), s685.

[4] J. Cleymans, H. Oeschler, K. Redlich, S. Wheaton, [axXiv:hep-ph/0510283].

[5] M. Gaździcki and M.I. Gorenstein, Acta Phys. Polon. **B 30** (1999), 2705.

[6] S. Salur et al. (for the STAR collaboration), [arXiv:nucl-ex/0509036].

[7] A. Laszlo and T. Schuster (for the NA49 collaboration), [arXiv:nucl-ex/0510054].

[8] C. Alt et al. (NA49 collaboration)., GSI-Report 2004, NQMA-EXP-14.

[9] C. Alt, Diplomarbeit 2005, Universität Frankfurt.

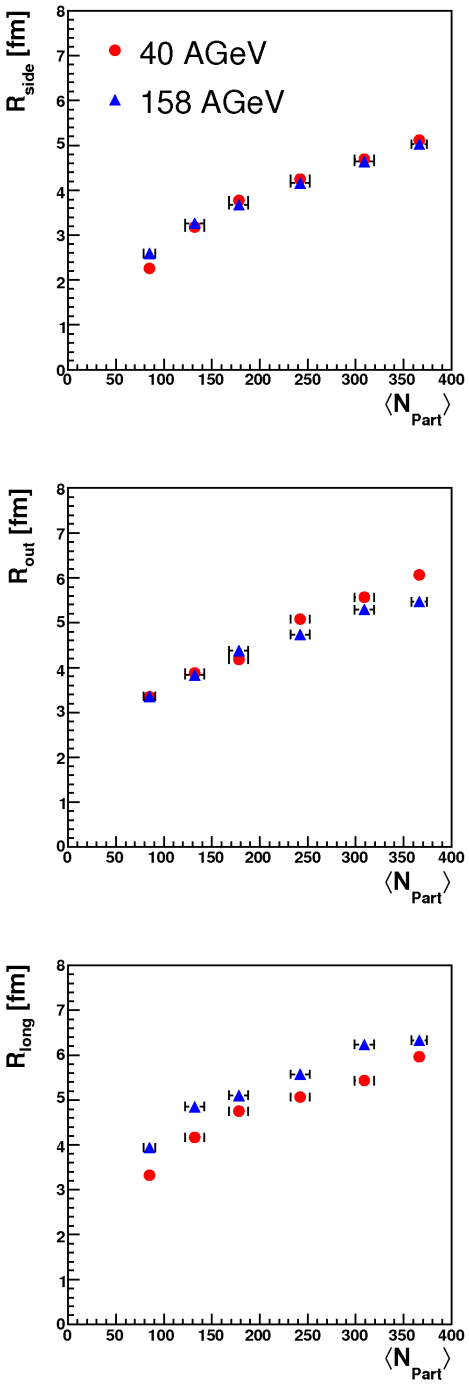


Figure 3: Radius parameters as function of number of participant nucleons as measured in minimum bias Pb+Pb collisions at 40A and 158A GeV.

Production of φ mesons in central Pb+Pb collisions at SPS energies

V. Friese, GSI, Darmstadt, Germany
for the NA49 collaboration

Abstract

The NA49 experiment has measured φ production in central Pb+Pb collisions at the CERN SPS at beam energies from 20 to 158 AGeV. We present preliminary results on the energy dependence of tranverse spectra as well as of the mean multiplicities.

.

Strangeness production in heavy-ion collisions is believed to give insight into the collision dynamics. The φ meson is of special interest due its s-anti-s quark content. Being strangeness-neutral as a hadron, it should be sensitive to whether the strangeness content is determined on a partonic or hadronic level.

NA49 [1] is a fixed-target hadron spectrometer operated at the CERN-SPS. Previously, the NA49 experiment has reported on φ production in central Pb+Pb collisions at 158 AGeV beam momentum [2]. This measurement has been extended towards lower beam energies in the context of the NA49 energy scan programme.

The φ meson is measured via its decay into charged kaons (branching ratio 49.1 %). The daughter kaons are detected in the MTPCs; kaon candidates are selected based on the energy loss measurement in the TPC gas. The ±1.5 σ selection results in a 75 % identification efficiency for the pair.

The φ signal was obtained by calculating the invariant mass of all combinations of oppositely charged kaon candidates. The combinatorial background was reconstructed by event mixing and subtracted. The φ yield is then obtained from a fit of a relativistic Breit-Wigner distribution, folded with the detector resolution, to the background-subtracted spectrum. This procedure is done differentially in p_t, integrated over a large rapidity range, and in rapidity. By extrapolation of the rapidity distribution to full phase space, the φ multiplicity is obtained.

The acceptance corrections are calculated by a GEANT3 based simulation of the decay $\varphi \rightarrow K^+K^-$ in the NA49 detector system. For the track selection applied, track density effects are negligible. The acceptance covers forward rapidities and transverse momenta from 0 to 2.1 GeV. Typically, about 20 % of the decays are reconstructed. Additional correction factors take into account the branching ratio and the kaon identification efficiency.

The transverse momentum distributions were fitted by thermal distributions. Figure 1 shows the extracted inverse slope parameters as a function of collision energy. They exhibit a plateau-like behaviour in the measured energy range, except for top SPS energy. This resembles the observations reported for pions, kaons and protons, which can be interpreted as a signal of the mixed phase of a first order phase transition at SPS energies [3].

The energy dependence of the integrated φ multiplicity, normalised to the pion multiplicity, is shown in figure 2. The excitation function is similar to that observed for the K^- [4]. The full equilibrium hadron gas model [5] overestimates this ratio from low SPS energies on, similar to the K/π ratio. Statistical models allowing for strangeness undersaturation parameter γ_s [6] seem to account better for the data. In contrast, the hadron-string transport model UrQMD strongly underpredicts the φ yield at all energies. In comparison to proton-proton collisions, the φ/π ratio shows an enhancement of a factor of about three at AGS and SPS energies.

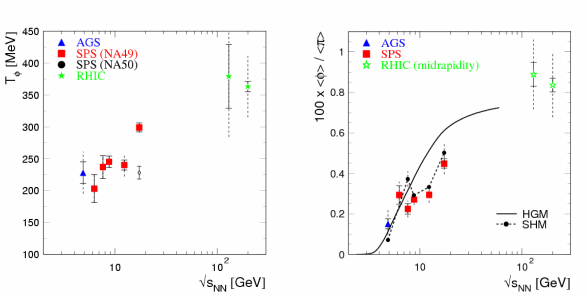


Figure 1: Energy dependence of (left) the φ inverse slope parameter and (right) the φ/π ratio in central A+A collisions. The data are compared to the results of the statistical hadron gas models with strangeness equilibrium [4] (full line) and with strangeness undersaturation [5] (dotted line).

The fact that the φ meson seems to be sensitive to strangeness enhancement and/or to the strangeness undersaturation parameter γ_s suggests that the strangeness content in the heavy-ion reaction is determined in a partonic stage. This conclusion is strengthened by the failure of hadronic transport models to describe the measured yields.

References

[1] S. Afanasiev *et al.* (NA49 collaboration), Nucl. Instr. and Meth. A 430 (1999) 210.
[2] S. Afanasiev *et al.* (NA49 collaboration), Phys. Lett. B 491 (2000) 59.
[3] M. Gazdzicki for the NA49 collaboration, J. Phys. G 30 (2004) S701
[4] V. Friese for the NA49 collaboration, J. Phys. G 31 (2005) S911
[5] P. Braun-Munzinger *et al.*, Nucl. Phys. A 697 (2002) 902.
[6] F. Becattini et al., Phys. Rev. C 69 (2004) 024905

Charged particle multiplicity in Pb+Au collisions at 158 GeV per nucleon

D. Miśkowiec, GSI, Darmstadt, Germany (CERES)

The absolute multiplicity of charged particles in Pb+Au collision events at a beam energy of 158 GeV per nucleon, recorded by the CERES experiment at the CERN SPS, was determined by counting correlated hits in the two silicon drift detectors (SD) located 100 mm and 138 mm downstream from the target. The analysis was done in bins of pseudorapidity and centrality, and was entirely data driven (no Monte Carlo). The main steps, random background subtraction, two-track efficiency correction, and delta electron correction, are briefly described below.

In order to distinguish genuine particle tracks from accidental hit coincidences the Θ coordinates of all SD1-SD2 hit combinations with $\Delta\phi < 0.2$ were translated to vertex positions along the beam z. The obtained z-distribution shows a narrow target peak sitting on a broad background of random hit combinations, the latter being perfectly reproduced by a distribution obtained with one of the detectors rotated (Fig. 1). The multiplicity $dN_{ch}/d\eta$ was calcu-

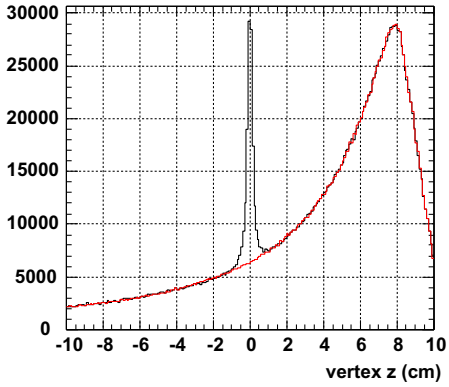


Figure 1: Vertex z distribution for hit pairs SD1-SD2.

lated by dividing the integral of the peak by the number of analyzed events.

The procedure, described above, was repeated requiring that the hits have no neighbours within certain Δr and $\Delta\phi$. The multiplicities $dN_{ch}/d\eta$, obtained for a fixed $\Delta\phi$, turn out to depend exponentially on Δr. The extrapolation to $\Delta r = 0$ gave the multiplicity corrected for two-track efficiency; the result was independent on the choice of $\Delta\phi$.

The delta electrons were estimated from the special run with a trigger on each beam particle rather than on nuclear interaction. The result was 16 electrons on average into the η interval from 2 to 3. Half of this was then subtracted from the interaction data to account for electrons knocked out of the targets preceding the one in which the interaction occured.

An example of a pseudorapidity distribution of charged particles obtained for one centrality bin is shown in Fig. 2.

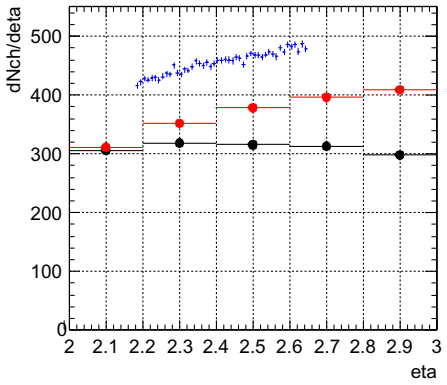


Figure 2: Pseudorapidity distribution of charged particles in the 5% most central Pb+Au collisions at 158 GeV per nucleon: raw (bottom) and corrected for two-track efficiency (middle). For comparison, the charged tracks measured in the TPC, which include resonance decay products, are shown (top).

The distribution can be parametrized by fitting a Gaussian centered at 3.1 where, according to event generators, the maximum should be located for this beam energy. The centrality dependence of the maximum dN_{ch}/dy, shown in Fig. 3, is in a reasonable agreement with NA57 and NA50. The systematical error, estimated by varying parameters of the analysis and combining the maximum observed deviations squared, is 12%.

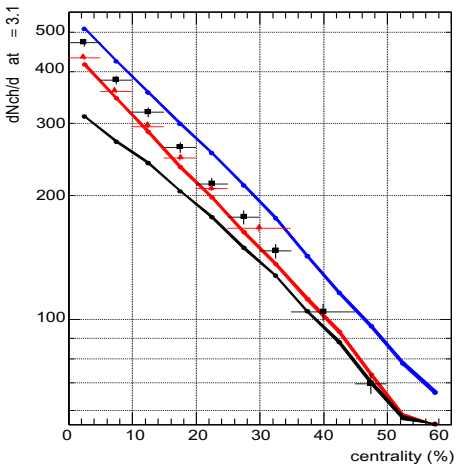


Figure 3: Centrality dependence of the $dN_{ch}/d\eta$ at $\eta = 3.1$. The bottom, middle, and top curves represent the raw, the two-track efficiency corrected, and, for comparison, TPC track multiplicities, respectively. The full squares and triangles represent the data of NA57 and NA50 and should be compared with the middle line.

Multiplicity fluctuations in nuclear collisions at 158A GeV

C. Alt[1], C. Blume[1], P. Dinkelaker[1], D. Flierl[1], V. Friese[2], M. Gaździcki[1], C. Höhne[2], S. Kniege[1], M. Kliemant[1], B. Lungwitz[1], M. Mitrovski[1], M. Otto[1], R. Renfordt[1], A. Sandoval[2], T. Schuster[1], R. Stock[1], C. Strabel[1], H. Ströbele[1] for the NA49 Collaboration and E. Bratkovskaya[3] and M. Gorenstein[3] for the HSD and UrQMD Collaboration

[1]Fachbereich Physik der Universität Frankfurt, [2]GSI Darmstadt, [3]Frankfurt Institute for Advanced Studies

Multiplicity fluctuations in nuclear collisions are dominated by an event-by-event variation of the number of nucleons participating in a collision, N_P. This is caused by the fluctuations of the initial states of the colliding nuclei and probabilistic character of an interaction process. The fluctuations of N_P form usually a large and uninteresting background. In order to minimize its contribution NA49 at the CERN SPS selected samples of nuclear collisions with fixed numbers of projectile participants, N_P^{proj} [1].

This selection is possible due to measurement of the spectator energy in each individual collision by use of a forward calorimeter. However, even in the samples with $N_P^{proj} = const$ the number of target participants fluctuates considerably. Hence, an asymmetry between projectile and target participants is introduced. It was recently proposed [2] to use this difference to locate the final state flows related to the projectile and the target. Qualitatively, one expects large multiplicity fluctuations in the domain related to the target and small fluctuations in the domain related to the projectile. When both flows are mixed intermediate fluctuations are predicted. The whole procedure is presented in a graphical form in Fig. 1. Clearly, the fluctuations measured in the target momentum hemisphere are larger than those measured in the projectile hemisphere in transparency (T-)models. The opposite relation is predicted for reflection (R-)models, whereas for mixing (M-)models the fluctuations in the projectile and target hemispheres are the same. The difference between these approaches are expected to be the largest for semi-peripheral collisions of heavy nuclei, where the relative fluctuations of N_P^{proj} reach a maximum. The NA49 results on scaled variance of multiplicity fluctuations ($V(n)/\langle n\rangle \equiv (\langle n^2\rangle - \langle n\rangle^2)/\langle n\rangle$) in Pb+Pb and p+p interactions at 158A GeV are presented in Fig. 2. The measurements were performed for negatively charged hadrons in the projectile rapidity domain ($1.1 < y_{cm} < 2.6$). The scaled variance increases with decreasing number of projectile participants, N_P^{proj}. A comparison with the predictions for the T-, M- and R-models suggests a large degree of mixing of projectile and target flows, as expected in approaches assuming a significant thermalization of the matter at early stage of collisions.

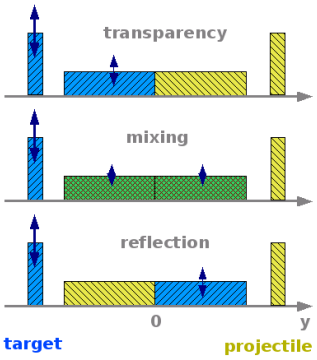


Figure 1: The sketch of the rapidity distributions of the particle production sources (horizontal rectangles) in nucleus-nucleus collisions resulting from the transparency, mixing and reflection models [2]. The spectator nucleons are indicated by the vertical rectangles. In collisions with the fixed number of projectile spectators only matter related to the target shows significant fluctuations (vertical arrows).

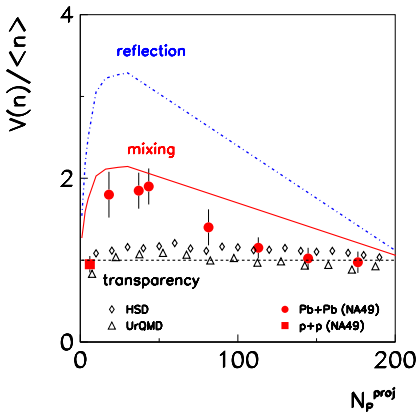


Figure 2: The dependence of the scaled variance of negatively charged particle multiplicity on N_P^{proj} measured in Pb+Pb (circles) and p+p (square) interactions at 158A GeV in comparison to models.

The string-hadronic models, HSD and UrQMD, follow [3] the trend expected for the transparency scenario (see Fig. 2) and thus they under-predict the measured fluctuations for peripheral Pb+Pb collisions.

References

[1] M. Rybczynski *et al.* [NA49 Collaboration], J. Phys. Conf. Ser. **5**, 74 (2005).

[2] M. Gazdzicki and M. Gorenstein, arXiv:hep-ph/0511058.

[3] V. P. Konchakovski, S. Haussler, M. I. Gorenstein, E. L. Bratkovskaya, M. Bleicher and H. Stocker, arXiv:nucl-th/0511083.

Pion-proton correlations in central Pb+Au collisions at 158 AGeV

D. Antończyk, GSI, Darmstadt, Germany
for the CERES collaboration

The two-dimensional pion-proton correlation functions were analyzed in the central Pb+Au collision data taken by CERES at the top SPS energy. The correlations between the same- and the opposite-sign particles exhibit a minimum and a peak, respectively, at low relative momentum $q := p_2 - p_1$, caused by the mutual Coulomb interaction. A difference between the average freeze-out position or time of two particle species reveals itself as an asymmetry of the correlation function at small q [1]. The high statistics of the CERES data set and the power of the two-dimensional analysis allow to study how the observed displacement between the sources of pions and protons evolves with the transverse momentum.

The CERES spectrometer at the CERN SPS was upgraded in 1998 with a cylindrical Time Projection Chamber (TPC), which allows to measure charged hadrons and leptons with the momentum resolution of $\Delta p/p = 2\% \oplus 1\% \cdot p/\mathrm{GeV/c}$. For the analysis presented here mainly information from the TPC were used. More detailed information about experimental setup one will find in [3, 4].

In the 2000 run about 32 millions central Pb+Au collision at energy of 158 AGeV events were recorded. A subset of this statistics was used in this analysis (about 23 M). The tracks chosen for the analysis came mainly from the vertex and fulfill a set of cuts. To avoid inefficiency due to the two-track resolution a minimum opening angle requirement was applied to pairs from the signal and the background distribution. Background distribution was generated using event mixing. Only events with similar centrality and originating from the same reaction target were mixed. Particle identification was based on the information from the TPC. The correlation functions were calculated for $\pi^-\pi^+$, $\pi^- p$, and $\pi^+ p$ pairs in the pair center of mass frame in five bins of pair transverse momentum. In this frame, variables $q_\parallel$, $q_\perp$ are defined as $q_\parallel = q_{out}$, $q_\perp = \sqrt{q_{side}^2 + q_{long}^2}$, where q_{out}, q_{side}, q_{long} are the well-known components of the Bertsch-Pratt coordinate system [2]. Two-dimensional histograms $n(q_\perp, q_\parallel)$ for the signal and background distribution were projected in the direction parallel to the pair momentum with condition on $q_\perp \in \{0, 50\}$ MeV. Projection results were divided to obtain a one-dimensional correlation function. For the quantitative parameterization of the asymmetry, a Lorentz curve with two widths was fitted to the spectra. The asymmetry is defined as the ratio between these two widths.

The clearly visible asymmetry in the pion-proton correlations indicates that the proton source on average is located at a larger radius than the pion source or that protons are emitted earlier than pions. The preliminary result on the asymmetry as a function of the transverse momentum is shown in Fig. 1. The straight solid line is a fit to the data points. It points to unity at $p_\perp = 0$ as expected from symmetry consideration.

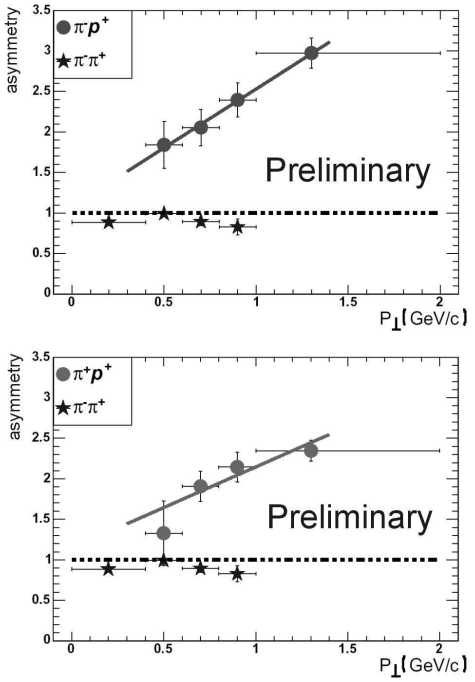


Figure 1: The pair transverse momentum dependence of the asymmetry for the pion-proton pairs and the comparison with the unlike pion pairs.

In order to study the asymmetry as a function of the displacement between particle sources a Monte-Carlo generator was written. Simulation shows that the best agreement with the data was obtained for the displacement between pion and proton sources equal to about 6.5 fm. This result is similar to the value observed by STAR [5]. A more quantitative analysis of the asymmetry is in progress.

References

[1] R.Lednický et al., Phys. Lett. B373 (1996) 30.

[2] G.F.Bertsch, Nucl. Phys. A498 (1989) 173c.

[3] A.Marín et al., Nucl.Phys. A661 (1999) 673c.

[4] D.Miśkowiec, Proceedings of QM2005, Budapest, Hungary.

[5] F.Retière for the STAR collaboration, arXiv:nucl-ex/0212026v1.

Scale dependence of mean transverse momentum fluctuations at 158 AGeV

G. Tsiledakis, GSI, Darmstadt, Germany
for the CERES collaboration

Non-statistical event-by-event fluctuations of mean transverse momentum, p_T, have been proposed as a possible signature for the QCD phase transition, in particular for the critical point. A surprising finding was that a small but practically beam energy independent value was found for the broad energy range of 40 AGeV SPS beam up to top RHIC energy [1]. On the other hand, the fluctuations seem to be a non-monotonic function of centrality [2].

Since fluctuations were characterized so far by one single (integral) number, it was difficult to estimate the many possible contributions to them. Taking into account the high available statistics offered by the CERES experiment combined with the full azimuthal acceptance, a differential study of mean p_T fluctuations is performed, which by allowing to discriminate among various correlation sources, provides the sensitivity to the fluctuations related to the vicinity of critical point. For the first time at SPS energy, the charge-dependent mean p_T fluctuations have been analyzed as a function of the angular pair separation, $\Delta\phi$, and of the separation in pseudorapidity, $\Delta\eta$, using the average momentum correlator $\langle \overline{\Delta} p_{t,1} \overline{\Delta} p_{t,2} \rangle$ as a measure [3].

Here we present recent results from the CERES collaboration on event-by-event fluctuations of the mean p_T in Pb-Au collisions at 158 AGeV/c, obtained with a sample of about 10 million central events. Fig. 1 shows the covariance map which reveals several structures and demonstrates that if the fluctuations were to be characterized by one single number the result would depend on the experiment's acceptance. The landscape is dominated by the short range correlation peak at small opening angles ('near-side'), most probably originating from Bose-Einstein and Coulomb effects between pairs of particles emitted with similar velocities. Another important contribution is a broad maximum at $\Delta\phi$=180° ('away-side') originating from back-to-back (dijet-like) correlations. Concerning the observed away-side peak, we demonstrate that it comes from high-p_T correlations that cannot be attributed to elliptic flow.

The centrality dependence of the measured correlator $\langle \overline{\Delta} p_{t,1} \overline{\Delta} p_{t,2} \rangle$, scaled by number of participating nucleons, for several regions of $\Delta\phi$ is shown in Fig. 2. Since the overall fluctuations seem to be dominated by the short range and the away-side two-particle correlations, we can analyse separately these two components and observe their non-monotonic centrality dependence (two upper sets of points in Fig. 2). Since the critical point fluctuations should be present for all opening angles, the best strategy seems to be to focus on the fluctuations in the region of $30^o < \Delta\phi < 60^o$, free of the influence of the two mentioned components, and where the elliptic flow cancels out. The p_T fluctuations in this region turn out to be close to zero and independent on centrality within the error bars [4].

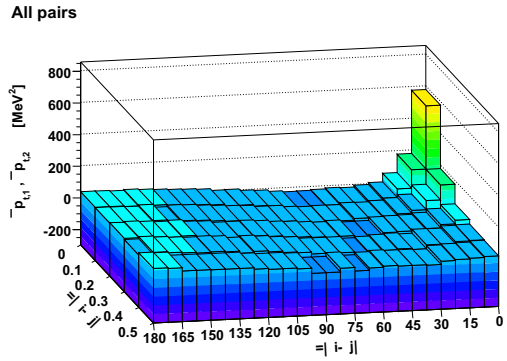


Figure 1: The $\langle \overline{\Delta} p_{t,1} \overline{\Delta} p_{t,2} \rangle$ map in $\Delta\eta$-$\Delta\phi$ for all pairs

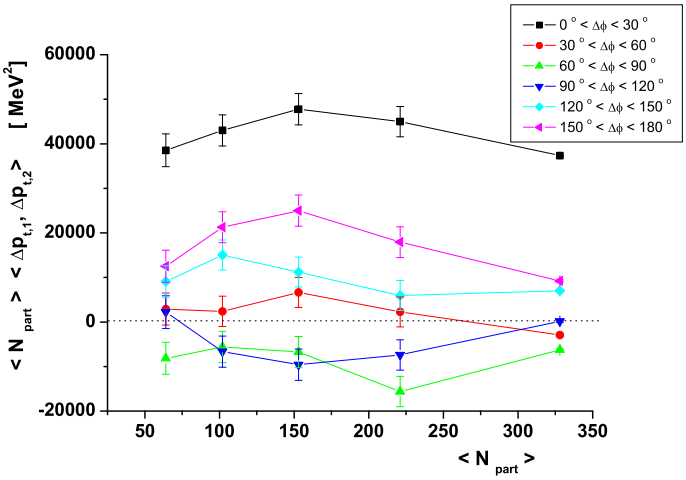


Figure 2: Centrality dependence of the measured correlator $\langle \overline{\Delta} p_{t,1} \overline{\Delta} p_{t,2} \rangle$, scaled by number of participating nucleons, for several regions of $\Delta\phi$.

References

[1] D. Adamova et al. (CERES), Nucl. Phys. A727 (2003) 97.

[2] H. Appelshäuser *et al.* (CERES), J. Phys. G: Nucl. Part. Phys. **30** (2004) S1376.

[3] S. Voloshin, nucl-th/0206052.

[4] D. Miśkowiec (CERES), Proceedings of QM2005, Budapest, Hungary.

Two-particle azimuthal correlations at high transverse momentum in Pb-Au at 158 AGeV/c

M. Płoskoń, S. Kniege and H. Appelshäuser for the CERES Collaboration,
Institut für Kernphysik, Universität Frankfurt, Germany

Abstract

We present new results of two-particle azimuthal correlations at high transverse momentum emerging from the analysis of the year 2000 data set recorded with the CERES Time-Projection Chamber.

Introduction

It has been reported that a dense color charged medium created in nucleus-nucleus collisions would strongly enhance the energy loss of a hard-scattered parton and modify its fragmentation function, resulting in the suppression of high-p_t hadrons in the final state observed at RHIC [1, 2]. A statistical analysis of the azimuthal angular correlation with respect to a leading hadron is suitable to verify the jet and di-jet production and address the question of their in-medium modification [3]. Due to its full azimuthal coverage at mid-rapidity the CERES spectrometer at the CERN-SPS is ideally suited for angular correlation studies.

Experiment and data analysis

The present study of leading hadron azimuthal correlations is based on the analysis of 30 million Pb-Au events at 158 AGeV/c recorded with the CERES spectrometer at SPS in the year 2000. The momenta of the charged particles are determined by the curvatures of their tracks in the radial Time Projection Chamber (TPC). The detector acceptance is 2π in azimuth and 2.1 to 2.7 in pseudo-rapidity. Due to the limited two-track resolution a separation cut of $\Delta\theta > 10$ mrad has been applied.

For the analysis of leading hadron correlations, we follow a scheme presented by the PHENIX collaboration [3]. We select trigger particles in the range 2.5 GeV/c $< p_t^{trigger} <$ 4.0 GeV/c and calculate the azimuthal angular difference $\Delta\phi^{same}$ with respect to associated particles with 1.0 GeV/c $< p_t^{assoc.} <$ 2.5 GeV/c in the same event. The normalized yield $Y(\Delta\phi^{same})$ has been divided by the normalized yield $Y(\Delta\phi^{mixed})$ obtained from mixed event pairs to form a correlation function $C(\Delta\phi) = \frac{Y_{same}(\Delta\phi)}{Y_{mixed}(\Delta\phi)}$. Subtracting the 2-particle flow [4, 5] contribution from the correlation function (*Zero Yield at Minimum* method [3]), it is possible to reconstruct the conditional yield distribution of jet-associated particles per trigger given by:

$$\frac{1}{N_{trig}}\frac{dN^{AB}}{d\Delta\phi} = \frac{J(\Delta\phi)}{\int(C(\Delta\phi')d(\Delta\phi'))}\frac{N^{AB}}{N^{A}}, \qquad (1)$$

where N^A is the number of triggers and N^{AB} the total number of AB pairs in the event sample. The conditional yields have been corrected for the single hadron efficiency.

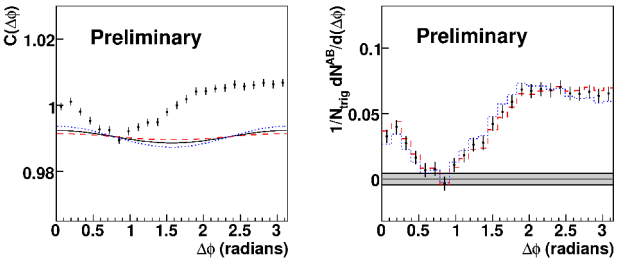


Figure 1: *Left:* Correlation function for $0-5\%$ most central events. The full lines indicate flow contributions estimated with the ZYAM method. *Right:* Conditional yield of the jet-pair distributions (Eq. 1). The full, horizontal bands represent the systematic uncertainty resulting from the flow constant estimation by the ZYAM method. The dashed and dotted lines estimate the systematic uncertainties due to the statistical uncertainty of flow contribution.

Results and conclusions

The correlation function and conditional yield of the (di-)jet associated particles are shown in Fig. 1. It is observed that the away-side structure is rather a plateau, revealing the existence of a local minimum at π. This significant modification of the back-to-back structure is possibly caused by substantial re-interaction of the scattered partons in the medium. The present findings at top SPS energy show features which are qualitatively similar to results obtained by the PHENIX collaboration from Au+Au $\sqrt{s} = 200$ GeV at RHIC [3]. These observations had been discussed in the context of conical flow patterns emerging from supersonic partons in a thermalized colored medium [6, 7]. It is remarkable that such mechanisms may also be at work at SPS energies.

References

[1] C. Adler *et al.*, Phys. Rev. Lett. **89**, 202301 (2002)

[2] K. Adcox *et al.*, Nucl. Phys. A **757**, 184 (2005)

[3] S. S. Adler *et al.*, [arXiv:nucl-ex/0507004].

[4] G. Agakichiev *et al.*, Phys. Rev. Lett. **92** (2004) 032301

[5] J. Milosevic, [arXiv:nucl-ex/0510057].

[6] H. Stöcker, *Nucl. Phys. A* **750** (2005) 121, [arXiv:nucl-th/0406018]. L. M. Satarov, H. Stoecker and I. N. Mishustin, Phys. Lett. B **627**, 64 (2005)

[7] J. Casalderrey-Solana, E.V. Shuryak, and D. Teaney, (2004) [arXiv:hep-ph/0411315].

Leading hadron azimuthal correlations in ALICE central barrel

Mateusz Płoskoń and Harald Appelshäuser,
Institut für Kernphysik, Universität Frankfurt, Germany

Abstract

Leading hadron azimuthal angular correlations in the ALICE central barrel are studied with the HIJING event generator employing scenarios with and without in-medium jet quenching. We investigate the potential of leading hadron correlation studies in the high multiplicity environment of a Pb-Pb collision at $\sqrt{s_{NN}} = 5.5$ TeV in the central barrel of the ALICE detector.

Introduction

For the first time in heavy-ion collisions, *exclusive* jet reconstruction will be possible at LHC. This will allow for a detailed study of medium-induced modifications of the jet fragmentation, providing a sensitive probe to investigate the properties of the QGP produced at LHC.

On the other hand, most of our present knowledge about jet modification in heavy-ion collisions at SPS and RHIC [1] is based on *statistical* methods. These methods employ azimuthal correlations between a high-p_t leading hadron (the *trigger* particle) and other particles from the same event, selected in a lower p_t range (the *associated* particles). A significant suppression of moderate p_t associated particles on the away-side ($\Delta\phi \approx \pi$) has been observed in central Au-Au collisions, interpreted as a consequence of medium-induced energy loss of the leading parton in the dense partonic matter at RHIC.

HIJING Simulation

For the present investigation, central Pb-Pb HIJING events ($\sigma/\sigma_{\rm geo} < 10\%$) at $\sqrt{s_{NN}} = 5.5$ TeV have been studied. The HIJING events have been processed by a fast simulation, applying the acceptance filter of the ALICE central barrel $|\eta| < 0.9$ and a parametrized momentum resolution. We compare the results of HIJING event samples in quenched and unquenched mode. For each sample, $4 \cdot 10^5$ events have been generated.

Charged trigger particles with transverse momentum $8 < p_t^{trig} < 15$ GeV/c have been selected in the acceptance of the ALICE central barrel $|\eta| < 0.9$. Pairs are created with associated particles in the same acceptance and in a lower p_t-range and plotted as a function of their azimuthal separation $\Delta\phi$ (see Fig. 1). The choice of this range of p_t^{trig} allows a comparison to recent results from RHIC for which the same p_t^{trig} had been chosen [3].

In all investigated cases of $z_t = p_t^{assoc}/p_t^{trig}$, a considerable amount of combinatorial background is observed, even at the highest selection of p_t^{assoc}. The signal-to-background ratio S/B has been determined in $\pm 2\sigma$ windows around the peaks, using the fit results for σ and the integral. The dependence on p_t^{assoc} of S/B at the near-side is shown in Fig. 1.

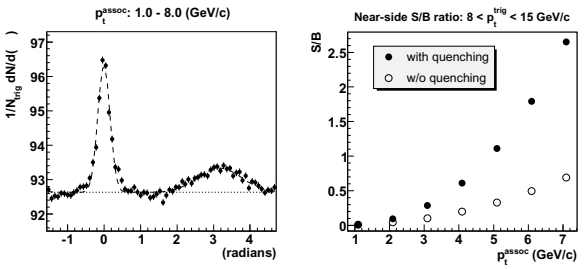


Figure 1: *Left:* Leading hadron azimuthal correlations in quenched central Pb-Pb HIJING events at $\sqrt{s_{NN}} = 5.5$ TeV for $8 < p_t^{trig} < 15$ GeV/c and $1 < p_t^{assoc} < 8$ GeV/c. *Right:* Near-side signal-to-background ratio S/B in quenched and unquenched HIJING events as function of p_t^{assoc} for $8 < p_t^{trig} < 15$ GeV/c.

As expected, S/B improves with increasing p_t^{assoc}. In the quenched scenario, this improvement is much more pronounced than in the unquenched events, reflecting the softer p_t spectrum of the background in the quenched events.

The observed signal-to-background ratios are in contrast to preliminary results from central Au-Au collisions at RHIC, presented by STAR. At these energies and for the same choice of p_t^{trig}, the signal-to-background ratio at the near-side is close to unity for $3 < p_t^{assoc} < 4$ GeV/c. At $p_t^{assoc} > 6$ GeV/c, the STAR measurement is essentially free of combinatorial background [3]. This is expected from the much softer background spectrum at RHIC energies. We note, however, that the results of the present study rely strongly on the details of final-state interactions implemented in HIJING.

References

[1] K. Adcox et al. (PHENIX Collaboration), Phys.Rev.Lett.88, 022301 (2002); C. Adler et al. (STAR Collaboration), Phys.Rev.Lett.89, 202301 (2002); S.S. Adler et al. (PHENIX Collaboration), Phys.Rev.Lett.91, 072301 (2003); J. Adams et al. (STAR Collaboration), Phys.Rev.Lett.91, 172302 (2003); C. Adler et al. (STAR Collaboration), Phys.Rev.Lett.90, 082302 (2003); G.Agakichiev et al. (CERES Collaboration), Phys.Rev.Lett.92, 032301 (2004). M. Ploskon et al. (CERES Collaboration), nucl-ex/0511043.

[2] J. Adams et al. (STAR Collaboration), nucl-ex/0501016.

[3] D. Magestro (STAR Collaboration), nucl-ex/0510002.

Quarkonia measurements with the central detectors of ALICE*

W. Sommer†, H. Appelshäuser, C. Blume, M. Hartig, M. Kessenbrock,
M. Kliemant, S. Kniege, F. Kramer, M. Ploskon, R. Renfordt, D. Wegerle
for the ALICE-TRD collaboration,
Institut für Kernphysik, Universität Frankfurt a.M., Germany

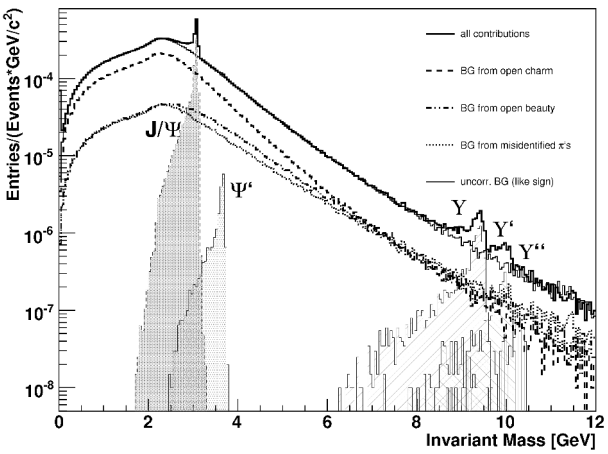


Figure 1: The invariant mass distribution of e^+-e^- pairs corresponds to $2{\cdot}10^8$ events reflecting the expected statistics of one ALICE running year. The centrality was 10 % at a multiplicity of 3000. A p_t-cut on single electrons of 1 GeV/c was applied.

With the unprecedented energies of 5.5 TeV in PbPb collisions, available at the LHC, detailed measurements of the various heavy-quarkonia states in heavy ion collisions will be possible for the first time. The ALICE detector will be able to measure quarkonia in the dimuon and dielectron channel in different kinematical regions. These simulation studies investigate the physics capabilities of quarkonia measurements with the inner tracking system (ITS), the time projection chamber (TPC) and the transition radation detector (TRD) covering a rapidity range from -0.9 to 0.9.

The presented simulations are based on calculations for quarkonia rates within the Color Evaporation model [Acc03]. The expected cross sections for the various quarkonia states are calculated for pp-collisions at $\sqrt{s}$=5.5 TeV. From these cross sections the PbPb-cross sections are calculated using N_{coll} scaling obtained by Glauber model calculations. In addition nuclear shadowing is included using the EKS98 parametrisation.

Due to the cross sections for the rare quarkonia states detailed simulations cannot be performed with todays computer facilities in an acceptable amount of time. For this reason a fast simulator was developed. It consists of three modules: A generator, a detector parametrisation and the analysis. The quarkonia states are generated according to the calculated rates and to the kinematical distributions obtained by scaling the distributions measured by the CDF experiment. In addition two main sources of background electrons are considered: electrons coming from charm and bottom decays are simulated using the CDF scaled distributions and background due to misidentified pions is simulated by a parametrised HIJING generator tuned to the multiplicity of dN/dy_{ch}=3000.

The detector response is then evaluated using parametrisations describing detection probability, momentum resolution and particle identification. The parametrisations were obtained using microscopic simulations of HIJING events with embedded electrons. For a detailed description of the parametrisation see [Gro05].

As can be seen from Fig. 1 and the values from Tab. 1 the J/Ψ and the Υ are detectable with good signal to background ratio and significance. The higher mass states are clearly distinguishable from the background, however the accumulated statistics was not sufficient to give quantitative values. A Gaussian fit to the observed peaks gives a width of 33 MeV for the J/Ψ and 90 MeV for the Υ. Given this resolution the distinction of the different Υ-states will be possible.

For more results and a more detailed description of the performed studies see [PPRVII].

Table 1: Expected signals (S), signal to background ratio (S/B) and significance (SGN) corresponding to $2{\cdot}10^8$ events.

Particle	S	S/B	SGN
J/Ψ	120.000	1.4	260
Υ	1.250	1.6	28
Υ′	470	0.6	13.1

References

[Gro05] J.F. Grosse-Oetringhaus, *Determination of the Physics Performance of the ALICE Central Barrel using a Distributed GRID Computing Environment*, Diploma thesis, Institut für Kernphysik, Münster, 2005

[Acc03] A. Accardi *et al.*, arXiv:hep-ph/0308248.

[PPRVII] ALICE PPR Volume II, CERN/LHCC 2005-030, 2005

* Work supported by BMBF
† sommer@ikf.uni-frankfurt.de

Chiral extrapolation of nucleon properties from lattice QCD

M. Procura, B.U. Musch, T.R. Hemmert and W. Weise
Physik Department, Technische Universität München, Garching, Germany

Lattice QCD on one side and chiral effective field theory on the other are progressively developing as important tools to deal with the non-perturbative nature of low-energy QCD and the structure of hadrons. At present, however, there is a gap between the relatively large quark masses accessible in full-QCD lattice simulations of nucleon properties and the small quark masses relevant for comparison with physical observables. In our work we study how to merge Chiral Perturbation Theory (χPT) which predicts the quark mass dependence of a nucleon observable and lattice simulations where the quark mass is a tunable parameter.

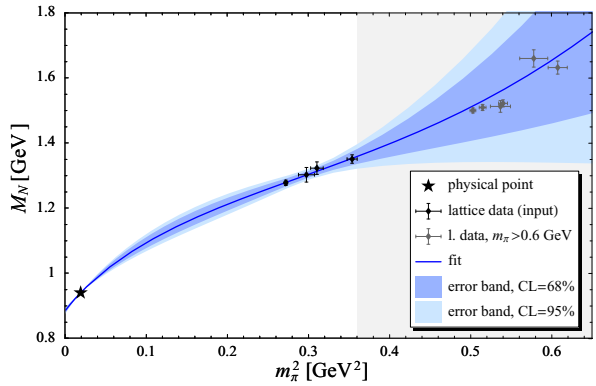


Figure 1: $M_N(m_\pi)$ at order p^4.

The quark mass dependence of the nucleon mass M_N is the subject of Refs.[1, 2]. An interpolation of this observable, between a selected set of full-QCD two-flavor lattice data and its physical value, is studied using $SU(2)$ Baryon χPT up to next-to-leading one-loop order. Different regularization and power counting schemes have been investigated. Both Heavy Baryon and manifestly Lorentz invariant formulations of chiral effective field theory have been analyzed and compared in this context. Lattice artifacts due to finite spatial volume have also been studied within χPT and have been incorporated in the analysis, improving the interpolations. From our numerical analysis we deduce the nucleon mass in the chiral limit, $M_0 \approx 0.88\,\mathrm{GeV}$, and the pion-nucleon sigma-term $\sigma_N = (49 \pm 3)\,\mathrm{MeV}$. The inclusion of explicit $\Delta\,(1232)$ degrees of freedom turns out to be not essential for a satisfactory description of the quark mass dependence of M_N [2, 3]. We have also performed a careful statistical analysis [2] which confirms and sharpen our previous results in Ref.[1]. In Fig.1 we show the statistical error bands corresponding to the 68% and 95% joint confidence regions for the fit parameters in $M_N(m_\pi)$ at next-to-leading one-loop order, $\mathcal{O}(p^4)$ [2]. The errors on the lattice pion masses have been taken into account as well.

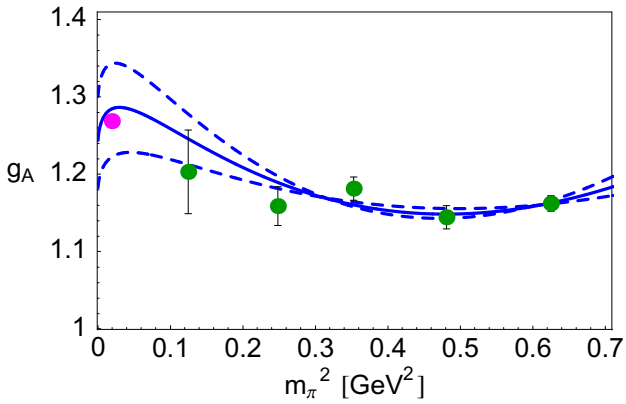


Figure 2: Chiral extrapolation of lattice data in Ref.[6].

We have compared also for the axial-vector coupling g_A, $SU(2)$ chiral effective field theory schemes with and without explicit $\Delta\,(1232)$ degrees of freedom, both in their non-relativistic [4] and manifestly Lorentz invariant form with infrared regularization [3, 5]. The inclusion of *explicit* $\Delta\,(1232)$ degrees of freedom is crucial in this context to obtain successful interpolations between present lattice data and the physical point. Fig.2 shows a chiral *extrapolation*, based on the leading-one-loop expression in the scheme with explicit $\Delta\,(1232)$, of very recent lattice data provided by the LHP collaboration [6]. Incorporating information about an effective coupling from low-energy $\pi N \to \pi\pi N$ scattering, our chiral extrapolation function works well from the chiral limit across the physical point into the region of present lattice data. The dashed curves reflect the uncertainty in the determination of the above-mentioned coupling.

References

[1] M. Procura, T.R. Hemmert and W. Weise, Phys. Rev. **D69**, 034505 (2004).

[2] M. Procura, B.U. Musch, T.R. Hemmert, T. Wollenweber and W. Weise, *forthcoming*.

[3] M. Procura, B.U. Musch, T.R. Hemmert, T. Wollenweber and W. Weise, `hep-lat/0512026`.

[4] T.R. Hemmert, M. Procura and W. Weise, Phys. Rev. **D68**, 075009 (2003).

[5] M. Procura, T.R. Hemmert and W. Weise, Nucl. Phys. **A755**, 649 (2005).

[6] J.W. Negele *et al.*, `hep-lat/0509101`; R.G. Edwards *et al.*, `hep-lat/0510062`; D. Richards, private communication.

Coupled-channel study of baryon resonances with charm

J. Hofmann and M.F.M. Lutz, GSI, Darmstadt, Germany

Empirically the QCD spectrum of charmed baryon states is poorly studied so far. It is important to correlate the properties of charmed states to those firmly established, applying a unified and quantitative framework. Our strategy is to extend previous works [1, 2, 3, 4] that performed a coupled-channel study of the s-wave scattering processes where a Goldstone boson hits an open-charm baryon ground state. The results of [1, 2, 3, 4] were based on the leading order chiral Lagrangian, that predicts unambiguously the s-wave interaction strength of Goldstone bosons with baryon states in terms of the pion decay constant. Including the light vector mesons as explicit degrees of freedom in a chiral Lagrangian gives an interpretation of the leading order interaction in terms of the t-channel exchange of vector mesons.

Extending those computations to include D- and η_c-mesons in the intermediate states leads to additional baryon resonances [5]. Identifying a zero-range exchange of vector mesons as the driving force for the s-wave scattering of pseudo-scalar mesons off the baryon ground states, a rich spectrum of molecules is formed. We argue that chiral symmetry and large-N_c considerations determine that part of the interaction which generates the spectrum. The latter couple universally to any matter field in this type of approach. Given the assumption that the interaction strength of D- and η_c-mesons with the baryon ground states is also dominated by the t-channel exchange of the light vector mesons, we are in a position to perform a quantitative coupled-channel study of charmed baryon resonances.

The interaction strengths of the channels that drive the resonance generation are predicted by chiral and large-N_c properties of QCD. The spectrum of s-wave molecules obtained is amazingly rich of structure. Results are obtained in all charm sectors [5]. Particularly striking are the crypto-exotic resonances in the charm-zero sector. The spectrum is shown in Fig. 1 in terms of coupled-channel speed plots. In the charm one sector we recover the $\Lambda_c(2593)$ as a narrow state coupling strongly to the $(D\,N)$ and $(D_s\,\Lambda)$ states. The $\Xi_c(2790)$ is interpreted as a bound state of the $(\bar K\,\Sigma_c), (\eta\,\Xi_c')$ system. We argue that the $\Lambda_c(2880)$ discovered by the CLEO collaboration can not be a s-wave state. About ten additional narrow s-wave states are predicted in this sector with masses below 3 GeV (see Fig. 2).

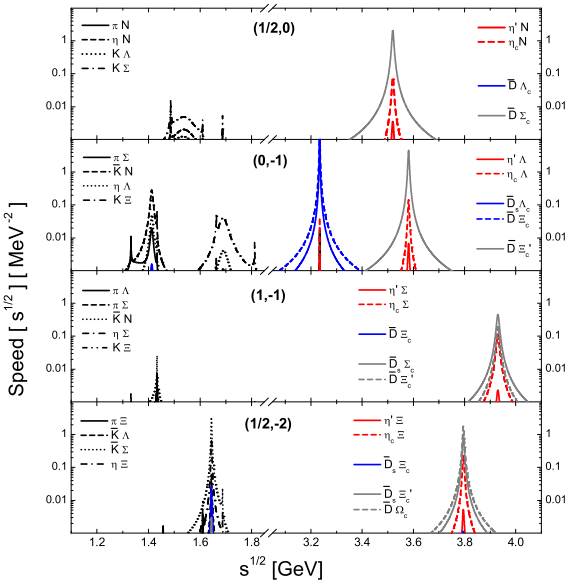


Figure 1: Spectrum of $J^P = \frac{1}{2}^-$ molecules with $C = 0$.

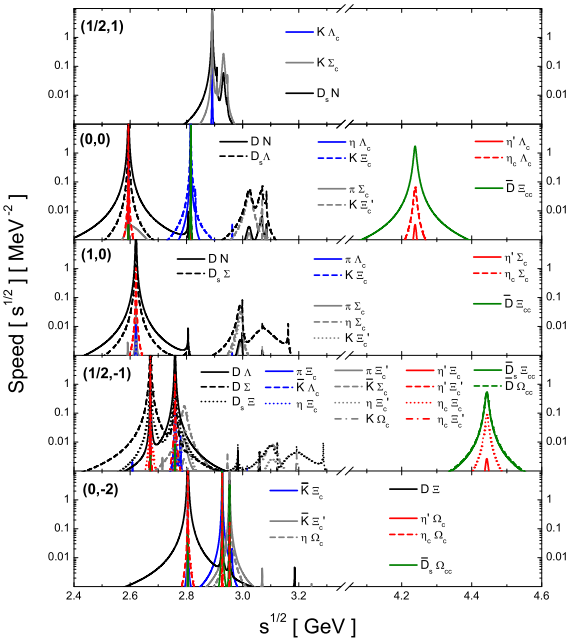


Figure 2: Spectrum of $J^P = \frac{1}{2}^-$ molecules with $C = 1$.

References

[1] C. García-Recio, M.F.M. Lutz and J. Nieves, Phys. Lett. B 582 (2004) 49.

[2] E.E. Kolomeitsev and M.F.M. Lutz, Phys. Lett. B 585 (2004) 243.

[3] M.F.M. Lutz and E.E. Kolomeitsev, Nucl. Phys. A 730 (2004) 110.

[4] M.F.M. Lutz and E.E. Kolomeitsev, Nucl. Phys. A 755 (2005) 29c.

[5] J. Hofmann and M.F.M. Lutz, Nucl. Phys. A 763 (2005) 90.

Quantum interferences in the $\gamma N \to e^+e^-N$ reaction close to the vector meson production threshold

M.F.M. Lutz (GSI, Darmstadt, Germany) and M. Soyeur (DAPNIA, CEA/Saclay, France)

The study of the $\gamma N \to e^+e^-N$ reaction [1] close to the vector meson production threshold ($1.40 < \sqrt{s} < 1.75$ GeV) complements our work on the $\pi N \to e^+e^-N$ reaction [2] aiming at understanding the coupling of vector fields (ρ^0 and ω) to low-lying baryon resonances. These couplings are not well-known and important for baryon structure studies and for dynamical descriptions of vector meson propagation in the nuclear medium. The complementarity comes from the result that the $\pi N \to e^+e^-N$ reaction is very sensitive to the couplings of selected baryon resonances to both the $\rho^0 N$ and the ωN channels while the $\gamma N \to e^+e^-N$ process reflects mostly the coupling of low-lying baryon resonances to the $\rho^0 N$ channel. The $\pi N \to e^+e^- N$ and $\gamma N \to e^+e^- N$ reactions underlie the more complex $\pi A \to e^+e^- X$ and $\gamma A \to e^+e^- X$ nuclear processes whose measurement is planned at GSI (with HADES) and under analysis at JLab (CLAS collaboration).

The photoproduction of e^+e^- pairs from nucleons close to the vector meson production threshold results from two main processes: the emission of Bethe-Heitler pairs and the photoproduction of ρ^0- and ω-mesons decaying into e^+e^- pairs. The Bethe-Heitler amplitudes are purely electromagnetic. The $\gamma N \to e^+e^-N$ amplitudes arise from vector meson production and decay and are derived from $\gamma N \to \rho^0 N$ and $\gamma N \to \omega N$ amplitudes using the Vector Meson Dominance assumption. The vector meson photoproduction amplitudes are calculated using the relativistic and unitary coupled-channel approach to meson-nucleon scattering of Ref. [3], i.e. in exactly the same theoretical framework as the $\pi N \to e^+e^-N$ reaction in Ref. [2].

The $\gamma N \to e^+e^-N$ differential cross sections display interference patterns. The interference of Bethe-Heitler pair production with vector meson e^+e^- decay is quite small in the domain of validity of our model for all angles of the emitted e^+e^- pair. If the leptonic phase space is fully integrated out, the interference terms between the Bethe-Heitler and vector meson amplitudes cancel. The interference of ρ^0- and ω-mesons in the e^+e^- channel can be large. We found it constructive for the $\gamma p \to e^+e^-p$ reaction and destructive for the $\gamma n \to e^+e^-n$ reaction [1].

We illustrate our results in Figs. 1 and 2 for the $\gamma p \to e^+e^-p$ reaction. Integrated spectra at $\sqrt{s}$=1.75 and 1.65 GeV, i.e. just above and just below the vector meson threshold, are shown in Fig. 1. They indicate the relative importance of the Bethe-Heitler and vector meson contributions in these kinematics and the interplay of the ρ and ω contributions in both J channels. Fig. 2 displays the relative smallness of the asymmetric contribution, reflecting the interference between Bethe-Heitler pairs and vector meson decays, and its different vector meson components. We refer to [1] for a complete presentation of the results.

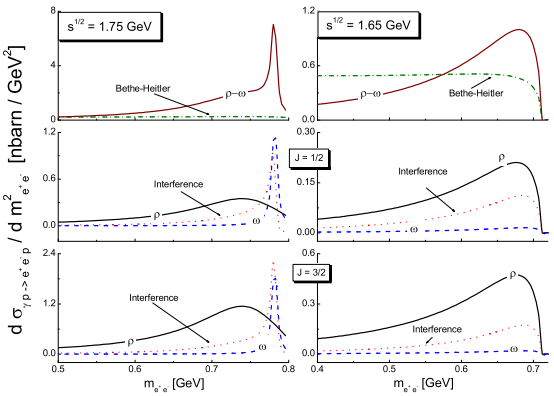


Figure 1: Integrated spectra for the $\gamma p \to e^+e^-p$ reaction at $\sqrt{s}$=1.75 and 1.65 GeV. The figure displays the Bethe-Heitler and the vector meson cross sections (upper part), the ρ- and ω-meson contributions and their interference in the J=1/2 and J=3/2 channels (middle and lower parts).

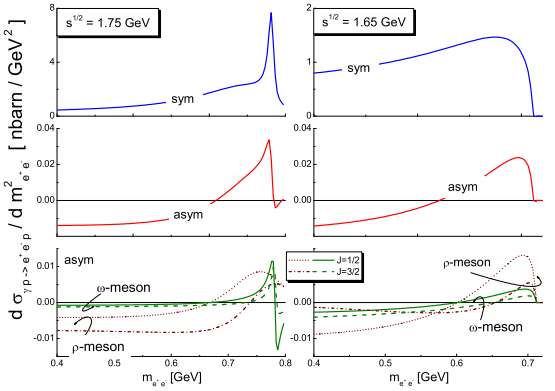


Figure 2: Same as Fig. 1 for the asymmetric contributions to the $\gamma p \to e^+e^-p$ cross section.

References

[1] M.F.M. Lutz, M. Soyeur, Nucl. Phys. A 760 (2005) 85.

[2] M.F.M. Lutz, B. Friman, M. Soyeur, Nucl. Phys. A 713 (2003) 97.

[3] M.F.M. Lutz, Gy. Wolf and B. Friman, Nucl. Phys. A 706 (2002) 431.

Hadron Resonances from Lattice-QCD with Chiral Fermions*

A. Schäfer, T. Burch, M. Göckeler, C. Hagen, D. Hierl, S. Solbrig, T. Wettig,
Institut für Theoretische Physik, Universität Regensburg, D-93040 Regensburg, Germany
C. Gattringer, C.B. Lang,
Institut für Theoretische Physik, Universität Graz, A-8010 Graz, Austria
P. Hasenfratz, F. Niedermayer,
Institut für Theoretische Physik, Universität Bern, CH-3012 Bern, Switzerland

While ground state spectroscopy is a well understood problem, the spectroscopy of excited states is still quite challenging. The reason is that euclidean two-point functions are given by a sum of exponentials and it is a non-trivial task to extract the subleading contributions which correspond to the excited states.

A powerful tool for this task is the variational method [1]. The central equation of this method is the generalized eigenvalue problem

$$C(t)\vec{\psi}^{(k)} = \lambda^{(k)}(t)C(t_0)\vec{\psi}^{(k)} \qquad (1)$$

which has to be solved. $C(t)$ denotes the matrix of two-point functions, $\lambda^{(k)}(t)$ are the resulting eigenvalues from which one extracts the masses of the individual states and $\vec{\psi}^{(k)}$ are the corresponding eigenvectors.

We have applied this technique to several mesonic and baryonic systems and successfully calculated the masses of several resonances. A subset of our results are shown in Fig. 1, further results can be found in [2, 3, 4]. In some cases the results still show quite significant deviations to the numbers obtained from experiment. This is partly caused by the quenched approximation we make for our calculations.

One problem which arises from this approximation is the occurance of unphysical states, often refered to as "ghosts". Until dynamical calculations at light quark masses become feasible, there is no way to avoid these states. However, after a closer inspection [5], the variational method proves to be very useful also in this case because it enables us to disentangle proper states from ghosts, as is shown in Fig.2.

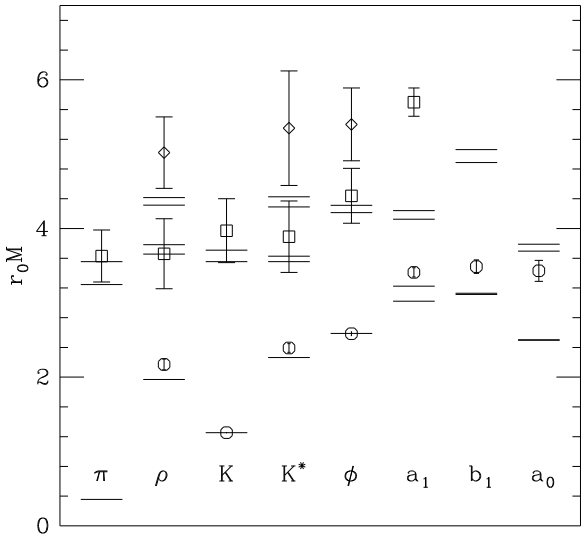


Figure 1: Some results for the excited meson masses. The horizontal lines correspond to $M \pm \sigma_M$ experimental values.

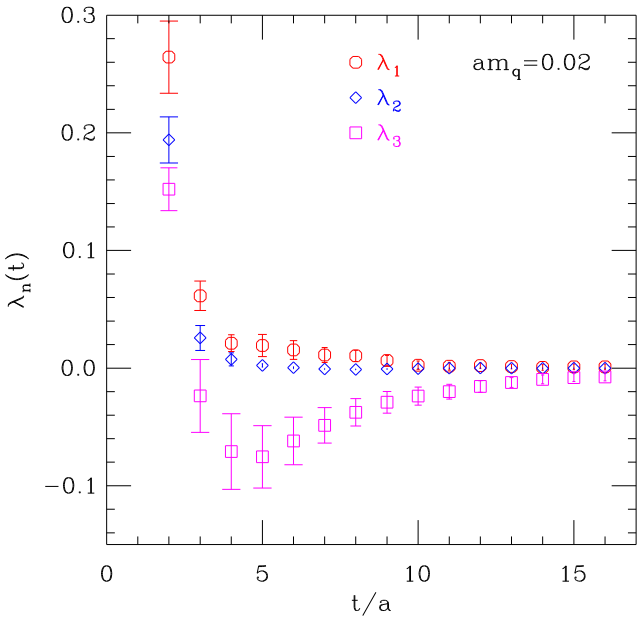


Figure 2: Euclidean time dependence for the eigenvalues of the generalized eigenvalue problem at quark mass $am_q = 0.02$. All "ghost" contribution have moved to eigenvalue $\lambda^{(3)}$.

References

[1] C. Michael, Nucl. Phys. B **259**, 58 (1985). M. Lüscher and U. Wolff, Nucl. Phys. B **339**, 222 (1990).

[2] C. Gattringer *et al.*, Nucl. Phys. B **677** (2004) 3; T. Burch *et al.*, Phys. Rev. **D70** (2004) 054502.

[3] T. Burch, C. Hagen, D. Hierl, A. Schäfer, C. Gattringer, L. Y. Glozman and C. B. Lang, PoS **LAT2005**, 097 (2005) [arXiv:hep-lat/0509086].

[4] T. Burch, C. Hagen, D. Hierl, A. Schäfer, C. Gattringer, L. Y. Glozman and C. B. Lang, PoS **LAT2005**, 075 (2005) [arXiv:hep-lat/0509051].

[5] T. Burch, C. Gattringer, L. Y. Glozman, C. Hagen and C. B. Lang, arXiv:hep-lat/0511054.

* Work supported by DFG, GSI, EU(I3HP), ...

Transversity from Lattice QCD*

A. Schäfer, A. Ali Khan, T. Burch, M. Göckeler, N. Warkentin, Institut für Theoretische Physik, Universität Regensburg, 93040 Regensburg; D. Brömmel, DESY, 22603 Hamburg; Ph. Hägler, T.R. Hemmert, Physik-Department, TU München, 85747 Garching; R. Horsley, J.M. Zanotti, School of Physics, University of Edinburgh, Edinburgh EH9 3JZ, UK; H. Perlt, A. Schiller, Institut für Theoretische Physik, Universität Leipzig, 04109 Leipzig; D. Pleiter, G. Schierholz, NIC, DESY, 15738 Zeuthen; P.E.L. Rakow, University of Liverpool, Liverpool L69 3BX, UK; H. Stüben, ZIB, 14195 Berlin

QCDSF/UKQCD Collaboration

Experiments with polarised protons and antiprotons at FAIR will provide information on the transversity in the nucleon. The theoretical description uses so-called generalised parton distributions. Their moments are given by linear combinations of generalised form factors (GFFs), which appear in the decomposition of (off-forward) nucleon matrix elements of local operators. Relevant for transversity are operators involving the Dirac matrix $\sigma^{\mu\nu}$. For example, the nucleon matrix element of the tensor density can be written as [1]

$$\begin{aligned}&\langle P'\Lambda'|\,\bar{\psi}(0)i\sigma^{\mu\nu}\psi(0)\,|P\Lambda\rangle\\&\quad=\overline{U}(P',\Lambda')\Big\{i\sigma^{\mu\nu}A_{T10}(t)+\frac{\overline{P}^{[\mu}\Delta^{\nu]}}{m^2}\widetilde{A}_{T10}(t)\\&\quad+\frac{\gamma^{[\mu}\Delta^{\nu]}}{2m}B_{T10}(t)\Big\}U(P,\Lambda)\,.\end{aligned}$$

The GFFs $A_{T10}(t)$, $\widetilde{A}_{T10}(t)$ and $B_{T10}(t)$ depend on $t = \Delta^2$, where $\Delta = P' - P$ is the momentum transfer. Such matrix elements can be calculated on the lattice from suitable combinations of two- and three-point functions.

On gauge field configurations generated with two flavours of dynamical clover fermions [2] we have evaluated a large number of hadron matrix elements of the above type and extracted the corresponding GFFs. As an example we show in Fig. 1 $A_{T10}(t)$ for the up-quark in the proton, extrapolated to the chiral and continuum limits together with a dipole fit [1].

From such dipole parameterisations one can extract quark densities in the transverse plane [3]. In Fig. 2 we present results [4] for unpolarised up-quarks in a polarised proton and for polarised up-quarks in an unpolarised proton.

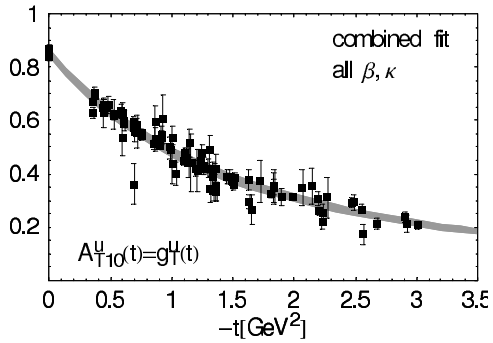


Figure 1: The form factor $A_{T10}(t)$ for the up-quark in the proton together with a dipole fit.

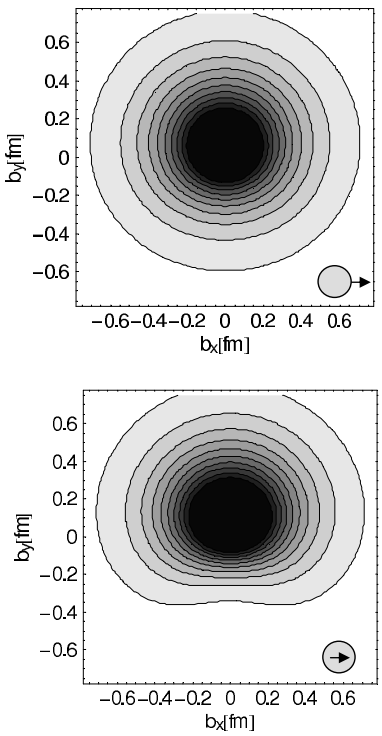


Figure 2: Densities of up-quarks in the proton. The proton and quark spins are oriented in the transverse plane as indicated, where the inner arrow represents the quark and the outer arrow the proton spin. A missing arrow represents the unpolarised case.

References

[1] M. Göckeler et al., Phys. Lett. B627 (2005) 113.

[2] C.R. Allton et al., Phys. Rev. D65 (2002) 054502.

[3] M. Burkardt, Phys. Rev. D62 (2000) 071503; Erratum ibid. D66 (2002) 119903.

[4] M. Diehl et al., arXiv:hep-ph/0511032.

* Work supported by DFG, GSI, EU (I3HP), HGF, LRZ and NIC.

On the Faddeev-Popov operator in topological field configurations*

Axel Maas, GSI, Darmstadt, Germany†

The confinement of colored objects in QCD is, even after more than thirty years, still a challenging problem. The progress which has been made in its understanding during the last years has been mainly along two directions, which are at first sight quite different. One is based on topological field configurations, like vortices [1]. The other investigates the properties of Green's functions [2].

The latter approach is currently most successful in a class of gauges, which includes the Landau and Coulomb gauges. In this context, the (Euclidean) Faddeev-Popov operator (FP)

$$M^{ab} = -\partial_\mu(\partial_\mu\delta^{ab} + g f^{abc} A^c_\mu) \qquad (1)$$

has been found to be of importance. Here A is a gauge field configuration, g the coupling constant, and f^{abc} the structure constants of the gauge group. E. g. in Landau gauge the expectation value of the inverse of the FP equals the propagator of the Faddeev-Popov ghosts. This propagator has been found to be infrared divergent [2]. This requires an enhancement of zero or near-zero eigenmodes of the FP, as is predicted by the Gribov-Zwanziger confinement scenario. This has been explicitly observed on the lattice [3].

It is thus an interesting question, whether such an enhancement is related to topological field configurations. This has been investigated in lattice calculation, and it has been found that a removal of thin center-vortices also removes the observed enhancement [4]. In the continuum, a possible alternative approach is to consider analytically the spectrum of the FP (1) in a purely topological field configuration [5], like a single center vortex, given in cylindrical coordinates for the gauge group SU(2) by [1]

$$A^a_\eta = \delta^{3a}\frac{1}{g}\frac{\mu(\rho)}{\rho}.$$

μ is the profile of the vortex, satisfying $\mu(0) = 0$ and $\mu(\infty) = 2n+1$, giving the flux of the vortex. The eigenequation of the FP for eigenvalue ω^2 then reads

$$(\partial^2\delta^{ab} + g f^{abc} A^c_\mu \partial_\mu + \omega^2)\phi^b = 0.$$

Due to the antisymmetry of the structure constants, the 3-component decouples. The remaining set of equations can be solved by first separating the trivial coordinates t and z. Then the angular part is a spin problem. Thus eigenfunctions for a fixed eigenvalue ω^2 can be labeled by a 'quantum number' m. The radial equations can then be reduced to the solution of an ordinary differential equation, which determines the allowed combinations of m and ω^2. It is found [5] that $\omega^2 \geq 0$ is required. For any $\omega^2 > 0$, m runs over all integers, including zero, so there is no enhancement of near-zero eigenvalues compared to the vacuum. However, there are $4n$ new non-trivial zero-modes for a vortex of flux $2n+1$. Thus vortices can be the origin of the observed enhancement. The corresponding radial solutions, shown in figure 1, exhibit strong non-localization.

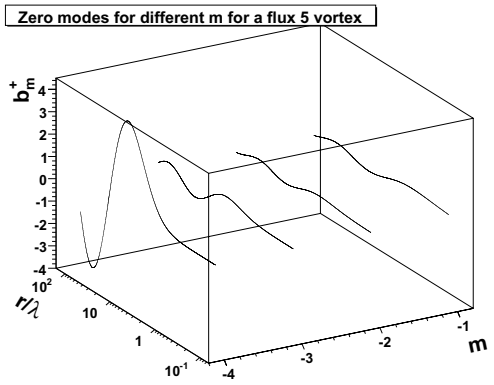


Figure 1: Radial behavior of zero-modes in a flux 5 vortex for different (negative) values of m. λ is the intrinsic scale of the profile function μ.

Furthermore, this vortex gives rise to an infinite energy of an unscreened color charge, a necessary condition for confinement [5]. Thus also in this analytical approach, a connection between vortices, an enhancement of the FP eigenspectrum, and confinement is found, indicating how the different aspects of confinement may fit together.

Nonetheless, many open questions remain. One is the relation to other topological configuration. E. g. also an instanton provides additional zero-modes of the FP, although only a very limited number [5]. Many further questions remain. Thus although a new piece of the confinement puzzle has been uncovered, it is neither yet really clear how it fits in, nor has a complete picture been obtained.

References

[1] J. Greensite, Prog. Part. Nucl. Phys. **51** (2003) 1 [arXiv:hep-lat/0301023] and references therein.

[2] R. Alkofer and L. von Smekal, Phys. Rept. **353** (2001) 281 [arXiv:hep-ph/0007355] and references therein.

[3] A. Sternbeck, E. M. Ilgenfritz and M. Mueller-Preussker, arXiv:hep-lat/0510109.

[4] J. Greensite, Š. Olejník and D. Zwanziger, JHEP **0505** (2005) 070 [arXiv:hep-lat/0407032].

[5] A. Maas, arXiv:hep-th/0511307.

* Work supported in part by the DFG under grant MA 3935/1-1.

† Present address: Instituto de Física de São Carlos, Universidade de São Paulo, Brazil

Phases of QCD

C. Ratti, M. A. Thaler, W. Weise
Physik Department, Technische Universität München, Garching, Germany

Recent years have seen an expansion of activities devoted to the study of the QCD phase diagram. The equation of state of strongly interacting matter is now at hand as a function of temperature T and in a limited range of quark chemical potential μ.

In our work [1] we have studied the thermodynamics of two-flavour QCD at finite quark chemical potential. Our investigation is based on a synthesis of a Nambu Jona-Lasinio (NJL) model and the non-linear dynamics involving the Polyakov loop [2, 3]. In this Polyakov-loop-extended (PNJL) model, quarks develop quasiparticle masses by propagating in the chiral condensate, while they couple at the same time to a homogeneous background (temporal) gauge field representing Polyakov loop dynamics. The main aim of our work is to investigate whether results from lattice QCD thermodynamics can be understood and interpreted in terms of quasiparticle degrees of freedom.

The thermodynamic potential of the PNJL model is:

$$\Omega = \mathcal{U}\left(\Phi,\bar{\Phi},T\right) + \frac{\sigma^2}{2G} \qquad (1)$$
$$-2N_f\,T\int\frac{\mathrm{d}^3p}{(2\pi)^3}\left\{\mathrm{Tr}_c\ln\left[1+L\,\mathrm{e}^{-(E_p-\mu)/T}\right]\right.$$
$$\left.+\mathrm{Tr}_c\ln\left[1+L^\dagger\,\mathrm{e}^{-(E_p+\mu)/T}\right]\right\} - 6N_f\int\frac{\mathrm{d}^3p}{(2\pi)^3}E_p\,\theta\left(\Lambda^2-\vec{p}^{\,2}\right)$$

where we have introduced the quark quasiparticle energy $E_p = \sqrt{\vec{p}^{\,2}+m^2}$, with a constituent quark mass given by their interaction with the chiral condensate (related to the σ scalar field): $m = m_0 - \langle\sigma\rangle = m_0 - G\langle\bar{\psi}\psi\rangle$. Φ and $\bar{\Phi}$ are the traced Polyakov loop and its conjugate: $\Phi = (\mathrm{Tr}_c\,L)/N_c$, $\bar{\Phi} = (\mathrm{Tr}_c\,L^\dagger)/N_c$. The Polyakov loop L is a matrix in colour space explicitly given by $L\left(\vec{x}\right) = \mathcal{P}\exp\left[i\int_0^\beta d\tau\,A_4\left(\vec{x},\tau\right)\right]$, with $\beta = 1/T$ the inverse temperature and $A_4 = iA^0$. The effective potential for the Polyakov loop, $\mathcal{U}(\Phi,\bar{\Phi},T)$, has a polynomial form reflecting the $Z(3)$ symmetry of pure-gauge QCD and its spontaneous breaking in the deconfined phase.

All parameters of the model are fixed a priori: the results are predictions of the model, which we will compare to the available lattice data. Minimizing the thermodynamic potential (1) gives the behaviour of Polyakov loop and chiral condensate as functions of temperature and chemical potential. We obtain the non-trivial result that chiral and deconfinement phase transitions take place at the same critical temperature, around 200 MeV (see Fig. 1). We have also evaluated the quark number density $n_q = -\partial\Omega(T,\mu)/\partial\mu$. We show an example in Fig. 2 in comparison with available lattice data [4], and with the results obtained in the standard NJL model. The improvement due to the inclusion of the Polyakov loop, resulting in a suppression of the quark degrees of freedom in the forbidden (confinement) region at $T < T_c$, is evident.

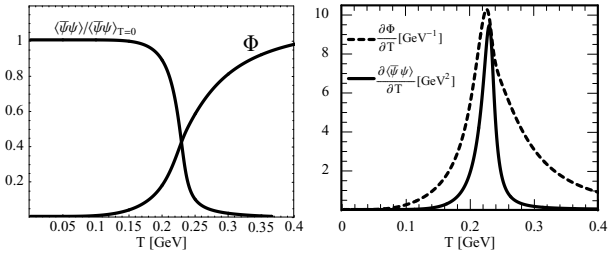


Figure 1: Left: scaled chiral condensate and Polyakov loop $\Phi(T)$ as functions of temperature at zero chemical potential. Right: plots of $\partial\langle\bar{\psi}\psi\rangle/\partial T$ and $\partial\Phi/\partial T$.

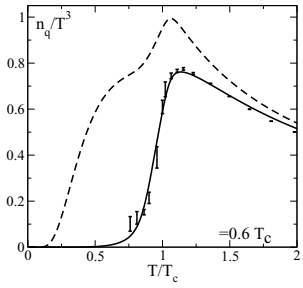


Figure 2: Scaled quark number density calculated in the PNJL model as a function of temperature at finite chemical potential (continuous line), compared to lattice data [4], and to the standard NJL results (dashed line).

Considering the simplicity of the PNJL model, the conclusion that can be drawn at this point is promising: it appears that a relatively straightforward quasiparticle approach, with its dynamics rooted in spontaneous chiral symmetry breaking and confinement and with parameters controlled by a few known properties of the gluonic and hadronic sectors of the QCD phase diagram, can account for essential observations from two-flavour $N_c = 3$ Lattice QCD thermodynamics.

References

[1] C. Ratti, M. A. Thaler and W. Weise hep-ph/0506234, accepted for publication in Phys. Rev. **D**.

[2] P. N. Meisinger and M. C. Ogilvie, Phys. Lett. B **379**, 163 (1996).

[3] K. Fukushima, Phys. Lett. B **591**, 277 (2004).

[4] C. R. Allton *et al.*, Phys. Rev. D **68**, 014507 (2003).

Realistic phase diagram in a chiral hadronic model*

S. Schramm, G. Zeeb, D. Zschiesche
Institut für Theoretische Physik, J.W. Goethe Universität, Max-von-Laue Str. 1, 60438 Frankfurt, Germany

In a current picture of the QCD phase diagram in the plane of temperature T versus quark-chemical potential μ_q, a line of first-order phase transitions starts at the zero temperature axis and ends in a critical point. Lattice QCD calculations at finite chemical potential locate that point at $T \approx 160$ MeV, $\mu_q \approx 120$ MeV [1]. Since lattice simulations at $\mu_q = 0$ give a rather weak dependence of the critical temperature on the pion mass, the physics around the phase transition cannot be dominated by the light degrees of freedom alone [2]. Furthermore, a hadron resonance gas approach gives a reasonable description of the pressure obtained from lattice calculations up to the critical temperature [3]. Thus, heavy states are important around the phase boundary and seem to "drive" the phase change. If this is true, it should be possible to reproduce the structure of the QCD phase diagram in a model calculation, which effectively includes these degrees of freedom.

To this end, we investigate the phase diagram of a relativistic field theoretical model built on a nonlinear realization of chiral $SU(3)_L \times SU(3)_R$ symmetry and broken scale invariance. The model incorporates the complete set of the lowest baryon and meson multiplets. In lowest order the expectation values of scalar mesons relevant for symmetric nuclear matter are the non-strange and strange chiral quark condensates, namely the scalar field σ and its $s\bar{s}$ counterpart ζ, respectively, and further the ω and ϕ vector meson fields. [1]

Schematically the Lagrangian of this model reads

$$\mathcal{L} = \mathcal{L}_{\rm kin} + \mathcal{L}_{\rm BM} + \mathcal{L}_{\rm BV} + \mathcal{L}_{\rm vec} + \mathcal{L}_0 + \mathcal{L}_{\rm SB} \ , \qquad (1)$$

with the kinetic energy term $\mathcal{L}_{\rm kin}$, the interaction of baryons with scalar- and vector mesons $\mathcal{L}_{\rm BM}$, the vector mass term and self-interaction $\mathcal{L}_{\rm vec}$, the scalar self-interaction $\mathcal{L}_0$, and finally the explicit symmetry breaking $\mathcal{L}_{\rm SB}$. All parameters of the model discussed so far are fixed by symmetry relations, observables in the vacuum (masses, decay constants,...) and properties of saturating nuclear matter (for details see [4]). If the members of the lowest lying octet represent the only baryonic degrees of freedom, the model shows a smooth decrease of the chiral condensates for high temperatures and high densities. However, additional baryonic degrees of freedom may change the behaviour towards a first order phase transition in certain regimes of the $T - \mu_q$ plane, depending on the chosen couplings. In order to model the influence of heavy states we include a resonance [2] with a mass given by $m_R = m_{R,esb} + g_R\sigma$ and a vector coupling $g_{R\omega} = r_V g_{N\omega}$. The mass parameters, $m_{R,esb}, g_R$ and the relative vector coupling r_V represent free parameters that are adjusted to reproduce the above described picture of the QCD phase diagram. It turns out that certain ranges for these parameters exist (e.g. $m_R = 2$ GeV, $r_V = 0.4$ and $m_{R,esb} = 0.57$ GeV in fig 1), for which the endpoint of the first order phase transition line is in reasonable agreement with the lattice results and simultaneously the phase transition at zero temperature is considerably above the nuclear matter saturation point. This is in contrast to models that do not account for heavy degrees of freedom and usually give too small values for the temperature of the endpoint (see e.g. [5] for a summary).

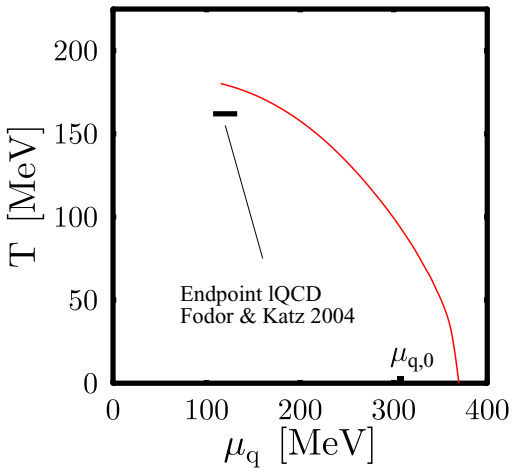


Figure 1: First order phase transition line in the T-μ plane.

References

[1] Z. Fodor and S. D. Katz, JHEP **0404** (2004) 050.

[2] A. Dumitru, D. Roder and J. Ruppert, Phys. Rev. D **70** (2004) 074001.

[3] F. Karsch, K. Redlich and A. Tawfi k, Phys. Lett. B571 (2003) 67.

[4] P. Papazoglou, D. Zschiesche, S. Schramm, J. Schaffner-Bielich, H. Stoecker and W. Greiner, Phys. Rev. C **59** (1999) 411.

[5] M. A. Stephanov, Prog. Theor. Phys. Suppl. **153** (2004) 139 [Int. J. Mod. Phys. A **20** (2005) 4387]

* Work supported by GSI and CSC Frankfurt.

[1] Another scalar isoscalar fi eld, the dilaton χ, which simulates the breaking of the QCD scale invariance, can be identifi ed with the gluon condensate, which is found to only be of importance if it couples rather strongly to baryonic degrees of freedom. Otherwise, the change in dense or hot matter is negligible. Thus, we want to focus here on the role of the quark condensates and keep the gluon condensate frozen ($\chi = \chi_0$).

[2] In principle, the whole resonance spectrum should be included in the Lagrangian. However, to keep the number of couplings small, we effectively describe the influence of the baryonic spectrum by a single resonance with adjustable couplings and mass.

Approaching the strongly coupled regime of color-superconductivity*

D. Nickel, TU Darmstadt, Darmstadt, Germany
R. Alkofer, U Graz, Graz, Austria
J. Wambach, TU Darmstadt & GSI, Darmstadt, Germany

Quark matter at sufficiently high density and low temperatures is expected to be a color-superconductor. Due to asymptotic freedom, it can be systematically studied at high densities in a weak coupling expansion [1, 2]. At low densities, i.e. in the strongly coupled regime, such an expansion is lacking.

Therefore non-perturbative methods such as truncated Dyson-Schwinger equations have to be applied here [3]. In our approach, we extend the scheme proposed in [4], which is in quantitative and qualitative agreement with lattice calculations for the vacuum, to finite densities. For this purpose, we work in the framework of the Nambu-Gor'kov formalism (see [2]) and add the medium polarization of undressed quarks to the inverse gluon propagator for describing screening and damping effects by particle-hole excitations in a first step. As a result, our Dyson-Schwinger equation for the quark propagator is closed under the input of the strong running coupling constant, which is taken from [4] and we recover the weak coupling results at asymptotically large densities. In this way, we bridge the gap to the non-perturbative regime, which is usually investigated within phenomenological, NJL-type models.

In Fig.(1) we present our results for the quasiparticle gap-functions in the chiral limit for the the superconducting 2SC and CFL phase as a function of the chemical potential and compare those to the extrapolated weak coupling results [5]. We observe, that the extrapolated weak coupling results differ from our self-consistent solutions by more than a factor of five at moderate chemical potentials around $500\mathrm{MeV}$, where the gap function are of order $100\mathrm{MeV}$, although converging towards each other at larger values.

Including a strange quark mass in our investigations opens the question, at which mass the 2SC phase becomes favored compared to the CFL phase due to the separation of the Fermi surfaces (see [6]). In contrast to phenomenological models, we find significantly larger values for the critical value of the renormalized strange quark mass, which is shown in Fig.(2). Especially for a physical value of the strange quark mass, we find that the CFL phase is preferred. The reason for the difference to former results in NJL-type models originates in our inclusion of the medium modification of the interaction and is therefore considered as an advantage of our approach.

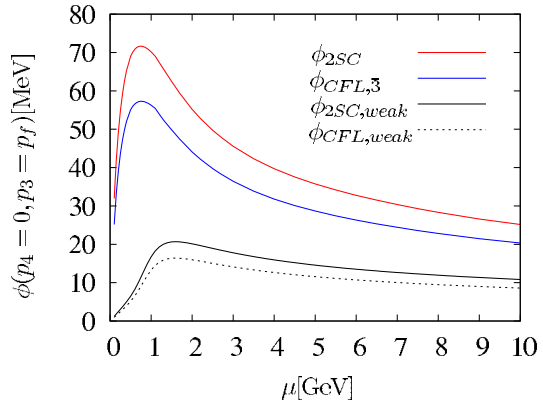


Figure 1: Quasiparticle gap-functions on the Fermi surface for the 2SC and CFL phase within our approach, ϕ_{2SC} and ϕ_{CFL}, and from the extrapolation of the weak coupling result, $\phi_{2SC,weak}$ and $\phi_{CFL,weak}$, as a function of the chemical potential μ.

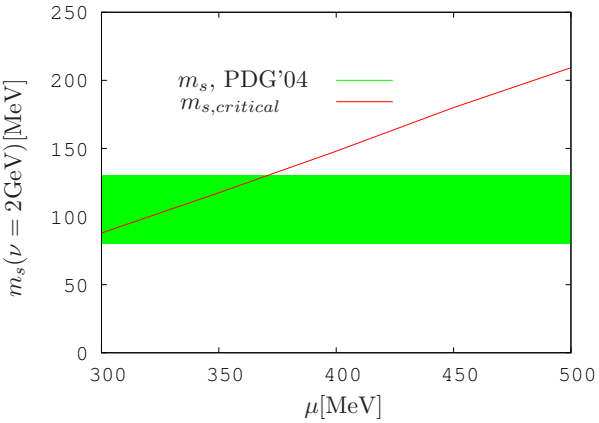


Figure 2: Critical renormalized strange quark mass $m_{s,critical}$ for color-flavor unlocking as a function of the chemical potential μ compared to its physical value $m_{s,\mathrm{PDG'04}}$ from the particle data group.

References

[1] T. Schäfer and F. Wilczek, Phys. Rev. D60, 114033(1999).

[2] D.H. Rischke, Prog. Part. Nucl. Phys. 52(2004) 197-296.

[3] C.D. Roberts, S.M. Schmidt, Prog. Part. Nucl. Phys. 45(2000) 1-103.

[4] C.S. Fischer and R. Alkofer, Phys. Rev. D67, 094020(2003).

[5] D. Nickel, R. Alkofer, J. Wambach, in preparation.

[6] M. Alford, J. Berges and K. Rajagopal, Nucl.Phys. B558(1999)219-242.

* Work supported by BMBF and DAAD.

Phase diagram of neutral quark matter: Self-consistent treatment of quark masses*

V. Werth, M. Buballa, TU Darmstadt, Germany
D. H. Rischke, S. B. Rüster, I. A. Shovkovy, J.W. Goethe Universität, Frankfurt, Germany

Theoretical studies suggest that quark matter at sufficiently high densities and sufficiently low temperatures may be a color superconductor. (For a review on color superconductivity see for example, Ref. [1].) In nature such conditions appear in the central regions of neutron stars. Therefore it is possible that matter is color superconducting in the cores of these objects.

In compact stars matter has to be neutral with respect to electric and color charges. It should also remain in β equilibrium. Taking these constraints into account may have a strong effect on the competition between different phases of deconfined quark matter at large densities [2, 3]. We studied locally neutral three-flavor quark matter within the framework of a Nambu–Jona-Lasinio model [4]. In the analysis we take dynamically generated quark masses into account self-consistently.

For each point in the plane of temperature T and quark chemical potential μ we have to compute nine quantities for each of the competing phases. These are the three constituent quark masses, M_u, M_d, and M_s, the three gap parameters, Δ_{ud}, Δ_{us}, and Δ_{ds}, which measure the diquark condensates, one electric and two color charge chemical potentials, μ_Q, μ_3, and μ_8, which are needed to ensure neutrality. These are obtained by solving a coupled set of six gap equations together with the three neutrality conditions.

In Fig. 1 the resulting phase diagram of neutral quark matter is displayed in the T-μ plane. In principle there could be seven color superconducting phases (different combinations of non-vanishing Δ_{ab}). We see that for our conditions only three appear as the ground state of neutral matter. These are the two-flavor color superconductor (2SC) with $\Delta_{ud} \neq 0$ and $\Delta_{us} = \Delta_{ds} = 0$, the color-flavor locked phase (CFL) with $\Delta_{ud}, \Delta_{us}, \Delta_{ds} \neq 0$, and the uSC phase with $\Delta_{ud}, \Delta_{us} \neq 0$ and $\Delta_{ds} = 0$.

In the region of small quark chemical potentials and not too high temperatures we find a non-superconducting phase in which the approximate chiral symmetry is spontaneously broken and quarks have relatively large constituent quark masses (χSB). At intermediate quark chemical potentials and very low temperatures there is a chirally restored normal (non color superconducting) quark matter phase (NQ). In this region quark pairing is not possible because charge neutrality disfavors a 2SC-type pairing and the strange quark mass is to high to allow cross-flavor pairing of light and strange quarks. For higher temperatures thermal smearing allows for up-down pairing. This feature of the phase diagram is sensitive to the choice of the diquark coupling. A stonger coupling enables 2SC-pairing also for low temperatures. For higher chemical potentials the strange quark mass drops and uSC- and CFL-pairing become possible.

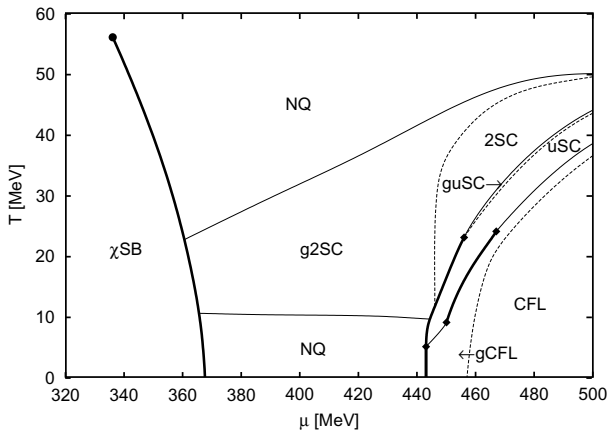


Figure 1: Phase diagram of neutral quark matter. First-order phase boundaries are indicated by bold solid lines, whereas the thin solid lines mark second-order phase boundaries. The dashed lines indicate the (dis-)appearance of gapless modes in different phases, and they do not correspond to phase transitions.

These results might be relevant for understanding the physics of (hybrid) neutron stars with quark cores, in which the deleptonization is completed. For protoneutron stars one has to take into account neutrino trapping which has a strong effect on the phase structure [5].

References

[1] K. Rajagopal and F. Wilczek, hep-ph/0011333.

[2] M. Alford and K. Rajagopal, JHEP **0206**, 031 (2002).

[3] S. B. Rüster, I. A. Shovkovy and D. H. Rischke, Nucl. Phys. A **743**, 127 (2004).

[4] S. B. Rüster, V. Werth, M. Buballa, I. A. Shovkovy and D. H. Rischke, Phys. Rev. D, **72**, 034004 (2005).

[5] S. B. Rüster, V. Werth, M. Buballa, I. A. Shovkovy and D. H. Rischke, hep-ph/0509073.

* Work supported in part by the Virtual Institute of the Helmholtz Association under grant No. VH-VI-041, and by Gesellschaft für Schwerionenforschung (GSI), and by Bundesministerium für Bildung und Forschung (BMBF). S. R. thanks for using the Center for Scientific Computing (CSC) of the Johann Wolfgang Goethe-Universität Frankfurt am Main.

Quark Fluctuations in a Chiral Model at finite chemical potential*

C. Sasaki, B. Friman, K. Redlich,† GSI, Darmstadt, Germany

During recent years the phenomenological importance of fluctuations in finite temperature/finite density QCD has been recognized [1]. The analysis of fluctuations is an essential method to characterize the thermodynamic properties of a system. Enhanced fluctuations signal the onset of a phase transition [2]. Thus, measuring modifications in the magnitude of fluctuations in heavy ion collisions on an event–by–event basis is considered as a phenomenological probe of deconfinement and chiral symmetry restoration [1].

Recently the quark susceptibilities have been computed in lattice QCD [3, 4]. Of particular interest are the results on isovector, quark number and the off-diagonal quark susceptibilites.

The quark number susceptibilities $\chi_{ff'}$ are defined by

$$\chi_{ff'} = \frac{\partial^2 \Omega}{\partial \mu_f \partial \mu_{f'}} \,, \qquad (1)$$

where $\Omega(T, \mu_f, V)$ is the thermodynamic potential and μ_f the chemical potential of quark flavour f. In this work [5] we explore the quark susceptibilities in the Nambu-Jona Lasinio (NJL) model in the chiral limit for isospin symmetric systems.

In two flavor QCD the (net) quark number susceptibility χ_q is expressed as the sum of the u and d quark susceptibilities: $\chi_q = 2(\chi_{uu} + \chi_{ud})$. According to universality arguments χ_q should diverge at the chiral end point independently of the quark masses. In the parameter range outside the chiral end point the net quark number fluctuations are expected to be finite. Thus, an observation of a non-monotonic structure of $\chi_q/\chi_q^{(free)}$ along the phase boundary is expected if the QCD phase diagram features a chiral critical point. This is illustrated in Fig. 1, where we show $\chi_q/\chi_q^{(free)}$ as a function of temperature for different values of the chemical potential. The susceptibility diverges at the phase transition for the critical value of the chemical potential, $\mu_q = 305$ MeV, at $T = 42$ MeV while it remains finite both for larger and smaller values of μ_q.

In Fig. 2 we show the phase diagram of the NJL model for different values of the isoscalar vector coupling constant. The parameters were adjusted so as to obtain a critical temperature at $\mu_q = 0$ of approximately 170 MeV. With increasing strength of the vector coupling, the critical point moves to smaller temperatures and larger values of μ_q and eventually for $G_V^{(S)} \gtrsim 0.6\, G_S$ the transition remains second order in the whole phase diagram. We note that the position of the critical point is strongly model dependent.

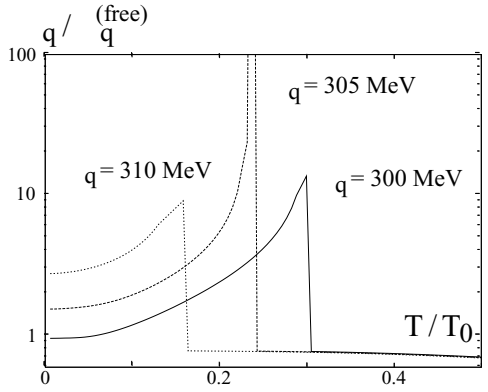


Figure 1: The quark number susceptibility near the critical point.

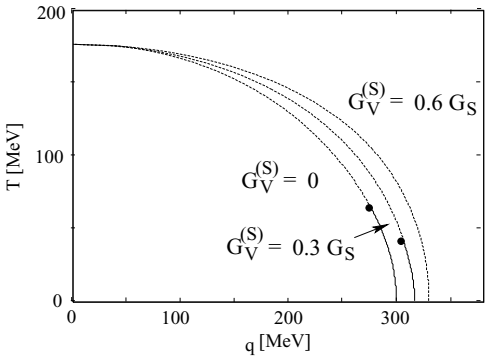


Figure 2: The phase diagram of the NJL model.

References

[1] For a recent review, see e.g., S. Jeon and V. Koch, *Quark Gluon Plasma 3*, R. C. Hwa and X.-N. Wang (Eds.), World Scientifi c 2004, p. 430 and references therein.

[2] T. Kunihiro, Phys. Lett. B **271** (1991) 395

[3] C. R. Allton, M. Doring, S. Ejiri, S.J. Hands, O. Kaczmarek, F. Karsch, E. Laermann and K. Redlich, Phys. Rev. D **71** (2005) 054508

[4] R.V. Gavai and S. Gupta, Phys. Rev. D73 (2006) 014004 ; Phys. Rev. D72 (2005) 054006 ; Eur. Phys. J. C43 (2005) 31

[5] C. Sasaki, B. Friman and K. Redlich, to be published

* Supported by the Helmholz Association under grant no. VH-VI-041

† Institute of Theoretical Physics, University of Wroclaw, PL–50204 Wrocław, Poland

Self-consistent in-medium masses of light, scalar and vector mesons from the linear σ-model

Stefan Strüber*, Institut für Theoretische Physik, Johann Wolfgang Goethe-Universität

Abstract

Within the linear σ-model consisting of the lightest scalar and vectorial degrees of freedom subject to a chiral $U(2)_R \times U(2)_L$-symmetry, the temperature dependent masses and the chiral condensate have been calculated self-consistently via the CJT-formalism [1] in the so-called "double-bubble" approximation.

Introduction

Focused on the lightest mesonic degrees of freedom a possible form of an effective-model Lagrangian for the mesonic physics of QCD is

$$\begin{aligned}\mathcal{L} \;=\; & \mathrm{Tr}[(D^\mu\Phi)^\dagger D^\mu\Phi] - m_0^2\mathrm{Tr}[\Phi^\dagger\Phi] - \lambda_1(\mathrm{Tr}[\Phi^\dagger\Phi])^2 \\ & -\lambda_2\mathrm{Tr}[(\Phi^\dagger\Phi)^2] + c(\det(\Phi^\dagger)+\det(\Phi)) \\ & +\mathrm{Tr}[H(\Phi^\dagger+\Phi)] - 1/4\mathrm{Tr}[(L^{\mu\nu})^2+(R^{\mu\nu})^2] \\ & +m_1^2/2\mathrm{Tr}[(L^\mu)^2+(R^\mu)^2]\,,\end{aligned}$$

where $\Phi = (\sigma + \mathrm{i}\eta)t_0 + (\vec{a}_0 + \mathrm{i}\vec{\pi})\vec{t}$, $L_\mu, R_\mu = (\omega_\mu \mp f_\mu^1)t_0 + (\vec{a}_\mu^1 \mp \vec{\rho}_\mu)\vec{t}$, $L_{\mu\nu} = \partial_\mu L_\nu - \partial_\nu L_\mu - \mathrm{i}g[L_\mu, L_\nu]$ and $D_\mu\Phi = \partial_\mu\Phi + \mathrm{i}g(\Phi L_\mu - R_\mu\Phi)$. The λ-terms are the possible scalar self-interactions, the c-term generates the $U(1)_A$ anomaly and the H-term breaks the chiral symmetry due to degenerated nonzero u and d masses. The covariant coupling of the scalar and vector mesons as well as the vectorial self-interaction is subject to local $U(2)_R \times U(2)_L$ gauge symmetry and thus restricts strongly the number of possible terms. Working out the isospin algebra, the ω-meson completely drops out consistent with neglecting the Wess-Zumino anomaly [2], while the f_1 only couples to scalars and the $\vec{\rho}$ to triplets.

A convenient nonperturbative resummation method circumventing problems correlated to the nonanalyticity of the coupling constant at finite temperature is the CJT-formalism, which is a generalisation of the concept of the effective action for one-particle irreducible diagrams to two-particle irreducible diagrams. This formalism was used in the "double-bubble" approximation to calculate the temperature dependence of the upper meson masses and the chiral condensate, χ, self-consistently.

Results

The parameters in the above Lagrangian have been adjusted to the vacuum masses and the pion decay constant under neglecting the divergent vacuum selfenergies. For a vacuum σ-mass of 600MeV, as shown in Fig. 1, the chiral phase transition turns out to be a crossover transition with a critical temperature of 167MeV. Around this phase transition the chiral partners start to degenerate, except for the f_1 and the ω owing to the complete decoupling of the latter. Assuming a vacuum mass for the σ of 700MeV the phase transition turns out to be of second order with an critical temperature of 171MeV. For higher vacuum σ masses the phase transitions are of first order corresponding to higher critical temperatures. However, none of these latter phase transitions goes into the complete restored phase, but jumps to significantly lower values of the order parameter.

Comparing the scalar sector of this two-flavour model with mere scalar linear σ-models with different numbers of flavours [3], it evinces that the influence from the vector-mesons on the scalars is much bigger than the influence coming from additional scalar degrees of freedom like the strange and the charm, due to the fact, that the coupling between scalars and vectors is about ten times stronger than the coupling between the scalars.

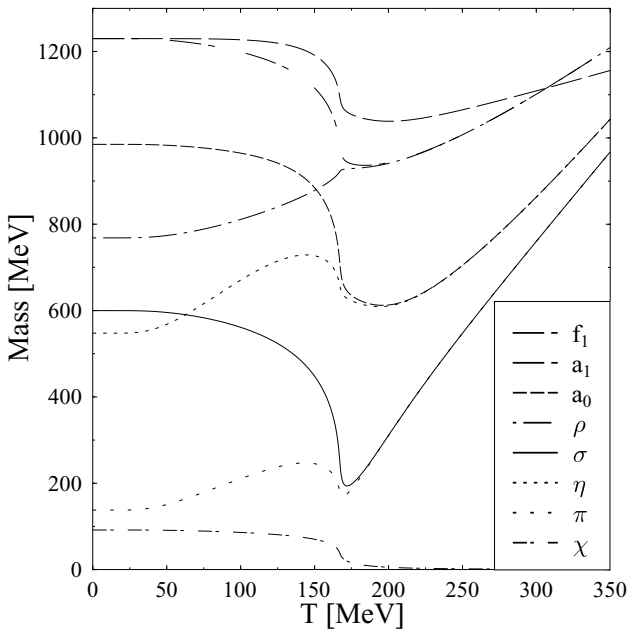


Figure 1: The meson masses and the chiral condensate as a function of the temperature.

References

[1] J. M. Cornwall, R. Jackiw and E. Tomboulis, Phys. Rev. D **10**, 2428 (1974).

[2] J. Wess and B. Zumino, Phys. Lett. B **37** (1971) 95.

[3] D. Roder, J. Ruppert and D. H. Rischke, Phys. Rev. D **68** (2003) 016003 [arXiv:nucl-th/0301085].

* strueber@th.physik.uni-frankfurt.de

Critical Region around the QCD Critical End Point

B.-J. Schaefer,[a,b] and J. Wambach,[a,c]

[a] Institut für Kernphysik, TU Darmstadt, Germany [b] Institut für Physik, Karl-Franzens-Universität, Graz, Austria
[c] GSI, Darmstadt, Germany

There is growing evidence that the phase diagram of QCD with two-flavors has a critical end point (CEP). Recently, its implications to the phenomena in the heavy ion physics are intensively under debate in order to identify its location experimentally. It is a genuine second-order phase transition, where the first-order transition line at lower temperatures T and higher quark chemical potentials μ terminates. Because this point lies in the universality class of the three-dimensional Ising model it implies the existence of a massless scalar mode and a singular power-law behavior with Ising critical exponents. It is expected that the fluctuations of the scalar sigma field will be reflected in the event-by-event fluctuations of pion observables.

The structure of the critical region near the CEP is not point-like but has a much richer structure. We define the critical region around the CEP as the region where the mean-field theory breaks down and nontrivial critical exponents emerge.

In order to estimate the size of this region we have performed a mean-field calculation and a proper-time renormalization group (PTRG) analysis within the two-flavor quark-meson model [1, 2]. The Lagrangian of the model is determined by

$$\mathcal{L} = \bar{q}\left(i\partial\!\!\!/ - g(\sigma + i\gamma_5\vec{\tau}\vec{\pi}) + \mu\gamma_0\right) q + \frac{1}{2}(\partial_\mu\vec{\phi})^2 - U(\vec{\phi}) \; .$$

The purely mesonic potential is given by $U(\vec{\phi}) = \frac{\lambda}{4}(\vec{\phi}^2 - v^2)^2 - c\sigma$. The isoscalar-scalar σ field and the three isovector-pseudoscalar pion fields $\vec{\pi}$ together form the chiral vector field $\vec{\phi} = (\sigma, \vec{\pi})$. Without the explicit symmetry breaking term c in the potential the Lagrangian is invariant under global chiral $SU(2)_L \times SU(2)_R$ rotations.

The scalar susceptibility χ_σ corresponds to the zero-momentum projection of the scalar propagator and encodes all fluctuations of the chiral order parameter. It is related to the inverse sigma mass squared.

In Fig. 1 the contour regions for four different ratios of the scalar susceptibilities $R_s = \chi_\sigma(T,\mu)/\chi_\sigma(0,0)$ in mean-field approximation around the CEP are shown. The region where the susceptibility is enhanced is elongated in the direction parallel to the first-order transition line.

The deeper reason for the elongated shape of the critical region parallel to the first-order transition line can be understood by a study of the critical exponent of the susceptibility at the critical point. The form of this divergence depends on the route by which one approaches the critical point. For the path asymptotically parallel to the first-order transition line the divergence of the susceptibility scales with an certain exponent. For any other path to the CEP which is not parallel to the first-order line the divergence scales with another exponent. Including fluctuations will change the critical exponents and therefore the shape of the critical region. This is demonstrated in Fig. 2 where the same contour plot as in Fig. 1 but within an RG analysis is shown.

In conclusion, including fluctuations changes the critical region around the CEP drastically. It becomes more compressed.

References

[1] B.-J. Schaefer and J. Wambach, *in preparation*.

[2] B.-J. Schaefer and J. Wambach, Nuclear Physics A **757**, 479 (2005).

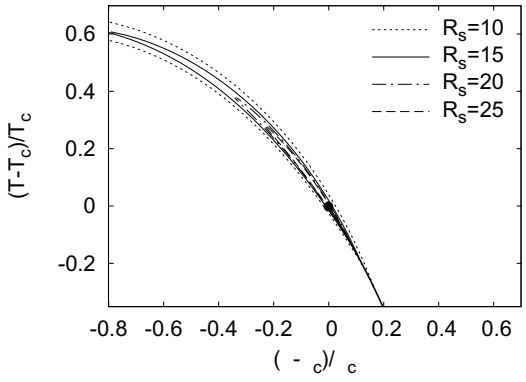


Figure 1: Contour region of different ratios R_s of the scalar susceptibilities near the CEP in mean-field approximation.

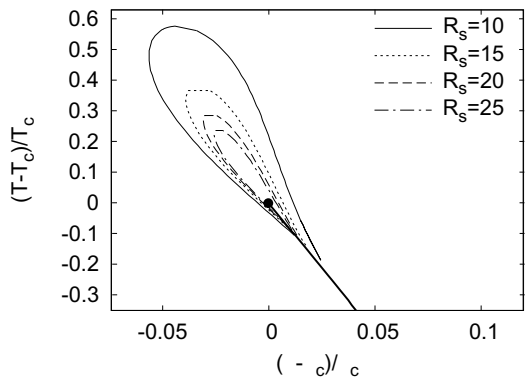


Figure 2: Same contour plot as Fig. 1 but within a RG calculation.

The D-meson spectral density in hot and dense nuclear matter *

L. Tolós[1,2,3], J. Schaffner-Bielich[2] and H. Stöcker[2,3]
[1]Gesellschaft für Schwerionenforschung, D-64291 Darmstadt, Germany
[2]Institut für Theoretische Physik & [3]FIAS, D-60438 Frankfurt am Main, Germany

Understanding the properties of matter under extreme conditions of density and temperature is a topic of high interest over the last years due to the implications in heavy-ion experiments as well as in the study of astrophysical phenomena. The CBM experiment of the FAIR project at GSI will investigate highly compressed nuclear matter, permitting the exploration of the QCD phase diagram for high-baryon density. In particular, the research program will address, among others, the investigation of the in-medium modifications of mesons with charm-quark content.

The D-meson spectral density under conditions resembling those expected at FAIR has been obtained by performing a microscopic self-consistent coupled-channel calculation in dense nuclear matter [1] at finite temperature [2], assuming a separable potential for the s-wave DN interaction. The parameters of this model, such as coupling constant and cutoff, have been determined by generating dynamically the position and width of the $\Lambda_c(2593)$ resonance. The introduction of temperature in the in-medium DN interaction affects the intermediate channels (DN, $\pi\Lambda_c$, $\pi\Sigma_c$, $\eta\Lambda_c$ and $\eta\Sigma_c$) by modifying the Pauli blocking of the nucleons, the Bose distribution on the pionic intermediate states together with the dressing of D-mesons, nucleons and pions.

In Fig. 1 the D-meson spectral density at zero momentum and T=120 MeV is shown together with the spectral density at T=0 MeV for nuclear matter saturation density, $\rho_0 = 0.17$ fm^{-3}. The spectral density is displayed for two approaches: self-consistent calculation of the D-meson self-energy including the dressing of the nucleons in the intermediate states (left panel) and the self-consistent calculation including not only the dressing of nucleons but also the self-energy of pions (right panel). Compared to the zero temperature case, the quasiparticle peak at finite temperature stays close to its free position for the range of densities analyzed (from ρ_0 up to $3\rho_0$). This is due to the fact that the Pauli blocking is reduced with increasing temperature. Furthermore, structures present in the spectral distribution at T=0 are washed out. However, the spectral density still shows a considerable width.

This small shift of the D-meson mass in the hot nuclear medium is in stark contrast with the large changes (-50 to -200 MeV) claimed in previous mean-field calculations. In our model, the self-consistent coupled-channel calculation together with finite temperature effects result in an overall reduction of the in-medium modifications independently of the in-medium properties of the intermediate states. In fact, based on the mean-field predictions, an enhancement of open-charm in nucleus-nucleus collisions was predicted

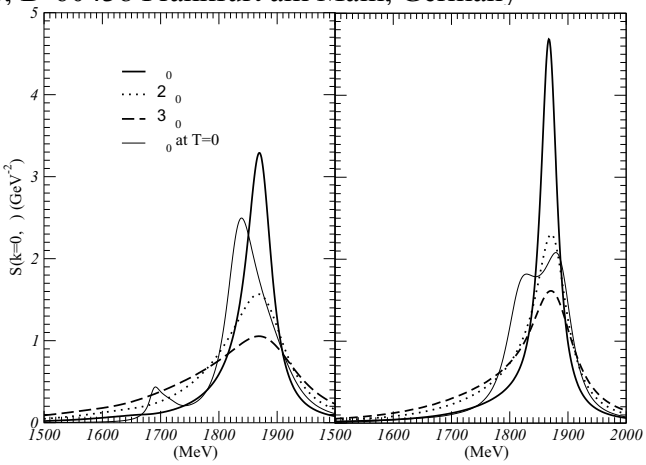


Figure 1: D-meson spectral density at $k_D = 0$ and T=120 MeV as a function of energy for different densities, together with the D-meson spectral density at $k_D = 0$ and T=0 MeV for normal nuclear matter density ρ_0 in the two approaches considered.

in order to understand the enhancement of 'intermediate-mass dileptons' in Pb+Pb collisions at the SPS energies [3]. According to our model, the inclusion of a considerable width of the D-meson in the medium (40-50 ρ/ρ_0 for T=120 MeV) is the only source which could lead to an enhanced in-medium D-meson production, as studied for kaons in Ref. [4].

The in-medium effects devised here can be tested experimentally by the CBM experiment at the future International Facility at GSI. Our results imply that the effective mass of the D-meson, however, may not be drastically modified in dense matter at finite temperature, but the D-meson develops an important width in this hot and dense environment. Therefore, the abundance of D-mesons in nucleus-nucleus collisions should be calculated in off-shell transport theory. Our calculation indicates that the medium modifications to the D-mesons in nucleus-nucleus collisions will be dominantly on the width and not, as previously reported, on the mass.

References

[1] L. Tolos, J. Schaffner-Bielich and A. Mishra, Phys. Rev. C **70**, 025203 (2004) [arXiv:nucl-th/0404064].

[2] L. Tolos, J. Schaffner-Bielich and H. Stoecker, arXiv:nucl-th/0509054.

[3] W. Cassing, E. L. Bratkovskaya and A. Sibirtsev, Nucl. Phys. A **691** (2001) 753 [arXiv:nucl-th/0010071].

[4] L. Tolos, A. Polls, A. Ramos and J. Schaffner-Bielich, Phys. Rev. C **68** (2003) 024903 [arXiv:nucl-th/0302082].

* Work partially supported by the Alexander von Humboldt Foundation

Open-charm systems in cold nuclear matter

M.F.M. Lutz, GSI, Darmstadt, Germany
C.L. Korpa, University of Pecs, Hungary

It has been suggested to explore the possible mass modifications of D mesons with the FAIR project at GSI. It is planned to study such effects by detecting D mesons in heavy-ion reactions but also in antiproton-nucleus reactions. The two approaches are complementary, with the second focusing on the properties of D mesons in cold nuclear matter. Thus it is of importance to develop a thorough theoretical understanding of how the D mesons may change their properties in nuclear matter.

At present there are only few works published on the properties of non-strange D mesons. An important step towards a realistic approach to the D^+ meson in nuclear matter was taken by Tolos et al. [1], who did not insist on a mean field approach exploring the possible influence of the $\Lambda_c(2594)$ resonance on the nuclear dynamics of the D^+ meson. The key ingredient of a realistic description are the $D^+N \to D^+N$ scattering amplitudes, that determine the D^+ meson self energy at least for dilute nuclear matter. In turn the results of [1] depend decisively on their particular form of the coupled-channel amplitudes. Recently a more complete computation [2] arrived at scattering amplitudes that differ significantly from those of [1]. The interaction was saturated by a t-channel vector meson exchange. As an important new result of [2] the isospin zero amplitude shows two resonance structures around 2.6 GeV. A narrow state that couples dominantly to the $DN, D_s\Lambda$ channels and a broader state that is interpreted as a chiral excitation of the open-charm sextet $\frac{1}{2}^+$ ground states [3]. The narrow state should be identified with the observed state $\Lambda_c(2594)$. The broader one, which couples strongly to the $\pi\Sigma_c$ channels, awaits experimental confirmation and couples very weakly to the DN channel. In contrast to [1] the isospin one amplitude of [2] reflects a narrow resonance of mass 2.62 GeV which couples dominantly to the $DN, D_s\Sigma$ channels. This additional resonance affects the properties of D^+ mesons in nuclear matter significantly.

Given the isospin averaged D^-N scattering length of [2] the mass shift of a D^- meson in nuclear matter is fully determined by the low-density theorem. The low-density mass shift of 17 MeV is quite close to the self consistent result shown in Fig. 1. Self-consistency leads to a mass shift of 18 MeV at saturation density and 38 MeV at twice saturation density. The result of a self-consistent computation for the D^+ mass distribution is shown also in Fig. 1. The spectral function has a two-mode structure, which is a consequence of important resonance-hole contributions [4]. Note that the masses of the $\Lambda_c(2594)$ and $\Sigma_c(2620)$ are almost degenerate. At saturation density the main mode is pushed up by about 32 MeV as compared to the free-space meson. The repulsive shifts are an immediate consequence of the negative scattering lengths feeded into the low-density theorem.

We turn to the mesons with non-zero strangeness. The study of [2] predicts the existence of a coupled-channel molecule in the $(D_s^-N,\ \bar{D}\Lambda,\ \bar{D}\Sigma)$ system. The latter carries exotic quantum numbers that can not be arranged by three quarks only. The binding of about 190 MeV for the $N_{s\bar{c}}(2780)$ state predicted in [2] awaits experimental confirmation. If confirmed the s-wave $D_s^-N \to D_s^-N$ scattering amplitude must show a prominent pole structure at subthreshold energies. The presence of the $N_{s\bar{c}}(2780)$ leads to a well separated two-mode structure of the D_s^- spectral distribution [4]. The main mode is pushed up by less than 10 MeV at nuclear saturation density.

An exotic state $N_{c\bar{s}}(2892)$ about 75 MeV below the D_s^+N threshold is generated in [2]. As a consequence the in-medium spectral distribution of the D_s^+ is most striking [4]. The two modes expected from the possible existence of the $N_{\bar{c}s}(2892)$ state are almost merged into one broad structure, in particular at intermediate meson momenta 400 MeV. Clearly this result is an immediate consequence of the small binding energy of the $N_{\bar{c}s}(2892)$ state.

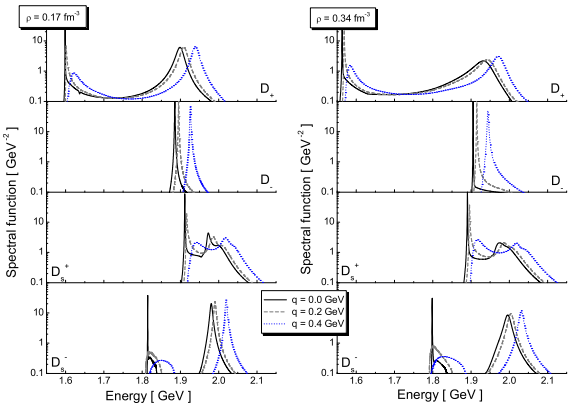


Figure 1: Spectral distribution of D mesons in cold nuclear matter.

References

[1] L. Tolos, J. Schaffner-Bielich and A. Mishra, Phys. Rev. 70 (2004) 025203.

[2] J. Hofmann and M.F.M. Lutz, Nucl. Phys. A 763 (2005) 90.

[3] M.F.M. Lutz and E.E. Kolomeitsev, Nucl. Phys. A 730 (2004) 110.

[4] M.F.M. Lutz and C.L. Korpa, Phys. Lett. B 633 (2006) 43.

Asymmetric neutrino emission in quark matter and pulsar kicks

I. Sagert, Institute for Theoretical Physics, J. W. Goethe University, Germany
J. Schaffner-Bielich,Institute for Theoretical Physics, J. W. Goethe University, Germany

Observations show that pulsars have large spatial velocities in the range of 100 km/s up to 1600km/s [1]. We propose a propulsion mechanism for neutron stars based on asymmetric neutrino emission from the direct Urca process in quark matter in the presence of a strong magnetic field. Due to the large central densities in neutron stars quark matter is considered to be present in the core where the magnetic field strength can also be much higher than on the surface. The strong magnetic field forces the electrons into the lowest Landau Level polarising their spin and accordingly the neutrino spin and momentum due to parity violation. The degree of polarisation χ depends on the neutron star's temperature T, the electron chemical potential μ_e and the magnetic field strength B. The neutrinos propagate along the magnetic field axis in one direction and work as a propulsion mechanism for the neutron star accelerating it to a velocity v_{ns} in dependance of given initial temperature T_0, neutron star's mass, radius R of the neutrino emiting quark phase and μ_q, the quark chemical potential. For a typical proto-neutron star T_0 is in the range of 10 MeV but drops very quickly below 1 MeV and the neutrino emisson doesn't contribute significantly to v_{ns} any more. Fig.1 shows the constraints on the magenetic field strength to fully polarise the electrons for a given electron chemical potential μ_e and T, showing that the necessary magnetic field for full polarisation increases with both, μ_e and T.

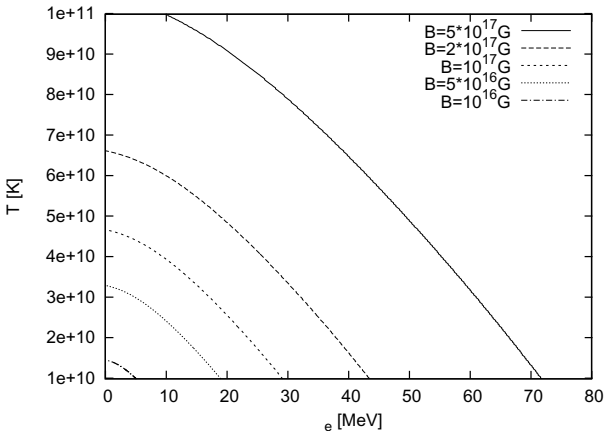


Figure 1: T, μ_e and magnetic field strength B for $\chi = 1$

Fig.2 displays different neutron star velocities for given T_0, quark phase radius R and fully spin polarised electrons. The lowest curve corresponds to v_{ns} =100 km/s whereas the velocity increases with each curve in steps of 100 km/s, i.e. the highest curve represents neutron stars with 1000 km/s. The stars have a total mass of $1.4M_\odot$ and the quark and electron chemical potentials were set to 400 MeV and 100 keV, respetively. The strong coupling constant was assumed to be $\alpha_s = 0.5$. In Fig.2 we additionally plot the neutrino mean free paths in quark matter l_q and neutron matter l_n as given in [2], combining the neutrino mean free paths for absorption and scattering for a neutrino energy of $E_\nu = 3T$. It can be seen from Fig.2 that v_{ns} ∼500 km/s can

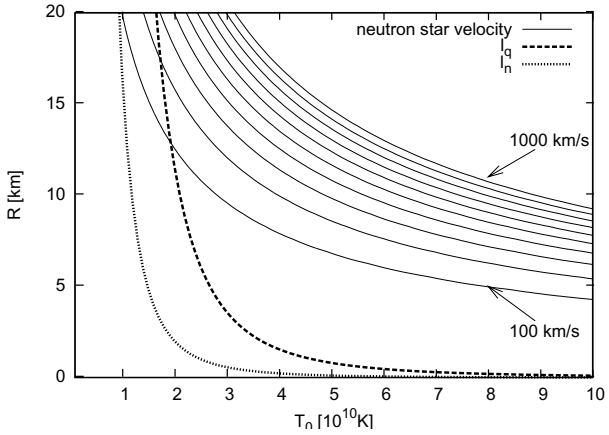


Figure 2: v_{ns} and ν mean free paths

be reached for T∼ $6 \cdot 10^{10}$K and a quark phase radius R∼10 km. As we require fully polarised electrons the necessary magnetic field can be taken from Fig.1. Assuming $T_0 =$ 6 MeV and μ_e <1 MeV the core magnetic field should be in the range of $2 \cdot 10^{17}$G. The neutrino mean free paths in Fig.2 are very small causing the neutrinos to interact with the medium on their way to the surface. Due to these interactions the neutrinos isotropise, thus the propulsion mechanism is not produced. This so called no-go theorem could be resolved for processes in quark matter by decreasing the electron chemical potential which therefore implies a core consisting of strange quark matter in the CFL or where their mean free path is expotentially enhanced. Furthermore [2] calculated the neutrino mean free paths in quark matter for $\mu_e \gg$T which isn't granted any more, therefore a further assignment is the calculation of neutrino mean free paths for $\mu_e \ll$T.

References

[1] G. Hobbs, D.R. Lorimer, A.G. Lyne and M. Kramer, " A statistical study of 233 pulsar proper motions", MNRAS, July 2005, p.974-992

[2] N. Iwamoto, "Neutrino Emissivities and Mean Free Paths of Degenerate Quark Matter",Annals of Physics, 1981, p.1-49

Decoherence time and entropy production in high energy Heavy Ion Collisons*

B. Müller, Duke University, USA and A. Schäfer†, Regensburg, Germany

Abstract

In high-energy hevy-ion collisons a sigificant amount of entropy can be produced merely by the decoherence of the individual nuclear multi-particle states. We argue that the time scales on which this happens are much shorter than 1 fm/c. Decoherence can therefore explain the very rapid onset of a behaviour which resembles that of a thermalised state of matter.

The mechanisms responsible for the creation of entropy in a high energy heavy ion collision (HIC) are still purely understood. One aspect is that the decoherence of a quantum mechanical state (like the ground states of the colliding nuclei) leads to a loss of information and thus to the production of entropy according to

$$S = \mathrm{Tr}\{\mathcal{D}\log\mathcal{D}\} \tag{1}$$

with the time-dependent density matrix $\mathcal{D}$. For a pure state this ratio is 1; for a completely incoherent state it is $1/N$, where N is the number of states in the region of phase space under consideration. We define as decoherence time $\tau_{\rm deco}$ the time by which this ratio has decayed to 1/e.

In the transverse plane the quark-gluon distribution of a fast moving nucleus is characterized by a saturation scale Q_s. Irrespective of details the general order of magnitude of the produced entropy per unit of rapidity is proportional to the number of independent transverse regions, which is of the order $Q_s^2R^2$, where R denotes the nuclear radius, and to the logarithm of the number of decohering partons in each region. For realistic values of Q_s this gives an entropy from decoherence of the order of 1500 per unit rapidity in Au+Au collisions [1], which is a sizeable fraction of the total produced entropy ($dS/dy \approx 5000$).

The role played by this "decoherence entropy" depends crucially on the decoherence time scale $\tau_{\rm deco}$. In [2] we have calculated this time scale and found it to be substantially smaller than 1 fm/c.

The dynamics of decoherence is a theoretically intricate and sometimes ambiguous problem. Any such calculation has, therefore, to be based on model assumptions. We analysed the nuclear collision in the rest frame of nucleus 1 (see Fig.1) and studied the interactions of virtual gluons in the nucleus at rest with Weizsäcker-Williams (WW) gluons from the fast moving nucleus 2, which populate an originally empty part of the gluon phase space. Our calculation is based on the assumption that the density matrix of gluons in the nucleus at rest can be described by a Gaussian

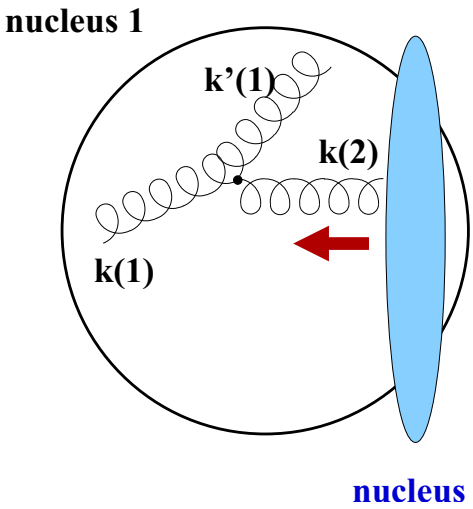


Figure 1: The process under investigation. A correlated gluon is scattered by a WW gluon and decoheres.

ansatz:

$$D^{\mu}{}_{\nu}(b,b;p^0,\vec{p},p^0,\vec{p}) = \frac{16}{VT}\pi^2\lambda^4 \tag{2}$$
$$\exp\Big\{-\lambda^2[(p_\perp)^2+(p_-)^2+(p_+)^2]\Big\}\frac{1}{2}\delta_{\mu\nu}|_{\mu,\nu\neq\perp}.$$

The correlation function of the WW gluons from nucleus 2 has been derived in [3, 4] in terms of the saturation scale Q_s.

A rather lengthy and involced calculation gives the result:

$$\tau_{\rm deco} = f(\lambda Q_s)\ \frac{1}{Q_s} \tag{3}$$

where $f(\lambda Q_s)$ denotes a double integral, which is of the order of 1. For the typical values $\lambda = 0.3$ fm and $Q_s = 1$ GeV, we find $f(\lambda Q_s) = 1.55$. We conclude that the decoherence time is roughly 0.3 fm/c, short enough for decoherence to be an important contribution to the entropy production in the pre-equilibrium stage of a heavy ion collision.

References

[1] B. Müller and A. Schäfer, hep-ph/0306309.

[2] B. Müller and A. Schäfer, hep-ph/0512100.

[3] Y. V. Kovchegov and A. H. Mueller, Nucl. Phys. B **529**, 451 (1998), hep-ph/9802440.

[4] Y. V. Kovchegov, Nucl. Phys. A **692**, 557 (2001), hep-ph/0011252.

* Work supported by BMBF and GSI

† andreas.schaefer@physik.uni-r.de

Dilepton production in heavy ion reactions at intermediate energies*

C. Fuchs, D. Cozma, E. Santini and Amand Faessler
Institut für Theoretische Physik, Universität Tübingen, Auf der Morgenstelle 14, D-72076 Tübingen

Dileptons represent a unique probe for studying nuclear matter under the extreme conditions reached during a heavy-ion collision. They allow in particular the study of meson properties, like mass and decay width, at various density and temperature regimes. For the energy regime of a few AGeV, the low mass region of the dilepton spectra measured by the DLS Collaboration [1] is underestimated by present transport calculations, in contrast to the p+p and p+d systems. In contrast to the ultrarelativistic case, the situation does not improve when in-medium spectral functions or the dropping mass scenarios are taken into account (DSL puzzle). Other scenarios like possible contributions from a quark-gluon plasma or in-medium modifications of the η mass have been excluded as a possible resolution of this puzzle. Decoherence effects [2] have been proven to be partially successful in explaining the difference between the DLS data and the theoretical predictions.

Here we investigate the dilepton production in C+C reactions at 2.0 AGeV where first data from HADES will be available. The vector meson and dilepton production is described within the framework of the resonance model in combination with the (R)QMD transport model [2]. The influence of medium effects such as quantum decoherence, collisional broadening and a dropping vector meson mass are included in the present calculations. For more deatils see [3]. Fig. 1 shows the RQMD results for C+C at 2 AGeV after the application of the HADES acceptence filter including the corresponding mass resulution [4]. The contributions from π^0 and η Dalitz decays are shown as well. The 'in-medium' calculation contains the combination of all medium effects under consideration, i.e. ρ and ω collisional broadening, mass shifts and decoherence. The corresponding spectra are normalized to the number of events $N_{\rm ev}$ and to the π^0 multiplicity. The difference between the vacuum and the 'in-medium' calculation is clearly visible, in particular around the $\rho - \omega$ peak where the collisional broadening of the ρ and ω leads to a strong suppression of the peak. The comparision to preliminary HADES data [5] is shwon in Fig.2 for the in-medium scenario. There is no doubt that the experimental spectra can only be explained under the assumption of strong medium effects. In particular the dissolution of the ρ and ω peaks due to a strong broadening of their spectral functions seems to be proven. The in-medium enhancement of low mass dilepton yield is less pronounced, though still visible. Forthcoming data for heavier systems than C+C will allow to investigate this region in more detail.

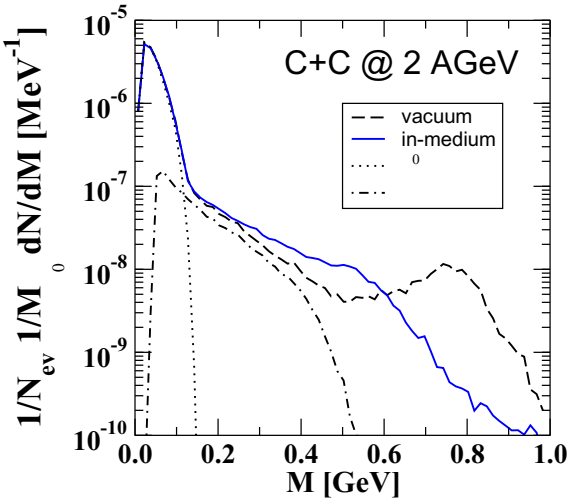


Figure 1: Dilepton spectra in C+C reactions at 2.0 AGeV after the application of the HADES acceptance filter. RQMD calculations w/o and with in-medium effects are shown.

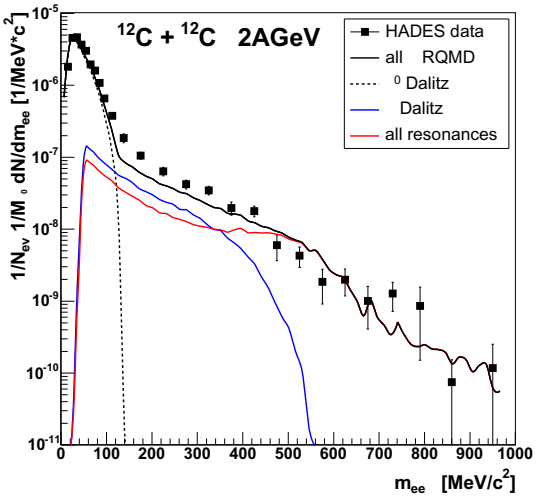


Figure 2: Comparison of the RQMD results including in-medium effects to the preliminary HADES data.

References

[1] R.J. Porter *et al.*, Phys. Rev. Lett. 79, 1229 (1997).
[2] K. Shekter *et al.*, Phys. Rev. C **68**, 014904 (2003).
[3] D. Cozma, C. Fuchs, E. Santini, A. Faessler, in preparation.
[4] C. Sturm, private communication.
[5] R. Holtzmann, talk at Quark Matter 2005.

* Work supported by BMBF (06TU202) and HGF (VH-VI-041).

Entropy per baryon of dense QCD matter at GSI-FAIR*

A. Dumitru, S. Schramm, G. Zeeb, D. Zschiesche
Institut für Theoretische Physik, J.W. Goethe Universität, Max-von-Laue Str. 1, D-60438 Frankfurt

Effective theories predict that a line of first-order phase transitions in the plane of quark-chemical potential μ_q versus temperature T ends in a critical point as the chemical potential is lowered [1]. Presently, the lattice locates that point at $T \approx 160$ MeV, $\mu_q \approx 120$ MeV [2]. The Compressed Baryonic Matter experiment at GSI-FAIR is planned to perform a dedicated experimental effort to detect that line of first-order phase transitions and its second-order critical point in relativistic heavy-ion collisions. It is hoped that by varying the beam energy, for example, one could trigger phase transitions of variable strength and perhaps even reach the critical point.

Here, we employ a non-linear $\sigma - \omega$-model with spontaneously broken $SU_L(3) \times SU_R(3)$ symmetry to model interacting hadrons on the mean-field level [3, 4]. The model is able to reproduce not only the sketched qualitative phase structure but also the location of the endpoint. The phase transition is "driven" by baryonic resonance degrees of freedom, as suggested e.g. by the dependence of the critical temperature on the quark mass as observed in lattice calculations. The properties of the high mass states (masses and couplings) are important for the actual location of the phase transition region [4].

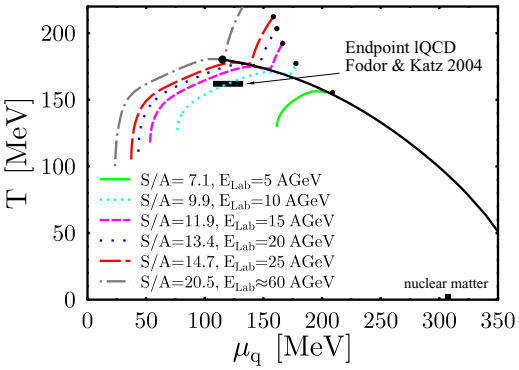


Figure 1: Phase transition line and adiabats in the T-μ_q phase diagram.

Lines of constant entropy per net baryon (adiabats) in the phase diagram correspond to perfect-fluid expansion trajectories (neglecting possible weak hadronization shocks). Fig. 1 depicts such trajectories in the T-μ_q phase diagram. On the first-order phase transition line, they "bend" towards smaller chemical potential along the phase transition/critical line. For the present EoS, the $S/A \approx 20$ adiabat goes right through the endpoint of first-order transitions, higher specific entropies then correspond to crossovers.

It is, of course, most interesting to match the adiabats to collision energies. We have done so using a simple geometrical overlap model for central collisions of large nuclei,

$$\rho_B^{ini} = 2\,\gamma_{\rm CM}\,\rho_0 \;\;,\;\; e^{ini} = \sqrt{s}\,\rho_0\,\gamma_{\rm CM}\,. \qquad (1)$$

This assumes that the entire initial beam energy and baryon number equilibrates in a Lorentz-contracted volume determined by the overlap of projectile and target in the center-of-mass frame, independent of the EoS. In the energy range of interest here, this simple model in fact reproduces the specific entropy from more elaborate three-fluid models quite well [5]. The initial energy density e^{ini} and baryon density ρ_B^{ini} then determine all other thermodynamic quantities such as the entropy per baryon.

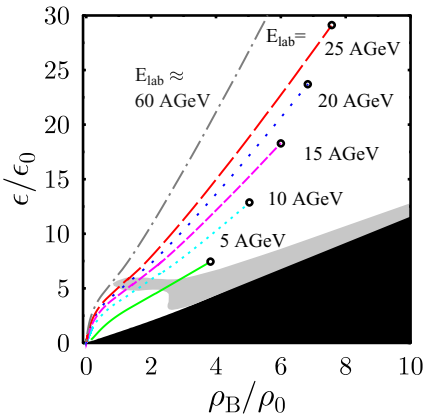


Figure 2: Adiabats in the e-ρ_B phase diagram. The grey area represents the mixed phase.

In this model beam energies between 5-10A GeV are sufficient to overshoot the shaded phase coexistence region (Fig. 2). In the considered energy range from 5-25A GeV, adiabatic expansion leads to a first-order phase transition back to the symmetry broken state with a latent heat of $\approx 120 - 160$ MeV/fm^3. Higher collision energies lead to weaker (more "critical") first order transitions. For the present model, crossover transitions correspond to beam energies in excess of 60A GeV.

References

[1] M. Stephanov, K. Rajagopal and E. Shuryak, Phys. Rev. Lett. **81** (1998) 4816.

[2] Z. Fodor and S. D. Katz, JHEP **0404** (2004) 050.

[3] P. Papazoglou, D. Zschiesche, S. Schramm, J. Schaffner-Bielich, H. Stoecker and W. Greiner, Phys. Rev. C **59** (1999) 411

[4] D. Zschiesche *et al.*, J. Phys. G **31** (2005) 935; and contribution to this volume.

[5] M. Reiter *et al.*, Nucl. Phys. A **643** (1998) 99; Y. B. Ivanov, V. N. Russkikh and V. D. Toneev, arXiv:nucl-th/0503088.

* Work supported by GSI and CSC Frankfurt.

Thermal production of glueballs in high–energy heavy–ion collisions*

I.N. Mishustin, W. Greiner, FIAS, Frankfurt am Main, Germany
L.M. Satarov, Kurchatov Institute, Moscow, Russia

Abstract

Within a simple thermal model we estimate possible multiplicities of glueballs in central Au+Au collisions in a broad range of bombarding energies. Assuming the glueball mass in the region 1.5–1.7 GeV, the model predicts on average 0.6–1.5 glueballs per event at the energy $\sqrt{s_{NN}} = 200$ GeV.

Glueballs are probably the most interesting particles predicted by the QCD but not established experimentally yet. Their mass is estimated in the range 1.5–1.7 GeV but uncertainty is introduced by the mixing with the $\bar{q}q$ states (see recent discussion in Ref. [1]). We think that relativistic heavy-ion collisions might be a right tool to produce and study these exotic particles. If the quark–gluon plasma is indeed produced in such collisions, then a significant fraction, more than 30%, of its entropy should be represented by thermal gluons. If these gluons survive until the hadronization stage, they will inevitably form glueballs as two-gluon bound states.

Analyses of experimental data on hadron production in relativistic heavy-ion collisions show [2, 3] that ratios of hadron multiplicities are well reproduced within a simple thermal model. It is assumed that all hadrons are formed in an equilibrated system characterized by a certain volume and the temperature T. Following Refs. [2, 4] we introduce a strangeness suppression factor γ_s accounting for deviations from chemical equilibrium for hadrons, containing nonzero number of strange quarks and antiquarks.

In our previous paper [5] we have used this model to predict possible yields of exotic baryonia. In this paper we apply the same model with the same parameters to estimate expected yields of glueballs, assuming that they are in thermal equilibrium with other hadrons. In order to eliminate unknown volume we consider the ratio of the glueball multiplicity to the multiplicity of $\phi(1020)$ mesons. Assuming further that the glueball is a flavor–neutral scalar particle characterized by zero chemical potential we get for this ratio:

$$\frac{N_G}{N_\phi} \simeq \frac{1}{3}\left(\frac{m_G}{m_\phi}\right)^{3/2} \gamma_s^{-2} e^{(m_\phi - m_G)/T}, \qquad (1)$$

where m_G (m_ϕ) is the glueball (ϕ–meson) mass. The r.h.s. of Eq. (1) is obtained in the Boltzmann approximation and in the lowest order in T/m.

In Fig. 1 we show the G/ϕ multiplicity ratio calculated within this model. As one can see, for the most central Au+Au collision at $\sqrt{s_{NN}} = 200$ GeV this ratio is predicted in the range of 1.5–4%. Using the measured ϕ/π multiplicity ratio at midrapidity [6, 7] and known total pion multiplicity [8] we estimate the total glueball multiplicitiy per event in the range 0.6–1.5 for $m_G = 1.5$–1.7 GeV. An order of magnitude larger multiplicities may be expected at the future LHC facility.

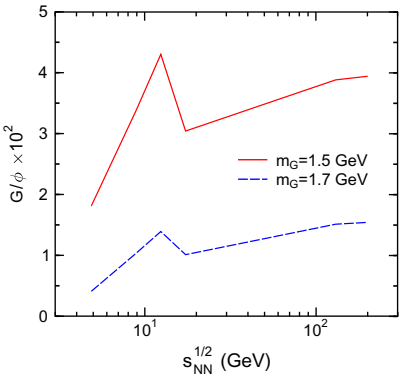


Figure 1: Ratio of average multiplicities of glueballs and ϕ–mesons in central Au+Au collisions at different c.m. bombarding energies calculated within the thermal model. Solid and dashed lines show results for the glueball mass 1.5 and 1.7 GeV, respectively.

For the experimental identification of glueballs one can use the decay mode $G \to K\overline{K}$ with predicted partial width in the range 10–40 MeV. For typical conditions when glueballs are slow in the c.m. frame one should look for the back–to–back correlated kaon and antikaon with characteristic momenta of about 0.6–0.7 GeV/c.

* Work supported by the GSI, the DFG, and the RFBR Grant 05–02–04013.

References

[1] F. Giacosa, T.H. Gutsche, V.E. Lyubovitskij, A. Faessler, Phys. Rev. D72 (2005) 094006.

[2] F. Becattini et al., Phys. Rev. C69 (2004) 024905.

[3] A. Andronic, P. Braun–Munzinger, J. Stachel, nucl-th/0511071.

[4] J. Letessier, J. Rafelski, Phys. Rev. C59 (1999) 947.

[5] I.N. Mishustin, L.M. Satarov, D. Strottman, W. Greiner, J. Phys. G31 (2005) 803.

[6] C. Adler et al., STAR Collab. Phys. Rev C65 (2002) 041901(R).

[7] S.S. Adler et al., PHENIX Collab. Phys. Rev C72 (2005) 014903.

[8] I.G. Bearden et al., BRAHMS Collab., Phys. Rev. Lett. 94 (2005) 162301.

Probability of n-body collisions in BUU*

A.B. Larionov[1,2], K. Gallmeister[1], U. Mosel[1]
[1]Institut für Theoretische Physik, Universität Giessen, D-35392 Giessen, Germany
[2]RRC "I.V. Kurchatov Institute", 123182 Moscow, Russia

The n-body ($n = 3, 4, ...$) extensions of a two-body collision scheme in the transport theory of heavy-ion collisions (HIC) were done by several groups of authors (c.f. [1, 2, 3]). These extensions have been applied to HIC [1, 2] as well as to p- and d- induced reactions [3] in 1 A GeV energy region and are shown to broaden the proton angular distributions [1] and enhance the kaon yield [2, 3].

The present work is an attempt to estimate the role of n-body collisions in HIC at 20 A GeV on the basis of the Giessen BUU model [4]. Once particles 1 and 2 collide, we start looking for other particles in a sphere of a radius $\sqrt{\sigma_0/\pi}$ centered at the collision point. Here σ_0 is a parameter which should be of the order of the total interaction cross section of 1 and 2 [2, 3]. For simplicity, we consider only baryonic many-body collisions. Thus, we put $\sigma_0 = 40$ mb which corresponds to the asymptotic high energy value of the total pp cross section. If m baryons are found in the sphere, we call this event as a $(m + 2)$-body collision.

In the upper panel of the figure we present the time evolution of the baryon density in the central 1 fm^3 cubic cell for the central Au+Au collision at 20 A GeV. The lower panel of the figure shows the frequency of n-body collisions vs time for various n. To have enough statisticks, we have counted collisions in the $(7$ fm$)^3$ central cubic cell. The contribution of the higher n's grows with the baryon density. We have checked that the n-body frequencies at a given time t can be well fitted by a Poissonian distribution

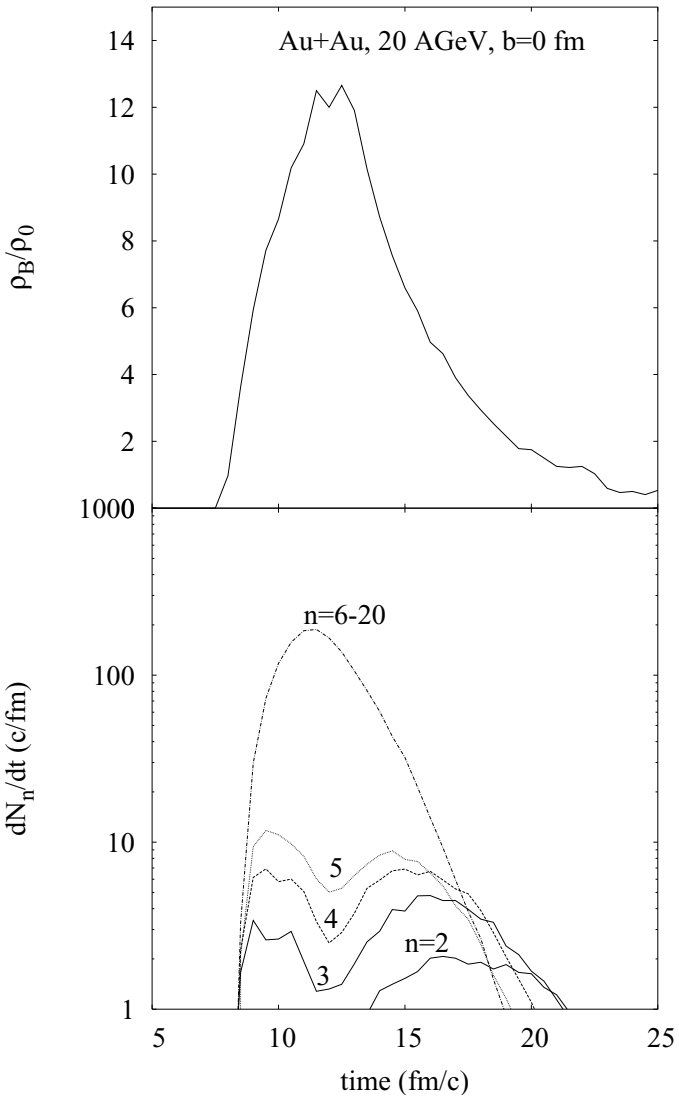
$$\frac{dN_n}{dt} = a\frac{\lambda^{n-2}}{(n-2)!}\exp\{-\lambda\}\ ,$$

where $a(t)$ and $\lambda(t)$ are the fit parameters. It turned out that $\lambda(t)$ is quite close to the average baryon number in the interaction sphere

$$\lambda(t) \simeq \frac{4}{3}\pi\left(\frac{\sigma_0}{\pi}\right)^{3/2}\rho_B(t)\ .$$

This means that our results for a relative n-body frequencies are consistent with the baryon density values reached in the central cell.

Finally, we have only counted the *attempted* n-body collisions by letting the system evolve within the usual two-body collision scenario. The actual simulation of the n-body collision events is the next step and left for future work.



References

[1] T. Kodama, S.B. Duarte, K.C. Chung, R.A.M.S. Nazareth, Phys. Rev. Lett. **49**, 536 (1982).

[2] G. Batko, J. Randrup, T. Vetter, Nucl. Phys. A **536**, 786 (1992); ibid. **546**, 761 (1992).

[3] A. Bonasera and T. Maruyama, Prog. Theor. Phys. **90**, 1155 (1993); A. Bonasera, F. Gulminelly, J. Molitoris, Phys. Rep. **243**, 1 (1994).

[4] O. Buss, L.-A. Ruso, P. Mühlich, U. Mosel, R. Shyam, in preparation.

* Work supported by GSI, Darmstadt

Charge Fluctuations from Cluster Hadronization and the D-puzzle*

S. Scherer†, M. Bleicher
Institut für Theoretische Physik, J. W. Goethe-Universität, Frankfurt am Main, Germany

Abstract

Event-by-event fluctuations of electric charge have been proposed as signals of quark-gluon plasma creation in ultra-relativistic heavy ion collisions, but can not be confirmed in experiments. We apply a quark molecular dynamics model which describes dynamically the transition from a gas of interacting quarks to hadrons via the formation of colour neutral clusters. We find a corresponding change of the fluctuation measure from the QGP value to the hadron gas value. This vindicates expectations formulated for quark recombination models and speaks in favour of the scenario of recombination as the mechanism of hadronization.

Charge fluctuations as probes of deconfinement

Event-by-event fluctuations of electric charge in ultra-relativistic heavy ion collisions,

$$D = \langle N_{\rm ch}\rangle \left\langle \delta R^2 \right\rangle \approx 4 \langle N_{\rm ch}\rangle \left\langle \delta F^2 \right\rangle \approx 4 \frac{\left\langle \delta Q^2 \right\rangle}{\langle N_{\rm ch}\rangle} \qquad (1)$$

where Q is the electric charge, $N_{\rm ch}$ is the number of charged particles, $F = Q/N_{\rm ch}$, and $R = (1+F)/(1-F)$, have been proposed as signals for the formation of a deconfined, partonic phase. Taking into account appropriate corrections for finite rapidity windows, one expects to find $D \approx 1$ for a quark gluon plasma, $D \approx 2.8$ for a resonance gas, and $D \approx 4$ for an uncorrelated pion gas [1].

Experimental measurements of D, however, consistently yield results close to the hadron gas value, even for collisions where the formation of a deconfined, partonic phase can not be doubted. This situation has been dubbed the "D paradox". It has been argued that this result can be explained naturally if hadronization is understood as the coalescence of constituent quarks [2].

Charge fluctuations in cluster hadronization

Here, we use a quark molecular dynamics model which describes dynamically the transition from a gas of interacting quarks to hadrons via the formation of colour neutral clusters [3]. This allows a detailed study of the time dependence of the fluctuations in electric charge, of the numbers of charged particles, and the mean mass of the particles and clusters in the system. We apply the model to SPS energies at 160 GeV/N.

In our study, we find an increase of D from the QGP values in the initial quark phase to the hadron gas value, going hand in hand with the transformation of quarks into hadrons. Final state resonance decays result in a slight decrease of the fluctuation model, in line with the expectations (figure 1). At upper SPS energies, this model picture includes entropy conservation, since high cluster masses compensate for temporarily decreasing total numbers of particles.

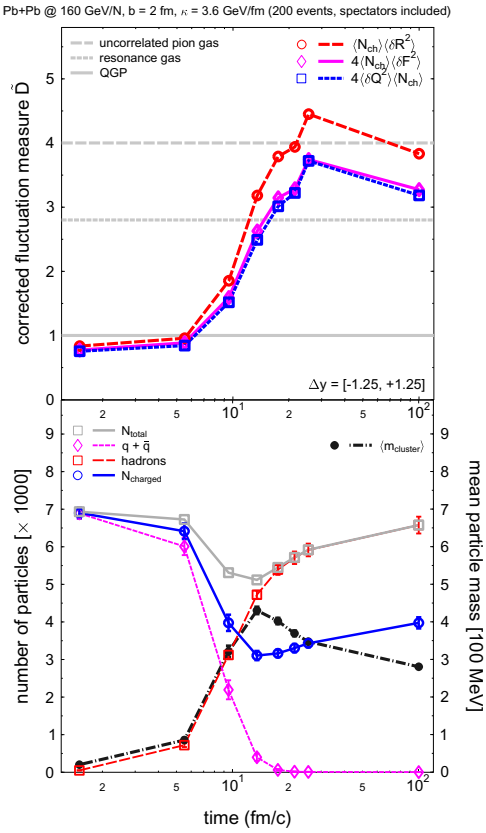


Figure 1: The time evolution of the fluctuation measures defined in (1) (upper panel) shows an increase from the QGP value to the hadron gas value with a slight final decrease, going hand in hand with the formation of hadronic clusters (□, dashed line) from quarks and antiquarks (♢) and the final decay of resonances (lower panel). High average masses (●) compensate for temporarily lower numbers (□), keeping entropy constant.

We conclude that the experimentally observed fluctuation measures favour the scenario of recombination of constituent quarks for the description of hadronization.

References

[1] S. Jeon and V. Koch, Phys. Rev. Lett. **85**, 2076 (2000); M. Asakawa, U. W. Heinz, and B. Müller, Phys. Rev. Lett. **85**, 2072 (2000); M. Bleicher, S. Jeon, and V. Koch, Phys. Rev. **C62**, 061902 (2000).

[2] A. Bialas, Phys. Lett. **B532**, 249 (2002); C. Nonaka, B. Müller, S. A. Bass, and M. Asakawa, Phys. Rev. **C71**, 051901 (2005).

[3] M. Hofmann, S. Scherer, M. Bleicher, L. Neise, H. Stöcker, and W. Greiner, Phys. Lett. **B478**, 161 (2000); S. Scherer et al., New J. Phys. **3**, 8 (2001).

* Work supported by supported by GSI, DAAD, and DFG. Calculations were performed with the CSC cluster, Frankfurt am Main.

† scherer@th.physik.uni-frankfurt.de

Di-Jet Suppression plus Mono-Jet Emission - induced Mach Shocks in the Quark-Gluon Plasma at the LHC

H. Stöcker*, FIAS- Frankfurt Institute for Advanced Studies, Institut für Theoretische Physik, Johann Wolfgang Goethe - Universität, Frankfurt am Main, Germany

The production of Large Extra Dimension (LXD) Black Holes (BHs), with a new, fundamental mass scale of $M_f = 1$ TeV, has been predicted to occur at the Large Hadron Collider, LHC, with the formidable rate of 10^8 per year in p-p collisions at full energy, 14 TeV, and at full luminosity (see Fig. 1).

We show that such LXD-BH formation will be experimentally observable at the LHC by the complete disappearance of all very high pt (> 500 GeV) back-to-back correlated Di-Jets of total mass $M > M_f = 1$TeV, in the large detectors ALICE, ATLAS and CMS.

We suggest to complement this clear cut-off signal at $M > 2 * 500$ GeV in the di-jet-correlation function by detecting the subsequent, hard Hawking-decayproducts of the LXD-BHs, namely multiple high energy (> 100 GeV) SM Mono-Jets (i.e. away-side jet missing), sprayed off the evaporating BHs into all directions.

With Heavy Ion beams at the LHC, strong Di-Jet suppression is also expected, due to Quark-Gluon-Plasma- induced jet attenuation, at medium to low jet energies, pt < 200 GeV. The (Mono-)Jets in these events can be used to trigger for Tsunami-like emission of secondary compressed QCD-matter at Machshock-angles, both at the trigger side and at the awayside missing jet. The Machshock-angles allow a direct measurement of the equation of state EoS and the speed of sound Cs of the primordial "big bang" matter at the LHC (see Fig. 2).

We discuss the importance of the underlying strong collective motion - the gluon storm - of the QCD-matter for the formation and evolution of these Machsock cones. We predict a significant deformation of Mach shocks by the gluon storm in central Au+Au collisions at RHIC and LHC energies as compared to the case of jet propagation in a static medium.

Complete stopping of 50 GeV jets at the LHC in 2-3 fm can yield nonlinear high density Mach shocks in the quark gluon plasma, which will be clearly visible in the disintegration pattern of the matter in crescents of revolution, with complex emission patterns. We report on strong effects of a first order phase transition in the EoS for the dynamics and geometrical evolution of the QCD- matter and the Tsunami-like Mach shock emission, as studied in a full 3-dimensional fluid dynamical model [3].

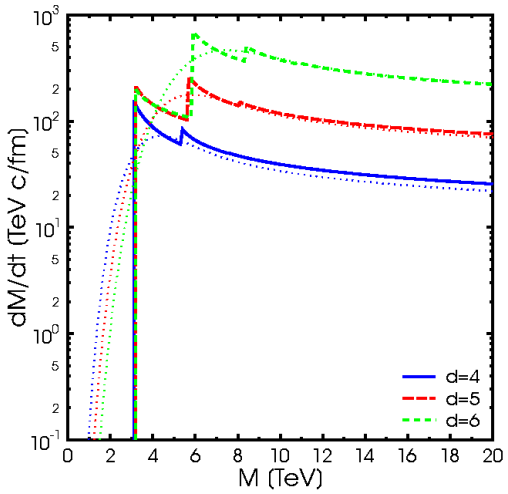


Figure 1: Black hole evaporation rate per degree of freedom as a function of mass, from top to bottom for $d = 6, 5, 4$. The thinn dotted lines show the standard micro-canonical scenario. The thick lines denote the calculations with the discrete energy spectrum[1].

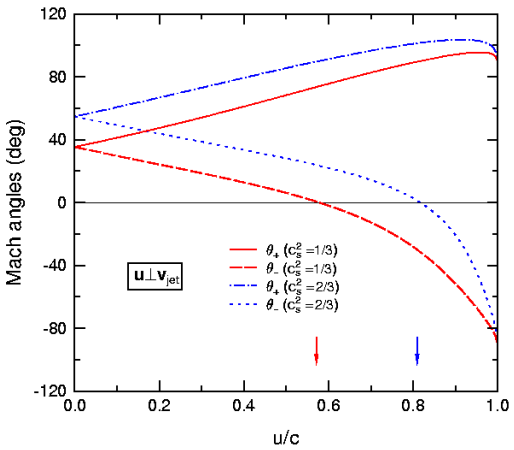


Figure 2: Angles of Mach region created by a jet moving transversely to the fluid velocity u in the CMF. Lower (upper) set of curves corresponds to the case $c_s 2 = 1/3\,(2/3)$. Arrows mark the values $u = c_s$ [2].

References

[1] S. Hossenfelder, M. Bleicher, S. Hofmann, H. Stoecker and A. V. Kotwal, Phys. Lett. B **566** (2003) 233 [arXiv:hep-ph/0302247].

[2] L.M. Satarov, H. Stöcker and I.N. Mishustin, *Phys. Lett.* **B627**, 64 (2005).

[3] H. Stöcker, IJMPD-Astro, accepted to be published

* stoecker@th.physik.uni-frankfurt.de

Improving the Hartree-Fock approximation by including nonzero decay widths

Dirk Röder*, Institut für Theoretische Physik, Johann Wolfgang Goethe-Universität,
Jörg Ruppert†, Department of Physics, Duke University

Abstract

We studied the linear sigma model with $O(N)$ symmetry at nonzero temperature in the framework of the Cornwall-Jackiw-Tomboulis formalism [1, 2]. Extending the set of two-particle irreducible diagrams by adding sunset diagrams to the usual Hartree-Fock contributions, we derived a new approximation scheme which extends the standard Hartree-Fock approximation by the inclusion of nonzero decay widths. In this approximation, in-medium modifications of the meson masses as well as decay and collisional broadening effects are self-consistently taken into account.

Introduction

At nonzero temperature T, ordinary perturbation theory in terms of the QCD coupling constant g breaks down in the sense that one can no longer order different contributions according to powers of g. The reason is that all terms of order gT/p have to be taken into account which requires the resummation of certain classes of diagrams. A convenient resummation method is provided by the extension of the Cornwall-Jackiw-Tomboulis (CJT) formalism [3] to nonzero temperatures and chemical potentials. It generalizes the concept of the effective action $\Gamma[\bar{\phi}]$ for the expectation value $\bar{\phi}$ of the one-point function in the presence of external sources to that for the effective action $\Gamma[\bar{\phi},\bar{G}] = S[\bar{\phi}] + 1/2\mathrm{Tr}\ln\bar{G}^{-1} + 1/2\mathrm{Tr}(G^{-1}\bar{G}-1) + \Gamma_2[\bar{\phi},\bar{G}]$ for $\bar{\phi}$ and the expectation value $\bar{G}$ of the two-point function in the presence of external sources. Here, $S[\bar{\phi}]$ is the tree-level action, G^{-1} the inverse tree-level two-point function, and $\Gamma_2[\bar{\phi},\bar{G}]$ the sum of all two-particle irreducible (2PI) vacuum diagrams with internal lines given by $\bar{G}$. The stationary points of this functional provide self-consistent equations for the expectation values of the one- and two-point functions. Since it is practically impossible to compute all 2PI diagrams, and one has to truncate Γ_2, for instance at some order in the number of loops. In the Hartree-Fock approximation Γ_2 solely contains diagrams of so-called "double-bubble" topology, and the self-energies only consist of "tadpole" diagrams, which is a very simple approximation scheme, since tadpole self-energies do not have an imaginary part and, consequently, all particles are stable quasiparticles. Our goal in this work was to include the nonzero decay width of the particles. To this end one has to add other diagrams to Γ_2 which yield self-energies with nonzero imaginary part. The leading diagrams which are the only ones considered in the following are those of the so-called "sunset" topology.

* roeder@th.physik.uni-frankfurt.de
† ruppert@phy.duke.edu

Results

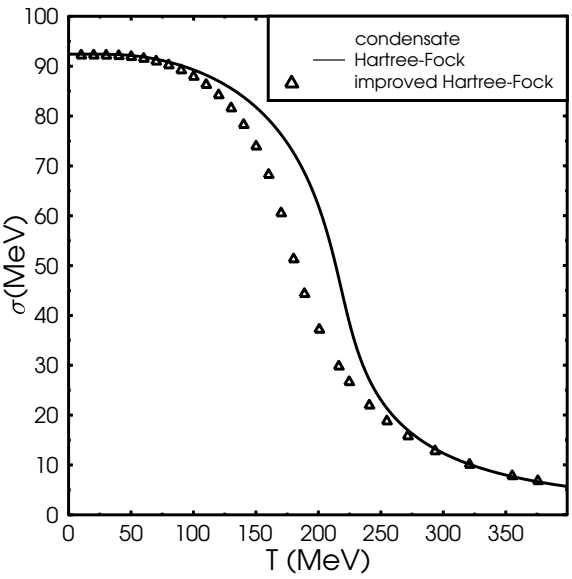


Figure 1: The chiral condensate σ as a function of temperature for the standard and the improved Hartree-Fock approximation.

The qualitative behavior of the chiral condensate, shown in Fig. 1, is similar in the Hartree-Fock and the improved Hartree-Fock approximation: the condensate drops significantly with temperature indicating the restoration of chiral symmetry. Since we considered the case of explicit $O(4)$ symmetry breaking, the chiral phase transition is a crossover transition. Nevertheless, one can define a transition temperature, T_χ, as the temperature where the chiral susceptibility $\partial\sigma/\partial T$ assumes a maximum. Quantitatively, the inclusion of a nonzero decay width lowers T_χ as compared to the standard Hartree-Fock approximation by about 20%. The transition temperature $T_\chi \simeq 160$ MeV agrees well with recent lattice results for the two-flavor case [4].

References

[1] D. Röder, J. Ruppert and D. H. Rischke, arXiv:hep-ph/0503042.

[2] D. Röder, arXiv:hep-ph/0509232.

[3] J. M. Cornwall, R. Jackiw and E. Tomboulis, Phys. Rev. D **10**, 2428 (1974).

[4] E. Laermann and O. Philipsen, Ann. Rev. Nucl. Part. Sci. **53**, 163 (2003) [arXiv:hep-ph/0303042].

Finite Volume effects from Renormalization Group flows

J. Braun*, H.-J. Pirner, Universität Heidelberg
B. Klein, GSI, Darmstadt

In recent years, the accuracy of lattice QCD calculations has increased considerably, and simulations with dynamical fermions have reached rather low pion masses. In agreement with observations, a famous result by Lüscher [1] predicts that finite volume effects are strongly suppressed for large pion masses, but should become much more important for small, realistic values. For this reason, there is an interest in the calculation of such effects by other means, in addition to the direct investigation on the lattice. The principal method used for this purpose is chiral perturbation theory (chPT), the low-energy effective field theory of QCD.

The application of chPT to finite-volume QCD is almost as old as the theory itself [2]. In an effective field theory, unknown higher-momentum effects are encoded in the values of the low-energy couplings (LECs). These values in the low-energy effective Lagrangian remain the same when introducing a finite temperature, but not necessarily when the underlying QCD is put into a finite Euclidean volume. While the boundary conditions for quark fields must be anti-periodic in the time direction, they can be chosen freely in the space directions. In [2], it is argued that due to the symmetry between spatial and temporal directions, the LEC remain unchanged for a choice of anti-periodic quark boundary conditions in the high-energy theory. However, they might change for periodic quark boundary conditions.

In order to investigate the effects of quark boundary conditions, we turn to the quark-meson model, in which constituent quarks are coupled to a linear σ model [3]. In this model system, chiral symmetry is broken dynamically through the formation of a quark condensate. We use non-perturbative Renormalization Group (RG) flow equations to systematically integrate out quantum fluctuations and obtain the effective action. Since the bare couplings of the model are fixed at some UV scale in order to reproduce observables for infinite volume, only the behavior in finite volume is predicted [3, 4].

In accordance with the predictions of [2], we find agreement between chPT and our results for anti-periodic boundary conditions, but qualitatively different behavior for periodic boundary conditions (Fig. 1). In general, finite volume effects are much smaller for periodic boundary conditions, the usual choice in lattice calculations.

The chiral phase transition temperature in finite volume is affected by the boundary conditions as well (Fig. 2), even for volumes $L \simeq 2 - 2.5$ fm [5]. While the absolute value of the transition temperature in the chiral limit is too low compared to lattice or QCD RG investigations [6], we expect qualitatively similar behavior on the lattice.

* supported by GSI

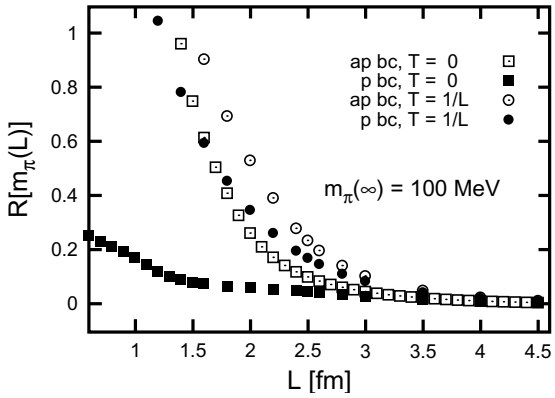


Figure 1: The pion mass shift $R[m_\pi(L)] = (m_\pi(L) - m_\pi(\infty))/m_\pi(\infty)$ in a finite volume $V = L^3\frac{1}{T}$, as a function of L. Results are for anti-periodic (solid) and periodic (open symbols) quark boundary conditions, for fixed $T = 0$ (boxes), and for $T = \frac{1}{L}$ varying with the volume size (circles), for a pion mass $m_\pi(\infty) = 100$ MeV.

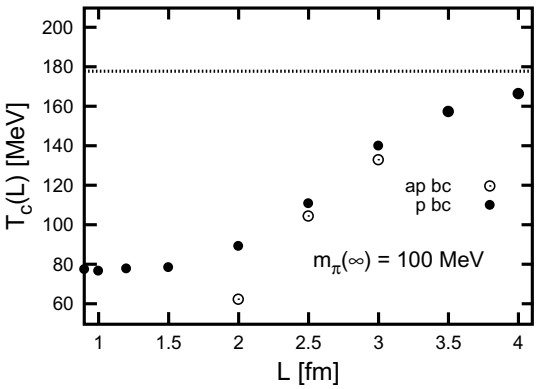


Figure 2: Chiral phase transition temperature in a finite volume $V = L^3\frac{1}{T}$ as function of L, for periodic and anti-periodic quark boundary conditions, for a pion mass $m_\pi(\infty) = 100$ MeV. The crossover temperature is defined via the minimum of the σ mass.

References

[1] M. Lüscher, Commun. Math. Phys. **104** (1986) 177.

[2] J. Gasser and H. Leutwyler, Nucl. Phys. B **307** (1988) 763.

[3] J. Braun, B. Klein, and H.-J. Pirner, Phys. Rev. D **72** (2005) 034017.

[4] J. Braun, B. Klein, and H.-J. Pirner, Phys. Rev. D **71** (2005) 014032.

[5] J. Braun, B. Klein, H.-J. Pirner, and A.H. Rezaeian, submitted to Phys. Rev. D, [arXiv:hep-ph/0512274].

[6] J. Braun and H. Gies, arXiv:hep-ph/0512085.

A Multiple-Reflection Time-of-Flight Mass Spectrometer for Resolution of Isobaric Ions

T. Dickel, M. Petrick, W. R. Plaß, C. Jesch, Z. Wang, Justus-Liebig-Universität Gießen
Z. Di, H. Geissel, C. Scheidenberger, GSI, Darmstadt

A multiple-reflection time-of-flight mass spectrometer (MR-TOF-MS) has been developed, in which isobaric ions can be separated and measured with a cycle time of about 1 ms. It is based on a principle proposed by Wollnik et al. [1] and on an ion-optical reflector design developed by Verentchikov et al. [2].

The layout of the MR-TOF-MS is shown schematically in Fig. 1. In its present configuration, it consists of an electron-impact ion source, a time-of-flight analyzer with two electrostatic mirrors, and a microchannel-plate detector. Ions formed in the source are injected into the analyzer, in which they travel for a defined number of turns, until they are ejected and impinge on the detector. Injection and ejection is realized by pulsing of the electric potentials on the reflector electrodes. Since the overall time-of-flight can be increased by the repeated passage of the ions through the analyzer, the mass resolution of the MR-TOF-MS can be significantly higher than that of single-reflecting TOF-MS. According to simulations, a mass resolving power (FWHM) of the device of 65000 can be expected. In first measurements, a mass resolving power of 35000 was achieved (Fig. 2). Currently, the performance of the MR-TOF-MS is limited by the stability of the applied voltages, by the lack of cooling of the ion population before injection into the analyzer, and by collisions of the ions with residual gas in the analyzer. For further improvement, the ion source will be replaced by an RF trap for ion cooling. The trap will also allow injection of externally created ions into the MR-TOF-MS. Thus, mass measurements of very short-lived nuclei with half-lives of ~ 1ms could be performed.

An additional application of the MR-TOF-MS could be the pre-separation of a beam of exotic nuclei for mass-resolved nuclear spectroscopy and for Penning trap mass measurements in the presence of strong isobaric contamination. Here, the temporal separation of the ions is converted to a spatial separation by a pulsed ion gate. The energy spread of the separated ions is then reduced in a dynamic energy buncher, and the ions are accumulated in an RF trap to make them available for precision experiments. Applications of the MR-TOF-MS are envisaged for direct mass measurements at SHIPTRAP and the FRS Ion-Catcher [3] and as a high-resolution mass separator at SHIPTRAP and MATS.

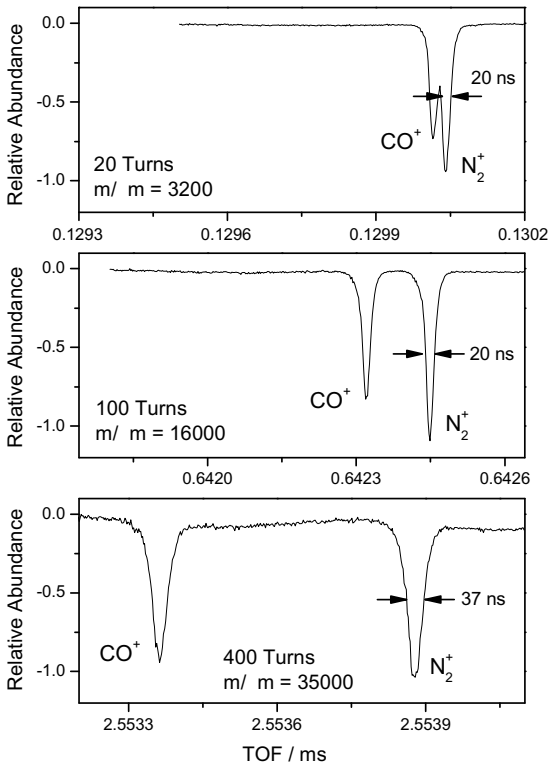


Figure 2: Mass spectra of the isobaric doublett of CO^+ and N_2^+ obtained with the MR-TOF-MS for different number of passes through the instrument. After 400 turns, a peak width of 37 ns is achieved, corresponding to a mass resolving power (FWHM) of about 35000.

References

[1] H. Wollnik *et al*., Int. J. Mass Spectrom. Ion Processes 96 (1990) 267.
[2] A. N. Verentchikov *et al*., Tech. Phys. 50 (2005) 73.
[3] M. Maier et al., GSI Scientific Report 2005, 331.

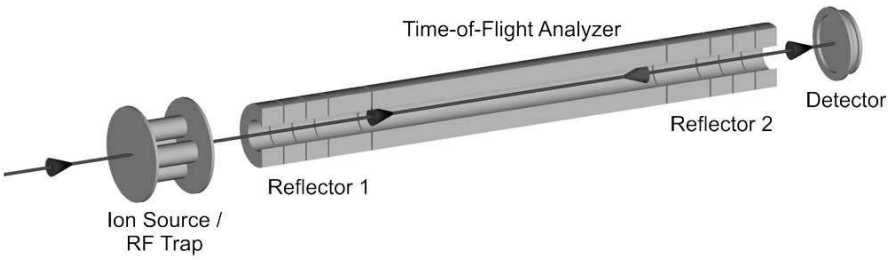


Figure 1: Schematic figure of the MR-TOF-MS and the path of the ions in the device.

A modular setup to monitor a detector's operation conditions

B. Voss, M. Henske, T. Knapp, A. Heinz; GSI, Darmstadt, Germany

Motivation and Requirements

Every active (gas-) detector in nuclear physics has to be operated in a specific regime concerning e.g. temperature (T), gas-flow (F), -pressure (P), bias (VDD), high voltage (HV) and ambient conditions (H) to perform as designed. In order to monitor and protocol theses quantities, a modular, flexible and universal set of hard and software with interlocking capabilities has been built [1,2].

System architecture and implementation

The design of all hardware components with grouped function (e.g. detection, checking, interlocking, communication, test, protocol etc.) has been built in a modular way for flexibility in maintenance and in functional changes [3] (see fig.1).

A set of sensors, all based on one layout to achieve synergy effects, take the required data where they are relevant, which means inside the gas volume of the detector. Each one has its unambiguous ID and the calibration information stored in an EEPROM on board for ease of maintenance and operation. Their analogue bipolar output is accessible at the detector itself and is fed into a set of discrete as well as software-programmable window comparators. The hardware limits may be modified only by opening the detector e.g. in case of maintenance. A subsequent CPLD circuit serves to generate hierarchical step-by-step alarm functions (warnings and interlocks) without the use of software and sends these via fail-safe LWL connections to a control system.

The whole operation is supervised by a controller setup directly flanged to the detector (see fig.2). It serves to write-up all error events and main operation changes in an exchangeable MMC-card (ring-buffered). The generated interlock signals have to be acknowledged by a user interaction, either manually at the detector or via remote control. There is no possibility provided to override theses conditions except by changing the software thresholds for the comparators which is also an action being recorded. Proper operation of every component may be checked by requesting a self test either manually or remote controlled. The operation of the µ-controller has been made fail-safe by a battery-buffered real-time clock and a watch-dog monitor therein.

The whole set may be remote controlled via Ethernet as well as locally via a RS232 and a JTAG port which also serve as programming interface. In addition, a compact, graded display for the status of the whole setup and the high voltage in a clear way is implemented at the detector itself. At start-up, the controller operates autarkical without the need for a user interaction.

The work on the hard and software is still in progress. Especially the setup of failsafe software is a challenging task.

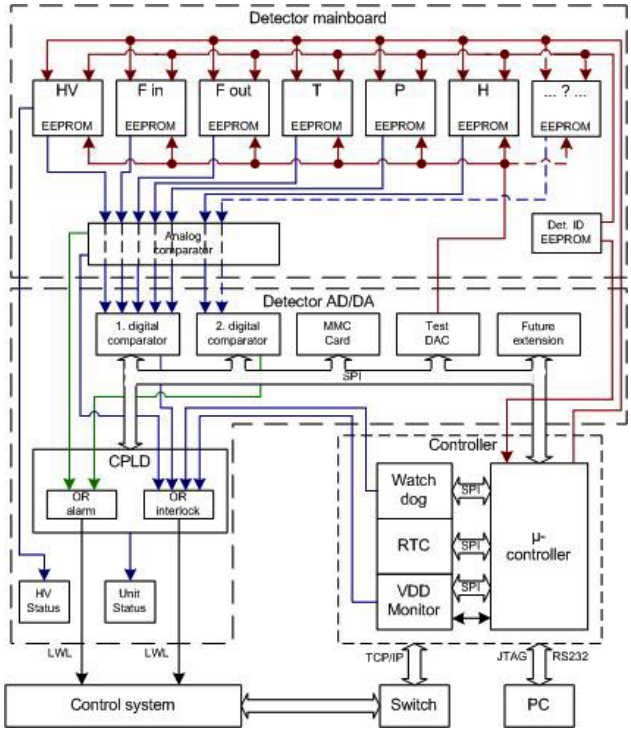


Figure 1: System architecture of grouped components inside and outside of the detector.

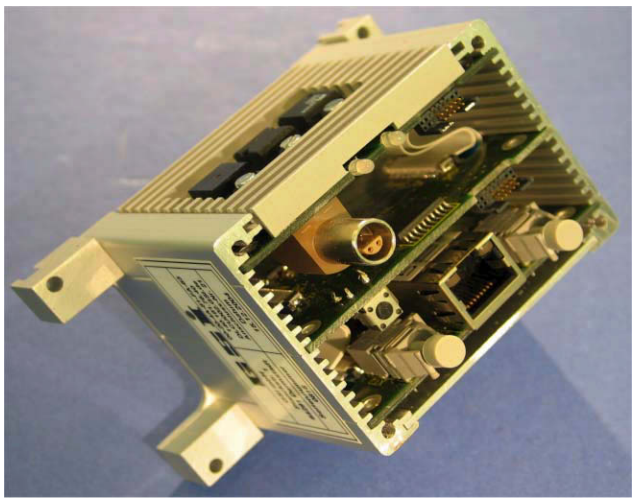


Figure 2: Picture of the external controller unit with front cover removed.

References

[1] T. Knapp, Diploma thesis, Fachhochschule Darmstadt, Germany, 2004

[2] M. Henske, Diploma thesis, Fachhochschule Darmstadt, Germany, 2005, in preparation

[3] B. Voss et al., Patient monitors for HIT and transfer of know-how to Siemens-Med, contribution to this report

The TASCA Project

M. Schädel[1], D. Ackermann[1], A. Semchenkov[1, 2], and A. Türler[2] for the TASCA collaboration
[1] GSI Darmstadt, Germany; [2] TUM Garching, Germany

The **T**rans**A**ctinide **S**eparator and **C**hemical **A**pparatus, **TASCA**, project started early in 2005. The envisioned research program will focus on the separation and investigation of neutron-rich transactinide nuclides produced in hot-fusion reactions with actinide targets. While novel chemical investigations of transactinide elements - after preseparation with a physical recoil separator - is one of the main goals, a rich nuclear structure investigation program is foreseen complemented by typical hot-fusion nuclear reaction studies; see [1] for a coverage of preparatory and ongoing activities.

As the central device for all these research programs we opted for a gas-filled separator [2] making at least partially use of existing components from the former NASE [3]. To optimize all separator components, new and old ones, ion-optical calculations were performed [2] based on the model fusion reaction of 5-6 MeV/u ^{48}Ca on 0.5 mg/cm^2 actinide targets (^{238}U, ^{244}Pu).

The DQQ configuration, which was selected as the best choice [2], allows operation in two possible modes. While the DQ_hQ_v mode gives the highest possible transmission the smallest image size results from the DQ_vQ_h mode. New ducts were designed and built for the dipole and the quadrupoles to maximize the transmission in both modes.

For the "high transmission" DQ_hQ_v mode, see Fig. 1, a horizontal and vertical acceptance of 110 and 40 mrad is achieved which corresponds to a solid angle of 13.3 msr. Assuming a 30% reduction for the operation as a gas-filled separator, a transmission of about 45% is estimated which would yield a slightly higher value as compared with the Dubna gas-filled separator, DGRRS, or GARIS at RIKEN. With a dispersion of 9 mm/% a "vacuum" image area of 27 cm^2 is calculated.

In the DQ_vQ_h mode a reduced horizontal acceptance of 34 mrad presumably yields only 30% transmission. However, an extraordinarily small image area of 7 cm^2 (in vacuum) should be achievable - a key issue to build small recoil transfer chambers for a fast transport of products into any chemistry set-ups and something unique for TASCA. Monte-Carlo simulations [4] making use of existing models of the dipole and quadrupole magnets [5] are under way.

All magnets, including ducts and water cooling, are now installed in the newly built cave at the UNILAC beam line X8, and they are connected to power supplies. A LabVIEW control program and communication via MIL-bus was established and first tests of the power supplies and magnets are promising. The control program for the power supplies will be part of a general TASCA control program described in a separate contribution [6].

To make use of highest available beam intensities, a windowless differential pumping section was installed and successfully tested. Details are given elsewhere [7].

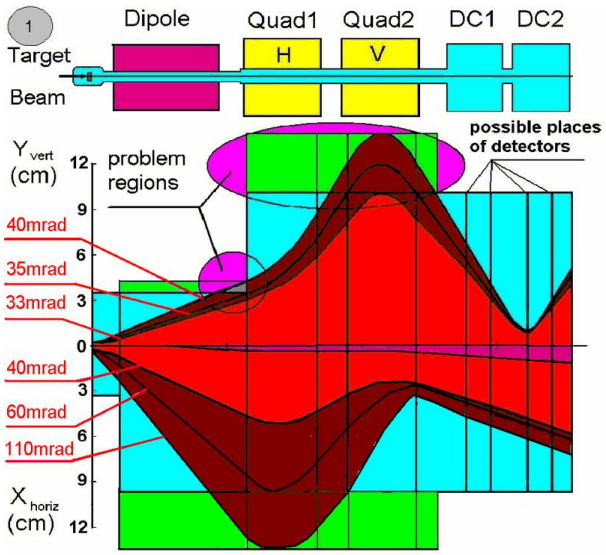


Figure 1: DQ_hQ_v configuration and simulation for the vertical and horizontal beam shape. Inner lines demonstrate constraints from the old NASE set-up. Outer lines show the present TASCA situation with new ducts.

A new target chamber was designed and built which accommodates (i) the rotating actinide target wheel in an easily removable cassette, (ii) the newly built drive [8], (iii) collimators, and (iv) beam diagnostic components. A beam current transformer upstream of the target shall allow for continuous monitoring of the beam current.

Last not least it is important to mention not only the new TASCA cave at X8 with its concrete shielding – designed and built for the highest envisioned beam intensities – and its access system, but also all the infrastructure components – a crane, electrical power for magnets, pumps, detectors and data acquisition systems, cooling water, pressurized air and nitrogen, filtered exhaust systems, air conditioning, and many other components - which were installed in 2005 [9].

References

[1] http://www.gsi.de/tasca ; http://www.gsi.de/tasca05
[2] A. Semchenkov et al., GSI Scientific Report 2004, GSI Report 2005-1, p. 332.
[3] V. Ninov et al., Nucl. Instr. Meth. A 357 (1995) 486.
[4] K. E. Gregorich, private communication.
[5] T. Belyakova et al., GSI Scientific Report 2004, GSI Report 2005-1, p. 333.
[6] E. Jäger et al., contribution to this report.
[7] A. Semchenkov et al., contribution to this report.
[8] H.-J. Schött, E. Jäger, private communication.
[9] Many thanks to everybody who contributed to this.

Development of the TASCA Control System

E. Jäger[1], W. Brüchle[1], E. Schimpf[1], M. Schädel[1], A. Semchenkov[1, 2], A. Türler[2], A. Yakushev[2]
[1]GSI, Darmstadt, Germany, [2]TUM Garching, Germany

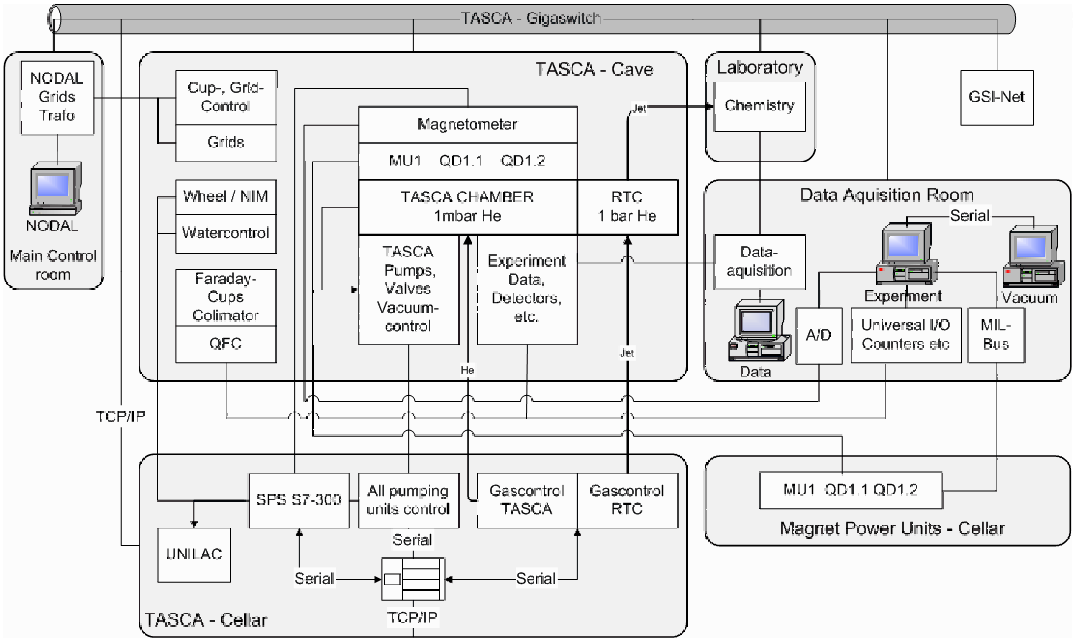


Fig.1. Scheme of the TASCA control system presently under development.

The TASCA [1] control system will be based on Siemens SPS microcontrollers as low level control units, and PCs for the high level control. For safety reasons we opted for SPS controllers at the lower level. All safety critical fast signals like interlocks will be processed by hardware components or by the SPS. PCs will be applied as the user interface and to control processes which are not time critical, like the routine operation of the pumping system, magnet controls, beam current reading and others. High level programming will be performed under LabVIEW.

The common scheme of the TASCA control system is presented in Fig.1. It consists of modules to control (i) dipole and quadrupole magnets, (ii) gas pressures and differential pumping, and (iii) all heavy-ion beam and irradiation related aspects including the target wheel control. Communication links will be established to the NODAL system, our data acquisition system and automated chemistry set-ups.

Components of the control system will be located in (i) the TASCA cave, (ii) the cellar below TASCA, (iii) the data acquisition room, (iv) the UNILAC control room, and (v) the radiochemistry laboratory. All parts will be connected by Internet (TCP/IP), MIL-bus or serial interfaces. We plan to have two main control PCs, one for the gas-vacuum system and the second one to control magnets and for beam monitoring. The latter one will work as a server. All other computers, linked by TCP/IP protocol, will have the possibility to read data from these main computers to visualize the actual status of the TASCA operation.

The Magnet control system consists of a low-speed control shell (0.1-0.5Hz control and visualization frequency) operated under LabVIEW installed in a PC. Connections to the magnet power supplies are made by PC cards via MIL-bus. The main program will work as a server and it will solely control the power supplies. These two connected to the quadrupoles allow maximum currents of 630 A while the third one for the dipole is limited to 700 A. All power supplies are located in the cellar. Tests of the quadrupole power supplies show good short and long term stabilities ($< 10^{-5}$).

A 3-channel Tesla-meter will be used for magnetic field measurements. Connected to the control system by a serial port or ADC PC-card, it will be part of the online experimental monitoring.

The gas-vacuum control subsystem, including its differential pumping aspects, will be described in [2].

Beam current readings from collimators, Faraday cups and the beam dump are based on readouts from charge-frequency converters (QFCs). In addition, a beam current transformer will allow continuously monitoring the beam. Wire grids and luminescent screens are installed to properly focus the beam. This information will be visualized in the control room.

References

[1] M. Schädel et al., contribution to this report.
[2] A.Semchenkov et al., contribution to this report

Modelling the Differential Pumping of the TASCA Gas-Vacuum System

A. Semchenkov[1, 2], W. Brüchle[1], E. Jäger[1], E. Schimpf[1], M. Schädel[1], A. Türler[2], A. Yakushev[2]
[1]GSI, Darmstadt, Germany,[2]TUM Garching, Germany

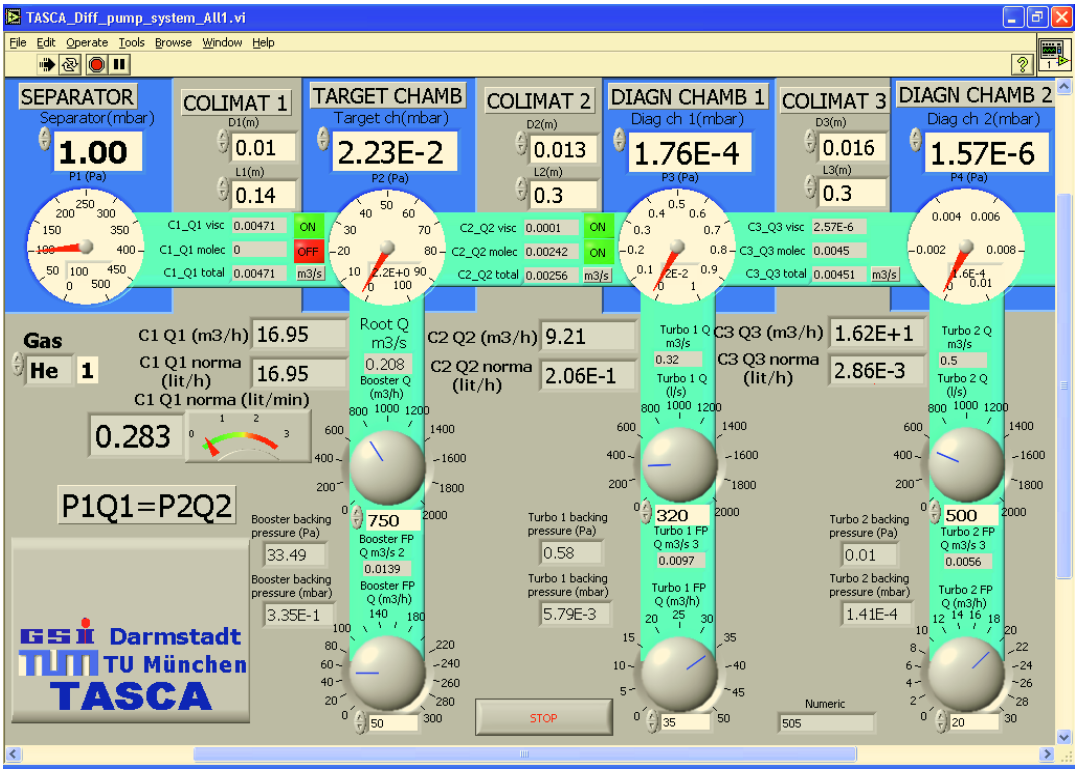


Fig.1. User interface of the program to model the differential pumping situation at TASCA

The scientific program at the TASCA gas-filled separator [1] requires the highest possible UNILAC beam intensities. Presently, they are of the order of one particle microampere and a significant increase is in preparation. To make use of these intensities a windowless differential pumping system (DPS) was installed and a computer program was developed to simulate vacuum conditions at various sections along the beam line as a function of parameters like gas composition and pressure in the separator, pumping capacity and the geometry of the collimator; see Fig. 1 for the program interface. The goal was to maintain a stable pressure in the separator (typically about 1 mbar He) and get a rapid pressure drop over a short distance to obtain 10^{-6} mbar in the beam line.

The system consists of three pumping sections and our design strongly profited from the experience obtained at RITU [2]. Our first section will have a 1070 m^3/h (volume flow rate, N_2) Roots pump with a 62 m^3/h backing pump (test and comparisons with simulations were performed with smaller pumps). The second section has a 400 L/s (N_2) turbomolecular pump with the specific feature that it can operate at a relatively high pressure coupled to a 32 m^3/h backing pump. The third section consists of a 1400 L/s (N_2) turbo and a 20 m^3/h backing pump.

One envisioned configuration, which is depicted in Fig. 1, has collimators of 10x140, 13x300 and 16x300 (inner diameter x length / mm). Calculations with the DPS simulation program show a pressure drop of about a factor 100 for each section; see Fig. 1. The program is written in LabVIEW and was tested experimentally with different gases. A good agreement between calculated and measured pressures was obtained. The program calculates the pressure and flow through collimators in a static regime of selected gases based on the following equations:

1. For viscous flow:

$$Q_v = (\pi D^4 \Delta P)/(256 \eta L),$$

with η: viscosity of gas at t=20°C, D: collimator diameter [m], L: collimator length [m], P: pressure [Pa].

2. For molecular flow:

$$Q_m = (1/6)(2\pi KT/M)^{1/2}(D^3/L),$$

with K: Boltzmann constant, T: absolute temperature [K], M: mass of one molecule of gas [kg].

Set parameters of the program are the pressure in the separator, the filling gas, the collimator size and the pumping speed.

References

[1] M. Schädel et al., contribution to this report.
[2] J. Uusitalo, http:/www-wnt.gsi.de/tasca04/images/contributions/4.1_Uusitalo.pdf

TASCA Target Group Status Report

K. Eberhardt, J. V. Kratz, D. Liebe, P. Thörle, Johannes Gutenberg-Universität, Mainz (UMZ)
H.-J. Maier, J. Szerypo, Sektion Physik, Ludwigs-Maximilians-Universität München, (LMU)
W. Brüchle, Ch. Düllmann, W. Hartmann, A. Hübner, E. Jäger, B. Kindler, B. Lommel,
M. Schädel, B. Schausten, E. Schimpf, A.Semchenkov, J. Steiner, GSI, Darmstadt, Germany
A. Türler, A. Yakushev, Institut für Radiochemie, Technische Universität München (TUM)
K. E. Gregorich, R. Sudowe, Lawrence Berkeley National Laboratory, Berkeley (LBNL)

The **T**rans-**A**ctinide **S**eparator and **C**hemistry **A**pparatus **TASCA** is currently installed at cave X8 and is dedicated to investigate the chemical and physical properties of the heaviest elements. An overview of the current status is given in a separate report [1].

For the production of Rf and Db isotopes, cold fusion reactions can be applied using Ti-beams with Pb- or Bi targets, respectively. Low melting metals can be substituted by compounds for application in high intensity beams [2]. However, to produce longer-lived isotopes of neutron-rich heavier actinides and transactinides hot fusion reactions with actinide targets are required. Here, possible target materials range from Th up to Cm or heavier elements.

We combined the different methods and capabilities of the four target laboratories involved to solve the challenging task of developing appropriate backings and targets. For first tests, we kept the geometry of the existing target wheel of the nuclear chemistry experiments at GSI unchanged. As we plan to install thinner backings for TASCA – so far 15 to 20 µm thick Be foils were used - it is necessary to fix the backing on an adequate frame, as can be seen in Figure 1.

Al backings and Ti backings, supplied from different companies with different qualities, were produced by cold rolling. C backings were produced by resistance heating and applied without annealing. After two test beam times with ^{12}C beam (500 pnA) and ^{40}Ar beam (800 pnA), we now focus on 3 µm Ti or 35 µg/cm² annealed C, alternatively, which will be tested with thermally evaporated UF_4, a target material in the near future.

As the target laboratory at GSI is specialised in evaporation, sputtering, and rolling of stable elements up to natural uranium, the foils discussed above were prepared there. The other three laboratories have the expertise of handling highly radioactive materials including the chemical purification of target material and the recovery of rare target material from used targets. After the decision for the appropriate backing has been made, backing foils will be given to the target laboratory at the LMU, where radioactive targets (Ra, Ac, Th, U, Pu, Cm) can be prepared by microevaporation. The group at the TUM offers the analytical capabilities to measure concentrations of actinide elements in solution (also Pu, Cm). For the nuclear chemistry experiments at GSI the radioactive actinide targets are prepared by electrochemical deposition at UMZ.

The search for optimal conditions for the electrochemical deposition of U (as uranylnitrate) from organic solution by molecular plating on thin Al- and Ti-backing foils is currently going on at LBNL and UMZ [3]. Figure 1 shows a picture of a 265 µg/cm^2 ^{238}U-layer produced by molecular plating on a 25 µm thick Al-backing [3]. Target performance - when exposed to an ion beam - has not been tested yet. At UMZ a new electrochemical cell for improved deposition yield and uniformity of the target layer is under construction based on the design and the experience obtained at RIKEN [4]. Furthermore, optical microscopy, electron microscopy, and energy dispersive x-ray analysis are used for monitoring target thickness, chemical purity and homogeneity of the target surface. UMZ is testing a commercially available autoradiographic imager (Packard Instant Imager).

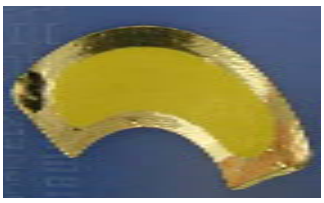


Figure 1: ^{238}U-target (265 µg/cm^2) produced by molecular plating of uranylnitrate from isobutanolic solution.

A new target station for TASCA is currently developed at GSI. This device is designed so that it can be used with the existing rotating actinide target wheel from GSI and with the new rotating target wheel system that is presently under development at LBNL for the Berkeley Gas-filled Separator (BGS), as well.

All contributions to the TASCA Working Group meetings and Workshops are accessible via www-w2k.gsi.de/tasca.

References

[1] M. Schädel et al., this report
[2] B. Kindler et al., accepted for NIM A
[3] D. Liebe et al., this report
[4] H. Haba, TASCA 05, Oslo, 2005; http://www-w2k.gsi.de/tasca05/images/contributions/TASCA05_Haba.pdf

A High-Resolution Time-of-Flight Spectrometer with Tracking Capabilities for Fission Fragments and Beams of Exotic Nuclei

N. Nankov*, E. Grosse†, A. Hartmann, A. R. Junghans, K. Kosev, K. D. Schilling, M. Sobiella, A. Wagner, Forschungszentrum Rossendorf, Dresden, Germany

The spectrometer consists of 2 micro-channel plate (MCP) detectors with position sensitive delay-line anodes for registration of secondary electrons (SEs) knocked out by the ion beam from few 100 μg/cm^2 thin foils and deflected by 90° by an electrostatic mirror towards the MCPs (see ref. [1]). The device has been used to identify heavy ions like ^{12}C, ^{35}Cl and ^{127}I at energies up to 2 MeV/u delivered from the FZ-Rossendorf 5 MV tandem accelerator. The experimental setup consists of the spectrometer, 2 silicon detectors serving as beam monitors installed directly in front of and after the device. The first beam monitor used to monitor the primary beam is movable. In order to reduce the primary beam intensity an aperture with the diameter of 0.5 mm was installed in front of it. A movable Faraday cup was also installed in front of the aperture to monitor directrly the primary beam current. The identification of fission fragments produced via photo-induced fission at the ELBE accelerator at FZR will be performed in the near future in order to test the influence of the background and the time and space resolution at realistic conditions. Finally, the setup will be applied to identify and track incoming exotic relativistic ions at the heavy ion accelerator at GSI. In the double-arm TOF spectrometer, both the charge and the mass of each fragment will be determined by two independent TOF measurements.

To test and optimize the setup, a mixed α-source containing ^{226}Ra and its daughter products as well as the heavy ion beam from the tandem accelerator were used. In the experiment, the energy of the ions in front of and after the spectrometer was additionally determined using the beam monitors.

Three major characteristics namely detection efficiency, time and position resolution have been measured and optimized. Efficiency measurements for the forward as well as for the backward emitted and accelerated secondary electrons were made. A stable efficiency of more than 95% has been reached at an accelerating potential beyond 1 kV. The ratio between the forward and backward efficiency taken in the saturation area was determined to be 1.9(2).

In order to determine the position resolution, the blend was replaced with a mask with several apertures of 0.5 mm diameter. An investigation of the dependence of the position resolution of the detector on the accelerating potential was carried out (see Fig. 1). The maximum position resolution of 1.8(3) mm was achieved. The time resolution was determined for different ion-energy combinations

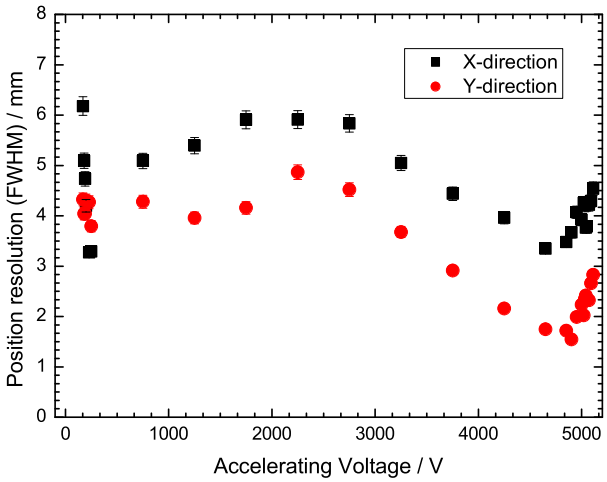


Figure 1: Position resolution for forward emitted SEs as a function of the accelerating potential for ^{35}Cl ions at 40 MeV. X-axis is taken to be transversal to the beam direction and paralel to the MCP detector plane. Y-axis is perpendicular to the X-direction and the beam direction.

and for different ion flight paths. Simulations using SRIM (see ref. [3]) have been performed in order to determine the time uncertainty due to the initial beam spread, taken from the beam monitor and the energy loss straggling inside the foil. Both these effects account for up to 210 ps time uncertainty. Unfolding the measured time resolution with the calculated one, an apparent time resolution of about 280 ps (FWHM) was derived. The foil inhomogeneities were not taken into account because the beam diameter was limited by the aperture.

The longitudinal and transversal SEs energy distributions were measured (see ref. [2]) in order to determine their influence on the position and time resolution of the spectrometer. They were determined to be about 400(80) eV (σ) and 150(30) eV (σ) respectively. The angular distribution of the SEs was also determined and its value was estimated to be 14(5)° (σ).

References

[1] N. Nankov, E. Grosse *et al.*, Proc. 3rd Proc. Int. Workshop on Nuclear Fission and Fission-Product Spectroscopy, France, May 2005, AIP vol. 798 (2005) p. 357

[2] N. Nankov, M. Friedrich *et al.*, K.Kosev, N. Nankov *et al.*, IKH Annual Report, FZR-442 2005(2006).

[3] http://www.srim.org, 2003.

* also INRNE, Sofi a, Bulgaria
† also Technical University of Dresden, Germany

Single-Crystal CVD-Diamond Detectors Progress Report*

E. Berdermann, GSI Darmstadt Germany, for the NoRHDia Collaboration

In 2005, systematic characterisation data obtained from more than 10 Single-Crystal CVD-Diamond Detectors (SC-DD) have been analyzed (ID = BDS resp. EBS). The size of the samples varies from 3x3 mm^2 to 5x5 mm^2 and the thickness from 300 µm to 500 µm. Different contacts were tested including Guard Ring (GR) electrodes.

IV Characteristics

Consecutive hysteretic measurements with Keithley electrometers are performed avoiding parasitic currents caused by humidity or air ionization and minimizing pick-up distortion. Figure 1 shows the dark-current behaviour of 10 BDS samples in a glance, all metallized with sputtered Cr-Au electrodes.

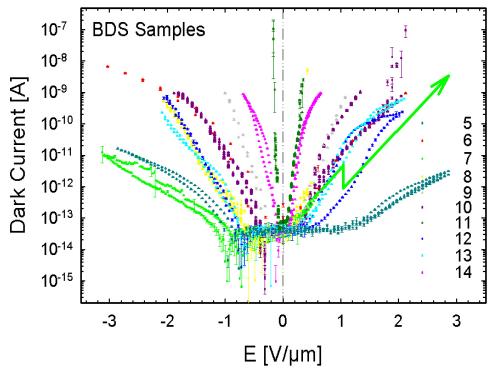


Figure 1: Dark current behaviour of BDS samples metallized with sputtered Cr-Au electrodes.

The measurements are performed in an electric-field range E_{max}= ± 3.0 V/µm by controlling dI/dV < 1nA/10V. At E = ± 1 V/µm, low currents of absolute values < 10 pico amps are measured for most of the samples. These are by orders of magnitude lower currents than those obtained from electronic-grade PolyCrystalline Diamond Detectors (PC-DD) [1].

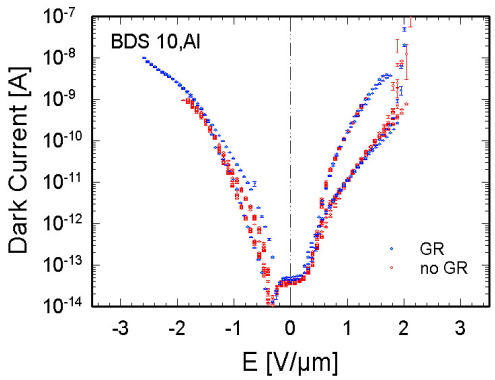


Figure 2: Influence of Guard Ring (GR) electrodes

However, the polarity-dependend behaviour and particularly the steep current increase in some cases at rather low bias is unexpected for material of nominal resistivity > 10^{14} Ωcm. Moreover, real break down occurs occasionally (lightning bolts) followed in some cases by persistent hysteretic behaviour as demonstrated in Figure 2 (BDS 10 at positive bias). The excellent reproducibility of this measurement with GR electrodes is a strong indication of a bulk origin of the dark current. However, currents injected from the contact interface are not recognizable.

Micro-Beam Mapping with ^{12}C ions

Micro-beam data allow detailed studies, illuminating peculiarities that are invisible for real, extended particle beams of beam spots on target ≥ 1 mm in diameter. Carbon ions of two differnt beam energies, 3.6 AMeV and 9.515 AMeV, respectively, were used for an experiment at GSI's micro-beam facility. We exploited the weak (0.6%) beam contamination with ^{18}O ions (top of Figure 3, right line) of same A/Q for energy calibration of the spectra. The long-term stability of the electronics and of the detector performance was pulser controlled. We observed rather similar pictures from both layers around Bragg-Maxima (27 µm and 126µm depth, respectively). The data shown in the following are from the 3.6 AMeV run.

Energy calibrated, one-dimensional spectra measured with a sample of 350µm thickness are shown in logarithmic scale on the right part of Figures 3 and 4. The selected amplitudes (dashed lines) are processed event by event and plotted on the Z-axis of the maps (left part of the Figures) over the corresponding XY-coordinate given by the raster scan magnets with an accuracy of ≈ 1µm. The uniformly distributed micro-pattern is unavoidable binning artefact. Dominant colours indicate the most probable energy measured within the selection.

This SC-DD shows high uniformity of the bulk material within the investigated ion range, as demonstrated by the homogeneous matrix area. All measured carbon events are processed in this case (Figure 3 top right, central line). On the other hand, completely congruend, large (x ≈ 20µm, y ≈ 5 µm), ellipsoidal structures are observed selecting the main peak- respective near-to-peak tail events (Figure 3 central- and bottom plot), obviously of lower intensity and almost hidden if a linear scale is used (Figure 5).

It is difficult to characterize unambiguously the origin of such structures by this simple method. Additional irradiations from the side may clarify the issue. The "missing-energy", is either lost upon entry into the diamond surface or by charge trapping along the particles path inside the bulk.Tthe energy loss is determined.comparing the full-energy peak of the high-efficiency regions (= 42.81 MeV, Figure 4, top right) with the peak value of the spectrum obtained from the low-efficiency regions (= 42.61 MeV, Figure 4, bottom right).

* Work supported by the EU/FP6 HADRONPHYSICS

A lot more experience needed to judge such structures. The stepwise broadening of the one-dimensional distributions shape in Figure 4 (bottom right) includes additional information.

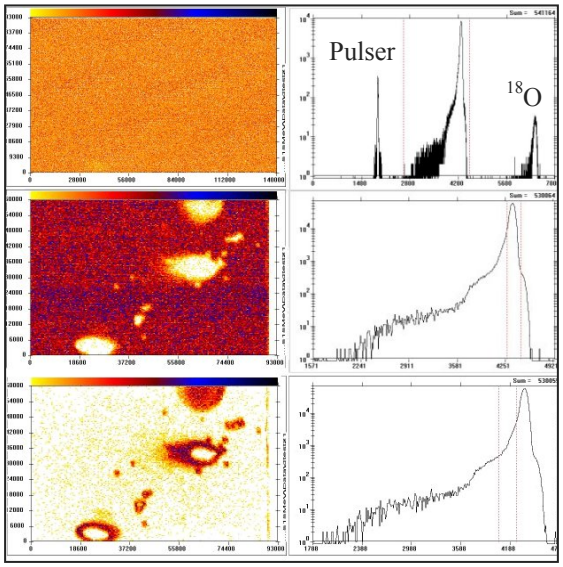


Figure 3: Distributions of selected energy signals of a SC-DD of 350 µm thickness over a homogeneously irradiated area of 140 x 93 µm^2 (left plots). The selected range is indicated by dashed lines in the corresponding one-dimensional spectra (right plots).

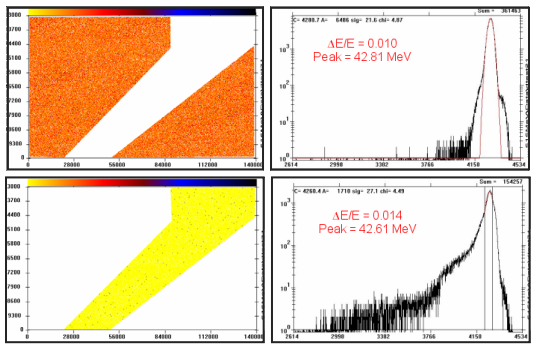


Figure 4: Comparison of energy distributions observed from 'good' and 'bad' regions (see text). The energy shifts found to be compatible with metallic pile-up due to scratch marks on the metallisation.

However, considering the appearance of the structures on a diagonal straight line and the development of the structures shape by selecting systematically lower amplitudes, we are convinced that in this case the measured 200 keV peak-shift is compatible with metallic pile-up due to scratches on the metallization. The circular structure observable at the top edge of the map in Figures 3 may be a liquid dropped on the surface during sample preparation.

For completion, all data collected in two runs have been calibrated in MeV and plotted in Figure 5 versus the beam energy. The excellent resolution obtained is ΔE/E = 0.01 for the lower energy of 43.2 MeV (left peak) and ΔE/E = 0.007 for the higher energy of 114.2 MeV (right peak), confirming convincingly the conclusion of bulk homogeneity of this SC-DD.

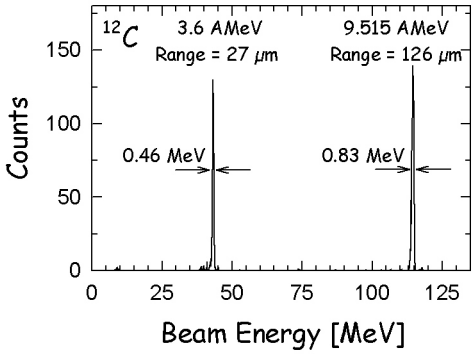


Figure 5: Energy spectra obtained from stopped ^{12}C ions probing different layers in 27 ± 5 µm depth (left line) and 126 ± 10 µm depth (right line), respectively. Homogeneity is mirrored in the resolution of ΔE/E = 0.01 for E = 43.2 MeV, respective ΔE/E = 0.007 for E = 114.2 MeV.

Timing Properties

Applying the intrinsic α-ToF technique and data analysis [2] the measured drift velocities of 10 SC-DD have been calculated and plotted in Figure 6 versus the electric field. First indications [2] of systematically faster holes drift is now established as a common feature of this material. Fitting the data, a $\mu_0^h \approx 2330$ [cm^2/Vs] and a $v_{sat}^h \approx 140$[µm/ns] are computed for the holes, whereas the electron data show more spread: $1400 < \mu_0^e$ [cm^2/Vs] < 3100 and $v_{sat}^e \approx 190$ [µm/ns] are determined. However, saturation velocity is never achieved.

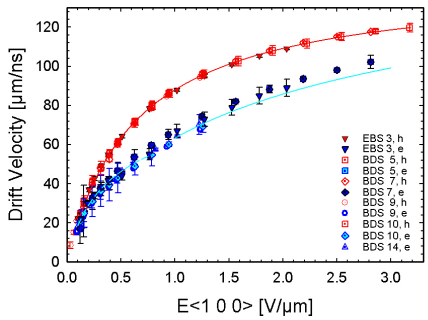


Figure 6: Drift velocities in <1 0 0> direction measured for 10 SC samples metallized with different contacts.

Intrinsic time resolution has been measured from the FOPI Collaboration using relativistic ^{27}Al ions (2 AGeV). The detailed description of this experiment is a contribution to this annual report: "A Diamond Start Detector for FOPI". σ_{int} = 28 ps was obtained for both types of CVD-DD-a clear limitation from the electronic noise.

References

[1] Dirk Meier, PhD Thesis, Univ. of Heidelberg, 1999
[2] GSI Scientific Report 2004, INSTMETH-35

A diamond start detector for FOPI*

M. Kiš, E. Berdermann, M. Ciobanu, K.D. Hildenbrand, A. Martemiyanow,
M. Pomorski, A. Schüttauf, A. Zhilin, GSI, Darmstadt, Germany
M. Rogowska, Warsaw University, Warsaw, Poland

At present FOPI uses an in-beam start detector with 2 PMTs and plastic scintillator foil for the ToF measurement. In a typical heavy-ion experiment a time resolution of $\sigma_t \approx$ 50-70 ps can be obtained. In conjunction with FOPI's ToF detector system (Plastic Barrel and Plastic Wall) this guaranties a decent combined ToF resolution. However, for the ongoing upgrade of the FOPI ToF barrel with the RPC detectors [1] a start detector with a time resolution that is better than the time resolution of the RPC detector ($\sigma_t \leq 60$ ps) by approximately factor of 2 is needed. To meet this requirement a new start detector based on diamond crystal material is planned to be constructed. In order to evaluate such a detector feasibility tests were performed on which we report here.

Two different types of detector-grade diamond crystals produced by CVD (chemical vapor deposition) technology are available: polycrystalline (PC) and single-crystals (SC) material. At the GSI there is an ongoing development program of diamond based detectors [2], so various samples of detectors are available.

In a test with a Ta beam in November 2004 a time resolution better than $\sigma_t \leq 25$ ps (shown in Fig. 1) with an

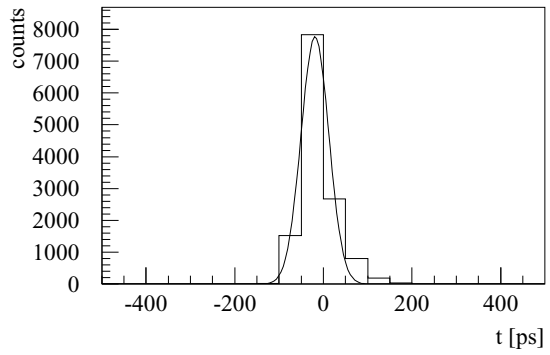


Figure 1: Time difference between two PC diamond detectors in a test with Ta beam was fitted with a Gaussian to estimate a time resolution.

efficiency $\varepsilon \leq 94\%$ had been obtained with a PC diamond detector (10x10 mm^2, active area $\phi = 8$ mm, thickness $d = 500$ μm). This is a solution for a new start detector as long as heavy-ion beams are used. However, if one wants to measure MIPs (minimum-ionizing particle) the intrinsic signal of the PC diamond becomes too small for the present state-of-the-art preamplifiers.

The possible solution are SC diamonds which have a much better carrier collection efficiency (close to 100%). Nevertheless, the intrinsic signal of a MIP traversing a SC diamond is still quite small (electron-hole pair creation energy is about 13 eV) so a special preamplifier electronics has to be developed for such a detector.

In 2005 two tests with SC diamonds have been carried out at FOPI. During our Al production run in August the pre-amp card originally built as the front-end electronics (FEE) part for the RPC detectors was used together with standard CAMAC electronics. The setup consisted out of two SC diamonds (4.3x4.3 mm^2, active area $\phi = 3$ mm, thickness $d = 300$ μm) placed behind each other with complete overlap into the direct beam. The measured time spectrum is shown in Fig. 2. We obtained a time resolution

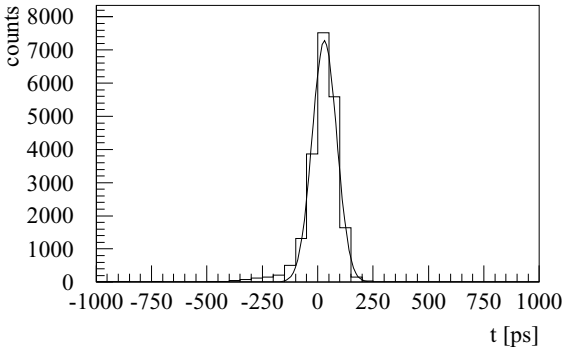


Figure 2: Time difference between two SC diamond detectors in a test with Al beam.

$\sigma_t \leq 40$ ps with an efficiency of $\varepsilon \leq 92\%$. However, the test showed that FEE gain is barely sufficient for a diamond application. Therefore, for the second test with protons in November we have used a modified FEE connected to the RPC time measuring electronics. During the run only a limited statistics was acquired yielding a time resolution of about $\sigma_t \leq$195 ps. In this modest preliminary result one has to keep in mind that it was obtained under non-optimal conditions; detectors were placed under a finite polar angle with seeing a lot of reaction background and in addition used pre-amps were still not optimized for the small signals of MIPs.

References

[1] A. Schüttauf *et al.*, NIM A 533 (2004) 65

[2] E. Berdermann *et al.*, Diamond and Related Materials 10 (2001) 1770,
NoRHDia Collaboration (this Ann. Rep.)

* Supported by EU/FP6 HADRONPHYSICS (see Annex)

Go4 Analysis Framework v3.0

J. Adamczewski, H. G. Essel, S. Linev; GSI, Darmstadt, Germany

Abstract

The Go4 version 3.0 released in November 2005 features improved inter-task communication, a new object management, and more convenient and powerful GUI functionality. Standard root macros may now be controlled via Go4 GUIs. Vice versa, a Go4 analysis may steered by a regular root session. A windows XP version of Go4 is now available (without Qt GUI).

Status of Go4

The Go4 (GSI Object Oriented Online Offline) analysis framework is well established in the atomic and nuclear structure physics community. The new version is fully compatible with existing analysis codes. To enhance functionality and maintainability some internal components have been redesigned, like the object management and the inter-task communication. Go4 v3 can be downloaded from the Go4 website [1] under GPL conditions

New Developments for v3.0

Inter-task Communication

The design upgrade of the task handler architecture [2] provides more flexible communication schemes. This means that a GUI can disconnect from a running analysis. Several GUIs may connect with authorization to the same analysis. The dependencies between analysis and GUI processes were decreased by modifications of the command pattern speeding up the GUI start up and reducing memory consumption.

Object Manager

The new object manager is now a general registry for data from different sources, using full pathname identifiers. It implements a common API also suitable for interactive work. It is implemented as a hierarchical structure of containers, data access proxies, a message passing mechanism, and standard ROOT cleanup techniques. In the GUI the object management is completely decoupled from the views. Thus another Go4 GUI could be implemented using other widget libraries than Qt, e.g. ROOT.

GUI Enhancements

The **object browser** was completely re-implemented as one browser panel with branches for different data sources, e.g. local work space, analysis, histogram servers, multiple root files, etc (see fig.1). It supports a local memory workspace with copy and paste, drag and drop, clipboard, and renaming functionalities. Other features are context menus (right in fig.1), a general monitoring management, and a property filter.



Figure 1: New browser for all data sources

Because the object management separates data and view, the same object may be displayed with different draw options and ranges simultaneously. Besides the known Go4 on-line features [3] a new **mbs status widget** monitors an MBS data acquisition node directly.

Standard ROOT Sessions

Starting a Go4 analysis server environment in a root CINT session this can be controlled from a Go4 master process (Qt GUI or other root session, see below). The GUI process may request data from a running analysis macro or control it via the Start/Stop buttons, if the macro uses some methods of the Go4 API. Therefore, any ROOT based analysis may easily benefit from Go4 remote communication and GUI.

The separation of the Go4 object management from the Qt layer made it possible to connect and control any remote (Go4) analysis task from a plain ROOT session. Additionally, a lightweight Go4 GUI was realised by supplying extensions for the regular ROOT TBrowser. Thus, Go4 v3.0 may also run in environments where Qt graphics is not available, i.e. Windows XP

References

[1] http://go4.gsi.de

[2] J.Adamczewski et al., *Go4 multitasking class library with ROOT*, IEEE TNS Vol.49, No.2, April 2002, pp 521-524

[3] J.Adamczewski et al., *Go4 online monitoring*, IEEE TNS Vol.51, No.3, June 2004, pp 565-570

Extension of ROOT I/O for XML Files and SQL Databases

S. Linev, GSI, Darmstadt, Germany

Abstract

ROOT framework of CERN [1] has powerful I/O system. Practically any kind of object can be stored in ROOT files. Until recent time ROOT supports only binary format and does not provide possibility for external (non-ROOT) access to object data. New development, started in GSI in 2004, allows alternative object data representations. Object I/O for XML files and SQL databases was introduced. Main efforts were done to support all ROOT I/O features: custom objects streamers, schema evolution and TFile interface for object manipulation.

ROOT I/O for XML Files

XML (eXtensible Markup Language) is a widely used standard for markup-based structured documents. Once stored in XML file, object data can be easily viewed/edited by a lot of existing XML tools. XML is also good candidate to be used as data exchange format between different applications.

Streaming of object data in ROOT is done via TBuffer class. Several methods of TBuffer class, responsible to streaming of basic data type, were declared as virtual and redefined in new TBufferXML class. Standard streaming procedure of ROOT was improved in the way, that TBufferXML object can identify data of which class member is streaming.

Custom streamers, which are widely used in ROOT classes, are also supported by TBufferXML class. The mandatory condition for usage of custom streamers is that sequence of input and output operations should be the same. Therefore, several ROOT classes were modified to fulfil that condition.

Several modifications in ROOT were done to enable schema evolution mechanism for non-binary objects streaming.

New TXMLFile class was introduced in ROOT. It provides TFile interface to write/read objects to/from XML file. Several layouts of XML file are supported. Special XML parser was implemented to improve speed of file I/O and memory consumption.

There are several limitations in usage of TXMLFile class. First, TTree and TDirectory are not supported while they internally use low-level I/O functions beside TBuffer. And second, size of XML file is limited by size of available memory.

ROOT also provides a method to access objects written to XML files by other applications. Special TXMLPlayer class can generate C++ code for I/O of user classes. Such code can be used to read/write XML files without ROOT environment.

ROOT I/O for SQL Databases

SQL (Structured Query Language) is common standard, supported by most of existing relational data base management systems (RDBMS). RDBMSs in physical experiments are typically used as storage for different kind of configuration and parameters. This can be detectors geometry, experimental conditions, slow-control data and so on.

Starting from ROOT version 5.08, support of object I/O for SQL databases was introduced. TSQLFile class allows storing arbitrary object, supported by ROOT, in SQL data base. The only exception is the TTree class, which has special TTreeSQL implementation for SQL database. TSQLFile fully supports custom streamers, schema evolution and subdirectory structure. User can configure different modes of usage database indexes and transaction.

Normally object data are stored column-wise, when for each class member exists appropriate column in class table. Normally each class version has one table, for example “TH1_ver4”. If data member can not be stored in single column (for example, list of objects), it is converted to “raw” format and stored in additional table with name like “TH1_streamer_ver4”. Each object stored in data base gets special id and registered in objects table.

Similarly to TBufferXML, new TBufferSQL2 class for object streaming was introduced. When writing object, TBufferSQL2 produces SQL INSERT queries, which applied then to SQL database. When reading, TBufferSQL generates appropriate SQL SELECT queries and gets object data from selected table's rows.

Tables, created by TSQLFile, have clear format and can be easily be accessed (for data reading) with simple SELECT queries. Typically data of one object is distributed between several tables because data of parent classes are always stored in other tables. TSQLFile can generate special SELECT query, which aggregate object data, distributed over several tables, in one resulting row.

At the moment TSQLFile class was tested together with MySQL 4.1 and Oracle 9 RDBMS. With minimum adjustments it should be possible to use TSQLFile for other kinds of RDBMS, supported by ROOT via TSQLServer interface.

References

[1] http://root.cern.ch

EPICS - Experimental Physics and Industrial Control System at GSI

J. Adamczewski, H.G. Essel, and M.R. Stockmeier*, GSI, Darmstadt, Germany

Abstract

EPICS (Experimental Physics and Industrial Control System) is a widely used scalable control system. At GSI the HADES group uses EPICS since its startup [1]. In order to build a GSI wide knowledge base on EPICS some other projects than HADES are started. For example FOPI is a nice target for different controls developments like the LabView based CS [2] and EPICS. For the FUTURE DAQ project of CBM and the HADES tdc readout board an "embedded" EPICS will be ported to these embedded boards.

EPICS - a small introduction

EPICS is an open source control system framework which allows to build huge distributed control systems. It can run on several OSs (operating systems) like Linux, Vxworks (originally developed on this OS), RTEMS (A real time OS), and Windows. The communication is based on the channel access (CA) protocol using Ethernet as transport layer. The IOC (Input Output Controller) is the application which provides process variables (PV) via CA. Once a PV is published it is network wide visible. EPICS gives the freedom to use any CA client to display the acquired data. As a default solution MEDM (Motif Editor and Display Manager) is at the moment used at GSI. But in the near future other means of displaying CA data will be tested. Any other service than displaying, like archiving, histograming, and alarm handling are available as CA clients. These tools can be found at the central webpage [3].

EPICS is fully documented and available on the world wide web. In addition to that the very active email list "tech-talk" gives access to the wide knowledge of the worldwide EPICS users. For the first start reference [3] is the best starting point to evaluate EPICS.

In order to have access to EPICS from all computers, a GSI wide installation was initiated on linux. A detailed HowTo is available at [4]. All experiment groups are invited to test EPICS for their setup.

EPICS @ FOPI

The FOPI collaboration is open for new ideas on controls on either LabView or EPICS. In addition, FOPI is a running complex experiment which has a great variety of hardware.

MBS monitor

The GSI standard DAQ system MBS [7] provides DAQ status information server socket. An EPICS IOC on a Linux machine was implemented to retrieve this status structure. The full MBS monitor setup connects to 5 different MBS nodes (FOPI uses up to 5 event builder). Every second the MBS status is updated and computed to a DC data and event rate. The usage of this IOC and the displaying tool based on MEDM is documented at [5].

MBS monitor archiver

A second CA client for the MBS monitor was used. As an archiving tool the Channel Archiver from SNS (spallation neutron source) was introduced. It connects, as any CA client, to process variables which are available by the MBS monitor.

EPICS on embedded systems

One of the advantages of EPICS is that it is possible to run EPICS even on embedded systems. This gives the possibility to get the slow control data very "fast" into the control system. It is not needed to invent other means of data transportation in order to reach the overall control system. Two embedded linux boards were selected as target architectures:

The HADES tdc readout boards are based on the ETRAX 100LX multi chip module [6]. EPICS cross compilation for the linux running on this board is currently under development. For the FUTURE DAQ for CBM the Virtex 4 evaluation board ML403 [8] will be the target platform.

The general steps to run EPICS on different embedded systems will be available soon.

References

[1] Burkhard Kolb, "HADES slow control", http://www-hades.gsi.de/scs/

[2] D. Beck et al., "A new control system for ISOLTRAP" Nucl. Instr. Meth. A 527, 2004, p. 567-579

[3] Argonne National Laboratory EPICS Homepage, "Experimental Physics and Industrial Control System", http://www.aps.anl.gov/epics/index.php

[4] M.R. Stockmeier, "EPICS wiki at GSI", http://wiki.gsi.de/-cgi-bin/view/Epics/WebHome

[5] M.R. Stockmeier, "FOPI MBS monitor", http://wiki.gsi.de/-cgi-bin/view/Fopi/HowToUseEPICSmbsMonitor

[6] AXIS communication, "ETRAX 100 LX", http://developer.axis.com/products/mcm/index.html

[7] N. Kurz, "MBS - Multi Branch System", http://daq.gsi.de

[8] Xilinx, Inc., "Xilinx web page", http://www.xilinx.com/

* M.Stockmeier@gsi.de

New Slow Control System for FOPI

P. Koczoń, D. Beck, H. Brand, M. Kugler, Y. Leifels, A. Schwinn, U. Thiemer, H. Vranesić

GSI, Darmstadt, Germany

FOPI-detector upgrade

A high resolution time-of-flight shell build of newly developed MMRPC [1] detectors is being installed at present at FOPI [2]. The upgrade will allow a high momentum measurements of Kaons. The achieved time resolution of MMRPCs (<100ps) can be assured only if the working conditions, e.g. counting gas parameters, high voltage and low voltages power supply are stable within required accuracy. The surroundings' temperature has to be monitored with a precision of 0.1 °C. Additional requirements concerning the new FOPI Control System itself like availability, scalability, flexibility, multi-user capability and security aspects should be guaranteed as well.

CS framework

The Control System (*CS*) based on National Instruments LabView [3] lately developed at and supported by GSI has been chosen as a framework for the FOPI slow *CS*. It provides event-driven local and network communication mechanisms, an object-oriented programming approach as well as SCADA functionality. It is already used by other GSI experiments [4]. The client-server architecture of the system allows to concentrate the data readout and archiving in one place – on the server machine. The alarming and trending processes are also running on the Server Computer. The User GUIs are running on Windows XP or Linux PCs what allows every user to open his own *CS* session controlling a subsystem of interest.

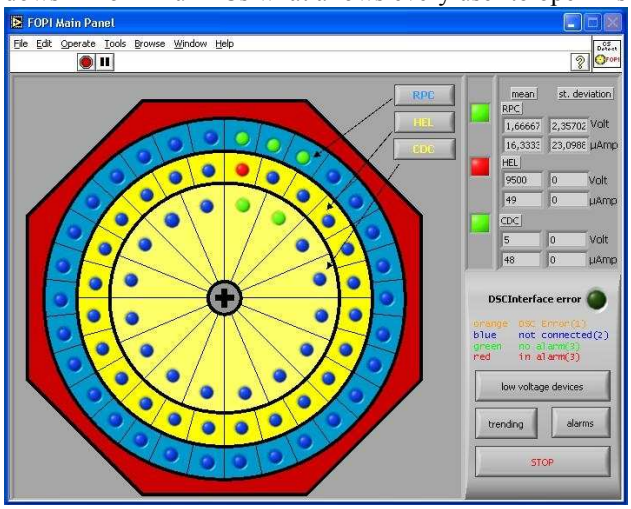


Figure 1: FOPI Control System – GUI.

FOPI *CS* implementation

The main window of the user GUI in its present status is shown in Fig. 1. Setting and monitoring of the most important parameters (main voltages and currents) of the FOPI subdetectors CDC, Helitron and RPC is available in this place.

The graphic depicts the detector setup in a form reminding the detector itself what allows easier orientation to the user. It will also allow setting or monitoring the parameters for each sector of the given subdetector separately. Indicators colour code is used to inform the user about the sector status: normal/subcritical/alarm.

Fig.2 presents an expert view of the CAEN 1527 high voltage supply for one sector. Every parameter of the channel can be set and monitored in this panel by an advanced user.

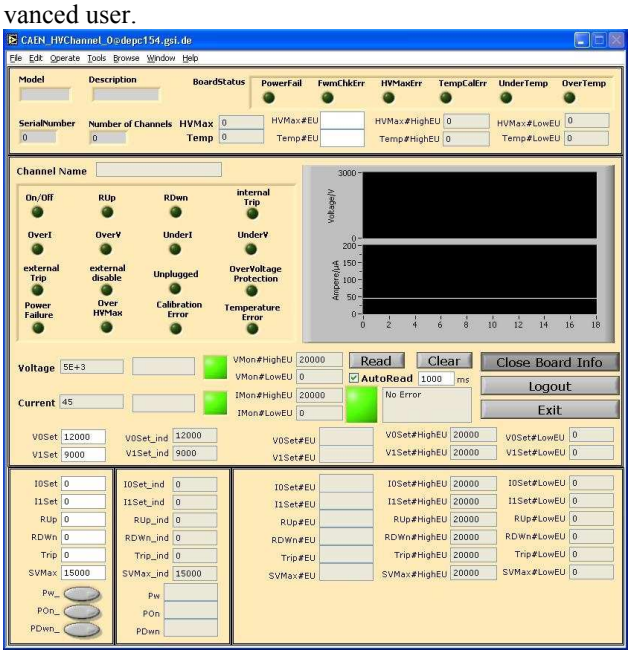


Figure 2: CAEN 1527 Control Panel – expert view

First test runs proved needed functionality and stability of the system.

References

[1] J.L.Ritman and the FOPI Collab. Nucl. Phys. B – Proc.Suppl. 44 (1995) 708

[2] A.Schuettauf NIM A 533 (2004) 65-68

[3] http:// ni.com/LabVIEW

[4] D.Beck and H.Brand GSI Scientific Report 2002 (2003) 210 and references therein

InfiniBand Test Cluster for FAIR DAQ[1]

J. Adamczewski, H.G. Essel, S. Linev, W.F.J. Müller; GSI, Darmstadt, Germany.

Abstract

FAIR experiments like CBM require a new approach for the data acquisition system, since event tagging and selection will be done triggerless [1]. Thus a most effective and fast data transport between many nodes is necessary. To evaluate possible techniques and performance, a small Linux cluster of CBM with InfiniBand (IB) connections is being tested at GSI. C++ software was implemented for IB data transport benchmarking, wrapping the uDAPL library. Here a data scheduling method using inter-node time synchronization was also developed. Investigations on the CMS XDAQ system have been started, as one example of a powerful DAQ framework.

Cluster Setup

The cluster consists of four double-opteron machines with 2GB memory each and 160 GB SATA disks, using SuSE 9.3 Linux. The nodes are connected both with Gigabit Ethernet and 10 Gb InfiniBand (IB), via a crossbar switch each. IP protocol is configured for both networks with different IP addresses. Mellanox IB Gold distribution v1.8 [2] was installed for usage of the IB interfaces. The cluster will be extended for a CBM DAQ prototype system.

InfiniBand Data Transport

In order to verify the InfiniBand connection performance, a set of standard benchmark suites were carried out. These tests applied both the MPI (Message Passing Interface) [3] and the uDAPL (user Direct Access Programming Library) [4]. Typically, a maximum bandwidth of 953 Mb/s, and a minimum latency of 4 µs could be achieved.

For advanced testing developments, a set of C++ classes was defined to wrap the uDAPL library C API. As a first simple test, the remote direct memory access (RDMA) between two nodes was implemented. This resulted in maximum bandwidth of 930 Mb/s for 1Mb buffer size.

To optimize the IB data traffic, a packet scheduling mechanism has been developed. It implies data sending at predefined times and controls retrieving on receiving side. A time calibration procedure between nodes was invented to compensate clock frequency differences and time shifts. Precision of few µs during 100 seconds was achieved. Different kind of traffic patterns was tested: “all-to-all”, “all-to-one”, and “one-to-all”. Both, uDAPL messages (Msg) and RDMA transfers were tested showing almost no difference. Fig.1 shows the results for the “all-to-all” case.

1 Supported by EU/FP6 HADRONPHYSICS (see Annex)

XDAQ Framework

XDAQ [5] is a C++ data acquisition framework developed for the CMS experiment. It was installed on the IB cluster after some code modification due to the 64 bit architecture that was not covered by the original distribution. XDAQ features, e.g. SOAP Messaging between cluster nodes, state machines, Hyperdaq web server, work loops (threads), and exception handling, were tested successfully.

The standard XDAQ peer-to-peer roundtrip benchmark for the I2O transport layer was carried out for the TCP protocol over InfiniBand, and over Ethernet connections of the cluster, respectively. This test yielded values of 97 Mb/s for Ethernet, and 196 Mb/s for IB (50kB packages). The latency (i.e. 28 byte I2O package roundtrip time) was 42 µs, and 55 µs , respectively. The complete transfer rate results are shown in Fig.1.

The RDMA client-server test with uDAPL as described above was adopted into an XDAQ application to run a pseudo roundtrip benchmark for IB under similar conditions as the I2O/tcp test. This gave values of 619 Mb/s (50 kB buffer), and a saturation maximum of 906 Mb/s (4.5 Mb buffer). The minimum latency was 30 µs. For further tests, it is planned to develop a direct IB/uDAPL implementation of the XDAQ I2O messaging interface.

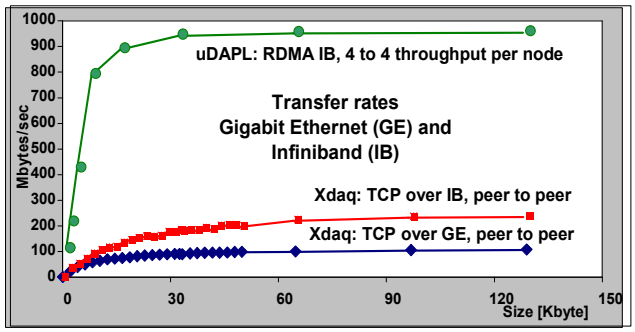


Figure 1: Transfer rates benchmarks

XDAQ turned out to offer powerful components for configuration and control of a DAQ system. Possible problems, like compatibility on different platforms, scalability, error handling, and failure recovery, still have to be investigated.

References

[1] Technical Status report CBM experiment, GSI (January 2005), pp. 235

[2] http://www.mellanox.com/

[3] http://www.mpi-forum.org/

[4] http://www.datcollaborative.org/

[5] http://xdaqwiki.cern.ch/index.php/Main_Page

PCI to GTB (GTBP) Interface for Data Acquisition.

J. Hoffmann , N. Kurz, W. Ott,
GSI Darmstadt

The new GTBP module allows access to GTB [1] with a standard PC. The GTB interface bus was originally developed for the therapy project and is used in the meantime in many different applications. The GTBP has a form factor of a standard PCI card and can be plugged in any free PCI slot of a PC. It performs as GTB Master and can be connected to any GTB slave module. E.g. in combination with the GTBC CAMAC controller, up to 15 CAMAC crates can be read out with one PC.

The GTBP module has the following features:

- readout and control of up to 15 GTB slaves.
- 1 GTB channel
- Master and slave PCI interface
- 4 LEDs
- on board TMS320C6711 DSP for readout and control
- 128MB SDRAM
- PCI communication memory, dual-port RAM 32K x 32 bit
- FPGA configuration via PCI

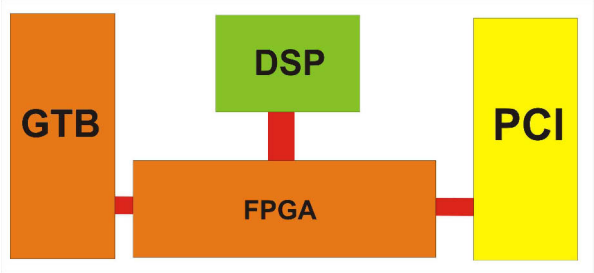


Fig. 1: Block Diagram of GTBP

MBS [2] , GTBP and GTBC

The first working application of the GTBP is the replacement of the old intelligent CAMAC controller CVC in the framework of the data acquisition system MBS. This solution utilizes a PC equipped with one GTBP running the real-time operating system LynxOS. Via GTB up to 15 of the newly developed CAMAC controllers GTBC can be connected in a chain, allowing thus the control and readout of up to 15 CAMAC crates. A LynxOS driver has been developed and integrated into the MBS to control the GSI CAMAC trigger module. The new system is fully in operation, i.e. it works with the standard ESONE server/client system for slow control applications. Care has been taken to make the adoption of old user applications running on the CVC very easy.

In addition the new system gives a substantial performance gain compared with a CVC system. With a CVC about 2000 events per second could be achieved for small data event sizes. Now, typically 20000 events per second can be reached under the same conditions, even with "old" 400MHz PCs.

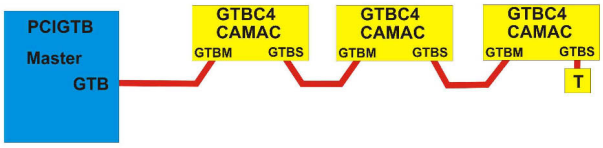


Fig 2: GTBP to GTBC connections

Future possible applications with the GTBP

One application could be a Multi Channel Analyzer (MCA), which can be set up together with Silena ADCs and the AMUX [3] modules. The histograming is done with the DSP on the GTBP card and the histograms are stored in the SDRAM. Possibly the visualisation of this MCA could be done with Labview.

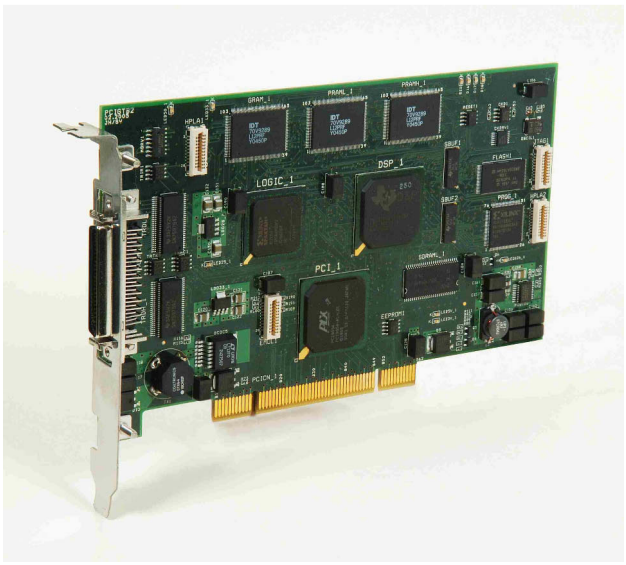


Fig 3: View of GTBP PCI module

[1] J.Hoffmann GTB The General Purpose Token Bus, http://www.gsi.de/informationen/wti/ee/elekt_entwicklung/GTB.html
[2] H.G.Essel and N.Kurz The General Purpose Data Acquisition System MBS. IEEE Transactions Apr. 2000
[3] AMUX Development of ADC multiplexer for SHIP, GSI Scientific Report 2004 http://www.gsi.de/informationen/wti/library/scientificreport2004/PAPERS/INSTMETH-13.pdf

Interface between CAD (CATIA) and ROOT/Geant4

P. Biryukov, GSI, Darmstadt, Germany.

Abstract

The main objective of the work is a proposal for the interplay between physics simulation software (ROOT/Geant4) and CAD (CATIA v5) systems. The results of the work could be used during future GSI experiments, in particular CBM (Compressed Baryonic Matter).

Overview

The goal of the work [1] is to make ROOT/Geant4 [3, 4] geometry available in CATIA [2] and vice versa. The work mostly targeted to the future GSI project, where CATIA v5 is used as a CAD system. It also should be evaluated which parts of the processing chain can be done automatically, partial automatically, or completely manually.

In the first approach geometry from ROOT/Geant4 was converted into STEP format (ISO 10303) [6] that could be read by many CAD systems (including CATIA). However, backward conversion from STEP to ROOT/Geant4 was problematic due to quite different hierarchy and geometry representations in CAD/STEP and ROOT/Geant4; to solve this problem other file format were used during geometry conversion from CATIA to ROOT in the first approach and in the entire second approach.

The first approach

On the way from ROOT to CATIA the program performs ROOT/Geant4 geometry tree traversal, converts geometry into Open CASCADE [5] representation and saves a STEP [6] file with the geometry that could be read with many modern CAD systems (including CATIA).

On the way from CATIA to ROOT/Geant4 the program restricts CATIA to produce only limited set of solids that could be stored using a custom file format. These files are read by another part of the program that recreates the geometry in ROOT.

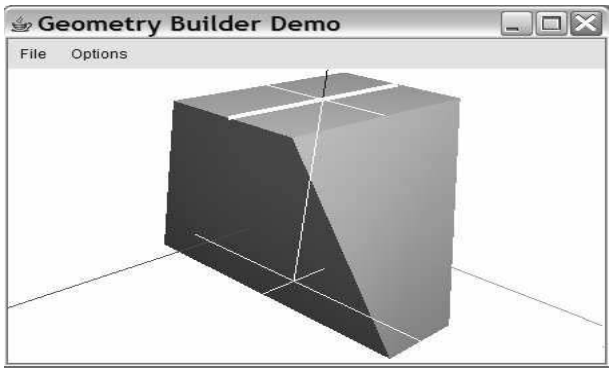


Figure 1: Early stage of Geometry Builder development (TRD2 has activated markers for size changes).

This approach is currently being improved. The idea is to create a stand-alone conversion utility between CAD and ROOT/Geant4. It should be the program that provides advanced functionality for ROOT-like geometry editing, with strong points of CAD and ROOT, such as well developed visual tools of geometry edition (as in CAD) with the orientation for the certain set of 3D shapes (as in ROOT); and without weak points such as geometry inadaptability to sophisticated editing (as in ROOT), or too general geometry definitions that are hard to convert into ROOT's style (as in CAD).

The second approach

On the way from ROOT to CATIA the program performs ROOT geometry tree traversal, and saves a text file with the geometry description. On CATIA's side the program reads this file and recreates geometry inside CATIA. The HADES and CBM geometries were processed using this method.

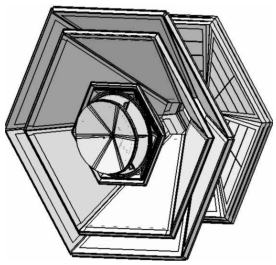


Figure 2: Geometry of HADES detectors loaded into CATIA.

The way from CATIA to ROOT is more complicated. Geometry in CATIA must be marked with key points and some additional information must be entered for the exporting script (manually), then the script saves a STEP file with key points and a text file with additional information such as hierarchy information required by ROOT. On ROOT's side the program converts both STEP and geometry description files into ROOT's geometry.

Summary

Both approaches have strong and weak points, however software such as the mentioned Geometry Builder that could create ROOT-like geometries using CAD style and export it into both CAD and ROOT seems to have good chances for success. More information about this work could be found on the author's website [1].

References

[1] http://www-hades.gsi.de/~biryukov/
[2] http://www.3ds.com/
[3] http://www.root.cern.ch/
[4] http://geant4.web.cern.ch/geant4/
[5] http://www.opencascade.org/
[6] http://www.iso.org/

Electronic gain dependence of the time resolution for FOPIs Multi-strip Multi-gap Resistive Plate Counters (MMRPCs)

A. Schüttauf, K.D.Hildenbrand, M. Ciobanu, P.Koczon, Y.J. Kim, M.Kis, Y.Leifels, M. Marquardt, J. Weinert, X.Zhang, GSI, and E. Cordier, N. Herrmann, Phys. Institut Univ. Heidelberg

In order to improve the Kaon identification up to 1 GeV/c the FOPI detector will be upgraded by an array of 150 Multi-strip MRPCs [1][2]. This requires a time resolution $\sigma_t \leq 100$ ps for single and double-hits in the counters [3][4]. The counter design is finalized (cf. Fig. 1): active area 46 x 900 mm^2, 8 gaps of 220 μm, 16 separate anode strips, operation voltage 9 to 10 kV; a gas mixture Freon/i-But/SF6 (85/5/10)is used. The mass production has started, the system shall be operational by the end of 2006.

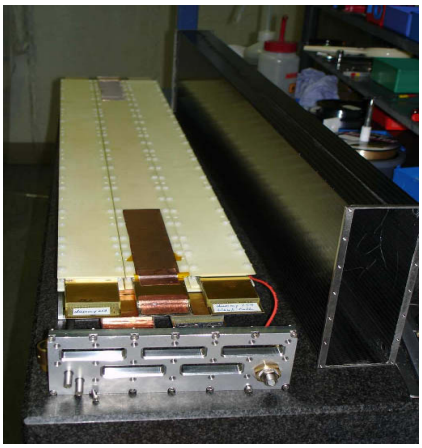


Figure 1: *Super-module consisting of a carbon fiber box and two aluminum flanges which houses 5 counters with common gas and high voltage supply.*

To optimize the final electronic settings we investigated the influence of the electronic gain on time resolution, efficiency and cluster size. Especially the cluster size is crucial for the multi-hit performance: To resolve clusters even for the highest multiplicities (60 particles), a mean cluster size $\langle nstr \rangle \leq 3$ strips is needed.

The charge avalanche in Timing RPCs grows exponentially through the gap in first order [**?**]. To keep its lateral and transverse size small we use gaps of only 220 μm , also in view of an optimum in time resolution. This, however, reduces the number of primary electrons: Minimum ionizing particles deliver 75 fC of primarry charge in our counters with signal rise times of 0.3-0.5 ns. This explains the need of a high gain (G $\sim$ 100) and high bandwidth ($\delta f \sim$ 1.5 GHz) preamplifier.

Fig. 2 shows the dependence of time resolution and efficiency on the applied electric field (defined as Cathode voltage divided by total gap size) for 4 different preamplifier gain settings (G $\sim$ 77,130,160 and 220). Qualitatively the detector response is similar for the various gain settings, a higher gain leads to a shift of the curves to lower fields. At given field a higher gain provides a better resolution, likewise at given gain a certain resolution is reached at a lower field strength. For example we reach at G $\sim$ 77 a time resolution of $\sigma_t \leq$75 ps at E$\geq$ 120 kV/cm; at G $\sim$ 220 a resolution $\sigma_t \leq$ 50 ps is reached at E$\geq$ 108 kV/cm already. Similarly the detector becomes fully efficient at lower electric fields when the gain is higher.

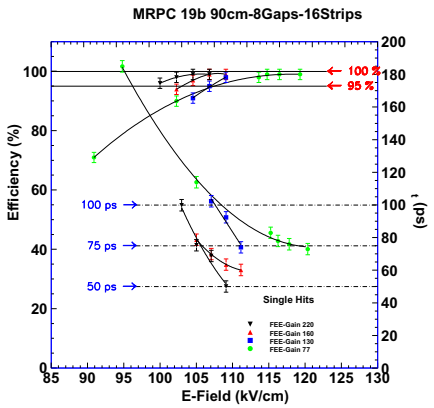


Figure 2: *HV dependence of time resolution and efficiency for four FEE-gain settings.*

From these results one might conclude that a high FEE-gain would deliver an optimum in counter performance. However, our systematic study of the cluster size [5] revealed an increase by more than 75 % between the two extreme gain settings at given field strength and discriminator threshold, too high a value to be tolerated for the expected multiplicities.

In summary we conclude that a FEE-gain of G $\sim$ 160 fulfils best FOPI's needs in terms of timing, efficiency and cluster size. With this setting we reach at 110 kV/cm a resolution of $\sigma_t \leq$ 60 ps at an efficiency of $\epsilon \geq 99\%$ and a mean cluster size of $\langle nstr \rangle \leq 2.5$.

References

[1] E.C. Zeballos et. al., *NIM A 374 (1996) 1322*,

[2] P.Fonte et al., *NIM A 443 (2000) 201*

[3] M.Petrovici et. al., *NIM A 487 (2002) 337*,

[4] A.Schüttauf et. al., *NIM A 533 (2004) 65*

[5] A.Schüttauf et. al., *NIM A (2006) in press*

Status of the HADES RPC Project*

The HADES RPC Group

In recent years, timing RPCs (Resistive Plate Chambers) [1] have emerged as a novel, cost-effective technology to achieve high timing resolutions $\sigma_t \leq 100$ ps as well as high granularities, which are required for high particle multiplicities. In order to cope with rates of $\Phi \leq 700$ Hz/cm^2 (expected for Au+Au collisions), the HADES detector is being upgraded. As a part of the upgrade project, an RPC-based Time-of-Flight (TOF) wall, ESTRELA (Electrically Shielded Timing RPC Ensemble for Low Angles) is being constructed. The final setup will consist of 1024 RPCs with two-sided readout, an active area of $\simeq$8 m^2 ($18^o \leq \vartheta \leq 45^o$, $0 \leq \varphi \leq 2\pi$) and will be integrated into the HADES level-1 and level-2 trigger systems. The RPC cells are electrically shielded, with a typical size of (150-600)$\times$(20-60)$\times$11.2 mm^3, and comprising of 4 gas gaps formed by 3 aluminium electrodes separated by electrically-floating glass electrodes [2] of 2 mm thickness.

Front-End Electronics

In 2005, a new concept for the RPC front-end electronics (FEE) has been developed, which consists of two different boards, namely a daughterboard (DB) and a motherboard (MB).

The DB has 4 channels, 6 layers and a size of 5×4.5 cm^2. It consists of two different parts, an analog and a digital part. In the analog part, since the input signal has frequency components up to the GHz range, Monolithic Microwave Integrated Circuit (MMIC) amplifiers are used. In the 3^{rd} iteration of the DB, two staged amplifiers were used, a Philips BGA-2712, with a 1 GHz bandwidth, 21 dB power gain and 3.9 dB noise figure, and a Mini-Circuits GALI-S66, with a 2 GHz bandwidth, 18 dB power gain and 2.8 dB noise figure. As we found that the GALI-S66 provides sufficient gain for the RPC signals, in the 4^{th} iteration the GALI-S66 amplifier will be used exclusively. Two parallel branches follow behind the amplifying stage. In one branch there is an integration stage using a TI OPA-690 wide-band voltage-feedback operational amplifier, which is used for a Time-Over-Threshold (ToT) measurement. In the other branch, which is the digital part, the amplified and the integrated signals are input to a MAXIM 9601, a dual ECL/PECL, 500 ps propagation delay, ultra-high speed comparator. A PECL/LVDS converter, Philips PTN3311, follows the comparator in order to obtain a digital output signal (LVDS, Low Voltage Differential Signal). The latch enable of the MAX9601 comparator is used to provide the leading (using the TOF) and the trailing (using the TOT) edge of the LVDS signal. A multiplicity trigger for the HADES level-1 trigger is also delivered to the MB.

The MB has 32 channels (8 DBs per 1 MB), 8 layers per board and a size of 40×6 cm^2. The DB is connected to the MB through a SAMTEC QSS connector with 16 differential pin pairs of 0.635 mm pitch. The connector is specified for a crosstalk of $\leq$3.6% and an impedance mismatch of $\leq$10% up to frequencies of 2 GHz. DB and MB are connected geometrically in a 90^o way. Thus, in the end, the FEEs on the front-side and the back-side of the RPC gasbox will form a channel for air cooling. The MB provides voltage supply to the DB, DACs for analog signal thresholds (programmed by SPI, serial peripheral interface), a 3-stage summing circuit for a level-1 trigger multiplicity signal, and repeater and fan-out for test signals. The MB layout is impedance matched to 100 Ω, and uses newest generation multilayer ceramic capacitors as noise filters. The MB sends all LVDS signals to a TDC board which is described elsewhere [3].

Test with a pulse generator

The DB has a test signal circuit, which, for an external test pulse (a square input signal of 0.5-2.5 V amplitude and 1 μs duration) generates a narrow RPC-like test signal of a few ns width. The time difference between these test signals on two channels of one DB was measured with a Digital Tektronix oscilloscope TDS7104 (1 GHz, 4 GSa/s per channel). The width of the distribution is a measurement of the DB time resolution and was determined to be σ_t=16 ps for signal charges above 100 fC and thresholds of 25 fC.

Test with a ^{60}Co source

In a second test, the prototype described in [4] (using a standard gas mixture [5]) was illuminated with $\leq$1.3 MeV photons from a ^{60}Co source. The RPC cell was read out at both sides, and the analog signals were input to two channels on the same DB. The time difference $\Delta t = t_l - t_r$ between the leading edges of the LVDS signals of the both RPC sides (l denotes left, r denotes right) for well defined source positions was measured, and a raw time resolution of σ=40$\pm$5 ps was determined, uncorrected for signal charge. For a threshold of 25 fC, crosstalk was determined to be $\leq$1%.

Test with ^{12}C beam

In November 2005 a prototype setup of 24 RPCs has been mounted into the HADES frame and tested at GSI

* This work was supported under the following contracts: EU 6^{th} FP No. RII3-CT-2004-506078, Ministerio de Ciencia y Tecnología No. FPA2003-07581-C02-02, Xunta de Galicia No. PGIDT-02-PXIC-20605-PN, MCYT No. FPA2000-2041-C02-02, FEDER and FCT No. POCTI/FP/FNU/50171/2003, and POCI/FP/63411/2005.

with ejectiles from reactions of a 1.5 AGeV ^{12}C beam on a Pb Target. Fig. 4 and Fig. 5 show the time difference Δt=$(t_l^1+t_r^1)/2-(t_l^2+t_r^2)/2$ for two superimposed, neighbouring RPCs, measuring twice the identical particle (i=1,2 denote the RPC index). Fig. 4 shows σ_t measured using standard reference electronics (CAMAC) as described in [6]. A resolution of σ_t=78 ps was measured, corresponding to the resolution of a single RPC of 78 ps/$\sqrt{2}$=55 ps. This time resolution was measured on 14 individual RPCs, ranging the results from $50 \leq \sigma_t \leq 80$ ps, with an average of σ_t=60.1 ps. The low relative fraction of 0.90% in the tails for $\Delta t \geq 700$ ps also indicates a negligible level of crosstalk. The value of $\Delta t \geq 700$ ps corresponds to a $\pi^{\pm}$-$K^{\pm}$ TOF separation for 1 GeV/c particle momentum and a flight path of 2 m, approximately matching the HADES RPC conditions. Fig. 5 shows the same time difference Δt, but measured with the new electronics (DB and MB and TDC board) to 113 ps for the two combined RPCs, and $\simeq$80 ps for the single RPC resolution. A position resolution can be derived from $(t_r^1$-$t_l^1)$-$(t_r^2$-$t_l^2)$, translated into coordinates ($v \simeq 2/3c$), and was determined to be Δz=9.8 mm (FWHM). The detector was operated at 33^oC, reaching counting rates up to 800 Hz/cm^2 without any discernible impact on the performance.

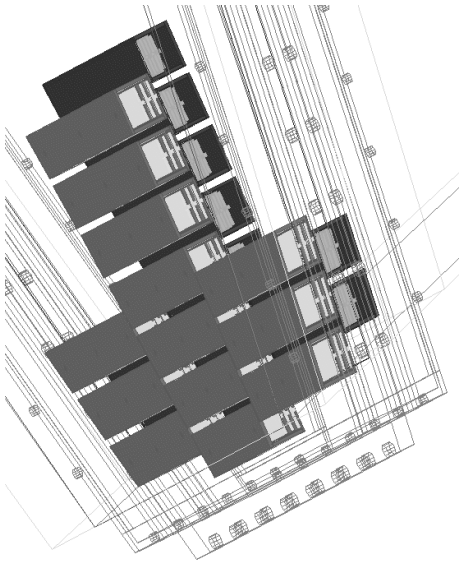


Figure 1: The geometrical RPC setup for the beam test.

References

[1] P. Fonte, A. Smirnitski, M. C. S. Williams, NIM A443(2000)201
[2] E. Cerron Zeballos at al., NIM A374(1996)132
[3] M. Traxler et al., 128 channel high resolution TDC with integrated DAQ-system, GSI Scientific Report 2005
[4] H. Alvarez Pol et al., NIM A535(2004)277.
[5] P. Camarri at al., NIM A414(1998)317.
[6] H. Alvarez Pol et al., NIM A533(2004)79.



Figure 2: The daughterboard.

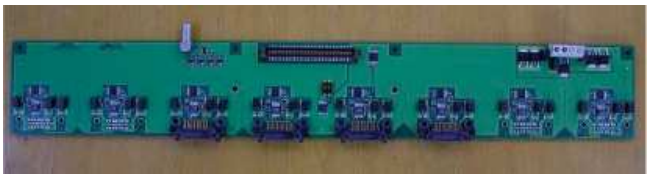


Figure 3: The motherboard.

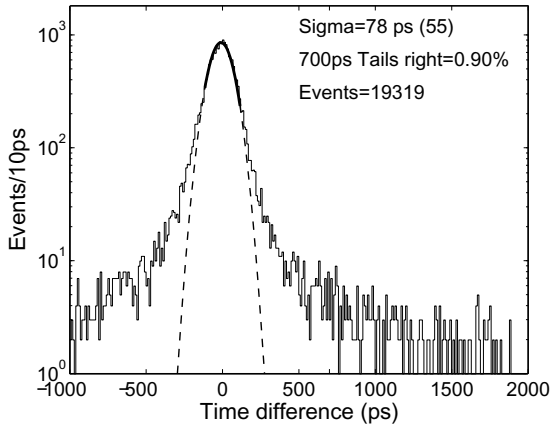


Figure 4: Time resolution for the beam test, using reference CAMAC electronics.

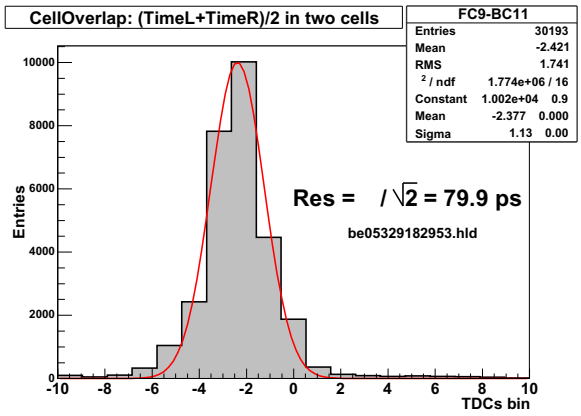


Figure 5: Time resolution for the beam test, using the new front-end electronics.

Progress on Pion Beam for HADES*

B. Spruck[1], W. König[2], S. Visotski[3], R. S. Simon[2], R. Novotny[1], V. Metag[1]
[1]II. Physikalisches Institut, Universität Gießen, [2] GSI Darmstadt, [3]ITEP

In August 2005 a three day high intensity machine development test in SIS was combined with investigations of the pion beam and scintillation detector tests in the HADES cave. Average intensities of $4-5*10^{10}$ particles (^{14}N) in SIS were routinely achieved over extended periods of time (several hours). Such intensities, however, are still about a factor three lower than the SIS space charge limit of $14*10^{10}$ particles. The maximum intensity achieved was $6.5*10^{10}$ particles in SIS. For this peak intensity $1.8*10^{6}$ π^- were registered per burst (4s cycle time) in front of the HADES detector at a momentum of 1.17 GeV/c. The increase in intensity compared to the experiment of May 2004 (described in [1]) mainly results from improved extraction at SIS. These numbers have to be compared to the pion intensities of 1.0 and $1.1*10^{6}$/s assumed in the proposal for 800 MeV/c and 1.3 GeV/c, respectively. The present intensities fully confirm the extrapolations used in the proposal. Provided the space charge limit of SIS is reached the intensity will be sufficient to perform the planned pion beam experiments. At a constant extraction time of 4s rapid ramping would decrease the cycle time from 7s to 5s. This future option will allow for long term operation in the production runs.

The intensity and profile of the beam were measured with two scintillating fiber arrays of 96 fibers, subtending an area of 6.5*6cm each. The count rate was determinded by requiring coincidences between both arrays. Two different setups for the fiber hodoscopes were used during this experiment. In one configuration they were set up within a distance of 10cm to measure x and y distributions of the pions at 2.2m behind the last quadrupole. The measured profiles in x and y have 10.5mm and 9mm FWHM, respectively. While the x distributions has large asymmetric tails, there is no significant deviation from a Gaussian shape in y direction.

In a second step, the fiber hodoscopes were installed in parallel at 1.2m and 2.35m behind the last quadrupole. A better focus in x with 8mm FWHM was achieved near the quadrupole with tails reaching up to $\pm$15mm. With two x position measurements, the pion tracks could be reconstructed along the beamline as illustrated in fig. 1. Due to the momentum spread of the π-beam the focus extends over about a meter in beam direction, consistent with beam transport calculations.

An additional test has been done by running the beam transport system in a setting for positive polarity particles, where protons dominated the secondary particle beam. The resulting total intensity was $5-6*10^{6}$ particles/spill at the HADES target position for $4-5*10^{10}$ ^{14}N ions in SIS.

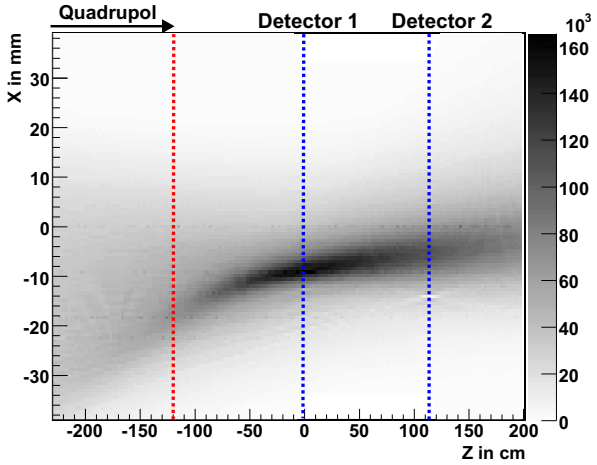


Figure 1: Reconstruction of beamfocus in the x-z plane. The end of the last quadrupole and the positions of the two fiber arrays are indicated by lines.

Beam Transport Simulation

Beam optics calculations suggest that the tails in x direction can be further reduced by using an additional 3rd quadrupole. Simulations have been done with a beam transport programm (Trace 3D), using a beamline setting for nominal momentum while varying the energy of the pions. This results in a second order appoximation of the momentum spread of the beam. Table 1 lists the envelope sizes for nominal and $\pm 2\%$ energy. The simulated first order momentum spread is 4% and 2%, respectively. It is clearly visible that the beamspot size is dominated by second order effects, which can be reduced by the third quadrupol.

Table 1: Simulated beamspot sizes for actual (doublet) and future setup (triplet).

	Doublet		Triplet	
Energy	X_{max}	Y_{max}	X_{max}	Y_{max}
1020MeV	47mm	4.0mm	10.3mm	4.1mm
1044MeV	3.2mm	4.7mm	4.2mm	4.5mm
1067MeV	73mm	4.8mm	10.3mm	2.9mm

References

[1] B. Spruck et.al., GSI Annual Report 2004

*Supported also by EU under RII3-CT-2004-506078 and BMBF 06GI146I

128 channel high resolution TDC with integrated DAQ-system*

M. Traxler[1], D. Gil[2], M. Kajetanowicz[3], K. Korcyl[2], M. Palka[2], P. Salabura[2], P. Skott[1], R. Trebacz[2]
[1]EE, GSI, Darmstadt, Germany, [2]Jagiellonian University, Krakow, Poland, [3]Nowoczesna Elektronika, Krakow, Poland

A multi-purpose 128-channel Time to Digital Converter (TDC) electronics based on the HPTDC [1] with on-board DAQ functionality has been developed. The main usage will be the RPC-detector upgrade of the HADES-detector (2600 channels) with a needed time resolution of $< 100ps$ and the required possibility to measure the time of the rising and falling edge of the signal to make a Time-over-Threshold (TOT) measurement for a walk-correction of the RPC-detector. Additionally, it will be used for the Forward-Wall and Pion-Hodoscope upgrades (640 channels). The readout-electronics is on board and the data is transported via 100 MBit Ethernet and Internet-Protocol.

The Time to Digital Conversion of the 128 channels is done in 4 HPTDC chips (as shown in Fig. 1). The

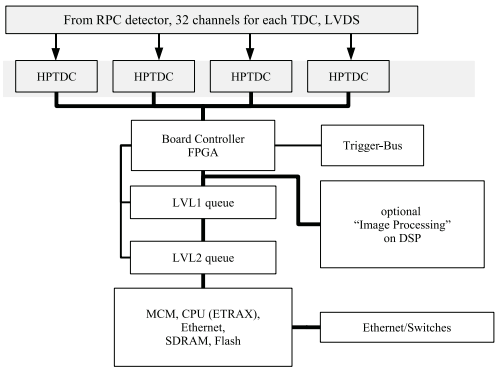


Figure 1: TDC Readout Board block diagram.

TDC-Readout-Board (TRB) has 4 input connectors (80-pins, high density), where each has 31 LVDS timing input signals and several I/O-signals for general purpose. The 32nd channel of each HPTC is connected to an external reference timing signal (LVDS). The HPTDC ASICs are highly configurable [1] and allow to choose the TDC bin-width in the range of $780ps$ and $25ps$ (at $25ps$ one only has $1/4$ of the channels available), detect rising and falling edge of the timing-signal and allow to define a matching-window, so that delay cables are not necessary anymore. An external trigger signal starts the selection of data in the HPTDCs and the board-controller FPGA initiates the readout. This data is then first stored in a FIFO (128 kB) where it is waiting for an external LVL2 trigger decision, which decides if the data can be discarded or has to be transported to mass storage (the LVL2 trigger is needed for the HADES DAQ but optional). If the trigger was positive, the data is stored in a second memory (128 kB) and then readout by a single chip computer (ETRAX [2]) with linux running on it. Then the data is formatted and transported via UDP over 100MBit Ethernet to the event-builder, which collects and orders the data from many different sources. The UDP transport performance of the ETRAX has been measured to be 4 MB/s [3]. Having the DAQ-system with a full featured computer so close to the FEE allows the implementation of the slow-control on the TRB (EPICS), e.g. for setting the thresholds of the attached FEE. The TRB uses a 48V galvanic isolated power-supply which simplifies power-distribution, prevents ground-loops and allows to mount the TRB directly on the detector. The time resolution between two reference channels (different HPTDCs) resulted ($100ps$ bining) in $\sigma = 40ps$, as expected from the known HPTDC performance. Great care has been taken for the layout of the PCB to assure impedance matched and decoupled transmission lines of the LVDS-timing signals, which is rewarded in a crosstalk influence to the resolution of less than $20ps$ (preliminary result, still under test).

In November 2005 a full system RPC-beam-test was performed, which included the full electronics chain with detector, FEE, TRB and beam in the HADES-cave. An integral time resolution of $\sigma = 80ps$ has been reached, without any corrections (Fig. 2, for details see [4]). The TRB (without any speed optimizations) was fully integrated into the HADES-DAQ system and running stably with up to 80 kHz LVL1 (for small events) and 2 kHz LVL2 rate, which corresponds to 1.2 MB/s with the given occupancy.

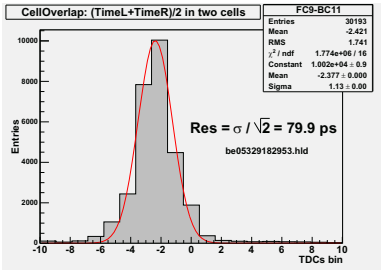


Figure 2: Time resolution of full electronics chain.

References

[1] HPTDC, J. Christiansen, Digital Microelec. Group, CERN
[2] ETRAX, AXIS Communications, Sweden
[3] R. Trebacz, Single-Chip-Linux-Computer for the HADES-experiment Data-Acquisition, GSI Summer Student Programm 2004
[4] J.S. Lange, Status of the HADES RPC Project, GSI Scientific Report, 2006

* Work supported by EU FP6 grant, contract number 515876 and EU FP6 grant RII3-CT-2004-506078 (JRA1)

Status of the ALICE Time Projection Chamber

G. Augustinski, P. Braun-Munzinger, U. Frankenfeld, J. Hehner, C. Garabatos, H.R. Schmidt, S. Schwab, H. Stelzer, D. Vranic, J. Wiechula, GSI, Darmstadt, Germany
R. Renfordt, IKF, University of Frankfurt, Germany
I. Kraus, H. Öschler, TU Darmstadt, Germany
M. Pikna, M. Siska, B. Sitar, Comenius University, Bratislava, Slovak Republic
P. Glässel, J. Stachel, B. Windelband, PI, University of Heidelberg, Germany
J. Bächler, CERN, Geneva, Switzerland

The TPC is the central detector of the CERN-LHC experiment ALICE. The LHC is scheduled to commence operation in 2007; the first heavy-ion collisions are foreseen in fall 2007. In a central Pb-Pb event up to 20000 charged particles are expected in the TPC acceptance. The simultaneous detection of densely phase-space packed tracks puts high constraints on the mechanical tolerances of the TPC.
In 2005, an important milestone has been reached: all of the 72 readout chambers [1, 2], built at both at GSI, Heidelberg and Bratislava, were installed into the TPC field cage. The mounting procedure itself is highly delicate due to the requirement of minimized dead zones. This implies that the chambers in the final mounting step have to be retracted from the inside of the field cage against the end plate (the mechanical structure holding all chambers). This requires the manipulation of heavy-weight chambers (> 50kg) with a precision of tens of microns with large lever arms.
The tool, designed and optimized for this purpose is shown in Fig. 1. This manipulation tools is an adapted version of a device previously employed by the ALEPH-collaboration. Intricate mechanics allows movements in all six degrees of freedom of rotation and translation.



Figure 1: Mounting tool to insert the readout chambers into the TPC field cage

To allow access to all 36 chamber positions, the tool was mounted on rails on a hydraulic platform, which was used consecutively at the two sides of the TPC.
To achieve the required flatness (300 μm) of the entire readout plane over the full surface (~17 m^2) the positions of the chambers have been surveyed by means of photogrammetry and accordingly corrected to the desired position.
Besides the mechanical tolerances of the TPC the temperature homogeneity and stability plays an essential role for the overall performance of the TPC [3, 4]. To monitor the temperature profile of the sensitive volume of the TPC about 500 Pt-1000 temperature probes were mounted. The sensors were installed both on the field cage outer hull and onto the readout chamber bodies close to the readout electronics. To achieve a resolution below the required temperature uniformity of 0.1 K all sensors have been calibrated to a precision of 50 μK at the operating temperature.

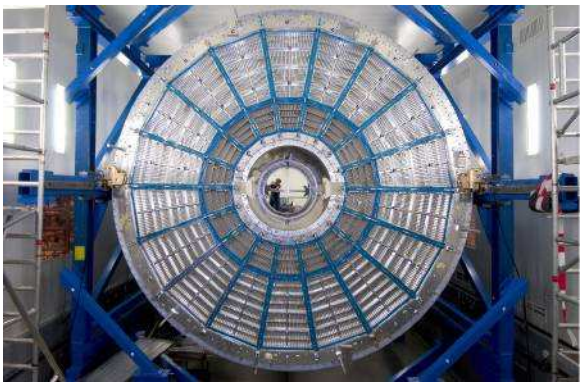


Figure 2: Front view of the TPC with all readout chambers installed

References

[1] U. Frankenfeld et al., "The ALICE TPC Readout Chamber: From prototypes to Series Production", ALICE-INT-2003-017.
[2] H. Stelzer et al.; "The ALICE TPC Inner Readout Chamber: Results of Beam and Laser Tests", ALICE-INT-2002-030.
[3] U.Frankenfeld, S.Popescu, H.R.Schmidt, "Temperature Monitoring System for the ALICE TPC", ALICE-EN-2005-001.
[4] U.Frankenfeld, S.Popescu, H.R.Schmidt, "Experimental Evaluation of the ALICE TPC Front-End Electronics Cooling Strategy", ALICE-INT-2005-001.

Alice TRD Manufacturing at GSI, Status of Chamber Production and Testing

S. Altipnar, G. Augustinski, J. Hehner, Ch. J. Schmidt, S. Schwab, A. Steffen, and H. Stelzer,
GSI, Darmstadt, Germany
A. Radu, NIPNE, Bukarest, Rumania

Abstract

The Alice TRD system is comprised of a total of 540 TRD wire chambers in 12 different sizes, 60% of which are scheduled to be produced in a first batch beginning of 2008. The entire production load is distributed among fife institutions, GSI being responsible for the 72 largest modules, measuring up to 1100 x 1226 mm^2. During 2005 TRD production was started at GSI immediately after the Alice TPC production was completed. By now, production and testing procedures have been established for Alice TRD so that chamber output is about to pick up speed towards the final two chambers per week production rate projected for GSI.

TRD Chamber Manufacturing

A complete line of production was set up at the GSI detector laboratory: Chambers are assembled from pre-fabricated parts like chamber side walls, various spacer ledges, the radiator assembly, pad plane pcbs and a honeycomb backpanel. For each chamber, two wire planes, a



Figure 1: Wire plane assembly line at GSI.

cathode as well as an anode wire plane are first prepared on a dedicated wire winding machine developed at GSI. They are then allocated and glued precisely ($\delta \sim 10\mu m$) onto the pre-fabricated chamber.

Chamber Testing

Alice TRD detector modules are designed as non serviceable, completely glue-sealed MWPC. During production, each chamber is tested extensively twice: Just prior to final sealing, operating potentials are applied and the chamber is inspected for potential dark currents. Dark currents, if present, can mostly be attributed to pieces of lint or dust present in the chamber. In this first test, they can be localized to an area of about 10 cm^2 and removed before finally sealing the chamber. Likewise, in this first test, gain uniformity is determined, using a mobile X-ray source or, alternatively, an ^{55}Fe radioactive X-ray source. The measurements are then employed as a guideline for corrective actions on these large wire chambers, which allow to meet the specified corridor of +- 15% on spatial gain variation across the chamber. An additional scan of very fine granularity is also performed across the chamber, perpendicular to all the wires. Very localized signal variations of 5% or more in this case give an indication to non-connected individual wires, a fault that can be corrected at this stage.



Figure 2: ALICE TRD chamber at the GSI detector lab.

Once neither leakage currents nor disconnected wires are detectable, the chamber can finally be sealed with glue. It is then again subjected to a final extensive testing procedure that serves as quality control prior to shipment.
Here, gain uniformity as well as gain as a function of Anode voltage are determined for documentation purposes. Likewise, chamber gas tightness is measured through the determination of Oxygen contamination in the counting gas. Leaks detected at this stage are sealed with glue until the integral leak rate below 1 mbar l/h is attained. Finally, each chamber is continuously operated for at least 12 hours taking pulse height spectra of 55Fe X-rays. Chambers are then finally declared “ready for shipping”.

Chamber Production Status

The chamber production status at the end of 2005 is depicted in table 1.

Chamber Type	L4C1	L5C1
Ready for shipment	6	8
Assembled, non tested	1	14
In assembly	8	3

Table 1

References

Alice TRD Technical Design Report, CERN/LHCC 2001-021 (Oct. 2001)

Mass production of the ALICE TRD chambers at IKF Frankfurt *

M. Hartig, W. Amend, H. Appelshäuser, C. Blume, H. Hinke, M. Kliemant,
F. Kramer, M. Kessenbrock, W. Sommer
J.W. Goethe University Frankfurt/Main, Germany

ALICE is a general-purpose heavy-ion experiment designed to study the physics of strongly interacting matter and the quark–gluon plasma in nucleus–nucleus collisions at the new Large–Hadron–Collider (LHC) at CERN [1]. One of its major detector components is the Transition Radiation Detector (TRD). It consists of 540 readout chambers. Each chamber has a 4.8 cm thick radiator, attached to it a gas chamber with a 3 cm long drift region and a 0.7 cm amplification gap. The induced charge is read out at the back via copper pads [2]. The mass production of these chambers has started in 2005. It is a joint project between JINR Dubna, GSI Darmstadt, NIPNE Bucharest, IKP Münster, University of Heidelberg and IKF Frankfurt.

From January till September 2005, a new laboratory for the assembly of the TRD chambers was equipped at the IKF Frankfurt. Motivated by the three major steps of the chamber construction, the laboratory was divided in three different rooms namely a room for the preparation and gluing of the chamber frames, a room for wiring the chambers and a room for the final assembly.

In the first room the radiators are mounted in the chamber frame and the pad planes are glued on the inner back side of the chamber.

The major component of the second room is the winding machine, as it is shown in figure 1. It was developed by the GSI detector laboratory and is used to wind the wires with a well defined wire tension and wire spacing on an aluminum frame. This frame is used in the next production step to glue the wires into the chambers in a reproducible way. As the wiring has to be done in a clean environment the room is equipped with a local air filter system.

Finally, the two parts of a chamber are put together and the back panel is glued on the frame with the radiator and the wires. All steps of construction go along with a thoroughly quality assurance.

Furthermore, another laboratory was established to check the quality of the chambers, before they are installed in one of the 18 TRD super modules. Figure 2 shows the setup, which was developed at GSI with financial support from the " Stern-Gerlach-Zentrum für Experimentelle Physikalische Forschung ". The test setup consists of a movable xy-table to scan the surface of the chamber with an X-ray tube and a ^{109}Cd-source. The aim of these tests is to measure the relative gain over the whole chamber area and to determine the absolute gas gain. The maximum tolerance for the gain uniformity is $\pm$ 15 %. The design value for the gas gain is $5 \cdot 10^3$ at the nominal high voltage setting.

The schedule for 2006 is to build a total of 50 chambers at the IKF in Frankfurt.

* Work supported by BMBF Verbundforschung, GSI–F&E and Stern-Gerlach-Zentrum für Experimentelle Physikalische Forschung

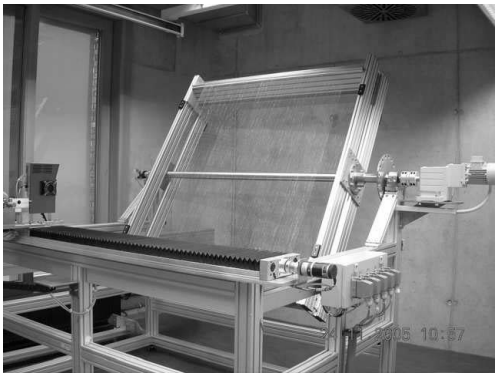


Figure 1: Winding machine



Figure 2: Test setup

References

[1] ALICE Physics Performance Report, J. Phys. G: Nucl. Part. Phys. 30 (2005), 1517-1763

[2] ALICE TRD, Technical Design Report, CERN/LHCC 2001-021

Surface electrical conductivity of cured Araldite 2011 Epoxy, a study initiated during Alice TRD production

Ch. J. Schmidt and H. Risch, GSI, Darmstadt, Germany

Abstract

Leakage currents, occurring systematically in newly assembled Alice TRD chambers in various production sites all over Europe, could be attributed to an uncontrolled surface conductivity of the Araldite epoxy compound 2011 (AW106/HV953U) employed. These unexpected occurrences triggered systematic investigations correlating the compound´s resulting surface conductivity with environmental conditions during the curing process. Directed by previous experiences, the atmospheric humidity was quickly identified as the culprit, that would compromise the expoxy´s resulting electrical surface properties during the curing process. Based upon these investigations, a practical procedure could be set up for production that will guarantee adequate surface resistivity for the proper, reliable operation of the Alice TRD chambers.

Araldite 2011 surface resistivity and ambient humidity

Practical experience had shown in the past that excessive ambient atmospheric humidity during compound curing of Araldite 2011 and other epoxy systems like Araldite AY103-1/HY991 or AW116/HV953U will result in "sticky" surfaces showing unreliable, finite surface conductivity, which does not cease even during months of waiting. The occurrence of very steady leakage currents in finally assembled Alice TRD chambers thus triggered a systematic study of the dependence of resulting surface resistivity upon the exposure to a humid atmosphere during curing. In view of the chamber production process, the allowable period of exposure to the atmosphere that would yield adequate surface resistivity was to be determined for this and an alternative epoxy system.

To this end, a series of samples were prepared under identical conditions and exposed to the environmental atmosphere for a certain amount of time prior to immersion in dry nitrogen. After curing the samples at least 18 hours, surface conductivity was determined according to DIN 53482, employing Hewlet Packard HP 4339A with HP 16008B and applying an electrical field along the surface very similar to the field strengths encountered for the Alice TRD-chamber insulating surfaces.

It is found that terminal surface resistivity dropped rapidly upon exposure to an atmosphere of 34% rel. humidity an 20° C during curing. Yet after exposure of only 10 min to humid air and successive curing in dry Nitrogen, surface resisitivity degraded by six orders of magnitude from a best value 10^{17} Ohm/square to an unacceptable level between 10^{10} to 10^{11} Ohm/square. This behaviour was observed for Araldite AW106/HV953U as well as for alternative epoxy systems such as AW116/HV953U and AY103-1/HY991, allowing less than 5 min handling time in practical environments if surface resistivity was not to be compromised.

Interestingly, samples that were sealed in a small volume of dry Nitrogen after exposure all resulted bad, leading to the conclusion that some component (supposedly the hardener which does smell) fractionally evaporates from and condenses onto the curing epoxy surface, likewise compromising the electrical properties. Only when ventilated in a weak flow of dry Nitrogen could good surface properties be achieved at all.

Surface Cleaning

The indication for conductive residues on the surfaces impairing electrical performance initiated an investigation concerning the feasibility of cleaning relevant surfaces as a means to insure adequate surface resistivity. Isopropanol as well as Ethanol p.a. were employed as cleaning agents. Two sets of fife samples were prepared simultaneously and cured in ambient atmosphere to result with a surface resistivity of 3 10^{11} Ohms/square. Cleaning these samples with Ethanol resulted in an average surface resistivity of (3.7 +- 1.4) 10^{15} Ohms/square, about an order of magnitude higher than the results achieved with Isopropanol. Acetone was not investigated as it is considered critical for ageing properties in particle detectors.

Conclusion

Presence of a humid atmosphere during the curing period drastically impairs the insulating properties of surfaces for the epoxy systems Araldite AW106/HV953U, AW116/HV953U as well as AY103-1/HY991.To inhibit these effects, handling time in humid atmosphere must be limited to well below 5min, a very impractical limit for Alice TRD chamber production. Adequate surface insulating properties can be re-established through cleaning with Ethanol after curing.

A combined procedure is employed for Alice TRD production: rapid application of glue with immediate immersion of the surfaces in a flow of dry Nitrogen (flushing the closed chamber), together with an Ethanol cleaning step after the epoxy has cured.

The ALICE HLT Read-Out Receiver Card

T.Alt, Kirchhoff Institut for Physics, Heidelberg, Germany
V.Lindenstruth, Kirchhoff Institut for Physics, Heidelberg, Germany

Abstract

The High-Level Trigger Readout Receiver Card (H-RORC) is an FPGA based PCI card located inside the Front End processors of the ALICE High-Level Trigger computing farm. The main fields of application are to transfer raw detector data into the main memory of the HLT framework and to process the data online inside the FPGA. The card was designed not only to match the requirements of the ALICE experiment but to provide an inexpensive and flexible multi-purpose solution. However about 200 cards will be produced for ALICE this year.



Figure 1: Picture of the H-RORC (top)

Fields of application

Receiving detector data

The frond end electronics of the ALICE TPC detector will send raw data over optical links with a maximum data rate of 153MByte/s per link. Two optical links can be connected to the H-RORC via CMC connectors. A DMA capable PCI design will transfer the data directly into the main memory of the computing farm. Benchmarks have shown that data rates > 380MByte/s can be achieved.

Pre-Process raw data : Cluster Finder

With the possibilities of a modern FPGA not only data can be transferred but also processed. With 42.000 logic cells, 64 digital signal processing units and 2 Mbit fast, internal dual-port memory the Virtex4 LX40 allows massive parallel processing.. For the HLT, a fast cluster finder algorithm has been developed. The centre of gravity of a particle's charge distribution in the TPC can be computed "on the fly" while the data is transferred from the optical links to the PCI interface.

Single board computer

The infrastructure of the card incorporates everything needed for a single board computer including volatile and non-volatile memory, a serial and a fast Ethernet interface. Free and commercial softcore processors are available for the Virtex4.

Functional Overview

Key Features

- Xilinx Virtex4 LX40FF1148-11
- PCI 64/66 and PCI-X 64/133(optional) interface
- Up to 4 independent modules of DDR400 SDRAM with up to 1Gbit/module
- 256 User I/Os grouped in 2 CMC-J11/J12
- 2 4-bit bidirectional fast LVDS links : TAGNET
- Fast Ethernet with RJ-45 10/100
- RS232 serial interface
- 2 Flash memories with up to 64MBit/device
- Xilinx XC95144XL CPLD for configuration
- Optional Xilinx Platform Prom
- 2 Oscillators : 100MHz System, 1 User selectable
- Linux capable

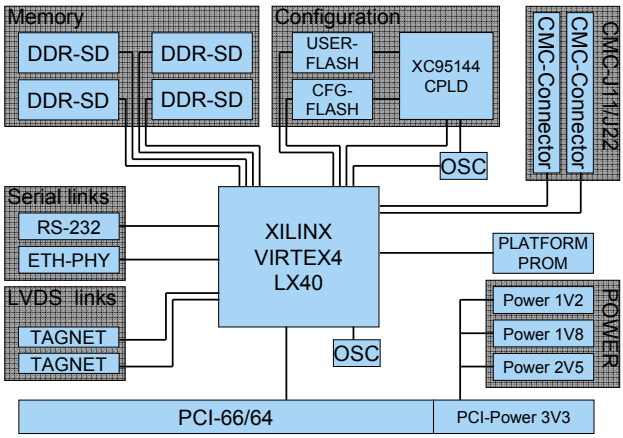


Figure 2: H-RORC functional overview

Secure Remote Update:

In order to update the card remotely the firmware can be stored in the CFG-Flash via PCI. The CPLD will automatically detect the new firmware, load it into the FPGA and start a watchdog which can only be disabled by a user command. If not disabled it will time out, assume that an error has occurred and will reload a safe default configuration.

Summary

The H-RORC was designed carefully to match the requirements of high-speed digital design. All critical parts were simulated and tested successfully. In October 2005 it passed CERN's Production Readiness Review.

The Readout Boards for the ALICE TRD

I. Rusanov, J. Stachel
Physikalisches Institut, University of Heidelberg

One of the major components of the ALICE TRD front-end electronics is a readout board (ROB). General requirements of the ROB can be found in [1]. This is a 6-layer board, which connects multichip modules. The MCM module carries a PASA and an ADC/Digital chip (TRAP). The ROBs have the essential functions: amplifying and shaping, digitizing and sending of DATA. The ALCE TRD detector needs 4104 ROBs (228 readout boards per Super Module). Each Super Module consists of 6 chambers with 6 readout boards (36 ROBs) and 24 chambers 8 readout boards (192 ROBs). Some additional functions are implemented on the readout boards, which include "half chamber mergers" (two per chamber) and the board of the "Detector Control System" (one per chamber). Therefore, in order to minimize the number of different readout boards, the chambers will hold boards with the same board outline and a fixed (the same) position of the MCM modules. Each readout board includes all traces that the electronics system needs for the transfer of DATA, CLK, Pre-trigger/Trigger, Slow control and Shutdown signals from/to and trough the board. Therefore 7 different types of ROBs (Fig. 1) were designed and produced.

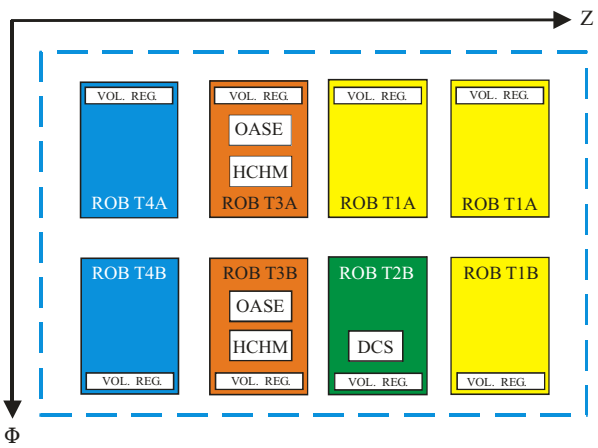


Fig.1. The ALICE TRD Chamber with 8 ROBs. DCS – board of detector control system, HCHM – half chamber merger, OASE – boar for optical link.

Voltage regulators. For the ALICE TRD one of the essential challenges is power dissipation. In this context, to avoid the high voltage drop on the voltage regulators of 1.8 V (TRAP and ADC's), on the ROBs ultra low dropout voltage regulators are used. The devices operate with two input voltages (Vbias and Vin). To provide Vbias = 5 V on each ROB a charge pump is used, which converts 3.3 V to 5.0 V. To have more effective filtering on of the charge-pump's output voltage a "C-C-R-C-C" filter is used. The bandwidth of the filter is from 0 Hz to 10 kHz, which is far from the first harmonic of the charge-pump's output signal. With these changes the "stand alone" readout board with all FEE chips contributes to the detector noise 500 electrons (0.5 LSB).

Slow control network within one TRD chamber. On each TRD chamber there is one DCS board, which can drives 4 slow control links. The DCS board is mounted on the ROB type 2B. Each SCSN link, to which two readout boards in Φ belong, includes two slow control rings.

DATA, CLK, Trigger and reset distribution. Within each TRD chamber the transfer of the signals is "point-to-point" type. The routing of the CLK, Trigger and Reset signals is done in the following way: from DCS board to the "half chamber mergers", located on ROBs type3A/3B, and trough the readout tree to each MCM module.

Shutdown links. The source of the shutdown signals is the DCS board. Always two ROBs in Φ belong to one SD link. The ALICE TRD readout board has 3 groups of voltage regulators. Therefore each shutdown link includes 6 signal lines – 3 per board. The distribution of the shutdown signals follows of slow control signals. To minimize the current flow between the DCS board and ROBs the shutdown logic scheme was changed. Each ROB has only 3 SD inputs, which decreases the current flow by a factor of 4.

Prototypes of all readout board types are produced and one TRD chamber has been fully equipped. This was used for the improvement of grounding scheme. The measured noise of the system "TRD chamber and Readout boards" is 1.3 LSB (1300 electrons).

References:

[1] ALICE TRD Technical Design Report, CERN/LHCC 2001-021, October.

FPGAs – Reconfiguration for Radiation Tolerance

G. Tröger*, U. Kebschull*, V. Lindenstruth*
J. Alme#, K.Røed#, D. Röhrich#, R. Campagnolo‡, L. Musa‡

* Kirchhoff-Institut für Physik, Heidelberg, Germany
# Institutt for fysikk og teknologi, Universitetet i Bergen, Norway
‡ CERN, Genève, Switzerland

Introduction

A major concern with any kind of detector electronics is their exposure to the irradiation environment. For ASICs, radiation-hardness can be taken into account during their design. But while radiation-hard FPGA technology exists, the most common types of FPGAs used today are SRAM-based. The reasons for this can be easily identified as costs and complexity.

The problem with SRAM-based FPGAs is that, in addition to the issues known from ASICs, their configuration itself is highly sensitive to single event upsets (SEUs) induced by ionizing particles. These upsets have been identified as the main cause for functional errors of these devices, and therefore need to be addressed in detector electronics systems.

ALICE TPC

In 2003/2004, the first prototypes for the Readout Control Unit (RCU) board of the ALICE [1] Time Projection Chamber (TPC) were designed and the planned components tested for their radiation tolerance. Simulations show the radiation environment for the RCU will be up to 800 hadrons/cm² sec with a distribution peak at 100-200 MeV. The irradiation results for the Altera APEX20K400E FPGA, originally intended to be used on the RCU board, were at the limit of what could accepted.

Subsequent testing of a replacement candidate, a Xilinx Virtex-II Pro XC2VP7, gave cross-section results in the same order of magnitude (see Table 1 on the right; beam tests were performed at the cyclotrons of the Oslo University and The Svedberg Laboratory, Uppsala). However, the Virtex offers the possibility of active partial reconfiguration, which can be used to mitigate the effects of single event upsets as explained below.

Active partial reconfiguration allows reading and modifying the configuration of the device without interrupting its operation. For this, the configuration bits are organized in columns of individually addressable data frames. By continuously monitoring and repairing the contents of the configuration memory, one can repair errors caused by SEUs in-situ without fully resetting the system. The monitoring part is optional, as one could just blindly overwrite the configuration all the time, but it allows checking for the occurrence of errors and tagging of data processed at that time as possibly corrupted.

A test setup using this technique was subjected to further irradiation testing. Results show that it can be expected to reduce the influence of SEUs on the operation of the RCU to a negligible level.

Radiation-Tolerance Setup

The task of scrubbing the configuration of the main FPGA has to be performed by a radiation-hardened controller. For the RCU, an Actel ProASIC+ APA075 was chosen. It is a small flash-based FPGA which is not sensitive to configuration upsets in the ALICE TPC irradiation environment.

A new RCU board has been developed, using the XC2VP7 and the APA075. The complete radiation-tolerance setup for the new RCU is illustrated in Fig. 1. The flash memory connected to the Actel contains the correct configuration data for the main FPGA.

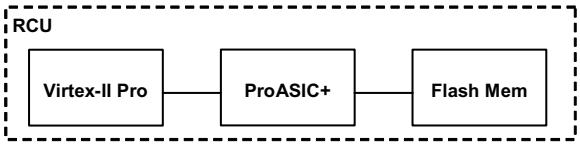


Figure 1: Radiation-Tolerance setup on the new RCU

Summary and Outlook

With the results of the beam tests, the RCU has been redesigned to achieve higher radiation tolerance based on the active partial reconfiguration technique. The new board is shown in Fig. 2. Preliminary irradiation tests of the full system show promising results, and the scheme has already been incorporated in other boards in ALICE.

References

[1] ALICE – A Large Ion Collider Experiment at CERN LHC, see http://aliceinfo.cern.ch/

	26 MeV p+	180 MeV p+
APEX20K400E	$3.3\times10^{-9}\pm1.9\times10^{-9}$	$6.0\times10^{-9}\pm1.1\times10^{-9}$
XC2VP7	$9.4\times10^{-9}\pm5.5\times10^{-9}$	$2.8\times10^{-9}\pm1.3\times10^{-9}$

Table 1: SEFI cross-section in [cm²] vs. energy for the Altera APEX02K400E and Xilinx XC2VP7

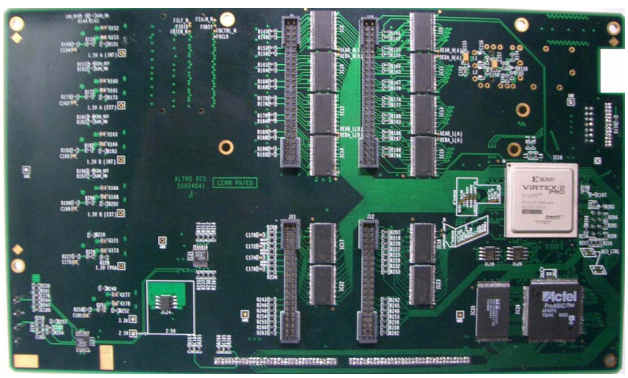


Figure 2: The new ALICE TPC RCU board

Optical Readout Interface for the ALICE TRD

V. Lindenstruth, V. Angelov, F. Rettig, P. Popov
Kirchhoff Institut für Physik, Ruprecht-Karls-Universität Heidelberg, Germany.

Abstract

A module with 240 Mbytes/s parallel LVDS input and 2.5 Gbit/s optical output was developed for ALICE TRD.

Introduction

The ALICE TRD Detector employs 1080 optical links for the data readout. The FEE chips (TRAP [1]) form a readout tree running at 8 bit 120 MHz double data rate. The Optical Readout Interface (ORI) performs LVDS to LVCMOS level translation, double to single data rate (DDR to SDR) conversion, data resynchronization, serialization and optical transmission at 2.5 Gbit/s.

Architecture

The module is built using commercially available components. Texas Instruments TLK2501 is used as serializer, Linear Technology LTC5100 as optical driver for a VCSEL diode at 850nm from ULM. The interface between TRAP output and TLK input is implemented using a Lattice CPLD ispMACH 4k. A CPLD is sufficient for the interface logic and is favoured over a FPGA because of better radiation tolerance and no configuration memory is needed. The application of a freely configurable CPLD makes this low-cost device adoptable to a large range of driving signal standards.

The TRAP chip drives 10 data lines - 8 data bits, a parity and a spare bit - along with a strobe signal. The positions of the parity/spare bits within the 10 data lines are freely programmable. This feature is implemented in the CPLD design as well. The TRAP provides the data with each edge of the strobe signal. When no data are sent, the strobe remains high.

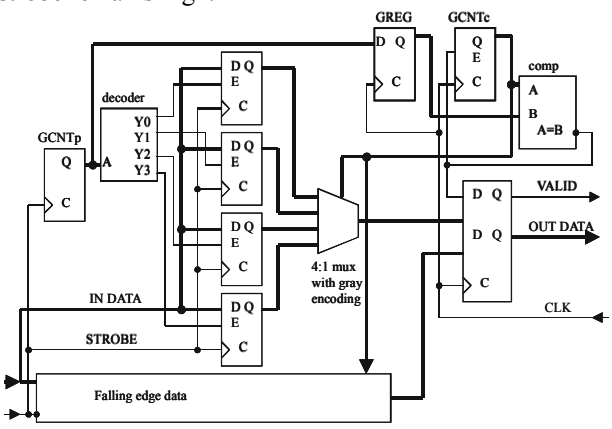


Fig. 1: Block diagram of the DDR to SDR conversion and resynchronization in the CPLD

A circuit similar to that in the TRAP chip implements the DDR to SDR conversion and the resynchronization (see Fig. 1) in the CPLD. There are four input registers for each edge (pos/neg) of the strobe signal. A grey counter GCNTp, triggered by the corresponding strobe edge, controls the write enables to the data registers. GCNTp is copied to a register GREG in the output clock domain. If any difference is detected between the GREG and GCNTc, the data valid is set and the gray counter GCNTc is enabled for one clock. The output data and the valid flag are synchronized again with the output clock and are fed to the serializer inputs.

The clock resynchronization is necessary, because the serializers normally require a very high clock quality, which is hardly to achieve with the clock distribution on the readout board. The proposed resynchronization technique has the lowest possible latency and size.

The board has JTAG and I²C interfaces. The JTAG interface permits later reprogramming of the CPLD within the detector. It is also used to build a custom serial interface to some configuration registers in the CPLD design and to read the parity counters. The I²C interface is used to program and control the laser driver chip.

Test setup and results

The current test setup consists of a TRAP chip delivering data to the ORI board, which drives the serial data into a 60m long fiber optic cable. The receiver system is implemented based on the TLK2501 as deserializer. Its output data are captured by a FPGA-PCI card and can be read out by test software.



Fig. 2: Photo of the ORI on the readout board

This test software generates four 16-bit random numbers, which serve as seeds for pseudo-random generators running on the four TRAP CPUs. These generators fill the TRAP data packets, which are then sent over the optical link. After the serial transmission of the data is completed, the captured data are read out by the test software and checked with the correct values. No errors were found up to now after more than 200 GBytes of data were sent and checked. Outgoing tests are for radiation tolerance of the ORI board. The board is ready for production. A photo of the board is shown on Fig. 2.

References

[1] GSI Scientific Report 2004, p. 353

Electronics Integration for the ALICE TRD

C. Lippmann*, GSI, Darmstadt, Germany
K. Oyama and I. Rusanov, Physikalisches Institut, Universität Heidelberg

In the year 2005 the first efforts to integrate the readout electronics on the ALICE TRD [1] detectors have started. These electronics utilize two custom chips: an 18 channel analog preamplifier and shaper (PASA) and a mixed-signal chip, performing 10 bit analog-todigital conversion, event buffering and local tracking (TRAP). Both chips together are packaged as a multi chip module (MCM).The first integration tests and noise measurements have been carried out on a detector which is situated at the Kirchhoff Institut für Physik, Universität Heidelberg. The integration of 30 detectors and readout electronics (almost 4.000 MCMs) into the first supermodule will start there in early 2006.

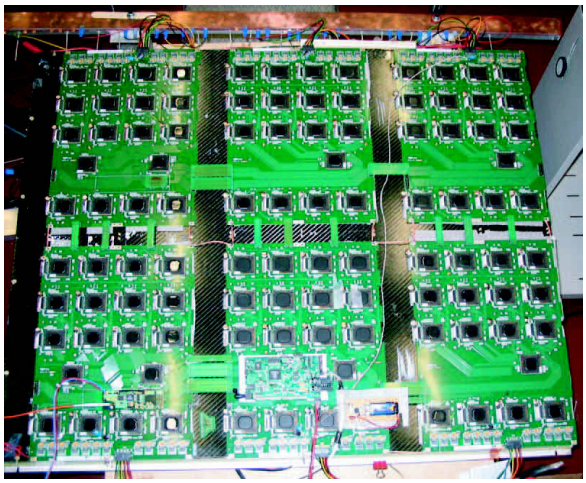


Figure 1: TRD chamber with final readout electronics.

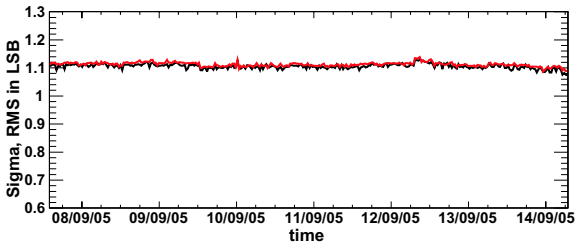


Figure 2: Noise results (average sigma and r.m.s. on one readout board) as a function of time over six days.

A TRD readout chamber (Type L1C0) equipped with six readout boards of the final version is shown in Fig. 1. Of the seven different existing types of TRD readout boards (1A, 1B, 2B, 3A, 3B, 4A and 4B) that can be integrated on all of the ALICE TRD detectors of the 12 different sizes (L0C0, ...,L5C0, L0C1, ..., L5C1) five (all except the type 4 boards) can be seen on Fig. 1. The slow control, pretrigger, clock and data signal lines are distributed from board to board via short cable boards. The 2B board (in the lower center) carries a DCS (detector control system) board which combines hard- and software to control the functionality of the detector (controlling, monitoring). The data path begins at the MCMs, and ends with the data shipment via the readout tree to the Global Tracking Unit (GTU) and the optical detector links (DDL) to the High Level Trigger (HLT) and the data aquisition. The 3B board (in the lower left) carries a special board which has the task of converting the data to optical signals and sending them to the readout tree.

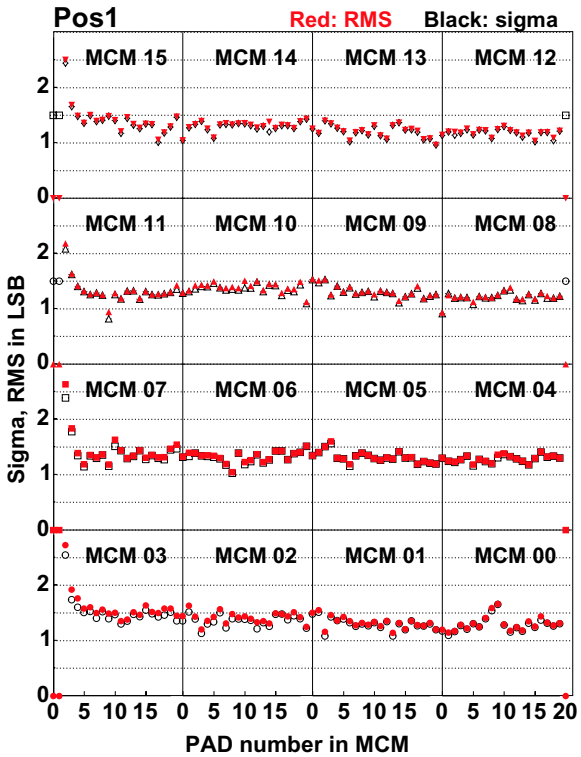


Figure 3: Noise results (sigma and r.m.s.) on all channels (16 MCMs) of one readout board.

Fig. 2 shows the average noise performance (on-chamber) on one of the six readout board mounted on the TRD detector measured continuously over about a week. The performance is very stable. The distribution of the noise on the different channels of a different readout board is shown in Fig. 3. We find an overall performance around 1.3 LSB, which is close to the aimed at value of 1 LSB. A systematic increase towards the chamber border (to the left) is clearly visible. This can partly be explained by an increase of capacity in this region.

References

[1] ALICE Transition Radiation Detector Technical Design Report, ALICE TDR 9, CERN/LHCC 2001-021.

* C.Lippmann@gsi.de

Grid Activities at GSI*

P. Malzacher, A. Manafov, R. Manteufel, V. Penso, C. Preuss, K. Schwarz

Abstract

This article describes the summarised work of the GSI Grid Group with the aim to set up an ALICE tier2 centre within the global environment of the LHC Computing Grid LCG [1].

ALICE tier2 centre

To fulfill the storage requirements of an ALICE tier2 centre new fileservers have been bought with altogether 12 TB of disk space. The fileservers have been installed with dCache [2] and interfaced via SRM (Storage Resource Manager) to LCG. An SRM is the agreed Grid interface to storage resources (disk or tape) with a standard set of required functionality. One fileserver has been installed with xrootd [3] to serve as an AliEn Storage Element for ALICE Data Challenges.

PROOF

The login script for setting up an individual PROOF environment [4] has been redeveloped in Python and extended by a GUI. By authenticating via Grid certificates first extensions of GSI based PROOF Clusters to GridKa using Globus methods and a self developed TCP router, succeeded. Similar tests have been done with LCG, too. Facilitating the xrootd installation mentioned above file access reliability is being measured and compared with NFS. On the experience gained at GSI a PROOF course has been given during the GridKa School 2005 [5].

The EGEE project

The EGEE project will come to its end, soon, and EGEE II will start in April 2006. GSI will continue participating, being a primary partner for regional certification of new middleware releases as well as user training in the Swiss/German Federation (DECH). The EGEE based middleware gLite [6] came to version 1.5 and will be merged with the current production software LCG 2.7 to gLite 3.0 at the beginning of this year. A gLite testbed is maintained within the DECH VO (Virtual Organisation).

The integration of the current LCG software into the GSI Debian environment has been successfully completed. Additionally the LCG Grid services have been extended by a Resource Broker (RB), which assigns Grid jobs to connected sites according to job requirements and site capabilities, and a ”Local File Catalogue” (LFC) which provides the physical location of the files stored in the GSI Grid SE’s. Several of the Grid services are installed on virtual XEN [7] machines.

D-Grid

The D-Grid initiative [8], announced March 2004, follows similar programs in the USA and the UK. and shall help to set up a German Grid infrastructure.

At GSI distributed analysis tools under usage of grid resources are being developed within work package 3 of the HEP community Grid. A starting point is the analysis framework ROOT. Making use of a set of abstract classes provided by ROOT (TGrid ...) an interface to gLite is being created to enable Grid access directly from within ROOT. This includes querying the File Catalogue, job submission, getting job status and output. By combining several stand-alone PROOF based analysis facilities using existing Grid Middleware large dynamically generated Grid Analysis Clusters can be created.

The WLCG project

To clarify the difference between the LCG Grid middleware and the LCG project the latter has been renamed in Worldwide LHC Computing Grid (WLCG). One of the large ongoing WLCG activities is Service Challenge 3 (SC3), in which reliable file transfers from CERN to participating tier 1 centres and transfer speed is being tested. The target to write data with a total rate of 150 MB/s to disk and 60 MB/s to tape has been achieved by most sites. A second goal is a long term Grid service stability test. The ALICE experiment has made use of the Grid services provided during SC3 to accomplish Physics Data Challenge ’05 (PDC’05) in which up to now 28000 jobs doing MC simulation, tracking, and reconstruction of Pb+Pb and p+p events have been completed. GSI takes part in PDC’05 since November 2005 having produced so far 4% of the data, mainly on the new batch farm nodes installed with Debian Sarge.

In SC4, starting April 2006, the globally distributed data produced in SC3 will be analysed by using Grid Methods.

References

[1] GSI Annual Report (2002) 212.

[2] http://www.dcache.org/.

[3] http://xrootd.slac.stanford.edu/.

[4] http://wiki.gsi.de/Grid/TheParallelRootFacility

[5] http://gks05.fzk.de/.

[6] http://glite.web.cern.ch/glite/.

[7] http://www.cl.cam.ac.uk/Research/SRG/netos/xen/.

[8] www.d-grid.de.

* Work supported by BMBF, Förderkennzeichen 01AK802G

Research to the Programme in Atomic Physics, Plasma Physics and Materials Research

AP
Atomic Physics with Heavy Ions

- AP-EXP-SPECTROSCOPY : Spectroscopy and Atomic Properties (293p.)
- AP-EXP-COLLISIONS : Atomic Collision Processes (302p.)
- AP-METHODS : Instruments and Methods (310p.)
- AP-THEORY : Theories to Atomic Physics (319p.)

PLPY
Plasma Physics

- PLPY: General (328p.)
- PLPY-EXP : Experimental Plasma Physics (329p.)
- PLPY-METHODS : Instruments and Methods (335p.)
- PLPH-THEORY : Plasma Physics Theories (336p.)

MATERIALS
Materials Research with Heavy Ions (341p.)

PHELIX
Plasma and Single-Particle Research with Laser and Ion Beams (356p.)

Test of Relativistic Time Dilation at the ESR

C. Novotny, G. Huber, S. Karpuk, W. Nörtershäuser, University Mainz, Germany
S. Reinhardt, G. Saathoff, D. Schwalm, A. Wolf, MPI for Nuclear Physics, Heidelberg, Germany
G. Gwinner, Dept. of Physics and Astronomy, University of Manitoba, Winnipeg, Canada
G. Ewald, University Tübingen, Germany
F. Bosch, C. Geppert, H.-J. Kluge, T. Kühl, M. Steck, Th. Stöhlker, GSI Darmstadt, Germany
T.W.Hänsch, R.Holzwarth, T.Udem, M.Zimmermann, MPI of Quantum Optics, Garching, Germany

Lorentz Invariance and Time Dilation

Lorentz invariance is the principle underlying all currently accepted theories describing the fundamental interactions of nature - the quantum field theories of the strong and electroweak forces and general relativity. This is a strong motivation to test the theory of Special Relativity (SR) experimentally with ever higher precision, as any deviation from its predictions would have profound consequences for our understanding of nature. In particular, many unifying theories, such as string theory, allow for violations of Lorentz invariance at some level [1]. While kinematic test theories describe possible violations of the observer Lorentz transformation (e.g. the rest frequency of an atomic transition is assumed to be the same in all inertial frames, while the transformation between the frames is tested), dynamical test theories like the Standard Model Extension [1] deal with possible breakdowns of the particle Lorentz transformation. Time dilation experiments can put unique constrains not only on kinematic test theories but also on Lorentz-violating extensions of the Standard Model [2, 3] not obtainable from other experiments.

Time dilation can be measured via the optical Doppler effect. The first experiment of this kind was performed by Ives and Stilwell (IS) [4], who measured the Doppler-shifted frequencies ν_p and ν_a of the H_β line (ν_0) of a hydrogen beam in parallel and antiparallel direction. In SR, these frequencies are given by the relativistic Doppler-formula $\nu_{p,a} = \gamma_{SR}(1 \pm \beta)\nu_0$, where the Lorentz factor γ_{SR} appears as a direct consequence of time dilation. Kinematic test theories parameterize possible deviations of time dilation from SR by introducing a test parameter α by $\gamma = \gamma_{SR}(1 + \alpha\beta^2 + ...)$. The result of the original IS experiment set an upper bound on α of $\alpha < 1 \times 10^{-2}$ [4].

Preliminary experiments at the TSR

As heavy-ion storage rings are providing ion beams of superb quality at high velocities they allow for Ives-Stilwell type experiments with increased sensitivity. A first time dilation measurement was performed at the storage ring TSR at the Max-Planck-Institut für Kernphysik in Heidelberg in 1990-1994 using metastable $^7Li^+$ ions at a velocity of $\beta = 0.064$ [5]. More recently, an improved experiment was carried out at the TSR using collinear saturation spectroscopy on a closed two-level system in metastable $^7Li^+$. This led to an upper bound of $\alpha < 2.2 \times 10^{-7}$ [6], which could most recently be lowered by another factor of about 2 [7]. Further improvements of this limit, however, will require higher ion velocities as available at the ESR.

Experiments at the ESR

In October 2005 a first test was performed at the ESR. During this beam time metastable $^7Li^+$ ions were extracted from an electron cyclotron resonance (ECR) ion source, accelerated by the heavy ion synchrotron SIS to a velocity of $\beta = 0.34$, and subsequently transferred from the SIS into the ESR. Furthermore, collinear laser spectroscopy with the lithium beam has been performed using a Ti:Sa laser (λ=780nm).

These test measurements showed already, that an improved time dilation experiment is possible at the ESR. In particular, the ion beam's longitudinal relative momentum spread of the $^7Li^+$ ions of $\Delta p/p < 10^{-5}$ is smaller than in the TSR, and due to the high velocity also the lifetime of the metastable $^7Li^+$ ions is higher than in TSR, approaching the natural lifetime of the $^3S_1$ state of 50 s. It turned out, however, that the fraction of metastable $^7Li^+$ ions from the ECR ion source was below 10^{-3}. To enhance the number of metastable ions, it is proposed to change the source material from the used LiF to another Li-compound (e.g. Li_2CO_3), to avoid the quenching of the metastable $^7Li^+$ by the fluoride ions. Corresponding tests of the production efficiency of metastable $^7Li^+$ in an ECR ion source are in progress in Gießen.

We expect that the planned experiment at the ESR will allow us to improve the sensitivity to the time dilation test parameter α by one order of magnitude to the 5×10^{-9} level. Data collection and analysis should also consider cosmological constraints due to the motion of the ions in the sidereal frame.

References

[1] V. A. Kostelecky and S. Samuel, Phys. Rev. D 39 683-685 (1989)
[2] C. D. Lane, Phys. Rev. D 72 016005-(1-9) (2005)
[3] M. E. Tobar, P. Wolf, A. Fowler, and J. C. Hartnett, Phys. Rev. D 71, 025004-(1-15) (2005)
[4] H. E. Ives and G. R. Stilwell, J. Opt. Soc. Am. 28 215-226 (1938)
[5] R. Grieser *et. al.*, Appl. Phys. B 59 127-133 (1994)
[6] G. Saathoff *et al.* , Phys. Rev. Lett. 91 190403-(1-4) (2003)
[7] S. Reinhardt, PhD-thesis, Univ. Heidelberg (2005)

Laser Spectroscopy of Heavy Elements at SHIPTRAP

H. Backe[1], T.Kolb[1], P. Kunz[1], W. Lauth[1], M. Sewtz[3], A. Sharafutdinov[1] and N. Trautmann[2]
[1]Institut für Kernphysik, Universität Mainz, Germany, [2]Institut für Kernchemie, Universität Mainz, Germany, [3]Ludwig-Maximillians-Universität, München, Germany

The aim of this project is the investigation of atomic and nuclear properties of heavy elements with charge numbers Z≥100 by laser spectroscopy. Any atomic spectroscopy, even with the most sensitive laser methods, is seriously hampered by the fact that no information on the atomic structure is available for these elements. To get acquainted with such a spectroscopy experiments were performed for the element fermium (Z = 100) [1]. A first experiment for the elements with Z>100 is being prepared on the element nobelium with the charge number Z = 102. Since the production rate is only in the order of 5 ions/s and the beam projectile isotope ^{48}Ca is very expensive, the experimental method is being developed at the chemical homolog ^{155}Yb which is also α-active with a half-life $t_{1/2}$ = 1.75 s. The reaction products, separated by SHIP, are stopped in a buffer gas cell in which Resonance Ionization Mass Spectroscopy (RIS) is performed with the detection of the ionization process by the α-decay [2].

A large gain factor in the efficiency can be obtained if the 85% fraction of the thermalized ions is transported to a filament from which the ions will be re-evaporated as atoms with the aid of high temperature pulses. This way, a localized atom cloud will be generated and the overlap with the laser beams can also be improved. This idea was pursued in the last year.

The improved experimental setup was tested off-line in two ways. First a mass of about 0.3 mg of the stable element Yb was electrolytically deposited on a tantalum filament. By the evaporation of Yb atoms and their subsequent laser ionization it is possible to simulate thermalized ions from SHIP in the buffer gas. Two dye laser beams, were used for resonance ionization. The first one had a wave length of λ_1 = 398.912 nm, the second of λ_2 = 399.587 nm excited a Rydberg state. By a relative comparison of the collected ion charges the efficiency of the resonance ionization process was determined to be in the order of 10^{-2}. The second testing method makes use of a radioactive ^{223}Ra source. In the decay series ^{211}Pb recoils are produced and the charged fraction is transported in the buffer gas by electrical fields on a catcher electrode. After a suitable activation time in the order of 1 hour the catcher is moved into the buffer gas cell in front of a filament. Thereafter, ^{207}Tl recoils from the α-decay of ^{211}Bi can be employed for the simulation of a particle beam. This setup was used to optimize the extraction potentials, to determine the energy shift of α-decays in the buffer gas and to measure the efficiency of the resonance ionization of ^{207}Tl. For the latter test, ^{207}Tl ions were captured on the catcher filament, re-evaporated at a temperature of about 800°C, laser ionized and extracted to a Passivated Implanted Planar Silicon (PIPS) detector which detects the β-decay of ^{207}Tl. Recoil ^{207}Tl ions, directly transported to the detector, served as a reference to determine the resonance ionization efficiency. In good agreement with the experiments with the above described experiment using stable Yb, these measurements yielded also efficiencies in the order of 10^{-2}.

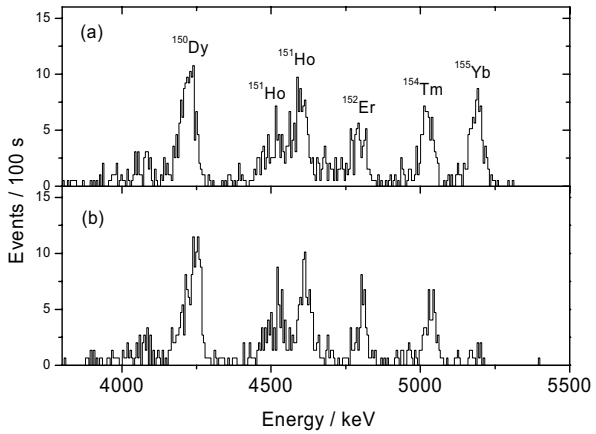


Figure 1: The α-particle spectrum with assignments of the isotopes collected on the filament. (a) at room temperature, (b) after heating up the filament for about one second to 1400 ° C.

An on-line test experiment with the improved setup was performed at the beginning of July, 2005 at the SHIP facility. ^{155}Yb recoil ions were produced by the reaction ^{107}Ag(^{52}Cr,p3n)^{155}Yb at a projectile energy of 4.57 MeV/u. The secondary ^{155}Yb recoil beam was focused into the buffer gas cell. The ions were guided in the electrical field of about 100 V/cm to the Ta-filament catcher. The isotopes on the catcher were identified by the energy of the α particles and their half-lifes. For that purpose, an additional semiconductor detector was moved periodically in front of the catcher in the beam-off periods. The evaporation temperature of the collected Yb ions on the filament was determined by performing measurements with stepwise increased temperatures of the filament for which a decrease of the alpha decay rate of the ^{155}Yb isotope was observed. In figure 1 two measured α spectra are shown, (a) for a cold filament and (b) for a filament heated up to 1400 °C. At the high temperature the α intensity of the ^{155}Yb isotope decreased significantly. Laser spectroscopic measurements at the Yb atoms could not be performed in the running beam time because of a short circuit of one of the electrodes in the cell.

References

[1] M. Sewtz, et. al., Phys. Rev. Lett. **90** (16), 163002-1 (2003)
[2] H. Backe, et. al., Phys. Rev. Lett. **80,** 920 (1998)

Nuclear Charge Radius of Lithium-11*

R. Sánchez,[1] W. Nörtershäuser,[1,2,3] G. Ewald,[1,2] D. Albers,[4] J. Behr,[4] P. Bricault,[4] B. Bushaw,[5] A. Dax,[1] J. Dilling,[4] M. Dombsky,[4] G.W.F. Drake,[6] S. Götte,[1] R. Kirchner,[1] H.-J. Kluge,[1,7] Th. Kühl,[1,3] J. Lassen,[4] C.D.P. Levi,[4] M.R. Pearson,[4] E. Prime,[4] V. Ryjkov,[4] A. Wojtaszek,[1,†] Z.-C. Yan,[8] and C. Zimmermann[2]
[1]GSI, Darmstadt, Germany; [2]Univ. Tübingen, Germany; [3]Univ. Mainz, Germany; [4]TRIUMF, Vancouver BC, Canada; [5]PNNL, Richland, USA; [6]Univ. Windsor, Canada; [7]Univ. Heidelberg, Germany; [8]Univ. New Brunswick, Canada.

The nucleus of the isotope ^{11}Li exhibits a halo structure—a diluted two-neutron component surrounding a ^{9}Li-like core [1]. An important question that has not been firmly established up to now is whether the ^{9}Li core is decoupled from the halo in the sense that is not modified from the free ^{9}Li. This can be determined by observing a change in the nuclear charge radius from ^{9}Li to ^{11}Li. A measurement of the isotope shift in an atomic transition provides model-independent values for the nuclear charge radius. A shift in frequency (the isotope shift) of a spectral resonance is produced by the change in the nuclear mass (mass shift) and the nuclear charge distribution (field shift). In the case of lithium the mass shift is 10^5 times larger than the field shift. Therefore both, high resolution isotope shift measurements and accurate atomic calculations for the mass shift are required to be able to extract nuclear charge radius information with a relative precision of few percents.

Recently this could be accomplished. On the experimental side, an on-line laser and mass spectroscopic technique was developed at GSI [2] to overcome the short half-live and low abundance of the radioactive lithium isotopes. The isotope shift in the $2s\,^2S_{1/2} \rightarrow 3s\,^2S_{1/2}$ Doppler-free two-photon electronic transition of all lithium isotopes could be measured at a 10^{-5} level. The experiments were performed for $^{6-9}$Li at GSI in 2003 [3] and for $^{6-11}$Li at TRIUMF in 2004 [4]. On the theoretical side [5], the quantum mechanical three-electron problem for low Z was solved to high accuracy in the non-relativistic limit and the effects of relativity and QED were included by perturbation theory.

Nuclear charge radii of Li isotopes extracted from the combination of isotope shift measurements and mass shifts calculations are shown in Fig. 1 [4]. The charge radius decreases continuously from ^{6}Li to ^{9}Li and increases from 2.217(35) fm to 2.467(37) fm for ^{11}Li. Different nuclear theoretical predictions are also shown. From those models which were able to predict the ^{11}Li charge radius, the Stochastic Variational Multi-Cluster Model show the best agreement with the experimental result. This model considers light nuclei as composed of smaller clusters namely the α particle, the triton nucleus, and the nucleons p and n. This clustering allows to focus on those degrees of freedom thought to be the most relevant to the physical behavior of a given nucleus. Calculations for ^{11}Li were performed including neutron correlations as well as polarization of the ^{9}Li core by the halo neutrons. If core-excitation is not included, the model predicts a much smaller charge radius, only slightly larger than that of ^{9}Li. Thus, in the frame of this model it is possible to conclude that perturbations of the core are a significant contribution and must be included in order to reproduce the increase to the charge radius of ^{11}Li.

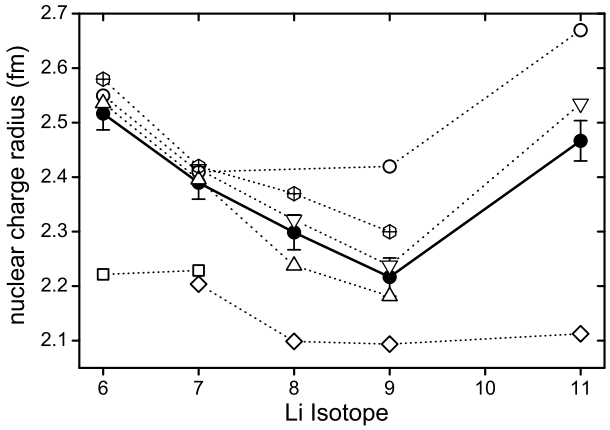


Figure 1: Experimental charge radii of lithium isotopes (•) compared with theoretical predictions: △: Greens-Function Monte Carlo Calculations, ▽: Stochastic Variational Multi-Cluster Model, ⊕: Fermionic Molecular Dynamics, ○: Dynamic Correlation Model, □ and ◇: ab-initio No-Core Shell Model.

References

[1] A. S. Jensen *et al.*, Rev. Mod. Phys. **76**, 215 (2004).
[2] W. Nörtershäuser *et. al.*, NIMB **204**, 644 (2003).
[3] G. Ewald *et al.*, PRL **93**, 113002 (2004).
[4] R. Sánchez *et al.*, PRL **96**, 033002 (2006).
[5] Z.-C. Yan, G. W. F. Drake, PRA **66**, 042504 (2002).

* Supported by BMBF Contract No. 06TU203 and EU/FP6 EURONS (see Annex).
† Supported by a Marie-Curie Fellowship of the EU Community Programme IHP, Contract No. HPMT-CT-2000-00197.

Isotope Shift Measurements of Li-like ^{142}Nd^{57+}-^{150}Nd^{57+} by Means of Dielectronic Recombination

C. Brandau[a], C. Kozhuharov[a], A. Müller[b], K. Beckert[a], P. Beller[a], D. Bernhardt[b], F. Bosch[a,c], S. Böhm[b], F.J. Currell[d], J. Jacobi[b], H.-J. Kluge[a,e], P.H. Mokler[a,b], F. Nolden[a], R. Reuschl[a], S. Schippers[b], E.W. Schmidt[b], U. Spillmann[a], Z. Stachura[f], M. Steck[a], Th. Stöhlker[a,g], A. Wolf[h]

[a]GSI Darmstadt, Germany; [b]Universität, Giessen, Germany;
[c]Universität, Kassel, Germany; [d]Queen's University, Belfast, U.K.;
[e]Universität Heidelberg, Germany; [f]IFJ Kraków, Poland;
[g]Universität Frankfurt, Germany; [h]MPI-K Heidelberg, Germany

As has been detailed in [1, 2], dielectronic recombination (DR) of few-electron heavy-ions is a promising novel approach to study nuclear properties like charge radii and hyperfine effects. Isotope shift measurements of highly charged ions by means of DR complement nicely optical (laser) spectroscopic techniques in neutral atoms or moderately charged ions since the interpretation of the energy shift is not hampered by many-body effects. A combined analysis offers the opportunity to link together highly accurate data from Laser measurements with the DR isotope shift data and hence to significantly improve the overall accuracy. In contrast to experiments with muonic atoms and—up to now—the technique of high-energy electron scattering, DR isotope shift experiments with unstable exotic species seem feasible.

In August 2005, a first pilot experiment with the two stable Li-like neodymium isotopes ^{A}Nd^{57+} with A=142 and A=150 was successfully performed at the electron cooler of the ESR. Special care has been taken to ensure identical experimental conditions in the individual runs with the two different isotopes. In particular, this concerned the mutual alignment of electron and ion beam in the electron cooler, cooling and measurement cycles, and the sequences of measurement voltage ramps applied.

Figure 1 nicely demonstrates the sensitivity of DR to nuclear size effects. Shown are the energetically lowest resonance groups with $1s^2 2p_{1/2} 18\ell_j$ configurations. The spectrum in Figure 1 was obtained within $\sim$1 hour of data acquisition for each isotope with less than 10^7 particles stored in the ring. The isotope shift, which is clearly visible, is mostly due to the change in the nuclear size contribution to the $2s - 2p_{1/2}$ excitation energy. The captured, loosely bound $n = 18$ Rydberg electron can be considered as a mere spectator that does not contribute to the energy shift. Corrections like normal as well as specific mass shifts and radiative contributions are small and can easily be accounted for. It should be emphasized that the spectrum only depicts a small fraction of the experimental data. The next higher Rydberg states with $n = 19, 20, \ldots$ and resonances from the $2s \rightarrow 2p_{3/2}$ excitation have also been recorded and show corresponding isotope effects. ^{142}Nd is a semi-magic nucleus and thus possesses a spherical shape. With increasing number of neutrons the nucleus becomes strongly deformed. Deviations from the liquid drop model, that predicts a $A^{1/3}$ charge radius scaling, can be used to infer information about the deformation of the isotope ^{150}Nd (see e.g. [3]).

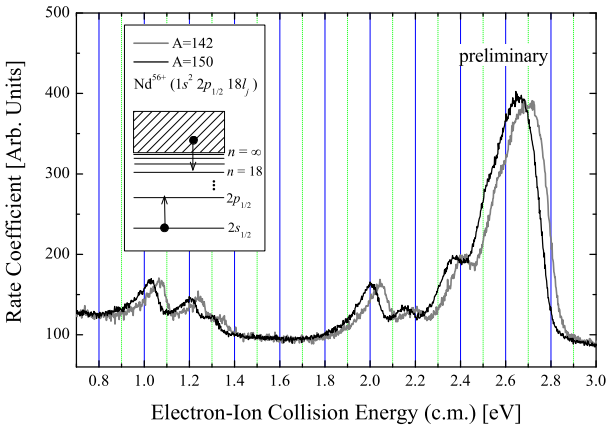


Figure 1: Preliminary experimental data on dielectronic recombination of the two Li-like neodymium ^{A}Nd^{57+} isotopes with A=142 (grey line) and A=150 (black line). The initial dielectronic capture populates intermediate doubly excited states, i.e., $e + \mathrm{Nd}^{57+}(1s^2 2s_{1/2}) \rightarrow \mathrm{Nd}^{56+}(1s^2 2p_{1/2} 18\ell_j)$.

These exciting first results employing the novel method of isotope shift measurements by means of DR pave the road towards further experimental studies with other stable species, and—in the near future—also radioactive ions. The new opportunities at FAIR, with high production yields of radioactive ions from the SuperFRS and a dedicated ultracold electron target at the NESR, will furthermore increase the precision and range of accessible species.

References

[1] C. Brandau, et al., GSI Report 2003, GSI 2004-1, 104.

[2] C. Brandau, et al., in: *Schriften des FZ Jülich, Matter and Material*, Vol 30, ed. D. Chiladze et al., ISBN 3-89336-404-8, 209ff.

[3] E. W. Otten, in: *Treatise on Heavy-Ion Science*, Vol 8, ed. D. A. Bromley, Plenunm Press, New York, p. 515 ff.

High-precision mass measurements with ISOLTRAP *

G. Audi[1], S. Baruah[2], D. Beck[3], K. Blaum[3,4], G. Bollen[5], M. Breitenfeldt[2], P. Delahaye[6], M. Dworschak[4,7], S. George[3,4], C. Guénaut[1], U. Hager[8], F. Herfurth[3], A. Herlert[2,6], A. Kellerbauer[6], H.-J. Kluge[3,9], D. Lunney[1], M. Marie-Jeanne[6], S. Schwarz[5], L. Schweikhard[2], C. Weber[3,4], and C. Yazidjian[3,6] for the ISOLTRAP collaboration
[1]CSNSM-IN2P3-CNRS, Orsay, France [2]Universität Greifswald, [3]GSI, [4]Universität Mainz, [5]NSCL, Michigan State University, East Lansing, USA, [6]CERN, Switzerland, [7]Universität Würzburg, [8]University of Jyväskylä, Finland, [9]Universität Heidelberg

Introduction

The mass of an atomic nuclide is directly related to the nuclear binding energy and thus it reflects nuclear structure. In astrophysics the mass values enter as parameters in the calculations of the nucleosynthesis. Especially in the case of the r-process, where elements heavier than iron are formed by rapid neutron capture, nuclear structure data of nuclides far from the valley of stability are required.

Nuclear masses are also important for fundamental tests, where the mass needs to be known with a relative uncertainty of $\delta m/m = 1 \cdot 10^{-8}$ or smaller. One example is the test of the Standard Model with respect to the conserved-vector-current hypothesis of the weak interaction and the unitarity of the Cabibbo-Kobayashi-Maskawa quark-mixing matrix, where the masses of superallowed β-decaying nuclides are required [1].

Experimental setup and procedure

The ISOLTRAP experiment at ISOLDE/CERN comprises three ion traps for precise mass measurements. The first linear radiofrequency ion trap cools and bunches the continuous radioactive ion beam coming from the ISOLDE target. The ion bunches are sent to a cylindrical Penning trap where in a helium buffer-gas environment isobaric contaminants are removed. The further cooled short-lived ions are finally transferred to the precision Penning trap, where the mass m is determined via the cyclotron frequency $\nu_c = qB/(2\pi m)$ of the stored ions with a time-of flight cyclotron-resonance detection technique. The magnetic field B is calibrated with the measurement of ν_c of a reference nuclide with well-known mass.

Technical developments

A conversion-dynode channeltron detector has been installed which has a 2.5-times higher efficiency than a standard MCP detector. This reduces the ion-ion-interaction in the precision Penning trap since a smaller number of ions can be stored in each experimental cycle.

Furthermore a pressure and temperature regulation system has been installed and tested. It allows the stabilization of the magnetic field in the precision trap for a reduction of any significant fluctuation in the frequency determination.

Finally a new detection scheme has been tested that employs a Ramsey scheme for the quadrupolar rf-excitation in the precision trap. This leads to a decrease of the width of the central peak by about 50% and an increase in the precision of the frequency determination by a factor of 2-3.

Mass measurements

With ISOLTRAP about 300 masses of radionuclides have been measured to date. In 2005 the atomic masses of 28 nuclides have been investigated: For the first time doubly charged ions have been studied for mass measurements with ISOLTRAP. The masses of ^{126}Xe and ^{136}Xe have been measured, where the uncertainty was improved by a factor of two [2]. In the case of ^{126}Xe a significant deviation to the literature value was found.

Mass measurements around the doubly magic ^{132}Sn give valuable information on nuclear structure. The Sn isotopes with masses $A = 127, 128, 131 - 134$ have been investigated with a special interest on ^{131}Sn, where the excitation energy of the first isomeric state is still not determined. However, even rf-excitation durations at ISOLTRAP of up to 9 s, which is equal to a resolving power of $R = 5 \cdot 10^6$ in the respective mass range, could not resolve the two isomers.

Furthermore, Cd isotopes with masses $A = 118 - 124$ have been investiagted. Some mass values are important input parameters for the δV_{pn} values that probe the average interaction of the last proton(s) with the last neutron(s) [3] and thus reveal information on nuclear structure.

A highlight of the 2005 beam-time period was the investigation of the neutron-rich zinc isotopes. The masses of $^{71-81}$Zn have been measured, in the case of ^{79}Zn and ^{81}Zn for the first time. The waiting point nuclide ^{80}Zn is of special interest for the study of the r-process pathway.

References

[1] M. Mukherjee *et al.*, Phys. Rev. Lett. 93 (2004) 150801.

[2] A. Herlert *et al.*, Int. J. Mass Spectrom., accepted (2006).

[3] R.B. Cakirli *et al.*, Phys. Rev. Lett. 94 (2005) and 95 (2005) 119903.

* Financial support by GSI, the BMBF (06GF151), the EU (HPRI-CT-2001-50034 and RII3-CT-2004-506065), and the HGF (VH-NG-037)

Mass Measurements of Rare-earth Radionuclides at SHIPTRAP*

M. Block[1], D. Ackermann[1], D. Beck[1], K. Blaum[1,2], A. Chaudhuri[1,3], S. Eliseev[1,4], D. Habs[5], F. Herfurth[1], F.P. Heßberger[1], S. Hofmann[1], H. Geissel[1,6], H.-J. Kluge[1,7], A. Martín[1], G. Marx[3], J.B. Neumayr[5], M. Mukherjee[8], W.R. Plaß[6], S. Rahaman[9], C. Rauth[1], D. Rodríguez[10], C. Scheidenberger[1,6], L. Schweikhard[3], P.G. Thirolf[5], G. Vorobjev[1,4], C. Weber[1,2]

[1]GSI Darmstadt, [2]Universität Mainz, [3]Universität Greifswald, [4]PNPI RAS, Gatchina, [5]Ludwig-Maximilians-Universität München, [6]Universität Gießen, [7]Universität Heidelberg, [8]Universität Innsbruck, [9]University of Jyväskylä, [10]LPC Caen

With the Penning trap mass spectrometer SHIPTRAP [1] at GSI mass measurements of radionuclides are performed, which are produced in fusion-evaporation reactions and separated by the velocity filter SHIP [2]. A schematic overview of the set-up is shown in Fig. 1. The reaction

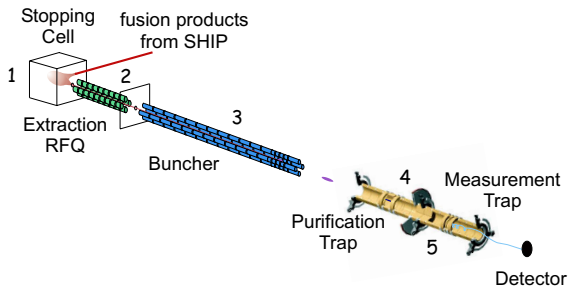


Figure 1: Schematic overview of SHIPTRAP.

products from SHIP are stopped in a gas-filled stopping cell [3] at helium pressures around 50 mbar. The extracted ions are pre-cooled in the extraction radiofrequency quadrupole (RFQ) and transferred to a second RFQ operated as ion beam cooler. In this RFQ the ions are transversally and longitudinally cooled within a few milliseconds to be finally extracted as a low-emittance bunched beam. Such a beam can be efficiently injected into the Penning trap system, consisting of two cylindrical traps in one superconducting 7-T magnet. The first trap with a mass resolving power of about 10^5 is utilized for isobar purification. High-accuracy mass measurements are performed in the second trap using the time-of-flight cyclotron resonance technique. A mass resolving power of $\mathrm{m}/\Delta\mathrm{m} = 10^6$ is routinely achieved.

In 2005, mass measurements of radionuclides in the rare-earth region near the proton drip-line were performed. Several nuclei in that region are energetically unbound to the emission of a proton and, hence, are located beyond the proton drip line. From mass measurements proton separation energies can be determined allowing for a mapping of the drip line. In addition, the $\mathrm{Q_p}$ value can be obtained from the mass of the proton emitter and its daughter, which allows to identify potential proton emitters. At present, many masses in that region are only known from extrapolations [4] of systematic trends.

* Work supported by the EU, BMBF, HGF (VH-NG-037) and within the GSI F&E program

The investigated nuclides around ^{147}Ho were produced in the reaction $^{58}\mathrm{Ni} + ^{92}\mathrm{Mo} \rightarrow ^{150}\mathrm{Yb}^*$ with primary beam energies between 4.3 - 4.6 MeV/u. The masses of the nuclides ^{147,148}Tm, $^{146-148}$Er, $^{144-148}$Ho, $^{143-148}$Dy and ^{143,147}Tb were measured in two runs with relative uncertainties between $1 \cdot 10^{-7}$ to $5 \cdot 10^{-8}$ using ^{133}Cs and ^{85}Rb as reference. For eight of these nuclides the mass has been experimentally determined for the first time, while for the others the mass uncertainty has been improved compared to [4]. The data are presently analyzed. An example of a

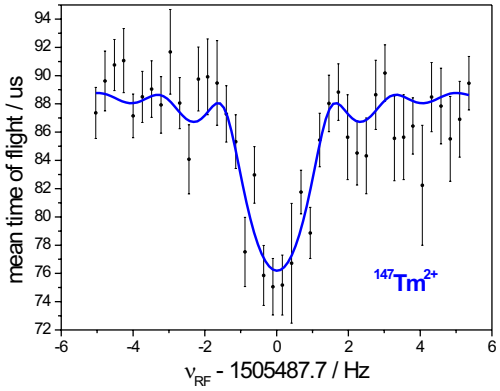


Figure 2: Time-of-flight cyclotron resonance of $^{147}\mathrm{Tm}^{2+}$ ions.

cyclotron resonance of $^{147}\mathrm{Tm}^{2+}$ ions is shown in Fig. 2. It should be noted that the gas cell was very clean resulting in the extraction of a large fraction of doubly-charged ions which were used for most of the measurements.

The measured nuclides include the proton emitter ^{147}Tm ($\mathrm{T}_{1/2} = 580$ ms) and its daughter ^{146}Er. The production cross section for ^{147}Tm in the 1p2n-channel is only about a factor of ten higher than the production cross section for ^{254}No in the reaction $^{208}\mathrm{Pb}(^{48}\mathrm{Ca}, 2\mathrm{n})^{254}\mathrm{No}$. Hence, a nobelium mass measurement at SHIPTRAP is in reach.

References

[1] M. Block *et al.*, Eur. Phys. J. A **25**, s1.49 (2005).

[2] S. Hofmann and G. Münzenberg, Rev. Mod. Phys. **72**, 733 (2000).

[3] J. Neumayr *et al.*, Nucl. Inst. Meth. B in print.

[4] G. Audi, A.H. Wapstra and C. Thibault, Nucl. Phys. A **729**, 337 (2003).

First Observation of the Lyman-α Transition in Hydrogen-like Heavy Ions with High Resolution Calorimetric Low Temperature Detectors

V. Andrianov[1], K. Beckert[1], P. Beller[1], A. Bleile[1,2], P. Egelhof[1,2], A. Gumberidze[1], S. Ilieva[1,2], C. Kilbourne[3], H. J. Kluge[1], S. Kraft-Bermuth[1,2], D. McCammon[4], J. P. Meier[1,2], U. Popp[1], R. Reuschl[1], T. Stöhlker[1], and S. Trotsenko[1]

[1]GSI Darmstadt, Germany; [2]Institut f. Physik, Univ. of Mainz, Germany; [3]NASA/Goddard Space Flight Center, Greenbelt, USA; [4]Dept. of Physics, Univ. of Wisconsin, Madison, USA

The precise determination of the Lamb shift in hydrogen-like heavy ions provides a sensitive test of quantum electrodynamics in very strong Coulomb fields, not accessible otherwise. For increasing accuracy on the 1s Lamb shift in $^{238}U^{91+}$ in measurements performed at the ESR, high resolving X-ray detectors for hard X-rays ($E \leq 100$ keV) are required. As one option to replace the presently used conventional semiconductor detectors, the concept of calorimetric low temperature detectors was proposed [1], and consequently such a detector system, optimized for the high resolution detection of hard X-rays, was developed and recently tested at the ESR under running conditions. The detector modules for the present setup are designed on the basis of silicon micro-calorimeters which were developed by the Goddard/Wisconsin groups for astrophysical applications. Each detector pixel consists of a silicon thermistor and of an X-ray absorber glued on top of it by means of an epoxy varnish. Thermistor arrays, consisting of 36 pixels each, are provided from the collaborating group from Goddard Space Flight Center. For the Lamb shift measurement, the experimental setup was optimized with respect to energy resolution and detection efficiency for hard X-rays at the experimental area of the storage ring ESR. The final detector concept foresees three calorimeter arrays with about 100 detector channels. In order to reach sufficient photopeak efficiency, the absorber should be a high-Z material and have a volume of at least V > 0.5 mm² x 40 µm. To obtain a reasonable detection solid angle, a special $^3He/^4He$-dilution refrigerator with a side arm which fits to the internal target geometry at the ESR gas-jet target was designed. The operating temperature can be chosen around 50 mK.

pixel no.	absorber material	active area [mm²]	ΔE [eV] @ 70 keV	efficiency [10^{-8}]
31	Pb	0.41	188(40)	2.57
32	Sn	0.41	115(59)	3.18
35	Sn	0.27	277(71)	3.41
36	Pb	0.39	329(96)	3.45

Table 1: Detector geometry and results of the Lyman-α measurement at the ESR with the 4-pixel prototype array

Recently, a prototype array of 4 pixels was for the first time applied to detect Lyman-α X-rays produced by a 90 MeV/u $^{238}U^{92+}$ beam interacting with an internal Ar gas-jet target. The detector, covering a total solid angle of 1.3 x 10^{-5} sr, thus reaching an overall Lyman-α detection efficiency of 1.3 x 10^{-7}, was positioned at $\theta_{lab} = 145°$. As an example, a spectrum obtained with a Sn pixel (pixel 32) is displayed in Fig. 1. The two Lyman-α lines are clearly identified. For the Lyman-α1 line at 70 keV, an energy resolution of ΔE = 115 eV is obtained. The detector geometry as well as the performance for all 4 pixels is summarized in Table 1. The significantly worse energy resolution obtained for pixels 35 and 36 is due to a worse signal-to-noise ratio for these channels, which needs to be improved for future measurements. With the energy resolution obtained, it may be possible to improve the accuracy of the absolute Lyman-α energy measurement in a dedicated long-time experiment.

This work has been supported by I3 EURONS under EC contract No. 506065.

[1] P. Egelhof et al., NIM A **370** (1996) 263

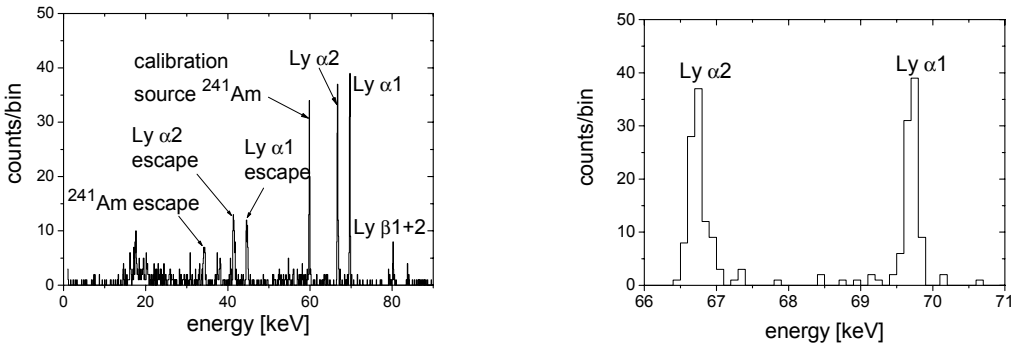


Fig. 1: Total energy spectrum (left side) obtained with a calorimetric low temperature detector (pixel 32, see Table 1) placed at the internal gas-jet target of the ESR. The extension (right side) displays the region of the Lyman-α lines emitted from the charge-exchanged $^{238}U^{91+}$ ions. An energy resolution of ΔE = 115 eV was obtained.

State Selective Formation of Excited L-Shell Levels in Li-Like Uranium

S. Trotsenko[1,2], Th. Stöhlker[1,2], D. Banas[5], C. Z. Dong[3], S. Fritzsche[7], A. Gojska[6], A. Gumberidze[1,2], S. Hagmann[1], S. Hess[1,2], P. Indelicato[4], C. Kozhuharov[1], D. Liesen[1], M. Nofal[1], R. Reuschl[1,2], J. Rzadkiewicz[1,6], U. Spillmann[1,2], A. Surzhykov[7]

[1]GSI Darmstadt, [2]IKF, Univ. of Frankfurt, Germany, [3]Northwest Normal University, Lanzhou, China, [4]Université P. et M. Curie, Paris, France, [5]Institute of Physics, Swietokrzyska Academy, Kielce, Poland, [6]The Andrzej Soltan Institute for Nuclear Studies, Swierk, Poland, [7]Universität Kassel, Germany

In relativistic collisions with gaseous targets in the ESR storage ring at GSI the process of *K*-shell ionization of Li-like high-*Z* ions was studied. This process has proven to be a highly-selective mechanism for the population of excited (n=2) *s*-states [1]. In the present study, these investigations were extended to initially Be-like uranium allowing us to produce almost exclusively the $1s(2s)^2$ level in the Li-like species which is expected to undergo predominantly an exotic two-electron one-photon decay (TEOP). Recently at low-*Z*, similar studies have been performed for Li-like aluminum ions in laser produced plasmas [2] and for the process of dielectronic recombination in an electron-beam ion trap using Li-like iron [3]. The decay properties of the $1s2s^2\ 2S_{1/2}$ state are of particular interest for atomic structure investigations because of the sensitivity of the TEOP transition to electron correlation. Therefore, studies of these exotic transitions along the isoelectronic sequence up to the heaviest ions probe uniquely our understanding of the interplay of relativistic and correlation effects on the atomic structure of few electron systems. The experiment was performed with cooled Be-like uranium ions colliding with N_2 gas target at the energy of 90 *MeV/u* in the storage ring ESR. The x-rays produced in this process were measured under different angles with respect to the propagation direction of the ion beam. For details concerning the experimental setup we refer to [1]. In Fig.1, we present preliminary x-ray spectra as recorded by the detector at the observation angle of 35 deg. By the coincident registration of x-rays with the charge state of the ions after the collision, two different radiative processes can be separated: *K*-shell excitation of the Be-like ions and the formation of excited states of the Li-like ions produced by *K*-shell ionization. As can be seen in Fig. 1, *K*-shell ionization appear again (compare result for He-like ions [1]) to be a very selective population process and in the associated photon spectrum only one single x-ray line is observed stemming from the decay of the $1s(2s)^2$ state. We note, that in contrast to the low-*Z* ions, this state my also decay by a fast M1 transitions. However, interestingly, even for the case of uranium the TEOP is predicted to be dominant decay mode. Following theoretical predictions, the various decay modes of the $1s(2s)^2$ state in U^{89+} (decay rates and energies) are given in Fig. 2. Currently, the data evaluation is in progress, aiming on a determination of the M1 and TEOP branching ratio from the observed spectra via an accurate line centroid determination (the transitions are separated by about 280 eV).

Acknowledgment: This work has been supported by I3 EURONS under EC contract No. 506065.

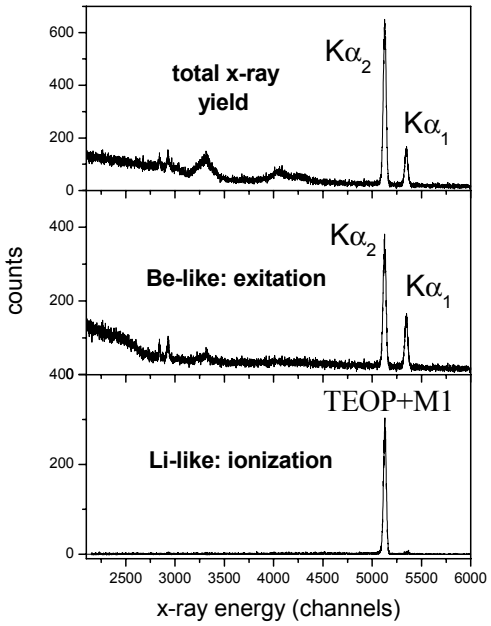


Figure 1: Preliminary x-ray recorded for $U^{88+} \rightarrow N_2$ (for details compare text).

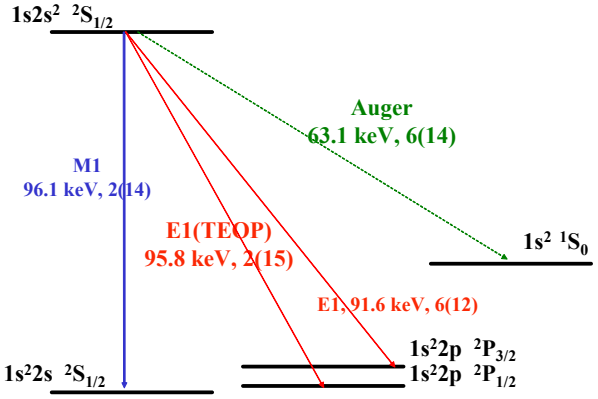


Figure 2: Level scheme and decay modes of U^{89+}. The transition energies and the radiative rates are given [5].

[1] D. Banas et al., NIMB, 235, p.326-330, 2005
[2] F. B. Rosmej et al., Phys. Rev. A 63 (2001) 032716
[3] Y. Zou et al., Phys. Rev. A 67 (2003) 042703
[4] P. Beiersdorfer et al., Phys. Rev. Lett. 95, 233003 (2005)
[5] C. Z. Dong et al., to be published.

Radiative Processes Studied in Collisions of Decelerated Bare Uranium Ions with H_2 Target

A. Gumberidze[1,2], Th. Stöhlker[1,2], S. Hagmann[1,2], S. Hess[1,2], C. Kozhuharov[1], U. Popp[1], R. Reuschl[1,2], J. Rzadkiewicz[1,3], U. Spillmann[1,2], S. Trotsenko[1,2], G. Weber[1]

[1]GSI, Darmstadt, Germany, [2]University of Frankfurt, Germany, [3]IPJ Swierk, Poland

Projectile X-ray emission arising from collisions of high-Z ions with the gas-target atoms and molecules has proven throughout the years to be a unique tool for accurate studies of atomic structure and dynamics in the domain of extreme electromagnetic fields. The ideal conditions offered by the ESR storage ring along with the internal gasjet target enables for detailed investigations of various fundamental atomic processes occurring in the ion-atom collisions. In the present experiment, the X-ray emission study was carried out for collisions of bare uranium (U^{92+}) ions with the H_2 gas target at the beam energy of 98 MeV/u. Here, we like to emphasize that the H_2 gas target was used for the first time since its commissioning in 2001 [1] and offered an improved performance, in particular a better long-term stability. The use of hydrogen as a target provides many advantages with respect to beam lifetimes and also spectroscopic resolution due to a very narrow Compton-profile. For the x-ray recording, the experimental chamber at the ESR gas target was utilized. The x-rays were measured by an array of Ge(i) detectors mounted at different observation angles with respect to the beam. In Fig. 1, we present x-ray spectra as recorded by the detector at 150 deg. Exploiting a coincidence technique (with the down-charged ions), two different radiative processes can be rigorously identified/separated; the Radiative Electron Capture (REC) into the bare uranium ions (b) and the Bremsstrahlung stemming from inelastic scattering of initially bound target electrons by the nucleus of the projectile (c). The latter process is of particular importance since up to now only few experimental studies have been conducted for such collisions [2]. In addition, the case of bare ions attracts the greatest interest since here the interaction of the electrons with the pure Coulomb potential of the projectile can be studied in the absence of many-body effects. Therefore, the reliability of theoretical models can be most precisely examined in such experiments. In particular, high-Z projectiles are of interest, as they exclusively probe the coupling between the continuum states and the radiation field in the presence of strong external potentials. Moreover, the tip region is very clearly identified in the experiment, (Fig.1 c)) owing to the very narrow Compton-profile of the target electron. The shape of the spectrum near to the tip is, in particular, sensitive to Coulomb distortions caused by the large nuclear charge of the projectile. Besides, this hard-photon bremsstrahlung is closely related to the REC, i.e. the time-reversed Photo Effect and therefore, its study is complementary to the investigations of the REC extending them to final electron states of positive energy.

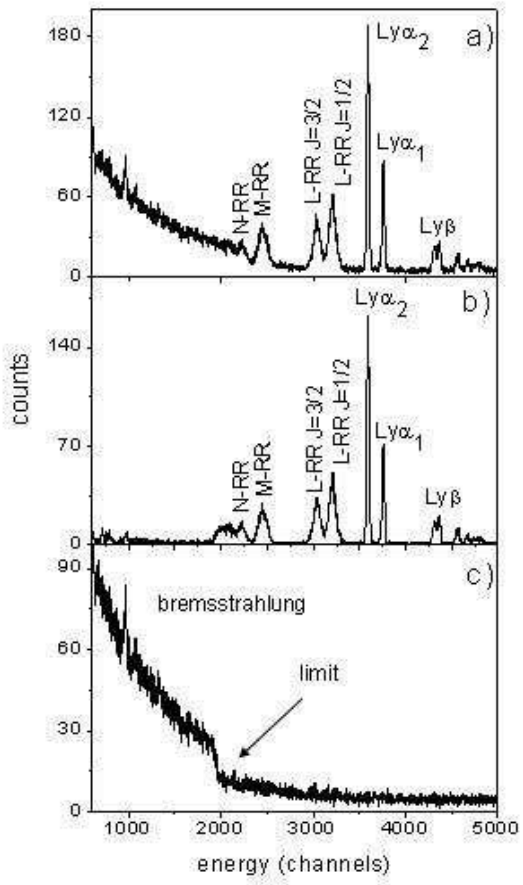


Fig 1; a) Total x-ray spectrum from $U^{92+} \rightarrow H_2$ collisions at 98 MeV/u, b) x-ray spectrum acquired in coincidence with capture of one electron into a projectile ion, c) difference between the total spectrum and the coincident one; corresponding to collisions where no charge exchange took place.

Acknowledgements

This work has been supported by I3 EURONS under EC contract No. 506065.

References

[1] A. Krämer et al., NIM B, 174, p205, 2001.
[2] T. Ludziejewski et al., J. Phys. B, 31, p2601 1998.

Mutual Ionization in 200 keV H^- - He Collisions

T. Ferger, D. Fischer, B. Najjari, R. Moshammer, J. Ullrich, A.B. Voitkiv, MPIK Heidelberg
M. Schulz, UMR Rolla Missouri, USA

By now many experimental data on fully differential cross sections (FDCS) exist for single target ionization covering a broad range of different collision systems. At this stage it therefore seems reasonable to turn to somewhat more complex ionization processes and to fully exploit the opportunities provided by heavy projectiles, in order to advance our understanding of collision-induced few-particle quantum-dynamics. One fundamental step forward is to study double ionization of the target atom, where electron-electron correlations have to be taken into account [1]. Another important step is to investigate mutual ionization of both collision partners, whereby two-center effects can be studied. Although this process is more complicated than double ionization in that it requires a structured projectile, one important advantage is that the mutual ionization can proceed through a single interaction (between the two electrons to be ionized), while double ionization requires at least two interactions. In that sense mutual ionization is the more simple process.

Experimentally, following numerous total cross section studies, multiple differential data became only available quite recently [2, 3]. In fact, the very first measurement of FDCS for MeV C^{2+} + He collisions was performed at GSI just a few years ago [3]. There the question was addressed to what extend mutual ionization proceeds through the interaction between the two active electrons and how this particular reaction channel can be separated from other ionization mechanisms. However, because of the comparable binding energies of projectile and target (48 and 24 eV), a considerable contribution of nucleus-electron interaction was found. Only under certain kinematical conditions features typical for electron impact ionization (e,2e) were observed.

In the present work we chose 200 keV H^- as projectiles and investigated the simultaneous ionization of the projectile and the He target by means of a kinematically complete experiment using a reaction microscope [4]. Here, compared to all previous studies, the binding energy of the projectile electron is much smaller (0.7 eV). Thus, one might expect that during the collision the weakly bound quasi free projectile electron interacts with the target giving rise to ionization of both, projectile and target. Since the projectile nucleus is just a spectator in this scenario we expect to approach a situation very similar to free electron impact ionization.

Theoretically, if the above assumptions hold, a first order treatment in the projectile-target interaction should be adequate to describe the H^- - He collisions. We use a first Born approximation (FBA) where the projectile and the target are assumed to have just one active electron and mutual ionization can only proceed through an interaction between these active electrons. The initial and final electronic states in H^- were found by solving the Schrödinger equation for a Yukawa-like potential used to model the short-range force experienced by the active electron in H^-.

In Fig. 1 the experimental longitudinal momentum spectra of electrons ionized form the target and the projectile are shown in comparison with our FBA calculation (thick lines). The projectile electron distribution exhibits a main peak at about 2.3 a.u. as well as a "bump" approximately at the projectile velocity (indicated by the arrow in Fig.1). Both features are very well reproduced by our first order theory. The projectile electron has to deliver the energy to ionize the He (24.7 eV) which leads to a change in the projectile electron momentum from initially v_p to at least 2.48 a.u. in agreement with experiment. Because of very similar arguments a forward shifted momentum distribution for the target electrons is predicted (thick line in Fig.1). However, the experimental data show a pronounced cusp shape with a maximum at $p_z = 0$. This discrepancy can only be removed if a more advanced theory is used for the target ionization. Taking a CDW-EIS calculation for pure target ionization, where the H^- projectile is treated as an anti-proton (thin curve in Fig. 1) the data are very well described. It appears that the post-collision-interaction of the target with the projectile electron, which is not included in the FBA, is essential.

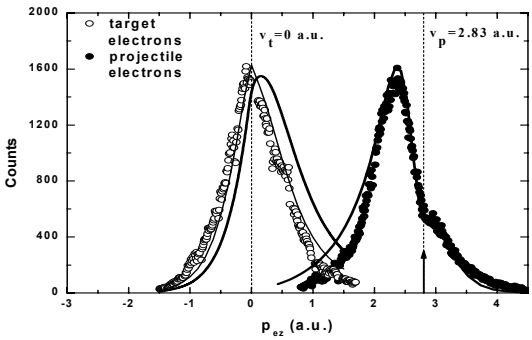


Figure 1: Longitudinal electron momemtum spectra. Thick lines, FBA for mutual ionization. Thin line, CDW calculation for target ionization by negative ion impact.

In conclusion, the above analysis demonstrates that mutual ionization indeed can be understood as an interaction between the two active electrons. However, it also shows that our understanding of the underlying many-particle dynamics is still premature. The latter becomes even more apparent when the angular correlations between both electrons are inspected (see [4]).

References

[1] D. Fischer, et al., Phys. Rev. Lett. 90, 243201 (2003)
[2] H. Kollmus et al., Phys. Rev. Lett. 88, 103202 (2002)
[3] W. Wu et al., Phys. Rev. Lett. 72, 3170 (1994)
[4] T. Ferger, et al., Phys. Rev. A 72, 062709 (2005)

Longitudinal Momentum Distributions in Simultaneous Ionization of Target and Projectile in 3.6AMeV Ne^{3+} +Ar Collisions

M. Nofal[1,3], S. Hagmann[2,3], Ch. Kozhuharov[3], R. Moshammer[1], N. Lineva[3], X. Wang[4]

[1]Max Planck Inst. f. Kernphysik, Heidelberg, [2]Institut f. Kernphysik, Univ. Frankfurt, [3]GSI-Darmstadt, [4]Fudan University, Shanghai

Ionization of target atoms by ion impact represents a suitable test ground for the many particle problem which is not fully understood up to this date. Recoil-Ion Momentum Spectroscopy (RIMS) has been developed to provide an efficient and precise experimental tool to explore the correlated dynamics of collision induced atomic many-particle reactions in kinematically complete experiments by measuring all the momentum components (and thus angle and energy) of all involved particles in coincidence [1] with nearly 4π detection efficiency. In the present work we present our preliminary experimental results obtained with a reaction microscope (see Fig.1) for the single ionization of Argon in 3.6 AMeV Ne^{3+} +Ar $\rightarrow$ Ne^{4+} +Ar^{1+} +$2e^-$ collisions.

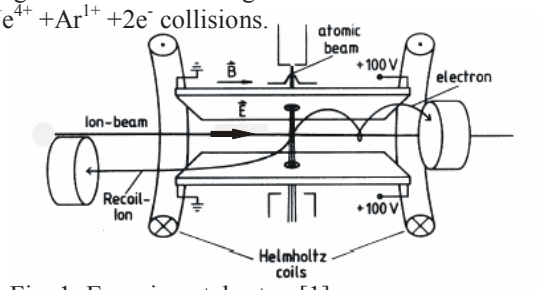


Fig. 1: Experimental setup [1]

Recoil ions and electrons are extracted along the beam axis in a solenoidal magnetic guiding field to 2D position sensitive detectors on opposite sides of the target zone. We have measured coincidences between singly ionized projectiles ($Ne^{3+}\rightarrow Ne^{4+}$), recoil ions, and target- and projectile-electrons. The time of flight of electrons and recoils ions, respectively and thus the longitudinal momentum components are calculated from the coincident time spectra between electrons/recoil ions and charge-changed projectiles Ne^{4+}. Fig. 2 shows the sum of the low energy electron and recoil ion longitudinal momentum. Using momentum conservation it follows that recoil and low energy electron longitudinal momentum change is compensated by the momentum change of projectile and projectile-electron: $\Delta P_{R\|} + \Delta P_{e\|} = -(\Delta P_{p\|} + \Delta P_{e\text{-}proj})$. The half width measured is 0.6 a.u. and thus 3 times larger than found for pure single target ionization (SI) at the same collision velocity [2]. The difference is attributed mostly to the larger momentum spread of the Ar compared to a He supersonic jet target.

Fig. 3 shows the longitudinal momentum distributions for Ar^{1+} recoil ions and low energy electrons ionized out of the target during simultaneous single ionization of the projectile. The low energy electron emission is not nearly isotropic as expected for the present small perturbation with a Sommerfeld parameter q_{proj}/v_{Proj}=0.25 but unexpectedly exhibits the same strong forward asymmetry for low energy electron emission as observed for pure SI in strong perturbation by the 3.6AMeV Ni^{24+} projectile (with a Sommerfeld parameter q/v=2) resulting in atomic dissociation [2]. Moreover, the half width of the electron distribution is clearly larger than that of the corresponding recoil distribution and appears to mirror the momentum fraction inferred for the projectile electron. We argue that the condition of simultaneous projectile and target ionization emphasizes the small impact parameter region so that for q/v=0.25 the electron nucleus (e-N) and the electron-electron (e-e) channel both contribute with similar strength to the simultaneous projectile and target ionization. The analysis of disentangling the (e-N) and (e-e) channels to identify these 3- and 4-body channels [1] is still ongoing.

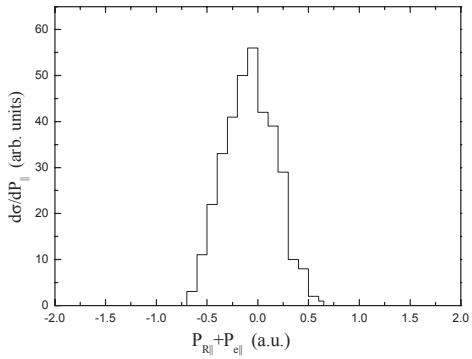


Fig. 2 The sum of the electron and recoil ion longitudinal momentum

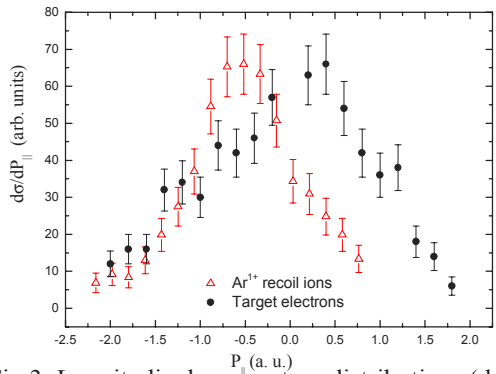


Fig.3: Longitudinal momentum distributions ($d\sigma/dP_{\|}$) for Ar^{1+} recoil ions, and target electrons

[1] J. Ullrich et al., Rep. Prog. Phys. **66**(2003) 1463

[2] R. Moshammer et al, Phys. Rev. Lett. **73**(1994) 3371

Radiative Electron Capture to the Continuum Cusp (RECC) in 90AMeV U^{88+} + N_2

M. Nofal[1,3], S. Hagmann[2,3], Th. Stöhlker[3], Ch. Kozhuharov[3], X.Wang[4],A. Gumberidze[3],U. Spillmann[3], R. Reuschl[3], S. Heß[3] S.Trotsenko[3], D. Banas[3], F. Bosch[3], D. Liesen[3], D. Jakubassa[5] ,R. Moshammer[1],J. Ullrich[1],R. Dörner[2], M. Steck[3], P. Beller[3], K. Beckert[3], B. Franczak[3],
[1]Max Planck Inst. f. Kernphysik, Heidelberg, [2]Institut f. Kernphysik, Univ. Frankfurt, [3]GSI-Darmstadt, [4]Fudan University, Shanghai, [5]Rechenzentrum,LMU-München

Electron transfers from bound states of a target atom into continuum states of a highly charged projectile still represent a major challenge for ab initio theoretical treatments almost over the entire velocity range due to the very large momentum transfer $|\Delta p_e|$ $|v_{Proj.}|$ involved/1/. At high collision velocities above v_e 40a.u. the radiative electron capture to continuum (RECC) increasingly competes with the non radiative capture (ECC). It is of basic interest to compare the nature of both processes as the RECC comprises the additional radiative degree of freedom. Moreover, the RECC process as seen in the projectile frame – a quasifree electron from the target is decelerated from velocity v_{proj} to v 0 while emitting a photon of energy E_x= (-1)mc^2 – is the kinematic inverse of the electron nucleus bremsstrahlung at the short wavelength limit (SWL). Interestingly, the inverse kinematic where the electron is detected with v_e v_{Proj} offers the only configuration to investigate total differential cross sections (TDCS) at the SWL of electron nucleus Bremsstrahlung; this has never been accomplished in the standard configuration as it implies detecting an electron of zero energy. As a first step towards measuring TDCS we have studied forward electron emission in 90AMeV U^{88+} +N_2 and measured coincidences between cusp electrons around v_e v_{Proi} and x rays.

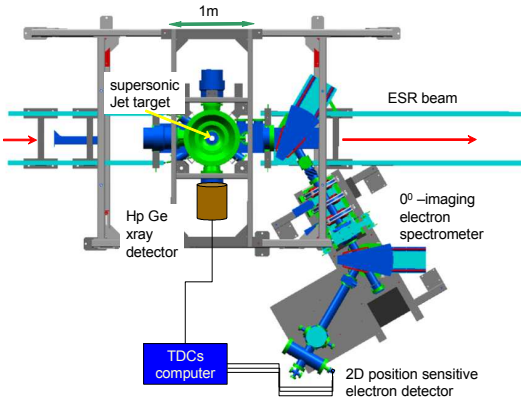


Figure 1: Imaging forward electron spectrometer in the jet target zone of the ESR

Electrons were analyzed with the imaging forward electron spectrometer in the ESR and x rays were detected with a HpGe detector at 90^0 with respect to the beam axis (see Fig.1). In the coincident x ray spectra (Fig.2) we observe for the very first time nearly exclusively photons from the short wavelength limit of electron nucleus bremsstrahlung, corroborating identification of the coincident electrons as RECC cusp. We found a strong asymmetry of the coincident RECC electron cusp distribution which is skewed towards the high energy side of the electron spectrum (Fig.3), as predicted by theory/2/.

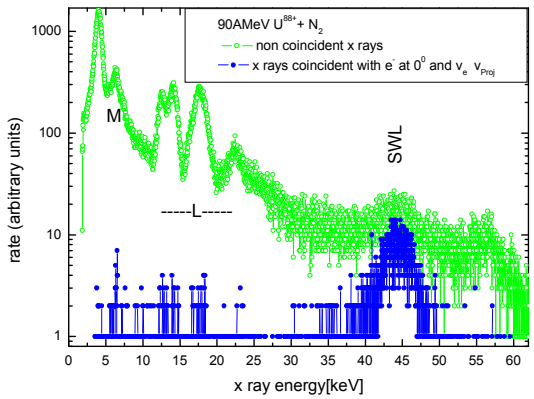


Fig.2 X ray spectrum coincident with forward electrons with v_e $v_{Proj.}$; the SWL of bremsstrahlung is indicated. For comparison a random x ray spectrum is shown.

This asymmetry is opposite to the one found for the non-radiative electron capture to the continuum ECC/2/. The electron decelerates in the projectile frame from ' = (-1)mc^2 to '≈0 during photon emission. This means that the electron bounces back with subsequent forward emission in the laboratory frame/2/.

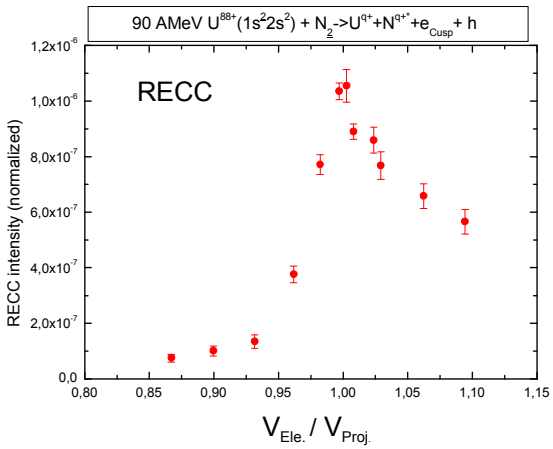


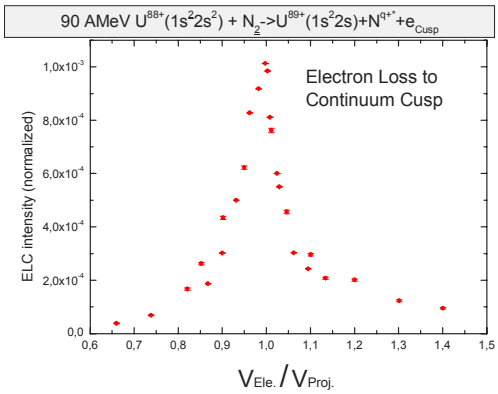
Figure 3: Radiative electron capture to continuum cusp in 90AMeV U^{88+} + N_2 collisions. The relative probability for electron-photon coincidences is given as function of electron velocity normalized to the projectile velocity.

1. J. Burgdörfer, Lecture Notes in Physics Vol. **213**(1984),32, Springer Verlag, Berlin
2. D.Jakubassa, J.Phys.**B36** (2003)1971

Simultaneous Electron Capture to Bound and Continuum States in 90AMeV U^{88+} + N_2 Collisions

M. Nofal[1,3], S. Hagmann[2,3], Th. Stöhlker[3], Ch. Kozhuharov[3], X.Wang[4],A. Gumberidze[3], U. Spillmann[3], R. Reuschl[3], S. Heß[3], S.Trotsenko[3], D. Banas[3], F. Bosch[3], D. Liesen[3],D. Jakubassa[5], J. Ullrich[1],R. Moshammer[1],R. Dörner[2], M. Steck[3], P. Beller[3], K. Beckert[3], B. Franczak[3],
[1]Max Planck Inst. f. Kernphysik, Heidelberg, [2]Institut f. Kernphysik, Univ. Frankfurt, [3]GSI-Darmstadt, [4]Fudan University, Shanghai, [5]Rechenzentrum, LMU-München

Electron transfer processes in relativistic ion-atom collisions have been at the center of attention in ion collision dynamics for a variety of reasons: a) they are a basic ingredient in relativistic ion accelerator design/1,2/, b) the large recombination energy of highly charged ions (HCI) contributes to both, extended multiple ionization of target atoms, even of strongly non-sequential character, and population of otherwise non accessible, even "custom made", multiply excited configurations. Moreover, ab initio theories for single and multiple electron capture/3/ are in dire need of data for critical tests. Theories have up to now widely failed to describe the intrinsic many-electron processes in the capture channel/5/. This may partially be attributed to a peculiarity of the electron capture to continuum, as it is characterized by large momentum transfers/4/ and thus is mostly not in the realm of first order perturbation theories. We have begun a study of the non-radiative electron capture to continuum (ECC) in the relativistic domain with 90 AMeV $U^{88+}(1s^22s^2)$ + N_2 → $U^{87+}(1s^22s^22p)$ + $\{N^{q+*}\}$ + e_{Cusp}, where at least two active electrons are involved. Using the imaging forward electron spectrometer in the ESR target zone we have measured electrons emitted into a narrow cone around the projectile axis with $\mathbf{v_e \approx v_{proj}}$ in coincidence with the down charged projectile $U^{87+}(1s^22s^22p)$ i.e. a projectile asymptotically having captured one electron into the 2p shell and one electron into its continuum.



Fig,1 Electron loss to continuum(ELC) cusp for forward emitted electrons coincident with projectile after single electron loss.

For comparison we have measured simultaneously coincidences between electrons emitted into a narrow cone around the projectile axis with $\mathbf{v_e \approx v_{proj}}$ and projectiles which experienced a single electron loss. The resulting electron loss to continuum cusp exhibits a nearly symmetric line shape in agreement with theory/4/ (Fig.1). Contrary to the ELC cusp we observe in the electron continuum spectrum coincident with capture to a projectile bound state a cusp line shape skewed towards the low-energy side which points towards a non-radiative ECC process/6/ as the active mechanism (fig.2).

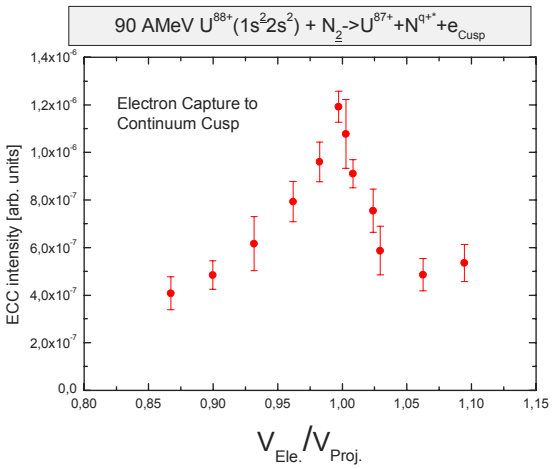


Figure 2: Non radiative electron capture to continuum cusp coincident with bound state capture

On the other hand, double capture processes as $U^{88+}(1s^22s^2)$ + N_2 → $U^{86+}(1s^22s^2nln'l')$ + $\{N^{q+*}\}$ with subsequent autoionization via electron and/or photoemission to $U^{87+}(1s^22s^22p)$ + $\{N^{q+*}\}$ + e_{Cusp} +hν may also contribute as the asymptotic final state for the pure bound state and the continuum plus bound state capture reactions are identical. However, the asymmetric line shape of the observed cusp disproves such a double capture process as dominant channel and supports identification as simultaneous continuum and bound state capture. Calculations of a non-radiative ECC simultaneous with bound state capture are in progress.

1. H. Gould et al, Phys. Rev. Lett.**52**(1984)180
2. P. Thieberger et al, IEEE Tran. Nuc. Sci. **32**(1985)1767
3. W. Meyerhof et al, Phys. Rev. **A32**(1985)3291
4. J. Burgdörfer, Lect. Notes in Physics Vol**213**(1984),32 Springer Verlag, Berlin
5. A. Skutlartz et al., J. Phys.**B21**(1988)3609
6. D. Jakubassa , J. Phys.**B36**(2003)1971

X-ray study of the enhancement effect in radiative recombination of bare U^{92+} ions with low-energy electrons

M. Pajek, D. Banaś, M. Czarnota, Świętokrzyska Academy, 25-406 Kielce, Poland
Th. Stöhlker, H. F. Beyer, F. Bosch, C. Brandau, S. Chatterjee, A. Gumberidze, S. Hagmann, C. Kozhuharov, D. Liesen, P. H. Mokler, R. Reuschl, U. Spillmann, S. Tachenov, S. Trotsenko, P. Verma, GSI, Darmstadt, Germany
D. Sierpowski, A. Warczak, Jagiellonian University, Cracow, Poland
S. Böhm, A. Müller, E. W. Schmidt, Justus-Liebig Universität, Giessen, Germany
J.-Cl. Dousse, J. Szlachetko, University of Fribourg, Switzerland

The radiative recombination (RR) process has been studied extensively in the last years in ion storage rings, where ion beams are cooled by dense, equal-velocity electron beams in an electron cooler. The radiative recombination of high-Z bare ions with cooling electrons can be treated within the nonrelativistic dipole approximation (NDA) which is expected to be well-suited for low-energy electrons. However, the RR experiments performed at different heavy ion storage rings (TSR, CRYRING, ESR) revealed that the measured recombination rates exceed substantially the theoretical predictions for relative electron energies below the transverse electron beam temperature $kT_\perp$. This so-called "enhancement" effect is well evidenced experimentally for a number of bare ions up to U^{92+} [1]. Additionally, the influence of the magnetic guiding field and the longitudinal electron beam temperature $kT_\parallel << kT_\perp$ on the measured RR rates was observed [1, 2]. The RR for high-Z bare ions has also been studied in the context of spectroscopic x-ray measurements [3, 4].

In order to explain the enhancement effect an x-ray recombination experiment has been performed at the ESR storage ring allowing to study the RR enhancement in a state-selective way for the relative electron energy range 0-1000 meV. In this experiment uranium ions accelerated in the UNILAC/SIS complex, stripped to U^{92+} , stored and decelerated in the ESR to an energy of 23 MeV/amu were used. The x-rays emitted from RR between ions and electrons in the electron cooler, for fixed relative electron energies, were measured by two germanium detectors placed nearly at 0^o and 180^o with respect to the ion beam direction. This allowed to measure the photons originating from RR to low n-states, namely K-RR, L-RR, as well as the Lyman and Balmer x-ray photons from radiative cascades following the RR to high n-states. In this way the RR was studied in a state-selective manner for a wide range of n-states, including high Rydberg states.

In the first part of the experiment performed in 2004 a dependence of the recombination enhancement on the electron detuning energy was investigated by selecting one value of the B-field (70 mT) and measuring the recombination rates for six off-cooling electron cooler voltage settings, corresponding to the relative electron energies of about $\pm$ 69 meV, $\pm$ 190 meV and $\pm$ 930 meV. The measurements were performed by changing the effective cooler voltage by modifying the electron cooler drift tubes voltage.

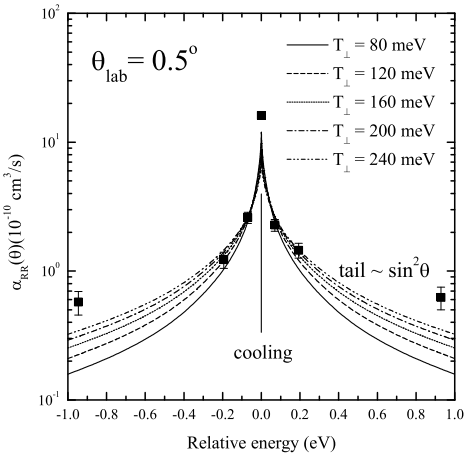


Figure 1: The measured K-RR recombination rate coefficient versus the relative electron energy. The data are normalized to the predictions of the NDA for $kT_\perp$=120 meV at E_{rel}=190 meV.

The measured dependence of the K-RR rates on the relative electron energies are compared with the nonrelativistic dipole approximation calculations in Fig. 1. This figure clearly demonstrates both the enhancement of the measured K-RR rates at zero relative energy (cooling condition) as well as the underestimation of the data by NDA calculations for higher electron energies. The latter observation suggest the importance of relativistic effects [5] to explain the measured K-RR rates at zero degree for higher detuning energies, due to strong suppression of the dipole term ($\sim \sin^2\theta$) for this direction. The calculations of relativistic RR rates are presently in progress.

References

[1] W. Shi *et al*. Eur. Phys. J. D 15, 145 (2001)
[2] G. Gwinner *et al.*, Phys. Rev. Lett. 84, 4822 (2000).
[3] H.F. Beyer *et al.*, Z. Phys. D 35, 169 (1995).
[4] A. Gumberidze *et al.*, Phys. Rev. Lett. 92, 203004-1 (2004).
[5] M. Pajek *et al.*, Proc. of ICPEAC-2005 (in press).

X-ray emission in few-electron heavy ion – atom collisions

S. Salem[1, 2], A. Bräuning-Demian[1], R.W. Dunford[3], F. Bosch[1], H. Bräuning[4], S. Chatterjee[1], S. Hagmann[5], C. Kozhuharov[1], D. Liesen[1], P.H. Mokler[1, 4], M. Nofal[1, 2], Z. Stachura[5], A. Warczak[6], A. Wilck[6]

[1]GSI, 64291 Darmstadt, Germany; [2]J. W. Goethe University, 40638 Frankfurt, Germany; [3]ANL, Argonne, Illinois 60439, USA; [4]Justus-Liebig University, D-35392 Giessen, Germany; [5]INP, Cracow, Poland; [6]Institute of Physics, Jagiellonian University, Cracow, Poland.

The interaction of few-electron heavy ions with atoms in solid state targets provides a tool to investigate fundamental processes which lead to the population of different excited states in projectiles under the influence of strong central fields, i.e. in highly charged ions with high nuclear charge number Z [1]. We concentrated our measurements on transition energies and identification of these transitions resulting from the decay of excited lead ions with only one, two or three incoming electrons.

The experiment has been performed using H-like (q=81+), He-like (80+) and Li-like (79+) ions produced by stripping the SIS beam at 113 MeV/u in a thick Al foil. The different charge states, magnetically selected from the emerging beam, were excited by collisions in a 105 μg/cm^2 Al foil. X-rays emitted by the projectile ions have been measured in coincidence with the projectile charge state. For this purpose three different photon detectors (two intrinsic Ge detectors and a Si(Li) detector) and a position sensitive particle detector have been used [2, 3]. The schematic experimental setup with top view is shown in Fig. 1. In order to correct for Doppler broadening one of the Ge detectors is segmented, i.e. it consists of 7 independent strips. The solid angles of the 7-fold Ge and the single Ge detectors were 0.231 sr and 0.217 sr, respectively.

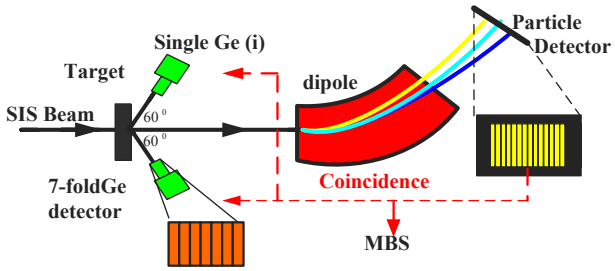


Figure 1:The experimental setup showing the Ge x-ray detectors, the magnet spectrometer and the particle detector [3].

Typical singles spectra, Doppler-corrected, recorded by the 7-fold Ge detector for Pb^{81+} , Pb^{80+} and Pb^{79+}- ions incident on the target are shown in Fig. 2. Depending on the incoming projectile charge state, different contributions of K and L x-rays can be observed. The L x-ray emission, referring mainly to electron capture to the higher projectile shells, are quite similar for all the spectra. For H-like projectiles the x-ray yields from the

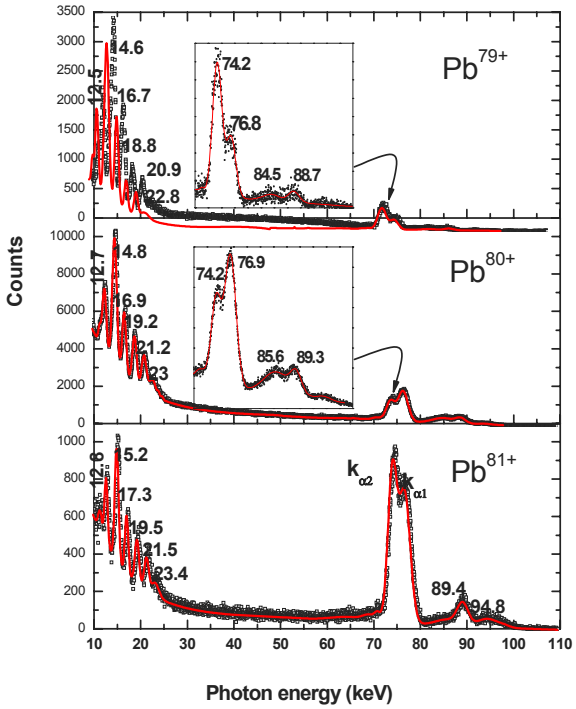


Figure 2: X-ray singles spectra in the emitter frame for 110 MeV/u Pb^{81+}, Pb^{80+} and Pb^{79+}- ions incident on an Al-target.

decay to the K and L states are comparable. In contrast to the L x-ray emission, the K_α yield changes considerably with the projectile charge state. This is true for both, the intensity compared to the L-shell and the relative intensity within the K_α doublet. This difference can be assigned to the different population mechanisms: in the case of Pb^{80+} mainly to ground-state excitation and in the case of Pb^{81+} preferentially to electron capture.
Presently, the aquired coincident x-ray / x-ray / particle spectra are analyzed for two-photon transitons in the heavy projectile [4].

References

[1] S. Fritzsche, et al., J. Phys. B38 (2005) S707-S726.
[2] H. W. Schäffer, in GSI-report Diss. 99-16, (1999).
[3] A. Braeuning-Demian, et al., GSI Report 2004, 219.
[4] P.H. Mokler, R.W. Dunford, Phys. Scr. 69, C1-9, (2004).

Deceleration of H-like uranium ions in a crystal

D. Dauvergne[1], A. Bräuning-Demian[2], F. Bosch[2], H. Bräuning[3], M. Chevallier[1], C. Cohen[4], A. Gumberidze[2], S. Hagmann[2], A. L'Hoir[4], C. Kozhuharov[2], D. Liesen[2], P.H. Mokler[2], J.-C. Poizat[1], C. Ray[1], J.-P. Rozet[4], Th. Stöhlker[2], E. Testa[1], M. Toulemonde[5] and P. Verma[2].

[1] IPNL, Villeurbanne, France, [2]GSI, Darmstadt, Germany, [3]JLU, Giessen, Germany, [4]GPS, Paris, France, [5]CIRIL, Caen, France.

Abstract

The E052 crystal channeling experiment has allowed us to decelerate U^{91+} ions from 12 MeV/u down to 9.5 MeV/u, with a fraction of frozen H-like transmitted ions of ~0.3 %.

Highly-charged, decelerated ions (below 20 MeV/u), such as H-like Pb or U ions, are very far from their equilibrium charge state in matter. They offer a unique opportunity to study ion-matter interaction in extreme perturbation regimes. In a random medium, highly charged ions capture electrons by means of the non-radiative capture MEC (Mechanical Electron Capture), the cross section of which is huge. In an aligned crystal, channeling, which leads to a redistribution of the ion flux inside the target, influences dramatically the charge exchange and energy loss conditions. In particular, ions traveling far from target atomic rows or planes experience a quasi-free electron gas, and electron capture can only occur by means of Radiative Electron Capture (REC).

Our previous studies with 20 MeV/u U^{91+} ions were devoted to detailed studies of the competition between these two processes as a function of the impact parameter [1,2,3]. We have also measured the very strong effect of the electron gas polarization induced by slow, highly-charged ions, which shifts the continuum energy levels by more than 100 eV at the ion position. This was observed by means of the REC photons emitted by channeled ions [4].

We have further focused our experiments on the energy loss by channeled highly-charged ions. Actually, ions keeping their very high charge q in matter have a very high energy loss rate, due to the q^2 dependence of the stopping force, although channeled ions experience a reduced electron density. We have shown that, below 15 MeV/u, H-like Pb or U ions lose more energy under channeling conditions than for a random incidence, where charge equilibrium is rapidly reached in thin targets [5]. During our last experience (May 2005) we have observed U^{91+} ions transmitted through a 18 µm thick silicon crystal under (110) planar channeling conditions (see figure 1). The energy loss of such ions amounts to 2.6 MeV/u, i.e. to more than 20% of their initial energy. The ions transmitted in random conditions emerge with the mean charge 65+, and their energy loss is 1.9 MeV/u. In <110> axial channeling conditions beam focusing problems prevented from distinguishing between the charge states. However, the fraction of transmitted H-like ions should be larger than for the planar case. Indeed, H-like transmitted ions in axial channeling conditions should have a smaller energy loss than for planar ones, which is compatible with the slight shift to the right side of the channeled component in fig.1.

We have thus demonstrated that thin crystals can be used efficiently to decelerate H-like ions below 10 MeV/u.

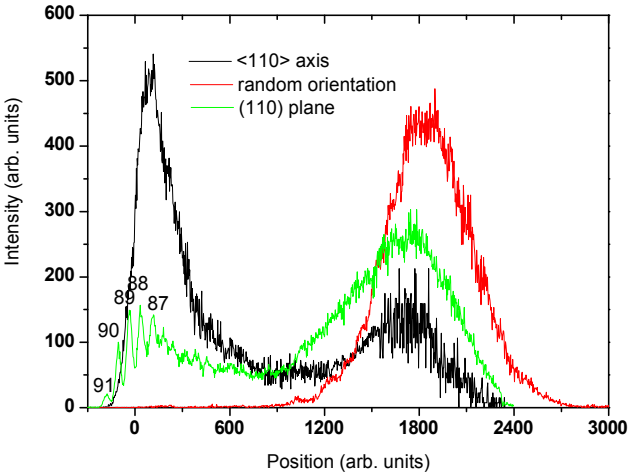


Figure 1: Charge state distributions of transmitted ions at the focal plane of Cave A, for 12 MeV/u U^{91+} incident ions, and for various orientations of an 18 µm thick Si crystal target.

References

[1] D. Dauvergne et al., Nucl. Instr. Meth. B205 (2003)773.

[2] D. Dauvergne et al., to be published in the Proceedings of the International Conference on the Physics of Electronic, Atomic and Photonic collisions, Rosario, Argentina, July 2005.

[3] E. Testa, thesis (Université Lyon 1, 2005)

[4] E.Testa et al., to be published in NIM B.

[5] D. Dauvergne et al., GSI Report 2004-1, p.108

Fragmentation of Acetylene in Collisions with 3.6 MeV/u Xe^{40+}-ions

U. Werner, Fakultät für Physik, Universität Bielefeld, Bielefeld, Germany
B. Siegmann, Institut für Physik, Universität Dortmund, Dortmund, Germany
R. Mann, GSI, Darmstadt, Germany

The multiple ionization and fragmentation of acetylene was studied in collisions with 3.6 MeV/u Xe^{40+} ions provided by the UNILAC at GSI. The fragmentation dynamics was studied using a position- and time-sensitive multiparticle detector [1] which allows the coincident measurement of the momenta of correlated fragment ions. If all fragment ions from a particular fragmentation are detected, a kinematically complete analysis of the molecular breakup is possible [2] and the released kinetic energies and several angular correlations can be derived.

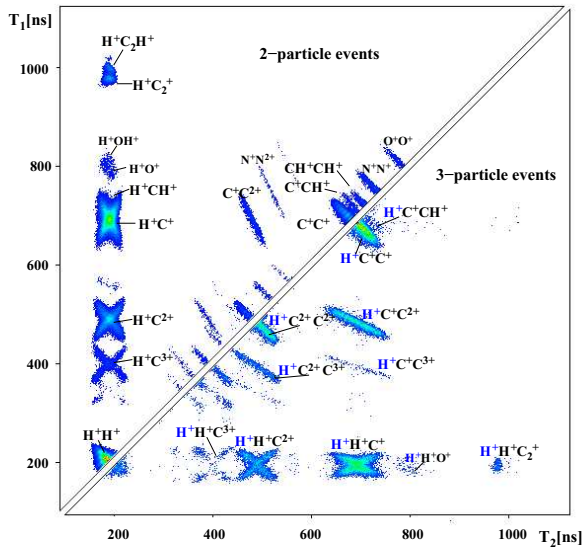


Figure 1: Coincidence maps of two- and three-particle events observed in collisions of 3.6 MeV/u Xe^{40+} with C_2H_2. The intensity increases from black towards light gray (blue towards red).

Fig. 1 gives an overview over the observed two- and three-particle coincidences. The measured intensity is shown as function of the flight times T_1 and T_2 of the fragments. In case of three particle events, it shows the flight times of the second and third fragment ions which were detected in coincidence with another H^+ ion. The applied coincidence mapping technique allows a detailed study of the characteristic fragmentation patterns [3]. In case of completely observed break-up processes, as e.g. $C_2H_2 \rightarrow CH^+ + CH^+$ or $C_2H_2 \rightarrow H^+ + C^+ + CH^+$, even more information can be derived from the measured momenta.

As an example Fig. 2 shows some results for the symmetric and asymmetric two-particle Coulomb fragmentations $C_2H_2 \rightarrow CH^+ + CH^+$ and $C_2H_2 \rightarrow H^+ + C_2H^+$.

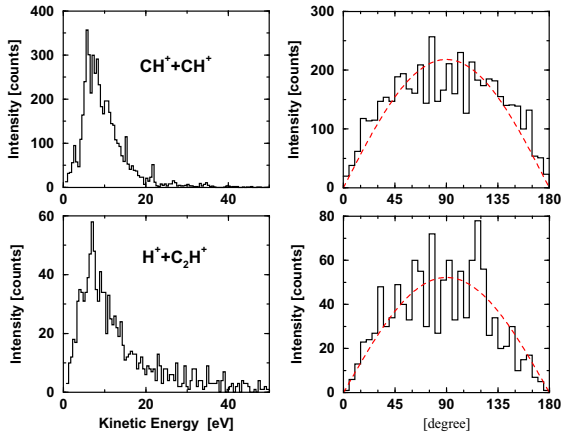


Figure 2: Total kinetic energy of coincident fragment ions: $CH^+ + CH^+$ (top) and $H^+ + C_2H^+$ (bottom). The right graphs show the corresponding dependences of the cross section on the orientation θ of the molecule axis; the dashed lines represent isotropic distributions.

The left graphs show the distributions of the total kinetic energy of both fragments. Apart from the narrower width of the symmetric process both spectra are rather similar with maxima around 7 eV.

By neglecting molecular vibrations acetylene may as a first approximation be considered as a linear molecule and the dependence of the cross sections on the orientation θ of the molecular axis with respect to the projectile beam may be studied. In this simple picture the fragment ions are driven apart by their mutual Coulomb repulsion along the molecular axis and the angle θ between the axis and the projectile beam can be derived from the velocity vectors of the fragment ions. The right graphs in Fig. 2 show the corresponding θ-distributions for the two-particle break-ups. As expected no significant orientation effects occur at this low degree of molecular ionization. Similar results were found for diatomic molecules [4].

References

[1] J. Becker, K. Beckord, U. Werner and H.O. Lutz, Nucl. Instrum. Methods **A 337**, 409 (1994).

[2] B. Siegmann U. Werner, H.O. Lutz, and R. Mann, J. Phy. B **35**, 3755 (2002)

[3] B. Siegmann U. Werner, and R. Mann, Nucl. Instr. and Meth. **B233**, 182 (2005)

[4] B. Siegmann, U. Werner, H. Lebius, B. Huber, H.O. Lutz, and R. Mann, Nucl. Instr. and Meth. **B205**, 629 (2003).

Status of the HITRAP Decelerator Project*

W. Barth[1], T. Beier[1], M. Bevcic[1], M. Block[1], K. Blaum[1,2], L. Dahl[1], S. Eliseev[1,3], H. Ernst[2], P. Forck[1], G. Gruber[1], S. Heinz[1], F. Herfurth[1], B. Hofmann[1,5], R. Kaminski[1], M. Kaiser[1], O. Kester[#1], H.-J. Kluge[1,4], C. Kozhuharov[1], S. Koszudowski[1,4], A. Krämer[1], G. Maero[1,4], F. Peldzinski[1], W. Quint[1,4], U. Ratzinger[5], H. Reich-Sprenger[1], A. Sauer[5], A. Schempp[3], T. Stöhlker[1,5], W. Vinzenz[1], M. Vogel[2], G. Vorobjev[1,3], C. Weber[1,2], G. Werth[2], H. Zimmermann[1,5]
[1]GSI, Darmstadt, Germany, [2]Universität Mainz, [3]St. Petersburg, [4]Universität Heidelberg, [5]Universität Frankfurt, [6]LMU München

The heavy ion trap facility (HITRAP) (fig.1) will provide unique beams of highly charged ions up to bare U at very low energies for a large variety of experiments. HITRAP will decelerate ions (e.g. U^{91+}) produced by the GSI accelerator facility at relativistic energies. The ions are first decelerated the ESR down to 4 MeV/u and further decelerated down to 6 keV/u in linear rf-accelerator structures [1]. Subsequently the highly charged ions will be injected into a long Penning trap for cooling [2]. The HITRAP decelerator linac employs a double drift buncher (DDB) for phase focusing, an interdigital H-type (IH) structure [3] and a 4-rod Radio Frequency Quadrupole (RFQ) [4]. At its low energy side a de-buncher will reduce the final energy spread in order to improve the injection efficiency into the cooler trap.

A complete beam dynamics calculation of the HITRAP decelerator from the ESR towards the RFQ has been performed. The beam dynamics design of the re-buncher, of the IH-structure and of the RFQ have been finalized. The lay-out of the cavity drift tube structures and the RFQ electrodes has been done. The DDB, which comprises two coaxial resonator structures, has been included in order to increase the efficiency of the matching of the phase spread of the ion bunch from the ESR into the phase acceptance of the IH-structure. 70% of the particles extracted from the ESR will be transmitted and decelerated. In order to improve the injection efficiency into the HITRAP cooler trap, a low-energy de-buncher has been designed and included into the RFQ set-up. The rf-design of all decelerator cavities, which comprises the cavity geometry, drift tube structure and the tuning plungers, has been completed. All geometry data of the IH-structure have been submitted to the GSI design office in order to finalize the cavity design drawings. The RFQ design and the low-energy de-buncher attached to the RFQ, will be performed by the manufacturer, based on a similar cavities built at the IAP Frankfurt. An order has been placed.

The infrastructure of HITRAP is presently being built up. The supply platform has been assembled in December 2005. The containers, which will house power supplies and electronics of the linac and of the experiments have been delivered and installed on the platform. The separation of the security control system of the re-injection channel from the ESR safety system is in preparation and the required hardware is ordered. Hence access to the HITRAP area in the re-injection channel will be possible while the ESR is in operation. The infrastructure for the linac and the experiment site is being prepared in order to provide all media for first tests of the DDB in 2006.

References

[1] O. Kester et al., *The HITRAP Decelerator Project at GSI*, Proc. of the HIAT 2005, 26-29. Sept. 2005 Port Jefferson, USA, to be published
[2] F. Herfurth et al., *Highly charged ions at rest: The HITRAP project at GSI*, AIP conference proceedings Vol. 793, 2005, p.278
[3] A. Sauer et al. *The HITRAP DTL*, this report
[4] B. Hofmann et al., *The HITRAP RFQ*, this report

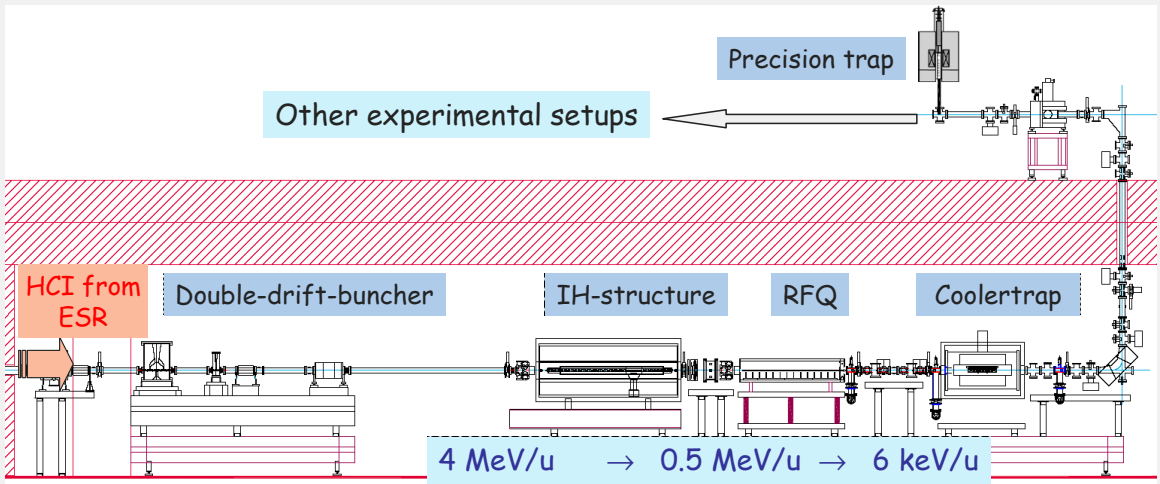


Figure 1: Overview of the HITRAP beam line.

*Work supported by the EU (HPRI-CT-2001-50036) an by the BMBF
#O.Kester@gsi.de

Status of the HITRAP DTL decelerator at GSI*

A. Sauer, U. Ratzinger, IAP, J.W. Goethe-Universität, Frankfurt/Main, Germany,

L. Dahl, O. Kester, H. Kluge, GSI, Darmstadt, Germany .

The heavy ion trap (HITRAP) linac will decelerate highly charged ions up to U^{92+}, provided by the GSI accelerator facility at 4 MeV/u down to 6 keV/u. The highly charged ions will subsequently be injected into a Penning trap for beam cooling. Therefore the HITRAP facility will provide unique pulsed beams of up to about 10^5 highly charged ions at very low energies for atomic physics experiments. The HITRAP decelerator LINAC consists of a double drift buncher (DDB) for phase focusing, an interdigital H-type (IH) structure and a 4-rod RFQ. The Drift Tube Linac (DTL) part of the decelerator section is tenor of this report. The deceleration stage from the ESR extraction energy of 4 MeV/u to 6 keV/u is done by an rf-linear accelerator [1]. Fig.1 gives an overview drawing of the HITRAP decelerator LINAC.

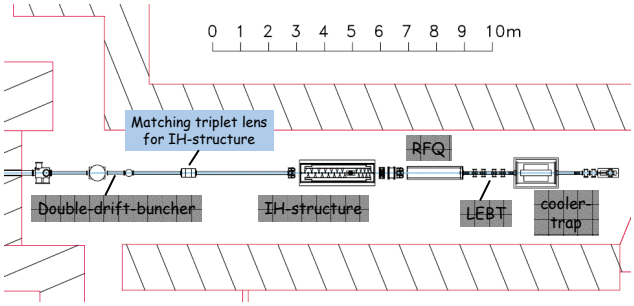


Fig. 1: Overview of the HITRAP decelerator LINAC structures including the cooler trap.

Table 1 summarizes the most important cavity parameters of the DDB and the IH resonator of HITRAP.

Table 1: Structure parameters of the HE part cavities of the HITRAP LINAC.

Parameters	Buncher		IH-DTL
P_{rf} [kW]	1.52	0.64	175.0
Z_{eff} [M /m]	64.8	42.1	285.0
f [MHz]	108.4	216.8	108.4
	0.092		0.092 - 0.035
Gaps	4	2	25
Length [m]	0.57	0.28	2.7

The DDB cavities are designed as coaxial quarter wave resonators with optimized shunt impedances and transit time factors. Fig 2 shows both cavities in a longitudinal 3D view calculated with Microwave Studio®. The subsequent IH-structure contains 25 gaps and one magnetic inner-tank-quadrupole triplet lens.

*Work supported by the EC under contract HPRI-CT-2001-50036 and by the BMBF

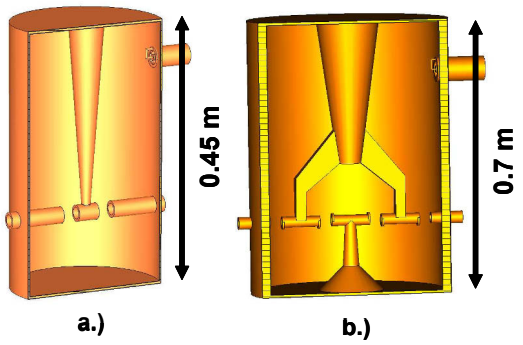


Fig. 2: Longitudinal 3D view of a.) 216 MHz 2-gap buncher; b.) 108 MHz 4-gap-buncher. The rf couplers are also shown.

Fig 3 gives a 3D sectional view of the HITRAP IH cavity with internal lens and rf coupler calculated with MWS®. Coupling and tuning of the cavities has been investigated and optimized for all cavities with MWS. Therefrom detailed geometry data of the cavities could be submitted to the GSI design office.

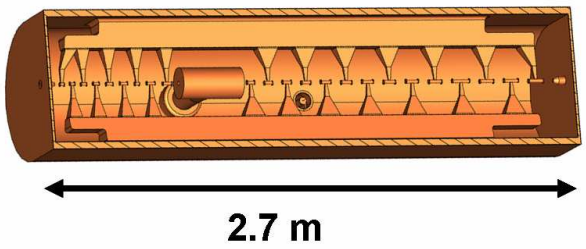


Fig. 3: 3D sectional view of the HITRAP IH-cavity with internal lens and rf coupler calculated with MWS®.

All cavities are now under mechanical design and first calls for tenders have been placed. Production of the buncher cavities will already start in the beginning of 2006. The magnetic quadrupole lens inside the IH-structure has been specified and will be ordered soon. The infrastructure for the LINAC and the experiment site is in preparation [2]. First power tests of the DDB's are planned in the middle of 2006. A beam test with beam from the ESR is prepared for fall 2006.

References

[1] C. Kitegi et al., "The IH-cavity for HITRAP", LINAC 2004, Lübeck, Germany.

[2] O. Kester et al., "The HITRAP Decelerator Project at GSI", HIAT Conference, October 2005, New York, USA.

The cooler Penning trap for the HITRAP project *

F. Herfurth[1,†], K. Blaum[1,2], S. Heinz[1], O. Kester[1], H.-J. Kluge[1,3], S. Koszudowski[1,3], G. Maero[1,3], D. Neidherr[2], W. Quint[1], S. Stahl[2] C. Weber[1]
[1]GSI Darmstadt; [2]University of Mainz; [3]University of Heidelberg

A decelerator will be installed at GSI in order to provide and study bare heavy nuclei or heavy nuclei with only few electrons at very low energies or almost at rest. Stripping at relativistic energies will produce highly charged ions. After electron cooling and deceleration in the Experimental Storage Ring the ions are extracted from the storage ring at 4 MeV/u and further decelerated in a combination of an IH and 4-rod RFQ structure. Finally, they are injected into a Penning trap where the ions are cooled to 4 K. From this trap, the ions can be transferred in a quasi-continuous or pulsed mode to different experimental setups [1].

The low energy beam line connects the radio-frequency quadrupole decelerator with the cooler trap. It provides the differential pumping to separate the extremely good vacuum required for the operation of the cooler trap from the standard high vacuum in the decelerator. Furthermore, the beam diagnosis and matching elements for injection into the strong magnetic field of the trap will be placed in this beam line. Presently the best choice seems to use electrostatic einzel lenses as described in [1].

The cooler trap finally captures the highly charged ions in flight and decreases their phase space volume by electron and resistive cooling. A cylindrical Penning trap in a magnetic field of 6 Tesla is used. The trap will consist of 23 electrodes that can be used to shape the electric potential very flexibly and to create five harmonic trap regions, three for ions and two for electrons (compare figure 1).

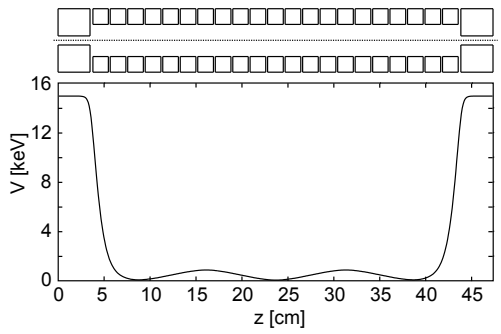


Figure 1: Schematics of the trap electrodes (top) and calculated potential on the axis of the cylindrical electrodes (bottom).

The first step is the in-flight capture. For this, the ion bunch with a pulse length of about 1 μs will be injected into the trapping region and decelerated further from 6 keV/u to approximately 2 keV/u while the ion beam is kept radially small by the strong magnetic field. The incoming bunch is reflected at the downstream trapping electrode and trapped by switching the upstream trapping electrode from the initial potential of $\approx$11 kV to about 18 kV just after injection of the ion bunch.

Then the HCI interact and thermalize with the simultaneously stored electrons. The electrons have a kinetic energy corresponding to 4 K since they emit synchrotron radiation during their storage in a high magnetic field and hence are in equilibrium with the surrounding that is cooled to 4K using a two stage closed cycle cryocooler. Since dielectronic recombination is not possible for bare ions and the electron densities are still to low for three-body recombination processes, only radiative recombination must be taken into account. Calculations show that more than 90% of the bare uranium ions sent initially into the trap remain in the original charge state within the projected cooling time of a few seconds [2].

After separation of electron and ion clouds the ions will be cooled further using resistive cooling. The ion cloud oscillating in the Penning trap induces image charges and hence an image current in the trap electrodes. If this signal is fed into a resonant circuit kept at 4 K, the signal will be damped in the circuit and consequently the ion motion is damped until it is in equilibrium with the environment of the circuit.

Two modes of extracting the cooled ion cloud are foreseen: slow extraction and bunched extraction. If extracted in a bunch, the scheme is very similar to existing trap facilities where up to 100 million singly charged ions are extracted in a 15 μs pulse. This mode is especially well suited for experiments where the ions need to be recaptured in a trap. In the slow extraction mode the stored ions will be ejected distributed over the 10 s that are available until the next decelerated ion bunch arrives. This mode is for example required by ion-surface interaction experiments in order to avoid detector saturation.

The cooler trap and low energy beam line are now under construction. The superconducting magnet has been ordered and many components have been designed. The cryogenic electronics has been specified and is in the design phase. After magnet delivery in the second half of 2006 commissioning will start off-line using medium-heavy, highly charged ions from the electron beam ion source MAXEBIS.

References

[1] F. Herfurth *et al.*, in: Y. Yamazaki, M. Wada (Eds.), Physics with ultra slow antiproton beams, AIP conference proceedings 793, 2005, pp. 278.

[2] J. Bernard *et al.*, Nucl. Instr. and Meth. A532 (2004) 224.

* Work supported by the HGF, the EC (HPRI-CT-2001-50036) and the BMBF

† F.Herfurth@gsi.de

The HITRAP RFQ

B. Hofmann#, A. Schempp, Universität Frankfurt, Germany
O. Kester, L. Dahl, H.-J. Kluge, GSI, Darmstadt, Germany

The HITRAP linac at GSI will decelerate ions from 4 MeV/u to 6 keV/u for experiments with highly charged ions at low energies [1]. The ions, provided by the GSI ESR, will be further decelerated via a drift tube LINAC down to an energy of 5oo keV/u. The following 4-Rod type RFQ will decelerate the ion beam from 500 keV/u to 6 keV/u (fig.1).

The design of the HITRAP 4-rod-RFQ is closely related to the design of the 108 MHz structure of the GSI-HLI LINAC, the high-charge state injector to the UNILAC. The low A/q allows a short structure of 143 cells that is only 1.9 m long. A maximum rod voltage of 78.5 kV is required. The mean aperture radius is about 4 mm which reduces the peak fields to safe values. The 45° phase spread of the ion bunches extracted from the IH-structure needs to be matched to the RFQ acceptance of 20°. Thus, in the matching section between IH-structure and RFQ an existing two gap 108 MHz spiral re-buncher from GSI will be installed. This cavity has been modified to the new synchronous particle velocity by changing its drift tubes. For this purpose Microwave Studio (MWS) calculations have been performed, which provide data for the new drift tube geometry. At 0.5 MeV/u the cell length $\beta\lambda/2$ is 45.3 mm and so is the distance between the two gap-centers.

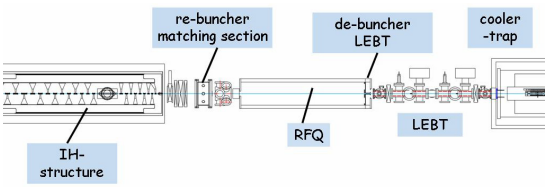


Fig. 1: Overview of the RFQ section of the HITRAP decelerator

Figure 2 shows a MWS simulation of the modified re-buncher cavity, where the thermal losses are shown in a colour code. With the MWS calculations, the power losses and the cavity frequency could be studied.

The modified spiral has been reinstalled in the cavity, the drift tubes have been exchanged. It is possible to cool the whole spiral arm, so that no thermal problems will occur. Frequency tuning of the cavity is being performed.

A de-buncher in the LEBT section is required in order to reduce the energy spread of the ion bunch coming from the RFQ from ±7% down to ±4%. A smaller energy spread of the ions is required for high injection efficiency into the HITRAP cooler trap.

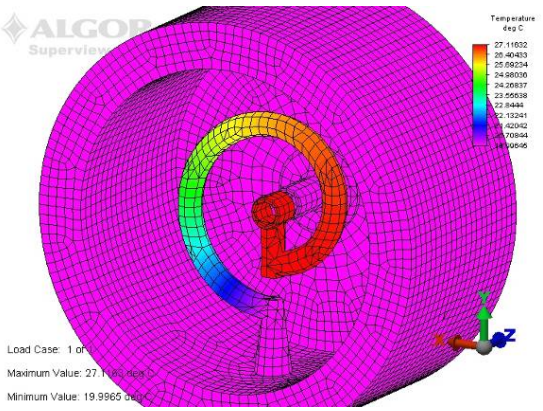


Fig. 2: thermal simulation of the re- buncher

Figure 3 shows the de-buncher cavity, which is directly mounted behind the RFQ so that both form a compact and short combined structure. Two copper plates ensure rf-separation of the cavities and the de-buncher can be used as first differential pumping stage towards the cooler trap.

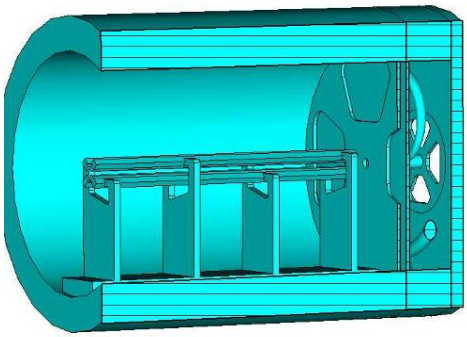


Fig. 3: Final section of the RFQ and the de-buncher cavity.

The modification of the re-buncher cavity will be finished in the first quarter of 2006, the vacuum tank of the RFQ and the electrode structure are ordered and will be assembled during 2006.

References

[1] O. Kester et al., *Status of the HITRAP decelerator project*, this report
[2] O. Kester et al., *The HITRAP Decelerator Project at GSI*, Proc. of the HIAT 2005, 26-29. Sept. 2005 Port Jefferson, USA

Chargebreeding with the MAXEBIS*

Holger Zimmermann[#1], R. Becker[3], O. Kester[2] M. Kleinod[3]

[1]Department für Physik, LMU München, Schellingstrasse 4, 80799 München
[2]GSI, Darmstadt, Planckstraße 1, 64291 Darmstadt, Germany
[3]J. W. Goethe-Universität Frankfurt, Max-von-Laue Straße 1, 60438 Frankfurt, Germany

The demand of exotic ions prior to their injection into an accelerator has driven the development of the charge breeding method. Existing facilities like REX-ISOLDE or ISAC at TRIUMF are already using a charge state booster for the post acceleration of radioactive ions. Planned facilities like MAFF, SPES, SPIRAL II and EURISOL have identified the need of a breeding system because of the demand for highly charged ions for low energy experiments and because of the available budget and space. Therefore the exploration and optimization of existing charge state breeders is mandatory and is supported by the I3-EURONS project.

Central part of the planed charge breeding experiments is the MAXEBIS [1]. The electron gun, the inner electrode structure and the collector of the MAXEBIS have been modified. The MAXEBIS is a cold source, the superconducting magnet can reach up to 5 T. The high current electron gun is based on a 2 mm IrCe cathode which can be driven to a maximum emission current density of about 95 A/cm^2. A new collector has been installed which can sustain 18 kW beam power. A small surface ion source has been designed, which will provide alkaline beams for the injection of the ions into the MAXEBIS. The full MAXEBIS set-up has been moved from Frankfurt to GSI, where the charge breeding measurements will be performed. The whole beamline is homed outside GSI at the Heckhalle.

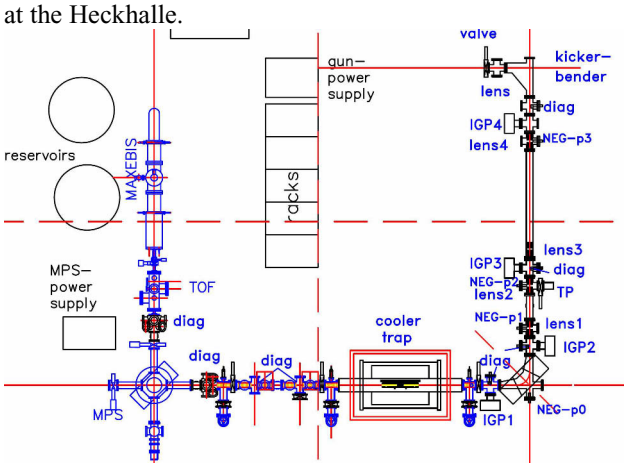


Fig. 1: Setup of the MAXEBIS for chargebreeding experiments and as the testinjector for the HITRAP cooler trap and RETRAP.

* supported by the EU, EURISOL-DS, RIDS 515768
#h.zimmermann@gsi.de

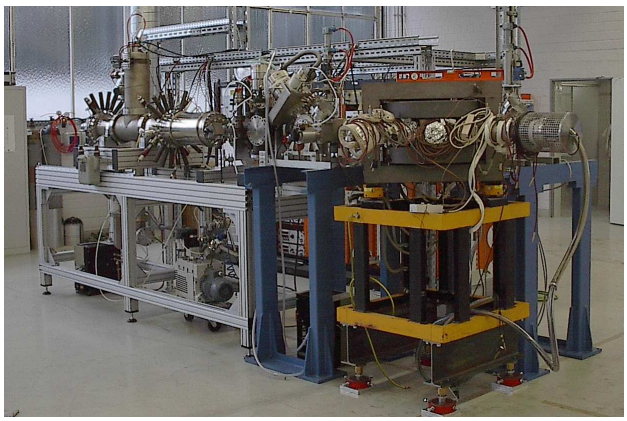


Fig.2: EBIS and diagnostic device mounted on a new rack.

For beam diagnostics we use a TOF spectrometer and a couple of faraday cups, which are mounted at both ends of the MPS (multi passage spectrometer) (Fig. 1,2).

In between the charge breeding measurement runs, the MAXEBIS will deliver highly charged ions for test of the HITRAP cooler trap and for atomic physics experiments in the RETRAP Penning trap, which will be installed at GSI within the next year.

First beam test in August 2005 demonstrated that the EBIS was not damaged after the transport from Frankfurt to GSI. These tests have been performed without baking of the system. A test of the electron gun, the collector and the superconducting solenoid was the first goal. The electron gun characteristics have been measured for the first time, at a 3 T field strength of the solenoid.

The electron beam current - gun voltage characteristic has been measured for different heating power to see the onset of the temperature limited regime. The measured perveance is 0.305 A/V$^{3/2}$. The calculation of the gun perveance via EGUN yields 0.33 A/V$^{3/2}$. The maximum electron current in the electron gun was 100 mA, which was only limited by the power supply [1]. The EBIS is now mounted on a new ITEM rack and a new electricity system is installed (Fig. 2). The next beam tests are planed for February 2006.

References

[1] O. Kester, R. Becker, M. Kleinod, H. Zimmermann, "The Frankfurt MAXEBIS Setup for Advanced Charge Breeding Experiments", to be published in Rev. Sci. In strum. 77 (2006)

Implementation of a sensitive, narrow-band Fourier-Transform Ion-Cyclotron-Resonance (FT-ICR) detection for short-lived radionuclides at SHIPTRAP*

R. Ferrer[1,#], K. Blaum[1,2], M. Block[2], J. Ketelaer[1], D. Neidherr[1], C. Weber[1,2],
and the SHIPTRAP collaboration
[1]Johannes Gutenberg-Universität, D-55099 Mainz.
[2]Gesellschaft für Schwerionenforschung mbH, D-64291 Darmstadt.

A very promising way towards establishing an accurate description of the inner structure of an atomic nucleus is the study of exotic nuclei. In the last few years a number of mass spectrometers based on Penning traps have been setup at rare isotopes facilities [1]. For instance SHIPTRAP at GSI is designed to provide clean and cooled beams of singly charged radioactive ions produced in a fusion-evaporation reaction and separated in-flight by the velocity filter SHIP. The scientific goals include mass spectrometry, atomic and nuclear spectroscopy, and chemistry of transuranium species which are not available at ISOL- or fragmentation facilities [2].

High precision Penning trap mass spectrometry on radionuclides was up to now only achieved with the destructive time-of-flight ion-cyclotron-resonance (TOF-ICR) detection method, which has established itself over the years to be the best choice for the investigation of short-lived nuclides. This detection scheme, however, is not applicable for exotic, transuranium nuclides with extremely low production rates, as investigated with the present SHIPTRAP setup. A sensitive single ion detection like the narrow-band Fourier Transform-ICR technique is ideally suited for the identification and characterization of these species.

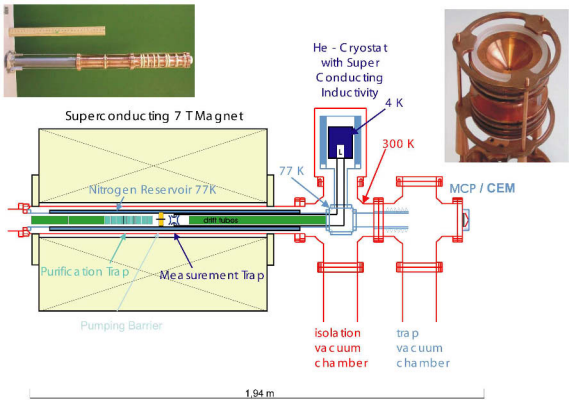


Figure 1. Cryogenic Penning trap setup for a non-destructive detection of image currents.

At the MATS group [3] at the University of Mainz in collaboration with GSI Darmstadt a cryogenic Penning-trap setup, as shown in Fig. 1, is currently build up and commissioned . It is foreseen to employ both the non-destructive ion detection as well as the TOF-ICR method.

* Work supported by the Association of Helmholtz Research Centers (contract VH-NG-037)

email: ferrer@uni-mainz.de

The setup consists of a cylindrical trap for isobaric cleaning under presence of a helium buffer gas at a pressure of $P_{PURIF.} = 10^{-4}$ mbar and a hyperbolical trap for the mass determination. Both traps are placed 20 cm apart from each other in a single superconducting magnet. In order to guarantee the required vacuum conditions of better than $P_{PREC.} = 10^{-8}$ mbar for a coherent ion motion while transient recording or excitation, they have to be separated by a pumping barrier. This barrier consists of a cylinder with a small diameter channel and it is fixed to the trap tube by pressuring a proper sealing. Different sealing materials as well as different diameters of the channel have been tested at room temperature and at 77 K.

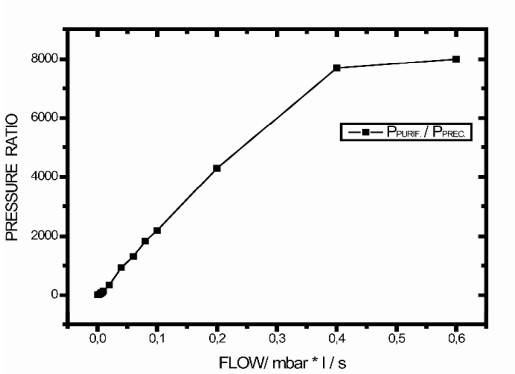


Figure 2. Differential pumping test through a 2 mm diameter and 50 mm long channel, sealed by a Viton ring at room temperature. $P_{PURIF.}$ / $P_{PREC.}$ represents the ratio between the pressure measured at the purification and the precision trap sides.

The measurements at room temperature show a differential pumping factor of 10^3 with a channel diameter of 2 mm, as can be seen in Fig. 2. According to calculations this factor is expected to be enhanced up to 10^4 by using a 1.5 mm channel. This will suppose an improvement of two orders of magnitudes compared to the current SHIPTRAP setup. At 77 K, indium has proven to be the best candidate to reproduce the differential pumping values achieved at room temperature. Further tests are in progress where commercial cryogenic sealings supported by springs will be employed.

References

[1] D. Lunney, *et al.*, Rev. Mod. Phys. **75,** 1021 (2003).
[2] M. Block, *et al.*, Eur. Phys. J. A. **25,** Suppl. 1, 49 (2005).
[3] http://www.quantum.physik.uni-mainz.de/mats/
[4] C. Weber, *et al.*, Eur. Phys. J. A. **25,** Suppl. 1, 65 (2005).

Efficiency improvement studies for ion-catcher devices*

J.B. Neumayr, D. Habs, S. Heinz, V.S. Kolhinen, M. Sewtz, J. Szerypo and P.G. Thirolf, LMU München, Germany and the SHIPTRAP collaboration

The ion-catcher device of SHIPTRAP at GSI presently provides a maximum overall stopping and extraction efficiency of 4-8% [1], thus allowing for mass measurements with reaction products from the SHIP facility [2]. In order to enable future measurements with ions having comparatively low production rates, optimisation efforts concerning the efficiency of the ion catcher are still going on at GSI, as well as at the MLL (Maier-Leibnitz-Laboratorium) in Garching. For these further studies the MLL-IonCatcher, a new and improved device, has been set up and characterised at the MLL [3].

The MLL-IonCatcher, schematically shown in Fig. 1, was designed by taking into account experiences with the SHIPTRAP buffer-gas cell. The stopping chamber has a length of 500 mm and a diameter of 200 mm. The extraction chamber is based on a DN150/DN200 cross and contains the RFQ ion guide with a length of 320 mm. In contrast to the almost perpendicular ion injection (relative to the extraction axis) at SHIPTRAP, the MLL-IonCatcher was designed for a parallel injection, resulting in a modified geometry of the stopping volume.

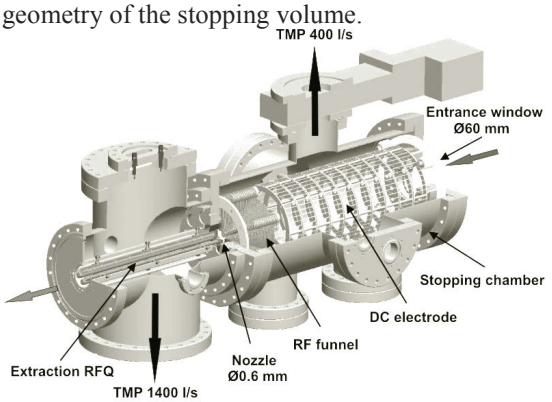


Figure 1: Schematic view of the MLL-IonCatcher.

While the nozzle was not changed and the RFQ and the DC electrode inside the cell were only adapted to the different sizes of the chambers, several changes were done at the RF funnel in order to achieve higher repulsive fields in the funnel region near the extraction nozzle. There the funnel of the MLL-IonCatcher consists of ring electrodes with a thickness/distance of 0.5 mm, while the first funnel of the SHIPTRAP gas cell (as described in [2]) consisted exclusively of electrodes with a thickness/distance of 1 mm. Presently these modifications were also inserted into the funnel geometry of the SHIPTRAP ion catcher. Like the SHIPTRAP buffer-gas cell, the MLL-IonCatcher was characterised at the MLL using the Munich test set-up [1], where for the tests ^{152}Er was produced via the reaction ^{121}Sb(^{35}Cl,4n). The number of injected and extracted ions was determined by the detection of the specific α-decay energy of ^{152}Er. The measurements were performed with gas pressures of 40-140 mbar and an entrance window (Ti) with a thickness of 3.5 μm. Inside the cell DC gradients of 2-4 V/cm were used and an RF voltage of 180-200 V_{pp} at 800 kHz was applied to the funnel. The extraction RFQ was operated with an RF voltage between 60-120 V_{pp} at 800-1100 kHz and a DC gradient of 0.2 V/cm. Fig. 2 shows exemplarily the overall efficiency as a function of the buffer-gas pressure. A common set of DC and RF voltages was used to find a relative optimum of the stopping efficiency. The maximum efficiency of ~10.5% for these parameters was reached in the range of 90-100 mbar. Compared to the measurements with the SHIPTRAP gas cell [1] the efficiency maximum was reached in a higher gas pressure region (90-100 mbar instead of 40-50 mbar), due to a thinner entrance foil (3.5 μm instead of 4 μm). Based on the optimum gas pressure of 100 mbar, the optimisation of all other operational parameters resulted in an overall efficiency of the set-up of about 16.4%±1.1%.

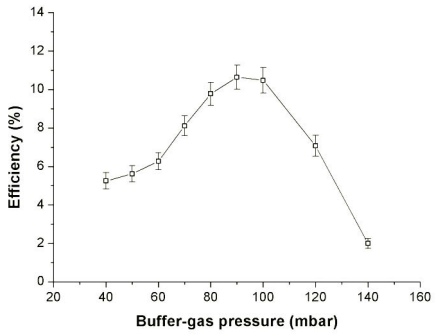


Figure 2: The overall stopping and extraction efficiency for ^{152}Er ions as a function of the buffer-gas pressure.

The efficiency improvement is also correlated with developments concerning the entrance window material. With the presently thinnest available metallic foil (Ti) in pinhole free quality (thickness 3.5 μm), transmission through the window is limited to energies of ≥180 keV/u (Z~80). However, experiments foreseen at SHIPTRAP will require the acceptance of recoil ion energies down to ~50 keV/u. Therefore presently tests of thin (1-3 μm) polyimide foils are performed, where pressure and temperature stability of these foils are studied as well as their impact on the purity of the UHV conditions. Further optimisation efforts will involve studying the effect of cryopanels inside the cell for the localisation of contaminations.

*Work supported by GSI F&E-LM-HA1 and EU-IONCATCHER-HPRI-CT-2001-50022

[1] J.B. Neumayr et al., Nucl. Instr. Meth. B in print.
[2] M. Block et al, this report.
[3] J.B. Neumayr et al., submitted to Rev. Sci. Instr.

Status of the g-factor experiment for highly charged calcium*

J. Alonso† [1,2], K. Blaum[1,2], S. Djekic[1,2], H.-J. Kluge[2], W. Quint[2], B. Schabinger[1], S. Stahl[1], J. Verdú[1], M. Vogel[2] and G. Werth[1]

[1] Institut für Physik, Johannes Gutenberg-Universität, 55099, Mainz, Germany

[2] GSI, Planckstraße 1, 64291, Darmstadt, Germany

The limb of the Standard Model which deals with the interaction between electrons and electromagnetic fields, quantum electrodynamics (QED), has been tested to an extremely high precision by means of different experiments. Perhaps the most outstanding agreement between theory and experiment is the result coming from the anomaly of the magnetic moment of the free electron [1], where the concordance was up to the 12^{th} digit. Also impressive are the 9 digits of agreement between the calculations of the *g*-factors of the electron bound to hydrogen-like carbon and oxygen ions and their corresponding measurements performed by the collaboration between GSI and the University of Mainz [2, 3]. In this case, bound-state quantum electrodynamics (BS-QED) is the subject of the tests, which can in addition lead to a more precise determination of fundamental constants such as the mass of the electron or the fine-structure constant α. Both, the relevance of the BS-QED tests and the precision of the determination of fundamental constants grow with the charge of the ions with which the experiments are performed.

Therefore, a new setup has been constructed [4] with which the *g*-factors of hydrogen- and lithium-like calcium ions are planned to be determined for two stable isotopes (masses 40 and 48). From proper comparison of these measurements, additional information can be obtained, e.g. BS-QED tests in the presence of electronic correlation effects or tests for the various methods employed in relativistic calculations of many-electron systems, as well as nuclear contributions to the magnetic moment (from the isotopic shifts in the *g*-factors).

The measurement process, described in [5], needs to be adapted to the higher charge of calcium ions when compared to carbon or oxygen ions, since the observation of the frequency jumps from which the magnetic moment is derived is more difficult. In that sense, mainly two techniques have been developed and tested. The first one, baptized as the 'three-dip method' [6], makes use of mode coupling of the ion motions in the Penning trap for simultaneous determination of two different frequencies. The second technique, the so-called phase sensitive detection, is based on the determination of the phase difference between two frequencies which lie very close to each other, rather than the direct measurement of both frequencies.

Another new challenge is the creation of the ions, i.e. the subsequent ionization. In our case, the ions will be produced inside the trap with a mini-electron beam ion source (EBIS), which can be driven with an energy up to 10 keV, enough to strip all electrons from the calcium atoms. The environmental requirements are very strict, $T = 4K$ and $p \sim 10^{-16}$ mbar. An FT-ICR (Fourier transform-ion cyclotron resonance) technique has also been implemented in order to be able to observe on-line the content of the trap, i.e. the different charge states of calcium. This tool enables the cross-section determination for electron impact ionization [7], which is only known for the noble gases and a few other elements in the periodic table.

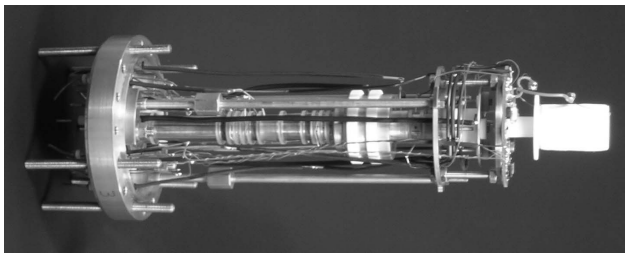


Figure 1: Details of the in-trap EBIS and a double-Penning-trap setup, which are located inside a vacuum chamber thermally connected to a liquid helium dewar in order to ensure the required vacuum and temperature conditions.

During 2005, the final assembly of the setup has been carried out. Figure 1 shows the trap setup inside the vacuum chamber, the heart of the experiment. Also part of the programming of the control system is finished. At the beginning of 2006, the setup has been closed and it will be soon cooled down to liquid helium temperature, to immediately start the creation of ions and the first test measurements. In the future at the HITRAP facility, the g-factor measurements will be performed up to the heaviest hydrogen-like ions, e.g. Pb^{81+} and U^{91+}, where the product of nuclear charge and the fine-structure constant ($Z\alpha$) approaches unity. This will provide a crucial test of QED calculations in extreme electromagnetic fields.

References

[1] V.M. Hughes and T. Kinoshita, Rev. Mod. Phys. **71**, 133 (1999).

[2] H. Häffner et al., Phys. Rev. Lett. **85**, 5308 (2000).

[3] J. Verdú et al., Phys. Rev. Lett. **92**, 093002 (2004).

[4] M. Vogel et al., Nucl. Instr. Meth. B **235**, 7-16 (2005).

[5] G. Werth et al., Nucl. Instr. Meth. B **205**, 1-8 (2003).

[6] J. Verdú et al., Physica Scripta **T112**, 68 (2004).

[7] J. Alonso et al., accepted for Rev. Sci. Instr. (2005).

* Work supported by the EU-Network HITRAP HPRI-CT-2001-50036, the BMBF, the DFG and the Helmholtz association (VH-NG-037)

† alonso@uni-mainz.de

The FOCAL Spectrometer for Accurate X-Ray Spectroscopy of Fast Heavy Ions

S. Chatterjee[1], H. F. Beyer[1], D. Liesen[1], Th. Stöhlker[1], A. Gumberidze[1], A. Simionovici[2], A. Warczak[3], B. Manil[4], D. Banas[5], D. Sierpowski[3], D. Protic[6], E. Förster[7], E. Ziegler[8], I. Mohos[6], J. Hoszowska[8], M. Trassinelli[9], O. Wehrhan[7], P. Indelicato[9], R. Reuschl[1], S. Tashenov[1], S. Trotsenko[1], Th. Krings[6], U. Spillmann[1], X. Ma[10], Z. Stachura[3]

[1]GSI, Darmstadt, Germany; [2]ENS, Lyon, France; [3]Institute of Physics Jagiellonian University, Cracow, Poland; [4]CIRIL-GANIL, rue Claude Bloche, Caen, France; [5]Institute of Physics, Swietokrzyska Academy, Kielce, Poland; [6]FZ Jülich, Institut für Kernphysik, Germany; [7]Inst. für Optik und Quantenelektronik, F. Schiller-Universität, Jena, Germany; [8]ESRF, Grenoble, France; [9]Lab. Kastler Brossel, Universite' P. Et M.Curie Paris Cedex 05, France; [10]Institute of Modern Physics, Lanzhou, China

A system of two crystal spectrometers has been completed for accurate wavelength measurements of hard x-rays emitted by heavy ions in flight. The configuration is working in the FOcusing Compensated Asymmetric Laue (FOCAL) mode along with high performance two-dimensional position sensitive micro-strip Ge detectors. Recent tests of the spectrometer have been performed securing quantitatively spectral resolving power and efficiency predicted by numerical simulations [1,2,3].

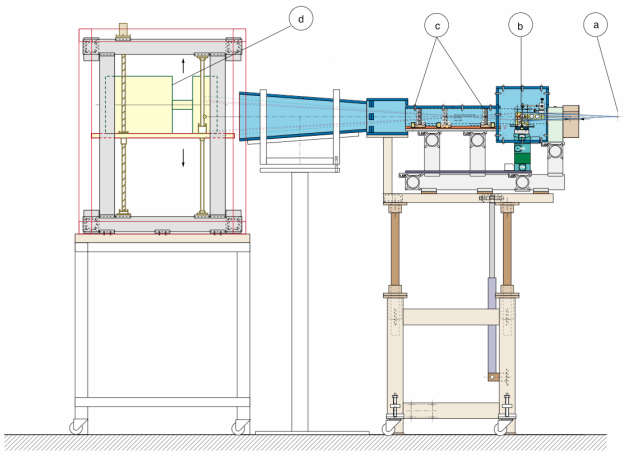


Fig. 1. The FOCAL spectrometer along with a detector stage on the left hand side. (a) is the position of the x-ray source, (b) the crystal part, (c) the slit assembly and (d) the detector. Each of the two spectrometers is approximately 3.2 m long.

Preliminary results have been obtained by mounting the micro-strip detector at the FOCAL test set-up. To investigate the position sensitivity of the detector, we have shifted the detector in steps of 50 µm and observed the centroid of the peaks from a radioactive ^{169}Yb source. The measurements of the Yb- Kα_2 line are shown in Fig. 2 and Fig. 3. The position of the line centroid shows a linear variation with the position of the detector. Therefore the consistency in all cases proves that the center of gravity of the lines observed can be determined with an accuracy better than 50 µm [4].

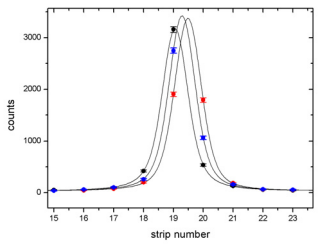


Fig. 2. The detector has been shifted in steps of 50 µm and the center of gravity of Yb- Kα_2 line was observed.

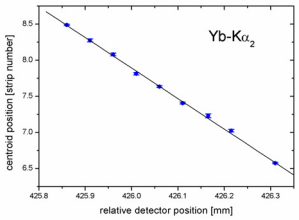


Fig. 3. The position (strip number) of the peak-centroid of Yb-Kα_2 is plotted as a function of the relative detector position.

The FOCAL spectrometer has been successfully tested reaching nearly all of its design goals. Important improvements are the boosted detection efficiency over other spectrometers, sufficiently high energy resolution and negligible Doppler broadening. Both the crystal optics and the two-dimensional position sensitive detector enable us to map complicated two dimensional intensity patterns on the detector plane.

This project is supported by a Marie Curie Fellowship of the European Community programme IHP under contract number HPMT-CT-2000-00197 and I3 EURONS under EC contract number 506065.

References

[1] H.F.Beyer, NIM A 400 (1997) 137.
[2] H.F.Beyer et al., Spectrochimica Acta Part B 59 (2004) 1535.
[3] D. Protic et al., IEEE Trans. Instr. Meas. 48 (2001) 1048.
[4] S. Chatterjee et al., to be published in NIM B.

Hyperfine Splitting in Heavy Ions with the Nuclear Magnetization Distribution Determined from Experiments on Muonic Atoms*

A.A. Elizarov, V.M. Shabaev†, N.S. Oreshkina, I.I. Tupitsyn, St. Petersburg State University, Russia
Th. Stöhlker, GSI Darmstadt, Germany

Abstract

The hyperfine splitting in hydrogenlike ^{209}Bi, ^{203}Tl, and ^{205}Tl is calculated with the nuclear magnetization determined from experimental data on the hyperfine splitting in the corresponding muonic atoms. The QED corrections are taken into account for both electronic and muonic atoms. The obtained results are compared with other calculations and with experiment.

High-precision measurements of the hyperfine splitting (HFS) in heavy hydrogenlike ions [1, 2] have triggered a great interest in calculations of this effect. The main goal of these experiments was to probe the magnetic sector of quantum electrodynamics (QED) in the presence of a strong Coulomb field. The uncertainty of the theoretical results is mainly determined by the uncertainty of the nuclear magnetization distribution correction, the Bohr-Weisskopf (BW) effect. In calculations [3, 4, 5] based on the single-particle nuclear model, which provide a reasonable agreement with the experiments, this uncertainty may amount up to about 100% of the BW effect and is generally few times larger than the total QED contribution. More elaborated calculations [6, 7] based on many-particle nuclear models, do not provide a desirable agreement with the experiments.

In the present work, we determine the BW correction to the hyperfine splitting of hydrogenlike ^{209}Bi, ^{203}Tl, and ^{205}Tl using experimental data on the hyperfine splitting in the corresponding muonic atoms. We consider the single-particle and configuration-mixing nuclear models. The parameters of the nuclear magnetization distribution are chosen to reproduce the experimental values of the nuclear magnetic moment as well as the BW contribution in muonic atoms extracted from the corresponding experiments. To increase the precision of the determination of the BW contribution, the QED corrections for the muonic atoms have been evaluated.

In Table 1 we compare our final theoretical results for the HFS in electronic hydrogenlike ions with previous ones and with experiment. Our results include the BW correction derived in the present work and the QED correction, which has been calculated by many authors (see, e.g., Ref. [8] and references therein). As one can see from the table, our results are closer to the experimental ones as compared to the results based on the direct calculations within the single-particle nuclear model. They are also stable enough with respect to a change of the nuclear model and have a better accuracy than the previous single-particle results. However, due to a higher accuracy of the present results, a small discrepancy between the theory and experiment occurs for ^{209}Bi^{82+}. The reason for this discrepancy is unclear to us.

For details we refer to Ref. [9].

Table 1: Ground-state hyperfine splitting in H-like ions, in eV.

	^{209}Bi^{82+}	^{205}Tl^{80+}	^{203}Tl^{80+}
This work [9]	5.098(7)	3.238(9)	3.220(20)
Shabaev et al. [5]	5.100(27)	3.261(18)	3.229(17)
Tomaselli et al. [6]	5.054(7)		
Sen'kov and Dmitriev [7]	$5.111\binom{+20}{-3}$		
Experiment [1, 2]	5.0840(8)	3.24410(29)	3.21351(25)

References

[1] I. Klaft, S. Borneis, T. Engel, B. Fricke, G. Grieser, G. Huber, T. Kühl, D. Marx, R. Neumann, S. Schröder, P. Seelig, L. Völker, Phys. Rev. Lett. 74 (1994) 2425.

[2] P. Beiersdorfer, S.B. Utter, K.L. Wong, J.R. Crespo Lopez-Urrutia, J.A. Britten, H. Chen, C.L. Harris, R.S. Thoe, D.B. Thorm, E. Träbert, M.G.H. Gustavsson, C. Forssén, and A.-M. Mårtensson-Pendrill, Phys. Rev. A 64 (2001) 032506.

[3] V.M. Shabaev, J. Phys. B 27 (1994) 5825.

[4] L.N. Labzowsky, W.R. Johnson, G. Soff, and S.M. Schneider, Phys. Rev. A 51 (1995) 4597.

[5] V.M. Shabaev, M. Tomaselli, T. Kühl, A.N. Artemyev, and V.A. Yerokhin, Phys. Rev. A 56 (1997) R2499.

[6] M. Tomaselli, S.M. Schneider, E. Kankeleit, and T. Kühl, Phys. Rev. C 51 (1995) 2989.

[7] R.A. Sen'kov and V.F. Dmitriev, Nucl. Phys. A 706 (2002) 351.

[8] A.N. Artemyev, V.M. Shabaev, G. Plunien, G. Soff, and V.A. Yerokhin, Phys Rev. A 63 (2001) 062604.

[9] A.A. Elizarov, V.M. Shabaev, N.S. Oreshkina, I.I. Tupitsyn, and Th. Stöhlker, Opt. Spectr. 100 (2006) 184.

* Work supported by INTAS-GSI (Grant No. 03-54-3604).

† shabaev@pcqnt1.phys.spbu.ru

Electron angular and energy distributions in relativistic ion–atom collisions

Stephan Fritzsche*, University of Kassel, Germany
Andrey Surzhykov, MPI–K, Heidelberg, Germany
Thomas Stöhlker, GSI-Darmstadt, Germany

Abstract

The projectile ionization of high–Z, hydrogen–like ions has been studied within the framework of first–order perturbation theory, based on Dirac's equation. In these studies, emphasis was placed on the energy distribution of the emitted electrons as observed within the laboratory frame.

For many years, first–order perturbation theory has been applied in order to analyze the excitation and ionization of high–Z projectiles in collision with light target materials [1]. At storage rings, these processes are of particular interest since the ionization of the projectiles leads to a loss of the ions from the beam. Apart from the *total* ionization cross sections, which were often found in good agreement with first–order computations, however, further details about the ionization mechanism can be obtained by studying the *angular* and/or *energy* distribution of the emitted electrons. For the energy distributions, for example, a clear deviation from theoretical predictions [1] were observed by Vane *et al.* [2] in collisions of 160 GeV/u hydrogen–like Pb^{81+} ions with an atomic Al target. Since up to the present this 'discrepancy' between the relativistic theory and experiment has not been resolved, computation of the *differential* ionization cross sections became desirable and have been carried out by us during the last few years [3].

For fast collisions, of course, the semi–classical approximation (SCA) is appropriate to describe the motion of the projectile along a straight–line trajectory with well–defined impact parameter b. In this approximation, an ionization of the projectile in the field of target atom may happen owing to the Liénard–Wiechert vector potential. From the first–order amplitudes $A_{fi}(b; \mu_i, m_s)$ of this potential, the angle and/or energy–differential electron-emission cross sections are obtained [3]

$$\frac{\mathrm{d}^2\sigma_{fi}}{\mathrm{d}\Omega_f \mathrm{d}E_f} = \frac{2\pi}{2j_i+1} \sum_{\mu_i\, m_s} \int_0^\infty \mathrm{d}b\, b\, |A_{fi}(b;\, \mu_i, m_s)|^2 \quad (1)$$

by integrating over all the impact parameters as well as by performing the average over the initial magnetic projections μ_i of the ionic bound states together with the summation over the spin states m_s of the emitted electron. In the laboratory frame any analysis of the energy and angular distribution of the emitted electrons can be traced back always to the *accurate* computation of the double–differential (ionization) cross section (1) in the rest frame of the projectile ions.

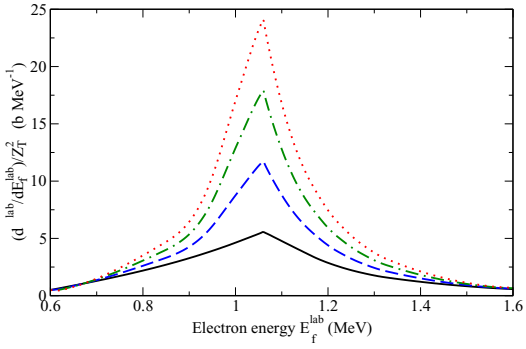


Figure 1: Energy–differential cross section for the ionization of hydrogen–like uranium ions U^{91+} as function of the energy of the emitted electron and with 0 % (—), 10 % (– –), 20 % (– - –) and 30 % (- - -) relative population of the excited $2s_{1/2}$ state. Results are presented in the laboratory frame.

To explore the above mentioned discrepancy from above, detailed computations have been carried for various high–Z ions and for different initial bound states. For relativistic U^{91+} ions, for instance, a small partial population of the excited $2s_{1/2}$ state results in a much narrower energy spectrum of the emitted electrons than obtained for the case of a pure K–shell ionization. In Figure 1, the single–differential cross sections are shown for the ionization of U^{91+} ions with energy T_p = 1 GeV/u, assuming various fractions of the projectile electrons to be initially excited into the $2s_{1/2}$ subshell. Apart from a pure ground state population (—), i.e. 100 % in the $1s_{1/2}$ shell, here we assume that 10 % (– –), 20 % (– - –), or even 30 % (- - -) of the projectiles are given in the $2s_{1/2}$ excited shell. As seen from this figure such an initial excitation of the projectile electrons into the $2s_{1/2}$ excited state may help explain the observations by Vane *et al.* [2] in the future.

References

[1] A. Voitkiv, Physics Reports **392** (2004) 191.

[2] C.R. Vane *et al.*, *Proc. 21st Int. Conf. of the Physics of Electronic and Atomic Collisions (Sendai, Japan)* (New York: AIP, 2000) 709.

[3] Surzhykov A and Fritzsche S, JPB **38** (2005) 2711.

* s.fritzsche@physik.uni-kassel.de

Kα_1 decay of helium–like uranium ions following radiative electron capture

Andrey Surzhykov* and Ulrich D. Jentschura, MPI–K, Heidelberg, Germany
Thomas Stöhlker, GSI-Darmstadt, Germany
Stephan Fritzsche, University of Kassel, Germany

Studies of the charge transfer in relativistic ion–atom collisions have a long tradition at the GSI storage ring [1]. In the radiative electron capture (REC), for example, a free (or quasi–free) electron is captured into a bound state of the projectile ion, accompanied by the simultaneous emission of a recombination photon. The angular and polarization properties of such photons have been explored in a number of experiments and have revealed important information on the dynamics of the electron capture in the presence of strong electromagnetic fields [1]. Apart from measuring the direct recombination photons, recent studies have also focused on the subsequent radiative decay which follows REC into excited ionic states. Several experiments have been performed, for example, to investigate the electron capture into the $1s_{1/2}2p_{3/2}\,{}^{1,3}P_{J=1,2}$ states of (initially) hydrogen–like U^{91+} uranium ions and its subsequent Kα_1 ($^{1,3}P_{J=1,2} \rightarrow {}^1S_{J=0}$) decay [2]. This bound–bound transition gave rise to an almost *isotropic* angular distribution of the characteristic radiation, quite in contrast to expectations from a "one–electron" model where the Lyman–α_1 ($2p_{3/2} \rightarrow 1s_{1/2}$) decay following REC into (initially) bare ions exhibits a strong angular dependence [1]. Although a qualitative explanation of such a 'discrepancy' has been recently proposed [3], a detailed theoretical analysis of the radiative transitions in helium–like heavy ions is required including a careful treatment of many–electron effects.

In this contribution, we apply the density matrix theory to investigate the angular distribution of the characteristic $K\alpha_1$ radiation following REC into the $1s\,2p_{3/2}\,{}^{1,3}P_{1,2}$ levels of (initially) hydrogen–like uranium ions. Within the density matrix approach, the population of the excited ionic states and their subsequent decay are treated as two independent steps, well separated in time. In the first step, radiative electron capture usually leads to an alignment of the resulting (excited) ion which is described by means of so–called alignment parameters $\mathcal{A}_k$. The properties of the decay photons, which are emitted in the second step, are then closely related to these alignment parameters. For instance, the angular distributions of the $1s\,2p_{3/2}\,{}^1P_1 \rightarrow 1s^2\,{}^1S_0$ electric dipole (E1) and $1s\,2p_{3/2}\,{}^3P_2 \rightarrow 1s^2\,{}^1S_0$ magnetic quadrupole (M2) transitions are given by:

$$W_{E1}(\theta) \sim 1 + 1/\sqrt{2}\;\mathcal{A}_2(J=1)\,\mathrm{P}_2(\cos\theta) \qquad (1)$$

and

$$W_{M2}(\theta) \sim 1 - \sqrt{5/14}\;\mathcal{A}_2(J=2)\,\mathrm{P}_2(\cos\theta)\,, \qquad (2)$$

where θ is the angle between the directions of the decay photon and the beam while $\mathcal{A}_2(J=1,2)$ refer to the alignment parameters of the $^1P_1$ and $^3P_2$ levels. Apart from the second–rank parameter $\mathcal{A}_2$, the alignment of the $^3P_2$ level is also described by the forth–rank parameter $\mathcal{A}_4$. For the REC into fast, high–Z projectiles, however, this parameter appears to be very small and, therefore, its contribution to the angular distribution of the decay photons can be neglected in expression (2).

* Electronic address: surz@mpi-hd.mpg.de

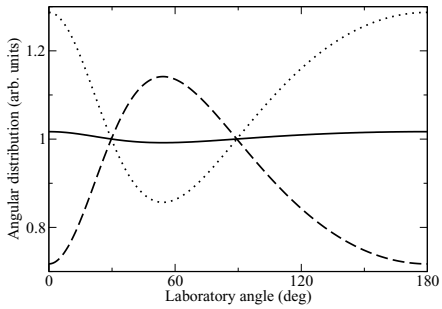


Figure 1: Angular distributions of the $^1P_{J=1} \rightarrow {}^1S_{J=0}$ (dashed line) and $^3P_{J=2} \rightarrow {}^1S_{J=0}$ (dotted line) transitions as well as their superposition (solid line) following REC into the $1s\,2p_{3/2}\,{}^{1,3}P_{J=1,2}$ states of (initially) hydrogen–like uranium ions with energy T_p = 217 MeV/u.

As seen from Eqs. (1) and (2), the angular dependence of the subsequent photon emission results from the Legendre polynomials $P_2(\cos\theta)$ weighted by the alignment parameters $\mathcal{A}_2$ and some geometrical factors which arise with the different signs for the decay of the $^1P_1$ and $^3P_2$ states. Therefore, as long as the $^1P_1 \rightarrow {}^1S_0$ and $^3P_2 \rightarrow {}^1S_0$ transitions are *not resolved* experimentally, their – measured – superposition (Kα_1 line) may exhibit an isotropic behaviour even if the individual components of this line are strongly anisotropic. Of course, a more detailed analysis of the angular dependence of the Kα_1 radiation requires the computation of the alignment as well as the relative populations of the $^{1,3}P_{1,2}$ exited states. We have performed these calculations within the Multiconfiguration Dirac–Fock (MCDF) approach for the different energies of projectile ions. In Fig. 1, for example, the angular distribution of the Kα_1 decay (solid line) is displayed for the collision energy T_p = 217 MeV/u, indicating an almost isotropic behaviour.

References

[1] Th. Stöhlker *et al.*, Phys. Scr. **T110** (2004) 384.

[2] A. Gumberidze *et al.*, Hyperfi ne Inter. **146/147** (2003) 133.

[3] E. G. Drukarev, GSI report 2005–1 (2005) APHY–THE–04.

Correlated double-electron capture with emission of a single photon

A.I. Mikhailov, I.A. Mikhailov, PNPI, St. Petersburg, Russia
A.V. Nefiodov and G. Plunien, Institut für Theoretische Physik, TU Dresden, Germany

Double photoionization of an atom caused by the absorption of a single photon, the so-called double photoeffect, is a fundamental phenomenon, in which correlation effects play a crucial role. Since the photon interacts only with a single electron, the simultaneous ejection of two electrons is exclusively caused by the electron-electron interaction. So far experiments have been performed with helium and a few neutral atoms in the region of moderate values of the nuclear charge number Z.

In contrast to neutral atoms, the study of the double photoeffect in multicharged ions is of particular interest. The photoionization processes on the simplest many-electron systems such as heliumlike ions allow for a rigorous treatment within the framework of QED perturbation theory. This problem could also serve as a testing ground for numerous theoretical approaches developed recently for the description of the complete photofragmentation of helium. An experimental study of the double photoeffect via the time-reversed process has been undertaken in fast collisions of bare ions with light target atoms [1, 2, 3]. However, several measurements, which have been performed at GSI, have provided only upper limits for the total cross sections of the process under investigation. The advantage of studying of the double photoeffect via its time-reversed version utilizing beams of multicharged ions is that it opens the possibility to investigate the process involving excited electron states.

We have investigated the correlated double-electron capture into the inner shells of a bare ion with the emission of a single photon [4, 5]. The total cross section for the correlated double-electron capture into the K shell of a bare ion can be expressed as

$$\sigma^{(2)}_{1^1S} = \sigma_0 \frac{2^{19} Z_{\rm t}^3}{3\mathcal{V} Z^5}\, Q(\xi), \qquad (1)$$

where $Z_{\rm t}$ is the nuclear charge number for the target atom, $\mathcal{V}$ is the normalization volume, Z is the charge of the incoming bare nucleus, $\sigma_0 = \alpha^3 a_0^2$, α is the fine-structure constant, and a_0 denotes the Bohr radius. The dimensionless variable ξ^{-1} is just the momentum of the captured electron calibrated in units of the characteristic momentum of the K-shell electron. Within the dipole approximation, Q is a universal function, which can only be obtained by numerical integration [4]. In the case of fast collisions ($\xi \ll 1$), the cross section (1) decreases rapidly. In the direct double photoeffect, it would correspond to the emission of both electrons with equal-energy sharing due to absorption of a high-energy photon. For slow collisions ($\xi \gg 1$), the cross section $\sigma^{(2)}$ significantly increases. The main uncertainty in the calculations of the absolute value of the total cross section appears due to the normalization volume $\mathcal{V}$, which to some extent can be chosen arbitrarily.

We have also performed calculations of the total cross section $\sigma^{(2)}_{2^1S}$ for the capture into the excited 2^1S state, which exhibits again the universal behavior similar to Eq. (1). To circumvent the ambiguity associated with the uncertainties in the description of the initial state, it is worthwhile to study the ratio $\sigma^{(2)}_{2^1S}/\sigma^{(2)}_{1^1S}$ of the cross sections for the correlated double-electron capture into the 2^1S and 1^1S states, respectively (see Fig. 1). Due to the cancelation of the normalization volume, evaluation of the ratio seems to be much more reliable.

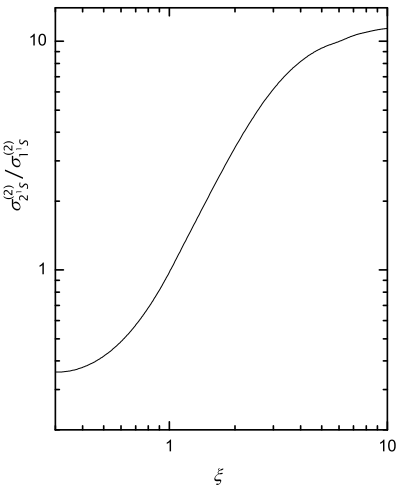


Figure 1: Universal ratio of total cross sections for capture into the excited 2^1S and the 1^1S state, respectively.

In fast collisions of ion beams with light target atoms, the correlated double-electron capture represents a charge-exchange channel, which turns out to be rather exotic. As we have shown, the total cross section of the process increases rapidly in the low-energy regime. In addition, the formation of the excited 2^1S heliumlike state can be much more probable than the 1^1S state.

This work has been supported partly by INTAS-GSI (Grant No. 03-54-3604).

References

[1] A. Warczak, *et al.,* Nucl. Instr. Meth. B **98** (1995) 303.

[2] G. Bednarz, *et al.,* Phys. Scr. T **92** (2001) 429.

[3] G. Bednarz, *et al.,* Nucl. Instr. Meth. B **205** (2003) 573.

[4] A.I. Mikhailov, *et al.,* Phys. Lett. A **328** (2004) 350.

[5] A.V. Nefi odov, *et al.,* Phys. Lett. A **346** (2005) 158.

Quantum interference between nuclear excitation by electron capture and radiative recombination

A. Pálffy, W. Scheid, Institut für Theoretische Physik, Justus-Liebig-Universität, Giessen
Z. Harman, Max-Planck-Institut für Kernphysik, Heidelberg

Experimental observations of atomic physics processes with regard to the internal structure of the nucleus have been reported, such as the bound-state internal conversion [1] and the nuclear excitation by electron transition (NEET) [2]. Closely related to NEET is the nuclear excitation by electron capture (NEEC). It is a resonant process in which a free electron is captured into an atomic shell with the simultaneous excitation of the nucleus. This is followed by a radiative nuclear decay.

Theoretical calculations of the NEEC occurring in scattering measurements are particularly useful in finding candidate isotopes and transitions suitable for experiments. In Refs. [3, 4] we derived NEEC rates and cross sections for the case of both electric and magnetic multipole transitions. The resonance strengths of NEEC followed by the radiative decay of the excited nuclear state are typically four orders of magnitude smaller than the ones of the analogous process of dielectronic recombination (DR). This is due to the small widths of the excited nuclear states.

If the initial and final states of NEEC and radiative recombination (RR) are the same, quantum interference between the two processes occurs. In the following we try to determine the magnitude of the interference term between NEEC and RR in the cross section.

The initial state $|\Psi_i\rangle$ of both RR and NEEC consists of the nucleus in its ground state and the free electron. The final state $|\Psi_f\rangle$ for both processes contains a photon of electric or magnetic multipolarity, the captured electron, and the nucleus which is again in its ground state. The total cross section of the process is given by

$$\sigma_{i\to f}(E) = \frac{2\pi}{F_i}\int_{4\pi} d\Omega_k \lim_{\epsilon\to 0+} |\langle\Psi_f|T(E+i\epsilon)|\Psi_i\rangle|^2 \rho_f \ , \tag{1}$$

where T is the transition operator, Ω_k is the solid angle of the emitted photon, and F_i and ρ_f denote the flux of the incoming electrons and the density of final photonic states, respectively. By means of the Feshbach projector formalism described in Ref. [3] we take the perturbation series of T and keep all the terms which account for NEEC and RR, so that the total cross section can be written as

$$\sigma_{i\to f}(E) = \sigma_{\rm RR} + \sigma_{\rm NEEC} + \sigma_{\rm int} \ . \tag{2}$$

Here, $\sigma_{\rm RR}$, $\sigma_{\rm NEEC}$ and $\sigma_{\rm int}$ are the cross sections for RR, NEEC and the interference term between both processes, respectively. For H-like ions, the RR cross section can be taken from the tabulation of Ref. [5]. The values for total cross sections of NEEC followed by radiative nuclear decay for various transitions in heavy elements are found in Ref. [3]. We calculated the interference cross section $\sigma_{\rm int}$ for the $M1$ transition of $^{173}_{70}$Yb, where the NEEC resonance strength is the largest, namely, $S = 0.86$ b eV. The nuclear part of this cross section can be traced back to experimental reduced radiative transition probabilities [6]. As in Ref. [3], in the calculation of the electronic matrix elements we used relativistic Coulomb-Dirac wave functions for the continuum electron and wave functions considering a homogeneously charged nucleus for the bound electron. In Fig. 1 we present $\sigma_{\rm int}$ and $\sigma_{\rm NEEC}$ as function of the continuum electron energy. The value of $\sigma_{\rm int}$ is smaller than $\sigma_{\rm NEEC}$ in this particular case. Calculations for various collision systems where a more pronounced interference enhancement is expected are in progress. The quantum interference effect may help in finding suitable isotopes for experiments aiming at the observation of NEEC.

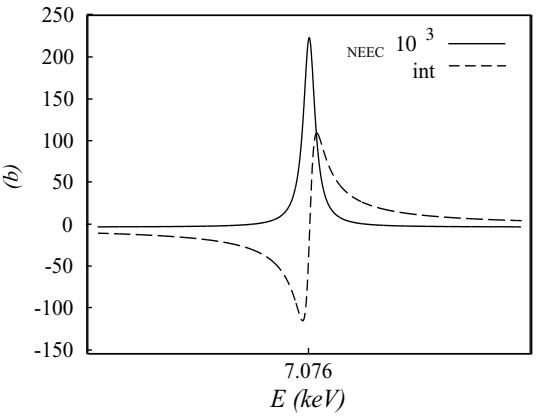


Figure 1: Interference and NEEC terms of the cross section for capture into bare $^{173}_{70}$Yb ions as a function of the continuum electron energy. The NEEC term is scaled by a factor of 10^{-3}. The widths of these resonances are approximately 10^{-6} eV.

References

[1] T. Carreyre *et al.*, Phys. Rev. C 62, 024311 (2001)

[2] S. Kishimoto *et al.*, Phys. Rev. Lett. 85, 1831 (2000)

[3] A. Pálffy, W. Scheid, and Z. Harman, Phys. Rev. A 73, 1 (2006), in print

[4] A. Pálffy, W. Scheid, and Z. Harman, GSI Report 2004, APHY-THE-02 (2005)

[5] A. Ichihara and J. Eichler, At. Data Nucl. Data Tables 74, 1 (2000)

[6] V. S. Shirley, Nucl. Data Sheets 54, 589 (1988)

Tests of Fundamental Interactions with Heavy Ions and Atoms

A.N. Artemyev, V.M. Shabaev, V.A. Yerokhin, St. Petersburg State University, Russia
S. Höche, G. Plunien, A.V. Volotka, Institut für Theoretische Physik, TU Dresden, Germany

Abstract

QED calculations of heavy two-electron ions and their applications to a feasible PNC experiment are discussed. Recent progress on calculations of the PNC effects in neutral alkali-metal atoms is also reported.

Heliumlike ions, being the simplest many-electron systems, serve as an important testing ground for investigations of few-electron QED effects in strong fields. In Ref. [1], all second-order two-electron QED corrections to the energy levels of the $n = 1$ and $n = 2$ states of He-like ions with the nuclear charge number within the range $Z = 12$-100 were calculated. As a result, a significant improvement in the accuracy of the theoretical predictions was achieved, especially in the high-Z region. To date, the most accurate experiment with heavy He-like ions was performed at GSI [2]. In this experiment the two-electron contribution to the ground state energy of He-like uranium has been measured. The experimental value of this contribution was found to be $2248(9)$ eV, while the corresponding theoretical result from Ref. [1] is $2245.89(18)$ eV.

Investigations of parity non-conservation (PNC) effects in atomic systems play a prominent role in tests of the Standard Model (SM). In Refs. [3, 4], the full gauge-invariant set of one-loop QED corrections to the PNC transition amplitudes in neutral cesium and francium was calculated. This resulted in a significant improvement of the corresponding PNC amplitudes. Compared with the most precise experiment for cesium [5], these calculations provided a new value for the weak charge of ^{133}Cs which deviates by 1.1 σ from the SM prediction. Further progress on tests of the Standard Model with neutral atoms from the theoretical side is mainly limited by difficulties with accurate calculations of the electron-correlation effects. For this reason PNC experiments with heavy few-electron ions, where the correlation effects can be evaluated to a high accuracy, seem highly desirable.

A promising situation for PNC tests occurs in heavy He-like ions with the nuclear charge number near Z=64 and Z=90, where the two levels 2^1S_0 and 2^3P_0 with opposite parity come close to each other thus enhancing the PNC effects significantly. Experimental identification of the PNC effects will require precise knowledge of the $2^3P_0 - 2^1S_0$ interval in He-like ions with nuclear charge numbers near these values of Z. The results of the calculations of this interval from Ref. [1] are shown in Table 1 . For comparison, the results obtained in other works are also presented in the table.

Table 1: The $2\,^3P_0 - 2\,^1S_0$ transition energy, in eV.

Ref.	$Z = 63$	$Z = 64$	$Z = 65$	$Z = 66$
[1]	$-0.224(69)$	$0.004(74)$	$0.32(12)$	$0.495(84)$
[6]	-0.591	-0.389	-0.153	0.016
[7]		-0.170		0.341
[8]	-0.168	0.067	0.328	0.614
Ref.	$Z = 89$	$Z = 90$	$Z = 91$	$Z = 92$
[1]	$1.61(46)$	$0.61(46)$	$-0.31(55)$	$-2.64(28)$
[6]			-1.971	-4.511
[7]		-0.095		-2.639
[8]	1.731	0.718	-0.209	-1.816

A feasible PNC experiment with heavy ions was suggested by Labzowsky *et al.* [9]. It was proposed to study a one-photon $2^1S_0 - 1^1S_0$ transition in polarized He-like Eu. The total amplitude of the one-photon $2^1S_0 - 1^1S_0$ transition is a mixture of the basic hyperfine-quenched (hfq) M1 and the additional hyperfine- and weak-quenched E1 amplitude. The probability for the emission of a photon in direction $\mathbf{n}$ is given by [9]

$$dW(\mathbf{n}) = \frac{W_{\rm M1}}{4\pi}[1 + \varepsilon(\boldsymbol{\nu}\cdot\mathbf{n})]d\Omega\,, \qquad (1)$$

where $W_{\rm M1}$ is the total probability of the hfq M1 $2^1S_0 - 1^1S_0$ transition, $\boldsymbol{\nu}$ is the unit vector directed along the ion polarization, and ε is the asymmetry parameter caused by the PNC effects. Our calculation for Eu^{61+} employing the transition energies from Ref. [1] (see Table 1) yields $\varepsilon \approx 0.0004\lambda_0$, where λ_0 is the degree of the ion polarization.

This work has been supported partly by INTAS-GSI (Grant No. 03-54-3604).

References

[1] A.N. Artemyev *et al.*, Phys. Rev. A 71 (2005) 062104.
[2] A. Gumberidze *et al.*, Phys. Rev. Lett. 92 (2004) 203004.
[3] V.M. Shabaev *et al.*, Phys. Rev. Lett. 94 (2005) 213002.
[4] V.M. Shabaev *et al.*, Phys. Rev. A 72 (2005) 062105.
[5] C.S. Wood *et al.*, Science 275 (1997) 1759.
[6] O.Y. Andreev *et al.*, Phys. Rev. A 67 (2003) 012503.
[7] D.R. Plante *et al.*, Phys. Rev. A 49 (1994) 3519.
[8] G.W.F. Drake, Can. J. Phys. 66 (1988) 586.
[9] L.N. Labzowsky *et al.*, Phys. Rev. A 63 (2001) 054105.

Preservation of the polarization of polarized ions in the magnetic system of a storage ring

G. Plunien, A. Volotka, Institut für Theoretische Physik, TU Dresden, Germany
L. Labzowsky, A. Prozorov, St. Petersburg State University, St. Petersburg, Russia
D. Liesen and F. Bosch, GSI Darmstadt, Germany

Experiments with polarized ion beams in storage rings can provide new testing grounds of fundamental physics. A feasible experiment for the search of space-parity nonconservation effects in He-like Eu and an experiment to search for time-reversal noninvariance with bare high-Z polarized nuclei have been proposed. Both goals can be achieved provided a polarized one-electron ion beam will be available. At present, the investigation of mechanisms for the polarization of highly-charged ion (HCI) beams and the preservation of polarization represents an urgent problem.

In [1] it has been argued, that the radiative polarization of HCI in storage rings could be achieved exploiting the idea of a selective laser excitation of hyperfine levels in an external magnetic field and the subsequent transitions to the ground hyperfine level in H-like HCI. As an example the $^{151}_{63}$Eu ion with nuclear spin $I = 5/2$ and total angular momentum values $F' = 3$ and $F = 2$ for the excited and ground hyperfine levels has been considered. For reasons of simplicity it has been assumed that the polarizing magnetic field is oriented along the beam direction. In storage rings with electron cooling such a longitudinal magnetic field is provided by cooler magnet.

The scenario considered in [1] assumes that the polarization state of the ion is not effected by the magnetic system of a storage ring. In order to address the problem of depolarization, we consider the time-evolution of a given initial polarization state of the ion described by the spin wave function $\chi_s(t_{\rm in})$, which may have been prepared in a constant polarizing magnetic field $\vec{B}(t_{\rm in})$ at times $t \le t_{\rm in} = 0$. Neglecting the additional coupling to the radiation field one has to solve the Schrödinger equation for $\chi_s(t)$ in the time-dependent external magnetic field $\vec{B}(t)$ arising with respect to the rest frame of the ion, while it moves through the magnetic system of the storage ring

$$\left[i\partial_t + \mu \left(\vec{B}(t) \cdot \hat{\vec{s}} \right) \right] \chi_s(t) = 0 \,. \qquad (1)$$

Here $\hat{\vec{s}}$ denotes the spin (total angular momentum) operator and μ is the magnetic moment of the electron. To investigate the most generic features one can utilize the following parameterizations for the spherical components of the magnetic field

$$\vec{B}(t) = \sum_q B^{in} \left\{ f(t)\delta_{0q} + g(t) d^1_{q0}(\beta) \right\} \vec{e}_q \qquad (2)$$

with arbitrary functions $f(t)$ and $g(t)$, respectively. The Wigner function $d^1_{q0}(\beta)$ corresponds to an active rotation of the magnetic field around the y-axis described by the time-dependent Euler angle $\beta = \beta(t)$. The initial (longitudinal) magnetic field is $\vec{B}(0) = B^{in}\,\vec{e}_0$ assuming e.g. the initial conditions $f(0) = 1, g(0) = 0$ and $\beta(0) = 0$, respectively. The spin wave-function can be decomposed as

$$\chi_s(t) = \sum_m a_m(t)\, \chi_{sm} \,, \qquad (3)$$

where χ_{sm} is the eigenfunction for the spin eigenvalue $s(s+1)$ and the spin projection m onto the instantaneous quantization axis in the direction of the magnetic field and $a_m(t)$ are the corresponding occupation amplitudes. Then the occupation numbers are $N_m(t) = |a_m(t)|^2$. Insertion into Eq. (1) yields a system of coupled differential equations for the amplitutes a_m.

The exact solutions can be found analytically for the initial conditions $a_m(0) = \delta_{mM}$ with M being the maximum value of the projection m as

$$a_m(t) = e^{i\Phi_m(t)}\, d^s_{Mm}(\beta) \,, \qquad (4)$$

where $\Phi_m(t)$ is a known time-dependent phase. This generic solution reveals that there is no conservation of the polarization with respect to the instantaneous axis, since also sublevels with $m \neq M$ get populated while time evolves. However, when the magnetic field returns to the initial direction after the time period T (the ions come back to the longitudinal magnet) $\beta(T) = \beta(0) = 0$ and the amplitudes differ from the initial ones only by some phase factor, i.e. $a_m(T) = e^{i\Phi_m(T)}\delta_{mM}$. Thus the corresponding initial population number will be restored after the time T, i.e., $N_m(T) = n_m(0) = \delta_{mM}$. A similar behaviour is found for the expectation value of the spin (polarization) operator

$$\vec{s}(t) = \langle \chi_s(t) | \hat{\vec{s}} | \chi_s(t) \rangle = M \sum_q d^1_{q0}(\beta)\, \vec{e}_q \,. \qquad (5)$$

This indicates the preservation of the ion polarization in the magnetic system of a storage ring provided that the polarization once has been prepared. In the considerations above the radiative transitions have been neglected. Accordingly, the preservation of ion polarization remains to be further investigated in more details [2].

This work has been supported partly by INTAS-GSI (Grant No. 03-54-3604).

References

[1] A. Prozorov, *et al.*, Phys. Lett. B **574**, 180, (2003)

[2] A. Prozorov, *et al.*, (in preparation)

New level diagrams for superheavy collision systems

J. Anton, B. Fricke, University of Kassel, Germany
A. Bräuning-Demian, P. H. Mokler*, P. Verma#, GSI Darmstadt, Germany

Asymmetric and symmetric heavy collision systems have been a subject of several theoretical and experimental investigations in the past, for a review see e.g. [1]. Superheavy quasimolecules are formed transiently during collisions of heavy-atoms by high-Z projectile ions, moving slowly (v_{ion}) with respect to the orbital velocities of the electrons of concern (v_{e-}), where the inner shell processes are governed by the adiabaticity parameter η (= v_{ion}/v_{e-}).

Due to advanced accelerator technologies moderately slow heavy ions are now available even in the highest charge states at SIS, and thus heavy projectiles can be provided with vacancies in the innermost shells prior to the collision. Experiments have been performed at SIS for an asymmetric (U-Au) and for a near symmetric (Bi-Au) very heavy collision system: a charge state selected U^{q+}-ion beam ($73 \le q \le 92$) and a Bi^{q+}-ion beam ($77 \le q \le 82$) of 69.2 MeV/u from the SIS was incident on thin Au targets (18 to 225 µg/cm^2 thick); for details and results see our earlier publication [2] and [3] respectively. As the adiabaticity factor for the inner shells of both the systems is smaller than 1, both lie in the quasiadiabatic regime and hence the transfer of inner shell vacancies can be considered within the quasimolecular picture using adiabatic level diagrams. Based on earlier work, see e.g. [4], advanced SCF-DFS multielectron level diagrams for the U-Au and Bi-Au collision systems have been newly calculated, see Figure 1 and 2 respectively, which are the systems that were considered experimentally.

In close collisions, K vacancies brought in by the projectile can be transferred to the target K-shell in the quasimolecule via the coupling of the 1sσ and 2pσ orbitals (the K-K sharing [5]) - the region of K-K sharing is indicated in the figures by rectangles. Transferred vacancies are then carried to the target K-shell in the outgoing part of the collision. The increase mainly in the Au-K X-ray emission for projectiles with initial K vacancies allowed an estimation of the relevant interaction distances [2, 3] in a simple model which are a little bit larger than the crossings of the 1sσ and 2pσ orbitals shown in the level diagrams. This suggests that this inner level crossing is only one of the ways to fill in the inner shell vacancies. Additional contributions are expected to result from the feeding from the L-shell at smaller internuclear distances, which are then transferred via the 1sσ and 2pσ crossing to the K-shell of the outgoing ion. The coupled channel calculations which hopefully will explain the values quantitatively are being performed presently.

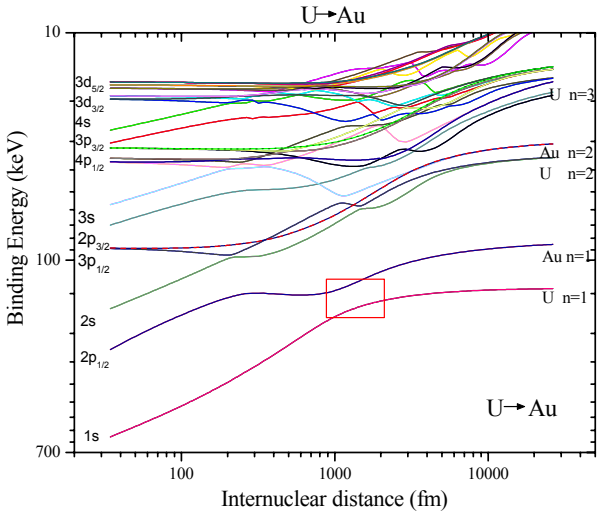


Figure 1: Adiabatic level diagram for the asymmetric U-Au collision system

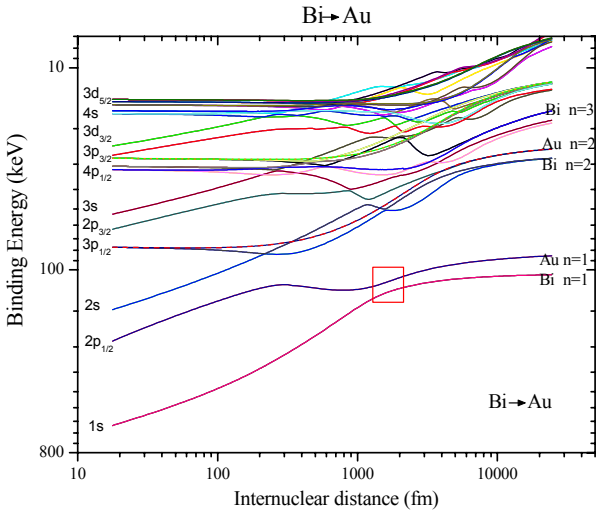


Figure 2: Adiabatic level diagram for the near symmetric Bi-Au collision system.

[1] P.H. Mokler and D. Liesen, in: Progress in Atomic-Spectroscopy, Vol.C (1984) p. 321.

[2] P. Verma, *et. al.*, Radiation Physics and Chemistry, in print, (2006).

[3] P. Verma, *et. al.*, Nucl. Instr. Meth. in Phys. Res. B 235 (2005) p. 309, and in print (2006).

[4] M. Mann *et al.,* J.Phys.B 15 (1982) 4199

[5] W.E. Meyerhof, Phys. Rev. Lett. 31 (1973) p. 1341.

* University of Giessen, Germany
# JMI, ND-110025, India, Vaish College, Haryana -124001, India

Electron Cooling of bare Uranium in HITRAP*

B. Möllers, C. Toepffer, G. Zwicknagel
Institut für Theoretische Physik II, Universität Erlangen, Germany

Electron cooling in HITRAP [1] is an essential tool for providing cold ions required for planned experiments. We study the evolution of the energy distribution of the trapped ions within the following model (see also e.g. [2] and references therein) which takes into account: (i) the deceleration of the N_i ions ($\mu = 1, \ldots, N_i$) by collisions with magnetized electrons

$$M\frac{d\vec{V}_\mu}{dt} = \vec{F}_\mu = \vec{F}[n_e, T_e, B, \vec{V}_\mu(t)]\,, \qquad (1)$$

(ii) the transfer of the ionic energy ($E_{i,\mu} = MV_\mu^2/2$) to the electrons, which are trapped together with the ions

$$N_i\langle\frac{dE_i}{dt}\rangle(t) = \sum_\mu^{N_i}\vec{V}_\mu\vec{F}_\mu = -\frac{dE_e}{dt} \stackrel{!}{=} -\frac{3}{2}N_e k_B\frac{dT_e}{dt}\,. \quad (2)$$

(iii) the heating of the N_e electrons and their cooling by synchrotron radiation (with a time constant τ)

$$\frac{dT_e}{dt}(t) = -\frac{2}{3k_B}\frac{N_i}{N_e}\langle\frac{dE_i}{dt}\rangle(t) \; - \; \frac{1}{\tau}\left(T_e(t) - T_0\right), \quad (3)$$

where $\tau \approx 0.1$ s for $B = 6$ T, and $T_0 = 4$ K is the ambient temperature supplied by the cryostat. These coupled differential equations for the velocities $\vec{V}_\mu(t)$ and the electron temperature $T_e(t)$ are solved numerically. Simultaneously we calculate for each ion the radiative ion-electron recombination rate

$$\nu_{\mathrm{RR},\mu}(t) = n_e\int d^3v_e\; v_{r,\mu}\;\sigma_{\mathrm{RR}}(v_{r,\mu})\, f\,(v_e, T_e(t)) \quad (4)$$

(with $\sigma_{\mathrm{RR}}(v_r)$ from [3], $v_{r,\mu}(t) = |\vec{V}_\mu(t) - \vec{v}_e|$, and $f(v_e)$ is a Maxwellian distribution), and the surviving probability $P_{\mathrm{RR},\mu}(t) = \exp\left(-\int_0^t dt'\nu_{\mathrm{RR},\mu}(t')\right)$. A similar treatment has already been applied, e.g. in [2]. There the energy loss dE_i/dt was, however, modeled by a rate equation for the ionic temperature, instead of the detailed description based on the cooling force $\vec{F}_\mu$ for individual ions as given by Eqs.(1) and (2).

Using this model we considered the case of bare Uranium, for an initial ($t = 0$) ion distribution of 500 ions which represents the ensemble of about 10^5 ions in the trap and which was obtained from a simulation of the injection into HITRAP [4]. For the cooling force $\vec{F}$ in Eq. (1) we employed here a linear response expression for strong magnetic fields, see [5]. Since the ions are only cooled when traveling through the electrons, the cooling force $\vec{F}$ was multiplied by a factor 0.4 (extension of the electron cloud/effective trap length). Fig. 1 shows the time evolution of $\langle E_i\rangle, T_e$ and $\langle P_{\mathrm{RR}}\rangle$ together with some snapshots of the energy distribution dN/dE_i for typical HITRAP conditions. The decrease of the average ion energy $\langle E_i\rangle$ indicates a cooling time of about one second. A strong heating of the electrons from initially $T_0 \approx 0.34$ meV to about $T_e = 2.2$ eV takes place. The recombination

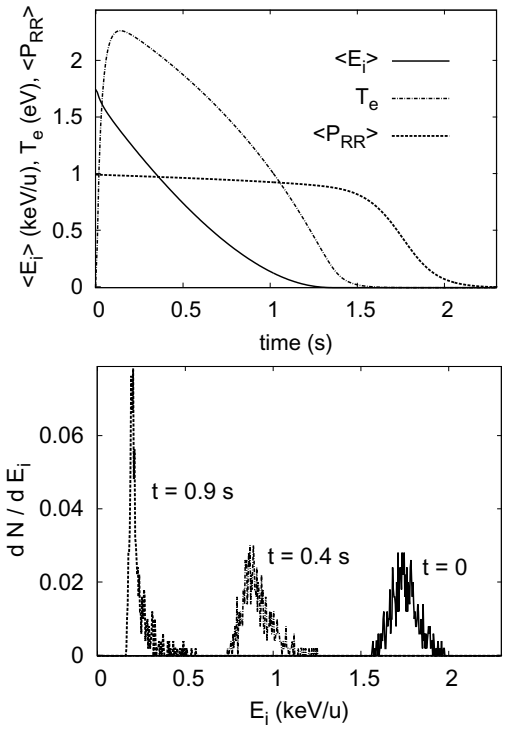


Figure 1: Top: Temporal evolution of $\langle E_i\rangle, T_e$ and $\langle P_{\mathrm{RR}}\rangle$ for U^{92+} ions at $B = 6$T, $n_e = 10^7$ cm^{-3}, $N_e = 10^4 N_i$. Bottom: some corresponding E_i-distributions.

becomes only effective at late times with small E_i and T_e. In(de)creasing the electron density by a factor 10 results in roughly 0.5(4) seconds cooling time and a maximal T_e of about 6(0.6) eV, whereas the overall qualitative picture remains unchanged. Roughly the same values are observed for in(de)creasing N_e by a factor 10 (at fixed $n_e = 10^7$ cm^{-3}). Altogether this analysis clearly indicates that cooling times around a second at recombination losses of about 10% are feasible for electron cooling of bare Uranium in HITRAP.

References

[1] Th. Beier et al., *HITRAP, TD report*, GSI, 2003.
[2] J. Bernard et al., NIM **A532** (2004) 224.
[3] M. Pajeck, R. Schuch, NIM **B93** (1994) 241.
[4] F. Herfurth, private communications.
[5] H.B. Nersisyan et al., Phys.Rev. **E61** (2000) 7022.

*Work supported by BMBF (06ER128) and GSI (ER/TOE)

Progress on HEDP/WDM experiments at GSI*†

D. Varentsov, D. Fernengel, A. Hug, J. Menzel, P. Ni, S. Udrea, TUD, Darmstadt, Germany
D.H.H. Hoffmann, P. Spiller, N.A. Tahir, H. Wahl, GSI, Darmstadt, Germany
V.E. Fortov, V.K. Gryaznov, M. Kulish, I.V. Lomonosov, V. Mintsev, D. Nikolaev,
N. Shilkin, A. Shutov, V.Ya. Ternovoi, IPCP, Chernogolovka, Russia
A. Fertman, A. Golubev, B.Yu. Sharkov, V. Turtikov, ITEP, Moscow, Russia

During the past year, significant progress has been achieved in experimental investigation on heavy-ion beam generated high-energy-density (HED) states in matter (warm dense matter, WDM). The main aims of the HEDP/WDM experiments performed at the HHT area of GSI were commissioning of recently developed diagnostic instruments and methods for the future HEDgeHOB experiments at FAIR; tests of different beam-target configurations for EOS studies; optimization of transport, focusing and diagnostics of intense heavy ion beams; obtaining new data on thermophysical properties and hydrodynamic response of various materials in HED states near boiling curve, two-phase liquid-gas and the critical point regions. In particular, HED properties of lead, tin, copper, aluminum, tungsten, tantalum, sapphire and uranium dioxide have been studied using the "plane-HIHEX" beam-target design concept (see Fig. 1).

In this beam-target configuration, solid or porous sample foil is placed along the elliptically-shaped ion beam, at the origin. Two sapphire plates are located parallel to the foil from both sides at variable distances, limiting the target expansion and defining the final volume. In order to avoid undesirable direct heating of the sapphire plates by the beam, a thick tungsten slit collimator is installed in front of the sample. The physics package is placed inside a solid brass container with additional sapphire windows at each face. The HIHEX design allows one to study 1D quasi-isentropic expansion of uniformly heated target material into a buffer gas or vacuum.

In the performed experiments, electron-cooled beam of $^{238}\mathrm{U}^{73+}$ ions with initial ion energy of 350 AMeV has been used. The intense, up to $2.5 \cdot 10^9$ ions/bunch, ion pulses have been compressed in time down to $\sim 110\,\mathrm{ns}$ (FWHM) and focused at the target to a spot of $\leq 300\,\mu\mathrm{m}$ diameter. The beam intensity and the pulse shape has been measured by current transformers installed in front of the target chamber whereas the upper limit for the focal spot size has been determined by recording beam-induced scintillation of argon gas at ionic lines.

A motorized achromatic 1:1 imaging system collects the light emitted by beam-heated target and transmits it to a fast radiation pyrometer and a streak-spectrometer via $400\mu\mathrm{m}$ quartz fiber lines. Using this advanced light collection system and an improved fast 12-channel pyrometer, the color temperatures up to 12000 K during direct ion-beam heating of tungsten targets have been recorded in the performed experiments. Target pressure is determined by measuring displacement history of the gold-coated outer surface of the sapphire plate (see Fig. 1). For this purpose, a modified $90°$ Michelson interferometer or an all-fiber VISAR system is used, registering pressures in the kilobar range at the moment of impact. The target expansion velocity is measured by visible backlighting/shadowgraphy system consisting of a diode laser or Xe flash lamp, interference filters and an electronic streak camera. The expansion velocities of more than $2\,\mathrm{km/s}$ has been detected for lead targets. In addition, the evolution of the electrical conductivity has been measured using a four-probe contact technique for lead and aluminum targets in plane and cylindrical (wires) geometries.

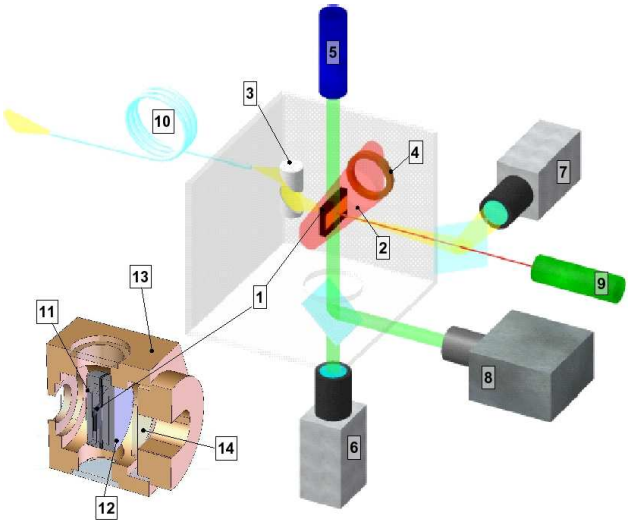


Figure 1: Scheme of the HEDP diagnostic instruments at HHT and plain-HIHEX target design: 1 – sample foil, 2 – ion beam with elliptic focal spot, 3 – pyrometer/spectrometer light collection system, 4 – beam current transformers, 5 – backlighting laser or Xe flash lamp, 6,7 – fast amplified CCD cameras (beam/target optical diagnostics and alignment), 8 – streak camera (target expansion shadowgraphy), 9 – displacement interferometer or VISAR system (pressure measurements), 10 – quartz fiber lines to pyrometer and streak-spectrometer (target temperature, spectroscopy), 11 – (gold-coated) sapphire plates, 12 – tungsten slit collimator, 13 – brass container, 14 – sapphire windows.

The obtained data on HED properties of various metals in hot expanded liquid, two-phase liquid-gas and near-critical states is currently being analyzed and prepared for publication. It is also planned to compare the experimental data with full-scale 3D hydro-simulations taking into account radiation transport phenomena.

* Supported by GSI-INTAS (03-54-4254), ISTC (2107) and BMBF.
† R&D work for the HEDgeHOB Collaboration experiments at FAIR.

Heavy-Ion-Beam Pumped Excimerlaser

A. Ulrich[1], A. Adonin[2], J. Jacoby[2], V. Turtikov[2,6], D. Fernengel[5], A. Fertman[6], A. Golubev[6], D.H.H. Hoffmann[3,5], A. Hug[5], R. Krücken[1], M. Kulish[7], J. Menzel[5], P. Ni[5], B. Sharkov[6], S. Udrea[5], D. Varentsov[3], H. Wahl[3], J. Wieser[4]

[1]TU-München, Garching, Germany, [2]Univ. Frankfurt am Main, Germany, [3]GSI, Darmstadt, Germany, [4]TuiLaser/ Coherent, München, Germany, [5]TU-Darmstadt, Germany, [6]ITEP, Moscow, Russia, [7]IPCP, Chernogolovka, Russia

The use of heavy-ion beams for pumping gas-lasers had first been demonstrated in 1983 by pumping an infrared He-Ar laser with a 100 MeV ^{32}S beam from the Munich Tandem van de Graaff accelerator [1]. Various schemes for ion beam pumped lasers have been studied [3-5] and amplified spontaneous emission was observed at GSI for the VUV xenon excimer transition at 172 nm [2]. In this report we describe the first successful operation of a UV excimer laser using a pulsed heavy ion beam from the heavy ion synchrotron SIS at GSI. The experiment has become possible due to the improved beam intensity and quality which is now available at the HHT target area.

The well known KrF^* excimer laser line at a wavelength of 248 nm has been selected for a first demonstrational experiment. The laser setup consisted of a 1.2 m long stainless steel tube of 30 mm diameter placed about 2 m behind an exit foil of the HHT beamline. A pulsed beam of ^{238}U ions with a particle energy of 250 MeV/u and ~110 ns pulse duration (FWHM) was used for pumping. The projectiles traversed 2 m of air, a 600µm thick scintillator, a stainless steel entrance foil, a 3 mm thick glass mirror substrate, and were then stopped in the laser gas mixture. Single shot pulses of up to 2.5×10^9 particles/pulse were focused into the laser cell. The optical resonator was formed by a flat, Al–coated mirror near the beam entrance and a second dielectrically coated, highly reflective mirror with 3 m radius of curvature at a distance of about 1 m. This end mirror was also used as a window for the cell and for decoupling the light from the resonator.

A laser gas mixture of approximately 50% Ar and 50% 99.5/0.5 Kr /F_2 was used as the laser medium. A constant gas flow was maintained to avoid F_2 depletion due to chemical reactions. Two fast UV enhanced photodiodes with 248 nm filters and two small monochromators with fiber optics input were used for laser diagnostics. Light emitted along the laser axis was diffusely reflected off an Al-plate before detection.

The ion beam was steered and focused into the laser cell with about 10^8 particles/pulse. Spontaneous emission near the end of the cell was observed with cameras. For a gas pressure of 1.6 bar the range of the ions matched the length of the cell. When the beam intensity was raised to about 2×10^9 particles/pulse laser effect was immediately observed by a strong appearance of the 248 nm line in the spectrum emitted along the laser axis. Laser threshold was reached with 1.25×10^9 particles/pulse for this specific setup. Spectra recorded with 1.0 and 1.3×10^9 particles/ pulse, respectively, just below and above threshold, are shown in Fig. 1. The broad-band Kr_2F^* emission around 400 nm shows only a slight difference in the two spectra as can be expected for a non-lasing transition in contrast to the 248 nm laser-light. Note, that the end mirror is highly reflective for 248 nm light and transmissive at 400 nm.

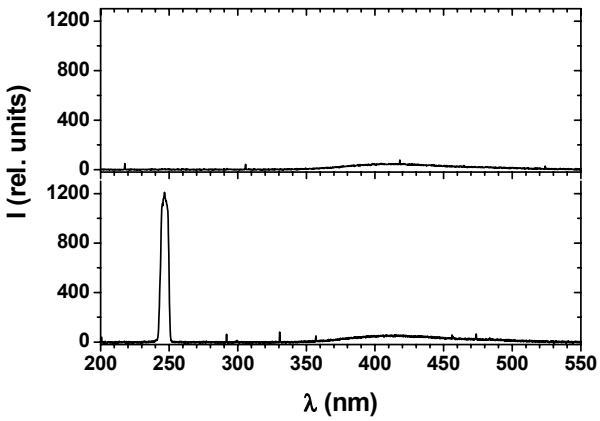


Fig. 1: Emission spectra from KrF along the laser axis just below (top) and above laser threshold. Laser effect is clearly visible by the strong 248 nm emission.

The time structure of the emission of spontaneous as well as laser light at 248 nm was recorded with the photodiodes. The half-width of spontaneous emission was 130 ns and the laser pulse duration ranged from 59 to 84 ns for pumping intensities between 1.4 and 2.5×10^9 particles/pulse. A first indication of spectral narrowing was also observed by comparing spectra of spontaneous and laser emission, respectively, recorded with one of the low resolution spectrometers.

In summary it could be shown that the pumping power and beam quality of the heavy-ion synchrotron SIS at GSI Darmstadt is now sufficient to pump UV lasers and it is planned in a next step to extend the laser experiments into the VUV range of the spectrum (λ<200 nm).

[1] A. Ulrich, H. Bohn, P. Kienle, and G.J. Perlow, Appl. Phys. Lett. **42**, 782 (1983)
[2] B. Busch, A. Ulrich, W. Krötz, G. Ribitzki, J. Wieser, and M. Winkler, J. Appl. Phys. **74**, 5960 (1993)
[3] A. Ulrich, J. Wieser, R. Pfaffenberger, B. Busch, W. Krötz, H.-J. Körner, G. Ribitzki, and D.E. Murnick, Z. Phys. **A341**, 111 (1991)
[4] A. Ulrich, R. Gernhäuser, W. Krötz, J. Wieser, and D.E. Murnick, Phys. Rev. **A50**, 1931 (1994)
[5] M. Salvermoser, A. Ulrich, and J. Wieser, Phys. Rev. **E58**,6531 (1998)

Supported by BMBF Project # 06F130 and Coherent Inc.

Influence of non-gaussian laser beam profiles on proton acceleration

M. Schollmeier*, M. Roth, TUD, Darmstadt, Germany
A. Blazevic, GSI, Darmstadt, Germany
B.M. Hegelich, J.C. Fernandez, K. Flippo, LANL, Los Alamos, New Mexico, USA

The irradiation of foil targets with ultra-intense short laser pulses leads to the generation of MeV ion beams from the non-irradiated target rear side [1]. The accelerating mechanism was identified to be the build up of a dense sheath of energetic electrons at the non-irradiated, rear surface of the target with an electric field strength exceeding 10^{12} V/m. The acceleration was found to take place within a few ps only. The beam always is directed normal to the rear surface of the target with an emittance being superior compared to conventional accelerator beams [2, 3]. The laser pulse accelerates electrons to relativistic energies in the front side preplasma formed by the prepulse. They penetrate the target and escape at the rear side. The target is charging up and the electrons are kept back from further escaping, forming the sheath. Assuming a quasineutral, electrostatic expansion the proton emission follows the gradient of the electron sheath.

For further investigstions the virtual laboratory *VIPBUL* was formed, including GSI as the participating Helmholtz center [4], for a further understanding of the acceleration mechanism of the ions. It was found in earlier experiments that the transverse shape of the laser beam strongly influences the transverse shape of the proton beam [5]. There the source size of the protons had to be estimated by the angular broadening of the electrons, transported through the target. It was fitted to 25°, a value that roughly fits the angle resulting from multiple Coulomb scattering. For further investigations of the influence of the laser beam profile on the proton beam, we have done experiments at the TRIDENT laser facility at LANL, Los Alamos. The targets were thin (10 - 50) µm gold foils, that had a micro-structured rear side with equally spaced grooves of 5 or 10 µm distance and less than 1 µm depth. This micro-structure leads to a micro-focussing of the protons that follow the local surface normal in the beginning of the acceleration [3]. While in former experiments by our group the laser was focussed to a nearly diffraction limited spot with a radially symmetric beam profile [2], we have changed the laser to form a line focus (see the left image in fig. 1). The target was a 13 µm thick Au-foil with 10 µm spaced lines on the rear side. The laser was focussed to an intensity of $2.5 \cdot 10^{18}$ W/cm^2. The image in the middle of fig. 1 shows the energy deposition of 5 MeV protons, recorded with a radiochromic film (RCF). The microstructured lines of the target rear side lead to the vertical lines in the lower part of the image. The most intense feature shows an ellipse rotated by 90° with respect to the laser ellipse. This can be understood as an effect of the electron sheath gradient. Applying the same procedure as described in ref. [5], and assuming only multiple Coulomb scattering, we cannot reproduce the image in the RCF. By simple line counting we determine the source size to be 130 µm for 5 MeV protons. This would correspond to an electron angular distribution of 150° full opening angle. The hot electron energy is $\approx$ 0.7 MeV [6], therefore the large angle is not due to scattering. Interpolating the laser focus image to the measured source size, a reasonable agreement with the RCF image can be simulated; see the right side of fig. 1. While for thick targets the main contribution to the broadening of the electrons forming the accelerating sheath is from multiple Coulomb scattering, this effect seems to be of minor importance for thin targets. Additionally for thin targets the assumption of an electrostatic acceleration seems to be wrong. One reason for the observed source size could be recirculating electrons that travel back and forth both sides of the target [7]. The target thickness allows for several round trips, this can lead to an additional broadening. Nevertheless the divergence of the protons in vertical direction seems to be reduced compared to shots with round foci. Overall we conclude that, both the shape of the laser focus as well as the target thickness, have strong influence in the ion beam profile. We plan to further investigate these results with additional experiments and 3D-PIC simulations in 2006.

We acknowledge the excellent support by the Trident laser team. We thank IMVT, Forschungszentrum Karlsruhe, as well as IHT, TU Darmstadt, for the target preparation. This work was performed within the Virtual Institute, VIPBUL, funded by the Helmholtz Foundation.

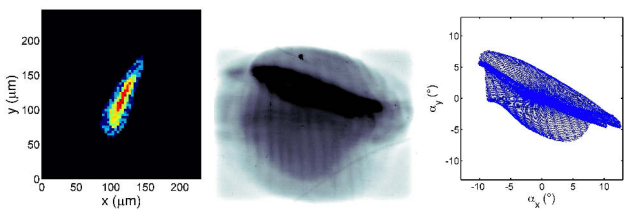


Figure 1: *l:* laser focus, *m:* 5 MeV proton beam, *r:* model

* m.schollmeier@gsi.de

References

[1] R.A. Snavely *et. al.*, Phys. Rev. Lett. **85**, 2945 (2000)
[2] E. Brambrink *et. al*, Annual report 2002, **GSI-2003-2**, 9 (2002)
[3] T.E. Cowan *et. al.*, Phys. Rev. Lett. **92**, 204801 (2004)
[4] Virtual Institute to investigate the generation of intense Particle Beams by Ultra-intense Lasers, `http://www.vipbul.de`
[5] J. Fuchs *et.al.*, Phys. Rev. Lett. **91**, 255002 (2003)
[6] S.C. Wilks *et.al.*, Phys. Plasma **8**, 542 (2001)
[7] A.J. Mackinnon *et.al.*, Phys. Rev. Lett. **88**, 215006 (2002)

Charge state and energy loss of heavy ion beam interacting with porous and solid matter.

A. Fertman [1], T. Mutin [1], V. Turtikov [1], A.A. Golubev[1], O. Rosmej [2], S. Korostiy [2], A. Blazevic [2], S. Pikuz [3], V.P. Efremov [3], D.H.H. Hoffmann [2, 4]

[1] ITEP, Moscow; [2] GSI-Darmstadt, Germany; [3] Institute High Energy Density, Moscow; [4] TU-Darmstadt, Germany

Materials with fine porous nano-structure are very promising as targets for ICF driven by laser or heavy ion beams [1] providing high uniformity of the energy deposition. Silica gel is one of them. Its structure is formed by chains of colloidal SiO_2–beads of 3 - 5 nm in diameter. The chains build the 3-D open cell structure, with pores of 30 - 50 nm [2]. The nm uniform silica-gel structure provides a continuously expanded interaction volume. In order to investigate the possible influence of the porous nano-structure on the ion stopping process, the energy loss and the charge state distribution of the 11.4 MeV/u Ca ion beam interacting with Al foils and silica-gel targets with approximately the same linear densities x were measured and analysed.

For energy loss measurements a time-of-flight (TOF) method was used. A stop detector consisting of a micro-sphere plate with a rise time of 150 ps was placed at the end of the 473 cm long time-of-flight path after the target.

At RFQ LINAC phase correlation between the beam microstructure and the accelerating rf voltage structure (~ 36 MHz sine wave) is well defined at any point of the beam line including the target and stop detector positions. The stop detector signal and the UNILAC rf signal were recorded simultaneously using a two-channel digital oscilloscope (sample rate 2.5 GS/s). The phase correlation between the ion beam micro bunches and rf-signal peaks measured without a target served as a time reference point. When the target is placed in the way of the ion beam, a phase shift of the beam microstructure relative to the rf signal occurs due to the ion energy loss in stopping medium. Together with an accurately measured target-detector distance this shift gives rise to the difference between the initial ion velocity and the velocity after the beam passed through the target. This procedure allows measuring of the ion energy loss in the target. As a result, 11.4 MeV/u calcium beam energy losses in aerogel and aluminium targets have been determined. The experimental results are summarized in the Table I.

Target/ Density g/cm^3	Linear density, mg/cm^2	Energy loss, MeV/u	
		experiment	SRIM2003
Al/ 2.7	6.9	1.572	1.558
Al	12	2.882	2.812
Al	13.81	3.141	3.283
Al	16.98	4.17	4.15
Silica-gel/0.023	7.015	1.692	1.77
Silica-gel/0.019	12.0	3.061	3.16
Silica-gel/0.048	13.6	3.384	3.635

Experimental data on the stopping power for fast ions are traditionally compared with the values predicted SRIM code. We also present such a comparison in Table I. One can see that our experimental results on the Ca ion energy loss in Al targets are in good agreement with SRIM2003 values.

For the analysis of the charge state distribution after interaction with the investigated target, the beam burst is deflected in the B=1–1.8 T magnetic field of a dipole magnet. The ions are split according to their charge-to-mass ratio Q/m and energy. The ion impacts were detected by a plastic scintillator of 1mm thickness, viewed by a camera which produces intensified images on a charge coupled device (CCD). The background picture of the foreign lighting and CCD noise was registered and subtracted for each image. The images were then projected along the direction of the dispersion. Since the beam energy after the target is known from the TOF measurements, the charge state distribution of the ion beam can be determined. Figure 1 shows the charge state distribution of the Ca ion beam with initial energy of 11.4 MeV/u after penetration of the 50-m-thick Al foil and the silica gel target of approximately the same linear density. The measured ion beam energies after the aluminium target are 8.3 MeV/u, and after the piece of gel 8.06 MeV/u.

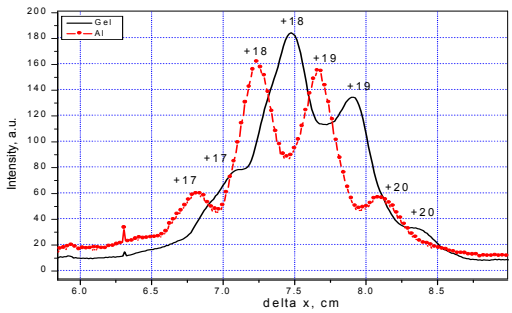


Fig.1 Ca ion charge state distribution

The curves are shifted along the x axis due to the difference in the final energy of the ion beam. The averaged Ca ion charge measured after the Al target is Z_{av}=18.5; the averaged ion charge measured after the gel target is Z_{av}=18.2 with the experimental accuracy of 1–2%. These results allow suggesting that at our experimental conditions the pore of 30–50 nm size does not seriously influence the ion stopping processes.

References:

[1] M. Desselberger *et al.,* Phys. Rev. Lett. **74**, 2961 (1995).
[2] N.G. Borisenko, Ya.A. Merkuliev, Targets for the spherical laser compression ,Proceedings of P.N. Lebedev Institute, Vol. 221, Nova Science Publishers, New Yorl, 1996 (in English).

This work was supported by WTZ grand 02/001-6.98

Energy Loss of C-ions in Ar-plasma and -gas in the Gap-target Configuration*

K. Weyrich, H. Wahl, D.H.H. Hoffmann, GSI, Darmstadt, Germany
A. Golubev, A. Kantsyrev, B. Sharkov, ITEP, Moscow, Russia
M. Kulish, S. Dudin, V. Mintsev, IPCP, Chernogolovka, Russia

Abstract

Plasma targets for measuring energy loss and charge state distribution of heavy ions in non-ideal Ar-plasmas (Γ-parameters 0.55–1) have been developed and the interaction with several ion species was studied. Here the results for 5.9 MeV/u C-ions are presented.

The Targets

The target scheme for explosively driven plasmas and the experimental set-up were described in [1,2]. For the experiments at Z6 at GSI a configuration called gap-target was developed, see fig. 1 The energy-loss of ions in Ar-gas is measured between the mylar foils sealing the target-head (~ 28 mm). The interaction zone with the plasma is the 4 mm gap between the Al-tubes, resulting in approximately the same line density (compression factor in the plasma ~ 10). So the straggling is equal and the shape of the signals of the TOF-measurements (MSP or phaseprobes) for determining the energy loss are comparable. Inhomogenities in the plasma due to plasma wall interactions are shaded by the tubes. For 5.9 MeV/u C-ions several beam-times were carried out.

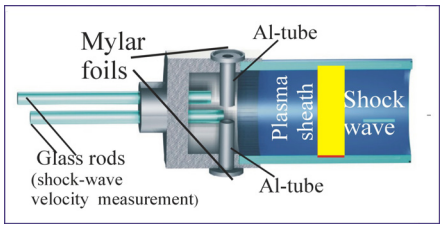


Fig. 1: Scheme of the head of the gap-target

Energy-Loss Results

The experimental results for the energy-loss in Ar-plasma are shown in figure 2. For plasma the results from the beam-times in December 2002 and August 2004 are reproducible within the error-bars and show a slight enhancement above the theoretically expected values for Ar-gas calculated with SRIM2003. The data for cold gas (not presented here) could not be reproduced. The development of the energy-loss in Ar-gas was systematically studied in two additional beam-times. Figure 3 shows the energy-loss of 5.9 MeV/u C-ions measured in a 100 µs long beam-pulse and at different time-windows in a 500 µs pulse at 300 mbar and 600 mbar. The later in the pulse the measurement was done, the lower is the energy-loss. The energy-deposition of the ion beam heats the gas which flows out of the interaction zone through the gap reducing the line-density.

Simulations with a code by D. Varentsov verify this. The process is sensitive to the beam-current. At 10 µA a decrease in the energy-loss of 15 % was measured at times < 100 µs, at 8 µA at 250 µs (fig. 3), and for 6 µA the decrease never reaches 10 %. This does not apply to the energy loss measurement in the plasma, for the plasma sheath travels throuh the gap in a few µs.

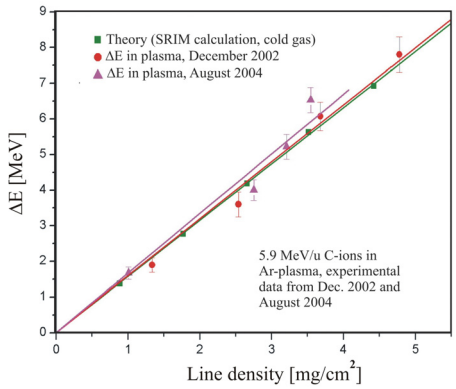


Fig. 2: Energy loss of C-ions in Ar-plasma (experiment) and Ar-gas calculated with SRIM2003

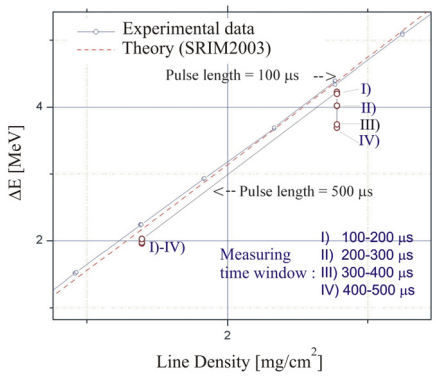


Fig. 3: Energy loss of C-ions in different times-windows in a beam-pulse

The measurements have shown, that the gap-target is optimized for the measurements in plasma and the results are reproducible. For measurements in Ar-gas to compare with the plasma for detecting any non-idealty effects, which will be very small [3], the experimental conditions have to be reproducible. More sensitive detectors have to be develloped to keep the beam-intensity below a threshold that initiates gas dynamics during the ion-pulse.

References

[1] V. Mintsev et al., NIM A 415 (1998) 715
[2] K. Weyrich et al. GSI-Scientific-Report 2002, p. 135
[3] G. Zwicknagel , Phys. Rep. 309 (1999) 117.

*Work supported by DFG 436 RUS 113/685/0-1

Calcium projectile ion radiation dynamics in gaseous target.

S. Korostiy [1], O. Rosmej [1], A. Blazevic [1], D. Varentsov [4], A. Fertman [3] V. Turtikov [3], V. P. Efremov [2], J. Rzhadkiewicz [5], A. Gójska [5], D.H.H. Hoffmann [1, 4]

[1] GSI-Darmstadt, Germany; [2] ITEP, Moscow; [3] Institute High Energy Density, Moscow; [4] TU-Darmstadt, Germany; [5] The Andrzej Soltan Institute for Nuclear Studies, Poland

Experimental investigations of the slowing-down process of calcium projectile ions traveling through the neon gas were carried out at the UNILAC facility at GSI in the frame of the project U-189 "X-ray spectroscopy of projectile ion and target radiation". The main goal was to demonstrate the influence of the target density on the charge state distribution inside matter. In order to analyze the projectile charge state distribution along the trajectory the X-ray spectroscopy of projectile ion *K-shell* radiation was applied. Ca projectile ion spectra were measured with high spectral ($\lambda/\delta\lambda$=3000) and spatial resolution (100μ) along the ion beam stopping path. The dependence of the characteristic ion spectrum on the ion beam penetration depth in the gaseous target was investigated.

The $48Ca^{+10}$ ion beam with initial energies of 5.9 and 11.4 MeV/u was delivered to the target chamber at Z6 experimental area. The ion beam was well collimated by means of two 2mm carbon apertures. The typical pulsed ion beam current in gas was 0.1-0.2 μA. The macro pulse duration was 5 - 5.5ms with a frequency of 2-5 Hz. The gas target was designed as a cylindrical copper box with a length of 210 and an inner diameter of 30mm filled with Ne gas under 1.9 bar pressure. The target was separated from 10^{-5} mbar vacuum in the experimental chamber by 5μm entrance Havar foil. The gas flow in the tube served for the renewal of the stopping medium. Three rectangular windows 4mm x 40mm used for X-ray diagnostic were oriented along the direction of the ion beam propagation. The distance between the entrance hole and the beginning of the first diagnostic window was 20 mm. The windows were covered with a 5μm Ti foils transmitting 60% of 3-4 keV photons and effectively protecting the crystal spectrometer from parasitic low energy radiation.

After passing through the entrance Havar foil, the $48Ca^{+10}$ ion beam enters the gas having an equilibrium charge state distribution. From the first diagnostic window we observed *K-shell* Ca radiation dynamics along 40mm of the ion stopping path. Spectra were measured by mean of Focusing Spectrometer with Spatial Resolution [1]. The mica spherically bend crystal was used as a dispersive element. An X-ray Kodak Direct Exposure Film (DEF) was exposed 10-12 hours.

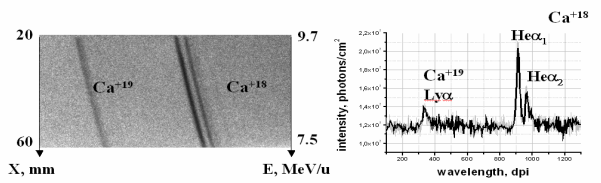


Fig.1. Radiation dynamics of Ca projectile ions with initial energy of 11.4 MeV/u slowed down in 1.9 bar Ne-gas. X, mm – penetration depth, measured from the entrance foil

The spectrum in Fig.1 shows radiation of Ca^{+19} and Ca^{+18} ions in 9.7-7.2 MeV/u energy region. We observe Lyα (1s-2p), Heα$_1$ ($1s^2$-1s2p $^1P_1$) and Heα$_2$ ($1s^2$-1s2p $^3P_1$) radiative transitions. Characteristic feature of the spatially resolved along the ion penetration depth spectrum is the tilted form of lines. Measured characteristic lines are shifted in wavelength due to the Doppler Effect. This shift depends on the projectile velocity and the observation angle. In the experiment the spectra were observed at the angle providing the shift to the higher photon energies - "blue" shift. Due to the ion energy loss in stopping media the line Doppler shift is decreasing continuously with the ion penetration depth, lines become tilted. This fact was used to determine projectile ion velocity depending on the penetration depth in stopping media [2, 3, 4].

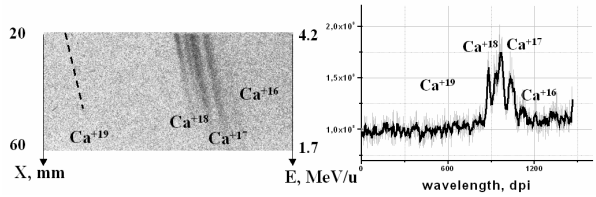


Fig.2. Radiation dynamics of Ca projectile ions with initial energy of 5.9 MeV/u slowed down in 1.9 bar Ne-gas

Fig.2 presents a *K-shell* spectrum of Ca ion beam at lower energies of 4.7 – 2.1 MeV/u. At these energies the radiation of Ca^{+19} (Lyα) ions is fully absent and the maximum of the spectra line intensity is shifted to the group of satellites originating from the autoionizing states of Ca^{+17} and Ca^{+16}. This shift to the lower charge states is due to the increase of the bound electron capture cross sections at lower projectile energies.

Spatially resolved *K-shell* spectra of Ca ions with initial energy of 11.4 MeV/u slowed down in solid and porous stopping media [3, 4] differ from those obtained in experiments with gaseous targets. In solid matter we observe long lasting intense radiation of highly charged ions Ca^{+19} and Ca^{+18} down to the energies of 2.5 - 3 MeV/u.

The "gas-solid" difference in projectile charge state distribution we attribute to the increase of the effective ionisation cross sections and suppression of the bound electron capture in dense stopping media [5]. Both processes tend to the increase of the projectile ion charge in dense matter.

References:

[1] A.Ya. Faenov et al, Phys. Scripta, **50**, 333 (1994)
[2] O.N. Rosmej et al, NIM A **74**, No12, 5039 (2002)
[3] O.N. Rosmej et al, RSI, **74**, No12, 5039 (2003)
[4] O.N. Rosmej et al.Phys.Rev.A **72**,052901 (2005)
[5] V.P.Shevelko et al, J.Phys.B: **37,** 201 (2004)

Influence of f number variation on the properties of laser produced plasmas

A. Ya. Faenov, T. Pikuz, Mendeleevo, Moscow region, Russia
G. Rodríguez Prieto*, G. Schaumann, S. Korostiy,
O. N. Rosmej, A. Blazevic, T. Heßling, GSI, Darmstadt, Germany

Experimental setup and results

The nhelix [1] system was used in experiments to test the f number influence on laser created plasma. The f number (f/#) is defined as the ratio of a lens focal length to the diameter of its entrance pupil. It has received some attention for its role on the laser produced plasma, as key parameter for the resonance absorption process [2]. The resonance absorption enhances the light absorption in the plasma. Therefore, it is important to understand the plasma physics and its applications.

In experiments perfomed at GSI with the nhelix facility a direct relation between f/# and the highly charged ions emission was found. This result is in agreement with previous works [2]. Figure 1 shows the experimental setup. The laser is focused onto the target with a lens (13 cm focal length) placed inside the vacuum chamber. The targets were magnesium slabs of 1 mm thickness. The laser beam incidence angle was fixed in 45°with respect to the target surface. The plasma spatial characteristics were recorded with X-ray pinhole cameras.

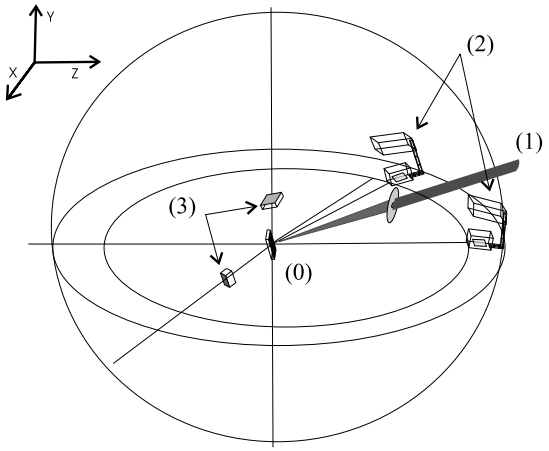


Figure 1: Experimental setup scheme: (0) Target, (1) Laser beam with last lens, (2) X-ray spectrometers and (3) Pinhole cameras.

The cameras were placed in perpendicular directions to probe the spatial characteristics in these two planes. Two X-ray spectrometers (FSSR [3]) were placed with angles of 0°(Fs1) and 90°(Fs2) with respect to the target surface. Their spectra were recorded using X-ray films. The spectral region between the He-β (7.85 Å) and He-γ (7.50 Å) magnesium lines was set up in the FSSR. The movement of the He-like ions is recorded on the FSSR in perpendicular to the wavelength axis. The comparison of the ion movement is then possible.

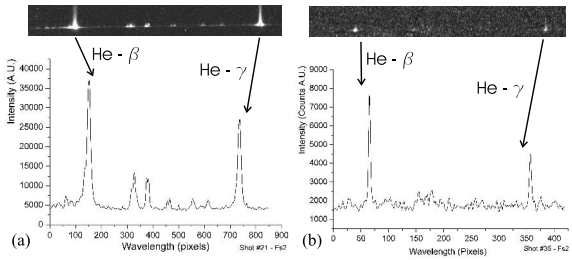


Figure 2: Fs2 spectra and their density traces for the two cases of f-number: (a) f/2.65 and (b) f/2.06

For the used lens a laser beam diameter variation from 49 mm to 63 mm implies that f/# goes from f/2.65 to f/2.06. These were the values used here. In fig. 2 the spectra and their total density trace are presented. The lines perpendicular to the wavelength axis show that with f/2.65 the plasma expansion is present. Such expansion does not appear with the smaller f/2.06. The ion emission measured with the peak value is five times higher with f/2.65 (37 000 counts) than with f/2.05 (7 700) in the He-β line. Similar results can be obtained with the He-γ line (right line in the figure 2).

Conclusions

The importance of f/# as key parameters in the laser plasma generation had been confirmed. With as litle change as 20% in f/# the ion peak emission has been increased 5 times. In order to use the nhelix as back iluminator the X-ray generated intensity must be maximized. As this works states, an increase in the f/# is very effective to obtain an incresaed X-ray flux. A non linear effect as the resonance absorption can explain the obtained results.

References

[1] G. Schaumann et al.,"High Energy Heavy Ion Jets Emerging from Laser Plasma Generated by Long Pulse Laser Beams from the NHELIX Laser System at GSI" , Laser and Particle Beams **23** (2005), p. 503

[2] S. Yu. Gus'kov et al., "Influence of Angles of Incidence of Laser Radiation on the Generation of Fast Ions", Journal of Experimental and Theoretical Physics Letters **73** (2001) 12, p. 655

[3] A. Ya. Faenov et al., "High-Performance X-Ray Spectroscopic Devices for Plasma Microsources Investigations", Physica Scripta **50** (1994), p. 333

* g.rodriguezprieto@gsi.de

CAST - Probing Axions from the Core of the Sun

M. Kuster, S. Gerhard, G. Hoffmeister, D. Weber, TU Darmstadt, Darmstadt, Germany
D. H. H. Hoffmann, GSI, TU Darmstadt, Darmstadt, Germany
K. Zioutas, University of Patras, Patras, Greece

The sun provides a deep insight into the physics of fusion, the physics of hot plasmas and is an excellent laboratory for astroparticle physics. As such the sun can be used to probe the existence of novel particles and dark matter candidates like the axion. The axion is a direct consequence (2; 3) of the theoretical solution of the CP problem in strong interactions proposed by (1). Inside the core of the sun axions could be produced by coherent conversion of thermal photons interacting with the electromagnetic field of charged particles of the solar plasma (Primakoff effect).

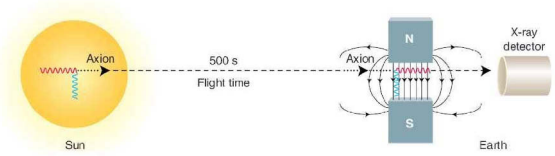


Figure 1: Physical principle of the CAST experiment.

With the *CAST* experiment at *CERN*, we aim to detect such solar axions on earth by "converting" them back to X-ray photons inside a strong transversal magnetic field (inverse Primakoff effect, see Fig. 1). The conversion probability of axions to photons is proportional to the square of the strength of the magnetic field and its length. Thus, a strong magnetic field is essential to achieve a high sensitivity of the experiment.

The heart of CAST is a prototype LHC superconducting magnet providing a dipole magnetic field of $\approx 9\,\mathrm{T}$ in the interior of two parallel pipes over a distance of $9.26\,\mathrm{m}$. On both ends of the magnet X-ray detectors are looking for a potential axion signal as an excess signal over detector background. A TPC detector covers two magnet bores on one end looking for axions during sunset. On the opposite side of the magnet, a micro mesh gas detector and an X-ray telescope with a pn-CCD detector are looking for axions at sunrise. The magnet can be pointed towards the sun for about $1.5\,\mathrm{h}$ during sunrise and sunset, resulting in $3\,\mathrm{h}$ observation time per day. The remaining time is used for systematic background studies. The most sensitive detector system of *CAST* is the Wolter I type X-ray telescope which enhances the signal-to-background ratio by a factor of ≈ 100 by concentrating the potential signal flux on a small spot on the pn-CCD detector.

During the last two years *CAST* was taking data for about twelve months, six months during 2003 and during 2004. The analysis of the data reveals no significant excess signal over background and allows us to set a new upper limit on the axion to photon coupling (4). Fig. 2 shows the preliminary corresponding upper limit for the axion to photon coupling constant $g_{a\gamma}$ derived from the data aquired

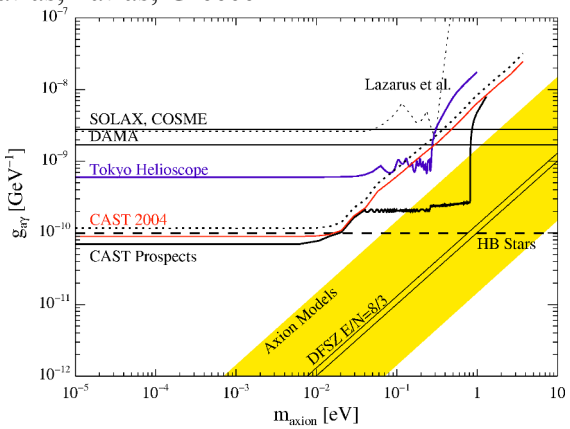


Figure 2: *Preliminary* upper limit (CL 95 %) on the axion to photon coupling $g_{a\gamma}$ depending on the axion mass m_a derived from the data of 2004 exploiting the full sensitivity of the X-ray telescope. The shaded area represents the parameter range of theoretical axion models. The results of earlier experiments *SOLAX*, *COSME*, *DAMA*, and the Tokyo helioscope are shown for comparison. The best astrophysical limit is indicated as "HB Stars".

with the X-ray telescopes during 2004. The analysis of the 2004 data is still in progress and we expect to further improve the upper limit in the *CAST* axion sensitive mass range $m_a < 0.02\,\mathrm{eV}$, although the present preliminary result is already comparable to the best astrophysical constraints (see Fig. 2). Due to coherence effects, the *CAST* helioscope in its configuration during 2004 was sensitive for axions with masses $m_a < 0.02\,\mathrm{eV}$, only. To extend the sensitivity of CAST to $m_a < 0.8\,\mathrm{eV}$, the refractive index of the conversion volume has to be changed using a buffer gas, either ^{4}He or ^{3}He. Then, the photon acquires an effective mass ($m_\gamma = m_a$) and the momentum exchange during the Primakoff process becomes negligible (phase II of CAST). During 2005 the CAST magnet has been transformed into its phase II configuration, allowing to be operated with a buffer gas (^{4}He) inside the conversion volume. First data has successfully been taken with the new experimental setup at the end of 2005 and data taking will be continued at the beginning of this year.

References

[1] Peccei, R. D., & Quinn, H. R., 1977, Phys. Rev. Lett., 38, 1440

[2] Weinberg, S., 1978, Phys. Rev. Lett., 40, 223

[3] Wilczek, F., 1978, Phys. Rev. Lett., 40, 279

[4] Zioutas, K., et al., 2005, Phys. Rev. Lett., 94, 121301, 2005

Hydrodynamic Stability of LAPLAS Target Using an Annular Focal Spot at the Future FAIR Facility*

N.A. Tahir, D.H.H. Hoffmann, GSI, Darmstadt, Germany
A.R. Piriz, G. Wouchuk, University of Castilla-La Mancha, Ciudad Real, Spain
A. Shutov, I.V. Lomonosov, V.E. Fortov, IPCP, Chernogolovka, Russia
C. Deutsch, LPGP, University of Paris–Sud, Orsay, France

Abstract

One of the important experiments that will be carried out at the Future Facility for Antiprotons and Ion Research (FAIR) has been named LAPLAS that stands for Laboratory Planetary Sciences [1, 2]. The target proposed for this experimental scheme is a multi-layered cylindrical target that contains a cylinder of frozen hydrogen that is enclosed in a heavy shell of a high-Z material like gold or lead. The target is irradiated facially along the length of the cylinder and the hydrogen is compressed due to the high pressure generated in the beam heated region of the surrounding shell. Two type of hydrodynamic instabilities, namely, Rayleigh–Taylor (RT) and Richtmeyer–Meshkov (RM) have the potential to destroy the implosion. In this contribution we present analysis to investigate the development of these two instabilities.

Introduction

The future **F**acility for **A**ntiprotons and **I**on **R**esearch (**FAIR**) [3], will generate a very intense uranium beam with an intensity of 10^{12} ions that will be delivered in a single bunch, 50 ns long. A wide range of particle energy between 400 MeV/u–2.7 GeV/u will be available which will provide great flexibility to the experiment designers. The beam focal spot geometry can either be circulary with a Gaussian transverse intensity profile, or one may generate an annular shape using an rf-wobbler that will rotate the beam with a high frequency (in GHz range) [4]. One face of the cylinder is irradiated with the beam and the particle energy is chosen in such a manner that the projectile range is larger than the target length (see Fig. 1) The high pressure produced in the beam heated part of the surrounding shell launches a shock inwards, along the radial direction that undergoes multiple reflection between the axis and the hydrogen-gold boundary. Such a scheme leads to a low–entropy compression that generates super–high densities (up to 30 times solid density) and ultra-high pressures (up to 30 Mbar) while teperature remains low (of the order of a few thousand K). However, the implosion can be destroyed due to the uncontrolled growth of Rayleigh–Taylor (RT) and/or Richtmeyer–Meshkov (RM) instabilities. In this contribution we present stability analysis of the LAPLAS target driven by a hollow beam with an annular focal spot.

* Work supported by BMBF

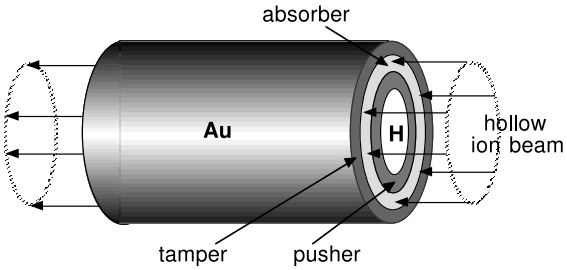


Figure 1: Beam–target geometry for the LAPLAS experiment using annula focal spot.

Rayleigh–Taylor Instability Analysis

The well known Rayleigh–Taylor (RT) instability occurs when two fluids of different densities are placed in contact and are accelerated in a direction normal to their interface and directed towards the denser fluid.

The linear growth rate for this instability is given by

$\gamma = \sqrt{A_t \cdot k \cdot a}$

where $A_t = (\rho_2 - \rho_1)/(\rho_2 + \rho_1)$

is the Atwood Number across the interface, k is the perturbation wave number and a is the acceleration.

The perturbation amplitude at time t is given by

$\eta = \eta_0 e^{(\gamma \cdot t)}$

The driver energy is deposited in part of the gold shell which expands, producing a low density region. The pusher part of the gold shell, on the other hand, is compressed to super solid densities due to shock compression and is accelerated by the high pressure in the beam heated region which may lead to the growth of RT instability.

We assume that the target is 1 cm long, the radius of the hydrogen is 0.4 mm and the outer radius of the gold shell is 3 mm. The beam intensity is considered to be 10^{12} ions of 2 GeV/u uranium with a bunch length of 50 ns., The inner and the outer radii of the annular focal spot are 0.6 mm and 1.6 mm, rspectively. The pusher acceleration in the implosion phase starts at t = 65 – 70 ns when the shock emerges from the Au and enters into the H. Since this moment, until the beginning of the deceleration phase that starts at t = 120 ns, the pusher acceleration is almost constant and is equal to a = 6 $\times$ 10^{12} cm s^{-2}. On the other hand, because of the absorber expansion, a density gradient is created at the interface pusher/absorber which has a minimum density scale length L = ρ/(dρ/dr) practically constant during the implosion and approximately equal to L = 0.015 cm (see Fig. 2).

These respective values of a and L allow us to estimate the maximum growth rate for the RT instabilities as:

$\gamma_{max} = \sqrt{a/L} = 2 \times 10^7\ s^{-1}$

During the implosion phase that lasts for a time interval, Δt = 50 – 70 ns the maximum number, n of e–foldings will be n = $\gamma_{max}\ \Delta$t = 1 – 1.5, and the perturbation amplitude η cannot growth beyond a factor of 3 to 5 times its initial value η_0:

η_{max}/η_0 = exp($\gamma_{max}\ \Delta$t) = 2.7 – 4.5. This means that if the initial perturbations are less than 1 % and at the end on the implosion phase the interface has imploded to a half of its initial radius, the final symmetry level will be better than 5to 10 %.

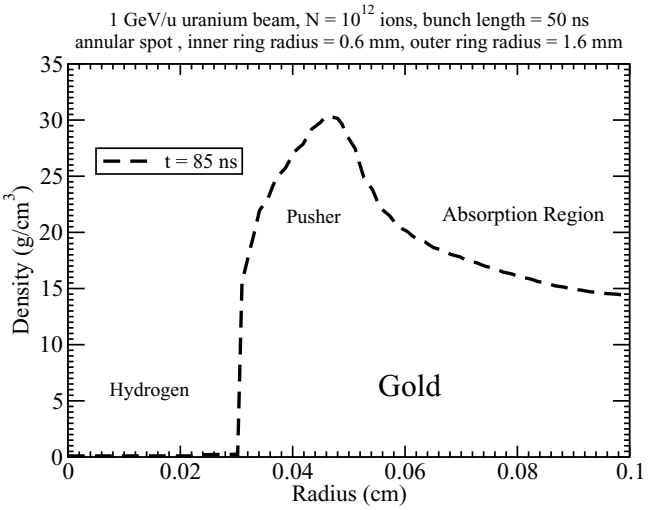


Figure 2: Density vs cylinder radius at t = 85 ns using an annular focal spot, hydrogen radius = 0.4 mm, outer gold radius = 3 mm.

It has been observed in the simulations that during the implosion phase the pusher remains mainly solid, although its internal layers are melted during the deceleration phase. This means that it will retain the elastic and plastic properties of the material. A detailed analytic study of the problem has shown that these effects will provide an additional stabilizing mechanism for the RT instability of the pusher during different phases of implosion [5].

Richtmeyer–Meshkov Instability Analysis

When a shock is transmitted across a corrugated interface, the corrugation appears in the transmitted shock front. The amplitude of corrugation may substantially increase at the contact surface due to RM instability. This problem can occur in the LAPLAS target if there is surface roughness across the hydrogen–gold interface in longituand or azimuthal direction. In case of a wobbler driven implosion, non–uniformities in energy deposition in azimuthal direction can also trigger this instability. It is also to be noted that this type of experiments can be used to study the problem of RM instability in cylindrical geometry in linear as well as non-linear regime. Such experimental studies will be very useful because no analytic theory exists to model such problems.

First we consider corrugation on the hydrogen–gold interface along the longitudinal direction. The cylinder length, L = 4 mm and we consider different perturbation wavelengths and amplitudes. For simplicity of numerical simulations, we assume that the facial boundaries of the target are fixed. The original target considered in LAPLAS calculations is 1 cm long and this approximation is therefore valid in the inner part of the target.

In a typical case we consider 4 wavelengths along the cylinder length which means λ = 1 mm that leads to a wavenumber, k = 62.857 cm^{-1}. Three different values for perturbation amplitude, A, namely, 0.1 μm, 1.0 μm and 10.0 μm, respectively, are considered. The respective values for the product kA become 6.28 $\times$ 10^{-4}, 6.28 $\times$ 10^{-3} and 6.28 $\times$ 10^{-2}. These numbers are very small which means that the instability will grow linearly througout the implosion till the maximum compression is achieved at t = 135 ns. In Fig. 3(a) and 3(b) we plot radial position of the hydrogen–gold interface at t = 0, 80 and 135 ns, assuming A = 0.1 μm and 1 μm, respectively. It is seen that in both cases, the perturbation amplitude does not grow during implosion. Figure 3(c) represents the case with an initial perturbation amplitude, A = 10 μm which is large and is clearly visible at t = 0 ns. It is seen that at t = 80 ns, the amplitude of perturbation has been reduced sustantially while at the time of maximum compression (at t = 135 ns) the amplitude has increased again, but has opposite phase compared to the initial perturbation. This is because when a shock propagates from a high–density (Au) medium to a low–density (H) medium, corrugated fronts in the expanding gold and hydrogen that is being compressed, deposit enough vorticity on the contact interface in such a way that it enhances the ripple growth in opposite direction from that at initial time [6, 7]. However, the implosion is successful even in the cases of a large perturbation with an initial amplitude of 10 μm.

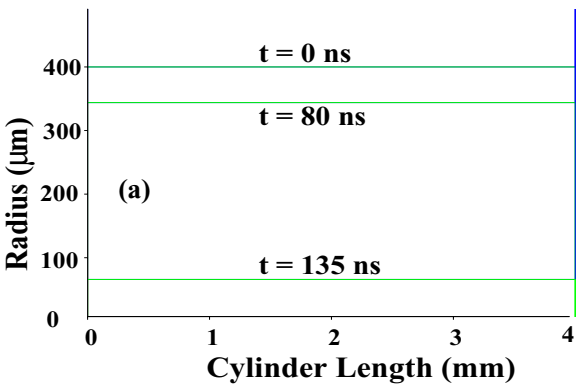


Figure 3: Radial position of hydrogen–gold interface at three different times using λ = 1 mm and A = 0.1 μm.

For larger wavenumbers, the implosion will be stable if smaller values of A $\leq$ 0.1 μm are considered, which is

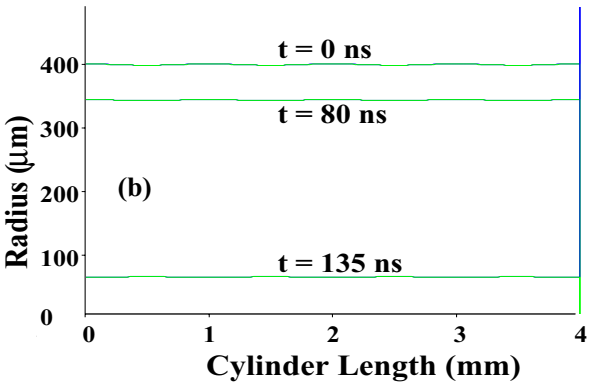


Figure 4: Radial position of hydrogen–gold interface at three different times using λ = 1 mm and A = 1.0 μm.

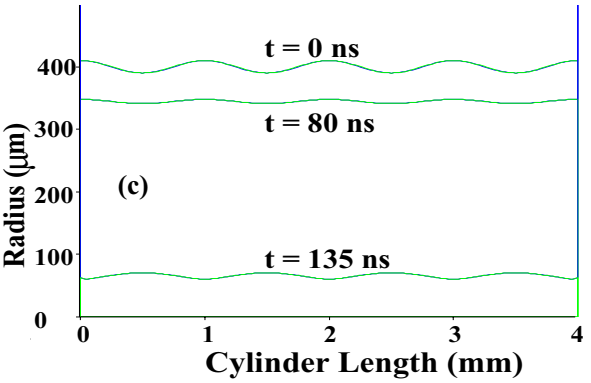


Figure 5: Radial position of hydrogen–gold interface at three different times using λ = 1 mm and A = 10.0 μm.

within the reach of the present day technology.

Figure 6 presents the cross sectional view of the target showing development of R–M instability due to azimuthal asymmetries at three different times. We assume 10 wavelengths over the circumfrence of the interface (radius = 0.4 mm that leads to k = 2.5 $\times$ 10^2 cm^{-1}) and A = 1 μm so that the product kA = 2.5 $\times$ 10^{-2} that represents a linear rigime. Figures 6(a)–(c) show that in this case the instability does not grow. For smaller modes, the compression is stable even if one considers larger amplitudes.

(please contact: n.tahir@gsi.de).

References

[1] N.A. Tahir et al., Phys. Rev. E 63 (2001) 016402.

[2] N.A. Tahir et al., Nucl. Instr. Meth. A 544 (2005) 16.

[3] W.F. Henning, Nucl. Instr. Meth. B 214 (2004) 211.

[4] A.R. Piriz et al., Plasma Phys. Controlled Fusion 45 (2003) 1733.

[5] A.R. Piriz et al., Phys. Rev. E 72 (2001) 056313.

[6] Y. Yang et al., Phys. Fluids 8, 1666 (1994).

[7] G. Wouchuk, Phys. Plasmas 8, 2890 (1994).

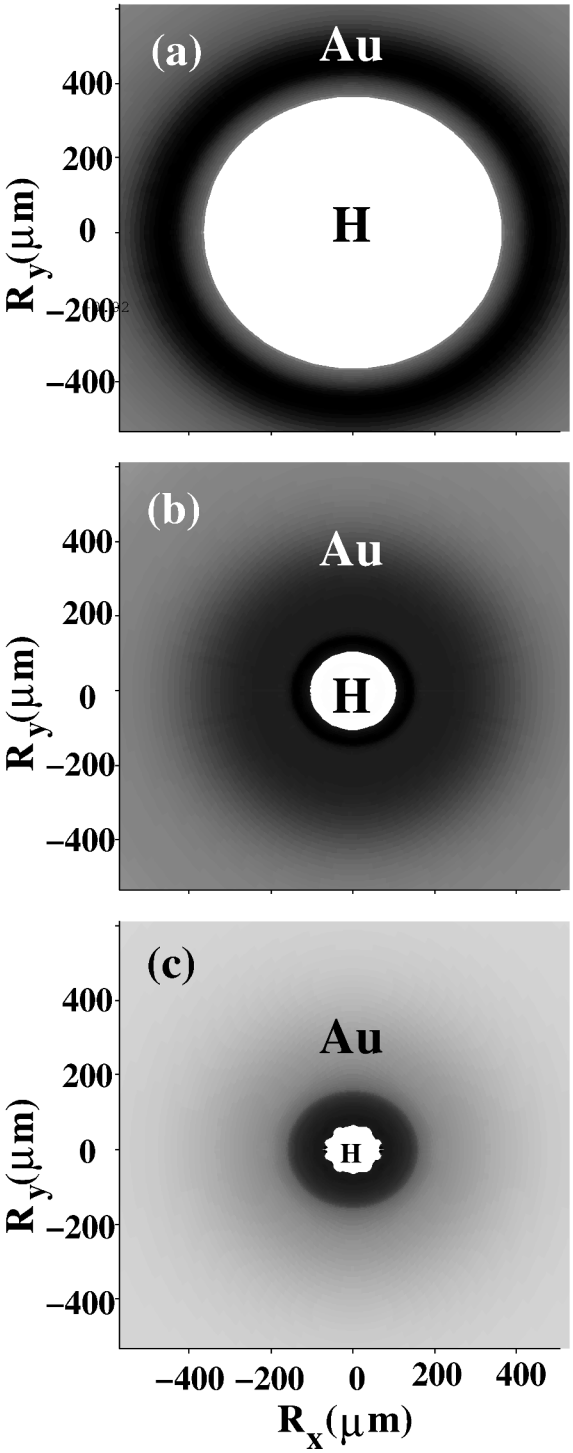


Figure 6: Cross sectional view of the target, (a) at t = 0 ns, (b) t = 120 ns, (c) t = 135 ns imploded by annular focal spot; λ = 2.5 $\times$ 10^{-2} cm, A = 0.1 μm.

Simulations of Damage to Carbon Collimators Caused Due to Full Impact of LHC Beam*

N.A. Tahir, GSI, Darmstadt, Germany
R.Schmidt, Y.Kadi, CERN, Geneva, Switzerland
A. Shutov, IPCP, Chernogolovka, Russia
A.R. Piriz, University of Castilla-La Mancha, Ciudad Real, Spain
D.H.H. Hoffmann, GSI, Darmstadt, Germany

Abstract

This contribution presents two-dimensional numerical simulations of heating of solid carbon target by full impact of an LHC beam. This work has been carried out to assess the damage caused to carbon collimators in case the beam is deflected towards them. The calculations show that the beam has the potential to cause substantial damage to the collimators.

Introduction

The LHC will operate at 7 TeV with a luminosity of $10^{34}\ cm^{-2}s^{-1}$. This requires two beams, each with 2808 bunches. The nominal intensity per bunch is 1.1×10^{11} protons and the transverse particle intensity profile is Gaussian with a standard deviation, σ = 0.2 mm. The bunch length is 0.5 ns and two neighboring bunches are separated by 25 ns. The energy stored in each beam of 362 MJ. In previous papers [1, 2] the mechanisms causing equipment damage in case of a failure of the machine protection system was discussed, assuming that the entire beam is deflected into a copper target. Another failure scenario is the deflection of beam, or part of it, into carbon material. Carbon collimators and beam absorbers are installed in many locations around the LHC to absorb beam losses, since carbon is the material that is most suitable to absorb the beam energy without being damaged. Since collimators and absorbers are close to the beam, it is very likely that they are hit first when the beam is accidentally deflected. In this paper the results of two-dimensional hydrodynamic simulations of the heating of a solid carbon cylinder with a radius of 5 cm whose one face is irradiated by the LHC beam with nominal parameters are presented. The hydrodynamic simulations have been carried out using the BIG-2 computer code [3] while the energy loss of the 7 TeV protons in carbon is calculated using the well known FLUKA code [4]. Our calculations suggest that the LHC beam may penetrate up to 10 m in solid carbon.

Simulation Results

In Fig. 1 we plot the specific energy deposited by a single bunch of 7 TeV protons and their cascade particles, calculated by the FLUKA code in solid carbon which is compressed powdered graphite with a density of 2.2 g/cm^3 along the beam axis. It is seen that the maxima of energy deposition occurs at a longitudinal position, L = 135 cm and is 0.16 kJ/g. In Fig. 2 are plotted specific energy deposition vs transverse coordinate at four different values of L = 40 cm, 135 cm, 240 cm and 350 cm respectively.

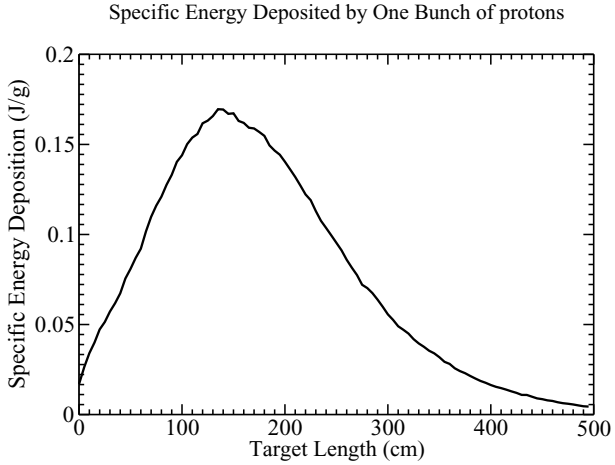


Figure 1: Specific energy deposited in solid carbon by a single LHC bunch along the axis.

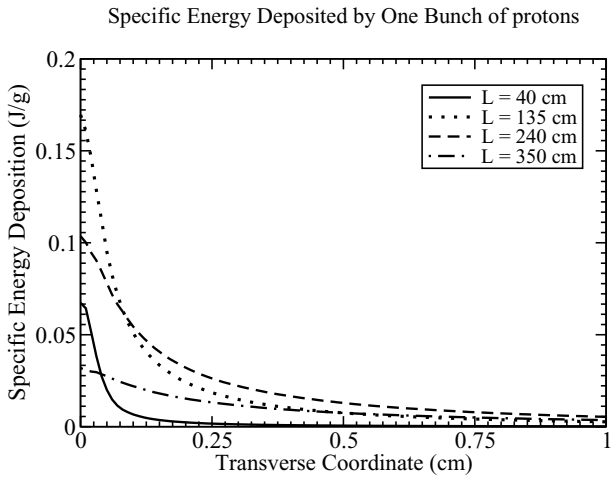


Figure 2: Specific energy deposited in solid carbon by a single LHC bunch in transverse direction at four different longitudinal positions.

Using the energy deposition data provided by the FLUKA code as input to to the BIG2 code, we have cal-

* Work supported by BMBF

culated the hydrodynamic and thermodynamic response of a solid carbon cylinder whose one face is irradiated with the LHC beam. We note that the energy deposition profile generated by the FLUKA code is three-dimensional while the BIG2 code is two-dimensional. To overcome this difficulty we consider four different longitudinal positions and study the hydrodynamic and thermodynamic response of the target along the transverse direction.

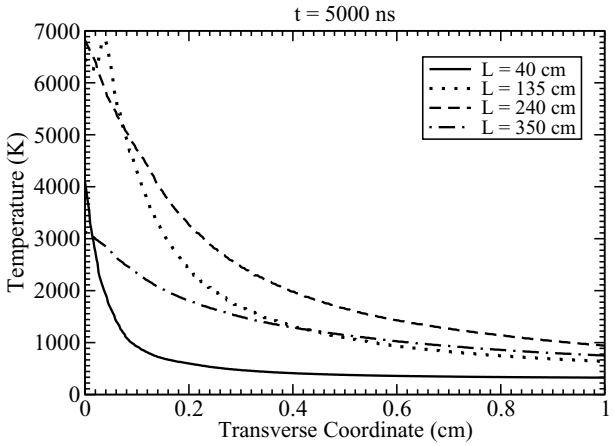


Figure 3: Temperature vs transverse coordinate at t = 5 microsecond at four different longitudinal positions.

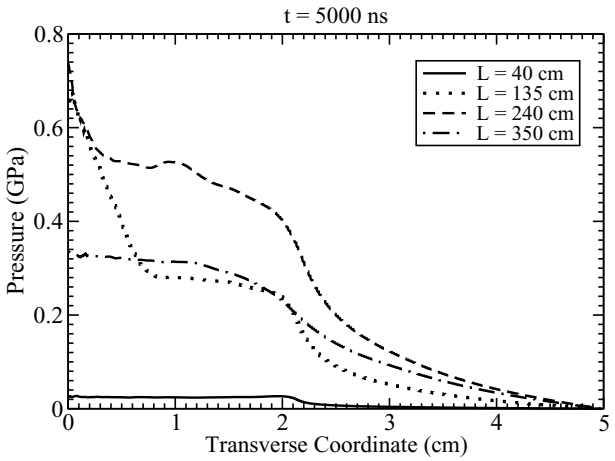


Figure 4: Pressure vs transverse coordinate at t = 5 microsecond at four different longitudinal positions.

In Fig. 3 we plot the target temperature vs transverse coordinate corresponding to the energy deposition profiles shown in Fig. 2 at t = 5 microsecond. By this time, only 250 out of 2808 bunches have been delivered. It is seen that a maximum temperature of 7000 K has been generated at the beam axis at L = 135 cm, where the maximum of energy deposition occurs. This leads to a maximum pressure of the order of 0.7 GPa, as is seen from Fig. 4. This high pressure drives a radially outgoing shock wave that leads to a substantial reduction in density (0.4 gm/cm^3) which is shown in Fig. 5. This means that the protons will penetrate further into the material thereby increasing the penetration depth of the beam. This means that the energy deposition peak that lies at L = 135 cm for solid density will continuously shift along the longitudinal direction.

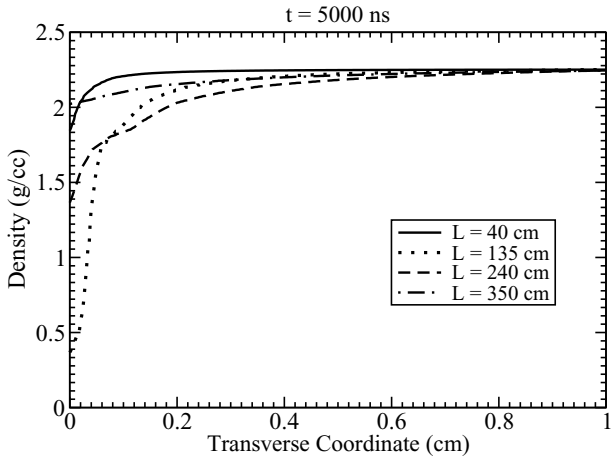


Figure 5: Density vs transverse coordinate at t = 5 microsecond at four different longitudinal positions.

Due to lower energy deposition at other longitudinal position, the material damage is relatively lower. We note that as the energy material density is reduced at a given position, the production of the secondary particle decreases that leads to a reduction in specific energy deposition. This in turn will slow down the hydrodynamic expansion of the material in transverse direction. This effect however is not included in the present calculations and is intended for the future work. We estimate that the LHC beam may penetrate about 10 m in solid carbon.

(please contact: n.tahir@gsi.de).

References

[1] N.A. Tahir et al., Phys. Rev. Lett. 94 (2005) 135004.

[2] N.A. Tahir et al., J. Appl. Phys. 97 (2005) 083532.

[3] V.E. Fortov et al., Nucl. Sci. Eng. 123 (1996) 169.

[4] A. Fasso et al., The physics models of FLUKA: status and recent development, CHEP 2003, LA Jolla, California, 2003.

Thermo-stimulated luminescence in LiF and NaCl crystals ion-irradiated at 8 K

K. Schwartz, K.-O. Voss, C. Trautmann, R. Neumann, GSI Darmstadt, Germany
A. Volkov, M. Sorokin, Kurchatov Institute, Moscow, Russia

Earlier defect studies on LiF and NaCl crystals irradiated at 8 K with swift heavy ions [1, 2] are complemented by thermo-stimulated luminescence (TSL) measurements.

Single crystals of LiF and NaCl were cooled to 8 K in the cryostat installed at the beamline XO of the UNILAC [1] and irradiated with ^{12}C (54 MeV), ^{58}Ni (370 MeV), ^{78}Kr (450 MeV), ^{197}Au (1100 and 2187 MeV), ^{208}Pb (1140 MeV), and ^{238}U (1400 MeV) ions. Fluences between 5 10^7 and 5 10^{11}ions/cm^2 were applied. Without dismounting the samples, TSL spectra were recorded in the range from 8 - 70 K (heating rate 4 K/min) using a photomultiplier (Hamamatsu, R374).

Independent of the irradiation parameters, all TSL spectra exhibit similar features, namely pronounced peaks in the low-temperature range (a broad peak at 12 K for LiF and several separated peaks at 10, 12, 15, and 20 K for NaCl), and a group of peaks of much weaker intensities at temperatures between 25 and 80 K. (Fig. 1). In LiF the lowest TSL maximum is at 12 K (a superposition of several elemental peaks) and in NaCl crystals the lowest peaks are in the range of 10 - 20 K. The spectra are very similar as those observed when performing irradiations with X-rays or fast electrons (see [3] and references therein). The TSL peaks at 10 – 20 K are ascribed to Frenkel pairs consisting of an α center (anion vacancy) and an I center (interstitial anion), whereas the peaks at higher temperatures (25 – 60 K) are mainly due to (F - H) Frenkel pairs (the F center is an anion vacancy with an electron and the H corresponds to an anion halogen molecule (X_2^-) replacing a regular anion). The intensity of the low-temperature peaks (10 – 20 K) depends on the total absorbed ion energy E_{abs} (beam energy times applied fluence). There is no threshold effect or any other pronounced dependence on the energy loss of the ions. Only at very high fluences, when E_{abs} exceeds 5 10^{18}eV/cm^2, the TSL peak intensity (normalized by E_{abs}) decreases. In this regime, the TSL emission is probably reduced due to pronounced absorption by color centers.

The TSL spectra do not give us information related to the defect concentration induced by the ion because of concomitant recombination processes. However, additional absorption studies demonstrate that the decrease of the concentration of F centers in the temperature range 8 - 25 K is smaller than that in the range of 25 - 60 K in agreement with the results described in [3].

The presence of the low-temperature TSL peaks demonstrates that under heavy-ion irradiation Frenkel pairs of type (α – I) are created in LiF as well as in NaCl. This type of defect cannot be detected by optical absorption spectroscopy, because their absorption maximum is close to the band gap. The results are important for the development of more detailed thermal spike models.

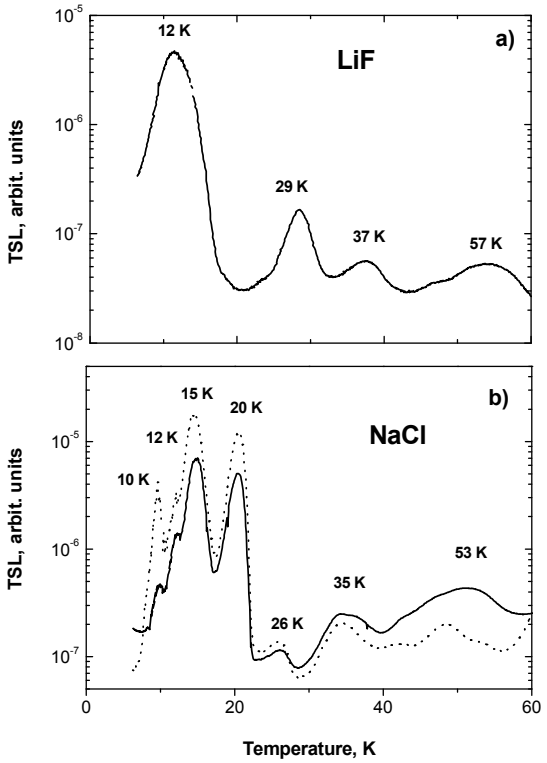


Figure 1: Thermo-stimulated luminescence spectra of (a) LiF irradiated with 1400-MeV U ions (10^8 ions/cm^2) and (b) NaCl irradiated with 1400-MeV U ions (solid line) at a fluence of 10^9 ions/cm^2 and 54-MeV C ions (dotted line) at a fluence of 5 10^{10} ions/cm^2.

References

[1] K. Schwartz, M. Sorokin, C. Trautmann, R. Neumann, A. Volkov, K.-O. Voss, GSI Scientific Report 2004, p. 256.

[2] K. Schwartz, A. Volkov, K.-O. Voss, M. V. Sorokin, C. Trautmann, R. Neumann, Nucl. Instr. Meth. B (2006) in press.

[3] E. Vasil`chenko, I. Kudryavtseva, A. Lushchik, Ch. Lushchik, V. Nagirnyi, Phys. Stat. (c) 2 (2005) 405.

Characterisation of surface hillocks formed on CaF_2 under ion irradiation

N. Khalfaoui, C.C. Rotaru, S. Bouffard, M. Toulemonde, CIRIL, Caen, France
J.P. Stoquert, INESS, F. Haas, IRES, Strasbourg, France
C. Trautmann, GSI, Darmstadt, Germany

For many amorphizable insulators (silicates, garnets, etc.) track observations by different techniques give coherent results concerning the track size at the surface and in the bulk [1, 2]. The situation is quite different for ionic crystals. Their strong ionic binding structure prevents amorphization, and under ion irradiation they respond by a complex damage mechanism. To date, there exists a large set of track data in particular for LiF and CaF_2 [3-7]. The experimental results give indications that tracks in these crystals are larger on the surface than in the bulk. Moreover, in contrast to amorphisable crystals, the diameter of tracks at the surface increases only slightly with the electronic energy loss (S_e).

In this study, we exposed single crystals of CaF_2 cleaved along the (111) plane to various ion projectiles between Ca and U (1-11 MeV/u), delivered from different accelerators (GANIL, Caen, UNILAC, Darmstadt, and VIVITRON, Strasbourg) covering a S_e range between 4.6 and 35.5 keV/nm.

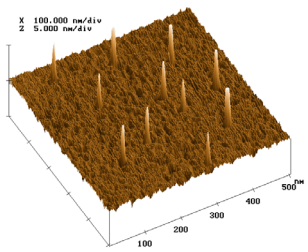


Fig. 1: 3-D SFM image of CaF_2 surface irradiated with 6.4-MeV/u Xe ions (5×10^9 cm^{-2}).

The irradiated surface was investigated by scanning force microscopy (SFM). Imaging was performed in the tapping mode using tips of nominal curvature 5-10 nm, which is smaller than tips typically used in the contact mode [5]. The SFM image of an irradiated CaF_2 surface is presented in Fig.1, showing hillocks of around 20 nm in diameter and a few nm in height [8]. For each hillock, the height as well as the corresponding diameter was recorded. For sufficiently high energy losses, the two parameters are clearly correlated (Fig. 2).

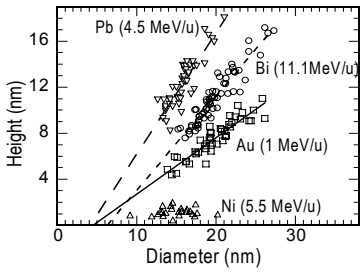


Fig. 2: Height versus corresponding diameter of surface hillocks produced by different ion irradiations.

For all different irradiation experiments, we analysed the efficiency (E_{eff}) of hillock creation, defined by the number of observable hillocks normalized to the incident ions. Hillocks appear only above an energy loss threshold of ~5 keV/nm (Fig. 3-right). For larger S_e values, E_{eff} increases reaching unity (each ion produces a hillock) at ~13 keV nm^{-1}. The height-diameter correlation coefficient [8] becomes constant at around the same S_e value, revealing a direct link between these two properties.

Plotting the mean value of the different heights and diameters versus the energy loss (Fig. 3-left) shows constant (~1 nm) hillock heights between 5 and 10 keV/nm which then increase linearly with S_e and reach 12.5 nm at 35.5 keV/nm. This evolution is in contrast to the hillock diameter which scatters around a constant value of 18 nm.

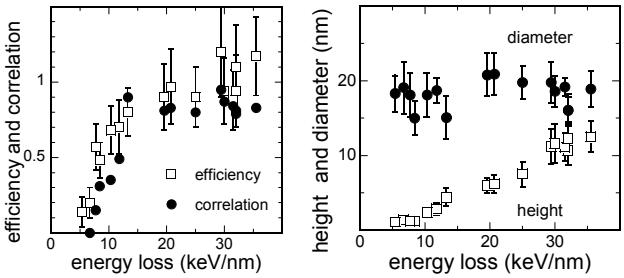


Figure 3: (left) efficiency and correlation coefficient versus energy loss; (right) mean height and diameter of hillocks versus energy loss.

For strong height-diameter correlations (coefficient >0.5), we could graphically deconvolute the measured diameter and the tip size. For each data set recorded with a given tip, the height-diameter data (as shown in Fig. 2) extrapolated to zero height gives us the tip curvature radius. Applying this procedure reduces the hillock diameters to about ~13 nm, constant in the entire S_e regime. We note that this value is almost a factor of two larger than track diameters obtained by transmission electron microscopy [7,8].

References

[1] N. Khalfaoui et al., Nucl. Instr. Meth. B 209 (2003) 165.
[2] R. Neumann, Nucl. Instr. Meth. B 151 (1999) 42
[3] K. Schwartz et al., Phys. Rev. B 58 (1998) 11232.
[4] C. Trautmann et al., Nucl. Instr. Meth. 164-165 (2000) 365.
[5] C. Müller et al., Nucl. Instr. Meth. B 212 (2003) 318.
[6] M. Boccanfuso et al., Prog. Nucl. Energ. 38 (2001) 271.
[7] J. Jensen et al., Nucl. Instr. Meth. B 141 (1998) 753.
[8] N. Khalfaoui et al., Nucl. Instr. Meth. B240 (2005) 819.

Influence of ion velocity on the track morphology in dark mica

M. Lang, K.-O. Voss, R. Neumann, C. Trautmann, GSI, Darmstadt, Germany
N. Medvedev, Moscow Engineering Physics Institute & Kurchatov Institute, Moscow, Russia
W. Hasenkamp, R. Papaléo, Pontifícia Univ. Católica do Rio Grande do Sul,Porto Alegre, Brazil
U.A. Glasmacher, Geologisch-Palaeontologisches Institut, Univ. Heidelberg, Germany
G.A. Wagner, Forschungsstelle Archäometrie der Heidelberger Akademie der Wissenschaften am MPI für Kernphysik, Heidelberg, Germany
N. Ishikawa, Japan Atomic Energy Agency (JAEA), Tokai-mura, Japan
T. Yamaki, Japan Atomic Energy Agency (JAEA), Takasaki, Japan

In many solids, swift heavy ions (MeV–GeV) produce long cylindrical damage trails with diameters of a few nm. The projectiles induce excitation and ionization processes, releasing electrons which spread their kinetic energy via collisions with secondary electrons radially to the ion trajectory. The energy density in this cylindrical zone is determined by the ion energy deposited per unit path length (dE/dx) and by the range of the electron cascades. Since this range is directly connected to the maximum energy transfer to the electrons, the kinetic energy of the projectiles comes into play. For a fixed *dE/dx* value, the resulting energy density is lower for higher ion velocities. This so-called *velocity effect* was evidenced for latent tracks [1] as well as for etched tracks [2], revealing that track radii increase with decreasing ion velocity.

We investigated how the velocity affects the damage morphology in phlogopite, a dark mica mineral. Track formation and etching are typically linked to the deposition of a critical *dE/dx*. Chemical etching of tracks of Ni ions (81 MeV) in phlogopite exhibits the interesting property that the etch-pit geometry changes at around *dE/dx* = (6.1 ± 0.5) keV/nm from triangular to hexagonal [3]. On the basis of this threshold behaviour, we tested the influence of the velocity on the track morphology.

Samples of natural phlogopite were irradiated with ^{58}Ni ions at different accelerator facilities (GSI, UFRGS Porto Alegre (Brazil), JAEA Tokai-mura and Takasaki (Japan)) covering a broad energy range from 4 to 650 MeV. The corresponding electronic energy-loss values are marked in Fig. 1, illustrating that the same *dE/dx* value can be reached at low and high beam velocities. The irradiated samples were etched in 4 % HF (10 min, room temperature). Scanning electron microscopy images of etched tracks reveal hexagonal cross sections for 12-MeV Ni ions and triangular etch pits for 650-MeV Ni ions (Fig. 2). Although the energy loss is 5.7 keV/nm for both irradiations, the different kinetic energies have obviously a significant influence on the track damage.

The shape transition is assigned to a change in the continuity of the damage along the tracks [3]. This is supported by the observation of step-like structures in the triangular etch pits implying a non-uniform track etch rate (Fig. 2 right). In contrast, the hexagonal structures are much deeper (larger track etch rate) and have a small distribution in size (Fig. 2 left), typical indications for a homogenous damage morphology [3].

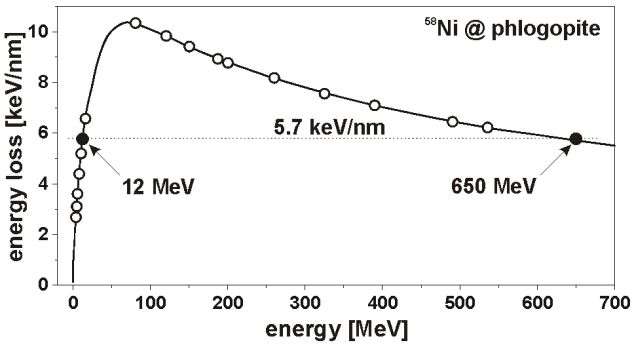


Fig. 1. Energy loss versus beam energy calculated with the SRIM00-code. Each dot represents an irradiation experiment.

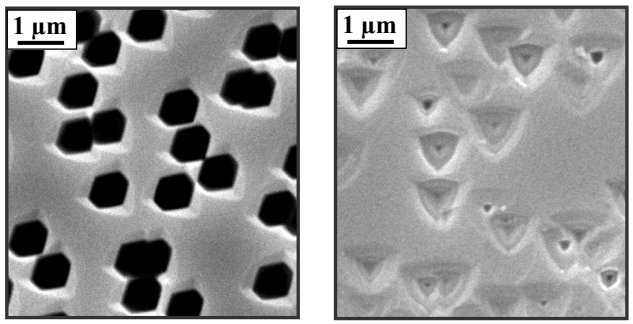


Fig. 2. Scanning electron microscopy images of etched tracks in phlogopite irradiated with Ni ions of *dE/dx* = 5.7 keV/nm using ions of (left) 12 MeV and (right) 650 MeV.

In phlogopite the sharp transition in etch-pit geometry at the threshold clearly demonstrates that the damage produced by low-velocity Ni ions of 12 MeV is more pronounced than that of 650-MeV ions. The threshold for homogeneous track etching is therefore shifted to a lower value, in agreement with observations made for tracks in vitreous SiO_2 [2].

References

[1] A. Meftah, F. Brisard, J.M. Costantini, M. Hage-Ali, J.P. Stoquert, F. Studer, M. Toulemonde, Phys. Rev. B 48 (1993) 920.
[2] J. Jensen, A. Razpet, M. Skupiński, G. Possnert, Nucl. Instr. and Meth. B (2006) in print.
[3] M. Lang, U.A. Glasmacher, B. Moine, R. Neumann, G.A. Wagner, Nucl. Instr. and Meth. B 218 (2004) 466.

Improved fission-track length measurements using ion irradiation

Raymond Jonckheere, Eva Enkelmann, Myo Min, Lothar Ratschbacher, Geologisches Institut,
Technische Universität – Bergakademie Freiberg, Germany
Christina Trautmann, GSI, Darmstadt, Germany.

Apatite [$Ca_5(PO_4)_3(F,Cl)$] is a common mineral in rocks that contains ~10 ppm U. ^{238}U disintegrates by spontaneous fission and the fission fragments produce linear damage trails of ~20 µm length and 5-10 nm width. The lattice damage along such a fission track is repaired at elevated temperatures, leading to a gradual decrease of its etchable length. Since fresh tracks are formed as existing tracks are annealed, the track-length *distribution* provides a record of temperature variations in the rock [1]. A temperature-time path, T(t), is reconstructed on the basis of measurements of the lengths of horizontally confined tracks in the interior of the grains [2,3].

The resolution of the modelled T(t)-path depends on the number of measured confined tracks. This number is often small because confined tracks are only etched via cracks or fission tracks that intersect the surface. The goal of 100 length measurements is often not reached and there are indications that even this number is not sufficient to constrain the T(t)-function. In the present investigation, we examine the effect of different ion irradiation conditions on the number of confined tracks in apatite. The irradiations were performed at the UNILAC, using 330-MeV Xe and 800-MeV U ions of fluence ~2.5×10^6 cm^{-2}.

For geometrical reasons, the confined-track densities (ρ_C) are proportional to the ion-track densities (ρ_{IT}) and lengths (l_{IT}), and to the fission-track densities (ρ_{FT}) and lengths (l_{FT}), i.e. with the combined fission- and ion-track lengths per unit area: $\rho_C \sim (\rho_{IT}\, l_{IT})\,(\rho_{FT}\, l_{FT})$. However, there exist important deviations from the geometrical model (Fig. 1). These are correlated with the orientation of the ion beam relative to the crystal symmetry, as indicated by the higher normalised confined-track densities for samples irradiated at 15° from the surface normal (DUR 5/6), compared to those irradiated under normal incidence (DUR 3/4). This, and the fact that higher confined-track densities are recorded when the azimuth direction of the ion tracks is parallel to the c-axis (DUR 6) than when it is perpendicular to the c-axis (DUR 5), indicates that the effect is, in part, related to the geometries of the etched ion tracks and fission tracks, and thus to the anisotropic etching properties of apatite. In contrast, the difference between the samples with fossil (DUR 3/4) and induced fission tracks (DUR 1/2) is not related to the track geometries, and assumed to result from a fundamental difference between "aged" fossil and "fresh" fission tracks or a fundamental difference in the structure of tracks produced by 330-MeV Xe (DUR 1/2) and 800-MeV U ions (DUR 3/4).

Figure 2 shows the increase of the normalised confined-track densities as a function of etching time (t_e). A geometrical model predicts a quadratic (or higher) increase if a modest increase of the ion-track length is taken into account. This is the case for DUR 1-4 up to step 3 (t_e = 35 s) and for DUR5-6 up to step 2 (t_e = 25 s). The deviations past these points result from track overlap.

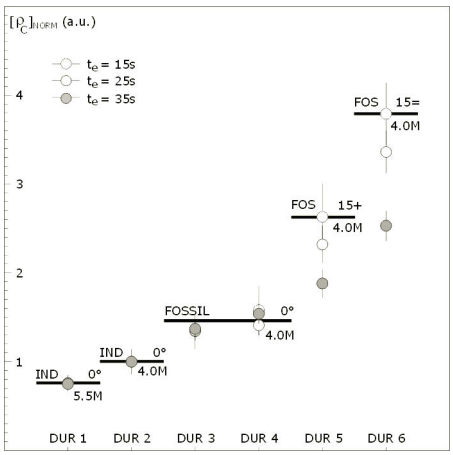


Figure 1: normalised confined fission-track densities in prismatic apatite surfaces irradiated under different conditions. IND: contains neutron-induced fission tracks; FOS: contains fossil fission tracks; 5.5M: etched in 5.5M HNO_3; 4.0M: etched in 4.0M HNO_3; 0°: ion-irradiated at normal incidence; 15+: irradiated at 15° from normal in the plane perpendicular to the crystallographic c-axis.

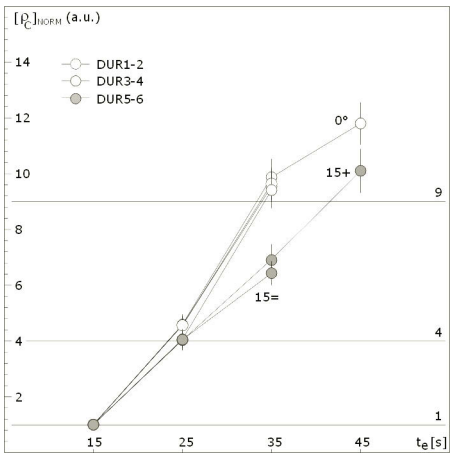


Figure 2: normalised confined fission-track densities in prismatic apatite surfaces as a function of etching time (t_e) in 4M HNO_3.

References

[1] P.F. Green et al., Chem. Geol. (Isot. Geosci.) 79 (1989) 155.
[2] K. Gallagher, Earth Planet. Sci. Lett. 136 (1995) 421.
[3] R. Ketcham et al., Geol. Mat. Res. 2 (2000) 1.

Quasi One-Dimensional Electrical Conductors Created by Swift Heavy Ion Tracks in Tetrahedral Amorphous Carbon Films *

D.Schwen†, H. Hofsäss, A. K. Nix, Universität Göttingen, Germany
J. Krauser, Hochschule Harz, Wernigerode, Germany
C. Trautmann, GSI, Darmstadt, Germany

Conduction mechanisms in swift heavy ion irradiated carbon films were studied using scanning probe microscopy and temperature dependent I-V spectroscopy.

Thin films of tetrahedral amorphous carbon (ta-C) were grown on low resistivity n-type Si substrates by mass selective ion beam deposition of 100 eV ^{12}C ions at room temperature. The films have a thickness of several hundred nm, exhibit an sp^3-content of about 80%, a density of about 3 g/cm^3, and a high resistivity at room temperature of up to 10^{10} Ωcm.

The films were irradiated at the UNILAC with swift heavy ions under normal incidence with fluences between 10^9 and 10^{11} ions/cm^2. Projectiles included uranium and lead with energies of about 1 GeV. The initial beam energy was degraded by Al foils to about 3-4 MeV/u close to the stopping power maximum.

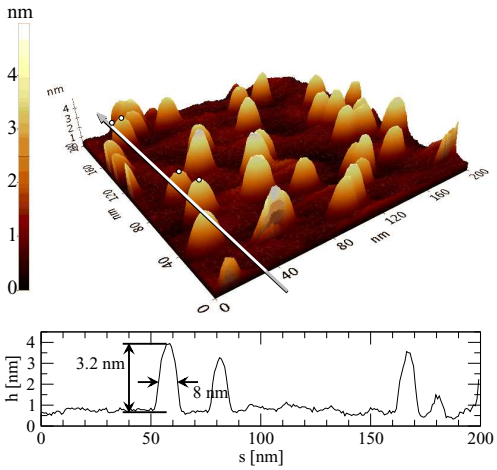


Figure 1: Topographical AFM image of a ta-C sample irradiated with 1 GeV Pb ions (10^{11} ions/cm^2). Bottom graph shows a topographical linescan (position indicated by the arrow). FWHM of the observed hillocks is about 8 nm, hillock height is about 3 nm.

The large electronic energy loss along the ion track of about 30 keV/nm causes a conversion of the dense and high-resistivity sp^3-phase into a conducting graphite-like sp^2-phase within a cylinder of about 10 nm in diameter[1], thus creating nanometer-sized conducting filaments within the ta-C matrix. On the surface above each track a hillock is formed (figure 1) due to the swelling associated with the local density reduction.

* Work supported by BMBF grant 05 KK4MGA/9
† dschwen@uni-goettingen.de

For individual conducting channels, the room temperature I-V curves were measured by contact-mode atomic force microscopy (AFM) using conducting metal-coated tips. Temperature dependent I-V measurements from 300-50 K were performed on ensembles of ion tracks sandwiched between the substrate as a back contact and evaporated Au pads as top contacts. The $e^{-\frac{T}{4}}$ temperature dependence of the I-V curves suggests a tunneling based variable-range hopping process. Strong voltage dependence is in agreement with a modified variable-range hopping model for moderate electrical fields [2] (Figure 2). This model considers the deduction of hopping ranges D. For temperatures below 50 K, D surpasses the track diameter, leading to a relative reduction of target states.

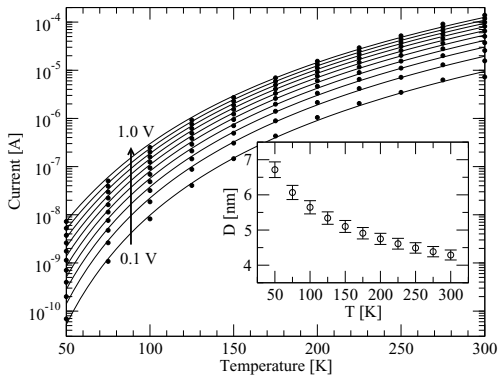


Figure 2: Temperature dependent I-V spectra fit with a modified variable-range hopping model. Inset shows hopping ranges extracted from the model. For temperatures below 50 K geometric confinement is expected.

Future experiments will focus on the measurement of temperature dependent I-V curves at individual conducting ion tracks, contacted by electro-deposition of Cu nanowires through self-aligned pores in a track etched polycarbonate film, spin-coated onto the ta-C prior to ion irradiation. This will allow us to investigate tracks as a possible model system for Luttinger liquid behaviour.

References

[1] Zollondz J.-H, Krauser J., Weidinger A., Trautmann C., Schwen D., Ronning C., Hofsäss H., Schultrich B., "Conductivity of ion tracks in diamond-like carbon films", Diamond Relat. Mater. **12** (2003) 938

[2] Pollak M., Riess I., "A percolation treatment of high field hopping transport", J. Phys. C **9** (1976) 2339

Laser Spectroscopy of the $^6P_{7/2}$ Multiplet of Gd^{3+} in a LaF_3 Host Crystal

K.-O. Voss*, R. Neumann, GSI Darmstadt, Germany

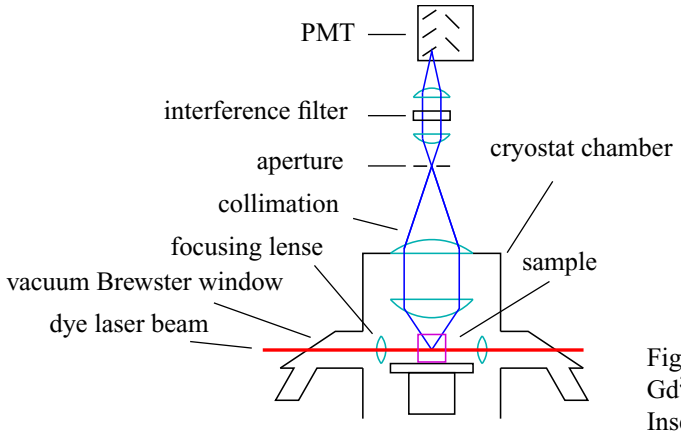


Figure 1: Scheme of the laser spectroscopy setup.

The 4f shell electrons of the lanthanides are deeply buried in a Xe-like electronic core. To a certain extent, they are thus shielded against any external electric field. As a consequence, when doping trivalent lanthanide ions into suitable crystals, optical transitions within the partly filled 4f shell are comparably narrow, especially at low temperatures, since line broadening effects are strongly reduced [1]. The remaining electrostatic crystal field introduces Stark splittings of the m_z-degenerate free-ion energy levels. We want to use such multiplets as probes of the crystal damage caused by ion irradiation.

Here, as a first step, we report the development of a setup for laser spectroscopy of lanthanide-doped solids and first measurements of laser-induced transitions within the 4f configuration as a function of sample temperature.

Specifically, we chose lanthanum trifluoride single crystals doped with Gd^{3+} ions at low concentration. Two-photon transitions from the 4f $^8S_{7/2}$ ground state of the Gd^{3+} dopand to its 4f $^6P_{7/2}$ excited state (see fig. 2) are induced by intense, narrow-band laser light tuned in the spectral region around 620 nm [2]. For this purpose, the light of a cw dye laser pumped by a frequency-doubled Nd:YVO_4 solid-state laser is focused into the LaF_3 crystal that is cooled by a helium compression cryostat (see fig. 1). The excitation is monitored via fluorescence at about 310 nm due to one-photon transitions back to the ground state. The fluorescence from the crystal passes a collimating system of lenses, is effectively separated from the laser stray light by means of interference filters and then detected by a cooled photomultiplier with high quantum efficiency in the near UV.

* K.-O.Voss@gsi.de

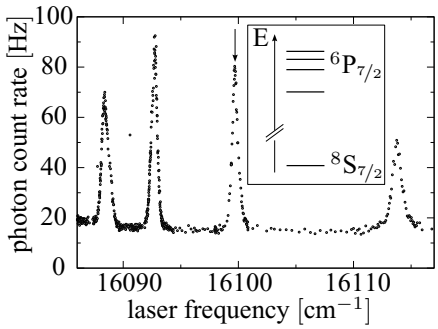


Figure 2: Excitation spectrum of the $^6P_{7/2}$ multiplet of Gd^{3+} in LaF_3 at about 8 K using two-photon absorption. Inset shows the Gd^{3+} ground state and the crystal-field split $^6P_{7/2}$ excited state.

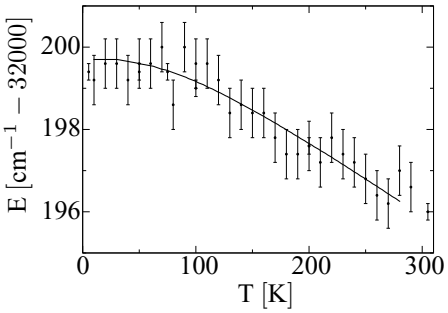


Figure 3: Energy of line from figure 2 (marked by arrow) as function of temperature. Solid line is computed for $\alpha = -21\,\mathrm{cm}^{-1}$, $T_D = 360\,\mathrm{K}$ after reference [4].

In figure 3, the transition energy E of the spectral line marked by an arrow in figure 2 is plotted as a function of temperature. For temperatures above 100 K, the energy shifts according to $\frac{\partial E}{\partial T} \approx -\frac{1.5}{100}\,\frac{cm^{-1}}{K}$. This observation can be explained by scattering of phonons at the Gd ions. Applying the formalism presented in [3] and [4], we find that an electron-phonon coupling constant of α = -21 cm^{-1} and a Debye temperature of $T_D = 360\,\mathrm{K}$ satisfactorily reproduce the temperature-dependent energy shift.

References

[1] S. Hüfner, *Optical Spectra of Transparent Rare Earth Compounds*, Academic Press (1978)

[2] M. Dagenais, M. Downer, R. Neumann and N. Bloembergen, Phys. Rev. Lett. 46 (1981) 561

[3] A. Ellens, H. Andres, A. Meijerink and G. Blasse, Phys. Rev. B 55 (1997) 173

[4] D. E. McCumber and M. D. Sturge, J. Appl. Phys. 14 (1963) 1682, and references therein.

Radiation sensitivity of polyimide at low irradiation temperatures

D. Severin, University of Marburg, Germany
W. Ensinger University of Technology Darmstadt, Germany
R. Neumann, C. Trautmann, G. Walter, GSI, Darmstadt, Germany
E. Balanzat, CIRIL, Caen, France

The aim of this study is to test the radiation sensitivity of polyimide (Kapton) proposed as insulators for the new superconducting magnets of FAIR. During long-term operation at low temperatures (4.5 K), some of the components will be exposed to strong radiation. To date, very little is known about radiation damage and degradation processes at such low temperatures. Although polyimide is known to exhibit excellent radiation resistance, there is particular concern due to the formation of small volatile molecule fragments frozen in during low temperature operation which may suddenly be released during warming up cycles. In degraded material this possibly induces small cracks or other defects deteriorating the insulating and mechanical properties of Kapton.

To test radiation damage induced at low-temperatures, first experiments were performed at the GANIL facility in Caen using a 9.3 MeV/u ^{78}Kr beam. The sample holder was connected to a cryostat that allows irradiation and infrared spectroscopy analysis at a controlled temperature down to 8K. Kapton foils of thickness 12 µm were exposed to different fluences. During beam stops they were analysed in-situ at temperatures between 8 and 300 K.

The infrared spectra show the same general trend as known from room-temperature irradiations [1,2], i.e. a decrease of structure-related bands such as the imide band at 725 cm^{-1} and an increase of bands due to the formation of unsaturated bonds, in particular triple bonds such as C≡N (2260cm^{-1}) [2].

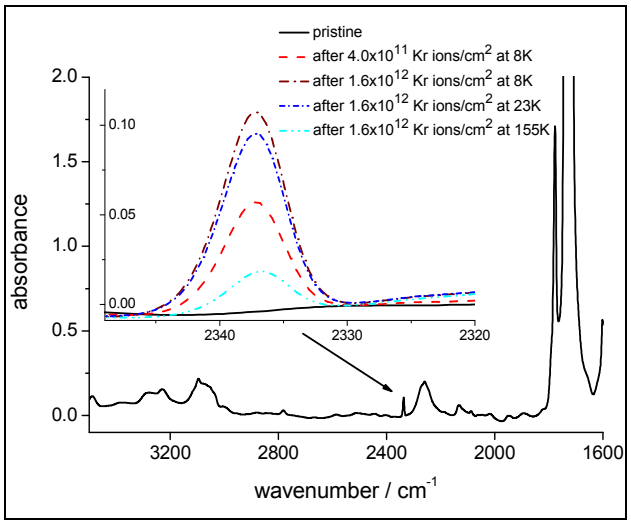


Fig. 1. Infrared spectra at 8 K after irradiation with 1.6 10^{12} Kr ions/cm^2. The inset illustrates how the CO_2 band (2337 cm^{-1}) rises with increasing fluence. The CO_2 band disappears during sample heating.

In addition to the indications of imide decomposition, the spectra recorded at 8 K show a new band at 2337 cm^{-1} ascribed to CO_2 (Fig. 1). The CO_2 band intensity becomes larger with increasing fluence and disappears when heating the samples after the irradiation (Fig. 2).

At low irradiation temperature, CO_2 fragments are obviously produced and trapped in the polymer matrix due to limited mobility or frozen at the sample surface. As soon as the temperature increases, the molecules can move and finally leave the sample by outgassing.

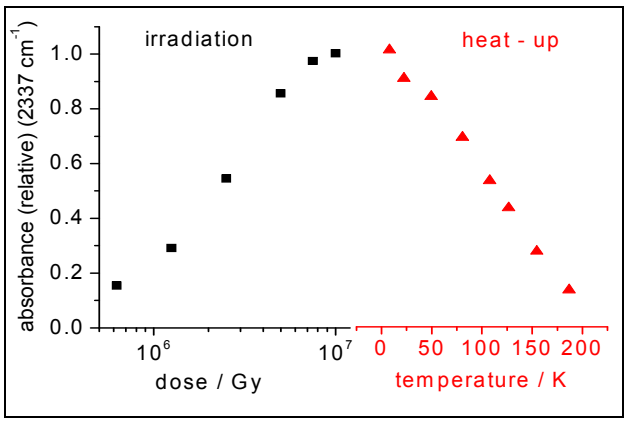


Fig. 2. Data from in-situ infrared measurement of the CO_2 band (2337 cm^{-1}) as a function of dose (squares) and temperature (triangles).

To better understand this complex process, additional low-temperature experiments are in preparation including online mass spectroscopy which will allow us to analyze volatile radiation fragments in combination with degradation products in the polymer bulk. By determining the yield of volatile degradation products, more quantitative estimations of the overall outgassing will become possible.

First low-temperature irradiations of polymer foils were already performed at GSI. The analysis of bulk modifications by infrared spectroscopy is in progress. To study the effect of low irradiation temperatures on the electrical properties, these Kapton samples will also be tested by dielectric relaxation spectroscopy.

References

[1] D. Severin, W. Ensinger, R. Neumann, C. Trautmann, G. Walter, I. Alig, S. Dudkin, Nucl. Instr. and Meth. B 236 (2005) 456.

[2] T. Steckenreiter, E. Balanzat, H. Fuess, C. Trautmann, Nucl. Instr. and Meth. B 151 (1999) 161.

Current–voltage curves in synthetic conical nanopores described by a simple Poisson/Nernst – Planck model

B. Schiedt, GSI, Darmstadt, Germany
J. Cervera, Universitat Jaume I, Castelló, Spain
R. Neumann, GSI, Darmstadt, Germany
P. Ramírez[#], Universidad Politécnica de Valencia, Valencia, Spain

We have developed a theoretical model [1] for ionic transport through synthetic conical nanopores. The results have been compared with experiments obtained for single, gold–coated conical nanopores.

The model [1] describes quantitatively the ionic transport through synthetic conical nanopores. It is based on the Poisson and Nernst-Planck (PNP) equations and allows the calculation of realistic profiles of average ionic concentration and electric potential along the pore. The only adjustable parameter is the surface charge density σ. Within this formalism, the concentration and potential profiles are computed together as self-consistent solutions of the PNP equations, in this way avoiding the assumption of a given potential distribution along the pore.

We have compared the results provided by the PNP model with recent experimental data by Siwy et al. [2] obtained for two poly(ethylene terephthalate) (PET) filters containing single gold–coated conical nanopores. They were produced by chemically etching a PET foil containing a single heavy ion track (irradiated at UNILAC, GSI) and subsequently covering the pore walls with gold by electroless plating. After this procedure, the small radius of the pores was ≈ 5 nm and the wide radius ≈ 300 nm. The length of the pores was ≈ 12 μm. In the experimental setup, the membrane separated the two halves of an electrolytic cell, containing 0.1 M KF solutions. I-V curves were recorded at several pH values, for pores with differently modified surfaces. The results in Fig. 1a were obtained from a nanopore modified with 2-mercaptopropionic acid, yielding a negative surface charge at pH = 6.6, and a neutral surface charge at pH = 3.5. In Fig. 1b, the nanopore surface contained mercaptoethylammonium groups and the measurements were conducted at pH = 6.6, yielding a positive surface charge. When the pore wall is uncharged, the *I–V* curve is linear (full circles in Fig. 1a). When the surface becomes charged, the corresponding *I–V* curves show rectification (open circles). For negative surface charge, the electric current is higher for $V > 0$ than for $V < 0$ (states "on" and "off"). If the charge on the pore wall becomes positive, the "on" and "off" states of the nanopore appear at $V < 0$ and $V > 0$, respectively.

The theoretical results in Fig. 1 (dashed and full lines) are parametric in the surface charge density σ (e is the elementary charge). In all the calculations we used the (infinite dilution) diffusion coefficients $D_+ = 1.47 \cdot 10^{-5}$ cm^2/s, and $D_- = 2.03 \cdot 10^{-5}$ cm^2/s of the ionic species.

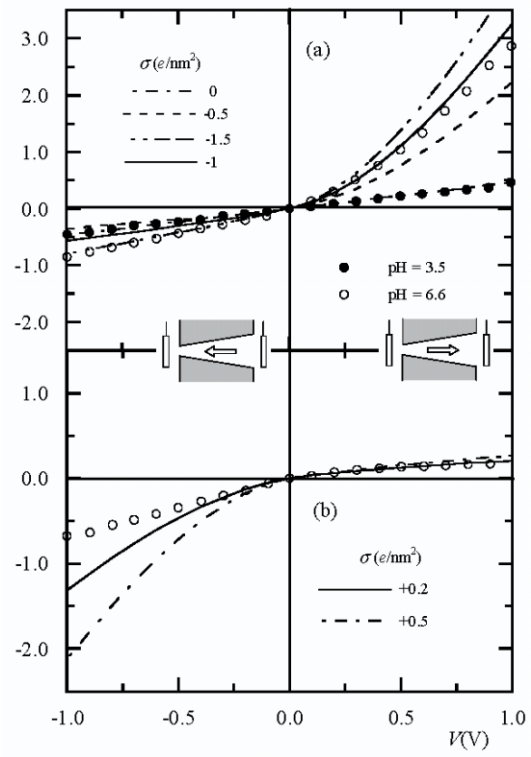


Figure 1: Experimental (circles) [2] and theoretical (curves) results for the negatively (a) and positively (b) charged nanopore. The curves are parametric in the surface charge density σ.

The theoretical curves in Fig. 1a account for the experiments at pH = 6.6 for $\sigma \approx 1 - 1.5$ e/nm^2, within the range of the surface charge densities reported for cylindrical and conical nanopores in PET filters. When the sign of the surface charge is reversed to positive (Fig. 1b), the theory follows again the experiments if the surface charge density is decreased. A better fit to the experimental points in Fig. 1b has not been attempted because it is not made clear in ref. 2 if the pore radii of the two samples measured were equal.

References

[1] J. Cervera, B. Schiedt and P. Ramírez**,** Europhys. Lett. 71 (2005) 35.

[2] Z. Siwy, E. Heins, C.C. Harrell, P. Kohli and C.R. Martin**,** J. Am. Chem. Soc. 126 (2004) 10850.

[#]patraho@fis.upv.es

Protein Biosensors Based on Conical Gold Nanotubes

Z. Siwy, L. Trofin, P. Kohli, L.A. Baker, C.R. Martin, University of Florida, USA
C. Trautmann, GSI, Darmstadt, Germany.

There is increasing interest in using nanopores as the sensing elements in biosensors [1]. The nanopore most often used is the α-hemolysin protein channel, and the sensor consists of a single channel embedded within a lipid bilayer membrane. An ionic current is passed through the channel, and analyte species are detected as transient blocks in this current associated with translocation of the analyte through the channel – stochastic sensing [1]. While this is a very promising sensing paradigm, it would be advantageous to eliminate the fragile lipid bilayer membrane, and to replace the biological nanopore with an abiotic equivalent.

We describe here a new type of protein biosensor that is based on a single conically shaped gold nanotube embedded within a polymeric membrane prepared by the track-etching technique [2]. The polymer template with a single nanopore was obtained by single-ion irradiation at the UNILAC in combination with the track-etching technique. The sensing protocol entails passing an ionic current through the nanotube, but unlike in previous devices [1], transient current pulses are not observed and analyzed. Instead, the protein analyte binds to a biochemical molecular-recognition agent immobilized at the small-diameter opening (or mouth) of the conical nanotube. Because the protein molecule and the nanotube mouth have comparable diameters, analyte binding effectively plugs the nanotube, which is detected as a corresponding permanent blockage of the ion current.

Single conically shaped nanopores were etched in 9 M NaOH from one side as described in [2]. The large diameter opening at one face of the membrane was ~600 nm, and the small diameter opening at the opposite face was ~30 nm. Electroless gold plating was used to deposit Au along the walls of this conical pore; also the two surfaces of the membrane are coated with Au [3]. The mouth diameter was controlled by varying the electroless plating time, and measured using a simple electrochemical method. Au nanotubes with mouth diameters in the range of 5 to 9 nm were used, depending on the analyte to be detected [4].

The final step is to attach the molecular-recognition agent (MRA) to the Au surfaces. Three different MRA/analyte systems were investigated: (i) biotin / streptavidin, (ii) protein-G / immunoglobulin (IgG), and (iii) an antibody to the protein ricin/ ricin as the analyte [4]. Biotin was attached to the Au by using a commercial thiolated biotin derivative. A commercial biotinylated protein G was used for the IgG sensor. The Au nanotube was first biotinylated, streptavidin was then attached to the surface-bound biotin, and the botinylated protein G was attached to the streptavidin. A similar strategy was used to attach biotinylated anti-ricin. The nanotube mouth diameter was remeasured after each of the functionalized steps [4]. The final mouth diameters (after all functionalization steps) were for the streptavidin and IgG sensors ~5 nm, and for the ricin sensor ~ 4nm.

The measurement procedure was as follows: 1. Current-voltage (I-V) measurement before exposure to protein. 2. Replace the solution facing the mouth of nanotube with an electrolyte solution of a protein that *does not bind* to the attached MRA and obtain a second I-V curve. 3. Replace this solution with a solution of protein that *does bind* to the MRA and record I-V curve. The ion currents were measured using Axopatch 200B and the signal was digitized by Digidata 1322 A (Molecular Devices Inc.).

The operation of such a sensor is illustrated in Fig. 1. The protein albumin BSA does not bind to the antibody of ricin, therefore it does not change the I-V curve of the Au tube in a significant way (Fig. 1). Adding ricin however led to shutting off the ion current. We demonstrated that this type of sensor can detect sub-picomolar concentrations of a protein analyte [4].

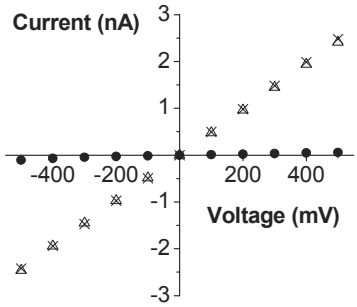


Fig. 1 Functioning of a single nanotube sensor for ricin. Current-voltage curves of a gold tube with antibody for ricin recorded at 1 M KCl, pH 4.3 (Δ), at 1 M KCl and 100 nM albumin BSA (×), and at 1 M KCl and 100 nM ricin (•) [4].

References

[1] H. Bayley, C.R. Martin, "Resistive-Pulsing Sensing – From Microbes to Molecules", Chem. Rev. 100 (2000) 2575.

[2] P.Y. Apel, Y.E. Korchev, Z. Siwy, R. Spohr, M. Yoshida, "Diode-like single-ion track membrane prepared by electro-stopping", Nucl. Instr. Meth. B 184 (2001) 337.

[3] M. Nishizawa, V.P. Menon, C.R. Martin, "Metal Nanotubule Membranes with Electrochemically Switchable Ion-Transport Selectivity", Science 268 (1995) 700.

[4] Z. Siwy, L. Trofin, P. Kohli, L.A. Baker, C. Trautmann, C.R. Martin, „Protein Biosensors Based on Biofunctionalized Conical Gold Nanotubes", J. Am. Chem. Soc. 127 (2005) 5000.

Morphological Changes in Au Nanowires Influenced by Rayleigh Instability

S. Karim, Department of Chemistry, Philipps University, Marburg, Germany
M.E. Toimil-Molares, T.W. Cornelius, and R. Neumann, GSI, Darmstadt, Germany
A.G. Balogh, W. Ensinger, Darmstadt University of Technology, Darmstadt, Germany

Metallic nanowires are important for potential applications in many future nanoscale devices [1]. Theories predicted that due to the high aspect ratio, nanowires become unstable particularly at elevated temperatures when the mobility of atoms by diffusion is higher [2]. Linear stability analysis by Nichols and Mullins demonstrated that a cylindrical wire is unstable to longitudinal perturbations whose wavelength exceeds its circumference. It was also found that the temporal growth rate of perturbation is maximum at a particular wavelength λ_{max} whose value is a function of mass transport mechanism (for surface diffusion-controlled morphological changes $\lambda_{max} = 8.89\ R_o$, where R_o is the radius of wire before annealing). Therefore, it was proposed that if a long cylinder decays into spheres, the spacing between the resulting spheres will represent the value of λ_{max}. Rayleigh instability was demonstrated recently in Cu nanowires [3].

Here, we present experimental results of a similar morphological instability of Au nanowires as a function of diameter. We fabricated Au wires with diameter 25-60 nm by electrochemical deposition in an etched ion-track membrane [3]. The polymer template was subsequently dissolved in CH_2Cl_2. The nanowires were dispersed on a SiO_2 substrate and annealed in an evacuated furnace at temperatures ranging between 200 and 500 ^oC (heating rate = 5 ^oC /min). After cooling down to room temperature, the samples were examined using HRSEM.

The series of images in Fig. 1 displays the morphological changes that occurred in 25nm diameter wires at different temperatures. Fig. 1a shows a wire before annealing. The wires annealed at 300 ^oC developed radial perturbations and fragmented into sections of various lengths (Fig. 1b). The wires annealed at 400 ^oC decayed into chains of short cylindrical particles. Finally, at 500 ^oC, the decay was complete and all wires transformed into chains of spheres.

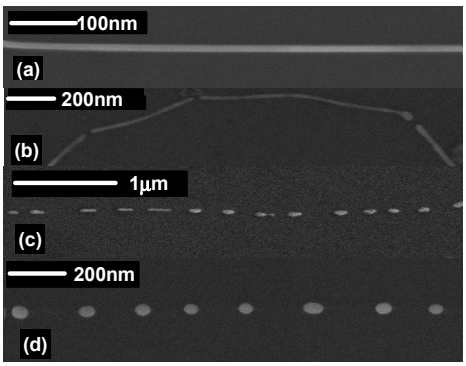


Fig.1. HRSEM images of Au wires (diameter 25 nm) at different temperatures: (a) RT, (b) 300 ^oC, (c) 400 ^oC, (d) 500 ^oC

In a subsequent experiment, we annealed Au wires with different diameters (d = 25-60 nm) until all wires decayed into spheres. The distance between adjacent spheres (λ_{max}) is plotted in Fig. 2 as a function of radius of wires before annealing together with theoretically predicted values. The experimental λ_{max} data is almost by a factor two larger than the values predicted by Nichols and Mullins.

Nichols and Mullins developed their model assuming isotropic surface energy. Subsequent models taking into account surface energy anisotropy predicted that the anisotropy can either promote or suppress the Rayleigh instability depending upon its magnitude and sign [4]. Accordingly, λ_{max} will become larger or smaller than $8.89\ R_o$ expected for isotropic materials.

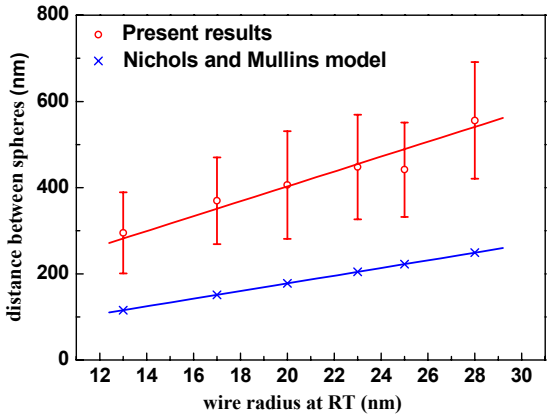


Fig. 2. Comparison of predicted and experimental values of λ_{max} as a function of nanowires radius at RT.

In conclusion, we have demonstrated experimentally that during isothermal annealing Au wires decay into linear rows of nanospheres at a temperature as low as 500 ^oC. Average values of λ_{max} are larger than that those predicted for materials with isotropic surface energy, indicating a stabilization effect due to surface energy anisotropy.

References

[1] A. Huczko, Appl. Phys. A 70, 2000, 365
[2] F.A. Nichols and W.W. Mullins, Trans. Metal. Soc. AIME 233, 1965, 1840
[3] M.E. Toimil Molares, A.G. Balogh, T.W. Cornelius, R. Neumann and C. Trautmann, Appl. Phys. Lett. 85, 2004, 5337
[4] J.W. Cahn, Scr. Metall. 13, 1979, 1069

Electrical transport properties of single bismuth nanowires

T.W. Cornelius, M.E. Toimil-Molares, R. Neumann, GSI, Planckstr. 1, 64291 Darmstadt, Germany
S. Karim, University of Marburg, Hans-Meerwein Str., 35032 Marburg, Germany.

Due to its unique electronic properties bismuth is of enormous interest for studies on the nanoscale. In particular, when the object size is comparable to the mean free path of charge carriers l_e (~ 100 nm and ~ 400 µm at 300 and 4 K, respectively [1]), mesoscopic effects such as electron scattering at both surface [2] and grain boundaries [3] become significant.

For investigating the influence of these two effects on the wire resistivity ρ, we fabricated and individually contacted single Bi nanowires. For an examination of the influence of grain boundary scattering, single wires of different crystallinity are created by varying the deposition parameters in a controlled manner [4].

In order to fabricate single Bi nanowires, polycarbonate foils are irradiated by single swift heavy ions at the UNILAC and subsequently etched in aqueous NaOH solution. After covering one side of a single-pore membrane by a conductive layer, a wire is electro-chemically deposited in the nanochannel. The process is continued until a cap is formed on top of the wire, which is then covered with an additional Au layer for electrical contact [5]. The electrical resistance of single wires is recorded at room temperature and as a function of temperature T.

Fig. 1 displays the specific wire resistivity versus diameter. The dashed lines represent the mean values of three different types of wire, that were created under three different deposition conditions. The solid line illustrates the resistivity of bulk Bi without taking into account any mesoscopic effects, while the dotted line represents the resistivity including totally diffuse electron scattering at the wire surface. The two approaches can neither explain the high resistivity values nor the difference of ρ for various kinds of wire. ρ can only be explained by incorporating electron scattering at grain boundaries. Since the grain size is larger for wires fabricated at higher T and smaller voltage U, wires created at these conditions exhibit smaller ρ values due to a lower contribution of scattering processes at grain boundaries.

Fig. 2 displays the resistance R of single Bi nanowires of diverse diameters, created at 60 °C and -17 mV as a function of temperature. All wires show a nonmonotonic R vs. T behaviour, the resistance maximum shifting to higher temperatures with decreasing wire diameter. In Bi the charge carrier density decreases while the mobility increases with diminishing temperature. In bulk Bi, the influence of growing mobility surpasses the effects of decreasing carrier concentration, leading to a reduction of ρ with lowering T. In contrast, in nanowires l_e is limited by the electron scattering at grain boundaries. Since thinner wires are expected to possess less grain boundaries, the influence of electron scattering is less pronounced.

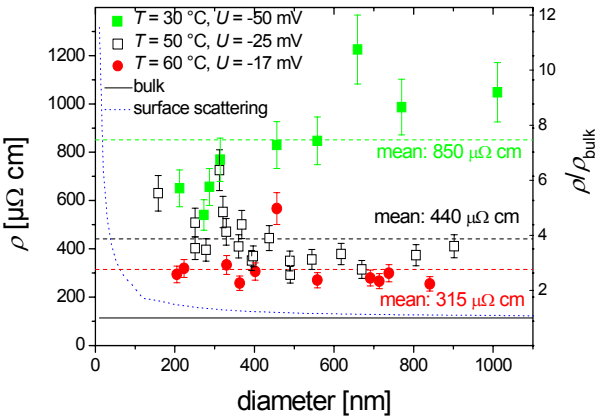


Fig. 1: Specific electric resistivity of single Bi nanowires of different crystallinity as a function of wire diameter.

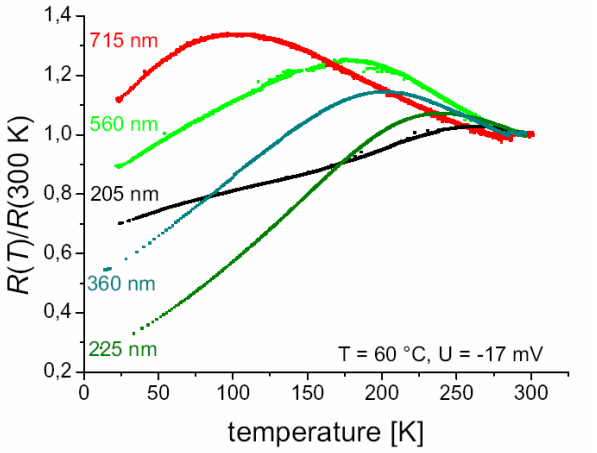


Fig. 2: Resistance of single Bi nanowires of different diameters d as a function of temperature.

In summary, we have shown that the electrical transport properties of single Bi nanowires are influenced by mesoscopic effects involving both a higher specific resistivity at room temperature and a nonmonotonic resistance versus temperature behaviour.

References

[1] S.B. Cronin et al., Nanotechnology 13 (2000) 653.
[2] R.B. Dingle, Proc. R. Soc. London A 201 (1950) 545.
[3] A.F. Mayadas, M. Shatzkes, Phys. Rev. B 1 (1970) 1382.
[4] T.W. Cornelius et al., Nanotechnology 16 (2005) S246.
[5] M.E. Toimil Molares et al., Nanotechnology 15 (2004) S201; T.W. Cornelius, Diploma Thesis, University of Heidelberg (2003).

Infrared properties of single metal nanowires

T. Kolb, F. Neubrech, R. Lovrincic, G. Fahsold, A. Pucci, Kirchhoff-Institut für Physik (KIP), University of Heidelberg, INF 227, 69120 Heidelberg, Germany
S. Karim, University of Marburg, Hans-Meerwein Str., 35032 Marburg, Germany
M.E. Toimil-Molares, T.W. Cornelius, R. Neumann, GSI, Planckstr. 1, 64291 Darmstadt, Germany

Nanostructures and especially nanowires (NW) are regarded as fundamental components of future key technologies. Of special interest is, e.g., the optical-field enhancement at the sharp ends of a thin NW. In surface enhanced spectroscopy, the optical-field enhancement can increase signals of single molecules to heights above the noise level. The maximum enhancement is expected at the fundamental antenna resonance of a NW.

We investigated resonances of single metal NWs by infrared (IR) spectroscopic microscopy. The NWs were prepared by template-directed growth of metal in ion track-etched polycarbonate membranes [1]. The wire diameters ranged from 200 down to 50 nm. After dissolution of the membrane, we dispersed the wires on IR-transparent substrates (e.g. KBr).

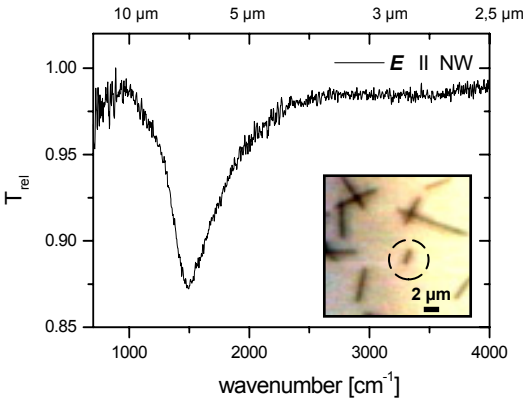


Fig. 1: Transmission spectrum of a single Cu nanowire of approximately 2.2 µm length and 200 nm diameter

The IR spectroscopic microscopy of single NWs was performed using the synchrotron light source ANKA (Forschungszentrum Karlsruhe). With an IR microscope coupled to an FTIR spectrometer we took spectra in a broad range between 600 and 6000 cm^{-1}. The IR spot size was 8.3 µm in diameter. In order to find the right IR spot position, a single NW was located by optical microscopy in the visible range (see inset of Fig. 1).

At nearly normal incidence we measured intensity (I) spectra at two positions: on the wire itself (I_{NW}) and, as reference, on the bare substrate (I_{ref}). The relative transmission $T_{rel} = I_{NW}(\omega) / I_{ref}(\omega)$ for a spot with a single NW is shown in Fig. 1.

IR spectra of NWs with length of a few micrometer show well pronounced antenna-like resonances (Fig. 1) [2]. The T_{rel} spectra reveal the resonant surface plasmon excitation only if the polarization of the electrical field is oriented parallel to the long wire axis. From such measurements, the ratio of the extinction cross-section σ_{ext} of a single NW to its geometric cross section σ_{geo} can be estimated by $\sigma_{ext} / \sigma_{geo} = A_0 \times (1 - T_{rel}) \times (n_s + 1) \times (L_{NW} \times D_{NW})^{-1}$, where A_0 denotes the IR spot size, n_s is the refractive index of the supporting substrate (n_s(KBr) =1.54), L_{NW} is the length (from VIS microscopy), and D_{NW} the NW diameter (known from the wire-growth process). At the resonance frequency of the NW in Fig. 1, we obtain $\sigma_{ext} / \sigma_{geo} = 38$. This corresponds to an intensity extinction by a factor of 38 larger than that of simple shadowing and to a local-field enhancement by $\sqrt{38} \approx 6$ (as spatial average).

According to the classical resonance condition for free-standing linear antennas consisting of perfectly conducting metal, the fundamental resonance occurs if L_{NW} matches with half the wavelength.

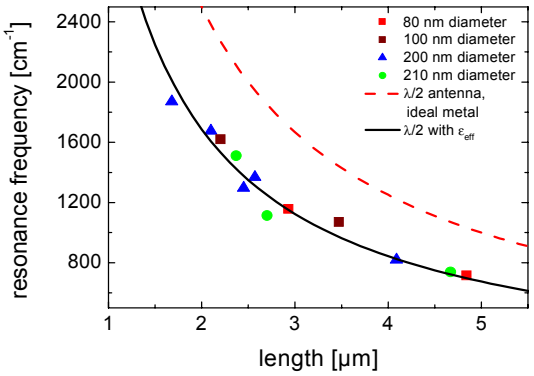


Fig. 2: Resonance frequencies of different nanowires versus their length (dots), calculation for an ideal metal in air (dashed line) and in a medium with an effective dielectric constant $\varepsilon_{eff} = 2.2$ (solid line), respectively.

For wires of various L_{NW} we found that the frequency of maximum extinction follows the law of antenna-like resonances, see Fig. 2. But a relatively big effective dielectric constant $\varepsilon_{eff} \approx 2.2$ has to be taken into account. For optical spectra of metal nanoparticles, $\varepsilon_{eff} = (1+n_s^2)/2$ (which gives 1.7 on KBr) is used to describe the substrate effect [see e.g. Ref. 3]. On the other hand, the NWs deviate from an ideal antenna since the skin depth is not small compared to the diameter.

We acknowledge valuable discussions with H. Eipel (KIP) and the IR beamline scientists Y.-L. Mathis, B. Gasharova, and D. Moss (ANKA, Forschungszentrum Karlsruhe). The members of the Kirchhoff-Institut acknowledge financial support by the DFG (SPP 1165)

[1] M.E. Toimil Molares et al., APL 82 (2003) 2139.
[2] G. Fahsold, et al., ANKA Annual report (2004) 103.
[3] M.M. Dvoynenko et al., Physica B 299 (2001) 88.

Field emission of copper nanowires grown in polymer ion-track membranes

F. Maurer*, J. Brötz, H. Fuess (Technische Universität Darmstadt, Darmstadt, Germany)
A. Dangwal, D. Lysenkov, G. Müller (Bergische Universität Wuppertal, Wuppertal, Germany)
M.E. Toimil-Molares, C. Trautmann (Gesellschaft für Schwerionenforschung, Darmstadt, Germany)

Nanowires with sharp tips, i.e. small radius of curvature, are expected to be ideal field emitters, because an externally applied electric field E can be amplified up to several orders of magnitude [1]. The probability of electron tunneling through the surface potential is enhanced, resulting in a field emission (FE) current. Since no elevated temperatures are required, such nanostructures could act as cold electron sources with many potential applications for vacuum nanoelectronics [2].

The field emission performance of a nanowire ensemble is influenced by the aspect ratio (ratio of length over diameter) of the wires and the mean spacing between the emitters. These geometrical parameters can be varied independently within a broad range by electrochemical deposition of metals into nanoporous polymeric ion-track templates.

Vertically-aligned nanowires were produced by Cu deposition into polycarbonate membranes. The irradiations were performed at the UNILAC using heavy ions such as Au, Pb or U of 11.4 MeV/u. Assuming a Poisson distribution [3], the mean spacing of neighboring ion tracks $\langle a \rangle$ was adjusted to 0.5 – 5 µm applying fluences f between 10^8 and 10^6 cm^{-2}, respectively. The diameter of the nanopores was controlled by the chemical etching process, increasing linearly with etching time. Pore diameters were chosen between 210 and 330 nm. Au was sputtered and electrochemically strengthened with a ∼10 µm Cu layer on one side of the template serving as working electrode. Wire growth in the nanopores was accomplished by potentiostatic ($-70 \leq U \leq -110$ mV) deposition at 50 °C using a high-conductive copper sulfate/sulphuric acid solution. As the length of the wires is directly proportional to the deposited charge q, the deposition was stopped at a defined value, corresponding to a certain wire length (online coulometry). The length of our wires was between 8 and 18 µm. The wires were released by dissolution of the polymeric template in CH_2Cl_2. Scanning electron microscopy (SEM) images of selected ensembles are imaged in Fig. 1. Wires of ensembles with low mean spacing and high aspect ratio tend to agglomerate to star-shaped bundles during or after dissolution of the template (Fig. 1b).

FE performance was examined in diode configuration with a luminescent screen under high-vacuum conditions (10^{-4} Pa). More detailed FE measurements were subsequently performed with a field-emission scanning microscope (FESM) under ultra-high vacuum conditions ($<10^{-7}$ Pa) [4] with µm resolution [5].

According to the modified Fowler-Nordheim (FN) theory, the current density J from a tip-like emitter with an electric field E amplified by the field enhancement factor β is given by

$$J = A(\beta E)^2/\phi \cdot \exp(-B\phi^{1.5}/\beta E)\,,$$

where ϕ is the work function of the emitting material ($\phi_{Cu} = 4.5$ eV), and A and B are summarized fundamental constants. For cylindrical emitters of height h and with a hemispherical tip of radius r, β is mainly given by the aspect ratio $\beta_{geo} = h/r + 2$ [1]. Integral and local FE investigations were accomplished on ensembles with different geometrical properties, obtaining emission site densities up to 1.4×10^5 cm^{-2} at 6 V/µm. Only 6 % of free-standing and vertically aligned nanowires were strong emitters. Nearly all wires showed unstable FN behavior (different values for ascending and descending voltage cycles) with a mean β value of 245, which is a factor three higher than expected from the emitter shape. The discrepancy is assumed to result from different tip geometries. We also observed field emission of the centers of the nanowire bundles shown in Fig. 1b.

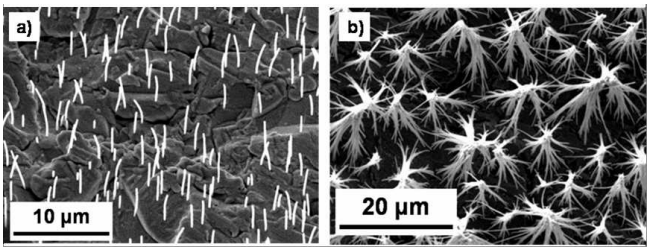


Figure 1: SEM images of Cu nanowire ensembles; a) $\langle a \rangle$ ∼1 µm, N ∼10^7 cm^{-2}; b) $\langle a \rangle$ ∼0.5 µm, N ∼10^8 cm^{-2}, single wires agglomerated to star-shaped wire bundles (∼10^6 cm^{-2} leading to a larger spacing between bundle centers compared to the parallel-aligned single wires).

References

[1] T. Utsumi; IEEE Transactions On Electron Devices 38 (1991) 2276.

[2] N.S. Xu, S. Ejaz Huq; Mat. Sci. Eng. R 48, 47 (2005).

[3] B.S. Barashenkov; JINR P 14 (1977) (German translation).

[4] E. Mahner, N. Minatti, H. Piel, N. Pupeter, Appl. Surf. Sci. 67 (1993) 23.

[5] D. Lysenkov, G. Müller, Int. J. Nanotechnology 2 (2005) 239.

* maurer@st.tu-darmstadt.de; fax: +49 6151 16 6023

Sharp metallic nanotips produced by the ion-track template technique

D. Dobrev, R. Neumann, C. Trautmann, GSI, Darmstadt, Germany.

In the recent past, micro- and nanowires of different materials and structures have been produced by means of the ion-track template technique [1]. This study focuses particularly on the creation of needles with sharp tips for the possible application as field emitters. In contrast to earlier approaches using cone-shaped pores [2], we are presenting here an alternative method. As usual the wires are grown in ion-track membranes produced from 30-µm thick polycarbonate (Makrofol N, Bayer). The foils were irradiated with 11.1 MeV/u uranium ions at the UNILAC accelerator applying a fluence of ~10^6 ions/cm^2 (Fig. 1a). Track etching in 5M NaOH at 50°C results in cylindrical pores with diameters 1-3 µm (Fig. 1b).

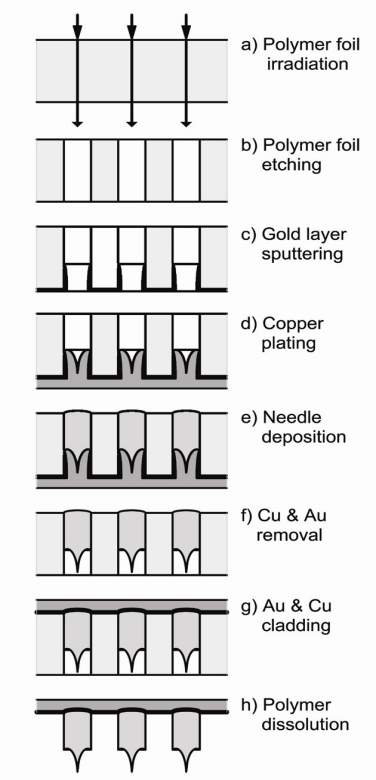


Fig. 1. Scheme of different preparation steps.

In contrast to the usual thin gold layer, we sputtered a rather thick gold film of 0.1 - 0.2 µm onto the mat side of the porous membrane. Due to the broad beam divergence, the gold is also deposited on the wall of the pores down to a depth of a few µm (Fig. 1c). The membrane was then inserted into the galvanic cell described in [3], the conductive gold layer facing the anode. The gold film was reinforced by a 20-µm thick copper layer deposited at room temperature (RT) and at a current density of 50 mA/cm^2. As electrolyte we used a Cupatierbad (Riedel Co) copper bath. Copper plating occurs on the regular membrane surface as well as on the Au covered wall close to the pore orifices. Once the pores are completely closed from this side (Fig. 1d), the membrane is turned around and remounted in the same cell. From the open pore side, needles of a desired metal are grown (Fig. 1e). After removal of the copper and gold layers, we obtain needles with sharp tips embedded in the polymer matrix (Fig. 1f). Free needles can bee produced by dissolving the polymer in a suitable solvent. If free-standing tips are needed, the filling side of the membrane has to be additionally sputter-coated (e.g. by a gold layer reinforced by Cu) (Fig. 1g) before the polymer matrix is removed (Fig. 1h).

Figs. 2 and 3 show scanning electron microscopy images of sharp tips on platinum and gold needles. The deposition of platinum was performed at RT using an alkaline solution containing 15g/l Pt (Pt-OH-bath, Mekatem Co) at effective current density of 1mA/cm^2. The gold needles were grown at 50°C from a sodium disulfitoaurate(I) Imabrite 24 bath (Schloeter Galvanotechnik Company) with 12.3 g/l gold at optimal current density of 0.3 A/dm^2.

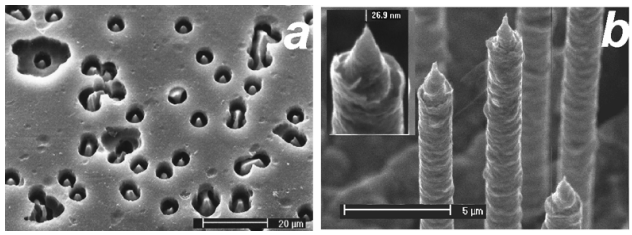


Fig. 2. Platinum nanotips: (a) embedded in the polymer matrix; (b) free-standing needles on a Cu-Au substrate

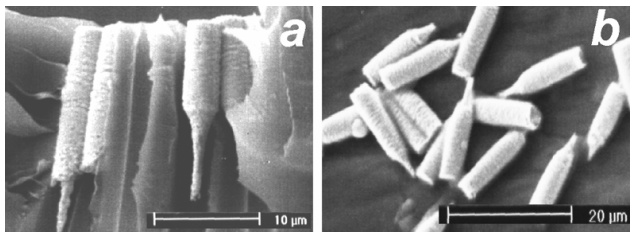


Fig. 3. Gold nanotips: (a) cross-section of ion-track membrane with pores filled with Au (step Fig. 1f); (b) free Au needles after dissolving the membrane in CH_2Cl_2.

This method is suitable for each metal that allows the preferential dissolution of the initial conductive and supporting layer without destroying the needle material. The needle density is limited by pore overlap and can vary from a single tip up to 10^6 - 10^8 tips/cm^2.

References:

[1] M.E. Toimil-Molares, N. Chtanko, T.W. Cornelius, D. Dobrev, I. Enculescu, R.H. Blick, R. Neumann, Nanotechnology 15 (2004) 201.
[2] D. Dobrev, J. Vetter, R. Neumann, N. Angert, J. Vac. Sci. Technol. B 19 (2001) 1385.
[3] D. Dobrev, J. Vetter, N. Angert, Nucl. Instr. Meth. B 149 (1999) 207.

Improvements of the GSI microprobe for the targeted irradiation of single cells*

M. Heiß, P. Barberet, G. Becker, G. Du, B. Fischer, C. Fournier, B. Jakob, G. Taucher-Scholz
GSI, Darmstadt, Germany

Since the first successful targeted cell-irradiation in 2003 the GSI heavy ion microprobe has been shown to be a useful tool for studies in radiation biology [1, 2]. To further enhance its performance several technical improvements have been installed in the past year.

A problem affecting the aiming precision were variations in temperature which caused thermal expansions of the setup and generated slowly increasing targeting inaccuracies, forcing a frequent readjustment of the irradiation settings. To prevent this, the irradiation area was temperature stabilised. For an additional thermal stabilisation the microscope lamp was thermally isolated and the setup is ventilated by a temperature controlled fan which blows cool pre-filtered air into the system. The filtering of the air also enhances the sterility of the irradiation area. In tests over several hours the formerly observed displacements between beamline and optics could be decreased by an order of magnitude with this installation.

A method for a fast online aiming verification has been developed that allows us to test the beam deflection precision over the whole optical field of view. For that, a thin copper micro-grid and an energy resolving particle detector are placed at the sample position as shown in figure 1. After an automatic recognition, single ions are targeted onto the bars of the grid. All well targeted particles have to traverse the copper and reach the detector with reduced energy while misplaced ions reach the detector with full energy. By plotting the coordinates of the ions with full energies, the misaligned area can easily be visualised.

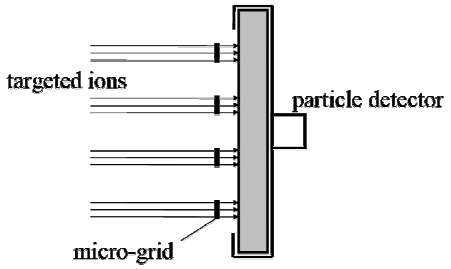


Fig. 1 Schematic setup of the online hit verification.

To test the targeting precision inside the cells, the ion tracks have been visualised by immunocytochemical staining of DNA damage response proteins [2]. To distinguish tracks from background foci, the ions were placed in cross patterns in which the single points were produced by one or twenty ions, respectively (see fig. 2). A comparison of the spots' sizes allows estimating the beams focal width. While the 1-hit spots have an average diameter of about 1.1 µm, the spot size increases for the 20-hit spots to roughly 1.8 µm. From these data one can conclude that all the 20 ions per spot have been placed in an area with a diameter of about 1µm.

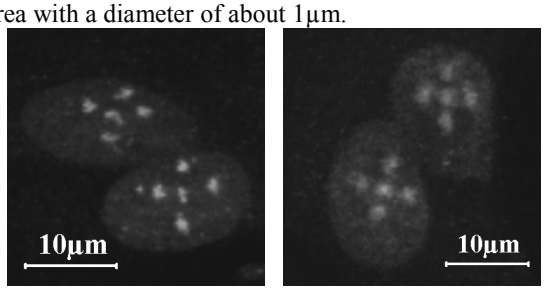


Fig 2: Cell nuclei irradiated with cross-patterns of C-ions with 4.8 MeV/u (5 points, 3 µm between the points) and stained for the damage response protein 53BP1. Left image: 1 hit/spot, right image: 20 hits/spot.

Regarding the biological application, the quantification of proteins involved in the cellular radiation response using immunofluorescence detection requires identical staining conditions. In order to control for this, special chambers were developed allowing the simultaneous staining of directly targeted cells, surrounding bystander cells and control cells. The control cells are completely separated from targeted and bystander cells by a stick in the middle of the chamber. Using this tool for targeted carbon irradiation, the analysis of the cell cycle regulating protein CDKN1A indicates a slightly increased CDKN1A induction in bystander cells (see fig. 3) confirming previous results obtained for low fluencies of carbon ions [4].

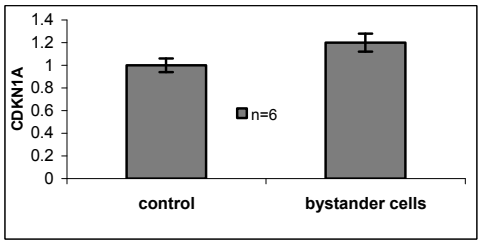


Fig 3: CDKN1A protein level in control and bystander cells following exposure to carbon ions (5 hits per nucleus, 3h after exposure)

References

[1] B. E. Fischer, M. Heiß, G. Taucher-Scholz, B. Jakob and G. Becker; GSI Scientific Report 2003.
[2] M. Heiß, B. E. Fischer, B. Jakob, C. Fournier, G. Becker and G. Taucher-Scholz; Radiation Research 165 (2006), in press
[3] Ph. Barberet, M. Heiss, G. Du, B.E. Fischer and G. Taucher-Scholz; Acta Physica Polonica A, submitted
[4] C. Fournier, M. Heiss, M. Scholz, S. Ritter and G. Taucher-Scholz; GSI Scientific Report 2003.

*Work supported by BMBF (0258203) and EU Grant CELLION MRTN-CT-2003-503923

PHELIX Progress Report*

V. Bagnoud[1,2], A. Blazevich[1], R. Bock[1], S. Borneis[1], H. Brand[1], C. Bruske[1], J. Caird[8], U. Eisenbarth[1], J. Fils[1,2], R. Fuchs[1], S. Götte[1], M. Hagemann[1,3] , T. Hahn[1], H.-M. Heuck[1,4], C. Hildebrandt[3], D. H. H. Hoffmann[1,2], D. Javorkova[1], H.-J. Kluge1, F. Knobloch[1], Th. Kühl[1,5], S. Kunzer[1], M. Kreutz[1], R. Lotz[1], T. Merz[1], P. Neumayer[1,6], E. Onkels[1], D. Reemts[1], M. Roth[1,2], H. Schmidt[3], C. Spielmann[6], R. Stenner[1], A. Tauschwitz[1], R. Thiel[1], U. Thiemer[1], D. Ursescu[1], K. Witte[1], U. Wittrock[4], B. Zielbauer[1,7]

[1]GSI, Darmstadt, Germany; [2]Technische Universität Darmstadt Germany; [3]Fachhochschule Darmstadt, Germany; [4]Fachhochschule Münster, Germany; [5]Universität Mainz; [6]Universität Würzburg, Germany; [7]Max- Born-Institut, Berlin/Germany, [8]Lawrence Livermore National Laboratory, USA.

Abstract

We report the progress of the physics and engineering design effort and the construction of PHELIX, which will be capable of producing pulses up to the peak power of 10^{15} W (1 PW) in 500 fs and the energy of 4 kJ in 10 ns, respectively.

The PHELIX Mission

GSI Darmstadt is currently building a Nd:glass Petawatt High-Energy Laser for Ion eXperiments called PHELIX. The project is established in close cooperation with Lawrence Livermore National Laboratory (LLNL) in the US and the Commissariat à l'Energie Atomique (CEA) in France. PHELIX will offer the unique combination of a high-current, high-energy (GeV/u), heavy-ion beam with a powerful laser beam thus providing the opportunity to investigate a variety of fundamental science issues in the field of atomic physics, nuclear physics, and plasma physics. Fig. 1 shows the schematics of the PHELIX PW-version. PHELIX is a member of the Laserlab Europe and the Optence network.

Pulsed power system and Timing

The PFN and control system of the preamplifier consisting of 2x19 and 1x45 mm diameter rod amplifiers (see Fig. 1) were changed to comply with the VDE safety standards and successfully put into operation. Extensive operation tests of the main amplifiers were performed. The electrical system was tested by discharging several times all capacitors for the double-pass amplifier simultaneously into dummy resistors at the full charging voltage of 18 kV. Modifications in the amplifier housings were checked to withstand the intense pump light pulses in a series of 50 shots at full energy for each amplifier. After an improvement of the cleaning procedure, all amplifiers passed the test which was done without laser disks. During these tests, two out of the 100 flash lamps failed to ignite and were disconnected from the capacitor bank for the rest of the tests.

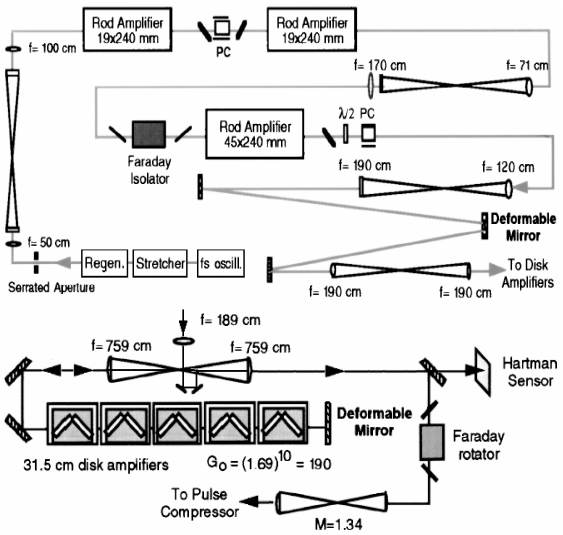


Figure 1: Schematics of the PHELIX PW-version. The front-end comprises the oscillator, stretcher, and two regenerative amplifiers. The pre-amplifier includes two 19-mm rods, one 45-mm rod, and four telescopes. The main amplifier consisting of five sections each containing two disks is double-passed.

Although 98% of the more than ten years old flash lamps survived, it was decided to replace them all since a visual inspection revealed a large number of cracks in the quartz tubes of almost each lamp. New flash lamps were specified and ordered with an expected delivery time April 2006. The setup of a dedicated test stand for the acceptance test of the new lamps was started in order not to interfere with the

extensive testing procedure with the setup of components in the laser bay.

To ensure synchronized operation of PHELIX with the accelerators at GSI, the communication hardware for the timing systems of UNILAC, SIS, and ESR were installed and the synchronization scheme was further finalized. To improve the long-term stability of the timing system, some critical connections to the accelerator timing were replaced by fibre optical connections which will ensure a stable synchronization to better than 1 ns under all circumstances.

Controls

The PHELIX Control System (PCS) is based on the framework of the CS which is in-house developed by the EE/KS group. In 2005, the PCS has grown up to about 30 PHELIX specific classes. About 700 Boolean and analogue values are read out or can be set by the PCS until now. The PCS is running distributed on about ten personal computers. The general architecture of the PCS is worked out. Important parts are already realized. According to the concept of object orientated programming, first the device layer instances are programmed which interact each with one device. Some of them are combined in application layer instances. These instances control the sequences of subunits. Thus the machine safety is guaranteed. On the highest level, the user interacts via an easy GUI. The necessary interfaces are implemented to add subsystems piece by piece according to the progress of hardware construction work.

In 2005, the main focus was the remote control of the pulsed power system which is a good example for the principle explained above. Device layer instances such as an electrical power supply unit, some high-power switches, diagnosis and so on are combined to a power unit (application layer) which pumps a laser head. Until now, six of these are running for the main amplifier section, while the preamplifier consists of four of these units. The shot sequencer of PHELIX controls all these units. From respect to the control system, the pulsed power system is ready to operate.

In 2006, the control system will focus on optical diagnosis and laser position monitoring and stabilization. A data collector documenting the shots and a data base storing default settings will follow to ease the operation of PHELIX. Finally the connection to the different experimental areas and the synchronization with the ion beam has to be set up.

PW compressor

In 2005, major milestones have been covered for the PW compressor. First, the compressor optical layout has been frozen offering the best trade-off between performance, cost, space, and versatility. The compressor will be hosted in a vacuum chamber. This chamber has been ordered in 2005; its fabrication has started and extends into 2006. It is made of two cylinders, connected by a middle piece and many flanges to allow the beam to get in and out. A top view of the chamber is presented in Figure 2. The chamber will first be installed in the laser bay to allow for its qualification and experimental suitability.

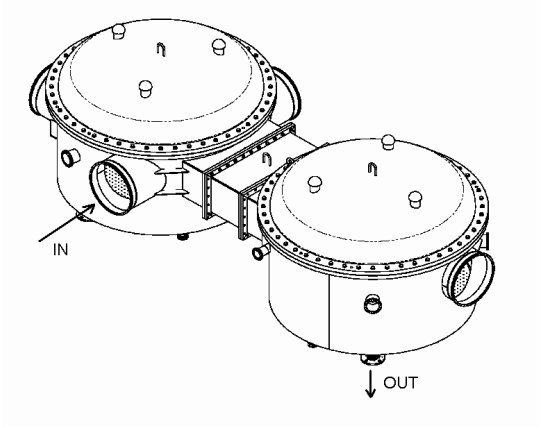


Figure 2: The Petawatt compressor tank.

Beam diagnostics

To characterize the fs-pulse precisely, we have developed a second-order scanning auto-correlator with a high-dynamic range serving as a pulse length etalon.

The diagnostic of the 28-cm beam of ns duration includes its total energy, its near- and far-field fluence patterns, and its wave front. The turning mirror following the 1:1 telescope (see Figure 1) has the transmission of 1%. The transmitted beam is first down-collimated in two steps to the diameter of 22 mm. A beam splitter then reflects 90% of the pulse energy into a calorimeter. The transmitted portion passes an attenuator whose dynamic range can be well matched to full power shots of 1-kJ energy and to low-power shots of much less energy as well such that the subsequent sensors recording the near- and far-field fluence patterns and the wave front can always be operated under optimal conditions.

The near-field sensor (Basler 601f digital camera) receives a real image of the actual beam de-magnified by the factor of 125. The far-field fluence pattern is recorded simultaneously with low and high resolution. The low-resolution image is for beams with relatively large phase front errors; it is obtained by placing the focus of the imaging lens directly on the camera chip (Basler 601f) yielding spot sizes of 30-µm. In the high-resolution case, the focal pattern is imaged onto the camera chip (Basler 601f) by a microscope objective providing the magnification of ~100. The wave front is measured using a Shack-Hartmann sensor that receives a real image of the

actual beam de-magnified by the factor of 80. Aberrations as small as /10 can be measured.

Except for the energy calorimeter, the full diagnostic system has been successfully tested using an auxiliary laser so that it is ready for the characterization of PHELIX pulses.

Simulations with Miró

We have continued simulations of the pulse propagation in PHELIX using the code Miró [1]. Particular attention was paid to super-Gaussian beams with elliptical cross section selected to optimally fill the rectangular compressor gratings. Two further issues concerned the effect of static aberrations of the optical components comprising the main amplifier including the disks, turning mirrors, 1:1 telescope, and Faraday rotator on the size of the pinhole in the telescope and the capability of the bimorph mirror placed behind the preamplifier (see Figure 1) to correct these aberrations. It turned out that the pinhole diameter has to be increased only slightly to avoid plasma formation. The focusability is more seriously affected by the aberrations as can be seen in Figure 3 showing three intensity profiles in the focal plane of the telescope following the double pass in the main amplifier. The aberrations reduce the Strehl ratio, , to 0.58. However, it can be almost fully recovered by the bimorph mirror leading to the conclusion that the static aberrations do not impair the PHELIX performance. Thermal aberrations and means to minimize their effect will be investigated next.

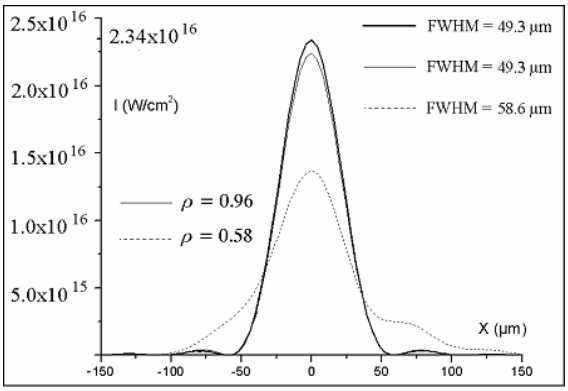


Figure 3: Intensity profiles along the x-axis for an aberration-free beam (thick solid line), for a distorted beam (dotted line), and for a corrected beam (thin solid line). The corresponding full width at half maximum (FWHM) and the Strehl ratio, , are also given.

In-situ inspection of large-sized lenses

The 1:1 telescope following the main amplifier serves for image relaying and simultaneously for spatial filtering as well thus requiring vacuum. Since outside the telescope atmospheric pressure prevails, the lenses have to withstand a difference pressure of 1 bar. Due to their large diameter of 520 mm, fracture is a non-negligible risk. By in-situ inspection of the lenses before and after each shot, surface and bulk damages usually preceding fracture can be detected.

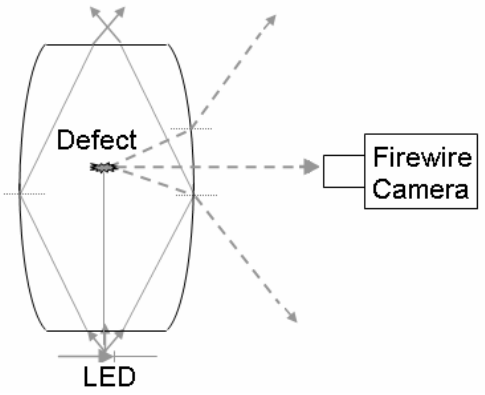


Figure 4: Sketch of the experimental setup. A defect in the middle of the lens is assumed to be present.

The inspection is made by the combination of an illuminating system and an image processing system both specifically designed for this purpose. The lens interior is illuminated by a couple of LEDs located in the lens holder as indicated in Figure 4. The setup relies on total internal reflection of the LED light entering the lens through its perimeter by the polished lens surfaces so that it is internally flooded with light. Imperfections inside the lens will scatter the LED light in all directions by acting as point-like sources. The high-resolution firewire camera looking either onto the front or back surfaces of the lens catches a fraction of this scattered light. It has been proven that defects with scale lengths >0.46 mm can be safely detected this way.

The image processing code written in LabView takes a reference image before each laser shot that is subtracted from the image taken after the shot. Thereby any changes resulting from the laser irradiation become visible. If there is any damage, it is marked on the on-line image that is then saved for further processing.

References

[1] O. Morice et al., *Miró V5 : Reference Manual*, CEA Internal Publication, October 2002.

Grazing Incidence Pumped Zr X-Ray Laser at PHELIX

D. Ursescu *[1,2], D. Javorkova[1], P. Neumayer†[1], O. Rosmej[1], T. Kühl[1,2], B. Zielbauer[1,2,3], K.A. Janulewicz[3], P.V. Nickles[3], W. Sandner[3], K. Cassou[4], S. Kazamias[4], A. Klisnick[4], D. Ros[4]
[1]GSI, Darmstadt; [2]Mainz University; [3]MBI, Berlin, Germany; [4]Universite Paris Sud, Paris, France

A **gr**azing **i**ncidence **p**umped (GRIP) Zr **x**-**r**ay **l**aser (XRL) was experimentally demonstrated at the PHELIX laser. Two lasing lines are observed, the strongest one in saturation. Analysis of the keV emission of the plasma is performed and the results are compared with the experiments performed at 45^o incidence on target.

GRIP XRL using Zr as active medium is reported for the first time. An extensive optimization of the laser output was performed. In the strong pumping regime used in the experiments, the peak-to-peak delay was found to influence the XRL output over large variations of the order of a few hundreds of ps only slightly. This is in contrast to the results of [1] where the delay of 50 ps was critical for obtaining lasing in the weak pumping regime.

Extended analysis of these results in comparison with earlier experiments under 45^o incidence on target [2] and similar conditions was performed. This way the understanding of the effect of the incidence angle was deepened. The optimum main pulse duration was found to be 0.5 ps (see fig. 1), considerably different from the result with normal incidence **t**ransient **c**ollisionally **e**xcited (TCE) XRL [3], where the optimum main pulse duration was 3 to 6 ps. A reduction of the plasma absorption was measured for shorter main pulse duration at constant pump energy (see fig. 2) which agrees qualitatively with the computations performed.

Gain curves were obtained for both lasing lines of the Ni-like GRIP Zr XRL. The small-gain signal is similar for the two lasing lines. Saturation of the main lasing line (22.02 nm) is inferred from the curve shape while for the second lasing line this is not seen, suggesting the possibility of enhanced lasing output at the second lasing line for a longer active medium.

An interesting result was obtained using the spatially resolved keV emission registered with the pinhole camera. Two side lobes in the emission showing increased temperature along the focal line of the main pulse were observed. The result correlates well with previous interference measurements of the plasma density profile and with near-field imaging of the TCE Ag XRL experiments at LULI [4].

The GRIP scheme will lead to a better performance of the XRL source for spectroscopy of Li-like ions. For this purpose, the laser will be transfered to the reinjection channel between ESR and SIS.

Another attractive perspective is the pumping efficiency in higher Z Ni-like lasers. Using the PHELIX laser, experiments employing pump energies of up to 150 J are planned. This should allow to create XRL output at several 100 eV photon energy, possibly reaching the water window.

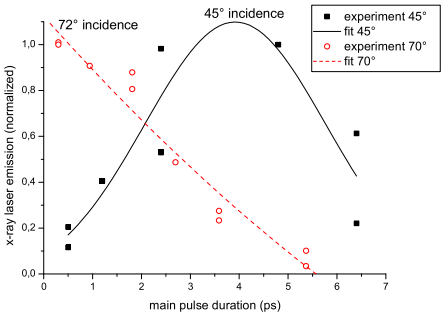


Figure 1: XRL emission versus main pulse duration at incidence angles of 45^o and 72^o.

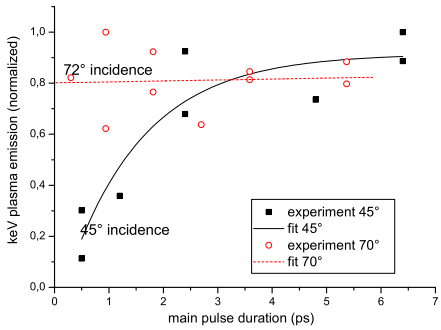


Figure 2: Plasma emission in the keV range versus main pulse duration at incidence angles of 45^o and 72^o.

References

[1] R. Keenan, J. Dunn, P. K. Patel, D. F. Price, R. F. Smith, and V. N. Shlyaptsev. *Physical Review Letters*, 94(10):103901, 2005.

[2] P. Neumayer, W. Seelig, K. Cassou, A. Klisnick, D. Ros, D. Ursescu, T. Kuehl *et al.*, *Applied Physics B: Lasers and Optics*, 78(7-8):957–959, 2004.

[3] P. V. Nickles, V. N. Shlyaptsev, M. Kalachnikov, M. Schnurer, I. Will, and W. Sandner. *Physical Review Letters*, 78(14):2748–2751, 1997.

[4] Olivier Guilbaud, Matthew Edwards, Annie Klisnick, David Ros, Gerard Jamelot *et al.*, *Soft X-Ray Lasers and Applications V*, 5197(1):17–28, 2003.

* d.ursescu@gsi.de
† Present address: Lawrence Livermore National Lab., USA

Laser produced proton beams as a tool for EOS measurements*

An. Tauschwitz, J.A. Maruhn, Johann Wolfgang Goethe-Universität, Frankfurt am Main, Germany
E. Brambrink, LULI, Ecole Polytechnique, France
M. Roth, Technische Universität Darmstadt, Germany
T. Schlegel, A. Tauschwitz, Gesellschaft für Schwerionenenforschung, Darmstadt, Germany

The protons generated at the backside of a thin solid target irradiated with an intense laser beam can be utilized for isochoric heating of solid matter. If the matter is heated homogeneously, the one-dimensional planar expansion will be isentropic and self-similar. In this case a measurement of the density profile of the expanded sample is enough to determine an $p(\rho)$ isentrope. These experiments are of special interest in the region of the phase diagram near the critical point. To explore the behavior of solid matter heated by a non-monoenergetic divergent proton beam the two-dimensional hydrodynamic code MULTI-2D was applied. The code utilizes the SESAME equation-of-state library; the energy deposition of the particle beam is modeled by ray-tracing.

In the calculations below the proton beam heats a foil placed behind a primary laser target, which emits the protons. The parameters of the proton beam were estimated for the PHELIX laser at GSI from measurements at the Vulcan Petawatt laser system [1]. A 500 J laser pulse of 500 fs length from the PHELIX laser is expected to generate $5 \cdot 10^{12}$ protons per pulse, having a Boltzmann-like energy distribution with a temperature of $T_{\mathrm{p}} = 18$ MeV. The beam heats a 20 μm thick aluminum foil which is placed 200 μm away from the primary target. The temperature distribution at the rear side of the target is rather homogeneous in a 2 μm thick layer and can be used for EOS measurements [2]. The rear surface of the target has a temperature of 16.5 eV. The simulations show that the expansion of this layer occurs in a planar 1-D geometry. Figure 1 shows that the discrepancy between isochoric and proton beam heating is about 4% in density and 9% in pressure. Note, that the obtained $p(\rho)$ isentrope also determines the Gr¨uneisen coefficient Γ at solid density $\Gamma(\rho_0) = \frac{P(\rho_0)}{\rho_0 \epsilon}$ without the challenging measurement of pressure in the energy deposition zone. By increasing the target thickness to 300 μm one can decrease the initial temperature for the expansion isentrope to 1.4 eV because of the Boltzmann energy spectrum and the divergence of the proton beam. The temperature profile is as homogeneous as in the previous case over a ten times longer layer which means less demanding requirements for the diagnostics. In the Fig. 2 the WDM region of the phase diagram for aluminum is depicted. The expansion isentropes are plotted for initial temperatures corresponding to the two cases considered above. The isentrope for the thick target crosses the two-phase region and allows EOS measurements in the vicinity of the critical point.

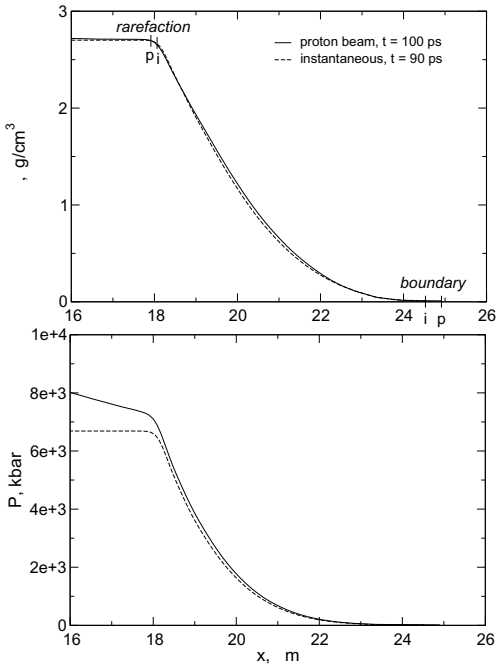


Figure 1: Longitudinal density and pressure expansion profiles at $R = 0$ for instantaneous homogeneous heating to 16.5 eV (i) and for proton beam heating (p). The positions of the plasma boundaries and the rarefaction fronts are marked by (i) and (p) correspondently.

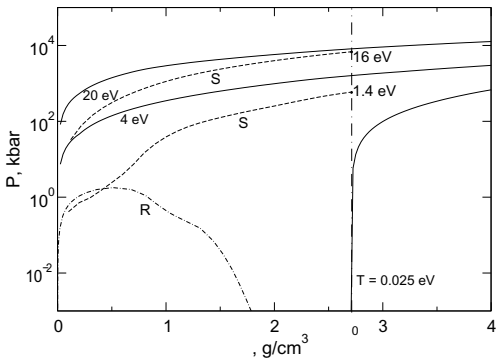


Figure 2: The $P - \rho$ phase diagram for aluminum; T indicates the isotherms, S the expansion isentropes, and R the vaporization curve.

References

[1] E. Brambrink, PhD thesis, TU Darmstadt (2004).

[2] An. Tauschwitz et al., accepted for publication in "High Energy Density Physics".

* Work supported by BMBF Project # 06 F 132

ILIAS - Ion and Laser beam Interaction and Application Studies

P. Mulser, Theoretical Quantum Electronics (TQE), Tech. Univ. Darmstadt, Germany
T. Schlegel, GSI, Darmstadt, Germany

Aim of the ILIAS study group

A great machine like PHELIX demands great ideas. In order to prepare an active environment for related theoretical research at GSI, the study group ILIAS has been founded in January 2005. Since the beginning its activities are directed towards fundamental as well as applied research geared to supporting the experimental projects within PHELIX and, eventually, to opening new directions in the field of superintense laser interaction with dense matter and particle beams. An additional important interest of ILIAS is focused on training young researchers to guarantee continuity of research in theoretical Petawatt (PW) physics at GSI. A detailed description of the scientific profile of the ILIAS study group is presented in [1].

Activities

The first steps towards such an ambitious goal were done during the course of the year by

- coordinating the expertises available in various groups at GSI and neighbouring Universities of Darmstadt, Frankfurt and Gießen on plasma physics, radiation hydrodynamics, atomic and nuclear physics, particle acceleration, nonlinear optics and numerical simulations;

- arranging a weekly workshop seminar, open to interested theoreticians, experimentalists and to guests from outside (ILIAS Arbeitsseminar);

- organizing a European theoretical workshop on Short Pulse PW Laser Plasma Interaction at the IBZ in Darmstadt, October 16 - 18, 2005;

- offering a lecture on Relativistic Intense Laser Interaction with Matter at TU Darmstadt.

At present, research in ILIAS is actively supported at

- GSI by T. Schlegel (radiation hydrodynamics, particle acceleration and radiation sources in laser matter interaction), M. Tomaselli (atomic and nuclear physics),

- Tech. Univ. Darmstadt by P. Mulser (collisionless absorption in clusters and solids)

- Univ. Frankfurt by J. Maruhn and Anna Tauschwitz (multidimensional hydrodynamics and applications)

- Univ. Gießen by W. Scheid (atomic physics, particle acceleration by PW laser)

Valuable support to ILIAS is given from outside:

P. Gibbon (complex atomistic modelling and simulation), Research Center Jülich; H. Ruhl (PIC and Vlasov simulations of relativistic PW laser interaction), Univ. Bochum; D. Bauer (multiphoton interaction, cluster physics), MPI Nuclear Physics, Heidelberg. H-J. Kull (laser-cluster interaction, relativistic plasma physics), RWTH Aachen.

Results

Planckian radiation sources in upcoming PHELIX experiments. The laser heated hohlraum physics is investigated and optimized for various experimental applications e.g. heavy ion stopping in hot plasmas, opacity and equation of state measurements [2].

Laser generated high energy protons and heavy ions. Further progress was achieved in understanding the laser induced acceleration of MeV proton and ion beams [3-4] .

Collective absorption mechanisms in clusters and solids. A break through in understanding the leading mechanisms of collisionless absorption in extended cluster media and in solid targets has been achieved at TU Darmstadt. The so far not explained phase shift between current density and driving electric field in the absence of friction (electron-ion collisions) is shown to happen as a consequence of the nonlinear resonance of plasma volume elements in their collective electric eigenfield [5-8]. In clusters the free electrons escaped from the core interact coherently with the Coulomb field of the individual ions thereby undergoing a giant enhancement of collision-type interaction by many orders of magnitude [8].

References

[1] P. Mulser, “ILIAS: Ion and Laser beam Interaction and Application Studies - A scientifi c portrait of the PHELIX theory group”, GSI Report 2005 - 04, June 2005

[2] E. Baldina, R. Ramis and T. Schlegel, “Multigroup kinetic description of x-ray transport in PHELIX driven hohlraums”, submitted to Phys. Rev. E

[3] E. Brambrink, A. Blazevic, M. Roth and T. Schlegel, “Modeling of the electrostatic sheath shape on the rear target surface in short-pulse laser-driven proton acceleration”, accepted by Laser and Particle Beams (2005)

[4] E.Brambrink, J.Schreiber, T. Schlegel et al., “Transverse characteristics of short pulse laser produced heavy ion beams - an approach to study the acceleration dynamics”, submitted to Phys. Rev. Letters

[5] P. Mulser, D. Bauer, “The physics of collisionless absorption of intense laser beams in solids and clusters”, Varenna 2005, accepted by Proc. Am. Inst. Phys.

[6] P. Mulser, M. Kanapathipillai, “Collisionless absorption in clusters out of linear resonance”, Phys. Rev. A 71, (2005) 063201

[7] D. Bauer, P. Mulser, “Irreversible energy gain by linear and nonlinear oscillations”, Journal of Physics, Conf. Series 11, (2005) 169

[8] P. Mulser, M. Kanapathipillai, and D.H.H. Hoffmann, “Two very effi cient nonlinear laser absorption mechanisms in clusters”, Phys. Rev. Letters 95, (2005) 103401

Research to the Programme Health in the Field of Cancer Research

RAD-BIOPHYSICS
Radiation Research and Biophysics with Heavy Ions (363p.)

EXTERNAL-HIT
Heidelberg Ion Therapy HIT/HICAT (396p.)

DNA fragmentation induced by ionizing radiation - AFM study.

K.Psonka*, E. Gudowska-Nowak*, G. Taucher-Scholz GSI, Darmstadt, Germany

DNA double-strand breaks (DSBs) produced by ionizing radiation are considered to be particularly malignant DNA lesions, with experimental evidence suggesting that misrepaired or unrepaired DSBs are the lesions leading to cell killing, mutations or carcinogenesis [1, 2]. DSBs production is determined by the spatial distribution of ionization events, dependent on the physical properties of the radiation and the chemical environment of the DNA. Differences in severity and complexity of the induced DNA damage depend on the radiation quality – the high LET radiation (ions) inducing more severe lesions compared to low LET radiation (X-rays) due to the induction of multiple lesion in close proximity [3].

Differences in the DSB yields induced in the DNA by ionizing radiation can be studied by fragmentation analysis. The conventional method to evaluate the fraction of fragmented DNA but not the fragments distribution is the gel electrophoresis. Atomic Force Microscopy (AFM) is a direct method allowing the detection and length measurements of individual fragments with a nanometer resolution.

Here we report on the fragmentation induced by X-rays and 3.5 MeV/u Ni ions in linear ΦX174 DNA diluted in 20 mM Hepes. The irradiation was done in a dose range of 0 – 3000 Gy. After irradiation the DNA samples were diluted in a cationic solution (28.6 mM $MgCl_2$ and 50 mM KCl) to the final concentration of 3 ng/μl. A drop of 10μl of DNA was deposited onto freshly cleaved mica and dried in the exccicator to enhance adhesion. The scanning was performed using AFM in liquid environment to provide physiological conditions. The DNA images (3 x 3 μm) with the scanning step 10 nm were collected for each dose and radiation quality (Fig. 1).

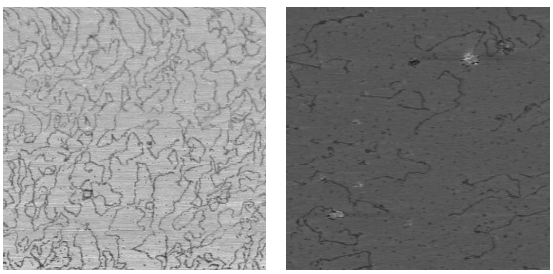


Figure 1: Exemplary AFM pictures of linear DNA irradiated with low (left) and high (right) dose of X-rays.

From each picture the individual fragments were detected and their lengths were measured using the Scion Image software. The obtained fragments lengths for different doses and radiation qualities were plotted as normalized histograms to obtain the probability of producing a DNA fragment with certain length (Fig. 2). The resulting fragment distributions for comparable doses of high and low LET radiation show that ions produce a considerably higher fraction of short DNA fragments than X-rays.

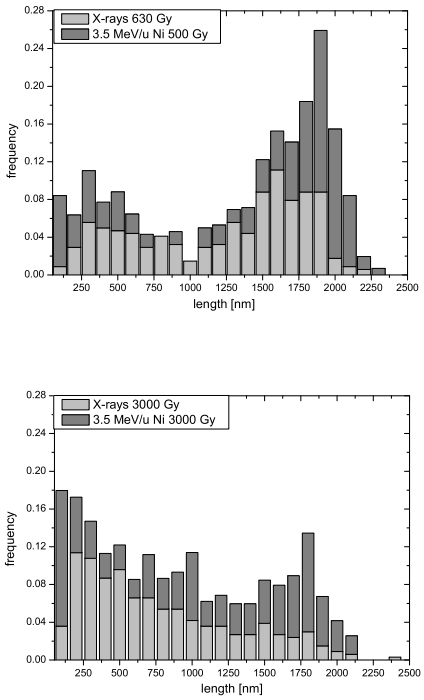


Figure 2: Measured fragment distribution of linear ΦX174 DNA irradiated with low (top) and high (bottom) dose of X-rays and Ni ions.

The enhancement in short fragment production can be explained based on locally correlated DSB induction along the particle track. The data presented here support the track structure concept. In the future, the fragment distributions derived from the theoretical model [4] will be compared with the AFM data to verify the fragmentation pattern dependence on the local energy deposition.

References

[1] E.L. Alpen: Radiation Biophysics Academic Press, San Diego, 1998

[2] S. Brons et al: Radiat. Environ. Biophys. 42 (2003) 63.

[3] S. Brons et al: Radiother. Oncology Suppl. 2 (2004) 112 – 114

[4] M. Scholz et al: Adv. Space Res. 18 (1995) 5 –14

* Jagiellonian University, Institute of Physics, Cracow, Poland

High resolution STM study on small dsDNA plasmid

M. Brezeanu, F. Hubenthal, F. Träger, Institute of Physics and CINSaT, Kassel, Germany

Abstract

Scanning Tunnelling Microscopy (STM) is a versatile tool to image the structure of biomolecules with high resolution [1,2]. New preparation methods were developed in the last years for imaging DNA molecules, but visualizing its structure remains a challenge. In this report we present our latest results of high-resolution imaging of linear dsDNA plasmids with 280 base pairs.

Introduction

Since DNA is the most important biomolecule, it was one of the first molecules studied with STM [2,3]. Aberrations of DNA molecules, for example, induced by heavy ion irradiation, have consequences that may lead to serious damages like single and double strand breaks. Several methods including gel electrophoresis and pulsed-field gel electrophoresis have been applied to analyse DNA strand breaks, but those methods are integral methods, which average over a large amount of DNA fragments. In contrast, STM can visualize the breaks at submolecular level with an accuracy of a few nanometers.

Materials and methods

A solution of dsDNA plasmids (with 280 base pairs) in 10 mM Tris and 1mM EDTA was diluted with 10 mM ammonium acetate (pH 7.5), until the concentration of dsDNA was 0.5 ng/µl. Highly oriented pyrolytic graphite (HOPG) purchased from SPI Supplies was used as conductive substrate. Several droplets of the diluted plasmid solution were deposited onto HOPG surfaces and dried in air at a humidity of 50%. The DNA samples were investigated with STM using a CP-R Scanning Probe Microscope from Veeco Instruments equipped with 5 µm scanner. STM tips, made by cutting a Pt/Ir wire at a 45^{o} angle, were used. The measurements were carried out under ambient conditions at a humidity of 50% to increase the plasmid conductivity [4]. All STM images of the DNA samples were recorded in constant current mode.

Experimental data

Figure 1 shows a high resolution STM image of an intercept of a linear dsDNA plasmid fragment. The helical structure of the dsDNA can be seen. In general, the imaged plasmids exhibit a smaller height and a larger width than usual, due to the plasmid stretching on the HOPG surface and the convolution with the STM tip. However, the measured dimensions and the calculated circumference are close to the theoretical predictions. Figure 2 depicts the cross section of the dsDNA as indicated in fig. 1.

Correspondence: brezeanu@physik.uni-kassel.de

A width of 4.8 nm and a height of 0.38 nm have been measured which are very close to the expected values. A detailed comparison of the dimensions of the plasmid between the experimental and theoretical values is summarized in table 1.

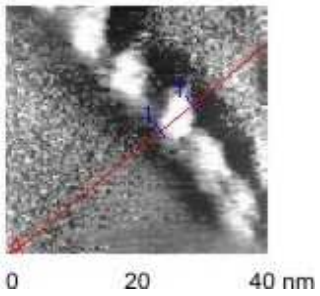


Figure 1: STM image of the linear dsDNA plasmid recorded in constant current mode with the bias voltage of 0.75 V and the set-point current of 0.17 nA, showing the helical turns.

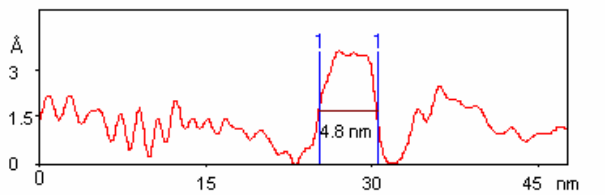


Figure 2: Cross-section of the dsDNA plasmid on HOPG.

dsDNA plasmid	ThData (nm)	ExpData (nm)
Length	95.2	98.9
Width	2.37	4.8
Height	2.37	0.38
Circumference	7.5	9.2

Table 1: Comparison between theoretical (ThData) and our experimental data (ExpData).

Conclusions

Small dsDNA plasmids on HOPG have been imaged by high resolution STM. The analysis of the plasmid dimensions with STM reveals good correspondence with theoretical predictions and demonstrates the potential of this method.

References

[1] W. Schonert, Ph.D thesis, University of Kassel, 1997.
[2] A. Ikai, Surface Science Reports 26 (1997) 261-33.
[3] S.M. Lindsay, et al., J Biomol. Struct. Dynam. 7 (1989) 279.
[4] D. Porath, et al., Nature 403 (2000) 635.

Quantification of ion-induced DNA double strand breaks using flow cytometry

J. Topsch, Y. Schweinfurth, M. Scholz, G. Taucher-Scholz

Biophysics, GSI, Darmstadt, Germany

Aimed at investigating the induction of DNA damage after irradiation the phosphorylated form of the histone H2AX was used as a marker of DNA double strand breaks (dsb). The latter can be visualized as γH2AX foci at a fluorescence microscope after immunostaining, but optimal evaluation is limited under conditions of overlapping foci. Furthermore, this analysis is very time consuming. With the help of flow cytometry one can detect thousands of single cells in suspension within minutes concerning their γH2AX expression. A further advantage of flow cytometry is that the cells analysed can be distinguished regarding their cell cycle phase simply by DNA staining. This differentiation between the cell cycle phases is important due to the increase of histones during DNA synthesis as well as the appearance of replication induced foci. In addition, flow cytometry provides a means to measure total fluorescence intensity in contrast to images from the confocal laser scanning microscope where after particle radiation individual dsbs in single tracks can not be resolved due to the high density of damages induced.

The first step was the establishment of the staining technique for the flow cytometric analysis. We compared the staining protocol of MacPhail et al. [1] using fixation with Ethanol (EtOH) with our procedure for microscopic foci staining, including fixation with paraformaldehyde (PFA) [2], and modified trypsinization and centrifugation steps. The preliminary results for CHO cells after x-ray irradiation are shown in Figure 1. The dsbs were stained with specific antibody against γH2AX (1:500) and Alexa 488 anti mouse antibody (1:400). The DNA was stained with 1µg/ml DAPI. The flow cytometric analysis was performed with identical parameters for all samples.

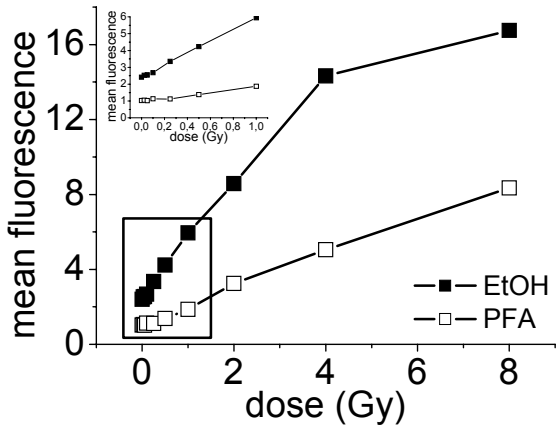


Figure 1: Dose dependency of γH2AX mean fluorescence after x-ray irradiation of CHO cells in G0/G1 phase comparing different staining procedures (see text).

For doses > 0.25 Gy we observed a dose dependent increase in mean fluorescence for both methods. The mean fluorescence of G0/G1 cells after EtOH fixation was in general (also the background) higher than after PFA fixation. Microscopy of the stained cells after PFA fixation showed a clear accumulation of γH2AX fluorescence above a lower stained nuclear background. But after fixation with EtOH no clear differentiation was visible because of bright (in part autofluorescent) staining of the whole nucleus. For a better comparability of foci counting and flow cytometric analysis we decided to use PFA fixation. First experiments with CHO cells using x-ray and Xe irradiation show the induction of γH2AX and the kinetic of γH2AX loss (Figure 2). The unirradiated control cells had a low level of γH2AX mean fluorescence that did not change over time. The irradiated cells showed a high level of fluorescence intensity 1-2 h after irradiation. In the case of x-rays the main part of the fluorescence decreased within 5 h. At 24 h after irradiation the remaining fluorescence intensity was only little above the control. For Xe-irradiated cells we also observed a decrease in the mean fluorescence with time for repair, but reaching a plateau at 3-24 h. At 48h after irradiation the fluorescence decreased further, but a high level of residual damage is still visible for the high-LET radiation. A comparison of the types of radiation is complicated by the inter-experimental variability of absolute values. Further optimization and a complementation with Western Blot analysis of H2AX phosphorylation are planned.

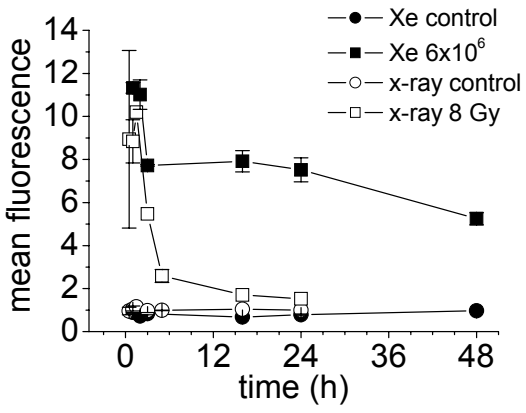


Figure 2: Time course of γH2AX mean fluorescence for unirradiated and Xe irradiated (fluence: $6x10^6$ particles/cm²; LET= 8816 keV/µm) CHO cells in G0/G1 phase.

References:
[1] MacPhail et al. (2003), Int. J. Radiat. Biol, Vol 79 (5)
[2] Jakob et al. (2000), Radiat. Res, 154 (4)

Repair of high-LET induced DSBs

A. Fricke, M. Kühne and M. Löbrich
Fachrichtung Biophysik, Universität des Saarlandes, Germany

It has been known for several years that high-LET-induced DSBs are generally more slowly repaired than breaks induced by X- or γ-rays. Moreover, the level of residual DSBs after prolonged repair incubation appears to correlate with the cell killing capacity of a given radiation quality over a substantial LET range. It is, therefore, important to understand the basis of the compromised DSB repair kinetics of high-LET radiations. One potential explanation relates to differences in the spatial distribution of DSBs induced by particles versus photons. Particles cause damage along their track, whereas DSBs induced by photon irradiation are more or less evenly distributed throughout the nucleus. It may well be possible that the repair of a DSB is compromised if additional DSBs are located nearby on the same DNA loop or on any other structural element of human chromatin. This idea would suggest that the repair of double stranded (ds) DNA fragments depends on the size of the fragments analyzed, with smaller fragments showing generally slower repair than larger fragments (because smaller fragments are generated by nearby DSBs). A second potential explanation is based on the high ionisation density of high-LET particles. It is possible that DSBs are generally more complex with additional lesions in very close proximity to the DSB. These additional lesions could include base and sugar damages or single-strand breaks, and may require processing before repair of the DSB can take place. For certain types of complex DSBs, it may be necessary to coordinate the repair of these lesions with the repair of the DSB and it may also be possible that the most severe forms of complex DSBs are refractory to repair.

In the present study we investigated DNA fragment distributions in the size range between 20 kbp and 3 Mbp after exposure to ionizing radiation. Primary human lung fibroblasts at the G_0 stage of the cell cycle were irradiated with carbon ions (LET=167 keV/µm) at the UNILAC accelerator of the GSI in Darmstadt. For comparison, X-ray and α-particle (114 keV/µm) experiments were performed in our laboratory. The cells were irradiated, incubated for repair times up to 24 h, embedded in agarose plugs und lysed. Two different electrophoretical conditions were applied to separate ds DNA fragments according to size. Southern hybridisation with radiolabelled genomic DNA probes was performed to quantify the DNA fragments. The data presented in figure 1 were obtained by transforming the fraction of DNA in a particular size range into the fraction of unrejoined DSBs for these sizes. For this, the fraction of DNA in a particular size range as a function of dose for samples without repair served as a calibration curve to obtain a "dose equivalent" for the repair samples. The "dose equivalent" value for a particular repair sample was then divided by the initial dose to give the fraction of unrejoined DSBs.

The similarity of the repair kinetics for different size ranges of all radiation qualities used suggests that the proximity of neighbouring DSBs (in the range analysed, i.e. >23 kbp) does not significantly affect the repair process. This finding and the observation that X-rays show faster repair relative to particle irradiations further suggests that the higher complexity of individual DSBs (as opposed to the proximity of DSBs) contributes substantially to the high biological effectiveness of high-LET radiation.

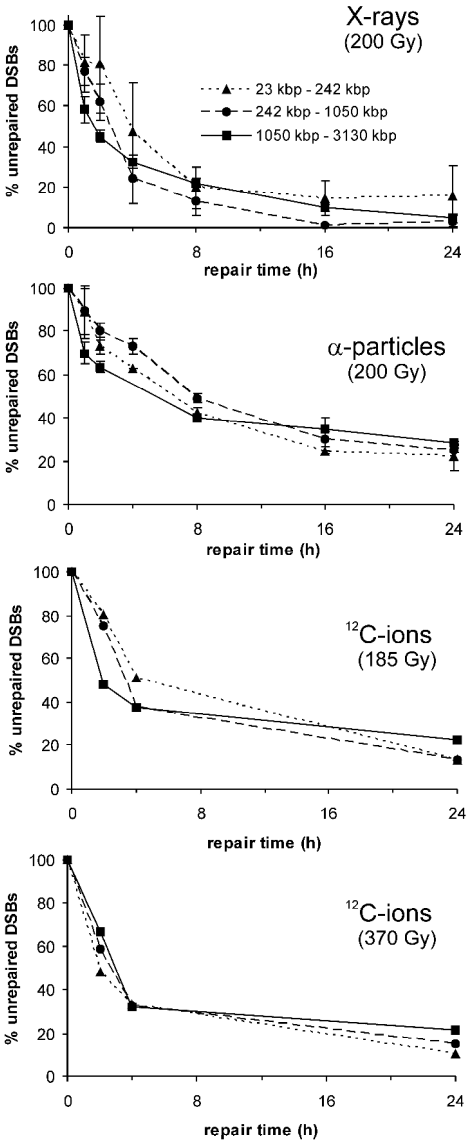


Figure 1: Repair kinetics for ds DNA fragments of three different size classes after irradiation with various radiation qualities.

Cluster Effects within the Local Effect Model (LEM)

Th. Elsässer, and M. Scholz, GSI, Darmstadt, Germany

The Local Effect Model (LEM) [1] has been successfully used in treatment planning for heavy ion therapy with carbon ions at the treatment facility at GSI. It predicts the radiobiological effectiveness (RBE) for different ions and different cell lines starting from the corresponding experimental photon data and an amorphous track structure model. Numerous comparisons of the results of LEM with experimental data prove its applicability to a variety of biological endpoints. However, so far the experimentally observed clustered damage at high doses has not been taken into account.

Cluster Extension

Here, we present an extension of the LEM which takes cluster effects of single strand breaks at the nanometer scale into account. In line with the main idea of the LEM, we take the yield of single (SSB) and double strand breaks (DSB) from experimental photon data and use a Monte-Carlo method to distribute them onto the DNA. We score clusters of SSBs where individual SSBs are separated by less than 25 bp as additional DSBs yielding the damage enhancement factor η defined by

$$\eta = \frac{N(DSB) + N(SSB + SSB)}{N(DSB)}$$

with N(DSB) being the number of DSBs and N(SSB+SSB) the number of clustered SSBs. The outcome of this modelling approach reveals an onset of a significant cluster effect for doses above several hundred Gy as well as a saturation due to more than one cluster within 25 bp for doses higher than 10^5 Gy (see Fig. 1). Assuming that the number of DSBs is a measure for cell lethality, we can calculate a modified survival curve for photons as the input for the LEM calculations.

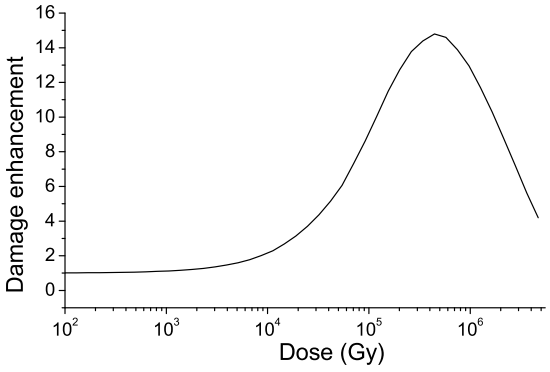


Figure 1: Damage enhancement factor η vs. dose

Results

We find that the extended LEM including cluster effects reproduces most experimental data better than the original LEM. As a consequence of the new approach, the ratio of maximum RBE values for at high LET to minimum RBEs at low LET is increased. This can be understood in terms of a higher radiation effect resulting from the cluster damage at high local doses. In Fig. 2, the RBE of the initial slopes for carbon ions at different LETs is depicted for two cell lines. It shows a comparison of the result of the original LEM with the extension of LEM including the cluster effects. It can be clearly seen that the maximum RBE for the cluster model is higher than in the original model. In addition there is a smaller radiobiological effect of heavy ions at lower LET, which was also observed in experiments.

In summary, this cluster extension enhances the accuracy of the LEM and will improve treatment planning for heavy ions [3].

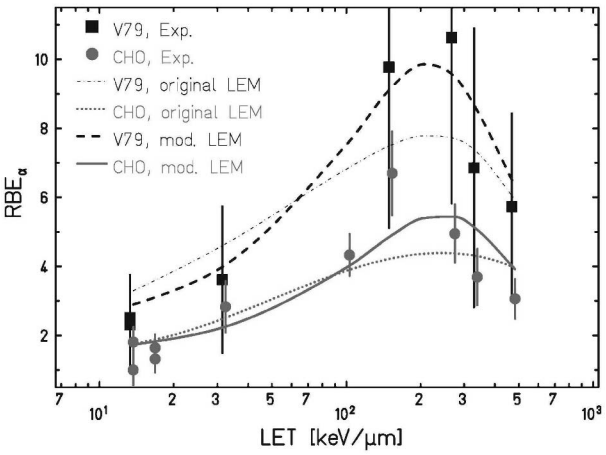


Figure 2: RBE dependence on LET for initial slopes for V79 and CHO hamster cells. The thin lines represent the original LEM, whereas the thick lines are the results of the cluster extension. The single points correspond to experimental data by Weyrather et. al [2]

References

[1] M. Scholz, G. Kraft, Radiat. Prot. Dosim. 52, 29-33 (1994).

[2] W. K. Weyrather, S. Ritter, M. Scholz, and G. Kraft, Int. J. Radiat. Biol. 75, 1357-1364 (1999).

[3] A. Schmidt et al., This report

Characterisation of p21 foci at heavy ion induced DNA lesions

D. Fink, J. H. Rudolph, B. Jakob, K. Knoop, G. Taucher-Scholz, GSI, Darmstadt, Germany.

The cyclin-dependent kinase inhibitor p21 is involved in a variety of different cellular processes, like cell cycle control, senescence and terminal differentiation. Recently, p21 was found to localize to discrete sites of DNA damage induced by heavy ions [1].
To investigate the functional significance of p21 at the DNA lesions, we designed a mammalian expression construct encoding translational fusions of human p21 to an enhanced green fluorescent protein (EGFP). HeLa cells transiently transfected with this construct were irradiated with low energy krypton ions to test the ability of the p21 fusion protein to form ionizing radiation induced foci (IRIF) at sites of ion traversals (Fig. 1).

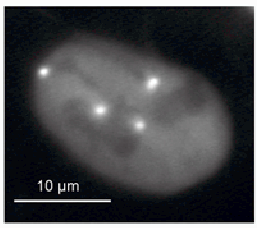


Figure 1: Nucleus of a HeLa cell expressing the p21-EGFP fusion construct 10 min after irradiation with Kr ions (5.0 MeV/u; LET: 5200 keV/µm). Bright spots indicate p21 accumulations in so called IRIF at sites of ion traversals.

With the help of the beamline microscope [2] the recruitment kinetic of EGFP-p21 to these IRIF was evaluated (Fig. 2).

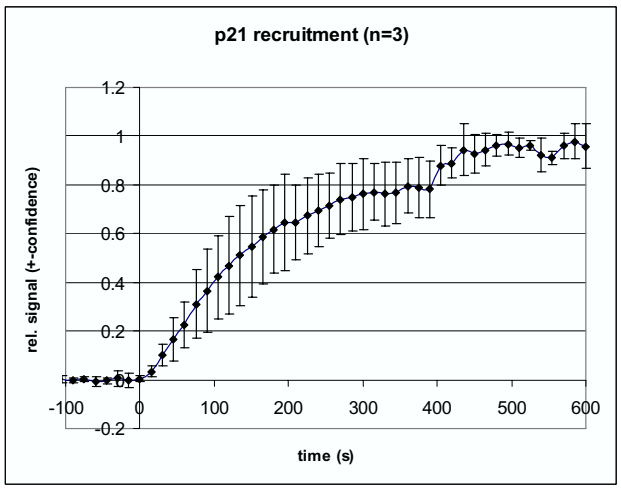


Figure 2: Kinetic of p21 recruitment to IRIF in HeLa cells. Increase of fluorescence intensity at sites of ion traversal over time. For details see [2].

The measured increase in EGFP-p21 fluorescence intensity shows a small lag-phase after the ion impacts and a recruitment time constant of about 200s. Altogether, this demonstrates, that p21 is one of the early participants in response to heavy ion produced DNA lesions, but, compared to the recruitment time constant of aprataxin [2], p21 may not belong to the first wave of damage sensing and processing proteins binding to charged particle-induced lesions.
To analyse the p21-foci formation in p21 "wildtype" cells after irradiation with charged particles on a biochemical level, we used a cellular fractionation protocol to separate the chromatin-bound proteins of irradiated and mock irradiated human fibroblasts as described in [3]. The cells were lysed in the presence of a detergent to release the soluble proteins. The detergent-insoluble fraction represented the chromatin-bound proteins, which were then solubilized by DNase digestion. By using this nuclear extraction procedure, we demonstrated an enhanced amount of p21 protein associated to chromatin in human fibroblasts 1 h after irradiation with chromium ions (6.5 MeV/u; LET 2630 keV/µm) compared to non-irradiated cells (Fig. 3, chromatin p21, ϟ and ━).

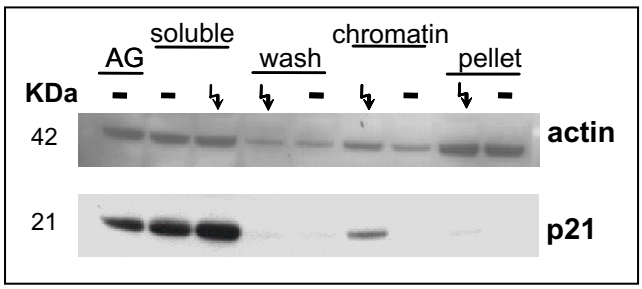


Figure 3: Western blot analysis for quantitative detection of p21 in fractionated chromium-irradiated and mock irradiated human fibroblasts (AG-cells). After extraction of the detergent-soluble protein fraction (soluble fraction) the chromatin-bound proteins were washed (wash fraction) and solubilized by DNase digestion (chromatin fraction). The remaining fraction of cell debris (pellet fraction) was used as a control for the quality of release of the DNA-bound proteins.

By monitoring the amount of the "housekeeping" gene actin in the different cellular fractions, we confirmed equal loading for the irradiated and the non irradiated probes. This result certified that the observed increase in chromatin-associated p21 protein is determined by the irradiation process.

In further experiments the fractions of chromatin associated proteins of irradiated and non irradiated cells will be used for p21-coimmunoprecipitations to define potential p21 binding partner and therewith illuminate a possible role of p21 in DNA repair.

References

[1] B. Jakob et al., Radiat Res 2000, 154(4), 398-405
[2] B. Jakob et al., Radiat Res 2005, 163, 681-690
[3] L. Stivala and E. Prosperi, Meth Mol Biol, vol. 281: checkpoint controls and cancer, Volume 2

Identification of TGF-β1-dependent signalling cascades mediating radiation-induced ATM activity

H. P. Rodemann, M. Blaese
Division of Radiobiology and Molecular Environmental Research,
Dept. of Radiation Oncology, Univ. of Tuebingen

Over the recent years our laboratory could demonstrate that the radiation-induced terminal differentiation of the fibroblast cell system, i.e. the induced differentiation of progenitor fibroblasts to postmitotic highly collagen synthesizing fibrocytes, is the key event in the induction and manifestation of the fibrotic tissue remodelling mainly independent of the radiation quality used. Molecular biological studies into the basic mechanisms of radiation, i.e. photon and heavy ion radiation induced terminal fibroblast differentiation revealed that the cytokine TGF-β1 is a key mediator regulating radiation-induced differentiation [1].
As a consequence of both photon and heavy ion irradiation in the previous research period, it could be postulated that radiation (photon and heavy ion radiation) rather leads to the proteolytic activation of latent TGF-β1 (LTGF-β1) to the active form of this cytokine than to a stimulation of gene expression [2]. For practical reasons, this hypothesis was tested first in photon-irradiated cells by the use of a specific inhibitor of the protease furin, which is known to be a major component of the proteolytic activation process of LTGF-β1 to TGF-β1. Preincubation with the furin inhibitor CMK resulted in a significant decrease of the phosphorylation of Smad-2 and –3 proteins involved in the intracellular TGF-β1 receptor-dependent signal transduction. Although not yet analyzed, it can be assumed that heavy ion irradiation will lead to a similar effect if not more pronounced activation of LTGF-β1 as shown for photon irradiation [2].

To enlight the underlying mechanisms in more detail, in the current project started in May 2004 different subclones of human fibroblasts and the p53 wild-type lung carcinoma cell line A549 genetically manipulated for the conditional expression (tet-on/tet-off) of various antisense constructs, i.e. α-TGF-β1, α-Smad2/3, α-Smad4 and α-Smad7 as well as α-furin, were established. Expression and functionality of the various antisense mRNAs was tested by conventional techniques and radiation response of stably transfected subclones was analyzed applying photon irradiation at different dose levels. So far, it could be demonstrated that clonogenic survival of stably transfected subclones of A549 cells presenting α-TGF-β1 as well as α-Smad2/3 is significantly altered as compared to the wild-type cells [3]. Suppression of TGF-β1 by α-TGF-β1 as well as repression of Smad2/3 by α-Smad2/3 caused a significant increase in clonogenic survival at the different dose levels (2 and 4 Gy) analyzed. At present the data indicate that blockage of the TGF-β1 signal transduction either at the level of the cytokine production or TGF-β1-dependent intracellular receptor signalling is able to downregulate radiation-induced ATM activity by nearly 50 % [3-4]. Furthermore, preliminary date indicate that independent of radiation exposure the active form of TGF-β1 can be found intracellularly and localized in the nuclear fraction. When tested with co-immunoprecipitation, it could be shown that nuclear TGF-β1 forms a complex with the nuclear ATM protein.

Consequently, the direct comparison of radiation effects, i.e. heavy ions versus photons/x-rays, with respect to radiation-induced TGF-β1 activation and stimulation of the ATM-dependent cell cycle responses can now experimentally be approached. The results to be obtained will allow detailed insights into the principle mechanisms of cellular responses underlying radiation-induced normal tissue consequences.

References

[1] A. von Pfeil, L. Hakenjos, C. Herskind, K. Dittmann, M. Weller, H. P. Rodemann, "Irradiated homozygous TGF-β1 knockout fibroblasts show enhanced clonogenic survival as compared with TGF-β1 wild-type fibroblasts," Int: J. Radiat. Biol. 78(5):331-339 (2002).
[2] O. Haase and H. P. Rodemann, "Fibrosis and cytokine mechanisms: Relevant in hadron therapy?" Radiother. Oncol. 73:S144-S147 (2004).
[3] M. A. Blaese, H. Loeffler, L. Santo-Hoeltje, H. P. Rodemann, "TGF-ß1 is involved in the induction of ATM-Kinase and downstream signaling in irradiated cells", Molecular Radiation Biology/Oncology, Vol. 5, p. 27, 2004, ISBN 3-9808819-1-1.
[4] M. A. Blaese, H. Loeffler, H. P. Rodemann, "Downregulation of ATM/p53-signaling by inhibition of the radiation induced TGFß-1 cascade", Molecular Radiation Biology/Oncology, Vol. 6, p. 50, 2005, ISBN 3-9808819-2-X.

Radiation-induced terminal differentiation and cellular senescence: Do they share common pathways?*

M. Winter, C. Fournier, P. Hessel, S. Ritter, Biophysics, GSI, Germany

In human skin fibroblasts, the DNA damage induced by irradiation has been shown to lead to the induction of cell cycle related proteins p53 and p21, followed by both a transient and persistent cell cycle arrest and a reduced proliferation [1, 2, 3]. A radiation-induced terminal differentiation, linked to an irreversible arrest, has also been observed [4].

An irreversible arrest and a concomitant induction of cell cycle inhibitors (p21, p16) are as well prerequisites of cellular senescence [5]. The driving force of senescence is discussed to be accumulation of DNA damage [6]. To investigate if radiation-induced terminal differentiation shares common pathways with cellular senescence, we analyzed the progeny of irradiated human skin fibroblasts up to 130 days after exposure. The proliferation index (BrdU labelling) as an indicator for persistent cell cycle arrest and the expression of the cell cycle- (p21) and senescence-related (p16) proteins were investigated at early (ca. 20 days) and late (130 days) times after carbon ion and X-ray irradiation. Carbon ions have been shown to be 3-4 times more efficient in inducing a early persistent cell cycle arrest [3], therefore the corresponding doses have been chosen for the experiments presented here.

Methods: Density inhibited, normal human foreskin fibroblasts (AG1522C) were irradiated with 250 kV X-rays or 9.8 MeV/u carbon ions and reseeded after irradiation and sub-cultured in intervals of two weeks. The levels of cell cycle- ($p21^{CIP/WAF1}$) and senescence-related proteins ($p16^{INK4a}$) were quantified by western blotting. Proliferation was measured with standard BrdU pulse labelling: The cells were labelled for one hour with 10μM BrdU followed by an immunocytochemical detection of BrdU incorporation.

At early times after irradiation, the proliferation index of the irradiated cells decreased with dose. In contrast to the 3-4 fold higher number of persistently arrested cells immediately after carbon exposure, the efficiency of carbon at 19 days after irradiation was less pronounced compared to X-irradiation (see fig. 1). Nevertheless, the relative increase of p21 at the same time was dose dependent and higher following carbon ions compared to X-ray exposure (fig. 2a), while the protein levels of p16 were only slightly elevated, without a clear dose dependency (fig. 2b). The p21 levels after 21 days indicate a dose dependent fraction of the fibroblasts undergoing a cell cycle arrest, which is confirmed by the labelling index. The less pronounced decrease of the proliferation index after carbon irradiation compared to X-rays may indicate a subpopulation of cells that continues proliferation, as well as a more pronounced induction of p21 within the fraction of arrested cells, probably due to the heterogeneous distribution of the number of particle traversals per nucleus. The slight increase of p16 could be caused by the arrested fibroblasts that enter terminal differentiation and subsequently cellular senescence.

* Work supported by BMBF 02S8203

At late times after irradiation p21 was increased about 1.5-fold compared to controls in all irradiated cultures (fig. 2c), but, unlike at early times after irradiation, no dependency on dose and radiation-type was observed. The increase of p16 correlated with the dose and was higher after X-ray than after carbon ion exposure (fig. 2d), suggesting a higher amount of terminally differentiated fibroblasts, which are probably entering senescence.

In addition to the direct effect of irradiation, the interpretation of the results obtained in mass cultures of cells has to take into account other complex factors, e.g. the composition of the fibroblast culture [7] and the inhomogeneous distribution of damage induction by particle irradiation. The data obtained so far indicate that subpopulations undergo terminal differentiation at early and late times after irradiation. The observed involvement of both cell cycle inhibitors suggests for X-ray as well as for carbon ion exposure an overlap between radiation induced terminal differentiation and senescence, which remains to be investigated in more detail.

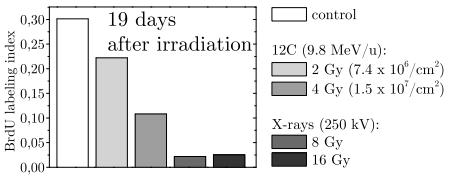


Figure 1: BrdU labelling index of human fibroblasts

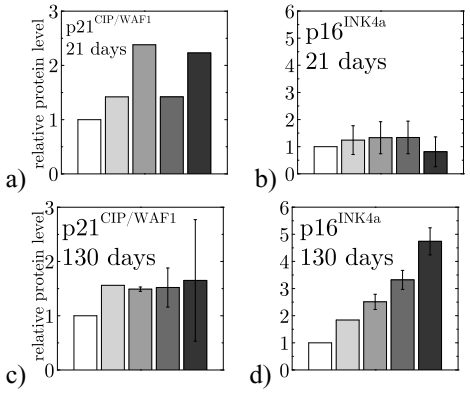


Figure 2: Protein levels of $p21^{CIP/WAF1}$ and $p16^{INK4a}$ in irradiated fibroblasts relative to non-irradiated controls. Bars: Standard deviation

References

[1] DiLeonardo, A. et al., Genes Dev. 1994, 8(21), 2540 pp
[2] Fournier, C. et al., Radiat. Res. 2004, 161(6), 675 pp
[3] Winter, M. et al., GSI Annual Report 2003, p. 166
[4] Rodemann H.P. et al., Scanning Microsc. 1991, 5(4), 1135 pp
[5] Stein, GH. et al, Mol. Cell Biol. 1999, 19(3), 2109 pp
[6] di Fagagna, F., Nature 2003, 426, 194 pp
[7] Drayton S. et al., Curr. Opin. Genet. Dev. 2002, 12(1), 98 pp

Radiation-induced telomerase activity in peripheral blood mononuclear cells

D. Milanovic, P. Maier, A.K. Schwegler, F. Wenz and C. Herskind
Dept. of Radiation Oncology, Mannheim Medical Center, University of Heidelberg, Germany

Telomeres are long terminal repeat sequences protecting the chromosomes from degradation. They do this by forming a t-loop structure, thus preventing the DNA ends from being recognized by the DNA double strand break repair machinery. Because of the so-called "end-replication problem", the terminal part of the lagging DNA strand cannot be replicated during S-phase and hence telomeres are shortened with each round of replication unless extended by other mechanisms.

In stem cells, telomeres are extended by a specialised enzyme, telomerase, consisting of telomerase reverse transcriptase, hTERT, and telomerase RNA component, hTERC. Most somatic cells have little or no detectable telomerase activity and thus telomere shortening is considered to play a major role in senescence of these cells. Lymphocytes represent an exception by having a low telomerase activity which may be increased by mitogenic stimulation with phytohemaglutinin (PHA) although this appears insufficient to maintain telomere length [*1*]. By contrast, cancer cells and immortal cell lines frequently express high levels of telomerase allowing them to escape senescence.

Experimental studies with hematopoietic cell lines have shown that telomerase activity can be increased by low doses of radiation [*2, 3*]. It has been speculated that this may contribute to chromosome stability by adding telomeric sequence to broken DNA ends by a process termed "chromosome healing" [*4-6*]. However, it is not known if radiation-induced telomerase activity plays a role in normal lymphocytes that have not been immortalised. Therefore, we tested if single doses of radiation could increase telomerase activity in PHA-stimulated peripheral blood mononuclear cells (PBMCs).

A newly established real-time PCR protocol for quantification of telomerase activity detected by the telomeric repeat amplification protocol (TRAP) was validated using the TK6 lymphoblastoid cell line. The telomerase activity of unstimulated PBMCs from young donors was low but increased to approximately 40% of the level for TK6 cells after 48-72h stimulation with PHA. Irradiation of 72h PHA-stimulated PBMCs with 2-10 Gy of 6 MV x rays showed a dose-dependent enhancement of telomerase activity of up to 2-2.5 fold 4h after irradiation with a maximum observed at approximately 7 Gy [*7*].

There is a considerable overlap of proteins participating in telomere maintenance and DNA double strand break (dsb) repair, and recent evidence suggests that telomerase may enhance DNA repair and increase genomic stability, or stabilise DNA dsbs [*8, 9*]. This might, in turn, influence the frequency of chromosome aberrations. Potential interactions between DNA repair and telomerase activity leading to increased genomic stability are shown schematically in Fig. 1.

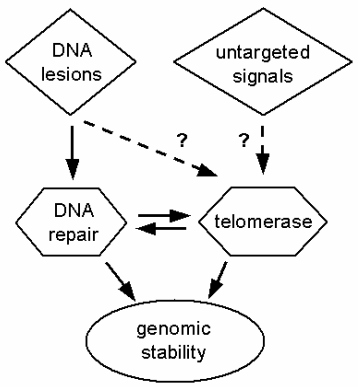


Fig. 1 Schematic model of processes involved in stabilising the genome after irradiation.

The finding that irradiation induces telomerase activity in PBMCs in a dose-dependent manner could have potentially important implications for radiation protection. Preliminary data from a clinical study on telomerase activity in PBMCs from radiotherapy patients were presented at MICROS2005, 14th Symposium on Microdosimetry, Venice, 13.-18. Nov. 2005. These studies are continued with the aim of comparing the effect of different radiation qualities given in vitro and in vivo. Furthermore, the relationship between telomerase activity and chromosome aberrations in cells from selected donors will be studied.

Acknowledgement: This study was supported by the BMBF, Bonn (contract no. 02S8203).

References

[1] C. Pan *et al.*, *Exp Cell Res* 231, 346-53 (1997).
[2] F. Leteurtre *et al.*, *Leukemia* 11, 1681-9 (1997).
[3] D. Neuhof *et al.*, *Radiat Res* 155, 693-7 (2001).
[4] R. J. Preston, *Radiat Res* 147, 529-34 (1997).
[5] M. P. Hande *et al.*, *Mutat Res* 404, 205-14 (1998).
[6] P. Slijepcevic, P. E. Bryant, *Int J Radiat Biol* 73, 1-13 (1998).
[7] D. Milanovic *et al.*, *Radiat. Prot. Dosimetry* (submitted).
[8] G. G. Sharma *et al.*, *Oncogene* 22, 131-46 (2003).
[9] D. Dubner *et al.*, *Int J Radiat Biol* 80, 593-605 (2004).

Induction of chromosomal aberrations in human primary B lymphocytes by ionising irradiation*

S. Conrad, TU Darmstadt, Germany, K. Nixdorff, TU Darmstadt, Germany
E. Nasonova, GSI Darmstadt Germany; S. Ritter, GSI, Darmstadt, Germany

In the current project the induction of chromosomal aberrations in human lymphocytes by ionizing radiation is investigated [1]. Types and frequencies of aberrations provide valuable information on health risks associated with radiation exposure such as cancer induction. Also aberration analysis in human lymphocytes is used to predict the individual radiosensitivity of patients before radiotherapy or to estimate the dose to which an individual has been accidentally exposed. However, cytogenetic studies are complicated by the fact, that irradiated human lymphocytes show a pronounced mitotic delay and there is evidence that cells arriving late at the first mitosis after irradiation carry more aberrations than those who arrive earlier.
Lymphocyte populations consist of T- and B-cells. Both cell types are a crucial part of the specific immune system. However, mainly T-cells are investigated so far, because phytoheamagglutinin (PHA), the standard mitogen used, predominantly stimulates T-cells. Based on survival studies, B-cells have been considered to be more radiosensitive than T-cells and this was also shown by measuring micronuclei induction [2, 3].
To investigate, if the higher chromosomal aberration rate in lymphocytes arriving late at the first mitosis results from a prolonged mitotic delay of heavily damaged T-cells or is due to the higher radiosensitivity of the B-lymphocyte subset, we intend to measured the induction of chromosomal aberrations in human primary B-lymphocytes by ionising irradiation and to compare the data with the aberration yield induced in T-cells

For this purpose, a new protocol was established, i.e. lymphocytes were irradiated and subsequently stimulated with pokeweed (PWA) instead of PHA. Because PWA is a T-cell dependent B-cell mitogen, T-cells are still required for B-cell activation. Therefore, B- and T-cells were co-cultured. Immediately before metaphase cells were collected, unwanted T-cells were removed from the culture.
This method is based on the capability of T-cells to form stable rosettes with sheep erythrocytes (SRBC). T-cell/erythrocyte rosettes were separated from B-cells by Ficoll-Hypaque centrifugation. Flow cytometric measurements, applying cell specific antibodies showed that the B-cell fraction contained less than less than 10% remaining T-cells.

This protocol was recently applied to investigate the effect of 100 MeV/u carbon ions and 250 kV X-rays. Lymphocytes were cultivated for 4 days in medium containing BrdU to differentiate first, second and third metaphase cells. Three hours before harvesting, colcemid was added to enrich metaphase cells. B-cells were purified as described above, fixed and analysed. Currently, mitotic index, stimulation index, distribution of first, second, third mitosis and type and number of chromosomal aberrations (Fig. 1) are scored together with the frequency of sister-chromatid-exchanges.

Counting the number of mitogen activated B-cells revealed that isodoses of carbon ions reduced the stimulation rate more than X-rays. Analysing the rosetted T-cells indicates that T-cells proliferate faster than B-cells, even if the mitogen PWA is used.
First cytogenetic results obtained for B- and T-cells irradiated with 1Gy X-ray showed no significant changes in the type or frequency of chromosomal aberrations induced in both lymphocyte subsets. As observed in T-cells, radiation did not influence the rate of sister chromatid exchanges in B-cells. The evaluation of chromosomal aberration induced by carbon ions and higher X-ray doses is in progress.

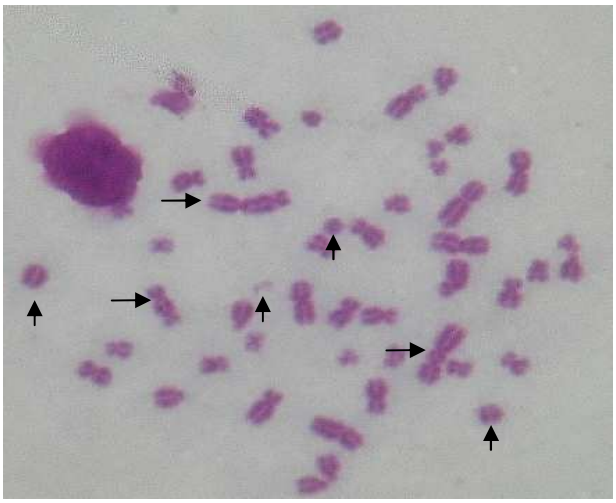


Fig. 1: First cycle metaphase of a B-cell, irradiated with 1Gy 100 MeV/u carbion ions, abberrations are indicated by arrows, (vertical arrows= dicentrics; horizontal arrows= fragments)

References

[1] Lee R. *et al*., Adv. Space Res.: 35, 268-275, (2005)
[2] Holmen A. *et al*., Mutation Research.: 309, 93-99, (1994)
[3] Lee TK. *et al*., Teratog Carc. Mutagen.: 14(1), 1-12, (1994)

*This study was supported by BMBF, grant 02S8203

Radiation-induced genetic instability in normal human fibroblasts*

S. Sommer, C. Fournier, P. Hessel, S. Ritter, M. Winter, GSI, Darmstadt, Germany
E. Nasonova, L. Melnikova, JINR, Dubna, Russia.

Accumulating evidence indicates that the exposure of cells to ionizing radiation can result in a delayed destabilisation of the genome manifested at chromosomal level in the *de novo* occurrence of chromosome aberrations many cell generations post-treatment (1,2). Genetic instability is considered as one of the most important aspects of carcinogenesis. For example, a relationship between a destabilisation of the genome and the induction of secondary tumours in the radiation field is discussed. However, the role of genetic instability in the response of normal human tissue to both high and low LET radiations is still unclear.

To contribute to this issue, we investigate to what extent chromosomal instability is induced in normal human cells. As a model system AG 1522 fibroblasts were chosen, since the early radiation response of these cells had been already extensively studied in our group, i.e. the induction of cytogenetic damage (3), the expression of cell cycle regulators (4) and fibrosis related markers (5) had been analysed.

In first long-term experiments AG 1522 fibroblasts were irradiated with different doses of X-rays and subcultured at 2 weeks intervals up to the end of their replicative life span. Chromosome samples were prepared between 60 and 230 days post-irradiation. To assay for genetic instability, 50 to 200 metaphases were examined by Giemsa-staining for the presence of non-transmissible aberrations such as dicentrics, rings, chromosome-type breaks and chromatid-type breaks or exchanges. Furthermore, to obtain information on the frequency of simple or complex translocations, 20 to 100 metaphases were analyzed by multiplex fluorescence in situ hybridisation (m-FISH).

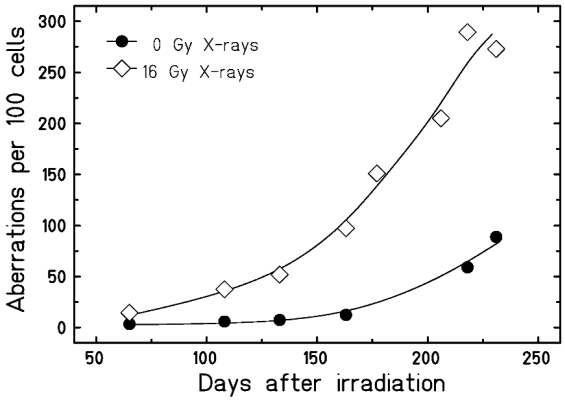


Fig. 1: Frequencies of non-transmissible aberration in the progeny of AG 1522 fibroblasts. Cells were irradiated with 0 and 16 Gy X-rays and aberrations were examined at different time-points by Giemsa-staining. Most aberrations were dicentrics.

*Work supported by BMBF (Bonn), grant 02S8203.

As shown in figure 1, 60 days after X-ray exposure the number of non-transmissible aberrations detected by Giemsa-staining was slightly higher in the progeny of irradiated cells than in the control. In both cultures the aberration frequencies increased with time and most aberrations were dicentrics, probably resulting from telomere fusion. However, in the control population aberrations appeared later and the level was much lower than in the offspring of irradiated cells.

When chromosome samples were analysed by m-FISH, higher aberration yields were detected than after Giemsa-staining due to the greater resolution power of this novel technique (see fig. 2). In the descendants of X-ray irradiated cells a high number of simple and complex translocations was found and the translocation frequency increased with culture time. In contrast, in the control culture a significantly lower number of translocations was measured and all translocations were classified as simple.

Altogether, these preliminary data indicate that in the progeny of X-irradiated fibroblasts chromosomal instability occurs earlier and is more pronounced than in control cells. Further studies investigating the fate of normal human fibroblasts after C-ion exposure are in progress.

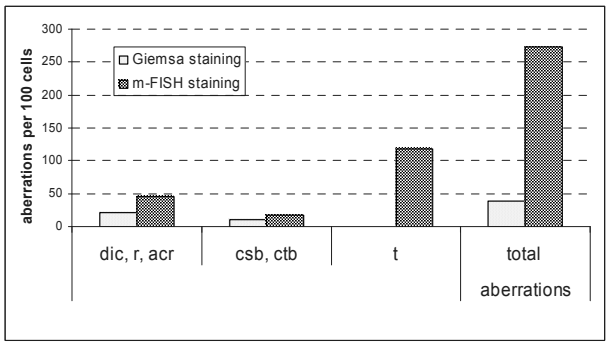


Fig. 2: Comparison of the aberration yields in the progeny of AG 1522 fibroblasts scored after Giemsa- or m-FISH staining. Cells were collected 108 days after irradiation with 16 Gy X-rays (dic: dicentrics; r: centric rings; acr: acentrics rings; csb: chromosome breaks; ctb: chromatid breaks; t: translocations).

References

[1] M.B. Martins et al., Mutat. Res. 285,(1993) 229-237.
[2] M.A. Kadhim et al., Int. J. Radiat. Biol. 73(1998), 143-148.
[3] E. Nasonova et al., Int. J. Radiat. Biol. 80 (2004) 621-634.
[4] C. Fournier et al., Radiat Res. 161 (2004) 675-684.
[5] C. Fournier et al., Int. J. Radiat. Biol. 77 (2001) 712

Chromosomal instability in T-lymphocyte long-term cultures irradiated with carbon ions and X-rays.*

H. Hofman-Hüther#, Dept. of Radiotherapy and Radiooncology, University of Göttingen, Germany
H. Peuckert, Dept. of Radiotherapy and Radiooncology, University of Göttingen, Germany
P. Virsik-Köpp, Dept. of Environm. Medicine, University of Göttingen, Germany

Introduction

Blood as well as other normal tissues are unavoidably exposed to ionising radiation during a radiation therapy of tumours. Damage to haematopoietic cells in cancer patients undergoing radiation therapy is one of the important side effects and might result in secondary malignancies of the haematopoietic system. Genomic instability induced during radiation therapy might play a role in responses of tumour and of normal tissues located in the treatment volume or in its close proximity. Since the radiation-induced genomic instability in normal tissues including haematopoietic system could significantly increase the risk of secondary malignancies, the potential of heavy ions with respect to instability induction must be addressed.

In this study, genomic instability induced by 250 kV X-rays and 100 MeV/u carbon ions in long-term lymphocyte cultures from two healthy donors was examined. The purpose of this analysis was to compare the instability effects induced by low LET X-rays and high LET carbon ions.

Material and Methods

The chromosomal instability was studied in descendants of cells from two healthy donors irradiated with 3 different doses of the particular radiation up to 22 population doublings. As cell system, we used primary long-term cultures of T-lymphocytes assayed from freshly separated mononuclear cells by stimulation with phyto-

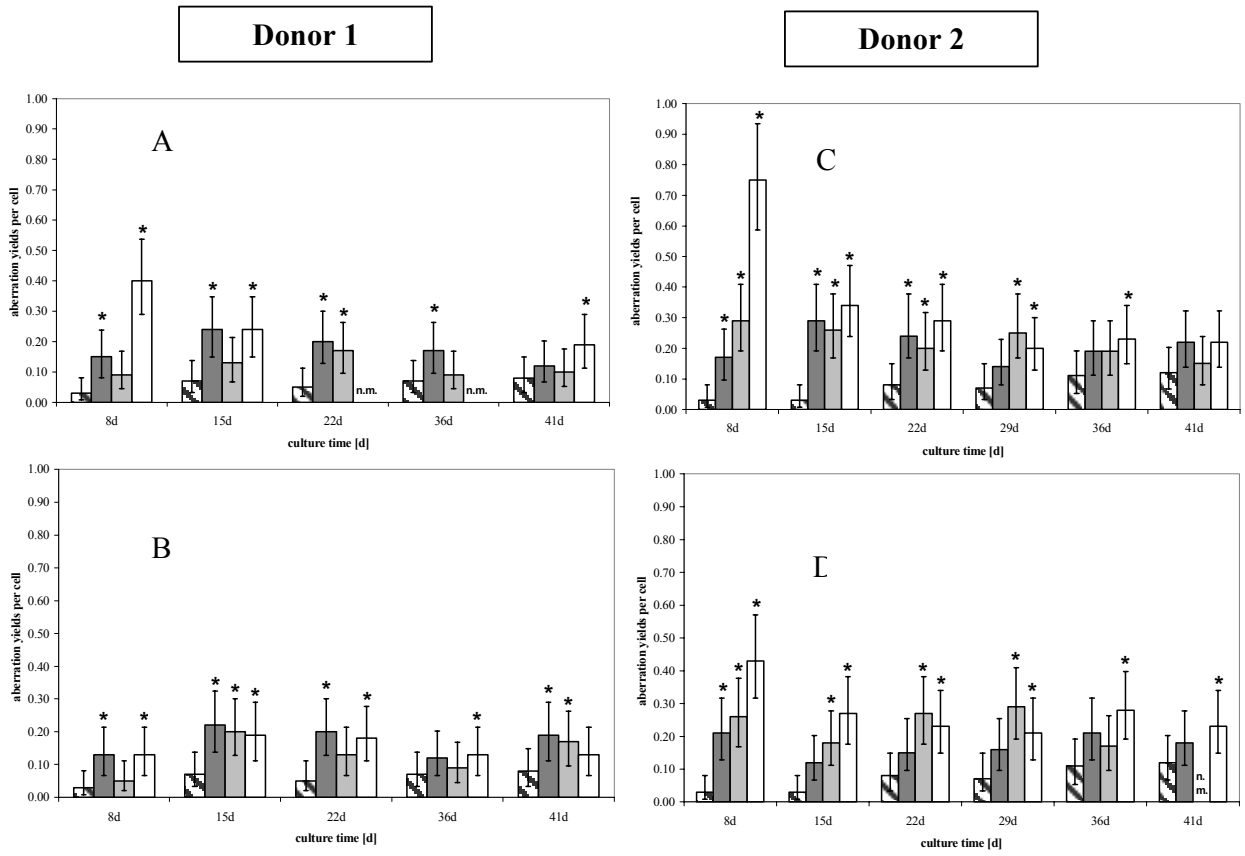


Fig.1 Time-course of spontaneous and radiation-induced aberration yields per cell in long-term lymphocyte cultures after irradiation with 250 kV X-rays and 100 MeV/u carbon ions. The aberration yields represent the sum of chromosome- and chromatid-type aberration. Aberration yields per cell in nonirradiated cells (▨) and in cells irradiated either with 250 kV X-rays (1Gy (■), 2 Gy (▩) and 4 Gy (□)) or with 100 MeV/u carbon ions (0.25 (■), 0.5 Gy (▩) and 2 Gy (□)) are shown for donor 1 (A and B) and for donor 2 (C and D) for X-rays and ions, respectively. Vertical error bars represent 95 % Poisson confidence limits. n.m. = no metaphases observed. (*): yields in irradiated cells are significantly different from spontaneous yields (α= 0.05) as tested by F-test.

haemagglutinin and addition of feeder cells as described by Fält et al. [1].

For the analysis of chromosomal aberrations, cells were collected at 8, 15, 22, 29, 36, 41, 49 and 56 days (~ 28 population doublings) post-irradiation after 4 hours colcemide treatment. Metaphase spreads were prepared according to standard techniques and stained with 5% Giemsa solution. At least 100 metaphases were analysed for each time- and dose-point. Chromosome aberrations were classified as chromosome-type (dicentrics, centric rings and acentric fragments) and chromatid-type (chromatid breaks and chromatid exchanges) aberrations. The mitotic indices were also scored for each point. Unirradiated lymphocytes of both donors displayed a mitotic index between 1 and 4 % until 41 days culture time. At later times, the mitotic index decreased down to zero, reflecting the culture deterioration. For control and irradiated cultures, there were only slight differences in mitotic indices, for both radiations, i.e. X-rays and carbon ions (data not shown).

Results

In Giemsa-stained cells, the spontaneous aberration yields amounted about 0.03-0.05 aberrations per cell for both donors on day 8 and 15 and then increased slightly up to 0.1-0.15 aberration per cell as shown in Figure 1.

Radiation-induced aberration yields as observed in cultures irradiated with X-rays or carbon ions are given in also in figure 1 for donor 1 and for donor 2. For both donors and radiations, the aberration yields observed for the highest doses (4 Gy of X-rays and 2 Gy of ions) were significantly increased in comparison to control values (F-test, $\alpha = 0.05$) up to day 36. Donor 2 displayed higher aberration levels than donor 1. For lower ion doses, the aberration yield pattern was quite complex. In donor 1, there was practically no dose-effect after irradiation with carbon ions in contrast to donor 2, where some dose-dependence could be observed for both lower doses. For both donors, the lowest ion dose used, D = 0.25 Gy, induced a significantly (F-test, $\alpha = 0.05$) increased amount of chromosomal instability as compared to controls.

The effectiveness of carbon ions was about twice as high as that of X-rays since the chromosomal instability induced by 2 Gy of ions was comparable to that of 4 Gy of X-rays.

Summary

For both donors and radiations, the aberration yields observed for the highest doses (4 Gy of X-rays and 2 Gy of ions) were significantly increased in comparison to control values up to day 36. Donor 2 displayed higher aberration levels than donor 1. The effectiveness of carbon ions was about twice as high as that of X-rays. Already a dose of 0.25 Gy of carbon ions corresponding to 1.4 ion traversals per cell nucleus was effective with respect to instability induction in our cell system.

References

[1] **S.** Fält, K. Holmberg, B. Lambert and A. Wennbor, "Long-term global gene expression patterns in irradiated human lymphocytes" Carcinogenesis, Vol. 24, No. 11, 1837-1845, November 2003.

*Work supported by BMBF-02S8203
#Hana.Hofman@gmx.de

Analysis of chromosome damage induced by 177 MeV/u Fe-ions based on the time-course of aberrations*

R. Lee, P. Hessel, S. Ritter, GSI, Darmstadt, Germany
E. Nasonova, JINR, Dubna, Russia
E. Gudowska-Nowak, Jagellonian University, Krakow, Poland

Health hazards resulting form the exposure to high-Z and high energy particles such as carcinogenesis, damage to the central nervous system or cataractogenesis are of major concern in planning manned missions to Moon and Mars. Among these effects carcinogenesis is currently considered to be the main risk factor for astronauts.

One important biomarker of cancer risk is the occurrence of chromosome aberrations. In humans aberrations are usually measured in peripheral blood lymphocytes. For cytogenetic analysis lymphocytes are cultivated *in vitro* for 48h. Then, chromosome spreads are prepared and aberrations are analysed in first generation metaphases [1]. However, evidence is accumulating that the conventional protocol underestimates the true frequency of heavy ion produced damages due to pronounced cell cycle perturbations [2, 3].

To contribute to this issue, we investigated the time-course of aberrations in human lymphocytes irradiated *in vitro* with 177 MeV/u Fe-ions (LET: 335 keV/µm). Cells were collected between 42 and 78 h post-irradiation and aberrations were analysed in first cycle metaphases identified by differential (FPG) staining [2]. For comparison an X-ray study was performed.

Exemplarily, data obtained for 2 Gy Fe-ions and X-rays are plotted in figure 1. While after exposure to Fe-ions the aberration yield increased drastically with sampling time, i.e. at 78h twenty times more aberrations were measured than at 42h, a stable yield was found after X-ray exposure. Thus, investigation of chromosomal damage at a single sampling time as recommended by the conventional protocol can result in a considerable under- or overestimation of the cytogenetic effects of high LET exposure, depending on the subpopulation of cells that is analysed. Accordingly, RBEs derived from single sampling time are not reliable.

To account for the time-dependent expression of chromosomal damage, the total amount of aberrations induced within the entire cell population was determined by means of the integration analysis [4]. In brief, for each collection time the aberration yield is weighted with the corresponding mitotic index. Furthermore, to consider the increase in population size due to cell division, a correction factor is applied. Finally, the frequencies are summed (integrated) yielding the number of aberrations induced in the initial cell population. Based on these integrated yields dose-response curves can be generated (see figure 2) and used for RBE calculation. Application of this method revealed that the RBE of 177 MeV/u Fe-ions is about 1, when doses up to 2 Gy are delivered. For higher Fe-ion doses an RBE close to zero is estimated due to the saturation of the aberration yield

Further studies investigating the cytotoxic effects of heavy charged particles over a wider range of LETs are in progress.

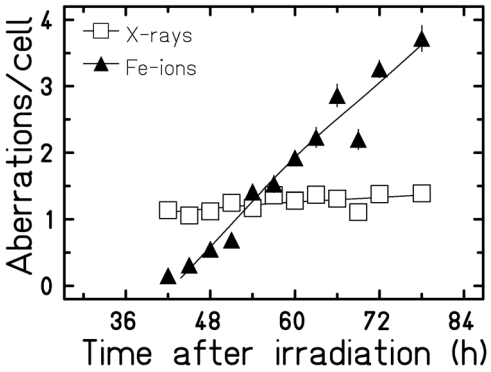


Fig. 1: Time-course of chromosome aberrations in first cycle human lymphocytes after irradiation with 2.2 Gy Fe-ions or 2 Gy X-rays. Lymphocytes were obtained from the same, healthy volunteer.

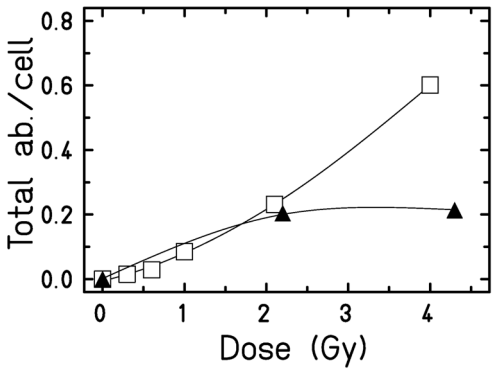


Fig. 2: Comparison of the total number of aberrations (ab.) per initial cell induced by X-rays or 177 MeV/u Fe-ions. The yields were determined by the integration analysis as described in [4]. Key as in figure 1.

References

[1] IAEA, Technical Report Series no. 405, International Atomic Energy Agency, Vienna, 2001.
[2] R. Lee et al., Advances in Space Research 35 (2005) 268-275.
[3] K. George et al., Radiation Research 160 (2003) 425-435.
[4] M. Scholz et al., International Journal of Radiation Biology 74 (1998) 325-331.

*Work supported by BMBF (Bonn), grant 02S8203.

Role of soluble factors in mediating bystander response after carbon ion exposure

D. Becker[1], C. Fournier[1], D. Pollet[2], G. Taucher-Scholz[1]

[1]GSI, Darmstadt, Germany; [2]FH-Darmstadt, Germany

Introduction

Biological effects in unirradiated cells, which are located near to irradiated cells, are of special interest in the context of the increased use of carbon ions in radiotherapy, especially to explore a potential bystander effect at the boarder line of the exposed tumor. We quantified the expression of the cell cycle regulator CDKN1A (p21), which is expressed at higher level after irradiation and has been described as part of the bystander response in human fibroblasts after exposure of a few cells to α-particles [Azzam *et al.*, 1998]. In parallel we measured the formation of intracellular reactive oxygen species (ROS) in bystander cells, which is discussed to be involved in the cellular response of bystander cells [Spitz *et al.*, 2004].

Material and Methods

Confluent monolayers of normal human fibroblasts strains (AG01522C) were used. Irradiation with fluences of carbon ions (170 keV/µm) was compared to similar X-ray doses. To get an improved understanding of the mechanisms underlying the effects in bystander cells, especially following densely-ionising irradiation, we separated irradiated (donor) and non-irradiated cells (acceptor cells) with a special coculture system (see figure 1), restricting the intercellular communication on soluble factors like cytokines or other signal molecules. The permeable membrane separates the donor from the acceptor cells but allows the passage of molecules, which can travel through the medium. After exposure, the donor cells were cocultured with the unirradiated acceptor cells for 5h. The amount of CDKN1A in the cells was measured by flow cytometry and the level of ROS was detected by measuring the fluorescence by Dichlorofluorescein (DCF)-assay.

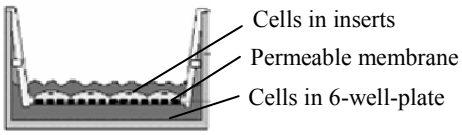


Figure 1: Insert-well-coculture system. The inserts are superposed in a distance from 0,9 mm to the 6-well-plate. Pore size of the membrane: 1 µm (1.6 x 10^6 pores/cm^2).

Results and Conclusion

With this experimental design, we detected an up to the twofold induction of CDKN1A in unirradiated acceptor cells 5h after irradiation with 5 Gy X-rays (not shown), confirming the data published by Yang *et al*. (2005). The involvement of soluble factors in the bystander response following low LET exposure was further investigated by measuring the intracellular level of ROS. It can be assumed that the lifetime of ROS formed during radiolysis is expired in a few seconds after irradiation. A detection of ROS at later times indicates a biological response of the cells. An increased level of intracellular ROS in the acceptor cells was only observed 3 days after exposure, but not in parallel to the induction of CDKN1A protein (not shown).

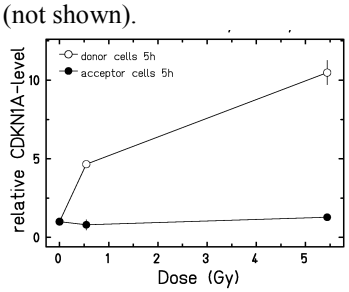


Figure 2: Induction of CDKN1A protein in irradiated donor and unirradiated acceptor cells 5h after carbon ion exposure (SEM, n=2)

Unlike the observation following X-ray exposure, for high LET (carbon ions) an induction of CDKN1A in acceptor cells based on the secretion of soluble factors was not observed (see figure 2). This is in contrast to the slight induction of CDKN1A in bystander cells located near or adjacent to irradiated cells [report GSI 2004]. Furthermore, no indication for the occurrence of enhanced ROS levels in unirradiated acceptor cells was obtained for carbon ions (see figure 3), whereas for α-particles an induction of intracellular ROS-level 1 day after coculturing was shown [Narayanan *et al.*, 1997].

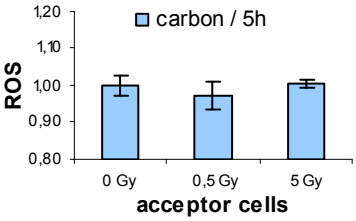


Figure 3: intracellular ROS in unirradiated acceptor cells 5h after coculture with carbon ion irradiated donor cells (SEM, n=2)

Taken together, carbon ion exposure leads neither to an induction of CDKN1A nor to an enhanced intracellular level of ROS in the acceptor cells, which is based on the secretion of soluble factors into the medium. An indication for the involvement of soluble factors and the participation of ROS at the bystander response was only obtained for X-ray, but not for carbon ions. This suggests a mechanistic relationship that may be relevant for low but not for high LET irradiation. [Partially supported by BMBF (02S8203)]

References

[1] Azzam *et al.*, Radiation Research 150:497-504 (1998)
[2] Narayanan *et al.*, Cancer Research 57(18):3963-3971 (1997).
[3] Spitz *et al.,* Cancer & Metastasis Reviews 23:311-322(2004)
[4] Yang *et al.*, Oncogene 24:2096-2103 (2005)

First insights into the cellular basis of different radiosensitivities of squamous carcinoma cells to high LET irradiation

G.Alphonse, M.Maalouf, C.Rodriguez-Lafrasse and S.Trajkovic-Bodennec -Molecular and Cellular Radiobiology Laboratory - EA3738–Oullins- France
C.Fournier and G.Taucher-Scholz - GSI- Darmstadt- Germany

The growing interest of the medical community in hadrontherapy stimulates studies on the molecular mechanisms underlying the cell death induced by exposure to high LET. In this context, the determination of RBE, the identification of the cellular death processes involved in the response to carbon ions and a better comprehension of molecular and biochemical bases of these responses represent an important point for the clinical application and the modulation of hadrontherapy.

Our laboratory and others [1-3] have previously demonstrated a correlation between the propensity of cell death by an apoptotic process, the radiosensitivity and the radiation induced ceramide production. Since, opposite to what is known with X-irradiation, the type of cell death induced after carbon ions is still not established. This study suggests the analysis of molecular events involved in cell death after high LET irradiation.

Two head and neck squamous carcinoma SCC61 (radiosensitive) and SQ20B (radioresistant) cell lines were irradiated with carbon ions (9,8 MeV/n). The survival curves, the extent of apoptosis and alterations in cell cycle were established.

In subsequent experiments, survival, apoptosis and alterations of the cell cycle distribution were determined for both cell lines after carbon irradiation and in parallel after X-irradiation. The results obtained (Figure 1) for both cell lines clearly indicate that carbon irradiation induces a higher level of clonogenic cell death than X-irradiation. RBE values for a survival of 10% were determined and were at 3.3 for SQ20B cells and at 3.5 for the radiosensitive SCC61 cell line.

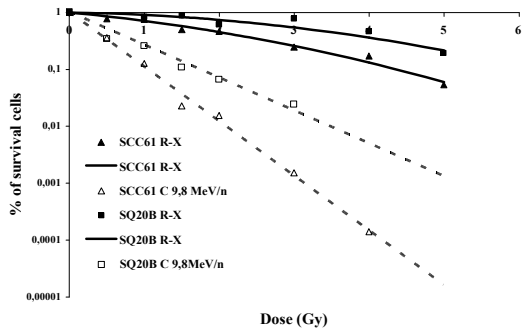


Figure 1: Survival curves after irradiation with carbon 9.8 MeV/n or x-rays on SCC61 and SQ20B cell lines.

Our studies on the cellular basis of observed differences in radiosensitivity between carbon and X-irradiation led us to examine the putative induction of apoptosis upon irradiation with carbon (9,8 MeV/n). First results have been obtained for the radioresistant cells. In order to evaluate the level of apoptosis in the SQ20B cell line in response to irradiation, the percentage of hypodiploid (apoptotic) cells was assessed by cell cycle analysis. As observed previously using X-irradiation, no induction of apoptosis could be observed in this cell line at least up to 72 hours post-irradiation with carbon whatever the dose used. (data not shown).

Since differences in apoptotic levels between two types of irradiation were not obvious, the role of cell cycle arrest in the lower survival was studied by flow cytometry using propidium iodide labelling. As shown in Figure 2, exposure to different doses of carbon ions induced, in a high percentage of SQ20B cells, a dose-dependent G2 phase arrest. This arrest was observed 24 hours after irradiation and was prolonged up to 72 hours. At the opposite, after X-irradiation of 10 Gy only a small reversible G2 arrest was previously observed at 24h.

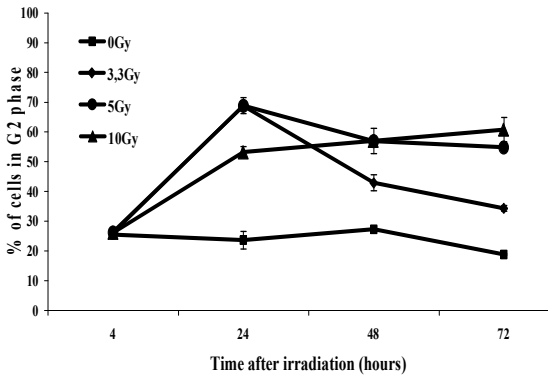


Figure 2: Percentage of SQ20B cells in G2 phase after a 3.3, 5 or 10Gy irradiation with carbon 9.8MeV/n.

These preliminary results show that irradiation with carbon ions results in important clonogenic cell death that may be explained, at least in part, by the cell cycle arrest within the G2 phase for the SQ20B cell line. No apoptosis induction could be detected upon irradiation with carbon up to 72 hours in this radioresistant cell line. These results have to be reassessed in SCC61 radiosensitive cells. Moreover evaluations of the induction of other type of cell death and the involvement of ceramide after exposure to carbon irradiations have to be performed.

References

[1] G. Alphonse *et al*. *Inl J Rad Biol* 2002, 78: 821-35.
[2] G.Alphonse *et al*. *Oncogene* 2004, 23: 2703-15.
[3] R.Kolesnick and Z.Fuks *Oncogene* 2003 22:5897-906

Neoplastic Transformation Induced by Carbon Ions*

Daniela Bettega, †, Paola Calzolari, Dept.Physics, Univ. of Milan and INFN, Italy,
Petra Hessel, Wilma K. Weyrather, GSI, Darmstadt, Germany

Abstract

Neoplastic transformation in vitro can be used as an indicator for risk assessment comparing different radiation types. In this work transformation of CGL1 cells by monoenergetic carbon ions has been measured and compared to photon irradiation.

Experiments

The human hybrid (Hela X skin fibroblast) cell line, developed by Stanbridge et al [1] and Redpath et al [2] and designated CGL1 has been used to compare carbon ion irradiation to conventional radiation (15 MeV photons). Preliminary results with high energy carbon ion at the SIS have been reported [3] [4]. In 2005 the series with track segment irradiation was completed with 11.4 MeV/u carbon ions at the Unilac. The complete set of used energies is shown in table 1.

Table 1: Physical characterisation of carbon beams used

Energy MeV/u	**Energy on target** MeV/u	**LET** keV/μm
270.0	266.4	13.7
100.0	86.5	29.5
11.4	9.65	172

The results for clonogenic survival and transformation frequency per surviving cell as function of particle fluence are shown in figure 1. Each data point is the result of two experiments. Figure 2 shows the data transferred to dose and compared to 15 MeV photons.
The RBE values at a level of 20% survival were 1.2 (266.4 MeV/u), 1.5 (86.5 MeV/u) and 4.6 (9.65 Mev/u).

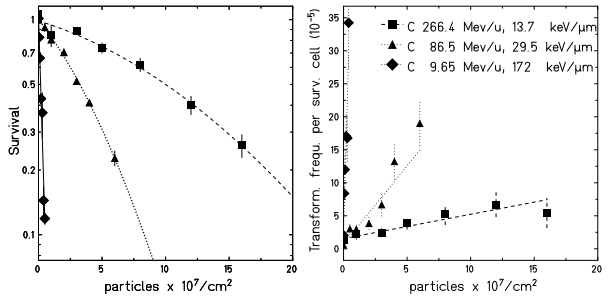


Figure 1: Survival and transformation frequency shown as a function of particle fluence

* Work supported by ...
† I3-EURONS (European Commission contract no. 506065)

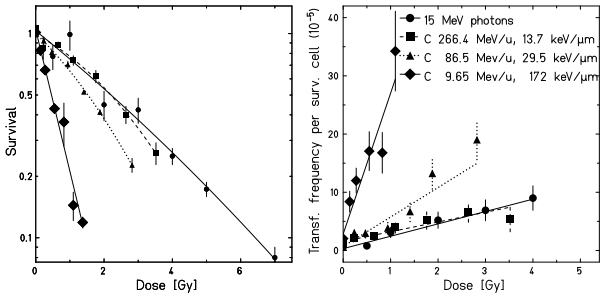


Figure 2: Survival and transformation as a function of dose and compared to photon irradiation

For the risk assessment the transformation frequency per cell at risk (the number of irradiated cells) is more relevant than the frequency per surviving cell. The results are shown in fig 3. As transformation induction and reproductive cell death are two competing processes, the transformation frequency per cell at risk decreases after a maximum. For higher doses the cell killing is the more important part. Our measurements showed that the transformation frequencies for photons and 270 MeV/u carbon ions are very similar and only slightly dose dependent with a not very pronounced maximum at around 2 Gy. For the 100 MeV/u carbon ions the maximum value is approx. 1.6 times higher than for photons and slightly shifted to lower doses. The Bragg-peak ions show a significant maximum at low doses.

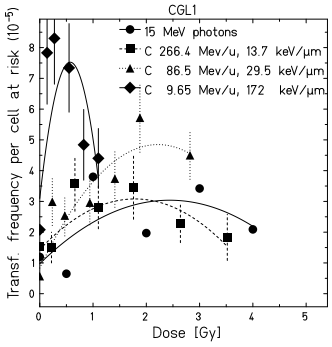


Figure 3: Transformation frequency for photons and carbon ions calculated for cell at risk.

References

[1] Stanbridge et al , Science, 215, 252 (1982)
[2] Redpath et al, Radiat. Res. 110, 468 (1987)
[3] GSI Scientifi c Report 2003, 169 (2004)
[4] GSI Scientifi c Report 2004, 286 (2005)

Impact of conventional and heavy ion irradiation on tumor cell migration *in vitro*

K. Goetze[1], W. Mueller-Klieser[1], G. Taucher-Scholz[2], M. Scholz[2]

[1]University of Mainz, Germany; [2]GSI Darmstadt, Germany

The formation of metastasis compromises most strategies for curing patients with solid malignant tumors. The metastatic process is directly linked to the ability of tumor cells to migrate. Consequently, tumor cell motility or migration has been intensely studied for a number of years with most of the studies being focused on attempts to inhibit cell migration. In contrast, only a few studies are concerned with the promotion of cell migration by common standard therapy. Wild-Bode et al. [1], for example, showed an enhanced migration of glioma cells after sublethal irradiation, and Cordes et al. [2] showed an upregulation of functional β1-integrins after ionizing irradiation of lung tumor cells. Preliminary data from our own group show conflicting results including radiation-mediated migration stimulation and inhibition. These data indicate that experimental conditions of the migration assay, such as the substrates used for the cell adhesion or the implemented cell density, are crucial for the outcome of the studies on pro- or anti-migratory stimuli; therefore, a series of experiments has been initiated to evaluate the influence of cellular microenvironment on radiation-induced changes in cell motility. Since information on the effect of heavy ion irradiation on the migratory behavior of tumor cells is very sparce (Ogata et al. [3]), the current project has its emphasis on the reaction of cell motility to carbon ion irradiation.

U87 human glioblastoma cells were irradiated with 10 Gy in monolayer culture under well-defined conditions using conventional or particle radiation. A standardized Boyden chamber assay was performed to quantify the migration of the cells through 8µm pores of a polycarbonate membrane. The membrane was covered with collagen IV in the (upper) starting compartment and with gelatin to arrest the cells at the (lower) arrival side. The cells were seeded in the migration chamber 24h after irradiation and the chamber containing complete culture medium in the upper and lower compartment was incubated for 16h.

Depending on the type of radiation, an opposite migratory behavior of the cells was registered following irradiation (Fig.1). After X-ray irradiation with 10 Gy the relative proportion of migrating cells was increased by 23%, whereas preliminary data using equivalent heavy ion irradiation indicate a number of migrating cells which was decreased by nearly 95% compared to untreated cells as controls (=100%).

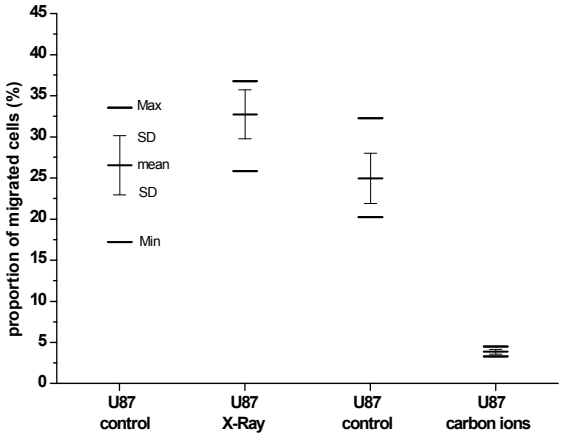


Fig. 1: Percentage of migrated U87 glioma cells irradiated with 10 Gy X-ray or heavy ions, respectively. Migration was quantified in a Boyden chamber assay.

These results suggest that irradiation of glioma cells can modulate tumor cell migration in opposing ways depending on the radiation quality. Conventional irradiation of glioma cells with X-rays seems to enhance the motility of these cells. During irradiation of solid tumors in the clinic, this effect may be overridden by a number of pro- and anti-migratory influencess *in vivo*. Still, it may reflect a certain risk of inducing metastasis, as has been shown to be true in animal studies (Rofstad et al., [4]). This situation is different with particle irradiation, where the *in vitro* data may be indicative of a reduced corresponding risk *in vivo*.

[1] Wild-Bode, C., Weller, M., Rimner, A., Dichgans, J., Wick, W., Cancer Res. 61: 2744-2750, 2001

[2] Cordes, N., Blaese, M.A., Meineke, V., van Beuningen, D., Int. J. Radiat. Biol. 78: 347-357, 2002

[3] Ogata, T., Teshima, T., Kagawa, K., Hishikawa, Y., Takahashi, Y., Kawaguchi, A., Suzumoto, Y., Nojima, K., Furusawa, Y., Matsuura, N., Cancer Res. 65: 113-118, 2005

[4] Rofstad, E.K., Mathiesen, B., Galappathi, K., Cancer Res. 64: 13-18, 2004

Investigation of substrate- and radiation-dependent cell motility using videomicroscopy

A. Müller, D. Pollet, FH Darmstadt, Germany
M. Scholz, G. Taucher-Scholz, J. Topsch, GSI Darmstadt, Germany

The outcome of tumor therapy like e.g. radiation therapy is closely related to the invasive potential of tumor cells. There are hints, that radiation might increase the motility and the invasive potential of tumor cells, thus counteracting the primary goal of radiotherapy for low-LET-radiation [1], whereas the opposite may be the case for high-LET-radiation [2].

Cell motility and migration can be investigated using e.g. the Boyden chamber assay (see [3]) or by means of video microscopy. For the work presented here, a video microscopy system for long-term observation of individual cells was established and tested. The system consists of a conventional inverted microscope equipped with a mini-incubator allowing to control for temperature, CO_2 and humidity. Aimed at the optimization of the system, the evaporation rate of medium was determined and the growth rate of cells was measured. By using gas permeable, but water impermeable foil lids the evaporation could be minimized, thus assuring optimal cell culture conditions during at least 48 hours.

Analysis of the video image sequences was based on the SIMI BioCell software, and average velocity, the velocity as a function time elapsed since cell birth and the type of movement were measured. The system was used to study in detail the motility of U87 glioblastoma cells with respect to dependence on the substrate and on irradiation with X-rays. The results for X-irradiation presented in this work will serve as reference data for a comparison with experiments using charged particle radiation.

The motility of U87 cells was slightly increased on collagene IV and fibronectin substrates as compared to uncoated culture dishes (see Fig. 1) . Furthermore, cells on fibronectin showed a higher frequency of directional changes during migration as compared to uncoated dishes or dishes coated with collagen IV; this becomes visible in the higher ratio of total to effective velocity. Cells immediately after mitosis showed the highest motility, and velocity steadily decreased with increasing time after mitosis (data not shown).
The proliferation of cells was not influenced by the substrate. However, radiation leads to a reduction of the proliferative capacity in a dose dependent manner.
There was no significant effect of radiation on the motility of cells, independent of the substrate. The variations observed were in the order of below 20% and thus in the range or inter-experimental variations (Fig. 2).

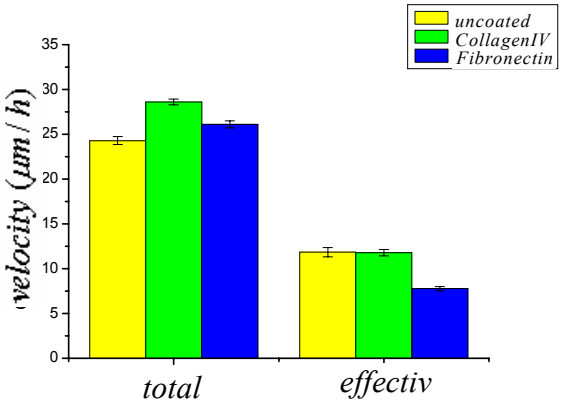


Fig. 1: Substrate dependence of cell motility as measured for U87 glioblastoma cells. Total velocity is defined by the total path length, whereas effective velocity is defined by the shortest distance between the starting and final position of the cell. Measurement interval: 48h

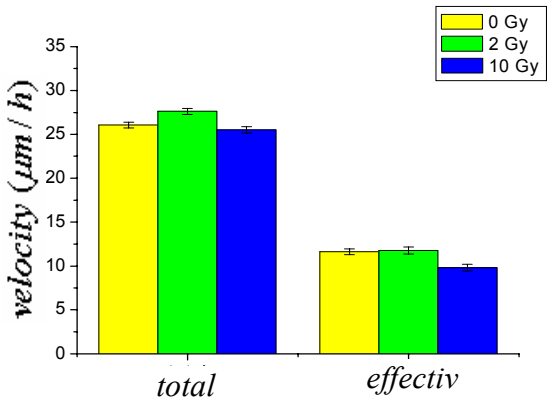


Fig. 2: Impact of X-irradiation on cell motility for U87 glioblastoma cells. Total velocity and effective velocity as defined in Fig. 1. Measurement interval: 48h

[1] Wild-Bode, C., Weller, M., Rimner, A., Dichgans, J., Wick, W., Cancer Res. 61: 2744-2750, 2001
[2] Ogata, T., Teshima, T., Kagawa, K., Hishikawa, Y., Takahashi, Y., Kawaguchi, A., Suzumoto, Y., Nojima, K., Furusawa, Y., Matsuura, N., Cancer Res. 65: 113-118, 2005
[3] Götze, K., Müller-Klieser, W., Taucher-Scholz, G., Scholz, M., this report

ALTEA: FM Particle Telescope tested at GSI*

L. Narici# for ALTEA collaboration

L. Narici, University of Rome Tor Vergata and INFN section of Rome Tor Vergata, via della Ricerca Scientifica 1, 00133 Rome, Italy
livio.narici@roma2.infn.it

Abstract

The ALTEA program, an international and multidisciplinary experiment scheduled to fly in the International Space Station (ISS) in 2006, is aimed at studying space radiation environment and its effects on astronauts. We present the results of the test of the Flight Model of the ALTEA particle detector obtained in two measurement sessions performed at the heavy ion accelerator of GSI laboratory.

Introduction

The increment of space mission duration requires investigation of the possible functional effects of 'space environment' on the Central Nervous System. The most evident of these effects is the anomalous perception of phosphenes ("light flashes", LF) due to the passages of ionizing nuclei through nervous tissues. ALTEA has been developed to conduct this investigation.

For a description of the ALTEA program see [1].

Here we present results of calibration of the Flight Model of ALTEA-space performed at the GSI heavy ion accelerator.

ALTEA-space apparatus

The ALTEA space hardware is composed by six particle detectors (SDS, Silicon Detector System) arranged on a helmet shaped support which also host a visual stimulator. A 32-channels electroencephalographer (EEG) and a pushbutton are also part of the hardware.

The SDS is composed by six identical particle telescopes (Silicon Detector Units, SDUs). Each SDU is composed by six stripped silicon planes alternatively oriented along X and Y directions. On each plane (DB, Detector Board) there are two $8 \cdot 8$ cm^2 silicon chips 380 ± 15 μm thick, placed side by side, with a 5.5-mm gap between them. Each chip is divided into 32 strips with 2.5 mm pitch, therefore a pair of X and Y planes features a $32 \cdot 64$ strip grid. The aluminium outer box is 1.3 mm thick. The bidirectional geometrical factor for one SDU is 160 cm^{2}sr, the maximum error of angular reconstruction is ±1.8°.

The dynamic range of the device varies from 5 to 2400 MIP. Simulations show the ALTEA SDU able to trigger particles from protons, with energy between 25 and 100 MeV, to Molybdenum (Z = 42) at minimum energy loss.

Beam test and result

The Training Model SDU-TM1 and the full ALTEA FM Model (6 SDUs) were tested in two measurement sessions with Carbon nuclei (beam at 100, 150, 400, 600 and 1000 MeV/n) and Titanium nuclei (beam at 200 and 600 MeV/n) [2]. In both measurement sessions a complete scan of each SDU was performed to check functionality and homogeneity of all strips of silicon detector planes. For each ion at different energies the instrument response was compared with Montecarlo simulations to study its linearity and to calculate instrument amplification. Linear fits show a good linearity (R^2 from 0.999 to 0.9997) and the conversion factor ranges from 0.62 to 0.66 MIP/ADC channel.

An aluminium absorber (6 mm) was also used to study fragmentations; it has been placed between the incoming beam (Ti at 600 MeV/n) and the SDU-TM1. After selected single track events, the energy distribution in Fig. 1 is obtained. Titanium peak is around 7200 ADC channels. Data from Montecarlo simulation are also showed; peak positions are in good agreement.

A neural network analysis of fragmentation data is in progress, nuclei from B to Sc can be recognised.

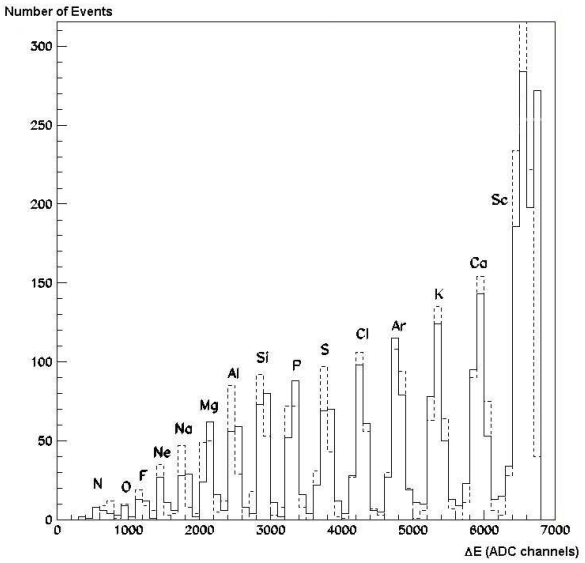


Figure 1: Experimental data (continuous line) in comparison with Montecarlo simulation (dashed line) of Ti fragmentation.

References

[1] Narici, L. et al., The ALTEA/ALTEINO projects: studying functional effects of microgravity and cosmic radiation. Advances in Space Research 33, 1352–1357, 2004.

[2] Zaconte V. et al., ALTEA: flight model calibration at GSI, *in press on Advances in Space Research*

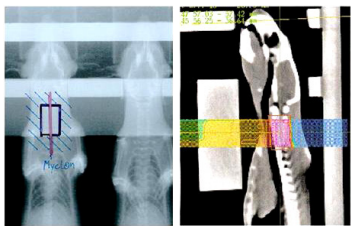
* Project funded by ASI

Radiation tolerance of the rat spinal cord after single and fractionated doses of photons and carbon ions

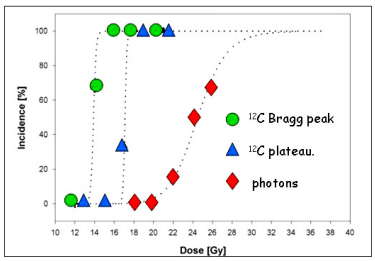
P. Peschke, C.P. Karger, R. Sanchez-Brandelik, DKFZ Heidelberg, Germany
M. Scholz, GSI, Darmstadt, Germany
J. Debus, University of Heidelberg, Germany

Particle beams have achieved growing interest for tumor therapy. The beneficial beam dose profile characteristics, in combination with active beam-shaping (rasterscan system) and biologically based treatment planning, allow for highly effective conformal target irradiations. For long-term local tumor control of extraneural neoplasms and tumors of the central nervous system (CNS) high radiation doses are required. Contradictive to a successful treatment is often the risk of late complications due to the limited radiation tolerance of the CNS. Clinical studies at the GSI, are accompanied by a biological program to assess the relative biological effectiveness (RBE) of carbon ion irradiations (^{12}C) relative to photons with special emphasis on late complications of the CNS.

In the first studies we have evaluated dose-response relationships for female Sprague Dawley rat spinal cord after 1, and 2 fractions of ^{12}C-ions in the plateau region and in the Bragg-peak. The upper segment of the cervical spinal cord with the cranial field limit at C2 was defined as the target point. The field size was 10 x 15 mm^2. In lateral direction a 4 mm safety margin was used to take into account potential set-up errors. The target point was localized by CT scans taken while the rat was immobilized in the holding device (Fig. 1). Markers, milled into the holding device, were used to align the target point to the isocenter of the irradiation facility, which is defined by crossed laser beams.



An intensity-controlled magnetic raster scanner, with active energy variation by the synchrotron, was used to generate the carbon ion irradiation fields. For irradiation of the rat spinal cords, the Bragg-peak was spread out to 10 mm in the target volume by energy variation of the synchroton. Due to the horizontal direction of the ion beam the anesthetized animals had to be immobilized in a vertical (”hanging”) position, using a specially designed holding device with a capacity for 12 rats. Photon irradiation was delivered by a linear accelerator (Siemens MPX, 15 MeV) with gantry angel at +90° for a horizontal beam. Positioning of the animals was identical to the ^{12}C irradiation. Treatment fields were defined by a multileaf collimator with an aperture of 10 x 15 mm. Dose-rate was 500 cGy/min, under reference conditions. In all the experiments, the dose–response relationship for paralysis of fore or hind limbs up to 300 days after irradiation was used as biological endpoint. Verification with portal-films clearly demonstrated that the raster scan method was accurate and highly reproducible with respect to position and homogeneity of dose. The median latency after ^{12}C irradiation was shorter in animals irradiated in the Bragg-peak (T_{50} = 157 days) than in those irradiated with plateau ions (T_{50} = 178 days). The ED_{50}-values (effective dose where 50% of the animals exhibited damage probability) for irradiation within the plateau region were 17.1±0.8 Gy for single dose (Fig. 2) and 24.9±0.7 Gy for split dose experiments. Irradiation in the Bragg-peak yielded ED_{50}-values of 13.9±0.8, and 15.8±0.7 Gy for 1 and 2 fractions, respectively. The corresponding RBE-values were **1.43**±0.08, **1.37**±0.12 (for 1 and 2 fx, plateau) and **1.76**±0.05, **2.16**±0.11 (for 1 and 2 fx, peak), respectively. For 6 fractions on consecutive days the ED_{50}-values were 57.0±4.0 Gy for photons, 42.8±1.5 Gy for ^{12}C plateau and 19.2±0.2 Gy for ^{12}C Bragg-peak irridiations. Based on these biological endpoints, we could calculated an RBE-value of **1.33**±0.10 for ^{12}C plateau and of **2.97**±0.21, for the ^{12}C Bragg-peak.



Taken in consideration the results from the first two studies, we can conclude that the latency period of myelopathy after Bragg-peak carbon ion irradiation is shorter than after plateau and photon irradiation. From the split dose and 6 fx experiments a clear fractionation effect was observed in the plateau phase, which allows more sparing of normal tissues. In contrast, no clinically relevant effect of fractionation was obtained when carbon ion irradiation was performed in the Bragg maximum.

After having established the technical set-up, the above described experiments were extended to 18 daily fractions of high energy ^{12}C and photons. Control experiments with 18 fractions of photons yielded an ED_{50} of 88.2 Gy. Studies using 18 fractions of ^{12}C, either in the Bragg-peak or in the plateau region have been completed in 2005. The D_{50}-values, fractionation efficacy as well as the responding RBEs are currently under evaluation.

The obtained data sets will be used to derive radiobiological parameters such as RBE and alpha/beta ratios. In addition, these data will be used to explore the precision of the local effect model (LEM) for estimation of RBE values for late effects after ^{12}C irradiation of neurological tissues such as the spinal cord.

Complete Double Differential Cross Sections for Low Energy Electron Emission in Solids Induced by Swift heavy ion Impact

N. Lineva[1], S. Hagmann[1,2], C. Kozhuharov[1]
[1]GSI, Darmstadt, Germany; [2]Institut f. Kernphysik, Univ. Frankfurt

The knowledge of double differential cross sections $d^2\sigma/d\Omega dv$ (DDCS) for electron emission after passage of swift heavy ions through condensed matter is an ingredient of the conformal modeling of the radiotherapy plans with ^{12}C-ions at GSI [1]. The currently used experimental input data of electron production and transport are provided by gas-phase collision experiments that do not include any solid-state effects. The latter can play an important role, especially for the emission of low-energy electrons, crucial for the biologically critical inner part (<10nm) of the ion tracks. The electron production at low energies E≤1keV is, thus, of great experimental interest.
For the measurement of the DDCS for electron emission, we use a toroidal electrostatic electron spectrometer (fig.1), installed in X3 at UNILAC. Its rotational symmetry allows us to measure DDCS in the entire range from 0° to 360°. It is set to a moderate energy resolution ΔE/E=2%, and the angular resolution amounts to 1.5°. A first experiment with 3.55 AMeV C^{2+} and a thin carbon target has been performed.

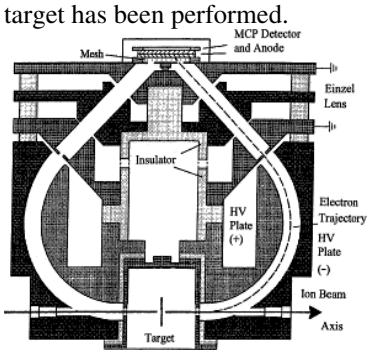


Fig.1 Cross section of the electrostatic toroidal electron energy analyzer

Highly collimated ion beams traverse inside the spectrometer a target foil oriented under 70° with respect to the ion beam axis and are integrated in a Faraday cup for normalization purposes.
The mean free path for low energy electrons is smaller then the thickness of the foil and decreases with decreasing electron energy. Even in the thinnest foils technically feasible for GSI target laboratory, 100 atomic layers carbon and gold foils, electrons undergo numerous elastic and inelastic collisions before leaving the target (see fig.2a). Their fixed energy and the nearly isotropic emission make Auger electrons suitable as a messenger of transport properties from tracks in solid state targets. Auger electrons emitted after the deexcitation of vacancies created through the heavy ion impact ionization have to travel a definite length in the solid state target to the surface that depends on the emission angle and depth of creation in the target (fig. 2b). Energy shift, broadening, and attenuation of Auger electron peaks due to secondary interactions are the objective of these studies in order to derive transport characteristics of electrons in condensed matter.

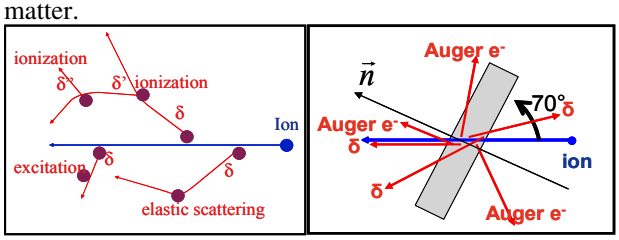


Fig.2(a,b) Emission and transport of electrons in condensed matter

Fig.2 shows a radial velocity distribution $d^2\sigma/d\Omega dv$ of electrons emitted in collisions of C^{2+}-projectiles with a carbon foil (4.5μg/cm2). The radius reflects the electron velocity in atomic units. Indicated are angular position of the target axis (T)-(T) and the position of four bridges in the cylinder aperture (O) positioned in the target zone of the spectrometer.

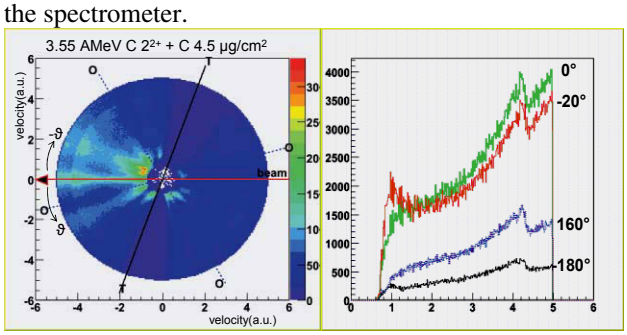


Fig.3a Radial velocity distribution of electrons emitted in collisions of 3.55 AMeV C^{2+} with a carbon foil

3b Electrons yields as a function of the velocity for different direction of emission with respect to the beam axis

Fig. 3a shows the angular and energy dependencies of the intensity of continuum and Auger electrons that leave the carbon foil in forward and backward directions. As expected, an increased intensity at the normal to the target surface direction is observed, since electrons emitted in this direction have to travel the shortest length inside the target. In fig. 3b yields of the electrons as a function of the velocity for four different emission angles are presented. The Auger electron peaks are clearly visible at the velocity of 4.2 a.u. The data are being currently analyzed.
A wide range of targets will be used in coming experiments in order to assess the influence of free electrons etc. on low energy electron emission. To derive a reliable scaling of DDCS, a sequence of projectiles with a range of Z between C up to U and energy between 3.6 and 15 AMeV from the UNILAC will be used.

[1] M.Kraemer and G.Kraft Adv. Space Res. Vol.14, No. 10, pp.(10)151-(10)159, 1994

Experimental Fragmentation Studies with ^{12}C Therapy Beams

E. Haettner, H. Iwase, D. Schardt, GSI, Darmstadt, Germany

High-energy fragmentation reactions occurring along the beam penetration path in tissue leads to attenuation of the primary beam flux and build-up of secondary lower-charge fragments which give rise to the characteristic dose tail behind the Bragg peak. These effects become most significant at large initial energy and correspondingly large penetration depth of the primary beam. New measurements were performed in order to expand and improve existing data [1,2] for the physical models used for treatment planning [3]. Similar investigations were reported by the HIMAC group at NIRS/Chiba [4].

Primary ^{12}C ions with specific energies of 200 or 400 MeV/u delivered from SIS-18 were detected by a beam counter (scintillator) which served also as start detector for time-of-flight (tof) measurements. The beam then entered into a water absorber, the thickness of which was adjustable with an accuracy of 10 µm over a wide range.

Secondary fragments emerging from the water absorber into the forward hemisphere were detected at about 3m distance by a 5 or 10 mm thick plastic scintillator (4x4 cm^2 area) which delivered an energy loss signal and the stop signal for the tof measurement. All charged fragments from carbon down to protons were identified and separated by the analysis of two-dimensional ΔE-tof-plots.

Angular distributions were measured by moving the stop detector on a linear precision drive perpendicular to the beam axis, covering forward angles up to 10°. Alternatively, for measurements of the primary beam attenuation a ΔE-E telescope detector consisting of a 9 mm thick scintillation detector (ΔE) and a 14 cm thick BaF_2-detector (E) was positioned at a short distance behind the exit window of the water phantom.

As a preliminary result of the data analysis the fraction of primary ^{12}C ions surviving the passage through the water absorber is shown in Fig.1 as a function of water depth, together with the corresponding measured Bragg curves. The beam attenuation is well described by an exponential function with a mean free path λ=259(16) mm. At 200 MeV/u still 70% of the primary ^{12}C ions are present at Bragg peak position, while this fraction decreases to 30% at 400 MeV/u.

The energy- and angular distributions of the emitted secondary fragments were investigated at seven different depths of the water absorber. Behind the Bragg peak the fragment spectrum is dominated by protons and α-particles. Their energy spectra are broad and peak at about 220 MeV/u and they also show the broadest angular distributions, while the heavier fragments (B, Be, Li) are emitted in a rather narrow cone of about 0° to 5°. The build-up curves shown in Fig.3 were obtained by integration of the angular distributions from 0° to 10°.

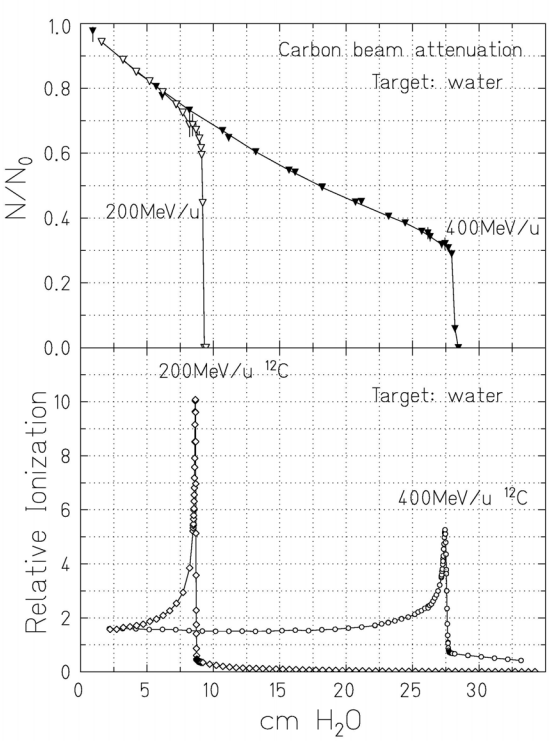


Figure 1: Attenuation of primary carbon beams and corresponding Bragg curves.

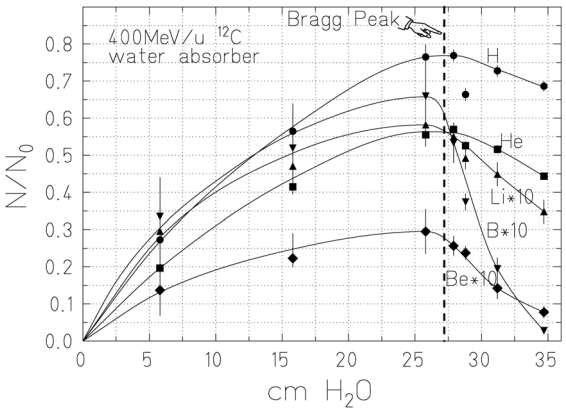


Figure 2: Build-up of secondary fragments produced by 400 MeV/u carbon ions in a water absorber

References

[1] I. Schall et al., Nucl. Instrum. Meth. B 117(1996)221
[2] K. Gunzert-Marx et al., Rad. Prot. Dos. 110 (2004) 595
[3] M. Krämer et al., Phys. Med. Biol. 45(2000)3299
[4] N. Matsufuji et al., Phys. Med. Biol. 50(2005)3393

Fragmentation of 200 MeV/u ^{3}He beams in water

H. Iwase, D. Schardt, S. Groezinger, and J. Naumann, GSI Darmstadt, Germany

^{3}He has a unique charge/mass ratio and it is considered as an alternative isotope instead of ^{4}He for the treatment of deep-seated tumors. For the physical characterisation of ^{3}He as a therapy beam the nuclear fragmentation in water (used as tissue-equivalent) was investigated in this study.

The measurements were performed in the biophysics cave at GSI using 200 MeV/u ^{3}He beams which were stopped in a 12.78 cm thick water target. In this study, (1) Attenuation and fragments buildup of ^{3}He in water, (2) Bragg curves of ^{3}He in water, and (3) Energy spectra of fragments emerging from the target at angles 0 to 30 degrees were measured with different detector arrangements.

Results of the attenuation measurement are shown in Fig.1. More than 35% of the primary 200 MeV/u ^{3}He undergo nuclear reactions and break up into p, d, and n before they reach the Braggpeak. The PHITS [1] calculations shown also in Fig.1 represent the measured data very well.

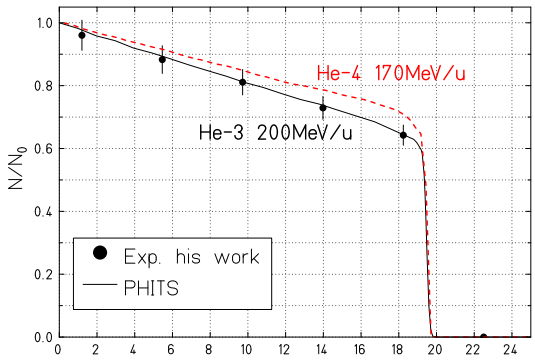


Figure 1: Measured and calculated attenuation of 200 MeV/u ^{3}He in water. For ^{4}He with the same range the calculated attenuation is shown (dashed line).

For five different energies Bragg curves of ^{3}He in water were measured with parallel-plate ionisation chambers and a water absorber with a high-precision linear drive for thickness variation. Results are shown in Fig.2 together with PHITS calculations. The shape of the Bragg curves reflects the complex interplay of stopping power dE/dx, angular- and energy-stragglings, nuclear interactions and emission of secondary fragments. In spite of this complexity all measured Bragg curves are well reproduced by the PHITS calculations. The lower part of Fig.2 compares calculated Bragg curves of 200 MeV/u ^{3}He, 170 MeV/u ^{4}He, and 170 MeV protons with the same position of the Bragg peak at 19.6 cm water. The Bragg curves of ^{3}He and ^{4}He are very similar with almost the same peak-to-entrance ratio. In both cases the dose contribution of nuclear fragments is small compared to the dose deposited by primary ions. The higher fragment dose for ^{4}He beam is explained by the formation of ^{3}He fragments whereas primary ^{3}He ions can only break into p, d, and n.

Spectral data were obtained by time-of-flight measurements. Energy spectra of secondary neutrons are shown in Fig.3. Comparison with PHITS shows very good agreement at 30 deg. but an underestimation at 0 deg.

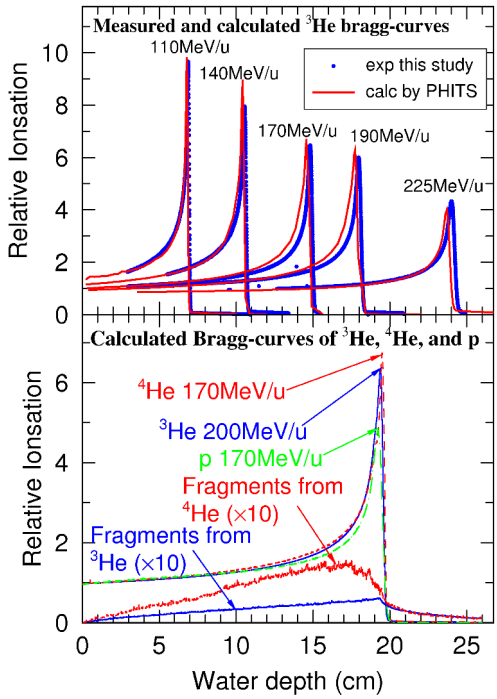


Figure 2: Measured and calculated Bragg curves of ^{3}He, ^{4}He and protons

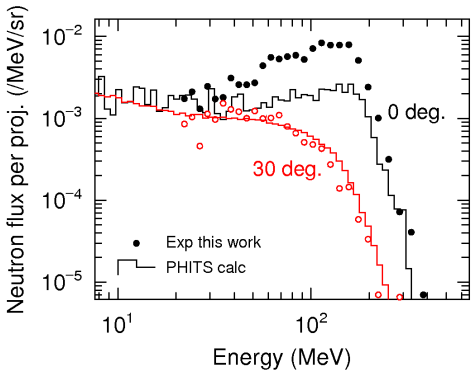


Figure 3: Measured and calculated neutron energy spectra emitted from 200 MeV/u ^{3}He stopped in water

References

[1] H. Iwase, K. Niita and T. Nakamura, Journal of Nucl. Sci. and Technol., Vol. 39, No. 11, p 1142-1151 (2002)

Synthetic diamonds for heavy-ion therapy dosimetry

M. Rębisz, B. Voss, E. Usenko, A. Heinz, M. Pomorski, E. Berdermann
GSI, Darmstadt, Germany

In this paper we report on first results obtained using polycrystalline CVD diamond detectors irradiated with heavily ionizing particles at GSI. At the UNILAC accelerator, ions with energies near the Bragg-Peak have been stopped inside the material whereas at the heavy-ion therapy facility of GSI these detectors are operated in transmission mode and have been studied in a carbon beam from SIS with energies ranging from 80 to 430 MeV/u.
In both energy regimes high-bandwidth electronics have been used to count the number of impinging particles. Furthermore, the thermoluminescence (TL) response of synthetic-diamond dosimeters to heavily ionizing particles has been studied.

To process the signals obtained from the active diamond detectors, an electronic based on a discrete high-bandwidth amplifier (DBA) [1] and alternatively a specially designed ASIC [2] amplified the current signals from the detectors. A 300 MHz Phillips discriminator together with a 225 MHz Phillips scaler served to count the number of detected particles. We tested unipolar as well as bipolar readout chains. Due to the better signal-to-noise ratio, the bipolar electronics based on the ASIC has been finally chosen.

As a result of the online beam-monitoring we achieved a counting efficiency of 95% for carbon ions with initial energies of 89 MeV/u as shown in fig. 1. At this energy, the mean generated charge is 120 fC from which only 10 to 30% (depending on the sample) is collected. The electronic threshold was fixed to 8 fC covering 95% of the collected-charge distribution. The efficiency of the measurement decreases with increasing energy and thus decreasing amount of charges generated inside the diamond samples. In this way, for a fixed setting of the electronic threshold of the ASIC, some of the particles generate a too low signal in the pCVD diamond to be detected. For the higher signals obtained at UNILAC (several 100 fC) this problem is not so pronounced. In this place, the multi-hit problematic is the dominating factor that spoils the counting efficiency.

For the thermoluminescence measurements, the sensitivity of all samples has been measured for an exposure to X-ray and carbon ions. All of them show a peak (180 to 230°C) in the high temperature region useful for dosimetry at a wavelength of maximum emission of 450 to 495 nm.

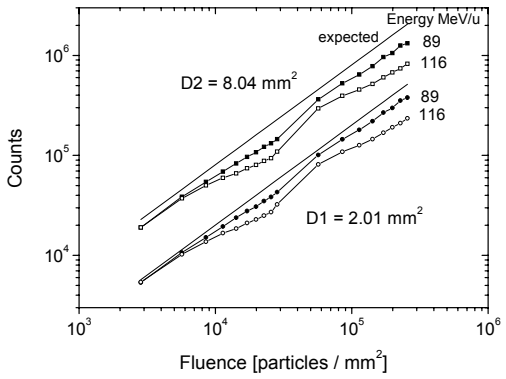


Fig.1 Efficiency of the pCVD diamond detectors 'D1' (lower curves) and 'D2' (upper curves) with different pad sizes for high-energetic carbon ions with initial energies of 89 MeV/u (full symbols) and 116 MeV/u (empty symbols), respectively. The expected gradients (straight lines) are also given.

During the irradiation with heavy charged particles (HCP), the energy is deposited in the densely ionized tracks which is different to the isotropic distribution assumed for low-LET radiation such as gamma or X-rays. The early saturation of the local volume gives rise to the linear dose response and lower sensitivity compared to low-LET irradiation. The efficiency decreases as the LET of the HCP increases. The TL output data for the irradiations done with carbon ions and x-rays, respectively for two pCVD samples called TM and PC, together with the ones for LiF, are used to derive the efficiency η.

For high-energetic particles (e.g. 350 MeV/u) we obtained 100% efficiency for the pCVD detectors. The efficiency decreases with decreasing initial particle energy. For low-energetic ions with an initial energy of 10.8 MeV/u the efficiency decreases to 41% for 'TM', 32% for 'PC' diamond and to 9 % for 'MTS-N' dosimeters, respectively. This is explained as a saturation effect due to the very high local dose around the ion path.

References

[1] P. Moritz et. al., Diamond detectors with sub nanosecond time resolution for heavy ion spill diagnostics, Workshop on Beam Instrumentation Stanford CA, (1998).
[2] F. Anghinolfi, et al., Nucl. Instr. and Meth. in Phys. Res. A 533 (2004) 183-187.

Recent progress in the development of a front-end electronic for diamond applications based on the NINO ASIC

B. Voss, E. Usenko, M. Rebisz; GSI Darmstadt, Germany

The NINO ASIC was originally designed as the front-end amplifier/discriminator for the MRPCs of the TOF array for the ALICE experiment [1]. Its basic design (see fig.1) is fully differential in input and LVDS output. The input capacity is 30 pF, input charge may vary from 5 fC up to 1.5 pC, input noise is below 3000 e^-*C_{Det}. The threshold of the discriminators is adjustable in the range of 10-100 fC in a linear way. The width of the digital output pulse depends on the charge of the input signal and may vary in the range of 0.5 to 10 ns for the input described above. Every chip incorporates eight channels with a bandwidth of 400 MHz.

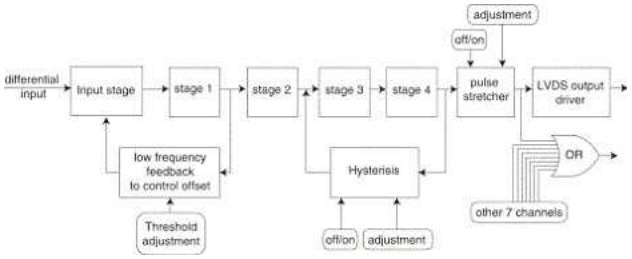


Figure 1: Block diagram of the NINO ASIC

It is our aim to apply the NINO chip to the signals of CVD diamond detectors mainly for beam monitoring and non-integrating dosimetry by particle counting. A first version of a set of boards has been designed and verified (fig.2). The setup is modular with respect to relevant functions for easy exchange and maintenance and to be adaptable to experimental needs. In order to be able to deal with many input channels in the future, a mezzanine board with 2 NINO chips was built which is attached to a motherboard providing remote controlled adjustments of threshold, width and hysteresis via a separate DAC board for all ASICS independently. In order to cope with the particles fluencies of up to several 10^{10} pps one may either adapt the size of the detector pixels and/or perform a rate division using ultra fast pre-scalers. This increases the maximum data rate to up to 1.2 GHz in the current setup. A test-input option rounds out the picture.

Measurements at the UNILAC and SIS facilities were performed with different ion species, energies and fluencies [3]. Stopping the particles inside the active detector volume one has to deal with input charges of up to several 100 fC in most cases (fig. 3) which may cause multi-hit counting problems. At SIS pCVD detectors of 100 µm thickness work in transmission mode generating signals of only several fC demanding an increased sensitivity e.g. by using single-crystal CVD. A counting efficiency of 95% for ^{12}C ions with an initial energy of 89 MeV/u was obtained under therapy conditions at CaveM.

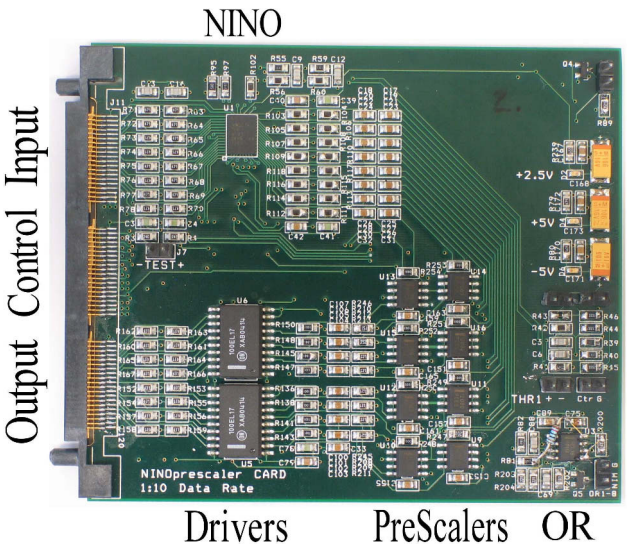


Figure 2: Picture of the mezzanine card carrying the NINO chip, optional 1:10 prescalers and the output drivers as well as an OR stage. The same layout is realized on the bottom side of the PCB thus allowing a 16 channel operation in total.

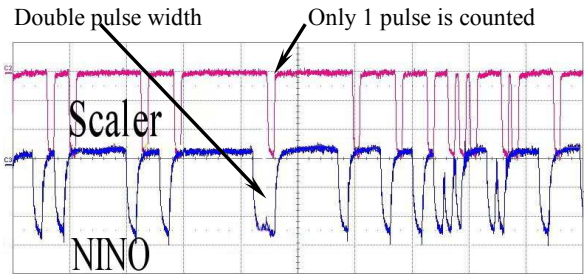


Figure 3: Oscillograph snapshot showing pulses from NINO and a scaler at the UNILAC. X-Axis unit is 50 ns.

The next version of the setup will incorporate the HV-distribution on-board and allow remote control via TCP/IP. An all-purpose input will be available allowing connection by bonding sc- or pc-CVD directly to the board or via strip-line cables.

References

[1] F. Anghinolfi et al., Nucl. Instr. and Meth. in Phys. Res. A 533 (2004) 183-187.

[2] www-norhdia.gsi/talks/2nd/usenko.pdf

[3] M. Rębisz, B. Voss, E. Usenko, A. Heinz, M. Pomorski, E. Berdermann, Synthetic diamonds for heavy-ion therapy dosimetry, contribution to this report & Diamond Relat. Mater. 2006, in press

Multiple field optimization and biological dosimetry of a 2D-treatment plan

A. Schmidt, M. Krämer, C. von Neubeck, W. K.-Weyrather, GSI, Darmstadt, Germany

Introduction

The software TRiP98 [1, 2, 3] is succesfully used for treatment planning. One of the major tasks of the planning procedure is the optimization step. During optimization the adequate fluencies for each of the many thousand pencil beams are calculated so that a target-conformal dose distribution is generated. Last year we reported on the implementation of a new optimization technique [4], namely multiple field optimization (MFO). Using MFO allows sparing of organs-at-risk (OAR), i.e. healthy, critical structures like the optical nerves or the brainstem which are closely situated to the tumor as shown in the left panel of figure 1. In simulations a dose reduction within critical structures by a factor 1.2-2 was observed. Yet, the challenge was to verify experimentally these results.

Materials and methods

We chose a U-shaped target area bending around an organ-at-risk as indicated in figure 1 (right panel). Chinese hamster ovary cells (CHO-K1) were grown at standard conditions and inserted into an irradiation box. The dose level was set to 6 GyE which corresponds to a survival level of 15 %. After irradiation the cells were carefully trypsinized, counted and seeded at an appropriate number. Finally, the cells were stained after 7 days and scored for survival.

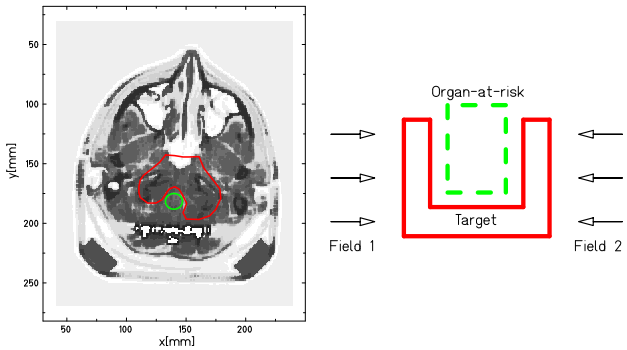


Figure 1: *Left*: typical CT-slice of a patient with a concave tumor bending around the brainstem. *Right*: the experimental target is chosen to be U-shaped enclosing an organ-at-risk. Two opposing fields, i.e. beam ports, are applied.

Results and discussion

The results of four cuts through the target volume are shown in figure 2. The enhanced tissue sparing effect using MFO is clearly approved. Yet, some deviations between measured and computed survival are observed. In the target areas, where mainly high-LET particles contribute to radiation damage, the cell killing effect calculated according to the classical local effect model (LEM) is underestimated, in accordance with other experimental results.
A new LEM version, which includes effects of clustered damage, yields better agreement as indicated by the dotted lines in figure 2. Details concerning the modifications of the LEM are presented in [5].

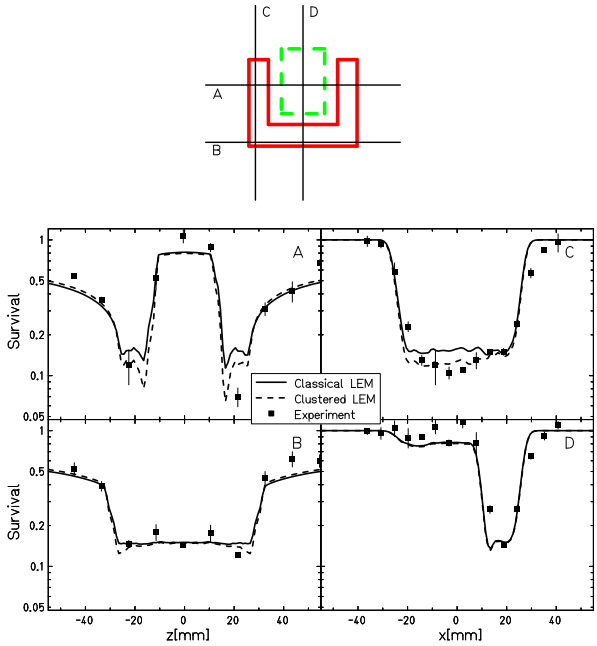


Figure 2: Comparison of calculated and measured survival (lower panel). Calculations based on the classical LEM approach are indicated by solid lines whereas the dashed lines represent the calculations including a modificated LEM version. Survival was measured in the cuts through the target indicated by the sketch in the upper panel.

References

[1] M. Krämer et al, Phys. Med. Biol., 45/11 (2000) 3299.

[2] M. Krämer et al, Phys. Med. Biol., 45/11 (2000) 3319.

[3] O. Jäkel et al, Phys. Med. Biol., 46/4 (2001) 1101.

[4] GSI report 2004

[5] T. Elsässer et al, This report

Verification of Complex 3D-Dose Distributions in Carbon Ion Irradiation *

U. Ramm, J. Licher, J. Moog, H.D. Böttcher, Uniklinikum-Strahlentherapie, Frankfurt/Main, Germany
S. Grötzinger, B. Spielberger, G. Kraft, GSI, Darmstadt, Germany

Introduction

In radiotherapy with swift carbon ions very complex dose distributions are applied to a desired target volume. Up to now at the GSI radiotherapy project only regide target volumes in the skull of patients are treated. Extending the benefit of carbon ion radiotherapy to the whole patients body, problems of target motion as heart beat or breathing will occur. Using raster scan technique this motion urgently needs to be compensated. At the GSI an active tool for compensation of patients movement is under construction [1]. Thus, a real three dimensional verification dosimeter is needed. BANG-Gel-Dosimeters (MGS, USA) are porposed to be a tool for verification of complex dose distributions in radiotherapy with swift carbon ions.

Material and Method

BANG-Gel-Dosimeters were irradiated at the raster scan facility in CAVE M at the GSI [2]. A realistic patients plan was irradiated under the conditions of (a) static target, (b) moving target, and (c) moving target compensated with the new online movement compensator (OMC). For movement compensation the OMC adapts the beam actively to the desired irradiation position. MR images were acquired at a 1.5 T whole body scanner (Magnetom, Siemens, Germany) using the standard quadrature head coil. The transverse MR relaxation rate R_2 of the water protons was taken as a measure of the radiation dose absorbed in the gel [3].

Results an Discussion

Figure 1 presents the results of online motion compensated raster scanning technique. The distributions of relaxation rate R_2 are shown under the three condition of static target (top), moving target (mid) and moving target with motion compensation (bottom).

Although, the geometry of the irradiated target volume is visible, the moving distribution differs significantly from the static one. The deviations exceed $\pm 25\%$. The online motion compensation eliminates the large differences. The deviations are reduced to less than $\pm 10\%$.

Conclusion

BANG-Gel-Dosimeters have been proven to be a suitable tool in verification even of complex irradiation techniques for applying three-dimensional dose distribution in radiotherapy with swift carbon ions.

* This work was supported by the Bundesministerium f¨ur Forschung und Technologie (BMFT, Germany) and the Paul and Ursula Klein Foundation (Germany).

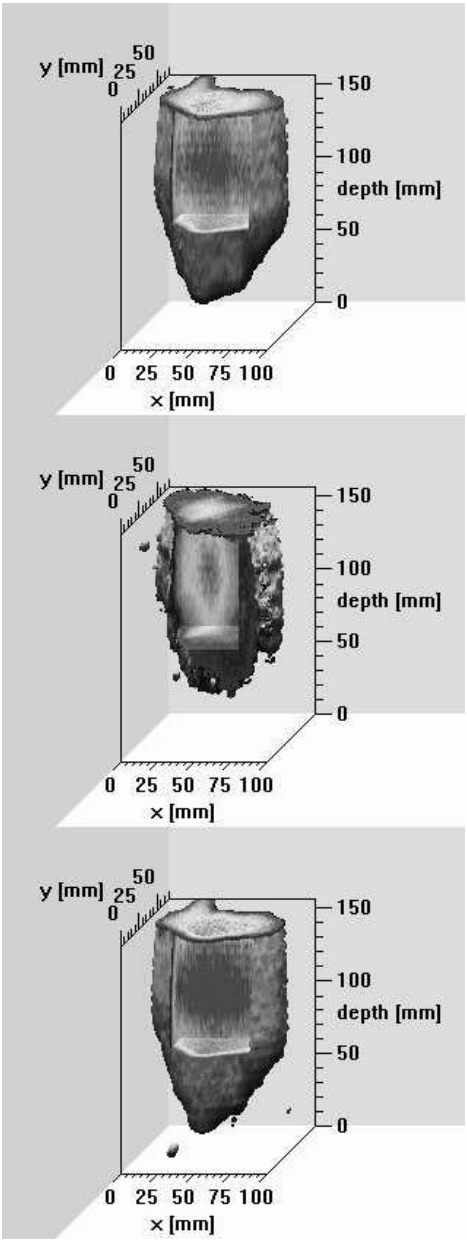


Figure 1: Distribution of relaxation rate R_2 after irradiation of a patients plan to BANG-Gel-Dosimeters.

References

[1] Q. Li, S.O. Groezinger, T. Haberer, E. Rietzel, and G. Kraft. Phys. Med. Biol. 49 (2004) 3029-3046.

[2] T. Haberer, W. Becher, D. Schardt, and G. Kraft. Nucl. Instr. and Meth. in Phys. Res. A 330 (1993) 296-305.

[3] U. Ramm, J. Moog, B. Spielberger, et al. Radiother. Onkol. 73 (2005) Suppl. 2: S99-101.

Dose calculation in the presence of organ motion

Ch. Bert, E. Rietzel, S.O. Grözinger, Th. Haberer, G. Kraft, GSI, Darmstadt, Germany

Introduction

In the presence of target motion, raster scanning beam delivery leads to significant interplay effects between dynamic beam delivery and target motion [1,2]. To extend the clinical applications for raster scanning from static to moving tumors, GSI is developing a motion compensation system. This system facilitates online adaptation of scan positions during beam delivery to compensate for tumor motion [3].

Motion compensation requires extended treatment planning capabilities that allow to calculate dose distributions as well as compensation parameters. Both are based on time resolved Computed Tomography (4DCT) data [4].

Material & Methods

4DCT data represents different respiratory motion states of a patient in time. Consequently, treatment plans have to be split into sub-plans corresponding to temporal 4DCT samples. Each of these sub-plans is used with the corresponding temporal CT data to compute the delivered sub-dose. For calculation of the total delivered dose, sub-dose distributions have to be summed after transformation into a common anatomical frame of reference.

Moving target extensions of the GSI treatment planning system TRiP were evaluated by comparing calculated to experimental dose distributions. A quadratic, homogeneous field was irradiated on a radiographic film. During irradiation, the film was moving sinusoidally, orthogonal to the beam in left-right direction. Distinct interplay patterns on the films were used to validate the calculations.

Calculation of dose distributions depends on the temporal sampling of the irradiation process. To assess the required temporal resolution, deviations between experimental and calculated dose distributions were analyzed for different numbers of motion phases.

Results

Figure 1 shows experimental and calculated film responses. The irradiated quadratic field is distorted. Interplay effects between film motion and scanning process

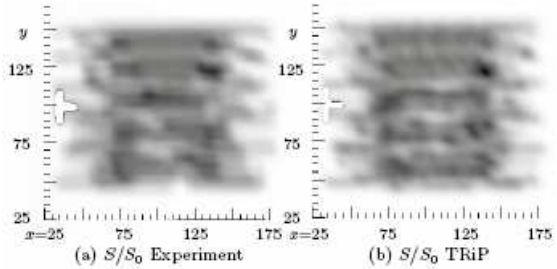


Figure 1: Experimental and calculated film responses in the presence of motion (amplitude 20 mm, period 7 s).

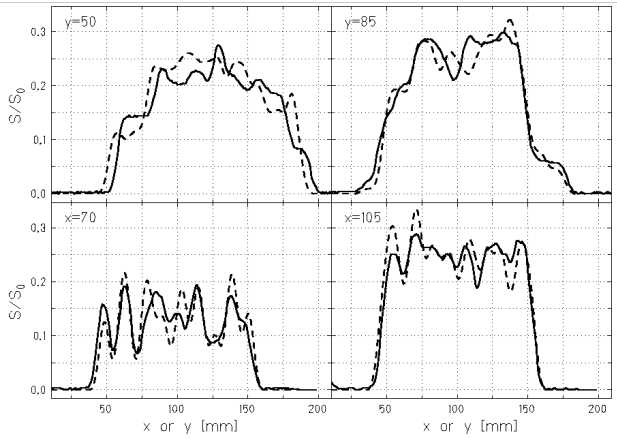


Figure 2: Line profiles of film response in Figure 1 at different positions: measured (solid) and calculated (dashed).

lead to a distinct dose pattern. Line profiles of the dose distributions are plotted in Figure 2. Calculations yield good agreement to experimental data.

Figure 3 shows the dependency of calculated dose distributions on temporal sampling for different motion parameters. Sufficient agreement between experiments and calculations is achieved with ~20 motion phases for amplitudes up to 20 mm.

Conclusion

Dose delivered to a moving target can be calculated by temporally sampling the treatment plan/delivery. Comparisons to experimental data show good agreement.

References

[1] Ch. Bert *et al.*, GSI scientific report 2003, pg 174
[2] Ch. Bert *et al.*, GSI scientific report 2004, pg 298
[3] S.O. Grözinger, PhD-thesis, TU Darmstadt 2004
[4] E. Rietzel *et al.*, Med. Phys. **32**, 874-889, 2005

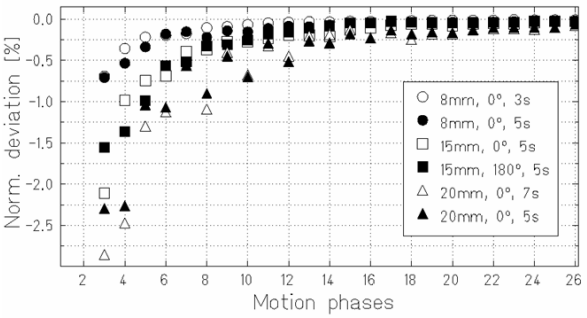


Figure 3: Comparison experiment calculation; dependency of mean normalized film response deviations on temporal sampling for different motion parameters.

Comparison of In-Beam PET Data Taken in the ^{3}He-Experiment with ^{12}C-Data*

F.Fiedler†, P. Crespo‡, M. Sellesk§, K. Parodi¶ and W. Enghardt‖, FZ Rossendorf, Germany

Abstract

Since more than 7 years in-beam PET has been clinically implemented at the experimental heavy ion treatment facility at GSI Darmstadt. For the ^{12}C-beam simulations are done and by comparisons with the measurement the beam portal position, anatomical changes and range information can be deduced. In the future it is expected to use further ion species to treat cancer patients. It is highly desirable to monitor also these irradiation by means of in-beam PET. To perform a simulation requires a precise knowledge of the spatial distribution of the beam induced positron emitters. Therefore, the β^+-activity induced by a ^{3}He-beam has been studied for the first time at the Gesellschaft für Schwerionenforschung (GSI) Darmstadt.

Materials and Methods

Pencil-like ^{3}He-beams with an energy 207.92 AMeV and a mean intensity of $2.0 \cdot 10^8$ ions / s were extracted from the heavy ion synchrotron of GSI. These beams were stopped in targets of polymethyl methacrylate (PMMA, $C_5H_8O_2$, $9 \times 9 \times 20$ cm^3, $\rho = 1.18$ g cm^{-3}), graphite ($9 \times 9 \times 15$ cm^3, $\rho = 1.795$ g cm^{-3}) and water, to which a very small amount of gelatine was added, in order to avoid thermal convection within the target and thus the deterioration of the β^+-emitter distributions. The water target had a stoichiometric composition of $H_{66.2}O_{33.1}C_{0.7}$ and a dimension of about $9 \times 9 \times 30$ cm^3 and a density of $\rho = 1.0$ g cm^{-3}. All targets were placed in the center of the field of view of the PET scanner. The time structure of the beam was comparable to that used during the therapy, which means the extraction took about 1.4 s followed by a pause of about 3 s. The energy of 337.5 AMeV of the ^{12}C-beam was chosen to get the same range as in the ^{3}He-irradiation, the intensity was $0.9 \cdot 10^8$ ions / s. The measurements were carried out by means of the PET scanner integrated into the GSI treatment facility consisting of two detector heads of bismuth germanate block detectors from the commercial ECAT EXACT PET scanner (CTI PET systems Inc. Knoxville, TN, USA) [1]. The PET measurement included 10 min of target irradiation followed by 20 min of decay.

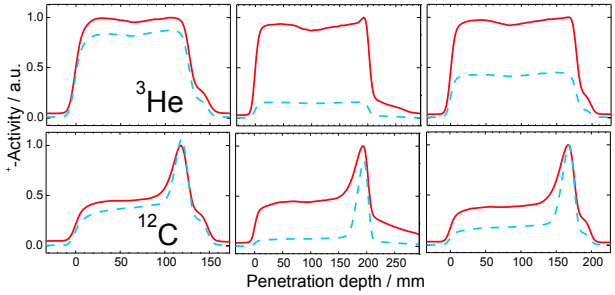


Figure 1: Depth profiles of β^+-activity induced by ^{3}He and ^{12}C-beams at 207.92 AMeV and 337.5 AMeV, respectively, in graphite (left), water (middle) and PMMA (right) targets. Upper row: β^+-activity depth profiles for ^{3}He-ions. The solid lines display the activity measured during the irradiation, the dashed lines give the activity from 10 to 20 min after the end of the irradiation normalized to the maximum of the activity measured during the irradiation. The ordinate is in arbitrary units. Lower row: same, but for ^{12}C-projectiles.

Results

The activity produced by carbon beams is about 2 times larger than in ^{3}He-irradiation for the same number of particles at the same range, whereas the dose related activity density is only a third. Fig. 1 shows β^+-activity depth profiles measured in the three different targets with pencil-like ^{3}He-beams and ^{12}C-beams. The displayed backprojections were obtained from the data measured during the irradiation as well as from a period of ten minutes starting ten minutes after the end of the irradiation, which also may be the time which is needed to bring a patient from the place were he was irradiated to an off-line PET scanner. In the case of ^{12}C-projectiles the main contribution to the signal arises from the β^+-emitting projectile fragments, which are absent in the ^{3}He-irradiation. So a larger difference in the counting statistics between these two time intervals in case of ^{3}He can be observed. In case of water target the largest difference was observed due to the short half life of the dominating positron emitter, ^{15}O. Since human tissue consists to about 65% of water the importance of measuring during the irradiation, that means of in-beam PET becomes even more important when going to projectiles which do not form β^+-emitting fragments.

References

[1] W. Enghardt et al. "Charged Hadron Tumour Therapy Monitoring by means of PET." Nucl. Instr. Meth. A, vol. 525, pp. 284-288, 2004.

* Work supported by the GSI Darmstadt, Germany and the European Union (QLRT-2001-01574)

† f.fi edler@fz-rossendorf.de

‡ p.crespo@fz-rossendorf.de

§ selleske@student.tu-freiberg.de, also with TU Freiberg, Germany

¶ kparodi@partners.org, now with Francis H. Burr Proton Therapy Center, Massachusetts, Boston, MA 02114, USA

‖ w.enghardt@fz-rossendorf.de, also with TU Dresden, Germany

Analysis of MLEM and OSEM Reconstruction Algorithms for Different Geometries of PET Scanners*

G. Shakirin, FZR, Dresden, Germany
P. Crespo, FZR, Dresden, Germany
W. Enghardt[#], FZR, Dresden, Germany

Abstract

At the experimental heavy ion tumor therapy facility at the GSI Darmstadt in-beam PET is operated. The in-beam PET data should be reconstructed as fast as possible (ideally, in real time), because they allow monitoring irregularities in beam delivery. To find a fast reconstruction algorithm with acceptable quality, MLEM [1] and OSEM [2] algorithms were compared for full-ring and dual-head geometries of the PET scanner with different parameters of reconstruction. An activity distribution to be reconstructed was generated by the simulation routine. Quality assurance of reconstructions was performed by numerical and visual comparison of the reconstructed and generated activity distributions.

Introduction

The simulated activity was homogeneously distributed within a hollow sphere. Then it was reconstructed using the projection data by means of MLEM and OSEM algorithms. Results of these reconstructions were compared using the Mean Absolute Error (MAE) [3]. For the OSEM algorithm projection data were grouped into different number of subsets.

Results for the full-ring PET scanner

Reconstructions with OSEM 6, 8, 10 and 12 subsets were compared with reconstruction result of 50-th iteration of MLEM (Fig. 1). Best result in terms of MAE showed the reconstruction with OSEM 8 subsets. It achieved the quality of 50-th iteration of MLEM in 9 iterations.

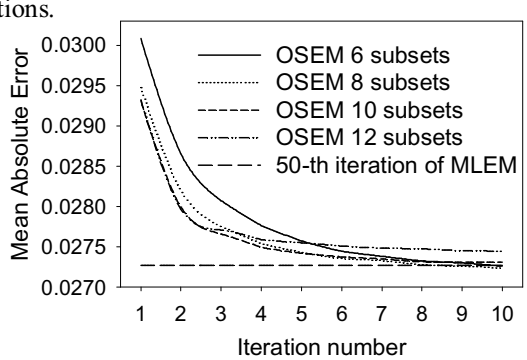


Figure 1: Mean Absolute Error for reconstructions within the full-ring PET scanner.

Results for the dual-head PET scanner

In case of a dual-head PET scanner MAE has a minimum at the 35-th iteration for MLEM and then increases. Finally MAE of MLEM and OSEM algorithms converges to the same value (Fig. 2).

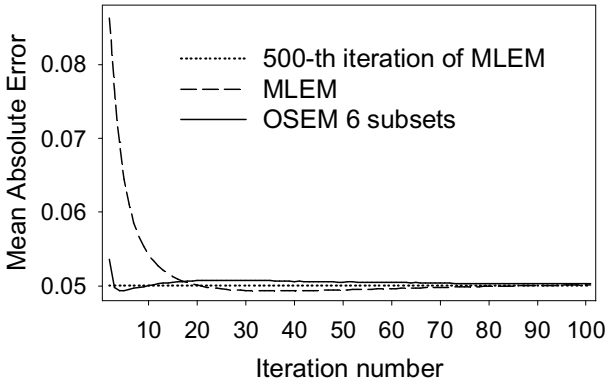


Figure 2: Convergence of MLEM and OSEM for the dual-head PET scanner geometry.

The best reconstruction result showed the OSEM algorithm with decreasing number of subsets from iteration to iteration. It achieved the quality of the 35-th iteration of MLEM in 2 iterations (Fig. 3).

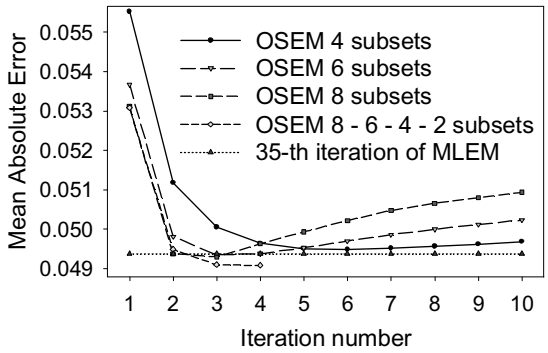


Figure 3: Mean Absolute Error for reconstructions within the dual-head PET.

References

[1] L.A. Shepp and Y. Vardi, "Maximum likelihood reconstruction for emission tomography", IEEE Trans. Med. Imag., vol MI-2, pp.113-122, 1982.

[2] H.M. Hudson and R.S. Larkin, "Accelerated Image Reconstruction Using Ordered Subsets of Projection Data", IEEE Trans., vol 13 No 4, pp.601-609, 1994.

[3] J. Sheng and D. Liu, "An Improved Maximum Likelihood Approach to Image Reconstruction Using Ordered Subsets and Data Subdivisions", IEEE Trans. Nucl. Science Vol 51 No 1, pp. 130-135, 2004.

*Work supported by GSI Darmstadt and EU
[#]also with Technische Universität Dresden

A Method of Processing of the Elements of the System Matrix for Iterative Reconstruction of PET Data*

G. Shakirin, FZR, Dresden, Germany
P. Crespo, FZR, Dresden, Germany
W. Enghardt#, FZR, Dresden, Germany

Abstract

At the experimental heavy ion tumor therapy facility at the GSI Darmstadt in-beam PET is operated. The in-beam PET data are highly desired to be reconstructed as fast as possible (ideally, in real time), because they allow deviations from the treatment plan to be detected. Precise calculation of the system matrix is required for performing such a very fast reconstruction. The system matrix defines the mapping from the image space to the projection data space and may contain around 10^{13} elements for fully 3D imaging systems. Such a huge size complicates the system matrix processing significantly. The proposed method allows a fast and accurate calculation of the system matrix in continuous image space.

Description of the method

The whole set of tubes of response (TORs) of a PET scanner is divided into symmetry groups. TORs belong to the same symmetry group if they have the same angles relative to the coordinate axes and the same angles with respect to the crystals surfaces (Fig. 1) and, therefore, such TORs have approximately the same system matrix values at respective points. It means that the calculation of the system matrix values for only one TOR per symmetry group is required. So, one TOR is selected from each symmetry group and a Net of Key Points (NKP) is created within the TOR. For each point-TOR pair the system matrix value equals to a probability that an event appeared at the point is registered by the TOR. This probability is calculated by means of a Monte-Carlo algorithm for all points of the NKP. Then approximation polynomials are created at the NKP using the least squares method. Finally, the coefficients of the approximation polynomials are saved to a file and for any point-TOR pair it is possible to calculate the system matrix value.

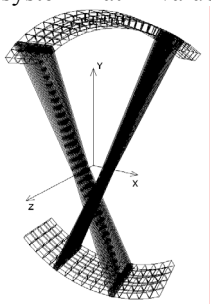


Figure 1: Schematic view of the dual-head PET scanner and one symmetry group.

For this, the coefficients of proper approximation polynomials are retrieved based on information to which symmetry group the TOR belongs and the system matrix value is calculated at the point.

Accuracy of the method

Quality assurance of the method has been performed by comparing system matrix values calculated by means of the Monte-Carlo method and by means of the proposed approximation (Fig. 2). The maximum of normalized difference did not exceed 12%. 88% percent of points had a normalized difference of less than 2%.

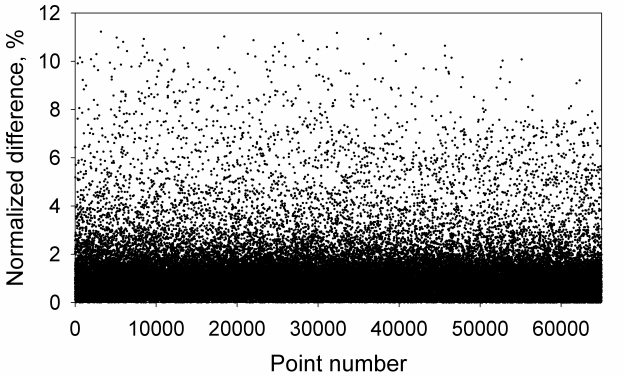


Figure 2: Normalized difference between values of the system matrix calculated using the Monte-Carlo method (as reference value) and the proposed approximation method. Calculations were done for more than 60000 points within the image space.

Practical application

The proposed method performs accurate (Fig. 2) and fast (200 000 calculations per second on 2.83 GHz processor) approximation for the system matrix elements. That allows to use this method in reconstruction algorithms which are sensitive to the system matrix quality (OSEM [1], RAMLA [2], FAIR [3]) and in real time reconstruction of in-beam PET data for the ion therapy.

References

[1] H.M. Hudson and R.S. Larkin, "Accelerated Image Reconstruction Using Ordered Subsets of Projection Data", IEEE Trans., vol 13 No 4, pp.601-609, 1994.

[2] Browne J., De Pierro A, "A row-action Alternative to EM algorithm for maximizing likelihoods in emission tomography", IEEE Vol. 15 pp. 687-699 1996.

[3] A. J. Reader, K Erlandsson et al, "Fast accurate iterative reconstruction for low-statistics volume imaging", Phys. Med. Biol 43 pp. 835-846 1997.

*Work supported by GSI Darmstadt and EU
#also with Technische Universität Dresden

Optimum detector arrangements for in-beam PET with direct time-of-flight*

P. Crespo, F. Fiedler, J. Pawelke, G. Shakirin, W. Enghardt, FZ Rossendorf, Dresden, Germany

Due to its effectiveness in monitoring highly tumour-conformed charged hadron therapy, in-beam positron emission tomography (in-beam PET [1]) is strongly desirable at charged hadron facilities under construction [2] or planning [3]. We present, therefore, optimized arrangements of the γ-ray detectors for next-generation in-beam PET scanners. A versatile, fully 3D, maximum likelihood expectation maximization (MLEM) algorithm coupled to a simulation routine was applied to several high-resolution closed-ring or dual-head tomographs. In order to evaluate the quality of images obtained with several camera configurations in real therapeutic situations, β^+-activity distributions calculated from a treatment plan with the PosGen Monte-Carlo code [4] were considered. Results regarding the optimisation of in-beam PET for monitoring head-and-neck irradiation can be found in [5, 6, 7]. Here we refrain to the more challenging situation, due to the large image volume, of monitoring the irradiation of the pelvis.

Fig. 1 depicts the positioning strategy for monitoring irradiation of the pelvis with in-beam PET and Fig. 2 shows the corresponding reconstructed images obtained without (top and middle rows) and with (bottom) time-of-flight (TOF) capable detectors. The sagittal views in Fig. 2 show the rectum of the patient, a radiosensitive organ, lying adjacent to the irradiated tumour and, therefore, elucidate how in-beam PET monitoring brings important information to the radiooncologist. Clearly, the closed-ring detector configuration (top row) yields the best images and its implementation feasibility is discussed in [5, 6]. Although the field of view of the dual-head tomograph with $\phi = 46\,^\circ$ (middle row) covers the irradiated volume completely, the corresponding reconstructed images contain less information due to the image degradation arising from the gaps between the two detector heads [5, 6]. This degradation is refrained [5, 7] if TOF-capable detectors with sufficiently good coincidence time resolution are used (bottom row).

In summary, in-beam PET monitoring of large fields benefits most from a closed-ring tomograph if ultra-fast TOF-capable detectors are not available at large production scales. A non-TOF dual-head tomograph with $\phi = 46^\circ$ yields satisfactory results for monitoring head-and-neck irradiation due to the smaller target volume (not shown).

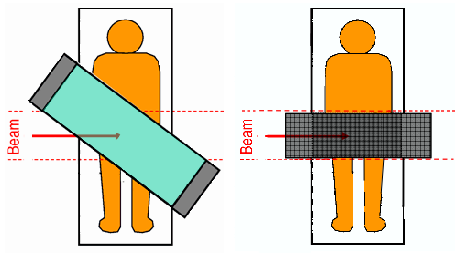


Figure 1: Patient positioning with closed-ring (left) and dual-head (right) tomographs for pelvis irradiation.

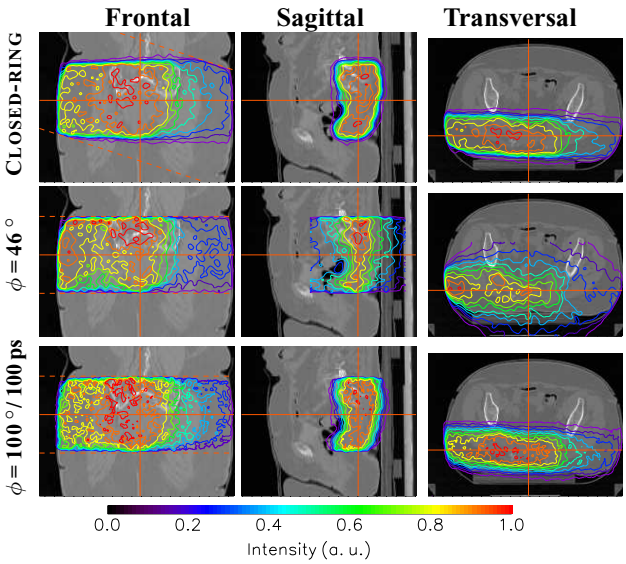


Figure 2: Reconstructions of a realistic pelvis irradiation (simulation). The angle ϕ (dual-head scanners only) is formed between the edge of the top and bottom detector heads with the isocenter of the tomograph. Top and middle rows obtained without TOF-capable detectors and MLEM reconstruction. Bottom row with detectors yielding 100 ps FWHM coincidence time resolution and with an ultra-fast, real-time direct-TOF algorithm.

References

[1] W. Enghardt et al., "Charged hadron tumour therapy monitoring by means of PET", NIM A 525 (2004) 284.

[2] H. Eickhoff et al., "HICAT - The German hospital-based light ion cancer therapy project", PAC'03, Portland, OR, p. 694.

[3] Siemens Medical Solutions, "Particle therapy, getting to the point", Order No. A91100-M2600-C689-2-7600.

[4] F. Pönisch et al., "The modelling of positron emitter production and PET imaging during carbon ion therapy", Phys. Med. Biol. 49 (2004) p. 5217.

[5] P. Crespo, Thesis, Technische Universität Darmstadt, 2005.

[6] P. Crespo et al., "On the detector arrangement for in-beam PET for hadron therapy monitoring", Phys. Med. Biol. (2005) submitted.

[7] P. Crespo et al., "Direct time-of-flight for real-time, in-beam PET: concept and feasibility study", Phys. Med. Biol. (2006) to be submitted.

* P. Crespo supported partly by Fundação para a Ciência e a Tecnologia, Lisbon, grant PRAXIS XXI/BD/18011/98. W. Enghardt is now with Zentrum für Innovationskompetenz Oncoray, TU Dresden. Work supported by the European Commission, grant QLRT-2001-01574, and by GSI.

Status Report of the HIT Project

U. Weinrich and B. Schlitt for the GSI therapy accelerator team

Abstract

Major progress of the Heidelberg ion beam cancer therapy center took place in 2005. The accelerator part of the building was finished to the point that the installation of the accelerator could be started. Many factory acceptance tests of accelerator components have been performed as well as numerous commissioning activities at GSI.

Organisational Aspects

Since April 2005 the University Clinic Heidelberg is responsible for the follow up of the medical part of the HIT facility. This includes the complete technique delivered by Siemens (eg. raster scanning, patient positioning, medical IT). Therefore, the corresponding GSI experts (4 persons) are now employed by the HIT-Service GmbH, a 100 % daughter of the university clinic, which is charged to operate the facility.

Progress of the Building

Since October 2005 the building was finished to the point that the accelerator assembly could be started. However, during all the time since then the building companies are still busy to finish their work in the accelerator rooms, especially for the commissioning of the technical infrastructure (Fig. 1). The mile stone of finishing of the accelerator part of the building was finally reached end of January 2006. GSI has pushed forward this process through intense follow up of the building process and substantial help for the understanding and handling of the accelerator specific technical infrastructure.

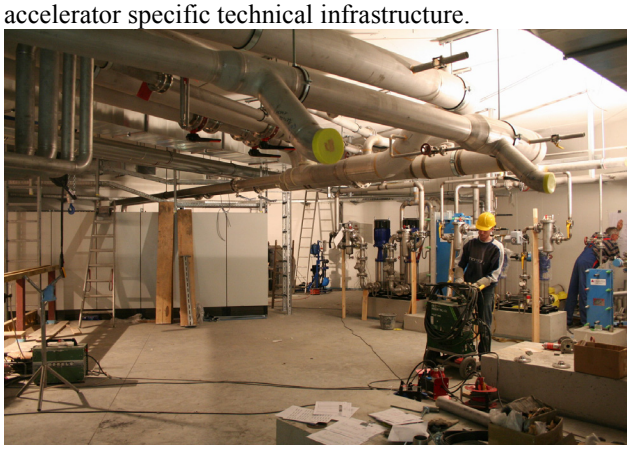


Figure 1: Installation of the accelerator cooling water system.

Progress of the Accelerator System

The year 2005 was marked by the follow up of the production process of the accelerator components. Factory acceptance tests took place for many magnets, vacuum chambers, power supplies, ion sources, LINAC RF amplifiers, synchrotron RF system, control system components as well as beam diagnostics for the LINAC and partly for the synchrotron.

At GSI, the magnetic measurements of the synchrotron dipoles have been started (Fig. 2) as well as the preassembly of the accelerator components to "ready for final assembly" modules.

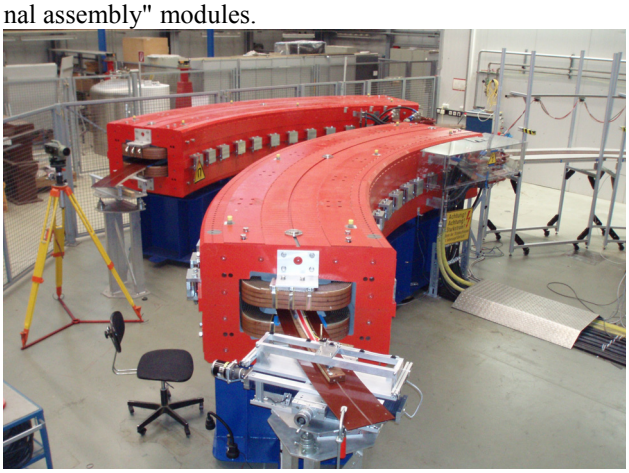


Figure 2: Synchrotron dipoles during magnetic measurements at GSI.

The 216 MHz LINAC RF system containing three amplifier chains for the RFQ, the IH tank and a small debuncher cavity has been almost completed. The 1.4 MW cavity amplifier from BERTRONIX Electronic GmbH, Munich, could be successfully commissioned at a GSI test setup [1]. After various tests and commissioning steps at GSI, the stage could be delivered early in January 2006 to THALES Broadcast & Multimedia AG in Turgi, Switzerland, for integration into the complete amplifier setup. All power supplies for the 1.4 MW stage have been finished by THALES B&M as well as the 120 kW driver amplifier. The 200 kW amplifier for the RFQ has been delivered by THALES B&M to GSI in August 2005 and has been operated successfully at GSI for RFQ beam tests [2]. Already in 2004 RFQ beam tests using proton beams have been performed at the Institute for Applied Physics (IAP) at Frankfurt University in order to check the main operating parameters of the RFQ and to measure the energy spread of the ion beam behind of the RFQ using an analyzing magnet. During 2005, a new RFQ test bench has been installed at GSI and precise time-of-flight measurements of the RFQ end energy could be successfully performed [2]. In addition, a number of further components for the HIT facility could be tested successfully at the RFQ test bench, in particular, major parts of the control system and several beam diagnostics devices like profile grids, Faraday cups, beam transformers, phase probes as well as the corresponding electronics equipment.

With the 20 MV IH-type drift tube linac cavity [1][3][4] several RF measurements and RF tuning steps have been performed successfully already at the factory at PINK

GmbH Vakuumtechnik in Wertheim (Fig. 3) [4]. Finally, the IH tank has been delivered to GSI in June 2005 and has been copperplated at GSI afterwards. After several vacuum tests and some mechanical refinishing operation, the assembly of the drift tubes within the final tank has started recently.

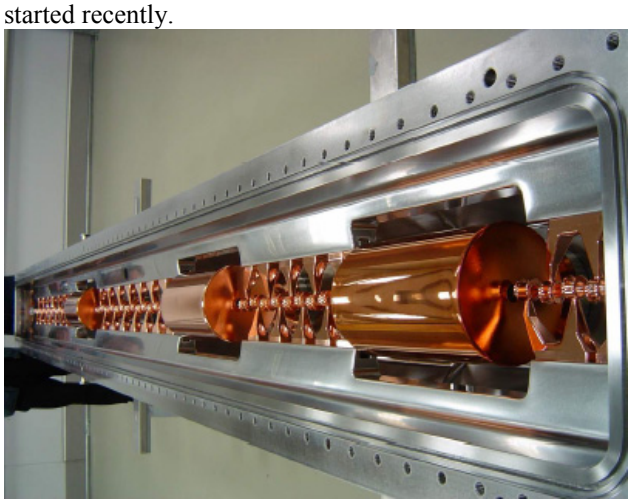


Figure 3: The open IH tank with drift tubes at PINK.

In October 2005, the installation of first components of the accelerator facility in the building in Heidelberg has started. At first, a complete surveying of the part of the building dedicated for the accelerator complex and for the treatment areas has been performed by METRONOM Automation GmbH, Mainz. The complete beam path has been marked on the floor and reference marks for the accelerator components and for the accelerator coordinate system have been fixed along the floor and the walls of the accelerator halls.

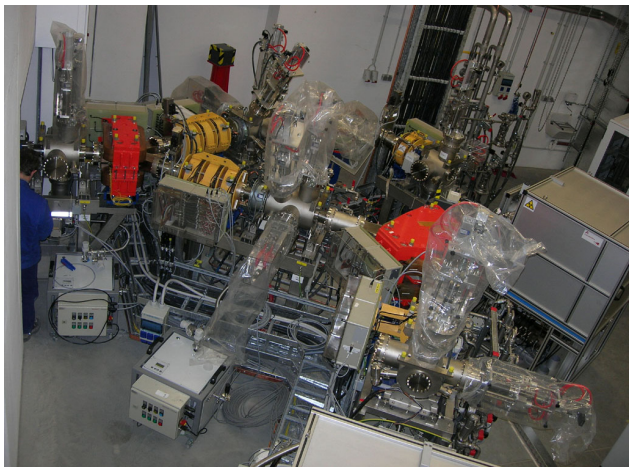


Figure 4: The LEBT with one of the ion source systems in February 2006.

Until February 2006, the low energy beam transport line (LEBT) has been assembled in the LINAC hall including the complete technical infrastructure required (Fig. 4). The corresponding power supplies as well as the ion sources have been delivered to Heidelberg and have been installed already. Commissioning has started in February 2006.

The electronic room was equipped with first electronic components. The accelerator control room was finished (Fig. 5) and the commissioning of the accelerator control system has started.

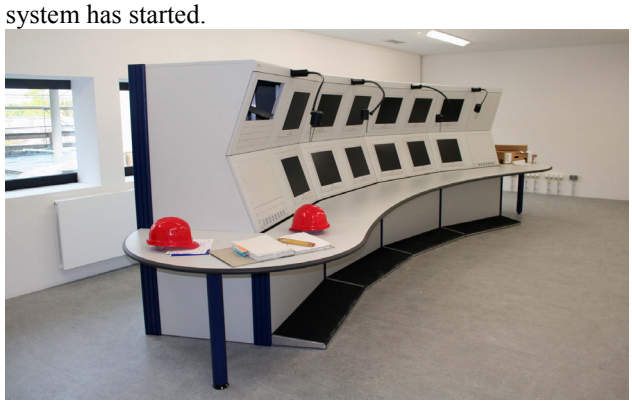


Figure 5: The accelerator control room.

In the Gantry part of the building the two 25 t cranes were set into operation and the Gantry room was prepared for the delivery of the main Gantry structure components.
During this time GSI has spent a lot of effort in coordinating the different companies from the accelerator and the building work since a lot of parallel work was necessary.

Accelerator and Treatment Technique

During the whole year 2005 the technical details at the junction between accelerator and treatment technique have been driven forward continuously. The gantry structure components will be delivered by MT Aerospace (formerly MAN Technologie) in spring 2006. Especially for the patient environment in the gantry treatment room further technical details have to be clarified.
There is also a permanent effort to coordinate the installation, commissioning and handing over between the accelerator and the treatment technique on the installation site.

General Project Evolution

The assembly of the accelerator has started and the first commissioning is taking place.
A lot of intense discussion took place between GSI and the university hospital to step by step set up the necessary procedures for the final operation such as the maintenance strategy including qualified personal and spare parts, the safety aspects, or the project documentation.

Since the therapy accelerator will be approved in accordance to the European Medical Device Directive, a lot of effort was and still has to be done into this direction as well.

References

[1] B. Schlitt et al., Proc. LINAC 2004, p. 51.
[2] C. Kleffner et al., this report.
[3] Y.R. Lu et al., Proc. LINAC 2004, p. 57.
[4] Y.R. Lu, PhD thesis, Johann Wolfgang Goethe University Frankfurt, July 2005.

Beam Diagnostics for the HIT and CNAO medical accelerators

A. Peters, M. Schwickert, A. Reiter and C. Dorn, GSI, Darmstadt, Germany

Introduction

In June 2003 it was decided that the GSI Beam Diagnostics (BD) group would act as contractor for the delivery of beam diagnostic devices for the heavy-ion cancer therapy facility HIT in Heidelberg. The contract included the production of the mechanical parts (feed-throughs, detectors etc.) as well as the integration of the 92 diagnostics devices of HIT to commercially available data acquisition systems and the software to control the devices.

All BD devices for the linac section were finished for the factory acceptance in November 2004 [1] and in 2005 the construction of BD components for the synchrotron and high-energy beam transport (HEBT) section was performed.

This report summarizes last year's activities on both projects HIT and CNAO, i.e. an Italian therapy project promoted by the CNAO foundation (Centro Nazionale di Adroterapia Oncologica). This medical facility, similar to HIT, is currently under construction in Pavia, 30 km south of Milan. In collaboration with CNAO the GSI beam diagnostics group is responsible for parts of the beam diagnostic devices.

Overall status of HIT beam diagnostics

At present, the accelerator area of the HIT building is being finished and the Low Energy Beam Transport (LEBT) section is mounted. Meanwhile all BD components for the LEBT section are readily installed.

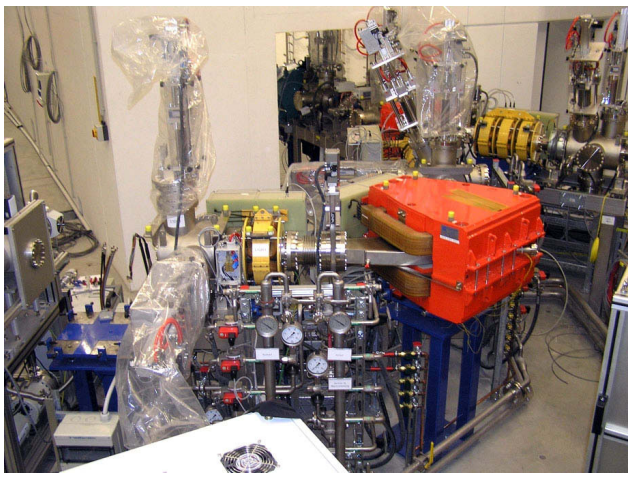


Figure 1: Left branch of the LEBT section

In Fig. 1 a recent picture of the LEBT section is shown. In the centre the 90°-dipole for mass separation can be seen. On the left side the exit of the extraction system of the ion source is visible. Right after the gap for the focusing magnet (not yet installed), the first diagnostic chamber is depicted, including a viewing screen and a water-cooled faraday-cup. To the right, behind the mass separator, a second diagnostic chamber houses a water-cooled slit system, a water-cooled faraday-cup and a profile grid.

Diagnostic components

Whereas in 2004 all BD components for the LEBT and linac section of HIT were finalized, all devices for beam diagnostics in the synchrotron and HEBT sections were, in accordance with the contract with the university clinics Heidelberg, finished in December 2005.

The HIT synchrotron will be equipped in each of the six synchrotron periods with 1 shoebox-type beam position monitor (BPM). These pick-ups have been optimized for the bandwidth of 0.1-100 MHz, thus allowing to measure up to 20 harmonics of the bunch frequency, i.e. 1.1-6.7 MHz [2]. In addition, two pairs of horizontal and vertical plates are installed in period 2 to perform Schottky diagnosis. Using one pair of plates of the Schottky chamber as an exciter and the BPM pick-ups as a detector, the synchrotron tune can be measured. Two viewing screens in the synchrotron allow observing the first turn and extraction of the ion beam. A vacuum chamber including an AC- and a DC-transformer has been developed to measure the beam intensity along the synchrotron cycle.

The GSI detector laboratory manufactured a total of 13 MWPC/IC detector pairs for the HEBT beam lines. The multi-wire proportional chamber (MWPC) at the front measures the beam profile, while, at the same time, the attached ionisation chamber (IC) determines the beam intensity.

As a second means for intensity measurements 5 scintillating counters were produced. Both types of detectors (MWPC/IC and scintillating counters) are mounted on a special pneumatic drive. This cylindrical vacuum feedthrough has 50µm stainless steel foil windows at the entry and exit direction of the ion beam. Thus the detector, during normal operation situated inside the cylindrical feedthrough, may be dismounted without breaking the vacuum. For the detection of the actual beam profile additional 8 viewing screens are ready to be mounted along the HEBT beam line, each equipped with a CCD camera and connected to a Firewire-network.

Electronics and Software

Whereas mechanical parts are manufactured and assembled at GSI, industrial solutions were mostly preferred for the software and electronics, in order to maintain the high performance of the accelerator and keep down-times to a minimum. Both are crucial factors for an efficient operation of the medical facility.

Beam diagnostics for HIT is subdivided into data acquisition (DAQ) systems and subsystems for the technical infrastructure. The subsystems control pressurized air, stepping motors, high-voltage supplies and the gas-flow for wire chambers throughout the facility.

The DAQ system consists of 11 PXI-crates with embedded controllers, connected to the front-end electronics via purpose-built connector-boxes. For the front-end electronics either commercially available parts, mainly from

small and highly specialised manufacturers, or trusted GSI systems were used. The software on the PXI-controllers runs under LabViewRT [3] and is divided into 7 different packages, one for each logical "device class": profile measurement, event counting, AC-current, DC-current, position monitors, phase probes and optical diagnostics. For example, the counter modules of the device class "event counting" digitize the signals of scintillators and ionization chambers with a sampling rate of up to 10 kHz.

The "manual control" software is being developed at Eckelmann AG [4], a company specialized on automation products. The industrial partner was chosen, because Eckelmann AG is responsible also for the implementation of the overall accelerator control system.

The software on the embedded controllers of the DAQ consists of two parts. Firstly, "manual control" software allows the user to control all functions of the front-end and detector electronics for commissioning and trouble-shooting. Secondly, the controller software implements an abstraction layer of the data acquisition hardware towards the accelerator control system.

All parts of the "manual control" software have been thoroughly tested at GSI. Additionally, the first modules of the BD devices were successfully integrated into the accelerator control system at a test setup for the RFQ commissioning.

Time Schedule and Outlook for Installation and Commissioning

Upon completion of the production of the BD components for the synchrotron and HEBT sections, these parts successfully passed the 2nd factory acceptance with the Heidelberg university clinics in December 2005. A last factory acceptance of the remaining parts, i.e. high-resolution viewing screens for iso-centre diagnostics, is scheduled for summer 2006. The production phase is accompanied by continuous software tests of the manual control software and the BD part of the accelerator control system. The first modules of the accelerator controls system are needed already in March 2006 for the commissioning of the ion sources on the site in Heidelberg. The installation of LEBT BD is scheduled until end of February 2006, followed by integration tests. Furthermore, installation and commissioning of the synchrotron BD devices are planned for May 2006 and HEBT BD is scheduled until September 2006.

Beam Diagnostics for CNAO

In summer 2004 GSI agreed to deliver technical support in planning and commissioning of the injector-linac for the CNAO facility [5] in Pavia, Italy. As a result of the initial contract, the GSI beam diagnostics group signed several addenda concerning not only the delivery of necessary diagnostic devices for the Linac, but also for the Medium Energy Beam Transport section. Beyond the hardware, a manual control software and support during commissioning were included in the contracts.

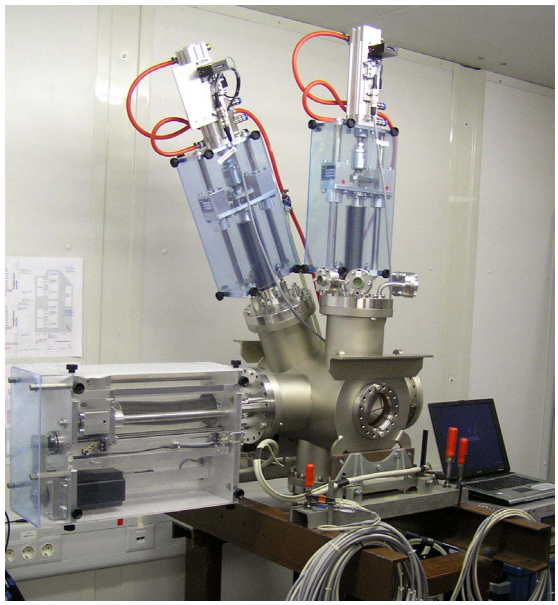


Figure 1: Stripper foil chamber with profile grid (front), stepping motor drive (middle) and Faraday cup (back).

Because the Linac is identical to the one in Heidelberg, components like the phase probes for the energy measurement, AC transformers or profile grids were adopted from the HIT project. Among the technical advances is a novel profile grid with 50% higher resolution (0.8 mm wire spacing) that meets the requirements of the different MEBT design and hence ion optics of the CNAO facility. The stripper foil chamber that will be installed behind the Linac has been fully equipped with a stepping motor drive for the foil ladder, a profile grid and a Faraday cup, both mounted on pneumatic actuators. Figure 1 shows the chamber on a test bench during inspection in December 2005 (together with the grid prototype and parts of the electronics) by members of the CNAO BD group.

The remaining production of mechanical components and final tests of software and electronics will take place until June 2006. After the factory acceptance in July all components will be transported to Pavia. Provided that the construction of the accelerator hall and the installations of the ion sources and LEBT section are finished on schedule, commissioning on site is expected to start in the following month

References

[1] GSI-Annual Report 2004, GSI, Darmstadt 2005.
[2] P. Kowina et al., DIPAC'05, Lyon 2005.
[3] http://www.ni.com
[4] http://www.eckelmann.de
[5] U. Amaldi, "CNAO-the Italian centre for light-ion therapy", Radiotherapy and Oncol., Vol. 73, Suppl. 2, Dec. 2004, p. S191-S201

Testbench of the HIT RFQ

C. Kleffner, R. Bär, M. Galonska, F. Heymach, R. Hollinger, M. Hörr, G.. Hutter, M. Maier, C. Mühle, A. Peters, A. Reiter, B. Schlitt, P. Spädtke, M. Schwickert, W. Vinzenz, GSI, Darmstadt
A. Bechtold, A. Schempp, IAP, J. W. Goethe-Universität Frankfurt am Main
R. Cee, E. Feldmeier, J. Suhm, S. Vollmer, HIT GmbH, Heidelberg

The RFQ cavity [1] for the HIT facility [2] was delivered to GSI in the first quarter of 2005. RF-tests with an rf power up to 200 kW and a pulse width of 500 µsec could be carried out successfully after a short time of rf-conditioning. A testbench for the RFQ cavity was constructed to allow for exact measurements of the output energy with the time of flight (ToF) method in addition to the beams tests at IAP Frankfurt [3].

The test bench for the RFQ was assembled in the GSI Betriebshalle. A MUCIS ion source produces a proton beam at 8 keV with approximately 2 mA beam current as well as H_3^+.

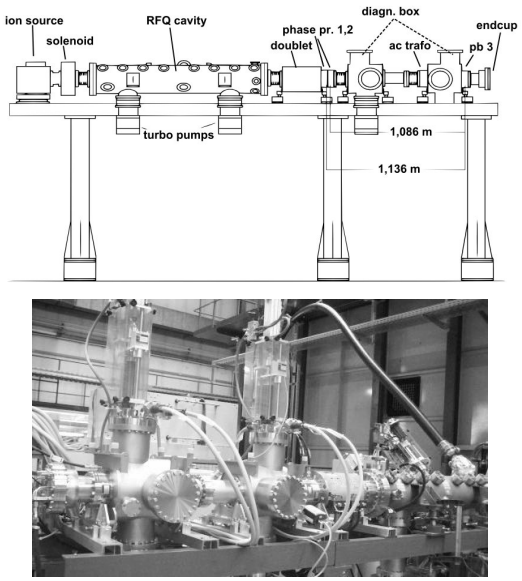


Figure 1: Layout of the testbench. The photo shows the beam direction from the right to the left.

As shown in fig. 1 a solenoid matches the protons to the RFQ entrance. A magnetic doublet focuses the accelerated beam transversaly into a drift section. Two capacitive pickups are followed by two profile grids inside the diagnostic boxes for the transverse position measurements and an AC transformer for the beam current measurement [4]. A third capacitive pick-up permits the exact and unambiguously energy determination.

ToF measurements without the integrated rebuncher have been carried out at different rf power levels and compared to particle tracking simulations with Parmteq. The estimated rf power consumption for the design RFQ electrode voltage of 23.3 kV is 19.0 kW as shown in fig. 2. The so called voltfactor is set to 1.0 at this rf level. At carbon level the expected power consumption will be 170 kW.

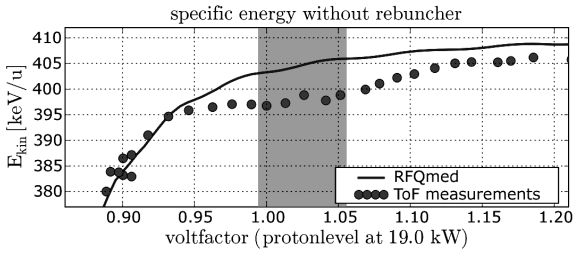


Figure 2: comparison of simulated vs. measured beam energies for calibration of the design rf power level.

The output energy of the protons depending on the voltfactor with integrated rebuncher shows the expected energy shift. Because the phase shift of the bunches to the rebuncher in relation to the voltfactor is known, the effective voltage can be estimated about 30 kV for protons. It is planned to move the rebuncher mechanically 1mm longitudinally and redo the measurements. This will change the working point with the maximum buncher voltage inside the working area (voltfactor between 1.00 and 1.06) of the RFQ.

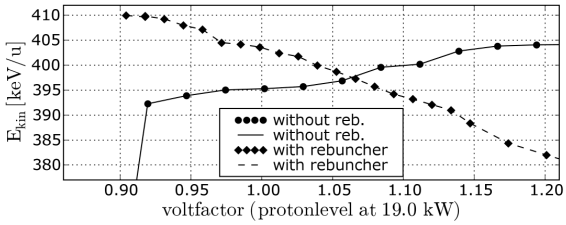


Figure 3: View on the testbench.

Outlook

It is expected that with the final mechanical adjustments of the internal rebuncher in the first quarter of 2006 an effective voltage of 90 kV for carbon level can be arrived within the working area.

References

[1] A. Bechtold, U. Ratzinger, A. Schempp, B. Schlitt, in: Proc. PAC 2001, p. 2485.
[2] H. Eickhoff et al., HICAT - The German Hospital-Based Light Ion Cancer Therapy Project; EPAC 2004
[3] A. Bechtold et al, Beam test stand of the RFQ-driftube-combination for the therapy center in Heidelberg. Proceedings of EPAC 2004, Lucerne, CH.
[4] A.Peters et al, Beam diagnostic devices and data adquisition for the HICAT facility. Proceedings of DIPAC 2005, Geneva, Switzerland.

Optimised raster scan dose delivery with RF-knockout extracted pencil beams

S. Brons, Th. Haberer, HIT, Heidelberg, Germany
H. Eickhoff, B. Franczak, P. Moritz, D. Ondreka, U. Scheeler, P. Schütt, GSI, Darmstadt, Germany

Introduction

External radiotherapy using the raster scan technique [1] has been successfully used at GSI to treat about 300 patients. Beam scanning requires pencil beams of high stability in terms of position and width as well as a predictable and adjustable intensity distribution.

RF-knockout ("KO") extraction, where the beam is slowly extracted from a synchrotron by exciting it by a transversal RF field perfectly matches these requirements, as during the extraction process the optics of the accelerator and the beam line are kept constant. This results in a superior stability of the extracted beam all over the extraction cycle. In addition, modulation of the amplitude of the transversal RF field allows reaching virtually any possible intensity distribution of the extracted beam. Therefore, RF-knockout extraction will be used as the standard extraction method at the Heidelberg Ion Therapy facility HIT [2].

Measurements

Measurements with scanned RF-knockout extracted pencil beams were performed at GSI in 2005 during one of the beam time blocks devoted to tumour therapy. A special test mode was introduced in the accelerator control system to allow definition of a ^{12}C beam of 250 $MeVu^{-1}$ extracted by RF-knockout extraction within volatile RAM without corrupting the therapy setting stored permanently in EPROMs. The beam was delivered to the raster scanner system of the tumour therapy facility. A set of time resolved multi-wire proportional chambers of the therapy control system were used to acquire spectra of beam intensity and width during the extraction cycle with a time resolution of 750 μs.

Results

Figure 1 shows the measured intensity distribution of a RF-knockout extracted ^{12}C-beam over one extraction cycle together with the intensity profile obtained for standard resonant extraction.

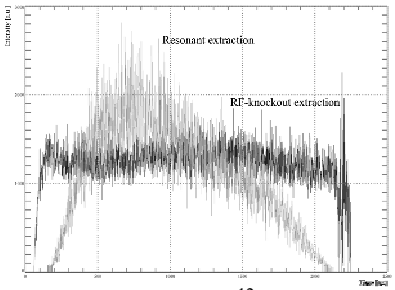


Figure 1: Intensity of extracted ^{12}C beam over one spill.

The figure shows that with RF-knockout extraction an almost rectangular intensity distribution can be reached (note, that the spike after 2100 ms is an artefact, due to the sweeping out of the synchrotron at extraction stop).

Figure 2 shows the variation in beam width over one extraction cycle for a ^{12}C-beam extracted by RF-knockout and by standard resonant extraction.

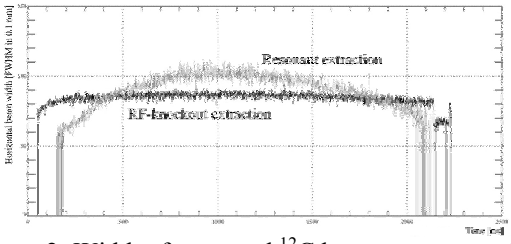


Figure 2: Width of extracted ^{12}C beam over one spill.

The figure illustrates that for RF-knockout extraction the beam spot size of the extracted beam stays almost constant all over the extraction cycle (safe the spike after extraction stop, see above). This is in contrast to the significant variation of beam width for resonant extraction.

Strong variation of beam spot size over the extraction cycle typically induces periodic patterns, when scanning the beam in 2D. In Figure 3 we show the film blackening obtained when scanning the RF-knockout extracted and the resonant extracted beams over a square area.

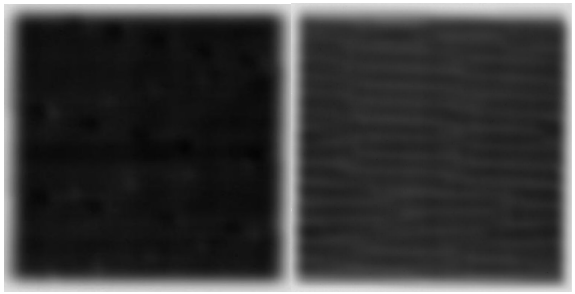


Figure 3: Blackening of a radiographic film by a scanned ^{12}C beam, Left: KO-extraction, right: Resonant extraction.

The figure shows that with the scanned RF-knockout extracted beam a remarkable homogeneity of the deposited dose is reached (actually far below the ±5 % limit required for tumour therapy at GSI).

Conclusions

Our measurements indicate that RF-knockout extracted ^{12}C beams exhibit a superior stability of the beam parameters over the extraction cycle when compared to resonance extraction. This results in a significantly improved raster scan dose delivery, particularly in terms of the homogeneity of the applied dose.

References

[1] T. Haberer, NIM **A 330** (1993) 296
[2] P. Heeg, Z. Med. Phys. **14** (2004) 17

Beam Monitors for the High-Energy Beam Line of HIT

B. Voss, A. Heinz, H. Risch; GSI Darmstadt, Germany

For the '**H**eidelberg **I**on **T**herapy' **HIT** [1] which is currently set up as a dedicated facility to treat cancer with heavy ions from Protons to Oxygen in Heidelberg/Germany, a small series of 13 beam-monitor detectors as part of the high energy beam line [2] have been designed and built in the detector laboratory of GSI.

Each unit consist of a mesh type ionization chamber (IC) and a current grid (CG) (see fig.1) with a symmetric design concerning high-voltage (HV) and signal (S) layers. They may be operated at max. ±1200 V (CG) and ±1500 V (IC) respectively for an Ar/CO_2 (80/20%) gas mixture, depending on the beam conditions. Each detector has been built out of a modular set of PCBs for ease of maintenance. CG and IC are densely flanged together only separated by a shielding foil in order to form one unit width a total thickness of 30.4±0.1 mm to be mounted in a common vacuum hood. Position adjustment to the optical axis was done with a precision of 0.1 mm. The relatively large active area of 72x72 mm^2 and the very limited space in the hood was a challenging restriction for the design especially of the position sensitive layers of the CG. These carry several high-precision resistor-arrays which provide the possibility to inject a test-pulse at each wire from the side which is not read out. As a result, the response of the whole chain from the wire to the read-out software can be tested in one step (fig.2a). During a test at CaveM, the detector has been proven to work 'as designed' (fig.2b).

Table 1: Layers in beam-direction (see also fig 1).

Part	Layer no.	Component	Material & Pitch	Thickness & Orientation
Hood	0, 0*	vacuum window	stainless steel	à 50 µm
	0 - 1 6* - 0*	'dead' gap	Ar/CO_2	à 11 mm
CG	1, 1*	shielding foil	aluminized Kapton©	25 µm
	1 - 3 5 - 1*	'dead' gap	Ar/CO_2	à 4.9 mm
	3, 5	signal layer (x, y)	W/Au wires 1.1 mm	50 µm 0°, 90°
	3 - 4 4 - 5	'active' gap	Ar/CO_2	à 4.8 mm
	4	high voltage layer	W/Au wires 2 mm	20 µm 45°
IC	1* - 6	'dead' gap	Ar/CO_2	2.1 mm
	6, 6*	high voltage layer	PE/Ni mesh	57 µm
	6 - 7 7 - 6*	'active' gap	Ar/CO_2	à 3.4 mm
	7	signal layer	PE/Ni mesh	57 µm

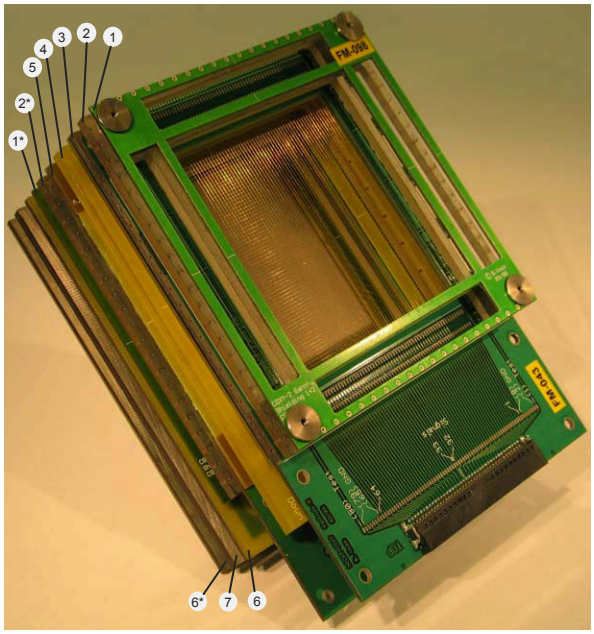


Figure 1: Picture of the detector unit with artificially separated layers and shielding foils removed.

See also tab.1 for the list of materials the beam has to traverse and their average thicknesses as measured during fabrication.

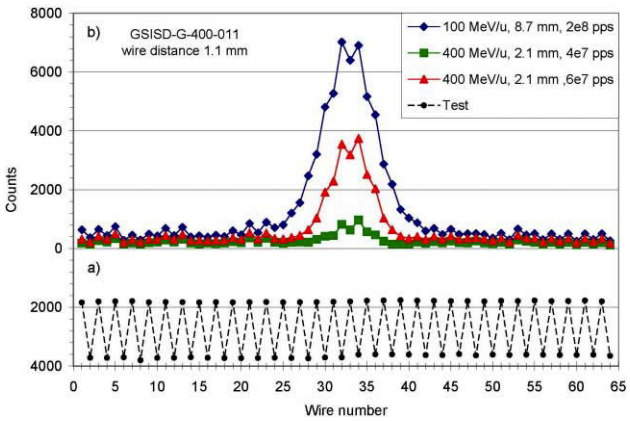


Figure 2a) Spectra of the test input (-2 V) for one position sensitive layer of the current grid. b) Profile data measured during a test at CaveM for different energies and foci of the carbon pencil-beam at -1200 V operating voltage.

References

[1] H. Eickhoff et al., HICAT-The German Hospital-Based Light Ion Cancer Therapy Project; EPAC 2004

[2] A. Peters et al., Beam diagnostic devices and data acquisition for the HICAT facility, DIPAC 2005

Patient monitors for HIT and transfer of know-how to Siemens-Med

B. Voss, A. Heinz, H. Risch; GSI Darmstadt, Germany

Abstract

At the therapy facility CaveM of GSI a set of two Multi-Wire Proportional Chambers (MWPC) (see fig.1) and three Ionization Chambers (IC) known as 'patient-monitor detectors' [1] serve to steer and control the irradiation of human patients with heavy ions. They measure the beam position, direction and intensity in front of the patient in a redundant and diverse way. Lacking an industrial supplier, the detector laboratory of GSI was charged in 2003 with the delivery of this system for the Heavy-Ion Therapy facility HIT which is currently under construction in Heidelberg.

Developments

In the framework of a hospital surrounding, the detectors have to be categorized as class 'II b' medical devices. Therefore their design and the respective manufacturing processes for a small series production have been adapted to be in accordance with the medical-device directive 93/42/EWG accomplishing the 'basic requirements' of the 'Act on Medical Devices' MPG. Besides already well established procedures involved in detector development additional tasks like e.g. 'risk assessment' and 'quality-controlled production' had to be implemented. Research effort and investments were made to build up knowledge, procedures and infrastructure. Especially the need for a detailed documentation and the composition of a 'technical file' was a challenge accepted. In some cases this led to the discovery of more general findings other projects [3] could benefit from.

Know-How Transfer

The developments were promoted up to the milestone of a possible type approval of the detector system according to addendum IV/MDD 93/42. This was the moment when the medical division of the Siemens-AG (SAG) joined the HIT project and was entrusted with the further development of all products concerning radiation techniques. Consequently, in 2004 the decision was made to transfer all required knowledge to this company. An iterative four-step process was implemented: a) theoretical and practical training and demonstration by GSI, b) action of SAG with guidance and supervision by GSI, c) single handed production by SAG with follow up control and finally d) fully autonomous production by SAG to gain experience and validate the processes. The whole procedure was successfully completed during 2005. Considerable efforts have been made to enable SAG to self-responsible produce parts of the beam-monitoring system using the infrastructure which has been set up in the detector laboratory of GSI in the framework of this project. The outcome of this work was successfully verified during beam times at CaveM.

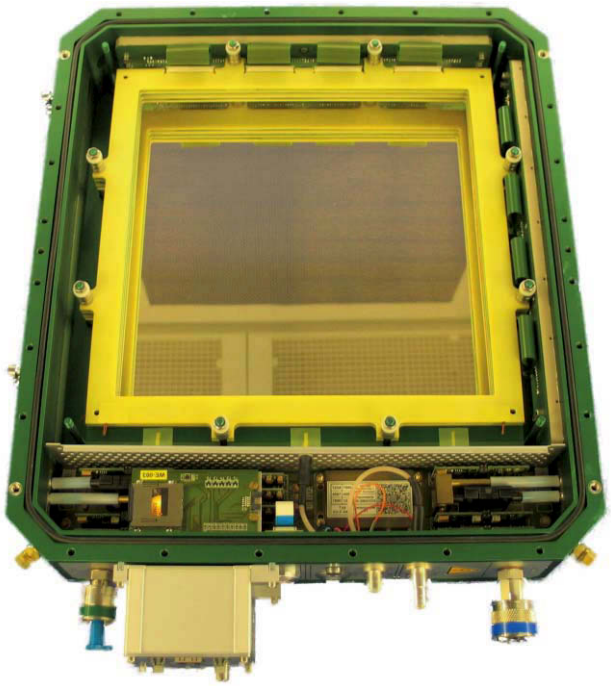


Figure 1: Picture of a MWPC with one of the chamber windows removed. The modular design is composed of the functional unit which forms either a parallel-plate ionization chamber or a multi-wire proportional chamber mounted on a carrier which serves as the exit window. The design also incorporated a set of sensors and a controller monitoring the operation conditions [2].

Outlook

Support and advisory service with respects to improvement in details, the risk assessment and the development of advanced concepts are still under way. The wire-winding machine DWM 2000 developed at GSI and sold to SAG as part of a technology transfer may be taken as an example. Here the adaptation to the special needs of the batched-flow production according the CE and FDA certification is still ongoing.

References

[1] B. Voss et al., The Monitor System of the Therapy Project, GSI Scientific report 1997, Volume 98-1, March 1998, page 187

[2] B. Voss et al., A modular setup to monitor a detector's operation conditions, contribution to this report

[3] Ch. J. Schmidt et al., Surface electrical conductivity of cured Araldite 2011 Epoxy, a study initiated during Alice TRD production, contribution to this report

Annex

ANNEX-PUBL
Publications (405p.)
ANNEX-PUBL-01 Publications to FAIR: Future experiments (405p.)
ANNEX-PUBL-02 Publications to FAIR: Accelerator Research & Development (407p.)
ANNEX-PUBL-03 Publications to the programme ’Physics of hadrons and nuclei’: Accelerator Research & Development (409p.)
ANNEX-PUBL-04 Publications to the programme ’Physics of hadrons and nuclei’: Experiments (413p.)
ANNEX-PUBL-05 Publications to the programme ’Large-scale facilities for research with photons, neutrons and ions’ (438p.)
ANNEX-PUBL-06 Publications to the programm ’Health’ in the field ’Cancer research’ (447p.)
ANNEX-PUBL-07 Patents and patent applications (448p.)
ANNEX-PUBL-08 GSI as publisher (449p.)

ANNEX-COLLABORATIONS
International and national collaborations of the GSI (451p.)

ANNEX-EVENTS
Workshops, Meetings, Seminars and Talks (484p.)

ANNEX-UNIV
Teaching Activities and Academic Works (510p.)

ANNEX-EXPERIMENTS
Experiments performed at the GSI (519p.)

ANNEX-ORGANIGRAM
Scientific bodies and the Organigram (521p.)

Index of authors (527p.)

Publications to FAIR: Future experiments

K. Große, GSI, Darmstadt, Germany

1. Reviewed publications

Eschke, J.*: **International facility for antiproton and ion research (FAIR) at GSI, Darmstadt.** *Journal of physics G, Nuclear and particle physics* **31**(6): S967–S973. DOI:10.1088/0954-3899/31/6/041

Gumberidze, A.*; Bosch, F.*; Bräuning-Demian, A.*; Hagmann, S.*; Kühl, T.*; Liesen, D.*; Schuch, R.; Stöhlker, T.*: **Atomic physics with highly-charged heavy ions at the GSI future facility: The scientific program of the SPARC collaboration.** *Nuclear instruments & methods in physics research, Section B, Beam interactions with materials and atoms* **233**: 28–30. DOI:10.1016/j.nimb.2005.03.082

Gutbrod, H. H.*: **International Facility for Antiproton and Ion Research (FAIR) at GSI, Darmstadt.** *Nuclear physics A, Nuclear and hadronic physics* **752**: 457C–469C. DOI:10.1016/j.nuclphysa.2005.02.137

Höhne, C.*; CBM Collaboration: **The compressed baryonic matter experiment at the future accelerator facility in darmstadt.** *Nuclear physics A, Nuclear and hadronic physics* **749**: 141C–149C. DOI:10.1016/j.nuclphysa.2004.12.023

Höhne, C.*; Kharlov, Y.; Khmelnikov, V.; Polishchuk, B.*; Rykalin, V.; Sadovsky, S.; CBM Collaboration: **Concept for a RICH detector for the CBM experiment at FAIR in Darmstadt.** *Nuclear instruments & methods in physics research, Section A, Accelerators, spectrometers, detectors and associated equipment* **553**(1): 91–95. DOI:10.1016/j.nima.2005.08.009

Hagmann, S.*; Beyer, H. F.*; Bosch, F.*; Bräuning-Demian, A.*; Kluge, H.-J.*; Kozhuharov, C.*; Kühl, T.*; Liesen, D.*; Stöhlker, T.*; Ullrich, J.; Moshammer, R.; Mann, R.*; Mokler, P.*; Quint, W.*; Schuch, R.; Warczak, A.: **Challenges and opportunities for atomic physics at FAIR: The new GSI accelerator project.** *Nuclear instruments & methods in physics research, Section B, Beam interactions with materials and atoms* **241**(1): 5–8. DOI:10.1016/j.nimb.2005.07.229

Henning, W.*: **Ups and downs, and the strange charm of roadmaps.** *Nuclear physics A, Nuclear and hadronic physics* **751**: 593C–603C. DOI:10.1016/j.nuclphysa.2005.02.049

Heuser, J. M.; Müller, W. F. J.*; Senger, P.*; Muntz, C.*; Stroth, J.*; CBM Collaboration: **A high-performance silicon tracker for the Compressed Baryonic Matter experiment at FAIR.** *Czechoslovak Journal of Physics* **55**(12): 1649–1653.

Lewandowski, B.: **A fast and compact electromagnetic calorimeter for the PANDA detector at GSI.** *Nuclear instruments & methods in physics research, Section A, Accelerators, spectrometers, detectors and associated equipment* **537**(1): 349–352. DOI:10.1016/j.nima.2004.08.041

Peters, K.: **Charmonium and exotic hadrons at PANDA.** *International Journal of Modern Physics A* **20**(2): 570–577. DOI:10.1142/S0217751X05021816

Piriz, A. R.; Temporal, M.; LópezCela, J. J.; Grandjouan, N.; Tahir, N. A.*; Moreno, M. C. S.; Portugues, R. F.; Hoffman, D. H. H.*: **Target design for the cylindrical compression of matter driven by heavy ion beams.** *Nuclear instruments & methods in physics research, Section A, Accelerators, spectrometers, detectors and associated equipment* **544**(1): 27–33. DOI:10.1016/j.nima.2005.01.191

Ritman, J.; PANDA Collaboration: **The PANDA detector at the GSI-FAIR project.** *International Journal of Modern Physics A* **20**(2): 567–569. DOI:10.1142/S0217751X05021804

Senger, P.*: **Strangeness and charm of compressed baryonic matter - the CBM experiment at FAIR.** *Journal of physics G, Nuclear and particle physics* **31**(6): S1111–S1114. DOI:10.1088/0954-3899/31/6/069

Senger, P.*: **The Compressed Baryonic Matter experiment at FAIR.** *Heavy ion physics* **22**(3): 363–370. DOI:10.1556/APH.22.2005.3-4.23

Senger, P.*: **The strangeness of dense baryonic matter.** *Heavy ion physics* **22**(1): 13–20. DOI:10.1556/APH.22.2005.1-2.3

Stöhlker, T.*; Beier, T.*; Beyer, H. F.*; Bosch, F.*; Bräuning-Demian, A.*; Gumberidze, A.*; Hagmann, S.*; Kozhuharov, C.*; Kühl, T.*; Liesen, D.*; Mann, R.*; Mokler, P. H.*; Quint, W.*; Schuch, R.;Warczak, A.: **Atomic physics with highly-charged heavy ions at the GSI future facility: The scientific program of the SPARC collaboration.** *Nuclear instruments & methods in physics research, Section B, Beam interactions with materials and atoms* **235**: 494–497. DOI:10.1016/j.nimb.2005.03.231

Stroth, J.: **The future at GSI and FAIR.** *Nuclear physics A, Nuclear and hadronic physics* **755**: 209C–218C. DOI:10.1016/j.nuclphysa.2005.03.104

Tahir, N. A.*; Deutsch, C.; Fortov, V. E.; Gryaznov, V.; Hoffmann, D. H. H.*; Kulish, M.; Lomonosov, I. V.; Mintsev, V.; Ni, P.; Nikolaev, D.; Piriz, A. R.; Shilkin, N.; Spiller, P.*; Shutov, A.; Temporal, M.; Ternovoi, V.; Udrea, S.; Varentsov, D.: **Proposal for the study of thermophysical properties of high-energy-density matter using current and future heavy-ion accelerator facilities at GSI Darmstadt.** *Physical review letters* **95**(3): 035001. DOI:10.1103/PhysRevLett.95.035001

Tahir, N. A.*; Deutsch, C.; Fortov, V. E.; Gryaznov, V.; Hoffmann, D. H. H.*; Lomonosov, I. V.; Piriz, A. R.; Shutov, A.; Spiller, P.*; Temporal, M.; Udrea, S.; Varentsov, D.: **Studies of strongly coupled plasmas using intense heavy ion beams at the future FAIR facility: the HEDgeHOB collaboration.** *Contributions to Plasma Physics* **45**(3): 229–235. DOI:10.1002/ctpp.200510025

Tahir, N. A.*; Weick, H.*; Iwase, H.*; Geissel, H.*; Hoffmann, D. H. H.*; Kindler, B.*; Lommel, B.*; Radon, T.*; Münzenberg, G.*; Shutov, A.; Sümmerer, K.*; Winkler, M.*: **Calculations of high-power production target and beamdump for the GSI future Super-FRS for a fast extraction scheme at the FAIR Facility.** *Journal of Physics D: Applied Physics* **38**(11): 1828–1837. DOI:10.1088/0022-3727/38/11/023

Welsch, C. P.; Grieser, M.; Ullrich, J.; Wolf, A.: **An ultra-low-energy storage ring at FLAIR.** *Nuclear instruments & methods in physics research, Section A, Accelerators, spectrometers, detectors and associated equipment* **546**(3): 405–417. DOI:10.1016/j.nima.2005.03.134

Wiedner, U.: **Hadron physics with antiprotons at FAIR.** *International Journal of Modern Physics A* **20**(8): 1772–1777. DOI:10.1142/S0217751X05023311

Wiedner, U.: **The PANDA experiment at FAIR.** *Nuclear Physics B - Proceedings Supplements* **147**: 119–123. DOI:10.1016/j.nuclphysbps.2005.03.014

2. Further external publications

Aumann, T.: **Prospects with rare isotope beams at the international facility for antiprotons and ion research (FAIR).** In: *Key Topics in Nuclear Structure, Proc. of the '8th International Spring Seminar on Nuclear Physics', May 2004, Paestum, Italy,* World Scientific ,

Peters, K.: **Charmonium and Exotic Hadrons at Panda.** In: Chen, H.; Du, D.; Li, W.; Li, C: *Proceedings of ICHEP 2004, Vol. 2,* World Scientific, 1068p.

Peters, K.: **FAIR: the future project at GSI.** In: *Proceedings of the VIIIth Biannual Low Energy Antiproton Physics Conference, LEAP2005, AIP Conf. Proc.* **796***,* 355p.

Simon, H.; ELISE collaboation: **The ELISe Experiment at FAIR.** In: Chiladze, David; Kacharava Andro; Ströher, Hans: *STORI'05, 6th International Conference on Nuclear Physics at Storage Rings, 23–26 May 2005, Jülich-Bonn,* Schriften des Forschungszentrum Jülich, Reihe Materie und Material Vol. 30, Jülich: Forschungszentrum Jülich,

Ullrich, J.; Dorn, A.; Fischer, D.; Moshammer, R.; Najjari, B.; Schulz, M.; Voitkiv, A.; Welsch, C. P.: **Sub-Femtosecond Correlated Dynamics Explored with Antiprotons.** In: *AIP Conf. Proc. 793 ,* 71p.

Welsch, C. P.; Grieser, M.; Dorn, A.; Moshammer, R.; Ullrich, J.: **Exploring Sub-Femtosecond Correlated Dynamics with an Ultra-low Energy Electrostatic Storage Ring.** In: *AIP Conf. Proc. 796,* 266p.

Wilms, A.: **A fast and compact electromagnetic calorimeter for the PANDA detector at FAIR", Proceedings of the VIIIth Biannual Low Energy.** In: *Antiproton Physics Conference, LEAP2005, AIP Conf. Proc.* **796***,* 373p.

Publications to FAIR: Accelerator Research & Development

K. Große, GSI, Darmstadt, Germany

1. Reviewed publications

Kaugerts, J. E.; Moritz, G.*; Muehle, C.*; Ageev, A.; Bogdanov, I. O.; Kozub, S.; Shcherbakov, P.; Sytnik, V.; Tkachenko, L.; Zubko, V.; Tommasini, D.; Wilson, M. N.; Hassenzahl, W.: **Design of a 6 T, 1T/s fast-ramping synchrotron magnet for GSI's planned SIS 300 accelerator.** *IEEE transactions on applied superconductivity* **15**(2): 1225–1227. DOI:10.1109/TASC.2005.849157

Khodzhibagiyan, H. G.; Fischer, E.*; Kovalenko, A. D.; Moritz, G.*; Potanina, L. V.; Shikov, A. K.; Vedernikov, G. P.: **Design and test of a hollow superconducting cable based on keystoned NbTi composite wires.** *IEEE transactions on applied superconductivity* **15**(2): 1529–1532. DOI:10.1109/TASC.2005.849157

Spiller, P.*; Blasche, K.*; Franczak, B.*; Kirk, M.*; Hülsmann, P.*; Omet, C.*; Ratschow, S.*; Stadlmann, J.*: **Accelerator plans at GSI for plasma physics applications.** *Nuclear instruments & methods in physics research, Section A, Accelerators, spectrometers, detectors and associated equipment* **544**(1): 117–124. DOI:10.1016/j.nima.2005.01.289

Tahir, N. A.*; Adonin, A.; Deutsch, C.; Fortov, V. E.; Grandjouan, N.; Geil, B.; Grayaznov, V.; Hoffmann, D. H. H.*; Kulish, M.; Lomonosov, I. V.; Mintsev, V.; Ni, P.*; Nikolaev, D.; Piriz, A. R.; Shilkin, N.; Spiller, P.*; Shutov, A.; Temporal, M. Ternovoi, V.; Udrea, S.; Varentsov, D.: **Studies of heavy ion-induced high-energy density states in matter at the GSI Darmstadt SIS-18 and future FAIR facility.** *Nuclear instruments & methods in physics research, Section A, Accelerators, spectrometers, detectors and associated equipment* **544**(1): 16–26. DOI:10.1016/j.nima.2005.01.178

2. Further external publications

Bobrov, E.; Fischer, E.; Kaugerts, J.; Moritz, G.: **A Detailed Mechanical and Thermal Evaluation of the Hollow Cable Conductor for the Fast Cyclic SIS 100 Synchrotron.** In: *Proceedings of MT19, Genova, Italy, Sep. 2005,*

Bogdanov, I.; Kozub, S.; Shcherbakov, P.; Tkachenko, L.; Zubko, V.; Muehle, C.; Moritz, G.; Tommasini, D.: **Optimization of a Dipole with Partially Keystoned Cable for the SIS 300.** In: *Proceedings of MT19, Genova, Italy, Sep. 2005,*

Franchetti, G.*; Hofmann, I.*; Orzhekovskaya, A.*; Spiller, P.*: **Intensity and Bunch-Shape Dependent Beam Loss Simulation for the SIS100.** In: Horak, C: *Proceedings of 2005 Particle Accelerator Conference, May 16-20, Knoxville, Tennessee, USA,* IEEE, 3807p.

Golubev, A.; Kantsyrev, A.; Luckjashin, V.; Fertman, A.; Kunin, A.; Vatulin, V.; Panova, Y.; Mustafin, E.*; Hofmann, I.*; Schardt, D.*; Weyrich, K.* Sobolevskiy, N.; Latysheva, L.: **Measurements of the Energy Deposition Profile for 238U Ions with Energy 500 and 950 MEV/U in Stainless Steel and Copper Targets .** In: Horak, C: *Proceedings of 2005 Particle Accelerator Conference, May 16-20, Knoxville, Tennessee, USA,* IEEE, 2318p.

He, M.; Becker, W.-J.; Ricken, W.; Peters, A.*; Reeg, H.*; Kowina, P.*: **High Dynamic Magnetic Beam Current Measurements by Means of Optimised Magneto-Resistance (MR) Sensor Engineering 102 .** In: *Proceedings of DIPAC 2005, Lyon, France,* 102p.

Kalimov, Alexander; Fischer, Egbert; Kurnyshov, Roman; Moritz, Gebhard; Muehle, Carsten; Shcherbakov, Petr: **Design of a Superferric Quadrupole Magnet with a High Field Gradient.** In: *Proceedings of MT19, Genova, Italy, Sep. 2005,*

Kauschke, M.; Schroeder, C. H.; Quack, H.: **FAIR-cryogenics – new task on the cryogenic system for the new research facility at GSI.** In: *Proceedings on CEC-ICMC 2005, Keystone, Colorado, USA, July 2005,*

Khodzhibagiyan, H.; Akishin, P.; Alfeev, A.; Bartenev, V.; Butenko, A.; Fischer, E.; Kovalenko, A.; Kuznetsov, G.; Mikhaylov, V.; Nikitaev, P.: **Progress in the Design of a Fast-Cycling Cos θstyle Dipole based on High Current Hollow Superconducting Cable.** In: *Proceedings of EUCAS 2005, Vienna, Austria, Sep. 2005,*

Khodzhibagiyan, H.; Fischer, E., Kovalenko, A.: **New Design for the SIS100/300 Magnet Cooling.** In: *Proceedings of MT19, Genova, Italy, Sep. 2005,*

Koch, S.; De Gersem, H.; Fischer, E.; Moritz, G.; Weiland, T.: **Simulation of Eddy-Current Losses in a Fast Ramped Superconductive Dipole Magnet.** In: *Proceedings of MT19, Genova, Italy, Sep. 2005,*

Kovalenko, Alexander; Agapov, Nikolay; Bartenev, Victor; Fischer, Egbert; Khodzhibagiyan, Hamlet; Nikitaev, Peotr;

Smirnov, Anatoly: **Progress in the Design of a Superconducting Synchrotron Dipole Magnet with Pulse Repetition Rate up to 20 Hz.** In: *Proceedings of MT19, Genova, Italy, Sep. 2005,*

Kovalenko, Alexander; Agapov, Nikolay; Fischer, Egbert; Khodzhibagiyan, Hamlet; Kuznetsov, Grigory; Moritz, Gebhard; Smirnov, Anatoly: **New Results on Minimizing AC Power Losses in a Fast Cycling 2T Superferric Dipole with a Cold Yoke.** In: *Proceedings of MT19, Genova, Italy, Sep. 2005,*

Kozub, S. S.; Bogdanov, I.; Pokrovsky, V.; Shcherbakov, P.; Shirshov, L.; Sytnik, V.; Tkachenko, L.; Zubko, V.; Kaugerts, J.; Moritz, G.: **Tests of Straight and Bent Superconducting Dipoles.** In: *Proceedings of MT19, Genova, Italy, Sep. 2005,*

Lehrach, A.; An, S.; Bongardt, K.; Dietrich, J.; Eichhorn, R.; Lorentz, B.; Maier, R.; Martin, S.; Prasuhn, D.; Senichev, E.; Senicheva, Y.; Stockhorst, H.; Tle, R.; Zaplatin, E.; Boine-Frankenheim, O.*; Dolinskii, A.*; Steck, M.*; Hinterberger, F.; Galnander, B.; Reistad, D.: **Design Work for the High-Energy Storage Ring for Antiprotons of the Future GSI Project.** In: Horak, C: *Proceedings of 2005 Particle Accelerator Conference, May 16-20, Knoxville, Tennessee, USA,* IEEE, 776p.

Moritz, G.*; Kaugerts, J.*; Escallier, J.; Ganetis, G.; Jain, A. K.; Marone, A.; Muratore, J. F.; Thomas, R.; Wanderer, P.; Auchmann, B.; de Maria, R.; Russenschuck, S.; Wilson, M.: **Recent Test Results of the Fast-Pulsed 4 T COSO Dipole GSI 001 .** In: Horak, C: *Proceedings of 2005 Particle Accelerator Conference, May 16-20, Knoxville, Tennessee, USA,* IEEE, 683p.

Mustafin, E.*; Kaugerts, J.*; Moritz, G.*; Walter, G.*; Latysheva, L.; Sobolevskiy, N.: **Radiation Damage to the Elements of the SIS300 Dipoles .** In: Horak, C: *Proceedings of 2005 Particle Accelerator Conference, May 16-20, Knoxville, Tennessee, USA,* IEEE, 3943p.

Nolden, F.*; Franzke, B.*; Peschke, C.*; Caspers, F.; Thorndahl, L.; Balk, M. C.; Schuhmann, R.; Weiland, T.: **Stochastic Cooling Electrodes for a Wide Velocity Range in the CR.** In: Horak, C: *Proceedings of 2005 Particle Accelerator Conference, May 16-20, Knoxville, Tennessee, USA,* IEEE, 799p.

Spiller, P.*: **Challenges and Progress in the FAIR Accelerator Project .** In: Horak, C: *Proceedings of 2005 Particle Accelerator Conference, May 16-20, Knoxville, Tennessee, USA,* IEEE, 294p.

Sytnikov, V. E.; Vysotsky, V. S.; Rychagov, A. V.; Taran, A. V.; Moritz, G.; Kauschke, M.; Fisher, E.; Egorov, S. A.; Rodin, Y. I.; Bottura, L.; Wilson, M. N.: **Development and test of a miniature novel Cable-In-Conduit-Conductor for use in fast ramping accelerators with superconducting magnets.** In: *Proceedings of MT19, Genova, Italy, Sep. 2005,*

Walter, Gertrud; Schroeder, Claus; Heß, Günther; Klos, Franz; Berlinghof, Stefan; Schnizer, Pierre; Floch, Eric; Kauschke, Marion; Moritz, Gebhard: **A test facility for fast-ramped superconducting magnets for FAIR.** In: *Proceedings of MT19, Genova, Italy, Sep. 2005,*

Wang, Q.; Zhao, B.; Moritz, G.: **Conceptual design of cryostat for the superconducting CR dipole magnet.** In: *Proceedings of MT19, Genova, Italy, Sep. 2005,*

Winkler, M.; Svedentsov, M.; Behr, K. H.; Geissel, H.; Iwase, H.; Moritz, G.; Muehle, C.; Weick, H.: **Radiation Resistant Quadrupole Magnet for the SuperFRS at FAIR.** In: *Proceedings of MT19, Genova, Italy, Sep. 2005,*

Xiang, Y.; Kauschke, M.; Moritz, G.; Kutzschbach, A.; Quack, H.: **Cryogenic distribution for beam transfer lines, radioactive secondary beam fragment separator at storage ring of FAIR.** In: *Proceedings on CEC-ICMC 2005, Keystone, Colorado, USA, July 2005,*

Publications to the programme 'Physics of hadrons and nuclei': Accelerator Research & Development

K. Große, GSI, Darmstadt, Germany

1. Reviewed publications

Al-khateeb, A. M.; Boine-Frankenheim, O.*; Hasse, R. W.*; Hofmann, I.*: **Longitudinal impedance and shielding effectiveness of a resistive beam pipe for arbitrary energy and frequency.** *Physical Review E* **71**(2): 026501. DOI:10.1103/PhysRevE.71.026501

Boine-Frankenheim, O.*; Shukla, T.: **Space charge effects in bunches for different rf wave forms.** *Physical Reviews Special Topics Accelerators and Beams* **8**(3): 034201. DOI:10.1103/PhysRevSTAB.8.034201

Calaga, R.; Tomas, R.; Franchi, A.*: **Betatron coupling: Merging Hamiltonian and matrix approaches.** *Physical Reviews Special Topics Accelerators and Beams* **8**(3): 034001. DOI:10.1103/PhysRevSTAB.8.034001

Czyzykiewicz, R.; Adam, H. H.; Budzanowski, A.; Grzonka, D.; Janusz, M.; Jarczyk, L.; Kamys, B.; Khoukaz, A.; Kilian, K.; Klaja, P.; Kowina, P.*; Moskal, P.; Oelert, W.; Piskor-Ignatowicz, C.; Przerwa, J.; Rozek, T.; Santo, R.; Sefzick, T.; Siemaszko, M.; Smyrski, J.; Taschner, A.; Winter, P.; Wolke, M.; Wustner, P.; Zipper, W.: **Production of η mesons in proton-proton collisions close to threshold.** *International Journal of Modern Physics* **20**(2): 708–711. DOI:10.1142/S0217751X05022238

Dimopoulou, C.; Moshammer, R.; Fischer, D.; Fainstein, P. D.; Höhr, C.; Dorn, A.; Urrutia, J. R. C. L.; Schroter, C. D.; Kollmus, H.*; Mann, R.*; Hagmann, S.*; Ullrich, J.: **Dissociative ionization of H_2 by fast protons: three-body break-up and molecular-frame electron emission.** *Journal of physics B, Atomic, molecular and optical physics* **38**(5): 593–601. DOI:10.1088/0953-4075/38/5/010

Franchetti, G.*; Hofmann, I.*; Aslaninejad, M.: **Collective emittance exchange with linear space charge forces and linear coupling.** *Physical review letters* **94**(19): 194801. DOI:10.1103/PhysRevLett.94.194801

Galonska, M.*; Hollinger, R.*; Krinberg, I. A.; Spaedtke, P.*: **Influence of an axial magnetic field on the electron temperature in a vacuum arc plasma.** *IEEE transactions on plasma science* **33**(5): 1542–1547. DOI:10.1109/TPS.2005.856504

Gutermuth, F.*; Wildermuth, H.; Radon, T.*; Fehrenbacher, G.*: **Radiation impact caused by activation of air from the future GSI accelerator facility fair.** *Radiation protection dosimetry* **115**(1): 437–440. DOI:10.1093/rpd/nci233

Hollinger, R.*; Galonska, M.*: **Status of vacuum arc ion source development for injection of high current uranium ion beams into the GSI accelerator facility.** *Nuclear instruments & methods in physics research, Section B, Beam interactions with materials and atoms* **239**(3): 227–244. DOI:10.1016/j.nimb.2005.04.062

Klingbeil, H.*: **A fast DSP-based phase-detector for closed-loop RF control in synchrotrons.** *IEEE Transactions on Instrumentation and Measurement* **54**(3): 1209–1213. DOI:10.1109/TIM.2005.847138

Parodi, K.; Crespo, P.; Eickhoff, H.*; Haberer, T.*; Pawelke, J.; Schardt, D.*; Enghardt, W.: **Random coincidences during in-beam PET measurements at microbunched therapeutic ion beams.** *Nuclear instruments & methods in physics research, Section A, Accelerators, spectrometers, detectors and associated equipment* **545**(1): 446–458. DOI:10.1016/j.nima.2005.02.002

Radon, T.*; Gutermuth, F.*; Fehrenbacher, G.*: **Monte Carlo simulations for the shielding of the future high-intensity accelerator facility fair at GSI.** *Radiation protection dosimetry* **115**(1): 212–215. DOI:10.1093/rpd/nci189

Spädtke, P.*; Tinschert, K.*: **Specific boundary conditions for the simulation of extraction for ECRIS, LIS, and H^--sources.** **160**(10): 451–456. DOI:10.1080/10420150500490200

Struckmeier, J.*: **Hamiltonian dynamics on the symplectic extended phase space for autonomous and non-autonomous systems.** *Journal of Phyiscs: Mathematical and General* **38**(6): 1257–1278. DOI:10.1088/0305-4470/38/6/006

Tahir, N. A.*; Adonin, A.; Deutsch, C.; Fortov, V. E.; Grandjouan, N.; Geil, B.; Grayaznov, V.; Hoffmann, D. H. H.*; Kulish, M.; Lomonosov, I. V.; Mintsev, V.; Ni, P.*; Nikolaev, D.; Piriz, A. R.; Shilkin, N.; Spiller, P.*; Shutov, A.; Temporal, M. Ternovoi, V.; Udrea, S.; Varentsov, D.: **Studies of heavy ion-induced high-energy density states in matter at the GSI Darmstadt SIS-18 and future FAIR facility.** *Nuclear instruments & methods in physics research, Section A, Accelerators, spectrometers, detectors and associated equipment* **544**(1): 16–26. DOI:10.1016/j.nima.2005.01.178

Tomas, R.; Bai, M.; Calaga, R.; Fischer, W.; Franchi, A.*; Rumolo, G.*: **Measurement of global and local resonance terms.** *Physical Reviews Spe-*

cial Topics Accelerators and Beams **8**(2): 024001. DOI:10.1103/PhysRevSTAB.8.024001

Winkler, M.*; Gammino, S.; Ciavola, G.; Celona, L.; Spädtke, P.*; Tinschert, K.*: **Transport of intense beams of highly charged ions.** *Radiation Effects and Defects in Solids* **160**(10): 535–543. DOI:10.1080/10420150500492453

Xiang, W.*; Spädtke, P.*; Hollinger, R.*; Galonska, M.*; Heymach, F.*: **Simulation of extraction of high current uranium beams.** *Review of scientific instruments* **76**(6): 063307. DOI:10.1063/1.1897669

2. Further external publications

Al-khateeb, A.; Boine-Frankenheim, O.; Hasse, R.; Hofmann, I.: **Longitudinal and transverse impedances and shielding effectiveness of a resistive beam pipe for arbitrary energy and frequency.** In: *High Intensity and High Brightness Hadron Beams, ICFA-HB2004, Bensheim, Germany,* AIP Conference Proceedings 773, 771p.

Benedetto, E.; Arduini, G.; Roncarolo, F.; Zimmermann, F.; Rumolo, G.; Franchetti, G.*; Ohmi, K.; Katsouleas, T.; Ghalam, A.; Feng, B.: **Effect of Lattice and Electron Distribution in Electron-Cloud Instability Simulations for the CERN SPS and LHC.** In: Horak, C: *Proceedings of 2005 Particle Accelerator Conference, May 16-20, Knoxville, Tennessee, USA,* IEEE, 387p.

Benedetto, E.; Schulte, D.; Zimmermann, F.; Franchetti, G.*; Ohmi, K.: **Emittance Growth Caused by Electron Cloud Below the Fast TMCI Threshold: Numerical Noise or True Physics?.** In: Horak, C: *Proceedings of 2005 Particle Accelerator Conference, May 16-20, Knoxville, Tennessee, USA,* IEEE, 1344p.

Bock, R. M.; Hofmann, I.; Hoffmann, D. H. H.; Logan, G.: **Inertial Confinement Fusion: Heavy Ions.** In: *Nuclear Energy,* Landolt-Börnstein: Numerical Data and Functional Relationships in Science and Technology, New Series; Energy Technologies, Vol. 3: Energy Technologies, Subvolume B, 529p.

Boine-Frankenheim, O.; Shukla, T.: **Stability of bunches for different rf wave forms.** In: *High Intensity and High Brightness Hadron Beams, ICFA-HB2004, Bensheim, Germany,* AIP Conference Proceedings 773, 360p.

Boine-Frankenheim, O.; Wei, J.: **Summary of the session on beam cooling and high brightness.** In: *High Intensity and High Brightness Hadron Beams, ICFA-HB2004, Bensheim, Germany,* AIP Conference Proceedings 773, 466p.

Calaga, R.; Abeytunge, A.; Bai, M.; Fischer, W.; Tomas, R.; Franchi, A.*: **Measurement and Optimization of Local Coupling from RHIC BPM Data .** In: Horak, C: *Proceedings of 2005 Particle Accelerator Conference, May 16-20, Knoxville, Tennessee, USA,* IEEE, 3553p.

Clemente, G.; Podlech, H.; Tiede, R.; Ratzinger, U.; Groening, L.*; Minaev, S.: **Development of a Normal Conducting CH-DTL.** In: Horak, C: *Proceedings of 2005 Particle Accelerator Conference, May 16-20, Knoxville, Tennessee, USA,* IEEE, 883p.

E. Mustafin, et al.: **Modeling of beam loss induced vacuum breakdown in heavy-ion rings.** In: *High Intensity and High Brightness Hadron Beams, ICFA-HB2004, Bensheim, Germany,* AIP Conference Proceedings 773, 222p.

Fischer, Egbert; Kurnyshov, Roman; Moritz, Gebhard; Shcherbakov, Peter: **3D Transient Process Calculations For Fast Cycling Superferric Accelerator Magnets.** In: *Proceedings of MT19, Genova, Italy, Sep. 2005,*

Forck, P.*; Bank, A. B.*; Giacomini, T.*; Peters, A.*: **Profile Monitors Based on Residual Gas Interaction.** In: *Proceedings of DIPAC 2005, Lyon, France,* 221p.

Forck, P.; Bank, A. B.*; Giacomini, T.*; Peters, A.*: **Profile Monitors Based on Residual Gas Interaction.** In: *Proceedings of DIPAC 2005, Lyon, France,* 221p.

Forck, P.*; Dorn, C.*: **Measurements with a Novel Non-Intercepting Bunch Shape Monitor at the High Current GSI-LINAC.** In: *Proceedings of DIPAC 2005, Lyon, France,* 48p.

Franchetti, G.; Hofmann, I.; Giovannozzi, M.; Martini, M.; Metral, E.: **Long term simulations of space charge and beam loss observed in the CERN PS.** In: *High Intensity and High Brightness Hadron Beams, ICFA-HB2004, Bensheim, Germany,* AIP Conference Proceedings 773, 137p.

Franchi, A.; Duperier, R.; Franchetti, G.; Gerigk, F.; Groening, L.; Hofmann, I.; Orzhekhovskaya, A.; Sauer, A.; Uriot, D.; Yaramyschev, S.: **Benchmarking linac code for the HIPPI project.** In: *High Intensity and High Brightness Hadron Beams, ICFA-HB2004, Bensheim, Germany,* AIP Conference Proceedings 773, 110p.

Galatis, A.*; Peters, A.*; Belleman, J.; Raich, U.; Zoubir, A.: **Digital Beam Position Measurement at GSI-SIS and CERN-PS.** In: *Proceedings of DIPAC 2005, Lyon, France,* 184p.

Hofmann, I.*; Franchetti, G.*; Giovannozzi, G.; Metral, E.; Qiang, J.; Ryne, R.; Cousineau, S.; Holmes, J.; Luccio, A.; Amundson, J.; Spentzouris, P.; Jones, F. W.; Machida, S.: **Benchmarking of Simulation Codes Based on the Montague Resonance in the CERN Proton Syn-**

chrotron. In: Horak, C: *Proceedings of 2005 Particle Accelerator Conference, May 16-20, Knoxville, Tennessee, USA,* IEEE, 330p.

Hofmann, I.; Franchetti, G.; Giovannozzi, M.; Martini, M.; Metral, E.; Qiang, J.; Ryne, R.: **Simulation aspects of the code benchmarking based on the CERN-PS "Montague-Resonance" experiment.** In: *High Intensity and High Brightness Hadron Beams, ICFA-HB2004, Bensheim, Germany,* AIP Conference Proceedings 773, 169p.

Kollmus, H.; Bender, M.; Bellachioma, M. C.; Mahner, E.; Krämer, A.; Westerberg, L.; Hedlund, E.; Malyshev, O. B.; Reich-Sprenger, H.: **Measurements on Ion-Beam Induced Desoprtion at GSI.** In: *High Intensity and High Brightness Hadron Beams, ICFA-HB2004, Bensheim, Germany,* AIP Conference Proceedings 773, 207p.

Kowina, P.; Kaufmann, W.; Schles, J.; Schwickert, M.*: **Optimisation of "Shoe-Box Type" Beam Position Monitors Using the Finite Element Methods.** In: *Proceedings of DIPAC 2005, Lyon, France,* 114p.

Liakin, A. D.; Skachkov, V.; Giacomini, T.*; Forck, P.*: **Improving the Reliability of IPM.** In: *Proceedings of DIPAC 2005, Lyon, France,* 150p.

Liakin, D.; Skachkov, Vl.; Barabin, S.; Forck, P.*; Giacomini, T.*; Skachkov, Vi.; Vetrov, A.; Paal, A.: **Current Status of the Advanced Residual Gas Monitor for Heavy Ion Synchrotron Applications.** In: *Proceedings of DIPAC 2005, Lyon, France,* 154p.

Mahner, E.; Bender, M.; Kollmus, H.: **oT.** In: *High Intensity and High Brightness Hadron Beams, ICFA-HB2004, Bensheim, Germany,* AIP Conference Proceedings 773, 219p.

Matos, M.*; Novikov, Y.; Attallah, F.*; Beckert, K.*; Beller, P.*; Bosch, F.*; Boutin, D.*; Franczak, B.*; Franzke, B.*; Geissel, H.*; Hausmann, M.; Hellström, M.*; Kaza, E.*; Klepper, O.*; Kluge, H.-J.*; Kozhuharov, C.*; Kratz, K.-L.; Litvinov, Y.*; Münzenberg, G.*; Nolden, F.*; Ohtsubu, T.; Patyk, Z.; Pfeiffer, B.; Schatz, H.; Scheidenberger, C.*; Stadlmann, J.*; Steck, M.*; Vorobjev, G.*; Weick, H.*; Winkler, M.*; Wollnik, H.; Yamaguchi, T.: **Direct mass measurements of neutron-rich nuclides from zink-70 fragmentation.** In: Penionzhkevich, Y. E.; Cherepanov, E. A. : *International Symposium on Exotic Nuclei: Petershof; Russia, July 5-12, 2004 EXON 2004,* New Jersey, London, Singapore, Beijing, Shanghai, Hong Kong, Tapei, Chennai: World Scientific, 96p.

Matos, M.*; Novikov, Y.; Beckert, K.*; Beller, P.*; Bosch, F.*; Boutin, D.*; Franczak, B.*; Franzke, B.*; Geissel, H.*; Hausmann, M.; Kaza, E.*; Klepper, O.*; Kluge, H.-J.*; Kozhuharov, C.*; Kratz, K.-L.; Litvinov, S.*; Litvinov, Y.*; Münzenberg, G.*; Nolden, F.*; Ohtsubu, T.; Ostrowski, A. N.; Patyk, Z.; Pfeiffer, B.; Portillo, M.; Schatz, H.; Scheidenberger, C.*; Stadlmann, J.*; Steck, M.*; Viera, D.; Vorobjev, G.; Weick, H.*; Winkler, M.*; Wollnik, H.; Yamaguchi, T.: **Direct mass measurements of short-lived neutron-rich fission fragments at the FRS-ESR facility at GSI.** In: Penionzhkevich, Y. E.; Cherepanov, E. A. : *International Symposium on Exotic Nuclei: Petershof; Russia, July 5-12, 2004 EXON 2004,* New Jersey, London, Singapore, Beijing, Shanghai, Hong Kong, Tapei, Chennai: World Scientific, 90p.

Peters, A.; Hoffmann, T.; Schwickert, M.: **Beam Diagnostic Devices and Data Acquisition for the HICAT Facility.** In: *Proceedings of DIPAC 2005, Lyon, France,* 145p.

Ronningen, R.; Bollen, G.; Blideanu, V.; Lawton, D.; Morrissey, D.; Sherrill, B.; Zeller, A.; Gomes, I. C.; Levand, A.; Momozaki, Y.; Nolen, J.; Reed, C.; Geissel, H.*; Iwase, H.*; Heilbronn, L.; Ahle, J.; Boles, J.; Reyes, S.; Stein, W.; Stoyer, M.; Beene, J. R.; Burgess, T.; Carter, K.; Conner, D.; Gabriel, T.; Mansur, L.; Remec, I.; Rennich, M.; Stracener, D.; Wendel, M.: **Radiation Simulations and Development of Concepts for High Power Beam Dumps, Catchers and Pre-separator Area Layouts for the Fragment Separators for RIA.** In: Horak, C: *Proceedings of 2005 Particle Accelerator Conference, May 16-20, Knoxville, Tennessee, USA,* IEEE, 3594p.

Rumolo, G.; Boine-Frankenheim, O.; Krämer, A.: **Estimations of Beam Lifetime in SIS18.** In: *High Intensity and High Brightness Hadron Beams, ICFA-HB2004, Bensheim, Germany,* AIP Conference Proceedings 773, 229p.

Schles, J.; Kaufmann, W.*: **New Single Shot Beam Position Monitor of the GSI High Energy Transfer Line.** In: *Proceedings of DIPAC 2005, Lyon, France,* 190p.

Schramm, U.; Bussmann, M.; Habs, D.; Khl, T.*; Beckert, K.*; Beller, P.*; Franzke, B.*; Nolden, F.*; Steck, M.*; Saathoff, G.; Reinhardt, S.; Karpuk, S.: **Laser Cooling of Relativistic Heavy Ion Beams.** In: Horak, C: *Proceedings of 2005 Particle Accelerator Conference, May 16-20, Knoxville, Tennessee, USA,* IEEE, 401p.

Spädtke, P.; Tinschert, K.; Lang, R.;Iannucci, R.: **Use of Simulations based on Experimental Data.** In: *Proceedings of the International Workshop on ECR Ion Sources, Berkeley, California,* AIP Conference Proceedings Vol. 749, 47p.

Steck, M.*; Beckert, K.*; Beller, P.*; Franzke, B.*; Nolden, F.*: **Experimental Progress in Fast Cooling in the ESR .** In: Horak, C: *Proceedings of 2005 Particle Accelerator Conference, May 16-20, Knoxville, Tennessee, USA,* IEEE, 615p.

Steck, M.*; Beckert, K.*; Beller, P.*; Franzke, B.*; Nolden, F.*: **Experimental Progress in Fast Cooling in**

the ESR. In: Horak, C: *Proceedings of 2005 Particle Accelerator Conference, May 16-20, Knoxville, Tennessee, USA,* IEEE,

Tinschert, K.; Spädtke, P.; Bossler, J.; Iannucci, R.; Lang, R.: **Experiments on Beam Extraction from the CAPRICE ECRIS.** In: *Proceedings of the International Workshop on ECR Ion Sources, Berkeley, California,* AIP Conference Proceedings Vol. 749, 241p.

Vodel, W.; Nietzsche, S.; Neubert, R.; Nawrodt, R.; Peters, A.*; Knaack, K.; Wendt, M.; Wittenburg, K.: **SQUID Based Cryogenic Current Comparator for Measurements of the Dark Current of Superconducting Cavities.** In: *Proceedings of DIPAC 2005, Lyon, France,* 163p.

Zenkevich, P.; Boine-Frankenheim, O.; Bolshakov, P.: **Kinetic effects in multiple intrabeam scattering.** In: *High Intensity and High Brightness Hadron Beams, ICFA-HB2004, Bensheim, Germany,* AIP Conference Proceedings 773, 425p.

Publications to the programme 'Physics of hadrons and nuclei': Experiments

K. Große, GSI, Darmstadt, Germany

1. Reviewed publications

Ackermann, D.*: **Beyond darmstadtium - Status and perspectives of superheavy element research.** *The European physical journal A, Hadrons and nuclei* **25**: 577–582. DOI:10.1140/epjad/i2005-06-147-4

Adamovich, M. I.; Alexandrov, Y. A.; Baranov, S. P.; Barberis, D.; Beck, M.; Berat, C.; Beusch, W.; Boss, M.; Brons, S.*; Bruckner, W.; Buenerd, M.; Busch, C.; Buscher, C.; Charignon, F.; Chauvin, J.; Chudakov, E. A.; Dersch, U.; Dropmann, F.; Engelfried, J.; Faller, F.; Fournier, A.; Gerassimov, S. G.; Godbersen, M.; Grafstrom, P.; Haller, T.; Heidrich, M.; Hubbard, E.; Hurst, R. B.; Konigsmann, K.; Konorov, I.; Keller, N.; Martens, K.; Martin, P.; Masciocchi, S.; Michaels, R.; Muller, U.; Neeb, H.; Newbold, D.; Newsom, C.; Paul, S.; Pochodzalla, J.*; Potashnikova, I.; Povh, B.; Ransome, R.; Ren, Z.; Rey-Campagnolle, M.; Rosner, G.; Rossi, L.; Rudolph, H.; Scheel, C.; Schmitt, L.; Siebert, H. W.; Simon, A.; Smith, V. J.; Thilmann, O.; Trombini, A.; Vesin, E.; Volkemer, B.; Vorwalter, K.; Walcher, T.; Walder, G.; Werding, R.; Wittmann, E.; Zavertyaev, M. V.; WA89 Collaboration: **Search for the pentaquark candidate $\Theta(1540)^+$ in the hyperon beam experiment WA89.** *Physical review C, Nuclear physics* **72**(5): 055201. DOI:10.1103/PhysRevC.72.055201

Adler, C.; Andronic, A.*; Angelov, V.; Appelshäuser, H.*; Baumann, C.; Blume, C.; Braun-Munzinger, P.*; Bucher, D.; Busch, O.*; Catanescu, V.; Chernenko, S.; Ciobanu, M.; Daues, H.*; Emschermann, D.; Fateev, O.; Foka, Y.*; Garabatos, C.*; Glasow, R.; Gottschlag, H.; Gunji, T.; Hamagaki, H.; Hehner, J.*; Heine, N.; Herrmann, N.; Inuzuka, M.; Kislov, E.; Lehmann, T.; Lindenstruth, V.; Lippmann, C.*; Ludolphs, W.; Mahmoud, T.; Marin, A.*; Miskowiec, D.*; Oyama, K.; Panebratsev, Y.; Petracek, V.; Petrovici, M.; Radu, A.*; Reygers, K.; Rusanov, I.; Sandoval, A.*; Santo, R.; Schicker, R.; Simon, R. S.*; Smykov, L.; Soltveit, H. K.; Stachel, J.; Stelzer, H.*; Stockmeier, M. R.; Tsiledakis, G.; Verhoeven, W.; Vulpescu, B.; Wessels, J. P.; Wilk, A.; Windelband, B.; Yurevich, V.; Zanevsky, Y.; Zaudtke, O.: **Electron/pion identification with ALICE TRD prototypes using a neural network algorithm.** *Nuclear instruments & methods in physics research, Section A, Accelerators, spectrometers, detectors and associated equipment* **552**(3): 364–371. DOI:10.1016/j.nima.2005.07.006

Adler, C.; Andronic, A.*; Appelshäuser, H.*; Bielcikova, J.; Blume, C.; Braun-Munzinger, P.*; Bucher, D.; Busch, O.*; Catanescu, V.; Ciolanu, M.*; Daues, H.*; Emschermann, D.; Fateev, O.; Foka, P.*; Garabatos, C.*; Gunji, T.; Herrmann, N.; Inuzuka, M.; Ivanov, M.; Kislov, E.; Lindenstruth, V.; Lippmann, C.*; Ludolphs, W.; Mahmoud, T.; Petracek, V.; Petrovici, M.; Radomski, S.*; Rusanov, I.; Sandoval, A.*; Santo, R.; Schicker, R.; Schwarz, K.*; Simon, R. S.*; Smykov, L.; Soltveit, H. K.; Stachel, J.; Stelzer, H.*; Tsiledakis, G.*; Vulpescu, B.; Wessels, J. P.; Windelband, B.; Yurevich, V.; Zanevsky, Y.; Zaudtke, O.: **Position reconstruction in drift chambers operated with Xe, CO_2 (15%).** *Nuclear instruments & methods in physics research, Section A, Accelerators, spectrometers, detectors and associated equipment* **540**(1): 140–157. DOI:10.1016/j.nima.2004.11.016

Adrich, P.*; Klimkiewicz, A.*; Fallot, M.*; Boretzky, K.*; Aumann, T.*; Cortina-Gil, D.; Datta Pramanik, U.*; Elze, T. W.; Emling, H.*; Geissel, H.*; Hellström, M.*; Jones, K. L.*; Kratz, J. V.; Kulessa, R.; Leifels, Y.*; Nociforo, C.; Palit, R.; Simon, H.*; Surówka, G.; Sümmerer, K.*; Waluś, W.; LAND/FRS Collaboration: **Evidence for pygmy and giant dipole resonances in ^{130}Sn and ^{132}Sn.** *Physical review letters* **95**(13): 132501. DOI:10.1103/PhysRevLett.95.132501

Agakichieva, G.*; Appelshäuser, H.*; Bielcikova, J.; Baur, R.; Braun-Munzinger, P.*; Cherlin, A.; Damjanovic, S.; Drees, A.; Esumi, S.; Faschingbauer, U.; Fraenkel, Z.; Fuchs, C.; Gatti, E.; Glässel, P.; Hering, G.*; de los Heros, C. P.; Holl, P.; Jung, C.; Lenkeit, B.; Marín, A.*; Messer, F.; Messer, M.; Miśkowiec, D.*; Nix, O.; Panebrattsev, Y.; Pfeiffer, A.; Rak, J.; Ravinovich, I.; Razin, S.; Rehak, P.; Richter, M.; Sampietro, M.; Sako, H.*; Saveljic, N.; Schmitz, W.; Schukraft, J.; Seipp, W.; Shimanskiy, S.; Socol, E.; Specht, H. J.; Stachel, J.*; Tel-Zur, G.; Tserruya, I.; Ullrich, T.; Voigt, C.; Voloshin, S.; Weber, C.; Wessels, J. P.; Wienold, T.; Wurm, J. P.; Yurevich, V.; CERES Collaboration: **e^+e^- -pair production in Pb-Au collisions at 158 GeV per nucleon.** *The European physical journal: C, Particles and fields* **41**(4): 475–513. DOI:10.1140/epjc/s2005-02272-3

Ageev, E. S.; Alexakhin, V. Y.; Alexandrov, Y.; Alexeev, G. D.; Amoroso, A.; Badelek, B.; Balestra, F.; Ball, J.; Baum, G.; Bedfer, Y.; Berglund, P.; Bernet, C.; Bertini, R.; Birsa, R.; Bisplinghoff, J.; Bordalo, P.; Bradamante, F.; Bravar, A.; Bressan, A.; Burtin, E.; Bussa, M. P.; Bytchkov, V. N.; Cerini, L.; Chapiro, A.; Cicuttin, A.; Colantoni, M.; Colavita, A. A.; Costa, S.; Crespo, M. L.; d'Hose, N.; Dalla Torre, S.; Dasgupta, S. S.; De Masi, R.; Dedek, N.; Denisov, O. Y.; Dhara, L.; Kavka, V. D.; Dinkelbach, A.

M.; Dolgopolov, A. V.; Donskov, S. V.; Dorofeev, V. A.; Doshita, N.; Duic, V.; Dunnweber, W.; Ehlers, J.; Eversheim, P. D.; Eyrich, W.; Fabro, M.; Faessler, M.; Falaleev, V.; Fauland, P.; Ferrero, A.; Ferrero, L.; Finger, M.; Fischer, H.; Franz, J.; Friedrich, J. M.; Frolov, V.; Fuchs, U.; Garfagnini, R.; Gautheron, F.; Gavrichtchouk, O. P.; Gerassimov, S.; Geyer, R.; Giorgi, M.; Gobbo, B.; Goertz, S.; Gorin, A. M.; Grajek, O. A.; Grasso, A.; Grube, B.; Grunemaier, A.; Hannappel, J.; von Harrach, D.; Hasegawa, T.; Hedicke, S.; Heinsius, F. H.; Hermann, R.; Hess, C.; Hinterberger, F.; von Hodenberg, M.; Horikawa, N.; Horikawa, S.; Ijaduola, R. B.; Ilgner, C.; Ioukaev, A. I.; Ishimoto, S.; Ivanov, O.; Iwata, T.; Jahn, R.; Janata, A.; Joosten, R.; Jouravlev, N. I.; Kabuss, E.; Kalinnikov, V.; Kang, D.*GAST; Karstens, F.; Kastaun, W.; Ketzer, B.; Khaustov, G.; Khokhlov, Y. A.; Khomutv, N. V.; Kisselev, Y.; Klein, F.; Koblitz, S.; Koivuniemi, J. H.; Kolosov, V. N.; Komissarov, E.; Kondo, K.; Konigsmann, K.; Konoplyannikov, A. K.; Konorov, I.; Konstantinov, V. F.; Korentchenko, A. S.; Korzenev, A.; Kotzinian, A. M.; Koutchinski, N. A.; Kowalik, K.; Kravchuk, N. P.; Krivokhizhin, G. V.; Kroumchtein, Z. V.; Kuhn, R.; Kunne, E.; Kurek, K.; Ladygin, M. E.; Lamanna, M.; Le Goff, J. M.; Leberig, M.; Lichtenstadt, J.; Liska, T.; Ludwig, I.; Maggiora, A.; Maggiora, M.; Magnon, A.; Mallot, G. K.; Manuilov, I. V.; Marchand, C.; Marroncle, J.; Martin, A.; Marzec, J.; Matsuda, T.; Maximov, A. N.; Medved, K. S.; Meyer, W.; Mielech, A.; Mikhailov, Y. V.; Moinester, M. A.; Nahle, O.; Nassalski, J.; Neliba, S.; Neyret, D. P.; Nikolaenko, V. I.; Nozdrin, A. A.; Obraztsov, V. F.; Olshevsky, A. G.; Ostrick, M.; Padee, A.; Pagano, P.; Panebianco, S.; Panzieri, D.; Paul, S.; Pereira, H. D.; Peshekhonov, D. V.; Peshekhonov, V. D.; Piragino, G.; Platchkov, S.; Platzer, K.; Pochodzalla, J.*; Polyakov, V. A.; Popov, A. A.; Pretz, J.; Quintans, C.; Ramos, S.; Rebourgeard, P. C.; Reicherz, G.; Reymann, J.; Rith, K.; Rozhdestvensky, A. M.; Rondio, E.; Sadovski, A. B.; Saller, E.; Samoylenko, V. D.; Sandacz, A.; Sans, M.; Sapozhnikov, M. G.; Savin, I. A.; Schiavon, P.; Schill, C.; Schmidt, T.; Schmitt, H.; Schmitt, L.; Shevchenko, O. Y.; Shishkin, A. A.; Siebert, H. W.; Sinha, L.; Sissakian, A. N.; Skachkova, A.; Slunecka, M.; Smirnov, G. I.; Sozzi, F.; Sugonyaev, V. P.; Srnka, A.; Stinzing, F.; Stolarski, M.; Sulc, M.; Sulej, R.; Takabayashi, N.; Tchalishev, V.; Tessarotto, F.; Teufel, A.; Thers, D.; Tkatchev, L. G.; Toeda, T.; Tretyak, V. I.; Trousov, S.; Varanda, M.; Virius, M.; Vlassov, N. V.; Wagner, M.; Webb, R.; Weise, E.; Weitzel, Q.; Wiedner, U.; Wiesmann, M.; Windmolders, R.; Wirth, S.; Wislicki, W.; Zanetti, A. M.; Zaremba, K.; Zhao, J.; Ziegler, R.; Zvyagin, A.: **Measurement of the spin structure of the deuteron in the DIS region.** *Physics letters B* **612**(3): 154–164. DOI:10.1016/j.physletb.2005.03.025

Aggarwal, M. M.; Ahammed, Z.; Angelis, A. L. S.; Antonenko, V.; Arefiev, V.; Astakhov, V.; Avdeitchikov, V.; Awes, T. C.; Baba, P. V. K. S.; Badyal, S. K.; Bathe, S.; Batiounia, B.; Bernier, T.; Bhatia, V. S.; Blume, C.; Bucher, D.; Büsching, H.; Carlen, L.; Chattopadhyay, S.; Decowski, M. P.; Delagrange, H.; Donni, P.; Dutta Majumdar, M. R.; Dubey, A. K.; El Chenawi, K.; Enosawa, K.; Fokin, S.; Frolov, V.; Ganti, M. S.; Garpman, S.; Gavrishchuk, O.; Geurts, F. J. M.; Ghosh, T. K.; Glasow, R.; Gupta, R.; Guskov, B.; Gustafsson, H. Å.; Gutbrod, H. H.*; Hrivnacova, I.; Ippolitov, M.; Kalechofsky, H.; Kamermans, R.; Karadjev, K.; Karpio, K.; Kolb, B. W.*; Kosarev, I.; Koutcheryaev, I.; Kugler, A.; Kulinich, P.; Kurata, M.; Lebedev, A.; Löhner, H.; Luquin, L.; Mahapatra, D. P.; Manko, V.; Martin, M.; Martínez, G.; Maximov, A.; Miake, Y.; Mishra, G. C.; Mohanty, B.; Mora, M.-J.; Morrison, D.; Moukhanova, T.; Mukhopadhyay, D. S.; Naef, H.; Nandi, B. K.; Nayak, S. K.; Nayak, T. K.; Nianine, A.; Nikitine, V.; Nikolaev, S.; Nilsson, P.; Nishimura, S.; Nomokonov, P.; Nystrand, J.; Oskarsson, A.; Otterlund, I.; Peitzmann, T.; Peressounko, D.; Phatak, S. C.; Pinganaud, W.; Plasil, F.; Purschke, M. L.*; Rak, J.; Raniwala, R.; Raniwala, S.; Rao, N. K.; Retiere, F.; Reygers, K.; Roland, G.; Rosselet, L.; Roufanov, I.; Roy, C.; Rubio, J. M.; Sambyal, S. S.; Santo, R.; Sato, S.; Schlagheck, H.; Schmidt, H.-R.*; Schutz, Y.; Shabratova, G.; Shah, T. H.; Sharma, A.; Sibiriak, I.; Siemiarczuk, T.; Silvermyr, D.; Sinha, B. C.; Slavine, N.; Söderström, K.; Sood, G.; Sørensen, S. P.; Stankus, P.; Stefanek, G.; Steinberg, P.; Stenlund, E.; Sumbera, M.; Svensson, T.; Tsvetkov, A.; Tykarski, L.; van der Phjll, E. C.; van Eijndhoven, N.; van Nieuwenhuizen, G. J.; Vinogradov, A.; Viyogi, Y. P.; Vodopianov, A.; Vörös, S.; Wysłouch, B.; Young, G. R.; WA98 Collaboration: **Azimuthal anisotropy of photon and charged particle emission in ^{208}Pb+^{208}*Pb* collisions at 158 A GeV/c.** *The European physical journal: C, Particles and fields* **41**(3): 287–296.

Aggarwal, M. M.; Ahammed, Z.; Angelis, A. L. S.; Antonenko, V.; Arefiev, V.; Astakhov, V.; Avdeitchikov, V.; Awes, T. C.; Baba, P. V. K. S.; Badyal, S. K.; Bathe, S.; Batiounia, B.; Bernier, T.; Bhatia, V. S.; Blume, C.; Bucher, D.; Büsching, H.; Carlén, L.; Chattopadhyay, S.; Decowski, M. P.; Delagrange, H.; Donni, P.; Dutta Majumdar, M. R.; Dubey, A. K.; El Chenawi, K.; Enosawa, K.; Fokin, S.; Frolov, V.; Ganti, M. S.; Garpman, S.; Gavrishchuk, O.; Geurts, F. J. M.; Ghosh, T. K.; Glasow, R.; Guskov, B.; Gustafsson, H. Å.; Gutbrod, H. H.*; Hrivnacova, I.; Ippolitov, M.; Kalechofsky, H.; Kamermans, R.; Karadjev, K.; Karpio, K.; Kolb, B. W.*; Kosarev, I.; Koutcheryaev, I.; Kugler, A.; Kulinich, P.; Kurata, M.; Lebedev, A.; Löhner, H.; Luquin, L.; Mahapatra, D. P.; Manko, V.; Martin, M.; Martínez, G.; Maximov, A.; Miake, Y.; Mishra, G. C.; Mohanty, B.; Mora, M.-J.; Morrison, D.; Mukhanova, T.; Mukhopadhyay, D. S.; Naef, H.; Nandi, B. K.; Nayak, S. K.; Nayak, T. K.; Nianine, A.; Nikitine, V.; Nikolaev, S.; Nilsson, P.; Nishimura, S.; Nomokonov, P.; Nystrand, J.; Oskarsson, A.; Otterlund, I.; Peitzmann, T.; Peressounko, D.; Petracek, V.; Phatak, S. C.; Pinganaud, W.; Plasil, F.; Purschke, M. L.*; Rak, J.; Raniwala, R.; Raniwala, S.; Rao, N. K.; Retiere, F.; Reygers, K.; Roland, G.; Rosselet, L.; Roufanov, I.; Roy, C.; Rubio, J. M.; Sam-

byal, S. S.; Santo, R.; Sato, S.; Schlagheck, H.; Schmidt, H.-R.*; Schutz, Y.; Shabratova, G.; Shah, T. H.; Sibiriak, I.; Siemiarczuk, T.; Silvermyr, D.; Sinha, B. C.; Slavine, N.; Söderström, K.; Sood, G.; Sørensen, S. P.; Stankus, P.; Stefanek, G.; Steinberg, P.; Stenlund, E.; Sumbera, M.; Svensson, T.; Tsvetkov, A.; Tykarski, L.; Pijll, E. C. V. D.; Eijndhoven, N. V.; Nieuwenhuizen, G. J. V.; Vinogradov, A.; Viyogi, Y. P.; Vodopianov, A.; Vörös, S.; Wysłouch, B.; Young, G. R.; WA98 Collaboration: **Centrality and transverse momentum dependence of collective flow in 158 A GeV Pb+Pb collisions measured via inclusive photons.** *Nuclear physics A, Nuclear and hadronic physics* **762**(1): 129–146. DOI:10.1016/j.nuclphysa.2005.08.004

Aguilera, D. N.; Blaschke, D.*; Buballa, M.; Yudichev, V. L.: **Color-spin locking phase in two-flavor quark matter for compact star phenomenology.** *Physical Review D* **72**(3): 034008. DOI:10.1103/PhysRevD.72.034008

Aguilera, D. N.; Blaschke, D.*; Grigorian, H.: **How robust is a 2SC quark matter phase under compact star constraints?.** *Nuclear physics A, Nuclear and hadronic physics* **757**(3): 527–542. DOI:10.1016/j.nuclphysa.2005.04.009

Alt, C.; Anticic, T.; Baatar, B.; Barna, D.; Bartke, J.; Betev, L.; Białkowska, H.; Billmeier, A.; Blume, C.*; Boimska, B.; Botje, M.; Bracinik, J.; Bramm, R.; Brun, R.; Bunčić, P.; Cerny, V.; Christakoglou, P.; Chvala, O.; Cramer, J. G.; Csató, P.; Darmenov, N.; Dimitrov, A.; Dinkelaker, P.; Eckardt, V.; Farantatos, G.; Flierl, D.; Fodor, Z.; Foka, P.*; Freund, P.; Friese, V.*; Gál, J.; Gazdzicki, M.; Georgopoulos, G.; Gładysz, E.; Grebieszkow, K.; Hegyi, S.; Höhne, C.; Kadija, K.; Karev, A.; Kliemant, M.; Kniege, S.; Kolesnikov, V. I.; Kollegger, T.; Kornas, E.; Korus, R.; Kowalski, M.; Kraus, I.*; Kreps, M.; van Leeuwen, M.; Lévai, P.; Litov, L.; Lungwitz, B.; Makariev, M.; Malakhov, A. I.; Markert, C.*; Mateev, M.; Mayes, B. W.; Melkumov, G. L.; Meurer, C.; Mischke, A.*; Mitrovski, M.; Molnár, J.; Mrówczyński, S.; Palla, G.; Panagiotou, A. D.; Panayotov, D.; Petridis, A.; Pikna, M.; Pinsky, L.; Pühlhofer, F.; Reid, J. G.; Renfordt, R.; Richard, A.; Roland, C.; Roland, G.; Rybczyński, M.; Rybicki, A.; Sandoval, A.*; Sann, H.*; Schmitz, N.; Seyboth, P.; Siklér, F.; Sitar, B.; Skrzypczak, E.; Stefanek, G.; Stock, R.; Ströbele, H.; Susa, T.; Szentpétery, I.; Sziklai, J.; Trainor, T. A.; Varga, D.; Vassiliou, M.; Veres, G. I.; Vesztergombi, G.; Vranić, D.*; Wetzler, A.; Włodarczyk, Z.; Yoo, I. K.; Zaranek, J.; Zimányi, J.; NA49 Collaboration: Ω^- **and** $\overline{\Omega}^+$ **production in central Pb+Pb collisions at 40 and 158A GeV.** *Physical review letters* **94**(19): 192301. DOI:10.1103/PhysRevLett.94.192301

Alt, C.; Anticic, T.; Baatar, B.; Barna, D.; Bartke, J.; Betev, L.; Białkowska, H.; Billmeier, A.; Blume, C.*; Boimska, B.; Botje, M.; Bracinik, J.; Bramm, R.; Brun, R.; Bunčić, P.; Cerny, V.; Christakoglou, P.; Chvala, O.; Cramer, J. G.; Csató, P.; Darmenov, N.; Dimitrov, A.; Dinkelaker, P.; Eckardt, V.; Farantatos, G.; Flierl, D.; Fodor, Z.; Foka, P.*; Freund, P.; Friese, V.*; Gál, J.; Gaździcki, M.; Georgopoulos, G.; Gładysz, E.; Grebieszkow, K.; Hegyi, S.; Höhne, C.*; Kadija, K.; Karev, A.; Kliemant, M.; Kniege, S.; Kolesnikov, V. I.; Kollegger, T.; Kornas, E.; Korus, R.; Kowalski, M.; Kraus, I.*; Kreps, M.; van Leeuwen, M.; Lévai, P.; Litov, L.; Lungwitz, B.; Makariev, M.; Malakhov, A. I.; Markert, C.; Mateev, M.; Mayes, B. W.; Melkumov, G. L.; Meurer, C.; Mischke, A.*; Mitrovski, M.; Molnár, J.; Mrówczyński, S.; Pálla, G.; Panagiotou, A. D.; Panayotov, D.; Petridis, A.; Pikna, M.; Pinsky, L.; Pühlhofer, F.; Reid, J. G.; Renfordt, R.; Richard, A.; Roland, C.; Roland, G.; Rybczyński, M.; Rybicki, A.; Sandoval, A.*; Sann, H.*; Schmitz, N.; Seyboth, P.; Sikler, F.; Sitar, B.; Skrzypczak, E.; Stefanek, G.; Stock, R.; Ströbele, H.; Susa, T.; Szentpétery, I.; Sziklai, J.; Trainor, T. A.; Trubnikov, V.; Varga, D.; Vassiliou, M.; Veres, G. I.; Vesztergombi, G.; Vranić, D.*; Wetzler, A.; Włodarczyk, Z.; Yoo, I. K.; Zaranek, J.; Zimányi, J.: **System-size dependence of strangeness production in nucleus-nucleus collisions at $\sqrt{s_{NN}}$=17.3 GeV.** *Physical review letters* **94**(5): 052301. DOI:10.1103/PhysRevLett.94.052301

Alt, C.; Anticic, T.; Baatar, B.; Barna, D.; Bartke, J.; Betev, L.; Białkowska, H.; Billmeier, A.; Blume, C.*; Boimska, B.; Botje, M.; Bracinik, J.; Bramm, R.; Brun, R.; Bunčić, P.; Cerny, V.; Christakoglou, P.; Chvala, O.; Cramer, J. G.; Csató, P.; Darmenov, N.; Dimitrov, A.; Dinkelaker, P.; Eckardt, V.; Farantatos, G.; Flierl, D.; Fodor, Z.; Foka, P.*; Freund, P.; Friese, V.*; Gál, J.; Gaździcki, M.; Georgopoulos, G.; Gładysz, E.; Grebieszkow, K.; Hegyi, S.; Höhne, C.; Kadija, K.; Karev, A.; Kliemant, M.; Kniege, S.; Kolesnikov, V. I.; Kollegger, T.; Kornas, E.; Korus, R.; Kowalski, M.; Kraus, I.*; Kreps, M.; van Leeuwen, M.; Lévai, P.; Litov, L.; Lungwitz, B.; Makariev, M.; Malakhov, A. I.; Markert, C.*; Mateev, M.; Mayes, B. W.; Melkumov, G. L.; Meurer, C.; Mischke, A.*; Mitrovski, M.; Molnár, J.; Mrówczyński, S.; Pálla, G.; Panagiotou, A. D.; Panayotov, D.; Petridis, A.; Pikna, M.; Pinsky, L.; Pühlhofer, F.; Reid, J. G.; Renfordt, R.; Richard, A.; Roland, C.; Roland, G.; Rybczyński, M.; Rybicki, A.; Sandoval, A.*; Sann, H.*; Schmitz, N.; Seyboth, P.; Siklér, F.; Sitar, B.; Skrzypczak, E.; Stefanek, G.; Stock, R.; Ströbele, H.; Susa, T.; Szentpétery, I.; Sziklai, J.; Trubnikov, V.; Varga, D.; Vassiliou, M.; Veres, G. I.; Vesztergombi, G.; Vranić, D.*; Wetzler, A.; Włodarczyk, Z.; Yoo, I. K.; Zaranek, J.; Zimányi, J.; NA49 Collaboration: **System size and centrality dependence of the balance function in A+A collisions at root S-NN=17.2 GeV.** *Physical review C, Nuclear physics* **71**(3): 034903. DOI:10.1103/PhysRevC.71.034903

Andreyev, A. N.; Ackermann, D.*; Antalic, S.; Darby, I. G.; Franchoo, S.; Heßberger, F. P.*; Hofmann, S.*; Huyse, M.; Kuusiniemi, P.*; Lommel, B.*; Kindler, B.*; Mann, R.*; Münzenberg, G.*; Page, R. D.; Saro, S.; Sulignano, B.*; Streicher, B.; Van de Vel, K.; Van Duppen, P.; Wise-

man, D. R.: **Cross section systematics for the lightest Bi and Po nuclei produced in complete fusion reactions with heavy ions.** *Physical review C, Nuclear physics* **72**(1): 014612. DOI:10.1103/PhysRevC.72.014612

Andronic, A.*; Barret, V.; Basrak, Z.; Bastid, N.; Benabderrahmane, L.; Berek, G.; Čaplar, R.; Cordier, E.; Crochet, P.; Dupieux, P.; Dželalija, M.; Fodor, Z.; Gasparic, I.; Grishkin, Y.; Hartmann, O. N.*; Herrmann, N.; Hildenbrand, K. D.*; Hong, B.; Kecskemeti, J.; Kim, Y. J.; Kirejczyk, M.*; Koczon, P.*; Korolija, M.; Kotte, R.; Kress, T.*; Lebedev, A.; Leifels, Y.*; Lopez, X.; Mangiarotti, A.; Merschmeyer, M.; Neubert, W.; Pelte, D.; Petrovici, M.; Rami, F.; Reisdorf, W.*; de Schauenburg, B.; Schüttauf, A.*; Seres, Z.; Sikora, B.; Sim, K. S.; Simion, V.; Siwek-Wilczyńska, K.; Smolyankin, V.; Stockmeier, M. R.; Stoicea, G.; Tyminski, Z.*; Wagner, P.; Wiśniewski, K.; Wohlfarth, D.; Xiao, Z.-G.*; Yushmanov, I.; Zhilin, A.; FOPI Collaboration: **Excitation function of elliptic flow in Au plus Au collisions and the nuclear matter equation of state.** *Physics letters B* **612**(3): 173–180. DOI:10.1016/j.physletb.2005.02.060

Appelshäuser, H.*; Sako, H.*; CERES Collaboration: **Event-by-event fluctuations at SPS.** *Nuclear physics A, Nuclear and hadronic physics* **752**: 394C–397C. DOI:10.1016/j.nuclphysa.2005.02.142

Aprahamian, A.; Langanke, K.; Wiescher, M.: **Nuclear structure aspects in nuclear astrophysics.** *Progress in particle and nuclear physics* **54**(2): 535–613. DOI:10.1016/j.ppnp.2004.09.002

Audouin, L.; Tassan-Got, L.; Armbruster, P.*; Schmidt, K.-H.*; Stéphan, C.; Taieb, J.*: **Recoil spectrometers for heavy-ion identification and secondary-beam production: Pushing the low-energy limit.** *Nuclear instruments & methods in physics research, Section A, Accelerators, spectrometers, detectors and associated equipment* **548**(3): 517–539. DOI:10.1016/j.nima.2005.04.073

Aumann, T.*: **Nuclear structure at the dripline.** *Nuclear physics A, Nuclear and hadronic physics* **752**: 289C–298C. DOI:10.1016/j.nuclphysa.2005.02.114

Aumann, T.*: **Reactions with fast radioactive beams of neutron-rich nuclei.** *The European physical journal A, Hadrons and nuclei* **26**(3): 441–478. DOI:10.1140/epja/i2005-10173-4

Bäumer, C.; van den Berg, A. M.; Davids, B.; Frekers, D.; De Frenne, D.; Grewe, E.-W.; Haefner, P.; Harakeh, M. N.; Hofmann, F.; Hollstein, S.; Hunyadi, M.; de Huu, M. A.; Jacobs, E.; Junk, B. C.; Korff, A.; Langanke, K.; Martínez-Pinedo, G.; Negret, A.; von Neumann-Cosel, P.; Popescu, L.; Rakers, S.; Richter, A.; Wörtche, H. J.: **Determination of the Gamow-Teller strength distribution from the odd-odd nucleus ^{50}V measured through V-50(d,^{2}He)^{50}Ti and astrophysical implications.** *Physical review C, Nuclear physics* **71**(2): 024603. DOI:10.1103/PhysRevC.71.024603

Ball, G. C.; Achtzehn, T.; Albers, D.; Al Khalili, J. S.; Andreoiu, C.; Andreyev, A.; Ashley, S. F.; Austin, R. A. E.; Becker, J. A.; Bricault, P.; Chan, S.; Chakrawarthy, R. S.; Churchman, R.; Coombes, H.; Cunningham, E. S.; Daoud, J.; Dombsky, M.; Drake, T. E.; Eshpeter, B.; Finlay, P.; Garrett, P. E.; Geppert, C.; Grinyer, G. F.; Hackman, G.; Hanemaayer, V.; Hyland, B.; Jones, G. A.; Koopmans, K. A.; Kulp, W. D.; Lassen, J.; Lavoie, J. P.; Leslie, J. R.; Litvinov, Y.*; Macdonald, J. A.; Mattoon, C.; Melconian, D.; Morton, A. C.; Osborne, C. J.; Pearson, C. J.; Pearson, M.; Phillips, A. A.; Ressler, J. J.; Sarazin, F.; Schumaker, M. A.; Schwarzenberg, J.; Scraggs, H. C.; Smith, M. B.; Svensson, C. E.; Valiente-Dobon, J. J.; Waddington, J. C.; Walker, P. M.; Wendt, K.; Williams, S. J.; Wood, J. L.; Zganjar, E. F.: **High-resolution gamma-ray spectroscopy: a versatile tool for nuclear beta-decay studies at TRIUMF-ISAC.** *Journal of physics G, Nuclear and particle physics* **31**(10): S1491–S1498. DOI:10.1088/0954-3899/31/10/019

Banu, A.*; Gerl, J.*; Fahlander, C.; Górska, M.*; Grawe, H.*; Saito, T. R.*; Wollersheim, H.-J.*; Caurier, E.; Engeland, T.; Gniady, A.; Hjorth-Jensen, M.; Nowacki, F.; Beck, T.*; Becker, F.*; Bednarczyk, P. L.*; Bentley, M. A.; Bürger, A.; Cristancho, F.; de Angelis, G.; Dombradi, Z.; Doornenbal, P.*; Geissel, H.*; Grebosz, J.*; Hammond, G.; Hellström, M.*; Jolie, J.; Kojouharov, I.*; Kurz, N.*; Lozeva, R.*; Mandal, S.*; Marginean, N.; Muralithar, S.*; Nyberg, J.; Pochodzalla, J.; Prokopowicz, W.*; Reiter, P.; Rudolph, D.; Rusu, C.; Saito, N.*; Schaffner, H.; Sohler, D.; Weick, H.*; Wheldon, C.*; Winkler, M.*: ^{108}**Sn studied with intermediate-energy Coulomb excitation.** *Physical review C, Nuclear physics* **72**(6): 061305. DOI:10.1103/PhysRevC.72.061305

Bastid, N.; Andronic, A.*; Barret, V.; Basrak, Z.; Benabderrahmane, M. L.; Čaplar, R.; Cordier, E.; Crochet, P.; Dupieux, P.; Dželalija, M.; Fodor, Z.; Gašparic, I.; Gobbi, A.*; Grishkin, Y.; Hartmann, O. N.*; Herrmann, N.; Hildenbrand, K. D.*; Hong, B.; Kecskemeti, J.; Kim, Y. J.*; Kirejczyk, M.*; Koczon, P.*; Korolija, M.; Kotte, R.; Kress, T.*; Lebedev, A.; Leifels, Y.*; Lopez, X.; Mangiarotti, A.; Manko, V.; Merschmeyer, M.; Moisa, D.; Neubert, W.; Pelte, D.; Petrovici, M.; Rami, F.; Reisdorf, W.*; Schuettauf, A.*; Seres, Z.; Sikora, B.; Sim, K. S.; Simion, V.*; Siwek-Wilczyńska, K.; Smolarkiewicz, M. M.; Smolyankin, V.; Soliwoda, I. J.; Stockmeier, M. R.; Stoicea, G.; Tyminski, Z.*; Wiśniewski, K.; Wohlfarth, D.; Xiao, Z.*; Yushmanov, I.; Zhilin, A.; Ollitrault, J. Y.; Borghini, N.; FOPI Collaboration: **First analysis of anisotropic flow with Lee-Yang zeros.** *Physical review C, Nuclear physics* **72**(1): 011901. DOI:10.1103/PhysRevC.72.011901

Becker, F.*; Banu, A.*; Beck, T.*; Bednarczyk, P.*; Door-

nenbal, P.*; Geissel, H.*; Gerl, J.*; Górska, M.*; Grawe, H.*; Grebosz, J.*; Hellström, M.*; Kojouharov, I.*; Kurz, N.*; Lozeva, R.*; Mandal, S.*; Muralithar, S.; Prokopowicz, W.*; Saito, N.*; Saito, T. R.*; Schaffner, H.*; Weick, H.*; Wheldon, C.*; Winkler, M.*; Wollersheim, H. J.*; Jolie, J.; Reiter, P.; Warr, N.; Burger, A.; Hubel, H.; Simpson, J.; Bentley, M. A.; Hammond, G.; Benzoni, G.; Bracco, A.; Camera, F.; Million, B.; Wieland, O.; Kmiecik, M.; Maj, A.; Meczynski, W.; Styczeń, J.; Fahlander, C.; Rudolph, D.: **Status of the RISING project at GSI.** *The European physical journal A, Hadrons and nuclei* **25**: 719–722. DOI:10.1140/epjad/i2005-06-170-5

Bednarczyk, P.*; Banu, A.*; Beck, T.*; Becker, F.*; Bentley, M. A.; Benzoni, G.; Bracco, A.; Brger, A.; Camera, F.; Doornenbal, P.*; Fahlander, C.; Geissel, H.*; Gerl, J.*; Górska, M.*; Grawe, H.*; Grebosz, J.*; Hammond, G.; Hellström, M.*; Hbel, H.; Jolie, J.; Kmiecik, M.; Kojouharov, I.*; Kurz, N.*; Lozeva, R.*; Maj, A.; Mandal, S.*; Meczyński, W.; Million, B.; Muralithar, S.*; Reiter, P.; Rudolph, D.; Saito, N.*; Saito, T. R.*; Schaffner, H.*; Simpson, J.; Styczeń, J.; Warr, N.; Weick, H.*; Wheldon, C.*; Wieland, O.; Winkler, M.*; Wollersheim, H.-J.*: **Status of the RISING project at relativistic energies.** *Acta physica Polonica B, Particle physics and field theory, nuclear physics, theory of relativity* **36**(4): 1235–1244.

Bielcik, J.*; Agakishiev, G.; Agodi, C.; Alvarez-Pol, H.; Balanda, A.; Bellia, G.; Böhmer, M.; Boyard, J. L.; Braun-Munzinger, P.*; Chernenko, S.; Christ, T.; Coniglione, R.; Djeridi, R.; Dohrmann, F.; Durán, I.; Eberl, T.; Fabbietti, L.; Fateev, O.; Finocchiaro, P.; Friese, J.; Fröhlich, I.; Garzón, J. A.; Gernhäuser, R.; Golubeva, M.; González-Daz, D.; Grosse, E.; Guber, F.; Hennino, T.; Hlavac, S.; Holzmann, R.*; Ierusalimov, A.; Iori, I.; Jaskula, M.; Jurkovic, M.; Kämpfer, B.; Kanaki, K.; Karavicheva, T.; Koenig, I.*; Koenig, W.*; Kolb, B. W.*; Kottel, R.; Kotulic-Bunta, J.; Krücken, R.; Kugler, A.; Kühn, W.; Kulessa, R.; Kurepin, A.; Lang, S.*; Lehnert, J.; Maiolino, C.; Markert, J.; Metag, V.; Mousa, J.; Münch, M.*; Müntz, C.; Naumann, L.; Novotny, R.; Novotny, J.; Otwinowski, J.; Pachmayer, Y. C.; Pant, L. M.; Pechenov, V.; Pérez, T.; Pietraszko, J.*; Pleskac, R.*; Pospísil, V.; Przygoda, W.; Rabin, N.; Ramstein, B.; Reshetin, A.; Ritman, J.; Roy-Stephan, M.; Rustamov, A.*; Sadovsky, A.; Sailer, B.; Salabura, P.; Sánchez, M.; Sapienza, P.; Schmah, A.*; Simon, R.*; Smolyankin, V.; Smykov, L.; Spataro, S.; Spruck, B.; Stroebele, H.; Stroth, J.*; Sturm, C.*; Sudol, M.*; Tlusty, P.; Toia, A.; Traxler, M.*; Tsertos, H.; Wagner, V.; Wisniowski, M.; Wojcik, T.; Wüstenfeld, J.*; Zanevsky, Y.; Zovinec, D.*; Zumbruch, P.*: **Dilepton analysis in the HADES spectrometer for C+C at 2 a GeV.** *Journal of physics G, Nuclear and particle physics* **31**(4): S231–S237. DOI:10.1088/0954-3899/31/4/028

Bielcikova, J.; Agakichiev, G.*; Appelshäuser, H.*; Baur, R.; Braun-Munzinger, P.*; Cherlin, A.; Drees, A.; Esumi, S. I.; Filimonov, K.; Fraenkel, Z.; Fuchs, C.; Glässel, P.; Hering, G.*; Lenkeit, B.; Marín, A.*; Messer, F.; Messer, M.; Milosevic, J.; Miśkowiec, D.*; Nix, O.; Panebrattsev, Y.; Petráček, V.; Pfeiffer, A.; Rak, J.*; Ravinovich, J.; Razin, S.; Rehak, P.; Sako, H.*; Saveljic, N.; Schmitz, W.; Shimansky, S.; Socol, E.; Specht, H. J.; Stachel, J.*; Tilsner, H.; Tserruya, I.; Voigt, C.; Voloshin, S.; Weber, C.; Wessels, J. P.; Wurm, J. P.; Yurevich, V.; CERES NA45 Collaboration: **Semihard scattering unraveled from collective flow at the SPS.** *The European physical journal: C, Particles and fields* **43**(1): 323–327. DOI:10.1140/epjc/s2005-02320-0

Blaschke, D.*; Fredriksson, S.; Grigorian, H.; Öztas, A. M.; Sandin, F.: **Phase diagram of three-flavor quark matter under compact star constraints.** *Physical Review D* **72**(6): 065020. DOI:10.1103/PhysRevD.72.065020

Blaschke, D.; Grigorian, H.; Khalatyan, A.; Voskresensky, D. N.*: **Exploring the QCD phase diagram with compact stars.** *Nuclear Physics B - Proceedings Supplements* **141**: 137–142. DOI:10.1016/j.nuclphysbps.2004.12.021

Block, M.*; Ackermann, D.*; Beck, D.*; Blaum, K.*; Breitenfeldt, M.; Chauduri, A.; Doemer, A.; Eliseev, S.*; Habs, D.; Heinz, S.; Herfurth, F.*; Heßberger, F. P.*; Hofmann, S.*; Geissel, H.*; Kluge, H.-J.*; Kolhinen, V.; Marx, G.*; Neumayr, J. B.; Mukherjee, M.*; Petrick, M.; Plass, W.; Quint, W.*; Rahaman, S.*; Rauth, C.*; Rodriguez, D.; Scheidenberger, C.*; Schweikhard, L.; Suhonen, M.; Thirolf, P. G.; Wang, Z.; Weber, C.*; SHIPTRAP Collaboration: **The ion-trap facility SHIPTRAP - Status and perspectives.** *The European physical journal A, Hadrons and nuclei* **25**: 49–50. DOI:10.1140/epjad/i2005-06-013-5

Braun, J.; Klein, B.*; Pirner, H. J.: **Influence of quark boundary conditions on the pion mass in finite volume.** *Physical Review D* **72**(3): 034017. DOI:10.1103/PhysRevD.72.034017

Braun-Munzinger, P.*: **Relativistic nuclear collisions and the QCD phase boundary.** *Nuclear physics A, Nuclear and hadronic physics* **751**: 127C–138C. DOI:10.1016/j.nuclphysa.2005.02.100

Brekiesz, M.; Papka, P.; Maj, A.; Kmiecik, M.; Beck, C.; Bednarczyk, P.*; Grebosz, J.*; Haas, F.; Meczynski, W.; Rauch, V.; Rousseau, M.; Zafra, A. S. I.; Styczen, J.; Thummerer, S.; Zieblinski, M.; Zuber, K.: **Study of deformation effects in the charged particle emission from ^{46}Ti.** *Acta physica Polonica B, Particle physics and field theory, nuclear physics, theory of relativity* **36**(4): 1175–1180.

Brger, A.; Saito, T.*; Al-Khatib, A.; Banu, A.*; Beck, T.*; Becker, F.*; Bednarczyk, P.*; Benzoni, G.; Bracco, A.; Bringel, P.; Camera, F.; Clement, E.; Doornenbal, P.; Geissel, H.*; Gerl, J.*; Górska, M.*; Görgen, A.; Grawe, H.*; Grebosz, J.*; Hammond, G.; Hellström, M.*; Hbel,

H.; Kavatsyuk, M.*; Kavatsyuk, O.*; Kmiecik, M.; Kojouharov, I.*; Kurz, N.*; Lozeva, R.*; Maj, A.; Mandal, S.*; Meczyński, W.; Mehta, D.; Million, B.; Muralithar, S.; Neusser, A.; Podolyák, Z.; Reddy, T. S.; Reiter, P.; Saito, N.*; Schaffner, H.*; Singh, A. K.; Weick, H.*; Wieland, O.; Wheldon, C.; Winkler, M.*; Wollersheim, H.-J.*: **Relativistic coulomb excitation of ^{54,56,58}Cr.** *Acta physica Polonica B, Particle physics and field theory, nuclear physics, theory of relativity* **36**(4): 1249–1252.

Bürger, A.; Saito, T. R.*; Grawe, H.*; Hubel, H.; Reiter, P.; Gerl, J.*; Górska, M.*; Wollersheim, H. J.*; Al-Khatib, A.; Banu, A.*; Beck, T.*; Becker, F.*; Bednarczyk, P.*; Benzoni, G.; Bracco, A.; Brambilla, S.; Bringel, P.; Camera, F.; Clément, E.; Doornenbal, P.; Geissel, H.*; Görgen, A.; Grebosz, J.*; Hammond, G.; Hellström, M.*; Honma, M.; Kavatsyuk, A.*; Kavatsyuk, O.*; Kmiecik, M.; Kojouharov, I.*; Korten, W.; Kurz, N.*; Lozeva, R*.; Maj, A.; Mandal, S.*; Million, B.; Muralithar, S.; Neusser, A.; Nowacki, F.; Otsuka, T.; Podolyák, Z.; Saito, N.*; Singh, A. K.; Weick, H.*; Wheldon, C.; Wieland, O.; Winkler, M.*; RISING Collaboration: **Relativistic Coulomb excitation of neutron-rich ^{54,55,56}Cr: On the pathway of magicity from N=40 to N=32.** *Physics letters B* **622**(1): 29–34. DOI:10.1016/j.physletb.2005.07.004

Buyukcizmeci, N.; Ogul, R.; Botvina, A. S.*: **Isospin and symmetry energy effects on nuclear fragment production in liquid-gas-type phase transition region.** *The European physical journal A, Hadrons and nuclei* **25**(1): 57–64. DOI:10.1140/epja/i2004-10281-7

Caamaño, M.; Walker, P. M.; Regan, P. H.; Pfützner, M.; Podolyák, Z.; Gerl, J.*; Hellström, M.*; Mayet, P.*; Mineva, M. N.; Aprahamian, A.; Benlliure, J.; Bruce, A. M.; Butler, P. A.; Cortina Gil, D.*; Cullen, D. M.; Döring, J.*; Enqvist, T.*; Fox, C.; Garc{éss Narro, J.; Geissel, H.*; Gelletly, W.; Giovinazzo, J.; Górska, M.*; Grawe, H.*; Grzywacz, R.; Kleinböhl, A.*; Korten, W.; Lewitowicz, M.; Lucas, R.; Mach, H.; O'Leary, C. D.; De Oliveira, F.; Pearson, C. J.; Rejmund, F.; Rejmund, M.; Sawicka, M.; Schaffner, H.*; Schlegel, C.; Schmidt, K.*; Schmidt, K.-H.*; Stevenson, P. D.; Theisen, C.; Vivés, F.; Warner, D. D.; Wheldon, C.*; Wollersheim, H. J.*; Wooding, S.*; Xu, F.; Yordanov, O.*: **Isomers in neutron-rich A $\approx$ to 190 nuclides from ^{208}Pb fragmentation.** *The European physical journal A, Hadrons and nuclei* **23**(2): 201–215. DOI:10.1140/epja/i2004-10079-7

Chakrawarthy, R. S.; Walker, P. M.; Smith, M. B.; Andreyev, A. N.; Ashley, S. F.; Ball, G. C.; Becker, J. A.; Daoud, J. J.; Garrett, P. E.; Hackman, G.; Jones, G. A.; Litvinov, Y.*; Morton, A. C.; Pearson, C. J.; Svensson, C. E.; Williams, S. J.; Zganjar, E. F.: **Discovery of a new 2.3 s isomer in neutron-rich ^{174}Tm.** *The European physical journal A, Hadrons and nuclei* **25**: 125–126. DOI:10.1140/epjad/i2005-06-169-x

Chulkov, L. V.*; Aksouh, F.*; Bleile, A.*; Bochkarev, O. V.*; Cortina-Gil, D.; Dobrovolsky, A.; Egelhof, P.*; Geissel, H.*; Hellström, M.*; Isaev, N. B.; Kiselev, O. A.; Komkov, B. G.; Matos, M.*; Moroz, F. N.; Münzenberg, G.*; Mutterer, M.; Mylnikov, V. A.; Neumaier, S. R.*; Pribora, V. N.*; Seliverstov, D. M.; Sergeev, L. O.; Shrivastava, A.; Sümmerer, K.*; Torilov, S. Y.; Weick, H.*; Winkler, M.*; Yatsoura, V. I.: **Quasi-free scattering with ^{6,8}He beams.** *Nuclear physics A, Nuclear and hadronic physics* **759**(1): 43–63. DOI:10.1016/j.nuclphysa.2005.05.148

Chulkov, L. V.*; Simon, H.*; Thompson, I. J.; Aumann, T.* L; Borge, M. J. G.; Elze, T. W.; Emling, H.*; Geissel, H.*; Grigorenko, L. V.*; Hellström, M.*; Jonson, B.; Kratz, J. W. V.; Kulessa, R.; Markenroth, K.; Meister, M.*; Münzenberg, G.*; Nickel, F.*; Nilsson, T.; Nyman, G.; Pribora, V.; Richter, A.; Riisager, K.; Scheidenberger, C.*; Schrieder, G.; Tengblad, O.; Zhukov, M. V.: **Three-body correlations in electromagnetic dissociation of Borromean nuclei: The ^{6}He case.** *Nuclear physics A, Nuclear and hadronic physics* **759**(1): 23–42. DOI:10.1016/j.nuclphysa.2005.05.001

Cleymans, J.; Redlich, K.*; Turko, L.: **Thermodynamic limit and semi-intensive quantities.** *Journal of physics G, Nuclear and particle physics* **31**(12): 1421–1435.

Cortina-Gil, D.; Fernandez-Vazquez, J.; Aumann, T.*; Baumann, T.; Benlliure, J.; Borge, M. J. G.; Chulkov, L. V.*; Datta Pramanik, U.*; Forssén, C.; Fraile, L. M.; Geissel, H.*; Gerl, J.*; Hammache, F.*; Itahashi, K.; Janik, R.; Jonson, B.; Mandal, S.*; Markenroth, K.; Meister, M.; Mocko, M.; Muenzenberg, G.*; Ohtsubo, T.*; Ozawa, A.; Prezado, Y.; Riisager, K.; Scheit, H.; Schneider, R.; Schrieder, G.; Simon, H.; Sitar, B.; Stolz, A.; Strmen, P.; Suemmerer, K.*; Szarka, I.; Weick, H.*: **Structure of neutron-rich oxygen isotopes.** *Journal of physics G, Nuclear and particle physics* **31**(10): S1629–S1632. DOI:10.1088/0954-3899/31/10/045

Cortina-Gil, D.; Fernandez-Vazquez, J.; Aumann, T.*; Baumann, T.; Benlliure, J.; Borge, M. J. G.; Chulkov, L. V.; Datta Pramanik, U.*.; Forssén, C.; Fraile, L. M.; Geissel, H.*; Gerl, J.*; Hammache, F.; Itahashi, K.; Janik, R.; Jonson, B.; Mandal, S.*; Markenroth, K.; Meister, M.; Mocko, M.; Münzenberg, G.*; Ohtsubo, T.; Ozawa, A.; Prezado, Y.; Pribora, V.; Riisager, K.; Scheit, H.; Schneider, R.; Schrieder, G.; Simon, H.; Sitar, B.; Stolz, A.; Strmen, P.; Sümmerer, K.*; Szarka, I.; Weick, H.*: **One-neutron knockout of ^{23}O.** *The European physical journal A, Hadrons and nuclei* **25**: 343–346. DOI:10.1140/epjad/i2005-06-149-2

Cowan, T. E.; Fuchs, J.; Ruhl, H.; Sentoku, Y.; Kemp, A.; Audebert, P.; Roth, M.*; Stephens, R.; Barton, I.; Blazevic, A.*; Brambrink, E.*; Cobble, J.; Fernández, J. C.; Gauthier, J. C.; Geissel, M.*; Hegelich, M.; Kaae,

J.; Karsch, S.; Le Sage, G. P.; Letzring, S.; Manclossi, M.; Meyroneinc, S.; Newkirk, A.; Pépin, H.; Renard-LeGalloudec, N.: **Ultra-low emittance, high current proton beams produced with a laser-virtual cathode sheath accelerator.** *Nuclear instruments & methods in physics research, Section A, Accelerators, spectrometers, detectors and associated equipment* **544**(1): 277–284. DOI:10.1016/j.nima.2005.01.221

Datta Pramanik, U.*; Adrich, P.*; Aumann, T.*; Boretzky, K.*; Cortina, D.; Elze, T. W.; Emling, H.*; Geissel, H.*; Hellström, M.*; Jones, K. L.*; Khiem, L. H.; Kratz, J. V.; Kulessa, R.; Leifels, Y.*; Münzenberg, G.*; Nociforo, C.; Palit, R.*; Scheif, H.; Simon, H.*; Sümmerer, K.*; Typel, S.*; Walus, W.; Weick, H.*: **Coulomb breakup of psd-shell neutron-rich nuclei.** *Journal of physics G, Nuclear and particle physics* **31**(10): S1583–S1587. DOI:10.1088/0954-3899/31/10/037

Datta Pramanik, U.*; Aumann, T.*; Boretzky, K.*; Cortina, D.; Elze, T. W.; Emling, H.*; Geissel, H.*; Hellström, M.*; Jones, K. L.*; Khiem, L. H.; Kratz, J. V.; Kulessa, R.; Leifels, Y.*; Münzenberg, G.*; Nociforo, C.; Palit, R.*; Scheit, H.; Simon, H.*; Sümmerer, K.*; Typel, S.*; Walus, W.; Weick, H.*: **Studies of light neutron-rich nuclei near the drip line.** *The European physical journal A, Hadrons and nuclei* **25**: 339–341. DOI:10.1140/epjad/i2005-06-173-2

Denisov, V. Y.*: **Entrance-channel potentials for hot fusion reactions.** *The European physical journal A, Hadrons and nuclei* **25**: 619–620. DOI:10.1140/epjad/i2005-06-106-1

Deveaux, M.*; Berst, J. D.; de Boer, W.; Caccia, M.; Claus, G.; Deptuch, G.; Dulinski, W.; Gaycken, G.; Grandjean, D.; Jungermann, L.; Riester, J. L.; Winter, M.: **Charge collection properties of X-ray irradiated monolithic active pixel sensors.** *Nuclear instruments & methods in physics research, Section A, Accelerators, spectrometers, detectors and associated equipment* **552**(1): 118–123. DOI:10.1016/j.nima.2005.06.020

Dzhioev, A.; Wambach, J.*; Vdovin, A.; Aouissat, Z.: **Symmetry conserving 1/N expansion and extended Holstein-Primakoff mapping for anharmonic O(N+1) oscillator model.** *Nuclear physics A, Nuclear and hadronic physics* **748**(3): 551–572. DOI:10.1016/j.nuclphysa.2004.11.016

Eberl, T.; Agakishiev, G.; Agodi, C.; Alvarez-Pol, H.; Balanda, A.; Bellia, G.; Bielcik, J.*; Bähmer, M.; Boyard, J. L.; Braun-Munzinger, P.*; Chernenko, S.; Christ, T.; Coniglione, R.; Djeridi, R.; Dohrmann, F.; Durán, I.; Fabbietti, L.; Fateev, O.; Finocchiaro, P.; Friese, J.; Fröhlich, I.; Garzón, J. A.; Gernhäuser, R.; Golubeva, M.; Gonzalez-Díaz, D.; Grosse, E.; Guber, F.; Hennino, T.; Hlavac, S.; Holzmann, R.*; Ierusalimov, A.; Iori, I.; Jaskula, M.; Jurkovic, M.; Kämpfer, B.; Kanaki, K.; Karavicheva, T.; Koenig, I.*; Koenig, W.*; Kolb, B. W.*; Kotte, R.; Kotulic-Bunta, J.; Krücken, R.; Kugler, A.; Kuhn, W.; Kulessa, R.; Kurepin, A.; Lang, S.*; Lehnert, J.; Maiolino, C.; Markert, J.; Metag, V.; Mousa, J.; Münch, M.; Müntz, C.; Naumann, L.; Novotný, R.; Novotny, J.; Otwinowski, J.; Pachmayer, Y. C.*; Pant, L. M.; Pechenov, V.; Pérez, T.; Pietraszko, J.; Pleskac, R.*; Pospísil, V.; Przygoda, W.; Rabin, N.; Ramstein, B.; Reshetin, A.; Ritman, J.; Roy-Stephan, M.*; Rustamov, A.*; Sadovsky, A.; Sailer, B.; Salabura, P.; Sánchez, M.; Sapienza, P.; Schmah, A.*; Simon, R.*; Smolyankin, V.; Smykov, L.; Spataro, S.; Spruck, B.; Stroebele, H.; Stroth, J.; Sturm, C.; Sudol, M.; Tlustý, P.; Toia, A.; Traxler, A.; Tsertos, H.; Wagner, V.; Wiśniowski, M.; Wójcik, T.; Wüstenfeld, J.; Zanevsky, Y.; Zovinec, D.; Zumbruch, P.*: **Di-electron measurements in C+C reactions at 2 GeV center dot A with HADES.** *Nuclear physics A, Nuclear and hadronic physics* **752**: 433C–438C. DOI:10.1016/j.nuclphysa.2005.02.123

Eeckhaudt, S.; Amzal, N.; Bastin, J. E.; Bouchez, E.; Butler, P. A.; Chatillon, A.; Eskola, K.; Gerl, J.*; Grahn, T.; Görgen, A.; Greenlees, P. T.; Herzberg, R.-D.; Heßberger, F. P.*; Hurstel, A.; Ikin, P. J. C.; Jones, G. D.; Jones, P.; Julin, R.; Juutinen, S.; Kettunen, H.; Khoo, T. L.; Korten, W.; Kuusiniemi, P.*; Le Coz, Y.; Leino, M.; Leppänen, A. P.; Nieminen, P.; Pakarinen, J.; Perkowski, J.; Pritchard, A.; Reiters, P.; Rahkila, P.; Scholey, C.; Theisen, C.; Uusitalo, J.; Van de Vel, K.; Wilson, J.; Wollersheim, H. J.*: **In-beam gamma-ray spectroscopy of ^{254}No.** *The European physical journal A, Hadrons and nuclei* **25**: 605–607. DOI:10.1140/epjad/i2005-06-015-3

Eeckhaudt, S.; Greenlees, P. T.; Amzal, N.; Bastin, J. E.; Bouchez, E.; Butler, P. A.; Chatillon, A.; Eskola, K.; Gerl, J.*; Grahn, T.; Görgen, A.; Herzberg, R. D.; Heßberger, F. P.*; Hürstel, A.; Ikin, P. J. C.; Jones, G. D.; Jones, P.; Julin, R.; Juutinen, S.; Kettunen, H.; Khoo, T. L.; Korten, W.; Kuusiniemi, P.*; Le Coz, Y.; Leino, M.; Leppänen, A. P.; Nieminen, P.; Pakarinen, J.; Perkowski, J.; Pritchard, A.; Reiter, P.; Rahkila, P.; Scholey, C.; Theisen, C.; Uusitalo, J.; Van de Vel, K.; Wilson, J.: **Evidence for non-yrast states in No-254.** *The European physical journal A, Hadrons and nuclei* **26**(2): 227–232. DOI:10.1140/epja/i2005-10163-6

Egelhof, P.*; Kraft-Bermuth, S.*: **Heavy Ion Physics.** *Topics in applied physics* **99**: 469–500.

Förster, A.; Böttcher, I.; Dohrmann, F.; Förster, A.; Grosse, E.; Koczon, P.*; Kohlmeyer, B.; Lang, S.; Laue, F.*; Menzel, M.; Naumann, L.; Oeschler, H.; Ploskon, M.*; Pühlhofer, F.; Scheinast, W.; Schmah, A.; Schuck, T.; Schwab, E.*; Senger, P.*; Shin, Y.; Ströbele, H.; Sturm, C.; Uhlig, F.*; Wagner, A.; Walus, W.; KaoS Collaboration: **Review of the results of the KaoS Collaboration.** *Journal of physics G, Nuclear and particle physics* **31**(6): S693–S700. DOI:10.1088/0954-3899/31/6/009

Fazio, G.; Giardina, G.; Mandaglio, G.; Ruggeri, R.; Muminov, A. I.; Nasirov, A. K.; Oganessian, Y. T.; Popeko, A. G.; Sagaidak, R. N.; Yeremin, A. V.; Hofmann, S.*; Hanappe, F.; Stodel, C.: **Strong influence of the entrance channel on the formation of compound nuclei ^{216,222}Th* and their evaporation residues.** *Physical review C, Nuclear physics* **72**(6): 064614. DOI:10.1103/PhysRevC.72.064614

Fernández-Dominguez, B.; Armbruster, P.*; Audouin, L.; Benlliure, J.; Bernas, M.; Boudard, A.; Casarejos, E.; Czajkowski, S.; Ducret, J. E.; Enqvist, T.*; Jurado, B.*; Legrain, R.; Leray, S.; Mustapha, B.; Pereira, J.; Pravikoff, M.; Rejmund, F.*; Ricciardi, M. V.*; Schmidt, K. H.*; Stephan, C.; Taieb, J.; Tassan-Got, L.; Volant, C.; Wlazlo, W.: **Nuclide cross-sections of fission fragments in the reaction ^{208}Pb+p at 500 A MeV.** *Nuclear physics A, Nuclear and hadronic physics* **747**(2): 227–267. DOI:10.1016/j.nuclphysa.2004.10.013

Fernández-Domínguez, B.; Lemmon, R.; Blank, B.; Chartier, M.; Cortina-Gil, D.; Geissel, H.*; Mandal, S.*; Rejmund, F.; Sümmerer, K.*: **Production cross sections of N $\simeq$ Z nuclei in the region around A N $\simeq$ Z to 80.** *Journal of physics G, Nuclear and particle physics* **31**(10): S1843–S1846. DOI:10.1088/0954-3899/31/10/084

Fernández-Domínguez, B.; Lemmon, R. C.; Blank, B.; Chartier, M.; Cortina-Gil, D.; Durell, J. L.; Geissel, H.*; Gerl, J.*; Mandal, S.*; Rejmund, F.; Sümmerer, K.*: **Production cross-sections from neutron-deficient ^{92}Mo at 500 A MeV.** *The European physical journal A, Hadrons and nuclei* **25**(2): 193–198. DOI:10.1140/epja/i2005-10104-5

Fernández-Domínguez, B.; Lemmon, R. C.; Blank, B.; Chartier, M.; Cortina-Gil, D.; Durell, J. L.; Geissel, H.*; Gerl, J.*; Mandal, S.*; Rejmund, F.; Sümmerer, K.*: **Production cross-sections from neutron-deficient ^{92}Mo at 500A MeV (vol 25, pg 193, 2005).** *The European physical journal A, Hadrons and nuclei* **25**(3): 473–474. DOI:10.1140/epja/i2005-10159-2

Frankland, J. D.; Chbihi, A.; INDRA Collaboration; ALADIN Collaboration: **Model-independent tracking of criticality signals in nuclear multifragmentation data.** *Nuclear physics A, Nuclear and hadronic physics* **749**: 102C–105C. DOI:10.1016/j.nuclphysa.2004.12.014

Frankland, J. D.; Chbihi, A.; Mignon, A.; Begemann-Blaich, M. L.*; Bittiger, R.*; Borderie, B.; Bougault, R.; Charvet, J.-L.; Cussol, D.; Dayras, R.; Durand, D.; Escano-Rodriguez, C.; Galichet, E.; Guinet, D.; Lautesse, P.; Le Fèvre, A.*; Legrain, R.; Le Neindre, N.; Lopez, O.; Łukasik, J.*; Lynen, U.*; Manduci, L.; Marie, J.; Müller, W. F. J.*; Nalpas, L.; Orth, H.*; Pârlog, M.; Pichon, A.; Rivet, M. F.; Rosato, E.; Roy, R.; Saija, A.*; Schwarz, C.*; Sfienti, C.*; Tamain, B.; Trautmann, W.*; Trzcinski, A.; Turzó, K.*; Van Lauwe, A.; Vient, E.; Vigilante, M.; Volant, C.; Wieleczko, J. R.; Zwieglinski, B.; INDRA/ALADIN Collaboration: **Model-independent tracking of criticality signals in nuclear multifragmentation data.** *Physical review C, Nuclear physics* **71**(3): 034607. DOI:10.1103/PhysRevC.71.034607

Friese, V.*; NA49 Collaboration: **Energy dependence of strangeness production.** *Journal of physics G, Nuclear and particle physics* **31**(6): S911–S918. DOI:10.1088/0954-3899/31/6/035

Fuster, A.; Henneaux, M.; Maas, A.*: **BRST-antifield quantization: A short review.** *International Journal of Geometric Methods in Modern Physics* **2**(5): 939–963. DOI:10.1142/S0219887805000892

Fynbo, H. O. U.; Diget, C. A.; Bergmann, U. C.; Borge, M. J. G.; Cederkall, J.; Dendooven, P.; Fraile, L. M.; Franchoo, S.; Fedosseev, V. N.; Fulton, B. R.; Huang, W. X.; Huikari, J.; Jeppesen, H. B.; Jokinen, A. S.; Jones, P.; Jonson, B. R.; Köster, U.; Langanke, K.; Meister, M.; Nilsson, T.; Nyman, G.; Prezado, Y.; Rilsager, K.; Rinta-Antila, S.; Tengblad, O.; Turrion, M.; Wang, Y. B.; Weissman, L.; Wilhelmsen, K.; Äystö, J.; ISOLDE Collaboration: **Revised rates for the stellar triple-alpha process from measurement of ^{12}C nuclear resonances.** *Nature* **433**(7022): 136–139. DOI:10.1038/nature03219

Görgen, A.; Clement, E.; Bouchez, E.; Chatillon, A.; Korten, W.; Le Coz, Y.; Theisen, C.; Andreoiu, C.; Becker, F.*; Blank, B.; Burger, A.; Butler, P.; Casandjian, J. M.; Catford, W.; Czosnyka, T.; Davies, P.; Fox, S. P.; De France, G.; Georgiev, G.; Gerl, J.*; Hübel, H.; Iwanicki, J.; Jenkins, D. G.; Johnston-Theasby, F.; Joshi, P.; Matea, I.; Napiorkowski, P.; De Oliveira Santos, F. D.; Sletten, G.; Timis, C.; Wadsworth, R.; Zielinska, M.: **Shape coexistence in light krypton isotopes.** *Acta physica Polonica B, Particle physics and field theory, nuclear physics, theory of relativity* **36**(4): 1281–1288.

Gadea, A.; Lenzi, S. M.; Napoli, D. R.; Axiotis, M.; Ur, C. A.; Martínez-Pinedo, G.; Górska, M.*; Roeckl, E.*; Caurier, E.; Nowacki, F.; de Angelis, G.; Batist, L.; Borcea, R.*; Brandolini, F.; Cano-Ott, D.; Döring, J.*; Fahlander, C.; Farnea, E.; Grawe, H.*; Hellström, M.; Janas, Z.*; Kirchner, R.*; La Commara, M.*; Mazzocchi, C.*; Nácher, E.; Plettner, C.; Plochocki, A.; Rubio, B.; Schmidt, K.*; Schwengner, R.; Tain, J. L.; Żylicz, J.: **Hindered E4 decay of the 12^{+} yrast trap in ^{52}Fe.** *Physics letters B* **619**(1): 88–94. DOI:10.1016/j.physletb.2005.05.073

Garnsworthy, A. B.; Thompson, N. J.; Podolyak, Z.; Walker, P. M.; Williams, S. J.; Dracoulis, G. D.; de France, G.; Lane, G. J.; Andgren, K.; Bruce, A. M.; Byrne, A. P.; Catford, W. N.; Cederwall, B.; Jones, G. A.; McGuirk, B.; Mandal, S.*; Paul, E. S.; Pucknell, V.; Redon, N.; Rosse, B.; Senior, R. J.; Sletten, G.: **Spectroscopy of ^{212}Po and ^{213}At using a ^{8}He radioactive beam and EXOGAM.**

Journal of physics G, Nuclear and particle physics **31**(10): S1851–S1854. DOI:10.1088/0954-3899/31/10/086

Geissel, H.*; Litvinov, Y. A.*: **Precision experiments with relativistic exotic nuclei at GSI.** *Journal of physics G, Nuclear and particle physics* **31**(10): S1779–S1783. DOI:10.1088/0954-3899/31/10/072

Geithner, W.; Brown, B. A.; Hilligsoe, K. M.; Kappertz, S.; Keim, M.; Kotrotsios, G.; Lievens, P.; Marinova, K.; Neugart, R.; Simon, H.; Wilbert, S.: **Nuclear moments of neon isotopes in the range from ^{17}Ne at the proton drip line to neutron-rich ^{25}Ne.** *Physical review C, Nuclear physics* **71**(6): 064319. DOI:10.1103/PhysRevC.71.064319

Gerl, J.*: **Gamma-ray imaging exploiting the Compton effect.** *Nuclear physics A, Nuclear and hadronic physics* **752**: 688C–695C. DOI:10.1016/j.nuclphysa.2005.02.068

Goetzen, K.; Lewandowski, B.; Peters, K. and the BABAR Collaboration: **Search for factorization-suppressed $B \to \chi_c K^{(*)}$ decays.** *Physical review letters* **94**(17): 171801. DOI:10.1103/PhysRevLett.94.171801

Goetzen, K.; Lewandowski, B.; Peters, K. and the BABAR Collaboration: **Search for the radiative decay $B \to \phi\gamma$.** *Physical Review D* **72**(9): 091103. DOI:10.1103/PhysRevD.71.091103

Goetzen, K.; Lewandowski, B.; Peters, K. and the BABAR Collaboration: $e^+e^- \to \pi^+\pi^-\pi^+\pi^-$ **,** $K^+K^-\pi^+\pi^-$ **, and** $K^+K^-K^+K^-$ **cross sections at center-of-mass energies 0.5 GeV – 4.5 GeV measured with initial-state radiation.** *Physical Review D* **71**(5): 052001. DOI:10.1103/PhysRevD.71.052001

Goetzen, K.; Lewandowski, B.; Peters, K. and the BABAR Collaboration: **.** *Physical review letters* **95**(12): 121802. DOI:10.1103/PhysRevLett.95.121802

Goetzen, K.; Lewandowski, B.; Peters, K. and the BABAR Collaboration: **.** *Physical review letters* **95**(15): 151803. DOI:10.1103/PhysRevLett.95.151803

Goetzen, K.; Lewandowski, B.; Peters, K. and the BABAR Collaboration: **An amplitude analysis of the decay $B^\pm \to \pi^\pm\pi^\pm\pi^\mp$.** *Physical Review D* **72**(5): 052002. DOI:10.1103/PhysRevD.72.052002

Goetzen, K.; Lewandowski, B.; Peters, K. and the BABAR Collaboration: **Branching fraction and CP asymmetries of B-0 -ANDgt;(KSKSKS0)-K-0-K-0.** *Physical review letters* **95**(1): 011801. DOI:10.1103/PhysRevLett.95.011801

Goetzen, K.; Lewandowski, B.; Peters, K. and the BABAR Collaboration: **Dalitz-plot analysis of the decays $B^\pm \to K^\pm\pi^\pm\pi^\pm$.** *Physical Review D* **72**(7): 072003. DOI:10.1103/PhysRevD.72.072003

Goetzen, K.; Lewandowski, B.; Peters, K. and the BABAR Collaboration: **Dalitz-plot analysis of the decays $B^\pm \to K^\pm\pi^\mp\pi^\pm$.** *Physical Review D* **72**(5): 052008. DOI:10.1103/PhysRevD.72.052008

Goetzen, K.; Lewandowski, B.; Peters, K. and the BABAR Collaboration: **Determination of $|V_{ub}|$ from measurements of the electron and neutrino momenta in inclusive semileptonic B decays.** *Physical review letters* **95**(11): 111801. DOI:10.1103/PhysRevLett.95.111801

Goetzen, K.; Lewandowski, B.; Peters, K. and the BABAR Collaboration: **Evidence for $B^+ \to \bar{K}^0K^+$ and $B^0 \to K^0\bar{K}^0$, and measurement of the branching fraction and search for direct CP violation in $B^+ \to K^0\pi^+$.** *Physical review letters* **95**(22): 221801. DOI:10.1103/PhysRevLett.95.221801

Goetzen, K.; Lewandowski, B.; Peters, K. and the BABAR Collaboration: **Evidence for the decay $B^\pm \to K^{*\pm}\pi^0$.** *Physical Review D* **71**(11): 111101. DOI:10.1103/PhysRevD.71.111101

Goetzen, K.; Lewandowski, B.; Peters, K. and the BABAR Collaboration: **Improved measurement of the CKM angle α using $B^0(\bar{B}^0) \to \rho^+\rho^-$ decays.** *Physical review letters* **95**(4): 041805. DOI:10.1103/PhysRevLett.95.041805

Goetzen, K.; Lewandowski, B.; Peters, K. and the BABAR Collaboration: **Limit on the $B^0 \to \rho^0\rho^0$ branching fraction and implications for the Cabibbo-Kobayashi-Maskawa angle alpha.** *Physical review letters* **94**(13): 131801. DOI:10.1103/PhysRevLett.94.131801

Goetzen, K.; Lewandowski, B.; Peters, K. and the BABAR Collaboration: **Measurement of CP asymmetries in $B^0 \to \phi K^0$ and $B^0 \to K^+K^-K^0_S$.** *Physical Review D* **71**(9): 091102. DOI:10.1103/PhysRevD.71.091102

Goetzen, K.; Lewandowski, B.; Peters, K. and the BABAR Collaboration: **Measurement of CP observables for the decays $B^\pm \to D^0_{CP}K^{*\pm}$.** *Physical Review D* **72**(7): 071103. DOI:10.1103/PhysRevD.72.071103

Goetzen, K.; Lewandowski, B.; Peters, K. and the BABAR Collaboration: **Measurement of branching fractions and charge asymmetries in B^+ decays to $\eta\pi^+$, ηK^+, $\eta\rho^+$ and $\eta'\pi^+$, and search for B^0 decays to ηK^0 and $\eta\omega$.** *Physical review letters* **95**(13): 131803. DOI:10.1103/PhysRevLett.95.131803

Goetzen, K.; Lewandowski, B.; Peters, K. and the BABAR Collaboration: **Measurement of double charmonium production in e^+e^- annihilations at $\sqrt{s}$ = 10.6 GeV.** *Physical Review D* **72**(3): 031101. DOI:10.1103/PhysRevD.72.031101

Goetzen, K.; Lewandowski, B.; Peters, K. and the BABAR Collaboration: **Measurement of the $B^+ \to$**

$p\bar{p}K^+$ **branching fraction and study of the decay dynamics.** *Physical Review D* **72**(5): 051101. DOI:10.1103/PhysRevD.72.051101

Goetzen, K.; Lewandowski, B.; Peters, K. and the BABAR Collaboration: **Measurement of the** $B^0 \to D^{*-}D_s^{*+}$ **and** $D_s^+ \to \phi\pi^+$ **branching fractions.** *Physical Review D* **71**(9): 091104. DOI:10.1103/PhysRevD.71.091104

Goetzen, K.; Lewandowski, B.; Peters, K. and the BABAR Collaboration: **Measurement of the branching fraction and decay rate asymmetry of** $B^- \to D_{\pi^+\pi^-\pi^0}K^-$**.** *Physical Review D* **72**(7): 071102. DOI:10.1103/PhysRevD.72.071102

Goetzen, K.; Lewandowski, B.; Peters, K. and the BABAR Collaboration: **Measurement of the branching fraction and the** CP**-violating asymmetry for the decay** $B^0 \to K_S^0\pi^0$**.** *Physical Review D* **71**(11): 111102. DOI:10.1103/PhysRevD.71.111102

Goetzen, K.; Lewandowski, B.; Peters, K. and the BABAR Collaboration: **Measurement of the branching fraction of** $\Upsilon(4S) \to B^0\bar{B}^0$**.** *Physical review letters* **95**(4): 042001. DOI:10.1103/PhysRevLett.95.042001

Goetzen, K.; Lewandowski, B.; Peters, K. and the BABAR Collaboration: **Measurement of the branching ratios** $\Gamma(D_s^{*+} \to D_s^+\pi^0)/\Gamma(D_s^{*+} \to D_s^+\gamma)$ **and** $\Gamma(D^{*0} \to D^0\pi^0)/\Gamma(D^{0*} \to D^0\gamma)$**.** *Physical Review D* **72**(9): 091101. DOI:10.1103/PhysRevD.72.091101

Goetzen, K.; Lewandowski, B.; Peters, K. and the BABAR Collaboration: **Measurement of the time-dependent** CP**-violating asymmetry in** $B^0 \to K_S^0\pi^0\gamma$ **decays.** *Physical Review D* **72**(5): 051103. DOI:10.1103/PhysRevD.72.051103

Goetzen, K.; Lewandowski, B.; Peters, K. and the BABAR Collaboration: **Measurement of time-dependent** CP **asymmetries and the** CP**-odd fraction in the decay** $B^0 \to D^{*+}D^{*-}$**.** *Physical review letters* **95**(15): 151804. DOI:10.1103/PhysRevLett.95.151804

Goetzen, K.; Lewandowski, B.; Peters, K. and the BABAR Collaboration: **Measurement of time-dependent** CP **asymmetries in** $B^0 \to D^{(*)\pm}D^{\mp}$ **decays.** *Physical review letters* **95**(13): 131802. DOI:10.1103/PhysRevLett.95.131802

Goetzen, K.; Lewandowski, B.; Peters, K. and the BABAR Collaboration: **Measurement of time-dependent** CP**-violating asymmetries and constraints on** $\sin(2\beta+\gamma)$ **with partial reconstruction of** $B \to D^{*\mp}\pi^{\pm}$ **decays.** *Physical Review D* **71**(11): 112003. DOI:10.1103/PhysRevD.71.112003

Goetzen, K.; Lewandowski, B.; Peters, K. and the BABAR Collaboration: **Measurements of branching fractions and time-dependent** CP**-violating asymmetries in** $B \to \eta' K$ **decays.** *Physical review letters* **94**(19): 191802. DOI:10.1103/PhysRevLett.94.191802

Goetzen, K.; Lewandowski, B.; Peters, K. and the BABAR Collaboration: **Measurements of the** $B \to X_s\gamma$ **branching fraction and photon spectrum from a sum of exclusive final states.** *Physical Review D* **72**(5): 052004. DOI:10.1103/PhysRevD.72.052004

Goetzen, K.; Lewandowski, B.; Peters, K. and the BABAR Collaboration: **Observation of a broad structure in the** $\pi^+\pi^- J/\psi$ **mass spectrum around 4.26 GeV/**c^2**.** *Physical review letters* **95**(14): 142001. DOI:10.1103/PhysRevLett.95.142001

Goetzen, K.; Lewandowski, B.; Peters, K. and the BABAR Collaboration: **Precision measurement of the** Λ_c^+ **baryon mass.** *Physical Review D* **72**(5): 052006. DOI:10.1103/PhysRevD.72.052006

Goetzen, K.; Lewandowski, B.; Peters, K. and the BABAR Collaboration: **Production and decay of** Ξ_{c0} **at BABAR.** *Physical review letters* **95**(14): 142003. DOI:10.1103/PhysRevLett.95.142003

Goetzen, K.; Lewandowski, B.; Peters, K. and the BABAR Collaboration: **Search for** $B \to J/\psi D$ **decays.** *Physical Review D* **71**(9): 091103. DOI:10.1103/PhysRevD.71.091103

Goetzen, K.; Lewandowski, B.; Peters, K. and the BABAR Collaboration: **Search for** CP **violation and a measurement of the relative branching fraction in** $D^+ \to K^-K^+\pi^+$ **decays.** *Physical Review D* **71**(9): 091101. DOI:10.1103/PhysRevD.71.091101

Goetzen, K.; Lewandowski, B.; Peters, K. and the BABAR Collaboration: **Search for** $b \to u$ **transitions in** $B^- \to D^0K^-$ **and** $B^- \to D^{*0}K^-$**.** *Physical Review D* **72**(3): 032004. DOI:10.1103/PhysRevD.72.032004

Goetzen, K.; Lewandowski, B.; Peters, K. and the BABAR Collaboration: **Search for decays of** $B^0 \to e^+e^-$**,** $B^0 \to \mu^+\mu^-$**,** $B^0 \to e^{\pm}\mu^{\mp}$**.** *Physical review letters* **94**(22): 221803. DOI:10.1103/PhysRevLett.94.221803

Goetzen, K.; Lewandowski, B.; Peters, K. and the BABAR Collaboration: **Search for lepton flavor violation in the decay** $\tau \to \mu\gamma$**.** *Physical review letters* **95**(4): 041802. DOI:10.1103/PhysRevLett.95.041802

Goetzen, K.; Lewandowski, B.; Peters, K. and the BABAR Collaboration: **Search for lepton-flavor and lepton-number violation in the decay** $\tau^- \to \ell^{\mp}h^{\pm}h'^-$**.** *Physical review letters* **95**(19): 191801. DOI:10.1103/PhysRevLett.95.191801

Goetzen, K.; Lewandowski, B.; Peters, K. and the BABAR Collaboration: **Search for strange-pentaquark production in** e^+e^- **annihilation at**

$\sqrt{s}$ **= 10.58 GeV.** *Physical review letters* **95**(4): 042002. DOI:10.1103/PhysRevLett.95.042002

Goetzen, K.; Lewandowski, B.; Peters, K. and the BABAR Collaboration: **Search for the W-exchange decays $B^0 \to D_s^{(*)-} D_s^{(*)+}$.** *Physical Review D* **72**(11): 111101. DOI:10.1103/PhysRevD.72.111101

Goetzen, K.; Lewandowski, B.; Peters, K. and the BABAR Collaboration: **Search for the decay $\tau^- \to 4\pi^- 3\pi^+(\pi^0)\nu_\tau$.** *Physical Review D* **72**(1): 012003. DOI:10.1103/PhysRevD.72.012003

Goetzen, K.; Lewandowski, B.; Peters, K. and the BABAR Collaboration: **Search for the rare decay $\bar{B}^0 \to D^{*0}\gamma$.** *Physical Review D* **72**(5): 051106. DOI:10.1103/PhysRevD.72.051106

Goetzen, K.; Lewandowski, B.; Peters, K. and the BABAR Collaboration: **Search for the rare decays $B^+ \to D^{(*)+} K_S^0$.** *Physical Review D* **72**(1): 011102. DOI:10.1103/PhysRevD.72.011102

Goetzen, K.; Lewandowski, B.; Peters, K. and the BABAR Collaboration: **Study of $B \to \pi l \nu$ and $B \to \rho l \nu$ decays and determination of $|V_{ub}|$ vertical bar.** *Physical Review D* **72**(5): 051102. DOI:10.1103/PhysRevD.72.051102

Goetzen, K.; Lewandowski, B.; Peters, K. and the BABAR Collaboration: **Study of $b \to c$ interference in the decay $B^- \to [K^+\pi^-]_D K^{*-}$.** *Physical Review D* **72**(7): 071104. DOI:10.1103/PhysRevD.72.071104

Goetzen, K.; Lewandowski, B.; Peters, K. and the BABAR Collaboration: **Study of the $\tau - \to ; 3h^- 2h^+ \nu_\tau$ decay.** *Physical Review D* **72**(7): 072001. DOI:10.1103/PhysRevD.72.072001

Golovkov, M. S.; Grigorenko, L. V.; Fomichev, A. S.; Krupko, S. A.; Oganessian, Y. T.; Rodin, A. M.; Sidorchuk, S. I.; Slepnev, R. S.; Stepantsov, S. V.; Ter-Akopian, G. M.; Wolski, R.; Itkis, M. G.; Denikin, A. S.; Bogatchev, A. A.; Kondratiev, N. A.; Kozulin, E. M.; Korsheninnikov, A. A.; Nikolskii, E. Y.; Roussel-Chomaz, P.; Mittig, W.; Palit, R.*; Bouchat, V.; Kinnard, V.; Materna, T.; Hanappe, F.; Dorvaux, O.; Stuttge, L.; Angulo, C.; Lapoux, V.; Raabe, R.; Nalpas, L.; Yukhimchuk, A. A.; Perevozchikov, V. V.; Vinogradov, Y. I.; Grishechkin, S. K.; Zlatoustovskiy, S. V.: **Correlation studies of the ^{5}H spectrum.** *Physical review C, Nuclear physics* **72**(6): 064612. DOI:10.1103/PhysRevC.72.064612

Grawe, H.*; Blazhev, A.*; Górska, M.*; Mukha, I.*; Plettner, C.*; Roeckl, E.*; Nowacki, F.; Grzywacz, R.; Sawicka, M.: **Shell structure from ^{100}Sn to ^{78}Ni: Implications for nuclear astrophysics.** *The European physical journal A, Hadrons and nuclei* **25**: 357–362. DOI:10.1140/epjad/i2005-06-025-1

Greenlees, P. T.; Amzal, N.; Bastin, J. E.; Bouchez, E.; Butler, P. A.; Chatillon, A.; Dorvaux, O.; Eeckhaudt, S.; Eskola, K.; Gall, B.; Gerl, J.*; Grahn, T.; Görgen, A.; Hammond, N. J.; Hauschild, K.; Herzberg, R.-D.; Heßberger, F.-P.*; Humphreys, R. D.; Hürstel, A.; Jenkins, D. G.; Jones, G. D.; Jones, P.; Julin, R.; Juutinen, S.; Kankaanpää, H.; Keenan, A.; Kettunen, H.; Khalfallah, F.; Khoo, T. L.; Korten, W.; Kuusmiemi, P.; Le Coz, Y.; Leino, M.; Leppanen, A. P.; Muikku, M.; Nieminen, P.; Pakarinen, J.; Rahkila, P.; Reiter, P.; Rousseau, M.; Scholey, C.; Theisen, C.; Uusitalo, J.; Wilson, J.; Wollersheim, H.-J.*: **In-beam and decay spectroscopy of transfermium elements.** *The European physical journal A, Hadrons and nuclei* **25**: 599–604. DOI:10.1140/epjad/i2005-06-026-0

Grigorian, H.; Blaschke, D.; Voskresensky, D.*: **Cooling of neutron stars with color superconducting quark cores.** *Physical review C, Nuclear physics* **71**(4): 045801. DOI:10.1103/PhysRevC.71.045801

Grigorian, H.; Voskresensky, D. N.*: **Medium effects in cooling of neutron stars and the 3P(2) neutron gap.** *Astronomy & astrophysics* **444**(3): 913–929. DOI:10.1051/0004-6361:20052799

Grüter, B.; Alkofer, R.; Maas, A.; Wambach, J.*: **Temperature dependence of gluon and ghost propagators in Landau-gauge Yang-Mills theory below the phase transition.** *The European physical journal: C, Particles and fields* **42**(1): 109–118. DOI:10.1140/epjc/s2005-02282-1

Gupta, R. K.; Manhas, M.; Münzenberg, G.*; Greiner, W.: **Theory of the compactness of the hot fusion reaction ^{48}Ca+^{244}Pu $\to$ ^{292}114.** *Physical review C, Nuclear physics* **72**(1): 014607. DOI:10.1103/PhysRevC.72.014607

Hagemann, M.; Bäumer, C.; van den Berg, A. M.; De Frenne, D.; Frekers, D.; Hannen, V. M.; Harakeh, M. N.; Heyse, J.; de Huu, M. A.; Jacobs, E.; Langanke, K.; Martínez-Pinedo, G.; Negret, A.; Popescu, L.; Rakers, S.; Schmidt, R.; Wörtche, H. J.: **Spin-isospin excitations in the medium-mass nucleus ^{58}Co investigated with the (d,^{2}He) reaction.** *Physical review C, Nuclear physics* **71**(1): 014606. DOI:10.1103/PhysRevC.71.014606

Hammer, J. W.; Fey, M.; Kunz, R.; Kiener, J.; Tatischeff, V.; Haas, F.; Weil, J. L.; Assuncao, M.; Beck, C.; Boukari-Pelissie, C.; Coc, A.; Correia, J. J.; Courtin, S.; Fleurot, F.; Galanopoulos, E.; Grama, C.; Hammache, F.*; Harissopulos, S.; Korichi, A.; Krmpotic, E.; Le Du, D.; Lopez-Martens, A.; Malcherek, D.; Meunier, R.; Papka, P.; Paradellis, T.; Rousseau, M.; Rowley, N.; Staudt, G.; Szilner, S.: **E1 and E2 capture cross section and astrophysical reaction rate of the key reaction ^{12}C(α,γ)^{16}O.** *Nuclear physics A, Nuclear and hadronic physics* **758**: 363C–366C. DOI:10.1016/j.nuclphysa.2005.05.066

Hammer, J. W.; Fey, M.; Kunz, R.; Kiener, J.; Tatischeff, V.; Haas, F.; Weil, J. L.; Assuncao, M.; Beck,

C.; Boukari-Pelissie, C.; Coc, A.; Correia, J. J.; Courtin, S.; Fleurot, F.; Galanopoulos, E.; Grama, C.; Hammache, F.*; Harissopulos, S.; Korichi, A.; Krmpotic, E.; Le Du, D.; Lopez-Martens, A.; Malcherek, D.; Meunier, R.; Papka, P.; Paradellis, T.; Rousseau, M.; Rowley, N.; Staudt, G.; Szilner, S.: **New determination of the C-12(alpha, gamma)O-16 reaction rate from gamma-ray angular distribution measurements..** *Nuclear physics A, Nuclear and hadronic physics* **752**: 514C–521C. DOI:10.1016/j.nuclphysa.2005.02.056

Hammond, G.*; Bentley, M. A.; Becker, F.*; Grebosz, J.*; Taylor, M. J.; Banu, A.*; Barton, C. J.; Beck, T.*; Bednarczyk, P.*; Bracco, A.; Bruce, A. M.; Bullock, L. C.; Brger, A.; Camera, F.; Chandler, C.; Doornenbal, P.*; Gerl, J.*; Geissel, H.*; Górska, M.*; Hellström, M.*; Judsond, D.; Kojouharov, I.*; Kurz, N.*; Lozeva, R.*; Maj, A.; Mandal, S.*; McGuirk, B.; Muralithar, S.*; Paul, E. S.; Podolyák, Z.; Prokopowicz, W.*; Rudolph, D.; Saito, N.*; Saito, T. R.*; Schaffner, H.*; Simpson, J.; Warner, D. D.; Weick, H.*; Weldon, C.*; Winkler, M.*; Wollersheim, H.-J.*: **Spectroscopy of T=3/2 mirror nuclei via two-step fragmentation using RISING.** *Acta physica Polonica B, Particle physics and field theory, nuclear physics, theory of relativity* **36**(4): 1253–1257.

Harissopulos, S.; Döring, J.*; La Commara, M.*; Schmidt, K.*; Mazzocchi, C.*; Borcea, R.*; Galanopoulos, S.; Górska, M.*; Grawe, H.*; Hellström, M.*; Janas, Z.*; Kirchner, R.*; Roeckl, E.*; Johnstone, I. P.; Schwengner, R.; Skouras, L. D.: β **decay of** ^{95}**Ag.** *Physical review C, Nuclear physics* **72**(2): 024303. DOI:10.1103/PhysRevC.72.024303

Heger, A.; Kolbe, E.; Haxton, W. C.; Langanke, K.; Martínez-Pinedo, G.; Woosley, S. E.: **Neutrino nucleosynthesis.** *Physics letters B* **606**(3): 258–264. DOI:10.1016/j.physletb.2004.12.017

Heilbronn, L.; Nakamura, T.; Iwata, Y.; Kurosawa, T.; Iwase, H.*; Townsend, L. W.: **Overview of secondary neutron production relevant to shielding in space.** *Radiation protection dosimetry* **116**(1): 140–143.

Henning, W.*: **Ups and downs, and the strange charm of roadmaps.** *Nuclear physics A, Nuclear and hadronic physics* **751**: 593C–603C. DOI:10.1016/j.nuclphysa.2005.02.049

Henzlova, D.*; Audouin, L.; Benlliure, J.; Botvina, A. S.*; Boudard, A.; Casarejos, E.; Ducret, J. E.; Enqvist, T.; Got, L. T.; Heinz, A.; Henzl, V.*; Junghans, A.; Jurado, B.; Kelic, A.*; Krasa, A.; Kurtukian, T.; Leray, S.; Napolitani, P.*; Ordonez, M. F.; Pereira, J.; Pleskac, R.*; Rejmund, F.; Ricciardi, M. V.*; Schmidt, K. H.*; Schmitt, C.*; Stephan, C.; Villagrasa, C.; Volant, C.; Wagner, A.; Yordanov, O.*: **Isotopically resolved residues frorn the fragmentation of projectiles with largely different N/Z - the isospin-thermometer method.** *Nuclear physics A, Nuclear and hadronic physics* **749**: 110C–113C. DOI:10.1016/j.nuclphysa.2004.12.016

Heßberger, F. P.*; Antalic, S.; Streicher, B.; Hofmann, S.*; Ackermann, D.*; Kindler, B.*; Kojouharov, I.*; Kusiniemi, P.*; Leino, M.; Lommel, B.*; Mann, R.*; Nishio, K.*; Saro, S.; Sulignano, B.*: **Energy systematics of low-lying Nilsson levels in odd-mass einsteinium isotopes.** *The European physical journal A, Hadrons and nuclei* **26**(2): 233–239. DOI:10.1140/epja/i2005-10171-6

Hix, W. R.; Frohlich, C.; Martinez-Pinedo, G.; Liebendorfer, M.; Thielemann, F. K.: **Influence of the explosion mechanism on the ejecta of core collapse supernovae.** *Meteoritics and Planetary Science* **40**(9): A68–A68.

Hofmann, J.*; Lutz, M. F. M.*: **Coupled-channel study of crypto-exotic baryons with charm.** *Nuclear physics A, Nuclear and hadronic physics* **763**: 90–139.

Hong, B.; Kim, Y. J.*; Herrmann, N.; Stockmeier, M. R.; Andronic, A.*; Barret, V.; Basrak, Z.; Bastid, N.; Benabderrahmane, M. L.; Čaplar, R.; Crochet, P.; Dupieux, P.; Dželalija, M.; Fodor, Z.; Gobbi, A.*; Grishkin, Y.; Hartmann, O. N.*; Hildenbrand, K. D.*; Kecskemeti, J.; Kirejczyk, M.*; Koczon, P.*; Korolija, M.; Kotte, R.; Kress, T.*; Lebedev, A.; Leifels, Y.*; Lopez, X.; Mangiarotti, A.; Merschmeyer, M.; Neubert, W.; Pelte, D.; Petrovici, M.; Rami, F.; Reisdorf, W.*; Schüttauf, A.*; Seres, Z.; Sikora, B.; Sim, K. S.; Simion, V.*; Siwek-Wilczyńska, K.; Smolyankin, V.; Stoicea, G.; Tyminski, Z.*; Wagner, P.; Wiśniewski, K.; Wohlfarth, D.; Xiao, Z. G.*; Yushmanov, I.; Zhilin, A.; FOPI Collaboration: **Charged pion production in** $^{96}_{44}$**Ru+**$^{96}_{44}Ru$ **collisions at 400A and 1528A MeV.** *Physical review C, Nuclear physics* **71**(3): 034902. DOI:10.1103/PhysRevC.71.034902

Ivanov, Y. B.*; Khvorostukhin, A. S.; Kolomeitsev, E. E.; Skokov, V. V.*; Toneev, V. D.*; Voskresensky, D. N.*: **Lattice QCD constraints on hybrid and quark stars.** *Physical review C, Nuclear physics* **72**(2): 025804. DOI:10.1103/PhysRevC.72.025804

Ivanov, Y. B.*; Riek, F.*; Knoll, J.*: **Gapless Hartree-Fock resummation scheme for the O(N) model.** *Physical Review D* **71**(10): 105016. DOI:10.1103/PhysRevD.71.105016

Ivanov, Y. B.; Riek, F.; van Hees, H.; Knoll, J.*: **Renormalization of a gapless Hartree-Fock approximation to a theory with spontaneously broken O(N) symmetry.** *Physical Review D* **72**(3): 036008.

Ivanov, Y. B.*; Skokov, V. V.*; Toneev, V. D.*: **Equation of state of deconfined matter within a dynamical quasiparticle description.** *Physical Review D* **71**(1): 014005. DOI:10.1103/PhysRevD.71.014005

Ivanyuk, F. A.*; Nörenberg, W.*: **Diabatic states from**

nodal structure conservation. *Physical review letters* **95**(8): 082501. DOI:10.1103/PhysRevLett.95.082501

Iwase, H.*; Wiegel, B.; Fehrenbacher, G.*; Schardt, D.*; Nakamura, T.; Niita, K.; Radon, T.*: **Comparison between calculation and measured data on secondary neutron energy spectra by heavy ion reactions from different thick targets.** *Radiation protection dosimetry* **116**(1): 640–646.

Janas, Z.; Batist, L.; Borcea, R.*; Döring, J.*; Gierlik, M.; Karny, M.; Kirchner, R.*; La Commara, M.; Mandal, S.*; Mazzocchi, C.*; Moroz, F.; Orlov, S.; Płochocki, A.; Roeckl, E.*; Żylicz, J.: **Lifetimes of proton unstable states in ^{113}I measured by the particle-X-ray coincidence technique.** *The European physical journal A, Hadrons and nuclei* **24**(2): 205–209. DOI:10.1140/epja/i2004-10137-2

Janas, Z.; Batist, L.; Döring, J.*; Gierlik, N.; Kirchner, R.*; Kurcewicz, J.; Mahmud, H.; Mazzocchi, C.*; Płochocki, A.; Roeckl, E.*; Schmidt, K.; Woods, P. J.; Żylicz, J.: **Total absorption spectroscopy of the β-delayed proton emitter ^{117}Ba.** *The European physical journal A, Hadrons and nuclei* **23**(3): 401–408. DOI:10.1140/epja/i2004-10103-0

Janas, Z.; Mazzocchi, C.*; Batist, L.; Blazhev, A.*; Górska, M.*; Kavatsyuk, M.*; Kavatsyuk, O.*; Kirchner, R.*; Korgul, A.; La Commara, M.; Miernik, K.; Mukha, I.; Plochocki, A.; Roeckl, E.*; Schmidt, K.: **Measurements of ^{110}Xe and ^{106}Te decay half-lives.** *The European physical journal A, Hadrons and nuclei* **23**(2): 197–200. DOI:10.1140/epja/i2004-10076-x

Jeppesen, H. B.; Ames, F.; Van den Bergh, P.; Bergmann, U. C.; Bollen, G.; Borge, M. J. G.; Cederkall, J.; Van Duppen, P.; Emhofer, S.; Forstner, O.; Fraile, L. M.; Fynbo, H. O. U.; Gómez-Camacho, J.; Habs, D.; von Hahn, R.; Huber, G.; Huyse, M.; Johansson, H. T.; Jonson, B.; Kester, O.; Liljeby, L.; Meister, M.; Moro, A. M.; Nilsson, T.; Nyman, G.; Oinonen, M.; Pantea, M.*; Podlech, H.; Ratzinger, U.; Reisinger, K.; Rensfelt, K. G.; Repnow, R.; Riisager, K.; Richter, A.; Rudolph, K.; Scheit, H.; Schempp, A.; Schmidt, P.; Schrieder, G.; Schwalm, D.; Sieber, T.; Simon, H.*; Tengblad, O.; Tengborn, E.; Turrión, M.; Weissmann, L.; Wenander, F.; Wolf, B.; ISOLDE Collaboration; REX-ISOLDE Collaboration: **Low energy reactions with radioactive ions at REX-ISOLDE - the ^{9}Li+ ^{2}H case.** *Nuclear physics A, Nuclear and hadronic physics* **748**(3): 374–392. DOI:10.1016/j.nuclphysa.2004.11.013

Jesinger, P.; Kopatch, Y. N.*; Mutterer, M.; Gönnenwein, F.; Gagarski, A. M.; Kalben, J. V.; Nesvizhevsky, V.; Petrov, G. A.; Trzaska, W. H.; Wollersheim, H. J.*: **New experimental studies on the quaternary fission of ^{233,235}U(n_{th}), f) and ^{252}Cf (sf).** *The European physical journal A, Hadrons and nuclei* **24**(3): 379–388. DOI:10.1140/epja/i2005-10026-2

Juodagalvis, A.; Langanke, K.; Martinez-Pinedo, G.; Hix, W. R.; Dean, D. J.; Sampaio, J. M.: **Neutral-current neutrino-nucleus cross sections for A $\sim$ 50-65 nuclei.** *Nuclear physics A, Nuclear and hadronic physics* **747**(1): 87–108. DOI:10.1016/j.nuclphysa.2004.09.005

Jurado, B.*; Schmitt, C.*; Schmidt, K.-H.*; Benlliure, J.; Junghans, A. R.: **A critical analysis of the modelling of dissipation in fission.** *Nuclear physics A, Nuclear and hadronic physics* **747**(1): 14–43. DOI:10.1016/j.nuclphysa.2004.09.123

Jurado, B.*; Schmitt, C.*; Schmidt, K.-H.*; Benlliure, J.; Junghans, A. R.: **Conditions for the manifestation of transient effects in fission.** *Nuclear physics A, Nuclear and hadronic physics* **757**(3): 329–348. DOI:10.1016/j.nuclphysa.2005.04.020

Kameoka, S.; Ajimura, S.; Aoki, K.; Banu, A.*; Bhang, H. C.; Fukuda, T.; Hashimoto, O.; Hwang, J. I.; Kang, B. H.; Kim, E. H.; Kim, J. H.; Kim, M. J.; Maruta, T.; Miura, Y.; Miyake, Y.; Nagae, T.; Nakamura, M.; Nakamura, S. N.; Noumi, H.; Okada, S.; Okayasu, Y.; Outa, H.; Park, H.; Saha, P. K.; Sato, Y.; Sekimoto, M.; Takahashi, T.; Tamura, H.; Tanida, K.; Toyoda, A.; Tsukada, K.; Watanabe, T.; Yim, H. J.: **Measurement of the π^- decay width of $^{5}_{\Lambda}$He.** *Nuclear physics A, Nuclear and hadronic physics* **754**: 173C–177C. DOI:10.1016/j.nuclphysa.2005.03.016

Kankainen, A.; Eliseev, S. A.*; Eronen, T.; Fox, S. P.; Hager, U.; Hakala, J.; Huang, W.; Huikari, J.; Jenkins, D.; Jokinen, A.; Kopecky, S.; Moore, I.; Nieminen, A.; Novikov, Y. N.; Penttilä, H.; Popov, A. V.; Rinta-Antila, S.; Schatz, H.; Seliverstov, D. M.; Vorobjev, G. K.*; Wang, Y.; Äystö, J.; IS403 Collaborat: **Beta-delayed gamma and proton spectroscopy near the Z=N line.** *The European physical journal A, Hadrons and nuclei* **25**: 129–130. DOI:10.1140/epjad/i2005-06-036-x

Kankainen, A.; Vorobjev, G. K.; Eliseev, S. A.*; Huang, W.; Huikari, J.; Jokinen, A.; Nieminen, A.; Novikov, Y. N.; Penttilä, H.; Popov, A. V.; Rinta-Antila, S.; Schatz, H.; Seliverstov, D. M.; Suslov, Y. P.; Äystö, J.: **Isomers of astrophysical interest in neutron-deficient nuclei at masses A = 81, 85 and 86.** *The European physical journal A, Hadrons and nuclei* **25**(3): 355–363. DOI:10.1140/epja/i2005-10141-0

Karny, M.; Batist, L.; Banu, A.*; Becker, F.*; Blazhev, A.*; Burkard, K.*; Brüchle, W.*; Döring, J.*; Faestermann, T.; Górska, M.*; Grawe, H.*; Janas, Z.; Jungclaus, A.; Kavatsyuk, M.*; Kavatsyuk, O.*; Kirchner, R.*; La Commara, M.; Mandal, S.*; Mazzocchi, C.*; Miernik, K.; Mukha, I.*; Muralithar, S.*; Plettner, C.*; Plochocki, A.; Roeckl, E.*; Romoli, M.; Rykaczewski, K.; Schädel, M.*; Schmidt, K.; Schwengner, R.; Żylicz, J.: **Beta-decay studies near ^{100}Sn.** *The European physical journal A, Hadrons and nuclei* **25**: 135–138. DOI:10.1140/epjad/i2005-06-037-9

Kavatsyuk, M.*; Kavatsyuk, O.*; Batist, L.; Banu, A.*; Becker, F.*; Blazhev, A.*; Brüchle, W.*; Burkard, K.*; Döring, J.*; Faestermann, T.; Górska, M.*; Grawe, H.*; Janas, Z.; Jungclaus, A.; Karny, M.; Kirchner, R.*; La Commara, M.; Mandal, S.*; Mazzocchi, C.*; Mukha, I.; Muralithar, S.; Plettner, C.; Płochocki, A.; Roeckl, E.*; Romoli, M.; Schädel, M.*; Schwengner, R.; Żylicz, J.: **Beta-decay spectroscopy of ^{103,105}Sn.** *The European physical journal A, Hadrons and nuclei* **25**: 139–141. DOI:10.1140/epjad/i2005-06-038-8

Kavatsyuk, O.*; Kavatsyuk, M.*; Batist, L.; Banu, A.*; Becker, F.*; Blazhev, A.*; Brüchle, W.*; Döring, J.*; Faestermann, T.; Górska, M.*; Grawe, H.*; Janas, Z.; Jungclaus, A.; Karny, M.; Kirchner, R.*; La Commara, M.; Mandal, S.*; Mazzocchi, C.*; Mukha, I.*; Muralithar, S.*; Plettner, C.*; Plochocki, A.; Roeckl, E.*; Romoli, M.; Schädel, M.*; Schwengner, R.; Zylicz, J.: **Beta decay of ^{103}Sn.** *The European physical journal A, Hadrons and nuclei* **25**(2): 211–222. DOI:10.1140/epja/i2005-10108-1

Kelić, A.*; Zinner, N.; Kolbe, E.; Langanke, K.*; Schmidt, K.-H.*: **Cross sections and fragment distributions from neutrino-induced fission on r-process nuclei.** *Physics letters B* **616**(1): 48–58. DOI:10.1016/j.physletb.2005.04.074

Kiselev, O. A.*; Aksouh, F.*; Bleile, A.*; Bochkarev, O. V.; Chulkov, L. V.; Cortina-Gil, D.*; Dobrovolsky, A. V.; Egelhof, P.*; Geissel, H.*; Hellström, M.*; Isaev, N. B.; Komkov, B. G.; Mátos, M.*; Moroz, F. V.; Münzenberg, G.*; Mutterer, M.; Mylnikov, V. A.; Neumaier, S. R.*; Pribora, V. N.; Seliverstov, D. M.; Sergueev, L. O.; Shrivastava, A.*; Sümmerer, K.*; Weick, H.*; Winkler, M.*; Yatsoura, V. I.: **Investigation of nuclear matter distribution of the neutron-rich He isotopes by proton elastic scattering at intermediate energies.** *The European physical journal A, Hadrons and nuclei* **25**: 215–216. DOI:10.1140/epjad/i2005-06-156-3

Kmiecik, M.; Maj, A.; Styczen, J.; Bednarczyk, P.*; Brekiesz, M.; Grebosz, J.*; Lach, M.; Meczynski, W.; Zieblinski, M.; Zuber, K.; Bracco, A.; Camera, F.; Benzoni, G.; Million, B.; Leoni, S.; Wieland, O.; Herskind, B.; Curien, D.; Dubray, N.; Dudek, J.; Schunck, N.; Mazurek, K.: **GDR feeding of the highly-deformed band in Ca-42.** *Acta physica Polonica B, Particle physics and field theory, nuclear physics, theory of relativity* **36**(4): 1169–1174.

Koch, K.*; Hardel, H.*; Schulze, R.*; Badura, E.*; Hoffmann, J.*: **A new TAC-based multichannel front-end electronics for TOF experiments with very high time resolution.** *IEEE transactions on nuclear science* **52**(3): 745–747. DOI:10.1109/TNS.2005.850957

Kolomeitsev, E. E.; Voskresensky, D. N.*: **Relativistic mean-field models with effective hadron masses and coupling constants, and ρ^- condensation.** *Nuclear physics A, Nuclear and hadronic physics* **759**(3): 373–413. DOI:10.1016/j.nuclphysa.2005.05.154

Korpa, C. L.; Lutz, M. F. M.*: **Kaon and antikaon properties in cold nuclear medium.** *Heavy ion physics* **22**(1): 21–28. DOI:10.1556/APH.22.2005.1-2.4

Korten, W.; Clément, E.; Bouchez, E.; Chatillon, A.; Görgen, A.; Le Coz, Y.; Theisen, C.; Casandjian, J. M.; de France, G.; Sletten, G.; Czosnyka, T.; Iwanicki, J.; Zielinska, M.; Becker, F.*; Gerl, J.*; Catford, W.; Timis, C.; Butler, P.; Andreoiu, C.: **Investigation of heavy N similar to Z nuclei using energetic radioactive ion beams.** *Nuclear physics A, Nuclear and hadronic physics* **752**: 255C–263C. DOI:10.1016/j.nuclphysa.2005.02.039

Kotte, R.; Alard, J. P.; Andronic, A.*; Barret, V.; Basrak, Z.; Bastid, N.; Benabderrahmane, M. L.; Čaplar, R.; Cordier, E.; Crochet, P.; Dupieux, P.; Dželalija, M.; Fodor, Z.; Gašparić, I.; Gobbi, A.*; Grishkin, Y.; Hartmann, O. N.*; Herrmann, N.; Hildenbrand, K. D.*; Hong, B.; Kecskemeti, J.; Kim, Y. J.; Kirejczyk, M.; Koczon, P.*; Korolija, M.; Kress, T.*; Lebedev, A.; Leifels, Y.*; Lopez, X.; Merschmeyer, M.; Mösner, J.; Neubert, W.; Pelte, D.; Petrovici, M.; Rami, F.; Reisdorf, W.*; de Schauenburg, B.; Schüttauf, A.*; Seres, Z.; Sikora, B.; Sim, K. S.; Simion, V.*; Siwek-Wilczyńska, K.; Smolyankin, V.; Stoicea, G.; Tyminski, Z.*; Wagner, P.; Wiśniewski, K.; Wohlfarth, D.; Xiao, Z. G.*; Yushmanov, Y.; Zhilin, A.; FOPI Collaboration: **Two-proton small-angle correlations in central heavy-ion collisions: A beam-energy- and system-size-dependent study.** *The European physical journal A, Hadrons and nuclei* **23**(2): 271–278. DOI:10.1140/epja/i2004-10075-y

Kraus, I.*; NA49 Collaboration: **System size dependence of strange particle yields and spectra at $\sqrt{s_{NN}} = 17.3$ GeV.** *Journal of physics G, Nuclear and particle physics* **31**(4): S147–S154. DOI:10.1088/0954-3899/31/4/018

Kuusiniemi, P.*; Heßberger, F.*; Ackermann, D.*; Hofmann, S.*; Sulignano, B.*; Kojouharov, I.*; Mann, R.*: **Decay studies of $^{215-217}$Th using ER-γ-α-γ coincidences.** *The European physical journal A, Hadrons and nuclei* **25**(3): 397–404. DOI:10.1140/epja/i2005-10117-0

Kuusiniemi, P.*; Heßberger, F. P.*; Ackermann, D.*; Hofmann, S.*; Kojouharov, I.*: **Decay studies of $^{210-214}$Fr using $\alpha - \gamma$-coincidences.** *The European physical journal A, Hadrons and nuclei* **23**(3): 417–428. DOI:10.1140/epja/i2004-10104-y

Lach, M.; Styczeń, J.; Meczynski, W.; Bednarczyk, P.*; Bracco, A.; Grebosz, J.*; Maj, A.; Merdinger, J. C.; Schulz, N.; Smith, M. B.; Spohr, K. M.; Zieblíński, M.: **Unnatural-parity states in $^{44}_{21}$Sc^{23}.** *The European physical journal A, Hadrons and nuclei* **25**(1): 1–4. DOI:10.1140/epja/i2005-10109-0

La Cognata, M.; Musumarra, A.; Spitaleri, C.; Tumino,

A.; Bonomo, C.; Cherubini, S.; Figuera, P.; Lamia, L.; Pellegriti, M. G.; Rinollo, A.; Pizzone, R. G.; Rolfs, C.; Romano, S.; Schürmann, D.; Strieder, F.; Tudisco, S.; Typel, S.*: **Study of the ^{3}He(d, p)^{4}He reaction through the Trojan Horse Method.** *Nuclear physics A, Nuclear and hadronic physics* **758**: 98C–101C. DOI:10.1016/j.nuclphysa.2005.05.021

La Cognata, M.; Spitaleri, C.; Tumino, A.; Typel, S.*; Cherubini, S.; Lamia, L.; Musumarra, A.; Pizzone, R. G.; Rinollo, A.; Rolfs, C.; Romano, S.; Schürmann, D.; Strieder, F.: **Bare-nucleus astrophysical factor of the ^{3}He(d, p)^{4}He reaction via the 'Trojan horse' method.** *Physical review C, Nuclear physics* **72**(6): 065802. DOI:10.1103/PhysRevC.72.065802

Langanke, K.*; Dean, D. J.; Nazarewicz, W.: **Thermal properties of N=40 isotones.** *Nuclear physics A, Nuclear and hadronic physics* **757**(3): 360–372. DOI:10.1016/j.nuclphysa.2005.04.023

Le Fèvre, A.*; Auger, G.; Begemann-Blaich, M. L.*; Bellaize, N.; Bittiger, R.*; Bocage, F.; Borderie, B.; Bougault, R.; Bouriquet, B.; Charvet, J. L.; Chbihi, A.; Dayras, R.; Durand, D.; Frankland, J. D.; Galichet, E.; Gourio, D.*; Guinet, D.; Hudan, S.; Imme, G.; Lautesse, P.; Lavaud, F.; Legrain, R.; Lopez, O.; Łukasik, J.*; Lynen, U.*; Müller, W. F. J.*; Nalpas, L.; Orth, H.*; Plagnol, E.; Raciti, G.; Rosato, E.; Saija, A.; Schwarz, C.*; Seidel, W.; Sfienti, C.*; Tamain, B.; Trautmann, W.*; Trzciński, A.; Turzó, K.*; Vient, E.; Vigilante, M.; Volant, C.; Zwiegliński, B.; Botvina, A. S.*; INDRA Collaboration; ALADIN Collaboration*: **Isotopic scaling and the symmetry energy in spectator fragmentation.** *Physical review letters* **94**(16): 162701. DOI:10.1103/PhysRevLett.94.162701

Leoni, S.; Benzoni, G.; Bracco, A.; Blasi, N.; Camera, F.; Grassi, C.; Million, B.; Paleni, A.; Pignanelli, M.; Vigezzi, E.; Wieland, O.; Matsuo, M.; Dossing, T.; Herskind, B.; Hagemann, G. B.; Wilson, J.; Maj, A.; Kmiecik, M.; Lo Bianco, G.; Petrache, C. M.; Castoldi, M.; Zucchiati, A.; De Angelis, G.; Napoli, D.; Bednarczyk, P.*; Curien, D.: **Warm rotating nuclei: Damping mechanisms and the order-to-chaos transition.** *Acta physica Polonica B, Particle physics and field theory, nuclear physics, theory of relativity* **36**(4): 1121–1132.

Leppanen, A. P.; Uusitalo, J.; Eeckhaudt, S.; Enqvist, T.; Eskola, K.; Grahn, T.; Heßberger, F. P.*; Greenlees, P. T.; Jones, P.; Julin, R.; Juutinen, S.; Kettunen, H.; Kuusiniemi, P.; Leino, M.; Nieminen, P.; Pakarinen, J.; Perkowski, J.; Rahkila, P.; Scholey, C.; Sletten, G.: **Alpha-decay study of ^{218}U; a search for the sub-shell closure at Z=92.** *The European physical journal A, Hadrons and nuclei* **25**: 183–184. DOI:10.1140/epjad/i2005-06-116-y

Linnemann, A.; Fransen, C.; Gorska, M.*; Jolie, J.; Kneissl, U.; Knoch, P.; Mucher, D.; Pitz, H. H.; Scheck, M.; Scholl, C.; von Brentano, P.: **Dipole excitations in ^{96}Ru.** *Physical review C, Nuclear physics* **72**(6): 064323. DOI:10.1103/PhysRevC.72.064323

Litvinov, Y. A.*; Bürvenich, T. J.; Geissel, H.*; Novikov, Y. N.; Patyk, Z.; Scheidenberger, C.*; Attallah, F.*; Audi, G.; Beckert, K.*; Bosch, F.*; Falch, M.; Franzke, B.*; Hausmann, M.; Kerscher, T.; Klepper, O.*; Kluge, H.-J.*; Kozhuharov, C.*; Lobner, K. E. G.; Madland, D. G.; Maruhn, J. A.; Münzenberg, G.*; Nolden, F.*; Radon, T.*; Steck, M.*; Typel, S.*; Wollnik, H.: **Isospin dependence in the odd-even staggering of nuclear binding energies.** *Physical review letters* **95**(4): 042501. DOI:10.1103/PhysRevLett.95.042501

Litvinov, Y. A.*; Geissel, H.*; Radon, T.*; Attallah, F.*; Audi, G.; Beckert, K.*; Bosch, F.*; Falch, M.; Franzke, B.*; Hausmann, M.*; Hellström, M.*; Kerscher, T.; Klepper, O.*; Kluge, H.-J.*; Kozhuharov, C.*; Löbner, K. E. G.; Münzenberg, G.*; Nolden, E.*; Novikov, Y. N.; Quint, W.*; Patyk, Z.; Reich, H.*; Scheidenberger, C.*; Schlitt, B.*; Steck, M.*; Sümmerer, K.*; Vermeeren, L.*; Winkler, M.*; Winkler, T.*; Wollnik, H.: **Mass measurement of cooled neutron-deficient bismuth projectile fragments with time-resolved Schottky mass spectrometry at the FRS-ESR facility.** *Nuclear physics A, Nuclear and hadronic physics* **756**(1): 3–38. DOI:10.1016/j.nuclphysa.2005.03.015

Liu, Z.; Kurcewicz, J.; Woods, P. J.; Mazzocchi, C.*; Attallah, F.*; Badura, E.*; Davids, C. N.; Davinson, T.; Doring, J.*; Geissel, H.*; Górska, M.*; Grzywacz, R.; Hellström, M.*; Janas, Z.; Karny, M.; Korgul, A.; Mukha, I.*; Pfützner, M.; Plettner, C.*; Robinson, A.; Roeckl, E.*; Rykaczewski, K.; Schmidt, K.*; Seweryniak, D.; Weick, H.*: **Decay spectroscopy of suburanium isotopes following projectile fragmentation of ^{238}U at 1 GeV/u.** *Nuclear instruments & methods in physics research, Section A, Accelerators, spectrometers, detectors and associated equipment* **543**(2): 591–601. DOI:10.1016/j.nima.2004.12.023

Liu, Z.; Woods, P. J.; Schmidt, K.; Mahmud, H.; Munro, P. S. L.; Blazhev, A.*; Döring, J.*; Grawe, H.*; Hellström, M.*; Kirchner, R.*; Li, Z. K.*; Mazzocchi, C.*; Mukha, I.*; Plettner, C.*; Roeckl, E.*; La Commara, M.: **Reinvestigation of direct proton decay of ^{105}Sb.** *Physical review C, Nuclear physics* **72**(4): 047301. DOI:10.1103/PhysRevC.72.047301

Lozeva, R.*; Gerl, J.*; Gorska, M.*; Mandal, S.*; Balabanski, D.; Kojouharov, I.*; Becker, F.*; Grebosz, J.*; Banu, A.*; Bednarczyk, P.*; Doornenbal, P.*; Wollersheim, H.-J.*: **Identification of heavy ion reaction channels with a new CAlorimeter TElescope within RISING.** *Journal of physics G, Nuclear and particle physics* **31**(10): S1917–S1920. DOI:10.1088/0954-3899/31/10/101

Lozeva, R.*; Mandal, S.*; Gerl, J.*; Górska, M.*; Grebosz, J.*; Kojouharov, I.*; Adamczewski, J.*; Banu, A.*;

Becker, F.*; Beck, T.*; Bednarczyk, P.*; Blazhev, A.*; Doornenbal, P.*; Geissel, H.*; Hellström, M.*; Kavatsyuk, M.*; Kavatsyuk, O.*; Kurza, N.*; Mutterer, M.; Muralithar, S.; Münzenberg, G.*; Prokopowicz, W.*; Saito, N.*; Saitoh, T.; Schaffner, H.*; Sümmerer, K.*; Weick, H.*; Winkler, M.*; Wheldon, C.*; Wollersheim, H.-J.*: **Calorimeter telescope for identification of relativistic heavy ion reaction channels.** *Acta physica Polonica B, Particle physics and field theory, nuclear physics, theory of relativity* **36**(4): 1245–1248.

Łukasik, J.*; Auger, G.; Begemann-Blaich, M. L.*; Bellaize, N.; Bittiger, R.*; Bocage, F.; Borderie, B.; Bougault, R.; Bouriquet, B.; Charvet, J. L.; Chbihi, A.; Dayras, R.; Durand, D.; Frankland, J. D.; Galichet, E.; Gourio, D.*; Guinet, D.; Hudan, S.; Lautesse, P.; Lavaudc, F.; Le Férea, A.*; Legraine, R.; Lopez, O; Lynen, A.*; Müller, W. F. J.*; Nalpas, L.; Orth, H.*; Plagnol, E.; Rosatog, E.; Saijah, H.; Schwarz, C.*; Sfienti, C.*; Tamaind, B.; Trautmann, W.*; Trzciński, A.; Turzó, K.*; Vient, E.; Vigilante, M.; Volant, C.; Zwiegliński, B.; INDRA Collaboration: **Directed and elliptic flow in ^{197}Au+^{197}Au at intermediate energies.** *Physics letters B* **608**(3): 223–230. DOI:10.1016/j.physletb.2004.12.076

Lutz, M. F. M.*; García-Recio, C.; Kolomeitsev, E. E.; Nieves, J.: **Quark-mass dependence of baryon resonances.** *Nuclear physics A, Nuclear and hadronic physics* **754**: 212C–220C. DOI:10.1016/j.nuclphysa.2005.01.037

Lutz, M. F. M.*; Kolomeitsev, E. E.: **Baryon resonances from chiral coupled-channel dynamics.** *Nuclear physics A, Nuclear and hadronic physics* **755**: 29C–39C. DOI:10.1016/j.nuclphysa.2005.03.110

Lutz, M. F. M.*; Soyeur, M.: **Quantum interferences in the γ N $\rightarrow e^+ e^-$ N reaction close to the vector meson production threshold.** *Nuclear physics A, Nuclear and hadronic physics* **760**(1): 85–109. DOI:10.1016/j.nuclphysa.2005.05.199

Lutz, M. F. M.*; Soyeur, M.: **The associated photoproduction of positive kaons and π^0 Λ or π Σ pairs in the region of the Σ(1385) and Λ(1405) resonances.** *Nuclear physics A, Nuclear and hadronic physics* **748**(3): 499–512. DOI:10.1016/j.nuclphysa.2004.11.007

Maas, A.*: **Gluons at finite temperature in Landau gauge Yang-Mills theory.** *Modern Physics Letters A* **20**(24): 1797–1811. DOI:10.1142/S0217732305018049

Maas, A.*; Wambach, J.*; Alkofer, R.: **The high-temperature phase of Landau-gauge Yang-Mills theory.** *The European physical journal: C, Particles and fields* **42**(1): 93–107. DOI:10.1140/epjc/s2005-02279-8

Mach, H.; Walker, P. M.; Julin, R.; Leino, M.; Juutinen, S.; Stanoiu, M.; Podolyak, Z.; Wood, R.; Bruce, A. M.; Bäck, T.; Cameron, J. A.; Cederwall, B.; Ekman, J.; Fogelberg, B.; Greenless, P. T.; Hellström, M.*; Jones, P.; Klamra, W.; Lagergren, K.; Leppänen, A. P.; Nieminen, P.; Orlandi, R.; Pakarinen, J.; Rahkila, P.; Rudolph, D.; Simpson, G.; Uusitalo, J.; Wheldon, C.: **Application of ultra-fast timing techniques to the study of exotic and weakly produced nuclei.** *Journal of physics G, Nuclear and particle physics* **31**(10): S1421–S1426. DOI:10.1088/0954-3899/31/10/007

Marín, A.*; CERES Collaboration: **New results from CERES.** *Journal of physics G, Nuclear and particle physics* **31**(6): S1175–S1178. DOI:10.1088/0954-3899/31/6/081

Maruta, T.; Ajimura, S.; Aoki, K.; Banu, A.*; Bhang, H.; Fukuda, T.; Hashimoto, O.; Hwang, J. I.; Kameoka, S.; Kang, B. H.; Kim, E. H.; Kim, J. H.; Kim, M. J.; Miura, Y.; Miyake, Y.; Nagae, T.; Nakamura, M.; Nakamura, S. N.; Noumi, H.; Okada, S.; Okayasu, Y.; Outa, H.; Park, H.; Saha, R.; Sato, Y.; Sekimoto, M.; Takahashi, T.; Tamura, H.; Tanida, K.; Toyoda, A.; Tsukada, K.; Watanabe, T.; Yim, H. J.: **Proton asymmetry in non-mesonic weak decay of light hypernuclei.** *Nuclear physics A, Nuclear and hadronic physics* **754**: 168C–172C. DOI:10.1016/j.nuclphysa.2005.02.159

Maruyama, T.; Tatsumi, T.; Voskresensky, D. N.*; Tanigawa, T.; Chiba, S.: **Nuclear 'pasta' structures and the charge screening effect.** *Physical review C, Nuclear physics* **72**(1): 015802. DOI:10.1103/PhysRevC.72.015802

Miura, Y.; Ajimura, S.; Fujii, Y.; Fukuda, T.; Hashimoto, O.; Hotchi, H.; Imai, K.; Imoto, W.; Kakiguchi, Y.; Kameoka, S.; Krutenkova, A.; Maruta, T.; Matsumura, A.; Miwa, K.; Mizunuma, K.; Nakamura, S. N.; Nagae, T.; Nomura, H.; Noumi, H.; Outa, H.; Saha, P. K.; Saitoh, T.*; Sato, Y.; Sekimoto, M.; Takahashi, T.; Tamura, H.; Tanida, K.; Toyoda, A.; Ukai, M.; Yamauchi, H.: **γ spectroscopy of $^{11}_{\Lambda}$B.** *Nuclear physics A, Nuclear and hadronic physics* **754**: 75C–79C. DOI:10.1016/j.nuclphysa.2005.02.131

Mocelj, D.; Rauscher, T.; Thielemann, F.-K.; Pinedo, G. M.; Langanke, K.*; Pacearescu, L.; Fäßler, A.: **Towards a parity-dependent level density for astrophysics.** *Journal of physics G, Nuclear and particle physics* **31**(10): S1927–S1930. DOI:10.1088/0954-3899/31/10/103

Montagnoli, G.; Stefanini, A. M.; Trotta, M.; Beghini, S.; Bettini, M.; Scarlassara, F.; Schiavon, V.; Corradi, L.; Behera, B. R.; Fioretto, E.; Gadea, A.; Latina, A.; Szilner, S.; Doná, L.; Rigato, M.; Kondratiev, N. A.; Chizhov, A. Y.; Kniajeva, G.; Kozulin, E. M.; Pokrovskiy, I. V.; Voskressensky, V. M.; Ackermann, D.*: **The large-area micro-channel plate entrance detector of the heavy-ion magnetic spectrometer PRISMA.** *Nuclear instruments & methods in physics research, Section A, Accelerators, spectrometers, detectors and associated equipment* **547**(2): 455–463. DOI:10.1016/j.nima.2005.03.158

Mukha, I.; Kavatsyuk, M.; Algora, A.; Batist, L.; Blazhev, A.*; Döring, J.*; Grawe, H.*; Hellström, M.*; Kavatsyuk, O.*; Kirchner, R.*; La Commara, M.; Mazzocchi, C.*; Plettner, C.; Roeckl, E.*: **The reaction of triple radiative capture $\alpha\alpha$(n,γ)^{9}Be studied in a beta decay of ^{9}Li.** *Nuclear physics A, Nuclear and hadronic physics* **758**: 647C–650C. DOI:10.1016/j.nuclphysa.2005.05.116

Mukha, I.*; Roeckl, E.*; Döring, J*.; Batist, L.; Blazhev, A.*; Grawe, H.*; Hoffman, C. R.; Huyse, M.; Janas, Z.; Kirchner, R.*; La Commara, M.; Mazzocchi, C.*; Plettner, C.*; Tabor, S. L.; Van Duppen, P.; Wiedeking, M.: **Observation of proton radioactivity of the (21^{+}) high-spin isomer in ^{94}Ag.** *Physical review letters* **95**(2): 022501. DOI:10.1103/PhysRevLett.95.022501

Mukha, I.*; Roeckl, E.*; Grawe, H.*; Döring, J.*; Batist, L.; Blazhev, A.*; Hoffman, C. R.; Janas, Z.; Kirchner, R.*; La Commara, M.; Dean, S.; Mazzocchi, C.*; Plettner, C.*; Tabor, S. L.; Wiedeking, M.: **Study of the (21^{+}) isomer in ^{94}Ag.** *The European physical journal A, Hadrons and nuclei* **25**: 131–133. DOI:10.1140/epjad/i2005-06-051-y

Muronga, A.*: **Viscous hydrodynamics.** *Journal of physics G, Nuclear and particle physics* **31**(6): S1035–S1039. DOI:10.1088/0954-3899/31/6/053

Nadtochy, P. N.*; Adeev, G. D.: **Dynamical interpretation of average fission-fragment kinetic energy systematics and nuclear scission.** *Physical review C, Nuclear physics* **72**(5): 054608. DOI:10.1103/PhysRevC.72.054608

Nagame, Y.; Tsukada, K.; Asai, M.; Toyoshima, A.; Akiyama, K.; Ishii, Y.; Kaneko-Sato, T.; Hirata, M.; Nishinaka, I.; Ichikawa, S.; Haba, H.; Enomoto, S.; Matsuo, K.; Saikal, D.; Kitamoto, Y.; Hasegawa, H.; Tani, Y.; Sato, W.; Shmohara, A.; Ito, M.; Saito, J.; Goto, S.; Kudo, H.; Kikunaga, H.; Kinoshita, N.; Yokoyama, A.; Sueki, K.; Oura, Y.; Nakahara, H.; Sakama, M.; Schädel, M.*; Brüchle, W.*; Kratz, J. V.: **Chemical studies on rutherfordium (Rf) at JAERI.** *Radiochimica acta* **93**(9): 519–526. DOI:10.1524/ract.2005.93.9-10.519

Neff, T.*; Feldmeier, H.*; Roth, R.: **Structure of light nuclei in fermionic molecular dynamics.** *Nuclear physics A, Nuclear and hadronic physics* **752**: 321C–324C. DOI:10.1016/j.nuclphysa.2005.02.092

Niedermaier, O.; Scheit, H.; Bildstein, V.; Boie, H.; Fitting, J.; von Hahn, R.; Kock, F.; Lauer, M.; Pal, U. K.; Podlech, H.; Repnow, R.; Schwalm, D.; Alvarez, C.; Ames, F.; Bollen, G.; Emhofer, S.; Habs, D.; Kester, O.; Lutter, R.; Rudolph, K.; Pasini, M.; Thirolf, P. G.; Wolf, B. H.; Eberth, J.; Gersch, G.; Hess, H.; Reiter, P.; Thelen, O.; Warr, N.; Weisshaar, D.; Aksouh, F.*; Van den Bergh, P.; Van Duppen, P.; Huyse, M.; Ivanov, O.; Mayet, P.; Van de Walle, J.; Aysto, J.; Butler, P. A.; Cederkall, J.; Delahaye, P.; Fynbo, H. O. U.; Fraile, L. M.; Forstner, O.; Franchoo, S.; Koster, U.; Nilsson, T.; Oinonen, M.; Sieber, T.; Wenander, F.; Pantea, M.; Richter, A.; Schrieder, G.; Simon, H.; Behrens, T.; Gernhauser, R.; Kroll, T.; Krucken, R.; Münch, M.; Davinson, T.*; Gerl, J.*; Huber, G.; Hurst, A.; Iwanicki, J.; Jonson, B.; Lieb, P.; Liljeby, L.; Schempp, A.; Scherillo, A.; Schmidt, P.; Walter, G.: **The neutron-rich Mg isotopes: first results from MINIBALL at REX-ISOLDE.** *Nuclear physics A, Nuclear and hadronic physics* **752**: 273C–278C. DOI:10.1016/j.nuclphysa.2005.02.071

Niedermaier, O.; Scheit, H.; Bildstein, V.; Boie, H.; Fitting, J.; von Hahn, R.; Köck, F.; Lauer, M.; Pal, U. K.; Podlech, H.; Repnow, R.; Schwalm, D.; Alvarez, C.; Ames, F.; Bollen, G.; Emhofer, S.; Habs, D.; Kester, O.; Lutter, R.; Rudolph, K.; Pasini, M.; Thirolf, P. G.; Wolf, B. H.; Eberth, J.; Gersch, G.; Hess, H.; Reiter, P.; Thelen, O.; Warr, N.; Weisshaar, D.; Aksouh, F.; Van den Bergh, P.; Van Duppen, P.; Huyse, M.; Ivanov, O.; Mayet, P.; Van de Walle, J.; Äystö, J.; Butler, P. A.; Cederkäll, J.; Delahaye, P.; Fynbo, H. O. U.; Fraile, L. M.; Forstner, O.; Franchoo, S.; Köster, U.; Nilsson, T.; Oinonen, M.; Sieber, T.; Wenander, F.; Pantea, M.*; Richter, A.; Schrieder, G.*; Simon, H.*; Behrens, T.; Gernhäuser, R.; Kroll, T.; Krücken, R.; Münch, M.; Davinson, T.; Gerl, J.*; Huber, G.; Hurst, A.; Iwanicki, J.; Jonson, B.; Lieb, P.; Liljeby, L.; Schempp, A.; Scherillo, A.; Schmidt, P.; Walter, G.: **'Safe' Coulomb excitation of ^{30}Mg-30.** *Physical review letters* **94**(17): 172501. DOI:10.1103/PhysRevLett.94.172501

Nociforo, C.; Jones, K. L.*; Khiem, L. H.; Adrich, P.*; Aumann, T.*; Carlson, B. V.; Cortina-Gil, D.*; Datta Pramanik, U.*; Elze, T. W.; Emling, H.*; Geissel, H.*; Hellström, M.*; Kratz, J. V.; Kulessa, R.; Lange, T.; Leifels, Y.*; Lenske, H.; Lubkiewicz, E.*; Münzenberg, G.*; Palit, R.*; Scheit, H.; Simon, H.*; Sümmerer, K.*; Typel, S.*; Wajda, E.; Walus, W.; Weick, H.*: **Coulomb breakup of ^{23}O.** *Physics letters B* **605**(1): 79–86. DOI:10.1016/j.physletb.2004.11.014

Nortershäuser, W.*; Bushaw, B. A.; Dax, A.*; Drake, G. W. F.; Ewald, G.*; Götte, S.*; Kirchner, R.*; Kluge, H.-J.*; Kühl, T.*; Sanchez, R.*; Wojtaszek, A*.; Yan, Z. C.; Zimmermann, C.: **Measurement of the nuclear charge radii of ^{8,9}Li - The last step towards the determination of the charge radius of ^{11}Li.** *The European physical journal A, Hadrons and nuclei* **25**: 199–200. DOI:10.1140/epjad/i2005-06-053-9

Ogul, R.*; Buyukcizmeci, N.; Botvina, A. S.*: **Nuclear fragmentation and critical temperature for the liquid-gas phase transition region.** *Nuclear physics A, Nuclear and hadronic physics* **749**: 126C–129C. DOI:10.1016/j.nuclphysa.2004.12.020

Ohtsubo, T.*; Bosch, F.*; Geissel, H.*; Maier, L.; Scheidenberger, C.*; Attallah, F.*; Beckert, K.*; Beller, P.*; Boutin, D.*; Faestermann, T.; Franczak, B.*; Franzke, B.*; Hausmann, M.; Hellström, M.*; Kaza, E.*; Kienle,

P.; Klepper, O.*; Kluge, H.-J.*; Kozhuharov, C.*; Litvinov, Y. A.*; Matos, M.*; Münzenberg, G.*; Nolden, F.*; Novikov, Y. N.*; Portillo, M.*; Radon, T.*; Stadlmann, J.*; Steck, M.*; Stöhlker, T.*; Sümmerer, K.*; Takahashi, K.*; Weick, H.*; Winkler, M.*; Yamaguchi, T.*: **Simultaneous measurement of β^- decay to bound and continuum electron states.** *Physical review letters* **95**(5): 052501. DOI:10.1103/PhysRevLett.95.052501

Okada, S.; Ajimura, S.; Aoki, K.; Banu, A.*; Bhang, H. C.; Fukuda, T.; Hashimoto, O.; Hwang, J. I.; Kameoka, S.; Kang, B. H.; Kim, E. H.; Kim, J. H.; Kim, M. J.; Maruta, T.; Miura, Y.; Miyake, Y.; Nagae, T.; Nakamura, M.; Nakamura, S. N.; Noumi, H.; Okayasu, Y.; Outa, H.; Park, H.; Saha, P. K.; Sato, Y.; Sekimoto, M.; Takahashi, T.; Tamura, H.; Tanida, K.; Toyoda, A.; Tsukada, K.; Watanabe, T.; Yim, H. J.: **π^0 decay branching ratios of $^{5}_{\Lambda}$He and $^{12}_{\Lambda}$C hypernuclei.** *Nuclear physics A, Nuclear and hadronic physics* **754**: 178C–183C. DOI:10.1016/j.nuclphysa.2005.02.128

Okada, S.; Ajimura, S.; Aoki, K.; Banu, A.*; Bhang, H. C.; Fukuda, T.; Hashimoto, O.; Hwang, J. I.; Kameoka, S.; Kang, B. H.; Kim, J. H.; Kim, M. J.; Maruta, T.; Miura, Y.; Miyake, Y.; Nagae, T.; Nakamura, M.; Nakamura, S. N.; Noumi, H.; Okayasu, Y.; Outa, H.; Park, H.; Saha, P. K.; Sato, Y.; Sekimoto, N.; Takahashi, T.; Tamura, H.; Tanida, N.; Toyoda, A.; Tsukada, K.; Watanabe, T.; Yim, H. J.: **Nucleon-nucleon coincidence measurement in the non-mesonic weak decay of $^{5}_{\Lambda}$ He and $^{12}_{\Lambda}$C hypernuclei.** *Nuclear physics A, Nuclear and hadronic physics* **752**: 196C–199C. DOI:10.1016/j.nuclphysa.2005.02.035

Otsuka, T.; Suzuki, T.; Fujimoto, R.; Grawe, H.*; Akaishi, Y.: **Evolution of nuclear shells due to the tensor force.** *Physical review letters* **95**(23): 232502. DOI:10.1103/PhysRevLett.95.232502

Otsuka, T.; Suzuki, T.; Fujimoto, R.; Matsuo, T.; Abe, D.; Grawe, H.*; Akaishi, Y.: **Evolution of shell and collective structures in exotic nuclei.** *Acta physica Polonica B, Particle physics and field theory, nuclear physics, theory of relativity* **36**(4): 1213–1219.

Otwinowski, J.; Agakichiev, G.*; Agodi, C.; Alvarez-Poll, H.; Balanda, A.; Bellia, G.; Bielcik, J.*; Bomer, M.; Bokemeyer, H.*; Boyard, J.; Braun-Munzinger, P.*; Chernenko, S.; Christ, T.; Coniglione, R.; Djeridi, R.; Dohrmann, F.; Duran, D.; Eberl, T.; Fabbietti, L.; Fateev, O.; Finocchiaro, P.; Friese, J.; Frohlich, I.; Garzon, J.; Gernhäuser, R.; Golubeva, M.; Gonzalez, D.; Grosse, E.; Gruber, F.; Hennino, T.; Hlavac, S.; Holzmann, R.*; Ierusalimov, A.; Iori, I.; Jaskula, M.; Jurkovic, M.; Kämpfer, B.; Kanaki, K.; Karavicheva, T.; Koenig, I.*; Koenig, W.*; Kolb, B.*; Kopf, U.*; Kotte, R.; Kotulic-Bunta, J.; Krücken, R.; Kugler, A.; Kuhn, W.; Kulessa, R.; Kurepin, A.; Lang, S.*; Lehnert, J.; Maiolino, C.; Market, J.; Metag, V.; Mousa, J.; Münch, M.; Müntz, C.; Naumann, L.; Novotny, J.; Novotny, J.; Pachmayer, Y.*; Pant, L. M.; Pechenov, V.; Perez, T.; Pietraszko, J.*; Pleskac, R.; Pospisil, V.; Przygoda, W.; Rabin, N.; Ramstein, B.; Reshetin, A.; Ritman, J.; Roy-Stephan, M.; Rustamov, A.*; Sadovsky, A.; Sailer, B.; Salabura, P.; Sanchez, M.; Sapienza, P.; Schmah, A.*; Simon, R.*; Smolyanikin, V.; Smykov, L.; Spataro, S.; Stroebele, H.; Stroth, J.*; Sturm, C.*; Sudol, M.*; Tlusty, P.; Toia, A.; Traxler, M.*; Tsertos, H.; Wagner, V.; Wisniowski, M.; Wojcik, T.; Wustenfeld, J.*; Zanevsky, Y.; Zoviniec, D.; Zumbruch, P.*; HADES Collaboration: **Dilepton analysis in the HADES spectrometer for ^{12}C+^{12}C at 2 AGEV.** *International Journal of Modern Physics* **20**(2): 602–605. DOI:10.1142/S0217751X05021907

Palacz, M.; Nyberg, J.; Bednarczyk, P.; Dworski, J.; Górska, M.*; Iwanicki, J.; Kapusta, M.; Kownacki, J.; Kulczycka, E.; Lagergren, K.; Moszyński, M.; Pienkowski, L.; Stolarz, A.; Wolski, D.; Zieblíński, M.: **Highly efficient charged particle veto detector CUP.** *Nuclear instruments & methods in physics research, Section A, Accelerators, spectrometers, detectors and associated equipment* **550**(1): 414–424. DOI:10.1016/j.nima.2005.04.093

Parkhomenko, A.; Sobiczewski, A.*: **Neutron one-quasiparticle states of heaviest nuclei.** *Acta physica Polonica B, Particle physics and field theory, nuclear physics, theory of relativity* **36**(10): 3115–3137.

Parkhomenko, A.; Sobiczewski, A.*: **Phenomenological formula for alpha-decay half-lives of heaviest nuclei.** *Acta physica Polonica B, Particle physics and field theory, nuclear physics, theory of relativity* **36**(10): 3095–3108.

Pershina, V.*: **Predictions of adsorption behaviour of the heaviest elements in a comparative study from the electronic structure calculations.** *Radiochimica acta* **93**(3): 125–131. DOI:10.1524/ract.93.3.125.61612

Pershina, V.*: **Theoretical investigations of the reactivity of MO_4 and the electronic structure of $Na_2[MO_4(OH)_2]$, where M = Ru, Os, and Hs (element 108).** *Radiochimica acta* **93**(7): 373–376. DOI:10.1524/ract.2005.93.7.373

Pershina, V.*; Bastug, T.: **Relativistic effects on experimentally studied gas-phase properties of the heaviest elements.** *Journal of Chemical Physics* **311**(1): 139–150.

Pershina, V.*; Bastug, T.; Fricke, B.: **Relativistic effects on the electronic structure and volatility of group-8 tetroxides MO4, where M=Ru, Os, and element 108, Hs.** *Journal of Chemical Physics* **122**(12): 124301.

Pichon, M.; Tamain, B.; Bougault, R.; Lopez, O.; INDRA Collaboration; ALADIN Collaboration: **Bimodality: a possible signature of the liquid-gas phase transition of nuclear matter.** *Nuclear physics A, Nuclear and hadronic physics* **749**: 93C–97C. DOI:10.1016/j.nuclphysa.2004.12.012

Pizzone, R. G.; Spitaleri, C.; Cherubini, S.; Cognata, M. L.; Lamia, L.; Miljanic, D.; Musumarra, A.; Romano, S.; Tumino, A.; Tudisco, S.; Typel, S.*: **Influence of the α-d motion in Li-6 on Trojan horse applications.** *Physical review C, Nuclear physics* **71**(5): 058801. DOI:10.1103/PhysRevC.71.058801

Płoskoń, M.*; KaoS Collaboration: **Azimuthal emission pattern of K^+ and K^- at SIS energies.** *Nuclear physics A, Nuclear and hadronic physics* **749**: 170C–173C. DOI:10.1016/j.nuclphysa.2004.12.027

Pomorski, M.*; Berdermann, E.*; Ciobanu, M.*; Martemyianov, A.*; Moritz, P.*; Rebisz, M.*; Marczewska, B.: **Characterisation of single crystal CVD diamond particle detectors for hadron physics experiments.** *Physica status solidi A, Applied research* **202**(11): 2199–2205. DOI:10.1002/pssa.200561929

Popescu, S.; Frankenfeld, U.; Schmidt, H. R.: **Thermal influences of the front-end electronics on the Alice TPC readout chamber.** *IEEE transactions on nuclear science* **52**(6): 2879–2888. DOI:10.1109/TNS.2005.862794

Redlich, K.*: **QPM thermodynamics below deconfinement and heavy-ion collisions.** *Journal of physics G, Nuclear and particle physics* **31**(6): S943–S950. DOI:10.1088/0954-3899/31/6/038

Reiter, P.; Becker, F.*; Bentley, M. A.; Bracco, B. A.; De Angelis, G.; Fahlander, C.; Gerl, J.*; Gorska, M.*; Grawe, H.*; Hübel, H.; Jolie, J.; Maj, A.; Mayet, P.; Saito, T.*; Speidel, K. H.; Wollersheim, H. J.*: **Future rising experiments at relativistic energies.** *Acta physica Polonica B, Particle physics and field theory, nuclear physics, theory of relativity* **36**(4): 1259–1268.

Ricciardi, M. V.*; Ignatyuk, A. V.; Kelić, A.*; Napolitani, P.*; Rejmund, F.; Schmidt, K.-H.*; Yordanov, I.*: **Complex nuclear-structure phenomena in the cooling down of highly excited nuclear systems.** *Nuclear physics A, Nuclear and hadronic physics* **749**: 122C–125C. DOI:10.1016/j.nuclphysa.2004.12.019

Rios, A.; Polls, A.; Ramos, A.; Vidaña, I.*: **Bulk and single-particle properties of hyperonic matter at finite temperature.** *Physical review C, Nuclear physics* **72**(2): 024316. DOI:10.1103/PhysRevC.72.024316

Rios, A.; Polls, A.; Vidaña, I.*: **Ferromagnetic instabilities in neutron matter at finite temperature with the Skyrme interaction.** *Physical review C, Nuclear physics* **71**(5): 055802. DOI:10.1103/PhysRevC.71.055802

Rivet, M. F.; Le Neindre, N.; Wieleczko, J. P.; Borderie, B.; Chbihi, A.; Frankland, J. D.; Parlog, M.; Pichon, M.; Tamain, B.; INDRA Collaboration; ALADIN Collaboration: **Correlations between signals of the liquid-gas phase transition in nuclei.** *Nuclear physics A, Nuclear and hadronic physics* **749**: 73C–82C. DOI:r:10.1016/j.nuclphysa.2004.12.010

Roth, R.; Hergert, H.; Papakonstantinou, P.; Neff, T.*; Feldmeier, H.*: **Matrix elements and few-body calculations within the unitary correlation operator method.** *Physical review C, Nuclear physics* **72**(3): 034002. DOI:10.1103/PhysRevC.72.034002

Salabura, P.*; Agakichiev, G.*; Agodi, C.; Alvarez-Pol, H.; Balanda, A.; Bellia, G.; Bielcik, J.*; Böhmer, M.; Boyard, J.; Braun-Munzinger, P.*; Chernenko, S.; Christ, T.; Coniglione, R.; Djeridi, R.; Dohrmann, F.; Duran, I.; Eberl, T.; Fabbietti, L.; Fateev, O.; Finocchiaro, P.; Friese, J.; Fröhlich, I.; Garzon, J.; Gernhäuser, R.; Golubeva, M.; Gonzalez-Diaz, D.; Grosse, E.; Guber, F.; Hennino, T.; Hlavac, S.; Holzmann, R.*; Ierusalimov, A.; Iori, I.; Jaskula, M.; Jurkovic, M.; Kämpfer, B.; Kanaki, K.; Karavicheva, T.; Koenig, I.*; Koening, W.*; Kolb, B.*; Kotte, R.; Kotulic-Bunta, J.; Krücken, R.; Kugler, A.; Kühn, W.; Kulessa, R.; Kurepin, A.; Lang, S.*; Lehnert, J.; Maiolino, C.; Markert, J.; Metag, V.; Mousa, J.; Münch, M.; Müntz, C.; Naumann, L.; Novotny, J.; Novotny, R.; Otwinowski, J.; Pachmayer, Y.; Pechenov, V.; Perez, T.; Pietraszko, J.; Pleskac, R.; Pospisil, V.; Przygoda, W.; Rabin, N.; Ramstein, B.; Reshetin, A.; Ritman, J.; Roy-Stephan, M.; Rustamov, A.*; Sadovsky, A.; Sailer, B.; Sanchez, M.; Sapienza, P.; Schmah, A.*; Smolyankin, V.; Smykov, L.; Spataro, S.; Spruck, B.; Stroebele, H.; Stroth, J.; Sturm, C.*; Sudol, M.*; Tlusty, P.; Toia, A.; Traxler, M.*; Tsertos, H.; Wagner, V.; Wisniowski, M.; Wojcik, T.; Wüstenfeld, J.; Zanevsky, Y.; Zovinec, D.; Zumbruch, P.*; HADES Collaboration: **Probing of in-medium hadron structure with HADES.** *Nuclear physics A, Nuclear and hadronic physics* **749**: 150C–159C. DOI:10.1016/j.nuclphysa.2004.12.024

Sato, T.; Sihver, L.; Iwase, H.*; Nakashima, H.; Niita, K.: **Simulations of an accelerator-based shielding experiment using the particle and heavy-ion transport code system PHITS.** *Advances in space research* **35**(2): 208–213. DOI:10.1016/j.asr.2005.01.041

Schaefer, B.-J.; Wambach, J.*: **The phase diagram of the quark-meson model.** *Nuclear physics A, Nuclear and hadronic physics* **757**(3): 479–492. DOI:10.1016/j.nuclphysa.2005.04.012

Scheidenberger, C.*: **The contribution of precision mass measurements to nuclear physics.** *Nuclear physics A, Nuclear and hadronic physics* **751**: 209C–225C. DOI:10.1016/j.nuclphysa.2005.02.006

Scheit, H.; Niedermaier, O.; Bildstein, V.; Boie, H.; Fitting, J.; von Hahn, R.; Köck, F.; Lauer, M.; Pal, U. K.; Podlech, H.; Repnow, R.; Schwalm, D.; Alvarez, C.; Ames, F.; Bollen, G.; Emhofer, S.; Habs, D. Kester, O.; Lutter, R.; Rudolph, K.; Pasini, M.; Thirolf, P. G.; Wolf, B. H.; Eberth, J.; Gersch, G.; Hess, H.; Reiter, P.; Thelen, O.; Warr, N.; Weisshaar, D.; Aksouh, F.*; Van den Bergh, P.;

Van Duppen, P.; Huyse, M.; Ivanov, O.; Mayet, P.; Van de Walle, J.; Äystö, J.; Butler, P. A.; Cederkall, J.; Delahaye, P.; Fynbo, H. O. U.; Fraile, L. M.; Forstner, O.; Franchoo, S.; Koster, U.; Nilsson, T.; Oinonen, M.; Sieber, T.; Wenander, F.; Pantea, M.; Richter, A.; Schrieder, G.; Simon, H.; Behrens, T.; Gernhäuser, R.; Kröll, T.; Krücken, R.; Münch, M.; Davinson, T.; Gerl, J.*; Huber, G.; Hurst, A.; Iwanicki, J.; Jonson, B.; Lieb, P.; Liljeby, L.; Schempp, A.; Scherillo, A.; Schmidt, P.; Walter, G.*: **Coulomb excitation of neutron-rich beams at REX-ISOLDE.** *The European physical journal A, Hadrons and nuclei* **25**: 397–402. DOI:10.1140/epjad/i2005-06-165-2

Schleifenbaum, W.; Maas, A.; Wambach, J.*; Alkofer, R.: **Infrared behavior of the ghost-gluon vertex in Landau gauge Yang-Mills theory.** *Physical Review D* **72**(1): 014017. DOI:10.1103/PhysRevD.72.014017

Schmah, A.; Lang, S.; Böttcher, I.; Dohrmann, F.; Förster, A.; Grosse, E.; Koczoń, P.*; Kohlmeyer, B.; Laue, F.*; Menzel, M.; Naumann, L.; Oeschler, H.; Scheinast, W.; Schuck, T.; Schwab, E.*; Senger, P.*; Shin, Y.; Ströbele, H.*; Sturm, C.*; Surówska, G.; Uhlig, F.*; Wagner, A.; Waluś, W.; Fuchs, C.; Faessler, A.; Mansour, H.; KaOS Collaboration: **Kaon and pion emission in asymmetric C+Au and Au+C collisions at 1.0A GeV and 1.8A GeV.** *Physical review C, Nuclear physics* **71**(6): 064907. DOI:10.1103/PhysRevC.71.064907

Schmitt, L. and the COMPASS Collaboration: **First measurement of the transverse spin asymmetries of the deuteron in semi-inclusive deep inelastic scattering.** *Physical review letters* **94**(20): 202002. DOI:10.1103/PhysRevLett.94.202002

Schmitt, L. and the COMPASS Collaboration: **Search for the phi(1860) Pentaquark at COMPASS.** *The European physical journal: C, Particles and fields* **41**(4): 469–474. DOI:10.1140/epjc/s2005-02281-2

Seyboth, P.; NA49 Collaboration: **Indications for the onset of deconfinement in Pb plus Pb collisions at the CERN SPS from NA49.** *Acta physica Polonica B, Particle physics and field theory, nuclear physics, theory of relativity* **36**(2): 565–573.

Sfienti, C.*; Adrich, P.*; Aumann, T.* L; Bacri, C. O.; Barczyk, T.; Bassini, R.; Boiano, C.; Botvina, A. S.*; Boudard, A.; Brzychczyk, J.; Chbihi, A.; Cibor, J.; Czech, B.; De Napoli, M.; Ducret, J.-E.; Emling, H.*; Frankland, J.; Hellström, M.*; Henzlova, D.*; Kezzar, K.*; Immé, G.; Iori, I.; Johansson, H.*; Lafriakh, A.; Le Fèvre, A.*; Le Gentil, E.; Leifels, Y.*; Lynch, W. G.; Lühning, J.*; Łukasik, J.*; Lynen, U.*; Majka, Z.; Mocko, M.; Müller, W. F. J.*; Mykulyak, A.; Orth, H.*; Otte, A. N.*; Palit, R.*; Pullia, A.*; Raciti, G.; Rapisarda, E.; Sann, H.*; Schwarz, C.*; Simon, H.*; Sokolov, A.*; Sümmerer, K.*; Trautmann, W.*; Tsang, M. B.; Verde, G.; Volaut, C.; Wallace, M.; Weick, H.*; Wiechula, J.*; Wieloch, A.; Zwieglinski, B.: **Mass and isospin effects in multifragmentation.** *Nuclear physics A, Nuclear and hadronic physics* **749**: 83C–92C. DOI:10.1016/j.nuclphysa.2004.12.011

Sharma, M. M.; Farhan, A. R.; Münzenberg, G.*: **α-Decay properties of superheavy elements Z=113-125 in the relativistic mean-field theory with vector self-coupling of omega meson.** *Physical review C, Nuclear physics* **71**(5): 054310. DOI:10.1103/PhysRevC.71.054310

Sikler, G.; Audi, G.; Beck, D.; Blaum, K.; Bollen, G.; Herfurth, F.*; Kellerbauer, A.; Kluge, H.-J.*; Lunney, D.; Oinonen, M.; Scheidenberger, C.*; Schwarz, S.; Szerypo, J.: **Mass measurements on neutron-deficient Sr and neutron-rich Sn isotopes with the ISOLTRAP mass spectrometer.** *Nuclear physics A, Nuclear and hadronic physics* **763**: 45–58. DOI:10.1016/j.nuclphysa.2005.08.014

Singh, B. S. N.; Hass, M.; Goldring, G.; Ackermann, D.*; Gerl, J.*; Heßberger, F. P.*; Hofmann, S.*; Kojouharov, I.*; Kuusiniemi, P.*; Schaffner, H.*; Sulignano, B.*; Brown, B. A.: **Parity non-conservation in the γ-decay of polarized 17/2$^-$ isomers in ^{93}Tc.** *The European physical journal A, Hadrons and nuclei* **25**: 703–704. DOI:10.1140/epjad/i2005-06-073-5

Singh, B. S. N.; Hass, M.; Goldring, G.; Ackermann, D.*; Gerl, J.; Heßberger, F. P.; Hofmann, S.; Kojouharov, I.; Kuusiniemi, P.; Schaffner, H.; Sulignano, B.; Brown, B. A.: **Parity nonconservation in the γ decay of polarized 17/2$^-$ isomers in ^{93}Tc.** *Physical review C, Nuclear physics* **72**(2): 027303. DOI:10.1103/PhysRevC.72.027303

Sohler, D.; Palacz, M.; Dombrádi, Z.; Hjorth-Jensen, M.; Fahlander, C.; Norlin, L.-O.; Nyberg, J.; Bäck, T.; Lagergren, K.; Rudolph, D.; Algora, A.; Andreoiu, C.; de Angelis, G.; Atac, A.; Bazzacco, D.; Cederkäll, J.; Cederwall, B.; Fant, B.; Farnea, E.; Gadea, A.; Górska, M.*; Grawe, H.*; Hashimito-Saitoh, N.*; Johnson, A.; Kerek, A.; Klamra, W.; Kownacki, J.; Lenzi, S. M.; Likar, A.; Lipoglavsek, M.; Moszynski, M.; Napoli, D. R.; Rossi-Alvarez, C.; Roth, H. A.; Saitoh, T.; Seweryniak, D.; Skeppstedt, O.; Timár, J.; Weisflog, M.; Wolińska, M.: **Maximally aligned states in the proton drip line nucleus Sb-106.** *Nuclear physics A, Nuclear and hadronic physics* **753**(3): 251–262. DOI:10.1016/j.nuclphysa.2005.02.153

Sohler, D.; Timár, J.; Rainovski, G.; Joshi, P.; Starosta, K.; Fossan, D. B.; Molnár, J.; Wadsworth, R.; Algora, A.; Bednarczyk, P.*; Curien, D.; Dombradi, Z.; Duchene, G.; Gizon, A.; Gizon, J.; Jenkins, D. G.; Koike, T.; Krasznahorkay, A.; Paul, E. S.; Raddon, P. M.; Scheurer, J. N.; Simons, A. J.; Vaman, C.; Wilkinson, A. R.; Zolnai, L.: **High-spin structure of ^{102}Ru.** *Physical review C, Nuclear physics* **71**(6): 064302. DOI:10.1103/PhysRevC.71.064302

Soyeur, M.; Lutz, M. F. M.*: **Study of the Σ(1385) and Λ(1405) resonances in K^+ photoproduction processes.** *Progress in particle and nuclear physics* **55**(1): 165–173. DOI:10.1016/j.ppnp.2004.12.003

Stroth, J.: **The future at GSI and FAIR.** *Nuclear physics A, Nuclear and hadronic physics* **755**: 209C–218C. DOI:10.1016/j.nuclphysa.2005.03.104

Tamura, H.; Ajimura, S.; Akikawa, H.; Alburger, D. E.; Aoki, K.; Banu, A.*; Chrien, R. E.; Franklin, G. B.; Franz, J.; Fujii, Y.; Fukao, Y.; Fukuda, T.; Hashimoto, O.; Hayakawa, T.; Hiyama, E.; Hotchi, H.; Imai, K.; Imoto, W.; Kakiguchi, Y.; Kameoka, M.; Kishimoto, T.; Krutenkova, A.; Maruta, T.; Matsumura, A.; May, M.; Minami, S.; Miura, Y.; Miwa, K.; Miyoshi, T.; Mizunuma, K.; Nagae, T.; Nakamura, S. N.; Nakazawa, K.; Niiyama, M.; Nomura, H.; Noumi, H.; Okayasu, Y.; Ota, S.; Ohtaki, T.; Outa, H.; Pile, P.; Quinn, B. P.; Rusek, A.; Saha, P. K.; Sato, Y.; Saitoh, T.; Sekimoto, M.; Sutter, R.; Takahashi, H.; Takahashi, T.; Tang, L.; Tanida, K.; Terashima, S.; Togawa, M.; Toyoda, A.; Ukai, M.; Yamauchi, H.; Yuan, L.; Zhou, S. H.: **γ-ray spectroscopy in Λ hypernuclei.** *Nuclear physics A, Nuclear and hadronic physics* **754**: 58C–69C. DOI:10.1016/j.nuclphysa.2005.01.034

Taylor, M. J.; Hammond, G.; Bentley, M. A.; Becker, F.*; Grebosz, J.; Banu, A.; Barton, C. J.; Beck, T.*; Bednarczyk, P.* L; Bracco, A.; Bruce, A. M.; Bullock, L. C.; Bürger, A.; Camera, F.; Chandler, C.; Doornenbal, P.*; Gerl, J.*; Geissel, H.*; Górska, M.*; Hellström, M.*; Judson, D. S.; Kojouharov, I.*; Kurz, N.*; Lozeva, R.; Maj, A.; Mandal, S.*; McGuirk, B.; Muralithar, S.; Paul, E. S.; Podolyák, Z.; Prokopowicz, W.*; Rudolph, D.; Saito, N.*; Saito, T. R.*; Schaffner, H.*; Simpson, J.; Warner, D. D.; Weick, H.*; Wheldon, C.; Winkler, M.*; Wollersheim, H. J.*: **Spectroscopy of nuclei approaching the proton drip-line using a secondary-fragmentation technique with the RISING detector array.** *Journal of physics G, Nuclear and particle physics* **31**(10): S1527–S1530. DOI:10.1088/0954-3899/31/10/025

Ter-Akopian, G. M.; Fomichev, A. S.; Golovkov, M. S.; Grigorenko, L. V.; Krupko, S. A.; Oganessian, Y. T.; Rodin, A. M.; Sidorchuk, S. I.; Slepnev, R. S.; Stepantsov, S. V.; Wolski, R.; Korsheninnikov, A. A.; Nikolskii, E. Y.; Roussel-Chomaz, P.; Mittig, W.; Palit, R.*; Bouchat, V.; Kinnard, V.; Materna, T.; Hanappe, F.; Dorvaux, O.; Stuttge, L.; Angulo, C.; Lapoux, V.; Raabe, R.; Nalpas, L.; Yukhimchuk, A. A.; Perevozchikov, V. V.; Vinogradov, Y. I.; Grishechkin, S. K.; Zlatoustovskiy, S. V.: **New insights into the resonance states of ^{5}H and ^{5}He.** *The European physical journal A, Hadrons and nuclei* **25**: 315–320. DOI:10.1140/epjad/i2005-06-080-6

Toneev, V. D.*; Parvan, A. S.: **Canonical strangeness and distillation effects in hadron production.** *Journal of physics G, Nuclear and particle physics* **31**(7): 583–597. DOI:10.1088/0954-3899/31/7/005

Trautmann, W.*: **Isoscaling and the symmetry energy in spectator fragmentation.** *Abstracts of papers American Chemical Society* **229**: U304–U304.

Trautmann, W.*: **Multifragmentation and the liquid-gas phase transition: an experimental overview.** *Nuclear physics A, Nuclear and hadronic physics* **752**: 407C–416C. DOI:10.1016/j.nuclphysa.2005.02.117

Typel, S.*: **Relativistic model for nuclear matter and atomic nuclei with momentum-dependent self-energies.** *Physical review C, Nuclear physics* **71**(6): 064301. DOI:10.1103/PhysRevC.71.064301

Typel, S.*: **The Trojan-Horse method for nuclear astrophysics.** *The European physical journal A, Hadrons and nuclei* **25**: 665–668. DOI:10.1140/epjad/i2005-06-086-0

Typel, S.*; Baur, G.: **Electromagnetic strength of neutron and proton single-particle halo nuclei.** *Nuclear physics A, Nuclear and hadronic physics* **759**(3): 247–308. DOI:10.1016/j.nuclphysa.2005.05.145

Uggerhøj, U. I.; Hansen, H. D.; Jessen, K.; Knudsen, H.; Uggerhøj, E.; Scheidenberger, C.*; Biino, C.; Clément, M.; Doble, N.; Elsener, K.; Gatignon, L.; Grafstrom, P.; Sona, P.; Mangiarotti, A.; Ballestrero, S.: **Strong suppression of nuclear-charge changing interactions for 18 TeV/c In ions channeled through a bent Si crystal.** *Physics letters B* **619**(3): 240–246. DOI:10.1016/j.physletb.2005.06.003

Uggerhøj, U. I.; Pshenichnov, I. A.; Scheidenberger, C.*; Hansen, H. D.; Knudsen, H.; Uggerhøj, E.; Sona, P.; Mangiarotti, A.; Ballestrero, S.: **Charge-changing interactions of ultrarelativistic In nuclei.** *Physical review C, Nuclear physics* **72**(5): 057901. DOI:10.1103/PhysRevC.72.057901

Uhlig, F.; Förster, A.; Böttcher, I.; Debowski, M.; Dohrmann, F.; Grosse, E.; Koczoń, P.*; Kohlmeyer, B.; Laue, F.*; Menzel, M.; Naumann, L.; Oeschler, H.; Scheinast, W.; Schwab, E.*; Senger, P.*; Shin, Y.; Ströbele, H.; Sturm, C.*; Surówka, G.*; Wagner, A.; Waluś, W.: **Observation of different azimuthal emission patterns of K^+ and of K^- mesons in heavy-ion collisions at 1-2A GeV.** *Physical review letters* **95**(1): 012301. DOI:10.1103/PhysRevLett.95.012301

Ukai, M.; Hashimoto, O.; Miura, Y.; Miyoshi, T.; Mizunuma, K.; Nakamura, S. N.; Okayasu, Y.; Tamura, H.; Ajimura, S.; Kishimoto, T.; Hayakawa, T.; Minami, S.; Akikawa, H.; Imai, K.; Takahashi, H.; Alburger, D. E.; Chrien, R. E.; Hotchi, H.; May, M.; Pile, P.; Rusek, A.; Sutter, R.; Nagae, T.; Sato, Y.; Banu, A.*; Franklin, G. B.; Quinn, B. P.; Franz, J.; Nakazawa, K.; Tanida, K.; Tang, L.; Yuan, L.; E930 2001 Collaboration: **Observation of hypernuclear fine structure in $^{16}_{\Lambda}$O.** *Nuclear*

physics A, Nuclear and hadronic physics **754**: 70C–74C. DOI:10.1016/j.nuclphysa.2005.02.127

Van de Vel, K.; Andreyev, A. N.; Ackermann, D.*; Boardman, H. J.; Cagarda, P.; Gerl, J.*; Heßberger/Hessberger, F. P.*; Hofmann, S.*; Huyse, M.; Karlgren, D.; Kojouharov, I.*; Leino, M.; Lommel, B.*; Münzenberg, G.*; Moore, C.; Page, R. D.; Saro, S.*; Van Duppen, P.; Wyss, R.: **Prolate structures in ^{189}Po and ^{185}Pb.** *The European physical journal A, Hadrons and nuclei* **24**(1): 57–62. DOI:10.1140/epja/i2004-10124-7

Vidaña, I.*; Bombaci, I.; Parenti, I.: **Quark deconfinement and neutrino trapping in compact stars.** *Journal of physics G, Nuclear and particle physics* **31**(6): S1165–S1169. DOI:10.1088/0954-3899/31/6/079

Wambach, J.: **The medium modification of hadrons.** *Nuclear physics A, Nuclear and hadronic physics* **755**: 198C–208C. DOI:10.1016/j.nuclphysa.2005.03.029

Wiechula, J.*; Braun-Munzinger, P.*; Daues, H.*; Frankenfeld, U.*; Garabatos, C.*; Hehner, J.*; Renfordt, R.; Schmidt, H. R.*; Stelzer, H.*; Vranić, D.*: **High-precision measurement of the electron drift velocity in Ne-CO_2.** *Nuclear instruments & methods in physics research, Section A, Accelerators, spectrometers, detectors and associated equipment* **548**(3): 582–589. DOI:10.1016/j.nima.2005.05.031

Wollersheim, H. J.*; Appelbe, D. E.; Banu, A.*; Bassini, R.; Beck, T.*; Becker, F.*; Bednarczyk, P.*; Behr, K.-H.*; Bentley, M. A.; Benzoni, G.; Boiano, C.; Bonnes, U.; Bracco, A.; Brambilla, S.; Brünle, A.*; Bürger, A.; Burkard, K.*; Butler, P. A.; Camera, F.; Curien, D.; Devin, J.; Doornenbal, P.*; Fahlander, C.; Fayz, K.; Geissel, H.*; Gerl, J.*; Górska, M.*; Grawe, H.*; Grebosz, J.*; Griffiths, R.; Hammond, G.; Hellström, M.*; Hoffmann, J.*; Hübel, H.; Jolie, J.; Kalben, J. V.; Kmiecik, M.; Kojouharov, I.*; Kulessa, R.; Kurz, N.*; Lazarus, I.; Li, J.*; Leske, J.; Lozeva, R.*; Maj, A.; Mandal, S.*; Meczyński, W.; Million, B.; Münzenberg, G.*; Muralithar, S.; Mutterer, M.; Nolan, P. J.; Neyens, G.; Nyberg, J.; Prokopowicz, W.*; Pucknell, V. F. E.; Reiter, P.; Rudolph, D.; Saito, N.*; Saito, T. R.*; Seddon, D.; Schaffner, H.*; Simpson, J.; Speidel, K. H.; Styczeń, J.; Sümmerer, K.*; Warr, N.; Weick, H.*; Wheldon, C.*; Wieland, O.*; Winkler, M.*; Ziebliński, M.: **Rare ISotopes INvestigation at GSI (RISING) using gamma-ray spectroscopy at relativistic energies.** *Nuclear instruments & methods in physics research, Section A, Accelerators, spectrometers, detectors and associated equipment* **537**(3): 637–657. DOI:10.1016/j.nima.2004.08.072

Yordanov, O.*; Gunzert-Marx, K.*; Adrich, P.*; Aumann, T.*; Boretzky, K.*; Emling, H.*; Fehrenbacher, G.*; Gutermuth, F.*; Iwase, H.*; Johansson, H.*; Jones, K. L.*; Kovalov, A.*; Radon, T.*; Schardt, D.*: **Neutron yields from 1 GeV/nucleon ^{238}U ion beams on Fe target.** *Nuclear instruments & methods in physics research, Section B, Beam interactions with materials and atoms* **240**(4): 863–870. DOI:10.1016/j.nimb.2005.06.199

Yurevich, S.; Adamová, D.; Agakichiev, G.*; Antonczyk, D.*; Andronic, A.*; Appelshäuser, H.*; Belaga, V.; Bielcikova, J.; Braun-Munzinger, P.*; Busch, O.*; Campagnolo, R.; Cherlin, A.; Damjanovic, S.; Dietel, T.; Dietrich, L.; Drees, A.; Esumi, S. I.; Filimonov, K.; Fomenko, K.; Fraenkel, Z.; Garabatos, C.*; Glässel, P.; Hering, G.; Holeczek, J.*; Kushpil, V.; Krobath, G.; Ludolphs, W.; Maas, A.*; Marín, A.*; Milošević, J.; Miśkowiec, D.*; Musa, L.; Ortega, R.; Panebrattsev, Y.; Petchenova, O.; Petráček, V.; Radomski, S.*; Rak, J.*; Ravinovich, I.; Rehak, P.; Sako, H.*; Schmitz, W.; Schukraft, J.; Sedykh, S.*; Seipp, W.; Shimansky, S.; Stachel, J.; Sumbera, M.; Tilsner, H.; Tserruya, I.; Tsiledakis, G.*; Wessels, J. P.; Wienold, T.; Windelband, B.; Wurm, J. P.; Yurevich, S.; Yurevich, V.; CERES Collaboration: **Latest results on e^+ e^- pair production in CERES.** *Nuclear physics A, Nuclear and hadronic physics* **749**: 160C–165C. DOI:10.1016/j.nuclphysa.2004.12.025

Zhou, S. H.; Zhou, J.; Meng, Q. Y.; Ajimura, S.; Akikawa, H.; Alburger, D. E.; Banu, A.*; Chrien, R. E.; Franklin, G. B.; Franz, J.; Hashimoto, O.; Hayakawa, T.; Hotchi, H.; Imai, K.; Kishimoto, T.; May, M.; Millener, D. J.; Minami, S.; Miura, Y.; Miyoshi, T.; Mizunuma, K.; Nagae, T.; Nakamura, S. N.; Nakazawa, K.; Okayasu, Y.; Pile, P.; Quinn, B. P.; Rusek, A.; Sato, Y.; Sutter, R.; Takahashi, H.; Tang, L.; Tamura, H.; Tanida, K.; Ukai, M.; Yuan, L.: **First observation of the Lambda N tensor interaction.** *High energy physics and nuclear physics Chinese edition* **29**(7): 627–631.

2. Further external publications

Baur, G.; Typel, S.: **Direct reactions with exotic nuclei.** In: *Proceedings of the 2nd Argonne/MSU/JINA/INT/RIA Workshop on Reaction Mechanism for Rare Isotope Beams, NSCL, Michigan State University, East Lansing, Michigan, USA, March 9-12, 2005,* AIP Conference Proceedings 791, 61p.

Berdermann, E.; NoRHDia Collaboration: **Single-Crystal CVD-Diamond Detectors for Hadron Physics.** In: *Proceedings of the XLIII International Winter Meeting on Nuclear Physics, Bormio, Italy, March 14-19, 2005,* 371p.

Cappuzzello, F.; Cunsolo, A.; Foti, A.; Lazzaro, A.; Orrigo, S. E A.; Winfield, J. S.; Nociforo, C.*; Lenske, H.: **New lines of research with the magnex large-acceptance spectrometer.** In: Penionzhkevich, Y. E.; Cherepanov, E. A. : *International Symposium on Exotic Nuclei: Petershof;*

Russia, July 5-12, 2004 EXON 2004, New Jersey, London, Singapore, Beijing, Shanghai, Hong Kong, Tapei, Chennai: World Scientific, 582p.

Chatillon, A.; Theisen, C.; Bouchez, E.; Clement, E.; Dayras, R.; Drouart, A.; Görgen, A.; Hürstel, A.; Korten, W.; Le Coz, Y.; Siemenel, C.; Wilson, J.; Eeckhaudt, S.; Grahn, T.; Greenlees, P. T.; Jones, P.; Julin, R.; Juutinen, S.; Kettunen, H.; Leino, M.; Leppänen, A.-P.; Maanselkä, V.; Nieminen, P.; Pakarinen, J.; Perkowski, J.; Rahkila, R.; Sare'n, J.; Scholey, C.; Uustialo, J.; van de Vel, K.; Auger, G.; Bouriquent, B.; Casandjian, J. M.; Cee, R.; de France, G.; de Tourreil, R.; St Laurent, M. G.; Stodel, C.; Villari, A.; Rejmund, M.; Amzal, N.; Bastin, J. E.; Butler, P. A.; Herzberg, R.-D.; Ikin, P. J. C.; Jones, G. D.; Pritchard, A.; Grevy, S.; Hauschild, K.; Korichi, A.; Lopez-Martens, A.; Heßberger, F. P.*; Lukyanov, S. M.; Penionzhkevich, Y. E.; Sobolev, Y. G.; Dorvaux, O.; Gall, B.; Kahlfallah, F.; Rousseau, M.: **Spectroscopy of the odd tansfermium ^{251} Md and ^{255}Lr nuclei using γ, electron and α spectroscopy .** In: Penionzhkevich, Y. E.; Cherepanov, E. A. : *International Symposium on Exotic Nuclei: Petershof; Russia, July 5-12, 2004 EXON 2004,* New Jersey, London, Singapore, Beijing, Shanghai, Hong Kong, Tapei, Chennai: World Scientific, 198p.

Egelhof, P.; EXL collaboation: **Nuclear Structure Studies on Exotic Nuclei by Light-Ion Induced Direct Reactions with Stored Radioactive Beams.** In: Chiladze, David; Kacharava Andro; Ströher, Hans: *STORI'05, 6th International Conference on Nuclear Physics at Storage Rings, 23–26 May 2005, Jülich-Bonn,* Schriften des Forschungszentrum Jülich, Reihe Materie und Material Vol. 30, Jülich: Forschungszentrum Jülich, 289p.

Emling, H.: **Nuclear Structure Studies with Exotic Nuclear Beams.** In: Gacsi, Z.; Dombradi, Z.; Krasznahorkay, A: *Exotic Nuclear Systems,* AIP Conference Proceedings, Vol. 802, 83p.

Emling, Hans*: **Neutron-rich nuclei studid in high-energy coulomb breakup of secondary beams.** In: Penionzhkevich, Y. E.; Cherepanov, E. A. : *International Symposium on Exotic Nuclei: Petershof; Russia, July 5-12, 2004 EXON 2004,* New Jersey, London, Singapore, Beijing, Shanghai, Hong Kong, Tapei, Chennai: World Scientific, 100p.

Feldmeier, H.*; Neff, T.*; Roth, R.: **Structure of light exotic nuclei in fermionic molecular dynamics.** In: Penionzhkevich, Y. E.; Cherepanov, E. A. : *International Symposium on Exotic Nuclei: Petershof; Russia, July 5-12, 2004 EXON 2004,* New Jersey, London, Singapore, Beijing, Shanghai, Hong Kong, Tapei, Chennai: World Scientific, 136p.

Geissel, Hans*: **Precision Experiments with exotic atoms and relativisitic exotic nuclei at GSI.** In: Penionzhkevich, Y. E.; Cherepanov, E. A. : *International Symposium on Exotic Nuclei: Petershof; Russia, July 5-12, 2004 EXON 2004,* New Jersey, London, Singapore, Beijing, Shanghai, Hong Kong, Tapei, Chennai: World Scientific, 68p.

Höhne, C. for the CBM Collaboration: **The compressed baryonic matter experiment at the future accelerator facility in Darmstadt.** In: *Proceedings of the 21st Winter Workshop on Nuclear Dynamics ,* 119p.

Henning, W.: **FAIR An International Accelerator Facility for Research with Ions and Antiprotons.** In: *Proceedings on High Intensity and High Brightness Hadron Beams, 33rd ICFA Advanced Beam Dynamics Workshop on High Intensity and High Brightness Hadron Beams, Bensheim, Germany, 18-22 October 2004,* AIP Conference Proceedings Volume 773,

Heßberger, F. P.: **Nuclear Structure Investigations of Heavy Actinide and Transactinide Isotopes.** In: Antonenko, N. V.; Scheid, W: *Proc. 'Workshop on Superheavy Elements', Schloss Rauischholzhausen, Germany, Sept. 6th, 2005,*

Hillebrandt, W.; Langanke, K.: **Challenges in Nuclear Astrophysics.** In: *Nuclear Physics News* **15***,* 21p.

Hofmann, S.: **Present status of experimebtal research on superheavy elements.** In: Antonenko, N. V.; Scheid, W: *Proc. 'Workshop on Superheavy Elements', Schloss Rauischholzhausen, Germany, Sept. 6th, 2005,*

Hofmann, S.*; Ackermann, D.*; Barth, W.*; Dahl, L.*; Heßberger, F. P.*; Kindler, B.*; Lommel, B.*; Mann, R.*; Münzenberg, G.*; Tinschert, K.*; Ratzinger, U.; Schempp, A.: **Heavy element research at SHIP.** In: Penionzhkevich, Y. E.; Cherepanov, E. A. : *International Symposium on Exotic Nuclei: Petershof; Russia, July 5-12, 2004 EXON 2004,* New Jersey, London, Singapore, Beijing, Shanghai, Hong Kong, Tapei, Chennai: World Scientific, 157p.

Kelic, A.; Schmidt, K.-H.: **Fission Barriers of Exotic Nuclei.** In: *Third International Workshop on Nuclear Fission and Fission-Product Spectroscopy, Cadarache, France, May 11-14, 2005,* AIP Conference Proceedings 798,

Kurtukian-Nieto, T., Benlliure, J.; Schmidt, K.-H.; Casarejos, E.; Cortina-Gil, D.; Fernandez-Ordonez, M.; Pereira, J.; Audouin, L.; Blank, B.; Giovinazzo, J.; Henzlova, D.; Jurado, B.; Rejmund, F.; Yordanov, O.: **Production and Half-lives on Neutron-rich Isotopes Near N=126.** In: *International Symposium on Exotic Nuclear Systems, Debrecen, Hungary, June 20-25, 2005,* AIP Conference Proceedings 802,

Lisetskiy, A. F.; Brown, B. A.; Horoi, M.; Grawe, H.*: **Shell model treatment of neutron-rich nuclei near ^{78}Ni.** In: Penionzhkevich, Y. E.; Cherepanov, E. A. : *International Symposium on Exotic Nuclei: Petershof; Russia, July*

5-12, 2004 EXON 2004, New Jersey, London, Singapore, Beijing, Shanghai, Hong Kong, Tapei, Chennai: World Scientific, 542p.

Łukasik, J.; Auger, G.; Begemann-Blaich, M. L..; Bellaize, N.; Bittiger, R.; Bocage, F.; Borderie, B.; Bougault, R.; Bouriquet, B.; Charvet, J. L., Chbihi, A.; Dayras, R.; Durand, D.; Frankland, J. D., Galichet, e.; Gourio, D.; Guinet, D.; Hudan, S.; Lautesse, P.; Lavaud, F.;Le Fèvre, A.; Legrain, R.; Lopez, O.; Lynen, U.; Müller, W. F. J.; Nalpas, L.; Orth, H.; Plagnol, E.; Rosato, E.; Saija, A.; Schwarz, C.; Sfienti, C.; Tamain, B.; Trautmann, W.; Trzciński, A.; Turzó, K.; Vient, E.; Vigilante, M.; Volant, C.; Zwiegliński, B.: **Directed and elliptic flow in Au+Au at intermediate energies.** In: Bauer, W.; Bellwied, R.; Panitkin, S: *Proceedings of the 21st Winter Workshop on Nuclear Dynamics, February 5-12, 2005, Breckenridge, Colorado,* Budapest: EP Systema,

Münzenberg, G.*: **NUSTAR: nuclear structure research within FAIR Objectives and organisation.** In: Penionzhkevich, Y. E.; Cherepanov, E. A. : *International Symposium on Exotic Nuclei: Petershof; Russia, July 5-12, 2004 EXON 2004,* New Jersey, London, Singapore, Beijing, Shanghai, Hong Kong, Tapei, Chennai: World Scientific, 614p.

Otsuka, T.; Suzuki, T.; Grawe, H.*; Akaishi, Y.: **Shell structure of exotic nuclei an nuclear force.** In: Penionzhkevich, Y. E.; Cherepanov, E. A. : *International Symposium on Exotic Nuclei: Petershof; Russia, July 5-12, 2004 EXON 2004,* New Jersey, London, Singapore, Beijing, Shanghai, Hong Kong, Tapei, Chennai: World Scientific, 467p.

Pershina, V.*; Bastug, T.: **Theoretical predictions for the chemical identification of superheaby elements role of relativistic effects.** In: Penionzhkevich, Y. E.; Cherepanov, E. A. : *International Symposium on Exotic Nuclei: Petershof; Russia, July 5-12, 2004 EXON 2004,* New Jersey, London, Singapore, Beijing, Shanghai, Hong Kong, Tapei, Chennai: World Scientific, 309p.

Ricciardi, M. V.*; Schmidt, K.-H.*; Kelic, A.*; Napolitani, P.*; Yordanov, O.*; Ignatyuk, A. V.; Rejmund, F.: **Complex nuclear-structure phenomena revealed from the nuclide production in fragmentation reactions.** In: Penionzhkevich, Y. E.; Cherepanov, E. A. : *International Symposium on Exotic Nuclei: Petershof; Russia, July 5-12, 2004 EXON 2004,* New Jersey, London, Singapore, Beijing, Shanghai, Hong Kong, Tapei, Chennai: World Scientific, 432p.

Ricciardi, M. V.; Schmidt, K.-H., Rejmund, F.; Enqvist, T.; Armbruster, P.; Benlliure, J.; Bernas, M.; Mustapha, B.; Tassan-Got, L.; Stephan, C.; Boudard, A.; Leray, S.; Volant, C.; Czajkowski, S.; Pravikoff, M.: **Experimental Cross Sections and Velocities of Light Nuclides Produced in the Proton-Induced Fission of 238U at 1 GeV.** In: *Third International Workshop on Nuclear Fission and Fission-Product Spectroscopy, Cadarache, France, May 11-14, 2005,* AIP Conference Proceedings 798,

Schmidt, K.-H.; Ignatyuk, A. V.; Rejmund, F.; Kelic, A.; Ricciardi, M. V.: **Statistical Approaches to the Even-odd Effect in Fission.** In: *Third International Workshop on Nuclear Fission and Fission-Product Spectroscopy, Cadarache, France, May 11-14, 2005,* AIP Conference Proceedings 798,

Sfienti, C.; Adrich, P.; Aumann, T.; Bacri, C. O.; Barczyk, T.; Bassini, R.; Boiano, C.; Botvina, A. S.; Boudard, A.; Brzychczyk, J.; Chbihi, A.; Cibor, J.; Czech, B.; De Napoli, M.; Ducret, J.-E.; Emling, H.; Frankland, J. D.; Hellström, M.; Henzlova, D.; Kezzar, K.; Immè, G.; Iori, I.; Johansson, H.; Lafriakh, A.; Le Fèvre, A.; Le Gentil, E.; Leifels, Y.; Lynch, W. G.; Lühning, J.; Lukasik, J.; Lynen, U.; Majka, Z.; Mocko, M.; Müller, W. F. J.; Mykulyak, A.; Orth, H.; Otte, A. N.; Palit, R.; Pawloswki, P.; Pullia, A.; Raciti, G.; Rapisarda, E.; Sann, H.; Schwarz, C.; Simon, H.; Sokolov, A.; Sümmerer, K.; Trautmann, W.; Tsang, M. B.; Verde, G.; Volan, C.; Wallace, M.; Weick, H., Wiechula, J.; Wieloch, A; Zwieglinski, B.: **Mass and Isospin effect in Multifragmentation.** In: *Proceeding of the XLIII International Winter Meeting on Nuclear Physics, Bormio (Italy), 13-20 March 2005, Ricerca Scientifica ed Educazione Permanente,*

Stodel, C.; Anne, R.; Auger, G.; Bouriquet, B.; Casandjian, J. M.; Cee, R.; de France, G.; de Oliveira Santos, F.; de Tourreil, R.; Khouaja, A.; Peghaire, A.; Saint-Laurent, M. G.; Villari, A. C. C.; Wieleczko, J. P.; Amar, N.; Grevy, S.; Peter, J.; Dayras, R.; Drouart, A.; Gilliert, A.; Theisen, C.; Chatillon, A.; Clement, E.; Lojek, K.; Sosin, Z.; Wieloch, A.; Hauschild, K.; Hannachi, F.; Lopez-Martens, A.; Stuttge, L.; Heßberger, F. P.; Hofmann, S.; Lichtenthäler, R.; Hanappe, F.: **Search fpr super-heavy elements at GANIL.** In: Penionzhkevich, Y. E.; Cherepanov, E. A. : *International Symposium on Exotic Nuclei: Petershof; Russia, July 5-12, 2004 EXON 2004,* New Jersey, London, Singapore, Beijing, Shanghai, Hong Kong, Tapei, Chennai: World Scientific, 180p.

Yakusehv, A.; Reitmeier, S.; Türler, A.; Werczinski, B.; Brüchle, W.*; Jäger, E.*; Schädel, M.*; Schimpf, E.*; Popeko, A.; Sagaidak, R.; Shutov, A.; Yeremin, A.: **Dependence of the production of heavy-element nuclei from complete-fusion neutron evaporation reactions.** In: Penionzhkevich, Y. E.; Cherepanov, E. A. : *International Symposium on Exotic Nuclei: Petershof; Russia, July 5-12, 2004 EXON 2004,* New Jersey, London, Singapore, Beijing, Shanghai, Hong Kong, Tapei, Chennai: World Scientific, 305p.

Yakusehv, A.; Türler, A.; Werczinski, B.; Brüchle, W.*; Jäger, E.*; Schädel, M.*; Schimpf, E.*: **Approach to first experiments with elements 114 and results of test ex-**

periments. In: Penionzhkevich, Y. E.; Cherepanov, E. A. : *International Symposium on Exotic Nuclei: Petershof; Russia, July 5-12, 2004 EXON 2004,* New Jersey, London, Singapore, Beijing, Shanghai, Hong Kong, Tapei, Chennai: World Scientific, 301p.

Zeitträger, H.*: **The Russian-German co-operation at GSI: an example of success and friendship.** In: Penionzhkevich, Y. E.; Cherepanov, E. A. : *International Symposium on Exotic Nuclei: Petershof; Russia, July 5-12, 2004 EXON 2004,* New Jersey, London, Singapore, Beijing, Shanghai, Hong Kong, Tapei, Chennai: World Scientific, 679p.

Publications to the programme 'Large-scale facilities for research with photons, neutrons and ions'

K. Große, GSI, Darmstadt, Germany

1. Reviewed publications

Abu Saleh, S.; Eyal, Y.: **Morphology of track cores and halos created by swift uranium ions in polycarbonate.** *Nuclear instruments & methods in physics research, Section B, Beam interactions with materials and atoms* **236**: 81–87. DOI:10.1016/j.nimb.2005.03.258

Abu Saleh, S.; Eyal, Y.: **Porous track cores along wakes of swift Pb ions in LiF.** *Nuclear instruments & methods in physics research, Section B, Beam interactions with materials and atoms* **230**: 246–250. DOI:10.1016/j.nimb.2004.12.049

Andriamonje, S.; Arsov, V.; Aune, S.; Aune, T.; Avignone, F. T.; Barth, K.; Belov, A.; Beltran, B.; Brauninger, H.; Carmona, J.; Cebrian, S.; Chesi, E.; Cipolla, G.; Collar, J.; Creswick, R.; Dafni, T.; Davenport, M.; Dedousis, S.; Delattre, A.; Delbart, A.; DeOliveira, R.; DiLella, L.; Eleftheriadis, C.; Engelhauser, J.; Fanourakis, G.; Farach, H.; Ferrer, E.; Fischer, H.; Formenti, F.; Franz, J.; Friedrich, P.; Geralis, T.; Giomataris, I.; Gninenko, S.; Golubev, N.; Hartmann, R.; Hasinoff, M.; Heinsius, F. H.; Hoffmann, D. H. H.; Irastorza, I.; Jacoby, J.; Joux, J. N.; Kang, D.; Königsmann, K.; Kotthaus, R.; Krcmar, M.; Kuster, M.; Lakic, B.; Lasseur, C.; Liolios, A.; Lippitsch, A.; Ljubicic, A.; Lutz, G.; Luzon, G.; Morales, A.; Morales, J.; Mutterer, M.; Nikolaidis, A.; de Solorzano, A. O.; Papaevangelou, T.; Placci, A.; Raffelt, G.; Rammos, P.; Robert, J. P.; Ruz, J.; Sarsa, M.; Schill, C.; Serber, W.; Semertzidis, Y.; Vieira, J.; Villar, J.; Vullierme, B.; Walckiers, L.; Zioutas, K.: **The CERN Axion Solar Telescope (CAST): An update.** *Nuclear Physics B, Pro. Suppl.* **138**: 41–44. DOI:10.1016/j.nuclphysbps.2004.11.008

Artemyev, A. N.*; Klasnikov, A. E.; Beier, T.*; Eichler, J.; Kozhuharov, C.*; Shabaev, V. M.*; Stöhlker, T.*; Yerokhin, V. A.*: **Negative-continuum dielectronic recombination into low-lying bound states of heavy ions.** *Nuclear instruments & methods in physics research, Section B, Beam interactions with materials and atoms* **235**: 270–275. DOI:10.1016/j.nimb.2005.03.188

Bachelet, C.; Audi, G.; Gaulard, C.; Guenaut, C.; Herfurth, F.*; Lunney, D.; De Saint Simon, M.; Thibault, C.; ISOLDE Collaboration: **Mass measurement of short-lived halo nuclides.** *The European physical journal A, Hadrons and nuclei* **25**: 31–32. DOI:10.1140/epjad/i2005-06-005-5

Banaś, D.*; Stöhlker, T.*; Ionescu, D. C.; Beyer, H. F.*; Bosch, F.*; Bräuning-Demian, A.*; Gumberidze, A.*; Hagmann, S.*; Kozhuharov, C.*; Ma, X.*; Mokler, P. H.*; Mann, R.*; Sierpowski, D.*; Tachenov, S.*; Stachura, Z.*; Warczak, A.*: **X-ray emission studies in relativistic collisions of Li-like uranium ions with gaseous target.** *Nuclear instruments & methods in physics research, Section B, Beam interactions with materials and atoms* **235**: 326–330. DOI:10.1016/j.nimb.2005.03.199

Bednarz, G.; Warczak, A.; Sierpowski, D.*; Stoehlker, T.; Hagmann, S.*; Bosch, F.*; Gumberidze, A.*; Kozhuharov, C.*; Liesen, D.*; Mokler, P. H.*; Ma, X.; Stachura, Z.: **Charge state dependence of L-REC into highly charged U-ions.** *Nuclear instruments & methods in physics research, Section B, Beam interactions with materials and atoms* **235**: 280–283. DOI:10.1016/j.nimb.2005.03.190

Beier, T.*; Dahl, L.*; Kluge, H. J.*; Kozhuharov, C.*; Ouint, W.*: **Trapping ions of hydrogen-like uranium: The HITRAP project at GSI.** *Nuclear instruments & methods in physics research, Section B, Beam interactions with materials and atoms* **235**: 473–478. DOI:10.1016/j.nimb.2005.03.193

Blaum, K.*; Audi, G.; Beck, D.*; Bollen, G.; Brodeur, M.; Delahaye, P.; George, S.; Guénaut, C.; Herfurth, F.*; Herlert, A.; Kellerbauer, A.; Kluge, H.- J.*; Lunney, D.; Mukherjee, M.*; Rodríguez, D.*; Schwarz, S.; Schweikhard, L.; Yazidjian, C.*: **ISOLTRAP pins down masses of exotic nuclides.** *Journal of physics G, Nuclear and particle physics* **31**(10): S1775–S1778. DOI:10.1088/0954-3899/31/10/071

Blaum, K.*; Audi, G.; Beck, D.*; Bollen, G.; Delahaye, P.; George, S.; Guénaut, C.; Herfurth, F.*; Herlert, A.; Kellerbauer, A.; Kluge, H.-J.*; Lunney, D.; Mukherjee, M.*; Schwarz, S.; Schweikhard, L.; Yazidjian, C.*: **ISOLTRAP mass measurements of exotic nuclides at δ m/m=10(-8).** *Nuclear physics A, Nuclear and hadronic physics* **752**: 317C–320C. DOI:10.1016/j.nuclphysa.2005.02.124

Block, M.*; Ackermann, D.*; Beck, D.*; Blaum, K.*; Breitenfeldt, M.; Chauduri, A.; Doemer, A.; Eliseev, S.*; Habs, D.; Heinz, S.; Herfurth, F.*; Heßberger, F. P.*; Hofmann, S.*; Geissel, H.*; Kluge, H.-J.*; Kolhinen, V.; Marx, G.*; Neumayr, J. B.; Mukherjee, M.*; Petrick, M.; Plass, W.; Quint, W.*; Rahaman, S.*; Rauth, C.*; Rodriguez, D.; Scheidenberger, C.*; Schweikhard, L.; Suhonen, M.; Thirolf, P. G.; Wang, Z.; Weber, C.*; SHIPTRAP Collaboration: **The ion-trap facility SHIPTRAP - Status and perspectives.** *The European physical journal A, Hadrons and nuclei* **25**: 49–50. DOI:10.1140/epjad/i2005-06-013-5

Bogdan, G.; Nesladek, M.; D'Haen, J.; Maes, J.; Moshchalkov, V. V.; Haenen, K.; D'Olieslaeger, M.: **Growth and characterization of near-atomically flat, thick homoepitaxial CVD diamond films.** *Physica status solidi A, Applied research* **202**(11): 2066–2072. DOI:10.1002/pssa.200561930

Bombaci, I.; Fabrocini, A.; Polls, A.; Vidaña, I.*: **Spin-orbit and tensor interactions in homogeneous matter of nucleons: accuracy of modem many-body theories.** *Physics letters B* **609**(3): 232–240. DOI:10.1016/j.physletb.2005.01.067

Borremans, D.; Balabanski, D. L.; Blaum, K.; Geithner, W.; Gheysen, S.; Himpe, P.; Kowalska, M.; Vermeulen, N.; Lassen, J.; Lievens, P.; Neyens, G.; Vermeulen, N.; Yordanov, D.: **New measurement and reevaluation of the nuclear magnetic andquadrupole moments of ^{8}Li and ^{9}Li.** *Physical review C, Nuclear physics* **72**(4): 044309. DOI:10.1103/PhysRevC.72.044309

Cervera, J.; Schiedt, B.*; Ramirez, P.: **A Poisson/Nernst-Planck model for ionic transport through synthetic conical nanopores.** *Europhysics letters* **71**(1): 35–41. DOI:10.1209/epl/i2005-10054-x

Chtanko, N.* Toimil-Molares, M. E.*; Cornelius, T. W.*; Dobrev, D.*; Neumann, R.*: **Ion-track based single-channel templates for single-nanowire contacting.** *Nuclear instruments & methods in physics research, Section B, Beam interactions with materials and atoms* **236**: 103–108. DOI:10.1016/j.nimb.2005.03.264

Cornelius, T. W.*; Brötz, J.; Chtanko, N.*; Dobrev, D.*; Miehe, G.; Neumann, R.*; Toimil Mollares, M. E. : **Controlled fabrication of poly- and single-crystalline bismuth nanowires.** *Nanotechnology* **16**(5): S246–S249. DOI:10.1088/0957-4484/16/5/020

Cowan, T. E.; Fuchs, J.; Ruhl, H.; Sentoku, Y.; Kemp, A.; Audebert, P.; Roth, M.*; Stephens, R.; Barton, I.; Blazevic, A.*; Brambrink, E.*; Cobble, J.; Fernández, J. C.; Gauthier, J. C.; Geissel, M.*; Hegelich, M.; Kaae, J.; Karsch, S.; Le Sage, G. P.; Letzring, S.; Manclossi, M.; Meyroneinc, S.; Newkirk, A.; Pépin, H.; Renard-LeGalloudec, N.: **Ultra-low emittance, high current proton beams produced with a laser-virtual cathode sheath accelerator.** *Nuclear instruments & methods in physics research, Section A, Accelerators, spectrometers, detectors and associated equipment* **544**(1): 277–284. DOI:10.1016/j.nima.2005.01.221

Daub, M.*; Enculescu, I.*; Neumann, R.*; Spohr, R.*: **Ni nanowires electrodeposited in single ion track templates.** *Journal of optoelectronics and advanced materials* **7**(2): 865–870.

Dimopoulou, C.; Moshammer, R.; Fischer, D.; Fainstein, P. D.; Höhr, C.; Dorn, A.; Urrutia, J. R. C. L.; Schroter, C. D.; Kollmus, H.*; Mann, R.*; Hagmann, S.*; Ullrich, J.: **Dissociative ionization of H_2 by fast protons: three-body break-up and molecular-frame electron emission.** *Journal of physics B, Atomic, molecular and optical physics* **38**(5): 593–601. DOI:10.1088/0953-4075/38/5/010

Dobrev, D.*; Baur, D.*; Neumann, R.*: **Crystallization of lysozyme in pores of etched heavy-ion tracks.** *Applied Physics A: Materials Science and Processing* **80**(3): 451–456. DOI:10.1007/s00339-004-3078-z

Drake, G. W. F.; Nörtershäuser, W.*; Yan, Z. C.: **Isotope shifts and nuclear radius measurements for helium and lithium.** *Canadian Journal of Physics* **83**(4): 311–325. DOI:10.1139/P05-020

Efremov, V. P.; Pikuz, S. A.; Faenov, A. Y.; Rosmej, O.*; Skobelev, I. Y.; Shutov, A. V.; Hoffmann, D. H. H.*; Fortov, V. E.: **Study of the energy release region of a heavy-ion flux in nanomaterials by x-ray spectroscopy of multicharged ions.** *JETP Letters* **81**(8): 378–382.

Enculescu, M.; Schwartz, K.*; Trautmann, C.*; Toulemonde, M.: **Heavy ion induced damage in NaCl and KCl crystals.** *Nuclear instruments & methods in physics research, Section B, Beam interactions with materials and atoms* **229**(3): 397–405. DOI:10.1016/j.nimb.2004.12.131

Ewald, G.; Knaak, K. M.*; Götte, S.*; Wendt, K. D. A.; Kluge, H.-J.*: **Development of narrow-linewidth diode lasers by use of volume holographic transmission gratings.** *Applied physics B, Lasers and optics* **80**(4): 483–487. DOI:10.1007/s00340-005-1735-3

Ewald, G.; Nörtershäuser, W.; Dax, A.; Götte, S.; Kirchner, R.; Kluge, H.-J.; Kühl, T.; Sanchez, R.; Wojtaszek, A.; Bushaw, B. A.; Drake, G. W. F.; Yan, Z.-C.; Zimmermann, C.: **Nuclear charge radii of ^{78,90}Li determined by laser spectroscopy (vol 93, art no 113002, 2004).** *Physical review letters* **94**(3): 039901. DOI:10.1103/PhysRevLett.94.039901

Feili, D.; Zimmermann, B.; Neacsu, C.; Bosselmann, P.; Schartner, K.-H.; Folkmann, F.; Livingston, A. E.; Trabert, E.; Mokler, P. H.*: **$2s^2\ {}^1S_0$-$2s2p\ {}^3P_1$ intercombination transition wavelengths in Be-like Ag^{43+}, Sn^{46+}, and Xe^{50+} ions.** *Physica scripta* **71**(1): 48–51. DOI:10.1088/0031-8949/71/1/008

Fritzsche, S.; Indelicato, P.; Stöhlker, T.*: **Relativistic quantum dynamics in strong fields: photon emission from heavy, few-electron ions.** *Journal of physics B, Atomic, molecular and optical physics* **38**(9): S707–S726. DOI:10.1088/0953-4075/38/9/018

Fritzsche, S.; Surzhykov, A.; Stöhlker, T.*: **Radiative recombination into high-Z few-electron ions: Cross sections and angular distributions.** *Physical review A,*

Atomic, molecular, and optical physics **72**(1): 012704. DOI:10.1103/PhysRevA.72.012704

Fuchs, J.; Sentoku, Y.; Karsch, S.; Cobble, J.; Audebert, P.; Kemp, A.; Nikroo, A.; Antici, P.; Brambrink, E.*; Blazevic, A.*; Campbell, E. M.; Fernandez, J. C.; Gauthier, J. C.; Geissel, M.; Hegelich, M.; Pepin, H.; Popescu, H.; Renard-LeGalloudec, N.; Roth, M.*; Schreiber, J.; Stephens, R.; Cowan, T. E.: **Comparison of laser ion acceleration from the front and rear surfaces of thin foils.** *Physical review letters* **94**(4): 045004. DOI:10.1103/PhysRevLett.94.045004

Galonska, M.*; Hollinger, R.*; Krinberg, I. A.; Spaedtke, P.*: **Influence of an axial magnetic field on the electron temperature in a vacuum arc plasma.** *IEEE transactions on plasma science* **33**(5): 1542–1547. DOI:10.1109/TPS.2005.856504

Geissel, M.; Roth, M.*; Allen, M.; Audebert, P.; Basko, M.; Blazevic, A.; Brambrink, E.; Cobble, J.; Cowan, T. E.; Cuneo, M. E.; Fernandez, J. C.; Fuchs, J.; Gauthier, J.-C.; Hegelich, M.; Karsch, S.: **M.I-12: short pulse laser generated ion beams for fast ignition.** *Nuclear instruments & methods in physics research, Section A, Accelerators, spectrometers, detectors and associated equipment* **544**(1): 55–60. DOI:10.1016/j.nima.2005.01.288

Ghiordanescu, V.; Sima, M.; Enculescu, I.; Grecu, M. N.; Mihut, L.; Secu, M.; Neumann, R.*: **Photoluminescence of manganese- and copper-doped CdS nanowires.** *Physica status solidi A, Applied research* **202**(3): 449–454. DOI:10.1002/pssa.200406927

Gregorian, L.; Kroupp, E.; Davara, G.; Starobinets, A.; Fisher, V. I.; Bernshtam, V. A.; Ralchenko, Y. V.; Maron, Y.; Fisher, A.; Hoffmann, D. H. H.: **Electron-temperature and energy-flow history in an imploding plasma.** *Physical Review E* **71**(5): 056402. DOI:10.1103/PhysRevE.71.056402

Guenaut, C.; Audi, G.; Beck, D.*; Blaum, K.*; Bollen, G.; Delahaye, P.; Herfurth, F.*; Kellerbauer, A.; Kluge, H.-J.*; Lunney, D.; Schwarz, S.; Schweikhard, L.; Yazidjian, C.*: **Extending the mass 'backbone' to short-lived nuclides with ISOLTRAP.** *The European physical journal A, Hadrons and nuclei* **25**: 35–36. DOI:10.1140/epjad/i2005-06-030-4

Guénaut, C.; Audi, G.; Beck, D.*; Blaum, K.*; Bollen, G.; Delahaye, P.; Herfurth, F.*; Kellerbauer, A.; Kluge, H.-J.*; Lunney, D.; Schwarz, S.; Schweikhard, L.; Yazidjian, C.*: **Is N=40 magic? An analysis of ISOLTRAP mass measurements.** *The European physical journal A, Hadrons and nuclei* **25**: 33–34. DOI:10.1140/epjad/i2005-06-029-9

Guénaut, C.; Audi, G.; Beck, D.*; Blaum, K.*; Bollen, G.; Delahaye, P.; Herfurth, F.*; Kellerbauer, A.; Kluge, H.-J.*; Lunney, D.; Schwarz, S.; Schweikhard, L.; Yazidjian, C.*: **Mass measurements of $^{56-57}$Cr and the question of shell reincarnation at N=32.** *Journal of physics G, Nuclear and particle physics* **31**(10): S1765–S1770. DOI:10.1088/0954-3899/31/10/069

Gumberidze, A.*; Stöhlker, T.*; Banaś, D.; Beckert, K.*; Beller, P.*; Beyer, H. F.*; Bosch, F.*; Hagmann, S.*; Kozhuharov, C.*; Liesen, D.*; Nolden, F.*; Ma, X.; Mokler, P. H.*; Steck, M.*; Sierpowski, D.; Tashenov, S.*: **Quantum electrodynamics in strong electric fields: The ground-state lamb shift in hydrogen-like uranium.** *Physical review letters* **94**(22): 223001. DOI:10.1103/PhysRevLett.94.223001

Healy, K.*G; Schiedt, B.*; Siwy, Z.*; Morrison, A. P.; Neumann, R.*: **Single-molecule DNA transport through individual conical polymer nanopores.** *Biophysical journal* **88**(1): 660A–660A.

Hegelich, B. M.; Albright, B.; Audebert, P.; Blazevic, A.; Brambrink, E.; Cobble, J.; Cowan, T.; Fuchs, J.; Gauthier, J. C.; Gautier, C.; Geissel, M.*; Habs, D.; Johnson, R.; Karsch, S.; Kemp, A.; Letzring, S.; Roth, M.; Schramm, U.; Schreiber, J.; Witte, K. J.; Fernandez, J. C.: **Spectral properties of laser-accelerated mid-Z MeV/u ion beams.** *Physics of plasmas* **12**(5): 056314. DOI:10.1063/1.1915350

Herfurth, F.*; Audi, G.; Beck, D.*; Blaum, K.*; Bollen, G.; Delahaye, P.; George, S.; Guénaut, C.; Herlert, A.; Kellerbauer, A.; Kluge, H.-J.*; Lunney, D.; Mukherjee, M.*; Rahaman, S.*; Schwarz, S.; Schweikhard, L.; Weber, C.*; Yazidjian, C.*: **Recent high-precision mass measurements with the Penning trap spectrometer ISOLTRAP.** *The European physical journal A, Hadrons and nuclei* **25**: 17–21. DOI:10.1140/epjad/i2005-06-031-3

Herlert, A.; Beck, D.*; Blaum, K.*; Carrel, F.; Delahaye, P.; George, S.; Guenaut, C.; Herfurth, F.*; Kellerbauer, A.; Kluge, H.-J.*; Lunney, D.; Mukherjee, M.*; Schweikhard, L.; Yazidjian, C.*: **Mass spectrometry of atomic ions produced by in-trap decay of short-lived nuclides.** *New Journal of Physics* **7**: 44. DOI:10.1088/1367-2630/7/1/044

Hoffmann, D. H. H.*; Blazevic, A.; Ni, P.*; Rosmej, O.*; Roth, M.; Tahir, N. A.*; Tauschwitz, A.*; Udrea, S.; Varentsov, D.; Weyrich, K.*; Maron, Y.: **Present and future perspectives for high energy density physics with intense heavy ion and laser beams.** *Laser and particle beams* **23**(1): 47–53. DOI:10.1017/S026303460505010X

Ishikawa, N.; Chimi, Y.; Michikami, O.; Hashimoto, T.; Kambara, T.; Neumann, R.*; Iwase, A.: **Ion-velocity dependence of high-density electronic excitation effects in oxide superconductors.** *Nuclear instruments & methods in physics research, Section B, Beam interactions with materials and atoms* **230**: 136–141.

DOI:10.1016/j.nimb.2004.12.031

Khalfaoui, N.; Rotaru, C. C.; Bouffard, S.; Toulemonde, M.; Stoquert, J. P.; Haas, F.; Trautmann, C.*; Jensen, J.; Dunlop, A.: **Characterization of swift heavy ion tracks in CaF_2 by scanning force and transmission electron microscopy.** *Nuclear instruments & methods in physics research, Section B, Beam interactions with materials and atoms* **240**(4): 819–828. DOI:10.1016/j.nimb.2005.06.220

Khaydarov, R. T.; Berdiyorov, G. R.; Kunishev, U.; Khalmuratov, M.; Tojikhonov, E.; Kanapathipillai, M.*: **Investigation of PbMg target characteristics by a laser mass-spectrometer.** *Laser and particle beams* **23**(4): 521–526. DOI:10.1017/S0263034605050706

Khoa, D. T.; Bohlen, H. G.; von Oertzen, W.; Bartnitzky, G.; Blazevic, A.; Nuoffer, F.; Gebauer, B.; Mittig, W.; Roussel-Chomaz, P.: **Study of refractive structure in the inelastic ^{16}O + ^{16}O scattering at the incident energies of 250 to 1120 MeV.** *Nuclear physics A, Nuclear and hadronic physics* **759**(1): 3–22. DOI:10.1016/j.nuclphysa.2005.04.027

Klasnikov, A. E.; Shabaev, V. M.; Artemyev, A. N.; Kovtun, A. V.; Stöhlker, T.*: **Polarization effects in radiative recombination of an electron with a highly charged ion.** *Nuclear instruments & methods in physics research, Section B, Beam interactions with materials and atoms* **235**: 284–289. DOI:10.1016/j.nimb.2005.03.191

Kowalskal, M.; Yordanov, D.; Blaum, K.; Borremans, D.; Himpe, P.; Lievens, P.; Mallion, S.; Neugart, R.; Neyens, G.; Vermeulen, N.: **Laser and β-NMR spectroscopy on neutron-rich magnesium isotopes.** *The European physical journal A, Hadrons and nuclei* **25**: 193–197. DOI:10.1140/epjad/i2005-06-041-1

Kuster, M.; Wilms, J.; Staubert, R.; Heindl, W. A.; Rothschild, R. E.; Shakura, N. I.; Postnov, K. A.: **Probing the outer edge of an accretion disk: a Her X-1 turn-on observed with RXTE.** *Astronomy & astrophysics* **443**(3): 753–767. DOI:10.1051/0004-6361:20042355

Kuusiniemi, P.*; Heßberger, F.*; Ackermann, D.*; Hofmann, S.*; Sulignano, B.*; Kojouharov, I.*; Mann, R.*: **Decay studies of $^{215-217}$Th using ER-γ-α-γ coincidences.** *The European physical journal A, Hadrons and nuclei* **25**(3): 397–404. DOI:10.1140/epja/i2005-10117-0

Lang, M.*; Glasmacher, U. A.; Neumann, R.*; Schardt, D.*; Trautmann, C.*; Wagner, G. A.: **Energy loss of 50-GeV uranium ions in natural diamond.** *Applied Physics A: Materials Science and Processing* **80**(4): 691–694. DOI:10.1007/s00339-004-3104-1

Litvinov, Y. A.*; Bürvenich, T. J.; Geissel, H.*; Novikov, Y. N.; Patyk, Z.; Scheidenberger, C.*; Attallah, F.*; Audi, G.; Beckert, K.*; Bosch, F.*; Falch, M.; Franzke, B.*; Hausmann, M.; Kerscher, T.; Klepper, O.*; Kluge, H.-J.*; Kozhuharov, C.*; Lobner, K. E. G.; Madland, D. G.; Maruhn, J. A.; Münzenberg, G.*; Nolden, F.*; Radon, T.*; Steck, M.*; Typel, S.*; Wollnik, H.: **Isospin dependence in the odd-even staggering of nuclear binding energies.** *Physical review letters* **95**(4): 042501. DOI:10.1103/PhysRevLett.95.042501

Litvinov, Y. A.*; Geissel, H.*; Radon, T.*; Attallah, F.*; Audi, G.; Beckert, K.*; Bosch, F.*; Falch, M.; Franzke, B.*; Hausmann, M.*; Hellström, M.*; Kerscher, T.; Klepper, O.*; Kluge, H.-J.*; Kozhuharov, C.*; Löbner, K. E. G.; Münzenberg, G.*; Nolden, E.*; Novikov, Y. N.; Quint, W.*; Patyk, Z.; Reich, H.*; Scheidenberger, C.*; Schlitt, B.*; Steck, M.*; Sümmerer, K.*; Vermeeren, L.*; Winkler, M.*; Winkler, T.*; Wollnik, H.: **Mass measurement of cooled neutron-deficient bismuth projectile fragments with time-resolved Schottky mass spectrometry at the FRS-ESR facility.** *Nuclear physics A, Nuclear and hadronic physics* **756**(1): 3–38. DOI:10.1016/j.nuclphysa.2005.03.015

López Cela, J. J.; Piriz, A. R.; Temporal, M.; Tahir, N. A.; Moreno, M. C. S.: **Elastoplastic effects on the Rayleigh-Taylor instability in an accelerated solid slab.** *European Physical Journal - Applied Physics* **29**(3): 247–252. DOI:10.1051/epjap:2004220

Morgan, B.; Spooner, N. J. C.; Armel-Funkhouser, M. S.; Hoffmann, D. H. H.; Jacoby, J.; Snowden-Ifft, D. P.; Zioutas, K.: **Searches for solar Kaluza-Klein axions with gas TPCs.** *Astroparticle Physics* **23**(3): 287–302. DOI:10.1016/j.astropartphys.2005.01.002

Mulser, P.; Kanapathipillai, M.*: **Collisionless absorption in clusters out of linear resonance.** *Physical review A, Atomic, molecular, and optical physics* **71**(6): 063201. DOI:10.1103/PhysRevA.71.063201

Mulser, P.; Kanapathipillai, M.*; Hoffmann, D. H. H.*: **Two very efficient nonlinear laser absorption mechanisms in clusters.** *Physical review letters* **95**(10): 103401. DOI:10.1103/PhysRevLett.95.103401

Neumayer, P.*; Bock, R.*; Borneis, S.*; Brambrink, E.*; Brand, H.*; Caird, J.; Campbell, E. M.; Gaul, E.; Goette, S.*; Haefner, C.*; Hahn, T.*; Heuck, H. M.*; Hoffmann, D. H. H.*; Javorkova, D.*; Kluge, H.-J.*; Kuehl, T.*; Kunzer, S.; Merz, T.*; Onkels, E.*; Perry, M. D.; Reemts, D.*; Roth, M.*; Samek, S.*; Schaumann, G.*; Schrader, F.*; Seelig, W.; Tauschwitz, A.*; Thiel, R.*; Ursescu, D.*; Wiewior, P.; Wittrock, U.; Zielbauer, B.*: **Status of PHELIX laser and first experiments.** *Laser and particle beams* **23**(3): 385–389. DOI:10.1017/S0263034605050548

Neyens, G.; Kowalska, M.; Yordanov, D.; Blaum, K.; Himpe, P.; Lievens, P.; Mallion, S.; Neugart,

R.; Vermeulen, N.; Utsuno, Y.; Otsuka, T.: **Measurement of the spin and magnetic moment of ^{31}Mg: Evidence for a strongly deformed intruder ground state.** *Physical review letters* **94**(2): 022501. DOI:10.1103/PhysRevLett.94.022501

Nortershäuser, W.*; Bushaw, B. A.; Dax, A.*; Drake, G. W. F.; Ewald, G.*; Götte, S.*; Kirchner, R.*; Kluge, H.-J.*; Kühl, T.*; Sanchez, R.*; Wojtaszek, A*.; Yan, Z. C.; Zimmermann, C.: **Measurement of the nuclear charge radii of ^{8,9}Li - The last step towards the determination of the charge radius of ^{11}Li.** *The European physical journal A, Hadrons and nuclei* **25**: 199–200. DOI:10.1140/epjad/i2005-06-053-9

Ohtsubo, T.*; Bosch, F.*; Geissel, H.*; Maier, L.; Scheidenberger, C.*; Attallah, F.*; Beckert, K.*; Beller, P.*; Boutin, D.*; Faestermann, T.; Franczak, B.*; Franzke, B.*; Hausmann, M.; Hellström, M.*; Kaza, E.*; Kienle, P.; Klepper, O.*; Kluge, H.-J.*; Kozhuharov, C.*; Litvinov, Y. A.*; Matos, M.*; Münzenberg, G.*; Nolden, F.*; Novikov, Y. N.*; Portillo, M.*; Radon, T.*; Stadlmann, J.*; Steck, M.*; Stöhlker, T.*; Sümmerer, K.*; Takahashi, K.*; Weick, H.*; Winkler, M.*; Yamaguchi, T.*: **Simultaneous measurement of β^- decay to bound and continuum electron states.** *Physical review letters* **95**(5): 052501. DOI:10.1103/PhysRevLett.95.052501

Olson, R. E.; Watson, R. L.; Horvat, V.; Zaharakis, K. E.; DuBois, R. D.; Stöhlker, T.*: **Electron stripping cross-sections for fast, low charge state uranium ions.** *Nuclear instruments & methods in physics research, Section A, Accelerators, spectrometers, detectors and associated equipment* **544**(1): 333–336. DOI:10.1016/j.nima.2005.01.229

Piriz, A. R.; Cela, J. J. L.; Cortazar, O. D.; Tahir, N. A.*; Hoffmann, D. H. H.*: **Rayleigh-Taylor instability in elastic solids.** *Physical Review E* **72**(5): 056313. DOI:10.1103/PhysRevE.72.056313

Pomorski, M.*; Berdermann, E.*; Ciobanu, M.*; Martemyianov, A.*; Moritz, P.*; Rebisz, M.*; Marczewska, B.: **Characterisation of single crystal CVD diamond particle detectors for hadron physics experiments.** *Physica status solidi A, Applied research* **202**(11): 2199–2205. DOI:10.1002/pssa.200561929

Protic, D.; Stöhlker, T.; Krings, T.; Mohos, I.; Spillmann, U.: **Two-dimensional microstrip germanium detector for the spectroscopy of hard x-ray transitions.** *IEEE transactions on nuclear science* **52**(6): 3194–3198. DOI:10.1109/TNS.2005.862932

Protic, D.; Stohlker, T.; Krings, T.; Mohos, I.; Spillmann, U.: **Two-dimensional microstrip germanium detector for the spectroscopy of hard x-ray transitions.** *IEEE transactions on nuclear science* **52**(6): 3194–3198. DOI:10.1109/TNS.2005.862932

Rodriguez, D.*; Kolhinen, V. S.; Audi, G.; Aysto, J.; Beck, D.*; Blaum, K.*; Bollen, G.; Herfurth, F.*; Jokinen, A.; Kellerbauer, A.; Kluge, H.-J.*; Oinonen, M.; Schatz, H.; Sauvan, E.; Schwarz, S.: **Mass measurement on the rp-process waiting point ^{72}Kr.** *The European physical journal A, Hadrons and nuclei* **25**: 41–43. DOI:10.1140/epjad/i2005-06-164-3

Rosmej, O. N.*; Blazevic, A.*; Korostiy, S.*; Bock, R.*; Hoffmann, D. H. H.*; Pikuz, S. A.; Efremov, V. P.; Fortov, V. E.; Fertman, A.; Mutin, T.; Pikuz, T. A.; Faenov, A. Y.: **Charge state and stopping dynamics of fast heavy ions in dense matter.** *Physical review A, Atomic, molecular, and optical physics* **72**(5): 052901. DOI:10.1103/PhysRevA.72.052901

Rosmej, O. N.*; Pikuz, S. A.; Korostiy, S.*; Blazevic, A.; Brambrink, E.; Fertman, A.; Mutin, T.; Efremov, V. P.; Pikuz, T. A.; Faenov, A. Y.; Loboda, P.; Golubev, A. A.; Hoffmann, D. H. H.*: **Radiation dynamics of fast heavy ions interacting with matter.** *Laser and particle beams* **23**(1): 79–85. DOI:10.1017/S0263034605050147

Roth, M.; Brambrink, E.; Audebert, P.; Basko, M.; Blazevic, A.*; Clarke, R.; Cobble, J.; Cowan, T. E.; Fernandez, J.; Fuchs, J.; Hegelich, M.; Ledingham, K.; Logan, L. G.; Neely, D.; Ruhl, H.; Schollmeier, M.: **Laser accelerated ions in ICF research prospects and experiments.** *Plasma Physics and Controlled Fusion* **47**: B841–B850. DOI:10.1088/0741-3335/47/12B/S66

Roth, M.; Brambrink, E.; Audebert, P.; Blazevic, A.; Clarke, R.; Cobble, J.; Cowan, T. E.; Fernandez, J.; Fuchs, J.; Geissel, M.; Habs, D.; Hegelich, M.; Karsch, S.; Ledingham, K.; Neely, D.; Ruhl, H.; Schlegel, T.*; Schreiber, J.: **Laser accelerated ions and electron transport in ultra-intense laser matter interaction.** *Laser and particle beams* **23**(1): 95–100. DOI:10.1017/S0263034605050160

Roudskoy, I. V.; Golubev, A. A.; Fertman, A. D.; Prokuronov, M. V.; Kantsyrev, A. V.; Sharkov, B. Y.; Turtikov, V. I.; Weyrich, K.*: **Gamma radiation measurements as a diagnostic tool of beam-induced dense plasmas.** *Laser and particle beams* **23**(4): 539–543. DOI:10.1017/S026303460505072X

Sahoo, B. K.*; Beier, T.*; Das, B. P.; Chaudhuri, R. K.; Mukherjee, D.: **Electron correlation effects in hyperfine interactions in Sc-45 and Y-89.** *Journal of physics B, Atomic, molecular and optical physics* **38**(24): 4379–4387. DOI:10.1088/0953-4075/38/24/004

Schaumann, G.; Schollmeier, M. S.; Rodriguez-Prieto, G.*; Blazevic, A.*; Brambrink, E.; Geissel, M.; Korostiy, S.*; Pirzadeh, P.; Roth, M.; Rosmej, F. B.; Faenov, A. Y.; Pikuz, T. A.; Tsigutkin, K.; Maron, Y.; Tahir, N. A.*; Hoffmann, D. H. H.*: **High energy heavy ion jets emerging from laser plasma generated by long pulse laser beams from the NHELIX laser sys-**

tem at GSI. *Laser and particle beams* **23**(4): 503–512. DOI:10.1017/S0263034605050688

Schiedt, B.*; Healy, K.; Morrison, A. P.; Neumann, R.*; Siwy, Z.: **Transport of ions and biomolecules through single asymmetric nanopores in polymer films.** *Nuclear instruments & methods in physics research, Section B, Beam interactions with materials and atoms* **236**: 109–116. DOI:10.1016/j.nimb.2005.03.265

Schweikhard, L.; Blaum, K.*; Herlerta, A.; Marx, G.: **Atomic clusters and ion cyclotron resonance mass spectrometry: a fruitful combination.** *European Journal of Mass Spectrometry* **11**(5): 457–468. DOI:10.1255/ejms.744

Severin, D.; Ensinger, W.; Neumann, R.*; Trautmann, C.*; Walter, G.*; Alig, I.; Dudkin, S.: **Degradation of polyimide under irradiation with swift heavy ions.** *Nuclear instruments & methods in physics research, Section B, Beam interactions with materials and atoms* **236**: 456–460. DOI:10.1016/j.nimb.2005.04.019

Sfienti, C.*; Adrich, P.*; Aumann, T.* L; Bacri, C. O.; Barczyk, T.; Bassini, R.; Boiano, C.; Botvina, A. S.*; Boudard, A.; Brzychczyk, J.; Chbihi, A.; Cibor, J.; Czech, B.; De Napoli, M.; Ducret, J.-E.; Emling, H.*; Frankland, J.; Hellström, M.*; Henzlova, D.*; Kezzar, K.*; Immé, G.; Iori, I.; Johansson, H.*; Lafriakh, A.; Le Fèvre, A.*; Le Gentil, E.; Leifels, Y.*; Lynch, W. G.; Lühning, J.*; Łukasik, J.*; Lynen, U.*; Majka, Z.; Mocko, M.; Müller, W. F. J.*; Mykulyak, A.; Orth, H.*; Otte, A. N.*; Palit, R.*; Pullia, A.*; Raciti, G.; Rapisarda, E.; Sann, H.*; Schwarz, C.*; Simon, H.*; Sokolov, A.*; Sümmerer, K.*; Trautmann, W.*; Tsang, M. B.; Verde, G.; Volaut, C.; Wallace, M.; Weick, H.*; Wiechula, J.*; Wieloch, A.; Zwieglinski, B.: **Mass and isospin effects in multifragmentation.** *Nuclear physics A, Nuclear and hadronic physics* **749**: 83C–92C. DOI:10.1016/j.nuclphysa.2004.12.011

Siegmann, B.; Werner, U.; Mann, R.*: **Fragmentation patterns of multiply ionized hydrocarbons in collisions with swift ions.** *Nuclear instruments & methods in physics research, Section B, Beam interactions with materials and atoms* **233**: 182–186. DOI:10.1016/j.nimb.2005.03.102

Sikler, G.; Audi, G.; Beck, D.; Blaum, K.; Bollen, G.; Herfurth, F.*; Kellerbauer, A.; Kluge, H.-J.*; Lunney, D.; Oinonen, M.; Scheidenberger, C.*; Schwarz, S.; Szerypo, J.: **Mass measurements on neutron-deficient Sr and neutron-rich Sn isotopes with the ISOLTRAP mass spectrometer.** *Nuclear physics A, Nuclear and hadronic physics* **763**: 45–58. DOI:10.1016/j.nuclphysa.2005.08.014

Siwy, Z. S.*; Trofin, L.; Baker, L.; Kohli, P.; Howorka, S.; Trautmann, C.*; Martin, C. R.: **Sensing binding affinities of proteins with a single abiotic nanopore.** *Biophysical journal* **88**(1): 658A–658A.

Siwy, Z.; Trofin, L.; Kohli, P.; Baker, L. A.; Trautmann, C.*; Martin, C. R.: **Protein biosensors based on biofunctionalized conical gold nanotubes.** *Journal of the American Chemical Society* **127**(14): 5000–5001. DOI:10.1021/ja043910f

Spohr, R.*: **Status of ion track technology - Prospects of single tracks.** *Radiation Measurements* **40**(2): 191–202. DOI:10.1016/j.radmeas.2005.03.008

Stahl, S.; Alonso, J.; Djekic, S.*; Kluge, H.-J.*; Quint, W.*; Verdu, J.; Vogel, M.; Werth, G.: **Phase-sensitive measurement of trapped particle motions.** *Journal of physics B, Atomic, molecular and optical physics* **38**(3): 297–304. DOI:10.1088/0953-4075/38/3/013

Stahl, S.; Galve, F.*; Alonso, J.; Djekic, S.; Quint, W.*; Valenzuela, T.; Verdu, J.; Vogel, M.; Werth, G.: **A planar Penning trap.** *The European physical journal: D, Atomic, molecular and optical physics* **32**(1): 139–146. DOI:10.1140/epjd/e2004-00179-x

Surzhykov, A.; Fritzsche, S.; Sepp, W. D.; Stöhlker, T.*; Orsic Muthig, A.*: **Polarization and alignment transfer in heavy hydrogen-like ions following radiative electron capture.** *Nuclear instruments & methods in physics research, Section B, Beam interactions with materials and atoms* **235**: 276–279.

Surzhykov, A.; Fritzsche, S.; Stöhlker, T.*; Tashenov, S.*: **Application of radiative electron capture for the diagnostics of spin-polarized ion beams at storage rings.** *Physical review letters* **94**(20): 203202. DOI:10.1103/PhysRevLett.94.203202

Tahir, N. A.*; Adonin, A.; Deutsch, C.; Fortov, V. E.; Grandjouan, N.; Geil, B.; Grayaznov, V.; Hoffmann, D. H. H.*; Kulish, M.; Lomonosov, I. V.; Mintsev, V.; Ni, P.*; Nikolaev, D.; Piriz, A. R.; Shilkin, N.; Spiller, P.*; Shutov, A.; Temporal, M. Ternovoi, V.; Udrea, S.; Varentsov, D.: **Studies of heavy ion-induced high-energy density states in matter at the GSI Darmstadt SIS-18 and future FAIR facility.** *Nuclear instruments & methods in physics research, Section A, Accelerators, spectrometers, detectors and associated equipment* **544**(1): 16–26. DOI:10.1016/j.nima.2005.01.178

Tahir, N. A.*; Deutsch, C.; Fortov, V. E.; Gryaznov, V.; Hoffmann, D. H. H.*; Kulish, M.; Lomonosov, I. V.; Mintsev, V.; Ni, P.; Nikolaev, D.; Piriz, A. R.; Shilkin, N.; Spiller, P.*; Shutov, A.; Temporal, M.; Ternovoi, V.; Udrea, S.; Varentsov, D.: **Proposal for the study of thermophysical properties of high-energy-density matter using current and future heavy-ion accelerator facilities at GSI Darmstadt.** *Physical review letters* **95**(3): 035001. DOI:10.1103/PhysRevLett.95.035001

Tahir, N. A.*; Goddard, B.; Kain, V.; Schmidt, R.; Shutov, A.; Lomonosov, I. V.; Piriz, A. R.; Temporal,

M.; Hoffmann, D. H. H.*; Fortov, V. E.: **Impact of 7-TeV/c large hadron collider proton beam on a copper target.** *Journal of Applied Physics* **97**(8): 083532. DOI:10.1063/1.1888031

Tahir, N. A.*; Kain, V.; Schmidt, R.; Shutov, A.; Lomonosov, I. V.; Gryaznov, V.; Piriz, A. R.; Temporal, M.; Hoffmann, D. H. H.*; Fortov, V. E.: **The CERN large hadron collider as a tool to study high-energy density matter.** *Physical review letters* **94**(13): 135004. DOI:10.1103/PhysRevLett.94.135004

Tahir, N. A.*; Weick, H.*; Iwase, H.*; Geissel, H.*; Hoffmann, D. H. H.*; Kindler, B.*; Lommel, B.*; Radon, T.*; Münzenberg, G.*; Shutov, A.; Sümmerer, K.*; Winkler, M.*: **Calculations of high-power production target and beamdump for the GSI future Super-FRS for a fast extraction scheme at the FAIR Facility.** *Journal of Physics D: Applied Physics* **38**(11): 1828–1837. DOI:10.1088/0022-3727/38/11/023

Temporal, M.; Lopez-Cela, J. J.; Piriz, A. R.; Grandjouan, N.; Tahir, N. A.*; Hoffmann, D. H. H.*: **Compression of a cylindrical hydrogen sample driven by an intense coaxial heavy ion beam.** *Laser and particle beams* **23**(2): 137–142. DOI:10.1017/S0263034605050226

Thungström, G.; Westerberg, L.; Spohr, R.*; Petersson, C. S.: **Fabrication and characterization of thin ΔE detectors for spectroscopic application.** *Nuclear instruments & methods in physics research, Section A, Accelerators, spectrometers, detectors and associated equipment* **546**(1): 312–318. DOI:10.1016/j.nima.2005.03.053

Toleikis, S.; Manil, B.; Bednarz, G.; Berdermann, E.*; Beyer, H. F.*; Bosch, F.*; Bräuning-Demian, A.*; Gumberidze, A.*; Indelicato, P.; Kozhuharov, C.*; Liesen, D.*; Marrus, R.; Mokler, P. H.*; Stachura, Z.; Stöhlker, T.*; Warczak, A.: **Lifetime measurement of the metastable 2 ^{3}P$_0$ state in He-like uranium.** *Nuclear instruments & methods in physics research, Section B, Beam interactions with materials and atoms* **235**: 197–200. DOI:10.1016/j.nimb.2005.03.172

Tomaselli, M.*: **Lithium transition energies and isotopic shift: three correlated electron states.** *Canadian Journal of Physics* **83**(4): 467–474. DOI:10.1139/P05-021

Tsigutkin, K.; Stambulchik, E.; Maron, Y.; Tauschwitz, A.*: **Determination of the LiI 4d-4f energy separation using active spectroscopy.** *Physica scripta* **71**(5): 502–506. DOI:10.1238/Physica.Regular.071a00502

Ursescu, D.*; Tomaselli, M.*; Kuehl, T.*; Fritzsche, S.: **Symbolic algorithms for the computation of Moshinsky brackets and nuclear matrix elements.** *Computer Physics Communication* **173**(3): 140–161. DOI:10.1016/j.cpc.2004.09.012

Varentsov, D.; Tkachenko, I. M.; Hoffmann, D. H. H.*: **Statistical approach to beam shaping.** *Physical Review E* **71**(6): 066501. DOI:10.1103/PhysRevE.71.066501

Verma, P.*; Mokler, P. H.*; Bräuning-Demian, A.*; Bräuning, H.; Berdermann, E.*; Chatterjee, S.*; Gumberidze, A.*; Hagmann, S.; Kozhuharov, C.*; Orsic-Muthig, A.*; Reuschl, R.; Schöffler, M.; Spillmann, U.*; Stöhlker, T.*; Stachura, Z.; Tashenov, S.*; Wahab, M. A.: **Charge exchange and X-ray emission in 70 MeV/u Bi-Au collisions.** *Nuclear instruments & methods in physics research, Section B, Beam interactions with materials and atoms* **235**: 309–314. DOI:10.1016/j.nimb.2005.03.196

Vogel, M.; Alonso, J.; Djekic, S.*; Kluge, H.-J.*; Quint, W.*; Stahl, S.; Verdu, J.; Werth, G.: **Towards electronic g-factor measurements in medium-heavy hydrogen-like and lithium-like ions.** *Nuclear instruments & methods in physics research, Section B, Beam interactions with materials and atoms* **235**: 7–16. DOI:10.1016/j.nimb.2005.03.136

Weber, C.*; Audi, G.*; Beck, D.; Blaum, K.*; Bollen, G.; Herfurth, F.*; Kellerbauer, A.*; Kluge, H.-J.*; Lunney, D.; Schwarz, S.: **Weighing excited nuclear states with a Penning trap mass spectrometer.** *Physics Letters A* **347**(1): 81–87. DOI:10.1016/j.physleta.2005.06.108

Weber, C.*; Audi, G.; Beck, D.*; Blaum, K.*; Bollen, G.; Herfurth, F.*; Kellerbauer, A.; Kluge, H.-J.*; Lunney, D.; Schwarz, S.: **Effects of the pairing energy on nuclear charge radii.** *The European physical journal A, Hadrons and nuclei* **25**: 201–202. DOI:10.1140/epjad/i2005-06-195-8

Weber, C.*; Blaum, K.*; Block, M.*; Ferrer, R.; Herfurth, F.*; Kluge, H.-J.*; Kozhuharov, C.*; Marx, G.; Mukherjee, M.*; Quint, W.*; Rahaman, S.*; Stahl, S.; SHIPTRAP Collaboration: **FT-ICR: A non-destructive detection for on-line mass measurements at SHIPTRAP.** *The European physical journal A, Hadrons and nuclei* **25**: 65–66. DOI:10.1140/epjad/i2005-06-167-0

Yazidjian, C.*; Beck, D.*; Blaum, K.*; Brand, H.*; Herfurth, F.*; Schwarz, S.: **Commissioning and first on-line test of the new ISOLTRAP control system.** *The European physical journal A, Hadrons and nuclei* **25**: 67–68. DOI:10.1140/epjad/i2005-06-096-x

Zioutas, K.; Andriamonje, S.; Arsov, V.*; Aune, S.; Autiero, D.; Avignone, F. T.; Barth, K.; Belov, A.; Beltrán, B.; Bräuninger, H.; Carmona, J. M.; Cebrián, S.; Chesi, E.; Collar, J. I.; Creswick, R.; Dafni, T.*; Davenport, M.; Di Lella, L.; Eleftheriadis, C.; Englhauser, J.; Fanourakis, G.; Farach, H.; Ferrer, E.; Fischer, H.; Franz, J.; Friedrich, P.; Geralis, T.; Giomataris, I.; Gninenko, S.; Goloubev, N.; Hasinoff, M. D.; Heinsius, F. H.; Hoffmann, D. H. H.*; Irastorza, I. G.; Jacoby, J.; Kang, D.; Königsmann, K.; Kotthaus, R.; Krčmar, M.; Kousouris, K.; Kuster, M.;

Lakić, B.; Lasseur, C.; Liolios, A.; Ljubičić, A.; Lutz, G.; Luzón, G.; Miller, D. W.; Morales, A.; Morales, J.; Mutterer, M.*; Nikolaidis, A.; Ortiz, A.; Papaevangelou, T.; Placci, A.; Raffelt, G.; Ruz, J.; Riege, H.*; Sarsa, M. L.; Savvidis, I.; Serber, W.; Serpico, P.; Semertzidis, Y.*; Stewart, L.; Vieira, J. D.; Villar, J.; Walckiers, L.; Zachariadou, K.: **First results from the CERN Axion Solar Telescope.** *Physical review letters* **94**(12): 121301. DOI:10.1103/PhysRevLett.94.121301

Zou, Y.; Hutton, R.; Feili, D.; Neacsu, C.; Ma, X.*; Schartner, K. H.; Mokler, P. H.*: **Precision lifetime measurement of the 2p $^2P_{3/2}$ level for Li-like Ni by beam-foil spectroscopy.** *Nuclear instruments & methods in physics research, Section B, Beam interactions with materials and atoms* **235**: 192–196. DOI:10.1016/j.nimb.2005.03.171

2. Further external publications

Bauer, D.; Mulser, P.: **Irreversible energy gain by linear and nonlinear oscillations.** In: *Journal of Physics, Conf. Series* **11**,

Berdermann, E.; NoRHDia Collaboration: **Single-Crystal CVD-Diamond Detectors for Hadron Physics.** In: *Proceedings of the XLIII International Winter Meeting on Nuclear Physics, Bormio, Italy, March 14-19, 2005,* 371p.

Bock, R. M.; Hofmann, I.; Hoffmann, D. H. H.; Logan, G.: **Inertial Confinement Fusion: Heavy Ions.** In: *Nuclear Energy,* Landolt-Börnstein: Numerical Data and Functional Relationships in Science and Technology, New Series; Energy Technologies, Vol. 3: Energy Technologies, Subvolume B, 529p.

Borneis, S.: **Hochenergie-Petawattlaser – die Erzeugung ultraintensiver Pulse.** In: *Photonik* **37***(3),*

Brandau, C.; Kozhuharov, C.; Müller, A.; Schippers, S.; Kluge, H.-J.; Mokler, P. H.; Stöhlker, T.; Wolf, A.: **Determination of Nuclear Ground State Properties with Large Atomic Cross Sections - Isotopic Shift Measurements by Means of Dielektronic Recombination.** In: Chiladze, David; Kacharava, Andro; Ströher, Hans: *STORI'05, 6th International Conference on Nuclear Physics at Storage Rings, 23–26 May 2005, Jülich-Bonn,* Schriften des Forschungszentrum Jülich, Reihe Materie und Material Vol. 30, Jülich: Forschungszentrum Jülich, 209p.

Hoffmann, D. H. H.*: **Editorial from the Editor in Chief.** In: *Laser and Particle Beams* **23***(1),* 1p.

Kester, O.; Dahl, L.; Eliseev, S.; Herfurth, F.; Heinz, S.; Kluge, H.-J.; Kozhuharov, C.; Maero, G.; Quint, W.; Vorobjev, G.; Ratzinger, U.; Schempp, A.; Hofmann, B.; Sauer, A.: **The HITRAP Decelerator Project at GSI .** In: *Proceedings of HIAT2005, Port Jefferson, USA,*

Manika, I.; Manika, J.; Schwartz, K.; Trautmann, C.; Toulemonde, M.: **Energy loss and fluence dependence of swift ion-induced hardening of LiF.** In: *Phys. Stat. Sol.(c) 2 ,* 434p.

Manika, I.; Maniks, J.; Schwartz, K.: **Hardening and long-range stress effects in LiF caused by high-fluence irradiation with fast Bi, Ni, Kr, and S ions.** In: *Optical Materials and Applications, Proceedings of SPIE, Volume 59460A-8,* A1p.

Matos, M.*; Novikov, Y.; Attallah, F.*; Beckert, K.*; Beller, P.*; Bosch, F.*; Boutin, D.*; Franczak, B.*; Franzke, B.*; Geissel, H.*; Hausmann, M.; Hellström, M.*; Kaza, E.*; Klepper, O.*; Kluge, H.-J.*; Kozhuharov, C.*; Kratz, K.-L.; Litvinov, Y.*; Münzenberg, G.*; Nolden, F.*; Ohtsubu, T.; Patyk, Z.; Pfeiffer, B.; Schatz, H.; Scheidenberger, C.*; Stadlmann, J.*; Steck, M.*; Vorobjev, G.*; Weick, H.*; Winkler, M.*; Wollnik, H.; Yamaguchi, T.: **Direct mass measurements of neutron-rich nuclides from zink-70 fragmentation.** In: Penionzhkevich, Y. E.; Cherepanov, E. A. : *International Symposium on Exotic Nuclei: Petershof; Russia, July 5-12, 2004 EXON 2004,* New Jersey, London, Singapore, Beijing, Shanghai, Hong Kong, Tapei, Chennai: World Scientific, 96p.

Matos, M.*; Novikov, Y.; Beckert, K.*; Beller, P.*; Bosch, F.*; Boutin, D.*; Franczak, B.*; Franzke, B.*; Geissel, H.*; Hausmann, M.; Kaza, E.*; Klepper, O.*; Kluge, H.-J.*; Kozhuharov, C.*; Kratz, K.-L.; Litvinov, S.*; Litvinov, Y.*; Münzenberg, G.*; Nolden, F.*; Ohtsubu, T.; Ostrowski, A. N.; Patyk, Z.; Pfeiffer, B.; Portillo, M.; Schatz, H.; Scheidenberger, C.*; Stadlmann, J.*; Steck, M.*; Viera, D.; Vorobjev, G.; Weick, H.*; Winkler, M.*; Wollnik, H.; Yamaguchi, T.: **Direct mass measurements of short-lived neutron-rich fission fragments at the FRS-ESR facility at GSI.** In: Penionzhkevich, Y. E.; Cherepanov, E. A. : *International Symposium on Exotic Nuclei: Petershof; Russia, July 5-12, 2004 EXON 2004,* New Jersey, London, Singapore, Beijing, Shanghai, Hong Kong, Tapei, Chennai: World Scientific, 90p.

Mokler, P. H.: **Higher Order QED Contributions to the Atomic Structure at Strong Central Fields.** In: *Proceedings of PEARL 2005,*

Schuch, R.; Stöhlker, T.: **SPARC: Atomic Physics with Highly-Charged Ions.** In: Chiladze, David; Kacharava Andro; Ströher, Hans: *STORI'05, 6th International Conference on Nuclear Physics at Storage Rings, 23–26 May 2005, Jülich-Bonn,* Schriften des Forschungszentrum Jülich, Reihe Materie und Material Vol. 30, Jülich: Forschungszentrum Jülich, 237p.

Surzhykov, A.; Fritzsche, s.; Stöhlker, T.; Tashenov, S.: **Diagnostics of Spin-Polarized Heavy Ion Beams at Storage Rings.** In: Chiladze, David; Kacharava Andro; Ströher, Hans: *STORI'05, 6th International Conference on Nuclear Physics at Storage Rings, 23–26 May 2005, Jülich-Bonn,* Schriften des Forschungszentrum Jülich, Reihe Materie und Material Vol. 30, Jülich: Forschungszentrum Jülich, 328p.

Tachenov, S.; Stöhlker, T.; Brandau, C.; Fritzsche, S.; Gumberdize, A.; Hagmann, S.; Kozhuharov, C.; Krings, T.; Protic, D.; Reuschl, R.; Rzadkiewicz, J.; Schneider, D., Spillmann, U.; Surzhykov, A.; Trotsenko, S.: **Diagnostics of Spin-Polarized Ion Beams by Hard X-Ray Polarimetry of Recombination Transition.** In: Chiladze, David; Kacharava Andro; Ströher, Hans: *STORI'05, 6th International Conference on Nuclear Physics at Storage Rings, 23–26 May 2005, Jülich-Bonn,* Schriften des Forschungszentrum Jülich, Reihe Materie und Material Vol. 30, Jülich: Forschungszentrum Jülich, 331p.

Tahir, N. A.; Deutsch, C.; Fortov, V. E.; Gryaznov, V.; Hoffmann, D. H. H.; Lomonosov, I. V.; Piriz, A. R.; Shutov, A.; Spiller, P.; Temporal, M.; Udrea, S.; Varentsov, D.: **Studies of High Energy Density Matter Including Strongly Coupled Plasmas Using Intense Heavy Ion Beams at the GSI Darmstadt and Future FAIR Accelerator Facilities.** In: *Bulletin of the American Physical Soceity 50,* 315p.

Tomaselli, M.; Kühl, T.; Ursescu, U.; Liu, L. C.: **Microscopic Correlations in Nuclear Structure Calculations.** In: *Proceedings8th Int. of the Spring Seminar in Nuclear Physics, Paestum, Italy, May 23 - 27, 2005,* World Scientific,

Verdu, J., K. Blaum, S. Djekic, S. Kreim, W. Quint, S. Stahl, S. Ulmer, M. Vogel, J. Walz, and G. Werth: **Penning trap measurement of the magnetic moment of the antiproton.** In: *Proceedings of the VIIIth Biannual Low Energy Antiproton Physics Conference, LEAP2005, AIP Conf. Proc.* **796***,* 260p.

Publications to the programme 'Health' in the field 'Cancer research'

K. Große, GSI, Darmstadt, Germany

1. Reviewed publications

Amaldi, U.; Kraft, G.*: **Radiotherapy with beams of carbon ions.** *Reports on Progress in Physics* **68**(8): 1861–1882. DOI:10.1088/0034-4885/68/8/R04

Bert, C.*; Metheany, K. G.; Doppke, K.; Chen, G. T. Y.: **A phantom evaluation of a stereo-vision surface imaging system for radiotherapy patient setup.** *Medical physics* **32**(9): 2753–2762. DOI:10.1118/1.1984263

Gudowska-Nowak, E.*; Kleczkowski, A.; Nasonova, E.*; Scholz, M.*; Ritter, S.*: **Correlation between mitotic delay and aberration burden, and their role for the analysis of chromosomal damage.** *International journal of radiation biology* **81**(1): 23–32. DOI:10.1080/09553000400027902

Gunzert-Marx, K.*; Schardt, D.*; Simon, R. S.*; Gutermuth, F.*; Radon, T.*; Dangendorf, V.; Nolte, R.: **Response of a BaF_2 scintillation detector to quasi-monoenergetic fast neutrons in the range of 45 to 198 MeV.** *Nuclear instruments & methods in physics research, Section A, Accelerators, spectrometers, detectors and associated equipment* **536**(1): 146–153. DOI:10.1016/j.nima.2004.07.168

Jakob, B.*; Rudolph, J. H.*; Gueven, N.; Lavin, M. E*.; Taucher-Scholz, G.*: **Live cell imaging of heavy-ion-induced radiation responses by beamline microscopy.** *Radiation research* **163**(6): 681–690.

Krämer, M.*; Jakel, O.: **Biological dose optimization using ramp-like dose gradients in ion irradiation fields.** *Physics M* **21**(3): 107–111.

Lee, R.*; Nasonova, E.*; Ritter, S.*: **Chromosome aberration yields and apoptosis in human lymphocytes irradiated with Fe-ions of differing LET.** *Advances in space research* **35**(2): 268–275. DOI:10.1016/j.asr.2004.11.020

Li, Q.; Groezinger, S. O.*; Haberer, T.*; Kraft, G.*: **Conformal irradiation for moving targets in heavy ion radiotherapy with raster-scanning beam delivery system (I) simulations.** *High energy physics and nuclear physics Chinese edition* **29**(10): 1006–1011.

Meller, B.; Sahlmann, C.; Horstmann, O.; Gerl, J.*; Baehre, M.; Meller, J.: **Conventional gamma and high energy probe for radioguided dissection of metastases in a patient with recurrent thyroid carcinoma with Tc-99m-MIBI and F-18-FDG.** *Nuklearmedizin - Nuclear Medicine* **44**(3): N23–N25.

Parodi, K.; Crespo, P.; Eickhoff, H.*; Haberer, T.*; Pawelke, J.; Schardt, D.*; Enghardt, W.: **Random coincidences during in-beam PET measurements at microbunched therapeutic ion beams.** *Nuclear instruments & methods in physics research, Section A, Accelerators, spectrometers, detectors and associated equipment* **545**(1): 446–458. DOI:10.1016/j.nima.2005.02.002

Paschen, A.; Song, M. X.; Osen, W.; Nguyen, X. D.; Berghaus, J. M.; Fink, D.*; Daniel, N.; Donzeau, M.; Nagel, W.; Kropshofer, H.; Schadendorf, D.: **Detection of spontaneous CD4(+) T-Cell responses in melanoma patients against a tyrosinase-related protein-2-derived epitope identified in HLA-DRB1∗ 0301 transgenic mice.** *Clinical Cancer Research* **11**(14): 5241–5247.

Psonka, K.*; Brons, S.*; Heiss, M.*; Gudowska-Nowak, E.*; Taucher-Scholz, G.*: **Induction of DNA damage by heavy ions measured by atomic force microscopy.** *Journal of physics Condensed matter* **17**(18): S1443–S1446. DOI:10.1088/0953-8984/17/18/002

Rietzel, E.*; Chen, G. T. Y.; Choi, N. C.; Willet, C. G.: **Four-dimensional image-based treatment planning: Target volume segmentation and dose calculation in the presence of respiratory motion.** *International journal of radiation oncology, biology, physics* **61**(5): 1535–1550. DOI:10.1016/j.ijrobp.2004.11.037

Rietzel, E.*; Pan, T. S.; Chen, G. T. Y.: **Four-dimensional computed tomography: Image formation and clinical protocol.** *Medical physics* **32**(4): 874–889. DOI:10.1118/1.1869852

Wang, J. F.; Weyrather, W. K.*; Krämer, M.; Scholz, M.*: **Biological equivalent dose and its verification in heavy ion treatment planning.** *High energy physics and nuclear physics Chinese edition* **29**(7): 709–712.

Patents and patent applications

M. Hensel, K. Große, GSI, Darmstadt, Germany

More information under:
<http://www.gsi.de/informationen/tt/index_e.html>

Granted patents and inventors

Schardt, D.; Heeg, P. **Vorrichtung zum Plazieren eines Tumor-Patienten.** European patent, January 2005 (GSI No. P159).

Bechthold, A.; Ratzinger, A.; Schempp, A.; Schlitt, B. **Apparatus for beam formation and pre-accelerating of ions.** US patent, February 2005 (GSI No. P169).

Yoshida, M.; Spohr, R. **Verfahren zum Steuern eines chemischen Ventils.** German patent, March 2005 (GSI No. P141).

Fehrenbacher, G.; Gutermuth, F.; Radon, T. **Abgeschirmter Raum für die Ionentherapie.** German patent, March 2005 (GSI No. P108).

Minaev, S.; Ratzinger, U.; Setzer, S. **Ionenstrahlimpulsverstärkung.** US patent, March 2005 and German patent, May 2005 (GSI No. P161).

Badura, E. **Vorrichtung und Verfahren zur Überwachung eines Signals.** US patent, May 2005 (GSI No. P140).

Spiller, P.; Bourgeois, W.; Fuchs, R. **Isokinetische Gantry-Anordnung.** US patent, May 2005 (GSI No. P192).

Haberer, T.; Ott, W. **Vorrichtung zur Anpassung einer Ionenstrahlfleckgröße.** US patent, February 2005 and European patent, May 2005 (GSI No. P167).

Siwy, Z.; Spohr, R.; Apel, Y. P.; Korchev, Y.; Yoshida, M. **Ätzen min. einer Ionenspur zu einer Pore in einer Membrane.** German patent, June 2005 (GSI No. P162).

Siwy, Z.; Dobrev, D.; Neumann, R.; Trautmann, C.; Voss, K.-O. **Nanostrukturen in Membranen und asymmetrische Membran.** US patent, June 2005 (GSI No. P177).

Vetter, J.; Angert, N.; Dobrev, D. **Folienmaterial mit Metallspitzen.** US patent, August 2005 (GSI No. P165).

Ott, W.; Haberer, T.. **Regelung eines Rasterscans in der Ionenstrahl-Therapie.** European patent, August 2005 (GSI No. P154).

Brüchle, W.; Fehrenbacher, G.; Gutermuth, F.; Radon, T. **Strahlungsschirmungsanordnung.** US patent, August 2005 (GSI No. P187).

Kraft, G. **Ionenstrahlanlage zur Bestrahlung von Tumorgeweben.** European patent, September 2005 (GSI No. P158).

Blasche, K.; Franczak, B. **Teilchenbeschleuniger für die Strahlentherapie mit Ionenstrahlen.** German patent, November 2005 (GSI No. P222).

Kraft, G.; Weber, U. **Ionenstrahl-Abtastsystem.** US patent, May 2005 and European patent November, 2005 (GSI No. P147).

Pavlovic, M.; Dolinskii, A.; Franczak, B. **Gantry with an ion-optical system.** European patent, November 2005 (GSI No. P153).

Reich-Sprenger, H. **Beschichtung aus einer Gettermetall-Legierung.** European patent, December 2005 (GSI No. P178).

Patent applications and inventors

Borneis, S.; Javorkova, D.; Neumayer, P.; Onkels, E. **Methods for increasing the damage threshold of diffraction gratins.** For German patent, February 2005 (GSI No. P229).

Apel, P.; Kiesewetter, H.; Spohr, R.; Skoczylas, M.; Zet, C. **Elektrolytische Bank.** For German patent, May 2005 (GSI No. P227).

Fehrenbacher, G. **Verfahren für die spektrometische Photonendosimetrie für Röntgen- und Gammastrahlung.** For German patent, June 2005 (GSI No. P231).

Fehrenbacher, G.; Radon, T. **Bestrahlungseinrichtung.** For German patent, July 2005 (GSI No. P232).

Hedlund, E.; Hjort, K.; Huber, T.; Neumann, R.; Westerburg, L. **Ratschenpumpe mit texturierter Oberfläche.** For German patent, November 2005 (GSI No. P230).

Bert, C.; Kraft, G.; Rietzel, E. **Vorrichtung zum Bestrahlen von Tumorgewebe eines Patienten mit einem Teilchenstrahl.** For German patent, December 2005 (GSI No. P237).

GSI as publisher

K. Große, GSI, Darmstadt, Germany

GSI; Groß, K.-D. et al. (Ed): **Wissenschaftliche Zielsetzungen und Forschungsprogramme: FAIR - Facility for Antiproton and Ion Research. [Statusbericht]** July 2005.

Smolyakov, A.; Fischer, W.; Omet, C.; Spiller, P.: **Comparison of the present and planned operation of the SIS18 and the AGS Booster with intermediate charge state heavy ions.** GSI-Acc-Report-2005-11-001.

Golubov, A. A.; Kantsyrev, A. V.; Luckjashin, V. E.; Fertman, A.; Kunin, A. V.; Vatulin, V. V.; Gnutov, A. S.; Panova, Y. V.; Mustafin, E.; Schardt, D.; Weyrich, K.; Sobolevsky, N. M.; Latysheva, L. N.: **Measurement of the energy deposition profiles for 238 U ions with energy 500 and 950 MeV/u in stainless steel and copper targets.** GSI-Acc-Note-2005-04-001.

Franchetti, G.; Giacomini, T.; Kirk, M.; Parfenova, A.: **Resonance Induced Beam Loss in SIS18.** GSI-Acc-Note-2005-12-001.

Kornilov, V.; Boine-Frankenheim, O.; Hofmann, I.; Doliwa, B.: **Damping of Transverse Instabilities for Coasting Beams.** GSI-Acc-Note-2005-10-001.

Latyscheva, L. N.; Mustafin, E. R.: **Modeling of energy deposition and fragment-spectra in the construction elements of the SIS300 dipole magnet irradiated by 37 GeV/u uranium ions.** GSI-Acc-Note-2005-04-002.

Golubov, A. A.; Kantsyrev, A. V.; Luckjashin, V. E.; Fertman, A.; Kunin, A. V.; Vatulin, V. V.; Gnutov, A. S.; Panova, Y. V.; Mustafin, E.; Schardt, D.; Weyrich, K.; Sobolevsky, N. M.; Latysheva, L. N.: **Measurement of the energy deposition profiles for 238 U ions with energy 500 and 950 MeV/u in stainless steel and copper targets.** GSI-Acc-Note-2005-04-001.

Franchetti, G.; Schuett, P.; Hoffmann, T.; Rumolo, G.; Franchi, A.: **Mapping of the resonances in SIS18.** GSI-Acc-Note-2005-02-001.

Ricciardi, M. V.; Armbruster, P.; Benlliure, J.; Bernas, M.; Boudard, A.; Czajkowski, S.; Enqvist, T.; Kelic, A.; Leray, S.; Legrain, R.; Mustapha, B.; Pereira, J.; Rejmund, F.; Schmidt, K.-H.; Stephan, C.; Tassan-Got, L.; Volant, C.; Yordanov, O: **Light Nuclides Produced in the Proton-Induced Spallation of ^{238}U at 1 GeV.** GSI Report 2005-6.

Egelhof, P.; Kraft-Bermuth, S.: **Calorimetric Low Temperature Detectors for Heavy Ion Physics.** GSI Report 2005-5.

PHELIX theory group: **ILIAS Ion and Laser beam Interaction and Application Studies: A scientific portrait of the PHELIX theory group.** GSI Report 2005-4.

Weyrich, K. (Ed.): **High Energy Density Physics with Intense Ion and Laser Beams: Annual Report 2004.** GSI Report 2005-3.

Geissel, H.; Winkler, M.; Weick, H.; Behr, K.-H.; Münzenberg, G.; Simon, H.; Sümmerer, K.; Achenbach, B.; Ahle, L.; Aumann, T.; Bleile, G.; Breitenberger, G.; Brünle, A.; Emling, H.; Fehrenbacher, G.; Gleim, M.; Hller, W.; Iwase, H.; Karagiannis, C.; Kaiser, R.; Kelic, A.; Kindler, B.; Klappich, T.; Kubo, N.; Kurz, K.; Kusaka, J.; Lettry, B.; Lommel, G.; Moritz, D.; Morrissey, B.; Mühle, C.; J.; Nolen, A.; Pschorn, I.; Radon, T.; Ronningen, R.; Savard, G.; Scheidenberger, C.; Shatunov, Y.; Sherrill, B. M.; Tahir, N. A.; Yavor, M.; Yoshida, A.; Yu, X.; Zeller, A. F.: **Technical Report on the Design, Construction, Commissioning and Operation of the Super-FRS of FAIR.** GSI Report 2005-2.

Große, K. (Ed.): **GSI Scientific Report 2004.** GSI Report 2005-1.

Ricciardi, M. V.; Armbruster, P.; Benlliure, J.; Bernas, M.; Boudard, A.; Czajkowski, S.; Enqvist, T.; Kelic, A.; Leray, S.; Legrain, R.; Mustapha, B.; Pereira, J.; Rejmund, F.; Schmidt, K.-H.; Stephan, C.; Tassan-Got, L.; Volant, C.; Yordanov, O.: **Light Nuclides Produced in the Proton-Induced Spallation of ^{238}U at 1 GeV.** GSI Report 2005-6.

Aumann, T.: **Reactions with fast radioactive beams of neutron-rich nuclei.** GSI Preprint 2005-12.

Geissel, H.; Litvinov, Y. A.; Pfeiffer, B.; Attallah, F.; Audi, G.; Beckert, K.; Beller, P.; Bosch, F.; Boutin, D.; Brvenich, T. J.; Chen, L.; Faestermann, T.; Falch, M.; Franzke, B.; Hausmann, M.; Kaza, E.; Kerscher, T.; Kienle, P.; Klepper, O.; Knöbel, R.; Kozhuharov, C.; Kratz, K.-L.; Litvinov, S. A.; Löbner, K. E. G.; Maier, L.; Matos, M.; Montes, F.; Münzenberg, G.; Nociforo, C.; Nolden, F.; Novikov, Y. N.; Ohtsubo, T.; Ostrowski, A.; Patyk, Z.; Plaß, W.; Portillo, M.; Radon, T.; Schatz, H.; Scheidenberger, C.; Stadlmann, J.; Steck, M.; Sun, B.; Takahashi, K.; Vorobjev, G.; Weick, H.; Winkler, M.; Wollnik, H.; Yamaguchi, T.: **Present and Future Experiments with Stored Exotic Nuclei at Relativistic Energies** GSI Preprint-11.

GSI Preprint 2005-10 did not come out.

Protic, D.; Stölker, T.; Krings, T.; Mohos, I.; Spillmann, U.: **Detector for the Spectroscopy of Hard X-Ray Transitions.** GSI Preprint-9.

Weber, C.; Audi, G.; Beck, D.; Blaum, K.; Bollen, G.; Herfurth, F.; Kellerbauer, A.; Kluge, H.-J.; Lunney, D.; Schwarz, S.: **Weighing excited nuclear states with a Penning trap mass spectrometer.** GSI Preprint 2005-8.

Kelic, A.; Schmidt, K.-H.: **Assessment of saddle-point-mass predictions for astrophysical applications.** GSI Preprint 2005-7.

Henzlova, D.; Botvina, A. S.; Schmidt, K.-H.; Henzl, V.; Napolitani, P.; Ricciardi, M. V.: **Symmetry energy of fragments produced in multifragmentation.** GSI Preprint 2005-6.

Litvinov, Y. A.; Geissel, H.; Radon, T.; Attallah, F.; Audi, G.; Beckert, K.; Bosch, F.; Falch, M.; Franzke, B.; Hausmann, M.; Hellström, M.; Kerscher, T.; Klepper, O.; Kluge, H.-J.; Kozhuharov, C.; Löbner, K. E. G.; Müzenberg, G.; Nolden, F.; Novikov, Y. N.; Quint, W.; Patyk, Z.; Reich, H.; Scheidenberger, C.; Schlitt, B.; Steck, M.; Sümmerer, K.; Vermeeren, L.; Winkler, M.; Winkler, T.; Wollnik, H.: **Mass Measurement of Cooled Neutron-Deficient Bismuth Projectile Fragments with Time-Resolved Schottky Mass Spectrometry at the FRS-ESR Facility.** GSI Preprint 2005-5.

Surzhykov, A.; Fritzsche, S.; Stöhlker, T.; Tashenov, S. : **Application of radiative electron capture for the diagnostics of spin-polarized ion beams at storage rings.** GSI Preprint 2005-4.

Gumberidze, A.; Stöhlker, T.; Banas, D.; Beckert, K.; Beller, P.; Beyer, H. F.; Bosch, F.; Hagmann, S.; Kozhuharov, C.; Liesen, D.; Nolden, F.; Ma, X.; Mokler, P. H.; Steck, M.; Sierpowski, D.; Tashenov, S.: **Quantum Electrodynamics at Strong Electric Fields: The Ground State Lamb Shift in Hydrogenlike Uranium.** GSI Preprint 2005-3.

Ivanyuk, F. A.; Nörenberg, W.: **Diabatic states from nodal structure conservation.** GSI Preprint 2005-2.

Fritzsche, S.; Indelicato, P.; Stölker, T.: **Relativistic quantum dynamics in strong fields: Photon emission from heavy, few-electron ions.** GSI Preprint 2005-1.

International and national collaborations

K. Große, GSI, Darmstadt, Germany

The FAIR Collaborations

FAIR: The AIC Collaboration

Anti-proton Ion Collider
Spokesperson: R. Krücken, Munich (Germany)

Beller, P.[3]; Bosch, F.[3]; Cargnelli, M.[7]; Fabbietti, L.[8]; Faestermann, T.[8]; Franzke, B.[3]; Fuhrmann, H.[7]; Hayano, R. S.[9]; Hirtl, A.[7]; Homolka, J.[8]; Kienle, P.[8]; Kozhuharov, C.[3]; Krücken, R.[8]; Lenske, H.[5]; Litvinov, Y.[3]; Marton, J.[4]; Nolden, F.[3]; Ring, P.[8]; Shatunov, Y. M.[2]; Skrinsky, A. N.[2]; Suzuki, K.[8]; Vostrikov, V.[2]; Widmann, E.[9]; Wycech, S.[1]; Yamaguchi, T.[6]; Zmeskal, J.[7]

1 Andrzej Soltan Institute for Nuclear Studies Warsaw (Poland)
2 BINP Novosibirsk (Russia)
3 GSI Darmstadt (Germany)
4 IMEP Wien (Austria)
5 Justus-Liebig University Giessen (Germany)
6 Saitama University (Japan)
7 Stephan Meyer Institute Vienna (Austria)
8 TU Munich (Germany)

FAIR: The BIOMAT Collaboration

The High-Energy Irradiation Facility for Biophysics and Materials Research
Spokespersons: M. Durante, Naples (Italy) S. Klaumünzer, Berlin (Germany)

Benyagoub, A.[5]; Bettega, D.[20]; Bolse, W.[26]; Bouffard, S.[5]; Chimi, Y.[27]; Cirio, R.[28]; Durante, M.[22]; Elsässer, T.[8]; Ensinger, W.[9]; Geissel, H.[8]; Glasmacher, U. A.[15]; Golubev, A.[21]; Hagmann, S.[12]; Hoffmann, D. H. H.[9]; Ishikawa, N.[27]; Iwase, A.[23]; Iwase, H.[8]; Jin, G. M.[19]; Kambara, T.[30]; Kawatsyuk, O.[8]; Keppler, H.[1]; Klaumünzer, S.[3]; Kraft, G.[8]; Krasavin, E.[11]; Lang, M.[8]; Langenhorst, F.[17]; Liu, J.[19]; Mewaldt, R.[24]; Miletich, R.[16]; Miller, J.[2]; Narici, L.[25]; Neumann, R.[8]; O'Sullivan, D.[10]; Okayasu, R.[7]; Picozza, P.[25]; Reitz, G.[18]; Ritter, S.[8]; Rothard, H.[5]; Schardt, D[8]; Schiwietz, G.[3]; Scholz, M.[8]; Schuhmacher, H.[4]; Sihver, L.[13]; Tahir, N.[8]; Ting, S. C. C.[6]; Toulemonde, M.[5]; Trautmann, C.[8]; Udrea, S.[9]; Valtonen, E.[29]; Varentzov, D.[9]; Wagner, G. A.[14]; Wang, Z. G.[19]

1 University of Bayreuth and Bayerische Akademie der Wissenschaften, Bayerisches Geoinstitut, Bayreuth (Germany)
2 Lawrence Berkeley Lab LBL, Berkeley (USA)
3 Hahn-Meitner-Institut HMI, Berlin (Germany)
4 Phys.-Techn. Bundesanstalt PTB, Braunschweig (Germany)
5 Centre Interdisciplinaire de Recherche Ions Laser CIRIL, Grand Acclerateur National d'Ions Lourds GANIL, Caen (France)
6 Massachusetts Institute of Technology MIT, Cambridge (USA)
7 National Institute of Radiation Science NIRS, Chiba (Japan)
8 GSI, Darmstadt (Germany)
9 University of Technology, Darmstadt (Germany)
10 Institute for Advanced Studies, Dublin (Ireland)
11 Joint Inst. f. Nucl. Research JINR, Dubna (Russia)
12 University of Frankfurt/Main (Germany)
13 Chalmers Univ. of Technology, Göteborg (Sweden)
14 Heidelberger Akademie der Wissenschaften, Heidelberg (Germany)
15 Max-Planck-Institut fr Kernphysik, Heidelberg (Germany)
16 University of Heidelberg, Heidelberg (Germany)
17 University of Jena, Jena (Germany)
18 Deutsches Inst. f. Luft-und Raumfahrt DLR, Köln (Germany)
19 Institute of Modern Physics, Chinese Academy of Sciences, Lanzhou (China)
20 University of Milano, Milano (Italy)
21 Institute of Theoretical and Experimental Physics ITEP, Moscow (Russia)
22 University of Naples, Naples (Italy)
23 Osaka Prefecture University, Osaka (Japan)
24 California Inst. of Technology CALTECH, Pasadena (USA)
25 University of Rome, Rome (Italy)
26 University of Stuttgart, Stuttgart (Germany)
27 Japan Atomic Energy Research Institute JAERI, Tokai (Japan)
28 Istituto Nazionale di Fisica Nucleare INFN, Torino (Italy)
29 University of Turku, Turku (Finland)
30 RIKEN, Wako (Japan)

Contributions in this report:
FAIR-APPA-BIOMAT-01
RAD-BIOPHYSICS-16

FAIR: The CBM Collaboration

The Condensed Baryonic Matter experiment
< http : //www.gsi.de/zukunftsprojekt/experimente/
CBM/index_e.html >
Spokesperson: P. Senger, Darmstadt (Germany)

Adamczewski, J.[6]; Adamova, D.[32]; Ahmad, Z.[17]; Aiftimiei, C.[2]; Akindinov, A.[22]; Akishin, P.[9]; Akishina, E.[9]; Al-Turany, M.[6]; Alyushin, M.[25]; Amar-Youcef, S.[10]; Ammosov, V.[30]; Andronic, A.[6]; Appelshäuser, H.[10]; Arefiev, A.[22]; Atanasov, D.[14]; Atkin, E.[25]; Badura, E.[6]; Baginyan, S.[9]; Baranova, N.[23]; Bashindjagyan, G.[23]; Basrak, Z.[40]; Baublis, V.[11]; Belogurov, S.[22]; Benabderahmane, L. M.[13]; Berdermann, E.[6]; Berdnikov, A.[36]; Berdnikov, Y.[36]; Bertini, D.[6]; Besson, A.[37]; Bezshyyko, O.[19]; Bocharov, Y.[25]; Bogdanovich, B.[25]; Bogolyubsky, M.[30]; Boldizsar, L.[4]; Bondar, N.[11]; Braun-Munzinger, P.[6]; Brenner, K.-H.[20]; Brzychczyk, J.[18]; Brüning, U.[20]; Bubak, A.[16]; Cai, X.[39]; Caplar, R.[40]; Caragheorgheopol, G.[2]; Catanescu, V.[2]; Chattopadhyay, S.[17]; Chen, H.[12]; Chepurnov, V.[7]; Chernenko, S.[7]; Chubarov, M.[35]; Ciobanu, M.[6]; Claus, G.[37]; Coi, K.-U.[31]; Cordier, E.[13]; Dželalija, M.[40]; Das, S.[6]; Deak, F.[3]; Denes, E.[4]; Deppe, H.[6]; Deveaux, M.[6]; Dohrmann, F.[33]; Dong, X.[12]; Dorokhov, A.[37]; Dulinski, W.[37]; DuttaMajumdar, M. R.[17]; Dyatchenko, V.[30]; Emelianov, V.[25]; Eschke, J.[6]; Essel, H.[6]; Fateev, O.[7]; Ferreira Marques, R.[5]; Fischer, P.[20]; Flemming, H.[6]; Fodor, Z.[4]; Fonte, P.[5]; Friese, V.[6]; Fröhlich,, I.[10]; Fröning, H.[20]; Futo, E.[4]; Gašparić, I.[40]; Galatyuk, T.[6]; Galkin, V.[28]; Garabatos, C.[6]; Ghosh, P.[17]; Gläß, J.[20]; Golovatyuk, V.[7]; Golovin, A.[28]; Golovtsov, V.[11]; Golubeva, M.[21]; Gonzales, D.[6]; Gousakov, J.[8]; Grishkin, Y.[22]; Grishuk, Y.[22]; Grosse, E.[33]; Grzeszczuk, A.[16]; Guber, F.[21]; Hartig, M.[10]; Heidel, K.[33]; Heini, S.[37]; Herrmann, N.[13]; Heuser, J.[6]; Himmi, A.[37]; Holzmann, R.[6]; Hong, B.[34]; Hoppe, M.[26]; Höhne, C.[6]; Ierusalimov, A.[7]; Igolkin, S.[35]; Ilyushenko, I.[25]; Im Kang, T.[34]; Ivanov, V.[11]; Ivanov, Va.[9]; Ivanov, Vi.[9]; Ivashkin, A.[21]; Izsak, R.[3]; Jaaskelainen, K.[37]; Kadenko, I.[19]; Kalisky, M.[6]; Karabowicz, R.[18]; Karasev, V.[35]; Karavichev, O.[21]; Karavicheva, T.[21]; Karmanov, D.[23]; Karpechev, E.[21]; Kazantsev, A.[24]; Kebschull, U.[14]; Kecskemeti, J.[4]; Kekelidze, G.[8]; Khanzadeev, A.[11]; Kharlov, Y.[30]; Khmelnikov, V.[30]; Kiš, M.[40]; Kim, J.[31]; Kim, Y.-J.[6]; Kirejczyk, M.[38]; Kisel, I[14]; Kiselev, S.[22]; Kiseleva, A.[6]; Kiss, A.[3]; Kiss, T.[4]; Klein-Bösing, C.[26]; Koch, K.[6]; Koczon, P.[6]; Kolb, B.[6]; Korolev, M.[23]; Korolko, I.[22]; Kostenko, B.[9]; Kotte, R.[33]; Kowalski, S.[16]; Krasnuk, A.[25]; Krauze, M.[16]; Kreidl, C.[20]; Kresan, D.[6]; Kryshen, E.[36]; Kugler, A.[32]; Kurepin, A.[21]; Kuznetsov, A.[30]; Kvaracheliya, T.[22]; Kämpfer, B.[33]; König, W.[6]; Ladygin, V.[7]; Lashaev, S.[35]; Laszlo, A.[4]; Lebedev, A.[22]; Lebedev, E.[9]; Leifels, Y.[6]; Leontiev, V.[30]; Li, C.[12]; Lindenstruth, V.[14]; Linev, S.[6]; Litvinenko, E.[9]; Lucenko, V.[8]; Maevskaya, A.[21]; Magureanu, C.[2]; Maiatski, V.[22]; Majka, Z.[18]; Malakhov, A.[7]; Malyshev, S.[22]; Mangiarotti, A.[13]; Manko, V.[24]; Martemiyanov, A.[22]; Matulewicz, T.[38]; Matyushevskiy, E.[7]; Merkin, M.[23]; Merschmeyer, M.[13]; Mialkovski, V.[8]; Mikhailov, K.[22]; Mishin, S.[8]; Mohanty, B.[17]; Moisa, D.[2]; Mousa, J.[27]; Murin, Y.[35]; Murthy, G. S. N.[17]; Muthers, D.[15]; Männer, R.[20]; Müller, W. F. J.[6]; Müntz, C.[10]; Nadtochii, A.[11]; Narayan, S. R.[17]; Naumann, L.[33]; Nayak, T.[17]; Niebur, W.[6]; Nüssle, M. N.[20]; Obraztsov, V.[30]; Onishchenko, E.[25]; Ososkov, G.[9]; Ossetski, D.[28]; Pal, S.[17]; Peshekhonov, D.[8]; Peshekhonov, V.[8]; Peshenichnov, I.[21]; Petracek, V.[29]; Petris, M.[2]; Petrovici, A.[2]; Petrovici, M.[2]; Piasecki, K.[38]; Plekhanov, E.[7]; Plujko, V.[19]; Plujschev, V.[35]; Polishchuk, B.[30]; Polozov, P.[22]; Pop, A.[2]; Popov, V.[25]; Pospisil, V.[29]; Pozdniakov, V.[7]; Prokudin, M.[22]; Rabin, N.[22]; Raduta, A.[2]; Rami, F.[37]; Raportirenko, A.[9]; Rasin, V.[21]; Reshetin, A.[21]; Reygers, K.[26]; Riabov, Y.[11]; Rogachevsky, O.[7]; Ryazantsev, A.[30]; Rykalin, V.[30]; Ryzhikov, D.[28]; Ryzhinskiy, M.[36]; Röhrich, D.[1]; Sadovsky, S.[30]; Sainis, Y.[17]; Samsonov, V.[11]; Sang Ryu, M.[34]; Saveliev, V.[28]; Schweda, K.[13]; Schüttauf, A.[6]; Seleznev, E.[35]; Seliverstov, D.[11]; Semak, A.[30]; Senger, P.[6]; Shao, M.[12]; Sharkov, G.[22]; Shelikhov, V.[30]; Shevshenko, V.[19]; Sikora, B.[38]; Silaev, A.[25]; Sim, K.-S.[34]; Simakov, A.[25]; Simion, V.[2]; Simon, R.[6]; Singhal, V.[17]; Siwek-Wilczynska, K.[38]; Skoda, L.[29]; Slogsnat, D.[20]; Slusarczyk, L.[38]; Smirnitskiy, A.[22]; Smolyankin, V.[22]; Soldatov, A.[30]; Soloviev, A.[9]; Soos, Cs.[4]; Sougonyaev, V.[30]; Staszel, P.[18]; Stavinskiy, A.[22]; Steinle, C.[20]; Stephan, E.[16]; Stoicea, G.[2]; Stolin, V.[22]; Strekalovsky, O.[8]; Stroth, J.[10]; Ströbele, H.[10]; Sviridov, Y.[30]; Tarassenkova, O.[11]; Tielert, R.[15]; Tiflov, V.[21]; Tlusty, P.[32]; Tolyhi, T.[4]; Tontisirin, S.[15]; Topilskaya, N.[21]; Torralba, G.[14]; Tröger, G.[14]; Tsertos, H.[27]; Uhlig, F.[6]; Ullaland, K.[1]; Uzhinsky, V.[9]; Valin, I.[37]; Vassiliev, I.[6]; Veretenkin, I.[21]; Vesztergombi, G.[4]; Victorov, V.[30]; Viriasov, K.[8]; Viyogi, Y.[17]; Volkov, Y.[25]; Voloshin, K.[22]; Voronin, A.[23]; Vznuzdaev, E.[11]; Wang, X.[12]; Wessels, J.[26]; Wilk, A.[26]; Winter, M.[37]; Wisniewski, K.[38]; Wohlfeld, D.[20]; Wu, J.[12]; Wu, T.[39]; Wurz, A.[20]; Xu, M.[12]; Yin, Z. B.[39]; Yoo, I.-K.[31]; Yushmanov, I.[24]; Zaboudko, M.[28]; Zaets, V.[30]; Zagreev, B.[22]; Zanevsky, Y.[7]; Zhalov, M.[11]; Zhang, Z.[12]; Zhilin, A.[22]; Zhou, D. C.[39]; Zipper, W.[16]; Zrelov, P.[9]; Zrjuev, V.[7]

1 Department of Physics and Technology, University of Bergen, Bergen (Norway)
2 National Institute for Physics and Nuclear Engineering, Bucharest (Romania)
3 Eötvös University, Budapest (Hungary)
4 KFKI Budapest (Hungary)
5 LIP, Coimbra (Portugal)
6 GSI, Darmstadt (Germany)
7 JINR-LHE, Dubna (Russia)
8 JINR-LPP Dubna (Russia)
9 JINR-LIT Dubna (Russia)
10 Institut für Kernphysik, Universität Frankfurt, Frankfurt (Germany)
11 Petersburg Nuclear Physics Institute PNPI, St. Petersburg (Russia)
12 Department of Modern Physics, University of Science & Technology of China, Hefei (China)
13 Physikalisches Institut, Universität Heidelberg, Heidelberg (Germany)
14 Kirchhoff-Institut für Physik, Universität Heidelberg, Heidelberg (Germany)
15 Universität Kaiserslautern, Kaiserslautern (Germany)
16 University of Silesia Katowice (Poland)
17 Variable Energy Cyclotron Centre VECC, Kolkata (India)[+]
18 Jagiellonian University, Krakow (Poland)
19 National University of Kyiv, Kyiv (Ukraine)
20 Inst. of Computer Engineering, Universität Mannheim, Mannheim

21 Institute for Nuclear Research, Moscow (Russia)
22 ITEP Moscow (Russia)
23 SINP-MSU, Lomonosov Moscow State University, Moscow (Russia)
24 Kurchatov Institute Moscow (Russia)
25 Moscow Engineering Physics Institute MEPhi, Moscow (Russia)
26 Institut für Kernphysik, Universität Münster, Münster (Germany)
27 Cyprus University, Nikosia (Cyprus)
28 Obninsk State Technical University for Nuclear Power Engineering, Obninsk (Russia)
29 Technical University, Prag (Czech Republic)
30 Institute for High Energy Physics IHEP, Protvino (Russia)
31 Pusan National University PNU, Pusan (Korea)
32 Czech Academy of Sciences, Rez (Czech Republic)
33 Institut für Kern- und Hadronenphysik, FZR, Dresden (Germany)
34 Department of Physics, Korea University, Seoul (Korea)
35 Khlopin Radium Institute KRI, St. Petersburg (Russia)
36 St. Petersburg State Polytechnic University SPbSTU, St. Petersburg (Russia)
37 Institut de Recherches Subatomiques IRes, IN2P3-CNRS and Univesité Louis Pasteur Strasbourg, Strasbourg (France)
38 Warsaw University, Institute of Experimental Physics, Warsaw (Poland)
39 Institute of Particle Physics, Hua-zhong Normal University Wuhan (China)
40 Rudjer Bošković Institute, Zagreb (Croatia)

Contributions in this report:
FAIR-QCD-CBM-02
FAIR-QCD-CBM-03
FAIR-QCD-CBM-04
FAIR-QCD-CBM-05
FAIR-QCD-CBM-06
FAIR-QCD-CBM-07
FAIR-QCD-CBM-08
FAIR-QCD-CBM-09
FAIR-QCD-CBM-10
FAIR-QCD-CBM-12
FAIR-QCD-CBM-13
FAIR-QCD-CBM-14
FAIR-QCD-CBM-15
FAIR-QCD-CBM-16

FAIR: The FLAIR Collaboration

A Facility for Low-energy Antiproton and Ion Research
< http://www-linux.gsi.de/∼flair/>
Spokesperson: E. Widmann (Austria)

Andler, G.[43]; Bagge, L.[43]; Balashov, V. V.[31]; Barna, D.[39]; Bassalleck, B.[51]; Beier, T.[18]; Beyer, H.[18]; Blaum, K.[26]; Bloch, I.[26]; Block, M.[18]; Borneis, S.[18]; Bosch, F.[18]; Boucard, S.[41]; Bräuning-Demian, A.[18]; Bureyeva, L. A.[35]; Burgdoerfer, J.[30]; Cargnelli, M.[49]; Charlton, M.[12]; Corradini, M.[13]; Danared, H.[43]; Dax, A.[11]; Djekic, S.[26]; Dörner, R.[23]; Eikema, K.[42]; Engström, M.[43]; Franzke, B.[18]; Fujiwara, M.[50]; Gabrielse, G.[7]; George, S.[26]; Gillitzer, A.[17]; Gotta, D.[17]; Grieser, M.[44]; Grzonka, D.[17]; Hagmann, S.[18]; von Hahn, R.[44]; Hayano, R.[11]; Herfurth, F.[18]; Hessels, E.[6]; Hogervorst, W.[42]; Holzscheiter, M.[45]; Hori, M.[11]; Horvath, D.[39]; Ichioka, T.[44]; Indelicato, P.[41]; Ishikawa, T.[11]; Jastrzebski, J.[19]; Jentschura, U.[44]; Juhász, B.[32]; Kanai, Y.[1]; Karshenboim, S. G.[2]; Kellerbauer, A.[18]; Kienle, P.[49]; Kilian, K.[17]; Kingsberry, P.[15]; Kluge, H.-J.[18]; Knudsen, H.[3]; Kobets, A.[38]; Komaki, K.-I.[33]; Korotaev, Y.[38]; Kostelecky, A.[20]; Kozhuharov, C.[18]; Kuroda, N.[1]; Källberg, A.[43]; Kühl, T.[18]; Labzowsky, L. N.[9]; Le Bigot, E.-O.[41]; Leali, M.[13]; Lemell, C.[30]; Liesen, D.[18]; Liljeby, L.[43]; Lindroth, E.[4]; Lodi Rizzini, E.[13]; Löfgren, P.[43]; Löhner, H.[40]; Madsen, N.[12]; Maggiore, C.[45]; Mann, R.[18]; Marton, J.[49]; McCullough, R.[46]; Meshkov, I.[38]; Minaev, S.[28]; Mohri, A.[1]; Mokler, P.[18]; Moshammer, R.[44]; Müller, A.[24]; Mller, S. P.[29]; Nagata, Y.[1]; Nefiodov, A. V.[48]; Nolden, F.[18]; Noordam, B.[16]; Nörtershäuser, W.[22]; Oelert, W.[17]; Orth, H.[18]; Pachucki, K.[36]; Paál, A.[43]; Pivin, P.[38]; Plunien, G.[27]; Quint, W.[18]; Ratzinger, U.[21]; Ray, A.[52]; Rensfelt, K.-G.[43]; Ritman, J.[17]; Saenz, A.[25]; Saito, H.[1]; Schempp, A.[21]; Schuch, R.[4]; Schuessler, H. A.[10]; Seleznev, I. A.[38]; Shabaev, V. M.[9]; Shibata, M.[1]; Sidorin, A.[38]; Simonsson, A.[43]; Skeppstedt, Ö.[43]; Smirnov, A. V.[38]; Stahl, S.[26]; Steck, M.[18]; Stöhlker, T.[18]; Syresin, E.[38]; Takács, E.[5]; Testera, G.[37]; Thompson, R.[8]; Tino, G. M.[14]; Tokési, K.[32]; Tomaselli, M.[18]; Torii, H. A.[33]; Trubnikov, G.[38]; Trzcinska, A.[19]; Ubachs, W.[42]; Uggerhj, U.[3]; Ullrich, J.[44]; Venturelli, L.[13]; Verdú, J.[26]; Vogel, M.[26]; Wada, M.[1]; Walz, J.[26]; Weber, C.[26]; Welsch, C.[44]; Werth, G.[26]; Widmann, E.[49]; Wolf, A.[44]; Wycech, S.[47]; Yakovenko, S.[38]; Yamazaki, Y.[34]; Yoshida, S.[30]; Zmeskal, J.[49]; Zurlo, N.[13]

1 Atomic Physics Laboratory, RIKEN (Japan)
2 D.I. Mendeleev Institute for Metrology/VNIIM (Russia)
3 Department for Physics and Astronomy, Aarhus University (Denmark)
4 Department of Atomic Physics, Stockholm University (Sweden)
5 Department of Experimental Physics, University of Debrecen (Hungary)
6 Department of Physics and Astronomy, York University (Canada)
7 Department of Physics, Harvard University, Cambridge (USA)
8 Department of Physics, Imperial College London, (U.K.)
9 Department of Physics, St. Petersburg State University (Russia)
10 Department of Physics, Texas A&M University, College Station (USA)
11 Department of Physics, University of Tokyo (Japan)
12 Department of Physics, University of Wales Swansea (United Kingdoms)
13 Dipartimento di Chimica e Fisica per l'Ingegneria e per i Materiali-Universita' di Brescia & INFN-Gruppo Collegato di Brescia (Italy)
14 Dipartimento di Fisica, Laboratorio LENS, INFN, Universita degli Studi di Firenze (Italy)
15 Duke University, North Carolina (U.S.A.)
16 FOM Institute for Atomic and Molecular Physics (Netherlands)
17 Forschungszentrum Jülich (Germany)
18 GSI Darmstadt (Germany)
19 Heavy Ion Laboratory, Warsaw University (Poland)
20 Indiana University, Bloomington, (USA)
21 Institut für Angewandte Physik, Universität Frankfurt (Germany)
22 Institut für Kernchemie, Universität Mainz (Germany)
23 Institut für Kernphysik, Universität Frankfurt (Germany)
24 Institut für Kernphysik, Universität Giessen (Germany)
25 Institut für Physik, Humboldt-Universität zu Berlin (Germany)
26 Institut für Physik, Universität Mainz (Germany)
27 Institut für Theoretische Physik, Technische Universität Dresden (Germany)
28 Institute for Experimental and Theoretical Physics (Russia)
29 Institute for Storage Ring Facilities, Aarhus University (Denmark)
30 Institute for Theoretical Physics, Vienna University of Technology (Austria)
31 Institute of Nuclear Physics, Moscow State University (Russia)
32 Institute of Nuclear Research of the Hungarian Academy of Sciences/ATOMKI (Hungary)
33 Institute of Physics, University of Tokyo (Japan)
34 Institute of Physics, University of Tokyo, and Atomic Physics Laboratory, RIKEN (Japan)
35 Institute of Spectroscopy of the RAS (Russia)
36 Institute of Theoretical Physics, Warsaw University (Poland)
37 Istituto Nazionale di Fisica Nucleare (Italy)
38 JINR Dubna (Russia)
39 KFKI Research Institute for Particle and Nuclear Physics, Budapest (Hungary)
40 KVI Groningen (Netherlands)
41 Laboratoire Kastler-Brossel, École Normale Supérieure et Université P. et M. Curie, Paris (France)
42 Laser Centre Vrije Universiteit, Faculty of Science (Netherlands)
43 Manne Siegbahn Laboratory/MSL (Sweden)
44 MPI für Kernphysik/MPI-K (Germany)
45 Pbar Labs, LLC Santa Fe (U.S.A.)
46 Queens University, Belfast (U.K.)
47 Soltan Institute for Nuclear Studies (Poland)
48 St. Petersburg Nuclear Physics Institute (Russia)
49 Stefan Meyer Institut für subatomare Physki/SMI, Österreichische Akademie der Wissenschaften, Wien (Austria)
50 TRIUMF (Canada)
51 University of New Mexico, Albuquerque (U.S.A.)
52 Variable Energy Cyclotron Center (India)

Contributions in this report:
AP-EXP-COLLISIONS-01
FAIR-APPA-FLAIR-01
FAIR-APPA-FLAIR-02
FAIR-APPA-FLAIR-03
FAIR-APPA-FLAIR-04

FAIR: The HEDgeHOB Collaboration

High Energy Density Matter generated by Heavy-iOn Beams
Spokesperson: D. H. H. Hoffmann, Darmstadt (Germany)

Adamyan, V.[29]; Adonin, A.[14]; Alcober Auban, J.[39]; Aleksandrova, I.[21]; Apfelbaum, E.[9]; Arkhipov, Yu.V.[2]; Audebert, P.[18]; Baimbetov, F.B.[2]; Ballester, D.[39]; Barigga, M.[38]; Basko, M.[11]; Batani, D.[44]; Benage, J. F.[22]; Blazevic, A.[8]; Bock, R.[8]; Borneis, S.[8]; Brambrink, E.[18]; Bret, A.[38]; Callahan, D.[20]; Caruso, A.[6]; Chtcherbakov, V.[21]; Constantin, C. G.[20]; Cortazar, O.[38]; Cowan, T.[45]; Davidson, R. C.[31]; Deutsch, C.[23]; Dewald, E. L.[20]; Dudin, S.[13]; Efremov, V.[9]; Faenov, A.[27]; Fernandez, J.[22]; Fertman, A.[11]; Fisher, V.[46]; Fortmann, C.[41]; Fortov, V.[13]; Friedman, A.[20]; Gauthier, J.-C.[42]; Geissel, M.[34]; Gericke, D.[4]; Glenzer, S.[20]; Golubev, A.[11]; Grandjouan, N.[18]; Gromov, A.[21]; Grubert, G.[4]; Gryaznov, V.[13]; Habs, D.[24]; Hegelich, M.[22]; Hoffmann, D. H.[35]; Iosilevski, I.[26]; Jacoby, J.[14]; Jungwirth,

K.[30]; Juranek, H.[41]; Kaganovich, I.[31]; Kain, V.[5]; Kalal, M.[3]; Kalinin, Y.[28]; Kanel, G.[13]; Khishchenko, K.[9]; Kietzmann, A.[41]; Kim, C. J.[16]; Kim, V.[13]; Kingsep, A. S.[28]; Knobloch, R.[35]; Kong, H.[15]; Konovalov, V.[26]; Koresheva, E.[21]; Koshelev, E.[21]; Krainov, V.[26]; Kuba, J.[3]; Kühl, T.[8]; Kuhlbrodt, S.[41]; Kulish, M.[13]; Kupriashin, A.[21]; Levashov, P.[9]; Li, R.[10]; Lim, C.[16]; Limpouch, J.[3]; Lisitsa, L.[28]; Logan, G.[19]; Lomonosov, I.[13]; Lopez-Cela, J.[38]; Lou, Q.[10]; Magunov, A.[27]; Maron, Y.[46]; Matveichev, A.[13]; Maynard, G.[23]; Mehlhorn, T. A.[34]; Merkuliev, Y.[21]; Meyer-ter-Vehn, J.[25]; Milyavskii, V.[9]; Minaev, S.[11]; Mintsev, V.[13]; Morozov, I.[9]; Murillo, M. S.[22]; Nardi, E.[46]; Nettelmann, N.[41]; Neumann, R.[8]; Ni, P.[35]; Niemann, C.[20]; Nikitenko, A.[21]; Nikolaev, D.[13]; Norman, G.[9]; Ogawa, M.[37]; Omar, B.[41]; Osipov, I.[21]; Pikuz, T.[27]; Piriz, A. R.[38]; Porter, J.[34]; Postnov, V.[13]; Povarnitsyn, M.[9]; Razorenov, S.[13]; Redmer, R.[41]; Reinholz, H.[41]; Riley, D.[32]; Romadinova, E.[26]; Röpke, G.[41]; Rosmej, F. B.[43]; Rosmej, O.[8]; Roth, M.[35]; Roudskoy, I.[11]; Ruhl, H.[33]; Sanchez-Duque, J.[38]; Sauerbrey, R.[7]; Schaumann, G.[35]; Schlanges, M.[4]; Schmidt, R.[5]; Schollmeier, M.[35]; Schurtz, G.[42]; Schwarz, V.[41]; Sharkov, B.[11]; Shen, B.[10]; Sheyko, A.[13]; Shilkin, N.[13]; Shutov, A.[13]; Skobelev, I.[27]; Smirnov, V.[28]; Son, E.[26]; Sosikov, V.[13]; Stamm, R.[43]; Starobinets, A.[46]; Suk, H.[17]; Sultanov, V.[13]; Tabak, M.[20]; Tahir, N. A.[8]; Tauschwitz, A.[8]; Tauschwitz, An.[14]; Temporal, M.[38]; Ternovoi, V.[13]; Thiele, R.[41]; Tikhonchuk, V.[42]; Timasheva, T.[21]; Tkachenko, I. M.[39]; Toepffer, C.[40]; Tolokonnikov, S.[21]; Trautmann, C.[8]; Tsigutkin, K.[46]; Turtikov, V.[11]; Udrea, S.[35]; Ullschmied, J.[30]; Ulrich, A.[36]; Utkin, A.[13]; Varentsov, D.[8]; Vorberger, J.[4]; Wahl, H.[8]; Weyrich, K.[8]; Wiewior, P.[45]; Wouchuk , J.[38]; Yu, W.[10]; Yuryev, D.[13]; Zaporoghets, Y.[13]; Zepf, M.[32]; Zhernokletov, M.[1]; Zhu, J.[10]; Zwicknagel, G.[40]

1 All-Russian Institute of Experimental Physics/VNIIEF (Russia)
2 Al-Farabi Kazakh National University/KNU (Kazakhstan)
3 Czech Technical University/CTU (Czech Republic)
4 Ernst-Moritz-Arndt-Universität Greifswald/UG (Germany)
5 European Organization for Nuclear Research/CERN (Switzerland)
6 Frascati Research Center/ENEA (Italy)
7 Friedrich-Schiller-Universität Jena/UJ (Germany)
8 Gesellschaft für Schwerionenforschung/GSI (Germany)
9 Institute for High Energy Densities RAS/IHED (Russia)
10 Institute for Optics and Fine Mechanics CAS/IOFM (China)
11 Institute for Theoretical and Experimental Physics/ITEP (Russia)
12 Institute for Theoretical and Mathematical Physics/ITMP (Russia)
13 Institute of Problems of Chemical Physics RAS/IPCP (Russia)
14 Johann Wolfgang Goethe-Universität Frankfurt/UF (Germany)
15 Korea Advanced Institute of Science and Technology/KAIST (Korea)
16 Korea Atomic Energy Research Institute/KAERI (Korea)
17 Korea Electrotechnology Research Institute/KERI (Korea)
18 Laboratorie pour lilisation des Lasers Intenses/LULI (France)
19 Lawrence Berkeley National Laboratory/LBNL (USA)
20 Lawrence Livermore National Laboratory/LLNL (USA)
21 Lebedev Physical Institute RAS/LPI (Russia)
22 Los Alamos National Laboratory/LANL (USA)
23 LPGP, CNRS-UMR8578, Université Paris XI/LPGP (France)
24 Ludwig-Maximilians-Universität München/LMU (Germany)
25 Max-Planck-Institut für Quantenoptik/MPQ (Germany)
26 Moscow Institute of Physics and Technology/MIPT (Russia)
27 Multi-charged Ion Spectra Data Center/MISDC of VNIIFTRI (Russia)
28 Nuclear Fusion Institute, Russian Research Center ”Kurchatov Institute”/NFI (Russia)
29 Odessa National University/ONU (Ukraine)
30 PALS Research Center, IPP/PALS (Czech Republic)
31 Princeton University/PU (USA)
32 Queens University of Belfast/QUB (UK)
33 Ruhr Universität Bochum/RUB (Germany)
34 Sandia National Laboratories/SNL (USA)
35 Technische Universität Darmstadt/TUD (Germany)
36 Technische Universität Munchen/TUM (Germany)
37 Tokyo Institute of Technology/TIT (Japan)
38 Universidad de Castilla La Mancha/UCLM (Spain)
39 Universidad Politecnica de Valencia/UPV (Spain)
40 Universität Erlangen/UE (Germany)
41 Universität Rostock/UR (Germany)
42 Université de Bordeaux/UB (France)
43 Université de Provence/UP (France)
44 University of Milano/UM (Italy)
45 University of Nevada/UNR (USA)
46 Weizmann Institute of Sciences/WIS (Israel)

Contributions in this report:
FAIR-APPA-HEDGEHOB-01
FAIR-APPA-HEDGEHOB-02

The PANDA Collaboration

<http://www.ep1.rub.de/∼panda/auto/_home.htm>
Spokesperson: U. Wiedner, Uppsala (Sweden)

Achenbach, P.[23]; Agnello, M.[37]; Alberto, P.[24]; Alexeev, G.[10]; Alexeev, M.[36]; Aliotta, M.[11]; Amoroso, A.[36]; Annand, J.[19]; Ardashev, E.[31]; Arefiev, A.[10]; Arestov, Y.[31]; Ayzenshtat, G.[31]; Baldin, E.[28]; Balestra, F.[36]; Ballantini, R.[17]; Barabanov, M. Y.[10]; Bargholtz, C.[34]; Bassini, R.[24]; Batyunya, B. V.[10]; Belostotski, S.[32]; Bendiscioli, G.[30]; Bertini, R.[36]; Bettoni, D.[14]; Birsa, R.[38]; Boca, G.[30]; Bogoslovski, D.[10]; Boiano, C.[24]; Bokova, T. Y.[10]; Borisov, V. V.[10]; Borissov, A.[19]; Botta, E.[37]; Bradamante, F.[38]; Branford, D.[11];

Bressani, T.[37]; Brinkmann, K.-T.[9]; Britvich, G.[31]; Budilov, V. A.[10]; Bugaenko, V.[10]; Bussa, M. P.[36]; Busso, L.[37]; Calén, H.[40]; Calabrese, R.[14]; Calvo, D.[37]; Cappellaro, F.[41]; Cargnelli, M.[43]; Cederwall, B.[33]; Chen, R.[22]; Chuiko, B.[31]; Clement, H.[39]; Colantoni, M. L.[35]; Döring, W.[18]; Dörner, R.[15]; Düren, M.[18]; Dalla Torre, S.[38]; Dalpiaz, P.[14]; Denisov, O.[36]; Destefanis, M.G.[18]; Diaz, J.[42]; Dodokhov, V. K.[10]; Dormenev, V. I.[25]; Doroshkevitch, E.[39]; Drexler, P.[18]; Drobychev, G. Y.[25]; Drochner, M.[20]; Duan, L.[22]; Efremov, A. A.[10]; Ehrhardt, K.[39]; Ekström, C.[40]; Eyrich, W.[12]; Föhl, K.[11]; Fava, L.[35]; Fedorov, A. A.[25]; Fedorov, O. I.[10]; Feliciello, A.[37]; Ferrero, A.[36]; Ferrero, L.[36]; Ferro, F.[37]; Feshchenko, A. A.[10]; Filippi, A.[37]; Fontana, A.[30]; Fröhlich, I.[18]; Fransson, K.[40]; Freiesleben, H.[9]; Frekers, D.[27]; Frolov, V.[36]; Fuhrmann, H.[43]; Götzen, K.[8]; Galoyan, A. S.[10]; Garfagnini, R.[36]; Gast, W.[20]; Gavrilov, G.[32]; Genova, P.[30]; Gianotti, P.[16]; Gillitzer, A.[20]; Giorgi, M.[38]; Golischewski, A.[3]; Golovnya, S.[31]; Gonser, P.[39]; Gorokhov, S.[31]; Grasso, A.[36]; Grisenti, R.[15]; Grzonka, D.[20]; Guaraldo, C.[16]; Guidal, M.[29]; Guzik, Z.[44]; Höistad, B.[41]; Hartmann, O. N.[16]; Hawranek, P.[7]; Hejny, V.[20]; Held, T.[3]; Hennino, T.[29]; Hinterberger, F.[4]; Holeczek, J.[21]; Hu, Z.[22]; Iazzi, F.[37]; Iliescu, M.[16]; Iori, I.[24]; Ireland, D.[19]; Ivanov, G.[10]; Jäkel, R.[9]; Jafarov, E.[10]; Johansson, T.[41]; Johnson, A.[33]; Kühn, W.[18]; Kłos, B.[21]; Kaesz, M.[15]; Kaiser, R.[19]; Kamys, B.[7]; Kaplin, V. I.[10]; Karmokov, A.[10]; Kellie, J.[19]; Kemmerling, G.[20]; Ketzer, B.[26]; Kholodenko, A.[31]; Khoukaz, A.[27]; Kienle, P.[43]; Kirschner, D.G.[18]; Kisiel, J.[21]; Kisielinski, M.[44]; Kistryn, S.[7]; Kleines, H.[20]; Koch, H.[3]; Konorov, I.[26]; Kopf, B.[3]; Korneev, A. E.[25]; Korzhik, M. V.[25]; Koshurnikov, E. K.[10]; Kotulla, M.[1]; Kozlowski, T.[44]; Krusche, B.[1]; Kudaev, V. C.[10]; Kupsc, A.[40]; Lavezzi, L.[30]; Lehmann, A.[12]; Lehmann, I.[41]; Lewandowski, B.[8]; Li, W.[22]; Lindberg, K.[34]; Lishin, V.[31]; Livingston, K.[19]; Lobanov, V. I.[10]; Lopatik, A. R.[25]; Lucherini, V.[16]; Lundborg, A.[41]; Luppi, E.[14]; Lynen, U.[8]; Mac Cormick, M.[29]; Macri, M.[17]; Maggiora, A.[36]; Maggiora, M.[36]; Magiera, A.[7]; Makarov, A. F.[10]; Malinina, L. V.[10]; Malyshev, V.[28]; Manara, A.[36]; Mann, A.[26]; Marcello, S.[37]; Marciniewski, P.[40]; Martin, A.[38]; Marton, J.[43]; Maslennikov, A.[28]; Mazza, G.[37]; McGeorge, C.[19]; Melnychuk, D.[44]; Metag, V.[18]; Mikhailov, K. V.[10]; Miklukho, O.[32]; Missevitch, O. V.[25]; Montagna, P.[30]; Morosov, B.[10]; Morra, O.[37]; Moskal, P.[7]; Mustafaev, G. A.[10]; Nakhushev, A. M.[10]; Nanova, M.[18]; Napoli, M. De[6]; Naryshkin, Y.[32]; Neubert, S.[26]; Nomokonov, P. V.[10]; Nordhage, O.[41]; Novotny, R.[18]; Nowak, H.[8]; Nyberg, J.[41]; Oelert, W.[20]; Oleks, I. A.[10]; Ong, S.[29]; Orth, H.[8]; Ottone, F.[18]; Pace, E.[16]; Panzarasa, A.[30]; Panzieri, D.[35]; Panzieri, D.[36]; Parakhin, V.[31]; Parodi, R.[17]; Paul, S.[26]; Peleganchyk, S.[28]; Peters, K.[8]; Petrascu, C.[16]; Pettersson, H.[41]; Pikalov, V.[31]; Piragino, G.[36]; Piskor-Ignatowicz, B.[7]; Piskor-Ignatowicz, C.[7]; Pismennaya, V.[10]; Pocheptsov, T. A.[10]; Pochodzalla, J.[23]; Polanski, A.[10]; Pontecorvo, G.[36]; Pospelov, G.[28]; Pouthas, J.[29]; Povtoreyko, A.[10]; Pozzo, A.[17]; Prasuhn, D.[20]; Protopopescu, D.[19]; Raciti, G.[6]; Ramstein, B.[29]; Rao, Y.-N.[41]; Rapisarda, E.[6]; Remigis, P. De[37]; Riboldi, S.[24]; Ritman, J.[20]; Rivetti, A.[37]; Rogov, N.[10]; Rosier, P.[29]; Rosner, G.[19]; Rotondi, A.[30]; Rudy, Z.[7]; Rufanov, I. A.[10]; Ryabtsun, S.[10]; Sadygov, Z. Y.[10]; Saitoh, T. R.[8]; Salabura, P.[7]; Salmin, R. A.[10]; Salvini, P.[30]; Salz, C.[18]; Sanchez-Lorente, A.[23]; Sapozhnikov, M. G.[10]; Sarantsev, A.[32]; Savriè, M.[14]; Schönning, K.[41]; Schadmand, S.[20]; Schiavon, P.[38]; Schmücker, H.[3]; Schmitt, L.[8]; Schneider, J.[18]; Schwarz, C.[8]; Seitz, B.[18]; Serbanut, G.-C.[18]; Sereda, T.[10]; Seth, K.[13]; Sfienti, C.[8]; Shabratova, G. S.[10]; Shelikhov, V.[31]; Shumeiko, N.[31]; Sibirtsev, A.[20]; Sirghi, D.[16]; Sirghi, F.[16]; Skachkov, N.[10]; Skachkova, A.[10]; Slowinski, B.[45]; Smyrski, J.[7]; Sokolov, A.[20]; Solin, A.[31]; Steinke, M.[3]; Stenzel, H.[18]; Stockmanns, T.[20]; Ströher, H.[20]; Strokovsky, E. A.[10]; Sukharev, A.[28]; Sun, Z.[22]; Täschner, A.[27]; Tegnér, P. E.[34]; Teshev, R. S.[10]; Tessarotto, F.[38]; Thöring, U.[18]; Thörngren Engblom, P.[41]; Tikhomirov, V.[10]; Tikhonov, Y.[28]; Tolbanov, O.[31]; Tosello, F.[36]; Tyazhev, A.[31]; Ucar, A.[20]; Ustenko, E. P.[10]; Uzhinsky, V. V.[10]; Van de Wiele, J.[29]; Vikhrov, V.[32]; Vlasov, N. V.[10]; Vlasov, P.[20]; Vodopianov, A. S.[10]; Vorobiev, A.[31]; Wüstner, P.[20]; Watts, D.[11]; Weitzel, Q.[26]; Wessels, J.[27]; Wheadon, R.[37]; Widmann, E.[43]; Wieczorek, P.[8]; Wiedner, U.[41]; Wilms, A.[8]; Wintz, P.[20]; Wojciechowski, M.[7]; Wojtkowska, J.[44]; Woods, P.[11]; Xiao, G.[22]; Xiao, Z.[22]; Xie, J. J.[2]; Xu, H.[22]; Zaporozhets, S. A.[10]; Zartova, I.[34]; Zehr, F.[1]; Zenoni, A.[5]; Zerguerras, T.[29]; Zhong, J.[3]; Zinchenko, A. I.[10]; Zlomanczuk, J.[41]; Zmeskal, J.[43]; Zosi, G.[36]; Zou, B. S.[2]; Zwieglinski, B.[44]

1 Universität Basel (Switzerland)
2 Institute of High Energy Physics, Chinese Academy of Sciences, Beijing (China)
3 Universität Bochum, I. Institut für Experimentalphysik (Germany)
4 Helmholtz-Institut für Strahlen- und Kernphysik, Bonn (Germany)
5 Università di Brescia (Italy)
6 Dipartimento di Fisica e Astronomia dell'Università di Catania and INFN, Sezione di Catania (Italy)
7 Instytut Fizyki, Uniwersytet Jagiellonski, Cracow (Poland)
8 Gesellschaft für Schwerionenforschung mbH, Darmstadt (Germany)
9 Technische Universität Dresden (Germany)
10 Veksler-Baldin Laboratory of High Energies (VBLHE), Joint Institute for Nuclear Research ([a]),Laboratory of Particle Physics (LPP) ([b]), Laboratory of Information Technologies (LIT) ([c]), Laboratory of Nuclear Problems (LNP) ([d]), Dubna, Kabardian-Balkarian State University ([e]) and Institute of Applied Mathematics and Automation ([f]), Nal'chik (Russia)
11 University of Edinburgh (United Kingdom)
12 Friedrich Alexander Universität Erlangen-Nürnberg (Germany)
13 Northwestern University, Evanston (USA)
14 Università di Ferrara and INFN, Sezione di Ferrara (Italy)
15 Johann Wolfgang Goethe-Universität Frankfurt (Germany)
16 INFN-Laboratori Nazionali di Frascati (Italy)
17 INFN, Sezione di Genova (Italy)
18 Justus Liebig-Universität Gießen, II. Physikalisches Institut (Germany)
19 University of Glasgow (United Kingdom)
20 Institut für Kernphysik ([a]), Zentralinstitut für Elektronik ([b]), Forschungszentrum Jülich (Germany)
21 Uniwersytet Slaski, Katowice (Poland)
22 Institute of Modern Physics, the Chinese Academy of Science, Lanzhou, P.R. (China)
23 Institut für Kernphysik, Johannes Gutenberg-Universität Mainz (Germany)
24 Politecnico di Milano ([a]), Physics Department, Università di Milano ([b]) and INFN, Sezione di Milano ([c]) (Italy)
25 Research Institute for Nuclear Problems, Belarus State University, Minsk (Belarus)
26 Technische Universität München (Germany)
27 Westfälische Wilhelms-Universität Münster (Germany)
28 Budker Institute of Nuclear Physics BINP, Novosibirsk (Russia)
29 Institut de Physique Nucléaire, Orsay (France)

30 Dipartimento di Fisica Nucleare e Teorica, Università di Pavia ([a]), INFN, Sezione di Pavia ([b]) (Italy)
31 Institute for High Energy Physics (IHEP)([a]), Protvino Tomsk State University (TSU)([b]), Tomsk (Russia) and National Center of Particle and High Energy Physics (NCPHEP)([c]), Minsk (Belorussia)
32 Petersburg Nuclear Physics Institute of Academy of Science PNPI, Gatchina, St. Petersburg (Russia)
33 Kungliga Tekniska Högskolan KTH, Stockholm (Sweden)
34 Stockholms Universitet (Sweden)
35 Università del Piemonte Orientale Alessandria, Torino and INFN, Sezione di Torino (Italy)
36 Dipartimento di Fisica Generale 'A. Avogadro', Università di Torino and INFN, Sezione di Torino (Italy)
37 Dipartimento di Fisica Generale Università di Torino ([a]), Dipartimento di Fisica Sperimentale, Università di Torino ([b]), INFN, Sezione di Torino ([c]), IFSI, Sezione di Torino ([d]) and Politecnico di Torino ([e]) (Italy)
38 INFN, Sezione di Trieste and Università di Trieste (Italy)
39 Physikalisches Institut, Universität Tübingen (Germany)
40 The Svedberg Laboratory, Uppsala (Sweden)
41 Institutionen för Strålningsvetenskap, Uppsala Universitet (Sweden)
42 Universitat de Valencia, Dpto. de Física Atómica, Molecular y Nuclear (Spain)
43 Stefan Meyer Institut für Subatomare Physik, Österreichische Akademie der Wissenschaften, Vienna (Austria)
44 Soltan Institute for Nuclear Studies, Warsaw (Poland)

Contributions in this report:
FAIR-QCD-PANDA-01
FAIR-QCD-PANDA-02
FAIR-QCD-PANDA-03
FAIR-QCD-PANDA-04
FAIR-QCD-PANDA-05
FAIR-QCD-PANDA-06
FAIR-QCD-PANDA-07
FAIR-QCD-PANDA-08

+ membership to be confirmed by the collaboration board

FAIR: The NUSTAR Collaboration

International Nuclear Structure and Astrophysics Community GSI
<http://www.gsi.de/forschung/kp/kp2/nustar.html>

The NUSTAR Board:
Spokesperson: W. Gelletly, University of Surrey (United Kingdom)
T. Aumann, GSI Darmstadt (Germany)
J. Benlliure, Santiago de Compostela (Spain)
R. Kücken, Munich (Germany)
B. Jonson, Chalmers University of Technology (Sweden)

Ackermann, D.[13]; Al-Khalili, J.[62]; Alamanos, N.[5]; Angulo, C.[28]; Aumann, T.[13]; Azaiez, F.[20]; Balabanski, D.[49]; Baur, G.[10]; Bazzacco, D.[19]; Benlliure, J.[60]; Blank, B.[6]; Bracco, A.[57]; Chulkov, L.[39]; Corradi, L.[27]; Cortina, D.[60]; Davids, B.[41]; De Angelis, G.[16]; Egelhof, P.[13]; Emling, H.[13]; Enders, J.[42]; Ershov, S. N.[21]; Faestermann, T.[43]; Feldmeier, H.[13]; Gadea, A.[16]; Geissel, H.[13]; Gelletly, W.[62]; Gerl, J.[13]; Gomez, J.[61]; Guttormsen, M.[58]; Górska, M.[13]; Habs, D.[29]; Hass, M.[44]; Heenen, P. H.[45]; Hencken, K.[47]; Hofmann, S.[13]; Huyse, M.[25]; Johansson, H.[13]; Jolie, J.[50]; Jonson, B.[8]; Jourdan, J.[47]; Kaeppeler, F.[11]; Kalantar, N.[26]; Kelic, A.[13]; Korten, W.[5]; Krasznahorkay, A.[2]; Kratz, J. V.[23]; Kratz, K.-L.[23]; Kulessa, R.[22]; Leino, M.[55]; Lenske, H.[24]; Lunardi, S.[59]; Maj, A.[15]; Martel, I.[54]; Maruhn, J.[53]; Meister, M.[8]; Motagnoli, G.[59]; Münzenberg, G.[13]; Nolan, P.[56]; Novikov, Y.[38]; Nyberg, J.[63]; Petrovici, A.[35]; Pfützner, M.[64]; Pierroutsakou, D.[18]; Pignanelli, M.[17]; Pla, W.[24]; Podolyak, Z.[62]; Regan, P.[62]; Reinhard, P.-G.[52]; Reiter, P.[50]; Riisager, K.[3]; Ring, P.[43]; Rolfs, C. E.[40]; Roy, A.[33]; Rubio, B.[14]; Rudolph, D.[30]; Rykaczewski, K.[37]; Savard, G.[1]; Scheidenberger, C.[13]; Scheit, H.[31]; Sherrill, B.[34]; Signorini, C.[46]; Simon, H.[13]; Simpson, J.[4]; Sitar, B.[9]; Sletten, G.[36]; Sorlin, O.[20]; Stefanini, A.[27]; Stevenson, P.[62]; Stoecker, H.[53]; Stoehlker, T.[13]; Sümmerer, K.[13]; Tengblad, O.[7]; Thielemann, F.[47]; Vaagen, J.[48]; Van Duppen, P.[25]; Wagner, A.[12]; Wolter, H.[29]; Woods, P.[51]; Zamfir, V.[32]; Zilges, A.[42]

1 ANL Argonne (USA)
2 ATOMKI Debrecen (Hungary)
3 Aarhus University (Denmark)
4 CCLRC Daresbury (United Kingdom)
5 CEA Saclay (France)
6 CEN Bordeaux-Gradignan (France)
7 CSIC Madrid (Spain)
8 Chalmers University of Technology (Sweden)
9 Comenius University Bratislava (Slovakia)
10 FZ Jülich (Germany)
11 FZ Karlsruhe (Germany)
12 FZ Rossendorf (Germany)
13 GSI Darmstadt (Germany)
14 IFIC Valencia (Spain)
15 IFJ PAN Krakow (Poland)
16 INFN Legnaro (Italy)
17 INFN Milan (Italy)
18 INFN Napoli (Italy)
19 INFN Padova (Italy)
20 IPN Orsay (France)
21 JINR Dubna (Russia)
22 Jagellonian University Krakow (Poland)
23 Johannes Gutenberg University of Mainz (Germany)
24 Justus-Liebig University Giessen (Germany)
25 KU Leuven (Belgium)
26 KVI Groningen (The Netherlands)
27 LNL / INFN (Italy)
28 Louvain-la-Neuve (Belgium)
29 Ludwig-Maximilians University of Munich (Germany)
30 Lund University (Sweden)
31 MPI für Kernphysik (Germany)
32 NIPNE Bucharest (Romania)
33 NSC New Delhi (India)
34 NSCL/MSU (USA)
35 National Institute for Physics and Nuclear Engineering (Romania)
36 Niels Bohr Institute (Denmark)
37 ORNL Oak Ridge (USA)
38 PNPI Gatchina (Russia)
39 RRC Kurchatov Institute Moscow (Russia)
40 Ruhr-University of Bochum (Germany)
41 TRIUMF (Canada)
42 TU Darmstadt (Germany)
43 TU Munich (Germany)
44 The Weizmann Institute of Science Rehovot (Israel)
45 Universite Libre de Bruxelles (Belgium)
46 University Padova and INFN Padova (Italy)
47 University of Basel (Switzerland)
48 University of Bergen (Norway)
49 University of Camerino (Italy)
50 University of Cologne (Germany)
51 University of Edinburgh (United Kingdom)
52 University of Erlangen (Germany)
53 University of Frankfurt (Germany)
54 University of Huelva (Spain)
55 University of Jyväskylä (Finland)
56 University of Liverpool (United Kingdom)
57 University of Milan (Italy)
58 University of Oslo (Norway)
59 University of Padova (Italy)
60 University of Santiago de Compostela (Spain)
61 University of Sevilla (Spain)
62 University of Surrey (United Kingdom)
63 Uppsala University (Sweden)
64 Warsaw University (Poland)

As part of FAIR-NUSTAR: The DESPEC Collaboration

Decay Spectroscopy
Spokesperson: B. Rubio, Valencia (Spain)
37 members form Belgium, Finland, France, Germany, Greece, Hungary, Poland, Romania, Spain, Sweden, Turkey, United Kingdom.

Contributions in this report:
FAIR-NUSTAR-DESPEC-01
FAIR-NUSTAR-DESPEC-02

As part of FAIR-NUSTAR: The HISPEC Collaboration

High resolution Spectroscopy
Spokesperson: Z. Podolyak, Surrey (United Kingdom)
95 members from Argentina, Australia, Belgium, Denmark, Finland, France, Germany, Hungary, India, Israel, Italy, Japan, Norway, Poland, Portugal, Romania, Russia, Spain, Sweden, Switzerland, The Netherlands, Turkey, United Kingdom.

Contributions in this report:
FAIR-NUSTAR-HISPEC-01
FAIR-NUSTAR-HISPEC-02
FAIR-NUSTAR-HISPEC-03

As part of FAIR-NUSTAR: The R^3B Collaboration

Reactions with Relativistic Radioactive Beams
<http://www-land.gsi.de/r3b/>
Spokesperson: T. Aumann Darmstadt (Germany)
181 members from Brasilia, Canada, China, Denmark, Finland, France, Germany, Hungary, India, Japan, Norway, Poland, Romania, Russia, Spain, Sweden, Switzerland, USA, United Kingdom.

Contributions in this report:
FAIR-NUSTAR-R3B-01
FAIR-NUSTAR-R3B-02
NUSTAR-THEORY-12

As part of FAIR-NUSTAR: The THEORY NETWORK Collaboration

Spokesperson: H. Lenske, Gießen (Germany)
12 members from Germany, Hungary, India, Norway, Romania, Russia, United Kingdom.

As part of FAIR-NUSTAR: The ELISe Collaboration

ELectron-Ion Scattering in a Storage Ring (eA collider)
<http://www.gsi.de/zukunftsprojekt/experimente/elise/>
Spokesperson: H. Simon, Darmstadt (Germany)
100 members form Germany, Japan, Russia, Spain, Sweden, Switzerland, The Netherlands, USA, United Kingdom.

Contribution in this report:
FAIR-NUSTAR-ELISE-01

As part of FAIR-NUSTAR: The EXL Collaboration

Exotic nuclei studied in light-ion induced reactions at the NESR storage ring
<http://ns.ph.liv.ac.uk/~mc/EXL/collaboration/EXL-collaboration.html>
Spokesperson: M. Chartier, Liverpool (United Kingdom)
134 members from Brasilia, Canada, France, Germany, Hungary, India, Italy, Japan, Russia, Spain, Sweden, Switzerland, The Netherlands, United Kingdom.

Contributions in this report:
FAIR-APPA-SPARC-03
FAIR-NUSTAR-EXL-01
FAIR-NUSTAR-EXL-02
FAIR-NUSTAR-EXL-03

As part of FAIR-NUSTAR: The EXO-pbar Collaboration

Exotic antiprotonic atoms
<http://www.gsi.de/NUSTAR/>
Spokesperson: M. Wada (Japan)
15 members from Finland, Germany, Japan, Poland.

As part of FAIR-NUSTAR: The ILIMA Collaboration

Isomeric Beams, Lifetimes and Masses
Spokesperson: Y. Novikov, Gatchina (Russia)
74 members from Belgium, China, France, Germany, Greece, Japan, Poland, Russia, USA, United Kingdom.

Contributions in this report:
FAIR-NUSTAR-ILIMA-01
FAIR-NUSTAR-ILIMA-02

As part of FAIR-NUSTAR: The LASPEC Collaboration

Laser Spectroscopy of short-lived isotopes at the FAIR Low Energy Beamline
Spokesperson: P. Campbell (United Kingdom)
33 memebers from Belgium, Finland, France, Germany, Switzerland, USA, United Kingdom.

Contributions in this report:
FAIR-NUSTAR-LASPEC-01
FAIR-NUSTAR-LASPEC-03

As part of FAIR-NUSTAR: The MATS Collaboration

Precision Measurement of vry short-lived nuclei using an Advanced Trapping System for highly-charged ions
Spokesperson: K. Blaum, Mainz (Germany)
60 members from Belgium, Canada, Finland, France, Germany, India, Russia, Sweden, Switzerland, USA.

Contributions in this report:
FAIR-NUSTAR-MATS-01
FAIR-NUSTAR-MATS-02
FAIR-NUSTAR-MATS-03

As part of FAIR-NUSTAR: The NCap Collaboration

Neutron Capture Measurements
<http://www.gsi.de >
Spokesperson: M. Heil, Karlsruhe (Germany)
13 members from France, Germany, Greece, Italy, Japan, Spain, Switzerland, USA.

The FAIR-NUSTAR Members

Ackermann, D.[34]; Adrich, P.[34]; Aksouh, F.[34]; Al-Khalili, J.[178]; Alamanos, N.[12]; Algora, A.[2]; Alvarez Rodriguez, R.[19]; Alvarez, H.[173]; Alvarez, R.[19]; Amaro Soriano, J.[36]; Ameil, F.[34]; Amzal, N.[172]; Andreev, A.[72]; Angulo, C.[83]; Antonenko, N.[67]; Appelbe, D.[10]; Arai, K.[178]; Armbruster, P.[34]; Arnould, M.[182]; Artukh, A.[67]; Asahi, K.[130]; Assmann, W.[84]; Äystö, J.[160]; Atac, A.[4]; Audi, G.[20]; Audouin, L.[29]; Auger, F.[12]; Aumann, T.[34]; Austin, S.[93]; Avdeichikov, V.[85]; Azaiez, F.[51]; Babilon, M.[123]; Bacelar, J.[74]; Bachelet, C.[20]; Backe, H.[72]; Bacri, C.[51]; Badura, E.[34]; Balabanski, D.[147]; Banu, L.[34]; Barton, C.[181]; Bauge, E.[11]; Baumann, T.[88]; Baur, G.[28]; Bazzacco, D.[47]; Beaumel, D.[51]; Beck, D.[34]; Becker, F.[34]; Beckert, K.[34]; Bednarczyk, P.[34]; Beller, P.[34]; Bender, M.[93]; Benlliure, J.[173]; Bentley, M.[75]; Berdermann, E.[34]; Bernas, M.[51]; Bertulani, C.[139]; Bhattacharya, S.[113]; Bhowmik, R.[92]; Billowes, J.[164]; Blank, B.[14]; Blazhev, A.[34]; Block, M.[34]; Blumenfeld, Y.[51]; Bochkarev, O.[56]; Bock, R.[34]; Bohlen, H.[37]; Boilley, D.[32]; Bollen, G.[93]; Bonaccorso, A.[48]; Borcea, C.[40]; Boretzky, K.[34]; Borge, M.[19]; Bortignon, P.[45]; Borzov, I.[52]; Bosch, F.[34]; Boston, A.[162]; Botvina, A.[49]; Boudard, A.[12]; Boutin, D.[34]; Bracco, A.[166]; Brancus, I.[29]; Braun-Münzinger, P.[34]; Bruchle, W.[34]; Bucurescu, D.[39]; Bushaw, B.[103]; Butler, P.[162]; Böhmer, M.[125]; Bürvenich, T.[87]; Caballero, J.[117]; Calen, H.[183]; Calvino, F.[133]; Camera, F.[45]; Campbell, P.[164]; Cano-Ott, D.[18]; Cappuzzello, F.[80]; Cargnelli, M.[119]; Carlen, L.[85]; Casarejos, E.[173]; Cata-Danil, G.[106]; Catford, W.[178]; Cederwall, B.[111]; Chapman, R.[172]; Chartier, M.[162]; Chatillon, A.[34]; Chen, L.[34]; Chmel, S.[144]; Choudhury, R.[61]; Chulkov, L.[110]; Coleman-Smith, P.[26]; Colo, G.[45]; Colonna, N.[44]; Corradi, L.[79]; Cortina, D.[173]; Crespo Lopez-Urrutia, J.[87]; Crespo, R.[136]; Creswell, J.[162]; Csatlos, M.[2]; Cullen, D.[164]; Cunsolo, A.[80]; Curien, D.[65]; Czajkowski, S.[14]; Czosnyka, T.[185]; Danilin, B.[110]; Das, P.[184]; Datta Pramanik, U.[113]; Davids, B.[122]; Dax, A.[15]; De Angelis, G.[44]; De Oliveira Santos, F.[33]; Debowski, M.[69]; Deloncle, I.[51]; Demetriou, P.[134]; Demonchy, C.[162]; Dendooven, P.[74]; Denisov, V.[34]; Dewald, A.[148]; Di, Z.[72]; Dickel, T.[72]; Dilling, J.[122]; Dillmann, I.[141]; Dolinskii, A.[34]; Dombradi, Z.[2]; Dracoulis, G.[6]; Drouart, A.[12]; Duchene, G.[65]; Ducret, J.[13]; Dudek, J.[65]; Duran, I.[173]; Durell, J.[164]; Döring, J.[31]; Dörner, R.[154]; Eberth, J.[148]; Egelhof, P.[34]; Eichler, B.[103]; Eichler, R.[103]; Ekstrom, C.[183]; Elisseev, S.[72]; Elze, T.[154]; Emling, H.[34]; Enders, J.[123]; Enghardt, W.[30]; Enqvist, T.[160]; Erduran, N.[66]; Ershov, S.[67]; Eschke, J.[34]; Espino, J.[175]; Ewald, G.[34]; Fabbietti, L.[84]; Faestermann, T.[125]; Fahlander, C.[85]; Farnea, E.[47]; Fedorov, D.[3]; Feldmeier, H.[34]; Fernandez Dominguez, B.[162]; Fernandez Ramirez, C.[23]; Fernandez, M.[173]; Ferreira, L.[17]; Fettouhi, A.[72]; Fioni, G.[12]; Flanagan, K.[73]; Fornal, B.[97]; Forssen, C.[82]; Fraile Prieto, L.[23]; Fraile, L.[15]; France III, R.[35]; Franczak, B.[34]; Fransson, K.[183]; Franzke, B.[34]; Freeman, S.[164]; Freer, M.[9]; Freiesleben, H.[124]; Friese, J.[125]; Friman, B.[34]; Fritioff, T.[176]; Fritsch, M.[112]; Fuhrmann, H.[119]; Fujita, Y.[101]; Fulton, B.[181]; Fynbo, H.[138]; Fässler, A.[180]; Gacsi, Z.[2]; Gadea, A.[44]; Gaeggeler, H.[143]; Gai, M.[149]; Galaviz Redondo, D.[123]; Garrido, E.[19]; Gast, W.[28]; Gastineau, B.[25]; Geissel, H.[34]; Gelletly, W.[178]; Genolini, B.[51]; George, S.[15]; Geppert, C.[34]; Gerl, J.[34]; Gernhauser, R.[125]; Gillibert, A.[12]; Gillitzer, A.[28]; Giot, L.[34]; Giovinazzo, J.[51]; Glasmacher, T.[88]; Gloeckle, W.[112]; Goennenwein, F.[180]; Goldring, G.[128]; Golovkov, M.[67]; Golubev, P.[85]; Gomez, J.[175]; Gomikawa, K.[179]; Goriely, S.[134]; Grawe, H.[34]; Grebosz, J.[41]; Greenlees, P.[160]; Greiner, W.[154]; Grigorenko, L.[67]; Gross, K.[34]; Grosse, E.[30]; Grzonka, D.[28]; Grzywacz, R.[100]; Guenaut, C.[20]; Guglielmetti, A.[45]; Gulyas, J.[2]; Gunsing, F.[12]; Gupta, M.[89]; Gupta, R.[105]; Gusev, Y.[102]; Gutbrod, H.[34]; Guttormsen, M.[170]; Grska, M.[34]; Habs, D.[84]; Haiduc, M.[91]; Hammache, F.[51]; Hanappe, F.[134]; Hannachi, F.[20]; Harakeh, M.[74]; Harissopulos, S.[59]; Hasegan, D.[62]; Hasper, J.[123]; Hass, M.[128]; Hausmann, M.[93]; Hayano, R.[179]; Heenen, P.[134]; Heil, M.[29]; Heinz, A.[186]; Heinz, S.[34]; Helariutta, K.[160]; Hellstroem, M.[34]; Hencken, K.[140]; Henning, W.[34]; Henzl, V.[34]; Henzlova, D.[34]; Herfurth, F.[34]; Herlert, A.[156]; Herraiz, J.[24]; Herskind, B.[150]; Herzberg, R.[162]; Hessberger, F.[34]; Hirenzaki, S.[168]; Hirtl, A.[119]; Hoffmann, J.[34]; Hofmann, S.[34]; Homolka, J.[125]; Hubel, H.[145]; Hunyadi, M.[2]; Huyse, M.[73]; Ignatyuk, A.[53]; Ikezoe, H.[71]; Ilie, C.[62]; Iordachescu, A.[94]; Ismael, M.[159]; Itahashi, K.[109]; Ivanov, V.[102]; Ivanyuk, F.[34]; Iwamoto, A.[71]; Iwasa, N.[109]; Iwasaki, M.[109]; Jakobsson, B.[85]; Janas, Z.[185]; Jastrzebski, J.[185]; Jenkins, D.[181]; Jensen, A.[3]; Johansson, H.[34]; Johnson, A.[120]; Johnson, R.[178]; Jokinen, A.[160]; Jolie, J.[148]; Jolos, R.[67]; Jones, K.[100]; Jonson, B.[21]; Jourdan, J.[140]; Julin, R.[68]; Jungclaus, A.[132]; Junghans, A.[30]; Jungmann, K.[74]; Jurado, B.[32]; Juutinen, S.[160]; Kaeppeler, F.[29]; Kailas, S.[7]; Kajetanowicz, M.[69]; Kalantar, N.[74]; Kamerdzhiev, S.[53]; Kanungo, R.[122]; Karataglidis, S.[11]; Karny, M.[185]; Kato, S.[187]; Kavatsyuk, M.[76]; Kavatsyuk, O.[76]; Kaza, E.[34]; Kelic, A.[34]; Kellerbauer, A.[15]; Kelley, J.[131]; Kester, O.[34]; Kettunen, H.[160]; Kezzar, K.[12]; Khan, E.[51]; Khanzadeev, A.[102]; Kiener, J.[20]; Kienle, P.[125]; Kindler, B.[34]; Kirchner, R.[34]; Kisselev, O.[34]; Klepper, O.[34]; Klimkiewicz, A.[34]; Kluge, H.[34]; Klygin, S.[67]; Kmiecik, M.[97]; Kneissel, U.[177]; Knodlseder, J.[16]; Knöbel, R.[72]; Koehler, P.[100]; Koester, U.[15]; Kohlmeyer, B.[165]; Kojouharov, I.[34]; Kolhinen, V.[84]; Koop, I.[8]; Kopatch, Y.[67]; Kopecky, S.[160]; Korcyl, K.[70]; Korichi, A.[20]; Korostelev, M.[8]; Korten, W.[12]; Koudriavtsev, I.[73]; Kownacki, J.[185]; Kozhuharov, C.[34]; Kozouline, E.[67]; Krasznahorkay, A.[2]; Kreiner, A.[121]; Kroell, T.[125]; Krolas, W.[58]; Krusche, B.[140]; Krücken, R.[125]; Kubo, T.[109]; Kuehl, T.[34]; Kulessa, R.[70]; Kupsc, A.[183]; Kurcewicz, W.[185]; Kurtukian, T.[173]; Kurz, N.[34]; Körner, G.[99]; La Commara, M.[135]; Labiche, M.[172]; Laird, A.[181]; Lalazissis, G.[5]; Lallena Rojo, A.[36]; Langanke, K.[34]; Lapoux, V.[12]; Lazarus, I.[10]; Le Blanc, F.[20]; Le Bleis, T.[34]; Le Gentil, E.[25]; Le Hong, K.[60]; Leifels, Y.[34]; Leino, M.[160]; Leleux, P.[163]; Lemmon, R.[26]; Lenske, H.[72]; Lenzi, S.[171]; Lepine-Szily, A.[174]; Leray, S.[25]; Letts, S.[26]; Lewitowicz, M.[32]; Leya, U.[55]; Liang, X.[104]; Lieb, K.[157]; Lieder, R.[28]; Lindberg, K.[176]; Lisin, V.[49]; Lister, K.[1]; Litvinov, S.[34]; Litvinov, Y.[34]; Litvinova, E.[114]; Lo Bianco, G.[147]; Loehner, H.[74]; Logatchov, P.[8]; Loiselet, M.[83]; Lombardo, U.[43]; Lommel, B.[34]; Lopez Herraiz, J.[24]; Lozeva, R.[34]; Lunardi, S.[171]; Lunney, D.[20]; Lynch, W.[93]; Lyne, U.[34]; Mach, H.[183]; Madland, D.[78]; Mahata, K.[34]; Maier, L.[125]; Maier, M.[34]; Maj, A.[41]; Mandal, S.[151]; Mann, R.[34]; Mao, R.[57]; Martel, I.[159]; Marton, J.[119]; Maruhn, J.[154]; Marx, D.[34]; Marx, G.[156]; Matos, M.[93]; Mazzocchi, C.[34]; Mazzocco, M.[27]; Meczinski, W.[41]; Meier, J.[34]; Meister, M.[21]; Menegazzo, R.[47]; Mengoni, A.[15]; Meshkov, I.[67]; Metag, V.[72]; Million, B.[45]; Mittig, W.[32]; Mitu, C.[63]; Moeller, P.[78]; Moore, I.[160]; Moreno, O.[19]; Morita, K.[109]; Morrissey, D.[88]; Moszynski, M.[118]; Motagnoli, G.[171]; Motizuki, Y.[109]; Motobayashi, T.[109]; Moya de Guera, E.[19]; Mueller, A.[51]; Mukha, I.[73]; Muralithar, S.[92]; Mushkarenkov, A.[49]; Mutterer, M.[123]; Müller, S.[123]; Müntz, C.[34]; Münzenberg, G.[34]; Nagai, Y.[108]; Nagy, S.[176]; Nakamura, T.[130]; Nalpas, L.[12]; Nankov, N.[72]; Navin, A.[7]; Nedorezov, V.[49]; Neff, T.[34]; Nesmiyan, I.[34]; Nesterenko, I.[8]; Neumaier, S.[34]; Neyens, G.[73]; Nickel, F.[34]; Nieminen, A.[160]; Nilsson, T.[123]; Nitsche, H.[146]; Nociforo, C.[43]; Nolan, P.[162]; Nolden, F.[34]; Nolen, J.[1]; Norenberg, W.[34]; Novikov, Y.[102]; Nyberg, J.[183]; Nyman, G.[21]; Nörtershäuser, W.[34]; Obradors, D.[19]; von Oertzen, W.[37]; Oganessian, J.[67]; Ohta, M.[77]; Ohtsubo, T.[98]; Oi, M.[178]; Orrigo, S.[72]; Ostrowski, A.[158]; Otboev, A.[8]; Otsu, H.[129]; Ott, W.[34]; Outa, H.[109]; Ozawa, A.[109];

Pachalis, S.[162]; Page, R.[162]; Palit, R.[126]; Pankaj, J.[92]; Pantea, M.[123]; Parkhomchuk, V.[8]; Paschalis, S.[162]; Patyk, Z.[185]; Paul, E.[162]; Pavlov, V.[8]; Penttillae, H.[160]; Pereira Conca, J.[173]; Pershina, V.[34]; Peräjärvi, K.[160]; Peschke, C.[34]; Peter, I.[34]; Peter, J.[81]; Petrache, C.[147]; Petrick, M.[72]; Petrovici, A.[95]; Peyre, J.[51]; Pfützner, M.[185]; Pierroutsakou, D.[46]; Pietralla, N.[148]; Pietri, S.[178]; Pignanelli, M.[45]; Pivovarov, Y.[107]; Plaß, W.[72]; Pleskac, R.[34]; Plettner, C.[186]; Plochocki, A.[185]; Ploskon, M.[34]; Podolyak, Z.[178]; Pollacco, E.[12]; Polonski, A.[49]; Popeko, A.[67]; Porquet, M.[51]; Portillo, M.[34]; Potlog, M.[63]; Pouthas, J.[51]; Prokopowicz, W.[70]; Protic, D.[28]; Pucknell, V.[26]; Quint, W.[34]; Radomski, S.[34]; Radon, T.[34]; Ramirez, C.[19]; Ramstein, B.[51]; Rathmann, F.[28]; Rauscher, T.[140]; Rauth, C.[34]; Ray, A.[184]; Redon, N.[51]; Redondo, D.[123]; Regan, P.[178]; Reifarth, R.[78]; Reinhard, I.[34]; Reinhard, P.[153]; Reiss, J.[34]; Reiter, P.[148]; Rejmund, F.[32]; Ricciardi, M.[34]; Richter, A.[123]; Riisager, K.[3]; Ring, P.[125]; Ripamonti, E.[166]; Rodriguez, D.[34]; Roeckl, E.[34]; Rohe, D.[140]; Rolfs, C.[112]; Rosner, G.[155]; Rossi, A.[47]; Rostchin, E.[102]; Roussel-Chomaz, P.[32]; Roy, A.[92]; Rubio, B.[38]; Rudnev, N.[49]; Rudolph, D.[85]; Rykaczewski, K.[100]; Rzaca-Urban, T.[70]; Saito, N.[34]; Saito, T.[34]; Salabura, P.[70]; Samyn, M.[134]; Santo, R.[167]; Saro, S.[22]; Sarriguren, P.[19]; Savajols, H.[32]; Savard, G.[1]; Scarpaci, J.[51]; Schaffner-Bielich, J.[154]; Schardt, D.[34]; Schatz, H.[93]; Scheid, W.[72]; Scheidenberger, C.[34]; Scheit, H.[87]; Schmidt, K.[34]; Schmitt, C.[50]; Schneider, D.[82]; Schoenfelder, V.[86]; Scholey, C.[160]; Scholz, M.[34]; Schrieder, G.[123]; Schuch, R.[176]; Schuck, C.[20]; Schwalm, D.[158]; Schwarz, S.[88]; Schweikhard, L.[156]; Schwengner, R.[30]; Schwertel, S.[125]; Schädel, M.[34]; Seleznev, I.[67]; Seliverstov, D.[102]; Seliverstov, M.[73]; Sereda, Y.[67]; Sevcenco, A.[64]; Sewtz, M.[84]; Shatilov, D.[8]; Shatunov, Y.[8]; Sherrill, B.[93]; Shindo, M.[179]; Shishkin, V.[34]; Shiyankov, S.[8]; Shotter, A.[122]; Shrivastava, A.[7]; Signorini, C.[137]; Simenel, C.[12]; Simon, H.[34]; Simpson, J.[10]; Singh, K.[105]; Sitar, B.[22]; Skarnemark, G.[21]; Skaza, F.[51]; Skrinsky, A.[8]; Sletten, G.[96]; Smith, A.[164]; Sohler, D.[2]; Sonnabend, K.[123]; Sorlin, O.[51]; Speidel, K.[145]; Spohr, K.[172]; Sprouse, G.[115]; Stadlmann, J.[34]; Stanoiu, M.[32]; Steck, M.[34]; Stefanini, A.[79]; Stelzer, H.[34]; Stephan, C.[51]; Stevenson, P.[178]; Stoecker, H.[154]; Stoehlker, T.[34]; Stolz, A.[93]; Strieder, F.[112]; Stroth, J.[34]; Styczen, J.[97]; Suda, T.[109]; Sun, Z.[57]; Suresh Kumar, S.[54]; Surowiec, A.[34]; Suzuki, K.[125]; Suzuki, T.[116]; Swetz, M.[20]; Syresin, E.[67]; Szerypo, J.[84]; Sümmerer, K.[34]; Tahir, N.[34]; Taieb, J.[32]; Tain, J.[38]; Takahashi, K.[134]; Tanihata, I.[1]; Tarasenkova, O.[102]; Tassan-Got, L.[51]; Tegner, P.[176]; Tengblad, O.[19]; Teterev, Y.[67]; Thielemann, F.[140]; Thirolf, P.[84]; Thoennessen, M.[93]; Thomas, H.[148]; Thompson, I.[178]; Thornhill, J.[162]; Thungstrom, G.[90]; Tinyakov, P.[161]; Tomaselli, M.[34]; Tostevin, J.[178]; Trautmann, D.[140]; Trautmann, W.[34]; Trzcinska, A.[185]; Tsang, B.[93]; Turinge, A.[49]; Turrion, M.[19]; Turzo, K.[14]; Typel, S.[34]; Türler, A.[84]; Udias-Moinelo, J.[24]; Ullrich, J.[87]; Utsunomiya, H.[77]; Uusitalo, J.[160]; Vaagen, J.[142]; Valishev, A.[8]; Van Duppen, P.[73]; Van den Berg, A.[74]; Varley, B.[164]; Vieira, D.[78]; Vignote, J.[24]; Villagrasa Cantom, C.[12]; Villari, A.[32]; Vitturi, A.[171]; Volant, C.[12]; Volkov, V.[110]; Von Brentano, P.[148]; Von Neumann-Cosel, P.[123]; Vorobjev, G.[102]; Vorontsov, A.[67]; Vostrikov, V.[8]; Vretenar, D.[125]; Wada, M.[109]; Wadsworth, B.[181]; Wagner, A.[30]; Walker, P.[178]; Walus, W.[69]; Wambach, J.[123]; Wang, Z.[72]; Warner, D.[10]; Weick, H.[34]; Westerberg, L.[127]; Wheldon, C.[34]; Widmann, E.[179]; Wieland, O.[45]; Wieleczko, J.[32]; Wiescher, M.[169]; Wilson, J.[96]; Wimmer, C.[154]; Winfield, J.[80]; Winkler, M.[34]; Witold, M.[58]; Woertche, H.[74]; Wohr, A.[169]; Wollersheim, H.[34]; Wollnik, H.[72]; Wolter, H.[84]; Woods, P.[152]; Wycech, S.[118]; Xiao, G.[57]; Yamaguchi, T.[116]; Yamazaki, T.[109]; Yamazaki, Y.[179]; Yazidjian, C.[15]; Yeremin, A.[67]; Yordanov, O.[34]; Zamfir, V.[91]; Zartova, I.[176]; Zeitelhack, K.[125]; Zerguerras, T.[51]; Zhang, Y.[42]; Zhou, Z.[72]; Zhukov, M.[21]; Zieblinski, M.[70]; Zilges, A.[123]; Zimmermann, C.[180]; Zmeskal, J.[119]; Zylicz, J.[185]

1 ANL Argonne (USA)
2 ATOMKI Debrecen (Hungary)
3 Aarhus University (Denmark)
4 Ankara University (Turkey)
5 Aristotle University of Thessaloniki (Greece)
6 Australian National University (Australia)
7 BARC Mumbai (India)
8 BINP Novosibirsk (Russia)
9 Birmingham University (United Kingdom)
10 CCLRC Daresbury (United Kingdom)
11 CEA Bruyeres-le-Chatel (France)
12 CEA Saclay (France)
13 CEA Saclay, DAPNIA/SPhN (France)
14 CEN Bordeaux-Gradignan (France)
15 CERN (Switzerland)
16 CESR (France)
17 CFIF/ Dep de Fisica, IST, Lisboa (Portugal)
18 CIEMAT (Spain)
19 CSIC Madrid (Spain)
20 CSNSM Orsay (France)
21 Chalmers University of Technology (Sweden)
22 Comenius University Bratislava (Slovakia)
23 Complutense University of Madrid (Spain)
24 Complutense University of Madrid (Spain)
25 DAPNIA CEA Saclay (France)
26 Daresbury Laboratory (United Kingdom)
27 Diparimento di Fisica 'Galileo Galilei' & INFN (Italy)
28 FZ Jülich (Germany)
29 FZ Karlsruhe (Germany)
30 FZ Rossendorf (Germany)
31 Federal Office for Radiation Protection Berlin (Germany)
32 GANIL (France)
33 GANIL/CNRS (France)
34 GSI Darmstadt (Germany)
35 Georgia College and State University (USA)
36 Granada University (Spain)
37 HMI Berlin (Germany)
38 IFIC Valencia (Spain)
39 IFIN-HH Bucharest (Romania)
40 IFIN-HH/CERN (Romania)
41 IFJ PAN Krakow (Poland)
42 IMPCAS (China)
43 INFN - LNS (Italy)
44 INFN Legnaro (Italy)
45 INFN Milan (Italy)
46 INFN Napoli (Italy)
47 INFN Padova (Italy)
48 INFN Pisa (Italy)
49 INR Moscow (Russia)
50 IPN Lyon (France)
51 IPN Orsay (France)
52 IPPE (Belgium)
53 IPPE Obninsk (Russia)
54 Indian Insitute of technology Roorkee (India)
55 Institute for Isotope Geology and Mineral Resources (Switzerland)

56 Institute of General and Nuclear Physics (Russia)
57 Institute of Modern Physics Lanzhou (China)
58 Institute of Nuclear Physics (Poland)
59 Institute of Nuclear Physics, NCSR 'Demokritos', Athens (Greece)
60 Institute of Physics (Vietnam)
61 Institute of Physics Bhubaneswar (India)
62 Institute of Space Sciences (Romania)
63 Institute of Space Sciences (Romania)
64 Institute of Space Sciences (Romania)
65 IreS Strasbourg (France)
66 Istanbul University (Turkey)
67 JINR Dubna (Russia)
68 JYFL Jyvaskyla (Finland)
69 Jagellonian University (Poland)
70 Jagellonian University Krakow (Poland)
71 Japan Atomic Energy Research Institute (Japan)
72 Johannes Gutenberg University of Mainz (Germany)
73 KU Leuven (Belgium)
74 KVI Groningen (The Netherlands)
75 Keele University (United Kingdom)
76 Kiev National University (Ukraine)
77 Konan University (Japan)
78 LANL Los Alamos (USA)
79 LNL / INFN (Italy)
80 LNS Catania (Italy)
81 LPC Caen (France)
82 Lawrence Livermore National Laboratory (USA)
83 Louvain-la-Neuve (Belgium)
84 Ludwig-Maximilians University of Munich (Germany)
85 Lund University (Sweden)
86 MPI for Extraterrestrial Physics (Germany)
87 MPI für Kernphysik (Germany)
88 MSU (USA)
89 Manipal Academy of Higher Education (India)
90 Mid Sweden University (Sweden)
91 NIPNE Bucharest (Romania)
92 NSC New Delhi (India)
93 NSCL/MSU (USA)
94 National Institute for Physics and Nuclear Engineering (Romania)
95 National Institute for Physics and Nuclear Engineering (Romania)
96 Niels Bohr Institute (Denmark)
97 Niewodniczanski Institute of Nuclear Physics (Poland)
98 Niigata University (Japan)
99 NuPECC (Germany)
100 ORNL Oak Ridge (USA)
101 Osaka University (Japan)
102 PNPI Gatchina (Russia)
103 PSI Villigen (Switzerland)
104 Paisly University (United Kingdom)
105 Panjab University Chandigarh (India)
106 Politechnical University of Bucharest (Romania)
107 Polytechnic University of Tomsk (Russia)
108 RCNP Osaka (Japan)
109 RIKEN (Japan)
110 RRC Kurchatov Institute Moscow (Russia)
111 Royal Institute of Technology (Sweden)
112 Ruhr-University Bochum (Germany)
113 SINP Kolkata (India)
114 SSC RF Obninsk (Russia)
115 SUNY Stony Brook (USA)
116 Saitama University (Japan)
117 Seville University (Spain)
118 Soltan Institute for Nuclear Studies (Poland)
119 Stephan Meyer Institute Vienna (Austria)
120 Stockholm University (Sweden)
121 TANDAR (Argentina)
122 TRIUMF (Canada)
123 TU Darmstadt (Germany)
124 TU Dresden (Germany)
125 TU Munich (Germany)
126 Tata Institute Mumbay (India)
127 The Svedberg Laboratory (Sweden)
128 The Weizmann Institute of Science Rehovot (Israel)
129 Tohoku University (Japan)
130 Tokyo Institute of Technology (Japan)
131 Triangle Universities Nuclear Laboratory and NCSU (USA)
132 UAM Madrid (Spain)
133 UPC Barcelona (Spain)
134 Universite Libre de Bruxelles (Belgium)
135 University Federico Napoli (Italy)
136 University Lisboa (Portugal)
137 University Padova and INFN Padova (Italy)
138 University of Aarhus (Denmark)
139 University of Arizona (USA)
140 University of Basel (Switzerland)
141 University of Basel/ FZK (Switzerland)
142 University of Bergen (Norway)
143 University of Bern (Switzerland)
144 University of Bonn (Germany)
145 University of Bonn (Germany)
146 University of California (USA)
147 University of Camerino (Italy)
148 University of Cologne (Germany)
149 University of Connecticut (USA)
150 University of Copenhagen (Denmark)
151 University of Delhi (India)
152 University of Edinburgh (United Kingdom)
153 University of Erlangen (Germany)
154 University of Frankfurt (Germany)
155 University of Glasgow (United Kingdom)
156 University of Greifswald (Germany)
157 University of Göttingen (Germany)
158 University of Heidelberg (Germany)
159 University of Huelva (Spain)
160 University of Jyväskylä (Finland)
161 University of Lausanne (Switzerland)
162 University of Liverpool (United Kingdom)
163 University of Louvain (Belgium)
164 University of Manchester (United Kingdom)
165 University of Marburg (Germany)
166 University of Milan (Italy)
167 University of Münster (Germany)
168 University of Nara (Japan)
169 University of Notre Dame (USA)
170 University of Oslo (Norway)
171 University of Padova (Italy)
172 University of Paisley (United Kingdom)
173 University of Santiago de Compostela (Spain)
174 University of Sao Paulo (Brasilia)
175 University of Sevilla (Spain)
176 University of Stockholm (Sweden)

177 University of Stuttgart (Germany)
178 University of Surrey (United Kingdom)
179 University of Tokyo (Japan)
180 University of Tübingen (Germany)
181 University of York (United Kingdom)
182 Univsite Libre de Bruxelles (Belgium)
183 Uppsala University (Sweden)
184 VECC Kolkata (India)
185 Warsaw University (Poland)
186 Yale University (USA)
187 Yamagata University (Japan)

FAIR: The SPARC Collaboration

Stored Particles Atomic Physics Collaboration
<http://www.gsi.de/zukunftsprojekt/experimente/sparc/index_e.html>
Spokesperson: R. Schuch, Stockholm (Sweden)

Afaneh, F.[59]; Ali, R.[59]; Andler, G.[80]; Andreev, O. Y.[35]; Andreev, O. Y.[68]; Anton, J.[39]; Artemyev, A.[68]; Aumayr, F.[3]; Backe, H.[38]; Bagge, L.[80]; Balashov, V.[72]; Banas, D.[61]; Baur, G.[28]; Beck, D.[30]; Becker, F.[30]; Beier, T.[30]; Beyer, H. F.[30]; Blaum, K.[81]; Block, M.[30]; Bosch, F.[30]; Braeuning-Demian, A.[30]; Brandau, C.[30]; Briggs, J.[29]; Bräuning, H.[31]; Bureyeva, L.[70]; Burgdoerfer, J.[2]; Cai, X.[10]; Chen, C.[9]; Chen, J.[13]; Ciortea, C.[66]; Cisneros, C.[60]; Currell, F[85]; Danared, H.[80]; Dangendorf, V.[43]; Dauvergne, D.[23]; Dilling, J.[6]; Ding, D.[11]; Djekic, S.[38]; Dong, C.[15]; Dousse, J.-C.[82]; Drukarev, E.[73]; DuBois, R.[89]; Dumitriu, D. E.[66]; Dörner, R.[37]; Egelhof, P.[30]; Eichler, J.[47]; Engström, M.[80]; Enss, C.[93]; Enulescu, A.[66]; Fainstein, P. D.[1]; Fischer, D.[34]; Fleischmann, A.[41]; Fluerasu, D.[66]; Fogle, M.[90]; Fricke, B.[39]; Fritzsche, S.[39]; Förster, E.[49]; Gao, K.[14]; Garcia, G.[75]; Gaul, E.[94]; Goidenko, I.[68]; Gotta, D.[28]; Gumberidze, A.[30]; Gwinner, G.[4]; Habs, D.[33]; Hagmann, S.[37]; Hahn, T.[30]; Hanafy, H.[20]; Hencken, K.[83]; Herfurth, F.[30]; Herlert, A.[27]; Horbatsch, M.[5]; Huber, G.[38]; Hutton, R.[79]; Jakubassa-Amundsen, D.[44]; Jentschura, U.[29]; Kamber, E.[91]; Karpuk, S.[38]; Keitel, C. H.[34]; Kirchner, T.[40]; Kluge, H.-J.[30]; Kozhuharov, C.[30]; Krings, T.[28]; Källberg, A.[80]; Kühl, T.[30]; Labzowsky, L. N.[68]; Lamour, E.[24]; Lanzano, G.[57]; Le Bigot, E.-O.[25]; Lemell, C.[2]; Lestinsky, M.[34]; Liesen, D.[30]; Liljeby, L.[80]; Lindgren, I.[76]; Lindroth, E.[77]; Löfgren, P.[80]; Ma, X.[10]; Macek, J.[90]; Madsen, L. B.[19]; Madzunkov, S.[77]; Manchikanti, K.[52]; Manil, B.[21]; Mann, R.[30]; Manson, S.[88]; Marinkovic, B.[74]; Marx, G. H.[27]; Mathur, D.[52]; Matrasulov, D.[98]; Mitra, D.[56]; Mohamed, T.[20]; Mokler, P.[30]; Moshammer, R.[34]; Mukherjee, M.[30]; Müller, A.[31]; Nagy, S.[77]; Nandi, T.[54]; Nefiodov, A.[68]; Novotny, C.[38]; Nörtershäuser, W.[36]; Pachucki, K.[63]; Pajek, M.[61]; Pal'Chikov, V.[69]; Paál, A.[80]; Penescu, L. C.[66]; Peter, G.[78]; Pisk, K.[17]; Plunien, G.[35]; Potvliege, R.[84]; Presnyakov, L.[67]; Protic, D.[28]; Quint, W.[30]; Radu, A. T.[66]; Rahaman, S.[30]; Rakhimov, K.[98]; Rathmann, F.[28]; Reinhardt, S.[34]; Renner, O.[18]; Rensfelt, K.-G.[80]; Richard, P.[95]; Rothard, H.[21]; Rozet, J.-P.[24]; Rzadkiewicz, J.[65]; Röpke, G.[46]; Saathoff, G.[34]; Saenz, A.[48]; Safvan, C. P.[54]; Salomonson, S.[76]; Samek, S. Warczak, A[62]; Sanchez, R.[30]; Savin, D. W.[96]; Scheid, W.[32]; Schenkel, R.[87]; Schippers, S.[31]; Schmidt-Böcking, H.[37]; Schneider, D.[87]; Schramm, U.[33]; Schuch, R.[77]; Schulz, M.[89]; Schweikhard, L.[27]; Schützhold, R.[35]; Segal, D.[86]; Sepp, W.-D.[39]; Shabaev, V.[68]; Shevelko, V.[67]; Simionovici, A.[22]; Simon, H.[30]; Simonsson, A.[80]; Skeppstedt, Ö.[80]; Sliver, E.[92]; Soff, G.[35]; Sprenger, F.[34]; Stachura, Z.[64]; Stahl, S.[38]; Stiebing, K. E.[37]; Stöhlker, T.[30]; Sulik, B.[51]; Suri, B.[55]; Suric, T.[17]; Surzhykov, A.[39]; Tanis, J.[97]; Thompson, R.[86]; Tokesi, K.[51]; Toleikis, S.[87]; Tomasseli, M.[30]; Trassinelli, M.[26]; Trautmann, D.[83]; Tribedi, L.[52]; Trotsenko, S.[30]; Ullrich, J.[34]; Varentsov, V.[71]; Verma, P.[53]; Vikor, G.[77]; Vogel, M.[38]; Volotka, A.[35]; Wang, J.[8]; Weber, C.[30]; Wei, B.[10]; Welsch, C.[34]; Winter, H.[3]; Winters, D.[86]; Wolf, A.[34]; Ximeng, C.[12]; Yamazaki, Y.[58]; Yerokhin, V.[68]; Yoshida, S.[2]; Zeng, X.[7]; Zhang, F. S.[10]; Zhu, L.[13]; Zhu, X.[10]; Zilges, A.[42]; Zou, Y.[16]; Zouros, T.[50]; Zwicknagel, G.[45]

1 Centro Atomico Bariloche (Argentina)
2 Vienna University of Technolgy, Wien (Austria)
3 Institut für Allgemeine Physik, TU Wien (Austria)
4 University of Manitoba (Canada)
5 York University (Canada)
6 TRIUMF National Laboratory Vancouver (Canada)
7 China Institute of Atomic Energy, Beijing (China)
8 Institute of Applied Physics and Computational Mathematics, Beijing (China)
9 Institute of Modern Physics, Fudan University, Shanghai (China)
10 Institute of Modern Physics, Chinese Academy of Sciences, Lanzhou (China)
11 Institute of Atomic and Molecular Physics, Jilin University, Jilin (China)
12 Lanzhou University, Lanzhou (China)
13 University of Science and Technology of China, Hefei (China)
14 Wuhan Institute of Physics and Mathematics, Wuhan (China)
15 Physics Department, Northwest Normal University (China)
16 Applied Ion Beam Physics Laboratoy, Fudan University (China)
17 Ruder Boskovic Institute, Zagreb (Croatia)
18 Institute of Physics, Czech Academy of Sciences (Czech Republic)
19 Department of Physics and Astronomy, University of Aarhus (Denark)
20 Physics Department, Beni-Suef Faculty of Science (Egypt)
21 CIRIL Ganil (France)
22 Ecole Normale Superieure - Lyon (France)
23 Institut de Physique Nucléaire de Lyon (France)
24 Groupe de Physique des Solides (France)
25 Univ. P. & M. Curie et Ecole Normale Supérieure (France)
26 Laboratoire Kastler Brossel
27 Ernst Moritz Arndt Universität Greifswald (Germany)
28 Forschungszentrum Jülich (Germany)
29 Freiburg University (Germany)
30 GSI, Darmstadt (Germany)
31 Institut für Atom- und Molekülphysik, Justus-Liebig-Universität Gießen (Germany)
32 Institut für Theoretische Physik der Universität Gießen (Germany)
33 Sektion Physik, LMU Munich (Germany)
34 Max-Planck-Institut für Kernphysik, Heidelberg (Germany)
35 Institut für Theoretische Physik, TU Dresden (Germany)
36 Tübingen University (Germany)
37 IKF, J.W.v.Goethe Universität Frankfurt am Main (Germany)
38 Institut für Physik, Universität Mainz (Germany)
39 Institut für Physik, Universität Kassel (Germany)
40 Institut für Theoretische Physik, TU Clausthal (Germany)
41 Kirchhoff-Institut für Physik, Universität Heidelberg (Germany)
42 TU Darmstadt (Germany)
43 Physikalisch-Technische Bundesanstalt (Germany)
44 Mathematics Institute, University of Munich (Germany)
45 Theoretische Physik, Universität Erlangen (Germany)
46 Institut für Physik, Universität Rostock (Germany)
47 Hahn-Meitner-Institut Berlin (Germany)
48 Humboldt-Universität zu Berlin (Germany)
49 Institute for Optics, Jena University (Germany)

50 University of Crete and IESL-FORTH (Greece)
51 Inst. of Nuclear Research (ATOMKI), Debrecen (Hungary)
52 Tata Institute of Fundamental Research (India)
53 Vaish College, Rohtak (India)
54 Nuclear Science Centre, New Delhi (India)
55 Bhabha Atomic Research Centre (India)
56 Saha Institute of Nuclear Physics (India)
57 Inst. Naz. Fisica Nucleare, Dip. di Fisica, Catania (Italy)
58 University of Tokyo & Atomic Physics Laboratory RIKEN, Wako (Japan)
59 Hashemite University (Jordan)
60 CCF Universidad Nacional Autónoma de México (Mexico)
61 Institute of Physics, Swietokrzyska Academy (Poland)
62 Institute of Physics, Jagiellonian University (Poland)
63 Institute of Theoretical Physics, Warsaw University (Poland)
64 Institute of Nuclear Physics of Polish Academy of Sciences (Poland)
65 The Soltan Institute For Nuclear Studies (Poland)
66 NIPNE National Institute for Physics and Nuclear Engineering (Romania)
67 Lebedev Physical Institute, Moscow (Russia)
68 Institute of Physics, St. Petersburg State University (Russia)
69 Institute of Metrology for Time and Space at VNIIFTRI (Russia)
70 Institute of Spectroscopy of the RAS (Russia)
71 V.G.Khlopin Radium Institute, St.Petersburg (Russia)
72 Institute of Nuclear Physics, Moscow State University (Russia)
73 Petersburg Nuclear Physics Institute (Russia)
74 Institute of Physics, Belgrade (Serbia and Montenegro)
75 CSIC (Spain)
76 Chalmers University of Technology and Goteborg University (Sweden)
77 Stockholm University (Sweden)
78 Mid-Sweden University (Sweden)
79 Lund University (Sweden)
80 Manne Siegbahn Laboratory MSL (Sweden)
81 CERN (Switzerland)
82 Department of Physics, University Fribourg (Switzerland)
83 Institut für Physik, Universität Basel (Switzerland)
84 Department of Physics, The University of Durham (United Kingdom)
85 Queen's University, Belfast (United Kingdom)
86 Imperial College (United Kingdom)
87 Lawrence Berkeley National Laboratory (USA)
88 Georgia State University (USA)
89 University of Missouri Rolla (USA)
90 Oak Ridge National Laboratory (USA)
91 Western Michigan University (USA)
92 Harvard-Smithsonian Center for Astrophysics (USA)
93 Brown University, Physics Department (USA)
94 Univeristy of Texas at Austin (USA)
95 Kansas State University (USA)
96 Columbia Astrophysics Laboratory, Columbia University (USA)
97 Western Michigan University (USA)
98 Heat Physics Department of the Uzbek Academy of Sciences (Uzbeksitan)
99 Arifov Institute of Electronics, Uzbek Acaemy of Sciences (Uzbeksitan)

Contributions in this report:
FAIR-NUSTAR-SuperFRS-01
FAIR-NUSTAR-SuperFRS-02
FAIR-NUSTAR-SuperFRS-03
FAIR-NUSTAR-SuperFRS-04
FAIR-NUSTAR-SuperFRS-05

The SIS/ESR/UNILAC Collaborations

The ALADiN 2000 Collaboration

<http://www-kp3.gsi.de/www/kp3/aladinhome.html>
Spoekesperson: W. Trautmann, Darmstadt (Germany)

Adrich, P.[1]; Aumann, T.[1]; Bacri, C. O.[2]; Barczyk, T.[8]; Bassini, R.[6]; Bianchin, S.[1]; Boiano, C.[6]; Botvina, A. S.[1]; Boudard, A.[3]; Brzychczyk, J.[8]; Chbihi, A.[4]; Cibor, J.[9]; Czech, B.[9]; De Napoli, M.[5]; Ducret, J. -E.[3]; Emling, H.[1]; Frankland, J.[4]; Hellström, M.[1]; Henzlova, D.[1]; Immè, G.[5]; Iori, I.[6]; Johansson, H.[1]; Kezzar, K.[1]; Lafriakh, A.[2]; Le Gentil, E.[3]; Leifels, Y.[1]; Le Fèvre, A.[1]; Lukasik, J.[1]; Lynch, W. G.[10]; Lynen, U.[1]; Lühning, J.[1]; Majka, Z.[8]; Mocko, M.[10]; Mykulyak, A.[7]; Müller, W. F. J.[1]; Orth, H.[1]; Otte, A. N.[1]; Palit, R.[1]; Pawłowski, P.[9]; Pullia, A.[6]; Raciti, G.[5]; Rapisarda, E.[5]; Sann, H.[1]; Schwarz, C.[1]; Sfienti, C.[1]; Simon, H.[1]; Sümmerer, K.[1]; Trautmann, W.[1]; Tsang, M. B.[10]; Volant, C.[3]; Wallace, M.[10]; Weick, H.[1]; Wiechula, J.[1]; Wieloch, A.[8]; Zwieglinski, B.[7]

1 GSI, Darmstadt (Germany)
2 Institut de Physique Nucléaire, IN2P3-CNRS et Université, Orsay (France)
3 DAPNIA/SPhN, CEA/Saclay, Gif-sur-Yvette (France)
4 GANIL, CEA et IN2P3-CNRS, Caen (France)
5 Dipartimento di Fisica dell'Universitá and LNS-INFN, Catania (Italy)
6 Istituto di Scienze Fisiche, Università degli Studi and INFN, Milano (Italy)
7 A. Sołtan Institute for Nuclear Studies, Warsaw (Poland)
8 M. Smoluchowski Institute of Physics, Jagiellonian Univ., Kraków (Poland)
9 H. Niewodniczański Institute of Nuclear Physics, Kraków (Poland)

The BIOPHYSICS Collaboration

Spokesperson: G. Kraft

Ando, K.[16]; Bettega, D.[21]; Beuve, M.[20]; Blattner, C.[30]; Böttcher, H.[33]; Cherubini, R.[6]; Cirio, R.[5]; Dangendorf, V.[35]; Debus, J.[40]; Durante, M.[22]; Enghardt, W.[31]; Furusawa, Y.[16]; Gudowska, E.[10]; Gueven, N.[17]; Huber, P.[27]; Hüttermann, J.[37]; Kanai, T.[16]; Kobayashi, Y.[9]; Kundrat, P.[1]; Lavin, M.[17]; Layer, P.[36]; Lind, B.[12]; Lokjicek, M.[1]; Löbrich, M.[37]; Matsufuji, N.[16]; Meijer, A. E.[12]; Mewaldt, R.[2]; Müller-Klieser, W.[32]; Narici, L.[23]; Nasonova, E. A.[11]; Nixdorff, K.[36]; O'Sullivan, D.[7]; Ottolenghi, A.[18]; Peschke, P.[27]; Picozza, P.[23]; Pollet, D.[28]; Raum, U.[33]; Rochat, J.[4]; Rodemann, H.[39]; Rodriguez-Lafrasse, C.[13]; Sandau, K.[29]; Semmler, W.[26]; Seppi, T.[19]; Stenerlöw, B.[25]; Tabocchini, M. A.[8]; Testard, I.[3]; Thiel, G.[36]; Tilly, N.[25]; Ting, S. C .C.[14]; Valtonen, E.[24]; Virsik-Köpp, P.[38]; Weber, K. J.[41]; Zink, D.[34]

1 Academy of Science of the Czech Republic, Praha (Czech Republic)
2 California Institute of Technology, Space Radiation Laboratory, Pasadena (USA)
3 CIRIL, Laboratory of Radiobiology and Oncology, Caen (France)
4 ETOILE, Lyon (France)
5 INFN, Torino (Italy)
6 INFN, Laboratori Nazionali di Legnaro, Legnaro (Italy)
7 Institute for Advanced Studies, School for Cosmic Physics, Dublin (Ireland)
8 Instituto Superiore di Sanita, Physics Laboratory, Rome (Italy)
9 JAERI, Research Group for Biotechnology Development, Takasaki (Japan)
10 Jagellonian University, Institute of Physics, Krakow (Poland)
11 JINR Dubna, Dept. of Radiation and Radiological Research, Dubna (Russia)
12 Karolinska Institutet, Division of Medical Radiation Physics, Dept. Of Oncology-Pathology, Stockholm (Sweden)
13 Lyon-Sud Medical School, Group of Radiobiology, Ollins (France)
14 Massachusetts Institute of Technology MIT, Dept. of Physics, Cambridge (USA)
15 Med-Austron, Vienna, Innsbruck (Austria)
16 NIRS, Research Center for charged Particle Therpaie, Chiba (Japan)
17 Queensland Institute of Medical Research (Australia)
18 Universita degli Studi di Pavia, Dipartimento di Fisica Nuclear e Teoria, Pavia (Italy)
19 Universitätsklinik für Strahlentherapie, Strahlenbiologie, Innsbruck (Austria)
20 Université Claude Bernard Lyon 1, LIRIS, Villeurbanne (France)
21 University of Milano, Dipartimento di Fisica, Milan (Italy)
22 University of Naples 'Federico II', Radiation Biophysics Group, Napoli (Italy)
23 University of Rome, Department of Physics, Rome (Italy)
24 University of Turku, Space Research Laboratory, Turku (Finland)
25 Uppsala University, Rudbeck Laboratory, Division of Biomedical Radiation Sciences, Uppsala (Sweden)
26 DKFZ, Abt. für Medizinische Physik in der Radiologie, Heidelberg (Germany)
27 DKFZ, Klinische Kooperationseinheit Radioonkologie, Heidelberg (Germany)
28 Fachhochschule Darmstadt, Fachbereich Biotechnologie, Darmstadt (Germany)
29 Fachhochschule Darmstadt, Fachbereich Optotechnik und Bildverarbeitung, Darmstadt (Germany)
30 FZ Karlsruhe, Institut für Toxikologie und Genetik, Karlsruhe (Germany)
31 FZ Rossendorf, Dresden (Germany)
32 Johannes-Gutenberg-Universität Mainz, Institut für Physiologie und Pathophysiologie, Mainz (Germany)
33 Klinik und Poliklinik der Johann-Wolfgang-Goethe-Universität, ZRAD-Strahlentherapie HS 21, Frankfurt (Germany)
34 LMU München, Institut für Anthropologie und Humangenetik, München (Germany)
35 Physikalisch-Technische Bundesanstalt PTB, Labor Neutronendosimetrie, Braunschweig (Germany)
36 Technische Universität Darmstadt, Fachbereich Biologie, Darmstadt (Germany)
37 Universität des Saarlandes, Fachrichtung Biophysik, Homburg/Saar (Germany)
38 Universität Göttingen, Medizinische Physik und Biophysik, Göttingen (Germany)
39 Universität Tübingen, Strahlenbiologie und Molekulare Umweltforschung, Tübingen (Germany)
40 Universitätsklinikum Heidelberg, Abt. für Radioonkologie und Strahlentherapie, Heidelberg (Germany)
41 Universitätsklinikum Heidelberg, Labor für Molekulare und Zelluläre Radioniologie, Heidelberg (Germany)

Contributions in this report:
RAD-BIOPHYSICS-04
RAD-BIOPHYSICS-15
RAD-BIOPHYSICS-17
RAD-BIOPHYSICS-18
RAD-BIOPHYSICS-20

FAIR: The CHARMS Collaboration

Collaboration for High-Accuracy Experiments on Nuclear Reaction Mechanisms with the FRS
<http://www-w2k.gsi.de/charms/>
Spokesperson: Karl-Heinz Schmidt, GSI

Armbruster, P.[1]; Benlliure, J.[2]; Bernas, M.[10]; Boilley, D.[3]; Botvina, A.[4]; Casarejos, E.[2]; Enqvist, T.[5]; Fernandez, M.[2]; Giot, L.[1]; Heinz, A.[6]; Henzl, V.[1]; Henzlova, D.[1]; Ignatyuk, A.[7]; Junghans, A.[11]; Kelić, A.[1]; Kurtukian, T[2]; Lukić, S.[1]; Nadtochy, P.[1]; Napolitani, P.[8]; Pleskač, R.[1]; Rejmund, F.[8]; Ricciardi, M.V.[1]; Schmidt, K.-H. [1]; Schmitt, C.[9]; Stéphan, C.[10]; Tassan-Got, L.[10]; Wagner, W.[11]; Yordanov, O.[1]

1 GSI Darmstadt (Germany)
2 University of Santiago de Compostela (Spain)
3 Universite de Caen Basse Normandie and GANIL (France)
4 Institute for Nuclear Research, Russian Academy of Sciences, Moscow (Russia)
5 CUPP project, Pyhäsalmi (Finland)
6 Yale University (USA)
7 IPPE Obninsk (Russia)
8 GANIL, Caen (France)
9 INP Lyon (France)
10 IPN Orsay, Orsay (France)
11 FZ Rossendorf, Rossendorf (Germany)

Contributions in this report:
NQMA-EXPERIMENTS-01
NQMA-EXPERIMENTS-02
NUSTAR-EXOTIC-BEAMS-04
NUSTAR-EXOTIC-BEAMS-05
NUSTAR-EXOTIC-BEAMS-06
NUSTAR-THEORY-13
NUSTAR-THEORY-17

The FOPI Collaboration

4π Detector System for Charged Particles
<http://www-fopi.gsi.de/>
Spokesperson: N. Herrmann, Heidelberg (Germany)

Andronic, A.[1]; Barret, V.[2]; Basrak, Z.[3]; Bastid, N.[2]; Benabderrahmane, M. L.[4]; Caplar, R.[3]; Cordier, E.[4]; Crochet, P.[2]; Dupieux, P.[2]; Dzelalija, M.[3]; Gasparic, I.[3]; Grishkin, Y.[6]; Hartmann, O. N.[1]; Herrmann, N.[4]; Hildenbrand, K. D.[1]; Hong, B.[7]; Kang, T. J.[7]; Kecskemeti, J.[5]; Kim, Y. J.[1]; Kirejczyk, M.[8]; Koczon, P.[1]; Korolija, M.[3]; Kotte, R.[9]; Kowalczyk, M.[8]; Lebedev, A.[6]; Leifels, Y.[1]; Lopez, X.[1]; Mangiarotti, A.[1]; Manko, V.[11]; Matulewicz, T.[8]; Merschmeyer, M.[4]; Moisa, D.[10]; Novosel, J.[7]; Petrovici, M.[10]; Rami, F.[2]; Reisdorf, W.[1]; Ryn, M. S.[7]; Schüttauf, A.[1]; Seres, Z.[5]; Sikora, B.[8]; Sim, K. S.[7]; Simion, V.[10]; Siwek-Wilczynska, K.[8]; Smolyankin, V.[6]; Stockmeier, M.[1]; Stoicea, G.[10]; Tyminski, Z.[8]; Wagner, P.[2]; Wisniewski, K.[8]; Xiao, Z. G.[12]; Xu, H. S.[12]; Yushmanov, I.[11]; Zhang, X. Y.[12]; Zhang, X. Y.[1]; Zhilin, A.[6]

1 GSI, Darmstadt (Germany)
2 Laboratoire de Physique Corpusculaire (LPC) / Université Blaise Pascal, Clermont-Ferrand (France)
3 Rudjer Boskovic Institute (RBI), Zagreb (Croatia)
4 Universität Heidelberg, I. Physikalisches Institut, Heidelberg (Germany.)
5 Central Research Institute of Physics (CRIP), Budapest (Hungary)
6 Institute for Theoretical and Experimental Physics (ITEP), Moscow (Russia)

7 Korea University, Depertment of Physics, Seoul (South Korea)
8 Institute of Experimental Physics, Nuclear Physics Division, Warsaw (Poland)
9 Forschungszentrum Rossendorf (FZR), Dresden (Germany)
10 National Institute for Physics and Nuclear Engineering (NIPNE), Bucharest (Romania)
11 Russian Research Center 'Kurchatov Institute', Moscow (Russia)
12 Institute of Modern Physics, Lanzhou (China)

Contributions in this report:
INSTRUMENTS-METHODS-09
INSTRUMENTS-METHODS-13
INSTRUMENTS-METHODS-17
NQMA-01
NQMA-EXPERIMENTS-06
NQMA-EXPERIMENTS-07
NQMA-EXPERIMENTS-08

The HADES Collaboration

High Acceptance Di-Electron Spectrometer
<http://www-hades.gsi.de/>
Spokesperson: P. Salabura, Cracow (Poland)

Agakishiev, G.[9]; Agodi, C.[1]; Balanda, A.[5]; Bannier, A.[7]; Bassini, R.[12]; Bellia, G.[1]; Bellia, G.[2]; Belver, D.[20]; Belyaev, A.[9]; Blanco, A.[3]; Boiano, C.[12]; Bortolotti, A.[12]; Boyard, J. L.[18]; Brambilla, S.[12]; Braun-Munzinger, P.[6]; Bröhmer, M.[16]; Cabanelas, P.[20]; Cavinato, M.[12]; Chernenko, S.[9]; Christ, T.[16]; Destefanis, M.[11]; Dohrmann, F.[7]; Durán, I.[20]; Díaz, J.[21]; Eberl, T.[16]; Enghardt, W.[7]; Fabbietti, L.[16]; Fateev, O.[9]; Finocchiaro, P.[1]; Fonte, P. J. R.[3]; Fonte, P. J. R.[4]; Friese, J.[16]; Fröhlich, I.[10]; Galatyuk, T.[10]; Garzón, J. A.[20]; Gernhäuser, R.[16]; Gilardi, C.[11]; Golubeva, M.[14]; Gonzalez-Diaz, D.[6]; Grosse, E.[7]; Grosse, E.[8]; Gruber, F.[14]; Hadjivasiliou, C.[17]; Heilmann, M.[10]; Heinz, T.[6]; Hennino, T.[18]; Holzmann, R.[6]; Ierusalimov, A.[9]; Iori, I.[12]; Iori, I.[13]; Ivashkin, A.[14]; Jurkovic, M.[16]; Kajetanowicz, M.[5]; Kanaki, K.[7]; Karavicheva, T.[14]; Kirschner, D.[11]; Koenig, I.[6]; Koenig, W.[6]; Kolb, B. W.[6]; Kopf, U.[6]; Korcyl, K.[5]; Kotte, R.[7]; Krizek, F.[19]; Krücken, R.[16]; Kugler, A.[19]; Kurepin, A.[14]; Kämpfer, B.[7]; Kühn, W.[11]; Lamas-Valverde, J.[20]; Lang, S.[10]; Lange, S.[6]; Maier, L.[16]; Markert, J.[10]; Marín, J.[20]; Metag, V.[11]; Michalska, B.[5]; Mishra, D.[11]; Moriniere, E.[18]; Mousa, J.[17]; Münch, M.[6]; Müntz, C.[10]; Naumann, L.[7]; Novotny, R.[11]; Ott, W.[6]; Otwinowski, J.[5]; Pachmayer, Y. C.[10]; Palka, M.[5]; Parpottas, Y.[17]; Pechenov, V.[11]; Pietraszko, J.[6]; Pinhao, J. M. A.[3]; Przygoda, W.[5]; Pullia, A.[12]; Pullia, A.[13]; Pérez, T.[11]; Rabin, N.[15]; Ramstein, B.[18]; Razin, S.[9]; Reshetin, A.[14]; Riboldi, S.[12]; Ritman, J.[11]; Rosier, P.[18]; Roy-Stephan, M.[18]; Rustamov, A.[10]; Rustamov, A.[6]; Sadovsky, A.[7]; Sailer, B.[16]; Salabura, P.[5]; Schmah, A.[6]; Schroeder, C.[6]; Schwab, E,[6]; Simon, R.[6]; Smolyankin, V.[15]; Spataro, S.[1]; Spruck, B.[11]; Stroth, J.[10]; Stroth, J.[6]; Strbele, H.[10]; Sudol, M.[10]; Sudol, M.[6]; Tarantola, A.[11]; Teilab, K.[10]; Tiflov, T.[14]; Tlusty, P.[19]; Toneev, V.[9]; Traxler, M.[6]; Trebacz, R.[5]; Troyan, A.[9]; Tsertos, H.[17]; Veretenkin, I.[14]; Wagner, V.[19]; Wen, H.[11]; Wisniowski, M.[5]; Wojcik, T.[5]; Wüstenfeld, J.[7]; Yahlali, N.[21]; Zanevsky, Y.[9]; Zumbruch, P.[6]

1 Istituto Nazionale di Fisica Nucleare - Laboratori Nazionali del Sud, Catania (Italy)
2 Dipartimento di Fisica e Astronomia, Università di Catania, Catania (Italy)
3 LIP-Laboratório de Instrumentação e Física Experimental de Partículas, Departamento de Física da Universidade de Coimbra, Coimbra (Portugal)
4 ISEC, Coimbra (Protual)
5 Smoluchowski Institute of Physics, Jagiellonian University of Cracow, Cracow (Poland)
6 GSI Darmstadt (Germany)
7 Institut für Kern- und Hadronenphysik, Forschungszentrum Rossendorf, Dresden (Germany)
8 Technische Universität Dresden (Germany)
9 Joint Institute of Nuclear Research, Dubna (Russia)
10 Institut für Kernphysik, Johann Wolfgang Goethe-Universität, Frankfurt (Germany)
11 II. Physikalisches Institut, Justus Liebig Universität Gießen, Gießen (Germany)
12 Istituto Nazionale di Fisica Nucleare, Sezione di Milano, Milano (Italy)
13 Dipartimento di Fisica, Università di Milano, Milano (Italy)
14 Institute for Nuclear Research, Russian Academy of Science, Moscow (Russia)
15 Institute of Theoretical and Experimental Physics, Moscow (Russia)
16 Physik Department E12, Technische Universität München, Garching (Germany)
17 Department of Physics, University of Cyprus, Nicosia (Cyprus)
18 Institut de Physique Nucléaire d'Orsay, CNRS/IN2P3, Orsay Cedex (France)
19 Nuclear Physics Institute, Academy of Sciences of Czech Republic, Rez (Czech Republic)
20 Departamento de Fíisica de Partículas, University of Santiago de Compostela. Santiago de Compostela (Spain)
21 Instituto de Física Corpuscular, Universidad de Valencia-CSIC, Valencia (Spain)

Contributions in this report:
INSTRUMENTS-METHODS-18
INSTRUMENTS-METHODS-19
NQMA-EXPERIMENTS-05

The HADES RPC Group

HADES Resistive Plate Chambers
<http://mars.fis.uc.pt/rpc_en.shtml>
Spokesperson: Paulo Fonte, Universitaet Coimbra (Portugal)

Alvarez-Pol, H.[10]; Belver, D.[10]; Blanco, A. [1]; Capela, C.[8]; Carolino, N.[1]; Díaz, J.[11]; Ferreira Marques, R.[1]; Ferreira Marques, R.[2]; Fonte, P.[1]; Fonte, P.[5]; Garzón, J.[10]; Gil, A.[11]; Gil, D.[6]; González-Díaz, D.[10]; Kajetanowicz, M.[7]; Koenig, W.[3]; Kolb, B.[3]; Korcyl, K.[6]; Lamas-Valverde, J.[10]; Lange, J. S.[3]; Lopes, L.[1]; Marín, J.[9]; Montes, N.[10]; Neves, C.[8]; Palka, M.[6]; Pereira, A.[1]; Pietraszko, J.[3]; Salabura, P.[6]; Skott, S.[3]; Sousa, C.[8]; Ströbele, H.[4]; Stroth, J.[4]; Traxler, M.[3]; Trebacz, R.[6]; Vieira, M.[8]; Zapata, M.[10];

1 Laboratório de Instrumentaçõ e Física Experimental de Partículas (LIP), Universidade de Coimbra (Portugal)
2 Departamento de Física, Universidade de Coimbra (Portugal)
3 GSI Darmstadt (Germany)
4 Johann Wolfgang Goethe-Universität, Institut für Kernphysik, Frankfurt/M (Germany)
5 Instituto Superior de Engenharia de Coimbra (Portugal)
6 Instytut Fizyki, Wydział Fizyki, Astronomii i Informatyki Stosowanej,Uniwersytet Jagielloński, Kraków (Poland)
7 Nowoczesną Elektroniką, 30-109 Kraków (Poland)
8 Escola Superior de Tecnologia e Gestão de Leiria (Portugal)
9 CIEMAT, Madrid (Spain)
10 LabCAF, Departamento de Física de Partículas, Universidade Santiago de Compostela (Spain)
11 IFIC, Instituto de Física Corpuscular, Valencia (Spain)

Contributions in this report:
INSTRUMENTS-METHODS-19

The ILIAS Collaboration

Ion and Laser beam Interaction and Application Studies
Spokesperson: P. Mulser, Darmstadt (Germany)

Bock, R.[2]; Gericke, D. O.[7]; Gibbon, P.[6]; Maruhn, J.[3]; Mulser, P.[1]; Ruhl, H.[5]; Scheid, W.[4]; Schlegel, T.[2]

1 Technische Universität Darmstadt (Germany)
2 GSI Darmstadt (Germany)
3 Universität Frankfurt (Germany)
4 Universität Gießen (Germany)
5 Universität Bochum (Germany)
6 Forschungszentrum Jülich (Germany)
7 Universität Greifswald (Germany)

The LAND-FRS Collaboration

Large Area Neutron time of flight Detector – Fragment Separator
Spokesperson: T. Aumann, Darmstadt (Germany)

Adrich, P.[4]; Aksyutina, Y.[1]; Aumann, T.[1]; Boretzky, K.[1]; Chatillon, A.[1]; Cortina-Gil, D.[5]; Emling, H.[1]; Geissel, H.[1]; Ickert, G.[1]; Johansson, H.[1]; Kiselev, O.[2]; Klimkiewicz, A.[4]; Kratz, J. V.[2]; Kulessa, R.[4]; Le Bleis, T.[1]; Mahata, K.[1]; Müntz, C.[3]; Nociforo, C.[1]; Rossi, D.[2]; Simon, H.[1]; Stroth, J.[3]; Sümmerer, K.[1]; Walus, W.[4]; Weick, H.[1]; Wimmer, C.[3]

1 GSI Darmstadt (Germany)
2 Univ. Mainz (Germany)
3 Univ. Frankfurt (Germany)
4 Univ. Kraków (Poland)
5 Univ. Santiago de Compostela (Spain)

The RISING Collaboration

<http://www-linux.gsi.de/EB_at_GSI/index.html>
Spokesperson: H.-J. Wollersheim, GSI, Darmstadt (Germany)

Algora, A.[30]; Appelbe, D.E.[24]; Atanasova, L.[5]; Bürger, A.[22]; Balabanski, D.L.[12]; Banu, A.[1]; Bassini, R.[13]; Beck, T.[1]; Becker, F.[1]; Bednarczyk, P.[1]; Belier, G.[7]; Benlliure, J.[6]; Bentley, M.A.[21]; Benzoni, G.[13]; Blasi, N.[13]; Blazhev, A.[2]; Boiano, C.[13]; Bonnes, U.[32]; Brünle, A.[1]; Bracco, A.[13]; Brambilla, S.[13]; Bruce, A.M.[27]; Burkhard, K.-H.[1]; Butler, P.A.[25]; Caceres, L.[1]; Camera, F.[13]; Caserejos, E.[6]; Catford, W.N.[4]; Chamoli, S.K.[11]; Clark, R.M.[20]; Cortina Gil, D.[6]; Cullen, D.M.[19]; Curien, D.[31]; Damyanova, G.[5]; Daugas, J.M.[7]; Davidson, T.[26]; Detistov, P.[5]; Devin, J.[31]; Doornenbal, P.[1]; Faestermann, T.[28]; Fahlander, C.[23]; Fayz, K.[24]; Freeman, S.J.[19]; Górska, M.[1]; Gelletly, W.[4]; Georgiev, G.[18]; Gerl, J.[1]; Gladnishki, K.[12]; Goldring, G.[11]; Gręboszz, J.[14]; Grawe, H.[1]; Griffiths, R.[24]; Grzywacz, R.[1]; Hübel, H.[22]; Hammond, G.[21]; Hass, M.[11]; Hellström, M.[23]; Herzberg, R.D.[25]; Hoffman, J.[1]; Ilie, G.[2]; Ionescu-Bujor, M.[16]; Iordachescu, A.[16]; Jolie, J.[2]; Jungclaus, A.[17]; von Kalben, J.[32]; Kindler, B.[1]; Kmiecik, M.[14]; Kojouharov, I.[1]; Korgul, A.[15]; Krücken, R.[28]; Kulessa, M.[33]; Kurtukian Nieto, T.[6]; Kurz, N.[1]; Lach, M.[14]; Lazarus, I.[24]; Leoni, S.[13]; Leske, J.[22]; Liu, Z.[4]; Lo Bianco, G.[12]; Lommel, B.[1]; Münch, M.[1]; Münzenberg, G.[1]; Męczyński, W.[14]; Mach, H.[29]; Maj, A.[14]; Mallion, S.[3]; Mandal, S.[1]; Matea, I.[9]; Mazurek, K.[14]; Meot, V.[7]; Million, B.[13]; Mutterer, M.[32]; Nara Singh, B.S.[11]; Neyens, G.[3]; Nolan, P.[25]; Orlandi, R.[19]; Page, R.D.[25]; Petrache, C.[12]; Pfützner, M.[15]; Podolyak, Zs.[4]; Pucknell, V.F.E.[24]; Regan, P.H.[4]; Regev, I.[11]; Reiter, P.[2]; Richard, A.[2]; Roig, O.[7]; Rubio, A.[30]; Rudolph, D.[23]; Sümmerer, K.[1]; Saitoh, N.[1]; Saitoh, T.[1]; Saltarelli, A.[12]; Schaffner, H.[1]; Scherillo, A.[2]; Schwengner, R.[10]; Seddon, D.[25]; Simpson, G.[8]; Simpson, J.[24]; Smith, A.G.[19]; Speidel, K.-H.[22]; Stelzer, H.[1]; Striepling, T.[2]; Styczeń, J.[14]; Tsekhanovich, I.S.[8]; Turzo, K[3]; Vaintraub, S.[11]; Van Duppen, P.[3]; Vermeulen, N.[3]; Wadsworth, R.[21]; Walker, P.M.[4]; Warr, N.[2]; Weick, H.[1]; Wieland, O.[13]; Williams, S.[4]; Winkler, M.[1]; Wollersheim, H.-J.[1]; Woods, P.[26]; Zamfir, V.[16]

1 Gesellschaft für Schwerionenforschung, Darmstadt (Germany)
2 Institut für Kernphysik, Universität zu Köln, Cologne (Germany)
3 K.U. Leuven, Leuven (Belgium)
4 University of Surrey, Surrey (UK)
5 University of Sofia, Sofia (Bulgaria)
6 Universidad de Santiago de Compostela, Santiago de Compostela (Spain)
7 CEA, Bruyères le Chatel (France)
8 Ill, Grenoble (France)
9 CENBG, Bordeaux (France)
10 IKHP, Rossendorf (Germany)
11 Weizmann Institute of Science, Herovot (Israel)
12 University of Camerino, (Italy)
13 University of Milano, Milano (Italy)
14 IFJ PAN Krakow, Cracow (Poland)
15 Warsaw University, Warsaw (Poland)
16 NIPNE, Bucharest (Romania)
17 Universidad Autonomia de Madrid, Madrid (Spain)
18 ISOLDE-CERN, Geneva (Switzerland)
19 Manchester University, Manchester (UK)
20 Lawrence Berkely National Lab, Berkely (USA)
21 University of York, York (UK)
22 University of Bonn, Bonn (Germany)
23 University of Lund, Lund (Sweden)
24 CLRC, Daresbury (UK)
25 University of Liverpool, Liverpool (UK)
26 University of Edingburgh, Edingburgh (UK)
27 University of Brighton, Brighton (UK)
28 TU München, Munich (Germany)
29 Uppsala University, Uppsala (Sweden)
30 IFIC Valencia, Valencia (Spain)
31 IRES, Strasbourg (France)
32 TU Darmstadt, Darmstadt, (Germany)
33 Jagiellonian University, Cracow (Poland)

Contributions in this report:
NUSTAR-SPECTROSCOPY-03
NUSTAR-SPECTROSCOPY-04
NUSTAR-SPECTROSCOPY-05
NUSTAR-SPECTROSCOPY-06
NUSTAR-SPECTROSCOPY-07

The SHIP Collaboration

Separator for Heavy Ion reaction Products
<http:/www.gsi.de/forschung/kp/kp2/ship/>
Spokesperson: S. Hofmann, GSI

Ackermann, D. [1]; Andreyev, A. N. [5]; Antalic, S.[3]; Bianco, L.[4]; Block, M. [1]; Burkhard, H. G.[1]; Cullen, D.[9]; Darby, I.[4]; Van Duppen, P.[8]; Eremin, A. V.[2]; Franchoo, S.[10]; Gan, Z.[12]; Hartmann, W. [1]; Heinz, S.[1]; Heßberger, F. P.[1]; Hofmann, S.[1]; Huebner, A.[1]; Huyse, M.[8]; Kindler, B.[1]; Kojouharov, I.[1]; Kuusiniemi, P.[1]; Leino, M.[6]; Leppänen, A. P. [6]; Lommel, B.[1]; Mann, R.[1]; Münzenberg, G.[1]; Nishio, K.[11]; Page, R. D. [4]; Pakarinen, J.[6]; Popeko, A. G.[2]; Ressler, J. J. [7]; Saro, S.[3]; Schött, H. J.[1]; Steiner, J. [1]; Streicher, B.[3]; Sulignano, B.[1]; Thomson, J.[4]; Uusitalo, J.[6]

1 Gesellschaft für Schwerionenforschung, Darmstadt (Germany)
2 Joint Institute for Nuclear Research, Dubna (Russia)
3 Comenius University, Bratislava (Slovakia)
4 University of Liverpool, Liverpool (United Kingdom)
5 TRI-University Meson Facility (TRIUMF), Vancouver (Canada)
6 University of Jyväskylä, Jyväskylä (Finland)
7 Simon Fraser University, Burnaby BC (Canada)
8 University of Leuven, Leuven (Belgium)
9 University of Manchester, Manchester (United Kingdom)
10 Institut de Physique Nucléaire d'Orsay, Orsay (France)
11 Japan Atomic Energy Agency, Tokai (Japan)
12 Institute of Modern Physics, Lanzhou (China)

The SHIPTRAP Collaboration

<http://www.gsi.de/forschung/ap/projects/shiptrap/index.html>
Spokesperson: M. Block, Darmstadt (Germany)

Ackermann, D.[1]; Backe, H.[2]; Blaum, K.[2]; Block, M.[1]; Breitenfeld, M.[3]; Chaudhuri, A.[3]; Di, Z.[5]; Eliseev, S.[1]; Ferrer, R.[2]; Geissel, H.[5]; Habs, D.[4]; Heinz, S.[4]; Herfurth, F.[1]; Hessberger, F. P.[1]; Hofmann, S.[1]; Kluge, H.-J.[1]; Kolhinen, V.[4]; Kunz, P.[2]; Lauth, W.[2]; Martín, A.[1]; Marx, G. H.[3]; Mukherjee, M.[7]; Neumayr, J. B.[4]; Novikov, Y.[9]; Petrick, M.[5]; Plaß, W.[5]; Quint, W.[1]; Rahaman, S.[8]; Rauth, C.[1]; Rodriguez, D.[6]; Scheidenberger, C.[5]; Schweikhard, L.[3]; Sewtz, M[4]; Szerypo, J.[4]; Thirolf, P. G.[4]; Vorobjev, G.[1]; Wang, Z.[5]; Weber, C.[2]

1 Gesellschaft für Schwerionenforschung, Darmstadt
2 Institut für Physik, Johannes-Gutenberg-Universität, Mainz (Gerrmany)
3 Institut für Physik, Ernst-Moritz-Arndt-Universität, Greifswald (Germany)
4 Sektion Physik, Ludwig-Maximilians-Universität,Garching (Germany)
5 II. Physikalisches Institut, Justus-Liebig-Universität, Giessen (Germany)
6 LPC, ENSICAEN, Caen Cedex (France)
7 Universität Innsbruck, Innsbruck (Austria)
8 University of Jyväskylä, Jyväskylä (Finland)
9 PNPI RAS, Gatchina, Leningrad district (Russia)

Contributions in this report:
AP-EXP-SPECTROSCOPY-02
AP-EXP-SPECTROSCOPY-06
AP-METHODS-06
AP-METHODS-07

The TASCA Collaboration

Transactinide Separator and Chemistry Apparatus
<http://www.gsi.de/tasca/>
Spokesperson: M. Schädel, GSI

Ackermann, D.[1]; Brüchle, W.[1]; Dressler, R. [6]; Düllmann, C. E.[1]; Eberhardt, K. [5]; Eichler, R.[6]; Fästermann, T.[3]; Gäggeler, H. W.[6]; Gregorich, K. E.[8]; Jäger, E.[1]; Kindler, B.[1]; Kratz, J. V.[5]; Krücken, R. [3]; Kuusiniemi, O.[7]; Leino, M.[7]; Liebe, D. [5]; Lommel, B.[1]; Maier, H.-J. [4]; Mann, R.[1]; Omtvedt, J. P.[9]; Schädel, M.[1]; Schött, H.-J.[1]; Scholey, C.[7]; Semchenkov, A[1]; Semchenkov, A. [2]; Sudowe, R.[8]; Szerypo, J.[4]; Türler, A. [2]; Uusitalo, J.[7]; Wierczinski, B. [2]; Yakushev, A.[2]

1 GSI Darmstadt (Germany)
2 Institut für Radiochemie, Technische-Universität, Garching (Germany)
3 Institut für Experimentalphysik, Technische-Universität, Garching (Germany)
4 Sektion Physik, Ludwig-Maximilians-Universität, Garching (Germany)
5 Institut für Kernchemie, Joahnnes-Gutenberg-Universität,

Mainz (Germany)
6 Labor für Radio- und Umweltchemie, PSI, Villigen (Switzerland)
7 University of Jyväskylä (Finland)
8 Nuclear Science Division, LBNL, Berkeley (USA)
9 University of Oslo (Norway)

Contributions in this report:
INSTRUMENTS-METHODS-03
INSTRUMENTS-METHODS-04
INSTRUMENTS-METHODS-05
INSTRUMENTS-METHODS-06
NUSTAR-SHE-CHEM-08

Collaborations in the theoretical fields

The HGF Virtual Institute with German Universities 'Dense Hadronic Matter and QCD Phase Transitions'

<http://theory.gsi.de/Vir-Institute/>
Speakers: D. Rischke; D. Blaschke
Blaschke, D.[6]; Cassing, W.[5]; Friman, B.[4]; Fäßler, A.[7]; Karsch, F.[1]; Rischke, D.[3]; Wambach, J.[2]

1 University of Bielefeld (Germany)
2 University of Darmstadt (Germany)
3 University of Frankfurt (Germany)
4 GSI (Germany)
5 University of Gießen (Germany):
6 University of Rostock (Germany)

Other collaborations at external institutions

The ALICE Collaboration

A Large Ion Collider Experiment at CERN LHC
<http://alice.web.cern.ch/Alice/AliceNew/collaboration/>
The collaborations contains 27 countries, 83 institutes, and about 1000 members. Here only the participants of the GSI are listed.
Leader at the GSI: P. Braun-Munzinger

GSI Darmstadt (Germany)
Andronic, A.; Antonczyk, D.; Bailhache, R.; Beck, D.; Bercuci, A.; Brand, H.; Braun-Munzinger, P.; Busch, O.; Ciobanu, M.; Dahlinger, M.; Daues, H.; Foka, P.; Frankenfeld, U.; Garabatos, J. Gutbrod, H.; Lippmann, C.; Malzacher, P.; Marin, A.; Masciocchi, S.; Maunder, R.; Miskowiec, D.; Müller, W. F. J.; Prybyla, A.; Radomski, S.; Schmidt, C. J.; Schmidt, H. R.; Schwarz, K.; Sedykh, S.; Simon, R.; Soyk, D.; Stelzer, H.; Tsiledakis, G.; Vranic, D.
Contributions in this report:
FAIR-QCD-CBM-01
INSTRUMENTS-METHODS-24
INSTRUMENTS-METHODS-26
NQMA-05

The ALICE TRD Collaboration

The Transition Radiation Detector of the ALICE experiment at LHC
<http://www-alice.gsi.de/trd>
Project leader: J. Stachel, Heidelberg (Germany)

Adler, C.[6]; Aiftimiei, C.[2]; Amend, W.[5]; Andronic, A.[4]; Angelov, V.[7]; Appelshäuser, H.[5]; Bablok, S.[11]; Bailhache, R.[4]; Baumann, C.[9]; Blume, C.[5]; Braun-Munzinger, P.[4]; Bucher, D.[9]; Busch, O.[4]; Chepurnov, V.[3]; Chernenko, S.[3]; Christakoglou, P.[1]; Ciobanu, M.[4]; Conner, E. S.[11]; Cătănescu, V.[2]; de Cuveland, J.[7]; Dietel, T.[9]; Emschermann, D.[6]; Fateev, O.[3]; Freuen, S.[6]; Garabatos, C.[4]; Glasow, R.[9]; Glssel, P.[6]; Gottschalk, D.[7]; Gottschlag, H.[9]; Grosse-Oetringhaus, J. F.[9]; Gunji, T.[10]; Gutfleisch, M.[7]; Hamagaki, H.[10]; Hartig, M.[5]; Hartung, G.[8]; Hehner, J.[4]; Heine, N.[9]; Herrmann, N.[6]; Hinke, H.[5]; Hoppe, M.[9]; Höbbel, H.[7]; Kebschull, U.[7]; Keidel, R.[11]; Kessenbrock, M.[5]; Kislov, E.[3]; Kiworra, V.[7]; Klein-Bösing, C.[9]; Kliemant, M.[5]; Kofler, E.[11]; Kramer, F.[5]; Krawutschke, T.[8]; Legrand, I.[2]; Lindenstruth, V.[7]; Lippmann, C.[4]; Mahmoud, T.[6]; Malzacher, P.[4]; Marin, A.[4]; Mercado, J.[6]; Miskowiec, D.[4]; Moisă, D.[2]; Morino, Y.[10]; Oyama, K.[6]; Panebratsev, Y.[3]; Petridis, A.[1]; Petriş, M.[2]; Petrovici, M.[2]; Ploskon, M.[5]; Radomski, S.[4]; Radu, A.[2]; Reichling, C.[7]; Reygers, K.[9]; Rusanov, I.[6]; Saito, S.[10]; Sandoval, A.[4]; Santo, R.[9]; Schiaua, C.[2]; Schicker, R.[6]; Schmidt, C. J.[4]; Schneider, R.[7]; Schwarz, K.[4]; Shukla, P.[6]; Simion, V.[2]; Simon, R. S.[4]; Soltveit, H. K.[6]; Sommer, W.[5]; Stachel, J.[6]; Stelzer, H.[4]; Stockmeyer, M. R.[4]; Stoicea, G.[2]; Tilsner, H.[7]; Tsiledakis, G.[4]; Vassiliou, M.[1]; Verhoeven, W.[9]; Vulpescu, B.[6]; Wessels, J. P.[9]; Wilk, A.[9]; Windelband, B.[6]; Yurevich, V.[3]; Zanevsky, Y.[3]

1 University of Athens (Greece)
2 NIPNE Bucharest (Romania)
3 JINR Dubna (Russia)
4 GSI Darmstadt (Germany)
5 Institut für Kernphysik, University of Frankfurt (Germany)
6 Physikalisches Institut, University of Heidelberg (Germany)
7 Kirchhoff-Institut für Physik, University of Heidelberg (Germany)
8 Fachhochschule Köln (Germany)
9 Institut für Kernphysik, University of Münster (Germany)
10 University of Tokyo (Japan)
11 Fachhochschule Worms (Germany)

Contributions in this report:
INSTRUMENTS-METHODS-21 INSTRUMENTS-METHODS-22
INSTRUMENTS-METHODS-23
INSTRUMENTS-METHODS-25
INSTRUMENTS-METHODS-27
INSTRUMENTS-METHODS-28
NQMA-04
NQMA-EXPERIMENTS-16
NQMA-EXPERIMENTS-17

The BABAR Collaboration

<http://www.slac.stanford.edu/BFROOT>
Spokesperson: D. MacFarlane, Stanford Linear Accelerator Center, CA (USA)

Abe, T. [68]; Abrams, G. S.[6]; Adye, T.[65]; Ahmed, M. [70]; Ahmed, S. [70]; Alam, M. S. [70]; Albert, J. [20]; Aleksan, R. [66]; Allison, J. [42]; Allmendinger, T. [54]; Altenburg, D.[25]; Andreassen, R. [21]; Andreotti, M.[28]; Angelini, C.[60]; Anulli, F. [29]; Arnaud, N. [36]; Aston, D. [68]; Aubert, B.[1]; Azzolini, V.[28]; Baak, M.[52]; Back, J. J.[79]; Bailey, S. [31]; Baldini-Ferroli, R. [29]; Band, H. R. [80]; Banerjee, S. [78]; Barate, R.[1]; Bard, D. J. [27]; Barlow, N. R. [42]; Barlow, R. J. [42]; Barrett, M. [7]; Bartoldus, R. [68]; Batignani, G.[60]; Bauer, J. M. [48]; Beck, T. W.[19]; Behera, P. K. [58]; Bellini, F.[63]; Benayoun, M.[57]; Benelli, G. [54]; Berger, N. [68]; Bernard, D. [26]; Berryhill, J. W.[18]; Best, D. [14]; Bettarini, S.[60]; Bettoni, D.[28]; Bevan, A. J. [38]; Bhimji, W. [33]; Bhuyan, B. [78]; Bianchi, F.[74]; Biasini, M.[59]; Biesiada, J. [62]; Blanc, F. [22]; Blaylock, G. [44]; Blinov, A. E. [13]; Blinov, V. E. [13]; Bloom, P. [22]; Bomben, M.[75]; Bona, M.[74]; Bondioli, M. [14]; Bonneaud, G. R. [26]; Borgland, A. W.[6]; Bosisio, L.[75]; Boutigny, D.[1]; Bowerman, D. A. [33]; Boyarski, A. M. [68]; Boyd, J. T. [9]; Bozzi, C.[28]; Brandenburg, G. [31]; Brandt, T.[25]; Brau, J.[55]; Breon, A. B.[6]; Briand, H.[57]; Brose, J.[25]; Brown, C. L.[40]; Brown, C. M. [78]; Brown, D. [41]; Brown, D. N.[6]; Bruinsma, M. [14]; Brunet, S.[49]; Bucci, F.[60]; Buchanan, C.[15]; Buchmueller, O. L. [68]; Bugg, W. [71]; Bukin, A. D. [13]; Bulten, H.[52]; Buono, L. Del[57]; Burchat, P. R. [69]; Burke, J. P. [9]; Button-Shafer, J.[6]; Buzzo, A.[30]; Côté, D.[49]; Cahn, R. N.[6]; Calabrese, R.[28]; Calcaterra, A. [29]; Calderini, G.[60]; Campagnari, C.[18]; Capra, R.[30]; Carpinelli, M.[60]; Cartaro, C.[75]; Cavallo, N.[51]; Cavoto, G.[63]; Chaisanguanthum, K. S. [31]; Chao, M. [14]; Charles, E.[6]; Charles, M. J. [34]; Chauveau, J.[57]; Chavez, C. A. [38]; Chen, A. [23]; Chen, C. [43]; Chen, E. [20]; Chen, J. C. [4]; Chen, S. [22]; Chen, X. [80]; Cheng, B. [80]; Cheng, C. H.[37]; Chevalier, N. [9]; Christ, S. [64]; Cibinetto, G.[28]; Clark, P. J. [27]; Claus, R. [68]; Cochran, J. [35]; Colecchia, F.[56]; Coleman, J. P. [38]; Contri, R.[30]; Convery, M. R. [68]; Cormack, C. M. [39]; Cossutti, F.[75]; Cottingham, W. N. [9]; Couderc, F.[1]; Covarelli, R.[59]; Cowan, G.[40]; Cowan, R.[45]; Crawley, H. B. [35]; Cremaldi, L. [48]; Cristinziani, M. [68]; Cuhadar-Donszelmann, T.[10]; Cunha, A.[18]; D'Orazio, A.[63]; Dahmes, B.[18]; Dallapiccola, C. [44]; Danielson, N. [62]; Dasu, S. [80];

Datta, M. [80]; Dauncey, P. D. [33]; David, P.[57]; Davier, M. [36]; Davis, C. L.[41]; Day, C. T.[6]; De Groot, N.[65]; Dickopp, M.[25]; Dingfelder, J. C. [68]; Dittongo, S.[75]; Dong, D. [68]; Dorfan, J. [68]; Dorigo, A.[56]; Druzhinin, V. P. [13]; Dubitzky, R. S.[32]; Dubois-Felsmann, G. P. [20]; Dujmic, D. [68]; Dunwoodie, W. [68]; Dvoretskii, A. [20]; Eckhart, E. A. [23]; Eckmann, R. [72]; Edwards, A. J. [69]; Egede, U. [33]; Eichenbaum, A. M. [80]; Eigen, G. [5]; Eisner, A. M.[19]; Elmer, P. [62]; Emery, S. [66]; Ernst, J. A. [70]; Eschenburg, V. [48]; Eschrich, I. [14]; Eyges, V. [35]; Fabozzi, F. [51]; Faccini, R.[63]; Fan, S. [68]; Farbin, A. [43]; Feltresi, E.[25]; Ferrarotto, F.[63]; Ferroni, F.[63]; Field, R. C. [68]; Finocchiaro, G. [29]; Flacco, C. J.[19]; Flack, R. L.[40]; Flaecher, H. U.[40]; Flood, K. T.[80]; Ford, K. E. [7]; Ford, W. T. [22]; Forster, I. J. [38]; Forti, F.[60]; Fortin, D. [78]; Foulkes, S. D.[16]; Franek, B.[65]; Frey, R.[55]; Fritsch, M.[8]; Fry, J. R. [38]; Gabathuler, E. [38]; Gaidot, A. [66]; Gaillard, J. R. [33]; Galeazzi, F.[56]; Gallo, F.[74]; Gamba, D.[74]; Gamet, R. [38]; Gan, K. K. [54]; Ganzhur, S. F. [66]; Gary, J. W.[16]; Gaspero, M.[63]; Gatto, C.[51]; George, K. A. [38]; Gill, M. S.[6]; Gioi, L. Li[63]; Giorgi, M. A.[60]; Giraud, P.-F. [66]; Giroux, X. [36]; Gladney, L. [58]; Glanzman, T. [68]; Godang, R. [48]; Goetzen, K.[11]; Golubev, V. B. [13]; Gopal, G. P.[65]; Gowdy, S. J. [68]; Gradl, W. [27]; Graham, M. [80]; Grancagnolo, S.[75]; Grauges, E.[2]; Graziani, G. [66]; Green, M. G.[40]; Greene, M. G. [81]; Grenier, G. J. [34]; Grenier, P. [26]; Gritsan, A. V.[6]; Grosdidier, G. [36]; Groysman, Y.[6]; Guo, Q. H. [58]; Höcker, A. [36]; Hadavand, H. K.[17]; Hadig, T. [68]; Haire, M. [61]; Halyo, V. [68]; Hamano, K. [78]; Hamel de Monchenault, G. [66]; Hamon, O.[57]; Harrison, P. F.[79]; Harrison, T. J. [7]; Hart, A. J. [7]; Hartfiel, B. L.[15]; Harton, J. L. [23]; Hast, C. [68]; Hauke, A.[25]; Hawkes, C. M. [7]; Hearty, C.[10]; Held, T.[8]; Hertzbach, S. S. [44]; Heusch, C. A.[19]; Hill, E. J.[17]; Hitlin, D. G. [20]; Hodgkinson, M. C. [42]; Hollar, J. J. [80]; Hong, T. M.[18]; Honscheid, K. [54]; Hryn'ova, T. [68]; Hufnagel, D. [54]; Hulsbergen, W. D. [43]; Hutchcroft, D. E. [38]; Igonkina, O.[55]; Innes, W. R. [68]; Ivanchenko, V. N. [13]; Izen, J. M. [73]; Jackson, P. D. [54]; Jackson, P. S.[40]; Jacobsen, R. G.[6]; Jawahery, A. [43]; Jayatilleke, S. [21]; Jessop, C. P. [53]; John, M. J. J.[57]; Johnson, J. R. [80]; Judd, D. [61]; Kadel, R. W.[6]; Kadyk, J.[6]; Kagan, H. [54]; Karyotakis, Y.[1]; Kass, R. [54]; Kelly, M. P.[9]; Kelsey, M. H. [68]; Kerth, L. T.[6]; Khan, A. [12]; Kim, H. [46]; Kim, P. [68]; Kirkby, D. [14]; Kitayama, I. [73]; Klose, V.[25]; Knecht, N. S.[10]; Koch, H.[8]; Kocian, M. L. [68]; Koeneke, K.[45]; Kofler, R. [44]; Kolomensky, G.[6]; Koptchev, V. B. [44]; Kovalskyi, D. [43]; Kowalewski, R. [78]; Kozanecki, W. [66]; Kravchenko, E. A. [13]; Krishnamurthy, M. [71]; Kroeger, R. [48]; Kroseberg, J.[19]; Kukartsev, G.[6]; Kutter, P. E. [80]; Kyberd, P. [12]; Lacker, H. M.[25]; Lae, C. K. [43]; Lafferty, G. D. [42]; Lanceri, L.[75]; Lange, D. J.[37]; Langenegger, U.[32]; Lankford, A. J. [14]; Latham, T. E.[79]; Lau, Y. P. [62]; Lazzaro, A.[47]; Le Diberder, F. [36]; Lees, J. P.[1]; Legendre, M. [66]; Leith, D. W. G. S. [68]; Lepeltier, V. [36]; Lewandowski, B.[11]; Li, H. [80]; Libby, J. [68]; Lillard, V. [43]; Lista, L.[51]; Liu, R. [80]; LoSecco, J. M.[53]; Lockman, W. S.[19]; Lodovico, F. Di[39]; Lombardo, V.[47]; London, G. W. [66]; Long, O.[16]; Lou, X. C. [73]; Lu, A.[18]; Lu, C. [62]; Lu, M.[55]; Luitz, S. [68]; Luppi, E.[28]; Lusiani, A.[60]; Luth, V. [68]; Lutz, A. M. [36]; Lynch, G.[6]; Lynch, H. L. [68]; MacFarlane, D. B.[17]; Macri, M.[30]; Majewski, S. A. [69]; Malclès, J.[57]; Mallik, U. [34]; Maly, E.[25]; Mancinelli, G. [21]; Mandelkern, M. [14]; Marchiori, G.[60]; Marco, E. Di[63]; Margoni, M.[56]; Marks, J.[32]; Marsiske, H. [68]; Martinez-Vidal, F.[76]; Mattison, T. S.[10]; Mayer, B. [66]; Mazur, M. A.[18]; Mazzoni, M. A.[63]; McKenna, J. A.[10]; McMahon, T. R.[40]; Meadows, B. T. [21]; Mellado, B. [80]; Messner, R. [68]; Meyer, W. T. [35]; Mihalyi, A. [80]; Mir, L. M.[6]; Mohanty, G. B.[79]; Mohapatra, A. K.[34]; Mommsen, R. K. [14]; Monge, M. R.[30]; Monorchio, D.[51]; Moore, T. B. [44]; Morandin, M.[56]; Morgan, S. E. [7]; Morganti, M.[60]; Morganti, S.[63]; Morii, M. [31]; Morton, G. W. [33]; Muheim, F. [27]; Muller, D. R. [68]; Naisbit, M. T. [42]; Nardo, G. De[51]; Narsky, I. [20]; Nash, J. A. [33]; Nauenberg, U. [22]; Neal, H.[81]; Negrini, M.[28]; Neri, N.[60]; Nesom, G.[19]; Nicholson, H.[50]; Nikolich, M. B. [33]; Nogowski, R.[25]; O'Grady, C. P. [68]; Ocariz, J.[57]; Oddone, P. J.[6]; Ofte, I. [5]; Olaiya, E. O.[65]; Olivas, A. [22]; Olsen, J. [62]; Onuchin, A. P. [13]; Orimoto, T. J.[6]; Otto, S.[25]; Ozcan, V. E. [68]; Paar, H. P.[17]; Paick, K. [61]; Palano, A.[3]; Palombo, F.[47]; Pan, Y. [80]; Panetta, J.[58]; Panvini, R. S.[77]; Paoloni, E.[60]; Paolucci, P.[51]; Pappagallo, M.[3]; Parry, R. J. [38]; Passaggio, S.[30]; Patel, P. M. [46]; Patrignani, C.[30]; Patteri, P. [29]; Payne, D. J. [38]; Pelizaeus, M.[8]; Perazzo, A. [68]; Perl, M. [68]; Peruzzi, I. M. [29]; Peters, K.[11]; Petersen, B. A. [69]; Petersen, T. C. [36]; Petzold, A.[25]; Piatenko, T. [20]; Piccolo, D.[51]; Piccolo, M. [29]; Piemontese, L.[28]; Pierini, M. [36]; Pioppi, M.[59]; Piredda, G.[63]; Plaszczynski, S. [36]; Playfer, S. [27]; Poireau, V.[1]; Polci, F.[63]; Pompili, A.[3]; Poropat, P.[75]; Porter, F. C. [20]; Posocco, M.[56]; Potter, C. T.[55]; Prell, S. [35]; Prepost, R. [80]; Pripstein, M.[6]; Pulliam, T. [54]; Purohit, M. V. [67]; Qi, N. D. [4]; Rahatlou, S.[17]; Rahimi, A. M. [54]; Rama, M.[60]; Rankin, P. [22]; Ratcliff, B. N. [68]; Raven, G.[52]; Re, D. del[17]; Reidy, J. [48]; Ricca, G. Della[75]; Ricciardi, S.[40]; Richman, J. D.[18]; Ritchie, J. L. [72]; Rizzo, G.[60]; Roat, C.[69]; Roberts, D. A.[43]; Robertson, S. H.[46]; Robutti, E.[30]; Rodier, S. [36]; Roe, N. A.[6]; Roethel, W. [14]; Ronan, M. T.[6]; Roney, J. M. [78]; Rong, G. [4]; Roodman, A. [68]; Roos, L.[57]; Rosenberg, E. I. [35]; Rotondo, M.[56]; Roudeau, P. [36]; Rubin, A. E. [35]; Ruddick, W. O. [22]; Ryd, A. [20]; Saeed, M. A. [70]; Safai Tehrani, F.[63]; Saleem, M. [70]; Salnikov, A. A. [68]; Salvatore, F.[40]; Samuel, A. [20]; Sanders, D. A. [48]; Sangro, R. de [29]; Santroni, A.[30]; Saremi, S. [44]; Sarti, A.[28]; Satpathy, A. [72]; Schalk, T.[19]; Schenk, S.[32]; Schindler, R. H. [68]; Schott, G.[25]; Schröder, H. [64]; Schrenk, S. [26]; Schroeder, T.[8]; Schubert, J.[25]; Schubert, K. R.[25]; Schumm, B. A.[19]; Schune, M. H. [36]; Schwiening, J. [68]; Schwierz, R.[25]; Schwitters, R. F.[72]; Sciacca, C.[51]; Sciolla, G.[45]; Seiden, A.[19]; Sekula, S. J.[45]; Serednyakov, S. I. [13]; Sharma, V.[17]; Shen, B. C.[16]; Simani, M. C.[37]; Simi, G.[60]; Simonetto, F.[56]; Sinev, N. B.[55]; Skovpen, I. [13]; Smith, A. J. S. [62]; Smith, J. G. [22]; Snoek, H. L.[52]; Snyder, A. [68]; Sobie, R. J.[78]; Soffer, A. [23]; Soha, A. [68]; Sokoloff, M. D.[21]; Solodov, E. P. [13]; Spaan, B.[24]; Spanier, S. M.[71]; Spradlin, P.[19]; Staengle, H. [44]; Steinke, M.[8]; Stelzer, J. [68]; Stocchi, A. [36]; Stoker, D. P.[14]; Stroili, R.[56]; Strom, D.[55]; Strube, J. [68]; Stugu, B.[5]; Su, D. [68]; Sullivan, M. K. [68]; Summers, D. J. [48]; Sundermann, J. E.[25]; Suzuki, K. [68]; Tan, P. [80]; Taras, P.[49]; Taylor, F.[45]; Taylor, G. P.[33]; Telnov, A. V.[62]; Teodorescu, L.[12]; Ter-Antonyan, R. [54]; Therin, G.[57]; Thiebaux, C. [26]; Thiessen, D.[10]; Tisserand, V.[1]; Toki, W. H. [23]; Torrence, E.[55]; Tosi, S.[30]; Touramanis, C.[38]; Ulmer, K. A. [22]; Uwer, U.[32]; Va'vra, J. [68]; Vasileiadis, G. [26]; Vasseur, G. [66]; Verderi, M.[26]; Verkerke, W.[18]; Vetere, M. Lo[30]; Viaud, B.[49]; Vitale, L.[75]; Voci, C.[56]; Voena, C.[63]; Vuagnin, G.[75]; Wagner, G. [64]; Wagner, S. R. [68]; Wagoner, D. E.[61]; Waldi, R.[64]; Walsh, J.[60]; Wang, K.[16]; Wang, P. [4]; Wappler, F. R.[70]; Watson, A. T.[7]; Weaver, M. [68]; Weidemann, A. W. [67]; Weinstein, A. J. R.[15]; Wenzel, W. A.[6]; Wilden, L.[52]; Williams, D. C.[19]; Williams, J. C.[42]; Willocq, S.[44]; Wilson, F. F.[65]; Wilson, J. R. [67]; Wilson, M. G.[19]; Wilson, R. J. [23]; Wisniewski, W. J. [68]; Wittgen, M. [68]; Won, E.[31]; Wong, Q. K.[54]; Wormser, G.[36]; Wright, D. H. [68]; Wright, D. M.[37]; Wu, J. [80]; Wu, S. L. [80]; Xie, Y.[27]; Yèche, C. [66]; Yamamoto, R. K.[45]; Yang, S.[20]; Yarritu, A. K. [68]; Ye, S.[73]; Yi, J.[35]; Young, C. C.[68]; Yu, Z.[80]; Yumiceva, F. X.[67]; Yushkov, A. N.[13]; Zallo, A.[29]; Zeng, Q.[23]; Zghiche, A.[1]; Zhang, J.[22]; Zhang, L.[16]; Zhao, H. W.[48]; Zhu, Y. S.[4]; Zito, M.[66]; von Wimmersperg-Toeller, J. H. [80]

1 Laboratoire de Physique des Particules, Annecy-le-Vieux (France)
2 IFAE, Universitat Autonoma de Barcelona, Bellaterra, Barcelona (Spain)
3 Università di Bari, Dipartimento di Fisica and INFN, Bari (Italy)
4 Institute of High Energy Physics, Beijing (China)
5 University of Bergen, Inst. of Physics, Bergen (Norway)
6 Lawrence Berkeley National Laboratory and University of California, Berkeley California (USA)
7 University of Birmingham, Birmingham (United Kingdom)
8 Ruhr Universität Bochum, Institut für Experimentalphysik 1, Bochum (Germany)
9 University of Bristol, Bristol (United Kingdom)
10 University of British Columbia, Vancouver, British Columbia (Canada)
11 Gesellschaft für Schwerionenforschung, Darmstadt (Germany)
12 Brunel University, Uxbridge, Middlesex (United Kingdom)
13 Budker Institute of Nuclear Physics, Novosibirsk (Russia)
14 University of California at Irvine, Irvine, California (USA)
15 University of California at Los Angeles, Los Angeles California (USA)
16 University of California at Riverside, Riverside California (USA)
17 University of California at San Diego, La Jolla California (USA)
18 University of California at Santa Barbara, Santa Barbara California (USA)
19 University of California at Santa Cruz, Institute for Particle Physics, Santa Cruz California (USA)
20 California Institute of Technology, Pasadena California (USA)
21 University of Cincinnati, Cincinnati Ohio (USA)
22 University of Colorado, Boulder, Colorado (USA)
23 Colorado State University, Fort Collins Colorado (USA)
24 Universität Dortmund, Institut fur Physik, Dortmund (Germany)
25 Technische Universität Dresden, Institut für Kern- und Teilchenphysik, Dresden (Germany)
26 Ecole Polytechnique, LLR, Palaiseau (France)
27 University of Edinburgh, Edinburgh (United Kingdom)
28 Università di Ferrara, Dipartimento di Fisica and INFN, Ferrara (Italy)
29 Laboratori Nazionali di Frascati dell'INFN, Frascati (Italy)
30 Università di Genova, Dipartimento di Fisica and INFN, Genova (Italy)
31 Harvard University, Cambridge Massachusetts (USA)
32 Universität Heidelberg, Physikalisches Institut, Heidelberg (Germany)
33 Imperial College London, London (United Kingdom)
34 University of Iowa, Iowa City Iowa (USA)
35 Iowa State University, Ames Iowa (USA)
36 Laboratoire de l'Accélérateur Linéaire, Orsay (France)
37 Lawrence Livermore National Laboratory, Livermore California (USA)
38 University of Liverpool, Liverpool (United Kingdom)
39 Queen Mary, University of London, London (United Kingdom)
40 University of London, Royal Holloway and Bedford New College, Egham, Surrey (United Kingdom)
41 University of Louisville, Louisville Kentucky (USA)
42 University of Manchester, Manchester (United Kingdom)
43 University of Maryland, College Park, Maryland (USA)
44 University of Massachusetts, Amherst Massachusetts (USA9
45 Massachusetts Institute of Technology, Laboratory for Nuclear Science, Cambridge Massachusetts (USA)
46 McGill University, Montréal, Quebec (Canada)
47 Università di Milano, Dipartimento di Fisica and INFN, Milano (Italy)
48 University of Mississippi, University, Mississippi (USA)
49 Université de Montréal, Laboratoire René J. A. Lévesque, Montréal, Quebec (Canada)
50 Mount Holyoke College, South Hadley Massachusetts (USA)
51 Università di Napoli Federico II, Dipartimento di Scienze Fisiche and INFN, Napoli (Italy)
52 NIKHEF, National Institute for Nuclear Physics and High Energy Physics, Amsterdam (Netherlands)
53 University of Notre Dame, Notre Dame Indiana (USA)
54 Ohio State University, Columbus Ohio (USA)
55 University of Oregon, Eugene Oregon (USA)
56 Università di Padova, Dipartimento di Fisica and INFN, Padova (Italy)
57 Universités Paris VI et VII, Laboratoire de Physique Nucléaire et de Hautes Energies, Paris (France)
58 University of Pennsylvania, Philadelphia Pennsylvania (USA9
59 Università di Perugia, Dipartimento di Fisica and INFN, Perugia (Italy)
60 Università di Pisa, Dipartimento di Fisica, Scuola Normale Superiore and INFN, Pisa (Italy)
61 Prairie View A&M University, Prairie View Texas (USA)
62 Princeton University, Princeton New Jersey (USA)
63 Università di Roma La Sapienza, Dipartimento di Fisica and INFN, Roma (Italy)
64 Universität Rostock, Rostock (Germany)
65 Rutherford Appleton Laboratory, Chilton, Didcot, Oxon (United Kingdom)
66 DSM/Dapnia, CEA/Saclay, Gif-sur-Yvette (France)
67 University of South Carolina, Columbia South Carolina (USA)
68 Stanford Linear Accelerator Center, Stanford California (USA)
69 Stanford University, Stanford California (USA)
70 State University of New York, Albany New York (USA)
71 University of Tennessee, Knoxville Tennessee (USA)
72 University of Texas at Austin, Austin Texas (USA)
73 University of Texas at Dallas, Richardson Texas (USA)
74 Università di Torino, Dipartimento di Fisica Sperimentale and INFN, Torino (Italy)
75 Università di Trieste, Dipartimento di Fisica and INFN, Trieste (Italy)
76 IFIC, Universitat de Valencia-CSIC, Valencia (Spain)
77 Vanderbilt University, Nashville Tennessee (USA)
78 University of Victoria, Victoria, British Columbia (Canada)
79 Department of Physics, University of Warwick, Coventry (United Kingdom)
80 University of Wisconsin, Madison Wisconsin (USA)
81 Yale University, New Haven Connecticut (USA)

The CERES Collaboration

Cherenkov Ring Electron Pair Spectrometer at the CERN SPS

<http://www.physi.uni-heidelberg.de/physi/ceres/>
Spokesperson: J. Stachel, Heidelberg (Germany)

Adamová, D.[7]; Agakichiev, G.[3]; Andronic, A.[3]; Antończyk, D.[3]; Appelshäuser, H.[4]; Belaga, V.[5]; Bielčíková, J.[4,6]; Braun-Munzinger, P.[3]; Busch, O[3]; Campagnolo, R.[4]; Cherlin, A.[9]; Damjanović, S.[4]; Dietel, T.[4]; Dietrich, L.[4]; Drees, A.[8]; Esumi, S. I.[4]; Filimonov, K.[4]; Fomenko, K.[5]; Fraenkel, Z.[9]; Garabatos, C.[3]; Glässel, P.[4]; Holeczek, J.[3]; Kalisky, M.[3]; Kniege, S.[10]; Kushpil, V. [7]; Ludolphs, W.[4]; Manafov, A.[3]; Marín, A.[3]; Milošević, J.[4]; Miśkowiec, D.[3]; Musa, L.[2]; Ortega, R.[4]; Panebrattsev, Y.[5]; Petchenova, O.[5]; Petráček, V.[4]; Płoskoń, M.[10]; Radomski, S.[3]; Rak, J.[3]; Ravinovich, I.[9]; Rehak, P.[1]; Sako, H.[3]; Schmitz, W.[4]; Schukraft, J.[2]; Sedykh, S.[3]; Seipp, W.[4]; Shimansky, S.[5]; Soualah, r.[4]; Stachel, J.[4]; Tilsner, H.[4]; Tserruya, I.[9]; Tsiledakis, G.[3]; Wessels, J. P.[4]; Wiemold, T.[4]; Windelband, B.[4]; Wurm, J. P.[6]; Xie, W.[9]; Yurevich, S.[4]; Yurevich, V.[5]; Šumbera, M.[7];

1 BNL, Upton (U.S.A.)
2 CERN, Geneva (Switzerland)
3 GSI Darmstadt, (Germany)
4 Heidelberg University (Germany)
5 JINR Dubna (Russia)
6 MPI, Heidelberg (Germany)
7 NPI ASCR, Řež (Czech Republic)
8 SUNY at Stony Brook (U.S.A.)
9 Weizmann Institute, Rehovot (Israel)
10 Frankfurt University (Germany)

Contributions in this report:
NQMA-EXPERIMENTS-11
NQMA-EXPERIMENTS-13
NQMA-EXPERIMENTS-14
NQMA-EXPERIMENTS-15

The NA49 Collaboration

Large Acceptance Hadron Detector for an Investigation of Pb-induced Reactions at the CERN SPS
<http://na49info.cern.ch/>
Spokesperson: P. Seyboth

Alt, C.[9]; Anticic, T.[21]; Baatar, B.[8]; Barna, D.[4]; Bartke, J.[6]; Betev, L.[10]; Białkowska, H.[19]; Blume, C.[9]; Boimska, B.[19]; Botje, M.[1]; Bracinik, J.[3]; Bramm, R.[9]; Bunčić, P.[10]; Cerny, V.[3]; Christakoglou, P.[2]; Chvala, O.[14]; Cramer, J. G.[16]; Csató, P.[4]; Dinkelaker, P.[9]; Eckardt, V.[13]; Flierl, D.[9]; Fodor, Z.[4]; Foka, P.[7]; Friese, V.[7]; Gál, J.[4]; Gaździcki, M.[11]; Gaździcki, M.[9]; Genchev, V.[18]; Georgopoulos, G.[2]; Grebieszkow, K.[20]; Gładysz, E.[6]; Höhne, C.[7]; Hegyi, S.[4]; Kadija, K.[21]; Karev, A.[13]; Kliemant, M.[9]; Kniege, S.[9]; Kolesnikov, V. I.[8]; Kornas, E.[6]; Korus, R.[11]; Kowalski, M.[6]; Kraus, I.[7]; Kreps, M.[3]; Lévai, P.[4]; Laszlo, A.[4]; Litov, L.[17]; Lungwitz, B.[9]; Makariev, M.[17]; Malakhov, A. I.[8]; Mateev, M.[17]; Melkumov, G. L.[8]; Mischke, A.[1]; Mitrovski, M.[9]; Molnár, J.[4]; Mrówczyński, St.[11]; Nicolic, V.[21]; Pühlhofer, F.[12]; Pálla, G.[4]; Panagiotou, A. D.[2]; Panayotov, D.[17]; Petridis, A.[2]; Pikna, M.[3]; Prindle, D.[16]; Renfordt, R.[9]; Roland, C.[5]; Roland, G.[5]; Rybczyński, M.[11]; Rybicki, A.[10]; Rybicki, A.[6]; Sandoval, A.[7]; Schmitz, N.[13]; Schuster, T.[9]; Seyboth, P.[13]; Siklér, F.[4]; Sitar, B.[3]; Skrzypczak, E.[20]; Stefanek, G.[11]; Stock, R.[9]; Ströbele, H.[9]; Strabel, C.[9]; Susa, T.[21]; Szentpétery, I.[4]; Sziklai, J.[4]; Szymanski, P.[10]; Szymanski, P.[19]; Trubnikov, V.[19]; Varga, D.[10]; Varga, D.[4]; Vassiliou, M.[2]; Veres, G. I.[4]; Veres, G. I.[5]; Vesztergombi, G.[4]; Vranić, D.[7]; Wetzler, A.[9]; Włodarczyk, Z.[11]; Yoo, I. K.[15]; Zimányi, J.[4]

1 NIKHEF, Amsterdam (Netherlands)
2 Department of Physics, University of Athens, Athens (Greece)
3 Comenius University, Bratislava (Slovakia)
4 KFKI Research Institute for Particle and Nuclear Physics, Budapest (Hungary)
5 MIT, Cambridge (USA)
6 Institute of Nuclear Physics, Cracow (Poland)
7 GSI, Darmstadt (Germany)
8 Joint Institute for Nuclear Research, Dubna (Russia)
9 Fachbereich Physik der Universität, Frankfurt (Germany)
10 CERN, Geneva (Switzerland)
11 Institute of Physics Świ etokrzyska Academy, Kielce (Poland)
12 Fachbereich Physik der Universität, Marburg (Germany)
13 Max-Planck-Institut für Physik, Munich (Germany)
14 Institute of Particle and Nuclear Physics, Charles University, Prague (Czech
15 Department of Physics, Pusan National University, Pusan (Republic of Korea)
16 Nuclear Physics Laboratory, University of Washington, Seattle, WA (USA)
17 Atomic Physics Department, Sofia University St. Kliment Ohridski, Sofia (Bulgaria)
18 Institute for Nuclear Research and Nuclear Energy, Sofia (Bulgaria)
19 Institute for Nuclear Studies, Warsaw (Poland)
20 Institute for Experimental Physics, University of Warsaw, Warsaw (Poland)

Contributions in this report:
NQMA-EXPERIMENTS-09
NQMA-EXPERIMENTS-10
NQMA-EXPERIMENTS-12

The RD42 Collaboration

Development of Diamond Tracking Detectors for High Luminosity Experiments at the LHC RD42
<http://rd42.web.cern.ch/RD42/>
Spokespersons: H. Kagan Ohio (USA), P. Weilhammer Geneva (Switzerland)

Adam, W.[1]; Berdermann, E.[2]; Bergonzo, P.[3]; de Boer, W.[4]; Bogani, F.[5]; Borchi, E.[6]; Brambilla, A.[3]; Bruzzi, M.[6]; Colledani, C.[7]; Conway, J.[8]; D'Angelo, P.[9]; Dabrowski, W.[10]; Delpierre, P.[12]; Doroshenko, J.[8]; Dulinski, W.[7]; van Eijk, B.[13]; Fallou, A.[12]; Fischer, P.[22]; Fizotti, F.[15]; Furetta, C.[3]; Gan, K. K.[16]; Ghodbane, N.[12]; Grigoriev, E.[4]; Hallewell, G.[12]; Han, S.[16]; Hartjes, F.[13]; Hrubec, J.[1]; Husson, D.[7]; Kagan, H.[16]; Kaplon, J.[17]; Kass, R.[16]; Keil, M.[14]; Knöpfle, K. T.[18]; Koeth, T.[8]; Krammer, M.[1]; Logiudice, A.[15]; Lu, R.[15]; mac Lynne, L.[8]; Manfredotti, C.[15]; Meier, D.[17]; Menichelli, D.[6]; Meuser, S.[14]; Mishina, M.[19]; Moroni, L.[9]; Noomen, J.[13]; Oh, A.[17]; Perera, L.[8]; Pernicka, M.[1]; Potenza, R.[23]; Riester, J. L.[7]; Roe, S.[17]; Rudge, A.[17]; Sala, J. S.[9]; Sampietro, M.[20]; Schnetzer, S.[8]; Sciortino, S.[6]; Stelzer, H.[2]; Stone, R.[8]; Sucera, C.[23]; Trishuk, W.[21]; Tromson, D.[3]; Tuve, C.[24]; Vincenzo, B.[23]; Weilhammer, P.[17]; Wermes, N.[14]; Wetstein, M.[7]; Zeuner, W.[11]; Zoeller, M.[16]

1 HEPHY, Vienna (Austria)
2 GSI, Darmstadt (Germany)
3 LIST CEA Saclay, Paris (France)
4 Inst. Exp. Kernphysik, Karlsruhe (Germany)
5 LENS, Florence (Italy)
6 Univ. of Florence, Florence (Italy)
7 LEPSI, IN2P3/CNRS-ULP, Strassbourg (France)
8 Rutgers University, New York (USA)
9 INFN, Milano (Italy)
10 UMM, Cracow (Poland)
11 II. Inst. für Exp. Physik, Hamburg (Germany)
12 CPPM, Marseille (France)
13 NIKHEF, Amsterdam (Netherlands)
14 Universität Bonn, Bonn (Germany)
15 Univ. of Torino Torino (Italy)
16 The Ohio State Univ., Columbus (USA)
17 CERN, Geneva (Switzerland)
18 MPI für Kernphysik, Heidelberg (Germany)
19 FNAL, Batavia (USA)
20 Polytechnico di Milano, Milano (Italy)
21 Univ. of Toronto Toronto (Canada)
22 Universität Mannheim, Mannheim (Germany)
23 University of Roma (Italy)
24 University of Catania (Italy)

The WA98 Collaboration

Large Acceptance Photon and Hadron Spectrometer
<http://wa98.web.cern.ch/WA98/>
Spokesperson: T. C. Awes (USA)
The collaboration contains serveral participating institutes. Here are only listed the members from the GSI.

GSI Darmstadt (Germany)
Gutbrod, H. H.; Kolb, B. W.; Schmidt, H. -R.

EU projects at GSI

R. Simon, M. Pantea, K. Große, GSI, Darmstadt, Germany

FAIR Design Study 'DIRACsecondary-Beams'/FP6 (515873)
<http://www.gsi.de/fair/EU-Design-Study/index.html>
Coordinator: GSI, Darmstadt (Germany)
Project coordinator: J. Eschke
Steering committee: J. Eschke (GSI, chair), H. H. Gutbrod (GSI), W. F. Henning (GSI), P. Gianotti (Frascati), R. Krücken (München), R. Maier (FZJ), B. Franzke (GSI), H. Eickhoff (GSI)
Contact at GSI: J. Eschke, K. Berghöfer

T1: Management – Management of Design Study, Spokesperson: J. Eschke (GSI)
T2: PANDA1 – Cherenkov Imaging Detectors, Spokesperson: C. Schwarz (GSI)
T3: PANDA2 – Silicon Microvertex Detector, Spokesperson: K.-T. Brinkmann (Dresden)
T4: PANDA3 – Magnet and detector integration, Spokesperson: G. Rosner (Glasgow)
T5: PANDA4 – Physics Performance, Spokesperson: B. Kopf (Univ. Bochum)
T6: NUSTAR1 – High-power production targets for fast extracted high-intensity primary beams, Spokesperson: K. Sümmerer (GSI)
T7: NUSTAR2 – Radiation-resistant large-aperture superferric dipole magnet, Spokesperson: G. Moritz (GSI)
T8: NUSTAR3 – Large-area beam tracking detectors for fast extracted beams, Spokesperson: B. Sitar (CUB)
T9: NUSTAR4 – Ion-optical design studies and application, Spokesperson: W. Plass (JLU-PHYSII)
T10: NUSTAR5 – Design of a superfluid-helium stopping cell, Spokesperson: J. Äysto (JYU)
T11: HESR1 – RF cavity (CAV), Spokesperson: A. Schnase (FZJ)
T12: HESR2 – Electron Cooling (EC), Spokesperson: D. Reistad (Uppsala)
T13: HESR3 – Stochastic Cooling (SC), Spokesperson: H. Stockhorst (FZJ)
T14: HESR4 – Beam Dynamics and Collective Effects (BD), Spokesperson: O. Boine-Frankenheim (GSI)
T15: COOLSB1 – Fast stochastic cooling of secondary beams, Spokesperson: F. Nolden (GSI)
T16: COOLSB2 – Ramped super-ferric dipole magnet for NESR, Spokesperson: G. Moritz (GSI)
T17: SIS100_1 – ERDA measurements, Spokesperson: H. Kollmus (GSI)
T18: SIS100_2 – Longitudinal feed back system, Spokesperson: H. Klingbeil (GSI)
T19: SIS100_3 – Fast high power switches for rf gaps, Spokesperson: P. Hülsmann (GSI)
T20: SIS100_4 – High current beam dynamics studies, Spokesperson: O. Boine- Frankenheim (TUD)
T20: SIS100_5 – Digital signal analysis electronics for BPMs, Spokesperson: U. Raich (CERN)
T20: SIS100_6 – Fast ramped superconducting magnets, Spokesperson: G. Moritz (GSI)

Contributions in this report:
FAIR-ACC-08
FAIR-ACC-11
FAIR-ACC-17
FAIR-ACC-20
FAIR-NUSTAR-SuperFRS-01
FAIR-NUSTAR-SuperFRS-02
FAIR-QCD-PANDA-03
FAIR-QCD-PANDA-04
FAIR-QCD-PANDA-05

FAIR Construction 'DIRAC-PHASE 1'/FP6 (515876)
<http://www.gsi.de/fair/EU-Construction/index.html>
Coordinator: GSI, Darmstadt (Germany)
Project coordinator: J. Eschke
Steering committee: J. Eschke (GSI, chair), H. H. Gutbrod (GSI), W. F. Henning (GSI), D. Krämer (GSI), J.-E. Ducret (CEA), H. Ströbele (U-Frankfurt/M.)

Contact at GSI: J. Eschke; K. Berghöfer

T1: Management – Management of the CNI, Spokesperson: J. Eschke (GSI)
T2: SIS18-1 – Two-harmonic cavity, HITR Spokesperson: P. Hülsmann (GSI)
T3: SIS18-2 – UHV vacuum upgrade, Spokesperson: H. Hartmut Reich-Sprenger (GSI)
T4: SIS18-3 – Collimator system, Spokesperson: P. Spiller (GSI)
T5: SIS18-4 – Injection/extraction upgrade, Spokesperson: U. Bell (GSI)
T6: SIS18-5 – Beam profile monitor, Spokesperson: P. Forck (GSI)
T7: SIS18-6 – Charge separator, Spokesperson: W. Bath (GSI)
T8: HADES1 – Resistive Plate Counter Time of Flight Wall (RPC), Spokesperson: P. Fonte (LIP-Coimbra)
T9: HADES2 – Forward Hodoscope (FH), Spokesperson: H. Ströbele (U-Frankfurt/M)
T10: HADES3 – Data Acquisition and Trigger upgrade (DAQ/Trigger upgrade), Spokesperson: M. Traxler (GSI)
T11: R3B – Superconducting Large Acceptance Dipole, Spokesperson: J.-E. Ducret (CEA)
T12: Overall Construction – All other construction tasks within the project duration period, Spokesperson: J. Eschke (GSI)

Contribution in this report:
INSTRUMENTS-METHODS-20

EURONS/FP6 (RII3-CT-2004-506065)
<http://www.gsi.de/informationen/jofu/EURONS/>
Coordinator: GSI, Darmstadt (Germany)
Project coordinator: A. C. Müller (IN2P3-IPNO), C. Scheidenberger (GSI, deputy coordinator)
Executive board: P. Butler (CERN), P. Van Duppen (U- Leuven), K.-D. Groß (GSI), S. Harissopoulos (NCSR Demokritos), R. Julin (Univ. Jyväskylä), S. Lenzi (INFN Padova)
Contact at GSI: I. Reinhard; M. Pantea

TA1: Transnational Access to GSI, Darmstadt, Spokesperson: K.-D. Groß (GSI)
TA2: Transnational Access to UCL-CRC, Louvain-la-Neuve, Spokesperson: G. Ryckewaert (CRC)
TA3: Transnational Access to GANIL, Cean, Spokesperson: S. Gales (GANIL)
TA4: Transnational Access to JYU-JYFL, Jyväskylä, Spokesperson: R. Julin (Univ. Jyväskylä)
TA5: Transnational Access to INFN-LNL, Legnaro, Spokesperson: E. Fioretto (INFN)
TA6: Transnational Access to ECT, Trento, Spokesperson: R. Leonardi (ETC)
TA7: Transnational Access to RUG-KVI, Groningen, Spokesperson: M. Koopmans (KVI)
TA8: Transnational Access to CERN-ISOLDE, Geneva, Spokesperson: K. Riisager (CERN)
N1: MANET – Management Network Spokespersons: A. C. Mueller (IN2P3- IPNO), C. Scheidenberger (GSI)
N2: CARINA – Challenges and Advanced Research in Nuclear Astrophysics, Spokesperson: C. Angulo (UCL)
N3: GAMMAPOOL – Coordination of the resources for gamma-ray spectroscopy in Europe, Spokesperson: S. Lenzi (INFN Padova)
N4: EWON – East-West-Outreach - European Nuclear Physics Network, Spokespersons: S. Harissopoulos (NCSR Demokritos), R. Broda (U-Warsaw)
N5: NuPECC – NuPECC Mapping Studies, Spokesperson: S. Körner (NuPECC)
N6: PANSI3 – Network for Enhanced Dissemination of Information on Nuclear Research within EURONS, Spokesperson: H. Leeb (AIAU)
N7: SHE – Transfermium element synthesis, properties and reactions, Spokesperson: A. Villari (GANIL)
N8: TNET – Network to coordinate the Nuclear Structure and Reaction Theory work, Spokesperson: I. Thompson (U-Surrey)
JRA1: ACTAR – Active Target Detectors for the Study of Extremely Exotic Nuclei using Direct Reactions, Spokespersons: H. Savajols (GANIL) / P. Roussel-Chomaz (GANIL)
JRA2: AGATA – Advanced Gamma Tracking Array, Spokesperson: W. Korten (CEA)
JRA3: Charge Breeding – Advanced charge breeding of radioactive ions, Spokesperson: O. Kester (GSI)
JRA4: DLEP – Detection of Low Energy Particles from exotic decays, Spokesperson: O. Tengblad (CSIC)
JRA5: EXL – Exotic nuclei studied with Light hadronic probes, Spokesperson: N. Kalantar (RUG-KVI)
JRA6: INTAG – Instrumentation for Tagging, Spokesperson: P. Butler (CERN)
JRA7: ISIBHI – Ion Sources for Intense Beams of Heavy Ions, Spokesperson: G. Ciavola (INFN-LNS)
JRA8: LASER – Laser techniques for Exotic nuclei Research, Spokesperson: P. Van Duppen (U- Leuven)
JRA9: RHIB – Reactions with High-Intensity Beams of exotic nuclei, Spokesperson: T. Aumann (GSI)
JRA10: SAFERIB – European Joint Research Activity on Radiation Protection Issues related to Radioactive Ion Beam Facilities,

Spokesperson: P. Thirolf (LMU)
JRA11: TRAPSPEC – Improvements and developments of ion traps, spectrometers and detectors for low-energy nuclear physics experiments, Spokesperson: N. Severijns (U-Leuven)

GSI participates as partner in TA1, N1, N5, N8, JAR1, JRA2, JRA3, JRA5, JRA6, JRA7, JRA8, JAR9, JA10, and JAR11.

Contributions in this report:
FAIR-APPA-SPARC-06
FAIR-APPA-SPARC-09
FAIR-NUSTAR-EXL-03
FAIR-NUSTAR-LASPEC-02
FAIR-NUSTAR-LASPEC-03
FAIR-NUSTAR-LASPEC-04
FAIR-NUSTAR-R3B-01
FAIR-NUSTAR-R3B-02
ACC-R+D-05
AP-EXP-SPECTROSCOPY-03
AP-EXP-SPECTROSCOPY-05
AP-EXP-SPECTROSCOPY-07
AP-EXP-SPECTROSCOPY-08
AP-EXP-SPECTROSCOPY-09
AP-METHODS-09
NUSTAR-SHE-PHYS-01
NUSTAR-SHE-PHYS-02
NUSTAR-SHE-PHYS-03
NUSTAR-SHE-PHYS-04
RAD-BIOPHYSICS-16

HADRONPHYSICS/FP6 (RII3-CT-2004-506078)
<http://hadronphysics.infn.it/>
Coordinator: INFN Frascati (Italy)
Project coordinator: C. Guaraldo (LNF-INFN)
Management board: M. Anselmino (INFN), T. Johansson (Univ. Uppsala), H. Koch (Univ. Bochum), L. Riccati (INFN), G. Rosner (Univ. Glasgow), R. Simon (GSI)
Project coordinator at GSI: R. Simon

A1: Transnational Access to INFN-LNF, Spokesperson: C. Guaraldo (INFN)
A2: Transnational Access to DESY-HERMES, Spokesperson: E.-C. Aschenauer (DESY)
A3: Transnational Access to FZJ-COSY, Spokesperson: D. Grzonka (FZJ)
A4: Transnational Access to FZJ-NIC/ZAM, Spokesperson: N. Attig (FZJ)
A6: Transnational Access to MAMI, Spokesperson: T. Walcher (Univ. Mainz)
A7: Transnational Access to ZIB, Spokesperson: H. Stueben (ZIB)
A8: Transnational Access to LU-MAXLAB, Spokesperson: B. Schroeder (Lund Univ.)
A9: Transnational Access to UU-TSL, Spokesperson: C. Eckström (Uppsala Univ.)
N1: CBMnet – Compressed Baryonic Matter, Spokesperson: P. Senger (GSI)
N2: ComHP – Computational (Lattice) Hadron Physics, Spokesperson: G. Schierholz (DESY)
N3: DIMUONnet – Dimuon physics in heavy-ion collisions at LHC, Spokesperson: E. Vercellin (INFN)
N4: EtaMesonNet – Production and Decay of Mesons and Resonances, Spokesperson: B. Höstad (Uppsala Univ.)
N5: HadronTh – Structure and Dynamics of Hadrons, Spokesperson: U.-G. Meissner (Univ. Bonn)
N6: SIM – Strongly Interacting Matter in Ultrarelativistic Heavy-Ion Collision, Spokesperson: J. Aichelin (CNRS)
N7: TRANSVERSITY – Exploring the Unknown Transverse Spin Structure of the Nucleon, Spokesperson: E. DeSanctis (INFN)
JRA1: FutureDAQ – Future Data Acquisition System, Spokesperson: W. F. J. Müller (GSI)
JRA2: FastEM Calorimeters – Fast Compact EM Calorimeters, Spokesperson: R. Novotny (Univ. Gießen)
JRA3: EuroTag – European Tagged Photon Facilities, Spokesperson: K. Livingston (Univ. of Glasgow)
JRA4: Gas Detectors – High Speed Gas Detectors with Integrated Electronics, Spokesperson: J. Wessels (Univ. Münster)
JRA5: GPD - Generalised Parton Distributions, Spokesperson: R. Kaiser (Univ. of Glasgow)

JRA6: HyperGamma – High Luminosity Hypernuclear Gamma-Spectroscopy, Spokesperson: A. Feliciello (INFN)
JRA7: Internal Targets – High Luminosity Internal Targets for Storage Rings, Spokesperson: H. Orth (GSI)
JRA8: Polarized Targets – Polarized Nucleon Targets for Europe, Spokesperson: W. Meyer (Univ. Bochum)
JRA9: RICH Detectors – Ring Imaging Cherenkov Counters for Particle Identification, Spokesperson: S. Dalla Torre (INFN)
JRA10: SIDDHARTA – Silicon Drift Detectors for X-ray Spectroscopy, Spokesperson: V. Lucherini (INFN)
JRA11: NoRHDia – Novel Radiation Hard CVD - Diamond Detectors, Spokesperson: E. Berdermann (GSI)
JRA12: ATOF – Advanced TOF Detection Systems, Spokesperson: N. Hermann (Univ. Heidelberg)

GSI participates as partner in A5, N1, JRA1, JRA2, JRA4, JRA6, JRA7, JRA11, and JRA12.

Contributions in this report:
FAIR-QCD-CBM-01
FAIR-QCD-CBM-02
FAIR-QCD-CBM-04
FAIR-QCD-CBM-05
FAIR-QCD-CBM-07
FAIR-QCD-CBM-09
FAIR-QCD-CBM-12
FAIR-QCD-CBM-14
FAIR-QCD-PANDA-06
FAIR-QCD-PANDA-07
INSTRUMENTS-METHODS-08
INSTRUMENTS-METHODS-09
INSTRUMENTS-METHODS-14
INSTRUMENTS-METHODS-18
INSTRUMENTS-METHODS-19
INSTRUMENTS-METHODS-20
NQMA-EXPERIMENTS-03
NQMA-EXPERIMENTS-05
NQMA-THEORY-04
NQMA-THEORY-05

CARE/FP6 (RII3-CT-2003-506395)
<http://esgard.lal.in2p3.fr/Project/Activities/Current/>
Coordinator: CEA Saclay (France)
Project coordinator: R. Aleksan (CEA)
Project coordinator at GSI: B. Franzke
Contact at GSI: L. Groening

GSI participates as partner in N2, N3, and JAR3.

Contributions in this report:
ACC-R+D-06
FAIR-ACC-04

EGEE/FP6 (INFSO-RI-508833)
<http://public.eu-egee.org/>
Coordinator: CERN (Switzerland)
Project coordinator: B. Jones (CERN), D. Kranzlmüller (CERN)
Project coordinator at GSI: P. Malzacher
Contact at GSI: P. Malzacher

Laserlab/FP6 (RII3-CT-2003-506350)
<http://www.laserlab-europe.net>
Coordinator: Forschungsverbund Berlin (Germany)

Project coordinator: W. Sandner (Berlin)
Project coordinator at GSI: H.-J. Kluge
Contact at GSI: T. Kühl

EUROTeV/FP6 (011899 RIDS)
<http://www.eurotev.org>
Coordinator: DESY, Hamburg (Germany)
Project coordinator: E. Elsen (DESY)
Project coordinator at GSI: H. Eickhoff
Contact at GSI: P. Schütt

Contribution in this report:
FAIR-ACC-22

Cellion/FP6 (MRTN-CT-2003-503923)
Network of Excellence
<http://cellion.ifj.edu.pl>
Project coordinator: Z. Stachura (PAN)
Contact at GSI: B. Fischer

Contribution in this report:
MATERIALS-15

HITRAP/FP5 (HPRI-CT-2001-50036)
<http://www-linux.gsi.de/∼hitrap>
Coordinator: GSI Darmstadt (Germany)
Project coordinator: H.-J. Kluge
Contact at GSI: T. Beier

Contributions in this report:
AP-METHODS-01
AP-METHODS-02
AP-METHODS-03
AP-METHODS-08

NIPNET/FP5 (HPRI-CT-2001-50034)
<http://www.kvi.nl/∼trimp/web/html/nipnet.html>
Coordinator: KVI (Netherland)
Project coordinator: H. Wilschut (KVI)
Project coordinator at GSI: H.-J. Kluge
Contact at GSI: M. Block

Contribution in this report:
AP-EXP-SPECTROSCOPY-06

EURISOL-Design Study/FP6 (515768 RIDS)
<http://www.eurisol.org>
Coordinator: INFN-LNL (Italy)
Project coordinator: G. Fortuna (INFN-LNL)
Project coordinator at GSI: K.-H. Schmidt
Contact at GSI: A. Kelic

Contributions in this report:
FAIR-ACC-26
NUSTAR-EXOTIC-BEAMS-06
AP-METHODS-05

EUROTRANS/FP6 (516520 F16W)
<http://nuclear-server.fzk.de/eurotrans/>
Coordinator: FZK, Karlsruhe (Germany)
Project coordinator: J. U. Knebel (NUCLEAR)
Project coordinator at GSI: K.-H. Schmidt
Contact at GSI: A. Kelic

EURATOM-Fellowships FISA2004/FP6 (012985 FI6W) and RESPA2004/FP6 (516352 F16W)
Project coordinator: K.-H. Schmidt
Contact at GSI: A. Kelic

Invited talks at conferences at other institutions

K. Große, GSI, Darmstadt, Germany

Ackermann, D.: **Exploring the Region of Superheavy Elements - Nuclear Structure and Reaction Mechanism.** Conference on Frontiers in the Physics of Nuclei, St. Petersburg (Russia), June 2005.

Ackermann, D.: **Nuclear structure and astrophysics at FAIR.** Helmholtz International Summer School Nuclear Theory and Astrophysical Applications, Dubna (Russia), May 2005.

Ackermann, D.: **A Separator/Spectrometer for AGATA at the SuperFRS Low Energy Branch (LEB).** HISPEC/DESPEC MEETING Valencia (Spain), June 2005.

Ackermann, D.: **Gamma-multiplicities in Fusion and K-isomers in Heavy Nuclei.** Workshop on Superheavy Elements, Schloss Rauischholzhausen (Germany), 06.09.2005.

Ackermann, D.: **SHE Production in Hot Fusion at SHIP - ^{48}Ca + ^{238}U.** European Science Foundation Exploratory Workshop on 'The Chemistry of Transactinide Elements', Oslo (Norway), October 2005.

Ackermann, D.: **Status and Perspectives of Superheavy Element Research.** International Workshop on Neutron-Rich Radioactive Ion Beams - Physics with MAFF - Kloster Banz (Germany), March 2005.

Ackermann, D.: **Superheavy Elements – Synthesis and Chemistry.** SPIRAL 2 Workshop on 'Reactions', GANIL, Caen (France), October 2005.

Ackermann, D.: **The Energy Buncher at the SuperFRS Low Energy Branch.** HISPEC/DESPEC MEETING Valencia (Spain), June 2005.

Andronic, A.: **Particle production at chemical equilibrium - from AGS to RHIC (and further to LHC).** School of Collective Dynamics in High-Energy Collisions - 'Twenty Years of Collective Expansion' Berkeley (USA), 19.-27.05.2005.

Andronic, A.: **The TRD of the CBM experiment at FAIR – GSI.** III workshop on advanced Transition Radiation Detectors for accelerator and space applications - 'TRDs for the 3rd Millenium', Ostuni (Italy), 07.-10.09.2005.

Aumann, T.: **Dipolanregung von neutronenreichen Kernen.** Forschungszentrum Rossendorf (Dresden), 28.11.2005.

Aumann, T.: **Dipolanregung von neutronenreichen Kernen.** Technische Universität Darmstadt (Germany), 29.06.2005.

Aumann, T.: **Electromagnetic excitation of soft and giant resonances in ^{132}Sn and neighboring nuclei.** Symposium on Science with Rare Isotope Beams at Pacifichem, Honolulu, Hawaii (USA), 20.12.2005.

Aumann, T.: **Experimental Studies of Reactions with Relativistic.** University of Surrey, Guildford (UK), 10.11.2005.

Aumann, T.: **Experiments with exotic beams at high energy.** Euroschool on Exotic Nuclei, Mainz (Germany), 25.08-02.09.2005.

Aumann, T.: **Giant and soft dipole excitations in neutron-rich nuclei.** Lawrence Berkeley National Laboratory (USA), 09.12.2005.

Aumann, T.: **Nuclear structure and reactions with relativistic rare-isotope beams.** IoP Nuclear Physics Summer School 2005, Chester (United Kingdom), 04.-17.09.2005.

Aumann, T.: **Nuclear-structure studies using high-energy radioactive.** University of Basel (Switzerland), 13.05.2005.

Aumann, T.: **The NUSTAR project at FAIR.** International Workshop on Neutron-Rich Radioactive Ion Beams - Physics with MAFF, Kloster Banz (Germany), 01.04.2005.

Barberet, P.: **Breaking Frontiers: Submicron Structures in Physics and Biology.** International Symposium XL Zakopane School of Physics, Zakopane (Poland), May 2005.

Berdermann, E.: **NoRHDia presentation.** 1st International Industrial Diamond Conference 'Diamond at Work', Barcelona (Spain), 20.-21.10.2005.

Berdermann, E.: **Radiation Hard Charged Particle Detectors made of CVD Diamond.** Kirchhoff Institute for Physics, University of Heidelberg (Germany),

30.06.2005.

Berdermann, E.: **Radiation Hard Charged Particle Detectors made of CVD Diamond.** Technical University of Munich (Germany), 22.06.2005.

Bert, C.: **3D surface imaging at MGH -QA and analysis of PBI setup.** Institut Curie, Orsay (France), January 2005.

Bert, C.: **3D surface imaging for PBI setup.** DKFZ, Medizin-Physik, Heidelberg (Germany), January 2005.

Bert, C.: **IGRT Workshop 2005, Boston, MA (USA).** 3D surface imaging for PBI setup, February 2005.

Bert, C.: **Tracking of moving targets in particle therapy.** Robotic Radiotherapy and IGRT, Universität Mannheim (Germany), August 2005.

Blaum, K.: **A Penning trap as a precision mass balance Mass measurements for fundamental studies.** Physics Colloquium, University of Jyväskylä, Jyväskylä (Finland), 08.04.2005.

Blaum, K.: **A Penning trap as a precision mass balance Mass measurements for fundamental studies.** Physics Colloquium, University of Stockholm, Stockholm (Sweden), 19.09.2005.

Blaum, K.: **A Penning trap as a precision mass balance Mass measurements for nuclear structure und fundamental studies.** Gordon Research Conference on Nuclear Chemistry, New London, New Hampshire (USA), 28.06.2005.

Blaum, K.: **A Penning trap as a precision mass balance Mass measurements for nuclear structure und fundamental studies.** Physics Seminar, Technical University of Darmstadt, Darmstadt (Germany), 06.07.2005.

Blaum, K.: **Atom- und kernphysikalische Experimente an ISOLDE/CERN.** Emanuel-Felke-Gymnasium, Bad Sobernheim, 01.02.2005.

Blaum, K.: **Atomic physics techniques for nuclear structure studies.** International workshop on Nuclear Structure Physics Near the Coulomb Barier: Into the 21st Century, Yale University, New Haven, CT (USA), 25.06.2005.

Blaum, K.: **Atomic physics tools in nuclear physics, 12th Euroschool on Exotic Beams.** Mainz (Germany), 30.08.2005.

Blaum, K.: **Aus dem Alltagsleben eines Physikers.** Wigbertschule, Hünfeld (Germany), 21.01.2005.

Blaum, K.: **EISOLTRAP pins down masses of exotic nuclei with 10-8 precision.** NUSTAR05 Conference, University of Surrey, Guildford (United Kingdom), 08.01.2005.

Blaum, K.: **Eine Penningfalle als ideale Waage Massenmessungen für fundamentale Studien.** Physikseminar, Universität Heidelberg (Germany), 17.05.2005.

Blaum, K.: **Exotische Kerne auf die Waage gestellt Präzisionsmassenmessungen für fundamentale Studien.** Justus-Liebig-Universität Gießen, Physikalisches Kolloquium, Gießen (Germany), 12.12.2005.

Blaum, K.: **Exotische Kerne auf die Waage gestellt Präzisionsmassenmessungen in der Kernphysik.** Universität zu Köln, Physikalisches Kolloquium (Germany), 25.01.2005.

Blaum, K.: **High-accuracy Penning trap mass spectrometry and its applications.** Physics Colloquium, Variable Energy Cyclotron Centre, Bidhanagar, Kolkata (India), 05.12.2005.

Blaum, K.: **High-precision mass measurements on neutron-rich radionuclides.** International Workshop on Neutron-Rich Radioactive Nuclei Physics with Maff, Kloster Banz (Germany), 03.03.2005.

Blaum, K.: **ISOLTRAP pins down masses of exotic nuclei 10^{-8} precision.** NUSTAR05 Conference, Univ. of Surrey, Guildfort (United Kingdom), 08.01.2005.

Blaum, K.: **Innovative Technologies A Penning trap as a precision mass balance.** BMBF, Perspektiv-Seminar 'Hadronen und Kernphysik', Bad Honnef (Germany), 13.05.2005.

Blaum, K.: **Laser spectroscopy and Penning trap mass spectrometry for atomic and nuclear structure studies.** Physics Colloquium, BARC Research Institute, Mumbai (India), 09.12.2005.

Blaum, K.: **Laser spectroscopy and Penning trap mass spectrometry A fruitful combination.** Symposium on 'Lasers and their Applications', Institute of Technology, Vellore (India), 07.12.2005.

Blaum, K.: **Laser spectroscopy and Penning trap mass spectrometry Atomic physics tools in nuclear physics.** Physics Colloquium, Nuclear Science Centre, New Delhi (India), 02.12.2005.

Blaum, K.: **MATS - Measurements with an Advanced Trapping System.** NUSTAR05 Conference, GSI Darmstadt (Germany), 09.02.2005.

Blaum, K.: **Nuclear-Structure Studies with Penning Trap Mass Spectrometry.** Workshop on Symmetries and low-energy phase transitions in nuclear-structure physics, Camerino (Italy), 09.10.2005.

Blaum, K.: **Physics Program of the MATS Collaboration: Measurements with an Advanced Trapping Syste.** SPARC Workshop, Piaski (Poland), 09.09.2005.

Blaum, K.: **Precision mass measurements for fundamental studies, Mattauch-Herzog Preisvortrag.** DGMS2005 Conference, Rostock (Germany), 08.03.2005.

Blaum, K.: **Standard Model Tests: Precision mass, half-life and branching-ratio measurements, Nuclear Physics and Astrophysics at CERN.** NuPAC Workshop, Geneva (Switzerland), 11.10.2005.

Blaum, K.: **Weight problems of physical kind A Penning trap as an ion balance for high-precision atomic mass measurements.** Physics Colloquium, University of Sussex, Brighton (United Kingdom), 16.02.2005.

Block, M.: **Experiments at SHIPTRAP: Mass Measurements of Heavy Elements.** NUSTAR Annual Meeting, GSI, 10.02.2005.

Block, M.: **Mass Measurements of Heavy Elements.** NSCL Seminar, Michigan State University, East Lansing (USA), 12.09.2005.

Block, M.: **Mass Measurements of Radionuclides in the Rare Earth Region at SHIPTRAP.** Seminar, Ludwig-Maximilians-Universität München (Germany), 19.12.2005.

Block, M.: **THE SHIPTRAP PROJECT: Mass Measurements of Heavy Elements.** Seminar über Atomphysik, Justus-Liebig-Universität Gießen, 10.11.2005.

Bogdan, G.; D'Hean, J.; Haenen, K.; D'Olieslager, M.; Nesladek, M.: **Growth and characterization of near-atomically flat, thick homoepitaxial CVD diamond films.** X International Workshop on Surface and Bulk Defects in CVD Diamond SBDD, Hasselt (Belgium), 23.-25.02.2005.

Boretzky, K.: **Dipole Excitation of Soft and Giant Resonances in 132Sn and neighboring unstable nuclei.** FINUSTAR International Conference on Frontiers in Nuclear Structure, Astrophysics and Reactions, Kos (Greece), 13.09.2005.

Boretzky, K.: **Elektromagnetische Anregung von exotischen Kernen.** Symposiums des Forschungsschwerpunkts Kern- und Strahlungsphysik, TU Darmstadt (Germany), 28.11.2005.

Bosch, F.: **Einstein und die ungelöste Frage nach der Zeit.** Evang. Akademie Arnoldshain, 20.-22.05.2005.

Bosch, Fritz: **Astrophysical Impact of Bound-State Beta Decay.** EXA05, Vienna (Austria, 21.-25.02.2005.

Bräuning-Demian, A.: **An international facility for antiproton and ion research: The FAIR Project.** Carpathian Summer School of Physics, Mamaia (Romania), 17.07.2005.

Bräuning-Demian, A.: **FLAIR Status Report.** SPARC Workshop, Piaski (Poland), 06.-11.09.2005.

Bräuning-Demian, A.: **Planning and Design of the FLAIR Building.** FLAIR/SPARC Workshop, Darmstadt (Germany), 12.-13.12.2005.

Brandau, C.: **Bestimmung von Ladungsradien mit elektromagnetischen Sonde.** Atomphysik-Seminar, Universität Gießen (Germany), 07.07.2005.

Brandau, C.: **Nuclear Ground State Properties with Large Atomic Cross Sections Isotopic Shift Measurements by Means of Dielectronic Recombination.** Nuclear Physics Group Seminar, University of Surrey, Guildford (United Kingdom), 29.09.2005.

Braun-Munzinger, P.: **Particle production and the QCD phase transition.** ICPAQGP, Kolkata (India), February 2005.

Braun-Munzinger, P.: **Quarkonia production at RHIC and prospects for LHC.** ALICE physics week, Erice (Italy), 2005.

Braun-Munzinger, P.: **Ultrarelativistic nuclear collisions and the QCD phase boundary.** Colloquium, München (Germany), July 2005.

Braun-Munzinger, P.: **Ultrarelativistic nuclear collisions.** Lecture series, 6th Nordic Summer School in Nuclear Physics, Hilleroed (Danmark), August 2005.

Brons, S.: **o. T..** Korean Institute of Radiobiological and Medical Sciences, Seoul (Korea), June 2005.

Brons, S.: **o. T..** Workshop for a Heavy Ion Accelerator Facility, Busan (South Korea), June 2005.

Brüchle, W.: **Simulation of elution curves for chromatography colums with a low number of theoretical plates.** 230th American Chemical Society National Meeting (USA), August 2005.

Brüchle, W.: **Simulation of elution curves for chromatography colums with a low number of theoretical**

plates. European Science Foundation Exploratory Workshop on The Chemistry of Transactinide Elements, Oslo (Norway), October 2005.

Ciavola, G.; Gammino, S.; Celona, L.; Torrisi, L.; Passarello, S.; Ando, L.; Cavenago, M., Galata, A.; Spädtke, p.; Tinschert, K.; Lang, R.; Iannucci, R.; Leroy, R., Barue, C. ;Hitz, D.; Seyfert, P.; Koivisto, H.; Suominen, P.; Tarvainen, O.; Beijers, H.; Brandenburg, S.; Vanrooyen, D.; Hill, C.; Küchler, D.; Homeyer, H.; Röhrich, J.; Schachter, L.;Dobrescu, S.: **MS-ECRIS The European Roadmap to 3rd Generation ECR Ion Source.** 11th International Conference on Ion Sources, Caen (France), 12.-16.09.2005.

Cornelius, T.: **Electrical and optical properties of bismuth nanowires.** Workshop 'Ionenstrahlphysik und technologie', Leipzig (Germany), April 2005.

Egelhof, P.: **Nuclear Structure Studies by Direct Reactions with Radioactive Beams.** Lectures presented at the INST School on Nuclear Physics and Astrophysics, Hanoi (Vietnam), 26.-31.08.2005.

Egelhof, P.: **Nuclear Structure Studies by Direct Reactions with Radioactive Beams.** Lectures presented at the INST School on Nuclear Physics and Astrophysics, Hanoi (Vietnam), August 2005.

Egelhof, P.: **Nuclear Structure Studies on Exotic Nuclei by Light-Ion Induced Direct Reactions with Stored Radioactive Beams.** 6th Int. Conf. on Nuclear Physics at Storage Rings, STORI05, Jülich-Bonn (Germany), May 2005.

Egelhof, P.: **Nuclear Structure Studies on Exotic Nuclei by Light-Ion Induced Direct Reactions with Stored Radioactive Beams.** CCG Collaboration Meeting, Uppsala (Sweden), March 2005.

Egelhof, P.: **Nuclear Structure Studies on Exotic Nuclei by Light-Ion Induced Direct Reactions with Stored Radioactive Beams.** CCG Collaboration Meeting, Uppsala (Sweden), March 2005.

Egelhof, P.: **Probing the Halo Structure of Exotic Nuclei by Elastic and Quasielastic Proton Scattering in Inverse Kinematics.** RIKEN, Tokyo (Japan), August 2005.

Egelhof, P.: **Probing the Halo Structure of Exotic Nuclei by Elastic and Quasielastic Proton Scattering in Inverse Kinematics.** RIKEN, Tokyo (Japan), August 2005.

Egelhof, P.: **Reaction Studies with Radioactive Beams at FAIR and Potential Synergies with SPIRAL2.** SPIRAL2 Reactions Workshop, Ganil (France), 19.-21.10.2005.

Egelhof, P.: **Reaction Studies with Radioactive Beams at FAIR and Potential Synergies with SPIRAL2.** SPIRAL2 Reactions Workshop, Ganil (France), October 2005.

Egelhof, P. for the EXL collaboation: **Nuclear Structure Studies on Exotic Nuclei by Light-Ion Induced Direct Reactions with Stored Radioactive Beams.** 6th Int. Conf. on Nuclear Physics at Storage Rings, STORI05, Jülich-Bonn, (Germany), 23.05-..2005.

Egelhof, P. for the EXL collaboation: **Nuclear Structure Studies on Exotic Nuclei by Light-Ion Induced Direct Reactions with Stored Radioactive Beams.** STI meeting, GSI (Germany), July 2005.

Emling, H.: **Giant Resonances.** Selected Topics in Nuclear and Atomic Physics, Fiera di Primiero (Italy), 01.10.2005.

Emling, H.: **Nuclear Structure Studies with Exotic Nuclear Beams.** Int. Symposium on Exotic Nuclear Systems, Debrecen (Hungary), 20.06.2005.

Emling, H.: **Physics with unstable nuclear beams at GSI and FAIR.** Changing Scales in Nuclear Physics, Kolkata (India), 14.06.2005.

Emling, H.: **Reaction Studies with Radioactive Beams at GSI and FAIR.** RIKEN, Tokyo (Japan), 17.12.2005.

Fischer, B.E.: **Die GSI Schwerionen-Mikrosonde: Ein Instrument zur gezielten Bestrahlung einzelner Zellen.** DPG Frühjahrstagung, Berlin (Germany), March 2005.

Fischer, B.E.: **Untersuchung von Strahlungseffekten in Biologie und Mikroelektronik: Beispiele zur Anwendung der Ionen-Mikrosonde bei der GSI.** Workshop Ionenstrahlphysik und technologie, Leipzig, Germany, May 2005.

Forck, P.: **Beam Profile Monitors Based on Residual Gas Interaction.** 7th European Workshop on Beam Diagnostics and Instrumentation for Particle Accelerators, DIPAC 2005, 06.-08.06.2005.

Fournier, C.: **Der strahleninduzierte Bystander-Effekt: Eine Übersicht über (in vitro-) Beobachtungen an Fibroblasten.** Jahrestagung der GBS, Buxtehude (Germany) April 2005.

Franchi, A.: **Measurement on nonlinearities in circular accelerators using BPM data.** INFN-Bologna University, Bologna, 24.07.2005.

Franchi, A.: **Progress in code benchmarking with tracking under space charge conditions.** RAL, HIPPI WP-5 annual meeting, 13.04.2005.

Franchi, A.: **Progress in linac code benchmarking.** RAL, HIPPI second annual meeting, 29.09.2005.

Franchi, A.: **Progress in the HIPPI code benchmarking.** CERN, CARE second annual meeting, 24.11.2005.

Franchi, A.: **Studies on linear coupling in the GSI SIS-18.** IAP, Frankfurt am Main, 08.06.2005.

Friman, B.: **Renormalization Group Approach to the Nuclear Many-Body Problem.** State University of New York in Stony Brook (USA), 21.06.2005.

Geissel, H.: **Experiments at the present and future rare-isotope facilities.** RIKEN, Tokyo (Japan), April 2005.

Geissel, H.: **Physics with exotic nuclei at GSI.** 12th Euroschool on Exotic Beams, Mainz (Germany), March 2005.

Geissel, H.: **Precision Experiments with Relativistic Exotic Nuclei.** International Conference NUSTAR05, Surrey (UK), January 2005.

Geissel, H.: **Precision Experiments with stored exotic nuclei.** APS Meeting, Tampas (USA), April 2005.

Geissel, H.: **Progress in mass- and lifetime measurements with sored exotic nuclei.** FINUSTAR, Kos (Greece), September 2005.

Geissel, H.: **Präzisionsmessungen mit relativistischen Ionen bei GSI.** Universität Wien (Austria), June 2005.

Geissel, H.: **Studies with in-flight separators at GSI.** PACIFICHEM 2005, Honolulu, Hawaii (USA), December 2005.

Geissel, H.: **The Super-FRS project.** STI-PAC-TAC-CORE Meeting, GSI (Germany), March 2005.

Götzen, K.: **Messung der CP-Verletzung bei BABAR.** XXXVI. Arbeitstreffen Kernphysik, Schleching (Germany), February 2005.

Götzen, K.: **Neue Teilchen bei BABAR und Belle.** Kernphysikalisches Kolloquium, HISKP, Bonn (Germany), January 2005.

Götzen, K.: **Search for Pentaquarks at BABAR.** 12th International QCD Conference 2005, Montpellier (France), June 2005.

Götzen, K.: **Suche nach Pentaquarks bei BABAR.** DPG Frühjahrstagung HuK, Berlin (Germany), March 2005.

Grawe, H.: **Shell model from a practitioners point of view : Two Lectures on Nuclear structure in the spherical shell model (I) and In-flight spectroscopy and nuclear structure far from stability (II).** 2nd Vistars Workshop on Nuclear Astrophysics, Russbach (Austria), 05.-12.03.2005.

Grawe, H.: **Nuclear structure far off stability Implications for nuclear astrophysics.** 20th Int. Nuclear Physics Divisional Conf. of the EPS Nuclear Physics in Astrophysics - II, Debreczen (Hungary), 16.-21.05.2005.

Grawe, H.: **The FAIR facility at GSI.** Faculty of Physics, University of Sofia, Sofia (Bulgaria), 14.04.2005.

Hartmann, Olaf: **FOPI – GSI's working house for nuclear reactions.** Stefan Meyer-Institut der ÖAW, Wien (Austria), 19.08.2005.

Hechler, l.; Höppner, K.; Kainberger, P.; Krause, U.; Schwarz, G.: **Replacement of Outdated VME Boards as Starting Point for Control System Modernization.** ICALEPCS 2005, International Conference on Accelerator and Large Experimental Physics Control Systems, Genf (Switzerland), October 2005.

Henning, W. F.: **A FAIR Approach to the Structure of Matter.** New Trends in Nuclear, Atomic and Molecular Physics, Heidelberg (Germany), 11.-12.03.2005.

Henning, W. F.: **Collaboration on accelerators and accelerator-based science between Germany and Japan.** RIKEN-GSI Joint Symposium: A hundred years of discovering new elements, Tokyo (Japan), 17.12.2005.

Henning, W. F.: **FAIR - Facility for Antiproton and Ion Research. Das Zukunftsprojekt an der GSI.** Kolloquium Universität Erlangen (Germany), 31.01.2005.

Henning, W. F.: **FAIR - Facility for Antiproton and Ion Research. The future project at GSI.** Seminar, DESY Hamburg (Germany), 08.02.2005.

Henning, W. F.: **FAIR - Facility for Antiproton and Ion Research. The future project at GSI.** Seminar, DESY Zeuthen (Germany), 09.02.2005.

Henning, W. F.: **GSI-Russian Collaborations: from heavy elements to quark matter, dense plasmas and the future FAIR Project.** Eröffnung des Helmholtz-Büros in Moskau (Russia), 07.02.2005.

Henning, W. F.: **Grundlagenforschung nur Geldverschwendung?.** Eröffnungsveranstaltung 'Wirtschaft trifft Wissenschaft', IHK Region Stuttgart (Germany), 16.02.2005.

Henning, W. F.: **Kern(e) der Materie, Brennstoff der Sterne.** Festkolloquium MinDir Dr. Hermann Schunck, DESY, Hamburg (Germany), 28.10.2005.

Henning, W. F.: **Kernphysik damals und heute.** Festkolloquium Homeyer, HMI, Berlin (Germany), 29.08.2005.

Henning, W. F.: **Nuclear physics at the beginning of the 21st century.** Symposium in Honour of the 80th Birthday of Igal Talmi, Zeev Fraenkel and Gvirol Goldring, Rehovot (Israel), 04.04.2005.

Henning, W. F.: **Nuclei and Hadrons: Perspectives for Europe.** D. Allen Bromley Memorial Symposium, Yale University, New Haven, Connecticut (USA), 09.12.2005.

Henning, W. F.: **Status of the FAIR Project.** NUSTAR Annual Meeting, 09.-11.02.2005.

Henning, W. F.: **The FAIR Project.** 2nd Swedish Workshop on FAIR Physics, Lund (Sweden), 12.09.2005.

Herfurth, F.: **Highly Charged Ions at Rest: The HITRAP Project at GSI.** Workshop on Physics with Ultra Slow Antiproton Beams, Tokio (Japan), 14.-16.03.2005.

Herfurth, F.: **Mass Measurements.** Workshop on Physics with Low Energy Beams at SPIRAL2 Caen (France), 01.-02.04.2005.

Heßberger, F.: **Nuclear Structure Incestigations of Heavy Actinide and Trans-Actinide Isotopes.** Havanna (Cuba), WONP 2005, February 2005.

Heßberger, F. P.: **Decay Spectroscopy of Heavy and Superheavy Elements.** Workshop on Future Prospects for High Resolution gamma Spectroscopy at GANIL, Caen (France), 06.10.2005.

Heßberger, F. P.: **GSI Experiments on Synthesis and Nuclear Structure Investigations of Heaviest Nuclei.** XII Nuclear Physics Workshop 'Marie and Pierre Curie', Kazimierz Dolny (Poland), September 2005.

Heßberger, F. P.: **Nuclear Structure Investigations of Heavy Actinide and Transactinide Isotopes.** Workshop on Superheavy Elements, Schloss Rauischholzhausen (Germany), 06.09.2005.

Heßberger, F.P.: **Nuclear Structure Investigations of Heavy Actinide and Transactinide Isotopes.** X International Workshop on Nuclear Physics WONP 2005, Havanna (Cuba), 10.02.2005.

Höhne, C.: **Results from NA49.** Quark Matter 2005, Budapest (Hungary), August 2005.

Höhne, C.: **Strangeness production and percolation.** 2nd International Workshop on the Critical Point and Onset of Deconfinement, Bergen (Norway), March 2005.

Höhne, C.: **The compressed baryonic matter experiment at the future accelerator facility FAIR in Darmstadt.** 21st Winter Workshop on Nuclear Dynamics, Breckenridge (USA), February 2005.

Höppner, K.; Hechler, L.; Kainberger, P.; Krause, U.: **Embedded Linux and CORBA in the GSI Control System.** PCaPAC 2005 (Workshop on Personal Computers and Particle Accelerator Controls) Hayama (Japan), March 2005.

Hoffmann, D. H. H.: **Dense Plasmas and High Energy Density Physics with Heavy Ion and Laser Beams.** Goa (India), March 2005.

Hoffmann, D. H. H.: **Frontiers of Dense Plasma Physics With Intense Beams and Accelerator Technology.** IFSA Conference, Biarritz (France), September 2005.

Hoffmann, D. H. H.: **Frontiers of Dense Plasma Physics With Intense Beams and Accelerator Technology.** IPP Summer University, Greifswald (Germany), 30.09.2005.

Hoffmann, D. H. H.: **Frontiers of Dense Plasma- and High Energy Density Physics with accelerator technology and Intense Heavy Ion and Laser Beams.** Int. Conf. on Strongly Coupled Coulomb Systems, Moscow (Russia), 20.06.2005.

Hoffmann, D. H. H.: **Frontiers of Dense Plasma- and High Energy Density Physics with accelerator technology and Intense Heavy Ion and Laser Beams.** Princeton Univ. (USA), 17.08.2005.

Hoffmann, D. H. H.: **Frontiers of Dense Plasma- and High Energy Density Physics with accelerator technology and Intense Heavy Ion and Laser Beams.** SHIM Aschaffenburg (Germany), June 2005.

Hoffmann, D. H. H.: **Frontiers of Physics with Intense Beams and Accelerator Technology.** ITEP Moscow (Russia), 15.12.2005.

Hoffmann, D. H. H.: **Frontiers of dense plasma physics with intense ion and laser beams and accelera-**

tor technology. Plasma Physics Summer School, Kudowa (Poland), 06.05.2005.

Hoffmann, D. H. H. for the CAST collaboration: **CAST and the search for solar axions.** High Energy Physics Conf., Thessaloniki (Greece), 23.04.2005.

Hoffmann, D. H. H. for the CAST collaboration: **CAST and the search for solar axions.** Phys. Kolloquium, Greifswald (Germany), 28.04.2005.

Hofmann, J.; Lutz; M. F. M.: **Coupled-channel study of baryon resonances with charm.** Hadron 2005, Rio de Janeiro (Brazil), 22.08.2005.

Hofmann, S.: **Heavy element program at GSI-SHIP Darmstadt.** PACIFICHEM 2005, Honolulu, Hawaii (USA), December 2005.

Hofmann, S.: **Present and Future at GSI-SHIP.** Third Sandanski Coordination Meeting on Nuclear Science, Albena (Bulgaria), September 2005.

Hofmann, S.: **Present status of experimebtal research on superheavy elements.** Workshop on Superheavy Elements, Schloss Rauischholzhausen (Germany), 06.09.2005.

Hofmann, S.: **Synthesis and Properties of superheavy elements.** X International Workshop on Nuclear Physics WONP 2005, Havanna (Cuba), 08.02.2005.

Hofmann, S.: **Synthesis of Superheavy Elements at SHIP.** Conference on Frontiers in the Physics of Nuclei, St. Petersburg (Russia), June 2005.

Hofmann, S. et al.: **Synthesis of SHE at SHIP.** Asia-Pacific Symposium on Radiochemistry 05 (APSORC-05), Beijing (China), October 2005.

Hofmann, S. et al.: **Synthesis of SHE at SHIP.** Carpathian Summer School of Physics 2005, Mamaia (Romania), June 2005.

Holzmann, R.: **The HADES experiment at GSI: status and outlook.** LIP Coimbra (Portugal), physics department, July 2005.

Holzmann, R.: **The physics program of at GSI.** LIP Lissabon (Portugal), physics department, July 2005.

Jakob, B.: **DNA-Schäden und Strahlenqualität: Dynamik von Reparaturproteinen an lokalisierten Schadensstellen.** DPG-Tagung Berlin (Germany), March 2005.

Kelic, A.: **Basic Research at GSI for the Transmutation of Nuclear Waste.** FAIR Road Show, Bucharest (Rumania), 24.02.2005.

Kelic, A.: **Fission barriers of exotic nuclei.** Third International Workshop on Nuclear Fission and Fission-product Spectroscopy, Cadarache (France), 11.05.2005.

Kelic, A.: **Spallation reactions studies in inverse kinematics at GSI.** n BANT Workshop, CERN (Switzerland), 22.03.2005.

Kester, O.: **Charge breeding of intense radioactive ion beams.** International Workshop on Neutron-Rich Radioactive Ion Beams - Physics with MAFF - Kloster Banz (Germany), 29.03-01.04.2005.

Kester, O.: **Charge breeding with EBIS/T within I3-EURONS.** TITAN Collaboration meeting and workshop, TRIUMF, Vancouver (Canada), 10.-11.06.2005.

Kester, O.: **HITRAP facility.** 4th Collaboration Meeting NIPNET, HITRAP and ION CATCHER, Munich (Germany), 26.-28.05.2005.

Kester, O.: **HITRAP: A status report.** Topical Workshop on Atomic Physics in Strong Fields, Piaski (Poland), 06.-11.09.2005.

Kester, O.: **Ladungsbrüten und Beschleunigen von Strahlen exotischer Nuklide.** Kolloquium des Graduiertenkollegs 410, Physik und Technik von Beschleunigern, 20.04.2005.

Kester, O.: **Status of the HITRAP Project at GSI.** HITRAP business meeting, GSI, 07.10.2005.

Kester, O.: **Teilchenfallen ein aktueller Überblick.** Seminar: Aktuelle Probleme der Beschleuniger- und Plasmaphysik, IAP, J. W. Goethe-Universität Frankfurt am Main, gemeinsam mit GSI Darmstadt, 11.01.2005.

Kester, O.: **The Frankfurt MAXEBIS Setup for Advanced Charge Breeding Experiments.** International conference on ion sources ICIS2005, Caen (France), 12.-16.09.2005.

Kester, O.: **The HITRAP Decelerator Project at GSI.** HIAT05, Port Jefferson (USA), 16.-20.10.2005.

Klepper, O.: **Fast Heavy Ions as a Microscope and as Tools - An Introduction to GSI.** Institute of Modern Physics - Chinese Academy of Science, Lanzhou (China), October 2005.

Klepper, O.: **GSI Darmstadt and IMP Lazhou - An illustrated personal review of 20 years of cooperation.** Meeting of Chinese Physicists Alumni to Germany,

Lanzhou (PR China), October 2005.

Klingbeil, H.; Kumm, M.; Moritz, P.; Zipfel, B.: **A Cavity Synchronization System For Heavy Ion Synchrotrons Based on DSP, DDS and FPGA Technology.** CERN LLRF05, CERN (Switzerland), October 2005.

Kluge, H.-J.: **(Halo) Nuclei in the Light of Lasers.** National Laser Symposium BARC, Bombay (India), 10.-13.01.2005.

Kluge, H.-J.: **(Halo) Nuclei in the Light of Lasers.** National Laser Symposium, BARC, Bombay (India), 10.01-13.10.2005.

Kluge, H.-J.: **Atomic Physics Techniques for Short-Lived Isotopes.** TARGISOL Workshop, El Escorial, 18.02.2005.

Kluge, H.-J.: **Atomic Physics at Accelerators Today (GSI) and Tomorrow (FAIR).** Instituto de Estructura de la Materia, Madrid (Spain), 17.02.2005.

Kluge, H.-J.: **Atomic Physics at Accelerators: Today (GSI) and Tomorrow (FAIR).** Tata-Institute, Bombay (India), 14.01.2005.

Kluge, H.-J.: **Atomphysik an Beschleunigern - oder Was tut die Atomphysik Gutes sich selbst, aber besonders der Kernphysik?.** XXXVI. Arbeitstreffen Kernphysik, Schleching (Germany), 24.02.2005.

Kluge, H.-J.: **Atomphysik an Beschleunigern: heute (GSI) and morgen (FAIR).** Quantum Seminar, Universität Mainz (Germany), 07.07.2005.

Kluge, H.-J.: **Atomphysikalische Präzisionsexperimente mit gekühlten und gespeicherten wasserstoffähnlichen Ionen.** Universität Erlangen (Germany), 28.11.2005.

Kluge, H.-J.: **Cooled and Trapped: Highly-Charged Ions in Extreme Fields for Tests of Quantum Electrodynamics and the Determination of Fundamental Constants.** University of Jyväskylä (Finland), 14.10.2005.

Kluge, H.-J.: **Gefangen und gekühlt: Hochgeladene Ionen zum Test der QED in extremen Feldern und zur Bestimmung von Fundamentalkonstanten.** Marburg (Germany), 06.06.2005.

Kluge, H.-J.: **Gefangen und gekühlt: Hochgeladene Ionen zum Test der QED in extremen Feldern und zur Bestimmung von Fundamentalkonstanten.** Universität Kassel (Germany), 24.11.2005.

Kluge, H.-J.: **Gerhard Soffs Contribution to Atomic Physics in Strong Fields.** SPARC Workshop, Piaski (Poland), 07.-10.09.2005.

Kluge, H.-J.: **HITRAP a Facility for Experiments on Stored and Cooled Highly-Charged Ions.** Topics in Heavy Ion Physics Memorial Symposium for Gerhard Soff, Frankfurt/Main (Germany), 25.-26.04.2005.

Kluge, H.-J.: **Halokerne im Laserlicht.** Kolloquium Optik und kondensierte Materie, Bonn (Germany), 12.04.2005.

Kluge, H.-J.: **High-Accuracy Experiments with Ion Traps.** Nuclear Science Center, Delhi (India), 19.01.2005.

Kluge, H.-J.: **High-Accuracy Experiments with Ion Traps.** Variable Energy Cyclotron Centre (VECC), 18.01.2005.

Kluge, H.-J.: **High-Precision Mass Measurements of Radionuclides in Storage Rings and Traps.** DPG Spring Meeting Symposium, 04.-09.03.2005.

Kluge, H.-J.: **LaSpec Laser Spectroscopic Determination of Nuclear Ground State Properties at the FAIR Low-Energy Branch Challenges and Opportunities.** SPARC Workshop, Piaski (Poland), 07.-10.09.2005.

Kluge, H.-J.: **Lasers for Nuclear Physics.** Saha Institute of Nuclear Physics, 17.01.2005.

Kluge, H.-J.: **Precise (and also Accurate) Atomic Mass Measurements in Traps.** Frontiers in the Physics of the Nucleus, St. Petersburg (Russia), 28.06-01.07.2005.

Kluge, H.-J.: **Present and Future of ISOLDE.** Nuclear Physics and Astrophysics at CERN - NuPAC, CERN, Geneva (Switzerland), 10.-12.10.2005.

Kluge, H.-J.: **Präzisionsmassenmessungen an Radionukliden in Ionenfallen und Speicherringen.** Jahrestagung der Deutschen Gesellschaft für Massenspektroskopie, Rostock (Germany), 06.-09.03.2005.

Kluge, H.-J.: **SHIPTRAP, HITRAP and MATS: Status and Plans for ion trap projects at GSI and FAIR.** TRIUMF, TITAN Workshop, Vancouver (Canada), 10.06-11.10.2005.

Kluge, H.-J.: **Trapping and Cooling for Fundamental Tests and Constants.** Third Sandanski Coordination Meeting on Nuclear Science, Albena (Bulgaria), 26.-30.09.2005.

Kollmus, H.: **Ion Beam-Loss Induced Desorption and Consequences for Heavy Ion Synchrotrons.** SHIM 2005, Aschaffenburg (Germany), 28.-31.05.2005.

Kollmus, H.: **Ionenstrahlinduzierte Desorption und deren Konsequenzen für Schwerionensynchrotrons.** Graduiertenkolleg Physik und Technik von Beschleunigern, Technische Universität Darmstadt, 20.04.2005.

Krämer, A.: **Ion Induced Desorption Measurements at GSI.** 25th Workshop on Physics of High Energy Density in Matte, Hirschegg (Austria), 2005.

Kraft, G.; Zeitträger, H.: **Tumor Therapy at GSI.** XXIV International Conference on Photonic, Electronic and Atomic Collisions, Rosario (Argentina), 20.-26.07.2005.

Kraft-Bermuth, S.: **Calorimetric Low Temperature Detectors for Heavy Ion Physics.** ESTEC/ESA (Netherlands), December 2005.

Kraft-Bermuth, S.: **Calorimetric Low Temperature Detectors for Heavy Ion Physics.** ESTEC/ESA (Netherlands), December 2005.

Kraft-Bermuth, S.: **Calorimetric Low Temperature Detectors for Heavy Ion Physics.** INFN, Milano (Italy), November 2005.

Kraft-Bermuth, S.: **Calorimetric Low Temperature Detectors for Heavy Ion Physics.** INFN, Milano (Italy), November 2005.

Kraft-Bermuth, S.: **Calorimetric Low Temperature Detectors for Heavy Ion Physics.** Saclay (France), November 2005.

Kraft-Bermuth, S.: **Calorimetric Low Temperature Detectors for Heavy Ion Physics.** Saclay (France), November 2005.

Kurdal, J.; Bellachioma, M. C.; Kollmus, H.; Krämer, A.; Reich-Sprenger, H.; Savino, G.: **Non evaporable getter films for the future GSI facility.** Olav Workshop, CERN (Switzerland), 11.-12.04.2005.

Kurtukian-Nieto, T., Benlliure, J.; Schmidt, K.-H.; Casarejos, E.; Cortina-Gil, D.; Fernandez-Ordonez, M.; Pereira, J.; Audouin, L.; Blank, B.; Giovinazzo, J.; Henzlova, D.; Jurado, B.; Rejmund, F.; Yordanov, O.: **Production and Half-lives on Neutron-rich Isotopes Near N=126.** Int. Symposium on Exotic Nuclear Systems, Debrecen (Hungary), June 2005.

Lang, M.: **Etch-pit morphology of tracks induced by ions in natural dark mica.** Workshop Erforschung kondensierter Materie mit nuklearen Sonden und Ionenstrahlen, München (Germany), April 2005.

Lang, M.: **Materials research at GSI.** Pontifcia Universidade Catlica do Rio Grande do Sul (PUCRS), Porto Alegre (Brazil), January 2005.

Lang, M.: **Phase Formation under High Pressure induced by Heavy Ions.** Lawrence Livermore National Laboratory (LLNL), Livermore (USA) July 2005.

Langanke, K.: **Astrophysical opportunities with MAFF.** MAFF workshop, Kloster Banz (Germany), 31.03.2005.

Langanke, K.: **Challenges in Nuclear Astrophysics.** MSU user's future workshop, East Lansing (USA), 19.08.2005.

Langanke, K.: **Introduction to nuclear astrophysics.** 4 lectures at the Mexican Summer School on Asytophysics, Morelia (Mexico), 18.-22.07.2005.

Langanke, K.: **Neutrino-nucleus reactions in supernova.** Colloquium at the FZ Karlsruhe (Germany), 13.12.2005.

Langanke, K.: **Neutrino-nucleus reactions in supernovae.** Erice school 2005, 18.-24.09.2005.

Langanke, K.: **Neutrino-nucleus reactions in supernovae.** INT Seattle (USA), 04.10.2005.

Langanke, K.: **Nuclear Astrophysics.** 5 lectures at the Nordic Summer School, Hillerod (Denmark), 08.-12.08.2005.

Langanke, K.: **Nuclear progress for supernova models.** SCiDAC Annual Meeting, Miami (USA), 17.01.2005.

Langanke, K.: **Nuclear structure and supernova.** 60th birthday workshop in honor of P.-G. Reinhard, Erlangen (Germany), 14.10.2005.

Langanke, K.: **Nuclear structure and supernova.** Colloquium at the University of Cologne (Germany), 20.12.2005.

Langanke, K.: **Nucleosynthesis issues and massive stars.** Isolde future workshop, CERN (Switzerland), 10.10.2005.

Langanke, K.: **Shell model and supernova.** Annual meeting of French nuclear physicists, Paris (France), 26.05.2005.

Langanke, K.: **Shell model and supernova.** Seminar at University of Mainz (Germany), 23.05.2005.

Langanke, K.: **Shell model and supernova.** Symposium for S-G. Nilsson, Lund (Sweden), 14.-17.07.2005.

Langanke, K.: **Supernova and nuclear physics.** Seminar at the University of Bonn (Germany), 07.07.2005.

Langanke, K.: **Weak-interaction processes in collapsing stars.** Max-Planck Institute for Astrophysics, Munich (Germany), 29.03.2005.

Lange, J. S.: **New resonance results from B factories.** International Workshop on Resonances in QCD, Trento (Italy), 11.-16.07.2005.

Lee, R.: **Chromosome abberation yields and apoptosis in human lymphocytes irradiated with Fe-ions of differing LET.** Marian Smoluchowski Institute of Physics Jagellonian University, Krakau (Poland), April 2005.

Lewandowski, B.: **Der PANDA Detektor.** DPG Frühjahrstagung HuK, Berlin (Germany), March 2005.

Lewandowski, B.: **Developement of Large Area APDs.** RA2 Fast Electromagnetic Calorimetry workshop during SCINT2005 at Alushta (Ukraina), 2005.

Lewandowski, B.: **PANDA - An Experimental Challenge.** JRA2 Fast Electromagnetic Calorimetry workshop during SCINT2005 at Alushta (Ukraina), 2005.

Lukasik, J.: **Directed and elliptic flow in Au+Au at intermediate energies.** 21st Winter Workshop on Nuclear Dynamics, Breckenridge, Colorado (USA), 05.02.2005.

Lukasik, J.: **INDRAGSI: Collective flow around the balance.** International Workshop on Multifragmentation and Related Topics-2005, Catania (Italy), 28.11.2005.

Lukasik, J.: **Stopping and flow, comparison of the INDRA and FOPI data.** WCI-III, Texas A&M University, College Station, Texas (USA), 12.02.2005.

Lutz, M.: **Chiral symmetry and resonances in QCD.** International Workshop XXII on Gross Properties of Nuclei und Nuclear Excitations, , FB Physik, January 2005.

Lutz, M. F. M.: **Chiral excitations in QCD.** Exotic states: challenges for QCD, Bad Honnef (Germany), 17.-21.01.2005.

Lutz, M. F. M.: **Dynamically generated baryon resonances.** NStar 2005, Tallahassee (USA), 12.-15.10.2005.

Lutz, M. F. M.: **Exotic baryons with charm.** Hadron physics at COSY, Bad Honnef (Germany), 25.-29.07.2005.

Lutz, M. F. M.: **New theoretical tools for nucleon resonance analysis workshop.** Argonne, 29. August - 3. September 2005, 29.08-03.09.2005.

Mann, R.: **Electron Spectroscopy at Storage Rings Aim and Status.** SPARC Workshop, Piaski (Poland), 06.-11.09.2005.

Mann, R.: **Online Target Diagnosis by an Electron Beam.** SPIRAL2 - International Workshop, GANIL Caen, (France), 19.-21.10.2005.

Miskowiec, D.: **CERES experiment.** Quark Matter 2005, 2005.

Mokler, P.: **Higher Order QED Contributions to the Atomic Structure at Strong Central Fields.** Physics at EBIT and Advanced Light Sources, Workshop, Sanya, Hainan (China), 09.-12.03.2005.

Mokler, P.: **QED Contributions to the Atomic Structure at Strong Central Fields.** X-Ray and Inner Shell Processes, 20th International Conference, Melbourne (Australia), 04.-08.07.2005.

Morse, J.: **NoRHDia presentation.** 1st International Industrial Diamond Conference 'Diamond at Work', Barcelona (Spain), 20.-21.10.2005.

Morse, J.: **Single-Crystal CVD, Diamond for Synchrotron Beam Monitoring.** X International Workshop on Surface and Bulk Defects in CVD Diamond SBDD, Hasselt (Belgium), 23.-25.02.2005.

Mulser, P.: **The physics of collisionless absorption and particle acceleration by superintense laser beams.** Topical problems of nonlinear wave physics NWP-2: High-field laser physics, St.-Petersburg - Nizhny Novgorod (Russia), 2.-09.10.2005.

Mulser, P.; Bauer, D.: **The physics of collisionless absorption of intense laser beams in solids and clusters.** 3rd International conference on superstrong fields in plasmas, Villa Monastero, Varenna (Italy), 19.-24.09.2005.

Mulser, P.; Bauer, D.; Kanapathipillai, M.: **The physical principle of collisionlessl absorption in superintense laser target interaction.** 2nd Interenational conference on the frontiers of plasma physics and technology, Goa (India), 21.02-..2005.

Mustafin, E.: **Analyses of the RHIC desorption experiments.** Accelerator seminar of BNL, Upton (USA), May 2005.

Neff, T.: **From the NN Interaction to Nuclear Structure and Reactions.** Breckenridge (USA), 21st Winter Workshop on Nuclear Dynamics, February 2005.

Neff, T.: **Nuclear structure within Fermionic Molecular Dynamics.** International Workshop XXII on Gross

Properties of Nuclei und Nuclear Excitations, , FB Physik, January 2005.

Neumann, R.: **Ionenstrahlen bei GSI.** Workshop Erforschung kondensierter Materie mit nuklearen Sonden und Ionenstrahlen, München (Germany), April 2005.

Neumann, R.: **Materialforschung mit relativistischen Ionenstrahlen im GSI-Zukunftsprojekt FAIR.** Workshop 'Ionenstrahlphysik und technologie', Leipzig (Germany), April 2005.

Neumann, R.: **Physics with Ions: from Analysis to Nanotechnology.** French-German Summer School PIANO, Blainville/Mer (France), September 2005.

Nörtershäuser, W.: **Electronic Eavesdropping on Nuclei: Determination of the ^{11}Li Charge Radius.** Physics in Canada - Canadian Association of Physicists Congress, Vancouver (Canada), 07.06.2005.

Nörtershäuser, W.: **Electronic Eavesdropping on Nuclei: Determination of the 11Li Charge Radius.** Vancouver (Canada), Physics in Canada – Canadian Association of Physicists Congress, June 2005.

Nörtershäuser, W.: **Electrons Spy on Nuclei: The nuclear charge radius of the halo nucleus Li-11.** Bode-Kolloquium, Max Planck-Institut für Kernphysik, Heidelberg (Germany), 25.05.2005.

Nörtershäuser, W.: **Electrons Spy on Nuclei: The nuclear charge radius of the halo nucleus Li-11.** Max-Planck Institut für Kernphysik, Heidelberg (Germany), CSR/TSR-Kolloquium, May 2005.

Nörtershäuser, W.: **Elektronischer Lauschangriff auf Kerne - Bestimmung des Ladungsradius von ^{11}Li.** Johannes Gutenberg-Universiät Mainz, Institut für Physik, QUANTUM Seminar, 10.02.2005.

Nörtershäuser, W.: **Elektronischer Lauschangriff auf Kerne: Bestimmung des Ladungsradius von Li-11.** Univ. Mainz (Germany), Institut für Physik, QUANTUM Seminar, February 2005.

Nörtershäuser, W.; Dax, A.; Ewald, G.; Sanchez, R.; Wojtaszek, A.: **Laserspektroskopische Bestimmung der Ladungsradien leichter Kerne.** Frühjahrstagung der Deutschen Physikalischen Gesellschaft, Fachverband : Hadronen und Kerne, Plenarvortrag, 04.03.2005.

Nörtershäuser, W.; Dax, A.; Ewald, G.; Sanchez, R.; Wojtaszek, A.: **Laserspektroskopische Bestimmung der Ladungsradien leichter Kerne: Von Wasserstoff zum Lithium.** Berlin (Germany), Frühjahrstagung der DPG, Fachbereich Atomphysik (Hauptvortrag), March 2005.

Nowak, H.: **Properties and Performance of Avalanche Photo Diodes.** Workshop on Physics with Antiprotons, GSI, Darmstadt (Germany), September 2005.

Nowak, H.: **Untersuchungen zur APD Auslese von Szintillationskristallen.** DPG Frühjahrstagung HuK, Berlin (Germany), March 2005.

Pershina, V.: **The chemistry of superheavy elements and relativistic effects.** First Joint NZ/FRG Workshop on Heavy and Superheavy Element Chemistry and Physics, Auckland (New Zealand), May 2005.

Pershina, V.: **Theoretical Predictions of experimentally studied properties of heaviest elements and relativistic effects.** European Science Foundation Exploratory Workshop on The Chemistry of Transactinide Elements, Oslo (Norway), October 2005.

Peters, K.: **Charm Spectroscopy in B-factories.** Stefan-Meyer Institut für subatomare Physik, Wien (Austria), 04.04.2005.

Peters, K.: **Exotics at LEAR.** 2. Internationaler Workshop 'Hadron Physics at COSY', Bad Honnef (Germany), 25.07.2005.

Peters, K.: **Experimental Status of QCD Exotics.** ECT Workshop 'Resonances in QCD', Trento (Italy), 12.07.2005.

Peters, K.: **FAIR: The future project at GSI.** Hadron 2005, Rio de Janeiro (Brazil), 22.08.2005.

Peters, K.: **FAIR: the future project at GSI.** VIIIth Biannual Low Energy Antiproton Physics Conference LEAP2005, Bonn (Germany), 19.05.2005.

Peters, K.: **GSI Physics Program.** Internationaler Workshop 'HIF 2005', Elba (Italy), 29.05.2005.

Peters, K.: **Hadron Physics Program FAIR.** Third Sandanski Coordination Meeting on Nuclear Science, Albena (USA), 30.09.2005.

Peters, K.: **Hadronenspektroskopie: Ein Streifzug von Gestern bis Übermorgen.** Physikalisches Kolloquium, Bochum (Germany), 31.10.2005.

Peters, K.: **Hadronenspektroskopie: Ein Streifzug von Gestern bis Übermorgen.** Physikalisches Kolloquium, Frankfurt (Germany), 02.11.2005.

Peters, K.: **Introduction to the hadron physics program at GSI.** Seminar am IHEP, Beijing (China), 29.04.2005.

Peters, K.: **QCD at FAIR: The future project at**

GSI. Seminar des INFN, Ferrara (Italy), 13.04.2005.

Peters, K.: **The FAIR Project at GSI.** SUPA Launch Event, Glasgow (Ireland), 07.10.2005.

Pomorski, M.: **NoRHDia Collaboration.** DPG Frühjahrstagung, Berlin (Germany), 04.-09.03.2005.

Pomorski, M.; Berdermann, E.; Ciobanu, M.; Fischer, B. E.; Martemiyanov, A.; Moritz, P.; Rebisz, M.; Voss, B.; Morse, J.; Salom, M.: **Single crystal CVD diamond detectors for Hadron Physics.** 7th International Conference on Advanced Technology and Particle Physics ICATPP, Como (Italy), 17.-21.10.2005.

Pomorski, M.; Berdermann, E.; Ciobanu, M.; Martemyianov, A.; Moritz, P.; Rebisz, M.; Marczewska, B.: **Characterisation of single crystal CVD diamond particle detectors for hadron physics experiments.** X International Workshop on Surface and Bulk Defects in CVD Diamond SBDD, Hasselt (Belgium), 23.-25.02.2005.

Quint, W.: **Atomic Physics at GSI.** Workshop on the Cooperation with KVI Groningen, GSI Darmstadt, 09.06.2005.

Quint, W.: **EU-Projektmanagement.** Informationsveranstaltung der Koordinierungsstelle KoWi, TU Darmstadt (Germany), 29.06.2005.

Quint, W.: **HITRAP - An Ion Trap Facility for Heavy Highly Charged Ions and Antiprotons.** FLAIR-SPARC Workshop, GSI Darmstadt, 12.-13.12.2005.

Quint, W.: **HITRAP Overview.** HITRAP EU Network Collaboration Meeting, Munich (Germany), 26.-28.05.2005.

Quint, W.: **Penning trap measurement of the g-factor of the (anti)proton.** LEAP Conference, Bonn (Germany), 16.-22.05.2005.

Quint, W.: **The HITRAP Project for Highly Charged Ions.** SPARC Collaboration Meeting, Piaski (Poland), 06.-10.09.2005.

Quint, W.: **g-Factor Experiments.** SPARC Collaboration Meeting, Piaski (Poland), 06.-10.09.2005.

Reich-Sprenger, H.: **Design considerations and actual status of the Vacuum System Design of FAI.** International Workshop on Heavy Ion Accelerators, Lanzhou (China), 11.-13.10.2005.

Reich-Sprenger, H.: **Grundlagen der UHV Technik.** Graduiertenkolleg, TU Darmstadt (Germany), February 2005.

Reich-Sprenger, H.: **Status report on the design work for UHV systems.** Working Meeting of CR Magnets and Vacuum System, Beijing (China), 20.-21.04.2005.

Reich-Sprenger, H.; Bellachioma, M. C.; Kollmus, H.; Krämer, A.; Bender, M.; Kurdal, J.; Welzel, K.; Bevcic, M.: **The SIS 18 UHV-upgrade program for high ion beam intensity operation of medium charged heavy ions.** Olav Workshop, CERN (Switzerland), 11.-12.04.2005.

Ricciardi, M.-V.: **Experimental Cross Sections and Velocities of the Light Nuclides Produced in the Proton-Induced Fission of 238U at 1 A GeV.** Third International Workshop on Nuclear Fission and Fission-product Spectroscopy, Cadarache (France), 11.05.2005.

Riek, Felix: **Selfconsistent description of vector-mesons in matter.** Hades Palaver, , Helmholtz International Summer School: Nuclear Theory and Astrophysical Applications, January 2005.

Roeckl, E.: **The 'truly exotic' (21+) isomer in ^{94}Ag.** IReS Strasbourg (France), February 2005.

Roeckl, E.: **One-proton and two proton radioactivity of the (21+) isomer in ^{94}Ag.** 12th Workshop on Nuclear Physics "Marie and Pierre Curie, Kazimierz Dolny (Poland), 21.-25.09.2005.

Sayed, M.; Panschow, W.: **Actual FPGAs -The Way Out of Manifold Hardware Problems?.** ICALEPCS 2005, International Conference on Accelerator and Large Experimental Physics Control Systems, Genf (Switzerland), October 2005.

Schädel, M.: **Chemical separation and characterization of superheavy elements - physical, chemical, technological and Metrological challenges.** First Joint NZ/FRG Workshop on Heavy and Superheavy Element Chemistry and Physics, Auckland (New Zealand), May 2005.

Schädel, M.: **Chemical separation and characterization of superheavy elements – physical, chemical, technological and metrological challenges.** Asia-Pacific Symposium on Radiochemistry 05 (APSORC-05), Beijing (China), October 2005.

Schädel, M.: **Perspectives of superheavy element chemistry with TASCA.** PACIFICHEM 2005, Honolulu, Hawaii (USA), December 2005.

Schädel, M.: **The TASCA Project.** European Science Foundation Exploratory Workshop on The Chemistry of Transactinide Elements, Oslo (Norway), October 2005.

Schädel, M.: **Two Decades of second generation superheavy element chemistry experiments.** International Workshop on Heavy Elements, Lanzhou (China), October 2005.

Schardt, D.: **Applied space research projects at GSI.** New Trends in Nuclear Physics Applications and Technology NPDC 19, Pavia (Italy), September 2005.

Schardt, D.: **Tumor Therapy with Heavy Ions at GSI Darmstadt.** International Symposium on Utilisation of Accelerators, Dubrovnik (Croatia), June 2005.

Scheidenberger, C.: **Antiprotonic radioactive beams.** STI-PAC-TAC Meeting, GSI, Darmstadt (Germany), March 2005.

Scheidenberger, C.: **EURONS.** Cortona (Italy), X Convegno su problemi di fisica nucleare teoretica, October 2005.

Scheidenberger, C.: **Effects of special relativity in heavy-ion accelerators and experiments.** International workshop on heavy-ion accelerators, Lanzhou (China), October 2005.

Scheidenberger, C.: **Experiments at the Low-Energy Branch of the SUPER-FRS.** International workshop on physics with Low energy beams at SPIRAL-2, Caen (France), July 2005.

Scheidenberger, C.: **First on-line results with the FRS Ion-Catcher.** 4th Combined Collaboration Meeting NIPNET-HITRAP-IONCATCHER, München (Germany), May 2005.

Scheidenberger, C.: **Massen- und Lebensdauermessungen von gespeicherten exotischen Nukliden.** TU Darmstadt (Germany), 28.06.2005.

Scheidenberger, C.: **Revolutioniert intensives Laserlicht die Teilchenbeschleunigung.** Habilitationsvortrag, Justus-Liebig Universität Gießen (Germany), 30.11.2005.

Scheidenberger, C.: **Simultaneous measurement of beta-minus decay to bound and continuum states of bare ^{207}Tl^{81+}.** EXA05, Wien (Austria), February 2005.

Scheidenberger, C.: **Status report: the Low-Energy Branch of the Super-FRS at FAIR.** STI-PAC-TAC Meeting, GSI, Darmstadt (Germany), March 2005.

Schepers, G.: **Antiwasserstoff in der Falle.** EP1 Seminar, Ruhr-Univ. Bochum, Bochum (Germany), December 2005.

Schepers, G.: **Using the Detectormodel in the Reconstruction.** Computing tutorial at the Ruhr-Univ. Bochum, Bochum (Germany), September 2005.

Schiedt, B.: **Single track-etched nanopores in polymer foils.** Seminar, MPI for Polymers Research, Mainz (Germany), October 2005.

Schiedt, B.: **Single track-etched nanopores in polymer foils.** Summer School 'Biosensing with channels', Bremen (Germany), August 2005.

Schmidt, K.-H.: **Nuclear Thermometry - Methods and Corrections.** World Consensus Initiative, Texas A&M University, College Station, Texas (USA), 12.02.2005.

Schmidt, K.-H.: **Nuclear-data Measurements at Relativistic Energies in Inverse Kinematics.** P(ND)^2 Perspectives on Nuclear Data for the Next Decade, Workshop on the future of theory- and experiment-based nuclear data evaluation, Bruyres-le-Chatel (France), 26.09.2005.

Schmidt, K.-H.: **Statistical Approaches to the Even-odd Effect in Fission.** Third International Workshop on Nuclear Fission and Fission-product Spectroscopy, Cadarache (France), 11.05.2005.

Schmitt, L.: **From COMPASS to PANDA - A Change of Paradigm in Data Acquisition and Triggering.** XXXVI. Arbeitstreffen Kernphysik, Schleching (Germany), September 2005.

Schmitt, L.: **The FAIR Project - Status and New Developments.** 19th Particles and Nuclei International Conference PANIC05, Santa Fe (New Mexiko), October 2005.

Scholz, M.: **The Increased Biological Effectiveness of Heavy Charged Particle Radiation: From Cell Culture Experiments to Biophysical Modelling.** Frankfurt Institute of Advanced Studies (FIAS), Frankfurt, 04.05.2005.

Scholz, M.: **Biophysics Research at FAIR.** Topical Workshop 'Atomic Physics in Strong Fields', Mazurian Lakes, PIASKI (Poland), 05.09.2005.

Scholz, M.: **Modelling of biological effects of high-LET radiation based on charged particle track structure and low-LET radiosensitivity.** PTCOG43 Educational Satellite Meeting, GSI (Darmstadt), 09.12.2005.

Scholz, M.: **The increased biological effectiveness of heavy charged particle irradiation: From cell culture experiments to biophysical modelling.** CERN Academic Training Programme, Genf (Switzerland), January 2005.

Schütt, P.; Krause, U.; Bär, R.; Franczak, B.; Fröhlich, G.; Hechler, L.; Redelbach, A.; Richter, S.; Schaa, V.; Schiebel, W.: **Operation Modes and Controls Aspects of FAIR.** ICALEPCS 2005, International Conference on Accelerator and Large Experimental Physics Control Systems, Genf (Switzerland), October 2005.

Schwartz, K.: **Heavy ion induced thermoluminescence in LiF and NaCl crystals.** Institute of Physics, Tartu University (Estonia), November 2005.

Schwartz, K.: **Radiation hardness of insulating materials and semiconductors.** Workshop on Novel Radiation Hard CVD Diamond Detectors for Hadron Physics, Darmstadt, Germany, September 2005.

Schwarz, C.: **FAIR: The GSI future project.** Int. Conf. on Exotic Atoms and Related Topics 2005, Wien (Austria), September 2005.

Senger, P.: **Dense baryonic matter.** XXIX Masurian Lakes Conference, Piaski, Poland, 30.08-06.09.2005.

Senger, P.: **Future Experiments on Hadron Physics and Dense Baryonic Matter at FAIR.** Kolloquium Institut für Kern- und Hadronenphysik, Forschungszentrum Rossendorf (Germany), 14.11.2005.

Senger, P.: **Probing superdense nuclear matter with heavy-ion reactions.** Graduierten Kolleg Univ. Tübingen (Germany), 20.05.2005.

Senger, P.: **Strangeness production in nuclear collisions at SIS energies.** Workshop HypHi05, Darmstadt (Germany).

Senger, P.: **The Compressed Baryonic Matter (CBM) experiment at the future Facility for Antiproton and Ion Research (FAIR) in Darmstadt/Germany.** Meeting of the Korean Physical Society, Seoul (Korea).

Senger, P.: **The Compressed Baryonic Matter Experiment at FAIR.** 2nd International Workshop on the Critical Point and Onset of Deconfinement, Bergen (Norway), 03.04.2005.

Senger, P.: **The Compressed Baryonic Matter Experiment at FAIR.** International Conference on the Physics and Astrophysics of the Quark-Gluon Plasma, Kolkata (India), 07.-12.02.2005.

Senger, P.: **The Compressed Baryonic Matter Experiment at FAIR.** Korean Heavy-ion Physics Meeting, Seoul (Korea), 21.04.2005.

Senger, P.: **The Compressed Baryonic Matter Experiment at FAIR.** Workshop RoFAIR, Perspectives on the Romanian participation in the FAIR Project, Bucharest (Romania), 24.-25.02.2005.

Senger, P.: **The future Facility of Antiproton and Ion Research (FAIR).** Institute of Physics, Bubhaneswar (India), 24.02.2005.

Sfienti, C.: **Il progetto FAIR al GSI.** Invited Talk XCI Annual Meeting of the Italian Physical Society SIF, Catania (Italy), 2005.

Sfienti, C.: **Mass and Isospin Effects in Multifragmentation.** DPG Frühjahrstagung HuK, Berlin (Germany), March 2005.

Sfienti, C.: **Mass and Isospin Effects in Multifragmentation.** XLIII International Winter Meeting on Nuclear Physics, Bormio (Italy), April 2005.

Sfienti, C.: **Mass and Isospin Effects in Multifragmentation.** XXIX Mazurian Lakes Conference on Physics, Nuclear Physics and the Fundamental Processes, Piaski (Poland), 30.08.2005.

Simon, H.: **Dripline nuclei: Properties, Means and Tools.** Seminar über Kernstruktur-, Elementarteilchen- und Astrophysik, Department Physik und Astronomie, Univ. Basel (Switzerland), 30.06.2005.

Simon, H.: **Dripline nuclei: properties, means and tools.** Seminar über aktuelle Themen aus Kosmochemie und Astrophysik, Institut für Kernchemie, Mainz (Germany), 05.12.2005.

Simon, H.: **Nuclear Physics Program at NESR.** Topical Workshop Atomic Physics in Strong Fields, Mazurian Lakes, Piaski (Poland), 07.09.2005.

Soyeur, M.; Lutz; M. F. M.: **e+ e- pair production from nucleon targets in the resonace region..** 29th Mazurian Lakes Conference on Physics: Nuclear Physics and the Fundamental Processes, Piaski (Poland), 30.08-06.09.2005.

Spädtke, P.: **28GHz ECR Source as Part of the UNILAC Upgrade Program.** International Workshop on Heavy Ion Accelerators, Lanzhou (China), 11.-13.10.2005.

Spädtke, P.; Tinschert, K.: **Specific Boundary Conditions for the Simulation of Extraction for ECRIS, LIS, and H- Sources.** 2nd Workshop on the Production of Intense Beams of Highly Charged Ions, Giardini Naxos (Italy), 11.06.2005.

Stöhlker, T.: **Atomphysik mit gekühlten Schwerionenstrahlen Präzisionsexperimente am wasserstoffähnlichen Uran.** Univ. Frankfurt (Germany), Physik,

June 2005.

Stöhlker, T.: **Challenges for Atomic Physics with Highly-Charged Ions and Antiprotons at the GSI Future Facility.** Physics Colloquium of the University of Fribourg (Switzerland), 08.06.2005.

Stöhlker, T.: **Challenges for Atomic Physics with Highly-Charged Ions and Antiprotons at the GSI Future Facility.** Physikalische Kolloquium der Universität Basel (Switzerland), 05.05.2005.

Stöhlker, T.: **Linear Polarization Properties of Radiative Electron Capture Revealed for Relativistic Projectiles.** International Seminar on Ion-Atom Collisions, Rio de Janeiro (Brazil), 28.-29.01.2005.

Stöhlker, T.: **Midterm Program at the ESR Storage Ring.** EXL collaboration meeting, Uppsala (Sweden), 01.03.2005.

Stöhlker, T.: **Photon Spectroscopy of Cooled HCI.** SPARC Collaboration Workshop, Piaski (Poland), 06.-11.09.2005.

Stöhlker, T.: **Physik starker Felder: Die Atomphysik auf dem Weg zu FAIR.** Physikalische Kolloquium der Universität Gießen (Germany), 07.11.2005.

Stöhlker, T.: **Recent Developments for the Investigation of Groundstate Transitions in Heavy One (Few)-Electron Ions.** PEARL2005, Physics at EBIT and Advanced Research Light Sources, Hainan (China), 09.-13.03.2005.

Stöhlker, T.: **SPARC: The Physics Program of the Stored Particle Atomic Physics Collaboration.** 6th International Conference on Nuclear Physics at Storage Rings, Jülich - Bonn, Germany, 23.-26.05.2005.

Stöhlker, T.: **Target development for EXL / SPARC.** EXL Collaboration Workshop, Santiago de Compostella (Spain), September 2005.

Stöhlker, T.: **Test of Bound-State QED at High-Z.** Topics in Heavy Ion Physics Memorial Symposium for Gerhard Soff, Frankfurt (Germany), 24.-25.04.2005.

Stöhlker, T.: **Test of bound state QED at the highest electric fields: Atomic structure of high-Z one - and few-electron ions.** RIKEN (Japan), International Workshop on Atomic Collisions of Slow/Trapped Highly-Charged Ions, March 2005.

Stöhlker, T.: **X-Ray Imaging and Compton Polarimetry of Atomic Transitions in Heavy Highly Charged Ions.** Seminar at the National Ignition Facility, Livermore Livermore National Laboratory (USA), 17.08.2005.

Struckmeier, J.: **Einstein Year 2005: The Lorentz Transformation as a Canonical Transformation in the Extended Phase Space.** Seminar des Instituts für Angewandte Physik, Universität Frankfurt am Main, May 2005.

Suemmerer, K.: **Coulomb dissociation of 8B: an indirect method to determine the low-energy astrophysical S-factor of the 7Be(p,g) reaction.** Seminaire CENBG Bordeaux-Gradignan, Gradignan (France), 17.06.2005.

Suemmerer, K.: **Experimental studies using radioactive beams at European large-scale facilities.** 1st CARINA workshop on Perspectives in European Nuclear Astrophysics, Girona (Spain), 08.06.2005.

Tahir, N.: **Studies of High-Energy-Density States of Matter Using Intense Heavy Ion Beams at the GSI Accelerator Facilities.** Autrans (France), Workshop: ILE Forum, March 2005.

Tahir, N. A.: **High Energy Density Matter Studies at the future FAIR Facility at Darmstadt: The HEDgeHOB Collaboration.** FORUM ILP: Worksop on Interation of Laser with Matter, Autrans (France), 13.-18.03.2005.

Tahir, N. A.: **Prospects of High-Energy-Density Matter Research at GSI Darmstadt and FUTURE FAIR Facility: the HEDgeHOB Collaboration.** Annual Moscow Workshop on the Non-ideal Plasma Physics (NPP-2005), Moscow (Russia), 30.11-01.12.2005.

Tahir, N. A.: **Studies of Equation of State Properties of High Energy Density Matter Using Intense Heavy Ion Beams at the Future FAIR Facility: the HEDgeHOB Collaboration.** Sixth International Symposium on Swift Heavy Ions in Matter (SHIM 2005), Aschaffenburg (Germany), 28.-31.05.2005.

Tahir, N. A.: **Studies of Warm Dense Matter Using Intense Beams of Energetic Heavy Ions at GSI Drmstadt Current and Future Facilities: the HEDgeHOB Collaboration.** International Workshop on Warm Dense Matter, Vancouver (Canada), 05.-08.10.2005.

Taucher-Scholz, G.: **Dynamics of Repair Protein Localization to Particle Tracks.** 52nd Annual Meeting Radiation Research Society, Denver, Colorado (USA), October 2005.

Taucher-Scholz, G.: **Imaging of Repair Protein Dynamics on Radiation Tracks.** 10th Japanese-German WS on Molecular Carcinogenesis, Universität Essen (Germany), September 2005.

Taucher-Scholz, G.: **Radiation Foci and Repair.** 10th WS on Heavy Charged Particles in Biology and Medicine, Oropa (Italy), June 2005.

Taucher-Scholz, G.: **Wie reagiert die Zelle auf Bestrahlung? Dynamik von Reparaturproteinen an Ionen-induzierten DNA-Schäden.** TU Darmstadt, Biologisches Kolloquium (Germany), November 2005.

Tauschwitz, A.: **Das PHELIX Kilojoule-Petawatt Laser Projekt bei der GSI - Status und erste Experimente.** Berlin (Germany), DPG Frühjahrstagung (Hauptvortrag), January 2005.

Tauschwitz, A.: **Das PHELIX Kilojoule/Petawatt Laser-Projekt bei der GSI und erste Experimente.** Universität Frankfurt (Germany), FB Physik, January 2005.

Toimil-Molares, M.E.: **Nanowires created by electrochemical deposition in etched ion-track membranes: investigation of novel properties.** 8th TESLA workshop: Nanoscience and Biomedicine with Ion Beams, Belgrade (Serbia and Montenegro), April 2005.

Trautmann, C.: **Hopping zwischen Beschleuniger-experimenten und Familie.** BerufsInformationsTag für Physiker/innen, Univ. Heidelberg (Germany), February 2005.

Trautmann, C.: **How energetic heavy ions modify solids: basic aspects and applications in micro- and nanoscience.** LLB Seminar, Saclay (France), January 2005.

Trautmann, C.: **Material modifications and nanoscience with MeV-GeV ions.** 9. Deutsche Physikerinnentagung, Darmstadt (Germany), October 2005.

Trautmann, C.: **Material modifications induced by MeV-GeV ions.** French-German Summer School PIANO, Blainville/Mer (France), September 2005.

Trautmann, C.: **Micro- and nanostructuring with energetic heavy-ions.** Indo German Workshop on Synthesis and Modification of Nano-Structured Materials by Energetic Ion Beams, NewDelhi (India), February 2005.

Trautmann, C.: **Nanotechnology with ion tracks.** French-German Summer School PIANO, Blainville/Mer (France), September 2005.

Trautmann, C.: **Track formation, sputtering, and applications with heavy ions of MeV to GeV energy.** 17th Intern. Conference on Ion Beam Analysis (IBA), Seville (Spain), July 2005.

Trautmann, C.: **How energetic heavy ions modify solids: Basic aspects and applications in micro- and nanoscience.** 19th Nuclear Physics Divisional Conference, New Trends in Nuclear Physics Applications and Technology, Pavia (Italy), September 2005.

Trautmann, W.: **Isoscaling and the symmetry energy in spectator fragmentation.** Glenn T. Seaborg Award Symposium, 229th American Chemical Society National Meeting, San Diego, California (USA), 13.03.2005.

Trautmann, W.: **Isoscaling and the symmetry energy in spectator fragmentation.** International Workshop on Multifragmentation, Catania (Italy), 01.12.2005.

Trautmann, W.: **The symmetry energy in nuclear reactions.** Seminaire de la Division de Recherche, IPN, Orsay (France), December 2005.

Typel, S.: **Coulomb dissociation of ^{230}Al and ^{27}P.** GSI, Darmstadt (Germany), Mini-Workshop on Coulomb Dissociation with radioactive beams at LAND/ALADIN, 15.07.2005.

Typel, S.: **Electromagnetic strength in neutron and proton single-particle halo nuclei.** Univerity Pisa (Italy), Workshop on Structure and Reactions of Exotic Nuclei, 24.-26.02.2005.

Typel, S.: **Electromagnetic strength in single-particle halo nuclei.** Technische Universität Berlin (Germany), DPG Spring Meeting, Section Hadrons and Nuclei, 04.-09.03.2005.

Typel, S.: **Indirect Methods for Nuclear Astrophysics.** Santa Tecla, Sicily (Italy), Third European Summer School on Experimental Nuclear Astrophysics, 02.-08.10.2005.

Typel, S.: **Indirect Methods in Nuclear Astrophysics.** Joint Institute of Nuclear Research (JINR), Dubna (Russia), Helmholtz International Summer School: Nuclear Theory and Astrophysical Applications, 26.07-04.08.2005.

Typel, S.: **Indirect methods for nuclear astrophysics.** Forschungszentrum Rossendorf/Dresden (Germany), Seminar, 07.01.2005.

Typel, S.: **Relativistic mean field model with momentum-dependent self-energies.** Technische Universität Berlin (Germany), , DPG Spring Meeting, Section Hadrons and Nuclei, 04.-09.03.2005.

Typel, S.: **Relativistic mean-field model with momentum-dependent self-energies.** Justus-Liebig-Universität Gießen (Germany), Colloquium of the Graduate School, 2005.

Ursescu, D.: **Risk Considerations, Measures and Procedures at PHELIX.** Laserlab: Europe Workshop on Radiation Safety at Ultra-High Intensity Lasers, Prague (Czech Republic), 01.09.2005.

Weber, C.: **Penningfallenmassenspektrometrie an ISOLTRAP und SHIPTRAP.** Institutsseminar, Institut für Kernphysik, Mainz, 23.05.2005.

Weber, C.: **The SHIPTRAP Cryogenic Penning Trap Setup.** Instituut voor Kern- en Stralingsfysica, Leuven (Belgien), 15.06.2005.

Welsch, C. P.: **Electrostatic Storage Devices.** CLIC meeting, CERN, Geneva (Switzerland), 04.02.2005.

Welsch, C. P.: **Exploring Sub-Femtosecond Correlated Dynamics with an Ultra-low Energy Electrostatic Storage Ring.** LEAP 05, Bonn (Germany), 15.-22.05.2005.

Welsch, C. P.: **FLAIR Project Proposal at GSI.** COOL05, Eagle Ridge, Galena, IL (USA), 18.-23.09.2005.

Weyrather, W.: **Basic principles for particle therapy.** First Danish Workshop on Particle Therapy, Kopenhagen (Denmark), November 2005.

Weyrather, W.: **Tumortherapie mit Ionenstrahlen.** Marienschule Offenbach, Aktion Brückenschlag, February 2005.

Wilms, A.: **A fast and compact electromagnetic calorimeter for the PANDA detector at FAIR.** VIIIth Biannual Low Energy Antiproton Physics Conference LEAP2005, Bonn (Germany), 19.05.2005.

Winkler, M.: **The NUSTAR facility at GSI.** Annual NUSTAR Collaboration meeting, GSI (Germany), February 2005.

Zeitträger, H.: **GSI's part at the Heidelberg Therapy Project (HIT).** China Institute of Atomic Energy, Beijing (China), 20.10.2005.

Zeitträger, H.: **GSI's part at the Heidelberg Therapy Project (HIT).** Institute of Modern Physics, IMP, Lanzhou (China), 17.10.2005.

Zeitträger, H.: **GSI's part at the Heidelberg Therapy Project (HIT).** Normal University, Beijing (China), 21.10.2005.

Zimmermann, H.: **Subtask: Charge breeding EURISOL-DS.** First EURISOL Design Study TOWN MEETING, GANIL, Caen (France), 28.-29.11.2005.

Zimmermann, H.: **The MAXEBIS test bench at GSI Darmstadt.** EURONS, EURISOL-DS joint collaboration meeting charge breeding, 14.09.2005.

Zipfel, B.; Klingbeil, H.; Moritz, P.; Kumm, M.: **Analysis of a digital beam phase control system.** CERN LLRF05, CERN (Switzerland), October 2005.

Zweig, M.: **Entwicklung eines Gatways von einem mobilen PC zu einem proprietären Feldbus.** SEI-Tagung, 06.04.2005.

Seminars and talks at the GSI

K. Große, GSI, Darmstadt, Germany

Bruening, U./Universität Mannheim (Germany): **Der ATOLL Chip.** IT/EE-Seminar, 11.01.2005.

Tsakiris, G. D./MPQ Garching (Germany): **Intense Attosecond Pulses Using Surface Harmonics: Generation and Detection.** Seminar der GSI, der TU Darmstadt und der Universitäten Frankfurt und Mainz, 11.01.2005.

Wagner, A./DESY Hamburg (Germany): **Matter, Energy, Space and Time – The International Linear Collider.** GSI Kolloquium, 11.01.2005.

Fischer, C./Durham (Great Britain): **Infrared properties of Landau gauge QCD.** Theorie-Seminar, 12.01.2005.

Gasques, L./JINA and University of Notre Dame (Russia and France): **The Sao Paulo potential: a parameter free description of the pycnonuclear reaction rate.** Theorie-Seminar, 12.01.2005.

Saenz, A./Humboldt-Universität zu Berlin (Germany): **Antihydrogen and its interaction with ordinary matter.** Atomphysik-Seminar, 12.01.2005.

Pistner, C./TU Darmstadt (Germany): **Abbau von Plutonium-Beständen: Neutronenphysikalische Untersuchungen zum Potenzial uranfreier Brennstoffe.** Atomphysik-Seminar, 18.01.2005.

Grisenti, R./Univ. Frankfurt (Germany): **Liquid Microjet Technology for Exploring Superfluidity in Highly Supercooled Molecular Hydrogen.** Atomphysik-Seminar, 19.01.2005.

Bürvenich, T.: **Joint Ventures of Experiment and Theory: Understanding Nuclear Ground State Properties.** KP2-Seminar, 20.01.2005.

Essel, E.: **DAQ und Slow Control für FAIR.** IT/EE-Seminar, 25.01.2005.

Rother, H.-P. /Fujitsu Services GmbH (Germany): **No more Moore? Forty years of exponential growth in IT: Myths and Methods (colloquium for Richter, Mathias).** GSI Kolloquium, 25.01.2005.

Ulrich, A./Technische Universität München (Germany): **Light sources and Gas Lasers using Low Energy Electron Beam Excitation.** Plasmaphysik-Seminar, 25.01.2005.

Aumann, T./GSI Darmstadt: **High-energy reactions and nuclear structure of unstable nuclei.** Theorie-Seminar, 26.01.2005.

Nogga, A./ Jülich (Germany): **Applying chiral interactions to light nuclei.** Theorie-Seminar, 26.01.2005.

Schiller, S./Heinrich-Heine-Universität Düsseldorf (Germany): **Interaction cooling of ions in traps: status and perspectives.** Atomphysik-Seminar, 26.01.2005.

Stöhlker, T.: **Die Physik starker Felder auf dem Teststand: Atomphysik an FAIR.** Wissenschaft für alle, 26.01.2005.

Corradi, L./Legnaro (Italy): **The Magnetic Spectrometer PRISMA - First Results.** KP2-Seminar, 27.01.2005.

Corradi, Lorenzo/Legnaro (Italy): **The Magnetic Spectrometer PRISMA - First Results.** Atomphysik-Seminar, 27.01.2005.

Sazaki, C./ GSI: **Chiral symmetry and its vector manifestation at the QCD phase transition phase transition.** Theorie-Seminar, February 2005.

Mosel, U./Universität Gießen (Germany): **Hadrons in Nuclei - Observables.** GSI Kolloquium, 01.02.2005.

Plasswilm, G.; Veskovski, S.: **Vorstellung der Produktpalette von National Instruments.** IT/EE-Seminar, 01.02.2005.

Drake, G. W. F./Dept. of Physics, Univ. of Windsor (Canada): **Helium, Relativity, and Quantum Electrodynamics.** Atomphysik-Seminar, 02.02.2005.

Riek, F.: **How to get a massless pion in Hartree Approximations?** PhD-Seminar, 02.02.2005.

Shklyar, V./Gießen (Germany): **Unified approach to photo- and meson-production of nucleon resonances.** Theorie-Seminar, 02.02.2005.

Dudek, J./Strasbourg (France): **Nuclear Symmetries of Potential Relevance for the Super-Heavy Nuclei Research Programs.** KP2-Seminar, 03.02.2005.

Ellis, J./CERN Genf (Switzerland): **Particle Physics and Cosmology.** Physikalisches Kolloquium der Technis-

chen Universität Darmstadt [Kolloquium gemeinsam mit der GSI], 04.02.2005.

Göringer, H.: **Der GSI Massenspeicher für Experimentdaten.** IT/EE-Seminar, 09.02.2005.

Rahaman, R.: **First on-line mass measurements at SHIPTRAP and mass determination of neutron-rich Fr and Ra isotopes at ISOLTRAP.** PhD-Seminar, 09.02.2005.

Zwicknagel, G./Inst. für Theoretische Physik, Universität Erlangen (Germany): **Electron cooling of highly charged ions in traps.** Atomphysik-Seminar, 09.02.2005.

Münzenberg, G./GSI, Univ. Mainz (Germany): **Research with Exotic Nuclei: New Experimental Developments lead to New Discoveries.** Spezialseminar, 10.02.2005.

Dudek, J./Strasbourg (France): **Nuclear Symmetries of Potential Relevance for the Super-Heavy Nuclei Research Programs.** Atomphysik-Seminar, 12.02.2005.

Sigmund, P./Odense (Denmark): **Lectures on basic ion penetration through matter.** PhD-Seminar, 14.02.2005.

Grosse, E./FZ Rossendorf (Germany): **Free Electron Laser.** GSI Kolloquium, 15.02.2005.

Masciocchi, S./DESY Hamburg (Germany): **Beauty Physics with the HERA-B Detector.** Spezialseminar, 15.02.2005.

Renault, G./SUBATECH Nantes (France): **Strange particle correlations measured by the STAR experiment in ultra-relativistic heavy ion collisions at RHIC.** Spezialseminar, 15.02.2005.

Walz, J./MPQ Garching (Germany): **Cold Antihydrogen Atoms.** GSI Kolloquium, 15.02.2005.

Hoffmann, D. H. H.: **Plasmaphysik: Hohe Energiedichte in ionisierter Materie.** Wissenschaft für alle, 16.02.2005.

Jacoby, J./Universität Frankfurt (Germany): **Plasmaphysik an FAIR: Hohe Energiedichte in ionisierter Materie.** Wissenschaft für alle, 16.02.2005.

Juodagalvis, A./GSI: **Shell Model Rates for Supernova Simulations.** Theorie-Seminar, 16.02.2005.

Maruyama, T./Nihon: **Kaon condensation and lambda-nucleon loop in the relativistic mean field.** Theorie-Seminar, 16.02.2005.

Masciocchi, S./DESY (Germany): **Beauty Physics with the HERA-B Detector.** Spezialseminar, 16.02.2005.

Strieder, F./Bochum (Germany): **^{12}C(α, γ) ^{16}O – 30 Years of Progress.** Atomphysik-Seminar, 17.02.2005.

Flemming, H.: **Vom NIM-Modul zum ASIC: Ein hochintegrierter Ladungs-Frequenz-Wandler für Ströme zwischen 3 pA und 150 uA.** IT/EE-Seminar, 22.02.2005.

Kavatsyuk, O./GSI: **Beta Decay of Light Tin Isotopes.** Theorie-Seminar, 24.02.2005.

Stöhlker, T./GSI: **Die Physik starker Felder auf dem Teststand: Atomphysik an FAIR.** Wissenschaft für alle, 26.02.2005.

Huhn, C.: **wiki.gsi.de als kollaboratives Dokumentationssystem.** IT/EE-Seminar, 01.03.2005.

Sedrakian, A./ Tübingen (Germany): **Pair correlations and clustering in extended nuclear systems.** Theorie-Seminar, 02.03.2005.

Schwarz, K.: **Konferenzbericht Grid Computing.** IT/EE-Seminar, 08.03.2005.

Starosta, K./MSU (USA): **Chirality and Triaxiality in Transitional Nuclei.** KP2-Seminar, 10.03.2005.

Scheidenberger, C.: **Ein Hauch von Exotik: Experimente mit kurzlebigen Kernen am Super-FRS.** Wissenschaft für alle, 16.03.2005.

Experimentausschuss: **Meeting of the GSI Experimentausschuss – Open Seminar.** Experimentausschuss, 21.03.2005.

Hsia, S./Fa. Tyan, Fremont (USA): **Opteron based Compute Servers.** IT/EE-Seminar, 22.03.2005.

Heßberger, F. P./GSI: **Nuclear Structure Investigation of Superheavy Nuclei.** KP2-Seminar, April 2005.

Shuryak, E./Stony Brook (USA): **New signals for the critical point.** Theorie-Seminar, 05.04.2005.

Bosch, F./GSI; Winter, M./GSI: **Im Schatten der langen Tage: Ein Streifzug durch den Abendhimmel im Frühling und Sommer.** Wissenschaft für alle, 13.04.2005.

Stanoiu, M./Orsay (France): **Study of Very Exotic Nuclei by Means of In-beam Gamma-ray Spectroscopy Using Radioactive Beams.** KP2-Seminar, 13.04.2005.

Grigorenko, L./GSI: **Two-proton radiative capture in astrophysics .** Theorie-Seminar, 15.04.2005.

Omet, C./ GSI: **High-Precision Studies of Few-Body**

Coulombic Systems. Atomphysik-Seminar, 15.04.2005.

Michel, N./Oak Ridge (USA): **Gamow shell model: Applications for weakly and unbound nuclei.** Theorie-Seminar, 19.04.2005.

Grigorenko, L./Dubna (Russia): **One Possibility to Study a Two-proton Halo in ^{17}Ne: Nuclear Fragmentation and Coulomb Dissociation.** KP2-Seminar, 20.04.2005.

Kester, O./GSI: **Charge state breeding with the Frankfurt MAXEBIS.** Atomphysik-Seminar, 20.04.2005.

Sazaki, C./GSI: **Chiral symmetry and its vector manifestation at the QCD phase transition.** Theorie-Seminar, 20.04.2005.

Milner, R./MIT (USA): **Spin dependent electron scattering from H and D using BLAST.** Sonderseminar, 22.04.2005.

Fricke, B./Kassel (Germany): **From Hydrogen to Superheavies, from Molecules to Clusters: On the Status of Relativistic Structure Calculations.** GSI Kolloquium, 26.04.2005.

Keyser, U. F./Delft University of Technology (Netherlands): **Probing polymer translocation through nanopores.** Seminar der Materialforschung, 26.04.2005.

Kunde, G. J./LANL (USA): **The PHENIX Silicon Vertex Tracker - Physics and Electronics.** Sonderseminar, 26.04.2005.

Spiller, P./GSI: **SIS18 upgrade Program Perspectives for Plasma Physics Experiments with Intense Heavy Ion Beams.** Plasmaphysik-Seminar, 26.04.2005.

Strieder, F./Bochum: **^{12}C$(\alpha,\gamma)^{16}$O - 30 Years of Progress.** KP2-Seminar, 26.04.2005.

Hoffmann, J.; Ott, W.: **ADC Multiplexer für Ship.** GSI-Palaver, 26.04.2005.

Adrich, P./Krakau (Poland): **Giant and Pygmy Dipole Resonances in ^{132}Sn and neighboring nuclei.** Seminar der Materialforschung, 27.04.2005.

Ullrich, J./MPI-K Heidelberg (Germany): **Sub-Femtosecond Correlated Dynamics Explored with Antiprotons.** Atomphysik-Seminar, 27.04.2005.

Langanke, K./GSI: **A FAIR chance for nuclear astrophysics (colloquium for Wolfgang Nörenberg).** GSI Kolloquium, 03.05.2005.

Malzacher, P.; Schwarz, K.: **Konferenzberichte EGEE (Grid).** IT/EE-Seminar, 03.05.2005.

Neff, S./GSI: **Transport von Schwerionen in Plasmakanälen - Transporteigenschaften und Kanalstabilität.** Plasmaphysik-Seminar, 03.05.2005.

Bert: **Dose calculation for C-12 therapy in the presence of organ motion.** PhD-Seminar, 04.05.2005.

Bender, M./GSI: **Ion Beam-Loss induced Desorption and other Vacuum Challenges for the GSI Future.** Theorie-Seminar, 10.05.2005.

Bittner, A./MPI for Solid State Research (Germany): **Chemical nanostructuring at and with viruses and clusters.** Seminar der Materialforschung, 10.05.2005.

Roth, M./TU Darmstadt (Germany): **Virtual Institutes and Real Photons/Next year's laser experiments at GSI.** GSI Kolloquium, 10.05.2005.

Meijer, G./FHI Berlin (Germany): **Manipulation of polar molecules with electric fields.** Atomphysik-Seminar, 11.05.2005.

Popeko, A./Dubna (Russia): **Gamma Spectroscopy of Transfermium Elements at the VASSILISSA Set up.** KP2-Seminar, 11.05.2005.

Scheidenberger, C./GSI: **Ein Hauch von Exotik: Experimente mit kurzlebigen Kernen am Super-FRS.** Wissenschaft für alle, 11.05.2005.

Banu, A.: **Study of 108-Sn by intermediate-energy Coulomb excitation.** PhD-Seminar, 18.05.2005.

Hotop, H./TU Kaiserslautern (Germany): **Resonanzen und Schwellenphänomene in niederenergetischen Stößen von Elektronen mit Atomen und Molekülen.** Atomphysik-Seminar, 18.05.2005.

Ivanov, Y. B./Kurchatov Institute (Russia): **Heavy-ion collisions within 3-fluid hydrodynamics: hadronic scenario.** Theorie-Seminar, 18.05.2005.

Nishio, K./GSI and Tokai (Japan): **Experimental Study of Fusion Reactions Using Deformed Targets.** KP2-Seminar, 18.05.2005.

Zioutas, K./CERN (Switzerland): **The Cern Axion Solar Telescope (CAST) and the search for solar axions.** GSI Kolloquium, 23.05.2005.

Das, B.P./Bangalore (India): **Parity Nonconservation in Heavy Ions.** Atomphysik-Seminar, 23.05.2005.

Piriz, A. R./Universidad de Castilla - La Mancha (Spain): **A heuristic approach to Rayleigh - Taylor instability.** Plasmaphysik-Seminar, 24.05.2005.

Zioutas, K./CERN (Swizerland) and Thessaloniki (Greece): **The Cern Axion Solar Telescope (CAST) and the search for solar axions.** GSI Kolloquium, 24.05.2005.

Schön, W: et al: **Konferenzberichte Hepix.** IT/EE-Seminar, 24.05.2005.

Gerl, J./GSI: **Mine Detection with gamma Back Scattering.** KP2-Seminar, 25.05.2005.

Schmidt, K. H./GSI: **High-resolution experiments on nuclear reactions an their implication for astrophysics and nuclear technology.** GSI-Palaver, 25.05.2005.

Vogel, M./Blackett Lab, Imperial College London (Great Britain): **Techniques for precision laser spectroscopy of trapped highly charged ions".** Atomphysik-Seminar, 25.05.2005.

Biryukov, P.: **An Interface between ROOT and CATIA.** GSI-Palaver, 31.05.2005.

Jarlskog, C./Lund (Sweden): **How did Einstein get the Nobel Prize?** GSI Kolloquium, 31.05.2005.

Jarlskog, C./Lund (Sweden): **How did Einstein get the Nobel Prize?** GSI Kolloquium, 31.05.2005.

Wouchuk Schmidt, J. G./Universidad de Castilla - La Mancha (Spain): **Perturbed flow evolution behind corrugated shocks and rarefaction waves, the Richtmyer-Meshkov instability.** Plasmaphysik-Seminar, 31.05.2005.

Ewald, G.: **Atomic electon probes its nucleus - Charge radius determination of radioactive lithium isotopes.** PhD-Seminar, 01.06.2005.

Manohar, A./San Diego (USA): **Large Nc QCD.** Theorie-Seminar, 01.06.2005.

Snchez, R./GSI: **Atomic Electrons Probe Halo Nuclei - Determination of the 11Li Nuclear Charge Radius.** Atomphysik-Seminar, 01.06.2005.

Kromm, E.: **GSI Computer Monitoring using Python based CGI Script.** IT/EE-Seminar, 07.06.2005.

Schilling, F. R./GeoForschungsZentrum Potsdam (Germany): **Geomaterial sciences at GFZ Potsdam.** Seminar der Materialforschung, 07.06.2005.

Shevelko, V. P./Lebedev Physical Institute Moscow (Russia): **Target Density Effects in Collisions of Fast Ions with Solid Targets.** Plasmaphysik-Seminar, 07.06.2005.

Wroblewski, A./Warschau (Poland): **Strangeness then and now.** GSI Kolloquium, 07.06.2005.

DuBois, B./University of Missouri-Rolla (USA): **Beam lifetimes and cross sections for low-charged heavy ions at UNILAC and SIS18 energies.** GSI-Palaver, 08.06.2005.

Henning, W. F./GSI: **Grundlagenforschung – Basis für Innovationen.** Wissenschaft für alle, 08.06.2005.

Kingsep, A./Kurchatov Institute, Moscow (Russia): **New Results with Z-Pinch Physics.** Plasmaphysik-Seminar, 08.06.2005.

Pochodzalla, J./Mainz (Germany): **Hypernuclei2.** KP2-Seminar, 08.06.2005.

Reuschl, R./GSI Darmstadt: **Radiative Recombination into bare and H-like Uranium Ions.** Atomphysik-Seminar, 08.06.2005.

Schuck, P./Orsay (France): **Alpha-particle condensation in nuclear systems.** Theorie-Seminar, 08.06.2005.

Brown, G./Stony Brook (USA): **Relation of Strangeness Nuggets to Strangeness Condensation and the Contribution of Neutron-Star Black-Hole Mergings to LIGO.** GSI Kolloquium, 14.06.2005.

Riley, D./University of Belfast (United Kingdom): **X-ray scattering from dense plasmas.** Plasmaphysik-Seminar, 14.06.2005.

Trautmann, C./GSI: **How energetic heavy ions modify solids: basic aspects and applications in micro- and nanoscience.** GSI-Palaver, 15.06.2005.

Watson, P./Gießen (Germany): **The Bethe-Salpeter description of light mesons beyond the ladder approximation.** Theorie-Seminar, 15.06.2005.

Batani, D./University Milano-Bicocca (Italy): **Recent experiments on electron transport.** Plasmaphysik-Seminar, 21.06.2005.

Dendooven, P./KVI Groningen (Netherlands): **Radioactive ions and atoms in superfluid helium.** Atomphysik-Seminar, 21.06.2005.

Mulser, P./TU Darmstadt (Germany): **Erzeugung quasimonochromatischer Elektronenjets im Multi-MeV-Bereich durch Höchstleistungslaser.** Theorie-

Seminar, 21.06.2005.

Myers, S./CERN (Switzerland): **Challenges of very large accelerator projects (Colloquium for K. Blasche).** GSI Kolloquium, 21.06.2005.

Kolbe, E./Basel (Switzerland): **Why should neutrino-nucleus cross sections be measured at the spallation neutron source?** Theorie-Seminar, 22.06.2005.

Verma, P./GSI, Darmstadt (Germany): **Probing superheavy quasimolecular collisions with incoming inner shell vacancies.** Atomphysik-Seminar, 22.06.2005.

Avasthi, D. K./Nuclear Science Centre NSC, Delhi (Indien): **Energetic ion beams in nano-structuring.** SSeminar der Materialforschung, 28.06.2005.

Deppe, H.: **ASICs für Zeitmessungen.** IT/EE-Seminar, 28.06.2005.

Düllmann, C./LBNL Berkeley (USA): **Heavy Element Research in Berkeley - Physics and Chemistry with the BGS.** KP2-Seminar, 28.06.2005.

Faenov, Y. Y.; Pikuz, T. A./VNIIFTRI Mendeleevo (Russia): **High-Resolution X-Ray Spectroscopy of Clusters and Powders Irradiated by Femtosecond Laser Pulses.** Plasmaphysik-Seminar, 28.06.2005.

Horowitz, C. J./Indiana University (USA): **Neutron rich matter in astrophysics and in the laboratory.** GSI Kolloquium, 28.06.2005.

Werner, U./Univ. Bielefeld (Germany): **Coulomb Fragmentation of Small Molecules by Fast Ions.** Atomphysik-Seminar, 29.06.2005.

Winter, M.: **Premature aging of human skin fibroplasts after irradiation with ^{12}C ions and X-rays.** PhD-Seminar, 29.06.2005.

Gratta, G./Stanford University (USA): **How much does a neutrino weigh ? Measuring the smallest mass in the Universe.** Atomphysik-Seminar, 30.06.2005.

Badziak, I./Institute of Plasma Physics and Laser Microfusion EURATOM, Warsaw (Poland): **Laser-driven generation of high-density ion beams by skin-layer ponderomotiv acceleration.** Plasmaphysik-Seminar, 06.07.2005.

Kavatsyuk, M./GSI: **Investigation of Nuclear Structure in the ^{100}Sn Region by Means of Total-Absorption.** KP2-Seminar, 06.07.2005.

Reinhart, H./Tübingen (Germany): **Yang-Mills theory in Coulomb gauge.** Theorie-Seminar, 06.07.2005.

Weinrich, U.: **HICAT - the ion therapy accelerator in Heidelberg.** GSI-Palaver, 06.07.2005.

Wöste, L./FU Berlin (Germany): **New Perspectives of Femtosecond Plasma Channels in Air.** GSI Kolloquium, 06.07.2005.

Brand, H.; et al.: **Konferenzberichte IEEE Real Time 2005.** GSI-Palaver, 12.07.2005.

Lips, O./TU Darmstadt (Germany): **NMR studies on LaF_3-type superionic conductors.** Seminar der Materialforschung, 12.07.2005.

Xiaokang, Y./IHM, Forschungszentrum Karlsruhe (Germany): **Optimization of a quasi-optical mode converter of a MW Gyrotron for fusion plasma heating and current drive and News from ITER.** Plasmaphysik-Seminar, 12.07.2005.

Blazhev, A.: **Nuclear Structure in the Region of the Doubly-magic ^{100}Sn^2.** Theorie-Seminar, 13.07.2005.

Henzl, V./GSI: **Spectator response to participant blast – experimental evidence and possible implications.** PhD-Seminar, 13.07.2005.

Heuck, H.-M./GSI: **Chromatic Aberration in Large Aperture fs-Lasers.** Atomphysik-Seminar, 13.07.2005.

Mahlke-Krüger, H./Cornell (USA): **Recent Results from CLEO-c.** GSI Kolloquium, 19.07.2005.

Petzold, A./TU Dresden (Germany): **Datenmanagement bei Barbar.** GSI-Palaver, 19.07.2005.

Chung, S. U./BNL (USA): **Current status and future prospects for exotic mesons.** Theorie-Seminar, 20.07.2005.

Henzlova, D./GSI: **How to reconstruct the temperature of the excited nucleus.** PhD-Seminar, 20.07.2005.

Kowal, M./Warsaw (Poland): **Entrance Channel Effects in the Synthesis of SHE.** KP2-Seminar, 20.07.2005.

Eliav, E./Tel Aviv University (Israel): **Multireference Relativistic Coupled Cluster Method: Recent Developments and Applications.** Spezialseminar, 27.07.2005.

Lepine, A./Sao Paulo (Brazil): **Measurements of Nuclear Masses and Radii at GANIL.** GSI-Palaver, 27.07.2005.

Souliotis, G./Texas A&M College Station (USA):

Projectile Residue Studies Around and Below the Fermi Energy. Theorie-Seminar, 05.09.2005.

Barty, C./Lawrence Livermore National Laboratory (USA): **Multi-kilojoule, short pulse lasers: Applications, technology and plans at LLNL.** Atomphysik-Seminar, 12.09.2005.

Huhn, C.: **Code Management mit Subversion.** GSI-Palaver, 13.09.2005.

Scheid, W./Univ. Gießen (Germany): **Ionen in intensiven Laserfeldern.** ILIAS-Seminar, 13.09.2005.

Witte, K./GSI: **Bericht IFSA.** ILIAS-Seminar, 13.09.2005.

Lüth, V./SLAC (USA): **Beauty in Particle Physics – as seen by BABAR.** Sonderseminar, 15.09.2005.

Höppner, K./GSI: **Grafikeinbindung mit LaTeX.** GSI-Palaver, 20.09.2005.

Katzenbach, R./TU Darmstadt (Germany): **Tunnel- und Tiefbau beim FAIR-Projekt der GSI - zur Statik und Kinematik von Bodenteilchen.** Wissenschaft für alle, 20.09.2005.

Fritzsch, H./LMU München (Germany): **Die Zeitabhängigkeit der Naturkonstanten.** GSI Kolloquium, 04.10.2005.

Guenaut, C./Orsay (France): **Optimized Ion Trapping of Exotic Nuclides for Mass Measurements in the N=40 Magic Region.** KP2-Seminar, 05.10.2005.

Shyh-Yuan Lee, Indiana University (USA): **Accelerator Modelling: Applications of the Orbit Response Matrix Method and the Independent Component Analysis in Beam Diagnosis.** Beschleuniger-Seminar, 06.10.2005.

Adamczewski, J. et al: **Berichte ROOT Workshop.** GSI-Palaver, 11.10.2005.

Haberer, T.: **Das Ionenskalpell - Status und Perspektive der Tumortherapie.** Wissenschaft für alle, 12.10.2005.

Hinde, D./Canberra (Australia): **Fusion Dynamics in Reactions Forming Heavy Elements.** KP2-Seminar, 12.10.2005.

Sikler, G./MPI-K Heidelberg (Germany): **Charge-Breeding of Radionuclides in an Electron Beam Ion Trap.** Beschleuniger-Seminar, 13.10.2005.

Basko, M./ITEP Moscow (Russia): **Charge-state energy-diffusion model for ion beam transport.** Plasmaphysik-Seminar, 18.10.2005.

Homeyer, H./Hahn-Meitner-Institut Berlin (Germany: **Ion Beam Physics at the ISL Berlin.** Atomphysik-Seminar, 19.10.2005.

Bret, A./Universidad Castilla la Mancha ETSI Industriales (Spain): **About the not so well-known most unstable modes encountered in relativistic beamplasma interaction.** Plasmaphysik-Seminar, 25.10.2005.

Schatz, H./MSU (USA): **Rare isotopes in cosmic explosions and terrestrial accelerators.** GSI Kolloquium, 25.10.2005.

Theory Group: **Nachlese Workshop 'Theory of Short Pulse Petawatt Laser Plasma Interaction' – Folgerungen für PHELIX-Experiment.** ILIAS-Seminar, 25.10.2005.

Jentschura, U./MPI-K Heidelberg (Germany): **Directions and Recent Developments in High-Precision Atomic Physics.** Atomphysik-Seminar, 26.10.2005.

Struckmeier, J./GSI: **Energy-Second-Moment-Map as a means for the regularity analysis of Hamiltonian systems.** Beschleuniger-Seminar, 27.10.2005.

Hoffmann, D.; Roth, M.; Witte, K.: **Neues von der IFSA (Biarritz, 5.–9. September 2005).** Plasmaphysik-Seminar, 01.11.2005.

Schlegel, T./GSI: **Erzeugung von Hohlraumstrahlung mit Lasern.** ILIAS-Seminar, 01.11.2005.

Block, M./GSI: **The SHIPTRAP project at GSI.** GSI-Palaver, 02.11.2005.

Martinez Pinedo, G./GSI: **Neutrino-induced Nucleosynthesis in Supernovae: The p-process.** KP2-Seminar, 02.11.2005.

Schmidt-Kaler, F./Uiversität Ulm (Germany): **Quantum information processing with ions.** Atomphysik-Seminar, 02.11.2005.

Tomasik, B./Copenhagen (Denmark): **The K/π horn and the lifetime of the fireball.** Theorie-Seminar, 02.11.2005.

Yaramyshev, S./GSI: **Beam Dynamics Study for the GSI-UNILAC.** Beschleuniger-Seminar, 03.11.2005.

Koonin, S. E./BP: **A Physicists View of the Worlds Energy Situation.** GSI Kolloquium, 08.11.2005.

Maynard, G./Universit Paris Sud 11, Orsay:(France): **Strongly coupled amplifying plasmas created by a high-intensity laser beam.** Plasmaphysik-Seminar, 08.11.2005.

Rosmej, O./GSI: **Experimente mit Nhelix: Ergebnisse.** ILIAS-Seminar, 08.11.2005.

Sartori Farenzena, L./Departamento de Fisica, Pontifcia Universidade Catolica, Rio de Janeiro (Brazil): **Secondary ion emission from frozen gases.** Seminar der Materialforschung, 08.11.2005.

Stockmeyer, M.: **Alice Detector Control System & EpicsGSI.** IT/EE-Seminar, 08.11.2005.

Parfenova, Y./Univ. Libre de Bruxelles (Belgium): **Study of hyperfine structure in ^{9,11}Be isotopes and the neutron distributions.** Atomphysik-Seminar, 09.11.2005.

Reuschl, R./GSI: **Radiative Recombination into Bare and H-like Uranium Ions.** PhD-Seminar, 09.11.2005.

Sümmerer, K./GSI: **Coulomb Dissociation of ^{8}B.** KP2-Seminar, 09.11.2005.

Machida, S./Rutherford Appleton Laboratory (United Kongdom): **Muon acceleration with the FFAG.** Beschleuniger-Seminar, 10.11.2005.

Bieniosek, F./LBNL, Berkeley (USA): **Intense Heavy Ion Beam Experiments in the USA.** Plasmaphysik-Seminar, 15.11.2005.

Deppe, H.; Flemming, H.: **Konferenzberichte Radiation Hardness, Berichte LHC Workshop.** IT/EE-Seminar, 15.11.2005.

Heinig, K.-H./FZR Dresden (Germany): **Ion beam synthesis and processing of nanostructures.** Seminar der Materialforschung, 15.11.2005.

Peters, K./GSI: **Facets of Hadron Spectroscopy.** GSI Kolloquium, 15.11.2005.

Damjanovic, S./Heidelberg :: **First measurement of the rho spectral function in high-energy collisions.** Theorie-Seminar, 16.11.2005.

Franchetti, G./GSI: **Progress of nonlinear dynamics studies for the design of FAIR.** Beschleuniger-Seminar, 16.11.2005.

Hagmann, S./GSI: **Electron Cusps in Ion-Atom Collisions: A New View of the Short-Wave Limit in Electron-Nucleus Bremsstrahlung.** Atomphysik-Seminar, 16.11.2005.

Holzmann, R./GSI: **Di-Electron Spectroscopy with the HADES Detector.** GSI-Palaver, 16.11.2005.

Kuhn, A./Regioplan: **Erde-Wasser-Luft: die komplexen Beziehungen des FAIR-Projektes zur Umwelt.** Wissenschaft für alle, 16.11.2005.

Schmidt-Böcking, H./Frankfurt: **Revealing the Off-shell Contributions in the He Ground State.** KP2-Seminar, 16.11.2005.

Habs, D./LMU München (Germany): **Neue Experimente mit Hochleistungs-Kurzpulslasern.** Plasmaphysik-Seminar, 22.11.2005.

Meijer, G./FHI Berlin (Germany): **Accelerator physics with neutral molecules.** GSI Kolloquium, 22.11.2005.

Stockebrand, B./Darmstadt (Germany): **TCP/IP Version 6 - Ein Überblick.** IT/EE-Seminar, 22.11.2005.

Wang, P.X./Institute of Modern Physics, Fudan University, Shanghai (China): **Exploring Electron Acceleration by Laser in Free Space.** ILIAS-Seminar, 22.11.2005.

Block, M./GSI: **Mass Measurements of Heavy Radionuclides at SHIPTRAP.** Atomphysik-Seminar, 23.11.2005.

Gasparyan, A./ITEP (Russia): **Pion-nucleon scattering up to 1.9 GeV in the framework of a coupled-channel model.** Theorie-Seminar, 23.11.2005.

Henzlova, D./GSI: **Systematic Investigation of the Isotopic Distributions Measured in the Fragmentation of ^{124}Xe and ^{136}Xe Projectiles.** KP2-Seminar, 23.11.2005.

Breitbach, G./GKSS (Germany): **Open Access in der Helmholtz Gemeinschaft.** Sonderseminar Wissenschaftlicher Ausschuss, 24.11.2005.

Fabjan, C./CERN (Switzerland): **Physics and Technology of Modern Particle Detectors.** GSI Kolloquium, 29.11.2005.

Hardt, M./FZ Karlsruhe (Germany): **Xen - Performance Measurements and LCG Installation.** IT/EE-Seminar, 29.11.2005.

Jacoby, J./Universität Frankfurt (Germany): **Frankfurter Perspektiven: Von dichten Plasmen bis zum Einzelteilchen.** Plasmaphysik-Seminar, 29.11.2005.

Mulser, P.: **Leonardo da Vinci: Naturforscher und Erfinder - Versuch einer Würdigung aus heutiger Sicht.** ILIAS-Seminar, 29.11.2005.

Quint, W./GSI (Germany): **HITRAP – An Ion Trap Facility for Heavy Highly Charged Ions and Antiprotons.** GSI-Palaver, 30.11.2005.

Shabaev, V. M./St. Petersburg State University (Russia): **Recent Progress on QED Calculations of Heavy Ions and Atoms.** Atomphysik-Seminar, 30.11.2005.

Strickland, M./FIAS: **Nonabelian plasma instabilities.** Theorie-Seminar, 30.11.2005.

Stöhlker, T./GSI (Germany): **Strong Field Effects on the Structure and Dynamics of High-Z Ions Studied at the ESR Storage Ring.** KP2-Seminar, 30.11.2005.

Grafström, S./TU Dresden (Germany): **Plasmonics: Optics on the Nanometer Scale.** GSI Kolloquium, 06.12.2005.

Krishnamurthy, M./Tata Institute of Fundamental Research, Mumbai, (India) and Max-Planck-Institut für Kernphysik, Heidelberg (Germany): **Mesoscopic Matter in Intense Laser Fields.** Plasmaphysik-Seminar, 06.12.2005.

Schaumann, G.: **Laser-geheizte Hohlraumtargets: Herstellung, Experimente, Diagnostik.** ILIAS-Seminar, 06.12.2005.

Grisenti, R. E./IKF, Univ. Frankfurt (Germany): **Cryogenic Rayleigh droplet beams: tool for novel studies in condensed matter and nuclear physics.** GSI-Palaver, 07.12.2005.

Mahata, K./GSI: **Shell Correction and Shape at the Saddle Point for A∼200.** KP2-Seminar, 07.12.2005.

Nefiodov, A. V./TU Dresden (Germany): **Double photoeffect on inner-shell electrons.** Atomphysik-Seminar, 07.12.2005.

Rubakov, V./Moscow (Russia): **Inflation, structure in the universe and Lorentz invariance.** Theorie-Seminar, 08.12.2005.

Welsch, C./CERN (Switzerland): **Beam Profile Measurements at CTF3.** Beschleuniger-Seminar, 08.12.2005.

Gabrielse, G./Harvard University (USA): **One-Electron Quantum Cyclotron: A New Measurement of the Electron Magnetic Moment and the Fine Structure Constant.** GSI Kolloquium, 13.12.2005.

Linev, S.: **Root I/O für SQL Database.** IT/EE-Seminar, 13.12.2005.

Mahnke, H,-E./HMI and Freie Universität Berlin (Germany): **From the Photo Effect to the Analysis of Nanostructures – X-Ray Absorption Spectroscopy.** Plasmaphysik-Seminar, 13.12.2005.

Rethfeld, Bärbel/TU Kaiserslautern (Germany): **Ultrashort dynamics of laser-excited solids: Time-resolved description from excitation to material removal.** Seminar der Materialforschung, 13.12.2005.

Tomaselli, M./TUD and GSI (Germany): **Electron Clusters in Strong Laser Fields.** Atomphysik-Seminar, 13.12.2005.

Audi, G./Univ. Paris (France): **The mass evaluation: Adjustment procedure and some comments on statistics.** Atomphysik-Seminar, 14.12.2005.

Bosch, F./GSI (Germany): **Warum und wie Einstein unsere Vorstellung von Raum und Zeit revolutioniert hat.** Wissenschaft für alle, 14.12.2005.

Reinosa, U./Heidelberg (Germany): **Exploring QCD Thermodynamics with the 2PI effective action.** Theorie-Seminar, 14.12.2005.

Trümper, J./MPI für Extraterrestrische Physik (Germany): **X-ray observations of neutron stars and the equation of state at high densities.** Sonderkolloquium, 14.12.2005.

Bender, M./GSI (Germany): **Status Report on Ion Induced Desorption Measurements.** Beschleuniger-Seminar, 15.12.2005.

Mulser, Peter/TU Darmstadt (Germany): **Leonardo da Vinci – Forscher und Erfinder.** ILIAS-Seminar, 20.12.2005.

Schneider, Jochen/Hamburg (Germany): **Status of the European Free Electron Laser Project for Hard X-rays, Experience from the VUV-FEL User Facility at DESY.** GSI Kolloquium, 20.12.2005.

Workshops and meetings

K. Große, GSI, Darmstadt, Germany

16.-22.01.2005: **Hirschegg 2005, Probing QCD with High Energy Nuclear Collisions.** Waldemar-Petersen-Haus, Kleinwalsertal (Austria).

24.-28.01.2005: **FAIR/CBM Tracking Week.** GSI, Darmstadt.

30.01-04.02.2005: **Hirschegg 2005 – Physics of High Energy Density in Matter.** Kleinwalsertal (Austria).

09.-11.03.2005: **5. Collaboration Meeting of the CBM Experiment at FAIR.** GSI, Darmstadt.

09.-11.03.2005: **FAIR/5. CBM Collaboration Meeting.** GSI, Darmstadt.

21.-23.03.2005: **FAIR/XII. PANDA Collaboration Meeting.** GSI, Darmstadt.

04.-06.04.2005: **SEI-Frühjahrstagung 2005, Studiengruppe für Elektronische Instrumentierung.** GSI, Darmstadt.

20.05.2005: **FAIR/STI Meeting.** GSI, Darmstadt.

28.-31.05.2005: **SHIM2005 – The Sixth International Symposium on Swift Heavy Ions in Matter.** Aschaffenburg (Germany).

30.05-01.06.2005: **FAIR/CBM Dilepton Workshop.** GSI, Darmstadt.

06.-08.06.2005: **First Workshop on Quark-Hadron Duality and the Transition to pQCD.** Laboratori Nazionali di Frascati (Italy).

06.-16.06.2005: **Helmholtz International Summer School: Heavy Quark Physics.** JINR Dubna (Russia).

13.-17.06.2005: **FAIR/3rd PANDA physics workshop, XIII. PANDA collaboration meeting.** Uppsala University (Sweden).

15.-16.06.2005: **FAIR/HISPEC/DESPEC Meeting.** Valencia (Spain).

20.-21.06.2005: **An International Workshop on Hypernuclei with Heavy Ion Beams (HypHI05).** GSI, Darmstadt.

20.-25.06.2005: **FAIR/HEDgeHOB Collaboration Meeting.** Moscow (Russia).

26.07-04.08.2005: **Helmholtz International Summer School: Nuclear Theory and astrophysical applications.** JINR Dubna (Russia).

28.-29.07.2005: **FAIR/STI Meeting.** GSI, Darmstadt.

30.08-01.09.2005: **2nd NoRHDia Workshop: Novel Radiation Hard Diamond Detectors for Hadron Physics.** GSI, Darmstadt.

06.-11.09.2005: **FAIR/SPARC topical workshop "Atomic Physics in Strong Fields".** Piaski, Mazurian Lakes (Poland).

08.-09.09.2005: **Workshop on Physics with Antiprotons: Probing QCD and fundamental symmetries.** GSI, Darmstadt.

12.09.2005: **Principles of Carbon Therapy – A PTCOG Satellite Meeting.** GSI, Darmstadt.

14.-16.09.2005: **Biology Program Advisory Committee BIO-PAC.** GSI, Darmstadt.

27.-28.09.2005: **FAIR/AFI Meeting.** GSI, Darmstadt.

28.-30.09.2005: **FAIR/Joint R3B/EXL Collaboration Meeting.** Santiago de Compostela (Spain).

11.-13.10.2005: **First FAIR FEE Workshop.** GSI, Darmstadt.

16.-18.10.2005: **Theory of Short Pulse Petawatt Laser Plasma Interaction.** GSI, Darmstadt.

26.10.2005: **FAIR p-linac meeting.** GSI, Darmstadt.

27.-28.10.2005: **FAIR Power Supplies Meeting.** GSI, Darmstadt.

14.11.2005: **FAIR Gemeinsame Sitzung AFI-FAIR/STI-FAIR.** GSI, Darmstadt.

15.-16.11.2005: **FAIR Cold Magnets Meeting.** GSI, Darmstadt.

PhD, Master, Bachelor, Habilitation and Diploma theses

K. Große, GSI, Darmstadt, Germany

In the following are listed academic works resulted from R&D at GSI or in the contact with GSI programs.

Adrich, Przemyslaw: **Observation of Pygmy and Giant Dipole Resonances in ^{132}Sn and.** Dissertation: Jagiellonian University, Krakow (Poland).

Alt: **Analyse, Implementierung und Test existierender Softwarealgorithmen in programmierbarer Hardware für das ALICE Experiment.** Dissertation: Universität Heidelberg.

Antalic, Stanislav: **Synthesis and properties of neutron deficient isotopes of elements around Z=100.** Dissertation: Comenius Universität Pressburg, Bratislava (Slowakei).

Atanasov: **Design and Implementation of a System for Data Traffic Management in a Real-Time Trigger Processing Farm Operated at 1 MHz.** Dissertation: Universität Heidelberg.

Aumann, Thomas: **Reactions with relativistic radioactive beams.** Habilitation: Johannes Gutenberg - Universität Mainz.

Backhaus, Thorsten: **Entwicklung eines Systems zum Laden und Kontrollieren von FPGAs via Ethernet auf Basis der Motorola Coldfire Architektur.** Diplom: Universität Mannheim.

Bailhache, R.: **Energieverlust und e/pi-Identifikation im ALICE Transition Radiation Detector.** Diplom: TU Darmstadt.

Balk, Monika C.: **Feldsimulation starrer Teilchenstrahlen beliebiger Geschwindigkeit und deren Anwendung in der Schwerionenbeschleunigerphysik.** Dissertation: Technische Universität Darmstadt.

Banu, Leontina Adriana: **^{108}Sn studied with intermediate-energy Coulomb excitation.** Dissertation: Johannes Gutenberg-Universität Mainz. GSI Diss 2005-11.

Barth, Joachim: **Entwicklung einer Testapparatur zur Resonanzionisation von Pd, Cu und Zn.** Diplom: Universität Mainz.

Blaum, Klaus: **Hochpräzisionsmassenspektrometrie mit Penningfallen und Speicherringen.** Habilitation: Johannes-Gutenberg Universität Mainz. GSI Habil 2005-01.

Blazhev, Andrey A.: **Nuclear Structure in the region of the double-magic 100Sn.** Dissertation: St. Kliment Ohridski University of Sofia (Bulgaria). GSI Diss 2005-15.

Boutin, David: **First Direct Observation of Bound-State Beta-Decay: Measurements of Branching and Lifetime of 207Tl81+ Fragments.** Dissertation: Justus-Liebig Universität Gießen. GSI Diss 2005-10.

Bramm, Roland: **Characterization of the ALICE-TPC Read-out Chip (ALTRO).** Dissertation: JWG-Universität Frankfurt.

Castillo Hernandez, Juan F.: **o. T.** Master: Universidad de Sevilla (Spain).

Chantelauze, Astrid: **Investigations on the Central Drift Chamber of the FOPI experiment at GSI.** Master: Universität Heidelberg.

Crespo, P.: **Optimization of an in-beam PE-Tomograph for monitoring Heavy Ion Tumor Therapy.** Dissertation: TU Darmstadt.

Cribeiro Santalla, Alberto: **Continuum States and their Boundary Conditions in a Collective-Coordinate Representation: Resonances and Phase Shifts in Fermionic Molecular Dynamics.** Dissertation: TU Darmstadt. GSI Diss 2005-13.

Crochet, Philippe: **Etude des collisions d'ions lourd aux énergies du SIS et du LHC.** Habilitation: Univ. Clermont-Ferrand (France).

Cuveland: **Entwicklung der ALICE TRD Global Tracking Unit.** Dissertation: Universität Heidelberg.

Damerau, Heiko: **Creation and Storage of Long and Flat Bunches in the LHC.** Dissertation: TU Darmstadt. GSI Diss 2005-12.

Deng, Jiajun: **Filter Design and Implementation for Realtime Applications.** Studienarbeit: TU Darmstadt.

Diehl, Andreas: **Umladung und Ionisation in Stößen zwischen mehrfach geladenen komplexen Ionen.**

Diplom: Universität Gießen.

Djeridi, Roukaia: **Untersuchung der elastischen Proton-Proton-Streuung mit dem HADES-Detektor.** Diplom: Universität Gießen.

Dmytro, Kresan: **Simulation of the Event-by-event Fluctuations of the Particle Yield Ratio Measurement in the CBM Experiment at FAIR.** Master: Taras Shevchenko National University of Kyiv (Russia).

Elfimow, Alexander: **Realisierung eines DDS-HF-Synthesizers für digitale Regelungssysteme.** Diplom: FH Fulda.

Enkelmann Eva: **Missing Links between Dabie and Sulu, the significance of the Tanlu fault and an integrated model of the exhumation of the ultrahigh-pressure crust in the Qinling-Dabie-Sulu orogen.** Dissertationertation: Technische Universität Bergakademie Freiberg.

Ewald, Guido: **Messung der Ladungsradien der radioaktiven Lithium-Isotope ^{8}Li und ^{9}Li.** Dissertation: Universität Heidelberg. GSI Diss 2005-04.

Fischer, Ulrich: **Entwurf und Implementierung eines echtzeitfähigen Network-on-Chip für den Einsatz in zeitkritischen Regelungsaufgaben.** Diplom: FH Fulda.

Funke, Tillmann: **Renormirungsgruppe in dimensional reduzierter QCD.** Diplom: Universität Bielefeld.

George, Sebastian: **Application of the Ramsey method in high-precision Penning trap mass spectrometry.** Diplom: Universität Münster. GSI Dipl 2005-03.

Giselbrecht, Stefan: **Polymere, mikrostrukturierte Zellkulturträger für das Tissue Engineering.** Dissertationertation: Universität Karlsruhe.

Gonser, Peter: **Modeling and testing straw-tube detectors for the PANDA-experiment.** Diplom: Universität Tübingen.

Greiche, Albert: **Einfluss statischer und quasistatischer Magnetfelder auf lasererzeugte Plasmen.** Diplom: TU Darmstadt.

Greiche, Albert: **Einfluss statischer und quasistatischer Magnetfelder auf lasererzeugte Plasmen.** Diplom: TU-Darmstadt.

Gutfleisch: **Local Signal Processing of the ALICE Transition Radiation Detector at LHC (CERN).** Dissertation: Universität Heidelberg.

Hagen, Christian: **Gitter Spektroskopie von Baryonen und exotischen Hadronen.** Diplom: Universität Regensburg.

Hendlmeier, Christof: **Two hadron production in longitudinally polarized lepton-nucleon collisions.** Diplom: Universität Regensburg.

Hessling, Thomas: **Herstellung und Charakterisierung von Hohlraumtargets.** Diplom: TU-Darmstadt.

Hildebrandt, Robert: **Elastic Copmton Scattering from the Nucleon and Deuteron.** Dissertation: TU München.

Hofmann, Julian: **Gekoppelte Kanaldynamik für Resonanzen mit Charm-Quarks.** Diplom: TU Darmstadt.

Hülsmann, Peter: **Neutrinoexperimente: Nachweismethoden und Produktion intensiver Neutrinostrahlen durch Beschleuniger.** Habilitation: Johann Wolfgang Goethe-Universität Frankfurt am Main.

Kalcher: **A Fault-Tolerant Mass Storage System for Clusters.** Dissertation: Universität Heidelberg.

Kavatsyuk, Myroslav: **Total-absorption studies of the Gamow-Teller transitions in light-tin isotopes.** Dissertation: National Taras Shevchenko University of Kyiv (Ukraine).

Kavatsyuk, Oksana: **Structure of excited states in nuclei near 100Sn studied in beta decay.** Dissertation: National Taras Shevchenko University of Kyiv (Ukraine).

Kezzar, K.: **Etude des effets de la masse et de l'isospin dans le processus de la multifragmentation.** Dissertation: Strasbourg, Universit Louis Pasteur (France).

Kniege, Stefan: $\pi^-\pi^-$ **Bose-Einstrein Korrelationen in zentralen Schwerionenkollisionen gemessen am Experiment NA49.** Master: Universität Frankfurt.

Laaroussi, Mohammed: **Ionenstrahl-Diagnose basierend auf einer PXI-LabVIEW-Realtime Client-Server-Applikation unter Einsatz von getriggerten und synchronisierten NI-ADC-Karten und einer NI-RIO-Karte (FPGA).** Diplom: Fachhochschule Darmstadt.

Lang, Kevin: **Entwicklung und Prototypenaufbau einer über Netzwerk ansteuerbaren Triggersignalquelle für Messsysteme der GSI-Strahldiagnose.** Diplom: Fachhochschule Darmstadt. GSI Dipl 2005-02.

Langwallner, Bernhard: **Improved QCD Sum Rules for the Nucleon.** Diplom: TU München.

Lara: **Entwicklung von Management verteilten Systeme.** Dissertation: Universität Heidelberg.

Le Bleis, Tudi: **Experiments with Radioactive Secondary Beams of Neutron-Rich Nuclei.** Diplom: Univ. Louis-Pasteur Strasbourg.

Leske, Jörg: **Schaleneffekte und kollektive Freiheitsgrade in ^{64,66,68}Zn- und ^{68,70}Ge- Isotopen.** Dissertation: Universität Bonn.

Loizides, Constantin: **Jet Physics in ALICE.** Dissertation: Universität Frankfurt/M.

Lovrincic, Robert: **Quanten-Size-Effekte und Phasenübergänge in Bismut-Nanodrähten.** Diplomarbeit: Universität Heidelberg.

Lozeva, Radomira: **A new developed calorimeter Telescope for identification of relativistic heavy-ion reaction channels.** Dissertation: St. Kliment Ohridski University of Sofia (Bulgaria). GSI Diss 2005-16.

Lu, Yuanrong: **Development of an IH-DTL Injector for the Heidelberg Cancer Therapy Project.** Dissertation: Johann Wolfgang Goethe-Universität in Frankfurt am Main. GSI Diss 2005-09.

Luca-Savim, Ovidiu: **Implementation of the Trigonometry Functions inside the FPGA for the Realtime Applications.** Bachelor: TU Darmstadt.

Marie-Jeanne, Melanie: **A temperature and pressure stabilization system for the Penning trap mass spectrometer ISOLTRAP.** Diplomarbeit: Universität Caen (France).

Markert, Jochen: **Untersuchung zum Ansprechverhalten der Vieldraht-Driftkammern niedriger Massenbelegung des HADES Experimentes.** Dissertation: Johann Wolfgang Goethe-Universität Frankfurt. GSI Diss 2005-14.

Miho, Jozsef: **Implementierung eines assoziativen Hit-Memories für die Spurverfolgung mit FPGAs.** Diplom: Universität Mannheim.

Mueller, A.: **Substrat- und Strahlungsabhängigkeit der Motilität von U87-Zellen.** Diplom: FH Darmstadt.

Musch, Bernhard: **Baryon Masses: Lattice QCD and Chiral Effective Field Theory.** Diplom: TU München.

Neff, Stephan: **Heavy-ion Beam Transport in Plasma Channels – Transport Properties and Channel Stability.** Dissertation: TU Darmstadt.

Nix, Anne-Katrin: **Elektrische Eigenschaften von graphitischen Ionenspuren in diamantartigen Kohlenstoffschichten.** Diplomarbeit: Universität Göttingen.

Omet, Carsten: **Auslegung eines Kollimationssystems zur Lokalisierung von Umladungsverlusten und Beseitigung von Desorptionsgasen hochenergetischer, intensiver Schwerionenstrahlen in Ringbeschleunigeranlagen.** Diplom: TU Darmstadt.

Paech, Kerstin: **Nichtgleichgewichtsdynamik des chiralen Phasenübergangs in relativistischen Kern-Kern Kollisionen.** Dissertation: Goethe Universität Frankfurt.

Panse: **A Hardware Based Cluster Health And Management System.** Dissertation: Universität Heidelberg.

Pelka, Alexander: **Bestimmung der Elektronendichte in lasererzeugten Plasmen mittels Laserinterferometrie.** Diplom: TU Darmstadt.

Pelka, Alexander: **Bestimmung der Elektronendichte in lasererzeugten Plasmen mittels Laserinterferometrie.** Diplom: TU-Darmstadt.

Prevor, Markus: **Deconfinement Phasenübergang der SU(4) Eichtheorie in 2+1 Dimensionen mit verbesserter Wirkung.** Diplom: Universität Bielefeld.

Procura, Massimiliano: **Quark Mass Dependence of Nucleon Observables and Lattice QCD.** Dissertation: TU München.

Rahaman, M. Saidur: **First on-line mass measurements at SHIPTRAP and mass determinations of neutron-rich Fr and Ra isotopes at ISOLTRAP.** Dissertation: Universität Heidelberg. GSI Diss 2005-01.

Reuschl, Regina: **Untersuchungen zur Photorekombination in Ion – Elektron Stößen.** Diplom: Johann-Wolfgang-Goethe-Universität Frankfurt, Fachbereich Physik, Institut für Kernphysik. GSI Dipl 2005-01.

Ricciardi, Maria Valentina: **High-resolution measurements of light nuclides produced in 1 A GeV ^{238}U-induced reactions in hydrogen and in titanium.** Dissertation: Santiago de Compostela (Spain). GSI Diss 2005-07.

Richter: **Schnelle Kalman Filter für den ALICE High Level Trigger.** Dissertation: Universität Heidelberg.

Riedl, Johann: **Produktion schwerer Quarks in hochenergetischen Prozessen.** Diplom: Universität Regensburg.

Rieth, Ulrich: **Beiträge zur Chemie der schwersten Elemente in den Bereichen Elektrochemie und Chromatographie.** Dissertation: Universität Mainz.

Schielke, Stefan: **Die Bedeutung der magischen Schalenabschlüsse N=Z=20 und N=28 für die Kernstruktur stabiler Ar- und Ca- sowie radioaktiver Ti-Isotope.** Dissertation: Universität Bonn.

Schneider: **Entwicklung des Triggerkonzeptes und die entsprechende Implementierung eines 200 GB/s Auslesenetzwerks für den ALICE Übergangsstrahlungsdetektor.** Dissertation: Universität Heidelberg.

Schönfeld, Andreas: **Untersuchungen zur Neutralisation eines energetischen H^--Strahls in einem EZR-Plasmatarget.** Dissertation: Universität Gießen.

Semke, Alexander: **Baryonenmassen in der Chrialen Störungstheorie.** Diplom: TU Darmstadt.

Sokolov, Andrei: **Development of proportional Chamber Detectors and Simulations to measure charm Hadrons in Antiproton-Proton Annihilation.** Dissertation: Universität Gießen.

Suo, Yun: **Analyse, Entwurf und Implementierung der aritmetische Division unter VHDL.** Diplom: TU Darmstadt.

Tashenov, Stanislav: **Hard X-Ray polarimetry with position sensitive germanium detectors - studies of the recombination transitions into highly charged ions.** Dissertation: Johann Wolfgang Goethe Universität, Fachbereich Physik. GSI Diss 2005-06.

Testa, Etienne: **Echanges de charge et perte d'nergie d'ions lourds ralentis, canaliss dans des cristaux de silicium.** Dissertation: Universit Claude Bernard, Lyon (France).

Thaler, Michael: **Phases of QCD: Lattice Thermodynamics and Quasipartricle Approaches.** Dissertation: TU München.

Topsch, Jana: **Schwerionenbestrahlung zwei- und dreidimensionaler Zellsysteme.** Dissertation: Johannes Gutenberg-Universität Mainz.

Tröger: **Improving Radiation Tolerance of FPGAs via Dynamic Reconfiguration.** Dissertation: Universität Heidelberg.

Vogel, Sascha: **Resonance Dynamics in Heavy Ion Collisions.** Diplom: Johann Wolfgang Goethe-Universität Frankfurt.

Wauschkuhn Bastian: **The apatite fission-track-age and confined-track-length profiles of the German continental deep drill-hole (KTB): implications for a recalibration of apatite fission-track temperature-time path modelling.** Diplomarbeit: Technische Universität Bergakademie Freiberg.

Wiebalck, Arne: **ClusterRAID: Architecture and Prototype of a Distributed Fault-Tolerant Mass Storage System for Clusters.** Dissertation: Universität Heidelberg.

Wiest, Alexander: **Optimierung des Führungsverhaltens und Inbetriebnahme einer längsgeregelten Stromversorgung für Bumpermagnet in einem Schwerionenbeschleuniger.** Diplom: FU Darmstadt.

Wietoska, Mirijam: **Pentaquarks in Neutronensternen.** Diplom: Johann Wolfgang Goethe-Universität Frankfurt.

Wolff, M.: **Aufbau eines Messstandes zur Restgasanalyse von Vorvakuumpumpen.** Diplomarbeit: Fachhochschule Wiesbaden, University of Applied Science.

Wollenweber, Tim: **Nucleon Properties and Lattice QCD: Finite Volume Effects.** Diplom: TU München.

Wüstenfeld, Jörn: **Auslese und Kontrolle der HADES Driftkammern.** Dissertation: Universität Frankfurt/M.

Wüstenfeld, Jörn: **Kaonen-Produktion in C + C und Si + Si Kollisionen bei 40 A und 158 AGeV.** Master: Universität Frankfurt.

Yuan, Jing: **Numerical Simulation of Hysteresis Effects in Ferromagnetic Material with the Finite Integration Technique.** Dissertation: Technische Universität Darmstadt.

Zeiser, Andreas: **Die Excalibur-Architektur und Ethernet zum Laden und Steuern von FPGAs.** Diplom: Universität Mannheim.

Zimmer, Kai: **Entwicklung eines Magneten für Elektronenstreuexperimente am S-DALINAC unter extremen Vorwärtswinkeln.** Diplom: TU Darmstadt.

Zumbruch, Peter W.: **Untersuchung zur Produktion von Pionen und Pion-Pion-Korrelationen in C + C - Reaktionen am HADES-Detektor bei einer Strahlenergie von 2 GeV pro Nukleon.** Dissertation: TU Darmstadt. GSI Diss 2005-08.

Teaching activities of GSI staff at universities

K. Große, GSI, Darmstadt, Germany

Appelshäuser, Bleicher, Blume, Dörner, Dumitru, Greiner, Greiner, Maruhn, Peters, Ratzinger, Rischke, Schaffner-Bielich, Schmidt-Böcking, Schramm, Stock, Stöcker, Ströbele, Stroth (WS 2005/06): **Interuniversitäres Schwerionenseminar gemeinsam mit der GSI in Darmstadt.** Universität Frankfurt, Seminar/seminar.

Appelshäuser, Bleicher, Blume, Dörner, Dumitru, Greiner, Greiner, Maruhn, Peters, Rischke, Schaffner-Bielich, Schmidt-Böcking, Schramm, Stock, Stöcker, Ströbele, Stroth (WS 2005/06): **Kolloquium zur Struktur der elementaren Materie – Astrophysik.** Universität Frankfurt, Kolloquium/collquium.

Appelshäuser, Bleicher, Blume, Dumitru, Greiner, Maruhn, Peters, Rischke, Schaffner-Bielich, Schmidt-Böcking, Schramm, Stock, Stöcker, Ströbele, Stroth (SS 2005): **Interuniversitäres Schwerionenseminar gemeinsam mit der GSI in Darmstadt.** Universität Frankfurt, Seminar/seminar.

Appelshäuser, Bleicher, Blume, Dörner, Dumitru, Greiner, Greiner, Maruhn, Peters, Rischke, Schaffner-Bielich, Schmidt-Böcking, Schramm, Stock, Stöcker, Ströbele, Stroth (SS 2005): **Kolloquium zur Struktur der elementaren Materie – Astrophysik.** Universität Frankfurt, Kolloquium/collquium.

Baeßler, S.; Bloch, I.; Blaum, K.; Egelhof, P.; Heil, K.; Huber, W.; Neugart, R.; Passler, G.; Wendt, K. (WS 2005/06): **Seminar über Quanten-, Atom- und Neutronenphysik.** , Seminar/seminar.

Baeßler, S.; Bloch, I.; Blaum, K.; Egelhof, P.; Heil, W.; Huber, G.; Neugart, R.; Passler, G.; Wendt, K. (SS 2005): **Seminar über Quanten-, Atom- und Neutronenphysik.** , Seminar/seminar.

Baeßler, S.; Bloch, I.; Blaum, K.; Egelhof, P.; Heil, W.; Huber, G.; Münzenberg, G.; Neugart, R.; Passler; G.; Wendt, K.; Werth, G. (WS 2004/05): **Seminar über experimentelle Atom- und Kernphysik.** , Seminar/seminar.

Beier (WS 2004/05): **Rechenmethoden der Elektrodynamik.** Dresden, Vorlesung/lecture.

Blaum (SS 2005): **Moderne Massenspektrometrie.** Mainz, Vorlesung/lecture.

Blaum (WS 2004/05): **Spektroskopie in Ionenfallen.** Mainz, Übung/exercise.

Blaum (WS 2004/05): **Spektroskopie mit Ionenfallen.** Mainz, Vorlesung/lecture.

Blaum (WS 2004/05): **Zusatzvorlesung Physik für Chemiker.** Mainz, Vorlesung/lecture.

Blaum, Nörtershäuser (WS 2005/06): **Laserspektroskopie, Fallen und ihre Anwendungen (M,F).** Mainz, Vorlesung/lecture.

Blaum, Nörtershäuser (WS 2005/06): **Laserspektroskopie, Fallen und ihre Anwendungen (M,F).** Mainz, Übung/exercise.

Boine-Frankenheim (WS 2005/06): **Einführung in die Beschleunigerphysik.** Darmstadt, Vorlesung/lecture.

Boine-Frankenheim (SS 2005): **Linear and circular accelerators.** 12th Euro Summer School on Exotic Beams, Vorlesung/lecture.

Bosch (WS 2005/06): **Physik der Elementarteilchen.** Kassel, Vorlesung/lecture.

Bosch (SS 2005): **Schlüsselexperimente der Atom-Kern und Experimentalteilchenphysik.** Kassel, Vorlesung/lecture.

Bosch, Fricke, Fritzsche (WS 2005/06): **Atomphysikalisches Seminar mit der GSI.** Kassel, Seminar/seminar.

Braun-Munzinger, P. (SS 2005): **Kernphysik I.** TU Darmstadt, Vorlesung/lecture.

Egelhof, P. (SS 2005): **Kernphysikalische Aspekte der Astrophysik.** , Vorlesung/lecture.

Egelhof, P.; Kraft-Bermuth, S. (SS 2005): **Übungen zur Vorlesung Kernphysikalische Aspekte der Astrophysik.** , Übung/exercise.

Egelhof, P.; Zeitnitz, Ch. (WS 2004/05): **Seminar zum physikalischen Praktikum für Fortgeschrittene I und II.** , Seminar/seminar.

Elsässer, T. (WS 2005/06): **Radiation Biophysics.** TU Darmstadt, Vorlesung/lecture.

Emling (WS 2004/05): **Physik V (Kern- und Teilchenphysik).** Heidelberg, Vorlesung/lecture.

Emling (WS 2004/05): **Physik an der zukünftigen Beschleunigeranlage bei GSI.** Heidelberg, Vorlesung/lecture.

Emling, H. (WS 2005/06): **Gruppenunterricht zur Physik V Vorlesung.** Heidelberg, Übung/exercise.

Feldmeier (WS 2005/06): **Kernphysik II: Theoretische Kernphysik.** Darmstadt, Vorlesung/lecture.

Feldmeier, Friman, Wambach, Langanke (WS 2005/06): **Theorie-Seminar zur Schwerionenphysik.** Darmstadt, Seminar/seminar.

Feldmeier, Roth, Langanke (SS 2005): **Kernstruktur und Nukleare Astrophysik.** Darmstadt, Seminar/seminar.

Feldmeier (WS 2004/05): **Informationstheorie und Quantenstatistik.** Darmstadt, Vorlesung/lecture.

Forck (WS 2004/05): **Beam Instrumentation and Diagnostic.** Joint University Accelerator School, Archamps, France, Vorlesung/lecture.

Fournier, C. (SS 2005): **Angewandte Strahlenbiologie.** FH Darmstadt, Vorlesung/lecture.

Friman (WS 2005/06): **Einführung in die Allgemeine Relativitätstheorie.** Darmstadt, Vorlesung/lecture.

Friman (SS 2005): **Einführung in die Allgemeine Elementarteilchenphysik.** Darmstadt, Vorlesung/lecture.

Friman, Braun-Munzinger, Wambach, Oeschler (WS 2004/05): **Relativistische Schwerionenphysik.** Darmstadt, Seminar/seminar.

Friman, Feldmeier, Wambach, Langanke (WS 2005/06): **Theorie-Seminar zur Schwerionenphysik.** Darmstadt, Seminar/seminar.

Fröhlich (2005): **Aufbau und Funktionsweise von digitalen Rechenanlagen.** FH Darmstadt, Vorlesung/lecture.

Fröhlich (2005): **Designprinzipien moderner Prozessoren.** FH Darmstadt, Vorlesung/lecture.

Fröhlich (2005): **Ion Beam Optics.** J.W.Goethe-Universität Frankfurt am Main, Vorlesung/lecture.

Fröhlich (2005): **Parallele Rechnerarchitekturen.** FH Darmstadt, Vorlesung/lecture.

Geissel, Scheidenberger (WS 2005/06): **Ziele des neuen internationalen FAIR Projektes.** Universität Gießen, Seminar/seminar.

Geissel (WS 2004/05): **Experimentelle Methoden der Kernstrukturforschung – Astrophysik.** Gießen, Vorlesung/lecture.

Geissel (WS 2004/05): **Experimentelle Methoden der Kernstrukturforschung – Wechselwirkung mit Materie.** Gießen, Vorlesung/lecture.

Genz, Hoffmann, Richter, Wambach, Zilges (WS 2005/06): **Saturday Morning Physics – Einführung in Probleme der modernen Physik.** Darmstadt, Vorlesung/lecture.

Görnitz, Korneck, Trautmann (WS 2005/06): **Moderne Physik.** Universität Frankfurt, Vorlesung/lecture.

Höppner (WS 2005/06): **Grundlagen der Programmierung II (C++).** FH Darmstadt, Vorlesung/lecture.

Höppner (SS 2005): **Grundlagen der Programmierung I (C++).** FH Darmstadt, Vorlesung/lecture.

Hoffmann (WS 2005/06): **Grundlagen der Trägheitsfusion.** Darmstadt, Seminar/seminar.

Hoffmann (WS 2005/06): **Ions and Atoms in Plasmas – Introduction to Plasma Physics with Heavy-Ions.** Darmstadt, Vorlesung/lecture.

Hoffmann, Bock, Roth (WS 2005/06): **Physik Dichter Plasmen mit Schwerionen und Laserstrahlen.** Darmstadt, Seminar/seminar.

Hoffmann, Richter, Roth, Wambach, Zilges (WS 2005/06): **Schwerionenphysik.** Darmstadt, Seminar/seminar.

Hoffmann, Roth (WS 2005/06): **High Energy Density in Matter.** Darmstadt, Seminar/seminar.

Hoffmann, Roth (WS 2005/06): **Wechselwirkung intensiver Laser- und Ionenstrahlen mit Materie.** Darmstadt, Seminar/seminar.

Hoffmann, Tauschwitz (WS 2005/06): **Dunkle Materie – Astroteilchenphysik.** Darmstadt, Seminar/seminar.

Hoffmann (SS 2005): **Einführung in die Plasmaphysik mit schweren Ionen.** Darmstadt, Seminar/seminar.

Hoffmann (SS 2005): **Grundlagen der Trägheitsfusion.** Darmstadt, Seminar/seminar.
Hoffmann (SS 2005): **Physik für Biologen.** Darmstadt, Vorlesung/lecture.

Hoffmann (SS 2005): **Physik für Biologen.** Darmstadt, Übung/exercise.

Hoffmann (SS 2005): **Project work in plamaphysics.** Darmstadt, Praktikum/practical course.

Hoffmann, Roth (SS 2005): **Physik Dichter Plasmen mit Schwerionen und Laserstrahlen.** Darmstadt, Seminar/seminar.

Hoffmann, Roth, Knoll, Oeschler (SS 2005): **International Student Program at GSI Research with heavy ions.** Darmstadt, Vorlesung/lecture.

Hoffmann (WS 2004/05): **Experimentelle Projektarbeiten in der Plasmaphysik.** Darmstadt, Praktikum/practical course.

Hoffmann (WS 2004/05): **Graduiertenkolleg: Physik und Technik von Beschleuniger.** Darmstadt, Vorlesung/lecture.

Hoffmann (WS 2004/05): **Grundlagen der Trägheitsfusion.** Darmstadt, Seminar/seminar.

Hoffmann (WS 2004/05): **Ions and Atoms in Plasmas - Introduction to Plasma Physics with Heavy Ions.** Darmstadt, Vorlesung/lecture.

Hoffmann, Kinsep (WS 2004/05): **Grundlagen nichtlineare Plasmaphysik.** Darmstadt, Vorlesung/lecture.

Hoffmann, Manakos, Panagiotis, Richter, Wambach (WS 2004/05): **Schwerionenphysik.** Darmstadt, Seminar/seminar.

Hoffmann, Richter, Wambach, Zilges (WS 2004/05): **Saturday Morning Physics – Einführung in die Probleme der modernen Physik.** Darmstadt, Vorlesung/lecture.

Hoffmann, Roth (WS 2004/05): **High Energy Density in Matter.** Darmstadt, Seminar/seminar.

Hoffmann, Roth (WS 2004/05): **Wechselwirkung intensiver Laser- und Ionenstrahlen mit Materie.** Darmstadt, Seminar/seminar.

Hoffmann, Roth, Bock (WS 2004/05): **Physik dichter Plasmen mit Schwerionen- und Laserstrahlen.** Darmstadt, Seminar/seminar.

Hoffmann, Tauschwitz (WS 2004/05): **Dunkle Materie – Astroteilchenphysik.** Darmstadt, Seminar/seminar.

Hofmann, I.; Struckmeier, J.; Ratzinger, U. (WS 2005/06): **Vielteilcheneffekte in dichten Teilchenstrahlen.** Universität Frankfurt, Seminar/seminar.

Hofmann, I.; Struckmeier, J.; Ratzinger, U. (WS 2004/05): **Vielteilcheneffekte in dichten Teilchenstrahlen.** Universität Frankfurt, Seminar/seminar.

Jakob, B. (WS 2005/06): **Biophysikalische Aspekte von Zellen und Zellnetzwerken: Molekulare Grundlagen der biologischen Strahlenwirkung, DNA-Schäden und zelluläre Strahlenreaktion.** TU Darmstadt, Vorlesung/lecture.

Kluge (WS 2004/05): **Modern Methods of Atomic and Molecular Physics.** Heidelberg, Vorlesung/lecture.

Kluge, Mokler, Hochschullehrer der Atomphysik (WS 2005/06): **Seminar über Atomphysik.** Liebig Universität Gießen, Seminar/seminar.

Kluge, Mokler, Hochschullehrer der Atomphysik (WS 2004/05): **Seminar über Atomphysik.** Liebig Universität Gießen, Seminar/seminar.

Knoll (SS 2005): **Internationales Studentenprogramm (Organisator).** Darmstadt, Praktikum/practical course.

Kraft (WS 2004/05): **Physik von Zellen und zellulären Netzwerken.** Darmstadt, Vorlesung/lecture.

Kraft, Elsaesser (WS 2005/06): **Strahlenbiophysik.** Darmstadt, Vorlesung/lecture.

Kraft, G.; Elsaesser, T.; Scholz, M.; Schardt, D.; Kraft-Weyrather, W.; Ritter, S.; Jakob, B. (WS 2005/06): **Radiation Biophysics.** TU Darmstadt, Vorlesung/lecture.

Kraft, Galuske, Langner, Thiel (WS 2005/06): **Physik von Zellen und zellulären Netzwerken.** Darmstadt, Vorlesung/lecture.

Kühl (WS 2005/06): **Ergänzungskurs für Chemiker zum Grundkurs I.** Mainz, Vorlesung/lecture.

Kühl (SS 2005): **Ergänzungskurs für Chemiker zum Grundkurs I.** Mainz, Vorlesung/lecture.

Kühl (WS 2004/05): **Relativistische Laser-Plasmaphysik.** Mainz, Vorlesung/lecture.

Kühl, Bock, Hoffmann, Jacoby, Maruhn, Mulser, Roth, Schlegel (WS 2004/05): **Physik dichter Plasmen mit Schwerionen- und Laserstrahlen.** Mainz, Seminar/seminar.

Lange, Blume (WS 2004/05): **Nuclear Physics III - Introduction into QCD.** Univ. Frankfurt, Vorlesung/lecture.

Lange, Blume (WS 2004/05): **Nuclear Physics III - Introduction into QCD.** Univ. Frankfurt, Übung/exercise.

Liesen (WS 2005/06): **Oberseminar über Atomphysik.** Heidelberg, Seminar/seminar.

Liesen (SS 2005): **Oberseminar über Atomphysik.** Heidelberg, Seminar/seminar.

Liesen (WS 2004/05): **Gruppenunterricht zur Physik III.** Heidelberg, Seminar/seminar.

Liesen (WS 2004/05): **Oberseminar über Atomphysik.** Heidelberg, Seminar/seminar.

Lutz, M. (SS 2005): **Effective field theories.** Hadrogenesis, Summerschool, Rez, Prague (Czech Republic), Vorlesung/lecture.

Lutz, M. (SS 2005): **Einführung in effektive Quantenfeldtheorien.** TU Darmstadt, .

Miskowiec, Lippmann, Busch (SS 2005): **Kernphysik I.** TU Darmstadt, Übung/exercise.

Mokler, Grün, Müller, Salzborn, Schartner, Scheid (WS 2004/05): **Seminar über Atomphysik.** Gießen, Seminar/seminar.

Mokler, Müller, Scheid, Schartner, Kluge (SS 2005): **Seminar über Atomphysik.** Liebig Universität Gießen, Seminar/seminar.

Münzenberg (WS 2004/05): **Experimentelle Atom- und Kernphysik.** Mainz, Vorlesung/lecture.

Münzenberg (WS 2004/05): **Seminar über aktuelle Themen aus Kosmochemie und Astrophysik.** Mainz, Seminar/seminar.

Neumann (WS 2005/06): **Materialforschung und Nanotechnologie mit energiereicher Strahlung II.** Heidelberg, Vorlesung/lecture.

Neumann (SS 2005): **Materialforschung und Nanotechnologie mit energiereicher Strahlung I.** Heidelberg, Vorlesung/lecture.

Neumann (WS 2004/05): **Hochauflösende Mikroskopie und Nanotechnologie II.** Heidelberg, Vorlesung/lecture.

Quint (WS 2005/06): **Struktur der Atome und Moleküle.** Heidelberg, Vorlesung/lecture.

Quint (WS 2004/05): **Struktur der Atome und Moleküle.** Heidelberg, Vorlesung/lecture.

Ratzinger, U.; Jacoby, J.; Klein, H.; Schempp, A.; Hofmann, I.; Podlech, H.; Struckmeier, J. (WS 2005/06): **Winterschule 'Aktuelle Probleme der Beschleuniger- und Plasmaphysik'.** Universität Frankfurt, Seminar/seminar.

Ratzinger, U.; Klein, H.; Schempp, A.; Jacoby, J.; Hofmann, I.; Struckmeier, J. (WS 2005/06): **Aktuelle Probleme der Beschleuniger- und angewandten Schwerionenphysik.** Universität Frankfurt, Seminar/seminar.

Ratzinger, U.; Jacoby, J.; Klein, H.; Schempp, A.; Hofmann, I.; Podlech, H.; Struckmeier, J. (WS 2004/05): **Winterschule 'Aktuelle Probleme der Beschleuniger- und Plasmaphysik'.** Universität Frankfurt, Seminar/seminar.

Ratzinger, U.; Klein, H.; Schempp, A.; Jacoby, J.; Hofmann, I.; Struckmeier, J. (WS 2004/05): **Aktuelle Probleme der Beschleuniger- und angewandten Schwerionenphysik.** Universität Frankfurt, Seminar/seminar.

Richter, Hoffmann,Jakoby, Weiland, Zilges (SS 2005): **Graduiertenkolleg: Physik und Technik von Beschleuniger.** Darmstadt, Vorlesung/lecture.

Rosmej (WS 2005/06): **Quantentheorie des Lichtes.** Bochum, Vorlesung/lecture.

Scheidenberger, C. (SS 2005): **Entstehung der Elemente in Sternen und im Labor.** Universität Gießen, Vorlesung/lecture.

Scheidenberger, C. (SS 2005): **Neue physikalische Möglichkeiten an FAIR.** Universität Gießen, Vorlesung/lecture.

Scheidenberger (WS 2004/05): **Experimentelle Methoden der Kernstrukturforschung – Wechselwirkung mit Materie.** Gießen, Vorlesung/lecture.

Scheidenberger, C. (WS 2004/05): **Ziele des neuen internationalen FAIR Projektes.** Universität Gießen, Seminar/seminar.

Scholz, M.; Weber, K. J. (WS 2005/06): **Radiologischer Kurs / Strahlenbiologie.** Universität Heidelberg, Vorlesung/lecture.

Scholz, M.; Weber, K. J. (WS 2004/05): **Radiologischer Kurs.** Heidelberg, Vorlesung/lecture.

Schwarz (WS 2005/06): **Kernphysikalisches Fortgeschrittenen-Praktikum.** Frankfurt, Praktikum/practical course.

Schwarz (SS 2005): **Kernphysikalisches Fortgeschrittenen-Praktikum.** Frankfurt, Praktikum/practical course.

Schwarz (WS 2004/05): **Praktikum für Fortgeschrittene im IKF.** Frankfurt, Praktikum/practical course.

Senger (WS 2004/05): **Ergänzungen zur Kernphysik 1.** Frankfurt, Vorlesung/lecture.

Spädtke, P. (SS 2005): **Beam Formation I/II.** Specialised CAS Course on 'Small Accelerators', Zeegse (Netherlands), Vorlesung/lecture.

Stöhlker (WS 2005/06): **Atomphysik I.** Frankfurt, Vorlesung/lecture.

Stöhlker (WS 2005/06): **Übungen zur Vorlesung: 'Atomphysik I'.** Frankfurt, Übung/exercise.

Stöhlker, Dörner, Dreizler, Jacoby, Lüdde, Maruhn, Schmidt-Böcking (WS 2005/06): **Hauptseminar: Neue Aspekte der Atomphysik.** Frankfurt, Seminar/seminar.

Stöhlker, Dörner, Groeneveld, Hagmann, Schmidt-Böcking, Stiebing (WS 2005/06): **Atomphysik mit schweren Ionen.** Frankfurt, Seminar/seminar.

Stöhlker (SS 2005): **Atomphysik IV.** Frankfurt, Vorlesung/lecture.

Stöhlker, Dörner, Groeneveld, Hagmann, Schmidt-Böcking, Stiebing (SS 2005): **Atomphysik mit schweren Ionen.** Frankfurt, Seminar/seminar.

Stöhlker (WS 2004/05): **Atomphysik I: Struktur und Dynamik von Ionen und Atomen.** Frankfurt, Vorlesung/lecture.

Stöhlker, Becker, Hagmann, Dreizler, Lüdde, Schmidt-Böcking (WS 2004/05): **Hauptseminar: Hochgeladene langsame Ionen - neue Aspekte in der Atomphysik.** Frankfurt, Seminar/seminar.

Stöhlker, Becker, Hagmann, Dreizler, Lüdde, Schmidt-Böcking (WS 2004/05): **Hauptseminar: Hochgeladene langsame Ionen - neue Aspekte in der Atomphysik.** Frankfurt, Seminar/seminar.

Stöhlker, Dörner, Groenefeld, Hagmann, Schmidt-Böcking, Stiebing (WS 2004/05): **Atomphysik mit schweren Ionen.** Frankfurt, Seminar/seminar.

Struckmeier, J. (SS 2005): **Ionenstrahldynamik.** Universität Frankfurt, Vorlesung/lecture.

Sylvia, R. (WS 2005/06): **Chromosomenkurs.** TU Darmstadt, Praktikum/practical course.

Trautmann (WS 2005/06): **Kernphysik für Studierende des Lehramtes an Haupt- und Realschulen.** Frankfurt, Vorlesung/lecture.

Trautmann, Sfienti (WS 2005/06): **Kernphysik für Studierende des Lehramtes.** Universität Frankfurt, Vorlesung/lecture.

Trautmann, Sfienti (WS 2004/05): **Kernphysik für Studierende des Lehramtes.** Universität Frankfurt, Vorlesung/lecture.

Wambach (WS 2005/06): **Mitarbeiterseminar.** Darmstadt, Seminar/seminar.

Wambach (WS 2005/06): **Theorie klassischer Teilchen und Felder I.** Darmstadt, Vorlesung/lecture.

Wambach, Braun-Munzinger, Friman, Oeschler (WS 2005/06): **Relativistische Schwerionenphysik.** Darmstadt, Seminar/seminar.

Wambach (WS 2004/05): **Rechenmethoden der Physik.** Darmstadt, Vorlesung/lecture.

Weber (WS 2005/06): **Spektroskopie in Ionenfallen.** Mainz, Übung/exercise.

Weber (SS 2005): **Spektroskopie in Ionenfallen.** Mainz, Übung/exercise.

Weber (WS 2004/05): **Spektroskopie in Ionenfallen.** Mainz, Übung/exercise.

Weyrather, W. K. (SS 2005): **Course Radiotherapy, Medical Imaging.** Universität Mannheim, Kurs/course.

Experiments performed at the GSI accelerators in 2005

compiled by Magdalena Górska, beam time coordinator 2005

∗In all tables 1 shift represents 8 hours of beam delivered to an experiment running in either main or parasitic mode.

Exp	Short title	Spokesperson	Status	Area	Ion	Shifts∗
U068	Bolometric Detectors	Egelhof	main	X8	^{12}C	4
U074	Energy loss of ions in dense plasmas	Blazevic	parasitic	Z6	^{40}Ar	15
U114	Multiple ionization	Hagmann	main	X4	^{54}CR	13
U120	Electron spectroscopy	Hagmann	parasitic	X4	^{48}Ca, ^{197}Au	11
U161	Electron spectroscopy	Hagmann	parasitic	X4	^{48}Ca, ^{40}Ar, ^{20}Ne	11
U165	Melecular fragmentation	Lutz	main	X4	^{136}Xe, ^{197}Au	15
U182	Element 106 and 108 Chemistry	Kratz	main	X1	^{40}Ar	12
U184	Heavy elements	Hofmann	main	Y7	^{20}Ne, ^{48}Ca	181
U189	Projectile spectroscopy	Rosmej	parasitic	Z6	^{48}Ca	15
U190	Stopping power measurements	Golubev	parasitic	Z6	^{12}C, ^{40}Ar	12
U201	Commissioning of SHIPTRAP	Quint	main	Y7	^{58}Ni	9
U205	Decay prperties near Z=108 and N=162	Tuerler	main	X1	^{48}Ca,^{26}Mg	57
U206	Rn isotopes	Andreyev	main	Y7	^{52,54}Cr	35
U207	Optical spectroscopy of Nobeium	Hessberger	main	Y7	^{52}Cr, ^{58}Ni	27
U209	Nuclear Structure Investigations No, Lr	Hessberger	main	Y7	^{48}Ca	34
U210	α-emitters in the transuranium region	Novikov	main	X1	^{12}C	11
U211	Even-even nuclaus ^{260}Sg	Sulignano	main	Y7	^{54}Cr	59
U213	Ion-plasma interaction	Blazevic	parasitic	Z6	^{26}Mg, ^{54}Cr	14
U216	ERDA: Oxide Laysers on stainless steel	Bender	main	UU	^{48}Ca, ^{136}Xe	11
UBIO	Radiobiology	Scholz	parasitic	X6	^{12}C, ^{48}Ca, ^{54}Cr, ^{238}U, ^{124}Sn, ^{136}Xe, ^{152}Sm	45
UMAT	Material Science	Trautmann /Fischer	main	X0	^{238}U, ^{12}C, ^{58}Ni, ^{78}Kr, ^{124}Sn, ^{197}Au, ^{208}Pb	64

Exp	Short title	Spokesperson	Status	Area	Ion	Shifts*
S104	Actinides by fragmentation	Schmidt	parasitic	HFS	^{197}Au, ^{208}Pb	17
S188	Dipole strangth in Ni isotopes	Aumann	main	FRS/HTC	^{40}Ar	7
S214	Bound states of eta and omega	Gillitzer	main	HFS	^{2}D	33
S247	Nuclear density distributions	Khanzadeev	main	FRS/HTC	^{12}C	30
S249	Precise measurement of stopping powers	Golubev	parasitic	HTA	^{238}U	9
S251	FOPI upgrade	Herrmann	parasitic	HTB	^{58}Ni, ^{86}Kr	1
S258	Gas catcher for FRS	Savard	main	HFS	^{58}Ni	22
S260	AMS	Ting	main	HTA	^{197}Au	8
S262	Dileptons	Salabura	parasitic	HAD	^{14}N	9
S269	RISING	Reiter	main	HFS	^{48}Ca, ^{40}Ca, ^{86}Kr, ^{132}Xe	63
S271	Two proton decay of ^{19}Mg	Mukha	parasitic	HFS	^{12}C	3
S280	RD on systhetic diamond detectors	Berdermann	parasitic	HTA	^{1}H	4
S282	Two-photon decay in heavy He-like ions	Dunford	main	HTA	^{208}Pb	18
S283	Spectroscopic investigation of ^{69}Br	Becker	main	HFS	^{78}Kr	21
S285	Triaxiality in even-even core nuclei	Saito	main	HFS	^{152}Sm	20
S287	Dipole strength in Ni isotopes	Aumann	main	FRS/HTC	^{58}Ni, ^{86}Kr	48
S291	Radioactivity induced by U ions	Mustafin	main	HTA	^{238}U	8
S295	Photodissociation experiments	Zilges	main	FRS/HTC	^{94}Mo	24
S297	Strange Barions/ Kaonic Clusters	Herrmann	main	HTB	^{2}D, ^{27}Al, ^{1}H	79
S301	HADES	Salabura	parasitic	HAD	^{12}C, ^{40}Ar, ^{40}Ca, ^{27}Al	88
S302	HED matter with intense beams	Mintsev	parasitic	HHT	^{238}U	24
S308	g-factor of the 11^- isomer in ^{196}Po	Maj	main	HFS	^{238}U	16
S310	g-factor of isomeric states near ^{100}Sn	Balabanski	main	HFS	^{136}Xe	20
S311	g-factors of isomeric states	Neyens	main	HFS	^{124}Sn, ^{238}U	27
SBIO	Biophysics experiments	Scholz/Schardt	main	HTA	^{12}C	28
SMAT	Material science	Trautmann	parasitic	HTA	^{86}Kr, ^{181}Ta	1

Exp	Short title	Spokesperson	Status	Area	Ion	Shifts*
E012	Direct mass measurement	Wollnik	main	ESR/HFS	^{238}U	20
E013/E017	Beta decay of highly charged ions	Bosch	main	ESR	^{152}Sm	15
E039	Precision X-ray spectroscopy	Beyer	main	ESR	^{238}U	17
E043	Charge tranfer from complex targets	Braeuning-Demian	main	X4	^{238}U	9
E049	Beta decay of highly charged ions	Bosch	main	ESR	^{152}Sm	13
E052	Deceleration of highle charged ions	Dauvergne	main	ESR	^{238}U	14
E056	Storage lifetimes and cross-sections	Dubois	main	ESR	^{132}Xe, ^{238}U	24
E062	Measurement of p,gamma rates	Heil	main	ESR	^{136}Xe	18
E064	Light-ion induced reactions in storage rings	Chartier	main	ESR	^{78}Kr, ^{136}Xe	13
E065	DR isotopic shift	Brandau	main	ESR	^{142}Nd, ^{152}Nd	23
E067	Test of time dilatation	Karpuk	main	ESR	^{7}Li	10

Scientific bodies of the GSI as at January 15th, 2006

K. Große, GSI, Darmstadt, Germany

Supervisory Board/Aufsichtsrat:

Dr. B. Vierkorn-Rudolph [chair],
Bundesministerium für Bildung und Forschung, Bonn/Berlin (Germany),
as representative of the Federal Republic of Germany

Ministerialrat Dr. R. Koepke,
Bundesministerium für Bildung und Forschung, Bonn/Berlin (Germany),
as representative of the Federal Republic of Germany

Ministerialdirigent Dr. R . Bernhardt,
Hessisches Ministerium für Wissenschaft und Kunst, Wiesbaden (Germany),
as representative of the State Hessen in Germany

Prof. Dr. R. Klanner,
Universität Hamburg/DESY (Germay),
as representatives of the Scientific Council of the GSI

Scientific Directorate/Wissenschaftliches Direktorium WD:

Prof. Dr. W. F. Henning [chair]
Dr. H. Eickhoff
Prof. Dr. P. Braun-Munzinger
Prof. Dr. K.-H. Langanke
Dr. A. Kurz

Divisions and department leaders/Bereichs- und Abteilungsleiter:

Dr. H. Eickhoff, Accelerator/Beschleunigerbereich
Prof. Dr. P. Braun-Munzinger, Infrastructure/Infrastruktur
Prof. Dr. K.-H. Langanke, Research/Forschungsbereich and
Theory: Nuclear structure and astrophysics/Theorie: Kernstruktur- und Astrophysik
Prof. Dr. H.-J. Kluge, Atomic physics/Atomphysik
Prof. Dr. G. Kraft, Biophysics/Biophysik
Prof. Dr. P. Braun-Munzinger, Nuclear physics I/Kernphysik I
Prof. Dr. H. Emling, Nuclear physics II/Kernphysik II
Prof. Dr. K. Peters, Nuclear physics III/Kernphysik III
Prof. R. Neumann, Materials research/Materialforschung
Prof. Dr. D. H. H. Hoffmann, Plasma physics/Plasmaphysik
Prof. Dr. J. Stroth, HADES
Prof. Dr. J. Wambach, Theory: QCD and hadron physics/Theorie: QCD und Hadronenphysik
Prof. Dr. K. Witte, PHELIX

Scientific Council/Wissenschaftlicher Rat WR:

<http://www.gsi.de/informationen/users/EAC/wr/>

R. Klanner [chair], Universität Hamburg (Germany); N. Holtkamp, Oak Ridge National Laboratory (USA); M. H. R. Hutchinson, Rutherford Appleton Lab, Central Laser Facility, Oxfordshire (Great Britain); C. Leemann, Thomas Jefferson National Accelerator Facility, Newport News (USA); V. Metag, Justus-Liebig-Universität, Gießen (Germany); B. Mueller, Duke University, Durham (USA); H. Requardt, Siemens AG Medical Solutions, Erlangen (Germany); D. O. Riska, Helsinki Institute of Physics, University of Helsinki (Finnland); W.-D. Schlatter, CERN EP, Geneva (Switzerland); B. M. Sherrill, Michigan State University, East Lansing (USA); A. Shotter, TRIUMF, Vancouver (Canada); M. Soyeur, DSM/DAPNIA/SPhN, Gif-sur-Yvette (France)

Scientific Committee/Wissenschaftlicher Ausschuss WA:

<http://www-w2k.gsi.de/wa/scientific_committee.htm>

S. Richter [chair]; A. Bräuning-Demian; L. Dahl; H. Essel; B. Friman; S. Götte; W. Henning; I. Hofmann; B. Lommel; P. Malzacher; D. Miskowiec; G. Moritz; W. F. J. Müller; R. Neumann; H. Reich-Sprenger; C. Scheidenberger; M. Scholz; P. Senger; A. Tauschwitz; M. Traxler

GSI Programme Advisory Committee PAC/ Experimentausschuss EA:

<http://www.gsi.de/informationen/users/EAC/ea/>

H. W. E. M. Wilschut [chair], Kernfysisch Versneller Instituut, Groningen (Netherlands); J. Aichelin, SUBATECH, Nantes (France); A. Drees, SUNY Stony Brook (USA); R. Krücken, Technische Universität München, Physik-Department (Germany); K. Langanke, GSI and Technische Universität Darmstadt (Germany); M. Lewitowicz, GANIL, Caen (France); S. Paul, Technische Universität München, Physik-Department (Germany); T. Peitzmann, Utrecht University (Netherlands); G. Savard, Argonne National Lab, Physics Division (USA); B. Sharkov, Inst. of Theoretical and Experimental Physics, Moscow (Russia); J. Ullrich, MPI für Kernphysik, Heidelberg (Germany); E. Widmann, Stefan-Meyer-Institut für subatomare Physik, Österreichische Akademie der Wissenschaften, Wien (Austria)

GSI Phelix and Plasmaphysics Program Advisory Committee (PPAC):

<http://www.gsi.de/informationen/users/EAC/ppac/>

M. H. R. Hutchinson [Chair], Rutherford Appleton Lab (United Kingdom); S. Jacquemot, LULI, Ecole Polytechnique, Palaiseau (France); G. Logan, LBL Berkeley (USA); T. A. Mehlhorn, Sandia National Laboratories, Albuquerque (USA); R. Sauerbrey, Friedrich-Schiller-Universität Jena (Germany); B. Sharkov, Inst. of Theoretical and Experimental Physics Moscow (Russia)

GSI Biophysics & Radio-Biology Program Advisory Committee (Bio-PAC):

<http://www.gsi.de/informationen/users/EAC/bio-pac/>

G. Iliakis [Chair], Institut für Medizinische Strahlenbiologie Universitätsklinikum Essen (Germany); M. Durante, Universita 'Federico II', Napoli (Italy); R. Engenhardt-Cabillic, Klinik für Strahlentherapie Philipps-Universität Marburg Klinikum (Germany); B. Michael, Gray Lab (Cancer Research Trust), Mount-Vernon-Hospital, Northwood (United Kingdom); R. Okayasu, National Institute of Radiological Sciences, Chiba-shi (Japan); E. Pedroni, Paul Scherrer Institut, Villigen (Switzerland)

Scientific Coordination:

Dr. K. D. Groß,

Committees of the FAIR Project

FAIR Project Coordinator: H. H. Gutbrod, GSI (Germany)

FAIR GSI-Project Division Leader: D. Krämer, GSI (Germany)

The International Steering Committee for the Facility for Antiproton and Ion Research (ISC-FAIR)

Chair: H. Schunck (Germany);
C. Alejaldre (Spain); M. Arajarvi (Finland); L. Borjesson (Sweden); D. Charalambidis (Greece); G. Fortuna (Italy); F. Gounand (France); X. Jiang (China); J. Koslov (Russia); R. Kulessa (Poland); J. Ma (China); S. Meng (China); D. Sakar (India); B. Vierkorn-Rudolph (Germany); J. Wood (United Kingdom); H. Yong (China); W. Zhan (China).

The working group for Scientific and Technical Issues STI for the international Facility for Antiproton and Ion Research (FAIR) at GSI

Chair: H. Wenninger (Switzerland), until Mach 2005; S. Gales;
W. Zhan (China); J. Aysto (Finland); D.-O. Riska (Finland); A. C. Mueller (France); W. Korten (France); P. Schroth (Germany); W. F. Henning (Germany); H. Stroeher (Germany); P. Dalpiaz (Italy); P. Fabbricatore (Italy); J. Benlliure (Spain); B. Rubio (Spain); U. Wiedner (Sweden); H. Danared (Sweden); B. Sharkov (Russia); G. Rosner (United Kingdom); NN (Greece); NN (India); NN (Poland).

The working group for Administrative and Funding Issues AFI for the international Facility for Antiproton and Ion Research (FAIR) at GSI

Chair: Ö. Seppstedt (Sweden) from Feb., 2006;
M. Arajarvi (Finland); B. Dormy (France); N. Godet (France); J. Grapentin (Germany); S. Hieber (Germany); A. Kurz (Germany); B. Maske-Demand (Germany); B. Vierkorn-Rudolph (Germany); Y. Bravo (Italy); C. Guaraldo (Italy); R. Pellegrini (Italy); L. E. Ruiz-López (Spain); L. Eriksson (Sweden); O. Skeppstedt (Sweden); P. Bogdanov (Russia); O. Patarkin (Russia); N. Pratt (United Kingdom); D. Schildt (United Kingdom).

AFI subcommittee FCI

Chair: B. Brandt;
B. Dormy (France); N. Godet (France); H. Fangohr (Germany); J. Grapentin (Germany); S. Hieber (Germany); A. Kurz (Germany); B. Maske-Demand (Germany); C. Scherf (Germany); K. Witte (Germany); L. Palumbo (Italy); L. Miralles (Spain); L. Eriksson (Sweden); S. Wells (United Kingdom).

LFI subcommittee FCI

Chair: B.-U. Jahn;
M. Arajarvi (Finland); N. Godet (France); T. Delissen (Germany); H. Fangohr (Germany); H. H. Gutbrod (Germany); A. Kurz (Germany); S. Hieber (Germany); N. Leclercq (Germany); B. Maske-Demand (Germany); C. Scherf (Germany); K. Witte (Germany); Yara Bravo (Italy); Carlo Guaraldo (Italy); L.-E. Ruiz-López (Spain); L. Eriksson (Sweden).

The Cost Review Group for Accelerators CORE-A (FAIR)

Chair: D. Plane (CERN);
K. Blasche (GSI); R. Bacher (DESY); M. Buhler-Broglin (CERN); W. Erdt (CERN); G. Fernqvist (CERN); H. Haseroth (CERN); I. Gardner (CCLRC); D. Kraemer (BESSY); L. Miralles (CELLS); G. Stevenson (CERN); P. Strubin (CERN); T. Taylor (CERN); E. Weisse (CERN).

The Cost Review Group for Experiments CORE-E (FAIR)

Chair: W. Bartel (DESY);
H.-J. Hilke (CERN); I. Lazarus (CCLRC); P. Lazeyras (CERN); H. G. Ritter (LBL); J. Simpson (CCLRC); A. Vacchi (INFN).

Atomic, Plasma Physics and Applications Programme Advisory Committee FAIR APPA-PAC

Chair: D. Schwalm (MPI Heidelberg);
S. Atzeni (University Rome); M. Basko (ITEP); G. W. F. Drake (University Windsor); P. Indelicato (University PM Curie Paris); G. Maynard (University Paris-Sud); T. A. Mehlhorn (SNL); P. Norreys (RAL); R. Sauerbrey (University Jena); B. Sharkov (ITEP); P. Spiller (GSI); M. Steck (GSI); D. Vernhet (GPS Paris); T. Yamazaki (RIBF-RIKEN).

Quantum Chromo Dynamics Programme Advisory Committee FAIR QCD-PAC

Chair: E. Chiavassa (INFN Torino);
S. J. Brodsky (SLAC); P. Dalpiaz (INFN); D. Geesaman (ANL); H. A. Gustafsson (University Lund); S. Kox (IN2P3); R. Landua (CERN); A. Magnon (CERN); R. Maier (FZ Jülich); B. Mueller (University Duke); J. Nelson (University Birmingham); E. Oset (IFIC); D.-O. Riska (University Helsinki); H. Stroeher (FZ Jülich); H. G. Ritter (LBL); I. Tserruya (Rehovot).

Nuclear Structure and Nuclear Astrophysics Programme Advisory Committee FAIR NUSTAR-PAC

Chair: R. Casten (University Yale);
F. Azaiez (IPNO); P. Butler (CERN); H. Grawe (GSI); R. Janssens (ANL); S. Kubono (CNS RIKEN); K. Kurz (FZ Jülich); H.-O. Meyer (University Indiana); A. Poves (University Madrid); B. Rubio (IFIC); B. Sherril (MSU); A. Shotter (TRIUMF); A. Villari (GANIL); H. Weick (GSI); M. Wiescher (University Notre-Dame).

The Technical Advisory Committee FAIR TAC

Chair: C. Yanglai (ANL);
P. Fabbricatore (INFN); R. Garoby (CERN); S. Ivanov (IHEP); M. Jacquemet (CEA); T. Junquera (IPNO); A. Mueller (IPNO); J. Nolen (ANL); S. Ozaki (BNL); F. Willeke (DESY); Y. Yamazaki (KEK).

miniTAC Beam Diagnostics

H. Schmickler (CERN); T. J. Shea (Oak Ridge National Laboratory).

miniTAC Power Supplies

J.-P. Jensen (DESY); H.-J. Eckoldt (DSEY); G. Fernqvist (CERN); F. Bordry (CERN); R. Fuja (Spallation Neutron Source); R. Cutler (Oak Ridge National Laboratory).

miniTAC Proton Linac

R. Cutler (Oak Ridge National Laboratory); R. Fuja (Spallation Neutron Source); H. Haseroth (CERN).

miniTAC Cryogenics

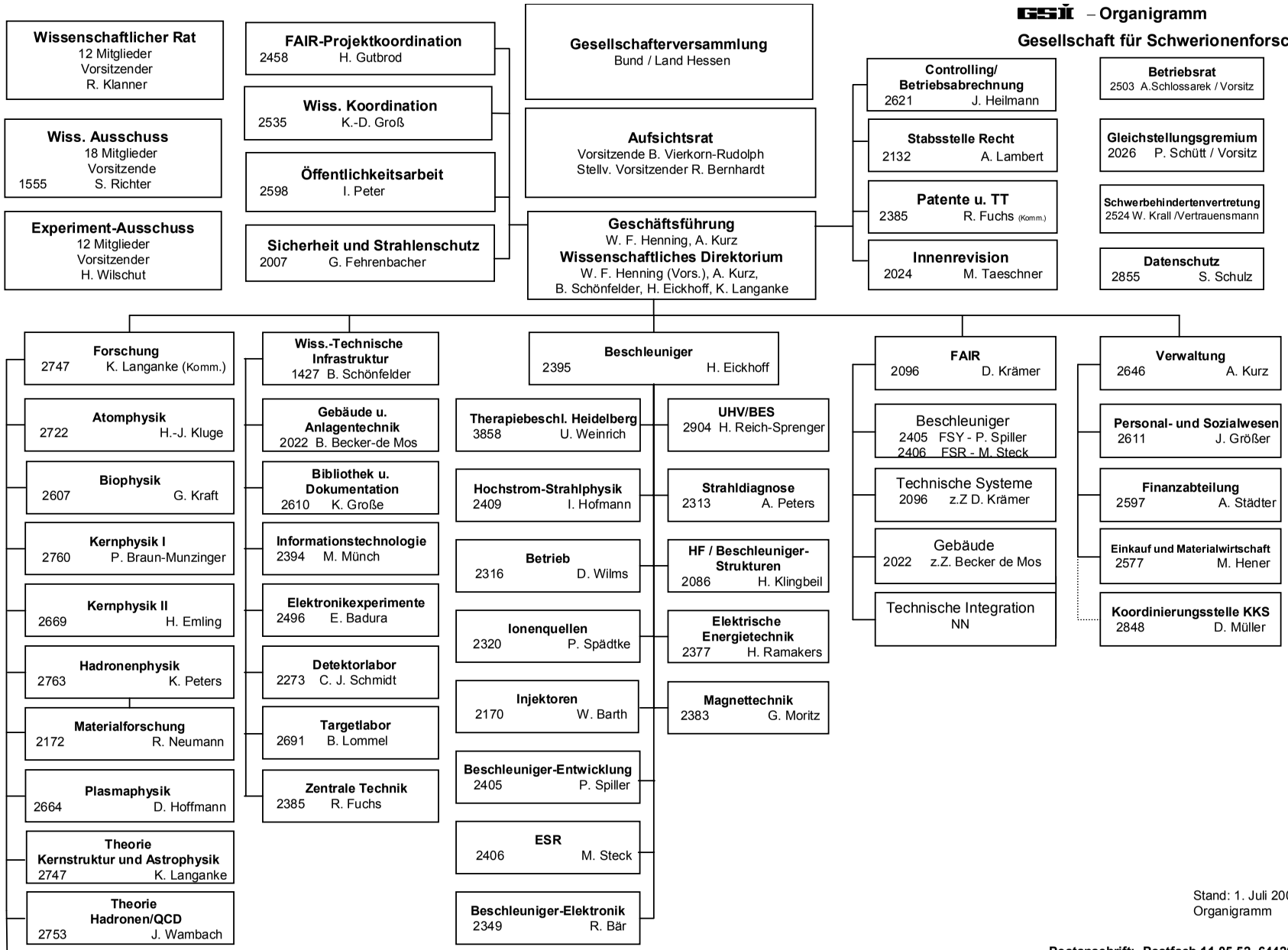
W. Erdt (CERN); G. T. Mulholland (Applied Cryogenics Technology); B. Petersen (DESY); H. Quack (Technical University Dresden); R. Trant (CERN); S. Wolff (DESY).

miniTAC Warm Magnets

J. Tuozzolo (Brookhaven National Laboratory); N. Marks (Daresbury National Laboratory); M. Muto (KEK).

miniTAC Cold Magnets

L. Bottura (CERN); P. Bruzzone (Paul-Scherrer-Institut); S. Gourlay (Lawrence Berkeley Laboratory); J. Kerby (Fermi National Accelerator Laboratory); M. Jacquemet (GANIL); P. Fabbricatore (Istituto Nazionale di Fisica Nucleare di Genova); T. Taylor (CERN); W. Scandale (CERN); E. Willen (Brookhaven National Laboratory); R. Wolf (CERN).



Stand: 1. Juli 2006
Organigramm

Postanschrift: Postfach 11 05 52 64420 Darmstadt
Telefon: 0 61 59/71– 0 Telefax: 0 61 59/71 – 27 85

Facts and Figures

J. Heilmann, K. Große, GSI, Darmstadt, Germany

Gesellschafter/Shareholders since 1969, December 17th

Federal Republic of Germany	90% of budget (and of share capital)
State of Hesse/Land Hessen	10% of budget (and of share capital)

Accelerators

FAIR	Facility for Antiprotons and Ion Research		pre-construction R&D
UNILAC	UNIversal Linear ACcelerator	13 MeV/u for U	in operation since 1976
SIS	Schwer-Ionen-Synchrotron	50–1000 MeV/u for U	in operation since 1989
ESR	Experimental Storage Ring	3–400 MeV/u for U	in operation since 1990

In 2005, GSI provided access to 25 experimental areas to about 1300 scientific users.

Total budget

Total budget in research and development:	81 million euros	
budget in the programme Structure of matter		67 million euros
budget in the programme Health		3 million euros
budget in the non-programme-bound research		11 million euros

Staff at 31.12.2005

Staff for research and development total	886 person years	
out of these in the programme Structure of matter		536 person years
out of these in the programme Health		36 person years
out of these for scientific infrastructure		192 person years
out of these for non-programme-bound research		122 person years
Staff for centre management and management support	63 person years	
Staff for basic infrastructure	9 person years	
Staff for special tasks	37 person years	

In total about 1000 employees including about 300 scientists and engineers.

List of Authors

Achenbach, B. 47, 51
Achenbach, P. 76, 79
Ackermann, D. 191, 194, 196, 197, 198, 262, 298
Adamczewski, J. 270, 272, 274
Adonin, A. 329
Albers, D. 295
Algora, A. 31
Ali Khan, A. 239
Al-khateeb, A. M. 115
Al-Khatib, A. 146
Alkofer, R. 243
Alme, J. 288
Alonso, J. 317
Alphonse, G. 378
Alt, C. 225, 229
Alt, T. 286
Altipnar, S. 283
Al-Turany, M. 66
Alvarez-Rodriguez, R. 29
Amar-Youcef, S. 59
Ameil, F. 159
Amend, W. 284
An, S. 94
Andre, C. 107
Andreyev, A. N. 196
Andrianov, V. 299
Andronic, A. 209, 210
Angelov, V. 289
Antalic, S. 191, 194, 196, 198
Anton, J. 201, 326
Antonczyk, D. 230
Appelshäuser, H. 232, 233, 234, 284
Armbruster, P. 159
Artemyev, A. N. 324
Assmann, W. 110
Atkin, E. 71
Audi, G. 297
Augustin, I. 1
Augustinski, G. 282, 283
Aumann, T. 45, 148
Azaiez, F. 148
Bacca, S. 182
Backe, H. 294
Bacquias, A. 158
Bächler, J. 282
Bär, M. 139
Bär, R. 400
Bagnoud, V. 356
Bailhache, R. 211
Baker, L. A. 349
Balanzat, E. 347
Balogh, A. G. 350
Balß, R. 101
Banas, D. 19, 21, 300, 306, 318, 304, 305
Banik, N. L. 205
Banu, A. 146, 149, 152
Barberet, P. 355
Barbieri, C. 163
Barth, W. 87, 88, 121, 310
Bartos, D. 67
Baruah, S. 297
Bassalleck, B. 7
Batist, L. 150, 152, 153
Baublis, V. 65
Baur, G. 17
Bayer, W. 87, 121
Beceiro, S. 120
Bechtold, A. 400
Beck, D. 273, 297, 298
Beck, T. 146
Becker, D. 377
Becker, F. 107, 152, 153, 146, 148, 156, 157
Becker, G. 355
Becker, R. 314
Beckert, K. 15, 39, 92, 125, 141, 143, 296, 299, 304, 305
Bednarczyk, P. 146, 148
Behr, J. 295
Behr, K. H. 41
Behr, K.-H. 47, 156, 157
Beier, T. 310
Beier, T. W. 1
Bellachioma, M. C. 112
Beller, P. 14, 15, 39, 92, 104, 125, 141, 143, 296, 299, 304, 305
Benabderrahmane, M. 223
Bender, M. 109, 110
Benlliure, J. 159
Benzoni, G. 148, 146
Berceanu, I. 67
Bercuci, A. 210
Berdermann, E. 267, 269, 387
Berghöfer, K. 1
Bergmark, T. 94
Bernas, M. 159
Bernert, M. 71
Bernhardt, D. 296
Bersani, A. 74
Bert, C. 391
Bertini, D. 66
Bertulani, C. A. 24
Berz, M. 47
Besson, A. 59
Bettega, D. 379

Bevcic, M. 310
Beyer, H. F. 21, 306, 318
Bianco, L 196
Biryukov, P. 276
Blaese, M. 369
Blasche, K. 90, 91, 124
Blaschke, D. B. 189
Blasi, N. 148
Blaum, K. 8, 33, 42, 44, 297, 298, 310, 312, 315, 317
Blazevic, A. 330, 331, 333, 334
Blazevich, A. 356
Blazhev, A. 150, 152, 153
Bleicher, M. 179, 256
Bleile, A. 299
Blell, U. 90, 124, 134
Block, M. 44, 298, 310, 315
Blume, C. 225, 229, 234, 284
Bock, R. 356
Böhm, S. 296, 306
Böttcher, H. D. 390
Boine-Frankenheim, O. 90, 96, 115, 94, 134
Bollen, G. 297
Bongardt, K. 94
Borneis, S. 13, 356
Bosch, F. 15, 39, 141, 143, 293, 296, 306, 307, 308, 325, 304, 305
Bossler, J. 122
Botvina, A. S. 180
Boudard, A. 159
Bouffard, S. 342
Boutin, D. 39, 49, 47, 141, 143
Bracco, A. 148, 146
Bräuning, H. 307, 308
Braeuning-Demian, A. 4
Bräuning-Demian, A. 307, 308, 326
Brambilla, S. 146
Brambrink, E. 360
Brand, H. 273, 356
Brandau, C. 15, 296, 306
Bratkovskaya, E. 229
Braun, J. 259
Braun-Munzinger, P. 209, 210, 282
Bravo, E. 187
Breckheimer, M. 205
Breitenfeldt, M. 297
Brezeanu, M. 364
Bricault, P. 295
Bringel, P. 146
Brinkmann, K.-T. 75
Brömmel, D. 239
Brötz, J. 353
Brons, S. 401
Brown, G. E. 171
Brüchle, W. 152, 153, 197, 204, 205, 206, 263, 264, 265
Brück, K. 33
Brüning, U. 71
Brünle, A. 41, 156, 157
Bruske, C. 356
Buballa, M. 244
Buda, R. 205
Bürger, A. 146
Bürvenich, T. J. 169
Burch, T. 238, 239
Burkard, K. 156, 157
Burkhard, H. G. 191, 194
Bushaw, B. 295
Bussmann, M. 14
Caballero, L. 31
Caceres, L. 41
Caird, J. 356
Calzolari, P. 379
Camera, F. 148, 146
Campagnolo, R. 288
Campbell, P. 32, 34
Carroll, J. J. 141
Casarejos, E. 159
Cassing, W. 183
Cassou, K. 359
Castoldi, M. 148
Catanescu, V. 67
Catford, W. 45
Caurier, E. 149
Cee, R. 400
Cervera, J. 348
Chakrawarthy, R. S. 141
Chartier, M. 45
Chatterjee, S. 306, 307, 318
Chau, L. 137
Chauduri, A. 298
Chen, L. 39, 141
Chevallier, M. 308
Chubaryan, G. 41
Chulkov, L. V. 24
Ciobanu, M. 269, 277
Clark, J. A. 41
Claus, G. 59
Clement, E. 146
Clemente, G. 88, 89
Cleymans, J. 212
Cohen, C. 308
Colonna, M. 178
Commenda, C. 136
Conrad, S. 372
Cordier, E. 68, 277
Cornelius, T. W. 350, 351, 352
Cortazar, O. D. 11
Cozma, D. 252
Crespi, F. 148
Crespo, P. 392, 393, 394, 395
Crespo López-Urrutia, J. 42, 43
Cribeiro, A. 181

Cullen, D. 141, 196
Currell, F. J. 296
Czajkowski, S. 159
Czarnota, M. 306
Dahl, L. 87, 88, 121, 310, 313
Dahl, U. 311
Damerau, H. 132
Danared, H. 5
Dangwal, A. 353
Danilin, B. V. 172
Daoutidis, J. 168
Darby, I. 196
Dauvergne, D. 308
Dax, A. 295
de Angelis, G. 148
De Gersem, H. 97, 134
de Lucio, O. 15
De Napoli, M. 215
Dean, D. J. 164, 165
Debus, J. 383
Delahaye, P. 297
Della Vedova, F. 148
Deppe, H. 71
Deutsch, C. 9, 336
Deveaux, M. 59
Dewald, A. 38
Di, Z. 41, 260
Di Toro, M. 178
Dickel, T. 260
Dietrich, J. 94
Dilling, J. 295
Dinkelaker, P. 225, 229
Djekic, S. 317
Dobrev, D. 354
Döring, J. 150, 152, 153
Dörner, R. 16, 110, 304, 305
Dolinskii, A. 40, 92, 94
Doliwa, B. 134
Dombsky, M. 295
Dong, C. Z. 300
Doornenbal, P. 145, 146
Dorn, C. 107, 398
Dorn, M. 71
Dorokhov, A. 59
Dousse, J. C. 21
Dousse, J.-Cl. 306
Dragojevic, I. 203
Drake, G. W. F. 295
Dressler, R. 191
Droba, M. 137
Du, G. 355
DuBois, R. D. 15
Dudin, S. 332
Düllmann, C. 265
Düllmann, C. E. 203
Dulinski, W. 59
Dumitru, A. 253
Dunford, R. 307
Dvorak, J. 204
Dworschak, M. 297
Eberhardt, K. 207, 265, 197
Efremov, V. P. 331, 333
Egelhof, P. 27, 45, 299
Eichhorn, R. 94
Eichler, R. 203
Eickhoff, H. 85, 401
Eisenbarth, U. 356
Eliav, E. 200
Eliseev, S. 298, 310
Elizarov, A. A. 319
Elsässer, T. 367
Emling, H. 45, 47, 148
Engeland, T. 149
Enghardt, W. 392, 393, 394, 395
Enkelmann, E. 344
En-qvist, T. 159
Ensinger, W. 347, 350
Epp, S. 43
Eppinger, K. 46
Ernst, H. 310
Ershov, S. N. 172
Eschke, J. 1
Essel, H. G. 270, 272, 274
Ewald, G. 35, 293, 295
Fabbietti, L. 222
Faenov, A. Y. 334
Faessler, A. 189, 252
Faestermann, T. 143, 152, 153
Fahlander, C. 149
Fahsold, G. 352
Falahat, S. 155
Farnea, E. 148
Farouqi, K. 188
Fehrenbacher, G. 119, 120
Feldmeier, E. 400
Feldmeier, H. 161, 175, 181, 182
Ferger, T. 302
Ferini, G. 178
Fernandez, J. C. 330
Fernengel, D. 328, 329
Ferrer, R. 44, 315
Fertman, A. 116, 329, 331, 333, 328
Fiedler, F. 392, 395
Fils, J. 356
Finelli, P. 170
Fink, D. 368
Fischer, B. 355
Fischer, D. 302
Fischer, E. 98
Fischer, P. 71
Fischer, W. 118
Flierl, D. 225, 229
Flippo, K. 330
Floch, E. 98

Förster, E. 318
Folden III, C. M. 203
Forck, P. 88, 90, 107, 124, 125, 129, 310
Fortov, V. E. 9, 336, 328
Fournier, C. 355, 370, 373, 377, 378
Franchetti, G. 90, 114, 124, 138
Franchi, A. 138
Franchoo, S. 196
Franczak, B. 90, 91, 124, 143, 401, 304, 305
Frankenfeld, U. 282
Franzke, B. 14, 92, 104, 125, 143
Freer, M. 45
Fricke, A. 366
Fricke, B. 326
Friese, V. 56, 62, 225, 227, 229
Friman, B. 245
Fritzsche, S. 300, 320, 321
Fröhlich, C. 187
Fröhlich, G. 129
Froese, M. 43
Fuchs, C. 189, 252
Fuchs, R. 356
Fuess, H. 353
Fukuda, M. 157, 156
Gadea, A. 148
Gaitanos, T. 178, 189
Galatis, A. 105
Galatyuk, T. 62
Gallmeister, K. 255
Galnander, B. 94
Galonska, M. 122, 133, 400
Garabatos, C. 69, 282
Garcia, M. A. 203
Gates, J. M. 203
Gattringer, C. 238
Gazdzicki, M. 225, 229
Geissel, H. 39, 40, 47, 49, 50, 51, 41, 141, 143, 146, 156, 157, 260, 298
George, S. 297
Geppert, C. 33, 35, 293
Gerhard, S. 335
Gerl, J. 30, 31, 36, 37, 146, 149, 141, 148
Gernhäuser, R. 46
Gevaert, F. 160
Giacomini, T. 107, 138
Giesen, F. 71
Gil, D. 281
Gillitzer, A. 7
Gläss, J. 70
Glässel, P. 282
Glasmacher, U. A. 343
Gleim, M. 47
Gniady, A. 149
Gnutov, A. 116
Göckeler, M. 238, 239
Görgen, A. 146
Görres, J. 155
Götte, S. 295, 356
Goetze, K. 380
Götzen, K. 77
Gojska, A. 300, 333
Golubev, A. 116, 329, 332, 328
Golubev, A. A. 331
Gorbunov, S. 60, 61, 63, 64, 65
Gorenstein, M. 229
Gorska, M. 30, 146, 149, 152, 148, 153, 519
Gostishev, V. 125
Graf, H. 107
Grawe, H. 145, 146, 149, 150, 152, 153
Grebosz, J. 146
Grebozs, J. 148
Gregorich, K. E. 203, 265
Greiner, W. 199, 254
Grieser, M. 6
Grigorenko, L. 150
Grigorian, H. 189
Grisenti, R. E. 16
Grishkin, Y. L. 24
Groening, L. 87, 88, 89, 121
Grötzinger, S. 390
Groezinger, S. 386
Groezinger, S. O. 391
Große, K. 405, 407, 409, 413, 438, 447, 448, 449, 451, 479, 484, 501, 509, 510, 514, 521, 526
Grosse, E. 266
Gruber, A. 74
Gruber, G. 310
Gryaznov, V. K. 328
Grzonka, D. 7
Gudowska-Nowak, E. 363, 376
Guénaut, C. 297
Gumberidze, A. 15, 299, 300, 301, 304, 305, 306, 308, 318
Gutbrod, H. H. 1
Gutermuth, F. 50, 119, 120
Gwinner, G. 293
Haas, F. 342
Haberer, T. 391, 401
Habs, D. 14, 298, 316
Hägler, P. 239
Hänsch, T. W. 293
Haettner, E. 385
Hagemann, M. 356
Hagen, C. 238
Hager, U. 297
Hagmann, S. 18, 15, 300, 301, 303,

304, 305, 306, 307, 308, 384
Hahn, T. 356
Hamar, G. 69
Hammond, G. 146
Harman, Z. 323
Hartig, M. 234, 284
Hartmann, A. 266
Hartmann, W. 207, 265
Hasenfratz, P. 238
Hasenkamp, W. 343
Hasse, R. W. 96, 115, 94
Hausmann, M. 141
Haxton, W. C. 186
Hedlund, E. 109
Hegelich, B. M. 330
Heger, A. 186
Hehner, J. 282, 283
Heil, M. 137
Heilmann, J. 526
Heini, S. 59
Heinz, A. 261, 387, 402, 403
Heinz, S. 312, 316, 310
Heiß, M. 355
Hellström, M. 146
Hemmert, T. R. 235, 239
Hempel, M. 184
Hensel, M. 448
Henske, M. 261
Henzl, V. 158, 214
Henzlova, D. 213
Herfurth, F. 42, 298, 312, 297, 310
Hergert, H. 162
Herghelegiu, A. 67
Herlert, A. 44, 297
Herrmann, N. 208, 223, 277
Herskind, C. 371
Heß, S. 304, 305
Heßberger, F. P. 191, 193, 194, 196, 198
Heßling, T. 334
Hess, G. 98
Hess, S. 21, 300, 301
Hessberger, F. P. 197, 298
Hessel, P. 370, 373, 376, 379
Heuck, H.-M. 356
Heuser, J. M. 58
Heymach, F. 122, 133, 400
Hierl, D. 238
Hildebrandt, C. 356
Hildenbrand, K. D. 269, 277
Himmi, A. 59
Hinke, H. 284
Hinterberger, F. 96, 94
Hix, W. R. 187
Hjorth-Jensen, M. 149
Ho, A. 189
Höche, S. 324
Höhne, C. 63, 225, 229
Hörr, M. 400
Hoffman, D. C. 203
Hoffmann, D. H. H. 9, 11, 51, 328, 329, 331, 332, 333, 335, 336, 339, 356
Hoffmann, J. 275
Hoffmann, T. 107, 129
Hoffmeister, G. 335
Hofman-Hüther, H. 374
Hofmann, B. 313, 310
Hofmann, I. 90, 114, 115
Hofmann, J. 236
Hofmann, S. 191, 193, 194, 196, 198, 298
Hofsäss, H. 345
Hollinger, R. 88, 122, 133, 400
Holzwarth, R. 293
Honma, M. 146
Hoppe, M. 67
Horsley, R. 239
Hosoi, M. 156, 157
Hoszowska, J. 318
Hubenthal, F. 364
Huber, G. 293
Hübel, H. 146
Hübner, A. 207, 265
Hüller, W. 47, 41
Hülsmann, P. 90, 101
Hug, A. 328, 329
Hummrich, H. 205
Hutter, G. 101, 400
Huyse, M. 41, 150, 196
Iannucci, R. 122
Ilieva, S. 299
Indelicato, P. 300, 318
Ishikawa, N. 343
Ivanyuk, F. A. 176
Iwase, H. 47, 50, 385, 386
Jaaskelainen, K. 59
Jacobi, J. 296
Jacoby, J. 13, 329
Jäger, E. 197, 204, 205, 263, 264, 265
Jäkel, R. 75
Jagodzinski, P. 19
Jakob, B. 139, 355, 368
Jakubassa, D. 304, 305
Janas, Z. 150, 152, 153
Janik, R. 156, 157
Janulewicz, K. A. 359
Javorkova, D. 359, 356
Jentschura, U. D. 321
Jesch, C. 260
Jessen, K. 38
Johnson, T. 94
Jolie, J. 36, 37, 38

Jonckheere, R. 344
Jones, G. 141
Joshi, N. 137
Jourdan, J. 24
Jungclaus, A. 31, 152, 153
Junghans, A. R. 266
Juodagalvis, A. 185
Kadi, Y. 339
Källberg, A. 5
Kaiser, M. 310
Kaiser, N. 170
Kajetanowicz, M. 22, 281
Kalantar-Nayestanaki, N. 28, 24
Kaldor, U. 200
Kalisky, M. 64
Kaminski, R. 310
Kant, M. 183
Kantsyrev, A. 116, 332
Karagiannis, C. 47, 41, 156, 157
Karger, C. P. 383
Karim, S. 350, 351, 352
Karny, M. 152, 153
Karpuk, S. 14, 293
Kaspar, K. 100
Katayama, T. 104
Kaufmann, W. 105, 129
Kaugerts, J. 98
Kauschke, M. 98
Kavatsyuk, M. 79, 153, 146, 152
Kavatsyuk, O. 152, 146, 153
Kavcic, M. 21
Kaza, E. 143
Kazamias, S. 359
Kebschull, U. 288
Kelic, A. 24, 47, 51, 158, 160, 173
Kellerbauer, A. 297
Kendziora, K. 74
Kessenbrock, M. 234, 284
Kessler, R. 154
Kester, O. 311, 312, 313, 314, 310
Ketelaer, J. 44, 315
Khalfaoui, N. 342
Kienle, P. 143, 222
Kikuchi, T. 104
Kilbourne, C. 299
Kilian, K. 7
Kim, V. 51
Kim, Y. J. 208, 223, 224, 277
Kimura, K. 156, 157
Kindler, B. 191, 194, 198, 207, 196, 265
Kingsberry, P. 7
Kirchner, R. 150, 152, 153, 295
Kirk, M. 117, 124, 138
Kis, M. 269, 277
Kisel, I. 60, 61, 63, 64, 65
Kiselev, O. A. 28, 45
Kiseleva, A. 65
Kishada, A. 141
Klähn, T. 189
Kleffner, C. 400
Klein, B. 259
Kleinod, M. 314
Klepper, O. 39, 141, 143, 152
Kliemant, M. 225, 229, 284
Kliemnant, M. 234
Klingbeil, H. 90, 124, 132
Klisnick, A. 359
Klüpfel, P. 169
Kluge, H. 311
Kluge, H. J. 299
Kluge, H.-J. 33, 35, 312, 313, 317, 293, 295, 296, 297, 298, 310, 356
Kmiecik, M. 146, 148
Knapp, A. 119
Knapp, T. 261
Kniege, S. 225, 229, 232, 234
Knobloch, F. 356
Knöbel, R. 39, 41, 141
Knoop, K. 368
Koch, S. 97
Koczon, P. 273, 277
Koenig, H. G. 100
Koenig, W. 46
König, W. 280
Kohli, P. 349
Kojouharov, I. 146, 191, 194, 196
Kolb, T. 294, 352
Kolhinen, V. S. 316
Kollmus, H. 109, 110
Kolomeitsev, E. E. 189
Korcyl, K. 281
Kornilov, V. 115
Korostiy, S. 331, 333, 334
Korpa, C. L. 249
Korten, W. 36, 37, 146
Kosev, K. 266
Koshurnikov, E. K. 80
Koszudowski, S. 312, 310
Kovalenko, A. D. 90
Kowina, P. 105
Kozhuharov, C. 15, 21, 39, 141, 296, 301, 303, 304, 305, 307, 308, 384, 300, 306, 310
Kozhurarov, C. 143
Kozlova, E. 120
Krämer, A. 109, 90, 310
Krämer, M. 389
Kraft, G. 390, 391
Kraft-Bermuth, S. 299
Kramer, F. 284
Kratz, J. V. 45, 205, 207, 265, 197

Kratz, K.-L. 154, 188
Kratz, L. 155
Kraus, I. 212
Krauser, H. 345
Kreim, S. 8
Kresan, D. 62, 64
Kreutz, M. 356
Krings, T. 20, 21, 27, 318
Krücken, R. 46, 222, 329
Kudryavtsev, Y. 41
Kühl, T. 14, 359, 293, 295, 356
Kühne, M. 366
Kühnel, K.-U. 6
Kugler, M. 273
Kulish, M. 332, 328, 329
Kumm, M. 132
Kunin, A. 116
Kunz, P. 294
Kunzer, S. 356
Kuo, T. T. S. 171
Kurcewicz, J. 39, 141
Kurdal, J. 112
Kurz, N. 275
Kuster, M. 335
Kuusiniemi, P. 191, 194, 197, 198
La Commara, M. 150, 152, 153
La Rana, G. 148
Labiche, M. 45
Labzowsky, L. 325
Lalazissis, G. A. 168
Lang, C. B. 238
Lang, K. 105
Lang, M. 343
Lang, R. 122
Langanke, K. 164, 175, 181, 183, 185, 186, 187
Larionov, A. B. 255
Lassen, J. 295
Latysheva, L. 116
Lauth, W. 294
Lebedev, S. 63
Lee, R. 376
Legrain, R. 159
Lehrach, A. 94, 96
Leible, K. D. 122, 133
Leibrock, H. 98, 47
Leifels, Y. 223, 273, 277
Leino, M. 191, 194
Lemmon, R. 45
Lenisa, P. 81
Lenzi, S. 148
Leoni, S. 148
Leppänen, A.-P. 196
Leray, S. 159
Levand, T. 41
Levi, C. D. P. 295
Lewandowski, B. 73
L'Hoir, A. 308
Licher, J. 390
Liebe, D. 205, 207, 265, 197
Liebendörfer, M. 187
Liebermann, H. 136
Liesen, D. 307, 318, 325, 300, 304, 305, 306, 308
Lindenstruth, V. 71, 286, 288, 289
Linev, S. 270, 271, 274
Lineva, N. 303, 384
Lippmann, C. 290
Litvinov, S. 141
Litvinov, S. A. 40, 39
Litvinov, Y. 41, 47, 141, 143
Litvinov, Y. A. 39, 40
Liu, Z. 141
Lo Bianco, G. 148
Löbrich, M. 366
Lofnes, T. 94
Lommel, B. 198, 207, 191, 194, 196, 265
Lomononsov, I. V. 51
Lomonosov, I. V. 9, 336, 328
Lopez, X. 208, 224
Lopez Cela, J. J. 11
Lorentz, B. 94
Lotz, R. 356
Lovrincic, R. 352
Lozeva, R. 146
Luckjashin, V. 116
Lühning, J. 74, 77, 80
Lukasik, J. 216
Lukic, S. 160
Lunardi, S. 148
Lungwitz, B. 225, 229
Lunney, D. 297
Lutz, M. F. M. 236, 237, 249
Lyakin, D. 107, 129
Lysenkov, D. 353
Ma, X. 318
Maalouf, M. 378
Maas, A. 240
Macri, M. 74
Männer, R. 70
Maero, G. 312, 310
Magureanu, C. 67
Mahjour-Shafiei, M. 28
Mahner, E. 109
Maier, H.-J. 265
Maier, L. 143
Maier, M. 41, 87, 400
Maier, P. 371
Maier, R. 94, 96
Maj, A. 146, 148
Malzacher, P. 291
Manafov, A. 291
Mandal, S. 141, 146, 153, 156, 157

Manikonda, S. 47
Manil, B. 318
Mann, R. 198, 309, 191, 194, 196
Manteufel, R. 291
Marie-Jeanne, M. 297
Marinelli, M. 74
Marquardt, M. 277
Martemiyanow, A. 269
Martin, A. 298
Martin, C. R. 349
Martin, S. 94
Martinez-Pinedo, G. 185, 186, 187
Maruhn, J. A. 13, 54, 169, 174, 360
Marx, G. 298
Mason, P. 148
Matos, M. 143
Matrasulov, D. U. 17
Matveev, V. I. 17
Maurer, F. 353
Mazzocchi, C. 152, 150, 153
Mazzocco, M. 39
McCammon, D. 299
Meczynski, M. 148
Medvedev, N. 343
Meier, J. P. 299
Melnikova, L 373
Melon, B. 38
Menzel, J. 328, 329
Merschmeyer, M. 208, 224
Merz, T. 356
Metag, V. 280
Meusel, O. 88, 137
Miernik, K. 152
Mikhailov, A. I. 322
Mikhailov, I. A. 322
Milanovic, D. 371
Miller, D. 74
Miller, M. C. 189
Million, B. 148, 146
Min, M. 344
Minaev, S. 89, 88
Mintsev, V. 332, 328
Mishustin, I. N. 180, 254
Miski-Oglu, N. 35
Miskowiec, D. 228
Mitrovski, M. 225, 229
Möhl, D. 104
Möller, O. 38
Möllers, B. 327
Mohos, I. 20, 318
Mohr, J. 101
Moisa, D. 67
Mokler, P. H. 307, 326, 296, 306, 308
Mol, A. 55
Montes, F. 141
Moog, J. 390
Moreno, O. 29
Moritz, G. 98, 47, 90
Moritz, P. 132, 401
Morrissey, D. 41
Mosel, U. 255
Moshammer, R. 302, 303, 304, 305
Moustafina, G. 119
Moya de Guerra, E. 29
Muehle, C. 98
Mühle, C. 47, 400
Müller, A. 296, 381, 306
Müller, B. 251
Müller, G. 353
Müller, I. 136
Müller, W. F. J. 56, 58, 274
Mueller-Klieser, W. 380
Müntz, C. 58, 59
Münzenberg, G. 49, 39, 41, 47, 141, 143, 155, 156, 157, 197, 191, 196
Mukha, I. 41, 150, 152, 153
Mukherjee, M. 298
Mulser, P. 361
Muralithar, S. 146, 153
Musa, L. 288
Musch, B. U. 235
Mustafin, E. 116
Mustapha, B. 159
Musumarra, A. 141
Muthers, D. 71
Mutin, T. 331
N. Kurz, N. 146
Nadtochy, P. N. 177
Najjari, B. 302
Nakajima, S. 156, 157
Nankov, N. 266
Napoli, D. 148
Narici, L. 382
Nasonova, E. 372, 373, 376
Nayak, D. 197
Nazarewicz, W. 164
Nedorezov, V. 24
Neff, T. 161, 175, 181
Nefiodov, A. V. 322
Neidherr, D. 44, 312, 315
Nelson, S. L. 203
Nesmiyan, I. 103, 104
Neubrech, F. 352
Neumann, J. 386
Neumann, R. 3, 341, 343, 346, 347, 348, 350, 351, 352, 354
Neumayer, P. 359, 356
Neumayr, J. B. 316, 298
Neußer, A. 146
Ni, P. 328, 329
Nickel, D. 243
Nickles, P. V. 359
Niedermayer, F. 238

Niewisch, L. 205
Nikolaev, D. 328
Niksic, T. 166
Nilsson, T. 45
Nishio, K. 198, 191, 194
Nitsche, H. 203
Nix, A.-K. 345
Nixdorff, K. 372
Nociforo, C. 39, 47, 141
Nörenberg, W. 176
Nörtershäuser, W. 32, 33, 35, 293, 295
Nofal, M. 303, 304, 305, 300, 307
Nolden, F. 14, 15, 92, 102, 103, 104, 39, 125, 141, 143, 296
Norman, G. 94
Novackova, Z. 204
Novikov, Y. 143
Novikov, Y. N. 197
Novotny, C. 293
Novotny, R. 280
Nowacki, F. 146, 149
Nowak, H. 78
Nyman, G. 45
Ochs, K. 122, 133
Oelert, W. 7
Oeschler, H. 212
Oezen, C. 165
Ohnishi, T. 156, 157
Ohtsubo, T. 143, 156, 157
Omet, C. 117, 118, 90, 124
Omtvedt, J. P. 202
Ondreka, D. 401
Onkels, E. 356
Oreshkina, N. S. 319
Orth, H. 74, 77, 80
Osborne, C. 43
Otsuka, T. 146
Ott, W. 275
Otto, M. 225, 229
Oyama, K. 290
Ozawa, A. 156, 157
Paar, N. 162
Page, R. D. 196
Pajek, M. 19, 306
Pakarinen, J. 196
Palffy, A. 323
Palka, M. 281
Pang, G. K. 203
Panova, Y. 116
Pantea, M. 479
Papakonstantinou, P. 162
Papaléo, R. 343
Parfenova, A. 138
Parkhomenko, A. 193
Parodi, K. 392
Passler, G. 33
Patyk, Z. 141
Pawelke, J. 395
Pearson, M. 295
Peldzinski, F. 107, 310
Penso, V. 291
Pereira Conca, J. 154
Peric, I. 71
Perlt, H. 239
Pershina, V. 200, 201, 202
Peschke, C. 92, 102
Peschke, P. 383
Peters, A. 105, 107, 113, 90, 124, 125, 129, 398, 400
Peters, K. 77
Petrache, C. 148
Petrick, M. 41, 260
Petris, M. 67
Petrovici, M. 67
Peuckert, H. 374
Pfeiffer, B. 188
Pietraszko, J. 46
Pignanelli, M. 148
Pikna, M. 282
Pikulskiy, M. 55
Pikuz, S. 331
Pikuz, T. 334
Piriz, A. R. 9, 11, 336, 339
Pirner, H.-J. 259
Plaß, W. 39, 41, 141
Plaß, W. R. 260, 298
Plass, W. 49, 47, 143
Pleiter, D. 239
Plettner, C. 152, 153
Plochocki, A. 152, 153
Ploskon, M. 232, 233, 234
Plunien, G. 322, 324, 325
Pochodzalla, J. 76, 79
Podlech, H. 89, 136
Podolyak, Z. 30, 36, 37, 141, 146
Poizat, J.-C. 308
Polakova, D. 202
Polishchuk, B. 63
Pollacco, E. C. 27
Pollet, D. 377, 381
Pomorski, M. 269, 387
Popeko, A. G. 191, 194
Popov, P. 289
Popp, U. 125, 301, 299
Portillo, M. 41, 143
Prasuhn, A. 96
Prasuhn, D. 94
Pravikoff, M. 159
Preuss, C. 291
Prime, E. 295
Prochazka, A. 156, 157
Procura, M. 235
Propri, R. 141

Protic, D. 20, 21, 27, 318
Prozorov, A. 325
Psonka, K. 363
Pucci, A. 352
Pyka, N. 90
Qin, Z. 197
Quick, W. 74, 77
Quint, W. 4, 8, 312, 317, 310
Radon, T. 50, 119, 120
Radu, A. 67, 283
Rahaman, S. 298
Rakhimov, K. Y. 17
Rakow, P. E. L. 239
Ramakers, H. 90, 124
Rami, F. 59
Ramm, U. 390
Ramírez, P. 348
Rathmann, F. 81
Ratschbacher, L. 344
Ratschow, S. 91
Ratti, C. 241
Ratzinger, U. 89, 88, 136, 137, 311, 310
Rauscher, T. 188
Rauth, C. 298
Ray, C. 308
Rębisz, M. 387
Rebisz, M. 388
Redelbach, A. 138, 124
Redlich, K. 210, 212, 245
Reeg, H. 107
Reemts, D. 356
Reich, H. 90, 124
Reich-Sprenger, H. 112, 310
Reinhard, P.-G. 139, 169, 174
Reinhard, S. 14
Reinhardt, S. 293
Reistad, D. 94
Reiter, A. 398, 400
Reiter, P. 145, 146, 148
Rejmund, F. 159
Renfordt, R. 234, 225, 229, 282
Ressler, J. J. 196
Rettig, F. 289
Reuschl, R. 15, 19, 21, 301, 304, 305, 296, 299, 300, 306, 318
Ricciardi, M. V. 158, 159, 160
Richter, S. 87, 121
Rietzel, E. 391
Rigby, S. 141
Ring, P. 166, 168
Risch, H. 285, 402, 403
Rischke, D. H. 244
Ritman, J. 7, 75
Ritter, S. 370, 372, 373, 376
Ritzert, M. 71
Rodemann, H. P. 369
Rodriguez, D. 298
Rodriguez Prieto, G. 334
Rodriguez-Lafrasse, C. 378
Roeckl, E. 150, 152, 153
Roed, K. 288
Röder, D. 258
Röhrich, D. 288
Röpke, G. 189
Rogowska, M. 269, 269
Rohe, D. 24
Romoli, M. 152, 153
Ros, D. 359
Rosmej, F. B. 13
Rosmej, O. 331, 333, 359
Rosmej, O. N. 334
Rotaru, C. C. 342
Roth, M. 330, 360, 356
Roth, R. 161, 162
Rozet, J.-P. 308
Rubio, B. 30, 31
Rudolph, J. H. 368
Rüster, S. B. 184, 244
Ruppert, J. 258
Rusanov, I. 72, 287, 290
Ryjkov, V. 295
Rykaczewski, K. 152
Rzadkiewicz, J. 301, 300
Rzadkjewicz, J. 15
Rzhadkiewicz, J. 333
Saathoff, G. 14, 293
Sagert, I. 250
Saito, N. 79, 141, 146
Saito, T. 141, 148
Saito, T. R. 79, 146, 149
Salabura, P. 217, 281
Salem, S. 307
Samek, S. 22
Sánchez, R. 35, 295
Sanchez Lorente, A. 79
Sanchez Majos, S. 76
Sanchez-Brandelik, R. 383
Sandner, W. 359
Sandoval, A. 225, 229
Santini, E. 252
Saro, S. 198, 191, 194, 196
Sarpe-Tudoran, C. 201
Sarriguren, P. 29
Sasaki, C. 245
Satarov, L. M. 254
Sauer, A. 311, 310
Savard, G. 41
Schabinger, B. 317
Schädel, M. 152, 197, 204, 262, 263, 264, 153, 205, 265
Schäfer, A. 238, 239, 251
Schaefer, B.-J. 171, 247

Schaffner-Bielich, J. 184, 248, 250
Schardt, D. 3, 116, 385, 386
Schatz, H. 141, 154
Schaumann, G. 334
Schausten, B. 197, 205, 265
Scheeler, U. 127, 124, 401
Scheid, W. 323
Scheidenberger, C. 41, 39, 47, 143, 141, 260, 298
Schempp, A. 313, 310, 400
Schempp, A. Tiede 88
Schepers, G. 77
Scherer, S. 256
Schiedt, B. 348
Schierholz, G. 239
Schiller, A. 239
Schilling, K. D. 266
Schimpf, E. 197, 204, 263, 264, 205, 265
Schippers, S. 296
Schlegel, T. 360, 361
Schlitt, B. 396, 400
Schmidt, A. 389
Schmidt, C. J. 283, 285
Schmidt, E. W. 296, 306
Schmidt, H. 356
Schmidt, H. R. 282
Schmidt, K. 152
Schmidt, K.-H. 24, 55, 158, 160, 173, 159
Schmidt, R. 339
Schmidt-Kaler, F. 35
Schmitt, L. 73, 80
Schnase, A. 94
Schnizer, P. 98
Schölles, J. 105, 129
Schött, H. G. 198
Schött, H. J. 191, 194
Schollmeier, M. 330
Scholz, M. 3, 365, 367, 380, 381, 383
Scholz, R. 101
Schramm, S. 242, 253
Schramm, U. 14
Schreiber, G. 132
Schrieder, G. 24, 45
Schroeder, C. 98
Schütt, P. 113, 124, 401
Schüttauf, A. 269, 277
Schulz, M. 302
Schuster, T. 225, 229
Schwab, S. 282, 283
Schwalm, D. 293
Schwartz, K. 341
Schwarz, C. 74, 77
Schwarz, K. 291
Schwarz, S. 33, 297
Schwegler, A. K. 371
Schweikhard, L. 297, 298
Schweinfurth, Y. 365
Schwen, D. 345
Schwengner, R. 152
Schwertel, S. 46
Schwickert, M. 398, 400
Schwinn, A. 125, 273
Scielzo, N. 41
Sefzick, T. 7
Sellesk, M. 392
Semchenkov, A. 262, 263, 264, 265
Senger, P. 56, 58, 62
Senichev, Y. 94
Senicheva, E. 94
Serna Moreno, M. C. 11
Severin, D. 347
Sewtz, M. 294, 316
Sfienti, C. 79, 215
Shabaev, V. M. 319, 324
Shakirin, G. 393, 394, 395
Sharafutdinov, A. 294
Sharkov, B. 332, 329
Sharkov, B. Y. 328
Shilkin, N. 328
Shindo, M. 141, 156, 157
Shovkovy, I. A. 244
Shrivastava, A. 45
Shutov, A. 9, 51, 336, 339, 328
Siegmann, B. 309
Sierpowski, D. 22, 318, 306
Sikler, G. 43
Simion, V. 67
Simionovici, A. 318
Simon, H. 24, 55, 45, 47
Simon, R. 479
Simon, R. S. 280
Simonsson, A. 5
Singh, A. K. 146
Siska, M. 282
Sitar, B. 156, 157, 282
Siwy, Z. 349
Skachkov, V. 107
Skott, P. 281
Smolyakov, A. 118
Sobiczewski, A. 193
Sobiella, M. 266
Sobolevskyi, N. 116
Solbrig, S. 238
Soltveit, H. K. 72
Sommer, S. 373
Sommer, W. 234, 284
Sorokin, M. 341
Soyeur, M. 237
Spädtke, P. 88, 122, 133, 400
Spielberger, B. 390
Spielmann, C. 356

Spiller, P. 15, 90, 91, 117, 118, 124, 328
Spillmann, U. 15, 19, 20, 21, 22, 301, 304, 305, 296, 300, 306, 318
Spruck, B. 280
Stachel, J. 72, 209, 210, 287, 282
Stachura, Z. 296, 307, 318
Stadlmann, J. 90, 117, 143
Stahl, S. 8, 312, 317
Stanoiu, M. 45
Starosta, K. 38
Stech, E. J. 155
Steck, M. 14, 15, 39, 92, 104, 94, 125, 141, 143, 293, 296, 304, 305
Steffen, A. 283
Steiner, J. 207, 265
Steinle, C. 70
Stelzer, H. 282, 283
Stenner, R. 356
Stephan, C. 159
Stevenson, P. 174
Stock, R. 225, 229
Stockhorst, H. 94
Stockmanns, T. 75
Stockmeier, M. R. 272
Stöcker, H. 248, 257
Stöhlker, T. 15, 17, 19, 20, 21, 22, 55, 300, 301, 304, 305, 306, 318, 319, 320, 321, 293, 296, 299, 308, 310
Stoquert, J. P. 342
Stork, A. 525
Strabel, C. 225, 229
Streicher, B. 191, 194, 196, 198
Strmen, P. 156, 157
Ströbele, H. 225, 229
Stroth, J. 58, 62, 59
Strüber, S. 246
Stüben, H. 239
Styczen, J. 148
Suda, T. 156, 157
Sudowe, R. 203, 265
Sümmerer, K. 51, 54, 45, 47, 156, 157
Sugawara, K. 156, 157
Suhm, J. 400
Sulignano, B. 194, 191, 196, 197, 198
Sun, B. 39, 141
Surzhykov, A. 320, 321
Surzykov, A. 300
Suzuki, K. 222
Suzuki, T. 156, 157
Svedentsov, M. 47
Szarka, I. 156, 157
Szerypo, J. 265, 316
Szlachetko, J. 21, 306
Tabor, S. L. 150
Tachenov, S. 306
Tahir, N. A. 9, 11, 51, 47, 328, 336, 339
Taieb, J. 159
Tain, J. L. 31
Takahashi, K. 143
Takechi, M. 156, 157
Takisawa, A. 156, 157
Tanaka, K. 156, 157
Tang, H. 113
Tashenov, S. 21, 318
Tassan-Got, L. 159
Taucher-Scholz, G. 355, 363, 365, 368, 377, 378, 380, 381
Tauschwitz, A. 13, 13, 54, 360, 360, 356
Ternovoi, V. Y. 328
Testa, E. 308
Thaler, M. A. 241
Thiel, R. 356
Thielemann, F.-K. 187, 188
Thiemer, U. 273, 356
Thirolf, P. G. 316, 298
Thörle, P. 207, 265, 197
Thomason, M. 15
Thomson, J. 196
Tiede, R. 89
Tiedemann, D. 35
Tielert, R. 71
Tinschert, K. 122, 135
Tölle, R. 94
Toepffer, C. 139, 327
Toimil-Molares, M. E. 350, 351, 352, 353
Tolos, L. 248
Tontisirin, S. 71
Topsch, J. 365, 381
Toulemonde, M. 342, 308
Träger, F. 364
Trajkovic-Bodennec, S. 378
Trassinelli, M. 19, 318
Trautmann, C. 3, 341, 342, 343, 344, 345, 347, 349, 353, 354
Trautmann, N. 294
Trautmann, W. 215, 216
Traxler, M. 281
Trebacz, R. 281
Tröger, G. 288
Trofin, L. 349
Trosenko, S. 21
Trotsenko, S. 15, 300, 301, 304, 305, 299, 306, 318
Trümper, J. 189
Tsiledakis, G. 231
Türler, A. 204, 262, 263, 264, 265

Tupitsyn, I. I. 319
Turinge, A. 24
Turtikov, V. 329, 331, 333, 328
Typel, S. 167, 189
Udem, T. 293
Udias Moinelo, J. 24
Udrea, S. 328, 329
Ugorowski, P. 141
Uhlig, F. 69
Ulllrich, J. 43
Ullrich, J. 6, 302, 304, 305
Ulmer, S. 8
Ulrich, A. 329
Ursescu, D. 359, 356
Usenko, E. 387, 388
Uusitalo, J. 191, 194
Vaagen, J. S. 172
Valin, I. 59
van Dahlen, E. N. E. 189
Van Duppen, P. 41, 150, 196
Varentsov, D. 328, 333, 329
Vassiliev, I. 61, 65
Vatulin, V. 116
Verdu, J. 8, 317
Verma, P. 326, 306, 308
Vinzenz, W. 88, 101, 310, 400
Virsik-Köpp, P. 374
Visotski, S. 280
Vogel, M. 317, 310
Vogel, P. 183
Vogel, S. 179
Voitkiv, A. 302
Volant, C. 159
Volkov, A. 341
Vollmer, S. 400
Volokov, V. 55
Volotka, A. 325
Volotka, A. V. 324
von Neubeck, C. 389
Vorobjev, G. 141, 298, 310
Voskresensky, D. N. 189
Voss, B. 261, 387, 388, 402, 403
Voss, K.-O. 341, 343, 346
Vovopianov, A. S. 80
Vranesic, H. 273
Vranic, D. 282
Vretenar, D. 166, 170
Wagner, A. 266
Wagner, G. A. 343
Wagner, M. 171
Wahl, H. 328, 332, 329
Walker, P. M. 141
Walter, G. 98, 347
Walz, J. 8
Wambach, J. 171, 243, 247
Wang, X. 18, 303, 304, 305
Wang, Z. 41, 47, 260
Warczak, A. 22, 318, 306, 307
Warkentin, N. 239
Weber, C. 44, 315, 297, 298, 310, 312
Weber, D. 335
Weber, F. 189
Weber, G. 15, 301
Weckenmann, B. 98
Wegerle, D. 234
Wehrhan, O. 318
Weick, H. 28, 39, 40, 49, 50, 55, 41, 47, 141, 143, 146
Weik, H. 51
Weiland, T. 97, 134
Weinert, J. 277
Weinrich, U. 396
Weise, W. 170, 235, 241
Welker, H. 90
Welsch, C. P. 6
Wendt, K. 33
Wenz, F. 371
Werner, U. 309
Werth, G. 317, 310
Werth, V. 244
Wessels, J. P. 67
Wettig, T. 238
Weyrather, W. K. 379, 389
Weyrich, K. 116, 332
Wheaton, S. 212
Wheldon, C. 146
Widmann, E. 4
Wiechula, J. 282
Wiehl, N. 205
Wieland, O. 148, 146
Wierczinski, B. 204
Wies, K. 33
Wiescher, M. C. F. 155
Wieser, J. 329
Wilck, A. 307
Wilk, A. 22, 67
Williams, S. 141
Wilms, A. 78
Wilms, D. 127
Winckler, N. 141
Windelband, B. 282
Winkler, M. 47, 49, 50, 51, 39, 41, 141, 143, 146
Winkler, S. 46
Winter, M. 59, 370, 373
Winter, P. 7
Witte, K. 356
Wittrock, U. 356
Wörtche, H. 24
Wojtaszeck, A. 295
Wolf, A. 6, 296
Wollersheim, H. 148

Wollersheim, H. J. 144, 146
Wollersheim, H.-J. 149, 141
Wollnik, H. 47
Wolter, H. H. 178, 189
Woods, P. J. 30
Woosley, S. E. 186
Wouchuk, G. 336
Wu, X. L. 197
Xiang, Y. 98
Yakushev, A. 204, 263, 264, 265
Yamaguchi, T. 143, 156, 157
Yamaki, T. 343
Yan, Z.-C. 295
Yang, J. 92
Yaramishev, S. 87, 121
Yaramyshev, S. 88
Yavor, M. 49, 47
Yazidjian, C. 44, 297
Yeremin, A. V. 191, 194
Yerokhin, V. A. 324
Yordanov, O. 160
Zabransky, B. J. 41
Zagrebaev, V. 199
Zanotti, J. M. 239
Zaplatin, E. 94
Zeeb, G. 242, 253
Zell, K. O. 38
Zhang, X. 277
278
Zhilin, A. 269
Ziegler, E. 318
Zielbauer, B. 359, 356
Zimmermann, C. 35, 295
Zimmermann, H. 314, 310
Zimmermann, M. 293
Zinner, N. T. 187
Zioutas, K. 335
Zipfel, B. 132
Zmeskal, J. 74
Zou, Y. 18
Zschiesche, D. 242, 253
Zucchiatti, A. 148
Zwicknagel, G. 140, 327
Zylicz, J. 152, 153